REPORT DOCUMENTATION PAGE

Form Approved
OMB No. 0704-0188

1. REPORT DATE *(DD-MM-YYYY)*	2. REPORT TYPE	3. DATES COVERED *(From - To)*
21/05/2024	FINAL	01/11/2017 - 31/01/2024

4. TITLE AND SUBTITLE

TURBULENCE TRANSPORT IN EXTREME NON-EQUILIBRIUM ENVIRONMENTS

5a. CONTRACT NUMBER

5b. GRANT NUMBER

N00014-18-1-3020

5c. PROGRAM ELEMENT NUMBER

6. AUTHOR(S)

RODNEY BOWERSOX, SIMON NORTH, ZACH BUEN, CASEY BROSLAWSKI, TYLER DEAN, ANDREW LIEDY, BRIANNE MCMANAMAN, BRYAN MOREALLE, IAN NEEL, FARHAN SIDDIQUI, AND MADELINE SMOTZER, TREVOR BLAIR, CALEB BRYAN, AND MCKENNA ROBERTS

5d. PROJECT NUMBER

5e. TASK NUMBER

5f. WORK UNIT NUMBER

7. PERFORMING ORGANIZATION NAME(S) AND ADDRESS(ES)

TEXAS A&M ENGINEERING EXPERIMENT STATION (TEES)
1111 RELLIS PARKWAY, SUITE 5226
BRYAN, TX 77807

8. PERFORMING ORGANIZATION REPORT NUMBER

9. SPONSORING/MONITORING AGENCY NAME(S) AND ADDRESS(ES)

DOD-NAVYOFFICE OF NAVAL RESEARCH
875 N. RANDOLPH STREET
SUITE 1425
ARLINGTON, VA 22203-1995

10. SPONSOR/MONITOR'S ACRONYM(S)

ONR

11. SPONSOR/MONITOR'S REPORT NUMBER(S)

12. DISTRIBUTION/AVAILABILITY STATEMENT

DISTRIBUTION STATEMENT A

13. SUPPLEMENTARY NOTES

NONE

14. ABSTRACT

A theoretical and experimental research project was performed to provide improved understanding and simulation of extreme temperature multi-physics gaseous turbulent flows, which have important science and engineering applications. The testbeds were (a) wall bounded turbulent flow at Mach 6, with DC glow discharge plasma activated thermal nonequilibrium and (b) high enthalpy (1.8 – 7.2 MJ/kg) hypervelocity Mach stem flows, with shock turbulence interactions and triple point initiated free shear layers. The project deliverables include: (i) database characterizing turbulence transport in the Mach 6 wall boundary layer, which includes the first known direct measurement of vibrational temperature surveys of NO(v=1) across a hypersonic boundary layer (laminar and turbulent) which allows for the advancement and validation of new theoretical treatments; (2) new database characterizing the role of thermochemistry on the basic structure turbulence generated by a Mach stem (shock-shock interaction) flow at extreme hypervelocity temperatures, which includes the first known first known laser based optical measurements velocity and temperature fluctuation amplification across a normal shock wave, and (3) development of a new national resource scale ground testing facility, which, at the time of this writing, was supporting additional research for the Army and Navy.

15. SUBJECT TERMS

TURBULENCE, HYPERSONIC, BOUNDARY LAYER FLOW, HIGH-TEMPERATURE, THERMOCHEMICAL NONEQUILIBRIUM, MACH STEM, SHOCK TURBULENCE INTERACTION, TURBULENCE MODEL, LASER/OPTICAL DIAGNSOTICS

16. SECURITY CLASSIFICATION OF:			17. LIMITATION OF ABSTRACT	18. NUMBER OF PAGES	19a. NAME OF RESPONSIBLE PERSON
a. REPORT	b. ABSTRACT	c. THIS PAGE			RODNEY DALE WELCH BOWERSOX
U	U	U	UU	486	19b. TELEPHONE NUMBER *(Include area code)* (979) 458-6811

Reset

FINAL REPORT FOR VANNEVAR BUSH FACULY FELLOWSHIP

(FOR DRS. BINDU NAIR, JEANLUC CAMBIER)

N00014-18-1-3020

TURBULENCE TRANSPORT IN EXTREME NON-EQUILIBRIUM ENVIRONMENTS

RODNEY D. W. BOWERSOX (PI), SIMON W. NORTH

Student Authors:

TREVOR BLAIR, CASEY BROSLAWSKI, CALEB BRYAN, ZACH BUEN, TYLER DEAN,

ANDREW LIEDY, BRIANNE MCMANAMAN, BRYAN MOREALLE, IAN NEEL,

MCKENNA ROBERTS, FARHAN SIDDIQUI, AND MADELINE SMOTZER

MAY 20, 2024

ABSTRACT

A theoretical and experimental research project was performed to provide improved understanding of extreme temperature multi-physics gaseous turbulent flows, which have important science and engineering applications. The testbeds were (a) wall bounded flows at Mach 6, with DC-glow-discharge activated thermal nonequilibrium and (b) high enthalpy (1.8 – 7.2 MJ/kg) hypervelocity Mach stem flows, with shock turbulence interactions and triple point initiated free shear layers. The wall bounded flow database was acquired to characterize the fundamental transport of turbulence with thermal nonequilibrium. These data include the first known measurements of the vibrational temperature of NO across a hypersonic boundary layer (laminar and turbulent), which, allow for advancement and validation of theoretical treatments for thermal nonequilibrium effects. The Mach stem database was acquired to characterize the role of extreme temperature thermochemistry (up to 7000K) on the basic structure the flow, which included shock turbulence interactions and measurements across the free shear layers. These data were acquired to facilitate validation of theories that account for shock turbulence interaction and/or include extreme temperature thermochemistry (air and nitrogen). The Mach stem data included the first known laser-based optical measurements of velocity and temperature fluctuation amplification across a normal shock wave (M = 4.4), which are useful to validate high fidelity methods.The diagnostics included planar laser induced fluorescence of nitric oxide (MHz and 0.1 Hz), focused laser differential interferometry, optical emission spectroscopy, schlieren photography, femtosecond electronic excitation molecular tagging velocimetry, IR thermography, constant temperature hot-film anemometry, thermocouples, and Kulite pressure sensors. Theoretical treatments were performed to advance mathematical models that include molecular energy exchange processes for turbulence closure. Complementary computational fluid dynamic simulations were also accomplished. Also, this program supported the final commissioning of a national resource scale hypervelocity ground test facility at Texas A&M University, which facilitated the extreme temperature experimentation. This project provided unique opportunities for twelve graduate students to perform research at the intersection of advanced hypervelocity experimentation, theoretical turbulence transport modeling, and thermochemical energy exchange. Interactions with the DoD included transferring a unique test apparatus to the Air Force with a graduate of this program. The PI was also subsequently selected by the Navy to lead a national working group in hypersonic turbulence. The results from this study were disseminated via this report, student theses and dissertations, archival articles, and conference proceedings. The databases and analyses produced in this study will serve the DoD research community for decades.

EXECUTIVE SUMMARY

Improved modeling of hypersonic turbulent shear layers is of national interest. Extreme temperature thermochemical effects remain a theoretical challenge. The objective of this project was to improve basic knowledge of gaseous turbulence when exposed to extreme hypervelocity environments. To that end, a theoretical and experimental research project was performed to provide improved understanding and simulation of extreme temperature multi-physics gaseous turbulent flows, which have important science and engineering applications. The testbeds were (a) wall bounded turbulent flows at Mach 6, with DC-glow-discharge activated thermal nonequilibrium and (b) high enthalpy (1.8 – 7.2 MJ/kg) hypervelocity Mach stem flows, with shock turbulence interactions and triple point initiated free shear layers. Of specific interest are mechanisms that couple turbulence to molecular energy exchange dynamics, mechanical forces (e.g., shock waves), and chemical reactions. The experiments took place in the Texas A&M University (TAMU) National Aerothermochemistry and Hypersonic Flight Laboratory. The following facilities were used: (i) actively controlled expansion (ACE) blow down tunnel (0.23 m x 0.36 m test section), which was operated at Mach 6, (ii) Mach 6 quiet tunnel (M6QT, 0.18 m exit diameter), (iii) a bench top (0.1 m x 0.1 m test section cross section) pulsed hypersonic adjustable contour expansion nozzle for aero-thermochemical test environments (PHACENATE) tunnel, which was operated at Mach 4.4, and (iv) hypervelocity expansion tunnel (HXT) that is capable of M = 3 - 25 at extreme thermal environments (stagnation enthalpies up to 16 MJ/kg for aerothermochemically clean air). The diagnostics included planar laser induced fluorescence of nitric oxide (MHz and 0.1 Hz), focused laser differential interferometry, optical emission spectroscopy, schlieren photography, femtosecond electronic excitation molecular tagging velocimetry, IR thermography, constant temperature hot-film anemometry, thermocouples, and Kulite pressure sensors. Mathematical treatments were performed to advance closure expression that include molecular energy exchange processes with turbulence.

The wall bounded experimental campaign was accomplished on a 2.75 degree half-angle wedge tested at M = 5.7 and Re = 6.0 million per meter in the TAMU ACE tunnel. Trips were used to force transition to turbulence over the test article and a direct-current glow discharge was employed to excite vibrational non-equilibrium. Both on- and off-body visualization, temperature, surface pressure frequency spectra, and velocity data were collected with the above listed techniques. These data includes the first known measurement of the vibrational temperature of NO(v=1) across hypersonic boundary layers (laminar and turbulent), which, allow for advancement and validation of new theoretical closure treatments. The data suggest that the vibrational relaxation and flow timescales were comparable allowing the possibility that the processes would interact. A complementary study of second mode boundary layer instability growth, with and without 3-D Görtler vortices, was also performed in the TAMU M6QT. The goal was to track second mode breakdown to turbulence, which was relevant to the processes observed with the trips. Mach stem experiments were conducted in two facilities by intersecting opposing oblique shock waves. Thermochemical effects on the Mach stem flow structure were examined in the TAMU HXT facility. Five Mach 8.5 flow fields with stagnation enthalpies ranging from 1.8 to 7.2 MJ/kg were studied. The database

was acquired to characterize the role of extreme temperature (up to 7000K) thermochemistry on the basic structure of a Mach stem flow, which included shock turbulence interactions and measurements across the triple point shear layers. These data were acquired to facilitate validation methods that address shock turbulence interactions and/or include extreme temperature air and nitrogen thermochemistry. Complementary laminar simulations were performed with the University of Minnesota US3D code, which effectively reproduced the effects of thermochemistry on the flow structure. Additional Mach stem data were acquired at low temperature, and include the first known laser-based optical measurements of velocity and temperature fluctuation amplification across a normal shock wave (M = 4.4). It important to note that both the wall boundary layer and Mach stem flow fields were designed to be accessible with current direct numerical simulation resources. Hence, these data are useful to validate high fidelity methods. The databases and analyses produced in this study will serve the DoD research community for decades. Finally, this program supported the final commissioning of the TAMU HXT, a national resource scale hypervelocity ground test facility, which facilitated the extreme temperature experimentation. At the time of this writing, experiments were underway in HXT supporting both the Army and Navy.

This Vannevar Bush Faculty Fellowship supported the graduate studies of twelve students (nine PhD, three MS) and five collaborators. All of the students graduated and entered into the workforce in closely related fields. Strong interactions with the DoD were also accomplished, e.g., the PHACENATE facility transitioned to the Air Force. with the PhD graduate. The PI was also subsequently selected by the Navy to lead a national working group in hypersonic turbulence. The results from this study are disseminated via this report, student theses and dissertations, archival articles, and conference proceedings. At the time of this writing, twenty-two articles/conference papers had been produced, with additional manuscripts in-progress. The descriptions presented in this document were drawn from selected dissertations, theses, articles produced over the execution of this project, in particular: McManamen [1], Buen et al. [2], McManamen et al. [3], Siddiqui [4], [5], Siddiqui et al. [6], Broslawski [7], Dean et al. [8], Bryan [9], Bryan et al. [10], Dean [11], Broslawski et al. [12], Broslawski et al. [13], Broslawski et al. [14], Smotzer et al. [15], and Dean et al. [16].

ACKNOWLEDGMENTS

The author gratefully acknowledges Drs. Bindu Nair and Jeanluc Cambier from the Department of Defense Office of the Undersecretary of Defense for Research and Engineering Vannevar Bush Faculty Fellowship (Grant N00014-18-1-3020) and Drs. Nafiz Karabudak, Barry Bauer, and John Rhoads from the Lockheed Martin Corporation for financial support and collaborative discussion for this (Project S20-004). The contents herein are solely the responsibility of the author and do not necessarily represent the official views of Texas A&M University, the DoD OUSD(R&E), or the Lockheed Martin Corporation. The PI also acknowledges the collaborations with Drs. Simon North (TAMU, Chemistry), Diego Donzis (TAMU, Aerospace Engineering), Richard Miles (TAMU, Aerospace Engineering), Arthur Dogariu (TAMU, Aerospace Engineering), William Saric (TAMU, Aerospace) and Mark Gragston (UTSI, Aerospace Engineering).

TABLE OF CONTENTS

Page

1. INTRODUCTION

1.1 Preamble

The descriptions presented in this final report were drawn from selected dissertations, theses, and articles produced in the execution of this project, in particular: McManamen [17], Buen et al. [2], McManamen et al. [3], Siddiqui [4], Siddiqui et al. [5], Siddiqui et al. [6], Broslawski [7], Dean et al. [8], Bryan [9], Bryan et al. [10], Dean [11], Broslawski et al. [12], Broslawski et al. [13], Broslawski et al. [14], Smotzer et al. [15], and Dean et al. [16]. The original citations are also included in the narrative.

1.2 Motivation

Hypersonic flows are perhaps the most extreme and technically challenging atmospheric flight environments. Nevertheless, there exists a relentless desire to travel higher and faster which motives continued dedication to their research. Technological advancements in this field have applications for space exploration and national security applications. Hence, progress in hypersonic science and technology is a national priority. In the National Defense Science and Technology Strategy 20238, the United States Government listed hypersonics as critical technology [18]. The characteristics that define hypersonic flow typically begin around Mach 5 [19]. Hypervelocity is a similarly defined term, where the velocity is flight matched or higher, whereas in some hypersonic ground test facilities, Mach 5 or above is achieved partically by operating at colder than flight temperatures, which, in turn, leads to lower than flight velocities.

An aim of modern hypersonics is to produce maneuverable hypersonic vehicles powered by air-breathing supersonic combustion engines called scramjets Urzay [20]. These maneuverable hypersonic vehicles introduce challenging, multidisciplinary problems. For example, these vehicles require advanced control systems that can make rapid decisions autonomously and adapt to changes in vehicle shape (e.g., ablation). Thermal management is a significant technical challenge for maneuverable vehicles because they need to withstand extreme temperatures for much longer durations than a vehicle on a ballistic trajectory. Strong radiative emission and ionization in the flow around a hypersonic vehicle also create communication and aero-optic challenges. A commonality among these challenges is that they arise due to the extreme conditions in the flow surrounding a hypersonic vehicle. This emphasizes the need for accurate understanding, prediction, and control of aerodynamics, thermodynamics, chemistry, viscous interactions, and radiation in hypersonic flows. ([7])

A small collection of data from the present study is provided in Figure 1.1 to qualitatively introduce underlying processes. The test article is shown in Figure 1.1a. The article had a slightly blunted leading edge. As indicated in Figure 1.1b, the shock layer (region between the shock and the body) was thin, and the shock was highly curved as it wrapped around the body, which led to a gradient in the entropy behind it. Also visible in these images was the viscous boundary layer, which grew moving downstream progressing from Figure 1.1b to d. The boundary layer governs the viscous drag and heating. Because of the low densities in the wind tunnel, discrete trips at $\sim$ 65mm were needed to accelerate transition from laminar to turbulence within the boundary

layer. The blue overlay is a planar laser induced fluorescence image showing what appeared to be trip excited second mode instability rope like structures in the boundary layer near the wall, which, when coupled with the 3-D trip wakes, led to transition. Beyond $\sim$ 130mm from the leading edge, the boundary layer was turbulent. Turbulent boundary layers effectively increase a vehicle's skin friction and thereby its drag and heating, so properly predicting and controlling their formation is often a key consideration for vehicle designers; e.g., Whitehead Jr. [21] found that if the proposed hypersonic National Aerospace Plane had a fully laminar boundary layer its payload-to-gross-weight would double what it would be with a fully turbulent boundary layer. Finally, electrodes mounted to the surface created a plasma which instilled thermal nonequilibrium. The electrodes were the two parallel copper colored strips upstream of the first window shown on Figure 1.1a. The boundary layer trips were just upstream of the electrodes. The flow features highlighted here, a thin shock layers, low-density effects, thick boundary layers, entropy layers due to curvature, and thermochemistry, define hypersonic flow [19]. In most cases, these characteristics are strongly coupled. Hence, as shown in Figure 1.2, this project was designed to advance basic understanding of turbulence in the presence of non-equilibrium effects. Two basic flow fields were examined, a hypersonic boundary layer and a hypervelocity Mach stem, which introduced shock turbulence interactions and allowed for the study of a wall-free turbulent shear layer. ([7, 12, 13, 14, 11, 16])

Bowersox [22] examined an algebraic energy flux approach for turbulence modeling, which was found to improve prediction in high speed flows for equilibrium flows [23, 24, 25]. Bowersox et al. [26] extended the model to include molecular effects. This analysis suggested that the timescales of vibrational and turbulent energy decay may interact. Fuller et al. [27] experimentally found this decay had a tangible impact on a subsonic turbulent channel flow exited by a radiofrequency plasma, and the work in Fuller [28] contextualized this effort within the energy flux theory. The pathways identified by Fuller et al. [27] were supported by the subsequent numerical exploration of Khurshid and Donzis [29]. Thus, at present, there exists a need for experimental data in a hypersonic environment to provide validation data to test these theories and models in high speed regimes. Ideally, these data would contain a high degree of detail, but involve relatively simple flows and modest thermodynamics (e.g., a two-temperature flow in air, with only $N_2^{v=1}$ excited) to allow for incremental progress to be made. In a prior study, our team quantified high-speed turbulent boundary layer (TBL) flow over canonical zero pressure gradient (ZPG) model [30]. The studies demonstrated the use of trips to generate low density hypersonic environment. In the present work the test article was again re-designed to include electrodes capable of producing a glow discharge plasma. This allowed the introduction of thermal nonequilibrium effects which introduced another element of the hypersonic environment to ZPG flows in the ACE tunnel. The ability to turn on turbulence or nonequilbrium using trips or a plasma allowed the effect of each to be isolated and controlled. ([7])

The Mach stem flow is shown schematically in Figure 1.3a. Key features of a Mach stem include an initial oblique shock, a normal shock, a triple point, a reflected oblique shock, and slip line, which are labeled in Figure 1.3a, where Mach stems are generated when the shock angle of a reflected oblique shock needed to turn flow back to parallel for a symmetry plane exceeds a critical value [31]. This flow allows for the study of two important phenomena: shock turbulence interactions and wall-free shear layers. shock turbulence interactions are important in high speed

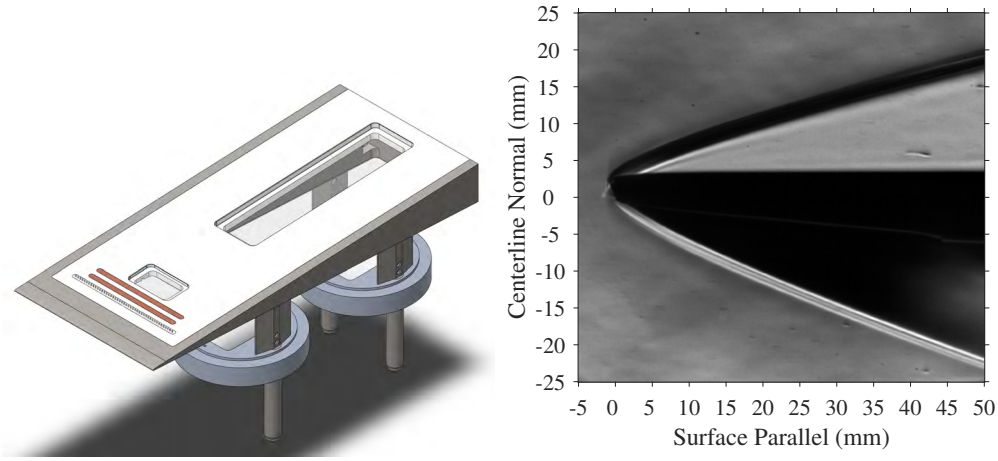

(a) CAD model

(b) Bow shock

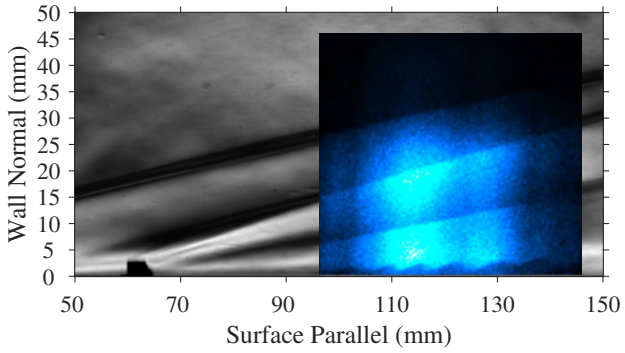

(c) Upstream view

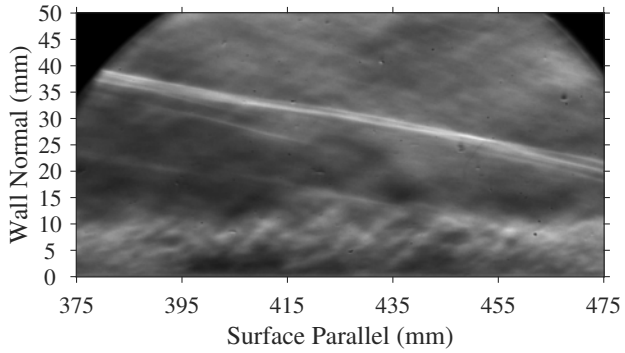

(d) Downstream view

Figure 1.1: Schlieren of the zero pressure gradient Mach 6 hypersonic turbulent boundary layer examined in this study. Flow is from left to right. [7].

aerodynamics and aeropropulsion flows because of the ability to alter underlying fluid dynamic processes through amplification of instability modes and modification of energy transport. Modern direct numerical simulation studies [32, 33] have brought into question classical theories [34, 35]. Experimental data suitable to distinguish theories were excessively rare, which was especially true

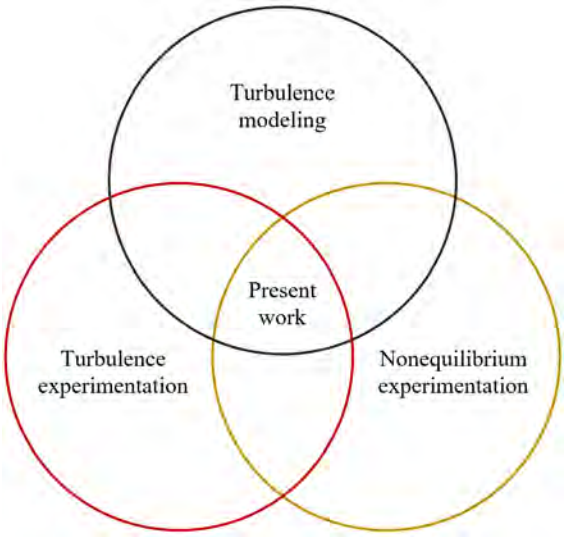

Figure 1.2: Venn diagram of the present research [7].

for non-intrusive measurements at high Mach number. Hence, our group performed a study of the amplification of turbulence across the normal shock. An example image is provided in Figure 1.3b. Also visible are Kelvin-Helmholtz instabilities in the free shear layer region, which corresponds to the slip line annotated in Figure 1.3a. At higher Reynolds number, it was expected that these shear layers would transition to turbulence. An example hypervelocity result at Mach 8.5 at elevated Reynolds number and stagnation enthalpy (7.2 MJ/kg) is shown in Figure 1.3c. As indicated, turbulent shear layers were observed. Hence, In this present study, the effects of thermochemistry on both the shock turbulence interaction and the shear layer were examined. ([17, 3, 8, 9, 11, 16])

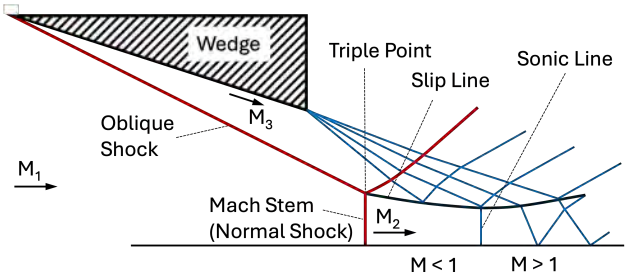

(a) Schematic

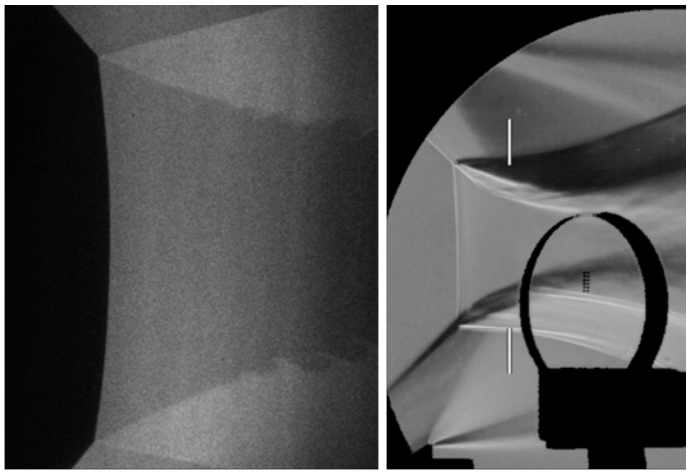

(b) Mach 4.4 (c) Mach 8.5

Figure 1.3: Mach stem flow structure. (a) Schematic of the flow structure. (b) Schlieren photograph of shock turbulence interactions (STI) study at Mach = 4.4 (cold flow) [1]. (c) Schlieren photograph at Mach = 8.5 (Enthalpy = 7.2 MJ/kg, Nitrogen) [11]. Flow is from left to right.

1.3 Research Objectives

The objective of this project was to improve basic knowledge of gaseous turbulence when exposed to extreme hypervelocity environments. Of specific interest were mechanisms that couple turbulence to molecular energy exchange dynamics, mechanical forces (e.g., shock waves), and chemical reactions. The vibrational energy flux model in [26] provided mathematical context. Two testbeds were examined: (1) wall bounded turbulent flow at Mach 6 with a DC glow discharge plasma to activate thermal nonequilibrium, as summarized in Figure 1.1 and (2) Mach 8.5 high enthalpy (1.8 – 7.2 MJ/kg) hypervelocity Mach stems, with shock turbulence interactions and triple point initiated free shear layers; see Figure 1.3. Additional studies of specific fundamental hydrodyanmic phenomena were also performed, which support the primary objective: (1) low enthalpy hypersonic boundary layer second mode instability and breakdown to turbulence and (2) low enthalpy shock turbulence interactions.

1.4 Approach

The wall bounded flows were accomplished on the (2.75° half-angle wedge) test article shown in Figure 1.1(a). The test article was based on the designs of Semper and Bowersox [30] and Leidy et al. [36], but fitted with electrodes to produced a glow discharge to introduced vibrational nonequiliubrium. This test article accomodated both traditional diagnostic techniques as well as modern optical approaches. Like their models, it used discrete trips to allow different boundary layers to be produced. A novel introduction, in addition to their recommended upgrades, were spanwise electrodes for the generation of a glow discharge. The plasma generated vibrational nonequilibrium in a controllable manner, which let its effect be isolated and studied. The wedge model also allowed for off-body optical diagnostics due to its flush windows and rigid yet translatable installation in the test section. The research goals were to (i) design a test article which could produce a canonical hypersonic turbulent boundary layer, (ii) allow for laminar, transitional, and turbulent boundary layers to be produced and studied, (iii) introduce thermal nonequilibrium, (iv) provide both on- and off-body measurements, including laser diagnostics, (v) formalize the derivation for the algebraic energy flux model introduced in Bowersox [22] to allow further development and easier extension to cases with thermal nonequilibrium, as in [26], (vi) provide experimental measurements to validate turbulence theories, (vii) provide experimental measurements of the vibrational energy through the boundary layer to explore how thermal nonequilibrium couples with hypersonic turbulence, and (viii) quantify relevant transition mechanisms on a NASA geometry designed specifically for this purpose. The experiments were performed in the Texas A&M University Actively Controlled Expansion (ACE) and Mach 6 Quiet Tunnels (M6QT). The flow conditions in the ACE tunnel were Mach 5.7, with unit Reynolds number of 6.0 million per meter, which, with boundary trips, provided access to a relatively thick (1 cm) turbulent boundary layer, which facilitated detailed measurements and provides an opportunity for direct numerical simulation. The M6QT provides Mach 5.9 flow, with unit Reynolds numbers between 5 and 10 million per meter. ([7, 4])

Two Mach stem experiment campaigns were performed. The goal for the low enthalpy shock turbulence interaction study was to quantify the role of a normal shock wave on the modification of turbulence through measurement of vortical and entropic fluctuations across a normal shock wave in a high Mach number wind tunnel environment. The vortical (velocity), entropy (temperature), and acoustic (pressure) disturbances commonly observed in high-speed wind tunnel freestreams was selected as the test-bed for the experiments. A Mach-stem generator was selected to produce a normal shock within the wind tunnel freestream. An open-wedge design was developed to enable optical access. An image of the Mach stem at Mach 4.4 is shown in Figure 1.3b. An interesting feature is the Kelvin-Helmholtz instability in the laminar slip line region downstream of the triple point. The goals for the high enthalpy campaign were quantify the role extreme temperature (up to 7,000K) thermochemistry on the structure of the Mach stem flow. The experiments took place in the TAMU Hypervelocity Expansion Tunnel (HXT). The Mach number was set to 8.5 and the enthalpy was varied from 1.8 to 7.2 MJ/kg. Air and nitrogen gases were tested. A schlieren photograph for a Mach stem at Mach 8.5 (H = 7.2 MJ/kg) is provided in the Figure 1.3c. An important observation is that the shear layer downstream of the triple point had transitioned to turbulence. Although this study had broad applications within the hypersonic field, the primary scientific ob-

jective was to provide improved understanding of the role extreme temperature on turbulence. Both shock turbulence interactions and the free shear layer flows were studied in the presence of thermal and chemical nonequilibrium. Measurements included index of refraction fluctuations, convective velocities, and internal molecular states. Results were produced for five enthalpies (1.8 - 7.2 MJ/kg) and/or gases (air and nitrogen). In addition, shock turbulence interactions were quantified using changes in refractive index fluctuations across normal shocks. Simulations of the hypervelocity Mach stem was performed using the University of Minnesota CFD code US3D Candler et al. [37]. The inlet flow conditions were Mach 8.5 with stagnation enthalpies of 3.8, 5.4, 6.9, and 11 MJ/kg. The simulation results enabled an understanding of the flow conditions in regions downstream of Mach stems measured using Focused Laser Differential Interferometry (FLDI) during the experimental campaign. The simulation results also provided great insight into the general structure and chemistry of high-enthalpy Mach stems. ([17, 3, 8, 9, 11, 16])

1.5 Contribution to the Field

The wall bounded flow database was acquired to characterize the fundamental transport of turbulence with thermal nonequilibrium. These data include the first known measurements of the vibrational temperature of NO across a hypersonic boundary layer (laminar and turbulent), which, allow for advancement and validation of theoretical treatments for thermal nonequilibrium effects. The Mach stem database was acquired to characterize the role of extreme temperature thermochemistry (up to 7000K) on the basic structure the flow, which included shock turbulence interactions and measurements across the free shear layers. These data were acquired to facilitate validation of theories that account for shock turbulence interaction and/or include extreme temperature thermochemistry (air and nitrogen). The Mach stem data included the first known laser-based optical measurements of velocity and temperature fluctuation amplification across a normal shock wave (M = 4.4), which are useful to validate high fidelity methods.The diagnostics included planar laser induced fluorescence of nitric oxide (MHz and 0.1 Hz), focused laser differential interferometry, optical emission spectroscopy, schlieren photography, femtosecond electronic excitation molecular tagging velocimetry, IR thermography, constant temperature hot-film anemometry, thermocouples, and Kulite pressure sensors. Theoretical treatments were performed to advance mathematical models that include molecular energy exchange processes for turbulence closure. Complementary computational fluid dynamic simulations were also accomplished. This program also supported the final commissioning of a national resource scale hypervelocity ground test facility at Texas A&M University, which facilitated the extreme temperature experimentation.

Finally, this Vannevar Bush Faculty Fellowship supported the graduate studies of twelve students and six collaborators. All of the students graduated and entered into the workforce in closely related fields. Strong interactions with the DoD were accomplished, e.g., the tabletop high-speed test facility transitioned to the Air Force with the graduating student. The PI was also subsequently selected by the Navy to lead a national working group in hypersonic turbulence. The results from this study are disseminated via this report, student theses and dissertations, archival articles, and conference proceedings. At the time of this writing, twenty-two articles/conference papers had been produced, with additional manuscripts in-progress.

2. BACKGROUND

2.1 Preamble

The present research effort had considerable breadth, encompassing compressible turbulence, Reynolds-averaged Navier-Stokes (RANS) modeling, high-temperature effects, and glow discharge physics. Hence, the following references are recommended Prandtl [38], van Driest [39], Clauser [40], Spalding [41], Jones and Launder [42], Cebeci and Smith [43], [44], Baldwin and Lomax [45], [46], Smits and Dussauge [47], White [48], [49], Schetz and Bowersox [50], and Pope [51]. The sections in this chapter were drawn directly from selected dissertations, theses, articles produced through support from this project, in particular: McManamen [17], Buen et al. [2], McManamen et al. [3], Siddiqui [4], [5], Siddiqui et al. [6], Broslawski [7], Dean et al. [8],Bryan et al. [52], Bryan et al. [10], Dean [11], Broslawski et al. [12], Broslawski et al. [13], Broslawski et al. [14], Smotzer et al. [15], and Dean et al. [16]. Original citations are also included in the subsequent text.

2.2 High-Temperature Effects

The review in this section follows from Broslawski [7]. A gas in thermal equilibrium can be described by a single temperature; that is, its external (translational) temperature and internal (rotational, vibrational, electronic) temperatures are all the same. A gas in chemical equilibrium is one not undergoing any spontaneous reactions. Past a strong hypersonic shock, rotational and translational temperatures equilibrate rapidly, while the vibrational temperature requires far more collisions to match the bath, see Table 2.1. Given the large numbr of collisions required for vibrational relaxation, it was expected that for some species, the relaxation time coul dbe comaprable to the those of the flow. Similarly, the reaction rate for dissociation and ionization could match those of the flow time scale. Of interest to the boundary layer work in this study was vibrational excitation, which, because it occurs at a relatively low temperatures, is the first internal mode to be excited, as rotational is generally assumed to be equilibrated with the external translational mode given the relatively small number of required collisions. Because the vibrational energy states are more greatly spaced than rotational and translational, activating the lower vibrational levels stores a disproportionate amount of energy and thus impacts the thermodynamics. At speeds approaching $10\frac{\text{km}}{\text{s}}$, viscous effects in the boundary layer and compression across the strong shocks produce temperatures sufficient excite internal energy modes, dissociate N_2 and O_2 and ionize species, which is relative to the hypervelocity Mach stem studies. ([7])

	Translation	**Rotation**	**Vibration**
Translation	1	10	10^6
Rotation	10	10	10^5
Vibration	10^6	10^5	$< 10^6$

Table 2.1: Estimate of collisions necessary for equilibration.

Local thermal equilibrium is defined as the case where a Boltzmann distribution at local temperature can be fit to each species at each point in the flow. Similarly, they define local chemical equilibrium as the case where, at each point in the flow, the chemistry is in equilibrium for the local temperature and pressure. Note that equilibrium is distinct from a frozen flow, wherein the rates for thermal or chemical equilibration are long enough to consider the nonequilibrium temperature or chemistry as constant for the relevant flow time scale. A simple model for hypersonic flows may contain five gas species, N_2, O_2, N, O, and NO. It is helpful to assume a mixture of thermally perfect gases, which requires that all species have the same volume and are not affected by intermolecular forces. This allows one to treat each species independently at the system's temperature and volume in accordance with Dalton's Law of Partial Pressures, and then produce a bulk property by summing each species' contribution scaled by its mass or molar average. ([7])

2.2.1 Vibrational Profile Assumptions

The review in this section follows from Broslawski [7]. The effect of plasma-initiated vibrational nonequilibrium on a turbulent freestream (channel) was studied by Fuller et al. [27] (see section 2.2.4). They showed that energy released by relaxing vibrational modes has a strong impact on $T^{rot-trans}$, viscosity, and ultimately Reynolds stress; this experiment and its affiliated work will be revisited in detail in Section 2.2.4. Thus accurate prediction of vibrational decay is critical. In addition to performing the experimental measurements described in [28, 27], Hsu [53] conducted an extensive simulation of the collisional kinetics of the channel flow. Their model contained six species (N_2, O_2, NO, O, H_2O, and CO_2) and 52 reactions covering chemical, vibration-vibration, and vibration-translation energy exchange collisions; the relevant rate constants Hsu calculated for their experiment are provided in Table 2.2. Neglecting the results in the presence of H_2O and CO_2, Hsu found N_2, O_2, and NO had a vibrational relaxation lifetimes of $\mathcal{O}(100\text{ms})$, $\mathcal{O}(100\text{ms})$, and $\mathcal{O}(0.1\text{ms})$ respectively. They attributed the rapid decay of NO to its rate constants being orders of magnitude larger than those for the other species, and noted that for both VT and VV collisions N_2 is the longest-lived molecule by orders of magnitude. This was critical, because it suggested air moving at $u = 850\text{m/s}$, a realistic speed for the ACE tunnel, will travel 85m before significantly decaying, but seeded NO will decay within 0.085m of excitation. Of course, the present test has different conditions than Hsu [53], but they are close enough that it is safe to assume the air is thermally frozen along the entire length of the test article, but the NO will decay somewhat. ([7])

For the continuum flows in the ACE tunnel velocity and external temperature slip at the wall is infeasible, but slip in the vibrational temperature profile is possible. Here vibrational slip analyzed analogously to the Maxwell model for velocity slip (see [58]), following Nompelis et al. [59]

$$e_{v,slip} - e_{v,wall} = \frac{2-\sigma_v}{\sigma_v}\lambda_v \left(\frac{\partial e_v}{\partial y}\right)_{wall} \tag{2.1}$$

Here $\lambda_v = \lambda = 2/\mu/\rho\bar{c}$ is equivalent to the momentum mean free path with $\bar{c} = \sqrt{8R_{specific}T/\pi}$. $e_{v,wall}$ is the vibrational energy of the wall, and $e_{v,slip}$ is the vibrational energy of the gas at the wall, with slip allowed; thus the degree of slip is controlled by the vibrational accommodation factor σ_v. When $\sigma_v = 0$, the above equation is meaningless, the wall is vibrationally adiabatic and e_v is uncorrelated to the wall. Conversely, when $\sigma_v = 1$ the flow is completely correlated. This

Reaction	Forward Rate Constant ($cm^3/molec/s$)	Ref.	Rxn No.
V-V Relaxation			
$N_{2,v=1} + O_2 \rightarrow O_{2,v=1} + N_2$	7.58×10^{-18}	[54]	1
$N_{2,v=1} + NO \rightarrow NO_{v=1} + N_2$	1.04×10^{-15}	[55]	2
$NO_{v=1} + O_2 \rightarrow O_{2,v=1} + NO$	1.00×10^{-14}	[56]	3
V-T Relaxation			
$N_{2,v=1} + N_2 \rightarrow N_2 + N_2$	4.13×10^{-24}	[55]	4
$N_{2,v=1} + O_2 \rightarrow N_2 + O_2$	4.13×10^{-24}	[55]	5
$N_{2,v=1} + NO \rightarrow N_2 + NO$	4.13×10^{-24}	[55]	6
$O_{2,v=1} + O_2 \rightarrow O_2 + O_2$	5.77×10^{-19}	[54]	7
$NO_{2,v=1} + N_2 \rightarrow O_2 + N_2$	5.58×10^{-19}	[54]	8
$O_{2,v=1} + NO \rightarrow O_2 + NO$	6.55×10^{-19}	[55]	9
$NO_{v=1} + NO \rightarrow NO + NO$	7.52×10^{-14}	[57]	10
$NO_{v=1} + O_2 \rightarrow NO + O_2$	2.58×10^{-14}	[57]	11
$NO_{v=1} + N_2 \rightarrow NO + N_2$	1.30×10^{-16}	[57]	12

Table 2.2: Relevant relaxation rate constants for the conditions in [53]

is perhaps more clearly explained by the definition in [60], who wrote that σ_v is the portion of the energy accommodated so $\sigma_v e_{v,wall}$ energy is accommodated by the wall and $(1-\sigma_v)e_{v,wall}$ is reflected back into the flow. ([7])

The macroscopic effect of vibrational accommodation is to increase wall heat flux; as $\sigma_v \rightarrow 1$ the wall absorbs more vibrational energy and becomes hotter, and *vice versa* [59, 61]. Furthermore, Yu et al. [60] showed a vibrational temperature boundary layer can only form when $\sigma_v \neq 0$, otherwise the frozen temperature will extend to the wall; their flat plate shock tunnel simulations showed no change in the external boundary layer profile regardless of the vibrational accommodation used. Sauerwein and Hruschkaand [61] compared their own simulations to shock tunnel data over a cone and found vibrational accommodation has no effect on surface pressure, and that its effect on heat flux is inversely proportional to density. Estimation of σ_v is important but difficult because it depends on both flow and material properties [60]. In their CFD replication of shock tunnel data over a double cone, Nompelis et al. [59] found a value of $\sigma_v = 0.001$ following the measurements of Black et al. [62] for stainless steel provided excellent agreement with the data (directly better than $\sigma_v = 0.1$), though its effect was coupled with other high-temperature corrections to the simulation; Moss and Bird [63] independently found that when adjusting σ_v alone better results were attained with full vibrational accommodation for the same experimental data set, though both the $\sigma_v = 0$ and 1 data were within the experimental uncertainty. Evidence for negligible vibrational accommodation is provided by the literature survey in [64]. Boyd et al. [65] also used $\sigma_v = 0.1$ for their calculations.Thus, it would seem vibrational equilibrium cannot be assumed at the wall. However, the previous studies were mostly concerned with high-temperature shock tube experiments, and none considered a turbulent boundary layer. The ACE tunnel runs

at modest Mach numbers, relatively negligible vibrational excitation, and comparatively (see [61]) high densities. Finally, here a glow discharge was used to locally seed in weak vibrational nonequilibrium. As such there is currently no truly analogous study of the vibrational slip condition in the literature. It was decided the best course of action would be to perform the experiment and for now accept the modest assumption that the vibrational excitation is collisionally quenched at the wall so $\sigma_v = 1$. This open question will be probed with optical techniques as part of the current work. ([7])

2.2.2 Flows in Thermochemical Nonequilibrium

The review in this section follows from Bowersox et al. [26], Bowersox [22]. and Broslawski [7]. In order to model a flow in thermochemical nonequilibrium, one must add conservation equations for both species conservation and the different energy modes to model chemical and thermal effects respectively. This is a direct departure from the above case of equilibrium, where no new conservation equations were introduced and the thermodynamic variables were calculated using the standard conservation laws supplemented with statistical thermodynamics results. The equations of motion shown below are for a weakly ionized plasma and were provided by Bowersox et al. [26]; to view the derivation of analogous forms see [66, 67]. In these equations n represents the species, m represents the energy modes, and $Y_{(n)}$ represents the mass fraction of each species.

- Global Conservation of Mass

$$\rho_{,t} + (\rho u_k)_{,k} = 0 \tag{2.2}$$

- Global Conservation of Momentum

$$(\rho u_i)_{,t} + (\rho u_i u_k)_{,k} = \sigma_{ik,k} + F_{bi} \tag{2.3}$$

  - Here $\sigma_{kl} = -P\delta_{ik} + \tau_{ik}$ and the body force due to electromagnetic forces is $F_{bi} = \sum_{(n)} \rho Y_{(n)} f_{b(n)}$

- Global Conservation of Energy

$$(\rho e)_{,t} + (\rho e u_k)_{,k} = -\left[q_k + \sum_n J_{(n)k} \left(h^{(ex)}_{(n)} + h^o_{f(n)} \right) \right]_{,k} + \sigma_{kl} u_{l,k} + \dot{W}_{F_b} - Q_{rad} \tag{2.4}$$

  - Here $q_k = -kT_{,k}$ and the three terms on the right hand side outside of the brackets represent, from left to right, work due to pressure and viscous forces, the rate of change of energy due to body forces, and radiation. The second bracketed term is the energy exchange due to species diffusion with, following Fick's Law, $J_{(n)k} = \rho_{(n)} u_{(n)k} \approx -D_{(n)(m)} Y_{(n),k}$ where $D_{(n)(m)}$ is the binary diffusion coefficient. $h^o_{f(n)}$ is the formation enthalpy.

- Conservation of Species

$$(\rho Y_{(n)})_{,t} + (\rho Y_{(n)} u_k)_{,k} = \dot{\omega}_{(n)} - J_{(n)k,k} \tag{2.5}$$

- Here $\dot{\omega}_{(n)}$ represents the rate of species change due to chemical reaction

- Conservation of External Energy of Heavy Particles

$$\begin{aligned}&\left(\rho_{(h)}e^{(ex)}_{(h)}\right)_{,t}+\left(\rho_{(h)}e^{(ex)}_{(h)}u_k\right)_{,k}=\\&-\left[q^{(ex)}_{(h)k}+\sum_{n\neq e}J_{(n)k}\left(h^{(ex)}_{(n)}+h^{o}_{f(n)}\right)\right]_{,k}+\sigma_{(h)kl}u_{l,k}+\dot{W}^{(ex)}_{F_b(h)}+Q^{(ex)}_{(h)}+\dot{W}^{(ex)}_{d(h)}\end{aligned} \tag{2.6}$$

  - Here $Q^{(ex)}_{(h)}=\sum_{(m)}\rho_{(h)}q^{(ex)-(m)}_{(h)}+Q^{(ex)}_{rad(h)}$; it covers energy exchange between external and internal energy modes and radiation.
  - Here $\dot{W}^{(ex)}_{d(h)}=\dot{W}_{(h)}-\left[\rho_{(h)}\left(u_iu_{(h)k}+u_{(h)i}u_k+u_{(h)i}u_{(h)k}\right)\right]_{,k}$; the first term covers the work due to collisions, force field interactions, and chemical reactions while the second term covers the effects of diffusion using the diffusion velocity $u_{(h)i}$. For weakly ionized plasmas $\dot{W}^{(ex)}_{d(h)}\approx 0$.

- Conservation of External Energy of Electrons

$$\begin{aligned}&\left(\rho_{(e)}e^{(ex)}_{(e)}\right)_{,t}+\left(\rho_{(e)}e^{(ex)}_{(e)}u_k\right)_{,k}=\\&-\left[q^{(ex)}_{(e)k}+J_{(e)k}e^{(ex)}_{(e)}\right]_{,k}+\sigma_{(e)kl}u_{l,k}+\dot{W}^{(ex)}_{F_b(e)}-\sum_{n=ions}I_{(n)}\dot{\omega}_{(n)}+Q^{(ex)}_{(e)}+\dot{W}^{(ex)}_{d(e)}\end{aligned} \tag{2.7}$$

  - Terms generally follow same interpretation as those of Equation 2.6.
  - $\sum_{n=ions}I_{(n)}\dot{\omega}_{(n)}$ represents energy transferred to an ion's potential energy during an ionizing collision between a neutral particle and an electron.

- Conservation of Internal Energy of Heavy Particles

$$\left(\rho_{(n)}e^{(in)}_{(n)}\right)_{,t}+\left(\rho_{(n)}e^{(in)}_{(n)}u_k\right)_{,k}=-\left[q^{(in)}_{(n)k}+J_{(n)k}e^{(in)}_{(n)}\right]_{,k}+e^{(in)}_{(n)}\dot{\omega}_{(n)}+Q^{(in)}_{(n)} \tag{2.8}$$

  - Terms generally follow same interpretation as those of Equation 2.6.
  - $e^{(in)}_{(n)}\dot{\omega}_{(n)}$ represents the rate of internal energy transfer during chemical reactions.
  - $Q^{(in)}_{(n)}=\sum_{(m)}\rho_{(n)}q^{(in)-(m)}_{(n)}+Q^{(in)}_{rad(n)}$. The radiation for the electric mode can manifest as visible light in a weakly ionized plasma, as is observed in the positive column of a glow discharge.

The above equations are generalized to be applicable to a variety of flows. However, for the present case of chemical equilibrium downstream of a weakly ionized plasma, several simplifications were appropriate; a similar philosophy, of reduction of the general form to suit a specific case, was employed by Fuller [28]. To begin, no electrons or ions were present, so Equation 2.7 and the heavy particle subscript (h) were removed. Without the presence of charged particles and

an electric field, the body force terms were removed. Technically, in the absence of chemical reactions one could remove Equation 2.5 and $e^{(in)}_{(n)}\dot{\omega}_{(n)}$, but for now these terms were kept for those who consider each internal energy mode and corresponding level to be a distinct species. Finally, the sum of the internal and external energy should be equal to the global energy (assuming perfect modeling), so Equation 2.4 was redundant. With these changes the equations of motion for the present case of thermal nonequilibrium were

- Conservation of Mass

$$\rho_{,t} + (\rho u_k)_{,k} = 0 \tag{2.9}$$

- Conservation of Momentum

$$(\rho u_i)_{,t} + (\rho u_i u_k)_{,k} = \sigma_{ik,k} \tag{2.10}$$

- Conservation of Species

$$(\rho Y_{(n)})_{,t} + (\rho Y_{(n)} u_k)_{,k} = \dot{\omega}_{(n)} - J_{(n)k,k} \tag{2.11}$$

- Conservation of External Energy

$$\begin{aligned} &\left(\rho_{(n)} e^{(ex)}_{(n)}\right)_{,t} + \left(\rho_{(n)} e^{(ex)}_{(n)} u_k\right)_{,k} = \\ &-\left[q^{(ex)}_{(n)k} + \sum_n J_{(n)k}\left(h^{(ex)}_{(n)} + h^{o}_{f(n)}\right)\right]_{,k} + \sigma_{(n)kl} u_{l,k} + \sum_{(m)} \rho_{(n)} q^{(ex)-(m)}_{(n)} \end{aligned} \tag{2.12}$$

- Conservation of Internal Energy

$$\left(\rho_{(n)} e^{(in)}_{(n)}\right)_{,t} + \left(\rho_{(n)} e^{(in)}_{(n)} u_k\right)_{,k} = -\left[q^{(in)}_{(n)k} + J_{(n)k} e^{(in)}_{(n)}\right]_{,k} + e^{(in)}_{(n)}\dot{\omega}_{(n)} + \sum_{(m)} \rho_{(n)} q^{(in)-(m)}_{(n)} \tag{2.13}$$

It is important to be explicit when defining the "external" and "internal" modes included in Equations 2.12 and 2.13 respectively. Because the translational and rotational modes equilibrate in just $\mathscr{O}(10)$ collisions, it is appropriate to include the rotational internal energy mode in Equation 2.12. Furthermore, for the present application one can assume there is no electronic excitation outside of the plasma, so the only active internal mode is vibrational excitation, but going forward this term is kept general to allow for electronic excitation. As a compromise, assume there is only one "internal" temperature covering both the vibrational and electronic modes as in [68]. Similarly, one must be clear in the definition of n. One could follow Deiwert and Candler [69] and assume each species is in vibrational nonequilibrium, whereby Equation 2.13 would need to be solved for each species. Alternatively, Park [70] and Gnoffo et al. [68] assumed all species are in vibrational equilibrium, so only one equation was needed and therefore one could completely drop the species subscript n; justification for this simplification is provided in the former publication. The same decision can be applied to the external energy equation as well, especially because it is far safer

to assume inter-species equilibrium. Here, for generality and based off the rate constants provided in [53], no inter-species equilibrium was assumed and the species subscript remained. It is noted that n could further represent each energy level of each energy mode of each species. Such a treatment is explored in [71, 72, 73, 74, 75]. Here the authors used rate and thermodynamics data tabulated [76, 77, 78, 79, 80] for 20 million N_2 and N subreactions to precisely study several classical assumptions for hypersonic flows, like ro-translational equilibrium and Boltzmann population distributions of internal modes within a set energy level. Even in these advanced studies, only N_2 and N were considered, and energy pools were developed to cluster internal energy levels into a tractable number for simulation. Again, the present study was limited to only include vibrationally excited molecules as distinct species (n) via the inclusion of Equation 2.11 despite the absence of chemical reactions; put another way, vibrationally excited molecules were assumed to be a separate species from the ground state bath, and only one internal temperature was considered. There are several new terms introduced which differentiate the above equations for a flow in thermal nonequilibrium from an equilibrium flow. $J_{(n)k}$ can be modeled with Fick's Law, and $\dot{\omega}_{(n)}$, which formally is only applicable to flows in chemical nonequilibrium, will be addressed as part of a later model. What remains is the energy exchange term, which is explored in the next section. ([26, 22, 7])

2.2.3 Vibrational Energy Relaxation

The review in this section follows from Anderson [19], Broslawski [7]. For the present application all of the internal energy was vibrational; there was no electronic excitation (or it was otherwise well described with a single internal temperature), and ro-translational equilibrium was assumed. Thus a model is needed to couple the vibrational and (ro-)translational modes. The Landua-Teller model [81] has been adopted as the standard model [82] for such relaxation between diatomic molecules. It is noted that in general the Landau-Teller approach is not limited to vibrational-translational relaxation, but can be extended to other internal energy modes, namely rotational-translational relaxation when equilibrium cannot be assumed [74].

Consider the following example from Vincenti and Kruger [67], noting that it assumes diatomic harmonic oscillators [67] and that it ignores all collisions except vibration-translation exchanges Anderson [19]. Begin with the rate equation for vibrational relaxation

$$\frac{de_{vib}}{dt} = \frac{1}{\tau}\left(e_{vib}^{eq} - e_{vib}\right) \tag{2.14}$$

where τ is a characteristic relaxation time. If one assumes the equilibrium temperature is constant and lets $e_{vib} = e_{vib_0}$ at $t = 0$, then the ordinary differential equation can be solved analytically

$$\frac{e_{vib} - e_{vib}^{eq}}{e_{vib_0} - e_{vib}^{eq}} = \exp\left(\frac{-t}{\tau}\right) \tag{2.15}$$

With this one can see that τ is the time required to let the vibrational energy reach $\frac{1}{e}$ its initial value. However, Vincenti and Kruger [67] noted that practically e_{vib_0} varies, especially as energy

is brought into rotational and translational states. This means the rate equation becomes

$$\frac{de_{vib}}{dt} = \frac{1}{\tau(T,P)}\left(e_{vib}^{eq}(T) - e_{vib}\right) \tag{2.16}$$

While $e_{vib}^{eq}(T)$ can be calculated from theoretical expressions, here it is not necessary as the main goal is to find a model for τ so vibrational decay can be predicted; note that due to the dependency on temperature and pressure, Vincenti and Kruger [67] stated that τ loses its exponential behavior and cannot formally be called a relaxation time, so instead they called it a local relaxation time.

It is at this point the Landau-Teller model [81] for τ is introduced,

$$\tau = \frac{K_1 T^{\frac{5}{3}} \exp\left(\frac{K_2}{T}\right)^{\frac{1}{3}}}{P\left(1 - \exp\left(-\frac{\Theta_v}{T}\right)\right)} \tag{2.17}$$

wherein K_1 and K_2 are molecule dependent constants, $\Theta_v \equiv \frac{h\nu}{k_B}$, h is Plank's constant, and ν is the fundamental frequency of the oscillator. For low temperatures, a simpler form is acceptable [67]

$$\tau = \frac{C_1}{P}\exp\left(\frac{C_2}{T}\right)^{\frac{1}{3}} \tag{2.18}$$

where the constants are determined from experimental data. For a pure N_2 environment, Blackman [83] provided $7.21 \times 10^8 \text{Pa} \cdot \text{s}$ and $1.91 \times 10^6 \text{K}$ for C_1 and C_2 respectively; these values were taken for the temperature range of $800 - 6000\text{K}$.

While the given constants far exceed the equilibrium temperatures in the ACE tunnel, the underlying theory was applicable. The development of the time constant for vibrational temperature decay is useful in closing the energy coupling terms in Equations 2.12 and 2.13. A calculation for the local relaxation time at the test conditions using another form of the Laundau-Teller equation was performed. ([7])

2.2.4 Foundational Experiment: Decaying Mesh Turbulence in Vibrational Nonequilibruim

The review in this section follows from Fuller et al. [27] and Broslawski [7]. Fuller et al. [27] studied the effect of a radiofrequency (RF) plasma on subsonic, decaying mesh turbulence in a channel. Of interest was the effect of bulk heating via the plasma, which increased viscosity and lowered the Reynolds number; this could either occur through direct heating of the external energy modes, or by the decay of excited internal energy modes downstream of the plasma. Optical emission spectroscopy was used to determine the ro-translational and vibrational temperatures of N_2, which were 335K and $\sim$ 2900K respectively; it was noted that the vibrational temperature corresponds to the C electronic state, and so did not correlate to the ground electronic state vibrational temperature experienced outside of the plasma [53]. Furthermore, no NO or OH peaks were observed in the spectra, which implied that the plasma could not produce these species; NO peaks were faintly present when the gas was seeded for PLIF measurements, however [53]. CARS was employed to measure the N_2 and O_2 vibrational temperatures in the ground electronic state;

the N_2 temperatures were 1230 and 1540K just downstream of the 150 and 300W plasmas respectively, and the O_2 data was below the noise floor. The absence of O_2 spectra was taken to imply a two-temperature flow outside of the plasma in the test domain, which in turn lent credence to this assertion for the present glow discharge experiment. The CARS data showed a significant decay in vibrational temperature along the streamline, which the authors demonstrated could be mostly attributed to the presence of water vapor in the humid room air. Modeling the decay with $N_2 - H_2O$ collisions produced strong agreement with the data while $N_2 - N_2$ collisions were found to be too ineffective to produce the observed decay on their own; more detail on modeling the kinetics was provided by Hsu [53]. Notably, in these models the N_2, O_2, and NO were assumed to be at an initial equilibrium vibrational temperature of 2000K after an electron collisional cross section calculation in the plasma put their estimated vibrational temperatures at 1700, 800, and 2000K respectively; NO was included as it was present for PLIF measurements. As the vibrational temperature decreased, NO PLIF ($\sim 1\%$ NO by mass) showed an increase in rotational temperature, which was assumed to be in equilibrium for all species. This was attributed to energy exchange between the internal and external modes and was explained by the equation $h_o = 2.73k_BT + 0.77e^{vib}_{N_2} + \frac{1}{2}u^2$, which assumed $h_o = Constant$ and a two-temperature only flow. To summarize, the thermal analysis showed that the plasma only weakly heated the external modes (to 335K), but due to the presence of H_2O the vibrationally excited species, N_2 and NO, were able to relax and heat up the bulk gas' external modes. Thus vibrational decay along the test domain, not Joule or cathode heating of the bath gas' ro-translational states in the plasma proper, was the dominant thermal mechanism in the experiment. Using Rayleigh theory for low Mach numbers to relate temperature and velocity ratios and then comparing PIV velocimetry and PLIF thermometry data yielded an estimate of 40% for the ratio of plasma power put into external energy modes; it was written $\sim 12\%$ of the N_2 molecules were vibrationally excited. ([7]) With the thermal effect of the plasma thus understood, PIV was employed to understand its impact on the turbulence. The mean velocity data were presented first. To begin, a decrease and increase in velocity before and after the electrodes respectively, and growing more pronounced as the plasma power was increased, was present and attributed to a pressure rise in the vicinity of the hot plasma. Along the channel, the peak velocity grew, which was expected for a relaminarizing channel flow. Indeed, plots of the normalized mean velocity profiles show they become more parabolic the farther one moves downstream, indicative of a classic Poiseuille flow [48]; when plotted in wall coordinates, the farther one moved downstream the more closely the data matched a theoretical laminar boundary layer plot. Across the electrodes, the Reynolds axial and shear stresses dropped 15 and 30% for the 150W case, and 30 and 50% for the 300W case, as compared to the "Off" condition. The Reynolds shear stress and molecular (laminar) stresses were plotted in wall coordinates at both the first and last test locations. At the first location, the molecular and Reynolds stresses were collapsed onto two separate curves for all three plasma cases ("Off", 150W, 300W). At the final location, the molecular stresses remained clustered together and of similar magnitude to before, but the Reynolds stresses were progressively reduced as the plasma strength was increased. Plots of the individual velocity components showed that the axial turbulence intensity (u') was reduced $10-15$, 30, and 40% at the final location for the "Off", 150W, 300W plasma cases respectively; there was not dependence on the plasma for reduction in the spanwise turbulence quantity. For

the same three test locations, the Reynolds stress fell 60, 75, and 85%. These two decays followed power law trends in the streamwise coordinate. The reduction in turbulence intensity and Reynolds stress even in the absence of a plasma was indicative of natural turbulence dissipation, and was supported by an analysis of the correlation coefficient $C_{xy} = \tau_{xy}/(-\tau_{xx})(-\tau_{yy})$; this quantity was reduced 30, 50, and 70% for the three plasma cases between the first and last test location. However, the increasing reduction of all included turbulence quantities after the introduction and strengthening of the plasma suggested it was causing relaminarization. Following the approaches of Bowersox et al. [26] and Bowersox [22], an effort was made to explain the flow physics via the transport equations for axial, spanwise, and mixed Reynolds stresses as well as turbulent energy flux $\theta_i^T = \rho\overline{e'u_i'}$ (to be introduced in Chapter 3). The analysis is too detailed to include here, but there is value in the technique; additional detail for the vibrational energy flux case was provided by Fuller et al. [27]. The authors started with a complex transport equation, simplified it to suit their application, then analyzed each term independently to try and isolate its effect and reconcile it with the bulk behavior experimentally observed. This lets one attempt to identify the exact function the nonequilibrium plays in relaminarization. In summary, though the experiment differed for the proposed conditions, the effect of plasma on turbulence is clear. When facilitated by a rapid-relaxer like H_2O, plasma-seeded vibrational energy can sufficiently relax to heat the gas enough to meaningfully increase the viscosity and reduce Reynolds stress. As the present experiment is expected to be vibrationally frozen in the freestream and potentially at least partially equilibrated at the wall, where turbulent boundary layers are the most sensitive, there is reason to believe interesting physics should develop. Furthermore, the techniques and data in [27] led to the adoption of identical or analogous methodologies here. ([27, 7])

2.2.5 Foundational Experiment: ACE Tunnel-Like Vibrational Nonequilibrium (NEQ) Experiments and Simulations

The review in this section follows from Broslawski [7]. Of particular interest to the present work was vibrational NEQ in the ACE tunnel's freestream. Hypersonic tunnels are particularly susceptible to this complexity due to the high temperatures required to prevent liquefaction of oxygen, low densities, and short time scales. Taken together, it is possible for the gases to be vibrationally frozen at or near the stagnation temperature. Both computational and experimental works studying this effect and its impact are reviewed here.

- Candler and Perkins [84] (1991): A computational paper which studied the effect of vibrational nonequilibrium has on the performance of a hypersonic nozzle. Most simulations were of a $M = 17$ nozzle with stagnation temperatures > 1500K, far more extreme than the ACE tunnel. The simple harmonic oscillator and Landau-Teller models were used for vibrational energy modeling and exchange. The effect of viscous boundary layers, both laminar and turbulent, were included, as well as possible mitigation effects. For a diatomic gas $\gamma_{neq} = 7/5$ while $7/9 \leq \gamma_{eq}(T) \leq 7/5$ as the flow equilibrates, so Mach numbers should naturally be higher in a nonequilibrium flow; exacerbating this effect, the external temperature should be lower in the equilibrium case if the flow freezes as energy becomes trapped in the internal mode (see [19]). The simulations showed the cases for $\gamma = 7/5$ and γ_{neq} produced higher Mach numbers than the γ_{eq} case. The similarity between the $\gamma = 7/5$ and γ_{neq} cases was also

established and occurred due to the vibrational energy freezing to $90\%T_o$ near the throat, effectively removing itself from relevancy in the subsequent thermodynamics. Still, in both cases the nozzle did not reach its specified performance; it was observed that the growing boundary layers caused recompression upstream of the nozzle exit which made the Mach number fall. The performance was worsened for thicker turbulent boundary layers. This prompted the authors to explore the validity of the Method of Characteristics nozzle design, specifically its assumption of perfect shock reflection at a thick boundary layer. They also showed that lengthening the nozzle's throat and increasing the stagnation pressure can both decrease the amount of energy stored in internal modes from $81\%T_o$ to 66 and 68% respectively, but the nonequilibrium remained strong.

- Neville et al. [85] (2014), Bowersox et al. [26] (2008), and Khurshid and Donzis [29] (2015): Fujii and Hornung [86] and Wagnild [87] numerically studied the effect vibrational nonequilibrium has on a single acoustic wave. They found that when the wave's frequency matched the vibrational timescale, there was optimal damping of the turbulent quantities. Neville et al. [85] and Neville et al. [88] extended this concept to compressible, isotropic turbulence and turbulent shear layers respectively. They varied the Mach numbers (turbulent [85] and convective [88]), as well as ratio between the large eddy and vibrational relaxation timescales from frozen to fully equilibrated; the latter was described by a vibrational Damköhler number $Da_v = \tau_{flow}/\tau_{vib}$. For the case of isotropic turbulence, the authors found there was indeed an optimal timescale ratio for damping between the two extremes related to the inverse of the turbulent Mach number (i.e.- for $Ma_t = 0.5$, $Da_{v(opt)} = 2$). This implied for higher turbulent Mach numbers, greater nonequilibrium was necessary to cause damping. Neville et al. [85] found the damping mechanism matched that in [86, 87]. Again, if vibrational energy lagged behind turbulent fluctuations in ro-translational temperature, energy could be stored in the internal modes during external temperature crests, and then dissipated back into the external mode during troughs; overall this dampened the turbulent fluctuations. For the case of a turbulent shear layer, again there existed some optimal Da_v which supported the claim that vibrational decay must be tuned to the flow timescale. Here the effect of vibrational relaxation was most pronounced in the dilatational energy mode, and because higher Mach numbers have stronger waves it was in these flows the physics were the clearest. In both cases the effect of vibrational relaxation was limited to temperature fluctuations; there was no significant effect on kinetic energy. It is noted all of the aforementioned works used CO_2 as the working medium.

  In their model Bowersox et al. [26] showed how a vibrational relaxation and turbulence (energy flux) timescale can mathematically communicate, which supports the experimental findings

$$\left(\frac{\delta_{ik}}{\overline{\tau}^{(vib)}_{(n)}} + \frac{\delta_{ik}}{\tau_{\theta^{T(ex)}_{(n)}}} + \tilde{u}_{i,k}\right)\theta^{T(in)}_{(n)k} \approx \tilde{Y}_{(n)}\tau^{T}_{(n)ik}\tilde{e}^{(vib)}_{(n),k} + \frac{\theta^{T(in)}_{(n)i,eq}}{\overline{\tau}^{(vib)}_{(n)}} \tag{2.19}$$

  where $\tau^{(vib)}_{(n)} \approx C_{(n)1}e^{(C_{(n)2/T_1})1/3}/P$, C is the energy flux correlation coefficient

$C_i = \theta_i^T / \sqrt{-\tau_{(i)(i)}^T}\overline{\rho}\overline{(e'')}^2$, θ_i^T is the turbulent energy flux $\theta_i^T \equiv \overline{\rho e'' u_i''}$ (discussed extensively in Chapter 3), and the remainder of lexicon is taken from the conservation equations in Section 2.2.2. Though these timescales were unique to this paper and the simplicity of Equation 2.19 belies the derivation's complexity and assumptions, the point here is to show that one can derive a link between vibrational and turbulence timescales. Indeed, in their paper Bowersox et al. [26] outlines the chain of dependencies which does indeed link their $\tau_{(n)}^{(vib)}$ to the Reynolds shear stress.

Khurshid and Donzis [29] further explored the effect of NEQ on decaying compressible turbulence through DNS simulations. They derived a nondimensional parameter β which combined the degree of initial NEQ and the ratio of the turbulent decay and vibrational and relaxation timescales. This allowed the study of regimes where the flow was vibrationally ($\beta \ll 1$) or mechanically ($\beta \gg 1$) frozen. In the latter case, the results matched those of Neville et al. [85] in that there was little effect of NEQ on the kinetic energy, though the authors attributed this moreso to the lack of NEQ at the outset of their simulations than the energy exchange itself. If the vibrational decay rate exceeded the turbulent time scale, then as the initial amount of NEQ was increased the more rapid its effect on the flow. This effect was identified as a decrease in the flow's kinetic energy; in the same process outlined in Section 2.2.4, the relaxing vibrational energy passed energy into the ro-translational states, which increased the temperature and thereby the viscosity which damped the turbulence. An asymptotic limit for the increase in viscosity as a function of increasing β was identified.

Khurshid and Donzis [29] also described the effect of turbulent fluctuations on the vibrational energy $\langle E_{vib} \rangle$; here angular brackets denoted a volume average. For $\langle E_{vib}^{eq} \rangle$ it was determined that approaching equilibrium $\langle E_{vib} \rangle < \langle E_{vib}^{eq} \rangle$ because equilibrating energy from vibrationally cold regions produced by the turbulent fluctuations required longer timescales than those for vibrationally hot regions because transferring energy from the ro-translational state into the vibrational state lowered the bath temperature, increasing τ_{vib} and decreasing $(E_{vib} - E_{vib}^{eq})$. The turbulent fluctuations have a greater effect on the equilibrium vibrational energy $\langle E_{vib}^{eq} \rangle$ than the vibrational relaxation time constant $\langle \tau_{vib} \rangle$, which Donzis and Maqui [89] traced back to the lag between E_{vib} and E_{vib}^{eq}. In the same paper, Donzis and Maqui [89] also write that for equilibrium ($\tau_v \ll \tau_{turb}$), and especially NEQ ($\tau_v \gg \tau_{turb}$) flows, a greater proportion of the total energy is stored in vibrational modes in the presence of bulk temperature fluctuations than in their absence (turbulent *versus* laminar flow). Put another way, with all other parameters fixed, a turbulent flow will have a higher mean vibrational temperature than a laminar flow.

- Nishihara et al. [90], Nishihara et al. [91], and Nishihara et al. [92] describe the development and characterization of a Mach 5 blowdown wind tunnel at The Ohio State University which uses a combination of pulsed and DC plasmas in the settling chamber to instill vibrational nonequilibrium. The tunnel's run time is $5 - 10$s and stagnation pressure is $50.66 - 101.33$kPa. Gases can be injected downstream of the plasma to act as a vibrational energy sink, furthering the thermal nonequilibrium. Nominal test articles were cylinders. Schlieren imaging and high speed (custom burst-mode laser) *NO* PLIF were used to visu-

alize the flow, and the system's thermodynamics were studied with optical emission spectroscopy, PLIF thermometry (for both rotational and vibrational temperature measurements), and picosecond CARS (best described in [93]). The work was also supported by CFD.

Calculations showed most of the plasma energy was stored in vibrational modes, and that in the absence of a "rapid-relaxer" species (ex.- H_2, H_2O, NO) it was frozen even after passing through the strong bow shock (recall this is a low temperature, low Mach number facility). The later CARS work in [93] showed how plasma power and relaxer species can be used to tailor the degree of nonequilibrium; notably, O_2 had little effect, which was important because the present experiment was conducted in air. Similarly, Nishihara et al. [94] showed how the injection of CO_2 could cause sufficiently fast relaxation to alter the trajectory of a free shear layer. In the settling chamber, theory and measurements showed $T_o = 300 - 400$K and $T_{o(v)}$ up to 2000K while in the test section $T_o = 300$K and $T_o = 500$K (stagnation at cylinder, plasma off and on respectively) and $T_v = 1000$K (freestream, plasma on); the calculated T_v of N_2 was 850K. No detectable change in the freestream ro-translational temperature in the presence of vibrational nonequilibrium was reported. The CARS work in [95], commendably performed at low density, showed there was no vibrational relaxation across a shock, which is expected in a low temperature, density, and Mach number flow. Calculations suggested as much as $50 - 80\%$ of the DC discharge's power went into vibrationally exciting the N_2 molecules, and very little went into its electronic modes; this was mostly confirmed by the CARS measurements in [93]. It was noted sufficient NO was generated by the plasma that weak PLIF was possible even without gas injection. Furthermore, spectroscopy showed between $200 - 300$nm $NO\,\gamma$ bands dominated the signal, and there was evidence of NO_2 chemoluminescence between $400 - 1000$nm.

These works showed that vibrational nonequilibrium is present in blowdown wind tunnels even without intentional excitation. While the temperatures and techniques used to generate the nonequilibrium were greater than what is experienced in the ACE tunnel, the underlying physics persist. The gas should have some vibrational energy near the throat conditions, and it should be mostly frozen in the freestream and through shocks. However, equilibrating the gas by the injection of relaxer species could have a significant impact on the fluid dynamics. If well-tuned to the turbulence, vibrational decay can significantly dampen temperature fluctuations, which matched the findings in [27]. Thus, a link between the current experiment's thermodynamics and turbulence was established, experimentally and mathematically. [26, 7])

2.3 Direct Current Glow Discharges

The review in this section follows from Broslawski [7]. Glow discharges are effective means to generate steady plasmas, which us state of matter wherein an equal balance of electrons, ions, and neutral atoms or molecules maintain quasi-neutrality but permit the passage of electrical current. The physics associated with glow discharges are well understood; e.g. see [96], Rajzer [97], Roth [98]. In a DC application it is convenient to measure Townsend's ionization coefficient $\alpha = \frac{\nu_i}{v_d}$ as opposed to ν_i directly [97]. Here v_d is the drift velocity and α describes the number of ionizing collisions per unit length. Measurements of α over a variety of conditions are reported in [96], but

Townsend provided a useful empirical formula

$$\alpha = AP\exp\left(-\frac{PB}{E}\right) \tag{2.20}$$

A and B are empirical and taken from tabulated experimental observations. Common values for air are, for $\frac{E}{P} = 100 - 800\frac{\text{V}}{\text{cm}\cdot\text{torr}}$, $15\text{cm}^{-1}\cdot\text{torr}^{-1}$ and $365\frac{V}{cm\cdot torr}$ respectively [99]. Despite A and B being empirical constants, under certain assumptions one can ascribe physical meaning to them. Rajzer [97] shows that by assuming every collision is an ionizing event, which is only valid for high $\frac{E}{P}$), given the context of Townsend's empirical formula for α one can write

$$A = (\lambda P)^{-1} = \left(\frac{k_B T}{\sigma}\right)^{-1} \text{ and } B = A\frac{I}{e} \tag{2.21}$$

where λ is the mean free path, I is the ionization energy, and e is unit charge. Thus A and B can be related to the system parameters, though it is noted that the exact agreement can be poor. For example, assuming room temperature, if $A = 15\text{cm}^{-1}\cdot\text{torr}^{-1}$ then $\sigma = 4.554\times10^{-20}\text{m}^2$, which is an order of magnitude away from the $43\times10^{-20}\text{m}^2$ reported in [100]; in this specific case the discrepancy is likely due to different definitions of molecular diameter in addition to the inherent limitation of the empirical model. A and B are dependent on temperature. Surzhikov [101] confirmed the feasibility of glow discharges for fomenting meaningful vibrational nonequilibrium, reasoning that because N_2 relaxation times are high a distinct vibrational mode can exist in a plasma between the electronically excited species and external energy bath. Furthermore, in a hypersonic environment these vibrationally excited molecules can easily convect out of the plasma before they have sufficient time to equilibrate. This effect can only be enhanced as one moves out of the plasma, and all electronically excited molecules and recombining ions relax, distributing themselves across ground electronic state's vibrational levels. Ideally, the goal here is the prediction of the concentration of vibrationally excited N_2 generated by the plasma and blown along the test article. However, one cannot neglect the complexity of the proposed test environment, a hot-wall boundary layer downstream of a plasma and trips. Because of the boundary layer, the number density was a function of the wall-normal coordinate. Estimation of $n(y)$ was complicated by the inclusion of the trips, which could create laminar, turbulent, or transitional boundary layers, as well as strong spanwise variation. A traditional glow discharge is difficult to analyze due to variation in the electric field from the sheaths and in some cases low pressures, but with the electrodes mounted in a flush configuration there were both streamwise and spanwise gradients in E. Finally, the system's thermal kinetics needed to be understood as the flow traveled downstream; just leaving the plasma itself caused electrically excited molecules to relax into a distribution of ro-translational and vibrational levels. Even under ideal circumstances each individual element of this system presented a significant theoretical challenge. Taken together, the problem became overwhelming. In such cases, the best course is often to conduct the experiment and collect enough data to fill in as many blanks as possible. This approach is risky because without any guidance it is easy to design an experiment which provides insufficient data or obfuscates key physics. To that end, here some relevant past work is reviewed which suggested that a meaningful population of vibrationally ex-

cited N_2 could be produced, albeit in a far simpler environment that the final experiment. This was perhaps the best prediction one could make of the proportion of vibrationally excited molecules in the final experiment without performing a dedicated and advanced simulation. Starikovskiy and Aleksandrov [102] commented that self-sustaining glow discharges form above $\frac{E}{N} = 120$Td, so the data suggested that for weakly-ionized air plasmas the majority of the energy is stored in the electronic state of N_2, with strong vibrational excitation in certain regions. The realities of operating in a tripped boundary layer, however, made this approach illustrative but only qualitatively accurate. Petrusev et al. [103] performed a simulation of a quiescent, low-density glow discharge with experimental parameters ($V_{PS} = 2000$V, $R_b = 300$kΩ, $P = 5$Torr, $T^{rot-trans} =$ Room temperature) very similar to those listed here and found a mass fraction of $N_2^{v=1} \approx 20\%$. They further estimated that as much as $60-70\%$ of all electron energy was spent collisionally exciting the vibrational modes of N_2 to any of the 50 vibrational states simulated. This number makes sense because vibrational energy levels are so much farther spaced than rotational ones [104], so a small portion of vibrationally excited molecules can store an outsized amount of energy; only the most energetic electrons can electronically excite or ionize molecules. Storozhev and Surzhikov [105] performed further calculations under the same conditions and found that if one were to sum the number densities of all molecules in the first 47 vibrationally excited levels of ground N_2 then the concentration of vibrationally excited molecules was 62%. That said, in the cathode layer they calculated more energy was lost to electronic modes than vibrational modes, which makes sense as this is where the electrons are the most energetic. Finally, in the proceeding section many authors [105, 103, 101, 106, 107] use $\eta \approx 0.5$ in their simulations of a very similar plasma environment to denote that half of the plasma's power goes into internal excitation, and half to external excitation. Taken together, these results show that a weakly ionized plasma can in fact generate a significant portion of vibrationally excited N_2, even though an exact predication is not offered at this time. ([7])

2.3.1 Foundational Experiment: AFRL/VA Plasma Channel Flat Plate Campaign

The review in this section follows from Broslawski [7]. The review papers by Starikovskiy and Aleksandrov [102], Adamovich et al. [108], and Semenov et al. [109] showed that plasmas are applicable to a variety of fields, and within a given discipline there are often multiple applications for them. For example, within hypersonics plasmas are studied for the external aerodynamics of a reentry vehicle, precombustion in high-speed engines, and active flow control. Here only the most relevant environment is considered, a glow discharge on a flat plate in a hypersonic flow.

An excellent facility for such experimentation was built in a collaboration between Wright State University and Wright-Patterson Air Force Base (AFRL/VA). This facility was described by Shang et al. [110]. It is a standard blow-down hypersonic wind tunnel with a 2D planar nozzle designed for $M = 5$ (nominally 5.15) and a free-jet test section. It runs at $Re = 1.15 \times 10^6/m$. Its stagnation conditions are $T_o = 300$K and $P_o = 10.1325 - 101.325$kPa, and for the nominal condition of $P = 300$Torr its freestream velocity, density, and temperature are $698.4\frac{\text{m}}{\text{s}}$, $0.005\frac{\text{kg}}{\text{m}^3}$, and 51.6K respectively; over the full range of stagnation pressures the freestream number density falls between $n = 3 \times 10^{16} - 3 \times 10^{17}/\text{cm}^3$. The test section is $177.8 \times 228.6 \times 73.4\text{mm}^3$ ($L \times H \times W$) and is lined with optical/instrument access ports. The facility can support Langmuir, Pitot,

static pressure, schlieren, optical emission spectroscopy, and lift/drag force balance measurements. The tunnel is not preheated as liquefaction was not predicted for the run conditions. Compare all of this to the ACE tunnel, summarized in Table 4.1, and the similarities in both design and flow conditions are clear. What sets the AFRL/VA tunnel apart is its construction from solely plastics and ceramics. This allows for the generation of a variety of plasmas (DC or RF glow discharges, see [111]) and the application of magnetic fields anywhere in the facility to study an array of electrohydrodynamic and magnetodynamic effects without any accidental ignition or field distortion. Furthermore, the low number density allows for plasma generation at low voltages and realistic flight altitudes, and the test section's small size aids with the uniform and precise application of magnetic fields. The AFRL/VA tunnel was carefully and purposefully designed to provide a testbed for hypersonic electro- and magnetohydrodynamic experimentation, and it has been put to great use. ([7].)

Of the many problems studied in the AFRL/VA tunnel, those of a spanwise DC glow discharge on a sharp leading edge (half-angle design) were the most pertinent; any work on this geometry including a magnetic field was neglected. As with the facility, the design of the test article was left as generalized as possible so the impact of many different factors could be independently studied. The experimental work was supported by computational efforts. A summary of each of these incremental campaigns is included:

- Menart et al. [112] (2003): Studied the effect of electrode orientation and polarity on surface pressure measurements in between the electrodes. The authors found that the plasma caused a measureable pressure rise in electrode gap, likely due to Joule heating, though the effect of cathode heating could not yet be discounted. Visual observations found spanwise electrodes provided the most predictable results.

- Estevadeordal et al. [113] (2004): Tested different illumination sources for schlieren imaging of a glow discharge in a low-density hypersonic facility. The authors found a continuous LED provided sufficient sensitivity without saturating the camera.

- Shang and Surzhikov [114] (2004): Drift-diffusion simulation of the plasma experiments using $V_{power\,supply} = 1200\text{V}$, $R_b = 12\text{k}\Omega$, and $I = 50 - 100\text{mA}$. This paper provided plots of charged particle number density, current density, electric field, temperature, and Joule heating. For the first time in this series the authors isolated the effect of Joule heating from electrode heating (assumed 600K) and found it was dominant. Heating effects were strongest over the electrodes. This effect was sufficient to cause oblique shocks, especially over the cathode, and alter the boundary layer thickness, causing deviation from leading edge inviscid-viscous leading edge interaction theory [115] (described in Section 4.5.2).

- Menart et al. [116] (2004): Compared Joule and cathode heating by making a plate with an embedded resistance heater and another with spanwise electrodes and using static pressure, Pitot, and thermocouple (not true temperature) measurements to compare their results; further evidence provided with computations. Both heat sources were run at a constant 60W. No correction was offered for the glow discharge's voltage drop across the ballast resistor, so one needed to assume the plasma itself was set to 60W, not the power supply; this

was a recurring issue in the experimental papers reviewed here. The data showed that the plasma approached steady state in approximately $20-40$s while the heater needed 20min; the plasma had a more immediate impact on the flow, and the heater tended to heat up the entire plate as it reached the test condition. Once both heat sources approached their steady state values, they had comparable effects on the flow. As expected, both techniques showed the strongest impact above the cathode/heater. The computations showed the heater was strongly dependent on the plate's thermal properties; this implied cathode heating due to a glow discharge should be similarly affected. In addition to the aforementioned experiments, a Langmuir probe was used to measure the ion number density; as expected [97], the concentration was the highest above the cathode.

- Kimmel et al. [117] (2004): Used Pitot, surface pressure, Langmuir, and total-temperature (uncalibrated) techniques to characterize a 60W (50mA, $1100-1200V$) glow discharge. Note that no ballast resistance was provided, leaving one to assume the 60W was entirely deposited into the flow; this is a recurring issue in the experimental papers reviewed here. The Pitot measurements were able to detect the oblique shock at the cathode, and the static pressure rise scaled roughly linearly with discharge power. The hot plasma thickened the boundary layer, which the authors postulated caused a pressure rise through viscous interaction; the 10% surface pressure rise was equivalent to the jump across an oblique shock from turning the flow an $0.8°$. The authors also studied the return of Pitot pressures to normal values following different plasma ignition durations to study the effect of cathode heating; the recovery time increased from nearly zero seconds for a five-second discharge to over sixty seconds for a forty second discharge, which implied cathode heating was significant and thus could not be discredited as a major source of flow perturbation for lengthy discharges.

- Surzhikov and Shang [106] (2005): A drift-diffusion simulation of the plate. The authors confirmed the model against the theoretical viscous-interaction theory [115]; this theory is described in Section 4.5.2. They then simulated cathode heating on an adiabatic plate and found it produced a strong enough pressure effect to produce a shock, and at excessive heats even separation. Next a glow discharge at $V_{power\,supply} = 1200$V and $R_b = 12\text{k}\Omega$ (the current was left to self-stabilize) was tested and the results were compared to those from the cathode heating; although a modest pressure rise was observed due to heating of the positive column, for the realistic electrode temperatures of 600K cathode heating was the dominant mechanism for flow perturbation. These mechanisms had a stronger affect on viscous-interaction the closer the electrodes were placed to the leading edge.

- Menart et al. [118] (2005): Used load cells to measure effectiveness of plasma for lift and drag control. While there was no effect on drag, a linear relationship was found between plasma power and lift. Due to insufficient information on the circuit, one needed to assume the listed power is spent entirely by the plasma; this is a recurring issue in the experimental papers reviewed here. This result persisted at both positive and negative angles of attack. For a 60W plasma, a 4% change in lift was observed; data was provided up to 230W which yielded a 18% change in lift, but at higher powers the plasma began to constrict.

- Shang et al. [119] (2005): Mostly a review paper, though some new plots such as skin friction and pressure coefficients reinforce the concept that the plasma actuates via pressure, not surface shear. The authors did write that for "a total power supply power" (how this relates to plasma power is unclear) of 60W, the power per unit length of electrode needed to provide an equivalent angle of surface actuation was $18.90\mathrm{W/cm/degree}$.

- Kimmel et al. [120] (2006): Journal article which mostly covered magnetohydrodynamics and reviews past findings; it confirmed the importance of uniform discharges to prevent localized pressure differentials as well as the linear relationship between input power and pressure rise. One novelty was the direct measurement of the copper cathode temperature immediately after the plasma was switched off via an embedded thermocouple. The cathode rose over 100K from below room temperature in as little as five seconds and reached temperatures above 500K after forty seconds of operation at 50mA; steady state was not attained. Temperature sensitive paint showed the ceramic model rose 50K and < 10K at the cathode and anode respectively after 40s of plasma operation.

- Menart et al. [121] (2006): Studied the effect of cathode size and placement using laser displacement. It was found moving the cathode closer to the leading edge and making it larger increased its effectiveness. The current and power never exceeded 24mA and 30W (without ballast resistance, one must gain assume this is the discharge power), and it is remarkable so little power had an effect. The authors note because the required voltage increased as the area and current are decreased, the discharge was likely in the abnormal glow regime.

- Stanfield et al. [122] (2006): Performed spatially resolved optical emission spectroscopy to measure the rotational temperature in the glow discharge. They measured the hottest temperature just above the cathode and a decrease at the cathode surface attributed to heat flux into the copper. The effect of spanwise, streamwise, wall-normal, and temporal gradients were discussed and where possible measured or resolved.

- Bennett et al. [123] (2008): A numerical study of the plasma. The simulated cathode was very large in the streamwise direction, but under this condition a plasma power as low as even 1W was enough to measurably alter the pressure distribution over the plate. Still, below 50W thermal gradients and flow modifications were weak. Of particular interest is the comparison of adiabatic *versus* conducting wall conditions. As expected, the conducting wall had a lower temperature, and thus weaker plasma effects, than the adiabatic case because the energy was being absorbed by the wall and not being directly deposited into the flow.

- Shang et al. [124] (2008): Mostly a review paper; its contents are deferred to the journal article by Shang et al. [125], which will be discussed shortly.

The above works were well-summarized in the journal articles [126, 107, 125]; the lattermost work was the most recent publication, so it was the main source for the present synopsis of the AFRL/VA plasma channel flat plate campaign. The numerical work included the derivation of a drift-diffusion

model for DC glow discharges [127, 128]. This was necessary because quasi-neutral and ambipolar models are generally used above 50Torr [126, 107]. These models are known to fail in plasma sheaths [97], but the freestream plasmas generated in [111, 112] validated their use for calculations of the bulk plasma. The viscous-interaction theory of Hayes and Probstein [115] showed how disturbances at the sharp leading edge of a hypersonic flat plate can have an outsized effect on the boundary layer; additional detail is provided in Section 4.5.2. There are two main mechanisms by which a glow discharge can introduce such a perturbation, Joule and cathode heating. The heat lowers the density and increases the size of the boundary layer, especially above the cathode, which can cause enough flow deflection for an oblique shock to form. This shock is strong enough to be captured by both Pitot [117] and schlieren Shang et al. [124, 125] measurements. Between the two heating mechanisms, no conclusive determination of which is more important was offered and one must assume they complement one another; this was evinced both computationally and numerically [107, 126, 112]. That being said, Shang et al. [129] wrote that Joule heating provides actuation in $\mathcal{O}(1\text{ms})$, three orders of magnitude faster than convective heating. Furthermore, the plot in [111, 129] shows that it takes longer for the cathode to approach its steady state temperature (here $>$ 500K [120]). Experimentation and computation [112, 118, 117, 121] showed that glow discharges are capable of significant flow control solely via pressure forcing (lift), not surface shear (drag). A consistent challenge with the above papers was the interpretation of "plasma power". Glow discharges waste power at their ballast resistor, so the power supply's full power is not delivered to the electrodes; without a complete description of the circuit, assumptions must unfortunately be made in interpreting the data. ([7])

2.4 Hypersonic Second Mode

The review in this section follows from Siddiqui [4]. Boundary layer transition has been the subject of investigation for nearly 80 years. As such, there are numerous definitive texts that describe the mathematical and experimental treatments, e.g., see Morkovin and Reshotko [130], Saric et al. [131], Saric [132], and Mack [133]. The latter is particularly relevant to hypersonic flows.

The current understanding of transition is founded in tracking the growth and breakdown of natural and forced instabilities within a laminar boundary layer. This began with the early work on low-speed instabilities. Schubauer and Skramstad conducted one of the earliest boundary-layer instability experiments that confirmed the presence of Tollmien-Schlichting waves [134]. Smith and Gamberoni [135] and Van Ingen [136] independently found that Tollmien-Schlichting waves undergo amplification of e^N times its initial amplitude leading to transition. The N-factor is thus defined as

$$N = ln(\frac{A}{A_0}) \tag{2.22}$$

where A is the disturbance amplitude at a location and A_0 is its initial amplitude. N ranged from 7.8 - 9 between the two studies. The e^N method for predicting transition works well for 2-D incompressible flows. However, receptivity is not accounted for in most models. Instabilities that are 3-D in nature, like crossflow and Görtler instabilities, are sensitive to small disturbances such

as surface roughness and initial amplitudes. Thus, Morkovin and Reshotko cautioned that the e^N method has to be used carefully for hypersonic flows where 3-D instabilities are the dominant cause of boundary-layer transition [130]. Of relevance to this study is the second mode instability, as this mode was observed downstream of the trips on the thermal non-equilibrium boundary layer experiment. There are several known mechanisms that lead to boundary layer transition from laminar to turbulent flow. Tollmien-Schlichting (T-S) waves are dominant causes of transition for 2-D flows at subsonic speeds, especially for incompressible flows. T-S waves are two-dimensional disturbances that grow in a shear layer and grow in amplitude, eventually causing transition of the boundary layer. At supersonic speeds there is a scalar transport of pressure in the spanwise directions and thus three-dimensional oblique disturbances appear. Mack [133] named these dominant disturbances at supersonic speeds the first-mode disturbances. Mack also found that a different disturbance was dominant at hypersonic speeds, at speeds above Mach 4. The relative Mach number ($\overline{M}$) is defined in terms of the difference between the local mean velocity and the speed of the instability. When $\overline{M}$<1, the solution is elliptic, which is the case for subsonic flows. When $\overline{M}$>1, the solution is hyperbolic and multiple modes exist, these are called Mack or second modes. Physically, the Mack mode disturbances are acoustic waves that reflect inviscidly between the solid wall and the sonic line ($\overline{M}$=1) in the boundary layer. Thus the sonic line acts as a wave guide. The first linear-stability mode is the most dominant instability at low Mach number. The Mack mode appears when M = 2.2, and it is a two-dimensional (streamwise) inviscid instability. Above Mach 4, the Mack mode is the most unstable instability in the boundary layer. Mack-mode waves have a wavelength dependent on the boundary-layer height as the sonic line location is dependent on the boundary-layer height. In general, $\lambda \sim 2\delta$. The different modes that lead to transition are separable in during the early small linear grown phases. However, as they grow, they can interact with each other. ([4])

2.4.1 Foundational Experiments: Recent Studies in the Texas A&M University M6QT

Kendall was the first to document the Mack-mode instability on a 5° cone at various Mach numbers between 1.6 and 8.5 [137]. He confirmed the Mack-mode instability dominance at higher Mach numbers [138]. These experiments were accomplished in conventional wind tunnels, where the freestream disturbance levels can be an order of magnitude (or more) higher that what is seen in flight. The disturbances are due to noise radiated from the tunnel turbulent boundary layers into the flow [139][140]. Mack noticed discrepancies between transition predictions from theory and actual transition locations in experiments and concluded the freestream disturbances may be the cause [141][142]. Schneider has written extensively on the need for quiet wind tunnel facilities for stability experiments [143][144]. Lachowicz conducted experiments over a straight cone and flared cone with interchangable tips in a NASA Langley Mach 6 quiet tunnel (M6QT now operational at Texas A&M University) and showed that the Mack mode was the dominant cause of transition. He also showed that increasing nosetip bluntness stabilized the boundary layer [145]. Lachowicz et al. studied a flared cone and showed that the amplification factors of the Mack-mode instability were within 5% of the predictions from LST [146]. The same flared cone was used by Doggett at an angle of attack and the Mack mode was observed to be destabilized on the leeward side and stabilized on the windward side [147]. Hofferth studied Mack-mode disturbances on the

93-10 cone in the M6QT [148] [149]. The 93-10 cone had a 254 mm (10 inch) straight fore section with a 5° half-angle. The straight section is follwed by a 254 mm (10 inch) flared section with a radius of curvature of 2.36 m (93.071 inch) for a total length of 508 mm (20 inch). This model had a detachable tip so the tip radius can be varied. The development of the Mack-mode instability was studied at a unit Reynolds number of $10\text{x}10^6$ /m using hot-wire anemometry and focusing schlieren. The Mack-mode instability was observed at 250 kHz < f_0 <310 kHz and exhibited substantial growth on the aft 20% of the cone. Focused schlieren data showed two additional harmonics of the Mack mode at $2f_0$ and $3f_0$. A bispectral analysis was used to identify the nonlinear interactions responsible for the development of these harmonics [150]. A sharp-tip 7° right-circular cone was designed by Craig to be used in the M6QT to study the crossflow instability [151]. The cone had a sharp detachable tip of length 155 mm (6.1 inch) and the total length is 430 mm (16.92 inch). The model was yawed 5.6° to induce crossflow on the surface. IR thermography was used to visualise the crossflow streaks and detect transition location. Hot-wire anemometry was used to map the mean flow and showed the structure of the crossflow vortices. A traveling crossflow wave was observed in addition to the stationary crossflow wave in a frequency band centered around 35 kHz. The boundary layer was not observed to transition and so distributed roughness was added to the tip. This caused the boundary layer to transition but not by exciting the crossflow instability, it appeared to be a different instability mechanism. ([4])

2.5 Mach Stems and Shock Turbulence Interaction

This review follows from Bryan et al. [52], Dean et al. [8], Dean [11], and Dean et al. [16]. Simulation of the complex flow field produced by a Mach reflection in high enthalpy, hypersonic flow is of great use to the academic community for studying thermal and chemical non-equilibrium. Whether a regular reflection or a Mach reflection, results from the intersection of two oblique shocks (or an oblique shock and a symmetry plane) in steady flow rely heavily on the incident oblique shock angle, α. If $\alpha < \alpha_N$ then a two-shock configuration will occur resulting in a regular reflection. On the other hand, if $\alpha > \alpha_D$ then a three-shock configuration will occur resulting in a Mach stem, also called a Mach reflection. Note that α_N is the von Neumann criterion and α_D is the detachment criterion. At sufficiently high enthalpies, extreme temperatures and chemical non-equilibrium are produced downstream of the normal shock. The flow downstream of the two oblique shocks does not get as hot. Therefore, the shear layer produced at the triple point has thermal and chemical non-equilibrium across it. Furthermore, a dual solution domain where either a regular reflection or Mach reflection exists when $\alpha_N \leq \alpha \leq \alpha_D$. Ivanov *et al.* [152] makes an important distinction that at the lower limit of the dual solution domain where $\alpha = \alpha_N$, then the pressure behind the Mach stem is equal to the pressure behind the reflected oblique shock. Ivanov *et al.* [152] further states that for $\alpha > \alpha_D$ a Mach stem must be present because the reflected oblique shock wave is not strong enough to turn the flow back to parallel with the symmetry plane. Azevedo *et al.* [153] sought to estimate the Mach stem height as a function of the body geometry and freestream conditions, but the predictions were often lower than the values obtained experimentally. Experiments from Dor *et al.* [154] determined that the wedge trailing edge angle had no effect on the location of the triple point or the height of the Mach stem. Unlike many of the experiments relating to Mach stems, Sharma *et al.* [155] focused on high enthalpy experi-

ments which significantly increased the amount of chemical dissociation and vibrational excitation present. Sharma *et al.* [155] utilized an expansion tube that could obtain stagnation enthalpies of $8-10$ MJ/kg and Mach numbers of $3-7.1$ paired with asymmetric wedges. The use of asymmetric wedges allowed for the comparison of triple points, shock patterns, chemical reactions, molecular dissociations, and shear layers. Burtschell *et al.* [156] utilized a two symmetrical wedge domain, a five species air model, and a freestream Mach number of 7 to study the shock patterns in hypersonic non-equilibrium flow. Burtschell *et al.* [156] discussed that a wedge angle that is outside the dual solution domain for a non-reacting gas, may lie in the dual solution domain once vibrational and chemical kinetics are considered. Both Li *et al.* [157] and Burtschell *et al.* [156] examined a phenomenon when simulating Mach stems in flow that is in thermal and chemical non-equilibrium. This phenomenon pertained to what prompts the formation of a regular reflection versus a Mach reflection computationally. If the flow around the wedge was uniform to the inlet conditions then a regular reflection would be the computational solution; however, if the flow around the wedge had zero velocity initially then a Mach reflection would be the computational solution [156, 157]. Grasso *et al.* [158] studied the crucial role thermal and chemical relaxations have on shock patterns for flow in non-equilibrium. Trotsyuk *et al.* [159] simulated steady supersonic flows with a combustible homogeneous air model and discovered that the Mach stem's axial location is not stationary and in reality, oscillates about an equilibrium point. Finally, McGilvray *et al.* [160] performed simulations to validate the facility and obtained values for variables that cannot be accurately obtained from the experiments conducted by Sharma *et al.* [155]. McGilvray *et al.* [160] also hypothesized that the discrepancies between the computational and experimental results could be caused by air contamination within the impulse facility. The air contaminants could be caused by several factors varying from particulates from the burst diaphragms [160] to other molecules that aren't strictly O_2 and N_2 based as simulated in their 5 species chemistry model. ([52])

Classical investigations of STI typically employ linear interaction analysis (LIA) first attributed to Ribner [34, 35, 161] and Moore [162]. A detailed background review of STI studies is provided in McManamen et al. [3]; the summary here follows from this manuscript. While linearized approaches inherently lose turbulence information, LIA methods have been accepted, particularly in the cases of strong shock waves and weak turbulence where the assumptions most closely match the environment. Attempts have also been made to apply rapid distortion theory (RDT) to the shock problem [163, 164]. With the rise of modern computation abilities, contemporary works have mainly transitioned to large eddy simulaiton (LES) and direct numerical simulation (DNS) approaches. These modern approaches have observed divergence from classic LIA solutions, particularly as Mach numbers of interest have increased. It has been shown [165, 166], however, that for small turbulent Mach number (M_t) DNS solutions converge to LIA. Lee et al. [167] observed that increasing M_t leads to a discrepancy in turbulent kinetic energy (TKE) enhancement, which may account for some of the disagreement between these approaches. Donzis [32] introduced a scaling parameter as the ratio of laminar shock thickness to Kolmogorov length scale, which allowed for easy categorization of shock-turbulence interactions. It was believed that some of the disparity between differing studies was a result of incomplete comparison, influencing variables typically left out in previous works (M_t, Re_λ) were captured in the parameter for a more clear indication of behavior. Chen and Donzis [168] was able to collapse all available data of amplification

factors, including simulations that stray from classic LIA assumptions. Another factor in simulations, separating experimental and computational results, is likely the influence of upstream correlations between Kovasznay modes [169, 170, 171]. Mahesh et al. [170] suggested that negative correlation between upstream velocity and temperature fluctuations would increase amplification of TKE as well as vortical and thermodynamic fluctuations across the shock wave. The majority of experimental works in canonical STI have been studied in shock tube facilities, observing decaying turbulent fields interacting with traveling shock waves. Measurements are typically made with the use of hot-wires and pressure transducers and the authors report significant amplification of turbulent intensities as well as length and time scales [172, 173, 174, 175, 176, 177, 178]. These results have shown moderate agreement with theory, though some limitations exist in these comparisons due to the experimental conditions and unknowns. Shadography, schlieren, and speckle photography [179, 180, 181] have been performed as well, though the results are rather limited and high errors have been reported. A few studies have been performed observing STI for a stationary shock wave using the laser Doppler velocimetry (LDV) technique in conventional wind tunnel facilities [182, 183]. It was determined in both cases, however, that the LDV was unable to fully capture the turbulent motion and thus was not sufficient for STI investigation. ([3])

3. MODEL DERIVATION

3.1 Preamble

The descriptions presented in this document were drawn fromBowersox et al. [26], Bowersox [22], and Broslawski [7]. The original references are also cited in the subsequent text.

Due simplicity and reasonable accuracy in the wall-normal direction, the gradient diffusion approach for calculating turbulent heat flux q_i^T in RANS solvers has become the standard White [48], Schetz and Bowersox [50]. Recall that it assumes one knows a turbulent Prandtl number (Pr_t) that can capture the physics of the turbulent heat flux. For many applications, it is indeed is sufficient to take $Pr_t = 0.9$. White [48], for example, made this argument by studying experimental data from Blackwell [184] and neglecting the measured deviation in Pr_t near the wall; the reasoning for the latter assumption was that most turbulence is dissipated in the viscous sublayer near the wall, so modest inaccuracies in Pr_t are inconsequential. Bowersox [22] analyzed both experimental and DNS data to show that this approach leads to inaccuracy in the estimation of the temperature profiles for high Mach numbers. A DNS replication of an experiment of a flat plate, cold wall boundary layer at $M = [11, 14]$ by Huang et al. [24] illustrated these discrepancies clearly (Figure 3.1), especially in streamwise predictions. Launder [185] argued the use of eddy viscosity and wall functions to capture the near wall convective heat transfer in high Reynolds number flows is an inferior modeling method to second moment turbulent energy flux closures. These inaccuracies prompted the derivation of a novel model for the turbulent heat flux. Building on earlier efforts Daly and Harlow [186], Launder [185], Bowersox provided a more formalized "algebraic energy flux" (AEF) model Bowersox [22]. These seminal efforts provided the groundwork for the current AEF model and its extension to high speed gaseous shear flows. A key advantage of the algebraic model includes explicit expressions for all three heat flux components. However, the model is explicitly dependent on the Reynolds stress tensor. In their original paper [22], Bowersox used a classical algebraic eddy viscosity model for the Reynolds shear stress with DNS based correlations to recover realistic axial stresses that the Boussinesq approximation cannot directly provide. In early testing, up to 20% improvements in the temperature profile were observed over the constant Pr_t model. The comparisons in Poggie [23], Huang et al. [24] abet these findings. Bowersox also examined the relationship between the AEF and the turbulent Prandtl number, which resulted in a simple near wall correction for the transverse component. However, this model remains beholden to the key issues behind the Boussinesq approximation.

This review expounds on our [26, 22] papers and the subsequent publications by Poggie [23] and Huang et al. [24]. The process will start with the governing equations and proceed all the way to implementation of the model in a 2D compressible boundary layer. Its contents were published in Broslawski et al. [25], and much of the same analysis is included here, but additional detail is provided in the derivation's steps.

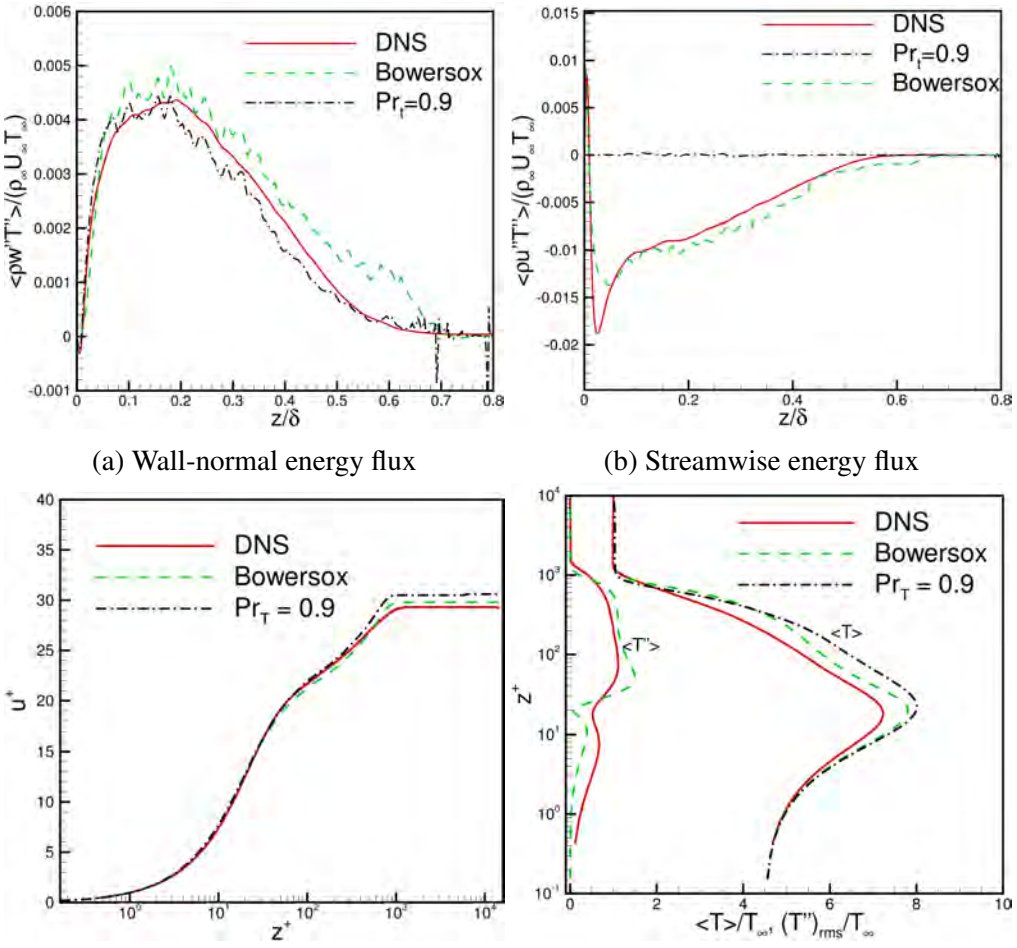

(a) Wall-normal energy flux

(b) Streamwise energy flux

(c) Wall-normal velocity profile

(d) Wall-normal temperature profile

Figure 3.1: Comparison of AEF, constant Pr_t, and DNS replication of a cold-wall, Mach 11 TBL over a flat plate; figures taken with permission from Huang et al. [24]

.

3.2 Governing Equations

The derivation begins by defining the governing equations for mass, momentum, and internal energy for a three-dimensional, compressible, viscous flow. The conservation (Eulerian) form:

$$Mass : \rho_{,t} + (\rho u_k)_{,k} = 0 \tag{3.1}$$

$$Momentum : (\rho u_i)_{,t} + (\rho u_i u_k)_{,k} = -P_{,i} + \tau_{ik,k} \tag{3.2}$$

$$Energy : (\rho e)_{,t} + (\rho e u_k)_{,k} = -q_{k,k} + \tau_{kl} u_{l,k} - P u_{k,k} \tag{3.3}$$

The nonconservative (Lagrangian) form is supplied in the same source:

$$Mass : \rho_{,t} + u_k \rho_{,k} + \rho u_{k,k} = 0 \tag{3.4}$$

$$Momentum : \rho u_{i,t} + \rho u_{i,k} u_k = -P_{,i} + \tau_{ik,k} \tag{3.5}$$

$$Energy : \rho e_{,t} + \rho e_{,k} u_k = -q_{k,k} + \tau_{kl} u_{l,k} - P u_{k,k} \tag{3.6}$$

In these equations, all body forces have been neglected, the heat flux is defined by Fourier's law $q_k = -kT_{,k}$, the shear stress tensor is $\tau_{ij} = \mu\left(u_{i,j} + u_{j,i}\right) + \delta_{ij}\lambda u_{k,k}$, and e represents the fluid element's internal energy. ([22, 7])

3.3 Turbulent Transport Equations

One can use the conservation equations to derive the exact turbulent energy transport equations. These equations can then be simplified via progressive assumptions to a form amenable to algebraic modeling. The process to produce such an equation follows a predictable pattern, so while as many as nine different transport equations will be needed, only those for the energy flux $\theta_i^T = \overline{\rho e'' u_i''}$, kinetic energy $k^T = \frac{1}{2}\overline{\rho u_i'' u_i''}$ (the diagonal of the turbulent Reynolds stress $\tau_{ij}^T = -\overline{\rho u_i'' u_j''}$), energy variance $\eta^T = \frac{1}{2}\overline{\rho e''^2}$, Favre-fluctuating velocity $\overline{\rho} \overline{u_i''}$ and Favre-fluctuating energy $\overline{\rho} \overline{e''}$ will be derived here. The steps are sufficiently generalized to be applicable to any subsequent transport equation one may need, and enough detail is included to allow for accurate reproduction of the final results shown; as an additional reference, the process for deriving transport equations in the manner shown here was illustrated by Cebeci and Smith [43] and Liou and Shih [187]. Here the most attention is paid to deriving $\frac{D\theta_i^T}{Dt} = \theta_{i,t}^T + (\theta_i^T \tilde{u}_k)_{,k}$, with the goal of expanding on the derivation in [22], as it is the most relevant to the final model. Clarifying the simplifying assumptions and limitations was necessary to allow for further refinement. ([22, 7])

3.3.1 Turbulent Energy Flux Transport Equation

Begin by taking the moment of the desired conservation equations; for θ_i^T, one must take the moment of the momentum (3.2) and energy (3.3) conservation equations, $e \cdot Momentum + u \cdot Energy$.

$$e\left[(\rho u_i)_{,t} + (\rho u_i u_k)_{,k} = -P_{,i} + \tau_{ik,k}\right] + u_i\left[(\rho e)_{,t} + (\rho e u_k)_{,k} = -q_{k,k} + \tau_{kl} u_{l,k} - P u_{k,k}\right] \tag{3.7}$$

$$e(\rho u_i)_{,t} + e(\rho u_i u_k)_{,k} + u_i(\rho e)_{,t} + u_i(\rho e u_k)_{,k} = -eP_{,i} + e\tau_{ik,k} - u_i q_{k,k} + u_i \tau_{kl} u_{l,k} - u_i P u_{k,k} \tag{3.8}$$

The left hand side can be simplified using the Multiplication Rule and mass conservation equation (3.1).

$$(\rho u_i e)_{,t} + (\rho u_i e u_k)_{,k} = -eP_{,i} + e\tau_{ik,k} - u_i q_{k,k} + u_i \tau_{kl} u_{l,k} - u_i P u_{k,k} \tag{3.9}$$

Now expand the velocity and energy terms with Favre [188] averaging ($X = \tilde{X} + X''$) and the shear stress with Reynolds averaging ($Y = \overline{Y} + Y'$). Because $\overline{\rho X''} = 0$ and $\overline{Y'} = 0$ the application of each expansion is strategic; depending on the presence of density in a term's coefficients it can be advantageous to perform one expansion over the other. Adopting the notation of Cebeci and Smith

[43], the approach taken here is as follows:

$$\begin{aligned}
&(\rho(\tilde{u}_i+u_i'')(\tilde{e}+e''))_{,t}+(\rho(\tilde{u}_i+u_i'')(\tilde{e}+e'')(\tilde{u}_k+u_k''))_{,k}= \\
&-(\tilde{e}+e'')(\overline{P}_{,i}+P'_{,i})-(\tilde{u}_i+u_i'')(\overline{P}+P')(\tilde{u}_k+u_k'')_{,k}-(\tilde{u}_i+u_i'')q_{k,k} \\
&+(\tilde{e}+e'')(\overline{\tau}_{ik}+\tau'_{ik})_{,k}+(\tilde{u}_i+u_i'')(\overline{\tau}_{kl}+\tau'_{kl})(\tilde{u}_l+u_l'')_{,k}
\end{aligned} \tag{3.10}$$

Perform all distributions, then Reynolds average and simplify the result to yield:

$$\begin{aligned}
&(\overline{\rho}\tilde{u}_i\tilde{e}+\overline{\rho u_i''e''})_{,t}+(\overline{\rho}\tilde{u}_i\tilde{e}\tilde{u}_k+\tilde{u}_k\overline{\rho u_i''e''}+\tilde{u}_i\overline{\rho e''u_k''}+\tilde{e}\overline{\rho u_i''u_k''}+\overline{\rho u_i''e''u_k''})_{,k}= \\
&-\tilde{e}\overline{P}_{,i}-\overline{e''}\,\overline{P}_{,i}-\overline{e''P'_{,i}}-\tilde{u}_i\overline{q_{k,k}}-\overline{u_i''q_{k,k}}+\tilde{e}\,\overline{\tau}_{ik,k}+\overline{\tau}_{ik,k}\overline{e''}+\overline{e''\tau'_{ik,k}} \\
&-\tilde{u}_i\overline{P}\tilde{u}_{k,k}-\overline{u_i''}\,\overline{P}\tilde{u}_{k,k}-\overline{u_i''P'}\tilde{u}_{k,k}-\tilde{u}_i\overline{P}\,\overline{u_{k,k}''}-\tilde{u}_i\overline{P'u_{k,k}''}-\overline{u_i''u_{k,k}''}\,\overline{P}-\overline{u_i''P'u_{k,k}''} \\
&+\tilde{u}_i\tilde{u}_{l,k}\overline{\tau}_{kl}+\overline{\tau}_{kl}\tilde{u}_{l,k}\overline{u_i''}+\tilde{u}_{l,k}\overline{u_i''\tau'_{kl}}+\tilde{u}_i\overline{\tau}_{kl}\overline{u_{l,k}''}+\tilde{u}_i\overline{\tau'_{kl}u_{l,k}''}+\overline{\tau}_{kl}\overline{u_i''u_{l,k}''}+\overline{u_i''\tau'_{kl}u_{l,k}''}
\end{aligned} \tag{3.11}$$

Repeat this process by taking mean moments of the Favre averaged momentum and energy equations to yield:

$$\begin{aligned}
&(\overline{\rho}\tilde{e}\tilde{u}_i)_{,t}+\tilde{u}_i(\overline{\rho e''u_k''})_{,k}+(\overline{\rho}\tilde{u}_i\tilde{u}_k\tilde{e})_{,k}=-\tilde{e}\overline{P}_{,i}+\tilde{e}\,\overline{\tau}_{ik,k}-\tilde{e}(\overline{\rho u_i''u_k''})_{,k} \\
&-\tilde{u}_i\overline{q_{k,k}}+\tilde{u}_i\overline{\tau}_{kl}\tilde{u}_{l,k}+\tilde{u}_i\overline{\tau}_{kl}\overline{u_{l,k}''}+\tilde{u}_i\overline{\tau'_{kl}u_{l,k}''}-\tilde{u}_i\overline{P}\tilde{u}_{k,k}-\tilde{u}_i\overline{P}\,\overline{u_{k,k}''}-\tilde{u}_i\overline{P'u_{k,k}''}
\end{aligned} \tag{3.12}$$

In order to derive the mean energy flux of the fluctuations transport equation, subtract the mean equation (3.12) from Equation (3.11) to give

$$\begin{aligned}
&(\overline{\rho u_i''e''})_{,t}+\tilde{u}_{i,k}\overline{\rho e''u_k''}+(\tilde{u}_k\overline{\rho u_i''e''}+\tilde{e}\overline{\rho u_i''u_k''}+\overline{\rho u_i''e''u_k''})_{,k}=\tilde{e}(\overline{\rho u_i''u_k''})_{,k} \\
&-\overline{e''}\,\overline{P}_{,i}-\overline{e''P'_{,i}}-\overline{u_i''q_{k,k}}-\overline{u_i''}\,\overline{P}\tilde{u}_{k,k}-\overline{u_i''P'}\tilde{u}_{k,k}-\overline{u_i''u_{k,k}''}\,\overline{P}-\overline{u_i''P'u_{k,k}''} \\
&+\overline{\tau}_{kl}\tilde{u}_{l,k}\overline{u_i''}+\overline{\tau}_{ik,k}\overline{e''}+\overline{e''\tau'_{ik,k}}+\tilde{u}_{l,k}\overline{u_i''\tau'_{kl}}+\overline{\tau}_{kl}\overline{u_i''u_{l,k}''}+\overline{u_i''\tau'_{kl}u_{l,k}''}
\end{aligned} \tag{3.13}$$

The left hand side can be simplified by using the material derivative, as well as with the Multiplication Rule $-(\overline{\rho u_i''u_k''})\tilde{e}_{,k}=-(\tilde{e}\overline{\rho u_i''u_k''})_{,k}+\tilde{e}(\overline{\rho u_i''u_k''})_{,k}$. The Multiplication Rule can also be used to write $\overline{e''P'_{,i}}=\left(\overline{e''P'}\right)_{,i}-\overline{e''_{,i}P'}$; this step is not intuitive, but it will be seen the result allows for simplification in Section 3.4.

$$\begin{aligned}
&\frac{D\theta_i^T}{Dt}=-\tilde{u}_{i,k}\theta_k^T+\tilde{e}_{,k}\tau_{ik}^T-\left(\overline{\rho u_i''e''u_k''}\right)_{,k}-\overline{e''}\,\overline{P}_{,i}-\left(\overline{e''P'}\right)_{,i}+\overline{e''_{,i}P'}-\overline{u_i''q_{k,k}}-\overline{u_i''}\,\overline{P}\tilde{u}_{k,k}-\overline{u_i''P'}\tilde{u}_{k,k} \\
&-\overline{u_i''u_{k,k}''}\,\overline{P}-\overline{u_i''P'u_{k,k}''}+\overline{\tau}_{kl}\tilde{u}_{l,k}\overline{u_i''}+\overline{\tau}_{ik,k}\overline{e''}+\overline{e''\tau'_{ik,k}}+\tilde{u}_{l,k}\overline{u_i''\tau'_{kl}}+\overline{\tau}_{kl}\overline{u_i''u_{l,k}''}+\overline{u_i''\tau'_{kl}u_{l,k}''}
\end{aligned} \tag{3.14}$$

For now all that remains is to group the transport/diffusion (defined here as $\overline{X_i''}_{,i}$ or $\overline{Y'}_{,i}$), dissipation (τ), triple correlation ($X''Y''Z''$ or $X'Y'Z'$), and molecular (q) terms into a dummy variable $\overline{\rho}\xi_i$. With this, the transport equation is of the form shown by [26, 22]. ([26, 22, 7])

$$\frac{D\theta_i^T}{Dt}=-\tilde{u}_{i,k}\theta_k^T+\tilde{e}_{,k}\tau_{ik}^T-\overline{e''}\,\overline{P}_{,i}+\overline{e''_{,i}P'}-\left[\overline{u_i''}\,\overline{P}+\overline{u_i''P'}\right]\tilde{u}_{k,k}-\overline{u_i''u_{k,k}''}\,\overline{P}+\overline{\rho}\xi_i \tag{3.15}$$

3.3.2 Turbulent Kinetic Energy Flux Transport Equation

The mean equation is similarly derived; see Cebeci and Smith [43]. The resulting equation is given by:

$$\frac{Dk^T}{Dt} = -\frac{1}{2}(\overline{\rho u_i'' u_i'' u_k''})_{,k} - \overline{u_i''}\,\overline{P}_{,i} - \overline{u_i'' P'_{,i}} + \overline{u_i''}\,\overline{\tau}_{ik,k} + \overline{u_i'' \tau'_{ik,k}} + \tilde{u}_{i,k}\tau^T_{ik} \tag{3.16}$$

3.3.3 Turbulent Energy Variance Transport Equation

The turbulent energy variance equation is similarly derived by taking the moment of the conservation of energy (3.3) with itself according to $e*(Energy)+e*(Energy)$. The result expression is given by:

$$\begin{aligned}\frac{D\eta^T}{Dt} &= -\tilde{e}_{,k}\theta_i^T - \frac{1}{2}(\overline{\rho e''^2 u_k''})_{,k} - \overline{e'' q_{k,k}}... \\ &+ \overline{e''}\overline{\tau}_{kl}\overline{u}_{l,k} + \overline{e''\tau'_{kl}}\overline{u}_{l,k} + \overline{\tau}_{kl}\overline{e''u''_{l,k}} + \overline{e''\tau'_{kl}u''_{l,k}} - \overline{e''}\,\overline{P}\tilde{u}_{k,k} - \tilde{u}_{k,k}\overline{e''P'} - \overline{P}\,\overline{e''u''_{k,k}} - \overline{e''P'u''_{k,k}}\end{aligned} \tag{3.17}$$

3.3.4 Favre-Fluctuating Velocity Transport Equation

The mean Favre velocity fluctuation equation is derived following Liou and Shih [187]. The first step is begin with the nonconservative form of the momentum equation

$$u_{i,t} + u_k u_{i,k} = \frac{1}{\rho}\left(\tau_{ik,k} - P_{,i}\right) \tag{3.18}$$

A linearized Taylor series expansion terms is applied to the density term: $\rho^{-1} \approx \overline{\rho}^{-1}\left(1 - \frac{\rho'}{\overline{\rho}}\right)$. Note this is only acceptable when $\frac{\rho'}{\overline{\rho}} < 1$. With this the conservation equation becomes

$$\overline{\rho}\tilde{u}_{i,t} + \overline{\rho}\overline{u''_{i,t}} + \overline{\rho}\tilde{u}_k\tilde{u}_{i,k} + \overline{\rho}\tilde{u}_k\overline{u''_{i,k}} + \overline{\rho}\overline{u''_k}\tilde{u}_{i,k} + \overline{\rho}\overline{u''_k u''_{i,k}} = \overline{\tau}_{ik,k} - \overline{P}_{,i} - \frac{1}{\overline{\rho}}\left(\overline{\rho'\tau'_{ik,k}} - \overline{\rho' P'_{,i}}\right) \tag{3.19}$$

Repeating for the mean nonconservative form of the momentum equation and subtracting from 3.19 provides:

$$\frac{D\overline{\rho}\overline{u''_i}}{Dt} = -\overline{\rho}\overline{u''_k}\tilde{u}_{i,k} - \overline{\rho}\overline{u''_k u''_{i,k}} - \frac{1}{\overline{\rho}}\left(\overline{\rho'\tau'_{ik,k}} - \overline{\rho' P'_{,i}}\right) - \tau^T_{ik,k} \tag{3.20}$$

The preceding equation can now be simplified. Firt group diffusion and triple correlation terms into D_{ik}. Next, expand $\tau^T_{ik,k} = -\left(\overline{\rho}\overline{u''_i u''_k}\right)_{,k} - \left(\overline{\rho' u''_i u''_k}\right)_{,k}$, then from the Chain Rule, $\tau^T_{ik,k} = -\overline{\rho}\left(\overline{u''_i u''_k}\right)_{,k} - \overline{\rho}_{,k}\overline{u''_i u''_k} - \left(\overline{\rho' u''_i u''_k}\right)_{,k} = -\overline{\rho}_{,k}\overline{u''_i u''_k} + D_{ik}$. Multiplying by $\frac{\overline{\rho}}{\overline{\rho}}$, this becomes $-\overline{\rho}_{,k}\frac{\overline{\rho u''_i u''_k}}{\overline{\rho}} + D_{ik} = -\overline{\rho}_{,k}\frac{\left(\overline{\rho u''_i u''_k} - \overline{\rho' u''_i u''_k}\right)}{\overline{\rho}} + D_{ik} = -\overline{\rho}_{,k}\frac{\left(\overline{\rho u''_i u''_k}\right)}{\overline{\rho}} + D_{ik}$. Therefore

$$\tau^T_{ik,k} = \frac{\overline{\rho}_{,k}\tau^T_{ik}}{\overline{\rho}} + D_{ik} \tag{3.21}$$

Substituting this result: ([22, 7])

$$\frac{D\overline{\rho}\overline{u_i''}}{Dt} = -\overline{\rho}\overline{u_k''}\tilde{u}_{i,k} - \overline{\rho}\overline{u_k''u_{i,k}''} - \frac{1}{\overline{\rho}}\left(\overline{\rho'\tau'_{ik,k}} - \overline{\rho'P'_{,i}} + \overline{\rho}_{,k}\tau^T_{ik}\right) + D_{ik} \tag{3.22}$$

3.3.5 Favre-Fluctuating Energy Transport Equation

The mean Favre fluctuation energy equation is similarly derived. The resulting expression is

$$\begin{aligned}\frac{D\overline{\rho}\overline{e''}}{Dt} &= \frac{1}{\overline{\rho}}\left(\overline{\rho' q'_{k,k}}\right) + \theta^T_{k,k} - \overline{\rho}\overline{u_k''}\tilde{e}_{,k} - \overline{\rho}\overline{u_k''e''_{,k}} \\ &- \frac{1}{\overline{\rho}}\left(\overline{\tau}_{kl}\overline{\rho' u''_{l,k}} + \overline{\rho'\tau'_{kl}}\tilde{u}_{l,k} + \overline{\rho'\tau'_{kl}u''_{l,k}} - \overline{P}\,\overline{\rho' u''_{k,k}} - \overline{\rho'P'}\tilde{u}_{k,k} - \overline{\rho'P'u''_{k,k}}\right)\end{aligned} \tag{3.23}$$

From the Multiplication Rule $\theta^T_{k,k} = \overline{\rho_{,k}e''u_k''} + \overline{\rho e''_{,k}u_k''} + \overline{\rho e''u''_{k,k}}$, which to second-order, simplifies to $\theta^T_{k,k} - \overline{\rho}\overline{e''_{,k}u_k''} = \theta^T_k\frac{\overline{\rho}_{,k}}{\overline{\rho}} + \overline{\rho}\overline{e''u''_{k,k}}$. With this

$$\begin{aligned}\frac{D\overline{\rho}\overline{e''}}{Dt} &= \frac{1}{\overline{\rho}}\left(\overline{\rho' q'_{k,k}}\right) + \theta^T_k\frac{\overline{\rho}_{,k}}{\overline{\rho}} + \overline{\rho}\overline{e''u''_{k,k}} - \overline{\rho}\overline{u_k''}\tilde{e}_{,k} \\ &- \frac{1}{\overline{\rho}}\left(\overline{\tau}_{kl}\overline{\rho' u''_{l,k}} + \overline{\rho'\tau'_{kl}}\tilde{u}_{l,k} + \overline{\rho'\tau'_{kl}u''_{l,k}} - \overline{P}\,\overline{\rho' u''_{k,k}} - \overline{\rho'P'}\tilde{u}_{k,k} - \overline{\rho'P'u''_{k,k}}\right)\end{aligned} \tag{3.24}$$

Finally, group the third order, molecular ($q_{k,k}$) and viscous (τ_{kl}) terms into the dummy variable M_{kl} to produce the final result. ([22, 7])

$$\frac{D\overline{\rho}\overline{e''}}{Dt} = \theta^T_k\frac{\overline{\rho}_{,k}}{\overline{\rho}} + \overline{\rho}\overline{e''u''_{k,k}} - \overline{\rho}\overline{u_k''}\tilde{e}_{,k} + \frac{1}{\overline{\rho}}\left(\overline{P}\,\overline{\rho' u''_{k,k}} + \overline{\rho'P'}\tilde{u}_{k,k}\right) + M_{kl} \tag{3.25}$$

3.4 Model Simplifications

A combination of dilatation, equation of state, and incompressible pressure scrambling models are derived and applied to Equation 3.15 to allow it to be algebratized and solved numerically. The derivation for each is shown below. The end result is closure, an equation written predominantly in terms of the turbulent energy flux (to be solved for) and Reynolds stress and mean parameters (known). The same simplifications are also applied to Equations 3.22 and 3.25 at this time. Additionally, it is noted that the terms $\overline{e''}\,\overline{P}_{,i}$ and $\overline{\rho}\xi_i$ will be addressed in later sections but will ultimately be removed.

- Turbulent Energy Flux Transport Equation

$$\frac{D\theta^T_i}{Dt} = -\tilde{u}_{i,k}\theta^T_k + \tilde{e}_{,k}\tau^T_{ik} - \overline{e''}\,\overline{P}_{,i} + \overline{e''_{,i}P'} - \left[\overline{u_i''}\,\overline{P} + \overline{u_i''P'}\right]\tilde{u}_{k,k} - \overline{u_i''u''_{k,k}}\,\overline{P} + \overline{\rho}\xi_i$$

The fourth term on the right hand side is removed by Equation 3.62, the bracketed terms modeled by Equation 3.61, and the seventh term modified according to Equation 3.37: $-\overline{u_i''u''_{k,k}}\,\overline{P} = -\overline{P}\frac{\overline{\rho}\overline{u_i''u''_{k,k}}}{\overline{\rho}} \approx -\overline{P}\frac{\overline{\rho}_{,k}\tau^T_{ik}}{\overline{\rho}^2}$. Again, these relations are derived below. With this the transport equation

becomes

$$\frac{D\theta_i^T}{Dt} = -\tilde{u}_{i,k}\theta_k^T + \tau_{ik}^T\left(\tilde{e}_{,k} - \overline{P}\frac{\overline{\rho}_{,k}}{\overline{\rho}^2}\right) - \overline{e''}\,\overline{P}_{,i} - \frac{R}{\overline{C_v}}\theta_i^T\tilde{u}_{k,k} + \overline{\rho}\xi_i \tag{3.26}$$

As a final simplification take the gradient of the specific enthalpy $\tilde{h} = \tilde{e} + \frac{\overline{P}}{\overline{\rho}}$ to define $\tilde{\psi}_{,k} \equiv \tilde{h}_{,k} - \frac{\overline{P}_{,k}}{\overline{\rho}} = \tilde{e}_{,k} - \frac{\overline{P}\overline{\rho}_{,k}}{\overline{\rho}^2}$ such that: ([22, 7])

$$\frac{D\theta_i^T}{Dt} = -\tilde{u}_{i,k}\theta_k^T + \tau_{ik}^T\tilde{\psi}_{,k} - \overline{e''}\,\overline{P}_{,i} - \frac{R}{\overline{C_v}}\theta_i^T\tilde{u}_{k,k} + \overline{\rho}\xi_i \tag{3.27}$$

- Favre-Fluctuating Velocity Transport Equation

$$\frac{D\overline{\rho}\overline{u_i''}}{Dt} = -\overline{\rho}\overline{u_k''}\tilde{u}_{i,k} - \overline{\rho}\overline{u_k''u_{i,k}''} - \frac{1}{\overline{\rho}}\left(\overline{\rho'\tau_{ik,k}'} - \overline{\rho'P_{,i}'} + \overline{\rho}_{,k}\tau_{ik}^T\right) + D_{ik}$$

The second term on the right hand side can be written $-\overline{\rho}\overline{u_k''u_{i,k}''} = \left(\overline{\rho' u_k''u_{i,k}''}\right) - \left(\overline{\rho u_k''u_{i,k}''}\right) = (D_{ik}) + \left(\left[\overline{\rho u_{k,k}''u_i''}\right] - \left[\overline{\rho(u_k''u_i'')_{,k}}\right]\right) = (D_{ik}) + \left(\left[\overline{\rho}\overline{u_{k,k}''u_i''} + \overline{\rho' u_{k,k}''u_i''}\right] + [D_{ik}]\right) = \overline{\rho}\overline{u_{k,k}''u_i''} + D_{ik}$ in order to cancel with the fifth term according to Equation 3.37; the dummy variable contains triple correlation and diffusion terms and is simply combined with the other such placeholder. Continuing, Equation 3.63 shows the fourth term is negligible. Finally, one can, under the present assumptions, consider the viscous term to be $\mathscr{O}(Diffusion)$ and add it to D_{ik}. With this the transport equation simplifies to:

$$\frac{D\overline{\rho}\overline{u_i''}}{Dt} \approx -\overline{\rho}\overline{u_k''}\tilde{u}_{i,k} + D_u \tag{3.28}$$

- Favre-Fluctuating Energy Transport Equation

$$\frac{D\overline{\rho}\overline{e''}}{Dt} = \theta_k^T\frac{\overline{\rho}_{,k}}{\overline{\rho}} + \overline{\rho}\overline{e''u_{k,k}''} - \overline{\rho}\overline{u_k''}\tilde{e}_{,k} + \frac{1}{\overline{\rho}}\left(\overline{P}\,\overline{\rho' u_{k,k}''} + \overline{\rho'P'}\tilde{u}_{k,k}\right) + M_{kl}$$

The first and second terms on the right hand side cancel according to Equation 3.38. Furthermore, Equation 3.44 modifies the fourth term. With this the transport equation simplifies to ([22, 7])

$$\frac{D\overline{\rho}\overline{e''}}{Dt} = -\overline{\rho}\tilde{e}_{,k}\overline{u_k''} + \frac{\overline{P}\,\overline{\rho}_{,k}\overline{u_{k,k}''}}{\overline{\rho}} + \frac{\tilde{u}_{k,k}\overline{\rho'P'}}{\overline{\rho}} + M_{kl} \tag{3.29}$$

3.4.1 Dilatation Models

The processes to derive a velocity ($\overline{\rho u_{k,k}''u_i''}$) and energy ($\overline{\rho u_{k,k}''e''}$) dilatation model are identical and thus both are shown simultaneously in terms of the dummy variable ϕ''. Begin by expanding the conservation of mass (Equation 3.1) with Favre averaging and the Multiplication Rule; immediately neglect the unsteady term. Next, take a moment with ϕ'' and then Reynolds average the result.

$$\cancel{\rho_{,t}} + (\rho u_k'' + \rho\tilde{u}_k)_{,k} \approx 0 \tag{3.30}$$

$$\rho_{,k}u_k'' + \rho u_{k,k}'' + \rho_{,k}\tilde{u}_k + \rho\tilde{u}_{k,k} \approx 0 \tag{3.31}$$

$$\overline{\phi''\rho_{,k}u_k''} + \overline{\phi''\rho u_{k,k}''} + \tilde{u}_k\overline{\phi''\rho_{,k}} + \tilde{u}_{k,k}\cancel{\overline{\phi''\rho}} \approx 0 \tag{3.32}$$

By the definition of Favre averaging, $\cancel{\overline{(\rho\phi'')}_{,k}} = \overline{(\rho_{,k}\phi'')} + \overline{(\rho\phi_{,k}'')} \implies \overline{(\rho_{,k}\phi'')} = -\overline{(\rho\phi_{,k}'')}$.

$$\overline{\phi''\rho_{,k}u_k''} + \overline{\phi''\rho u_{k,k}''} - \tilde{u}_k\overline{(\rho\phi_{,k}'')} \approx 0 \tag{3.33}$$

Consider the term $\overline{\phi''\rho_{,k}u_k''}$. Expand the density gradient and then neglect the triple correlation so it becomes $\overline{\phi''\rho_{,k}u_k''} \approx \overline{\rho}_{,k}\overline{\phi''u_k''} + \cancel{\overline{\phi''\rho_{,k}'u_k''}}$. Multiply it by $\overline{\rho}/\overline{\rho}$ to produce $\frac{\overline{\rho}_{,k}}{\overline{\rho}}\overline{\rho}\overline{\phi''u_k''}$. Because under the second-order assumption triple correlations are considered to be approximately zero, one can write $\frac{\overline{\rho}_{,k}}{\overline{\rho}}\overline{\rho}\overline{\phi''u_k''} + \frac{\overline{\rho}_{,k}}{\overline{\rho}}\overline{\rho'\phi''u_k''}$. The mean and fluctuating density terms can now be collapsed into one cumulative term; this is the exact opposite of what was done with $\rho_{,k}$. This last step provides $\frac{\overline{\rho}_{,k}}{\overline{\rho}}\overline{\rho\phi''u_k''}$. Applying these changes to the above equation and rearranging the terms produces

$$\overline{\phi''\rho u_{k,k}''} \approx -\frac{\overline{\rho}_{,k}}{\overline{\rho}}\overline{\rho\phi''u_k''} + \tilde{u}_k\overline{(\rho\phi_{,k}'')} \tag{3.34}$$

Now expand density on the left hand side and cancel the triple correlation. Meanwhile, on the right hand side the $\tilde{u}_k\overline{(\rho\phi_{,k}'')}$ term is assumed to be negligibly small in a shear layer.

$$\overline{\rho}\overline{\phi''u_{k,k}''} + \cancel{\overline{\phi''\rho'u_{k,k}''}} \approx -\frac{\overline{\rho}_{,k}}{\overline{\rho}}\overline{\rho\phi''u_k''} + \cancel{\tilde{u}_k\overline{(\rho\phi_{,k}'')}} \tag{3.35}$$

$$\overline{\rho}\overline{\phi''u_{k,k}''} \approx -\frac{\overline{\rho}_{,k}}{\overline{\rho}}\overline{\rho\phi''u_k''} \tag{3.36}$$

All that remains is to substitute in u_i'' for velocity dilatation and e'' for energy dilatation.

$$Velocity\,Dilatation: \overline{\rho}\overline{u_i''u_{k,k}''} \approx \frac{\overline{\rho}_{,k}}{\overline{\rho}}\tau_{ik}^T \tag{3.37}$$

$$Energy\,Dilatation: \overline{\rho}\overline{e''u_{k,k}''} \approx -\frac{\overline{\rho}_{,k}}{\overline{\rho}}\theta_{ik}^T \tag{3.38}$$

A density dilatation ($\overline{\rho'u_{k,k}''}$) model can be completed following an analogous process. As before, begin by taking a moment of the conservation of mass, here with density fluctuations ρ'; again neglect unsteady and triple correlation terms. This time it is necessary to expand both the velocity and density terms in Equation 3.1 with Favre and Reynolds averaging respectively.

$$\cancel{\rho_{,t}} + (\overline{\rho}\tilde{u}_k + \overline{\rho}u_k'' + \rho'\tilde{u}_k + \rho'u_k'')_{,k} \approx 0 \tag{3.39}$$

$$\overline{\rho_{,k}}\tilde{u}_k + \overline{\rho}\tilde{u}_{k,k} + \overline{\rho_{,k}}u_k'' + \overline{\rho}u_{k,k}'' + \rho_{,k}'\tilde{u}_k + \rho'\tilde{u}_{k,k} + \rho_{,k}'u_k'' + \rho'u_{k,k}'' \approx 0 \tag{3.40}$$

$$\cancel{\overline{\rho'}\overline{\rho_{,k}}\tilde{u}_k} + \cancel{\overline{\rho'}\overline{\rho}\tilde{u}_{k,k}} + \overline{\rho_{,k}}\overline{\rho'u_k''} + \overline{\rho}\overline{\rho'u_{k,k}''} + \overline{\rho'\rho_{,k}'}\tilde{u}_k + \overline{\rho'\rho'}\tilde{u}_{k,k} + \cancel{\overline{\rho'\rho_{,k}'u_k''}} + \cancel{\overline{\rho'\rho'u_{k,k}''}} \approx 0 \tag{3.41}$$

$$\overline{\rho}\overline{\rho' u''_{k,k}} \approx -\overline{\rho}_{,k}\overline{\rho' u''_k} - \overline{\rho' \rho'_{,k}}\tilde{u}_k - \overline{\rho'^2}\tilde{u}_{k,k} \tag{3.42}$$

From the Multiplication Rule $(\rho'^2)_{,k} = \rho'_{,k}\rho' + \rho'\rho'_{,k} = 2\rho'\rho'_{,k} \implies \rho'\rho'_{,k} = \frac{1}{2}(\rho')^2_{,k}$.
Also, $-\overline{\rho}_{,k}\overline{\rho' u''_k} = -\overline{\rho}_{,k}\overline{(\rho - \overline{\rho})u''_k} = -\overline{\rho}_{,k}\cancel{\overline{\rho u''_k}} + \overline{\rho}_{,k}\overline{u''_k}\overline{\rho} = \overline{\rho}_{,k}\overline{u''_k}\overline{\rho}$.

$$\overline{\rho}\overline{\rho' u''_{k,k}} \approx \overline{\rho}_{,k}\overline{u''_k}\overline{\rho} - \frac{1}{2}\overline{(\rho')^2_{,k}}\tilde{u}_k - \overline{\rho'^2}\tilde{u}_{k,k} \tag{3.43}$$

Divide both sides by $\overline{\rho}$. Also, the second and third terms on the right-hand side are assumed to be small. What remains is the model.

$$Density\,Dilatation: \overline{\rho' u''_{k,k}} \approx \overline{\rho}_{,k}\overline{u''_k} \tag{3.44}$$

Bowersox [22] used the DNS data from Pirozzoli et al. [189] to show these dilatation models are reasonably accurate. ([22, 7])

3.4.2 Equation of State Model

Both the caloric and thermal equations of state can be used to write the bracketed term in Equation 3.15 in terms of the energy flux θ_i^T. Here one makes the important assumption that the gas is thermally perfect, but caloric imperfections are permissible. That said, it is also necessary to assume $\frac{C'_v}{\overline{C_v}} \ll \frac{e''}{\tilde{e}}$, or by corollary $C'_v \approx 0$. Both the mean and fluctuating forms of the caloric and thermal equations of state must be derived. While the former will be substituted into the latter, in both cases the fluctuating equation will be derived by expanding the equation with Reynolds and Favre fluctuations and Reynolds averaging to get the mean equation, then subtracting this result from the expanded form. For the caloric equation of state $e = C_v T$ there is a unique substitution step before Reynolds averaging, to multiply both sides of the equation by density, which allows for greater simplification.

$$(\tilde{e} + e'') \approx (\overline{C_v} + \cancel{C'_v})(\tilde{T} + T'') \tag{3.45}$$

$$\rho\tilde{e} + \rho e'' \approx \overline{C_v}\rho\tilde{T} + \overline{C_v}\rho T'' \tag{3.46}$$

$$\overline{\rho}\tilde{e} + \cancel{\overline{\rho e''}} \approx \overline{C_v}\overline{\rho}\tilde{T} + \cancel{\overline{C_v \rho T''}} \tag{3.47}$$

$$\tilde{e} \approx \overline{C_v}\tilde{T} \tag{3.48}$$

Subtracting Equation 3.48 from Equation 3.46 and dropping the distributed density produces the fluctuating equation form.

$$e'' \approx \overline{C_v} T'' \tag{3.49}$$

The mean and fluctuating forms of the thermal equation of state $P = \rho RT$ are derived following the steps outlined above, but the results from Equations 3.48 and 3.49 are used to replace the temperature dependence with the gas constant and constant volume specific heat.

$$(\overline{P} + P') \approx \rho R\left(\frac{\tilde{e}}{\overline{C_v}} + \frac{e''}{\overline{C_v}}\right) \tag{3.50}$$

$$(\overline{P}+\cancel{\overline{P''}}) \approx \frac{R}{\overline{\overline{C_v}}}(\overline{\rho}\tilde{e}+\cancel{\overline{\rho e''}}) \tag{3.51}$$

$$\overline{P} \approx \frac{R}{\overline{\overline{C_v}}}\overline{\rho}\tilde{e} \tag{3.52}$$

Subtracting Equation 3.52 from Equation 3.50 produces the fluctuating thermal state equation, though additional steps are needed to put it into the desired form.

$$(\cancel{\overline{P}}+P') - [\cancel{\overline{P}}] \approx \rho R\left(\frac{\tilde{e}}{\overline{\overline{C_v}}}+\frac{e''}{\overline{\overline{C_v}}}\right) - \left[\frac{R}{\overline{\overline{C_v}}}\overline{\rho}\tilde{e}\right] \tag{3.53}$$

$$P' \approx \frac{R}{\overline{\overline{C_v}}}\left(\rho\tilde{e}+\rho e''-\overline{\rho}\tilde{e}\right) \tag{3.54}$$

$$P' \approx \frac{R}{\overline{\overline{C_v}}}\left(\cancel{\overline{\rho}\tilde{e}}+\rho'\tilde{e}+\rho e''-\cancel{\overline{\rho}\tilde{e}}\right) \tag{3.55}$$

$$P' \approx \frac{R}{\overline{\overline{C_v}}}\left(\rho'\tilde{e}+\rho e''\right) \tag{3.56}$$

Now use Equations 3.52 and 3.56 to simplify Equation 3.15

$$\overline{P'u_i''}+\overline{u_i''}\,\overline{P} \approx \overline{\frac{R}{\overline{\overline{C_v}}}\left(\rho'\tilde{e}+\rho e''\right)u_i''}+\overline{u_i''}\frac{R}{\overline{\overline{C_v}}}\overline{\rho}\tilde{e} \tag{3.57}$$

$$\overline{P'u_i''}+\overline{u_i''}\,\overline{P} \approx \frac{R}{\overline{\overline{C_v}}}\left(\overline{\rho'u_i''}\tilde{e}+\overline{\rho e''u_i''}+\overline{u_i''}\overline{\rho}\tilde{e}\right) \tag{3.58}$$

Combine two of the terms by collapsing the density with $\rho = \overline{\rho}+\rho'$. ([22, 7])

$$\overline{P'u_i''}+\overline{u_i''}\,\overline{P} \approx \frac{R}{\overline{\overline{C_v}}}\left(\overline{\rho'u_i''}\tilde{e}+\overline{u_i''}\overline{\rho}\tilde{e}+\overline{\rho e''u_i''}\right) \tag{3.59}$$

$$\overline{P'u_i''}+\overline{u_i''}\,\overline{P} \approx \frac{R}{\overline{\overline{C_v}}}\left(\cancel{\overline{\rho u_i''}}\tilde{e}+\overline{\rho e''u_i''}\right) \tag{3.60}$$

$$\overline{P'u_i''}+\overline{u_i''}\,\overline{P} \approx \frac{R}{\overline{\overline{C_v}}}\theta_i^T \tag{3.61}$$

3.4.3 Incompressible Pressure Scrambling Model

The incompressible pressure scrambling effect $\overline{P'e''_{,i}}$ can be removed from Equation 3.15. Begin by expanding P' according to Equation 3.56, producing $\overline{P'e''_{,i}} = \frac{R}{\overline{\overline{C_v}}}\left(\tilde{e}\overline{\rho'e''_{,i}}+\overline{\rho}\overline{e''e''_{,i}}\right)$. The Multiplication Rule shows $e''e''_{,i} = \frac{1}{2}(e''^2)_{,i}$, so assuming the gradient of the energy variance is negligible then $\overline{\rho}\overline{e''e''_{,i}} \approx D$, where D symbolizes terms on the order of diffusion. For $\tilde{e}\overline{\rho'e''_{,i}}$, assume statistical moments are homogeneous $P' \ll \rho', T' \implies \frac{\rho'}{\overline{\rho}} \sim \frac{T'}{\overline{T}}$; this is extended to the internal energy with the caloric equation of state such that $\frac{\rho'}{\overline{\rho}} \approx \frac{e''}{\tilde{e}}$. This allows $\tilde{e}\overline{\rho'e''_{,i}} \approx \tilde{e}\overline{\left(\frac{\overline{\rho}e''}{\tilde{e}}\right)e''_{,i}} \approx \overline{\rho}\tilde{e}\overline{e''e''_{,i}}$; as before, apply the Multiplication Rule and the same assumption to the gradient of the energy variance,

$\tilde{e}\overline{\rho' e''_{,i}} \approx \frac{\overline{\rho}}{2}\overline{(e'')^2_{,i}} \approx D$. Taken together,

$$\overline{P' e''_{,i}} \approx D \tag{3.62}$$

The same process can also be used to simplify $\overline{P'\rho'_{,i}}$ in Equation 3.22. Expanding P' with the fluctuating equation of state produces $\overline{P'\rho''_{,i}} = \frac{R}{\overline{C_v}}\left(\tilde{e}\overline{\rho'\rho'_{,i}} + \overline{\rho}\overline{e''\rho'_{,i}}\right)$. As before, through the Multiplication Rule the first term can be expressed as the gradient of a fluctuating quantity and can therefore be assumed to be negligible. For the second term, again use $\frac{\rho'}{\overline{\rho}} \approx \frac{e''}{\tilde{e}}$ to write $\overline{\rho}\overline{e''\rho'_{,i}} \approx \overline{\rho}\frac{\overline{\rho'\tilde{e}}}{\overline{\rho}}\rho'_{,i} \approx \tilde{e}\overline{\rho'\rho'_{,i}}$, which once again becomes the gradient of a fluctuating term and can therefore be grouped with diffusion. And so

$$\overline{P'\rho''_{,i}} \approx D \tag{3.63}$$

These assumptions, in particular, require additional study, which is now readily available via companion DNS works (e.g, [23, 24, 190]). ([22, 7])

3.5 Algebratization

The above transport equation has been heavily simplified, but it remains a partial differential equation. In order to solve this equation numerically, an algebratization technique proposed by Girimaji and Balachandar [191] is implemented. The Favre-fluctuating velocity and energy equations are also algebratized to allow for later simplification of the algebraic energy flux equation. This section follows from Bowersox [22] and Broslawski [7].

3.5.1 Algebraic Turbulent Energy Flux Transport

The simplified transport equation (3.27) is repeated for convenience.

$$\frac{D\theta_i^T}{Dt} = -\tilde{u}_{i,k}\theta_k^T + \tau_{ik}^T\tilde{\psi}_{,k} - \overline{e''}\,\overline{P}_{,i} - \frac{R}{\overline{C_v}}\theta_i^T\tilde{u}_{k,k} + \overline{\rho}\xi_i$$

Now define the correlation coefficient and differentiate it following the Quotient and Multiplication Rules.

$$F_i = \frac{\theta_i^T}{\sqrt{k^T}\sqrt{\eta^T}} \tag{3.64}$$

$$\frac{DF_i}{Dt} = \frac{\sqrt{k^T}\sqrt{\eta^T}\frac{D\theta_i^T}{Dt} - \theta_i^T\frac{D\sqrt{k^T}\sqrt{\eta^T}}{Dt}}{k^T\eta^T} \tag{3.65}$$

Apply the weak equilibrium assumption, that $\frac{DF_i}{Dt} \approx 0$; described verbally, this states that F_i is constant along a streamline.

$$0 \approx \frac{D\theta_i^T}{Dt} - \frac{\theta_i^T}{2}\left(\frac{1}{\eta^T}\frac{\eta^T}{Dt} + \frac{1}{k^T}\frac{Dk^T}{Dt}\right) \tag{3.66}$$

Now substitute in the transport equations for $\frac{D\theta_i^T}{Dt}$ (3.27), $\frac{Dk^T}{Dt}$ (3.16), and $\frac{D\eta^T}{Dt}$ (3.17), though it will be seen shortly the latter two need not be fully defined. It is useful to adopt the generalized notation $\frac{DX^T}{Dt} = P^X + D^X + A^X$ where P^X denotes production terms, D^X denotes diffusion terms, and A^X is

the aggregate of the remaining terms such as dissipation, molecular terms, pressure-strain, *etc*. Equation 3.27 has already been grouped such that $D^{\theta_i^T} + A^{\theta_i^T} = \overline{\rho}\xi_i$ and every remaining term is production $P^{\theta_i^T}$.

$$0 \approx \left[P^{\theta_i^T} + D^{\theta_i^T} + A^{\theta_i^T}\right] - \frac{\theta_i^T}{2}\left(\frac{1}{\eta^T}\left[P^{\eta^T} + D^{\eta^T} + A^{\eta^T}\right] + \frac{1}{k^T}\left[P^{k^T} + D^{k^T} + A^{k^T}\right]\right) \tag{3.67}$$

Here, one assumes that $\overline{\rho}\xi_i \approx 0$, or at least $P^{\theta_i^T} \gg \overline{\rho}\xi_i$. For some terms, there is some justification for this step. For example, in their model for turbulent kinetic energy Launder et al. [192] wrote dissipation as $\frac{2}{3}\delta_{ij}\varepsilon$, which implies dissipation is negligible for cross-correlation ($i \neq j$) terms; if one treats $\theta_i^T = \overline{\rho e'' u_i''}$ as a cross-correlation between energy and velocity, than one can assume its dissipation terms are also negligible. For a more general justification, one could invoke Launder's so-called WET hypothesis [193, 185], which states "Wealth" is proportional to "Earnings" multiplied by "Time". Philosophically, it means that the amount of something is equal to the rate at which it is produced multiplied by the time that rate has been applied. Laudner admits it is an oversimplification, but intuitively there is some logic to it. In the present context, the amount of energy flux θ_i^T is equal to its production terms $P^{\theta_i^T}$ multiplied by a time constant to be defined shortly, and $P^{\theta_i^T}$ dominates all other terms such as dissipation and diffusion. So while there is some reason to this step, in the end it remains a modeling necessity as it allows one to write

$$P^{\theta_i^T} \approx \frac{\theta_i^T}{2}\left(\frac{1}{\eta^T}\left[P^{\eta^T} + D^{\eta^T} + A^{\eta^T}\right] + \frac{1}{k^T}\left[P^{k^T} + D^{k^T} + A^{k^T}\right]\right) \tag{3.68}$$

where the right hand side lends itself naturally to the time constant

$$\tau_\theta^{-1} = \frac{1}{2}\left(\frac{1}{\eta^T}\left[P^{\eta^T} + D^{\eta^T} + A^{\eta^T}\right] + \frac{1}{k^T}\left[P^{k^T} + D^{k^T} + A^{k^T}\right]\right) \tag{3.69}$$

This is in and of itself too complex for feasible calculation, so it is modeled in Section 3.6. For now it is sufficient to consider the term closed. (Bowersox [22], Broslawski [7])

What remains is at last an algebraic expression for turbulent energy flux

$$-\tilde{u}_{i,k}\theta_k^T + \tau_{ik}^T\tilde{\psi}_{,k} - \overline{e''}\,\overline{P}_{,i} - \frac{R}{\overline{C_v}}\theta_i^T\tilde{u}_{k,k} \approx \frac{\theta_i^T}{\tau_\theta} \tag{3.70}$$

Or, written in the standard matrix notation,

$$a_{ik}\theta_k^T = b_i \tag{3.71}$$

where $a_{ik} = \left[\tau_\theta^{-1} + \frac{R}{\overline{C_v}}\tilde{u}_{m,m}\right]\delta_{ik} + \tilde{u}_{i,k}$ and $b_i = \tau_{ik}^T\tilde{\psi}_{,k} - \overline{e''}\,\overline{P}_{,i}$. The Kronecker delta is needed to align the indices between θ_i^T and θ_k^T. b_i can be further simplified by algebratizing the Favre-fluctuating velocity and energy transport equations. ([22, 7])

3.5.2 Algebraic Favre-Fluctuating Velocity Transport

The simplified transport equation (3.28) is repeated for convenience.

$$\frac{D\overline{\rho}\overline{u_i''}}{Dt} \approx -\overline{\rho}\overline{u_k''}\tilde{u}_{i,k} + D_u$$

Using Favre-averaging, $\overline{\rho}\overline{u_i''} = \cancel{\overline{\rho u_i''}} - \overline{\rho' u_i''} = -\overline{\rho' u_i''}$, which allows the definition of a correlation coefficient

$$F_i = \frac{-\overline{\rho' u_i''}}{\sqrt{\overline{\rho'^2}}\sqrt{\overline{u_i''^2}}} \tag{3.72}$$

The terms in the denominator are squared to prevent division by zero due to a $\overline{\rho'}$ term. Differentiate this expression following the Quotient Rule.

$$\frac{DF_i}{Dt} = \frac{-\sqrt{\overline{\rho'^2}}\sqrt{\overline{u_i''^2}}\frac{D\overline{\rho' u_i''}}{Dt} + \overline{\rho' u_i''}\frac{D\sqrt{\overline{\rho'^2}}\sqrt{\overline{u_i''^2}}}{Dt}}{\overline{\rho'^2}\,\overline{u_i''^2}} \tag{3.73}$$

Apply the weak equilibrium assumption, that $\frac{DF_i}{Dt} \approx 0$; described verbally, this states that F_i is constant along a streamline.

$$0 \approx -\frac{D\overline{\rho' u_i''}}{Dt} + \frac{\overline{\rho' u_i''}}{2}\left(\frac{1}{\overline{u_i''^2}}\frac{D\sqrt{\overline{u_i''^2}}}{Dt} + \frac{1}{\overline{\rho'^2}}\frac{D\sqrt{\overline{\rho'^2}}}{Dt}\right) \tag{3.74}$$

Now substitute in the transport equations for $-\frac{D\overline{\rho' u_i''}}{Dt}(=\frac{D\overline{\rho}\,\overline{u_i''}}{Dt})$ (3.28), $\frac{D\sqrt{\overline{u_i''^2}}}{Dt}$, and $\frac{D\sqrt{\overline{\rho'^2}}}{Dt}$. Because this equation never needs to be solved and only serves to simply Equation 3.71 in the theory, generalized notation and formal transport equations for $\frac{D\sqrt{\overline{u_i''^2}}}{Dt}$ and $\frac{D\sqrt{\overline{\rho'^2}}}{Dt}$ are unnecessary.

$$0 \approx -\overline{\rho}\overline{u_k''}\tilde{u}_{i,k} + D_u + \frac{\overline{\rho' u_i''}}{2}\left(\frac{1}{\overline{u_i''^2}}\frac{D\sqrt{\overline{u_i''^2}}}{Dt} + \frac{1}{\overline{\rho'^2}}\frac{D\sqrt{\overline{\rho'^2}}}{Dt}\right) \tag{3.75}$$

This time do not neglect the diffusion-order terms; because the goal here is not to model the above equation, there is less motivation to isolate P^u. Introduce a time constant

$$\tau_u^{-1} = \frac{1}{2}\left(\frac{1}{\overline{u_i''^2}}\frac{D\sqrt{\overline{u_i''^2}}}{Dt} + \frac{1}{\overline{\rho'^2}}\frac{D\sqrt{\overline{\rho'^2}}}{Dt}\right) \tag{3.76}$$

With this the algebratized equation becomes

$$0 \approx -\overline{\rho}\,\overline{u_k''}\,\tilde{u}_{i,k} + D_u + \frac{\overline{\rho' u_i''}}{\tau_u} \tag{3.77}$$

Re-writing $\overline{\rho' u_i''}$ as $-\overline{\rho}\,\overline{u_i''}$, absorbing $\frac{1}{\overline{\rho}}$ into D_u, and aligning indices with a Kronecker delta produces

$$\left(\tilde{u}_{i,k}\delta_{ik} + \tau_u^{-1}\right)\overline{u_k''} \approx D_u \tag{3.78}$$

Equation 3.78 suggests $\overline{u_k''} = \mathscr{O}(D_u)$ and therefore is negligible under the assumptions throughout this work. ([22, 7])

3.5.3 Algebraic Favre-Fluctuating Energy Transport

The simplified transport equation (3.29) is repeated for convenience.

$$\frac{D\overline{\rho}\,\overline{e''}}{Dt} = -\overline{\rho}\,\tilde{e}_{,k}\,\overline{u_k''} + \frac{\overline{P}\,\overline{\rho_{,k}}\,\overline{u_{k,k}''}}{\overline{\rho}} + \frac{\tilde{u}_{k,k}\overline{\rho' P'}}{\overline{\rho}} + M_{kl}$$

Using Favre-averaging, $\overline{\rho}\,\overline{e''} = \overline{\cancel{\rho e''}} - \overline{\rho' e''} = -\overline{\rho' e''}$, which allows the definition of a correlation coefficient

$$F_i = \frac{-\overline{\rho' e''}}{\sqrt{\overline{\rho'^2}}\sqrt{\overline{e''^2}}} \tag{3.79}$$

The terms in the denominator are squared to prevent division by zero due to a $\overline{\rho'}$ term. Differentiate this expression following the Quotient Rule

$$\frac{DF_i}{Dt} = \frac{-\sqrt{\overline{\rho'^2}}\sqrt{\overline{e''^2}}\frac{D\overline{\rho' e_i''}}{Dt} + \overline{\rho' e''}\frac{D\sqrt{\overline{\rho'^2}}\sqrt{\overline{e''^2}}}{Dt}}{\overline{\rho'^2}\,\overline{e''^2}} \tag{3.80}$$

Apply the weak equilibrium assumption, that $\frac{DF_i}{Dt} \approx 0$; described verbally, this states that F_i is constant along a streamline.

$$0 \approx -\frac{D\overline{\rho' e''}}{Dt} + \frac{\overline{\rho' e''}}{2}\left(\frac{1}{\overline{e''^2}}\frac{D\sqrt{\overline{e''^2}}}{Dt} + \frac{1}{\overline{\rho'^2}}\frac{D\sqrt{\overline{\rho'^2}}}{Dt}\right) \tag{3.81}$$

Now substitute in the transport equations for $-\frac{D\overline{\rho' e''}}{Dt}(=\frac{D\overline{\rho}\,\overline{u''}}{Dt})$ (3.29), $\frac{D\sqrt{\overline{e''^2}}}{Dt}$, and $\frac{D\sqrt{\overline{\rho'^2}}}{Dt}$. Because this equation never needs to be solved and only serves to simply Equation 3.71 in the theory, generalized notation and formal transport equations for $\frac{D\sqrt{\overline{e''^2}}}{Dt}$ and $\frac{D\sqrt{\overline{\rho'^2}}}{Dt}$ are unnecessary.

$$0 \approx \left(-\overline{\rho}\,\tilde{e}_{,k}\,\overline{u_k''} + \frac{\overline{P}\,\overline{\rho_{,k}}\,\overline{u_{k,k}''}}{\overline{\rho}} + \frac{\tilde{u}_{k,k}\overline{\rho' P'}}{\overline{\rho}} + M_{kl}\right) + \frac{\overline{\rho' e''}}{2}\left(\frac{1}{\overline{u_i''^2}}\frac{D\sqrt{\overline{u_i''^2}}}{Dt} + \frac{1}{\overline{\rho'^2}}\frac{D\sqrt{\overline{\rho'^2}}}{Dt}\right) \tag{3.82}$$

Now neglect the molecular term M_{kl}; because the goal here is not to model the above equation, there is less motivation to isolate P^e. Introduce a time constant

$$\tau_e^{-1} = \frac{1}{2}\left(\frac{1}{\overline{e''^2}}\frac{D\sqrt{\overline{e''^2}}}{Dt} + \frac{1}{\overline{\rho'^2}}\frac{D\sqrt{\overline{\rho'^2}}}{Dt}\right) \tag{3.83}$$

With this the algebratized equation becomes

$$0 \approx \left(-\overline{\rho}\tilde{e}_{,k}\overline{u_k''} + \frac{\overline{P}\,\overline{\rho}_{,k}\overline{u_{k,k}''}}{\overline{\rho}} + \frac{\tilde{u}_{k,k}\overline{\rho' P'}}{\overline{\rho}}\right) + \frac{\overline{\rho' e''}}{\tau_e} \tag{3.84}$$

Re-writing $\overline{\rho' e''}$ as $-\overline{\rho}\overline{e''}$ and re-arranging produces

$$\overline{\rho}\overline{e''} \approx \left(-\overline{\rho}\tilde{e}_{,k}\overline{u_k''} + \frac{\overline{P}\,\overline{\rho}_{,k}\overline{u_{k,k}''}}{\overline{\rho}} + \frac{\tilde{u}_{k,k}\overline{\rho' P'}}{\overline{\rho}}\right)\tau_e \tag{3.85}$$

Now recall Equation 3.78; by assuming diffusion-order terms are negligible, one can write $\overline{u_k''} \approx D_u$. Further assuming that the third term on the right hand side is negligible because it is a dilitation and second-order compressibility effect which both tend to be small, one is left with

$$\overline{e''} \approx D_e \tag{3.86}$$

Again, it is emphasized this result is only usable under the assumptions of the preceding derivation. ([22, 7])

3.6 Implementation

Using Equation 3.86 in Equation 3.71 one is left with the final, simplified form of the algebraic energy flux model:

$$a_{ik}\theta_k^T = b_i \tag{3.87}$$

where $a_{ik} = \left[\tau_\theta^{-1} + \frac{R}{\overline{C_v}}\tilde{u}_{m,m}\right]\delta_{ik} + \tilde{u}_{i,k}$ and $b_i = \tau_{ik}^T\tilde{\psi}_{,k}$. This approach has been successfully compared to a range of equilibrium flows [185, 22, 23, 24], including homogenous shear flows, wakes, and wall boundary layers (Mach $0-14$); recently, it was extended to high speed flows with both adverse and favorable pressure gradients [25]. However, because diffusion and dissipation are neglected, the current model is limited to the outer region of wall boundary layers and free shear layers until near wall corrections are produced. The purpose of this subsection is to provide some guidance on the application of the above theory to practical hypersonic, ZPG, RANS turbulent boundary layer modeling. A procedure to implement the model in an industry-level CFD package is provided in [25], but it provides detail beyond the scope of this report. In addition, a brief description is provided for implementation into an in-house research CFD code developed by the PI.

As the model is being actively researched, some parameters have changed with each publication (in order, Bowersox [22], Poggie [23], Huang et al. [24]). Bowersox's original paper [22] remains

both the theoretical and practical foundation for many of the concepts described below. Huang et al. [24] is taken as a useful reference regarding implementation. Additionally, note that in the model's recent publications [22, 23, 24] there is an extra term, placed either in a_{ik} or b_i, that is not present here; the derivation in [25] and the additional detail provided above show this term is indeed a simple typing error originating in [22] and carried through subsequent works. The authors of the affected sections confirmed in private communications it was never actually coded into any of the programs used to generate the data in these publications. (Broslawski [7])

Equation 3.87 can be solved explicitly using Cramer's Rule. Bowersox [22] recommended using $|a_{ik}| \approx \tau_\theta^{-3}$ for stability; Broslawski et al. [25] wrote that numerical instabilities grew in the determinant as greater pressure gradients were applied, and so this approximation should hold for ZPG flows. Hereafter x_1 is the streamwise coordinate, x_2 is the wall normal coordinate, and x_3 is the spanwise coordinate. ([22, 7])

$$\begin{aligned}
\theta_1^T &= \left(\frac{1}{\tau_\theta^{-3}}\right)\left[b_1\left(a_{22}a_{33}-a_{32}a_{23}\right)-b_2\left(a_{12}a_{33}-a_{32}a_{13}\right)+b_3\left(a_{12}a_{23}-a_{22}a_{13}\right)\right] \\
\theta_2^T &= \left(\frac{1}{\tau_\theta^{-3}}\right)\left[-b_1\left(a_{21}a_{33}-a_{31}a_{23}\right)+b_2\left(a_{11}a_{33}-a_{31}a_{13}\right)-b_3\left(a_{11}a_{23}-a_{21}a_{13}\right)\right] \\
\theta_3^T &= \left(\frac{1}{\tau_\theta^{-3}}\right)\left[b_1\left(a_{21}a_{32}-a_{31}a_{22}\right)-b_2\left(a_{11}a_{32}-a_{31}a_{12}\right)+b_3\left(a_{11}a_{22}-a_{21}a_{12}\right)\right]
\end{aligned} \tag{3.88}$$

For 2D thin shear layers, these equations reduce to, as written in [24],

$$\begin{aligned}
\theta_1^T &= \left(\tau_{12}^T-\tau_{22}^T\tilde{u}_{1,2}\tau_\theta\right)\tau_\theta\tilde{\psi}_{,2}/d_1 \\
\theta_2^T &= \tau_{22}^T\tilde{\psi}_{,2}\tau_\theta
\end{aligned} \tag{3.89}$$

where d_1 is a wall damping correction $d_1 = 1-\exp(-x_2^*/C_1^*)$ with semi-local scaling on the wall coordinate and the model constant C_1^*; x_2^+ and 12 are recommended, respectively [22]. In the absence of a pressure gradient $\tilde{\psi}_{,2} = \tilde{h}_{,2}$. The time constant τ_θ was calculated from $\tau_\theta \approx \sigma_\theta \tau_u$, where σ_θ was a tunable parameter set for all known implementations [22, 23, 24, 25] to $\sigma_\theta = 0.28/\gamma$; note that this assumed that the turbulent energy flux timescale was on the same order as that of the turbulent timescale. From the dimensional analysis of Jones and Launder [42], $\tau_u = \frac{k^T}{\varepsilon}$. The approximation ultimately used here was first written in [23] as $\tau_u \approx \frac{a_1}{C_\mu \tilde{u}_{1,2}}$ where $a_1 = 0.28$ and $C_\mu = 0.09$; as a numerical tip, add a small constant (ex.- 10^{-9}) to the derivative $\tilde{u}_{1,2}$ to prevent division by zero at all points throughout the domain. Additional explanation for the origin of the constants is found in [22]. ([22, 7])

For the flat plate case the Reynolds stress is solved with the Boussinesq approximation $\tau_{12}^T = \mu^T u_{1,2}$ and the streamwise stress with

$$\frac{\tau_{12}^T}{\tau_{22}^T} = -\frac{C}{1-\exp(-x_2^+/A^+)} \tag{3.90}$$

where $C = 0.68$ and $A^+ = 26.0$ [23], though here d_1 was used all the wall scaling coefficient.

This formula was purpose-built for a flat plate boundary layer, limiting its application. The use of μ^T does imply the Boussinesq approximation, even though it was not extended to the heat flux calculation. While this is acceptable for the flat plate case, in general it limits the application of the AEF approach under high speed conditions. In the proceeding section, it will be seen that DNS can be used to provide the Reynolds stresses, but as these remain highly specialized and expensive techniques improved RANS models for the Reynolds stresses under general hypersonic conditions are needed. (Broslawski [7].)

Finally, in order to relate the energy flux to heat flux for thermally perfect and calorically imperfect gases, begin with the enthalpy equation $\rho h = \rho e + P$. Expand it with Reynolds and Favre terms, multiply through by u_i'', then Reynolds average the result.

$$\tilde{h}\cancel{\overline{\rho u_i''}} + \overline{\rho h'' u_i''} = \tilde{e}\cancel{\overline{\rho u_i''}} + \overline{\rho e'' u_i''} + \overline{P}\,\overline{u_i''} + \overline{P' u_i''} \tag{3.91}$$

$$q_i^T = \theta_i^T + \overline{P}\,\overline{u_i''} + \overline{P' u_i''} \tag{3.92}$$

Using Equation 3.61 and $R = C_p - C_v$ yields

$$q_i^T = \gamma \theta_i^T \tag{3.93}$$

With this the AEF model supplies the turbulent heat flux. (Broslawski [7])

To summarize, for the numerical boundary layer solver, it was sufficient to calculate $q_2^T = \gamma \theta_2^T$ where $\theta_2^T = \frac{b_2 a_{11} a_{33}}{\tau_\theta^{-3}}$ with $a_{11} = a_{33} = \tau_\theta^{-1}$ and $b_2 = \tau_{22}^T \tilde{\psi}_{,2}$.

3.7 Extension to Flows with Pressure Gradients

The relevant work of Broslawski et al. [25] is summarized here as it extended the above theory to a real flow with pressure gradients. It used an in-house RANS code to model a 2D turbulent boundary layer in a wind tunnel at $M = 4.9$ and $Re = 45 \times 10^6/\text{m}$. Particle imaging velocimetry (PIV) provided the Reynolds stresses for both favorable [194] and adverse [195] pressure gradient cases. These data validated DNS for the favorable [196] and adverse [197] cases. These simulations in turn provided the wall normal and streamwise components of the turbulent heat flux q_y^T and q_x^T. Due to the pressure gradients, the authors used the Reynolds stresses provided by the DNS to calculate the turbulent heat flux using the AEF approach, completely removing all uses of the Boussinesq approximation. The Reynolds stresses from the experiments and simulations for the adverse (APG), weak favorable (FPG-WPG), and strong favorable (FPG-SPG) cases are compared in Figure 3.2. The under prediction of the experimental data was attributed a known phenomena of the PIV technique [198, 199, 200], and the agreement was considered satisfactory for the DNS to be used. The data suggested the favorable pressure gradient was re-laminarizing the flow, as evinced by the sign change in the Reynolds stress. This is noteworthy, because, by their very formulation, Boussinesq turbulence models cannot predict negative Reynolds stresses. As expected, the adverse pressure gradient tended to increase the production of the Reynolds stresses. ([7])

Nicholson et al. [196] observed that, given a large enough streamwise domain (beyond that shown in Figure 3.3) and for the case of the strong favorable pressure gradient, the wall normal component of the turbulent heat flux q_y^T had a similar sign change. Broslawski et al. [25] iden-

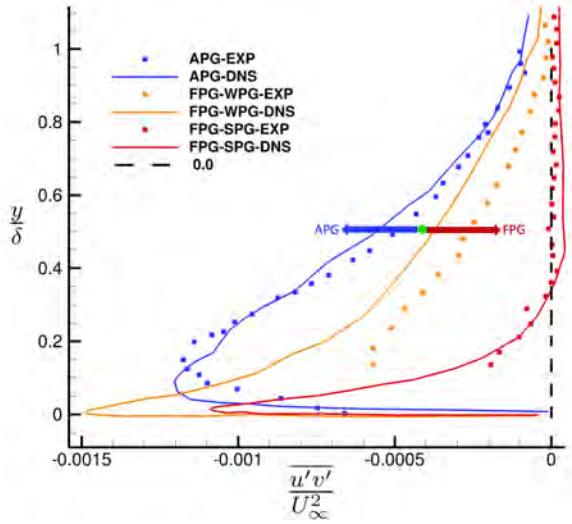

Figure 3.2: Reynolds stresses for AEF model study; figure taken with permission from [25].

tified two reasons these physics challenged the AEF model. The first was that they called into question the central weak equilibrum assumption, that the correlation coefficients F_i were constant along streamlines; in the case of pressure gradients, this appears to be violated, requiring direct investigation going forward. They also note the dominant dependence/scaling q_y^T had on $\overline{v'v'}$, an inherently positive parameter. These two factors were deemed problematic and may motivate further development of the AEF model for the generalized case of pressure gradients. Figure 3.3 compares the wall normal and streamwise components of the the turbulent heat flux as calculated with the AEF data (Reynolds stresses from DNS) and standard Boussinesq approach (constant Pr_t). The results were from the same test location as the Reynolds stresses in Figure 3.2. Beginning with q_x^T, it was immediately clear that the Boussinesq approach was completely incapable of predicting the streamwise component of the turbulent heat flux (Figure 3.3(a)). The AEF approach (Figure 3.3(b)) yielded improved agreement with the DNS for all three cases, though further development was needed to address an under prediction of the results in the case of the adverse pressure gradient. What was especially surprising was how well the AEF model performed near the wall, accurately capturing the spike in this region. Here diffusion, and especially dissipation, dominate the physics, and these were effectively omitted in the AEF model's derivation as part of the WET hypothesis. For q_y^T the Boussinesq approach (Figure 3.3(c)) did a better job matching the DNS, which made sense as it was specifically tuned to capture this component of the turbulent heat flux. However, the results were still inferior when compared to the agreement seen for the AEF approach (Figure 3.3(d)). Here it was noted again that there was a slight sign reversal in the case of the strong favorable pressure gradient, but the AEF model could not capture it. Finally, that $|q_x^T| \gg |q_x^T|$ underscored the importance of predicting all three components of turbulent heat flux and the gravity of Boussinesq models' inability to do so. ([7])

In summary, the work of Broslawski et al. [25] extended the AEF model to mechanically strained flows and showed it was able to outperform standard RANS techniques. The improve-

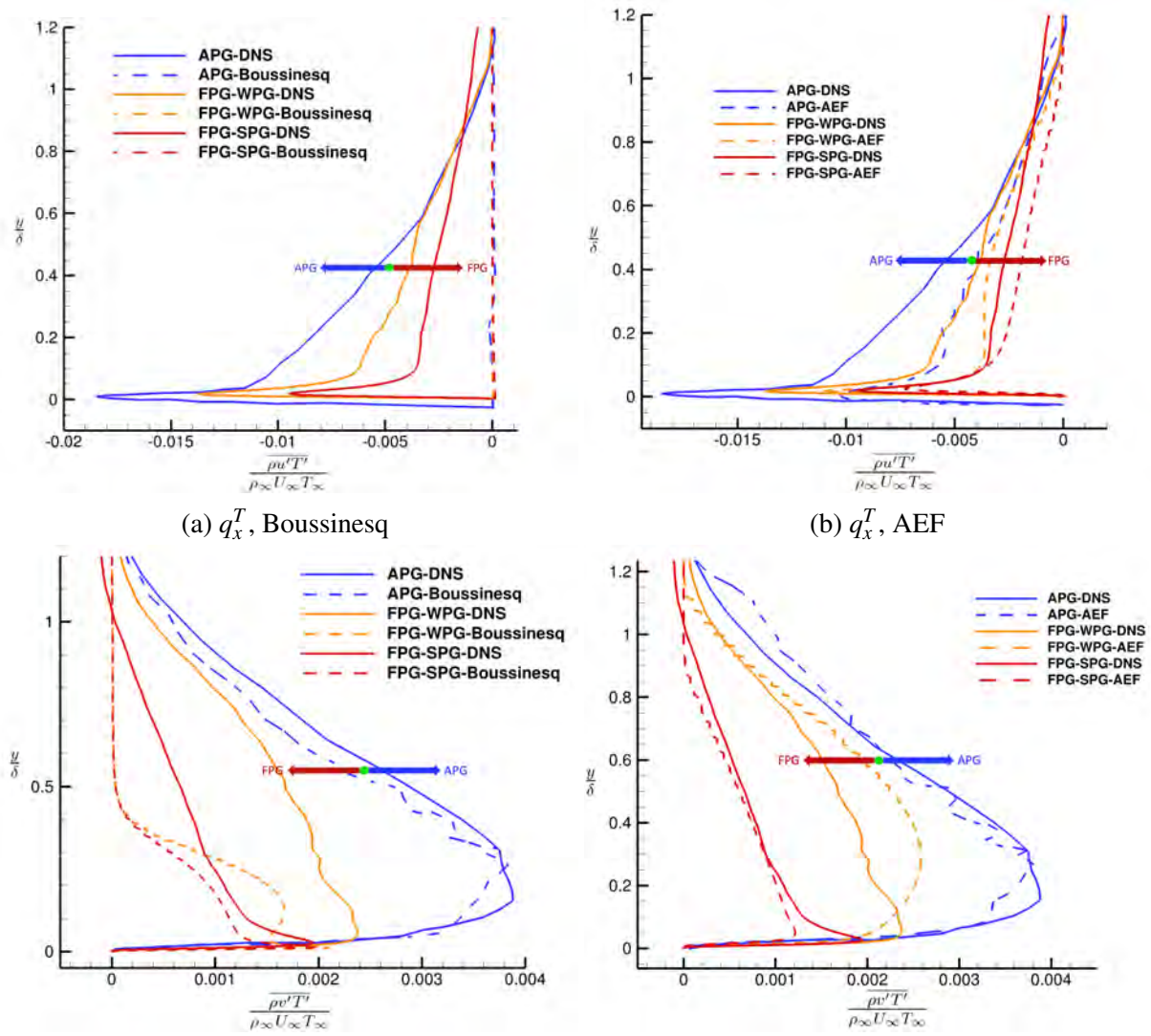

(a) q_x^T, Boussinesq

(b) q_x^T, AEF

(c) q_y^T, Boussinesq

(d) q_y^T, AEF

Figure 3.3: Comparisons of streamwise and wall normal turbulent heat flux as predicted by the Boussinesq and AEF models; figures taken with permission from [25].

ment was most profound in the case of q_x^T. This success motivated further development of the model, for example in the case of adverse pressure gradients. The derivation clarified the necessity and justification for the assumptions used throughout the process, which allowed each one to be studied individually. For example, the assumed dominance of production throughout the boundary layer, especially in the near wall region, and the weak equilibrium assumption could both benefit from an analysis like that by Nicholson et al. [190], which used DNS to individually plot each component of various transport equations and thereby study their individual behavior and importance. Such detailed work was invaluable in understanding the complex physics entrained in turbulence transport equations and deciding how each term should be treated in a model; for example, the au-

thors found production was in fact important in the near wall transport of q_x^T in the case of favorable pressure gradients and recommended these physics be included in models of such flows. Overall the current state of the AEF model as derived above has been shown to be effective in a variety of flows, improving the prediction of turbulent heat flux within a RANS framework. Further work, aided by ever-advancing computational resources, will only continue to drive it forward. ([7].)

3.8 Implementation into the In-House Research Codes

The PI implemented the equilibrium version of the algebraic energy flux model for perfect gases into two codes. The first code was a 2-D boundary layer solver similar to the one described above, and the second was a 2-D parabolized Navier-Stokes (PNS) solver. The Reynolds stress turbulence model utilized classical algebraic closure [22]. The equilibrium model was demonstrated with experimental and DNS data to reproduce flows over a Mach 0 - 14 range. It is important to note that ad hoc near wall corrections were required. For example, the simulations labeled "Bowersox" in Figures 3.1c and d were produced by the PI's PNS solver, with the model coded as described in Bowersox [22]. The simulated RMS temperature fluctuations in Figure 3.1d were based on an intermediate step not reported in [22], but described above for the energy flux formulation.

4.1 Preamble

This chapter covers all of the main facilities and hardware used throughout the campaign. The facility descriptions presented in this section were drawn from selected dissertations, theses, and articles associated with the execution of this project: McManamen [17], McManamen et al. [3], Broslawski [7], Bryan [9], Dean [11], and Siddiqui [4].This includes facility descriptions, along with its support infrastructure and any modifications made for the present work. The original citations are also included in the subsequent text.

4.2 Actively Controlled Expansion (ACE) Tunnel

This section follows from Broslawski [7]. All wind tunnel data included in this report were taken in the blowdown ACE tunnel at the NAL first introduced in Semper et al. [201]. Indeed, the entire campaign was designed to be conducted in this facility. Here the lab infrastructure is described in the sequential order it is used, starting with the air delivery system to the data acquisition system. Characteristic tunnel conditions are summarized in Table 4.1. Note that these values are a combination of theoretical calculations, personal experience, and published data and are intended only to provide a frame of reference. Modifications to the tunnel and the optimization of conditions may produce data outside the characteristic ranges shown here. Also included in Table 4.1 are the test conditions for the present campaign. Transience during a run and imperfect repeatability may cause slight deviation from these test conditions; tolerable experimental uncertainties are included in the table.

Parameter	Characteristic	Test Condition
M	$5-8$	5.70 ± 0.05
Duration (s)	$30-50$	40
$Re\,(\times 10^6/\mathrm{m})$	$0.5-8$	6.00 ± 0.25
$P_o\,(\mathrm{kPa})$	$48.26-689.48$	496.42 ± 20.68
$T_o\,(\mathrm{K})$	$300-533$	430 ± 15
$P\,(\mathrm{Torr})$	$0.05-10$	3.23 ± 0.13
$T\,(\mathrm{K})$	$40-70$	57.35 ± 2.00
$\rho\left(\frac{\mathrm{kg}}{\mathrm{m}^3}\right)$	$5.81\times10^{-4}-6.63\times10^{-2}$	$2.61 \pm 0.2 \times 10^{-2}$
$n\left(/\mathrm{cm}^3\right)$	$1.21\times10^{16}-1.38\times10^{18}$	$5.43 \pm 0.41 \times 10^{17}$
$\frac{P'_{RMS}}{\bar{P}}\,(\%)$	$0.1-2.0$	1.5 ± 0.25

Table 4.1: ACE tunnel conditions.

4.2.1 Support Infrastructure

As a blowdown facility, the ACE tunnel requires a large pressure differential to achieve hypersonic conditions. To reach high pressures on the supply side, air is compressed at 3.7 standard cubic meters per minute by two CompAir Reavell 5442 compressors before passing through a cyclone separator, two 99% efficient filters, a regenerative desiccant dryer and then finally being stored at 17.24MPa in an A.O. Smith 23.2m^3 tank. The conditioning process removes oil and particulates greater than 1μm and enough moisture reach a dew point of 233.15K. It takes $\sim$ 2.5hr for the tank to be fully recharged after a run, nominally from 10.34MPa, and this represents the largest limitation on the number of achievable runs in a campaign. To further increase the pressure differential through the tunnel, a 530Pa vacuum is supplied by a Fox Venturi Products two-stage air ejector pictured in Figure 4.1. This equipment operates on the Venturi principal and thus requires a motive air supply; here $\sim 25\frac{\text{kg}}{\text{s}}$ of air at 1MPa is supplied via a 10.16cm pipe (4 inch line) to drive the system. The mass flow through the ACE tunnel is $\mathcal{O}\left(1\frac{kg}{s}\right)$, making it clear that the limiting factor on run time, and thus on the facility's duty cycle, is the ejector. ([7])

Figure 4.1: The two-stage air ejector.

Air is supplied to the tunnels via a 5.08cm pipe (2 inch line). In doing so, it passes through a 0.5MW electrical resistance heater capable of temperatures of 530K; to prevent accidental overheat and improve repeatability, the heater is only used during the tunnel's preheat and not during a run. Blowdown hypersonic tunnels must be preheated to elevated stagnation temperatures in order to prevent liquefaction of oxygen during the expansion process [202]. A dome-loaded Stra-Val regulator upstream of the heater protects it from being over-pressurized. After passing through the heater, the air is passed through a second Stra-Val regulator followed by a final 1μm filter before

finally entering the settling chamber. A US Hose Corporation UFBX stainless steel braided hose formed the final connection between the support infrastructure and the tunnel as it provides flexibility during tunnel modifications. The use of two regulators in series prevents pressure oscillations in the line, and also provides better control of the tunnel's stagnation pressure. All infrastructure inside the laboratory space is covered with custom fiberglass insulation from the Advanced Thermal Corp. in order to prevent heat loss after preheat, and also for safety. It is noted that several redundant safety mechanisms are located throughout the air delivery system including fail-closed actuators, pop-off valves, and burst disks. ([7])

4.2.2 Design and Characterization

As was previously stated, the ACE tunnel is a blowdown facility; its flow path is shown in Figure 4.2. All materials were constructed in the Texas A&M Oran W. Nicks Low Speed Wind Tunnel's machine shop from stainless steel, which allows the use of NO for PLIF without risk of excessive corrosion. A full description of the tunnel design can be found in [201, 203, 202], though the reader is again cautioned that progressive upgrades to the facility may alter the values reported therein. Air is delivered into the settling chamber via a four 3.81cm flexible hoses split between ports on the top and bottom surfaces in order seed the flow throughout the entire plenum. Two 250W Omegalux HCS-080-240V heaters on the sides and a 1000W Omegalux HCS-120-240V on the top of the settling chamber help prevent heat loss after preheat and in between runs; these surfaces are covered with Advanced Thermal Corp. insulation for safety and to prevent heat loss. The uniformity is further improved by two aerogrids consisting of 0.32cm hole patterns in stainless steel plates [203]; if the flow is non-uniform some of the holes will choke and the flow will redistribute itself to become more even across the entire array [202]. The hole patterns between the two grids are offset to enhance this effect. Downstream of the aerogrids are three stainless steel screens of progressive refinement, from 7.87. then 23.62, and finally 59.06 grids per cm [203]. The meshes break up turbulent structures to pass laminar flow into the nozzle [202]. ([7])

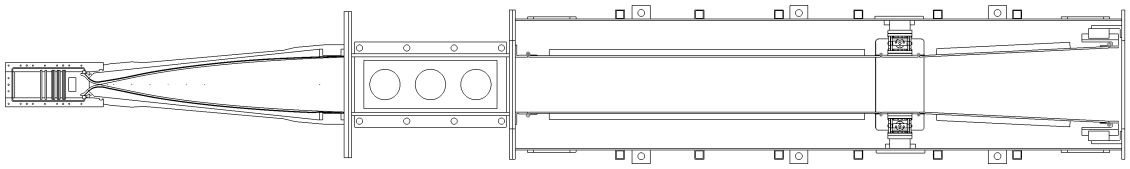

Figure 4.2: The Actively Controlled Expansion tunnel.

The contours for the 2D, planar, de Laval nozzle were designed using an in-house method of characteristics code following Shapiro [204] with a correction for the effect of the viscous boundary layer on the area ratio van Driest [39]. Simulations over the predicted experimental range were conducted with Aerosoft Inc.'s GASP CFD program. Semper et al. [201] provided a detailed explanation of the nozzle design. As with all supersonic flows, the Mach number is

controlled by the ratio between the nozzle's throat and exit via the following expression [205]

$$\left(\frac{A}{A^*}\right)^2 = \frac{1}{M^2}\left[\frac{2}{\gamma+1}\left(1+\frac{\gamma-1}{2}M^2\right)\right]^{\left(\frac{\gamma+1}{\gamma-1}\right)} \tag{4.1}$$

A unique design of the ACE tunnel's nozzle is the adjustable throat. The top and bottom surfaces of the nozzle are free floating, rigidly attached to the test section but otherwise held in place by pressure due to brackets along the two sidewalls and by resting on silicone O-rings inside the settling chamber. This allows operators to insert and remove shims at the throat to control the area ratio and thereby the Mach number. For the proposed test condition, $M = 5.7$, and for an exit area of $A = 831.70\text{cm}^2$ (including a 0.32cm step between the nozzle and test section), the theoretical throat area is $A^* = 19.43\text{cm}^2$. The actual throat height deviates from the theory, and indeed even changes at different Reynolds numbers, due to the presence and state (laminar/turbulent) of the nozzle's boundary layer. Mai [202] and Semper [206] provided Mach number and freestream acoustic noise calibrations of the freestream over a range of Reynolds numbers and for $M = [5,6,7]$. Using these results, for the current campaign $\frac{P'_{RMS}}{\langle P \rangle} = 1.0 - 1.5\%$ and the Mach number varied $0.5 - 1.5\%$ across the test section. There is a considerable jump in freestream noise at $Re \approx 3.0 \times 10^{-6}/\text{m}$ attributed to transition of the nozzle's sidewalls Semper et al. [207], so it was desirable to pick a test condition far from this Reynolds number to guarantee the nozzle's boundary layer had completely transitioned and was fully and consistently turbulent. The test section is 35.88cm wide, 23.18cm tall, and 66.04cm long. All internal surfaces are painted black to prevent reflection when performing optical measurements. A series of three 12.70cm ports on both the top and bottom surfaces allow for optical access or custom test article supports and probe mounts. One port on the top surface is reserved for a 101.325kPa pop-off valve in the event of accidental pressurization of the test section. $20.19 \times 55.75\text{cm}^2$ removable doors on both sides of the test section allow for further customization, be it for model support, further optical access, *etc*. A stainless steel table was constructed beneath the test section to form the base of an XT-95 optical rail cage that surrounded the entire test section. This is used to position equipment around the entire test section without being affected by the tunnel's vibration. The final stage of the tunnel's flowpath is the adjustable diffuser. It was originally designed following Bertram [208] and Wegener and Lobb [209]. The diffuser's outlet connects to the ejector system discussed above. ([7])

4.2.3 *NO* Injection

Under true hypersonic conditions, *NO* is naturally produced from dissociated nitrogen and oxygen atoms. However, the enthalpy in the ACE tunnel was too low to cause thermochemical effects. For this reason, aside from shock-type facilities capable of simulating flight conditions, *NO* needed to be artificially seeded into the flow; Danehy et al. [210] provided an example of *NO* PLIF MTV. On smaller-scale and pulse burst facilities, *NO* PLIF has been successfully conducted by pre-mixing *NO* into the N_2 supply McManamen et al. [3], Sanchez-Gonzalez [211], Hsu [53]. It was desirable to accelerate the *NO* through the nozzle like McManamen et al. [3], Sanchez-Gonzalez [211], Hsu [53] not only to ensure homogenous mixing, but also to allow adequate time for thermalization between the injected gas and the main air supply; this was especially important

for PLIF thermometry as it was assumed the *NO* was of the same temperature as the surrounding gas. This meant the ideal location for *NO* injection was the tunnel's settling chamber, pictured in Figure 4.3. The settling chamber was originally designed with replaceable plugs on all four sides of the box downstream of the flow conditioners; it is through one of these ports that 3.18mm total temperature and pressure probes are inserted into the flow. Because past tunnel characterizations had not found and effect on flow quality from to these probes Mai [202] and due to the ease of machining new plugs for different configurations, this was the primary candidate location for an *NO* seeder. ([7])

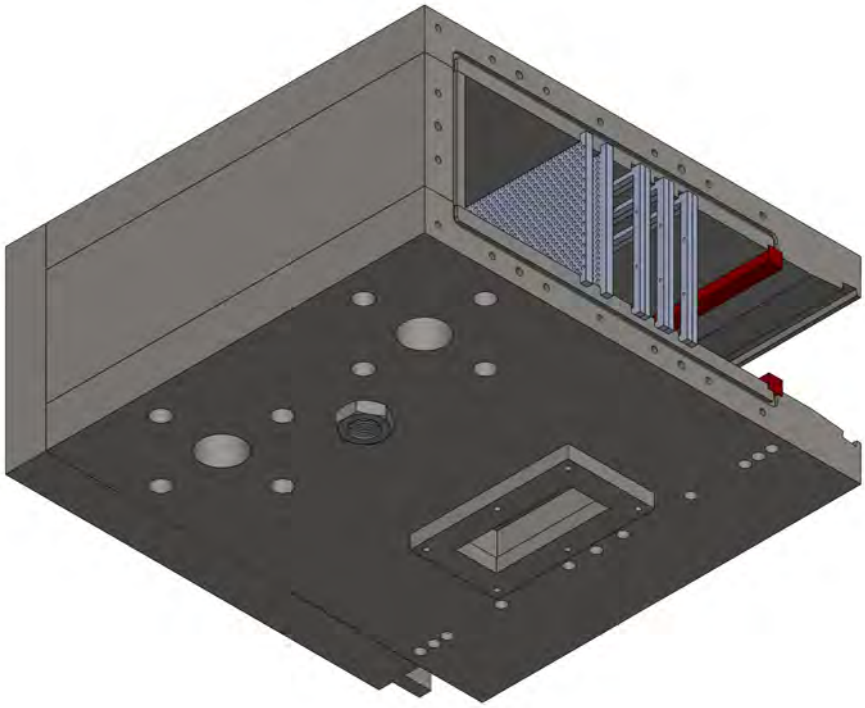

Figure 4.3: CAD model of the ACE tunnel's settling chamber; bottom corner view.

Many different seeder geometries were tested before the final design was selected. Design parameters included: the openings' geometry (slit or holes); the open area (length of slit or number/size of holes); the diameter of the pipe; the orientation of the pipe (straight from bottom or bent 90° to inject in the streamwise direction); the position of the slit/holes (before/after flow conditioners as well as vertical distance from the floor); and the injection pressure. All pipe designs were crimped to a roughly elliptical shape to simulate a symmetric airfoil and help reduce wakes. A characteristic seeder is shown in Figure 4.4. Many of the aforementioned design choices were answered in preliminary testing; for example, a water visualization test revealed in slit designs the momentum of the fluid travelling up the seeder caused non-streamwise injection. ([7])

Figure 4.4: A characteristic *NO* seeder.

An analysis of the independent impact of each parameter is included in [212], but a representative summary is provided in [2]. Three tests were conducted where a 9.53mm seeder, crushed roughly 2:1 for a final width of 4.77mm to reduce its cross-sectional area, was placed upstream and downstream of the flow conditioners, as well as removed completely such that the *NO* was injected as a plume from the floor of the settling chamber. The results are shown in Figure 4.5. The intricacy of the eddies Figure 4.5(a), which did not use a physical seeder inserted into the flow, suggest that even the act of injecting the gas itself could greatly impact the quality of the flow; this phenomenon was enhanced by the cross-flow direction of the injection. The physical seeder of 4.5(b) performed better. The streamwise injection of the gas removed many of the eddies, but a wake structure formed; even reducing the side of the seeder to a crushed 3.18mm pipe, the same size as the settling chamber's stagnation pressure and temperature ports created a wake [212]. Therefore it was necessary to inject the gas upstream of the settling chamber's flow conditioners. It was modified to allow for a pipe to be inserted $\sim$ 2.54cm upstream of the first aerogrid, as far upstream as space would allow. The resulting flow shown in Figure 4.5(c) was absent of any wake or injection artifact, so this injection location was used all subsequent experiments. It is noted that subtle streaks were present in the *NO* cloud in Figure 4.5(c), which Buen [212] attributed to be the result nonuniform *NO* seeding being passed through the aerogrids; these streaks tended to dissipate when a set of images were averaged. ([7])

Figure 4.5 also shows how PLIF flow visualization can be used to approximate the size and location of the *NO* cloud in the settling chamber. This was important because such visualization tests revealed the top-to-bottom location of the cloud was dependent on the location of the seeder's holes; the wedge, which effectively cut the test section into two regions, exacerbated this effect and made it very important to select a hole placement which puts the bulk of the cloud on the top

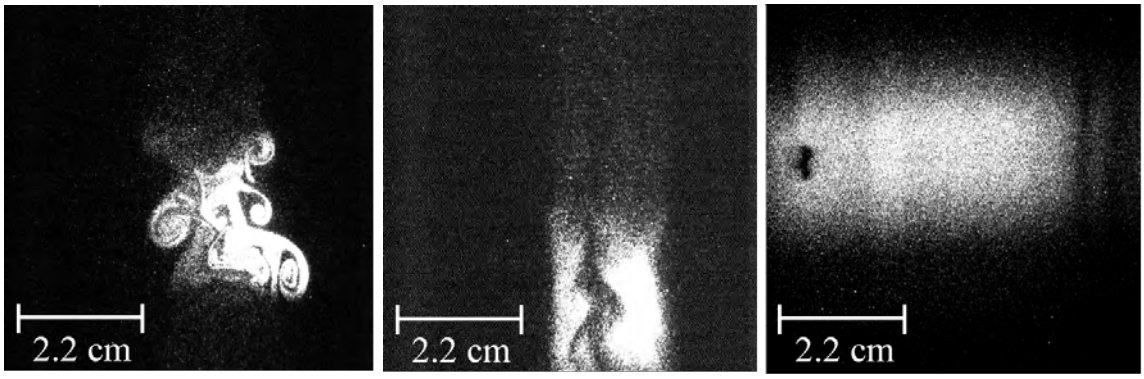

(a) (b) (c)

Figure 4.5: Effect of seeder body and placement. (a) No seeder, injection downstream of flow conditioners, (b) seeder dowstream of flow conditioners, (c) seeder upstream of flow conditioners. It is noted there is a burn spot in the camera visible in the fluorescing region in (c). The flow direction was bottom-to-top. Figures taken with permission from Buen et al. [2].

of test article in the core flow. Note that when the test article was not used the tunnel could not be run at $Re = 6 \times 10^6/\text{m}$ without risking unstart, so a slightly lower Reynolds number was used. The height of the seeder's hole was adjusted until the bulk of the gas was place above the plate in the region of interest; this success of the final placement, the dimensions of which will be quantified shortly, is demonstrated in Figures 4.6(a)-(d). The approximate placement of the test article was included via the red outline in Figures 4.6(c) and (d). The strong increase in signal directly above the plate in Figure 4.6(c) was due to the temperature and pressure increase across the bow shock. ([7])

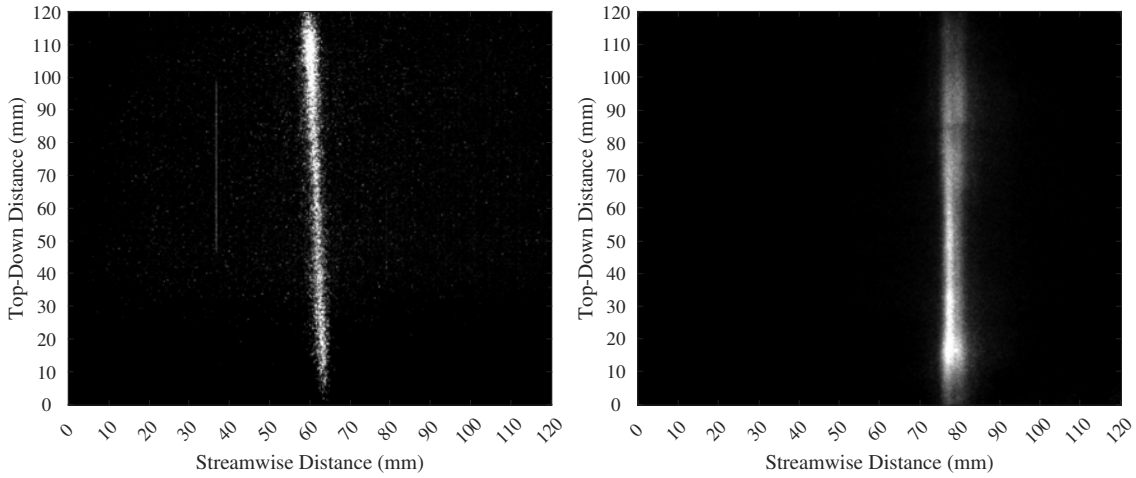

(a) Top-down, upstream

(b) Top-down, downstream

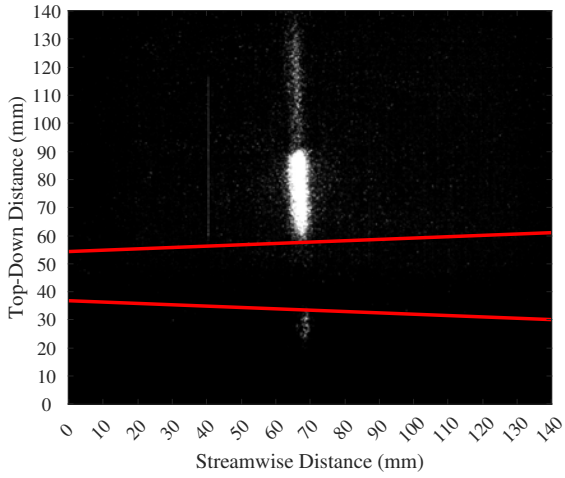

(c) Top-down with test article, upstream

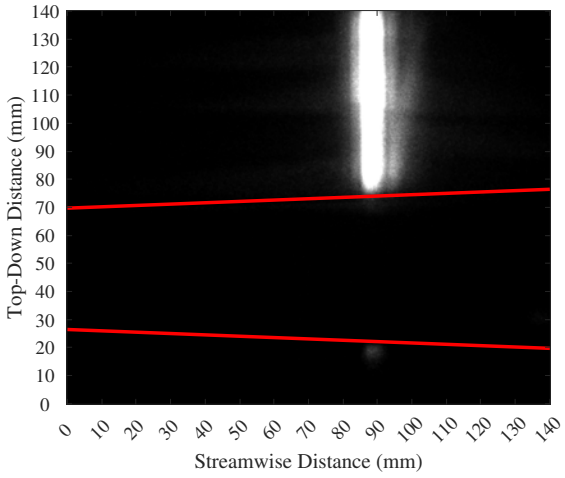

(d) Top-down with test article, downstream

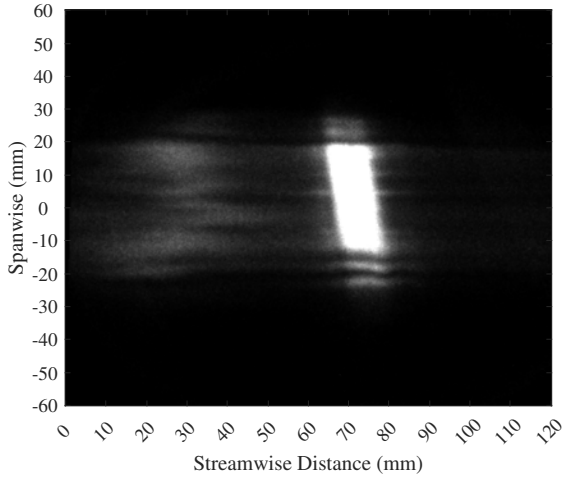

(e) Spanwise, upstream

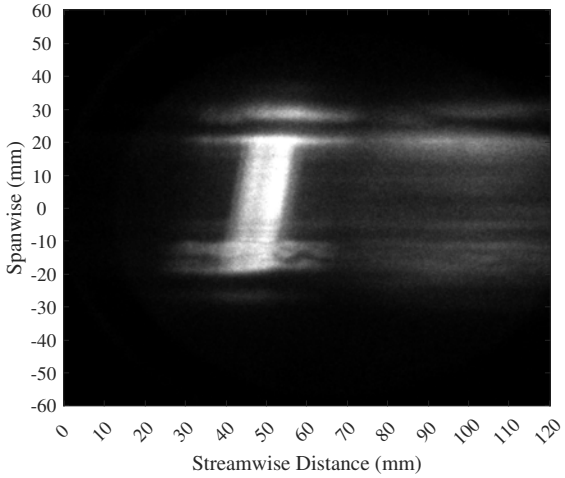

(f) Spanwise, downstream

Figure 4.6: Visualization of *NO* cloud in test section. All positions are relative, except for the spanwise position in (e) and (f); all beam positions approximately match final test locations, 125 and 405mm from the LE roughly along the test section's centerline. Flow was left to right.

It was surprising to see the gas spread nearly twice as far in the top-down direction than in the spanwise direction, but the compression and expansion of the ACE tunnel's nozzle occured in this only, which could help explain this distribution. At the extrema of the spanwise images, Figures 4.6(e) and (f), one can see evidence of two wake structures. It was believed these were the wakes cast by the 3.18mm tubes (these tubes were uncrimped) for the settling chamber's stagnation pressure and temperature probes. The probes' 50.8mm separation across the centerline matches the results. An analysis of the fluorescence in Figures 4.6(a) and (b) is discussed later. The size of the NO cloud could approximate the NO's concentration. From Figure 4.6 one could assume the gas had an elliptical shape with a major axis of 120mm and a minor axis of 60mm and uniform concentration. Estimating the the amount of NO in the region of interest required: the tunnel conditions (T_o, P_o, T, P, and M); cloud size (width and height); and the NO injection parameters (orifice diameter, number of orifices, NO concentration, and injected NO reservoir temperature and pressure). Note here the naming convention for gas injection was taken from John and Keith [205] where the "reservoir" pressure referred to the stagnation conditions of the injected gas (here NO), the "exit" conditions referred to those of the injected gas at the nozzle exit plane, and the "backing" conditions referred to those of the recipient gas (here the settling chamber) at the nozzle exit plane. A Microsoft Excel spreadsheet was produced to calculate injection conditions for a variety of cases. The user must input values for the parameters listed above, and then the spreadsheet performed the following steps:

1. Check to see if the orifices are choked; a choked nozzle has the sonic velocity at the throat and therefore cannot propagate information regarding the state of the "backing" conditions to the "reservoir", so it behaves independent of the backing conditions [205]. A nozzle is choked if
$$P_b < P_r \left(1 + \frac{\gamma - 1}{2}\right)^{-\frac{\gamma}{\gamma - 1}} \tag{4.2}$$
Note that, for the accuracy needed here, $\gamma = 1.4$ and $R_{specific} = 287 \frac{\mathrm{J}}{\mathrm{kg} * \mathrm{K}}$ for both air and NO.

2. Use isentropic flow relations to find the conditions at the orifice exit. If the orifice is not choked the flow is subsonic so $P_e = P_b$ and $\frac{P_e}{P_r}$ can be used in isentropic flow relations to find M_e and $\frac{T_e}{T_r}$ [205]. Analogously, if the flow is choked, $M_e = 1$ (again, this is not a converging-diverging nozzle so there is no acceleration beyond the sonic condition) and the isentropic flow relations can be used to calculate $\frac{P_e}{P_r}$ and $\frac{T_e}{T_r}$. These ratios are used with the reservoir conditions to provide T_e and P_e.

3. The Ideal Gas Law ($P = \rho R_{specific} T$) provides ρ_e.

4. The definition of Mach number, M_e, and T_e provides the exit velocity u_e.

5. The conservation of mass ($\dot{m} = \rho_e A_e u_e$) provides the mass flow through each orifice. Further multiplying by the total number of orifices and NO concentration provides $\dot{m}_{NO}$. Analogous calculations using the test section area and flow conditions provide $\dot{m}_{ACE}$.

6. Dividing the NO by the ACE mass flow rates provides the mass percentage of NO in the test section; this result is multiplied by the area ratio of the NO cloud and test section, which provides the "concentrated" mass percentage.

7. An alternate form of the Ideal Gas Law ($P = nk_BT$) provides the number density of NO in the cloud, n_{NO}.

The NO mix delivery system is described in [212]. In short, a LabVIEW Proportional-Integral-Derivative (PID) algorithm was used to provide customized mixtures of NO (99.95%, Praxair) and N_2 (99.999%, Brazos Valley Welding Supply). The gas concentration was set by MKS Mass-Flo 1179A mass flow controllers running of an MKS 247 power supply. The mixture was stored in a series of two Swagelok 304L-HDF4-1GAL 304L stainless steel ballast tanks with a total capacity of 7570cm^3; these tanks, as well as lines delivering the mixture, were evacuated with a Leybold D65Bvacuum pump prior to running to remove any humid air. An Omega Type PX309-200A5V pressure transducer reported the pressure in the ballast tanks, and an Omegadyne PX5500C0-250G5T pressure transducer (serial no. 47235; $0-1723.69$kPa range) connected to a static pressure tap just before the seeder entered the settling chamber provided the effective reservoir pressure. These measurements were necessary to record the NO delivery pressure drop during a tunnel run, which affected the NO concentration but not the size or shape of the NO cloud [212]. Several redundant shutoff, vacuum, vent, and purge valves were built into the NO delivery system for safety, and stainless steel was used exclusively for all components exposed to NO. Also for safety the NO was only introduced once the tunnel started, and it was shut off a few seconds before unstart to let the tunnel clear itself. ([7])

Through extensive testing, the final design was a 0.9525cm crimped pipe analogous to that in Figure 4.4; the top was sealed by completely crimping and then silver soldering it to prevent leaks. A single 0.1588cm hole was drilled into it and positioned approximately 6.668cm from the settling chamber floor. During a nominal run (Table 4.1) the nozzle is choked if $P_r > 939.693$kPa; the NO pressure typically falls from $1241.06 \rightarrow 551.581$kPa during a run, so it operates in both the choked and unchoked regimes. In testing any drop in NO number density during a run was not detectable. The ACE tunnel's mass flow rate was $\dot{m}_{ACE} = 1.8766$kg/s, and the NO mass flow rate fell from $\dot{m}_{inj} = 4.5858 \rightarrow 2.0381 \times 10^{-3}$kg/s. For the assumed elliptical NO cloud of uniform density and with NO mix percentages of 75% (velocimetry) and 0.5% (ro-translational thermometry) the approximate NO number densities throughout a run were $n_{NO(75\%)} = 4.568 \rightarrow 1.253 \times 10^{15}/\text{cm}^3$ and $n_{NO(0.5\%)} = 30.46 \rightarrow 8.354 \times 10^{12}/\text{cm}^3$. Using $n_{ACE} = 5.43 \times 10^{17}/\text{cm}^3$ from Table 4.1, then the flow by percentage would be $0.841 \rightarrow 0.231\%$ and $0.00561 \rightarrow 0.00154\%$ for the velocimetry and ro-translational thermometry runs respectively; note that $1\% = 10,000$ppm. The vibrational thermometry was conducted with an injection of 15% NO, which fell within the bounds of the other two campaigns. Using this technique, the local concentrations scale linearly based on the percentage at injection, so the local concentration in this case can be readily calculated from the listed data if so desired. Buen [212] estimated the local NO density by measuring the fluorescent lifetime of NO and modelings its decay through different pathways. They found that there was an approximately 100:1 reduction in the seeded NO concentration and the measured value in the test section; for example, if 75% NO was injected for a velocimetry measurement, the local con-

centration in the test section would be 0.75%. Thus the approximate method based off the choked flow relations agrees with Buen's independent measurement to within an order of magnitude. This means such an *a priori* estimation of the local *NO* number density can be used to check the feasibility of a proposed gas injection setup in the future. An additional consideration was the presence of the test article's hot wall (relative to the freestream temperature). A boundary layer assumption is that $\frac{\delta P}{\delta y} = 0$ [48], so $P_e = P_w$. However, here $T_e \ll T_w$ so from the Ideal Gas Law $n_e \ll n_w$; because the relationship is linear, for $T_e \approx 60\text{K}$ and $T_w \approx 360\text{K}$, there should be approximately a $\frac{1}{6}$ drop in the number density near the wall. Thus there was a considerable and unavoidable drop in PLIF signal in the critical region near the wall. Through intentional selection of the transitions to probe and rigorous data processing [212], measurements could be made near the wall, but as will be seen in all of the PLIF results, the uncertainty approaching the wall increased considerably due to fewer acceptable results; the statistical methodology by which results were filtered was described by Buen [212]. These physics set the bottom limit for the injection *NO* concentration, as data near the wall was critically important. ([7])

4.2.4 Instrumentation & Data Acquisition

The NAL's standard in-house LabVIEW VI "NALDAQ" was used to record tunnel conditions during a run. Data is read in through a 16-bit NI USB-6255 M-Series DAQ capable of recording at $1.25 \times 10^6 \frac{\text{samples}}{\text{sec}}$, though in practice most data is read at 100Hz and then averaged and recorded at 10Hz in a comma-separated variable file. Data from the entire system line is read through this system, including the air delivery system, the tunnel, and the ejector. A rise in pressure in a leg of the ejector tells the VI the tunnel is being run and that data should be saved; otherwise, data is simply printed out on a display. Two eight-channel NI USB-6366 X series "FASTDAQ"s provided a total of sixteen additional channels for experimental measurement. These DAQs could sample up to 2MHz, be synced to the NALDAQ by triggering from the same ejector condition, and could be linked together or run separately. Finally, a NI 9213 DAQ card mounted in a NI 9171 chassis to forms a "TCDAQ" for reading thermocouple data. Like the FASTDAQ it can be triggered off the same pulse as the NALDAQ and thus linked to it, and although its maximum repetition rate is lower it is capable of matching the 100Hz of the other DAQs. The stagnation pressure in the ACE tunnel is read from an Endevco 8540-200 pressure transducer connected to a Pitot tube located just before the settling chamber exit, and downstream of the flow conditioners. The sensor was located on the settling chamber at the end of the tube. Error introduced due to sensor heating was not corrected here, nor in [213, 214], though [202] took this step. The Endecvo's properties are listed in Table 4.2. The Endevco was re-calibrated just before the work in this campaign began, and the validity of the new calibration was tested. The stagnation temperature data comes from an Omega type K thermocouple with an exposed junction positioned alongside the Pitot probe; nominal error for such a thermocouple is the greater of 2.2K or 0.75% of the reading, so for the nominal condition of 430K the expected error is $\pm 3.23\text{K}$. Mai [202] estimated that the response time of the pressure transducer was negligible, but that of the thermocouple was $\mathcal{O}(1\text{s})$. To correct for this lag, Mai [202] used an average of 250ms worth of stagnation temperature data instead of the 100ms the rest of the sensors use, but this practice was not repeated here, nor in [213, 214]. The test section static pressure is recorded through a static pressure tap 11.4cm upstream of the

Property	Endevco 8540-200
Measurement Range	1378.95kPa (200psia)
Housing Diameter	3.86mm
Resolution	N/A
Sensitivity (typical)	0.218mV/kPa
Full-Scale Output (nominal)	0.3V at 10V
Resonant Frequency	450kHz
Temperature Range	$239-533$K
Temperature Sensitivity Shift	$\pm 4\%$ max
Temperature Zero Shift	$\pm 3\%$ FSO max
Combined Error (non-linearity, hysteresis, and repeatability)	$\pm 0.75\%$ FSO RSS max

Table 4.2: ACE tunnel settling chamber pressure sensor properties.

nozzle exit and downstream of the last characteristic. The pressure is fed into a MKS Baratron 631C-10 capacitance manometer thermally stabilized at 423K to provide an accuracy of $\pm 0.5\%$. While other sensors are employed to provide a detailed view of the health of the system, through isentropic flow relations and classic flow equations [205] these three values were sufficient to provide freestream values for ([7]):

- Mach number: $\frac{P}{P_t} = \left(1 + \frac{\gamma-1}{2}M^2\right)^{\frac{-\gamma}{\gamma-1}}$
- Static temperature: $\frac{T}{T_t} = \left(1 + \frac{\gamma-1}{2}M^2\right)^{-1}$
- Density (Ideal Gas Law): $P = \rho R_{air} T$
- Viscosity (Sutherland's Law [215], with constants for air from [216]): $\frac{\mu}{\mu_o} \approx \left(\frac{T}{T_o}\right)^{\frac{3}{2}} \frac{T_o+S}{T+S}$ where $\mu_o = 1.716 * 10^{-5} \frac{N*s}{m^2}$, $T_o = 273K$, and $S = 111K$
- Velocity: $U = M\sqrt{\gamma R_{air} T}$
- Unit Reynolds number: $Re = \frac{\rho U}{\mu}$

4.3 Quiescent Air Vacuum Chamber

Although the main experiment was conducted in the ACE tunnel, it is a difficult environment to work in: all materials must be securely fastened and rated to above the stagnation temperature; conditions are somewhat transient and difficult to replicate precisely; runs are brief and limited; and electrical and optical access is challenging. For these reasons prototypes and experiments critical to the development of the glow discharge and optical emission spectroscopy technique were done in a traditional quiescent air vacuum chamber.

The vacuum was produced by a Leybold Trivac D8B rotary vane pump capable of an ultimate pressure of 1×10^{-4}Torr and a nominal volumetric flowrate of $11.6\frac{\text{m}^3}{\text{hr}}$. The vacuum chamber was made from stainless steel components purchased predominantly from the Kurt J. Lesker Company. The bell jar was mounted to an automatic lift to allow for easy access to the test volume during setup, and it had a maximum height of 74.9cm and an inner diameter of 61.0cm. Its inner walls were wrapped in neoprene to help insulate against accidental ignition during plasma testing. Three 15.24cm CF flange windows, also purchased from the Kurt J. Lesker Company, allowed for optical access into the chamber; two of the windows were Kodial (Corning 7056 alkali borosilicate) windows with 8.99cm viewing diameters, while the third was high-purity fused silica (Corning 7980 HPFS) with a viewing diameter of 9.86cm. The HPFS window was used for all spectroscopic measurements because it was rated to maintain over 90% transmissivity above 250nm. The bell chamber sealed with Viton O-ring against a 20.3cm tall feedthrough collar, which itself sealed against a final end plate with another Viton O-ring. The feedthrough collar was ringed by eighteen 6.99cm CF blind flanges which could be easily modified to accommodate passing sensors or hardware into the chamber; such equipment included the manual pressure relief valve, wire throughputs, and pressure sensor. All CF flanges were sealed with annealed copper gaskets. A Duniway Stockroom Corporation CVT-275-101 pressure sensor, rated to 10% accuracy between $1 \times 10^{-3} - 4 \times 10^{2}$Torr, provided pressure data. It was connected to a Terranova 906A Convection Gauge Controller with its own 1% accuracy, so the Euclidean norm of the total error of pressure readings was 10.05%. The controller was calibrated per the manufacturer's instructions, by recording a point at atmosphere and another at a pressure an order of magnitude below the sensor's minimum readout of 1×10^{-3}Torr. Raw voltage from the controller was input into a custom LabVIEW "PlasmaDAQ" VI via the FASTDAQ and was calibrated such that the pressure matched what was displayed on the Terranova 906A's display. All flanges were sealed with annealed copper gaskets. The entire quiescent air vacuum chamber is shown in Figure 4.7. During testing, the electrodes were affixed in a channel cut into a custom ceramic holder and were polished and flush-mounted just as they would be in the ACE tunnel. The channel helped support the electrodes and allowed varying electrode widths to be tested. The wires were affixed by screws on the backside of the electrodes, which also held the electrodes in place. This approach ensured all hardware was securely fixed and centered, the electrodes were flat and flush with the channel, the test surface was clean, and, as best was possible, no breakdown occurred between the screws. For measurements across a gap (the electrodes facing each other), two ceramic mounts were used, and an aluminum extrusion was used during setup to guarantee planarity. ([7])

4.4 Plasma Hardware

The simple circuitry required for glow discharges is shown in Figure 4.8. A Spellman SL300 power supply provided up to 300W at 100mA and 3000V to the system. It had manual dials for current and voltage control as well as analog outputs so these values could be read into a custom "PlasmaDAQ" LabVIEW VI. When in the ACE tunnel for the main testing campaign, this "Switching" power supply always settled in a "Voltage Limited" configuration, which meant the delivered current was limited by the setting from the "Voltage" dial. For example, if the "Current" dial was maxed out, but the "Voltage" dial was low, the power supply could not provide the

Figure 4.7: The quiescent air vacuum chamber, bell jar open.

requested current and the amount delivered would depend on the "Voltage" setting. ([7])

A chassis mount Ohmite $10 \pm 5\%$kΩ resistor on the high-voltage side of the circuit acted as a ballast resistor. The maximum tolerable load was 100W and the total resistance, measured *in situ* to within 10Ω with a Fluke 117 multimeter (0.9% accuracy), was $R_b = 10.03$kΩ. For electrical and thermal protection the resistor rested on ceramic bricks and was stored in a plastic enclosure with a cooling fan. Alpha Wire 22AWG rated for 5000V at 473.15°K was selected to carry the power to the electrodes. For the ACE experiments, the wire simply passed through two small holes in a window plug which were sealed with tape on both the inside and outside of the test section. For the vacuum chamber, where leaks were a more serious concern, the high voltage wire was passed into the chamber with a custom high voltage throughput recommended by Dr. David Staack[1]. A length of high voltage wire had its braided core removed and replaced with a solid core lightly covered in vacuum grease. The modified wire was fed through one of the chamber's blind flanges tapped to accept a compression fitting which sealed against the silicone wire insulation. This approach provided a workable seal and electrical insulation. From here the wire was attached to the anode. The cathode was wired through a Kurt J. Lesker power throughput; while this throughput was rated for 5000V at 15A, it was designed for ultra-high vacuum applications and therefore offered no electrical insulation, so it was appropriate only for the ground side of the circuit. On the outside of the chamber, the ground wire was attached to the chamber itself and the building's ground before finally connecting back to the power supply, completing the circuit. The cathode wire for the ACE tunnel was grounded to the wind tunnel itself in a similar fashion. The power supply had analog

[1]Texas A&M University's Plasma Engineering and Diagnostics Laboratory

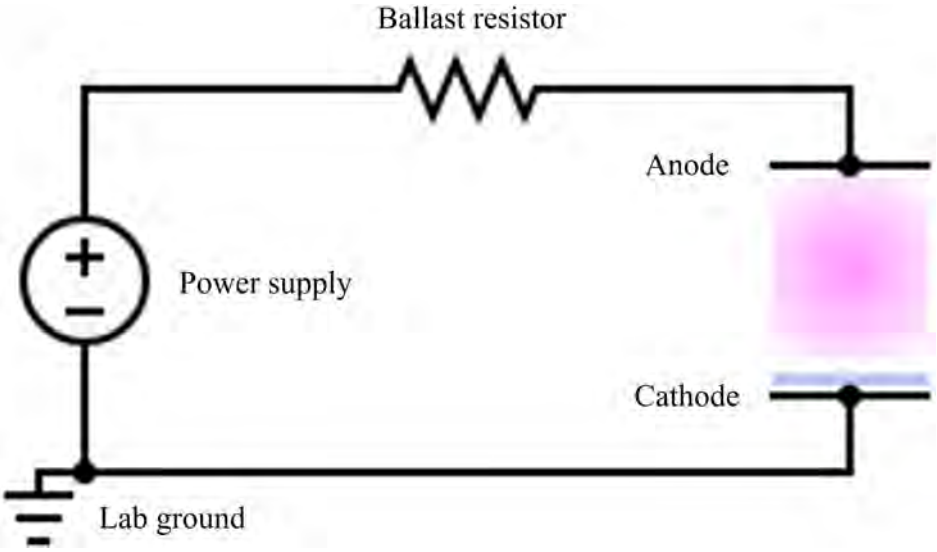

Figure 4.8: DC glow discharge wiring diagram.

outputs for the voltage and current which could be connected to the NI USB-6366 "FASTDAQ". A "PlasmaDAQ" VI was built which mimicked the design of the NALDAQ in that had the same sampling rate and trigger so the tunnel and plasma data were automatically synced to within 10Hz. The user needed to input the ballast resistance manually. With the power supply voltage V_{PS}, current I, and ballast resistance R_b known, one could use Ohm's law to calculate the voltage drop across the ballast resistor V_b (see [217]). Thus the voltage across the plasma was known from $V_{pl} = V_{PS} - V_b$. The total plasma power was then provided by Ohm's Law $P_{pl} = IV_{pl}$. The VI calculated, recorded, and displayed this information in real time, and these data were sufficient to estimate the Joule heating. ([7])

4.5 Test Article

The design of the test article was a direct result of its application, the study of vibrational nonequilibrium on hypersonic, ZPG TBLs in the ACE tunnel. All of the features and compromises to be discussed were intentionally chosen to provide a successful test environment for the planned experiments. Individual aspects of the design are discussed in their own subsections. The test article's final design is shown here in Figure 4.9 to provide a visual reference for subsequent discussions; measurements will be provided as they become relevant. Also, for reference, the test area/volume will hereafter refer to $\pm$25.4mm along the model's centerline and the flow above it as this was the core flow. ([7])

4.5.1 Past Work

The general design of the test article evolved from the recommendations in the doctoral works of Semper [206] and Leidy [213]. Both of these authors studied hypersonic, ZPG boundary layers in the ACE tunnel, and the former even focused on TBLs as well. Semper [206] used a true flat plate in their work, and designed it to span the entire test section. This successfully prevented edge

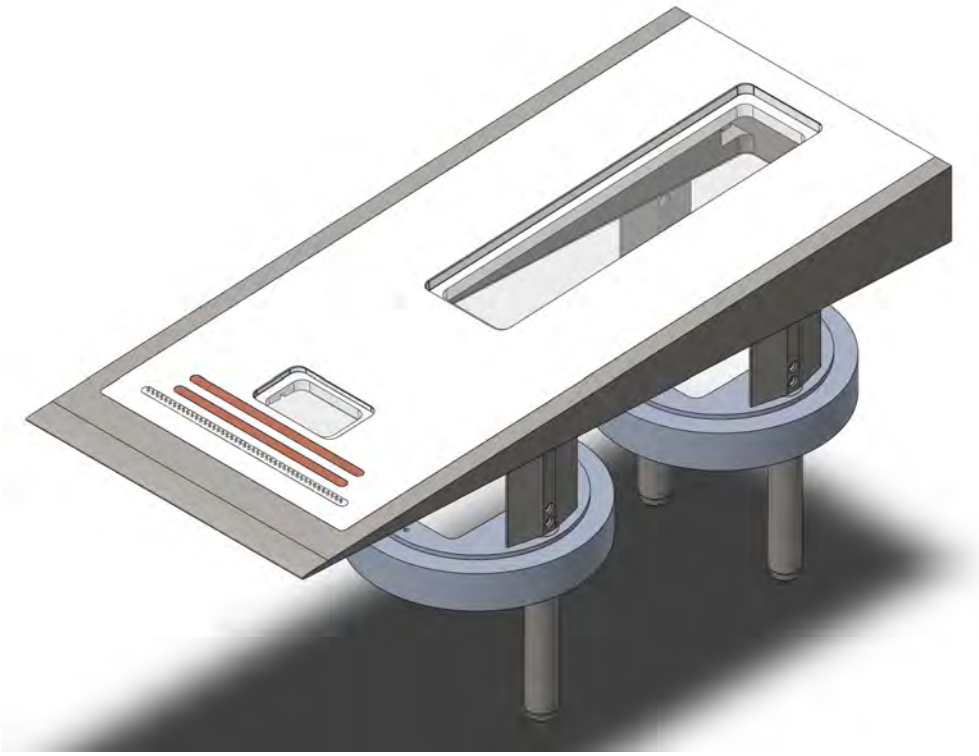

Figure 4.9: CAD model of the test article.

effects due to the pressure differential between the top and bottom surfaces, but oil flow results showed channeling of the streamlines due to tunnel sidewall interference. Notably, the model had a nonsymmetrical leading edge with 1.59mm bluntness and was mounted at a $-2°$ angle of attack to reliably produce stagnation on the top surface of the wedge. Finally, this model was constructed entirely out of aluminum, painted black for better contrast during oil flow studies, and was left in the tunnel during preheat as it mounted with four struts to the test section's floor. Leidy [213] made several attempts avoid sidewall interference before ultimately deciding to reduce the span of the model to 25.4cm, which left 5.24cm between the sides of the test article and the tunnel walls. Another notable feature was the use of a polyether ether ketone (PEEK) insert on the test surface, which allowed the use of infrared (IR) thermography as a diagnostic technique. Mounting fast response pressure transducers in a nonconductive material also reduced the data's noise. These properties, coupled with PEEK's high glass transition temperature and machinability, led Leidy [213] to attempt to make a test article entirely out of the material, but this resulted in warping in the thin section near the leading edge during manufacturing, so the plastic was instead mounted inside a larger stainless steel frame. The final model was mounted onto a sting attached to a door so the model could be quickly installed inside the tunnel after preheat; oil flow visualization showed the effect of the sting tangibly manifested on the test surface, but its effects never reached the core flow [213]. A long threaded rod connecting the test article to the floor of the test section allowed the model to be leveled before each run and helped prevent vibration. In moving the model

away from the test section's walls to reduce interference, Leidy [213] introduced the possibility of three dimensionality due to the pressure differential between the top and bottom surface of the test article. Early iterations of Leidy's model used a flat plate, leading edge, and angle of attack analogous to Semper [206], but it was found that without the aid of the tunnel sidewalls the effect of the pressure differential on the streamlines was severe [213]. In order to remove this effect, Leidy ultimately switched to a slender wedge mounted without any angle of attack and with a symmetric leading edge. The final design had a 1.3° half-angle, which according to the theoretical work of Cohen and Reshotko [218] should have only deviated slightly from true ZPG results. ([7])

4.5.2 Leading Edge

Because of the impact it has on the flow, special attention must be paid to the design of the leading edge. For example, failing to match the curvature of the leading edge with that of the wedge will produce a pressure spike and receptivity source [219]. Furthermore, if the leading edge is not sufficiently blunt the stagnation point may vacillate between the top and bottom surfaces, separating the flow and causing noise [131]. Neither of these effects were desirable even for the present study of TBLs because of their lack of predictability and uniformity; turbulence should come from uniform tunnel background noise or controllable trips, not design imperfections. Finally, slight bluntness should remove the viscous-inviscid interation which arises at sharp hypersonic leading edges (see [115, 48, 50]); this will be discussed in detail shortly. Leidy [213] used a mathematics-driven approach to design the polynomial $P(x)$ for the leading edge to account for these effects, and it was adopted here and programmed in Matlab. To begin, the user inputs a wedge half-angle δ and a polynomial-to-wedge transition point (x_{trans}, P_{trans}), where $P_{trans} \equiv P(x_{trans})$ is its distance from the leading edge and x_{trans} is its height from the centerline; this puts the streamwise direction along the vertical axis. In these coordinates, with the wedge angle now a known constant the slope of the polynomial at the transition point must be $P'_{trans} = \frac{1}{\tan(\delta)}$. The radius of curvature of a polynomial is $R = \left| \frac{\left(1+P'^2\right)^{\frac{3}{2}}}{P''} \right|$ and the curvature κ is its reciprocal, so for the constant-slope wedge the curvature must be zero. Therefore P''_{trans} must also be zero to match this condition at the transition point. With this there are three conditions for the polynomial, so it is possible to solve for three coefficients. The program will attempt to find suitable polynomials of the order $n = 2-10$, but for $n \neq 2$ only the highest order-terms are solved. For example, for a polynomial of order $n = 6$, the program solves

$$\begin{bmatrix} x_{trans}^6 & x_{trans}^5 & x_{trans}^4 \\ 6x_{trans}^5 & 5x_{trans}^4 & 4x_{trans}^3 \\ 30x_{trans}^4 & 20x_{trans}^3 & 12x_{trans}^2 \end{bmatrix} \begin{Bmatrix} A \\ B \\ C \end{Bmatrix} = \begin{Bmatrix} P_{trans} \\ P'_{trans} \\ P''_{trans} \end{Bmatrix} \tag{4.3}$$

to produce $P(x) = Ax^6 + Bx^5 + Cx^4$. In order to check the validity of the solution for each n, κ is calculated over the polynomial's domain, and if it becomes negative the solution is discarded. Using this technique, for a half-angle of $\delta = 2.75°$ and $(x_{trans}, P_{trans}) = (0.082, 0.813)$in, a sixth-order polynomial was produced in inches (Broslawski [7]):

$$P(x) = 4.2809 \times 10^6 x^6 - 1.1188 \times 10^6 x^5 + 8.0936 \times 10^4 x^4 \tag{4.4}$$

As was previously stated, sufficient leading edge bluntness is necessary to prevent flow separation [131]. It can be difficult to describe a polynomial with a single value of radius of curvature, especially for higher order polynomials which adopt a box-like shape (which in turn produces blunter profiles). It was therefore useful to adopt a new term, the "effective radius of curvature" R_{eff}, the x-coordinate where the traditional radius of curvature was minimized. Figure 4.10 visualizes the challenge of selecting a single radius of curvature for Equation 4.4, and shows the most pronounced feature is κ_{max} or R_{min}. The final result for Equation 4.4 was $R_{eff} = 1.25 \times 10^{-2}$in. This is sharper than the result in [213], $R_{eff} = 1.44 \times 10^{-2}$in, but it is blunter than the profile used for the $\delta = 2°$ wedge also studied in the ACE tunnel in [220], $R_{eff} = 5.51 \times 10^{-3}$in. Schlieren imaging of the leading edge in these studies did not show any separation, and the same technique was used to verify this claim for the current work. ([7])

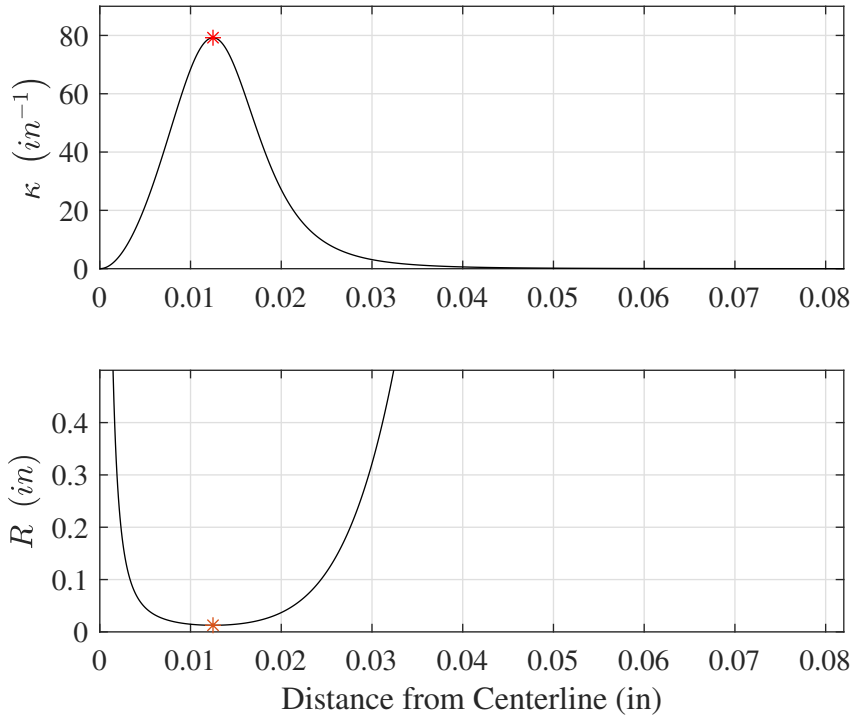

Figure 4.10: The curvature κ and radius of curvature R over the domain of the leading edge polynomial (Equation 4.4).

An additional consideration was the viscous interaction theory for hypersonic flows over flat plates with sharp leading edges, well described in [115, 50, 48, 19]. Due to the high Mach number and low density (Reynolds numbers) associated with hypersonic flows, a laminar boundary layer can grow rapidly at $\delta \propto \frac{xM_e^2}{\sqrt{Re_x}}$ [19]. So sudden is the growth at the leading edge it can create a shock and cause an "induced pressure" $\frac{P_e}{P_\infty}$ which decays along the length of the plate. An idealized

flat plate with a sharp leading edge and no angle of attach would otherwise not generate a shock as the streamlines would not deflect and $P_e = P_\infty$; even should a shock form due to real-world considerations, at the very least the pressure should be constant along the surface following the discrete jump across the shock [19]. This phenomena is governed by $\overline{\chi} = \frac{M_\infty^2}{\sqrt{Re_x}}\sqrt{C}$, where $C = \frac{\rho_w \mu_w}{\rho_w \mu_e}$. For $\overline{\chi} \gtrsim 3$, usually near the leading edge because of the $x^{-\frac{1}{2}}$ dependence, the flow is in a "strong interaction" regime. The flow "sees" the rapidly growing displacement boundary layer $\frac{d\delta^*}{dx}$, the streamlines turn, and a shock is formed which affects, most importantly, the boundary layer growth (decreased), skin friction (increased), and heat transfer (increased); these effects become negligible in the "weak interaction" region. In the strong interaction regime, Anderson [19] shows $\delta^* \propto x^{\frac{3}{4}}$, $\frac{d\delta^*}{dx} \propto x^{-\frac{1}{4}}$, and $\frac{P_e}{P_\infty} \propto x^{\frac{1}{2}}$, or $\frac{P_e}{P_\infty} = 1 + a_1\overline{\chi}$ where a_1 is a constant. In the weak interaction regime, $\delta^* \propto x^{\frac{1}{2}}$, $\frac{d\delta^*}{dx} \propto x^{-\frac{1}{2}}$, and $\frac{P_e}{P_\infty} = 1 + b_1\overline{\chi} + b_2\overline{\chi}^2$ where b_1 and b_2 are constants. Hayes and Probstein [115] ascribed values to these constants for the cases of adiabatic and cold-wall ($\frac{T_w}{T_{aw}} \ll 1$) flat plates. The point here is that even idealized, perfectly sharp leading edges are not without their own unique complexities which can manifest in practical environments. Because the test article was modeled after a flat plate in such an environment, the theory was worth reviewing. However, the bluntness of the leading edge and wedge's turning angle meant that a bow shock would form independent of any viscous effects. Furthermore, it was assumed the strength and curvature of the bow shock, the length of the plate, and the presence of the trips, would dominate a these leading edge effects. Indeed, a rough calculation showed the flow would enter the "weak interaction" regime $\lesssim$ 1cm from the leading edge, well ahead of the trips. ([7])

4.5.3 Half-Angle

In order to provide the greatest effect the electrodes should be placed as near the leading edge as possible. However, they must be insulated in order to prevent accidental ignition with the tunnel or test article. PEEK had suitable properties for this application, in addition to those for IR thermography and fast-response pressure measurement discussed above. Therefore a single, seamless PEEK insert was fit into the stainless steel wedge frame, following Leidy's [213] final model; an internal O-ring ensured there was no suction or blowing onto the test surface through the seam. As in the quiescent air vacuum chamber, the wires were attached to the electrodes with screws, which meant the electrodes needed a significant thickness. Additionally, they needed to mount flush inside a PEEK pocket, which itself needed to be attached to the metal wedge far enough upstream to prevent accidental ignition. All of these design requirements required a certain thickness, enough material for each feature to be machined, and the only way to provide it was to increase the wedge's half-angle. Ultimately a 2.75° half-angle yielded the thinnest realizable wedge. While $\delta = 2.75°$ should still behave like a flat plate [218], the increased cross-sectional area drove up tunnel blockage. This problem was exacerbated by the desire to keep the wedge as long as possible to provide testing locations at large Re_x. Taken together, it was necessary to reduce the test article's span to prevent tunnel unstart at the test condition due to excessive blockage. This makes the core flow more susceptible to edge effects, but the oil flow in [213, 220] assuaged these early design concerns and suggested a sufficient test area would be maintained. In the final design, the conservative tunnel blockage was approximately 13.2% without and 16.1% with the stands. If

the total tunnel blockage, including probes, was to be kept below the empirical upper limit of 20% then the wedge could not be made significantly longer or wider. ([7])

4.5.4 Translating Stands

In an effort to prevent interference due to the sting on the test surface seen by [213], and to minimize vibration during a run, the model was mounted in the test section with three stands. The stands were 1.27cm wide with angular leading and trailing edges to prevent the additional blockage produced by strong bow shocks and to prevent vortex-induced vibration. The stands could be attached via pins at one of three locations covering 7.62cm in the streamwise direction, allowing the test article to be translated in between runs. This was useful as optical access in the test section is somewhat limited. The stands themselves were connected to rods which extended through custom tunnel plugs. Outside of the tunnel three Mitutoyo 7850 Micrometer Jacks could be used to precisely raise or lower the test article while maintaining flatness in both the streamwise and spanwise directions; silicone O-rings ensured a hermetic dynamic seal between the rods and the tunnel. The ability to translate the model up and down was useful for laser diagnostic measurements of the boundary layer where it could be difficult to move the beams and maintain proper alignment. Only three stand/rod pairs were required to translate the model because adding a fourth would have over-constrained the test article and led to binding (a plane is defined by three points, not four). Note that wires could be passed into the test section through small holes in the custom plugs and then sealed with high temperature polymide (Kapton) tape or Permatex High Temperature Gasket Maker (room temperature vulcanizing (RTV) rubber). A $\pm 0.1^\circ$ tolerance in pitch and roll was maintained throughout the campaign, confirmed using a SPI-TRONIC Pro 3600 digital angle indicator ($\pm 0.05^\circ$ though $0 - 10^\circ$, overall accuracy $\pm 0.2^\circ$). Keeping the entire model support system constrained to custom plugs prevented permanent modification to the ACE tunnel's test section and restricted the design of the stands to a small area away from the test article's sides, where their influence may have affected the test surface. While this approach prevented all model vibration and guaranteed a level test surface, leaving the model in the tunnel during preheat meant all materials and sensors needed to be rated to above the tunnel stagnation temperature, especially those in contact with the test article's thermally conductive metal components. ([7])

4.5.5 Mounted Optics

The PLIF techniques require shooting a laser through the boundary layer at the wall. Directed exposure to a focused laser beam would degrade the test article, and the scatter thrown as the beam reflects off the model would be so strong it could damage the ICCD. Therefore it is necessary to have a means for the beam to pass through the model. To prevent these issues, custom fused silica windows were purchased from Technical Glass Products Inc. which should maintain $>$ 90% transmission at the wavelengths of interest. These windows were mounted on both the top and bottom surfaces of the test article, as well as the mounting plugs to allow the beam to pass completely though the model and out of the tunnel. They were specifically sized to maximize access to the test volume. This is illustrated in the model section view in Figure 4.11. The windows were hermetically sealed using Permatex High Temperature Gasket Maker RTV and were mounted flush with the test surface. This PEEK insert was only used for PLIF applications; a seamless PEEK insert was used for all other diagnostics. Small channels were left on the underside of the

test article to allow pressure relief in the space between windows as the model was thermally and barometrically cycled during a tunnel run. While a window blowout was unlikely, this approach should also help prevent any suction or blowing out through the top window's seam, which would directly affect the results. Figure 4.11 should communicate the effect wedge angle had on window placement. Neither the upstream nor downstream windows could be shifted farther upstream or made considerably thicker without making the test article too delicate to produce; this again shows why increasing the half-angle was the only way to increase the test area in the streamwise direction. Also, note how in the upstream location, the PEEK is directly exposed on both the top and bottom surfaces. The width of the windows was somewhat arbitrary and was selected to keep cost down and provide enough distance to collect off-centerline data without running into edge effects due to the windows' seams. In preliminary testing it was revealed that despite the high transmissivity, the reflections off of the windows were strong enough to conflate the results, so the glassware was sent to Newport Thin Film Laboratories where the top surface of each of the four windows was coated to reflect $< 0.5\%$ of the wavelengths of interest. The mounting plugs were also painted black to help prevent any scatter due to beam misalignment at the tunnel exit. ([7])

Figure 4.11: A section view of the test article.

4.5.6 Materials and Manufacturing

Most of the test article's components, most importantly the metal wedge frame, were made by Quicksilver Manufacturing, Inc. Wherever possible, SAE 304 stainless steel was used to add durability during handling, especially in thin sections like the leading edge. The wedge frame was heat treated to prevent warping of the leading edge during machining and was ground to a 0.813μm finish. A notable exception to the material restriction was the mounting plugs, which were made from 6061 aluminum due to an ultimately abandoned idea to surface treat them with an anti-reflective coating. The PEEK used for the insert was made from Victrex 450*G* granules extruded into a "Ketron 1000" sheet by Mitsubishi Chemical Advanced Materials and sold by Professional Plastics, Inc. Victrex supplied material properties, specifically the thermal conductivity and specific heat capacity, over a the range of temperatures expected in the ACE tunnel, which is critical for accurate heat flux calculation. Because of the need to use a known plastic source, the PEEK inserts were made in the Texas A&M Department of Chemistry's machine shop from stock purchased from the known supplier, Professional Plastics, Inc. Other versions of the PEEK insert without any window mounts were produced for testing with non-optical techniques without the risk of interference of any Mach waves produced by the windows' seams (ex.- one with static

pressure taps for Pitot measurements, one with holes for Kulite pressure transducers, *etc.*). Finally, the electrodes and trips were made in the Texas A&M Oran W. Nicks Low Speed Wind Tunnel due to its wire electric discharge machining capabilities. All materials used are either inert in the presence of *NO*, or could be easily replaced (ex.- the 3D printed trips). The full assembly's final dimensions are shown in Figure 4.12; the design and placement of the trips and electrodes is to be discussed. Each set of trips and electrodes were sanded to sit flush within their specific PEEK insert. ([7])

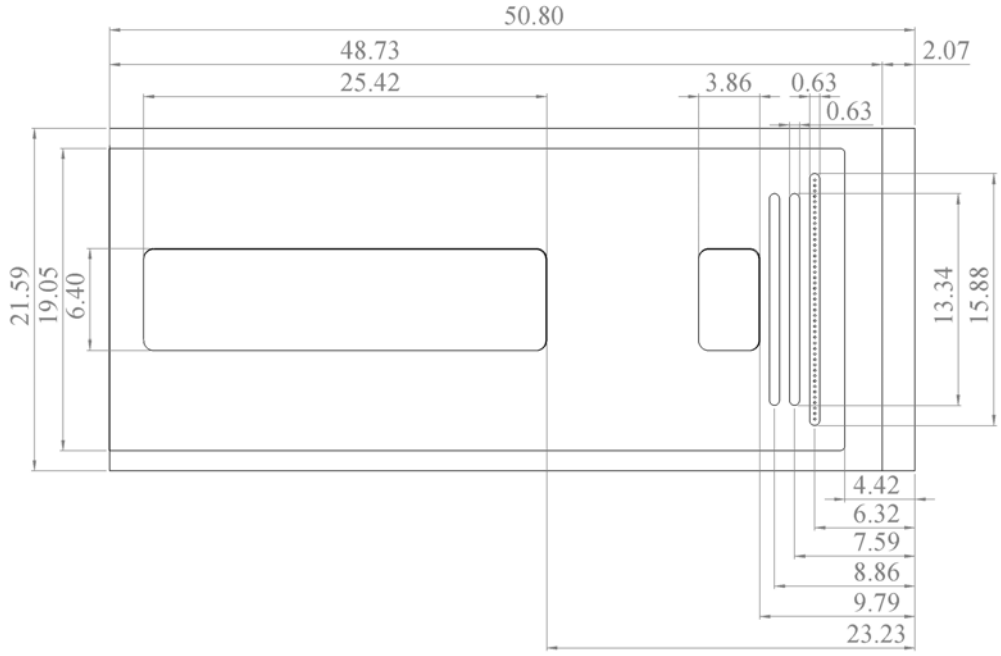

Figure 4.12: Drawing of the final test article. All dimensions are in centimeters.

4.5.7 Trips

In this study discrete trips were used to foment turbulence. The design selected are known colloquially as "pizza box" trips [206], but are more formally described as diamond trips. The width ("diameter", d), height (h), and spacing (w) of the diamonds are variable and impact the efficacy of the trips as a whole; these parameters are shown in Figure 4.13. Berry et al. [221] performed a comparative study of the diamond trips to other geometries typical for supersonic and hypersonic applications; this included a campaign at freestream Mach and Reynolds numbers attainable by the ACE tunnel, 6 and $7.22 \times 10^6/\text{m}$ respectively. Furthermore, the test article they used, the inlet to the Hyper-X scramjet, could be simplified without much loss to a slender wedge like the one used here. The authors scaled the trip geometry by the total enthalpy boundary thickness $\left(\delta_{H_o,99.5\%}\right)$, which was itself calculated from a laminar CFD simulation. The diamond diagonal

and center-to-center spacing were $d_{trip} = \delta_{H_o,99.5\%}$ and $w_{trip} = 2\delta_{H_o,99.5\%}$ respectively, while element heights ranging from $\frac{h_{trip}}{\delta_{H_o,99.5\%}} = 0.185 - 1.48$ were tested. Berry et al. [221] concluded that with the previously described size and spacing, the minimum "effective" diamond trip height was $\frac{h_{trip}}{\delta_{H_o,99.5\%}} = 0.74$, where "effective" meant turbulence was initiated immediately downstream of the trips. ([7])

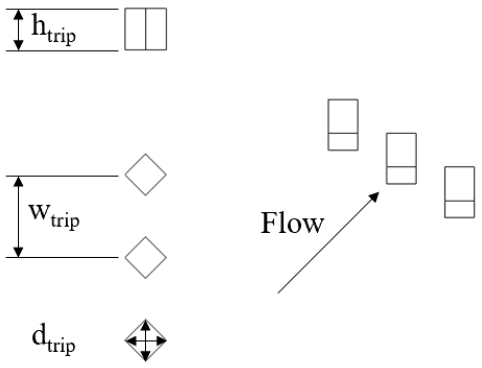

Figure 4.13: Diamond trip parameters; figure adapted with permission from Berry et al. [221]

.

While Berry et al. [221] ultimately recommended a different trip design for their specific application, the diamond trips have been used repeatedly on slender wedge geometries in the ACE tunnel. Semper and Bowersox [30] used said trips to study low Reynolds number $\left(4.4 \times 10^6/\text{m}\right)$ turbulent boundary layers on a true flat plate at $M = 5.92$ at a slight (2°), negative angle of attack. This study used the same $\delta_{H_o,99.5\%}$ and $2\delta_{H_o,99.5\%}$ width and spacing as Berry et al. [221], and used $\frac{h_{trip}}{\delta_{H_o,99.5\%}} = 1.48$, where $\delta_{H_o,99.5\%}$ was again determined from a laminar CFD simulation. The careful boundary layer surveys conducted by Semper and Bowersox [30] showed the trips were indeed effective at producing classical, fully-developed turbulent boundary layers in the ACE tunnel; it is noted that this effort included numerical and experimental studies of the flow physics around each trip. Semper and Bowersox [30] did remark, however, that optimal disturbance spacing should be $\sim 3\delta_{H_o,99.5\%}$ according to the work by Reshotko and Tumin [222]. In their work on transitional boundary layers tripped using the diamond elements over a 1.3° half-angle wedge at $M = 6$ in the ACE tunnel, Leidy [213] explored the effect of center-to-center spacing on the trip performance; trips in the range of $w_{trip} = (2-5)\delta$ were tested. Here it was assumed δ was where the velocity profile recovered 99% of its freestream value, which the Leidy [213] predicted with the self-similarity solutions of van Driest [223] and validated with schlieren imaging. Using oil flow visualization, Leidy [213] found that only $w_{trip} = 2\delta$ was able to produce a turbulent boundary layer for the trip heights studied; again, as the focus of that work involved transitional boundary layers, ultimately $h_{trip,max}/\delta_{H_o,99.5\%} = 0.6$ and $d_{trip} = \delta$ so laminar, transitional, and turbulent boundary layers could be achieved. These works provided a clear path for trip sizing to produce

TBLs in the ACE tunnel. The diamond trips were produced using Formlabs stereolithography 3D printing equipment in the Texas A&M Oran W. Nicks Low Speed Wind Tunnel's machine shop. A Form 3 "UltraHerbivore" model printer made the trips with 100μm layers from Gray Pro resin. The parts were washed in isopropyl alcohol in a FormWash "EbonyServal" part washer and cured in a FormCure "CoffeeTonkinese" UV chamber. The parts were lightly sanded to ensure they fit in the test article and all support material was removed, and they were manually tapped so they could be screwed into a pocket on the PEEK insert; these screws were covered with polymide tape to prevent suction or blowing onto the test surface through the holes. δ was determined from the boundary layer solver. The full boundary layer code was not run, just the self-similar solution as at the time it was the validated portion (van Driest's [223] results provided the comparison). The current wedge was slender enough to be handled by and compared to such a flat plate, 0° angle of attack technique. Eventually, schlieren imaging of the trips interacting with the boundary layer validated the choice of their height. It was desirable to use the smallest trips possible so as to reduce the effect of the trip itself on the flowfield. For this reason, four different trip heights were considered, $\frac{h_{trip}}{\delta} = [1, 1.25, 1.5, 1.75]$. Similarly, the spacings tested were $\frac{d_{trip}}{\delta} = [1, 1.5, 2]$ and $\frac{w_{trip}}{\delta} = [2, 3, 4]$. Analogous to the phosphor thermography in Berry et al. [221], IR imaging was used to determine the state of the boundary layer for each trip height over an array of Reynolds numbers. ([7])

The laminar boundary layer profile was solved for the 2.75° half-angle wedge used in the present study 63.5mm from the leading edge, which was where the trips were centered; note that this was as far upstream as the geometry of the test article would allow and was similar to that used by Leidy [213] (64mm) and significantly farther upstream than Semper and Bowersox [30] (95.2mm). The flow conditions conditions were $M = 5.75$, $P_o = 517.11$kPa, $T_o = 430$K, which yielded a pre-shock Reynolds number of 6.01×10^6/m. Following [30], who also left their model in the tunnel during preheat, an adiabatic wall condition was used; IR testing will show this assumption is in general not appropriate, but for a laminar boundary layer and for the fidelity needed at this point, the results remained usable. The simulation was conducted on an equally spaced grid with 250 points in the wall-normal direction simulating up to 10mm from the wall. The simulation was repeated with 1000 points and showed no meaningful change, implying the grid was converged. The resulting boundary layer thicknesses were: $\delta_{H_o,99.5\%} = 1.71$mm; $\delta_{u,99.5\%} = 1.64$mm; $\delta_{T,99.5\%} = 1.83$mm. There was little to choose, but for the sake of consistency with the work of Berry et al. [221] and Semper and Bowersox [30], the total enthalpy definition was used for trip sizing. This meant that $h_{trip} = [1.71, 2.14, 2.57, 2.99]$mm, $d_{trip} = [1.71, 2.57, 3.42]$mm, and $w_{trip} = [3.42, 5.13, 6.84]$mm. ([7])

4.5.8 Electrodes

Thermal NEQ was seeded into to the flow via a DC glow discharge, where electrical energy was used to create a plasma, which ionized the nitrogen molecules in the air and excited their electronic and vibrational states [102]. Broadband OES in [53] suggested molecular nitrogen would be preferentially excited, especially with respect to molecular oxygen. As the plasma recombined and relaxes from excited electronic states, energy was stored in elevated vibrational modes in the neutral nitrogen's ground electronic state. This process was central to the overall experiment, so

extra attention was paid to the design of this element of the test article.

4.5.8.1 Orientation

The plasma's primary role is to provide a uniform test area, perturbing nothing but thermal equilibrium. For this reason, flush electrodes spanning the width of the test article like those in [120] were selected. This configuration produced a manageably-sized, predictable, and uniform glow discharge. There are several practical considerations one must consider in regard to electrode placement such as plasma stability, efficacy, and shielding. As a starting point, the electrodes were placed as near the leading edge as possible, but downstream of the trips. This is because the space necessary for trips could act as insulation to prevent plasma formation between the anode and metal wedge frame. Following Kimmel et al. [120], the cathode was placed upstream of the anode. This made sense because it put the larger flow perturbation nearer to the leading edge to increase its effect, the negative glow was less likely to be distorted by the trip wakes, and it moved the high-voltage anode farther away from the metallic wedge body. Unfortunately, during preliminary testing streaks began to form on the PEEK between the two electrodes, their location corresponding with individual trip structures. It was unclear if these formed due to copper sputtering off the cathode or the PEEK degrading, but in either case there was a risk that over time they could allow breakdown across the surface of the PEEK. For this reason, the position of the cathode and anode were flipped. Streaks on the PEEK downstream of the cathode were formed throughout the remainder of the test campaign, but the risk of permanent damage to the test article was removed. Two physical phenomena related to this change should be mentioned. It noted that the ion velocity is of the same order as the flow velocity. It is not unreasonable to expect some ions clustered above the cathode may be blown into the test domain. Furthermore, the ions traveling towards the cathode were now sped along by the flow, increasing the ion current. This manifested in a $\sim 150\%$ increase in plasma power from the original electrode configuration and the formation of a positive column. The concern about a nonuniform positive column was assuaged by a visual inspection of the plasma and minor role the region plays in the first place, and accidental ignition was prevented by providing ample space on all sides of the electrodes and only supplying high voltage when the wind tunnel was started and stable. ([7])

4.5.8.2 Paschen's Curve to Determine Inter-Electrode Gap

A classic experiment for glow discharge facilities is the manifestation of Paschen's Law. Understanding this theory is important because it can be used to help set the electrode gap D. There is a delicate balance in selecting the electrode spacing, and getting it wrong risks either producing a nonuniform plasma, an abnormal glow discharge, or failing to even produce a glow discharge.

Breakdown is controlled by γ as well as A and B (Equation 2.21). γ is difficult to predict for a given setup, while the latter two were shown to be quasi-dependent on the system's temperature. Thus the presence of a strong thermal boundary layer further complicated the estimation of V_t because the exact temperature at which breakdown will occur (or, put another way, where in the boundary layer) was unknown. Here γ was determined experimentally. This ensured the electrode gap selected would produce an attainable V_t wherever in the boundary layer the gas ultimately broke down. Paschen's Law was experimentally replicated in the quiescent air vacuum chamber because it provided a relatively controllable pressure and temperature environment. Data

was recorded at each pressure condition with the "PlasmaDAQ" VI for 30s at 100Hz averaged into 10Hz intervals; this was conservatively several orders of magnitude slower than characteristic breakdown times Rajzer [97]. The electrodes used were rounded rectangles using 7.62cm long tip-to-tip and 1.27cm wide designed after the experiments in Kimmel et al. [120]. They were sanded down to P400 roughness and then polished with 800grit (10μm) lapping paste. Thus the electrodes were analogous to those ultimately mounted in the test article, but in order to remove all the ambiguity in measuring D for a flush electrode configuration, center-to-center or edge-to-edge, here the electrodes faced one another 2.54cm apart. During a data collection period, the current was maximized and the voltage was slowly ramped; because there was no current, no voltage was lost to the ballast resistor so $V_{PS} = V_t$ and $E = V_{PS}/D$. The time at which the current first exceeded 0.4mA for three consecutive samples determined V_t. Visual observations of the plasma confirmed this was an appropriate benchmark. Data was collected at a number of pressures and ceased when the plasma started being produced at the metal walls of the bell jar. The results are shown in Figure 4.14, with error bars due to the 10.05% uncertainty in the pressure reading. The experimental data were fit with Paschen's Law using A and B calculated from Equation 2.21 at $T_{room} = 294.82$K with σ and $\frac{I}{e}$ found from von Engel's measurements of $A = 15\text{cm}^{-1}\text{Torr}^{-1}$ and $B = 365\frac{\text{V}}{\text{cm}\cdot\text{Torr}}$ [99]. This approach was valid because the experiment was conducted at room temperature and $\frac{E}{P}$ was mostly within the listed $100 - 800\frac{\text{V}}{\text{cm}\cdot\text{Torr}}$. With this the only free parameter left was γ. Different values were used until a curve was produced which matched the data. In the end, $\gamma = 2.5 \times 10^{-4}$ provided reasonable agreement at both $V_{t,min}$ and on the right hand branch; the discrepancy in the left hand side of the branch was likely due to having $\frac{E}{P} > 800\frac{\text{V}}{\text{cm}\cdot\text{Torr}}$. This value for the secondary emission coefficient fell well within the bounds $\mathcal{O}(10^{-6}) < \gamma < \mathcal{O}(10^{-3})$ set by Francis [224] for N_2 on copper electrodes at $PD = 50\text{torr}\cdot\text{cm}$.([7])

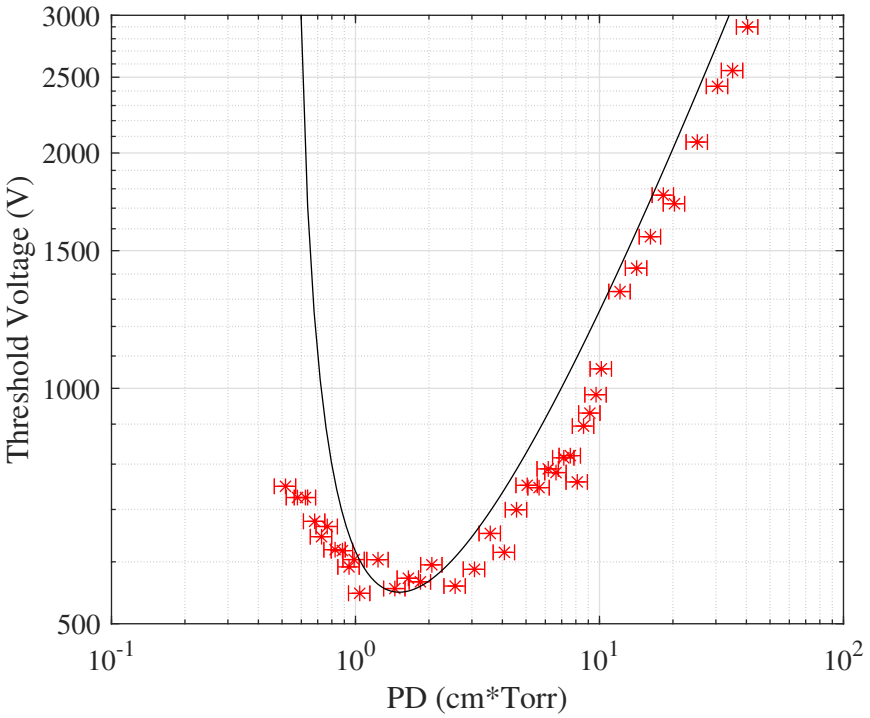

Figure 4.14: Paschen's curve in a the quiscient air vacuum chamber; $\gamma = 2.5 \times 10^{-4}$

With γ known, the effect of temperature on Pachen's Law could be explored. Here $\sigma = 4.554 \times 10^{-20}\text{m}^2$ and $\frac{I}{e} = 24.333\text{V}$, calculated from von Engel's measurements at room temperature [99], were used. Again, comparing with direct measurements like those by Atkins and Paula [100], these parameters are off, and the conditions under which they were found may not match the present experiment in the ACE tunnel, but they are sufficient to illustrate the effect of temperature on Paschen's Law and provide some approximation of V_t over the expected temperature range. Remember, the goal here is to ensure D is reasonably chosen, not precisely predict V_t as it is far easier to just measure it in the tunnel. To that end, temperatures between 50 and 450K were simulated and results are shown on Figure 4.15. The results suggest increasing the temperature decreases V_t on the right hand side of Paschen's curve, has no effect on $V_{t,min}$, and increases V_t on the left hand side of the curve. The 3000V power supply should be capable of providing breakdown up to $Pd \sim \mathcal{O}(10-100)\text{cm}\cdot\text{Torr}$, but in practice V_t should be limited to $< 1000\text{V}$ to ensure there is enough range to fully cover the cathode in plasma. This puts $PD \sim 1-10\text{cm}\cdot\text{Torr}$. Because the a nominal post-shock pressure was $\sim 5\text{Torr}$, the electrode gap was fixed at $D = 1.27\text{cm}$. This was the center-to-center distance, following the convention of Kimmel et al. [120], and although additional testing in the quiescent air vacuum chamber found that using the edge-to-edge distance had better agreement with Paschen's Law, it will continue to be used here. Finally, note that keeping the gap small had the additional benefit of helping to prevent accidental ignition between the electrodes and metal wedge frame.([7])

There was some concern that making the inter-electrode gap too small could cause the PEEK

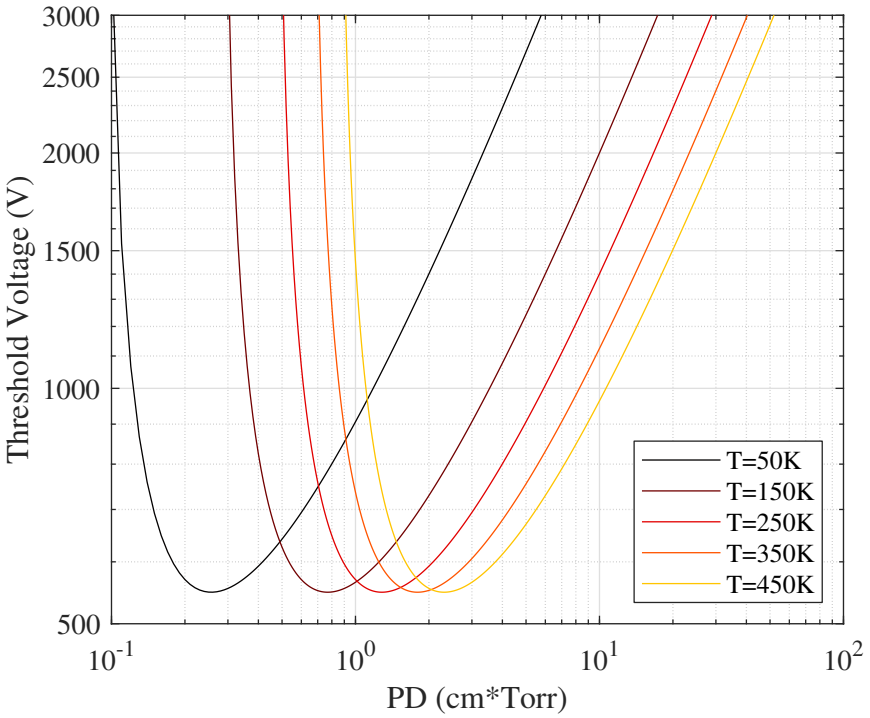

Figure 4.15: Theoretical Paschen's curves illustrating the effect of temperature on breakdown.

insulation between the electrodes to short, especially at higher temperatures or near the electrodes' rounded sides. Remember, D was a center-to-center measurement, and for the final design the PEEK thickness between the electrodes was only 0.635cm. Lacking applicable data from the manufacturer, this dielectric strength was tested with a leftover piece of PEEK with channels cut into it and an overpowered power supply. Electrodes matching the surface treatment and size of the final design were mounted into the PEEK. A 600W (10kV at 60mA) Glassman PS/EJ10R60.0 (serial no. N629111-01-NR190624) DC power supply provided the voltage. Three 50Ω and one 20Ω Ohmite chassis mount ballast resistors in series provided a total resistance of $R_b = 170\Omega$ and total power dissipation of 400W (the resistors were briefly overloaded during breakdown). To account for thermal effects, before testing the setup was heated face-down on a hot plate to $\sim 373.15K$, as measured with a Extech Inst. 42510A IR Thermometer; it is noted this setup did not provide uniform heating through the PEEK, but this was not a priority. The power supply was put into a "voltage limited" mode and the requested current maximized. The voltage was then increased until breakdown occurred. The experiment was conducted in open air, save for a cover for safety. The PEEK eventually shorted at $\sim$ 8kV, so the chosen gap was safe for the lower temperatures and 3kV power supply used throughout the campaign. Nevertheless, the power supply was only ever briefly turned on at low voltages before a run when the plate was cold and was shut off before tunnel unstart during a run to minimize the PEEK having to insulate the electrodes. ([7])

4.5.8.3 Size

In order to produce a glow discharge which completely covered the electrodes, a necessity for providing a constant test environment, one could either increase the power supply's current or decrease the size of the electrode. In practice, it was far easier to control the current than design multiple different electrodes of different size, so the approach taken here was to reduce the electrode area as much as reasonably possible and rely on current control thereafter. Following Kimmel et al. [120], the end result was a rounded rectangle 13.34cm long (tip-to-tip) and 0.635cm wide and with a total area of 8.381cm^2. The width was smaller than the trip insert to conserve area, but still large enough to prevent any plasma edge effects in the region of interest. The final width left 2.858cm on either side of the electrodes to prevent ignition between the the metal wedge frame; this distance is 4.5$\times$ the edge-to-edge electrode distance, 0.635cm, and was a minimum maintained around all sides of the electrodes. The thickness was set to provide ample material to tap support and conducting screws into and to provide sufficient rigidity for handling and polishing despite being made of soft copper. Preliminary testing showed that this size became fully covered around $I \approx 90$mA, so it was an excellent match for the 100mA power supply. Putting additional current through the electrodes once they are fully covered by plasma will lead one into the less well-characterized abnormal regime, where any power benefits are paid for with the necessity of more complex theory. ([7])

4.5.8.4 Construction, Wiring, and Support

The electrodes were made from a 0.476cm-thick 110 copper bar and machined with a wire electric discharge machine at the Oran W. Nicks Low Speed Wind Tunnel's machine shop; the thickness provided rigidity during production, sufficient thread length for fasteners, and, with proper tolerancing, provided some extra material to be sanded and polished away for a secure and flush fit. They were sanded down to P400 and polished with 800grit (10μm) lapping paste, just as those for the Paschen characterization. The electrodes were fit into pockets in the PEEK and fastened from below by three screws; the screws were covered in Permatex High temperature Gasket maker RTV to prevent plasma ignition and also sucking/blowing along the sides of the electrodes. Two screws were made from electrically insulative, thermally safe PTFE and one screw on each electrode was made from metal and acted to carry the current from the wire into the electrodes. The cathode's wire was connected to the center of the electrode to ensure a uniform glow discharge in the centerline, while for space the anode's wire was attached on one of the side screws; although a non-uniform positive column focused around the connection point would not be too problematic due to its relative lack of importance, it was nevertheless evenly distributed along the gap. ([7])

4.6 Mach 6 Quiet tunnel

This section follows from Siddiqui et al. [5]. The original NASA Langley Mach 6 Quiet Tunnel (M6QT) facility is installed at the TAMU National Aerothermochemistry and Hypersonics Laboratory, where it shares pressure-vacuum infrastructure with the ACE tunnel described above. The M6QT employs a long settling chamber with flow conditioning for the flow entering the nozzle. The nozzle has bleed slots to remove the boundary layer at the throat to start a fresh boundary layer, which helps delay transition. The nozzle is a highly polished surface to mitigate roughness-

induced transition. It is also a long expansion nozzle to delay the effects of the Görtler instability. All of these steps result in quiet flow up to a unit Reynolds number of 10.7×10^6/m. The freestream pressure fluctuations in the nozzle are 0.05% RMS along the centerline and gradually increase to 0.5% RMS at the nozzle exit [225]. The test section for the M6QT is an enclosed free-jet test section. The test section has an interior height and width of 0.81 m and contains the nozzle and diffuser bell mouth. The test section has room for any instrumentation and/or model mounting apparatus required. The test section also has doors on four sides and the doors have 8-inch windows providing optical access to the test area.

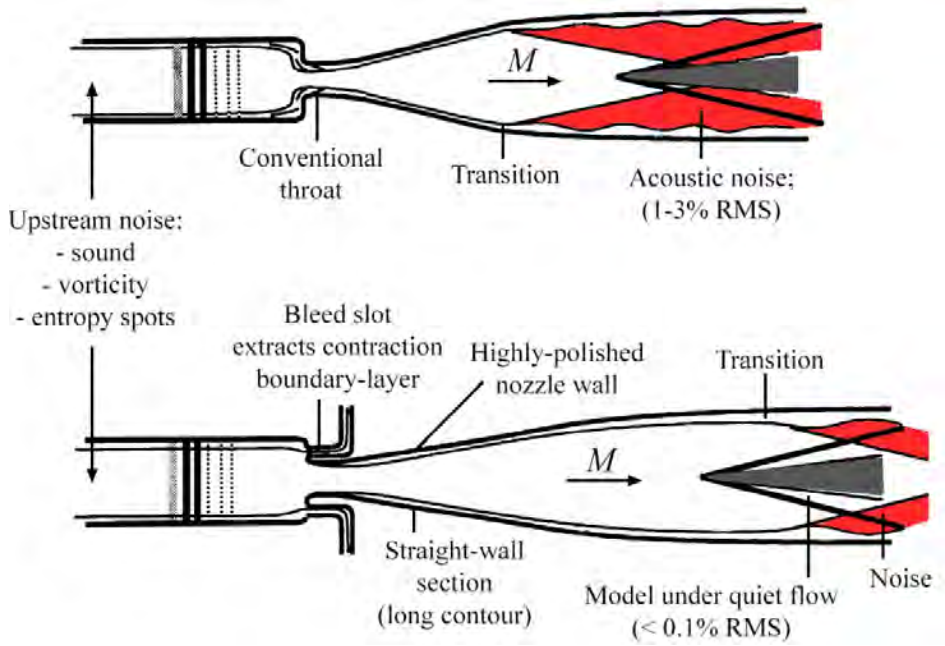

Figure 4.16: Schematic showing the general differences between conventional and quiet wind tunnels (Reprinted with permission from [225]).

4.6.1 Traverse

A 3-D traverse [150] was used to maneuver the hot-film probe to build 3-D measurement surveys in a cylindrical (r, θ,and z) coordinate system. This was well suited to probe around the axisymmetric nozzle and cone-shaped models. This traverse consists of a carriage with axial and radial motion stages moving on a ring using a rack-and-pinion gear system. The r and θ axes are in the plane parallel to the nozzle exit plane and the z-axis is streamwise, as seen in Fig. 4.17. Each axis has a specific range, minimum step size, and associated accuracy, these are summarized in Craig et al. [150]. ([5])

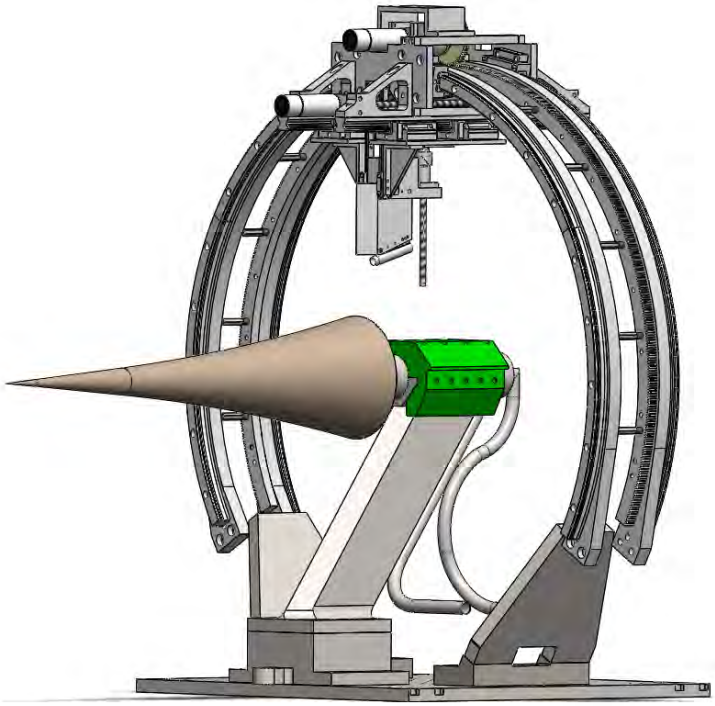

Figure 4.17: The 3-D traverse mechanism, shown here with the 91-6 cone model [150].

4.7 Model

4.7.1 91-6 cone

The model used was the 91-6 cone originally fabricated and tested by NASA. The model had a sharp detachable tip with a radius of 0.0635 mm (0.0025 in) and length 38.1 mm (1.5 in). The first 152.5 mm (6 in) of the model was straight with a 5° half-angle. After the straight section the model had a constant flare of radius 2322.7 mm (91.44 in) for 12 in. The total length of the model was 457.2 mm (18 in). The model is named the 91-6 cone for the 91.44 in flare and 6 in straight section, consistent with the naming of other similar models, such as the 93-10 cone [150]. The model had a 2.032 mm (0.08 in) thick Ni shell. On the inside was the coolant inlet that ran in the streamwise direction to just downstream of where the tip screwed in. The coolant then traveled between the coolant inlet passage and the model shell to the aft end of the cone and out through an exit. The coolant was continuously circulated by a recirculating chiller outside of the test section. Fig. 4.18 shows a diagram of the cone. ([5])

The 96-6 cone was one of several models used in the M6NTC at NASA Langley to study hypersonic boundary-layer stability. This cone specifically allowed for the study of the effect of wall cooling on second mode boundary-layer stability. Linear Stability Theory (LST) suggests the Mack-mode frequency increases with wall cooling. Mack observed that the first linear-instability mode was stabilized by wall cooling and the second or Mack-mode was destabilized. Mack-mode disturbances are acoustic waves that travel between the surface and the relative sonic line. As the temperature decreases the local speed of sound decreases thus increasing the local Mach

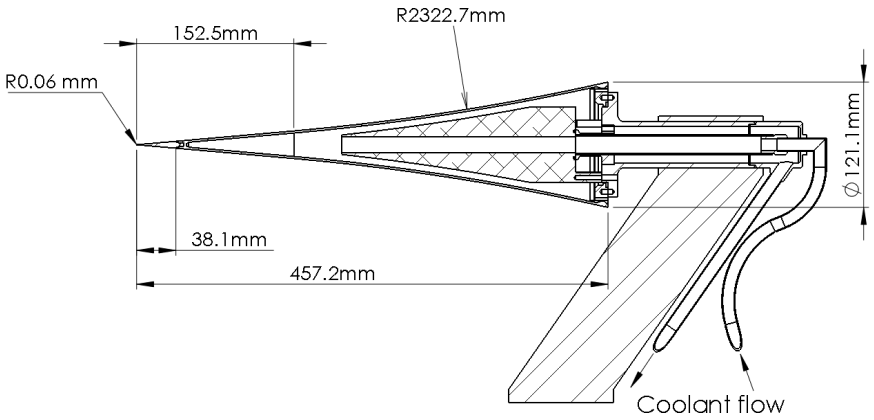

Figure 4.18: Diagram of the 91-6 cooled flared cone.

number which increases the frequency of Mack-mode disturbances. Blanchard and Selby [226] carried out the experiment in the M6NTC with the 91-6 cooled cone. The linear growth of Mack-mode disturbances, saturation and breakdown into developing turbulent flow was studied. That experiment serves as a benchmark for the susequent experiments. The present data were verified against previous results. Wilkinson [227] reviewed three separate experiments carried out in the M6NTC at NASA Langley to study low freestream disturbance stability. The cooled 91-6 cone was one of these studies. The conclusion was that the Mack mode dominated transition on this model. ([5])

4.7.2 Chiller

The chiller used in this study was a FTS Sytems Inc. RC211 model. The chiller works as a cascade refrigeration system with two loops to remove heat from the coolant. The high temperature loop was in contact with the coolant. The high temperature loop was in-turn cooled by the low temperature loop. The lowest possible minimum temperature was desired. Of the readily available coolants, ethanol met the requirements and was used for all the tests. ([5])

4.7.3 Distributed Roughness Elements (DREs)

Spatially-periodic Distributed Roughness Elements (DREs) were used to enhance and regulate the 3-D modulations of the boundary layer and study how they interact with the flow to increase increase the initial disturbance to hasten transition. A challenge was the precise application of the small and precise DREs without damaging the expensive and delicate model. Since this is a cooled model and has a cavity for coolant under the surface, machined roughness elements were not an option. DREs had to be adhered to the surface. The DREs were made by laser cutting them out of a strip of Kapton tape with thickness 0.051 mm (0.002 inch) that was adhered on to a Mylar sheet of thickness 0.178 mm (0.007 inch), the objective was to cut through the Kapton but not the Mylar. Precision laser cutting was enabled by a A-Laser, a division of FCT Assembly, in Milpitas, CA. The strip of DREs was cut into a suitable size for application to the model and then high-viscosity super glue applied to the strip. The tape was quickly pulled off the Mylar sheet leaving

the DREs in place with adhesive on them and the Mylar was very carefully applied to the model at the desired location and then pulled off leaving the DREs on the model. The placement of the DREs was decided by finding the neutral line from computations which is where the flare of the cone starts, at 152.4 mm from the tip. The DREs were placed at a wavenumber of 90 to interact with the observed fluctuation in mass flux at that wavenumber. A laser profilometer was used on flat plates and the blockage model to obtain the height and diameter of the DREs. They are 0.081 $\pm$ 0.0036 mm in height and the diameter and spacing are equal at 0.465 $\pm$ 0.0076 mm. Data were collected again after putting DREs on the model to compare with the results seen on the smooth cone. The DREs applied to the 91-6 cone can be seen in Fig. 4.19. ([5])

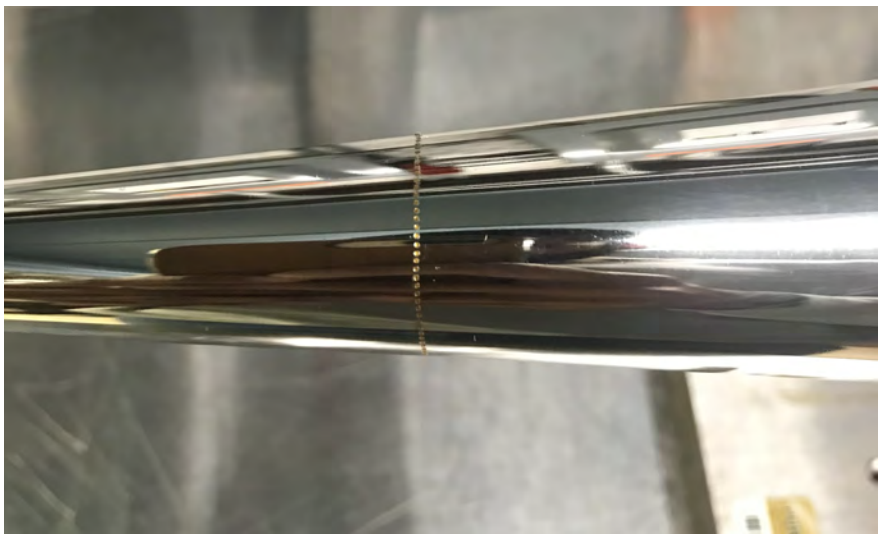

Figure 4.19: DREs on the 91-6 cone.

4.8 Pulsed Hypersonic Adjustable Contour Expansion Nozzle for Aero-thermochemical Test Environments

This section follows from McManamen et al. [3]. The low temperature STI experiments were conducted in the pulsed hypersonic adjustable contour expansion nozzle for aero-thermochemical test environments (PHACENATE) facility located at the National Aerothermochemistry and Hypersonics Laboratory (NAL) at Texas A&M University . The PHACENATE (pronounced 'fascinate') facility nominally operated with a 60 ms total run-time with 10-15 ms of stable flow and a duty cycle of 10-20 s. The pulsed operation was ideal for laser diagnostic based experiments, and allowed for large-sample data collection in order to analyze fluctuating quantities.

PHACENATE was a tabletop-scale facility with a converging-diverging planar nozzle (exit dimensions 10.2 cm x 10.2 cm) that exits into a rectangular test section (dimensions 25.4 cm H x 25.4 cm D x 58.4 cm L). The nozzle was designed using a method of characteristics approach, similar to the method described in Semper et al. [228]. The facility supported a variable Mach

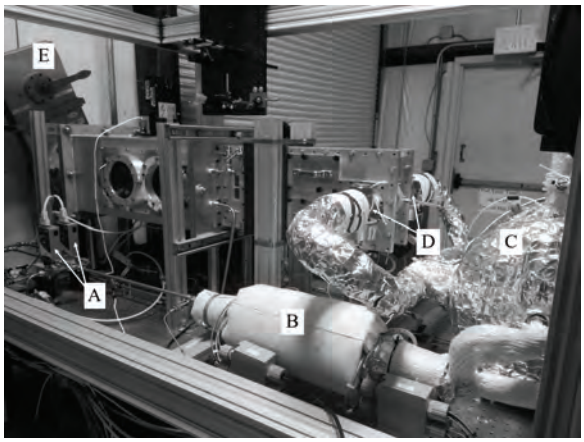

Figure 4.20: Image of the PHACENATE facility. Included labels are the mass flow controllers (A), pebble bed heater (B), inlet tank (C), poppet valves (D), and knife gate (E) leading to the dump tank and vacuum pumps through the wall. [3].

number range by allowing the height of the nozzle throat to be adjusted via a series of shims while the two nozzle planes were allowed to rotate in order to maintain a constant exit area. The test section had a series of mounting holes on the upper and lower walls of the cell for instrumentation capabilities. A series of rails was mounted to these holes, which were used to support a set of aerodynamic wedges with one degree of freedom. The test section provides optical access from all sides with 15.2 cm diameter schlieren quality windows in both sidewalls for imaging and 17.8 cm L x 2.5 cm W fused silica windows in the upper and lower walls for laser access. There were multiple window ports on the top and bottom walls of the tunnel allowing adjustment of diagnostic location. Several window blanks were outfitted as well, to allow additional pressure ports or sting assemblies to be used in the facility. To achieve hypersonic conditions, a set of vacuum pumps evacuated both the test cell and nozzle to 133 Pa (0.5 Torr) and the settling chamber was pressurized between 170-650 kPa. The facility was operated on a high pressure liquid nitrogen (N_2) tank running through a regulator to the supply line. A set of mass flow controllers were located in-line to allow controlled mixing of nitric oxide (NO) into the supply for optical diagnostic capabilities. The gas mixture entered a pebble bed heater which acts to pre-heat the supply and force mixing for even composition. The temperature of the heater was set such that the expansion process of the gas entering the tunnel and flowing through the nozzle would not result in liquefaction. The heated gas exited the pebble bed and filled a 0.1 m^3 reservoir which entered the settling chamber through a pair of 2.5 cm poppet valves, pictured in 4.20. The poppet valves operated with energize-times of 12 ms and were actuated by a series of MHJ Festo valves. ([17, 3])

A Quantum Composer 9520 series pulse delay generator was used to control tunnel operation. The Festo valves were triggered to open and closed the poppet valves and then the lasers, cameras, and data acquisition were triggered at optimal time delays. The pulse delay generator had picosecond resolution on 8 channels with $<$50ps jitter, and thus, was capable of controlling both tunnel operation and laser timing simultaneously. A custom program, written in LabVeiw, integrates tun-

nel control with data acquisition and system monitoring under a single graphical user interface. (McManamen et al. [3].)

4.8.1 Mach Stem Generator Model

The goal for the wind tunnel model used in this work was to produce a 'canonical STI' flowfield by forming a freestanding normal shock wave in an optically accessible location. This was achieved by creating a Mach stem at the nozzle exit, through a set of opposing aerodynamic wedges [229, 230]. Predictions of Mach stem height and growth rates are detailed in Mouton and Hornung [230]. The flow geometry was a function of incoming Mach number, specific heat ratio, and deflection surface geometry. From the work of Mouton and Hornung, only the angle and length of the leading edge of the deflection model was needed to satisfy the geometry unknowns. In an experimental work by Chpoun and Leclerc [231], it was shown that Mach stem formation and height was consistent between different model geometries, so long as the leading edge angle and length were kept constant. From this, Mach stem generator models could be developed for specific incoming flow conditions. The model design in this work was chosen by optimizing the leading edge angle and overall wedge height (easily related to leading edge length) using a Matlab procedure developed by Mai and Bowersox [232] following the routine of Mouton and Hornung [230]. For an expected Mach number range of 4 to 6, the ideal leading edge angle was found to be 32 degrees. This was determined by looking at the critical deflection angles for both the incident and reflected shocks and selecting an angle that remains between the two curves for the entire Mach number range. An overall height of 0.953 cm was chosen to optimize the Mach stem height within the bounds of tunnel blockage allowance and the expected core flow diameter of 5.1 cm. An additional consideration for the model design was optical access to the near region of the Mach stem from multiple directions. Camera access from the side of the tunnel was needed for imaging, as well as access for multiple laser sheets from the top or bottom of the tunnel. For this purpose, the model was designed with an open body concept where the leading edge is followed by an acute return angle creating a triangular profile, in contrast to a typical hypersonic body design. It was believed that the absence of a model structure downstream of the triple point may also help to stabilize the flow by removing the shock-boundary layer interaction of the reflected shock. Finally, the wedge implemented a swept back design to delay the influence of the shear layer of the nozzle sidewalls in hopes of minimizing blockage and stabilizing the flow. 4.21 shows a schematic of the model on its rail assembly as it would be installed in the tunnel, as well as a cut-out view that shows the leading edge profile. ([17, 3])

4.9 The HXT Facility

This section follows from Dean [11] and Dean et al. [16]. The high enthalpy Mach stem experiments were performed in the Hypervelocity Expansion Tunnel (HXT) at the National Aerothermochemistry and Hypersonics Laboratory (NAL). This facility is 30.5 m long with a 91.4 cm nozzle exit diameter. Although test times are on the order of 1 ms, a strength of this type of facility is the ability to produce high enthalpies with minimal freestream dissociation. The operational envelope of HXT, shown in Fig. 4.22, maps out the broad range of testing conditions that HXT can produce. The blue color maps out possible testing conditions with a static temperature of 65 K, and the red maps out testing conditions with a static temperature of 220 K, which is a representative static

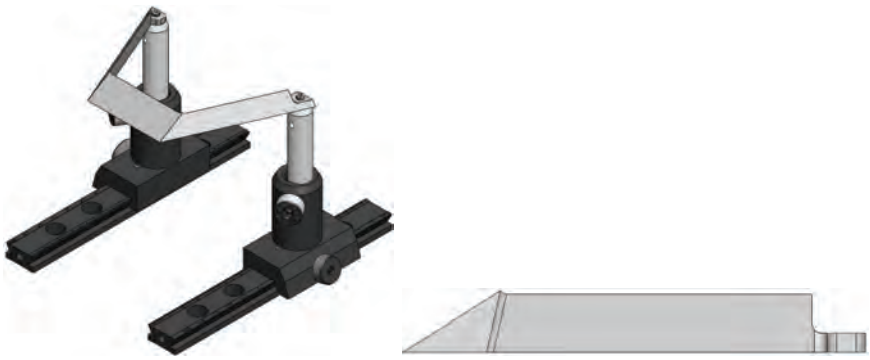

Figure 4.21: Schematic and cut-out view of final wedge design [3]

temperature for flight through the earth's atmosphere. Therefore, the red region also highlights that HXT can replicate the flight temperature, pressure, and velocity of many portions of hypersonic trajectories.

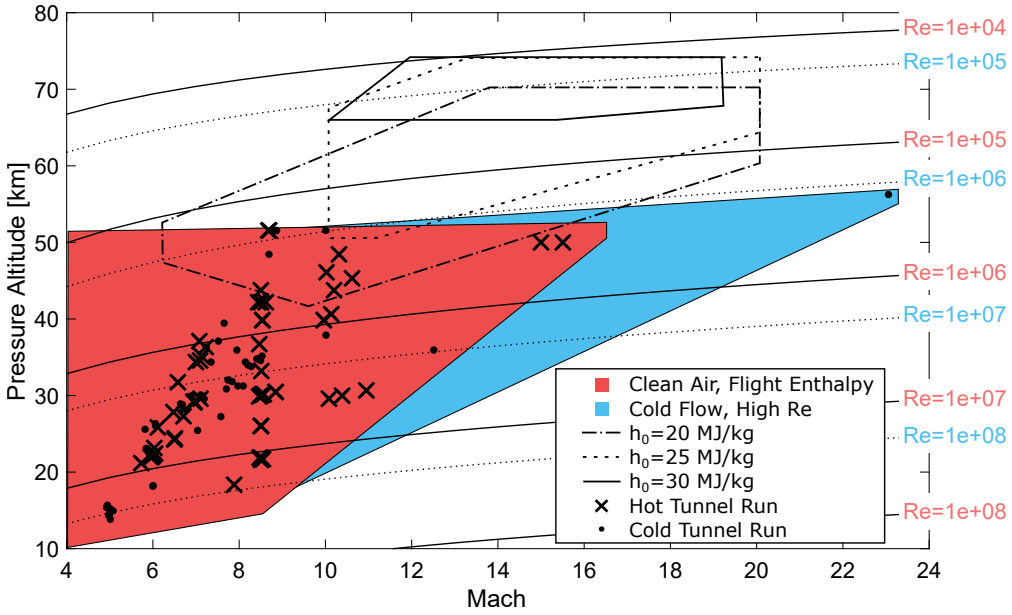

Figure 4.22: Pressure altitude vs. Mach for hot and cold air testing conditions. [11]

4.9.1 Expansion Tunnel Fundamentals

An expansion tube was first proposed in 1952 by Ressler [233]. This type of impulse wind tunnel is essentially a shock tube enhanced on the downstream end with a weak diaphragm followed by an additional length of pipe. Comprehensive explanations of shock tubes are widely available

in literature [234, 235]. The geometry and wave diagram of a basic expansion tunnel is shown schematically in Fig. 4.23, where the numbering system for the flow states follows Trimpi [236]. Diaphragms initially separate the three main parts of an expansion tube, typically called the driver, driven (or test gas), and expansion (or acceleration) sections. The inclusion of a diverging nozzle at the end of the expansion section results in a facility called an expansion tunnel. Although it is clipped from Fig 4.23, a dump tank (or tailpipe) is typically located on the downstream side of a test section to delay the reflected normal shock from interrupting the test time. ([11])

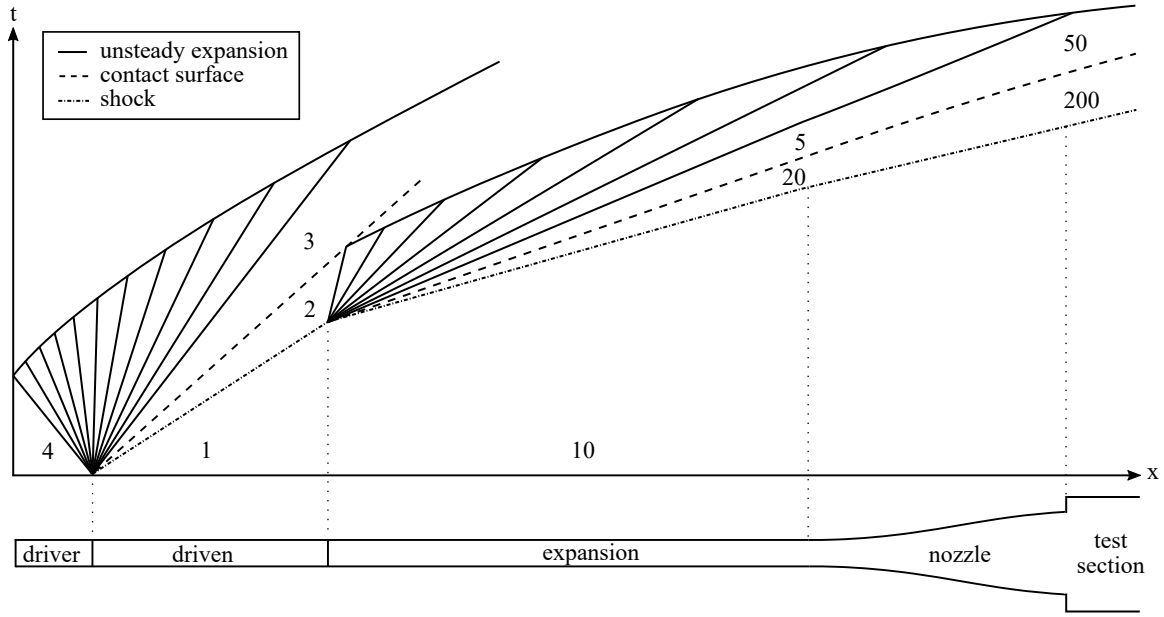

Figure 4.23: Expansion tunnel schematic and x-t wave diagram. [11]

The operation of an expansion tunnel starts with rupturing the diaphragm separating the driver and driven sections. The driver-driven pair of an expansion tunnel operates as an open-ended shock tube. The evolutions of the shock, contact surface, and expansion waves produced at the driver-driven interface for an arbitrary run condition are illustrated in Fig. 4.23. The driven section initially contains the test gas that will pass through the test section during the test time. The pressure and composition of the test gas depend on the desired test time conditions. The driver section is initially charged to a high pressure, where the pressure, gas composition, and temperature of the driver are used to control the strength of the shock that propagates through the driven section once the diaphragm ruptures. The test gas is compression heated and accelerated by the propagating shock, resulting in state 2 shown in Fig. 4.23. An air test gas remains clean of dissociation as long as the static temperature of state 2 remains lower than the dissociation temperature of oxygen. When the shock wave reaches the end of the driven section, the pressure of state 2 ruptures a second diaphragm. Similar to the driver-driven pair, the driven-expansion pair also operate like a shock tube when the secondary diaphragm ruptures. In this case, state 2 acts as the shock tube driver

gas, and state 10, which is the state of the gas initially in the expansion section, acts as the shock tube driven gas. The pressure, gas composition, and temperature of state 10 are used to control the strength of the unsteady expansion that propagates into state 2. When the secondary diaphragm ruptures, the resulting leftward moving unsteady expansion processes the high temperature, moderate velocity, and low Mach number state 2 gas into mild temperature, high velocity, and high Mach number state 5. The test gas, now in state 5, is then steadily expanded to the Mach number of state 50 through the diverging nozzle. State 50 represents the test time flow. More thorough explanations of the operation of an expansion tunnel are available in literature [237, 238, 239, 234]. The presence of test flow disturbances significantly limited the usefulness of early expansion tubes like the NASA Langley 6-inch expansion tube [240]. In the 1990s, Paull and Stalker [241] discovered that ensuring the speed of sound in state 2 is greater than the speed of sound in state 3 results in the suppression of acoustic disturbances. This discovery paved the way for modern expansion tunnels. ([11])

4.9.2 Infrastructure and Design

The design process for HXT started in the fall of 2015, and construction began in the summer of 2016 [242]. The length of each section of the facility was determined using a trade study considering the optimal length of each section for multiple operating conditions. The chosen configuration, illustrated in Fig. 4.24, was the best compromise over the range of operating conditions. The driver section is made from 50.8 cm (20 in) diameter, schedule 160 stainless steel pipe. It is 1.5 m long and rated for pressures up to 13.8 MPa. The driver gas is typically helium or air. The diaphragm box is a double diaphragm system that separates the driver and the driven sections. Two primary diaphragms were used instead of one to allow fine control of the initial pressure in the driver section, enabling highly repeatable testing conditions. The system was similar to the double diaphragm system of the Stanford expansion tube facility [243]. The driven section is made from the same schedule pipe as the driver section and is 4.6 m long. The secondary diaphragm holder consisted of two stainless steel rings bolted together to sandwich the secondary diaphragm. The rings acted as a frame for the delicate secondary diaphragm material and allowed easy diaphragm replacement. The acceleration section was made from 50.8 cm (20 in) diameter schedule 30 pipe and is 9.1 m long. The diverging nozzle was 6.1 m long and expanded the flow from a diameter of 48 cm to 91 cm. The test section was 1.8 m long and had a width and height of 1.5 m. The dump tank was made from a 1.06 m (42 in) diameter schedule STD pipe and was 6.1 m long. A noteworthy feature of the HXT was its ability to reconfigure for operation as a reflected shock tunnel [244]. ([11])

The facility was first operated as a shock tube to test and verify the operation of the primary diaphragm system. Many shock tube tests were performed to explore different diaphragm thicknesses, score depths, score shapes, and materials. Early tests used carbon steel diaphragms, but rust particles contaminated the post test time flow. As a result, 304 stainless steel diaphragms were the standard primary metal diaphragm material. During the first few years of operation, a piece of 6.1 m long acceleration pipe spanned the space currently occupied by the nozzle. The nozzle expanded the operational capabilities of the facility, making higher Mach numbers accessible. The contour of the nozzle was designed using an in-house method of characteristics code

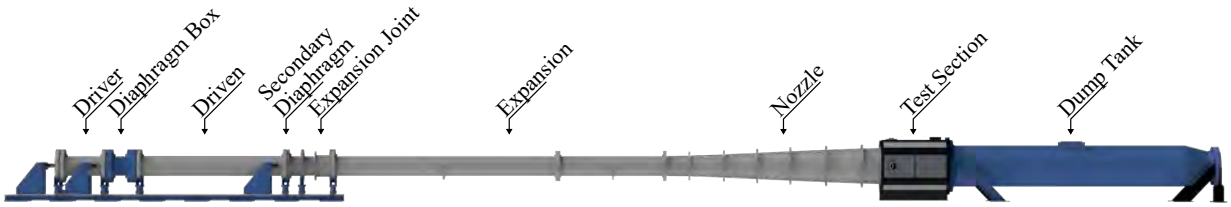

Figure 4.24: Full view of the HXT facility. [11].

(R. Bowersox), which incorporated a viscous correction. The final design shape was based on an intermediate testing condition and allowed for operation over a range of inlet Mach numbers. This nozzle was evaluated with viscous computational simulations using UnStructured 3D (US3D) [37] and provided acceptable flow uniformity over a valuable range of Mach numbers (3 - 12). The US3D simulation results plotted in Fig. 4.25 show the computed radial variation in Mach number at the nozzle exit for the highest Reynolds number testing conditions that the current version of the HXT could produce with static temperatures of 200 K. ([11])

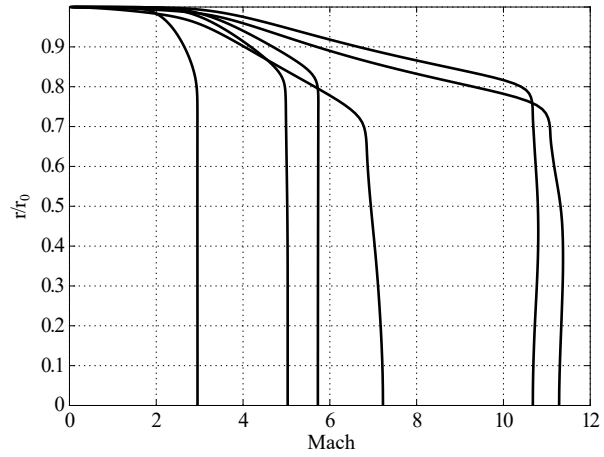

Figure 4.25: Mach number variation in the radial direction of the nozzle exit over a variety of run conditions. [11]

The secondary diaphragm had to reliably hold the initial pressure differential between the driven and acceleration sections. It was a best practice to use the thinnest and lightest secondary diaphragm material possible to minimize flow disturbances [245, 246]. Smaller diameter expansion tunnels are advantageous from this perspective because a smaller cross-sectional area means a smaller net force acting on the secondary diaphragm at a given initial pressure differential, allowing the use of thinner material. Mylar, Kapton, and other secondary diaphragm materials at various thicknesses were evaluated based on their ability to minimize losses, disturbances, and particles.

Also, tests were performed with a cross of blades similar to the primary diaphragm system of the hypervelocity expansion tube facility [247]. These blades were placed immediately downstream from the secondary diaphragm. Ultimately, Mylar without downstream blades offered the best performance. The results in Fig. 4.26 show the burst pressure differentials measured for various Mylar thicknesses inside the HXT. ([11])

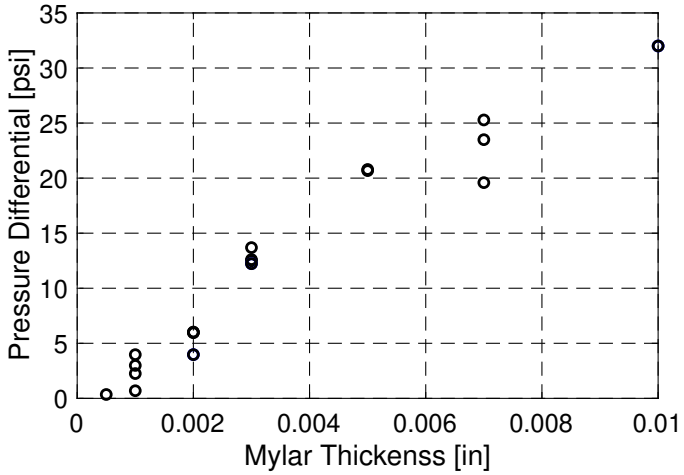

Figure 4.26: Mylar diaphragm burst pressure differentials. [11]

4.9.3 Characterization

4.9.3.1 High-Frequency Pressure Measurements

The HXT data acquisition was split between a control and a high-speed system. The control system continuously recorded the pressures and temperatures inside the various tunnel sections at a rate of 1 kHz. The controls system is also monitored in real-time as operators run the facility. The high-speed system measured shock speed, static pressure, pitot pressure, and other short-duration events at a rate of up to 2 MHz. The shock speeds were determined using measurements from PCB 132B38 pressure sensors located in the acceleration and nozzle sections. The static pressure at the exit of the nozzle was measured using a Kulite XCEL-25 pressure sensor. A static pressure comparison between runs 113 and run 114 is shown in Fig. 4.27. These two runs had relatively high Reynolds numbers of 2.8e7 /m and Mach numbers of 5. The results in Fig. 4.27 demonstrate the high repeatability of testing conditions within the HXT. In addition to closely matched static pressures, the shock speeds measured during these two runs differed by less than 0.2%.

As labeled in Fig. 4.27, many flow events inside the test section during runs 113 and 114 are visible in the static pressure traces measured at the nozzle exit. A noteworthy influence of the nozzle visible in Fig. 4.27 was the change in static pressure across the contact surface. Recalling the states labeled in Fig. 4.23, the static pressure was the same in states 5 and 20 before the nozzle inlet. However, a significant Mach number difference between states 5 and 20 meant that the states

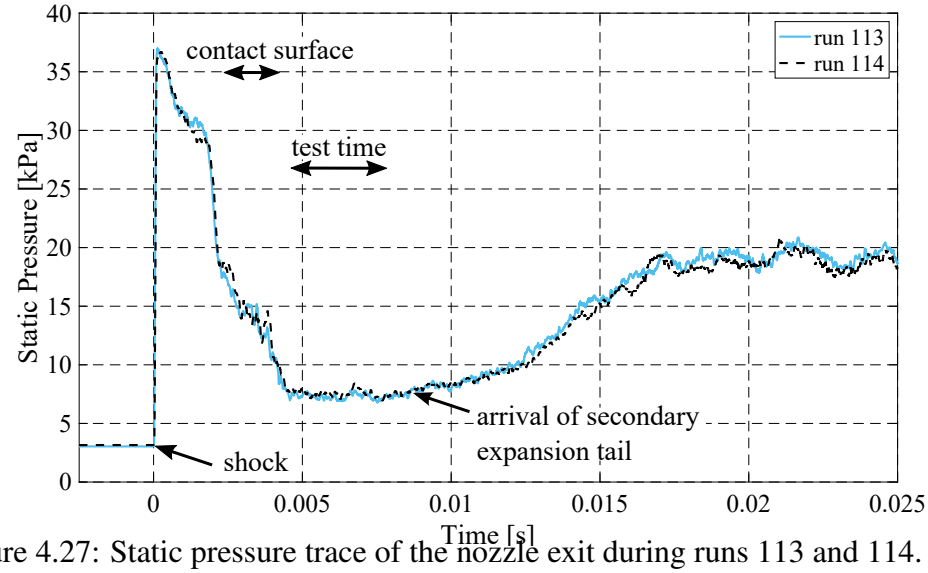

Figure 4.27: Static pressure trace of the nozzle exit during runs 113 and 114. [11].

were expanded differently through the nozzle, resulting in unequal static pressures between states 50 and 200. This resulting pressure difference also contributed to the broadening of the contact surface. It should also be noted that runs 113 and 114 were representative of testing conditions in the lowest and leftmost region of the operational envelope shown in Fig. 4.22. The nearly 3 ms test times shown in Fig. 4.27 were about the longest test times for this coampaign. Runs conducted at the opposite corner of the operational envelope had test times that were only a fraction of a millisecond. Static pressure at the nozzle exit and shock speed were measured during every wind tunnel run. In addition to these measurements, pitot rake measurements were occasionally performed to characterize the uniformity and size of the core flow. The rake pictured in Fig. 4.28 was designed for probe placement at 5.1 cm intervals ranging from a radius of 7.6 cm to 43.2 cm. PCB 102B16 and Kulite XCEl-100 pressure sensors were used in the rake for various runs. The PCB and Kulite sensors were flush-filled with RTV to protect against thermal loading. The image shown in Fig. 4.28 was taken before applying an RTV coating. During run 95, six PCB 102B16 sensors were placed in the rake at radial locations of 17.8 cm, 27.9 cm, and 38.1 cm. This run was approximately Mach 7.5 with a Reynolds number of 1e6 /m and a stagnation enthalpy of 2.5 MJ/kg. The pitot measurements acquired during the run are plotted in Fig. 4.29. The results indicate that the core flow was uniform to a radius between 27.9 cm and 38.1 cm. The lower pitot pressures measured by probes 1 and 6 indicated those probes were inside the boundary layer of the nozzle. ([11])

4.9.3.2 Schlieren

High-speed schlieren was used to examine the flow conditions in the test section during many shakedown tests. The basic z-type, 2-mirror schlieren setup included a constant light source LED, 20.3 cm diameter parabolic mirrors with focal lengths of 101.6 cm, and a Photron Fastcam SA-Z high-speed camera [248]. The schlieren videos were used to track the passing of shock waves

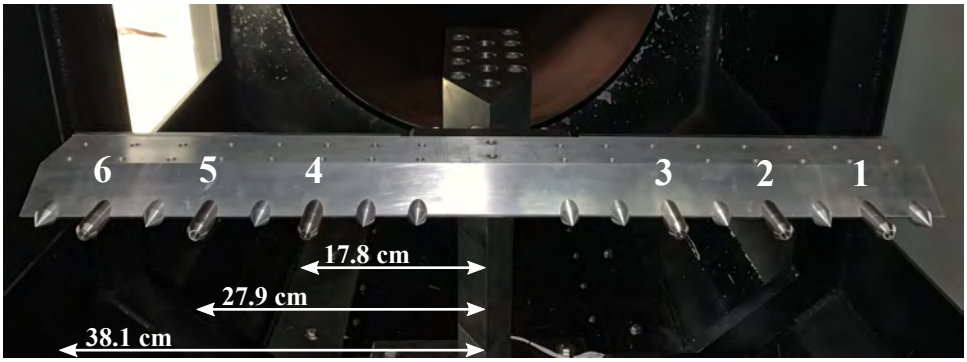

Figure 4.28: Pitot rake configuration during run 95. [11].

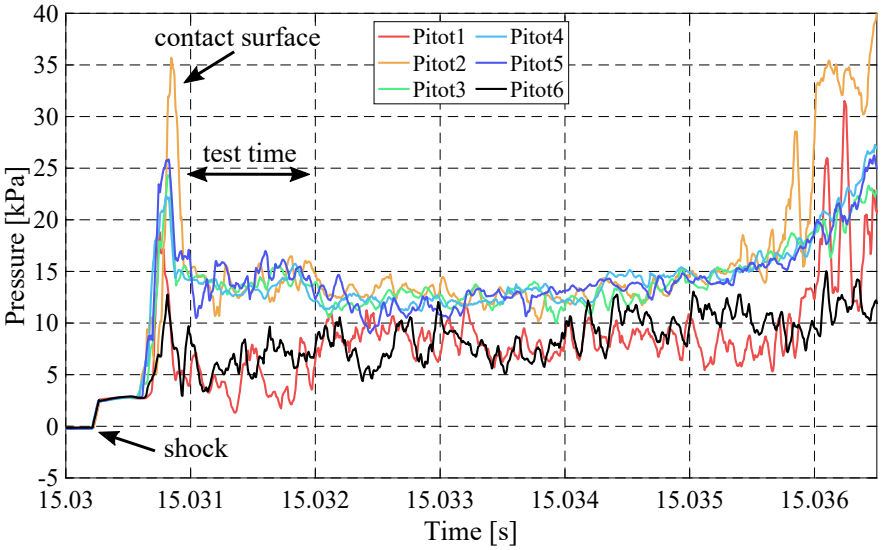

Figure 4.29: Pitot rake measurements during run 95. [11].

through the test section and investigate the flow establishment processes. This diagnostic technique was particularly useful when examining the flows around an 8.9 cm diameter model of the Orion spacecraft set to zero angle of attack. The shock standoff distance in front of this model enabled easy evaluation of test times and flow steadiness. In addition, any particles that happened to strike the face of the model would reflect upstream, creating small bow shocks that were easy to see. Schlieren images from run 77 showing the passing of the normal shock, the high temperature and low Mach number acceleration gas of state 200, the state 50 test time, and a particle impact are presented in Fig. 4.30. These select images were taken from a schlieren video captured at a rate of 100 kHz and processed by performing a background subtraction. The left-to-right moving flow was captured through windows with a diameter of 17.3 cm. The test time flow was approximately Mach 10 with a 4.7 MJ/kg stagnation enthalpy. Chemiluminescence from the hot flow downstream of the bow shock caused the bright regions in Figs. 4.30c and 4.30d. ([11])

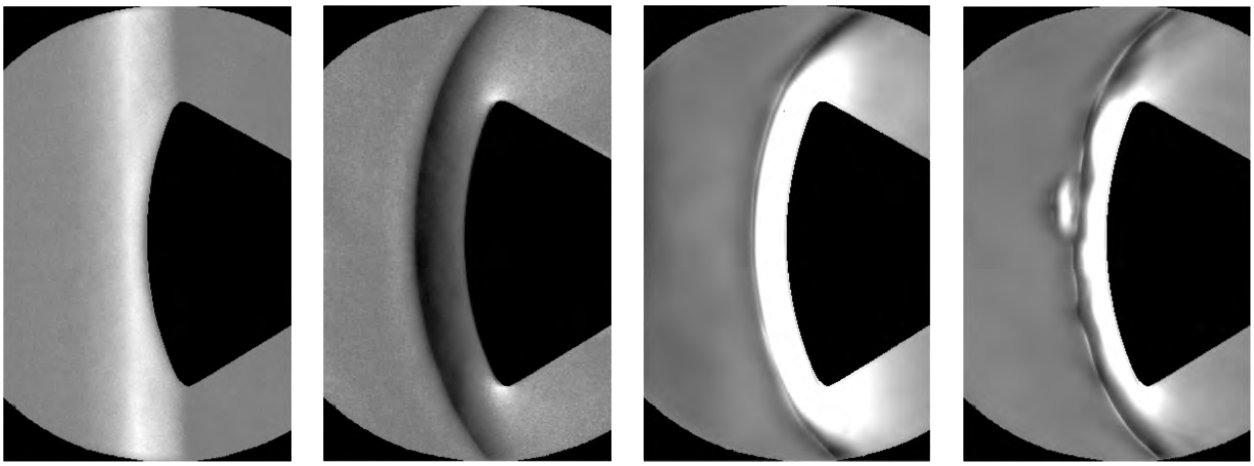

(a) (b) (c) (d)

Figure 4.30: Schlieren snapshot of flow around a model of the Orion spacecraft during a) passing of normal shock, b) passing of shock heated acceleration gas, c) high enthalpy Mach 10 test time, and d) post-test time flow with small particle impact. [11]

4.9.3.3 Mie Scattering

HXT was designed with experiments involving non-intrusive laser diagnostics measurements in mind. The test section, as shown in Fig. 4.31, was surrounded by a femtosecond laser, two 1 MHz pulse-burst lasers, and two sets of pulsed dye laser systems configured for vibrationally excited nitric oxide monitoring (VENOM) [249]. The second 1 MHz pulse-burst laser not pictured was located on the other side of the wall in the neighboring ALLEMO laboratory. An important goal during the shakedown testing was determining the best way to trigger the laser systems. Laser triggering was worked out during a series of Mie scattering experiments. The relatively simple setup involved using one of the pulse-burst lasers, a Photron Fastcam SA-Z high-speed camera, and a 9520 Series Pulse Generator made by Quantum Composers. The output from a PCB 132B38 shock arrival sensor was gained by a factor of 500 and used as the trigger input for the pulse generator. The pulse generator controlled delays and triggered both the camera and pulse-burst laser. The pulse-burst laser was configured to produce a laser sheet originating from the top of the test section with 375 pulses at a rate of 250 kHz. The high-speed camera, synchronized with the laser pulses, captured Mie scattering from particles through a window in a door on the side of the test section. A Mie scattering image of smoke and debris originating from the secondary diaphragm during run 67 is shown in Fig. 4.32. The flow moved left to right at a velocity of 2.1 km/s in the 7.6 cm by 11.4 cm region. The smoke vortices were isolated to a region about 22.9 cm long. ([11])

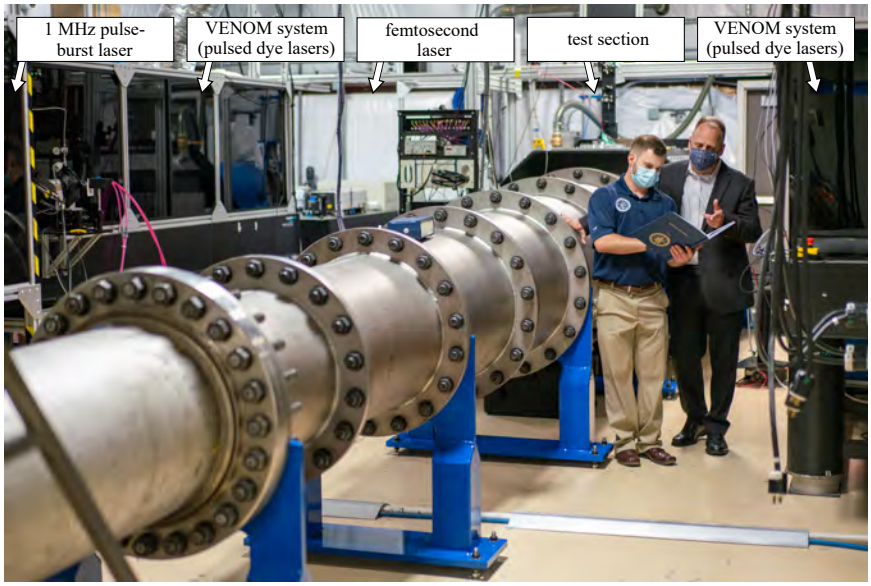

Figure 4.31: Layout around the test section. [11].


Figure 4.32: Mie scattering image of diaphragm debris from run 67. [11].

5.1 Preamble

The theory and practice behind each of the numerical techniques employed by the current work are covered herein. An effort was made to provide enough detail for the results to be independently replicated. The descriptions presented in this section were drawn from selected dissertations, theses, and articles associated with this project: Broslawski [7] and Bryan et al. [52]. Original citations are also included in the subsequent text.

5.2 Boundary Layer Solver

This section follows from Broslawski [7].

5.2.1 Problem Statement & Assumptions

The laminar, steady, 2D, planar boundary layer form of the conservation equations to be solved were provided by White [48]:

$$\frac{\partial}{\partial x}(\rho u) + \frac{\partial}{\partial y}(\rho v) = 0 \tag{5.1}$$

$$\rho u \frac{\partial u}{\partial x} + \rho v \frac{\partial u}{\partial y} \approx -\frac{dP_e}{dx} + \frac{\partial}{\partial y}\left(\mu \frac{\partial u}{\partial y}\right) \tag{5.2}$$

$$\frac{\partial P}{\partial y} \approx 0 \tag{5.3}$$

$$\rho u C_p \frac{\partial T}{\partial x} + \rho v C_p \frac{\partial T}{\partial y} \approx u \frac{dP_e}{dx} + \frac{\partial}{\partial y}\left(k \frac{\partial T}{\partial y}\right) + \mu \left(\frac{\partial u}{\partial y}\right)^2 \tag{5.4}$$

Again, the Prandtl number is defined as $Pr = \mu C_p / k$.

There were several key assumptions integral to the code, the most reasonable of which was the restriction to steady, 2D planar flows of perfect gases; this was all acceptable for simulating flows in the ACE tunnel, albeit without the thermal nonequilbrium introduced by the glow discharge. More general programs which considered thermochemical nonequilibrium were provided by Anderson and Lewis [250] and Blottner [251]. Leading edge complications like the Hayes-Probstein viscous-inviscid interaction Hayes and Probstein [115] and shock curvature (and thereby entropy layers) were not considered. A bolder simplification was the approximation of the 2.75° half-angle wedge used throughout the experimental campaign as a flat plate with zero pressure gradient. This was necessary as it greatly simplifies the code, and for the relatively slender 2D test article it was deemed acceptable. As a compromise, to accommodate the wedge's half-angle the program calculated the flow conditions across the oblique shock at the leading edge using isentropic flow relations [205]. It then used the results after the shock as the inputs to the flat plate solution. The simplification was further justified using the theoretical work on self-similar methods for flows with pressure gradients (wedges) by Cohen and Reshotko [218]. If one defines a parameter $\beta = \frac{\delta}{180\,\mathrm{deg}}$ then for the current wedge $\beta = 0.015$, which according to their data was sufficiently close enough to $\beta = 0$ for pressure effects to be neglected. ([7]).

5.2.2 Grid Generation with Clustered Spacing

A tacit requirement of turbulence modeling of any kind is clustered spacing [252]. When doing turbulent simulations, it is highly inefficient to use a uniform wall-normal grid because the resolution necessary to capture the sublayer is overly refined for the remainder of the boundary layer and especially the freestream [252], wasting computational effort is in these regions. Instead, a clustered wall-normal coordinate is used, which means extra nodes are added near regions of interest and the remainder of the domain is more sparsely discretized. Of the many ways achieve this, a popular technique for hypersonic flows is provided by Malik [253] which was adopted in this work; an alternative was described by Cebeci and Smith [43]. The central tenant of Malik's technique is to map a clustered, dimensional wall-normal coordinate ($y = [0, y_{max}]$) onto an equally-spaced domain ($\eta = [0,1]$) for numerical differentiation and integration, then bring it back to the dimensional frame for final processing. Here the clustering used was

$$y = \frac{a\eta}{(b-\eta)} \tag{5.5}$$

where $a = \frac{y_{max}y_{crit}}{(y_{max}-2y_{crit})}$ and $b = 1 + \frac{a}{y_{max}}$. This puts half of the nodes below y_{crit} and the other half above it Malik [253].

When using the Malik transformation, the program generated a clustered grid in physical coordinates and then mapped each point onto an equally spaced grid, which was necessary for finite difference differentiation and integration. Now everywhere there was differentiation or integration with respect to y in the finite difference equations, such as in the calculation of shear stress or momentum thickness, the Chain Rule is needed. However, if y was used by itself in a formula, then it did not need to be replaced by η. Similarly, when the results for u, T, v, *etc.* were output for all points through the boundary layer at a given streamwise location, no mapping was necessary to convert from η to y or *vice versa*. Because this was a $1:1$ mapping, when indexing a wall-normal coordinate the program did not need to know if it was referring to a clustered grid or equally spaced grid. The n^{th} node in a column of data referred to the same value, and whether it corresponded to $y(n)$ or $\eta(n)$ did not numerically matter. As a final example to emphasize that once the operation was complete parameters were independent of the grid used, the formula for the kinematic displacement thickness is shown in both physical and equally spaced coordinates.

$$\delta_k^* = \int_0^{y_{max}} \left(1 - \frac{u}{u_e}\right) dy = \int_{\eta(y=0)}^{\eta(y_{max})} \left(1 - \frac{u}{u_e}\frac{dy}{d\eta}\right) \partial\eta = \int_0^{\frac{by_{max}}{y_{max}+a}} \left(1 - \frac{u}{u_e}\right) \frac{ab}{(b-\eta)^2} d\eta \tag{5.6}$$

Throughout the remainder of this section, all formulas will be provided with the Malik coefficients included to ensure the more complicated forms of the equations are clearly shown. (Broslawski [7]).

5.2.3 Finite Difference Scheme

With the grid established, the boundary layer equations could be discretized. The following derivation follows White [48], though it was modified to include the Malik clustering; in the final implementation, Malik clustering could be turned off and the simplified equations solved.

It will be seen that the current AEF model was only amenable to an explicit scheme, but the

stability limitations on these equations made a solely explicit code overly restrictive. As a compromise, both explicit and implicit discretizations of the momentum and energy equations were derived and coded to solve for u and T respectively. The continuity equation, which provided v, was solved explicitly; this was acceptable as the final equation is stable White [48]. The implicit equations could be solved with any tridiagonal matrix algorithm such as the Thomas Aglorithm [252] or prebuilt, language-specific functions. Comparing the explicit and implicit discretizations, usually it was only the treatment of one term which distinguished the two. All derivations are shown below and follow White [48]. Streamwise derivatives were solved using first-order methods while wall-normal derivatives were solved with second-order methods, making all of the schemes $\mathscr{O}(\Delta x)+\mathscr{O}(\Delta y^2)$ accurate. While higher-order schemes could be used to make the code entirely second-order, for basic solvers first-order methods were sufficient [252]. When discretizing the boundary layer equations, it was important to maintain linearity of the $m+1$ variables Tannehill et al. [252]. Also, because this is a flat plate, perfect gas solver, C_p, ρ_e, and u_e were all constants and thus did not need to be discretized. That being said, wherever they could be removed entirely from the equations they were kept in for generality. Finally, some non-dimensional parameters to simplify the algebra are provided: ([7])

$$Let \quad \alpha = \frac{\mu_{m,n}\Delta x}{\rho_{m,n}u_{m,n}\Delta\eta^2}\left(\frac{ab}{(a+y)^2}\right)^2 \tag{5.7}$$

$$\beta = \frac{\nu_{m,n}\Delta x}{2u_{m,n}\Delta\eta^2}\left(\frac{ab}{(a+y)^2}\right) \tag{5.8}$$

$$\zeta = \frac{(\mu_{m,n+1}-\mu_{m,n-1})\Delta x}{4\rho_{m,n}u_{m,n}}\left(\frac{ab}{(a+y)^2}\right)^2 \tag{5.9}$$

5.2.4 Adding Turbulence

RANS turbulence modeling was accomplished with the Boussinesq approximation, which provided μ_t, which in turn was added to μ in the above equations. Analogously, using gradient diffusion one can use the turbulent Prandtl number and eddy viscosity to calculate k_t and then add it to k in the above equations. Thus no structural changes needed to be made to the finite difference scheme or derived equations to toggle between laminar or turbulent flow, the code only had to check and see if it was solving downstream of a user-specified trip. The problem was complicated by the introduction of the AEF model for turbulent heat flux derived in Chapter 3. The model still used the Boussinesq approximation to calculate μ_t, but it completely ignored k_t and solved for q_y^T directly. This was an issue for the implicit discretization of the conservation of energy. Recall that on the right hand side one takes the gradient of the heat flux $q_{,y} = (-kT_{,y})_{,y}$. Under an implicit scheme, the $\frac{\partial^2 T}{\partial y^2}$ portion was evaluated at T_{m+1}, which was ultimately brought to the left hand side. If one wanted to add a distinct q_y^T term, technically it must also be evaluated at $m+1$. To avoid adding an entire new unknown to the left hand side, the AEF model would need to be re-derived to be entirely in terms of temperature so the appropriate T_{m+1} terms could be moved to the proper place. For now, the simpler solution was to only apply the AEF model to explicit schemes where both the laminar and turbulent $q_{,y}$ were evaluated at m and thus remained on the right hand side.

From a practical perspective, the introduction of eddy viscosity and either gradient diffusion or AEF heat flux required a careful series of conditional statements. The user had to decide whether they wanted to run and implicit or explicit scheme, where they wanted to trip the boundary layer, and what turbulence models to use; the code would return an error if the implicit scheme was used with the AEF model. When $x < x_{transition}$, $\mu_t = k_t/q_y^T = 0$. If the flow was turbulent and a gradient diffusion model was requested, eddy viscosity was calculated from the specified model, eddy thermal conductivity was calculated with the turbulent Prandtl number, and both values were simply added to their laminar counter parts before the conservation equations were solved; $q_y^T = 0$ so the explicit energy equation could be solved without modification. In the AEF case, $k_t = 0$ and q_y^T was solved which "turned on" the extra term in the explicit energy equation. ([7])

5.2.5 Initial and Boundary Conditions

All finite difference schemes require initial and boundary conditions; recall that in every case above the solution began at the $(m+1)^{th}$ step but required data at m. Detailed instructions for the necessary starting conditions are provided below, and a summary of the process is as follows: The user specified the Mach number and upstream stagnation conditions. The code then used isentropic flow relations to calculate the conditions downstream of the bow shock. These results provided the initial conditions and freestream values for the finite difference solution, effectively simulating the wedge flow as a flat plate. The program used the shooting method to solve the self-similar equations, taking the freestream velocity and temperature (and if the flow is isothermal, wall temperature) as inputs. Once converged, the self-similar results were interpolated onto the user's dimensional grid, and standard equations were used to calculate some secondary variables through the boundary layer. With this boundary layer at a specific streamwise location was calculated and the code was ready to proceed to the finite difference scheme. ([7])

5.2.6 Initial Condition

The initial conditions required more effort to produce than the boundary conditions. Again, this code solved isentropic shock relations to simulate flow over a wedge as flow over a flat plate. Therefore one could start every simulation at the leading edge and assume the $(m-1,n)$ values are simply the freestream parameters, but it was found that doing so introduces a sharp numerical spike in the results as the code rapidly attempted to correct for the presence of a boundary layer. This was most apparent in v, which instantly went from being identically zero to being non-zero, causing a ripple effect through the rest of the variables that took $\mathcal{O}(10)$ steps to damp out. Furthermore, being forced to start at the leading edge could be a waste of numerical effort if one was only interested in the boundary layer far downstream. A better method was to solve the boundary layer equations at a given streamwise coordinate, then use this value as an input to the finite difference scheme. Because the code only considered laminar, 2D planar flows over flat plates as inputs, self-similar techniques were applicable; note that this was the technique used by van Driest [223] to generate exact compressible boundary layer solutions. A self-similar solution typically uses a coordinate transformation to reduce the number of independent variables; in boundary layers, the characteristic length scale is removed such that the solutions at one point on a plate are "similar" to the solution everywhere, effectively allowing for rapid scaling to the desired location [48]. Central to the self-similar solution of the boundary layer equations is the transformation used; the one used

here was adopted from Illingworth [254]. For both the adiabatic and isothermal cases there were five ODEs to be solved, but only three boundary conditions; put another way, this was a two-point boundary problem with two free variables [255]. The technique used to solve this system is called the Shooting Method and was described by Palmer [255], who solved the compressible boundary layer problem as an example. The philosophy of the shooting method is to guess values for the missing initial conditions, solve the system, and then compare the results at the farfield boundary to the known values. If the results match to within some tolerance, then the proper solution has been found, but if they do not new guesses are made and the process repeats. The challenge is therefore to find an efficient way to generate new guesses; following Palmer [255], the multi-dimensional, globally convergent Newton-Raphson technique was used. ([7])

Let $[V]$ be an array of the guesses, and $[E]$ be the array of the corresponding errors; for the current application, both were two-by-two arrays as there were two free variables. The problem is to find some perturbation $[\delta V]$ that will drive $[E]$ to zero. This can be done by solving the following expression, written in the classic $Ax = B$ form,

$$\frac{dE}{dV}\delta V = -E \tag{5.10}$$

Once $[V]$ has been calculated, the new values for each free variable can be found from,

$$V^{n+1} = V^n + \delta V \tag{5.11}$$

Palmer [255] suggested a finite difference approach to the calculation of $\frac{dE}{dV}$, namely $\frac{\Delta E}{\Delta V}$, admitting that it was not straightforward. Note that $\frac{\Delta E}{\Delta V}$ was a two-by-two array because, again, this is a multidimensional problem: there were two free variables to optimize at once, and changing one will affect the error of both. Therefore the code needed to study the effect of perturbing each free variables separately. The code was run with an initial guess for $[V]$, the system of ODEs was solved, and the errors were calculated. Next, one of the free variables was incremented by a small amount, say 1×10^{-4}, the system of ODEs was re-solved, and the errors were re-calculated. The first column of $\frac{\Delta E}{\Delta V}$ was the latest error array divided by the perturbation on the free variable (1×10^{-4}); in this way the effect of perturbing one variable on both errors was stored. This process was repeated once more by perturbing the second free variable, and the $\frac{\Delta E}{\Delta V}$ matrix was complete. With this, the $[V]$ array was updated. Note that it is recommended to under relax the solution by multiplying δV by a value ω between 0 and 1 before adding it to $[V]$. A formal review of so-called relaxation schemes was provided by Tannehill et al. [252], but here Palmer [255] used $\omega = 0.5$, which drove the error in both free variables below 1×10^{-6} in $\mathcal{O}(10)$ iterations. ([7])

Once the program converged, its results needed to be converted to physical coordinates and scaled before they could be used to set the initial and boundary conditions for the entire domain. The conversion between f and g and the physical variables was covered above. The edge conditions were provided by isentropic flow relations [48]. From these, the following critical variables could be calculated:

- Viscosity blended between Keyes' (air) and Sutherland's [215] Laws, as reported in [256]

  - Keyes: $\mu_K = 1.488 \times 10^{-6} \left(\frac{T^{1/2}}{1+122.1T_1/T} \right)$ where $T_1 = 10^{-5.0/T}$
  - Sutherland: $\mu_S = 1.458 \times 10^{-6} \left(\frac{T^{3/2}}{T+110.4} \right)$
  - Blending at $T_{switch} = 200\text{K}$: $\mu = f_{switch}\mu_K + (1 - f_{switch})\mu_S$ where $f_{switch} = \frac{1}{1+(T/T_{switch})^3}$

- Mach number by definition $M(\eta) = \frac{\sqrt{\gamma R_{specific} T(\eta)}}{u(\eta)}$, where for air $\gamma = 1.4$ and $R_{specific} = 287.058 \frac{J}{kg*K}$ [205]
- Density from the Ideal Gas Law $\rho(\eta) = \frac{P_e}{R_{specific} T(\eta)}$
- Thermal conductivity from the Prandtl number $k(\eta) = \frac{\mu(\eta) C_p}{Pr}$, where $C_p = 1004.5 \frac{J}{kg*K}$ and $Pr = 0.71$ [48]

Note the use of the boundary layer approximation $P(y) = P_e$ from $\frac{\partial P}{\partial y} = 0$. The self-similar solution used an arbitrary equally-spaced grid $\eta = [0, 10]$, where the upper value was deemed large enough to simulate infinity. This parameter needed to be converted back into dimensional "$y_{similarity}$"-coordinates. This required numerical integration; the Trapezoid Rule approximation is shown below, where $y_{j=0} = 0$:

$$y_j = (\eta_j - \eta_{j-1}) \sqrt{\frac{2x\mu_e}{U_e \rho_e}} \left(\frac{2\rho_e}{\rho_j + \rho_{j-1}} \right) + y_{j-1} \tag{5.12}$$

Just as with the Malik mapping, because this was a $1:1$ mapping any variable X could be called either with respect to η or $y_{similarity}$ provided the index of the wall-normal coordinate stayed the same; for example, if the code called $X(10)$, it did not matter what $\eta(10)$ or $y_{similarity}(10)$ are. This meant that once $y_{similarity}$ was known, linear interpolation could be used to map nearly all of the flow parameters onto the user-defined grid. The values of all parameters at locations above $y_{similarity,max}$ were simply set to the freestream value. With this, the initial condition was solved and the boundary conditions could be addressed. Before concluding, it is worth repeating that for laminar boundary layers the self-similar approach could be applied at all streamwise locations, completely ignoring the finite difference solution. Indeed, van Driest [223] used such an "exact" (without the inaccuracies of finite differencing) approach to great success. If information is only required at a few streamwise locations, this may be advisable. However, the iterative technique outlined here typically required $\mathcal{O}(10)$ iterations for each solution while the implicit finite difference scheme only required $\mathcal{O}(1)$. Thus for well-refined grids, the former was more efficient. ([7])

5.2.7 Boundary Conditions

As was previously mentioned, the freestream conditions were solved from isentropic flow conditions through the bow shock. Note again that this allowed the approximation of the thin wedge flows as flat plate flows. The oblique shock relations were provided in John and Keith [205]:

- Assume γ, M_1, P_{o1}, T_{o1}, and δ (wedge half-angle) were provided by the user

- $P_1 = \frac{P_{o1}}{(1+\frac{\gamma-1}{2}*M_1^2)^{\frac{\gamma}{\gamma-1}}}$
- $T_1 = \frac{T_{o1}}{(1+\frac{\gamma-1}{2}*M_1^2)}$
- θ was found approximately to within 1×10^{-6} using a brute force search between $\theta = \left[\sin^{-1}\frac{1}{M_1}, 30°\right]$. When $\left[\cot\theta\left(\frac{M_1^2\sin^2\theta-1}{\frac{\gamma+1}{2}M_1^2-(M_1^2\sin^2\theta-1)}\right)\right]$ was within 1×10^{-7} of $\tan\delta$ than θ had been found.
- $M_2 = \sqrt{\frac{1+\frac{1}{2}(\gamma-1)M_1^2}{\gamma M_1^2\sin^2\theta-\frac{1}{2}(\gamma-1)} + \frac{M_1^2\cos^2(\theta)}{1+\frac{1}{2}(\gamma-1)M_1^2\sin^2\theta}}$
- $T_2 = T_1\left(\frac{\left(1+\frac{\gamma-1}{2}M_1^2\sin^2\theta\right)\left(\frac{2\gamma}{\gamma-1}M_1^2\sin^2\theta-1\right)}{\left(\frac{(\gamma+1)^2}{2(\gamma-1)}\right)M_1^2\sin^2\theta}\right)$
- $P_2 = P_1\left(\frac{2\gamma M_1^2\sin^2\theta}{\gamma+1}-\frac{\gamma-1}{\gamma+1}\right)$
- $u_2 = M_2\sqrt{\gamma RT_2}$
- $P_{o2} = P_{o1}\left(\left(\frac{P_2}{P_1}\right)\left(\frac{T_2}{T_1}\right)^{\frac{\gamma}{1-\gamma}}\right)$

The freestream conditions along the entire domain could now be taken from the results after the shock because $\frac{\partial P}{\partial x} = 0$. This also meant that the pressure was known at all points as $\frac{\partial P}{\partial x} \approx 0$. Meanwhile, at the wall, both components of the velocity were zero along the entire domain, in accordance with the no-slip condition. If the wall was isothermal, then the user could input the known wall temperature to be applied along the entire wall. For adiabatic flows the wall temperature was set to the adiabatic wall temperature T_{aw}. For laminar flows T_{aw} was calculated by the self-similar solver, and for the turbulent portion of adiabatic-wall flows it was calculated using $r = Pr^{\frac{1}{3}}$ Dorrance [257]. It was found in testing that for laminar flows using the self-similar solver's result outperformed the differential solver with $r = Pr^{\frac{1}{2}}$, yielding q_w closer to zero. For this reason the self-similar solver's results were used for T_{aw}, though numerical prediction was output for consistency when comparing with other diagnostics. Similarly, even for laminar flows the turbulent adiabatic wall temperature was output for reference. ([7])

5.2.8 Convergence

When solving the finite difference equations at $m+1$ with lagged coefficients, the viscosity was taken at m. With viscosity known, one could calculate the thermal conductivity, solve the conservation equations, calculate density from the Ideal Gas Law, and so on. It was already stated that although lagging the coefficients is theoretically simple, it clearly introduces error throughout the entire code. However, if one could recalculate the coefficients once u_{m+1} and T_{m+1} were known, a more accurate result could be produced. The effect was exacerbated when implementing a RANS turbulence model, as even more coupled variables like δ_k^* were introduced. The solution taken here was a Predictor-Corrector-like iterative process (see Gilat and Subramaniam [258]) and

was applied in both laminar and turbulent cases. For the first iteration at a $m+1$ step, the previous μ_m value was used to solve for the thermal conductivity, eddy viscosity, conservation variables, *etc.* and values for u_{prev}, T_{prev}, and v_{prev} were taken from the results from the previous spatial step m. For all subsequent iterations, X_{prev} was the result from the previous iteration and μ was calculated from T_{prev}. The error for the three conservation equations was calculated from

$$X_{Error} = \frac{1}{n_{pts}} \sum_{n=1}^{n_{pts}} \left(X_{m+1,n} - X_{prev,n}\right)^2 \tag{5.13}$$

The three errors were then combined via a Euclidean norm

$$Error = \sqrt{\left(\frac{u_{error}}{u_e}\right)^2 + \left(\frac{T_{error}}{T_e}\right)^2 + \left(\frac{v_{error}}{u_e}\right)^2} \tag{5.14}$$

Note that v was normalized with u_e because theoretically $v_e = 0$. This process was repeated until a convergence tolerance was met. For $Tolerance = 1 \times 10^{-6}$ nominally < 5 and < 10 iterations were needed for laminar and turbulent cases respectively, though more iterations were typically needed exactly at the tripping point due to the sudden changes there. ([7])

5.2.9 Secondary Variables & Post Processing

The code produced a number of secondary results that, while not necessary to the solution of the conservation equations, provided useful data throughout the entire domain. These included:

- Mach number (neglect v): $M = \sqrt{\gamma R_{air} T}$
- Specific enthalpy (perfect gas): $h = C_p T$
- Total enthalpy (perfect gas): $H_o = h + \frac{1}{2}u^2$
- Number density: $n = \frac{P}{k_B T}$

The velocities, temperature, density, viscosity, and thermal conductivity were also returned throughout the entire domain. In the streamwise direction, the code calculated the wall shear stress and heat flux with a $\mathcal{O}(\Delta y)$ and $\mathcal{O}(\Delta y^2)$ forward difference scheme respectively

$$\tau_w = \mu_{n=wall} \frac{u_{(n=2)} - u_{(n=wall)}}{\Delta\eta} \left(\frac{ab}{(a+y)^2}\right) \tag{5.15}$$

$$q_{y(w)} = k \frac{-T_{(n=3)}/2 + 2T_{(n=2)} - 3T_{(n=wall)}/2}{\Delta\eta} \left(\frac{ab}{(a+y)^2}\right) \tag{5.16}$$

as well as the 99.5% boundary layer thickness by linearly interpolating the u, T, and H_o data; note that in the case temperature and/or total enthalpy fall through the boundary layer ($X_w > X_e$), δ was taken at 1.005% the freestream value. The lower order scheme was used for τ_w for simplicity, though in the future a higher order scheme could be used. 2D plots were made of the velocities, temperature, and Mach number, and the wall shear stress, wall heat flux, and boundary

layer thicknesses were plotted along the streamwise coordinate as well. A ".csv" file was generated containing the run inputs, for repeatability, as well as the values of the primary and secondary variables at the final streamwise location. If the flow was turbulent at this last position, then the velocity and temperature were reported in inner law coordinates and u_{eq}^{+} was plotted against y^{+}: $y^{+} = \frac{yv^{*}}{\nu_{w}}$ (with $v^{*} = \sqrt{\frac{\tau_{w}}{\rho_{w}}}$); $u^{+} = \frac{u_{eq}}{v^{*}}$; u_{eq}^{+}; and $T^{+} = \frac{T_{w}-\overline{T}}{T^{*}}$ (with $T^{*} = \frac{q_{w}}{\rho C_{p} v^{*}}$ for heat transfer case, $T^{*} = (v^{*})^{2}$ for adiabatic case to avoid division by zero). ([7])

5.3 Mach Stem Computational Fluid Dynamics Methods

This section follows from Bryan et al. [52]. The computational fluid dynamics (CFD) code utilized for this study was UnStructured 3D, or US3D Candler et al. [37]. US3D is a high-fidelity unstructured CFD code that is capable of modeling finite-rate thermochemical non-equilibrium flows for a variety of complex problems. US3D solves the fully compressible Navier-Stokes equations through finite-volume methods. US3D also takes into account finite rate chemical kinetics and internal energy excitation which was necessary for the hypersonic flow regimes simulated. Although US3D is able to run with unstructured grids, hexahedral grids generated with the commercial software Pointwise [259] were used in this work to minimize discretization error associated with poor shock alignment. US3D was configured to use the implicit Data-Parallel Line Relaxation (DPLR) time integration method with five linear subiterations to converge to steady solutions. Viscous, laminar flow simulations were performed using weighted least-square fits to compute gradients. Blottner viscosity fits with the Wilke mixing rule model were utilized to compute mixture viscosities. A simple harmonic oscillator was used to model vibrational energies. A constant Lewis number, defined as $Le = Pr/Sc$, model was selected to compute the species diffusion coefficients. In addition, since the time integration was implicit, a CFL schedule was used to ramp the timesteps to achieve steady-state convergence. The inviscid numerical method used second order fluxes in space with a MUSCL flux extrapolation via modified Steger-Warming inviscid flux-vector splitting. All of the simulations in this work used the same Mach stem geometry. This geometry was studied experimentally by Dean [8, 260, 11] and is the focus of several experimental projects in progress at the National Aerothermochemistry and Hypersonics Laboratory at Texas A&M University. Supporting these projects dictated the geometry and flow conditions that were simulated. In order to reduce computational time, a small subset of the full experimental flow field was simulated. The computational domain is shown in *Fig.* 5.1. The computational domain neglected the support structures needed to hold the wedges in the wind tunnel. It is also important to note that the small rectangular extrusion just aft of the wedge in *Fig.* 5.1 was much smaller than how it is depicted in the figure. The dimension of the top inlet plane was $\sim L/4$, the top outlet plane was $\sim 3L$, and the small rectangular extrusion was $\sim L/40$. ([52])

The computational domain boundary conditions are listed in *Fig.* 5.1 and include supersonic inlets, supersonic outlets, symmetry faces, and isothermal viscous walls. The most important boundary condition for the computational domain was the volume initialization condition. Initializing the flow with freestream values resulted in the formation of a strictly reflected oblique shock rather than a Mach stem. The volume initialization was set to zero velocity with the density and temperature matching the inlet flow properties. Doing so forced the simulations to follow the true characteristics of the experiments performed in the HXT, and resulted in the reliable formation of

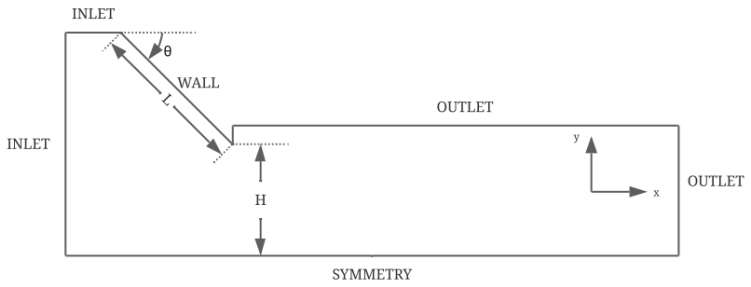

Figure 5.1: Computational domain with boundary conditions.

Mach reflections in the simulations. In addition to the volume initialization phenomena, another strictly numerical phenomena known as carbuncles were encountered. Carbuncles are spurious vortical structures that are said to arise from discretization errors near density inhomoegeneity and shock interactions. Carbuncles are most often found in the almost normal shock portion of a bow shock occurring at high Mach and high temperature. MacCormack [261] discusses the causes and possible remedies for carbuncles arising from bow shock waves. Although the Mach stems discussed are not directly bow shocks, the Mach stems do share the same properties where high Mach number flow is halted to subsonic flow over an infinitesimal distance, via a shock. Shock mesh alignment and increasing the dissipation in the Mach stem region were the two key remedies to alleviating the carbuncle problem. For the work presented here, a single mesh was used for all Mach number and stagnation enthalpy flows. Because the Mach number and stagnation enthalpy greatly affect the overall geometry of the Mach stem shock patterns, it would be impossible to have a single shock fit mesh that would work for all test conditions. As a result, in the presence of carbuncles, first order fluxes were specified in a small section across the Mach stem. It is important to note that the whole domain remained second order, with the exception of a small number of cells across the Mach stem. Essentially increasing the dissipation in the normal shock, or Mach stem, region eliminated the carbuncle effects and the solution could continue to converge smoothly to steady state. With the computational domain, boundary conditions, and initial conditions properly specified, it was possible to converge all Mach stem simulations to steady state. *Fig.* 5.2 shows the $x-$velocity for Mach 8.5 flow and stagnation enthalpy 11 MJ/kg as an example solution. From this point on, the bounds of the visualizations are refined to strictly highlight the region of interest around the Mach stem. ([52])

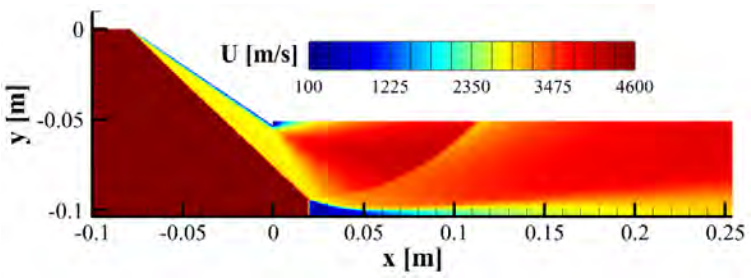

Figure 5.2: X-velocity for Mach 8.5 and stagnation enthalpy 11 MJ/kg.

5.4 In-House CFD Solver

A 2-D parabolized Navier Spokes (PNS) solver, developed by the PI, was used to assess the implementation of the algebraic model. The PNS code follows from Tannehill et al. [252], with the turbulence model following Bowersox [22]. This code was an invaluable resource to provide a first look at the model performance.

6. EXPERIMENTAL METHODS

6.1 Preamble

The theory and practice behind each of the techniques employed by the current work are covered herein. An effort was made to provide enough detail for the results to be independently replicated. The descriptions presented in this section were drawn from selected dissertations, theses, and articles associated with this project: McManamen [17], McManamen et al. [3], Broslawski [7], Dean [11], and Siddiqui [4]. The original citations are also included in the subsequent text.

6.2 Hypersonic Boundary Layer with Thermal Non-Equilibrium Diagnostics and Methods

6.2.1 Surface Profilometry

This section follows from Broslawski [7]. Past work on similar geometries [213] has shown the susceptibility of wedge models to deformation during manufacturing. This is especially important at the leading edge, where the flow is the most sensitive. In order to verify there were no machining errors, measurements were made of the leading edge using a surface profilometer. This work was conducted using a Keyence LK-H022 contactless laser distance sensor mounted to a custom traverse and resting on a vibration damping table. The system was described in [262], but the critical parameters are listed here. It offered an interrogation volume of $x \times y \times z = 950\text{mm} \times 75\text{mm} \times 6\text{mm}$ with a maximum resolution of $\Delta x = 2\mu\text{m}$, $\Delta z = 0.02\mu\text{m}$, and a user-defined Δy, here $250\mu\text{m}$. The on-target laser spot size was $25\mu\text{m}$ and data was recorded at 10kHz. It was advantageous to keep the laser in center of the z range in order keep the laser spot size small and maximize its sensitivity. This posed a problem for the test article which had a half-angle of 2.75°, so when rested on a flat surface it had a slope of $\tan(5.5^\circ) = 0.096\frac{\text{mm}}{\text{mm}}$. Therefore a custom aluminum block was made with a 5.5° cutout which would allow the wedge to lie flat. Screws and washers along the ends of the block ensured the test article was square with the block, and similarly screws in the breadboard tabletop ensured the block was square with the profilometer. The height of the profilometer could then be adjusted such that all measurements were $|z| < 1\text{mm}$. The profilometer supports were leveled by resting against two Stanridge Granite Corp. certified flat calibration blocks (Grade B, maximum deviation of $\pm 5\mu\text{m}$) and were squared by being screwed into the table's breadboard working surface. Even with these precautions, it was still necessary to zero the instrument relative to the test article. This was accomplished by fine-tuning the supports until the readings at four corners of a flat region $200 \times 20\text{mm}^2$ (starting 23mm from the leading edge, downstream of the polynomial profile) were all within $25\mu\text{m}$ of one another. The experimental setup is shown in Figure 6.1. (Broslawski [7].)

Once level, measurements were taken across the entire span of the test article over a total streamwise distance of $0 - 43\text{mm}$ from the leading edge, which was just upstream of the pocket for the PEEK insert; again, the spanwise scans were conducted at $\Delta y = 0.25\text{mm}$, which gave 172 lines of data per scan. The process was conducted three times for repeatability. Processing the profilometery data was a multi-step process conducted in a custom Matlab script which followed Leidy [213] and Neel [214]. Upon first visualizing the profilometer's ASCII data, it was observed that the results for the two opposite directions of laser travel were $\mathcal{O}(50\mu\text{m})$ apart. This was

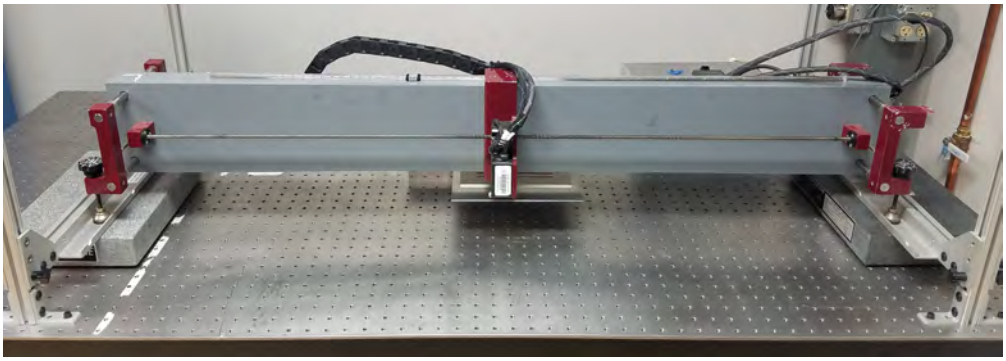

Figure 6.1: The laser profilometer during testing. [7].

a relatively small misalignment most likely due to a loose bearing or gear, but the results in a given direction remained valid. Thus the data were split into "even" and "odd" data sets each with $\Delta y = 0.5$mm; again no detail was lost during this process as the roughness parameters from each set should be identical and any deformations were still captured. Continuing with the data reduction, the results were median filtered to account for the width of the laser spot size. Erroneous data was smoothed out by linearly interpolating the results from the adjacent streamwise coordinates. Now each spanwise scan could be treated as its own independent signal. A second-order polynomial was fit to the data and then subtracted in order to remove any bulk trends and leave only the model's waviness. In order to separate the roughness from the wavy profile, the result was fit by a Zero-Order Gaussian Regression Filter provided in [263]; the filter was applied in sections of $\lambda_c =$ 0.3mm, which was sufficiently small to separate the roughness from the broader waviness. Once the filtered noise was subtracted, all that remained from the wavy profile was the true roughness. This process was depicted graphically in Figure 6.2. ([7])

There are multiple ways to define roughness [263], and here the center-line average R_{avg}, root-mean square R_{RMS}, and peak-to-peak R_{ptp} values were calculated. R_{avg} is the average of the absolute value of the difference between the data and the mean value for that scan. R_{ptp} is the maximum difference between the roughness values in a λ_c window; the average value was then taken as the average for all the windows in the scan. R_{RMS} is the root-mean square value for the scan. Roughness was measured in the flat region $23-43$mm from the leading edge across the entire span of the test article except for 1mm on either side to remove erroneous edge data. This meant that at the current resolution, there were 80 quasi-independent scans for each test, so for all three tests there were 240 scans. Each of the three roughness parameters was calculated for each of the 240 scans. For each set of 40 "even" or "odd" scans the 3σ outliers were removed; there were only a few outliers for a given scan. The results from all 240 scans were combined to provide a single value for each of the three parameters. ([7])

6.2.2 Oil Flow Visualization

This section follows from Broslawski [7]. Oil flow visualization is a simple technique which communicates even weak pressure gradients on test articles. It was used to ensure there were no unforseen pressure gradients on the test surface like those seen in [213], and to study the behav-

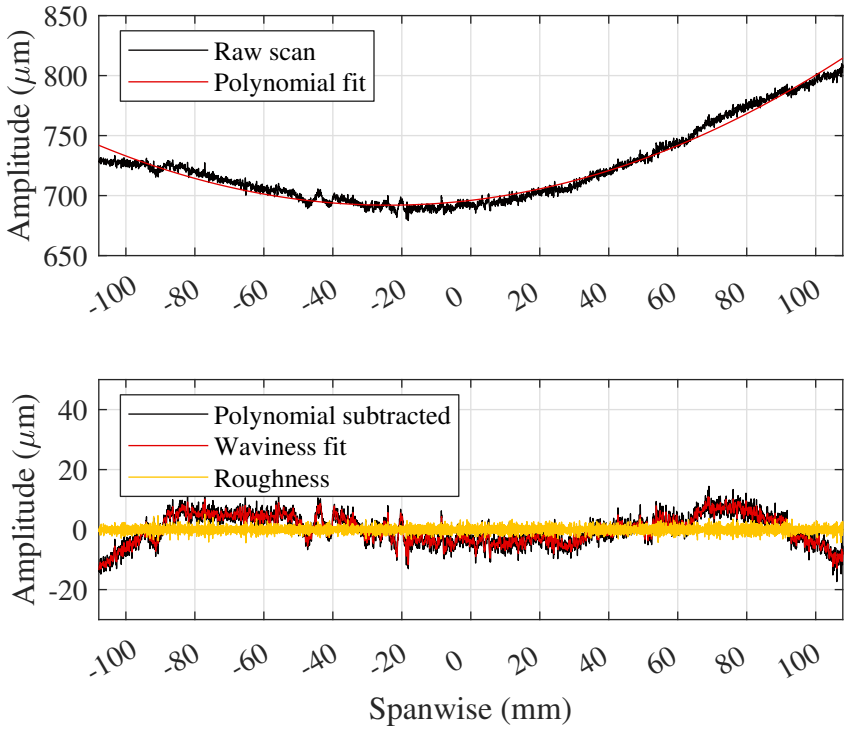

Figure 6.2: Reduction of the roughness data. [7]

ior of the trips; for example, would their wakes persist after the flow became turbulent? Here a UV-phosphorescent pigment, Day-Glo Color Corporation "Blaze Orange" was used to provide enhanced contrast on the model. A mix of 1.5g of pigment in 100mL of Esco E200 Silicone Fluid (100CS) provided good results. Increasing the viscosity of the oil reduces its sensitivity, but can help prevent excessive motion and a loss of signal as oil blows off the model. A foam brush was used to apply the oil across the model's PEEK insert after preheat. For laminar runs, the oil was applied in a thick strip just upstream of the camera's field of view so individual beads would roll across the test area, while for turbulent runs it was applied in an even coat over the entire PEEK insert and show the trips' structures. For safety, the plasma was never turned on during the oil flow tests, and the electrodes were completely removed from the PEEK and cleaned upon completion of the campaign as Leidy [213] found oil seeped into seams in the model during testing; this was another reason a single, seamless PEEK insert was designed for the present study. Once the model was preheated and coated with oil, data was recorded with a Nikon D5000 camera above the test section at 30fps with a manually adjusted, near-focus Nikkon Micro Nikkor (60mm, $f/2.8D$) lens which afforded 1280×720 pixels at a spatial resolution of $\sim 200 \frac{\mu\text{m}}{\text{pixel}}$. The camera angle was adjusted to the wedge's 2.75° to help keep the image focused and uniformly scaled across the entire test area. The camera's controls were tuned to maximize the contrast of the orange pigment; the shutter speed was $1/30$s, the f-number was 3.2, the ISO was 1000, and a fluorescent (high temperature mercury vapor) white balance further tuned to maximize the blue color ($A6$) were used. The lens' barrel distortion was removed. Two Feit Electric 13W BPESL15T/BLB UV lights were

directed onto the surface of the model from the sides of the test section to cause the oil to phosphoresce. UV-transmissible fused silica windows were used to pass the light into the tunnel, and to observe the phosphorescence as well. To maximize contrast, the lamps used nearly covered the entire window port and all other room lighting was switched off; it was found that despite manually specifying the camera's settings, for some as of yet unknown reason starting the recording before shutting off all the lights provided the best results. All windows on the test section not involved in data collection were replaced with blank plugs to prevent excess light from causing uneven illumination. The tunnel was typically only run for $10-15$s as this was sufficient to allow any structures to develop and after this time most of the oil had blown off the test article. All data was processed in a custom Matlab script. The data was imported, de-warped, rotated to account for camera misalignment, scaled, and then cropped. Under the current setup, attempts to identify tunnel start and unstart based off changes in the oil were unsuccessful, so all times were relative. The code saved data at user-specified times, and provided spanwise traces of the signal at a user-defined streamwise location. Both mean (5 frames, 0.167s) and instantaneous images and traces were saved. ([7])

6.2.3 Schlieren Imaging

This section follows from Broslawski [7]. Schlieren imaging is a ubiquitous technique for visualizing structures in fluids [264]. Here it was employed to interrogate the test article's boundary layer and shock structure. It provided a measurement on the state and size of the boundary layer, and ensured the test environment was clean (no impinging shocks, vacillating separation at the leading edge, *etc.*). It also provided information regarding the complex shock structure at the trips, and probed any pressure effects due to the plasma. Schlieren imaging's core concept is that light travels differently through media of different density, so by sending a collimated beam through the wind tunnel the intensity should change near the hot wall and across shocks as density gradients unevenly bend the light. Here a Z-type schlieren setup was used; it is outlined in Figure 6.3 and described in detail by Settles [264].

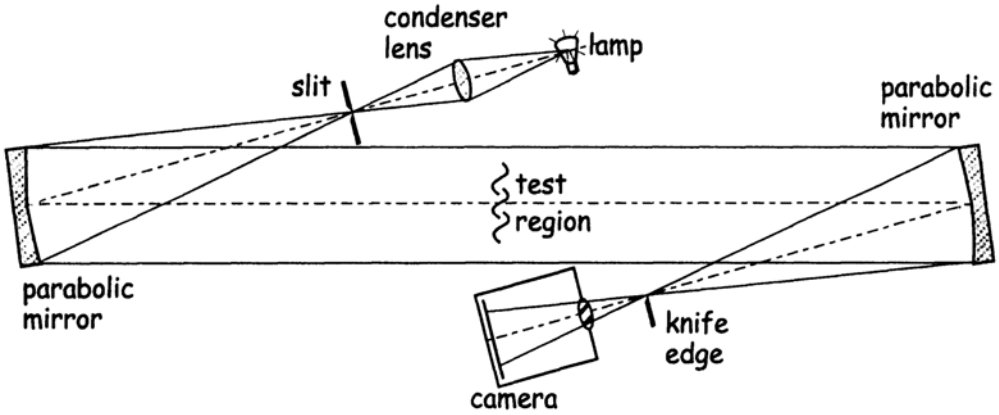

Figure 6.3: A characteristic Z-type schlieren setup. [264].

Light was produced by a Luminus Devices, Inc. PT-120-RAX-L15-MPK red-amber (613nm) continuous LED which was nominally powered with a Extech Instruments 382275 power supply at 3.4V and 21.5A for a total power of 73.1W; the LED was water-cooled with an external chiller, and red-amber was selected as the manufacturer's documentation stated the camera was most sensitive to this wavelength range. The light was condensed by a 55mm Nikon camera lens, which focused it onto a ThorLabs VA100 adjustable slit, which meant it effectively behaved as a point source. The slit was positioned at the focal point of a 152mm Edmunds Optics parabolic mirror with a 914mm focal length (f-number f/6), which directed the light through the test section. Because the slit was positioned exactly at the mirror's focal point, the light sent through the test section was collimated. On the opposite side of the test section, an identical mirror focused the light onto an adjustable horizontal knife edge. Because the knife edge was horizontal, just like the slit, the knife edge provided intensity gradients in the vertical direction by separating the light deflecting up from that deflecting down. The light was then collimated by a planoconvex lens and passed directly onto the camera's imaging plane; in addition to collimating the light, this lens also focused the image at the model's centerline. The camera used in this study was a Photron FASTCAM SA-Z CMOS with a full resolution of $1024 \times 1024 \text{pixels}^2$, a maximum frame rate of 2.1×10^6fps (with fewer active pixels), and a minimum exposure time of 159ns. The camera had 32GB of RAM, which was sufficient storage to record high-speed data over an entire tunnel run before it was downloaded through the control software Photron FASTCAM Viewer (PFV). It is noted that PFV can be used to adjust the shutter, frame rate, and active sensor area; the last two are also somewhat coupled, because for higher frame rates the camera reduced the number of active pixels. Furthermore, increasing the frame rate reduced the time the could camera record because its RAM filled more quickly. These parameters were adjusted in order to provide optimal conditions for the present application, boundary layer visualization. The frame rate was the highest amount possible to still have enough active pixels to record the flow across the entire width of one of the test section's windows (the orientation of the active pixels was customized to meet this requirement) and also allow recording for the entire duration of the run. Using a faster shutter could make the boundary layer more difficult to see, though using too slow of a shutter could blur turbulent structures. Ultimately a shutter of 1000fps, a gate of 1.25μs, and 1024×640 active pixels were selected. This provided a spatial resolution of $\sim 120 \frac{\mu \text{m}}{\text{pixel}}$, as measured with a gridcard placed along the model's centerline. It is noted that in this gridcard image a plumb bob was hung, the weight suspended in viscous oil, to provide a true vertical measurement which could be used to estimate the camera's roll, though in post-processing it was decided this step was not necessary. Schlieren data was processed using a custom Matlab script. All images were rotated to negate the wedge slope and scaled in this "flat" orientation. The streamwise scale was set from the known placement of the gridcard, but vertical scale was set manually by identifying the wall after the flow was starts and the test article shifted into its final position; similarly, the rotation was set from the data after the tunnel had started. The NALDAQ recorded conditions at 10Hz, so for each tunnel condition there were 100 frames of schlieren data. The code therefore used every hundredth frame to determine when unstart occured by checking when the signal in a region of interest suddenly changed; this was then used to link the DAQ data timeline to the camera timeline. The maximum temporal uncertainty using this approach was 0.1s which was tolerable, especially for runs when the tunnel

was held on a single condition. Once the timelines were set, the user could select specific run times at which to save schlieren images. The code also averaged together the 100 frames adjacent to that image (50 on each side) to provide a mean image. ([7])

6.2.4 Infrared Thermography

This section follows from Broslawski [7]. Infrared (IR) thermography is a popular technique for quantifying transition to turbulence in compressible flows. As the flow transitions, the increase in skin friction drag causes increased heating which signifies a turbulent front. The advent of laboratory-ready IR cameras provided a new way to quantify this thermal loading in high resolution and reasonable response time. Its main benefit is over surface-mounted thermocouples, which offer only pointwise readings and may perturb the flow.

The present work used a FLIR SC8100 mid-wavelength IR camera with a indium antimonide sensitive to $3-5\mu$m wavelengths. The camera's thermal resolution was 25mK, its 1024×1024 active pixel array offered for the current testing configuration a nominal spatial resolution of approximately $\sim 250\frac{\mu\text{m}}{\text{pixel}}$, and its maximum temporal resolution was 132fps though this required storing the data on a specialized FLIR high speed data recorded [265]; for this study, the camera wrote directly to a computer at 15Hz, which offered better temporal resolution than the NALDAQ and generally did not produce skipped or corrupt frames. Nevertheless, a catch was included in the code to account for any skipped frames by looking for gaps the camera's frame timeline, and should one exist, linearly interpolating to generate a new image to fill it. For this study the camera was mounted 21.6cm above the test article and tilted 2.75° ($\pm0.1°$)to account for the wedge's slope. It has been shown that excessive angles can effect perceived emissivity enough to affect temperature calculation [266, 267], though according to Running et al. [267] even if the camera was not normal to the surface for this study the angles were modest enough that any discrepancy would have a negligible effect. The camera collected data through a 11.43cm wide, 0.95cm thick II-VI Incorporated zinc-selenide window with a thin film, dual-band anti-reflective (DBAR) coating on both sides transmissible to $3-5$ and $8-9\mu$m; further reflections were reduced by exclusively conducting IR measurement with no other windows on the test-section and shrouding the gap between the lens and window with a lint-free shop rag. Two calibrations were necessary to get accurate IR images. The first was a temperature calibration to convert the sensor's counts into temperature readings. This was conducted *in situ* by Leidy [213], and because the same lens and window used here the results were used for the present application. Note that a central assumption of the calibration of the camera was that FLIR's black-coated aluminum calibration plate had the same emissivity as PEEK; the emissivity of PEEK is $0.91-0.95$ [268, 269, 270], which matches typical values for coated metal. In calibrating Leidy [213] noticed that the 2^{14}bit sensor was saturating for certain integration times, called "Presets" in FLIR's control software ResearchIR. This effectively provided an upper limit on the temperature that could be detected, and as the current test article was left in the tunnel during preheat, camera saturation was a real concern. For example, Leidy [213] reported that for an 8ms integration window, the camera saturated at $\sim$ 325K, while for a 1ms integration window it would saturate at $\sim$ 415K; both of these are well below the tunnel's stagnation temperature. It was desirable to use the preset which would provide the best sensitivity (the broadest span of bits), but would not saturate. Success was found using, in general, the

1ms preset near the leading edge and a 2ms preset everywhere else (this should provide data up to $\sim$ 380K [213]). It is noted a 4ms preset with a maximum operational temperature of $\sim$ 350K was also available [213]. The second calibration conducted was of the intrinsic camera properties. It was desirable to use the SC8100's 17mm lens as it had a slight fisheye effect which enabled it to see a span of approximately 20.32cm through the 11.43cm window. However, this introduced barrel/fisheye distortion in the final image, warping straight lines noticeably at the edges of the frame. MathWorks (Matlab) provides a detailed tutorial for performing a camera calibration[1] to remove this distortion, and it was closely followed here using the technique established by Neel [214]. In short, a precise, vinyl 1.27cm checkerboard was made into a custom $17.78 \times 20.32\text{cm}^2$ sticker by FastSigns; the final product then adhered to a 0.95cm thick piece of aluminum. This provided the Matlab tool a precise, easily identifiable (even in IR) grid of points which could be used to determine the distortion parameters. These parameters could then be applied to all subsequent images read into Matlab where a pre-defined function could be applied to reduce the distortion to a tolerable limit. As an added complication, it was expected that the internal parameters would change as the lens was focused. The procedure was conducted with the calibration plate focused 15.24, 17.78, 20.32, 22.86, and 25.40cm from the lens to provide an array of corrections from which users could pull the most applicable case; here the 20.32cm case was used exclusively. ([7])

PEEK was selected as the material for the test article's insert for its electrical insulation, machinability, and high service temperature, but what distinguishes it from other materials used for hypersonic wind tunnel testing are its advantageous thermal properties for IR measurement. The first is its low thermal conductivity, which means thermal events leave a lasting "fingerprint" on the material before becoming diffuse as the heat conducts throughout the material. PEEK's high emissivity is also critical because it makes it easily visible to IR cameras; it also lowers the material's reflectivity. Finally, because of its popularity in other applications, PEEK has been well-characterized over a range of conditions; the applicable examples are the thermal conductivity and specific heat capacity, both of which are shown in Figure 6.4. These data were supplied by Victrex, who supplied the raw PEEK granules eventually extruded into the sheets used here. Note that the jump observed in the plot of thermal conductivity was due to the room temperature value being reported separately from the main temperature sweep data and was otherwise unexplained by the manufacturer; for the present application, the room temperature value should never be needed and is only shown for completeness. ([7])

It will be seen that a critical part of heat flux calculation was the measurement of an internal temperature because it provided a boundary condition to the heat equation. An effort was made to measure this parameter directly as opposed to approximating it based on the surface temperature measured by the IR camera. To do so, custom East Coast Sensors Type K thermocouples were purchased. The TF1-KDTGC060A-05 design put the junction at the tip of a screw which could be threaded a specific amount into the material; here Techspray 1978-DP Heat Sink Compound was applied to improve the thermal connection. An analogous design, TE2-KF1C060A, had a flat junction covered by a piece of polymide tape to allow measurement of the surface temperature. This sensor was placed on the underside of the PEEK insert to provide a temperature reading at a third and final location; the surface thermocouple data was collected, but ultimately not used dur-

[1] https://www.mathworks.com/help/vision/ug/single-camera-calibrator-app.html

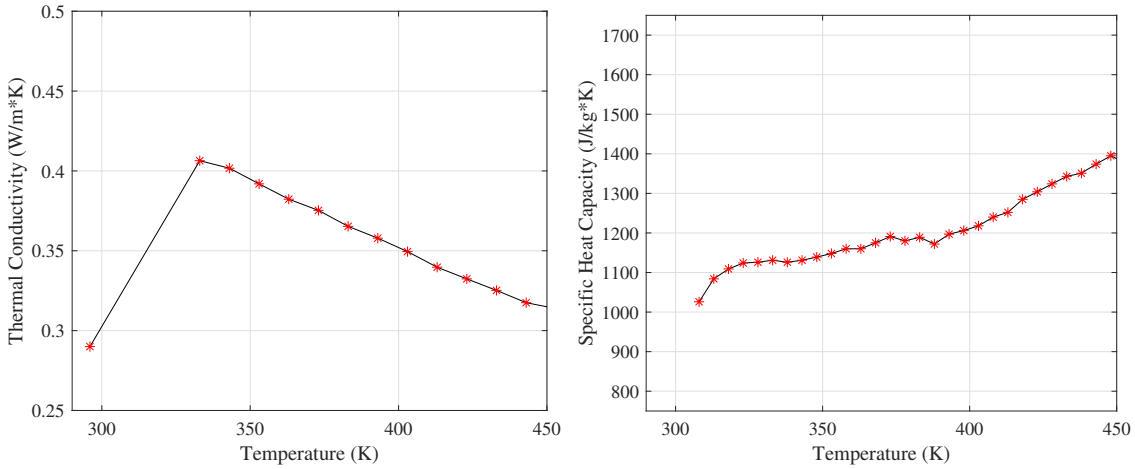

Figure 6.4: PEEK properties (a) thermal conductivity and (b) specific heat capacity as functions of temperature. All data available upon request from the manufacturer Victrex. [7]

ing the present analyses. During IR testing, a series of TF1 and TE2 thermocouples were mounted along the centerline article within the IR camera's field of view to provide the required internal temperatures. A linear polynomial fit provided the boundary condition in between the thermocouples, and data beyond the first and last thermocouple was neglected to prevent extrapolation; the streamwise temperature profile was assumed to be constant across the span of the test area. The manufacturer stated the accuracy of their thermocouples were the Type K standards of the greater of 2.2K or 0.75%. The thermocouples were connected to the TCDAQ and used its built-in cold junction for temperature calculation. The thermocouples were read with the same custom PlasmaDAQ VI as the plasma conditions, so they had the same read rate and triggering as the rest of the tunnel variables. The response time of the thermocouples was unknown, but rapid changes in the internal temperature were not expected. This technique removed the assumption that the internal temperature boundary condition was constant and equal to some initial condition at the surface necessary in [214, 213]. That said, one still needed to assume that the internal temperature was uniform throughout the insert despite some areas being in direct contact with the metal wedge and others, including where the thermocouples were, being free or even exposed to the flow; when exposed, the thermocouple's bodies were insulated with Permatex High-Temperature RTV gasket maker. This was a reasonable assumption because the portion in contact with metal is 15.62mm thick and the thermocouple is at a depth of 6.09mm from the top surface, well over halfway through the material. Nevertheless, to avoid all confusion, the test area was selected to be free of any metal on the underside, removing any interference in the final data. Still, the effect is checked in Section 7.2.3.3. Boyd and Howell [271] illustrated how one could use a 1D assumption to calculate heat transfer from thermocouples on a wind tunnel model. This was adopted to more modern IR measurements in [272, 273] and then introduced to the NAL by Neel et al. [274]. The core functionality of Neel's code, best described in [214], was adopted into a new Matlab program for IR data reduction custom-built for the current experiment. This program, whose outputs have

been validated against Neel's, will be described here to enough detail to permit its replication. Following Neel [214], atmospheric interference with IR signal was neglected due to the short distance between the test surface and camera, as were reflections off of the PEEK due to its high emissivity. The fundamental assumption was that the heat flux was 1D which greatly simplified the required calculation. In the context of IR thermography, this essentially allowed the code to consider each pixel as its own independent heat transfer problem. Boyd and Howell [271] and Running et al. [267] compared 1D results to 2D results and for the simple geometry, relatively low gradients, and high frame rate used here the 1D assumption was appropriate. The present code used interpolation to add in any dropped frames, so the time between frames was a constant $1/15\text{Hz} = 0.067\text{s}$. ([7])

The code began an analysis with standard bookkeeping, allowing the user to specify paths to the data, the region of interest, frame averaging. The raw .ats files from ResearchIR were read into Matlab arrays by a processing code provided by FLIR for Matlab. The thermal calibration was then performed for the user-specified preset, followed by rotation and distortion corrections before the final pixel-to-millimeter scale was set. Because the camera was triggered manually a few seconds before the 10.16cm line was opened and recorded at a different frame rate than the NALDAQ and PlasmaDAQ VI, it was necessary to unite the camera and tunnel's timelines. This is done using unstart, a dramatic even clearly visible in both data sets; in IR, it manifested as a sudden and uniform rise in temperature across the model. The code identified where the mean temperature on the whole plate suddenly rose, setting the IR camera's unstart, and where the Mach number suddenly fell, setting the NALDAQ's unstart. With a shared event marked in both timelines, the code then stepped backwards in time at the camera's known framerate and linearly interpolated tunnel conditions from the slower DAQ data, producing a "united" dataset between the IR camera and tunnel's DAQ. With this the code could proceed to the heat transfer calculation. The first step was to define the PEEK thermal properties, all of which were collected directly from the manufacturer Victrex. The density ρ of the Ketron 1000 PEEK was a constant $1300\frac{\text{kg}}{\text{m}^3}$, but the thermal conductivity k and specific heat capacity c_p were more complicated due to the temperature dependence illustrated in Figure 6.4. Every node in every pixel of every frame had its own unique temperature, so each node should then be able to interpolate from Victrex's data to determine the thermal properties. However, in practice this was unacceptably slow with any Matlab function attempted, standard or otherwise. As a compromise, a single characteristic temperature for a user-defined region of interest in each frame was used for the properties of that frame. The characteristic temperature was the average of the mean of the temperature of the top and inner surfaces. While the loss of fidelity was unfortunate, in testing it was discovered the temperature seldom rose more than 10K in the test area during a run, so there was little justification for the excessive computational expense of performing the ideal calculation. The thermal properties were used to calculate the thermal diffusivity $\alpha = \frac{k}{\rho c_p}$, which played an important role in the finite difference scheme. (Broslawski [7].)

The 1D equation for transient heat conduction through a wire is

$$\frac{\partial T}{\partial t} = \alpha \frac{\partial^2 T}{\partial \zeta^2} \tag{6.1}$$

This equation can be approximated with the following explicit, forward-time, central-space (FTCS)

scheme [252]

$$\frac{T_j^{i+1} - T_j^i}{\Delta t} = \alpha \frac{\left(T_{j-1}^i - 2T_j^i + T_{j+1}^i\right)}{(\Delta\zeta)^2} + \mathscr{O}\left(\Delta t, \Delta\zeta^2\right) \tag{6.2}$$

This represented a means to calculate the temperature at an internal node j at a future time step i provided the entire heating distribution was currently known through the wire. The variable ζ represented the spatial coordinate into the PEEK (with the origin at the surface). Its selection required care: more points improve fidelity, but the FTCS scheme was only stable if $\zeta \geq \sqrt{2\alpha\Delta t}$ [252]. Remember that α was now a function of temperature and changed with each frame, but ζ needed to be constant and amenable to all frames. To balance these concerns, ζ was calculated with the frame with the largest α, guaranteeing stability. Finally, both the surface and internal boundary conditions were "background corrected" by subtracting the data corresponding to $t = 0$s (or however many frames the user averaged together to temporally smooth the result) so as to help remove any artifacts like reflections, edge effects from the test article's walls or thermocouples, preheat gradients, *etc*. With the PEEK's properties set and the boundary conditions known at all times from the IR camera and thermocouples, the temperature through the PEEK for every pixel of every frame could be calculated. For the initial condition, the plate was assumed to be isothermal everywhere but the surface, with the temperatures measured from the thermocouples and IR camera respectively. The boundary conditions for each pixel were applied for each frame with the data from the thermocouple and IR camera for that frame. Once the temperature distribution within the model was known, the heat flux could be calculated from a second-order forward differencing approximation of Fourier's Law

$$q \approx -\frac{k\left(-\frac{3}{2}T_0^i + 2T_1^i - \frac{1}{2}T_2^i\right)}{\Delta\zeta} \tag{6.3}$$

Once the heat flux had been calculated all that remained was post processing. For the current work, this included averaging several frames (typically no more than five) together in order to smooth the final result; the images were median filtered for the same reason. It was also common [214, 213] to report the Stanton number, or the nondimensionalized form of the film coefficient h, to report the heating [48]. Doing so helped account for discrepancies in heat flux due to test article and tunnel heating as well as run-to-run variability. The Stanton number was

$$St = \frac{h}{\rho_e u_e c_p} = \frac{q}{\rho_e u_e c_p (T_{aw} - T_w)} \tag{6.4}$$

Here the density, velocity, and specific heat are for the fluid outside of the boundary layer, T_w was the wall temperature, and T_{aw} was the adiabatic wall temperature where, as was done throughout this report, T_{aw} could be found from $T_{aw} = T_e * (1 + \frac{1}{2}r(\gamma - 1) * M^2)$, where for laminar flows $r = Pr^{\frac{1}{2}}$ and for turbulent flows $r = Pr^{\frac{1}{3}}$. This procedure fails, however, if the state of the boundary layer was unknown. Thus for the trip sizing study, where quantitative results were unnecessary, the Stanton number was calculated with T_o instead of T_{aw}. Otherwise, for consistency if trips were installed, the flow was considered turbulent, which meant the Stanton number results just

downstream of the trips were unreliable. Temperature, heat flux, and Stanton number images were produced either at fixed Reynolds numbers or run times specified by the used. Spanwise traces of the variables at a user-specified location were also plotted. All heat flux and Stanton number figures were restricted by the domain of the internal thermocouples, the space between the first and last thermocouples in the streamwise direction. The effect of wall condition (metal contact, enclosed chamber, exposed to flow) was investigated. ([7])

6.2.5 High Frequency Pressure Transducers

This section follows from Broslawski [7]. Studying the pressure frequency content of a boundary layer can provide information regarding its condition (laminar, transitional, or turbulent), spatial and temporal growth, and spanwise uniformity. Past work on a similar geometry in the ACE tunnel [213] found meaningful content up to 300kHz. This work utilized Kulite XCE-062-15A Type A (screenless) ultra miniature, high temperature sensors for content below 80kHz, and then PCB 132B38 sensors for content up to 300kHz; these ranges were limited by the estimated flat-frequency response of each sensor (see [275] and [276] respectively). The sensors are compared in Table 6.1.

Property	**Kulite XCE-062-15A Type A**	**PCB 132B38**
Measurement Range	103kPa	345kPa
Housing Diameter	1.70mm	3.18mm
Resolution	Infinitesimal	7Pa
Sensitivity (typical)	N/A	$20.3\text{mV}/\text{kPa}$
Full-Scale Output (nominal)	0.1V	7V
Resonant Frequency	$200-250$kHz (empirical)	>1MHz
Temperature Range	$298-508$K (compensated)	$248-352$K
Temperature Sensitivity Shift	$\pm 1\%/100$K	N/A
Temperature Zero Shift	$\pm 1\%/100$K	N/A
Combined Error (non-linearity, hysteresis, and repeatability)	$\pm 0.1\%$ FSO BFSL (typical)	N/A

Table 6.1: High frequency pressure sensor properties.

The current test article was designed to stay in the tunnel during preheat, and so it reached temperatures considerably hotter than that in [213]; preliminary IR thermography data showed run temperatures of ~ 350K were nominal, and the temperature was known to rise even higher during unstart. According to the manufacturer's specification sheet, the PCBs used by Leidy [213] had a maximum operating temperature of 352K. Thus the PCBs would likely be damaged during the present application or, perhaps worse, provide misleading, inaccurate results. For this reason, PCBs were not used in this campaign. Kulite XCE-062-15A sensors (S/N 8534-3-79, -80, -81, -83) were fixed into the PEEK with Permatex high-temperature RTV as the cosmetic nail polish

used by Leidy [213] and Neel [214] would fail at the temperatures seen by the current model; RTV was recommended by the manufacturer to safely mount the sensors for repeated removal and reuse. Four Kulites were used at a time as limited by the available channels on the signal conditioning boxes to be introduced. They were placed in the three test locations used throughout this work, 130, 260, and 405mm from the leading edge; the 130mm location was slightly farther downstream than the PLIF measurements, but this was done to reduce the risk of the plasma damaging the sensors. In order to remove any chance of the 1.78mm holes for the upstream test locations interfering with the downstream test results, data was collected moving from the rear to the front of the test article, with each test location's holes only being drilled when that region was being studied. The sensors were placed 0 (K4, Kulite -80/-83), -3.42 (K3, -83), -6.84 (K2, -81), and -10.26mm (K1, -79/-81) from the centerline following a wake-trough pattern from the trips; their off-centerline locations were on the same side as all other measurements. This was done to study the behavior of being in the trips' wakes or troughs (especially relevant near the leading edge) and look for more generalized spanwise nonuniformity (especially relevant near the rear of the plate). As best as possible, the same sensors were kept in the same spanwise location across all tests, but by the time the "Front" test location was reached failed sensors necessitated moving the "inner" Kulites to "outer" locations in order to fill gaps in the data. Ideally, oil flow and IR thermography could have informed the placement of the sensors to ensure they were indeed in wakes or troughs, but the growth and movement of the structures along the plate, as well as the potential for misalignment, led to the more rigid approach. It was desirable to be just at the edge of a wake because it was the vortices cast by the corners of the trips which fomented turbulence and Neel [214] found the most distinct frequencies in these locations. Thus either the middle two sensors would validate the outermost sensor's results, or they would provide information on this third region. IR thermography was conducted concurrently with the Kulites to document exactly where each sensor was with respect to the flow structures; only temperature data was collected, a 2ms integration time was used for all cases, and all other specifications matched those discussed earlier. The Kulites were used to add extra fidelity to the scale of the IR images, as they provided exact coordinates on the test article with the flow on. ([7])

A Kulite's flat frequency response range is limited by the presence of a strong peak at its resonant frequency f_r [277]; this strong excitation can "bleed back" into lower frequencies, masking subtler effects and thereby defining the upper edge of the flat frequency response regime. Beresh et al. [275] showed that for the Type A variant, the flat response of Kulite XCE-062 sensors was $30-40\%$ of f_r and as low as 20% for the screened Type B. On the product specification sheet for the XCE-062-15A the manufacturer listed $f_r = 200$kHz, though in the NAL's facilites Neel [214] found the actual natural frequency to be $250-270$kHz; while such variability in piezoresistive Kulite sensors is not uncommon, the temperature and speed of sound effects of testing in a hypersonic environment also likely played a role [277]. Taking the manufacturer's value of f_r, one is left with a usable range of $0-80$kHz. In their PCB data Leidy [213] found meaningful results up to 300kHz, so there became a desire to increase the Kulites' usable bandwidth for the present work. The solution was the employment of a Kulite KSC-2 signal conditioning box with resonance frequency compensation (REZCOMP™). This signal conditioning box could provide the Kulites a clean 10V source, and, more importantly, filter the output signal to remove the natural frequency

spike as shown in Figure 6.5. According to the manufacturer, doing so allowed flat frequency responses up to 80% of f_r, and in some cases reliable data could be obtained above f_r. Hurst et al. [277] show improvements of the usable bandwidth of $200-300\%$, with varying results and temperature effects for different classes of sensors (the XCE class was not tested). The ability to measure up to 200kHz would cover most of the key features observed in Leidy's [213] analogous experiments and thereby negate the loss of the PCBs. The efficacy of the new REZCOMP was directly compared to a Kron-Hite Corporation Active Filter Module 8-pole Bessel 200kHz low-pass filter with unity gain housed in a Krohn-Hite FMB3002 chassis in the corresponding results section. As an input for the REZCOMP™ filter, the KSC-2's control software required an accurate measurement of the sensor's natural frequency and quality factor $Q = \frac{f_r}{\Delta f_{FWHM}}$. These quantities were determined experimentally *in situ* following Hurst et al. [277]. Performing a tunnel run with the REZCOMP™ feature turned off allowed one to identify f_r in the spectra, and from that an approximate Q; the results were clearer with the trips in as the turbulence better excited resonance in the sensor. This *in situ* calibration of tunnel data is preferable as the sensors had the same thermal loading as during a data collection run. Although resonant frequency is a function of the sensor construction, this procedure was repeated for every Kulite configuration, confirming only slight changes in each individual sensor's results. Following Leidy [213], the data were reduced using Matlab's implementation of Welch's power spectral density method. The number of samples per window was an input to Matlab's "pwelch" function, so a quasi-grid convergence study was performed where $2\times10^{8-16}$samples were used, in 10^2sample increments, until f_r changed by less than 1kHz, the resolution of the KSC-2's control software. Typically convergence occurred at 2×10^{12}samples, and 2×10^{10}samples were used for actual data reduction following Leidy [213]. The resonant frequencies fell between $225-246$kHz, with most above 240kHz. While the resonant frequency could be input into the KSC-2's software, Q was problematic. In its current form, the KSC-2 was not optimized to work with such high frequency sensors, and so the maximum programmable quality factor was $Q\leq50$. However, nominal results yielded $Q=50-100$ for window sizes of 2×10^{10}samples. Fortunately, Hurst et al. [277] showed that while accurate measurement of f_r is critical, that for Q was somewhat forgiving, even up to 25% from the correct value. Thus the filters were left at $Q=Q_{max}=50$. ([7])

The KSC-2 signal conditioning box provided two sensor channels which could be individually controlled by the affiliated software. Two boxes were generously loaned to the NAL for this work, one from Mr. Steve Carter at Kulite Semiconductor Products, Inc. (S/N 200469-014, calibrated 4/11/2021-5/18/2022) and another from Dr. Jerrod Hofferth at the Air Force Research Laboratory at the Arnold Engineering Development Complex (S/N 200469-015, calibrated 4/11/2018-9/12/2019). As best as possible, the same channels and wires were used for each spanwise test location throughout the entire campaign, and new cables were used throughout the system. Both boxes were powered through a Furman M-8x^2 surge protector for uniformity. The boxes were set to use their "Chassis Ground", and the sensors were connected to this chassis ground at the DB-9 connection to the box; thus in the affiliated software the "Shield" field was set to "Ground". While using new cables, common power, and the current grounding scheme did yield a tolerably low-noise environment, it was found to be critically important that USB control cable for each box be unplugged during testing; failure to do so introduced so much white noise the data were

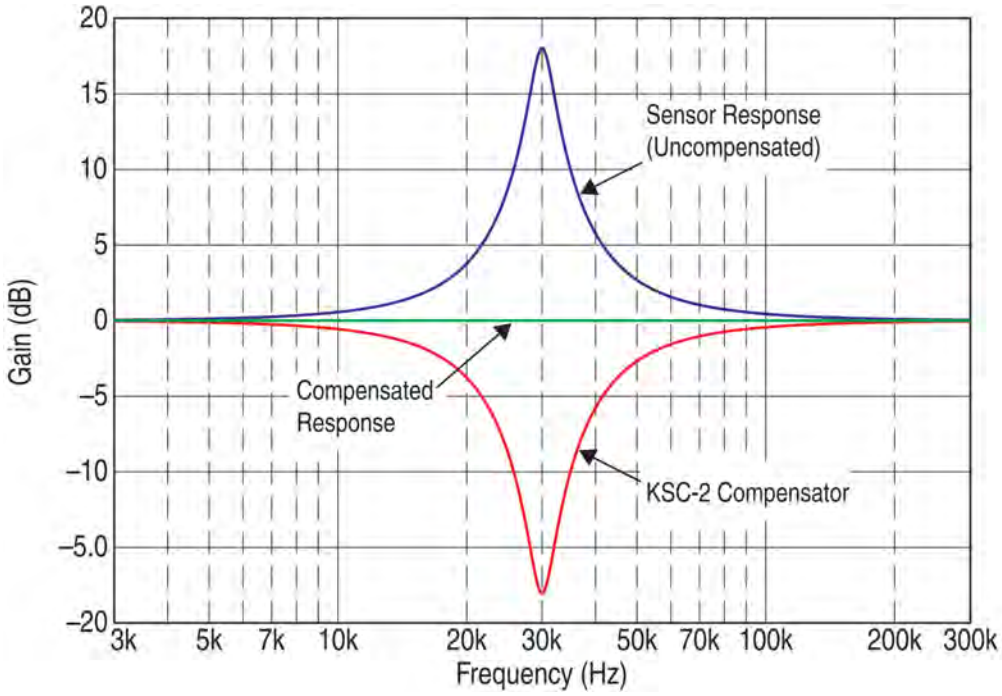

Figure 6.5: An example of the resonant frequency compensation with the KSC-2's REZCOMP™ filter. [277].

rendered nearly unusable. The KSC-2 boxes were programmed to provide 10V of bipolar excitation, which is required for the XCE class Kulites. The "Sense" field was set to "Local", another such requirement for this hardware. These Kulites return $0-100$mV from $0-103.421$kPa, and so for DC operation they could be amplified up to $100\times$ before saturating the NI USB-6366 DAQ's 10V limit. The boxes could output either DC- or AC-coupled data, and the former was chosen as it was more intuitive in noise reduction, data interpretation, and in checking sensor health. That being said, the Kulites were not calibrated or balanced as the temperatures experienced during a run would be challenging to replicate on a bench and pressure values were not needed to meet the experimental objectives, only voltage fluctuations. Because the KSC-2 box's control software only provides set amplification values, a pregain of $16\times$ and postgain of either $6\times$ or $5\times$ were used for a total of $96\times$ or $80\times$ amplification. This value allowed the full resolution of the DAQ to be used, but did not saturate the sensors at atmospheric pressure, which was necessary to determine the sensors' statuses; the lower amplification was used when daily temperature and humidity fluctuations led to slightly higher outputs to the DAQ. Common practice was to maximize the pregain as opposed to the postgain so any noise introduced by amplification can be filtered out. The KSC-2 boxes have programmable, custom 6-pole "flat" low-pass filters recommended for the current application, but their maximum cutoff of 127.5kHz was too low. Therefore the filter was switched off in the software and the boxes' inherent 3-pole Butterworth wideband amplifier frequency response was used to low-pass filter by -3dB frequency at 500kHz. Because the data were sampled at 2MHz the Nyquist frequency should be 1MHz, so low-pass filtering at 500kHz was sufficient to prevent

aliasing. The data were processed with a LabVIEW VI developed by Neel [214] and the power spectral density plots produced using Welch's method in a Matlab script following Leidy [213] and Neel [214]. The VI was modified to read in the plasma conditions. It was manually triggered before the air ejector was started, and then turned off after unstart, providing full context for the sensors' performances. During this time, the sensors were sampled at 2MHz in 100ms intervals, yielding 2×10^5samples at the NALDAQ's frequency of 10Hz. Matlab's "pwelch" method used 2×10^{10}samples in Hamming windows with the default 50% overlap, which yielded a resolution of approximately 2kHz. ([7])

6.2.6 Pitot Pressure

This section follows from Broslawski [7]. Pitot surveys were an integral part of the experimental campaign as they provided direct measurements of the Mach number, and by extension velocity and temperature, through the boundary layer. These data communicated the state of the boundary layer, which was especially important in transitioning/tripped flows, compared the flow in the trips' wakes as opposed to their troughs, and probed any effect of the plasma. They also provided a measurement of the wall shear stress, as well as validation for other experiments, including PLIF. This work was conducted alongside Joel White, another graduate student at the NAL who led the design and operation of the traverse system as part of their doctoral research. The resulting system had sufficient complexity to warrant a detailed description here; for clarity, this section is organized into discussions of the design of the traverse mechanism, the Pitot probes, the sensors, the measurement of the probes' positions, the data reduction, and an ancillary freestream measurement. A universal probe mount was designed to provide a platform for the present and future diagnostics. Motion was provided by two Aerotech PRO165 Mechanical-Bearing Ball Screw Linear Stage tables orthogonally mounted to afford 400mm of motion in the vertical and 200mm in either the streamwise or spanwise direction; the rig was mounted to the optical rail surrounding the ACE test section. Each stage had a factory High Accuracy Linear and Rotary calibration which provided a precision of $< \pm 5\mu$m at room temperature. These stages were controlled by Aerotech Ensemble HLe Controllers and linear drivers. Aerotech's Ensemble Motion Composer control software interfaced with LabVIEW to allow for control within a custom-built DAQ VI. This system was originally selected as it provided low electronic noise which could interfere with hot wire measurements [225], but due to the success and universality of the Aerotech platform subsequent students [206, 202, 213, 214] adapted it for use with both hot wire and Pitot probes. Any sting mounted to the traverse should capitalize on its two degrees of freedom. To do so necessitated a dynamic seal in both the vertical and horizontal plane, where the latter referred to motion in either the streamwise or spanwise direction. Mai [202] offered a solution which allowed for vertical and streamwise motion, and Neel [214] later simplified it, but due to the presence of sharp corners required to prevent excessive blockage and separation around the sting, both designs suffered from leaks at its interface with the O-ring. It was for this reason the Pitot mount was redesigned, with the final result included in Figure 6.6. Again, any sting required an aerodynamic shape to reduce blockage and vortex shedding, but such geometries are challenging to dynamically seal. Ultimately, all efforts to design such a seal were abandoned and instead the sting was divided into two distinct sections. The top half was a "piston" which had two standard Buna-A Durometer

70A 2-326 O-rings set inside a shaft; the shaft provided 55.8mm of vertical motion before the top O-ring would become exposed. Note that Dow Corning Vacuum Grease was applied to all O-rings for lubrication and to aid with the seals. The second half of the sting was a traditional blunted diamond shape 9.5mm wide and 25.4mm long; it extended a total length of 127mm, which was set to insert the Pitot probe into the region of interest with maximum protection. This component was made with the Oran W. Nicks Low Speed Wind Tunnel's FormLabs Form 3L SLA 3D printer from Rigid 10K as this material was shown to be mechanically and thermally durable enough to survive wind tunnel testing and made it trivial to produce complex parts [278]. The piston's shaft, shown in Figure 6.6(b), statically sealed against an adapter plate with a Buna-N Durometer 70A 2-141 O-ring. This adapter plate then dynamically sealed to the modified window plug with a custom $3/32$in fractional (0.103in actual) silicon O-ring. In order to translate in either the streamwise or spanwise direction, one must loosen the screws sealing the adapter plate to the window plug, actuate the traverse, then fasten all of the screws. The same procedure applied to the second plate on the inside of the tunnel as well, which prevented re-circulation inside the modified window plug's cavity. This system allowed the traverse to move 92.1mm in the spanwise direction, or, should the entire traverse be re-mounted 90°, 76.2mm in the streamwise direction. The reason the modified window plug needed to be so tall was to allow the adapter plate to slide over the other plugs on the top of the test section when the traverse was moving in the streamwise direction. It is noted that the system needed to be square with the tunnel to prevent binding when moving in the spanwise or streamwise directions. While this design was limited to moving the probe in the vertical direction while the tunnel was running, it provided sufficient functionality to precisely align the probe with test location on the test article, and sealed well. ([7])

The Pitot probe was constructed from two concentric stainless steel tubes joined with JB Weld Kwikweld Epoxy; the outer tube dynamically sealed through the piston head with a Swagelok Ultra-Torr vacuum fitting following [206]. This outer support tube had an outer diameter of 3.175mm, a wall thickness of 0.711mm, and an inner diameter of 1.753mm. The inner tube, meanwhile, had an outer diameter of 1.651mm, a wall thickness of 0.127mm, and an inner diameter of 1.397mm; the tip of this tube was crushed to an elliptic ratio with outer dimensions of nominally $2:1$mm to compensate for the large internal diameter. Semper [206] used an equally sized, crushed inner tube and collected data in the ACE tunnel, though their wall thickness was larger than that used here. The tubing used here was chosen to balance rigidity with near-wall measurements and venting; a thicker tube would be sturdier, but it would not be able to get as effectively close to the wall. Furthermore, its smaller hole would take longer to settle on the tunnel's near-vacuum conditions; near the wall Semper [206] noted it took 2s for the Pitot pressure to settle, as compared to 0.5s in the freestream. Because many different test locations were to be interrogated, the ability to quickly reach the stagnation conditions was a top priority if a decent density of test points were to be used. Crushing the tube had the added benefit of reducing the size in the direction with the strongest gradients, which helped reduce the sensed probe displacement [279, 280]. The probe's yaw was confirmed to be zero before each run by measuring the tip's distance from the side of the test article with a ruler and a camera positioned directly above the probe, and then by moving the camera to the leading edge, centering it relative to the probe using a ruler, and checking the angle with a camera looking head-on at the probe. A shaft collar "JB Welded" into the sting fixed the

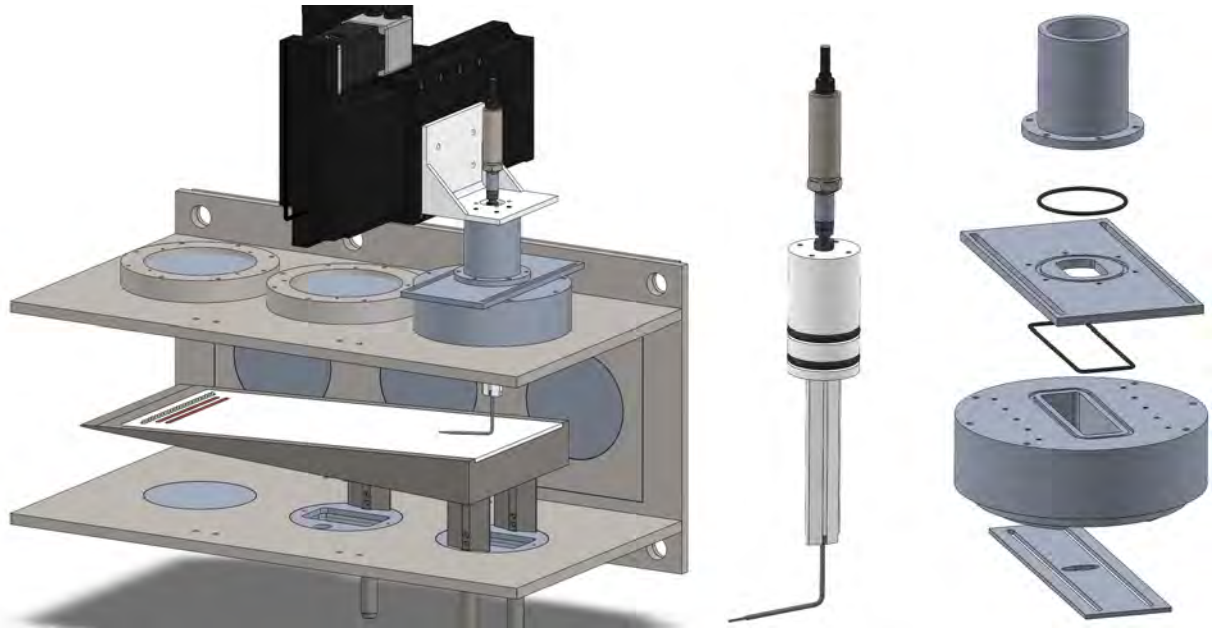

(a) Full view (b) Exploded view

Figure 6.6: CAD of 2D traverse. [7].

probe in place, and while the alignment was checked before every run, the probe seldom drifted. The probe's pitch was determined through careful trigonometry, as one needed to limit the angle between the test article and the probe, but also let the crushed tip of the inner tube touch the surface before the thicker outer tube. It was found that an angle of 7.5° relative to the centerline (4.75° relative to the test article) worked well, with no more than 25.4mm of the inner tube ever needing to be exposed to the flow. It is shown in [279] that this angle offset it expected to have only a minimal effect on the results. The tubing was manually bent with a 12.7mm radius following a stencil traced on paper. There were six test locations for this campaign, three streamwise locations and two spanwise locations; the test locations were selected to match those of other diagnostics, especially the PLIF data. The spanwise locations corresponded to the trips' theoretical wakes (0mm off-centerline) and troughs (-10.26mm off-centerline), though the IR thermography data show that these structures do move somewhat along the length of the test article. Streamwise data were collected at "Forward", "Middle", and "Back" test locations 140, 261, and 406.5mm from the leading edge respectively. The static pressure ports were positioned -6.84 and 3.42mm for the "Wake" and "Trough" measurements, respectively, taking advantage of the symmetry of the flow to maximize the distance between the holes and the probes to minimize interference. The static ports were 130, 260, and 405mm from the leading edge; the discrepancy between the Pitot probe and static ports in the "Forward" location was due to poor optical access at this point, a necessity which will be discussed shortly. For the "Rear" test location, the traverse was moved in the spanwise direction such that the same probe could take the "Wake" and "Trough" data. For the "Middle" and "Forward" locations, the traverse and test article (on its struts) were moved in the streamwise

direction so one probe could make the "Wake" measurements in both positions, and another could take the "Trough" data. In order to access the "Trough" without the ability to move the traverse in the spanwise direction, a Pitot tube was bent into position using screws drilled to trace out the proper horizontal "Z-shaped" displacement before the tube was turned in the streamwise direction as usual; this probe is shown in Figure 6.7. ([7])

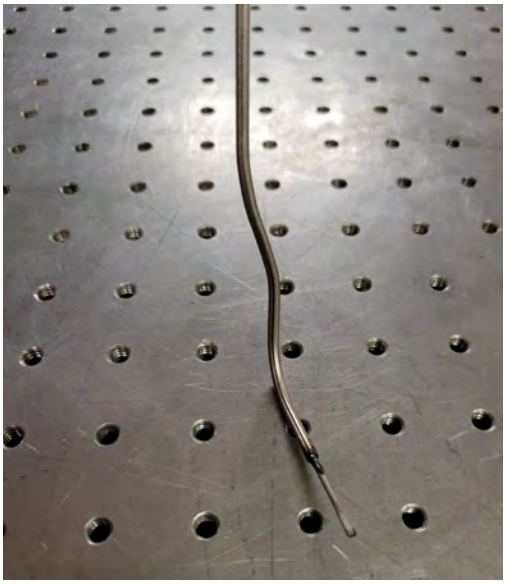

Figure 6.7: Trough Pitot probe. [7].

The static pressure taps were drilled with a 0.508mm bit to provide minimal flow disturbance, though it was later seen they still produced shocks. On the underside of the wedge, NPT-to-barb adapters connected the hole to Teflon PTFE tubing with an outer diameter of 3.175mm and an inner diameter of 1.588mm. This tubing was rated to above the temperatures of the ACE tunnel, was strong enough to endure the crushing effect of the vacuum, was flexible and workable, and had a small internal volume to reduce the settling time. It was passed out of the tunnel and into a series of adapters which connected it to the barometer. To ensure a hermetic seal, at the joint inside the tunnel JB Weld epoxy or Permatex RTV was applied, while outside the tunnel Dow Corning vacuum grease covered the barb adapter. When not in use, the underside of the static taps were covered in Kapton polymide tape, but the top remained uncovered as the holes were so small and effort to plug or cover them was likely to have a greater impact than the cavity itself. ([7])

The Pitot probe was connected to an Omega PX409-005A10V pressure transducer (serial no. 528724) which provided $0-10$V from $0-258.6$Torr. It was connected and sealed to the Pitot tube through a Swagelok Ultra Torr fitting and adapter set. The transducer came pre-calibrated from the manufacturer, and had a cumulative accuracy of 0.08% the full-scale voltage output. This sensor had an operating range of $-45-115°$C and a compensated temperature range of $-17-85°$C,

but as the transducer was mounted outside of the tunnel it was not expected to deviate from room temperature, a convenience Semper [206] confirmed. This device was powered to 24V and 5mA with a BK Precision 9110 100W Multi Range 60V/5A DC Power Supply. The static pressure was recorded with a Baratron 631C capacitance manometer (model no. 631C12TDFP, serial no. 07XX09 016522584) which had a range of $0-100$Torr and an accuracy of 0.5% of the reading. The Baratron 631C was thermally regulated to 200°C to provide thermal stability, though again, as it sat outside of the tunnel any such affect was likely to be minimal. Data were collected at 1000Hz while the probe was parked at a test location. This was chosen to provide an ample number of points, and to match the frequency of the schlieren images to be discussed. It was expected that there would be some settling time for both the Pitot and static pressure tubing owing to their small diameter. Preliminary testing showed that the Pitot tube settled within quarter of a second for any point in the boundary layer, showing the efficacy of the wider internal diameter than that in [206]. However, because stagnation pressure grew as the probe moved up from the hot surface, it was found starting each set of points near the surface and moving away from it produced quicker settling times; the effect was minor, but it was found vacuuming out the probe was less efficient then blowing into it, so taking full advantage of the hard vacuum achieved during the tunnel's startup was recommended. The static pressure probe took far longer to settle, perhaps due to the large internal volume of the Baratron 631C or small size of the static ports, but it ultimately converged within 0.5Torr by the final data point in a run. And so it was decided for each test point data would be collected for the conservative duration of one second, then in post processing stagnation pressures would be the average of the last half second of data and the static pressure would be the average of the full second of data for the last point. ([7])

Collecting data for one second per point meant that, including the time to ramp up the plasma and move between points, only as many as fourteen points could be collected per run. Wile this was sufficient resolution for the laminar boundary layers, for thicker, turbulent boundary layers this meant two runs would need to be combined to complete a survey. Initial efforts involved moving the probe in a staggered, "even/odd" pattern between two runs to prevent a step at the junction between the points from each run, but the concern was that due to inconsistent tunnel flexure it would be easy to either miss or repeat the critical points very near the wall. Instead, an "inner" and "outer" sweep was conducted for each sweep, where small steps as small as $\frac{1}{3}$mm were taken in the inner survey and as large as 5mm were taken in the outer survey; such large steps were susceptible to increased settling times, but none more than a quarter of a second were observed. In practice, no significant shift in Mach numbers was recorded at the junction between "inner" and "outer" runs at the same location. Both of these sensors were selected to be as accurate as possible. It is noted that the dynamic range of both sensors exceeded the predicted values of $\mathcal{O}(10)$ (including the probe's normal shock) and $\mathcal{O}(1)$Torr for the stagnation and static pressures, sensors which returned errors which scaled with the reading and not the full-scale output were preferred. The data reduction process will be reviewed shortly, but put simply the ratio of the stagnation to the static pressure provided the Mach number, which then yielded the temperature profile through the modified Crocco-Busemann correlation, and then the Mach number and temperature gave the velocity. Thus all of the variables of interest related to the pressure ratio, and both pressures had a conservative affiliated uncertainty from the sensors of $\frac{P_o \pm X}{P \pm Y}$. So, an upper bound for the cumulative

error of the pressure ratio would be $\frac{P_o+X}{P-Y}$ and the lower bound would be $\frac{P_o-X}{P+Y}$. This then tracked through all subsequent calculations; for example, the Mach number was calculated three times, once with the measured pressure ratio and again with both the upper and lower pressure ratio bounds. Repeating this process, the original sensor uncertainty could then follow all the way to the velocity. This approach yields large uncertainties, but it will be seen that even these were negligible. ([7])

During normal operation, the wind tunnel flexed, and while it was never more than a few millimeters, it was enough to throw off any pre-run calibration. The effect was exacerbated by the flexure of the Pitot probe itself. Therefore to accurately measure the position of the probe, it was necessary to record its position in real time. Here schlieren imaging was used alongside each Pitot run. It was triggered by the DAQ using the FASTDAQ's analog output channel and the Photron PFV4's "Random Reset" triggering feature at the start of each point's collection. With careful scaling using a dotcard, the probe's position in pixels could be converted into millimeters with a nominal resolution of $103\frac{\mu\text{m}}{\text{pixel}}$. A framerate of 1000fps was used at a shutter speed of 1.25μs, though the image resolution remained the default $1024 \times 1024\text{pixels}^2$ as PFV4 did not have the same customizability as Fastcam. A Matlab script was written which identified the wall and corner. Matlab's in-built image processing tools were key to this process. The code grayed then binarized the mean schlieren image such that all dark pixels became ones and all other pixels became zeros; the result was filtered, the edges were detected, and finally it was diagonally smoothed. The code identified the top corner of the probe by checking, for all pixels in the user-defined region of interest, if there were: no pixels in the twenty-five above it which were one (shocks could be erroneously labeled edges); no pixels upstream which were one; the neighboring pixels downstream and below were one. Should there be any issues identifying the corner, the code would prompt the user to manually select one. The wall identification was simpler, the code simply looked for the last nonzero pixel in the first and last column of the binary image; it then considered the wall to be the mean of those pixel locations, though with careful image rotation the identified points were never more than three pixels apart. The top corner of the probe was identified because the ACE tunnel and floor were not perfectly level, so seeing the precise pixel the probe touched the surface at was impossible without perfect alignment. While great care was taken when aligning to see as much of the probe as possible when it was touching the surface, only the top corner was ever definitively visible. For this reason, it was necessary to identify the offset between when the bottom of the probe was physically touching the surface and the observable, faux surface in the schlieren image. To do so, an image was taken with the bottom of the probe touching the surface. The top of the probe was identified, and its known thickness and angle were used to calculate the bottom pixel. Using the scale calculated from the gridcard, the height in millimeters between the bottom of the probe and the surface was calculated. The offset to be added to all subsequent calculated heights was the theoretical height minus the measured value. For mean run images at each position, an analogous process was carried out; the top corner and wall pixels were identified, scaled, and the offset was added, but here the center of the probe was output. The spatial uncertainty of the probe was taken to be 2pixels plus the scale uncertainty multiplied by the number of pixels between the measured probe position and the wall. The $mm/pixel$ uncertainty was half of the difference between the x- and y-scales as measured from the dotcard; this was acceptable as approximately the

same number of x- and y-points went into the mean "total" scale. No account of the effective probe centerline displacement was considered. This error came from the transverse velocity gradient over the probe and the unequal contribution the higher velocities have on the overall pressure reading, and it was especially relevant in the near-wall measurements of the turbulent boundary layer. Its effect could have been lessened experimentally by reducing the side of the probe, but that step was not taken here for fear of creating an unsustainable settling time in the Pitot probe. There exist empirical corrections [279, 280, 281], but none were found for hypersonic boundary layers. For this reason, no compensation could be applied, but in general it would seem the probe's effective reading would be for a position higher than it was actually placed. ([7])

The process to bring the measured stagnation and static pressures into a scaled velocity profile was as follows. The Mach number can be calculated from the following [205]

$$M < 1: \quad M = \sqrt{\left(\frac{2}{\gamma-1}\right)\left(\left[\frac{P_o}{P}\right]^{\frac{\gamma-1}{\gamma}} - 1\right)} \tag{6.5}$$

$$M \geq 1: \quad \frac{P_o}{P} = \left[\frac{(\gamma+1)^2 M^2}{4\gamma M^2 - 2(\gamma-1)}\right]^{\frac{\gamma}{\gamma-1}} \frac{1-\gamma+2\gamma M^2}{\gamma+1} \tag{6.6}$$

The first equation is the isentropic flow relation, and is valid for shock-free flows. For supersonic flows, the second equation must be used, the Rayleigh-Pitot formula; this equation solves for the supersonic Mach number upstream of the Pitot probe by working backwards from the subsonic flow in the tube and then across the probe's normal bow shock. The Rayleigh-Pitot formula must be solved iteratively, and here a Newton-Raphson method (see [258]) with a tolerance of 1×10^{-4} and the isentropic Mach number as a first guess was used. In order to convert from the Mach number to a velocity, the temperature must be known. While PLIF thermometry results could be used, the second Crocco-Busemann relation for non-adiabatic flows was more easily integrated into the process. This equation relied on the velocity, but it could be re-written in terms of solely the temperature, edge velocity, and Mach number using $u = M\sqrt{\gamma R_{air} T}$

$$T = T_w + (T_{aw} - T_w)\frac{M\sqrt{\gamma R_{air} T}}{u_e} + (T_e - T_{aw})\frac{M^2 \gamma R_{air} T}{u_e^2} \tag{6.7}$$

Recall that the recovery factor is $r_{lam} = Pr^{\frac{1}{2}}$ or $r_{turb} = Pr^{\frac{1}{3}}$ and the adiabatic wall temperature is $T_{aw} = T_e\left(1 + \frac{r}{2}(\gamma-1)M_e^2\right)$; note that in the "Turbulent/Front" case, where the flow was likely to be transitional and not fully turbulent, using r_{turb} was an unwanted but necessary approximation. The edge conditions were calculated using the measured tunnel conditions from the NALDAQ and oblique shock relations as was done in Section 5.2.7; this does introduce an inaccuracy in that this is not an ideal oblique shock due to the leading edge's bluntness, but it was deemed acceptable as the measured edge Mach number agreed with the theory satisfactorily well, even with the trips installed. From the results of the IR thermography campaign in Section 7.2.3.3, the wall conditions were set with the values in Table 6.2. It was clear from the results in Section 7.2.3.3 there was a high degree of variation between runs and exact placement in the heat flux, but here an effort was

made to choose an intermediate value agnostic of the presence of a wake or trough. Similarly, in the "Front/Turbulent" case, the flow was transitional, not fully turbulent, yet the turbulent T_{aw} was used in calculating St, so the wall shear stresses calculated using this parameter at this location were somewhat unreliable. A Newton-Raphson iteration scheme with a tolerance of 1×10^{-4} and T_w as a first guess was used to solve the Crocco-Busemann relation. ([7])

Location	**Laminar**			**Turbulent**		
	T_w (K)	q_w (W/m^2)	St $(\times 10^{-3})$	T_w (K)	q_w (W/m^2)	St $(\times 10^{-3})$
Front	365	700	2.5	365	1150	1.75*
Middle	355	300	0.6	355	1100	1.25
Back	345	300	0.5	345	975	1

Table 6.2: Wall thermal conditions for Pitot campaign calculations. *Calculated assuming turbulent T_{aw}, though flow was transitional.

With the temperature known, the velocity could be calculated as $u = M\sqrt{\gamma R_{air} T}$. For turbulent flows, it was desirable to scale the velocity with inner variables. Summarizing, for $v^* = \sqrt{\frac{\tau_w}{\rho_w}}$, $u^+ = \frac{\bar{u}}{v^*}$, and $y^+ = \frac{y v^*}{\nu_w}$ one can calculate

$$u_{eq} = \frac{U_e}{a}\left(\sin^{-1}\left(\frac{2a^2\frac{\bar{u}}{U_e} - b}{Q}\right) + \sin^{-1}\left(\frac{b}{Q}\right)\right)$$

such that in the viscous sublayer layer $u^+_{eq} = y^+$ and in the log layer $u^+_{eq} = \frac{1}{\kappa}\ln y^+ + C$ with $\kappa = 0.41$ and $C = 4.9$, following [40, 50]. As is customary, these theoretical results were plotted alongside the data. The viscosity used throughout these calculations was derived from the temperature, blending Keyes' and Sutherland's Laws in the cold and hot regions respectively. ([7])

Critical to the calculation of u^+_{eq} is the wall shear stress τ_w. There are many ways to approach this parameter both theoretically and experimentally, and several are reviewed here. Perhaps the first choice would be to calculate it from $\tau_w = \mu\frac{du}{dy}$, and indeed using the results from the numerical boundary layer solver this was tractable; it did, however, rely on an idealized model of the boundary layer, which was not desireable. To better anchor the result to the data, one could use a modified definition of the Reynolds Analogy from White's derivation of the Crocco-Busemann relations. In this equation the skin friction coefficient is $C_f = \frac{\tau_w}{\frac{1}{2}\rho_e U_e^2}$. Also, the van Driest II approach, which White [48] says is the superior model, is limited to adiabatic flows. Thus only the Reynolds analogy could be solved entirely from the tunnel's conditions, which made it at the very least a useful validation for the boundary layer solver's result. The Reynolds Analogy and van Driest II (for comparison) approaches were performed using the IR data available in Table 6.2 and the NALDAQ's run data as edge conditions were not measured for the "Inner" turbulent runs. P was taken from the NALDAQ's run data and not the static pressure port for consistency, though this

did remove any "Wake/Trough" dependence in the results, as well as any parameter changes across the trips' shock structure. To capture such effects, it was preferable to directly measure the wall shear stress. A serious effort was made using a new IC2 DirectShear Optical Shear Stress Sensor OS-210 (serial no. 102107) with an IC2 Differential Optical Sensor Unit OSU-1011-H2U (serial no. 103602), but the signal did not clearly rise above the noise floor, likely due to the low-density nature of the ACE tunnel and the large range of the sensor used. Nevertheless, there were other, somewhat more circuitous ways to measure the wall shear stress that stemmed from Pitot data. ([7])

One such approach is the Clauser chart method [40], a simple method well-summarized in [282]. The conceit is to try different values of τ_w until a good fit of the slope of the log layer on an inner variable plot is achieved. For compressible flows, mathematically this means

$$\frac{u_{eq}(y)}{v^*} = \frac{1}{\kappa}\ln\left(\frac{yv^*}{\nu_w}\right) + C \tag{6.8}$$

Multiplying by $\frac{v^*}{u_e}$ yields

$$\frac{u_{eq}(y)}{u_e} = \left[\frac{1}{\kappa}\frac{v^*}{u_e}\right]\ln\left(\frac{yu_e}{\nu_w}\right) + \left[\frac{1}{\kappa}\frac{v^*}{u_e}\ln\left(\frac{v^*}{u_e}\right) + C\frac{v^*}{u_e}\right] \tag{6.9}$$

Because the skin friction coefficient can be written $C_f = 2\left(\frac{v^*}{u_e}\right)$ then one can write

$$\frac{u_{eq}(y)}{u_e} = \left[\frac{1}{\kappa}\sqrt{\frac{C_f}{2}}\right]\ln\left(\frac{yu_e}{\nu_w}\right) + \left[\frac{1}{\kappa}\sqrt{\frac{C_f}{2}}\ln\left(\frac{v^*}{u_e}\right) + C\sqrt{\frac{C_f}{2}}\right] \tag{6.10}$$

While this equation could be solved for the log layer points, in practice, it was far simpler and tolerably accurate to allow the user to guess different values of τ_w until the results lined up with the theoretical line $u^+_{eq} = \frac{1}{\kappa}\ln y^+ + C$. Wei et al. [282] noted this method is susceptible to variability in the constants κ and C, as well as Reynolds number effects, but here the flow was simple and at a constant Reynolds number, so it was deemed worth investigation. Neeb et al. [283] added Coles' [284] Law of the Wake to the equation to get more points to fit, but here this step was not taken. It is noted, however, in their comparison of different means of finding τ_w in a turbulent, Mach 6 boundary layer this fitting method performed well. The final experimental approach attempted used a Preston tube to measure τ_w. A Preston tube is just a small Pitot tube placed directly on the surface, so here the first data point from every laminar and turbulent "inner" sweep was used to calculate a wall shear stress. Preston [281] used a functional analysis to relate this measurement to τ_w through the incompressible, pipe flow formula[2]

$$\log\frac{\tau_w d^2}{4\overline{\rho}\overline{v}^2} = -1.396 + \frac{7}{8}\log\frac{(\overline{P}-\overline{P}_o)d^2}{4\overline{\rho}\overline{v}^2} \tag{6.11}$$

[2]In the original publication, the constant -1.396 was written with the convention $-1.396 = -2 + .604 = \overline{2}.604$.

Here d refers to the outer diameter of the tube and an overline $\overline{X}$ denotes a variable at a constant property/incompressible condition. Hopkins and Keener [285, 286] would extend this theory to compressible boundary layers. They used $\frac{\tau_w d^2}{4\overline{\rho}\overline{\nu}^2} = \overline{R}_d \frac{\overline{C}_f}{8}$ and $\frac{(\overline{P}-\overline{P}_o)d^2}{4\overline{\rho}\overline{\nu}^2} = \overline{R}_d \frac{\overline{C}_p}{8}$ in Preston's equation to produce

$$\log R_d C_f = -1.283 + \frac{7}{8}\log R_d C_p \tag{6.12}$$

They also showed $R_d C_p \approx 1.4 R_{air} T_w \left(\frac{M_w d}{\nu_w}\right)^2$ such that only P, P_o, and T_w would be needed to calculate τ_w, where the pressures would be used to calculate the Mach number at the wall. The authors tuned this relation in non-adiabatic hypersonic flow and thus it was adopted here. There was some concern that the crimped tubing used here may have been problematic owing to the sensitivity probe size can have on the results, but Semper [206] successfully used a similarly crimped and sized tube for their work in the ACE tunnel and recovered a satisfactory value for τ_w. Furthermore, Preston recommended an internal-to-external diameter ratio of 0.6, though the authors in [287, 288] successfully used probes with ratios from $0.55-0.75$; again considering the minor axis of the probe to be d, then the probe used here had $d \approx 0.75$. Finally, it is noted that from Shang et al. [125]). there was no expectation the skin friction would be altered downstream of the plasma, though the above techniques were repeated for both the plasma "On" and "Off" cases regardless. At the beginning of this cumulative research effort, the settling chamber's Endevco 8540-200 High Temperature Pressure Sensor was re-calibrated, but not *in situ* due to the complexities of calibrating at an elevated temperature. Mai [202] took the additional step of manually adding temperature compensation factor into the sensor's results in post-processing, but from personal communication it seems this effort was generally not taken by other experimentalists at the NAL. Futhermore, in installing the *NO*'s injection pipe, the nozzle and settling chamber were disassembled several times. For these reasons, with a Pitot system installed in the tunnel, a test was conducted to confirm the freestream Mach number. For this test the probe was centered in the vertical and spanwise direction, and it was roughly centered in the streamwise direction as well. The probe was constructed from the 3.175mm tube bent to be parallel with the flow; there was no need to crimp the opening or use the smaller inner tube as they would only reduce the probe's response time. After preliminary testing revealed no probe motion during the run, no further schlieren data was taken. The tunnel was ramped to $Re = [2,4,6] \times 10^6/\text{m}$, with a few seconds of delay at each Reynolds number to ensure the probe would settle at each condition. ([7])

Mach number from $P_{o,SC}/P_{o,TS}$ (SC-settling chamber, TS-test section) was calculated from isentropic flow relations, and $P_{o,TS}/P_{TS}$ from the Rayleigh-Pitot formula. The $P_{o,TS}/P_{o,SC}$ Mach number was calculated from normal shock relations [205]

$$\frac{P_{o2}}{P_{o1}} = \left[\frac{\frac{\gamma+1}{2}M^2}{1+\frac{\gamma-1}{2}M^2}\right]^{\frac{\gamma}{\gamma-1}} \left[\frac{1}{\frac{2\gamma}{\gamma+1}M^2 - \frac{\gamma-1}{\gamma+1}}\right]^{\frac{1}{\gamma-1}} \tag{6.13}$$

This equation was solved using the bisection method (see [258]) to a tolerance of 10^{-4} using $M = [5,8]$ as the initial guesses. It is noted that the equation monotonically decreases, at least in the relevant range of Mach numbers, which was useful for the bisection method. These results were

compared to freestream PLIF measurements made by Buen [212], which included measurements of the ACE tunnel's freestream velocity and temperature fluctuations. (Broslawski [7].)

6.2.7 Optical Emission Spectroscopy (OES)

This section follows from Broslawski [7]. OES is a useful tool for determining the ro-translational, vibrational, and in some cases electronic, temperature of a plasma. It can communicate key chemical data such as species' formation and excitation; for example, Hsu [53] noted NO mixed into their flow for PLIF measurements was electronically excited by their RF glow discharge. The emission is passed into a spectrograph which contains gratings that diffract the light into its constituent wavelengths. An entrance slit controls the amount of light passed into the instrument and controls resolution by ensuring a portion of the source is perfectly aligned with the instrument's internal optics. Mirrors focus and redirect the light, increasing the optical path to allow for more divergence and thereby better resolution. The light is eventually directed onto a charge-coupled device (CCD), where, because of the physical width of the detector and divergent nature of the beam, after careful calibration with a known source each pixel can be correlated different wavelength. Through this technique discrete lines in the spectra from specific ro-translation, vibrational, and electronic transitions can be isolated. A detector's resolution is inversely proportional to pixel width, and its total width sets the device's bandwidth. Fine resolution is required to resolve certain features like ro-translational transitions as they are very closely spaced. It has been shown that the dominant spectroscopic peak in an air plasma was the second positive $N_2\left(C^3\Pi_u \rightarrow B^3\Pi_g\right)$ which manifests predominantly between $300-400$nm [53, 289]. In certain setups [290, 289] it was possible to see some electronic excitation of the first positive system of the nitrogen ions $N_2^+\left(B^2\Sigma \rightarrow X^2\Sigma\right)$ above ~ 390nm, and while this was unexpected for the low power glow discharge utilized here, it was worth avoiding quantitative analysis within this region. Indeed, one of the objectives of the broadband spectroscopic measurements was the determination of other excited species the N_2 ions or NO. Note that because of the fine spacing between vibrational levels in a given electronic state, the OES employed here was unable to directly measure vibrational temperature of the molecules in the ground electronic state. ([7])

In order to infer temperature from a spectra, a fitting code is required. N2SPECFIT [291, 122] is one such program specifically written for N_2 plasmas by Dr. Charles DeJoseph and graciously provided to the NAL; further explanation of the code is provided in [292], and it was previously used at the NAL by Hsu [53]. In general, it works by comparing an experimental spectra to a theoretical result calculated using tabulated constants. By running successive iterations at different temperatures and reducing the difference between the observed and synthetic spectra, the program can converge on a specific temperature. Several peaks must be fit as the ratio of their signal provides the temperature. Although N2SPECFIT must fit both vibrational and rotational peaks, it does not report vibrational temperatures; for such information, Specair [293, 294] is recommended. Pursuing vibrational temperatures was unnecessary here because they would only represent those of the elevated electronic state, not the desired ground state temperature. An important input parameter for any fitting code is the spectrograph's resolution as it allows the program to not only simulate the plasma physics, but the effect of the actual instrument itself. Even an idealized, Dirac delta-like signal will be broadened as it passes through a spectrograph's slits, mirrors, and gratings;

accurately measuring how this perfect signal distorts and passing it as an input allows the program to add in a proportional amount of experimental realism to its theoretical results via the so-called slit function. While it is calculable, here the resolution was measured as the full width at half maximum (FWHM) of a discrete peak. In order to measure this peak, four hollow cathode lamps (HCL) from Westinghouse Electric Corp. and Photron Pty. Ltd. were used; they are summarized in Table 6.3. All of the lamps were powered Photron Pty. Ltd. HCL power supply (P209). Each of these lamps produced at least one strong line in slightly different locations of the expected range of interest, so no matter where the spectrometer looked, a peak would be present. Assuming this peak was an ideal emitter and providing sufficient time to warm up ($5-10$min), the lamps allowed one to record a custom, experimental resolution measurement. It was important to change nothing about the spectrograph or CCD once the slit function was recorded unless another measurement was taken with the new settings. Using the HCLs was easier and safer, for both the detector and operator, than performing this measurement with a laser. ([7])

Element	**Manufacturer**	**Part No.**	**Dominant Wavelength (nm)**	**Current (mA)**	**Inert Gas**
Hg	Westinghouse	N/A	228.47	15	Ar
Rh	Photron	P844	343.5	6	Ne
Ti	Photron	P861	364.3	18	Ne
Cu	Photron	P814	324.8	4	Ne

Table 6.3: Summary of HCLs.

Additionally, the HCL's other strong lines were used to calibrate the detector by using tabulated data such as the National Institute of Standards and Technology Handbook of Basic Spectroscopic Data[3]; one needed to be careful to correctly attribute the lines from either the metal or the inert gas contained within each HCL. While this technique allowed a calibration, from pixel to wavelength, to be performed before a run and wavelength data to be directly exported, in practice it could be difficult to find exactly what lines appeared as compared to those listed on standard tables; furthermore, for the most resolved data sets the bandwidth did not always include multiple lines across the entire detector. Because N_2 plasmas are so well characterized it was in these cases better to use the plasma's known vibrational peaks calibrate the spectra. Gilmore et al. [295] provided the requisite wavelengths for each transition; this is one of the sources used for the constants in N2SPECFIT's libraries and was therefore deemed reliable. In applications such as the present project where the plasma was turned off faster than one could feasibly perform a calibration, one had to perform the calibration during post processing and apply it to the existing data. Note that it was important to read the CCD's manual in order to make sure the proper polynomial fit was used; the one used

[3]https://www.nist.gov/pml/handbook-basic-atomic-spectroscopic-data

here will be discussed shortly. As in [53], no intensity calibration was completed, though Stanfield et al. [122] took this step. Broadband spectroscopy probed three main questions. First, was the injected NO being electronically excited by the plasma, and would there be any other excited species like N_2^+? Next, would the trips affect the plasma's intensity? Finally, would there be any difference in the spectra between the negative glow and positive column regions? For example, Rajzer [97] stated that because of the high energy of the electrons emitted by the cathode, higher energy transitions should be visible in the negative glow than in the positive column, explaining the visible color difference between the two. It is sufficient to answer these questions qualitatively using spectroscopy, and the enhanced bandwidth of an OceanOptics USB2000+ spectrometer was desired. This spectrometer (CCD integrated into the spectrograph; serial no. USB2K10117) is sketched in Figure 6.8. The characteristics of the build used for the present experiments are included here. The usable bandwidth was approximately $175-875$nm and the theoretical resolution estimated by the manufacturer was 1.42nm. A fiber optic cable could be directly coupled via an SMA 905 connector, and the installed entrance slit was 25μm. It used OceanOptics' "Grating 01", which had: 600grooves/mm; a spectral range of 650nm; a blaze wavelength of 300nm; offered $>30\%$ efficiency between $200-575$nm. There were no internal filters or lenses, but the detector had OceanOptics' "Mfg B" coating, an "Array Wavelength" of 4, a capacity (WC) of 62500e$^-$, and 2048 pixels. When controlled by Ocean Optics SpectraSuite software, the spectrometer had a integration time range of 1ms-65s and a maximum acquisition rate of 30Hz under normal settings with the option to sample at $50-500$Hz using the program's high-speed mode. ([7])

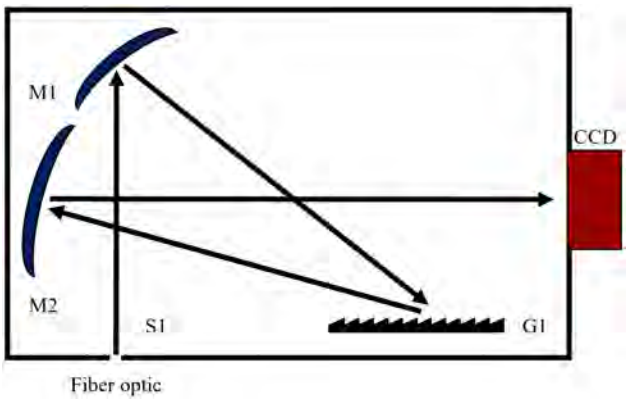

Figure 6.8: Diagram of the OceanOptics USB2000+ Spectrometer (S-Slit, M-Mirror, G-Grating). [7].

The OceanOptics spectrometer was calibrated using the $Hg-Ar$ HCL; this same calibration was used for all subsequent data taken with the instrument. Once it was calibrated, the spectrometer was used to record the spectra from the remainder of the HCLs, yielding a database of reliable lines. Note that for each HCL, spectra were taken such that the strong gas lines and then weaker metal lines each took up the full range of the spectrometer; this was accomplished by adjusting

the integration time. While the gas lines saturated during the latter set of measurements, this provided the clearest picture of the metal lines, which overlapped better with the plasma's spectra. For all HCL measurements, a single frame of background-subtracted data was recorded for both conditions for each HCL. With the spectrometer calibrated, the focus was shifted to recording spectra in the ACE tunnel. A series dummy runs were performed to optimize the placement of the fiber optic, as well as ensure the proper integration time to maximize the amplitude of the data and thereby improve the signal-to-noise ratio. Ultimately 15ms collections were taken for 15s of plasma-on run time, providing ample data to average out any imperfections; attempting to take more data caused problems with file corruption and was largely unnecessary. Background data was taken under the settings for each run to be subtracted from the full data; it was chosen to do this step manually, though SpectraSuite could do it automatically, to remain consistent between this spectrometer and the Andor EMCCD. All negative glow and positive column data were taken consecutively, so there was no variation in the signal due to minor adjustments from re-positioning the collimator; such physical considerations will be discussed shortly. When NO was introduced to study its behavior in the plasma, a 10% $NO-N_2$ mix was injected at 1378.95kPa. The moderate concentration (between that needed for PLIF thermometry and velocimetry) was selected for safety and conservation, and the higher pressure helped ensure better signal throughout the duration of the run. An image of the experimental setup for the broadband measurements is shown in Figure 6.9. ([7])

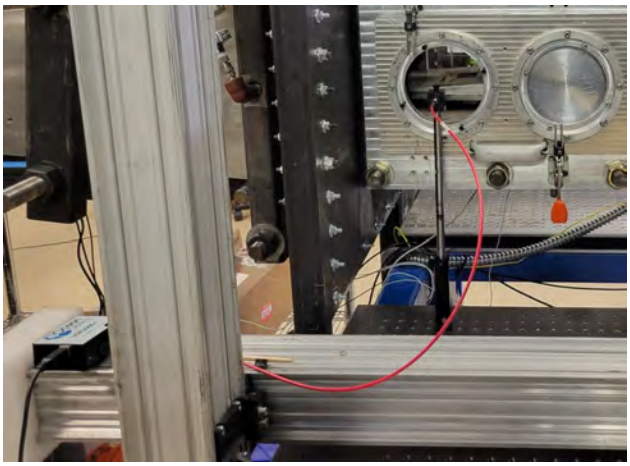

Figure 6.9: Picture of broadband OES setup. Note that for clarity in this picture the blackout sheet covering the window and fiber optic to block stray light was removed. [7].

In order to determine the rotational temperature of the bulk plasma, better resolution was required. To meet this objective, a Spex Industries 1877E Triple-Monochromator (serial no. 6768) was employed; this instruments is sketched in Figure 6.10. This device was donated to the NAL and brought into service with custom modifications by Dr. Andrea Hsu for the temperature measurements in [53]. The repairs mostly consisted of new stepper motors to control the wavelength

selector mirrors. This spectrograph used a series of three gratings, three slits, and a 0.6m optical path to achieve excellent resolution. In the first "bandpass" stage, two gratings were mounted on adjustable mounts controlled by two Anaheim Automation DPE25601 stepper motors, themselves controlled with the company's SMC60WIN program. Within this stage, empirically the first slit was found to reduce the intensity of the incoming light and the second reduced the bandwidth of the spectra; for the current application, best results were obtained when both were left entirely open. The second stage was a more standard layout. The inlet was controlled by a final slit which tuned the final resolution; here it was set to 40μm. There were three separate gratings on a carousel available for use: 600; 1200; and 1800lines/mm. Due to the instrument's age and background, little information was available regarding its gratings, bandwidth, theoretical resolution, *etc.* ([7])

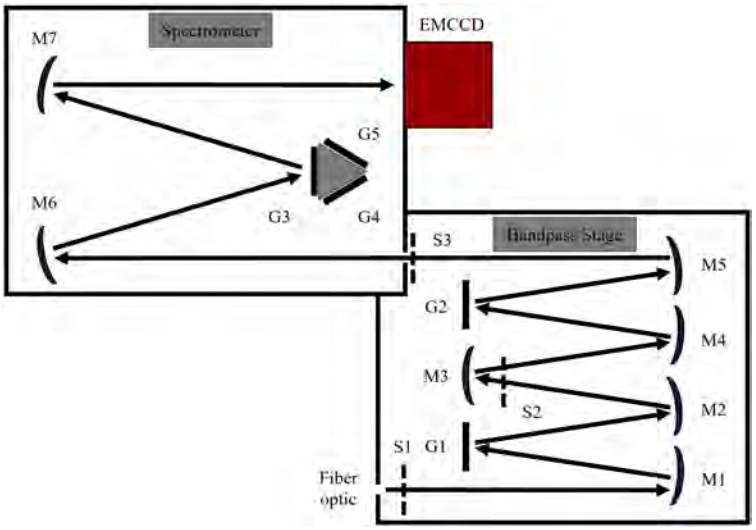

Figure 6.10: Diagram of the Spex 1877E Triple-Monochrometer (S-Slit, M-Mirror, G-Grating). [7].

An Andor Newton DU970N-BV EMCCD (serial no. CCD-8652) was coupled with the Spex spectrograph. This camera was back illuminated, water cooled, and electron multiplying to provide sufficient sensitivity for even single-photon events. The detector had 1600×200 square 16μm pixels for a total $25.6 \times 3.2\text{mm}^2$ image area. In electron-multiplying mode, it had an output node WC of $1.3 \times 10^6 \text{e}^-$ and a readout noise (RN) of $< 1\text{e}^-$ for a total dynamic range of $WC/RN > 1.3 \times 10^6$; in the conventional mode, these numbers were $3 \times 10^5 \text{e}^-$, 2.8e^-, and 1.07×10^5 respectively. The detector's spectral range at 298.15K was $200 - 1050$nm though it had a precipitous drop in quantum efficiency between $300 - 400$nm; regardless, in a similar glow discharge application with water cooling to the optimal 183.15K, Hsu [53] was able to get usable results for thermographic analyses. The EMCCD was controlled with Andor's Solis program. Resolved measurements were conducted in an analogous fashion to the broadband collections. Alignment at the tunnel matched the broadband measurements due to markings on the table and a shaft collar on the optical post,

and alignment at the spectrograph was set by adjusting the positioning of the fiber optic until the recorded signal from an HCL was maximized. Due to the complexity of this setup, the majority of the optimization was conducted in the quiescent air vacuum chamber as it allowed unlimited plasma-on time. Again, it was found that leaving the first and second slits fully open yielded the best results while the final slit reached a balance of resolution and signal at 40μm. Efforts to improve the resolution by closing the slit and compensating for the lower signal with increased intensification and/or integration times were ineffective. Setting the spectrograph to probe in the 380nm region with a 1800line/mm grating produced the clearest rotational lines. It is known that the transitions in this region are relatively weak [289], but the dropoff in intensity due to the fiber optic, Newton EMCCD, and potentially gratings below this value were significant and observable, and to go any higher would risk convolution with the first negative system. The Newton EMCCD was water cooled to -183.15K. Solis, the control software for the Newton EMCCD, suffered from several bugs of which Andor was made aware. Ideally, an "Accumulation" of background subtracted "Reference Data" frames would be collected, but this caused the program to crash. As a workaround, a "Kinetic" series of frames were taken; by selecting only one frame per series, and then repeating twenty times per acquisition, twenty separate frames could be taken and then summed in post-processing, mirroring the "Accumulation" mode. Background-subtracted data could not be collected due to another bug, so plasma-off data were recorded separately and then removed from the full spectra in post-processing. By taking twenty collections per run, not only was there enough data to reduce the noise via averaging, but the error for each pixel, represented by standard deviation, could be passed as an input into N2SPECFIT. To further improve signal-to-noise and to reduce the 2D image into a 1D trace as one would get from a linear pixel array, in Solis each frame was vertically binned, averaging all 200 pixels in the vertical direction. Solis' cosmic ray removal feature was also used to reduce noise. In both the vacuum chamber and in the ACE tunnel, a one second integration time with $4\times$ preamplifier gain and $100\times$ electron multiplication fully filled the range of the detector. Again, the integration time and intensification factors could have been fine-tuned, but these settings produced excellent results, yielded enough frames for averaging and statistical analyses, and with such a short duration of plasma-on time in the tunnel the amount of optimization that could feasible be performed was limited. With these settings, the bandwidth of the high-resolution setup was empirically known to be ~ 24nm. Even combining multiple spectra, the HCLs had insufficient strong lines across the range to provide a reasonable calibration. Thus the tunnel was first run and the data was recorded uncalibrated. In this region the second positive N_2 transition had vibrational bands at $(v',v'') = (0,2)$, $(1,3)$, and $(2,4)$ spanning ~ 10nm. With the inclusion of a strong Hg line, the total spread was ~ 15nm, so enough of the detector was covered to perform a calibration. It was found Solis' "Parabolic" calibration, recommended for when the control points are located near the center of the detector, outperformed the "Linear" and "Cubic" fits and thus was exclusively used. Once the calibrated pixel $\rightarrow$ nm data was saved, it could be applied to every dataset for each run: the plasma; the background; and the HCL. The added benefit of this approach is the strong Hg line could double as an isolated, slender peak for measurement of the spectrograph's resolution, a required input for N2SPECFIT. The Newton EMCCD was re-calibrated for every run, as it was found to drift slightly and more than the OceanOptics spectrometer. ([7])

There were several additional details worth discussing here. Perhaps the most important was the materials used for the transmission and measurement of UV light. As was mentioned previously, the Newton EMCCD begins to lose sensitivity below 400nm. While this was remedied by taking data at as high of a wavelength as possible and using a small bandwidth, the issue of optical losses persists in other equipment. For the tunnel window, the same UV transmissible fused silica window used for the *NO* PLIF was used for OES measurements. The light was collected by an Newport 77644 collimator which used an 11mm fused silica planoconvex lens to collimate the light; this ensured optimal transmission of light onto the fiber optic. Two separate Newport fiber optics were used, 78277 and 78303. The former "UV-VIS" cable was 1m long, had a 1mm diameter core, and was rated to transmit $280-1150$nm; because of its superior performance in the deep UV region, this cable was used for the broadband measurements with the OceanOptics spectrometer. The other "VIS-NIR" cable was 2m long, had a 1mm diameter core, and was rated to transmit $400-2200$nm; this longer cable was necessary to couple the larger Spex spectrograph to the wind tunnel, but its dropoff below 400nm was concerning. However, in reviewing the data listed by Newport, both cables performed identically $\gtrsim 350$nm, and the desired transition would be near 400nm due to the Newton EMCCD's limitations, so the cable's losses were deemed acceptable. All of this underscores the materials challenge of collecting UV spectra. Background light was removed at the tunnel side of the fiber optic by using blank plugs in every window port except the one used for data collection and then wrapping the assembly, from the test section around the collimator, in an opaque, black, and anti-reflective plastic sheet. For collecting HCL data, a custom housing was built to entirely encapsulate the HCL and place a collimator directly above the cathode, ensuring optimal alignment and reducing all stray light. For the OceanOptics spectrometer, the fiber optic's SMA connector mounted directly to the instrument's inlet, so no stray light was possible. For the Spex spectrograph, the cable's SMA was mounted into a Newport 77670 ferrule adapter, itself installed in another adapter and then positioned using a Newport 77612 mount such that the output from the fiber optic was as close to the slit as possible. The large openings into the spectrograph were covered with either aluminum tape or the same plastic sheeting. Alignment at the tunnel interface was set visually. The collimator was positioned so the center of the lens was just above the plate's surface, where the plasma was known to be brightest; this put a portion of the lens below the test surface. The height was fixed using a shaft collar on the optical post supporting the mount, and the apparatus was itself screwed into the laser table beneath the ACE tunnel. The streamwise position and planarity were visually set, but the data collected had strong signal so the placement was accepted. While it was positioned as close to the window as possible, the collimator did not touch the test section to prevent any vibrations from being transferred to the optic. For consistency, for each spectrometer all measurements at each streamwise location were taken consecutively and when moving between spectrometers the exact placement of the mount on the breadboard tabletop was clearly marked so it could be returned to that position as accurately as possible. The inlet into the Spex spectrograph showed remarkable sensitivity to alignment, so to optimize it the stable output from an HCL was passed into the spectrograph as both the fiber optic was moved vertically and rotated about the vertical axis until the signal was maximized; once set, the position did not change throughout the entire campaign. Again, the alignment at the HCL and into the OceanOptics spectrometer were automatically set. Finally, it is noted that the diam-

eter of the collimator, 11mm, was larger than both the width of the electrodes and interelectrode gap, 6.35mm; it was also taller than the plasma. Unfortunately, this removed the ability to take spatially-resolved species and temperature measurements as was done by Stanfield et al. [122]. It was decided that aligning a custom focusing lens during a comparatively brief ACE tunnel run would be infeasible and the improved data would be beyond the needs of the present work; the same sentiment precluded the use of a 2D spectroscopy setup. Indeed, de-resolved bulk temperatures would be sufficient, despite the expected thermal gradients in the plasma and the boundary layer because the goal was to provide an order of magnitude estimate of the plasma temperature. This in turn would allow the determination of the significance of any thermal perturbation and the likelihood of any species generation and excitation.([7])

6.2.8 Planar Laser Induced Fluorescence

This section follows from Broslawski [7]. The theory and general approach for the varying PLIF techniques described here are provided in the Background Chapter. To review, flow visualization uses a single sheet of fluorescing NO to provide a spatially and temporally resolved snapshot of the flow and is useful for studying the state of the boundary layer as well as identifying any large flow features. Thermometry uses the ratio of signal between two sheets exciting specific transitions to return a map of both the mean and fluctuating the ro-translational temperatures; vibrational temeratures can also be measured by changing the transitions probed. It is noted that flow visualization is a natural consequence of PLIF thermometry. Molecular tagging velocimetry writes a line or grid of NO into an excited state, captures its fluorescence, then uses a plane to repeat the process for only those molecules "tagged" by the first beam; the displacement between the structures and the known time delay provides one (line) or two (grid) components of the mean and fluctuating velocity. Note the 2D approach would also provide the Reynolds stress. ([7])

To summarize, laser diagnostics allow temporally and spatially resolved measurements of off-body flow parameters without any interference from a physical probe body. This makes them ideally suited for high speed, turbulent flows, and their data can validate theory and other experimental results. The laser diagnostic measurements were the purview of Zachary Buen's doctoral research and as such specifics on the hardware, calibration, experimental setup, and data analysis are best explained in their dissertation [2]. All data reduction was done by Buen with custom LabVIEW VIs. Only a comparatively brief overview is included here. Note that all "Trough" measurements were conducted in the first trough off centerline, -3.42mm, as opposed to the second trough off-centerline at -10.26mm due to the complexity of moving the beams a full centimeter. When aligning the beams, the measured location was ~ -4.95mm, but it was confirmed the beams fell precisely between the first and second trips at every streamwise test location; the source of the measurement discrepancy is unknown, but was likely due to the poor access to the test section during PLIF campaigns. Two injection seeded Spectra Physics PRO-290-10 Nd:YAG pump lasers provided 532 and 355nm beams, corresponding to the second and third harmonics, respectively. The injection seeder provided a linewidth of 0.003cm^{-1} and the flashlamps could provide a maximum repetition rate of 10Hz. In order to get the proper wavelengths for the desired NO transitions (~ 226.5 and ~ 223.8nm) the beams were each sent into a Sirah Cobra Stretch dye laser. The YAG's second harmonic passed through a methanol-Rhodamine 610/640 dye solution

and tunable grading optics to produce a beam in the range of $600-630$nm; this was then combined with the YAG's third harmonic in the Sirah's with a sum frequency mixing unit to provide the final desired output. Note that the methanol-Rhodamine 610/640 dye provided better performance for wavelengths necessary to probe excited vibrational states for applications like velocimetry, while a Rhodamine 640 in ethanol dye had better performance when probing ground vibrational states like those for thermometry. The linewidth was 0.08cm^{-1} and the energy delivered to the tunnel was estimated to be $\sim 8\text{mJ/pulse}$. The lasers were controlled by interfacing the manufacturer's software with a custom LabVIEW VI. The lasers were calibrated by scanning across a bandwidth with the beam in a small cell containing *NO*. As the laser passed through a transition, the fluorescence was recorded with a photo-multiplier tube. The signal was normalized against the beam power, captured by a photo diode with the portion of the beam reflected off a fused silica optic. The fluorescence *versus* wavelength was compared to theoretical spectra generated with SRI International's LIFBase. In order to calibrate an excited vibrational state, NO_2 was generated by mixing chilled *NO* and air, photodissociated with a YAG's third harmonic into a mixture containing excited *NO* [53, 211], and then probed with the beam being calibrated. Relevant theoretical spectra are shown in Figure 6.11; note the sub-Angstrom precision, and that no $v' = 1 \leftarrow v'' = 1$ transitions were predicted for a "Cold" (60K) flow. ([7])

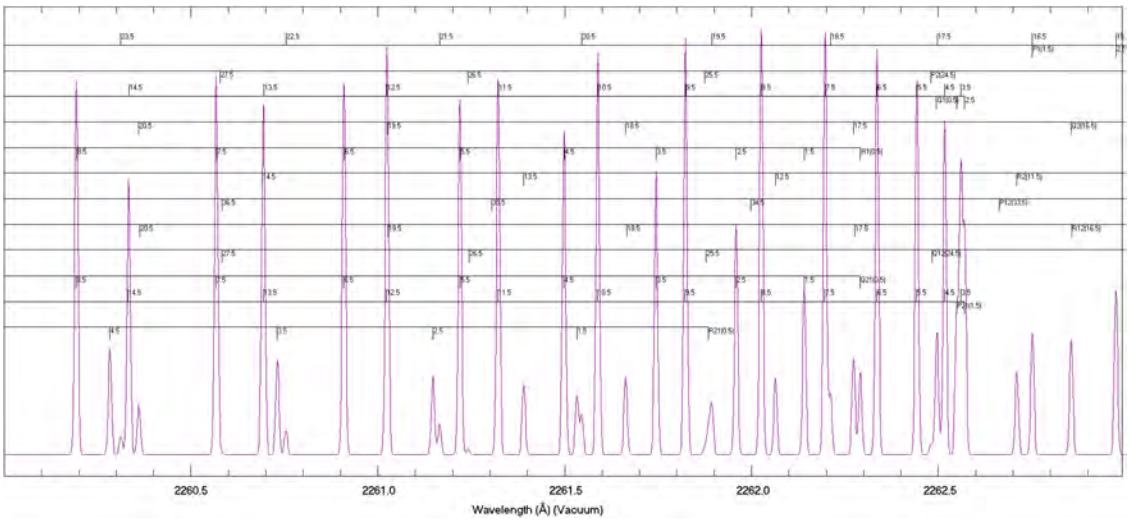

(a) "Hot" $v' = 0 \leftarrow v'' = 0$ spectra (thermal equilibrium at 350K)

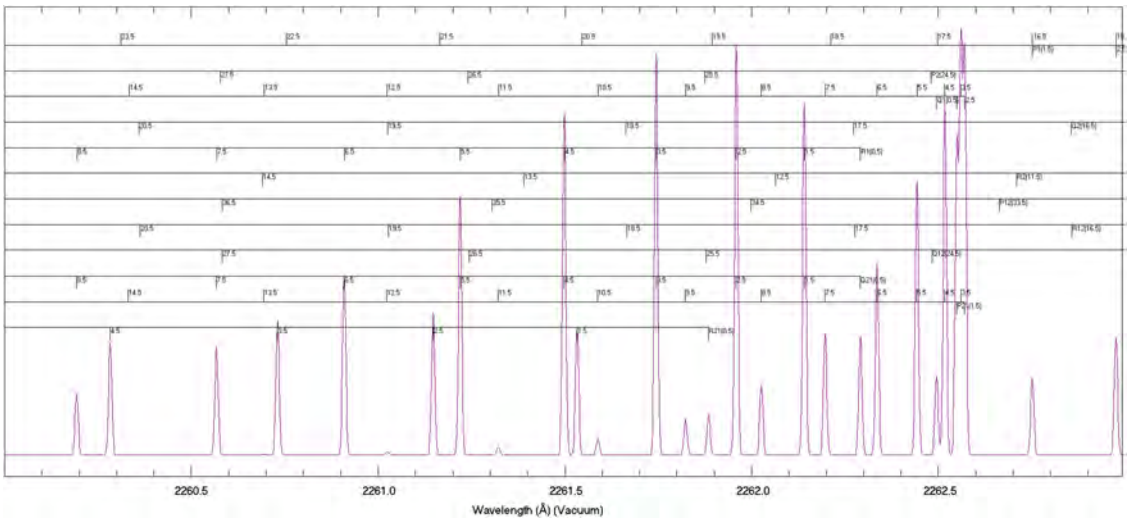

(b) "Cold" $v' = 0 \leftarrow v'' = 0$ spectra (thermal equilibrium at 60K)

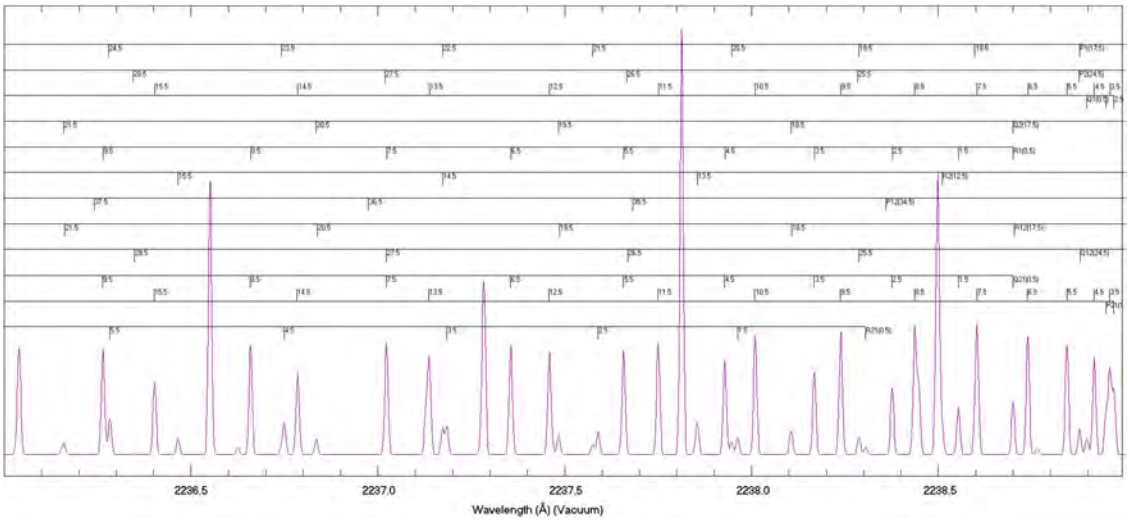

(c) "Hot" $v' = 1 \leftarrow v'' = 1$ spectra (thermal equilibrium at 350K)

Figure 6.11: Simulated *NO* spectra for two vibrational transitions using LIFBase. Rotational transitions are labeled. [7].

The beams were directed into the tunnel using 225nm dichroic mirrors, and they were shaped (focused into lines, planes, grids, etc.) using fused silica optics for high UV transmission. The tunnel's test section windows, both for passing the beam and observing the fluorescence, were fused silica as well. The beams were directed out of the test section through windows whenever feasible, but often the geometry of the problem made this impossible, and they reflected around the test section beneath the test surface. Fluorescence was detected with up to two Princeton Instrument PI-Max4 1024i ICCD cameras. The cameras could be intensified up to $100\times$, had lens extenders to improve their resolution, and were liquid-cooled to $-20\text{deg}\,\text{C}$ to reduce noise. The cameras' $1024 \times 1024\text{pixel}^2$ active area was 2×2 binned to improve their repetition rate to 10Hz. This trade-off, of resolution for faster cycles, was necessary as the ACE tunnel only provides $\sim 30-50$s of run time, whereas the pulse systems used by Sanchez-Gonzalez [211] and McManamen et al. [3] could run indefinitely. The spatial resolution was determined before a run by taking an image of a "grid card", a translucent piece of glass with a uniform grid, here $1 \times 1\text{mm}^2$, printed on it. The cameras were controlled either with Princeton Instrument's LightField program, or by interfacing with LightField through a custom LabVIEW VI. All camera and laser timing was set with a BNC Model 575 Pulse/Delay generator. Data acquisition was automatically triggered by the same pressure drop which starts the NALDAQ, syncing the two programs to within a tenth of a second, a tolerable amount for this constant Reynolds number study. In addition to the fluorescence, the NO tank pressure throughout the run was recorded, as well as the relative laser power. The latter was collected with a photodiode measuring the fluorescence of a 50mg Rhodamine 610/20mL dye when exposed to a portion of the output beam, split using a $92\%-8\%$ transmission-reflection fused silica window. This was useful in isolating the effect of laser power fluctuations. It is important to note the size of the laser beams and sheets as these dimensions limited the resolution of the laser diagnostics. The sizes were set to optimize power and signal and were often constrained by optical access and interference; for example, single beams were nominally "waisted" (focused to a minimum size) just above the camera's frame and then allowed to expand towards the surface of the test article to limit reflection, scatter, and damage to the windows. Each of the diagnostics will be introduced in the proceeding subsections, but for ease of comparison the sizes are discussed here. For rotational thermometry measurements, the 2D sheets were $\sim$ 2cm wide and $\sim 800\mu$m thick; for vibrational thermometry measurements, the dimensions were $\sim$ 1.5cm and $\sim 800\mu$m respectively. The wide sheets maximized the amount of data provided by each test. For the velocimetry measurements, the "Write" beams varied in diameter from $\sim 0.5-1.25$mm and the "Read" sheets were $\sim$ 1cm wide and $\sim 800\mu$m thick; the reduced width of the "Read" sheet relative to the thermometry measurements improved signal as the laser power was more concentrated. The spanwise thermometry "Write" beams were a thicker $\sim 0.85-1.5$mm due to the divergence of the beam along the larger test domain, but the "Read" sheets were the same size as they were for the wall normal campaign. It will be seen shortly that given the resolution of the cameras, the most experimental blurring in the thermometry measurements would be due to the thickness of the sheets. Still, the resolution in this spanwise dimension was excellent, and this coordinate was unimportant relative to the wall normal and streamwise directions. In both velocimetry campaigns, the streamwise measurement was the most directly affected by the beams' thicknesses. While this was of little consequence to the mean

velocity measurements, it could impact the fluctuation measurements by effectively averaging all perturbations within the beam. This was addressed as best as possible by allowing a large degree of displacement between velocimetry "Write" and "Read" measurements so fluctuations could better manifest, using high resolution cameras, and careful estimation of the beams' centerlines during image analysis. ([7])

6.2.9 Thermometry

This section follows from Broslawski [7]. The nominal conditions for ro-translational and vibrational thermometry are summarized in Tables 6.4 and 6.5 respectively. The "Cold" and "Hot" labels owe to the fact the lower J and v states are more populated at lower temperatures. For rotational thermometry, isolated J states were selected to provide high signal in the freestream and low signal near the wall ("Cold"), and *vice versa* for the "Hot" measurement. To visualize the effect, refer to the data in Figure 6.11(a) and (b) simulated at 350 and 60K, roughly showing the behavior near the test article's wall and freestream respectively. This effect was lessened in vibrational thermometry due to the high spacing between vibrational levels, and a relatively temperature invariant J state was used to prevent convolution with rotational heating as one moved towards the wall. For both thermometry campaigns, the time between the images was $\sim$ 500ns, which allowed sufficient time for thermalization any only allowed a displacement of $\sim$ 4.25pix in the freestream (assuming $850\frac{\text{m}}{\text{s}}$ flow.) ([7])

Stage	**Transition**	**Intensifier**	**Gate (ns)**	**Resolution (μm/pixel)**
Cold	$J = 1.5\,Q_{21}/R_1$ $A^2\Sigma^+(v'=0) \leftarrow X^2\Pi_{\frac{1}{2}}(v''=0)$	100×	20	$100\frac{\mu\text{m}}{\text{pix}}$
Hot	$J = 8.5\,Q_{21}/R_1$ $A^2\Sigma^+(v'=0) \leftarrow X^2\Pi_{\frac{1}{2}}(v''=0)$	100×	40	$100\frac{\mu\text{m}}{\text{pix}}$

Table 6.4: Nominal laser and camera settings for PLIF ro-translational thermometry. [7].

To collect these data, two cameras we placed at opposite sides of the test section to collect data in the same region of interest. The "Cold" and "Hot" beams were passed through a 300mm spherical plano-concave lens to tighten the beam, then a 500mm planar plano-convex lens to sheet it; because the beams were separated by a time delay, they could be passed through the same optics to conserve space. The sheets were overlapped in the wind tunnel covering the region of interest. One camera collected the fluorescence from the "Cold" beam, and the other collected the signal from the "Hot" beam. In post-processing, a grid card image was used to ensure both cameras were aligned. This setup is shown in Figure 6.12. ([7])

There were several interesting but complicating factors to take into account when performing the rotational and vibrational thermometry measurements. For rotational thermometry measurement, recall Figures 4.6(a) and (b), top-down freestream visualization experiments. These data

Stage	Transition	Intensifier	Gate (ns)	Resolution (μm/pixel)
Cold	$J = 4.5\,Q_{21}/R_1$ $A^2\Sigma^+(v'=0) \leftarrow X^2\Pi_{\frac{1}{2}}(v''=0)$	100×	3	$100\frac{\mu\text{m}}{\text{pix}}$
Hot	$J = 4.5\,Q_{21}/R_1$ $A^2\Sigma^+(v'=1) \leftarrow X^2\Pi_{\frac{1}{2}}(v''=1)$	100×	100	$100\frac{\mu\text{m}}{\text{pix}}$

Table 6.5: Nominal laser and camera settings for PLIF vibrational thermometry. [7].

showed a decrease in signal at the centerline of the NO cloud. Buen [212] hypothesized that this drop in signal was due to the formation of N_xO_y species as well as higher order clusters of the NO and these nascent species. The idea was the concentration of NO would be the highest along the centerline, and so it would be most susceptible to losses due to the formation of new species. To test this theory, Buen conducted simulations for a set of the most probable reactions and were carried out both in the settling chamber and at the variable temperature and pressure along the nozzle; they noted that the reaction rate constants were used outside of the temperature ranges for which they were found in the literature, owing to the ACE tunnel's low temperature. The injected concentrations tested were the limiting cases of 100 and 0.5%. The results suggested in the upper concentration limit N_2O_3 was the dominant nascent species, and in the lower concentration limit the concentrations of N_2O_3 and NO_2 converged. In both cases, however, there was little appreciable drop in the NO concentration, so Buen concluded the drop in signal was more probably due to the collisional quenching of the vibrationally excited NO by the nascent species, a process less covered by the literature. It was soon discovered, however, these nascent N_xO_y species would have a critical impact on the PLIF thermometry technique. When seeding in gas above $\geq 1\%$ NO, Buen [212] calculated nonphysical wall and freestream temperatures. They attributed this error to either collisional quenching of the vibrationally excited NO or the photodissociation of the N_xO_y species due to the lasers. A calculation found that collisional quenching, while likely not insignificant, would be unable to generate the unrealistic temperatures. Buen surveyed the literature to study the photodissociation of the most likely N_xO_y species, as well as NO dimers, and found it was reasonable to attribute the higher-than-expected temperatures to these species. This effect would be enhanced as one increased the NO concentration, be it due to injection or moving closer to the centerline. One of the benefits of injecting NO into the settling chamber instead of the boundary layer was that it allowed the assumption that the NO and air were fully thermalized. This meant the NO used was taken as a proxy for the bath temperature, so any uncertainty in T_{NO} had strong implications. Testing found a 0.5% NO mix injected at 1241.06kPa produced a uniform fluorescence signal and reasonable thermometric results. For vibrational thermometry, 15% NO was injected. This was necessary due to the lower signal of the vibrational readings. The photodissociation effects were more limited owing to the more invariant nature of the vibrational state (see the experiment in [90]), and the results were reasonable; still, ideally the experiments would have been conducted at lower NO concentrations. Pragmatically, having such a low gas concentration limits the types

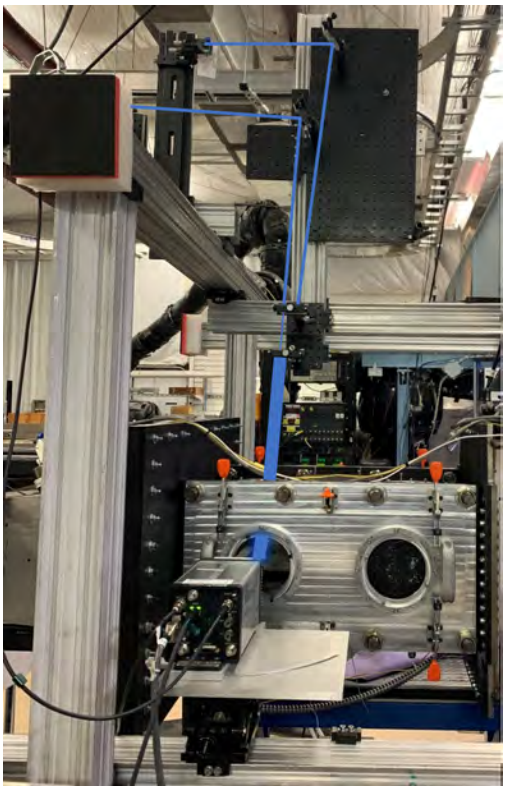

Figure 6.12: PLIF thermometry setup. Only one beam shown beyond focusing optic for clarity. [7].

of experiments one can perform because in order to obtain sufficient signal, on must open the gate for a long period of time. This is unacceptable for linear or point measurements like the VENOM measurements seen in [211] because the written structures can blur as they moved. It is noted that the pulsed facilities used by Sanchez-Gonzalez [211] and McManamen et al. [3] were run with only an NO and N_2 mix, so no N_xO_y species or NO dimers could form. Here the data collection was restricted to planar images which could provide 2D average and fluctuating temperature maps and be relatively unaffected by blurring, especially in the slow-moving boundary layer. These data were collected for the laminar and turbulent cases, with the plasma on and off, at the upstream and downstream location, and in the turbulent wakes and troughs. In order to scale PLIF thermometry data, one requires a known temperature. Ideally one could use the wall, but because the laser passed through glass, not PEEK, the wall temperature was not reliably known. Instead, for rotational thermometry measurements at the front test location included data both above and below the bow shock. It was decided that $T_{pre-shock}$, as measured by the NALDAQ from compressible flow theory, would provide the anchor temperature; this was nominally $\sim$ 58K. As will be discussed in detail later, this approach yielded reasonable wall temperatures, but provided an unexpected measurement of $T_{post-shock}$. In the back test location, the same $T_{post-shock}$ used in the front was used, with no correction for the Mach waves or trip shocks. Finding an anchor temperature for the vibrational thermometry was uniquely challenging and required a degree of temperature modeling.

The temperature in a portion of the flow must be known in order scale the remainder of the image. A natural choice would be the wall, thanks to the no-slip conditions, but an unknown degree of vibrational slip was possible, and even likely. This left the edge as the only available choice, but estimation of the vibrational temperatures here was more complex than the case for the rotational thermometry; there were no isentropic flow relations on which one could rely. ([7])

To produce an answer, Buen [212] performed a simulation of the vibrational decay of the N_2, O_2, and NO mixture from the ACE tunnel's throat all the way to its test section. The process is summarized here, but details are provided in [212]. At the throat, it was assumed the mix was at thermal equilibrium at 358K, taken from the same set of conditions as the previous species formation simulation. The rate constants were calculated from

$$k_{VT,v=1} = \frac{k_B T}{pt(T)\left(1 - e^{-\theta_v/T}\right)} \tag{6.14}$$

where θ_v was the vibrational characteristic temperature and $pt(T)$ were constants taken from [55], following Hsu [53]; it was noted these rate constants fell precipitously with the decreasing temperature along the length of the nozzle. Candler et al. [55] provided equations for $k_{VV,v=1}$ as well. The change in the relative $NO^{v=1}$ due to collisions was

$$Rate_{VT,v=1} = \sum_i \left[n_{NO,v=1} n_i k_{VT} - \exp\left(-\frac{\Delta E_v}{k_B T}\right) n_{NO,v=0} n_i k_{VT,v} \right] \tag{6.15}$$

where $n_{NO^{v=1}}$ was the total number density of the vibrationally excited NO, n_i was the total number density of the collisional partner, and ΔE was the energy difference between the $v = 1$ and 0 states of NO. These equations were also used to consider VV collisions. Finally, the Boltzmann equation (as reported in [212]) provided the vibrational temperature

$$N_{v=1} = N_{v=0} e^{-\frac{\Delta E}{k_B T}} \tag{6.16}$$

For the three species, Buen considered twelve reactions, the same shown in Table 2.2. Each of the vibrationally excited molecules $N_2^{v=1}$, $O_2^{v=1}$, and $NO^{v=1}$ could relax through collision with an other ground state molecule, for a total of nine reactions. The three VV reactions considered involved $N_2^{v=1} + O_2$, $N_2^{v=1} + NO$, and $NO^{v=1} + O_2$. The results showed the NO VT and $NO - O_2$ VV reactions dominated the relaxation process, and of these the former was the most important. The N_2 and O_2 were vibrationally frozen at the nozzle's throat temperature of 358K, but $T_{NO^{v=1}} = 230$K; this established the inherent NEQ of the ACE facility and was shown in Figure 6.13. The vibrational temperature decay ceased as the expansion rapidly reduced the bath temperature, highlighting the temperature dependence of the rate constants. It was shown in the experiments of Nishihara et al. [90] that there was little change in vibrational temperature across a normal bow shock in an analogous wind tunnel environment, so here the effect of the weaker oblique bow shock, Mach waves, trip shocks, *etc.* could be discounted and the edge condition of $T_{NO^{v=1}} = 230$K was used in the subsequent calculations. It is noted Buen [212] did attempt to provide an upper limit on the calculations by assuming vibrational equilibrium such that $T_{NO^{v=1}} = 358$K. The results using

$T_{NO^{v=1}} = 230$K were shown to follow the format in [212], but those for 358K were included in Appendix A. ([7])

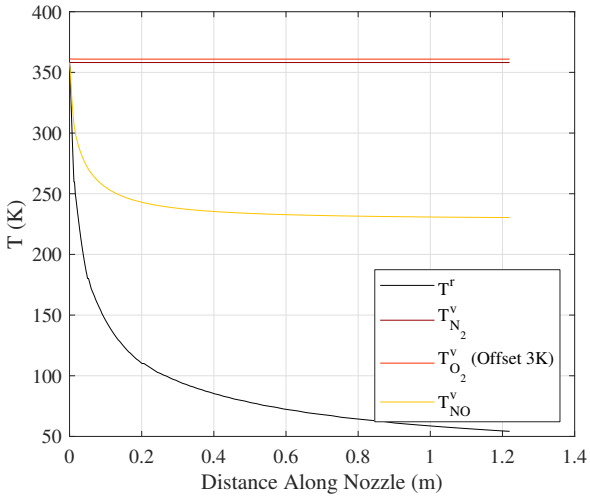

Figure 6.13: Simulated nozzle temperatures; note that $T^v_{O_2}$ was offset 3K to distinguish it from $T^v_{N_2}$. [7].

6.2.10 Velocimetry

This section follows from Broslawski [7]. Velocitmetry relies in probing the NO's rotational states within an excited vibrational state. Because of the relatively low number of NO molecules which can be "written" into this vibrational state as well as the low gas number density near the test article's hot wall, preliminary testing revealed a high gas concentration must be used to achieve usable signal. Even turning the YAG lasers to a power level which risked damaging the plate's glass was not a workable solution. In the end, a 75% NO injection at 1241.06kPa was selected; a higher concentration was not used because a noticeable pattern of diminishing returns made it not worth the safety risk and cost. Unfortunately, this meant one had to assume the nascent NO dimers and N_xO_y species did not affect the bath gas temperature and thereby the turbulence statistics excessively. Traditional PLIF MTV offered useful insight into the environment's fluid dynamics without the complexity of coupled velocity and temperature measurements (VENOM). A single-line experiment provided the streamwise velocity profile; in reality, two lines from two YAGs were used simultaneously write two parallel lines and double the data collected. This technique provided both the mean and fluctuating velocity profiles. The cameras were placed on opposite sides of the test section to probe the same region of interest, and their overlap was confirmed using a grid card image. One camera was used to collect "Write" images, and the other to collect "Read" images. A spherical plano-convex lens was used to focus the single-line "Write" beam for the 1D measurement (to save space, the same optic is used for both beams), but for the 2D measurements two micro-cylindrical lens arrays could be used to provide a focused grid of nodes. For both the 1D

and 2D measurements, the lasers would probe the same transition, so only the optical setup would change. The "Read" beam was sheeted through the same planar focusing and sheeting lenses as was done for the thermometry measurement. The experimental setup is summarized in Table 6.6 and shown in Figure 6.14; note that these measurements were the only ones collected on the P_{21}/Q_1 branch as it was determined the Q_{21}/R_1 yielded better results. In order to include chemistry effects in the calculation of the true time delay between the images, a temperature profile must be known at the measurement location; this had the added benefit of allowing longer integration times on the weak read signal. While this step was taken in the final analysis, for now it is sufficient to say $\sim 2\mu$s passed between each image. ([7])

Stage	**Transition**	**Intensifier**	**Gate (ns)**	**Resolution (μm/pixel)**
Write	$J = 8.5\, P_{21}/Q_1$ $A^2\Sigma^+(v' = 0) \leftarrow X^2\Pi_{\frac{1}{2}}(v'' = 0)$	100×	$3-15$	$50\frac{\mu\text{m}}{\text{pix}}$
Read	$J = 8.5\, P_{21}/Q_1$ $A^2\Sigma^+(v' = 1) \leftarrow X^2\Pi_{\frac{1}{2}}(v'' = 1)$	100×	150	$50\frac{\mu\text{m}}{\text{pix}}$

Table 6.6: Nominal laser and camera settings for PLIF velocimetry. [7]

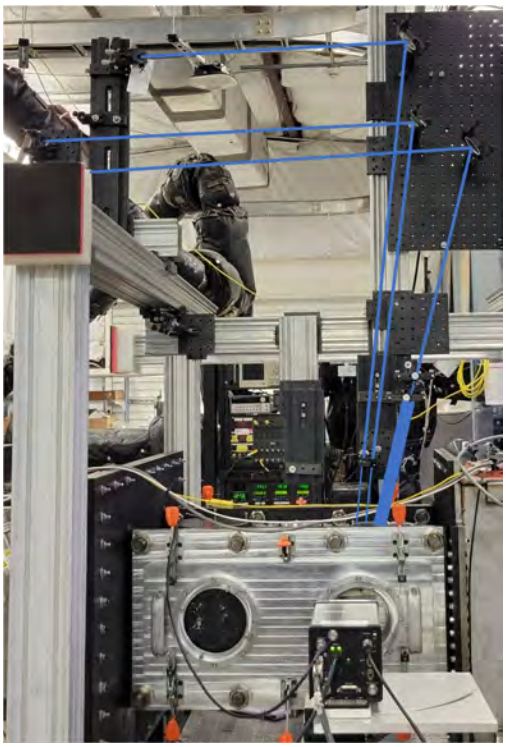

Figure 6.14: PLIF MTV setup. Two "Write" lines are used to double the usable data. [7]

6.2.11 Spanwise Velocimetry

This section follows from Broslawski [7]. As part of the broader velocimetry campaign, tests were conducted where the beam was passed horizontally across the span of the test article. These tests were carried out for both laminar and turbulent profiles at both the upstream and downstream test locations. The purpose of these tests was to look for any gradients across the test article, as well as to check the spanwise uniformity of the boundary layer. The effect of the plasma was not tested due to time constraints. For the laminar cases, the beam was positioned 2mm across the span of the test article, and for the turbulent cases, because the boundary layer was thicker, the beam was positioned 3mm above the surface. For these tests a 25% mix of NO was used as the beams were far enough from the wall so as to avoid the worst of the low density effects and to conserve the gas. A single camera was used to record both the "Write" and "Read" images through the use of the dual image feature, a special setting which allowed the camera to capture two images in rapid succession up to 2.5Hz, the frequency used here. This camera was tilted 2.75° to match the slope of the test article. A $\sim 4\mu$s delay was used between the "Write" and "Read" beams. The rotational states probed were relatively temperature invariant. The optics used generally matched those from the boundary layer MTV campaign; a single spherical plano-convex lens focused the "Write" beam, and a set of two planar optics were used to sheet and focus the beam. The "Read" beam was not pitched 2.75° as it only needed to overlap with the "Write" line, which had little streamwise component. Further experimental conditions are included in Table 6.7, and the setup

is shown in Figure 6.15; again, these measurements were taken on the Q_{21}/R_1 branch and not the P_{21}/Q_1 branch used for the wall normal measurements as it was found the former performed better. Note that additional data, spanwise flow visualization images originally taken as part of the model characterization are included in the corresponding results section for this campaign; whatever additional information regarding the simple setup for these few images that was not covered earlier is included alongside their analysis. ([7])

Stage	**Transition**	**Intensifier**	**Gate (ns)**	**Resolution (μm/pixel)**
Write	$J = 4.5\, Q_{21}/R_1$ $A^2\Sigma^+(v' = 0) \leftarrow X^2\Pi_{\frac{1}{2}}(v'' = 0)$	100×	3	$43\frac{\mu\text{m}}{\text{pix}}$
Read	$J = 4.5\, Q_{21}/R_1$ $A^2\Sigma^+(v' = 1) \leftarrow X^2\Pi_{\frac{1}{2}}(v'' = 1)$	100×	150	See above

Table 6.7: Nominal laser and camera settings for spanwise PLIF velocimetry. [7]

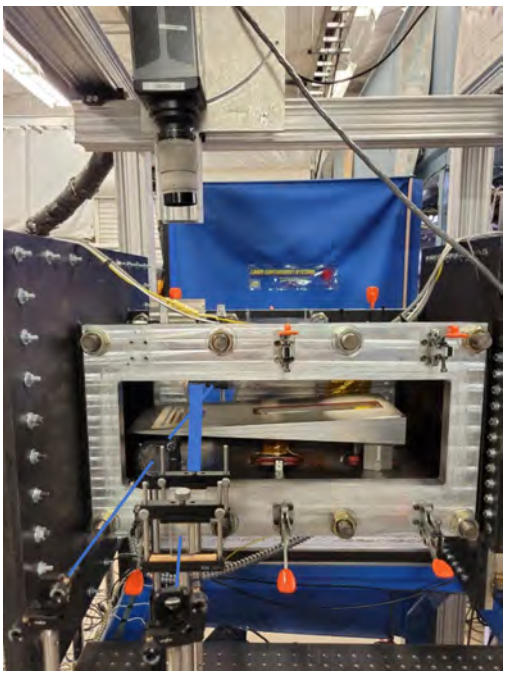

Figure 6.15: PLIF spanwise MTV setup. [7]

6.3 Mach 6 Quiet Tunnel Instrumentation

6.3.1 Test Article Surface Sensors

This section follows from Siddiqui [4]. The cone had fifty-one type-T thermocouples that were on the port side of the model along a streamwise line. There were thirty pressure ports on the starboard side also along a streamwise line. The thermocouples were used to track temperatures along the cone, since the model and tunnel were axisymmetric the temperature can be assumed to be the same all around the cone at the streamwise point where the thermocouple is reading data. The pressure ports were not used. The type-T thermocouples were guided out of the tunnel through a hole in a base plate that was machined specifically for these experiments, the plate also had the coolant inlet and outlet hoses running through it. The hole had a pipe nipple threaded through it so the wires could be taped together and then high-temperature RTV silicone used to seal the gap between the taped wires and the inside of the pipe nipple. The thermocouples were wired into two National Instruments SCXI-1303 32-channel isothermal terminal blocks. The blocks were plugged into a National Instruments SCXI-1001 chassis which held 12 modules and provided a low-noise environment for signal conditioning, supplying power, and control circuitry for the modules.

This section follows from Siddiqui [4].

6.3.2 Constant Temperature Anemometry

The anemometer was a A.A. Lab Systems AN-1003 hot-wire anemometry system. Hot-films were used to quantify the mass flux in the boundary layer. The film used was the TSI-1220-20, which is still a wire shaped sensor between two prongs. The diameter of the -20 film was 0.0508 mm (0.002 inch) and this results in the highest detectable frequency being $\sim$100 kHz. The films proved durable (not one film broke during tunnel runs), and fulfilled their purpose of collecting data that could be approximated to be mass flux in the boundary layer. The overheat ratio was set to be 0.6, this means the temperature would be 1.6 times the tunnel stagnation temperature, as this was just under the maximum temperature the film was rated for. The data were acquired at three channels:

1. The amplified output from the anemometer low-pass filtered at 200 kHz by an 8-pole Bessel filter element in a Krohn-Hite chassis.

2. The output from 1 was AC coupled, filtered (300 Hz - 300 kHz), and gained (x5) by a Stanford Research Systems SR560 low-noise preamplifier and filter.

3. The raw bridge voltage output from the anemometer.

The BNC outputs for each channel were sent to a NI USB-6366 DAQ system which had 8 channels capable of sampling at 2 MHz. The DAQ interfaces with a DAQ card installed in a computer which enabled a LabView VI to read the data and save it as a file to be processed. The data processing relied on the heat transfer relationship for a cylinder in a supersonic flow, where the dependence on Mach number is negligible [296]. For this case, and assuming $l/d \gg 1$, the Nusselt number depends on the following flow parameters:

$$Nu = f(\rho U, T_t, \tau) \tag{6.17}$$

where Nu is the Nusselt number, Re_d is the sensor diameter Reynolds number, Pr is the Prandtl number, M is the Mach number, $\tau = (T_w - \eta T_t)/T_t$ is the temperature loading factor[296], T_w is the operating temperature, T_t is the total temperature, $\eta = T_e/T_t$ is the recovery factor, and T_e is the film's equilibrium (or recovery) temperature. Smits et al. Smits et al. [297] showed that for sufficiently high τ the response is dependent solely on ρU and dependence on T_t becomes negligible. Thus, the hot-film measurements in the form of fluctuating anemometer voltages can be seen as fluctuating mass-flux measurements. Mean and dynamic mass-flux measurements can be made using hot films and the boundary layer resolved. Hot films are being used to acquire well-resolved mean flow and instability profiles. ([4])

6.3.3 Focusing Schlieren

Focusing schlieren is only sensitive in a narrow plane of interest. There are several ways that this can be achieved but the system used is a lens and grid type focusing schlieren system. The approach in Weinstein [298] was used as a guide when designing the focusing schlieren system. The initial design of the system was accomplished by Hofferth et al. [299] and further design details can be found in Craig et al. [150]. The constant light source is a Bridgelux C8000LM with an array of LEDs totaling 8000 lumens mounted to a heat sink and with a reflector to point light towards the Fresnel lens. The light source was driven by 2.2 A current at 36 V using a 80W Extech Instruments (M/N: 382260) DC power supply. A diffuser was added after the light source for the present work to homogenize the light as previously faint details of the array of LEDs could be seen all along the path. The light then travels through a Fresnel lens of diameter 317 mm and focal length 213 mm, the Fresnel lens improves the image brightness as found by Boedeker [300]. Classically source and cutoff grids were made from photographic film with one of them being the negative of the other but for this system originally the grids were made by printing on transparency film. This worked to some extent but the image quality was not ideal, attempts were made to stack multiple printed source grids on top of each other and this helped increase opacity of the grids but reduced the image quality due to the stacked grids not being perfectly aligned. The cutoff grid was too fine to stack and was left as a single layer. A new method of producing grids was used for the present work. FineLine Imaging in Colorado Springs, CO provided source and cutoff grids with a laser plotter on PET substrate. The optical density achieved using this method averaged $\sim$4.5 (0.00316% transmission) for the opaque areas and less than 0.05 (>90% transmission) for the clear areas. The resolution was 10k dpi which made for much sharper lines than the transparencies previously used. The new grids made for much sharper images and improved the quality of the diagnostic. The lens used is a three-element achromat with a diameter of 155 mm and focal length of 195 mm. The system was designed specifically for the M6QT with special consideration for the width of the test section and to keep the depth of focus inside of the nozzle shear layers. The depth of focus definition as stated in Weinstein [298] is

$$DS = 2\frac{l}{A}w \tag{6.18}$$

where l is the distance from the lens to the object plane, A is the lens aperture diameter, and w is the resolution limit of the image (calculated from image magnification and grid sizing). The length scale w can be replaced by the wavelength of the Mack-mode instability ($\sim$ 3 mm) to obtain the

depth of unsharp focus as

$$DU = 6\frac{l}{A} \tag{6.19}$$

This system was used to study Mack-mode disturbances on the 93-10 cone [299]. It was revived for the current work to be used as a flow visualisation tool at first. A Photron FASTCAM SA-Z high speed camera was placed at the image plane to visualize flow features. The camera settings were set to 1500 fps with a 160 nsec shutter. The camera was placed such that the field of view was on the aft end of the model that is not in the nozzle. Eventually the camera was replaced with a small-aperture (0.2 mm) fiber optic cable (Thor Labs M38L01) to make measurements at a point in the boundary layer and to analyze the spectral content. The fiber optic cable was connected to an avalanche photodetector (Thor Labs APD110A) with a bandwidth of 50 MHz. The signal from the photodetector was bandpass filtered from 1 kHz to 1 MHz and amplified by a factor of 50 by a Stanford Research Systems SR560 signal conditioner. The data were sampled at 2 MHz as this is the upper limit of the DAQ system. Welch's method was used to extract spectral data from the high-frequency voltage measurements. The camera and fiber optic were both placed on translation stages so the focal point could be adjusted. Note that the focal plane moves as the image plane moves, this is very helpful on a flat plate model as measurements can be taken at any point on the plate. This system was used on a wedge model in the ACE tunnel by Leidy [301] where the camera was moved during a tunnel run to study interaction between a shock wave and the boundary layer. For a cone model, as is the case for this experiment, the focal plane simply has to be placed at the center of the model/nozzle. This was achieved by placing a plastic bolt on the model as shown in Fig. 6.16 and moving the camera/fiber optic till the threads of the bolt came into sharp focus, this method is generally used to focus regular schlieren systems as well. ([4])

6.3.4 Focused Laser Differential Interferometry

Laser Differential Interferometry (LDI) was pioneered by Smeets and George [302], [303], [304], and [305] in the 1970's. Their system went through several iterations and was sensitive in changes to optical path lengths that are related to changes in density of the flow. Density profiles of laminar and turbulent boundary layers were created using this technique [305]. Laderman and Demetriades [306] used LDI to detect boundary-layer transition in supersonic flow by looking at the RMS fluctuations in the boundary layer and equating an increase in fluctuations to transition. Azzazy *et al.* [307][308] used LDI as a transition-detection tool at transonic and supersonic speeds with some success. LDI was compared to other methods of transition detection in Tunnel B at Arnold Engineering Development Center (AEDC) in a hypersonic (Mach 8) boundary layer and showed good agreement [309]. They were able to obtain spectral data and observed content that could be the Mack-mode instability, though the frequencies were lower ($\sim$150 kHz) owing to the thickness of the boundary layer. LDI is a path-integrated measurement and thus includes all fluctuations in the path of the laser including any boundary layers over tunnel windows or shear layers coming off nozzles. This results in a low signal-to-noise ratio (SNR). Building on the work done by Smeets [310], Parziale *et al.* [311] developed a focusing variant of LDI, aptly naming it Focused Laser Differential Interferometry (FLDI). FLDI does not integrate over the entire path but instead is sensitive only in the region around the focal point, which results in much higher SNR

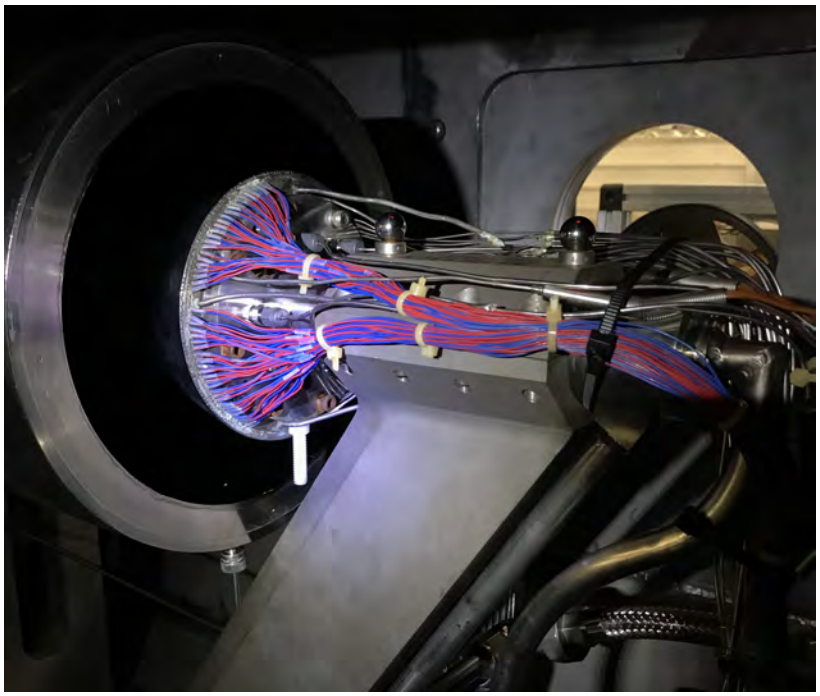

Figure 6.16: 91-6 cone with plastic bolt attached to underside to set imaging plane of focusing schlieren system in the region of interest. Siddiqui et al. [5]

than regular LDI. Parziale *et al.* used FLDI to measure freestream disturbance levels [312] and the Mack-mode instability [313]. Hameed *et al.* [314] used several Wollaston prisms to split the laser beam several times to create four beam pairs at the focus, thus simultaneously collecting data at four points in the boundary layer. Gragston *et al.* [315] used a diffractive optical element (DOE) to split the beam into 6 beams and collected data simultaneously at six points. Probing multiple points in the flow has the benefits of being able to track what is happening at multiple points and also be able to do some correlation studies by which velocities and other parameters can be quantified. Conventional FLDI would be something similar to what was first setup by Parziale *et al.* at Caltech [312]. Fig. 6.17 shows the single beam-pair setup. A continuous-wave laser is sent into a diverging lens to expand the beam. As the beam expands it passes through a polarizer and then a Wollaston prism that splits the beam in two orthogonally polarized beams with a certain separation angle (1-5 arcminute) between them. The beam pair is then focused by a converging lens to two points separated by a distance, this is called the beam-pair spacing. The beams then expand till they get to another focusing lens which is identical to the first one and get focused. The beam pair goes through a Wollaston prism that recombines the beam pair into one beam and then a polarizer that aligns the axes of polarization thus creating an interference fringe pattern. Like any other interferometer, the difference between the optical paths is what affects the fringe pattern. FLDI adds the focusing component by which the two beams share the same optical path except in the region where the beams focus to a point, thus making the system sensitive only in that region. This is very useful for measuring instabilities in a wind tunnel where there can be boundary layers

on the tunnel walls or shear layers coming off the nozzle in a free-jet test section, like in the M6QT. ([4])

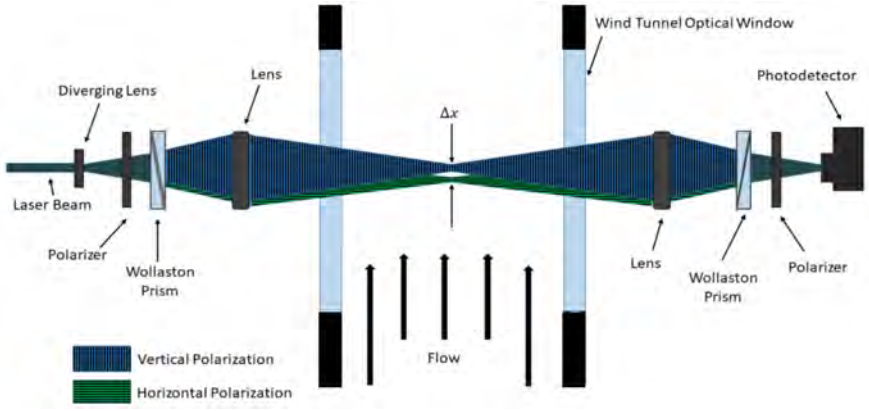

Figure 6.17: A basic single beam-pair FLDI setup (Reprinted with permission from [316]).

The index of refraction and density of a gas are related by the Gladstone-Dale relationship [317],

$$n - 1 = K\rho \tag{6.20}$$

where n is the index of refraction, K is a constant, and ρ is density. The optical path length difference (ΔOPL) between the two beams can be calculated,

$$\Delta OPL = \int_{s_1} n_1 \, ds \; - \int_{s_2} n_2 \, ds \tag{6.21}$$

where n_1, n_2 are indices of refraction and s_1, s_2 are the optical paths. The phase difference can then be defined and the Gladstone-Dale relation used to link the phase difference to the densities,

$$\Delta\phi = \frac{2\pi}{\lambda}(\Delta OPL) \tag{6.22}$$

$$\Delta\phi = \frac{2\pi}{\lambda}\left(\int_{s_1} n_1 \, ds \; - \int_{s_2} n_2 \, ds \;\right) \tag{6.23}$$

$$\Delta\phi = \frac{2\pi K}{\lambda}\left(\int_{s_1} \rho_1 \, ds \; - \int_{s_2} \rho_2 \, ds \;\right) \tag{6.24}$$

The last polarizer interferes the two beams along its transmission axis. The electric fields of the two beams can be defined,

$$E_1 = A_1 exp(j(kz - \omega t + \phi_1)) \tag{6.25}$$

$$E_2 = A_2 exp(j(kz - \omega t + \phi_2)) \tag{6.26}$$

where A is amplitude, k is wavenumber, ω is frequency, and ϕ is phase. The electric fields can be superimposed ($E = E_1 + E_2$) to find the irradiance at the photodetector (I_d) due to change in phase,

$$I_d = \langle EE^* \rangle = \langle (E_1 + E_2)(E_1 + E_2)^* \rangle \tag{6.27}$$

$$I_d = A_1^2 + A_2^2 + 2A_1A_2 cos(\phi_2 - \phi_1) \tag{6.28}$$

$$I_d = I_1 + I_2 + 2\sqrt{I_1 I_2} cos(\Delta\phi) \tag{6.29}$$

The voltage output from the photodetector is proportional to the irradiance received by the sensor, $V = \eta I_d$, where η is a constant having to do with response time and resistive load. Thus Equation 6.29 can be written in terms of output voltage. The interferometer is set to the most linear part of the fringe to avoid phase ambiguity as shown in Fig. 6.18 which adds a phase shift of $\pi/2$. When setting up FLDI this can be set by translating the recombination Wollaston prism perpendicular to the optical axis. The beams can be assumed to be evenly split ($I_1 = I_2 = I$), this gives a max intensity of $4I$ and intensity at reference point of $2I$. Thus the voltage can be written,

$$V - V_{ref} = V_{ref} cos(\Delta\phi) \tag{6.30}$$

where V_{ref} is the voltage at the reference point. The phase difference is adjusted to include the $\pi/2$ starting point and gives,

$$V = V_{ref}[1 - sin(\Delta\phi)] \tag{6.31}$$

The phase difference in Eq. 6.24 and Eq. 6.31 can then be equated to give,

$$sin^{-1}(1 - \frac{V}{V_{ref}}) = \frac{2\pi K}{\lambda}(\int_{s_1} \rho_1 \, ds \; - \int_{s_2} \rho_2 \, ds \;) \tag{6.32}$$

The beams traverse the same optical path throughout the system except for a characteristic length L near the focal point of the beams and so the equation can be simplified and written in terms of the densities,

$$\rho_2 - \rho_1 = \frac{\lambda}{2\pi KL} sin^{-1}(\frac{V}{V_{ref}} - 1) \tag{6.33}$$

This can also be written in terms of mean and fluctuation densities showing that the FLDI system is a useful tool to measure density fluctuations in the flow,

$$\frac{\rho'}{\langle\rho\rangle} = \frac{\lambda}{2\pi KL\langle\rho\rangle} sin^{-1}(\frac{V}{V_{ref}} - 1) \tag{6.34}$$

The system initially used was developed by Gragston *et al.* at UTSI [315][318], a Diffractive

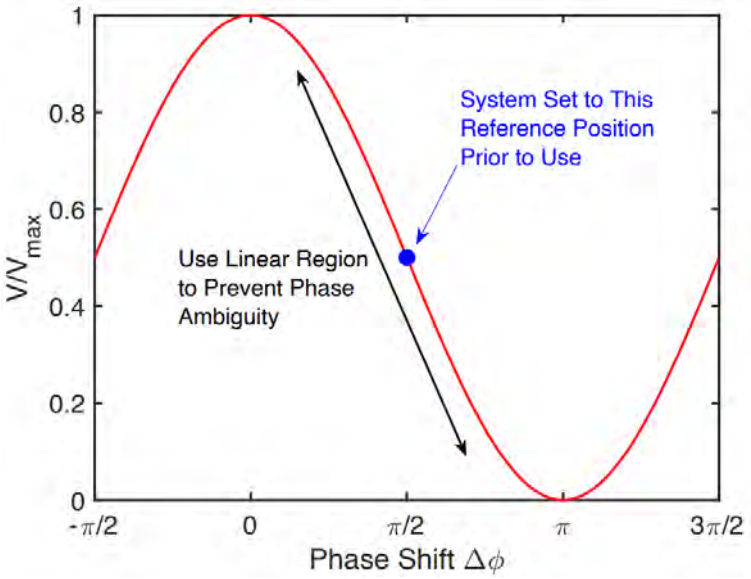

Figure 6.18: Photodetector voltage output and its relation to fringe intensity. [316].

Optical Element (DOE) (Holo-Or #MS-474-P-Y-A) was used to split the laser beam into a 1x6 array. The technique was named Linear Array-Focused Laser Differential Interferometry (LA-FLDI) as 1-D or 2-D arrays of linearly-spaced FLDI beam pairs can be created using this approach [315]. Fig. 6.19 shows the setup around the M6QT. ([4])

A 10 mW HeNe 633 nm laser beam (Edmund Optics Lumentum) is diverged using a f=-12 mm plano-concave lens and then split into six beams by the DOE with a 0.71° separation angle. The beams then pass through a polarizer and are split into beam pairs by a Wollaston prism (United Crystals) with 5-arcminute separation angle. A plano-convex lens with f=250 mm is used to focus the beam pairs on top of the cone. Another identical convex lens focuses the beam onto another 5-arcminute Wollaston prism which recombines the beam pairs. The six beams then pass through a polarizer again to get the interference fringe. An f=-30 mm plano-concave lens then collimates the beams before they travel into the collection optic, which is an array of six fiber optic cables (Thorlabs M35L01). The fiber optic cables are coupled to photodetectors (Thorlabs PDA36A2) that feed into a NI PXI Data Acquisition (DAQ) system (NI PXI system with components NI PXIe-8381, NI BNC-2110, and NI PXIe-6368) which samples each channel at 2 MHz [319]. A MATLAB code was written to use geometrical optics to predict beam-pair spacing and size optics suitable for the setup. This code helps design the setup as tunnel constraints can be accounted for, like the wide free-jet test section, and perhaps other obstacles outside of the test section. The code also helps order optics in the right size as the spread of the beams is predicted. To be safe bigger optics were ordered than necessarily needed. The first campaign used 5-arcminute Wollaston prisms, the ray trace diagram and close-up of beam pairs is shown in Fig. 6.20. The close-up of the beam pairs shows a predicted beam-pair spacing of 374 μm and spacing between beam pairs of 939.2 μm. (Siddiqui [4].)

A beam profiler (Ophir-Spiricon SP90425) was placed inside the test section very carefully

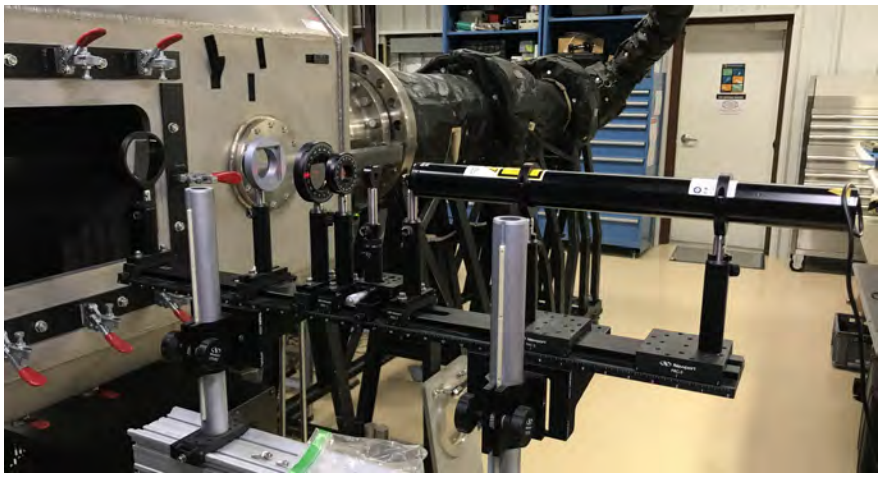

(a) Laser side

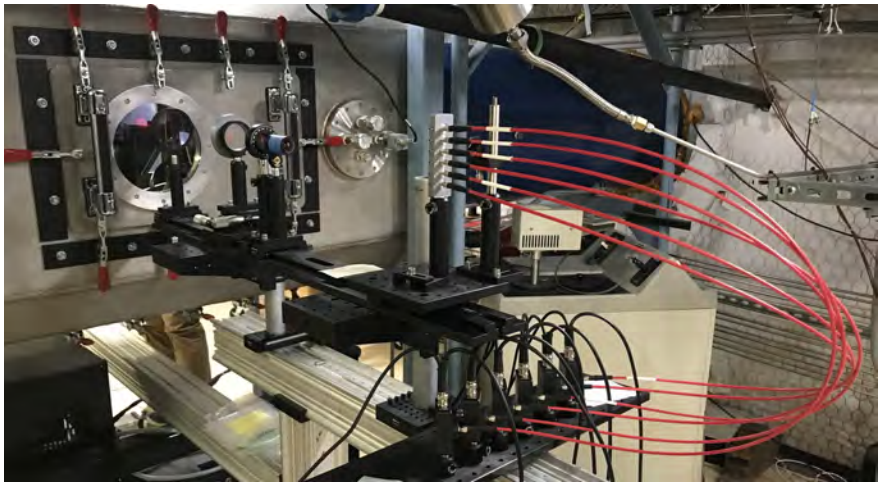

(b) Detector side

Figure 6.19: The LA-FLDI system setup on the M6QT. [5].

with the model pulled back and beam profiler suspended over it to characterize the beam pairs at the focal point. Fig. 6.21 shows the beam pairs as observed with and without the diffractive optic. The beam-pair spacing was measured to be 375 μm and distance between beam pairs was measured to be 933 μm. A slight smearing effect was observed in the beams furthest away from center due to the beams approaching the focus at an angle. Note that the beams are shown in a horizontal line but were angled to match the slope of the cone at the measurement location. The measurement location was such that the most downstream beam was 25.4 mm from the end of the cone and 1.2$\pm$0.5 mm from the surface. ([4])

The 5-arcminute Wollaston prisms were replaced with 1.5-arcminute Wollaston prisms to reduce the beam-pair spacing for the second campaign. Fig. 6.22 shows the prediction from the ray-trace diagram and a close-up of the beam pairs. The close-up of the beam pairs shows a predicted beam-pair spacing of 114 μm and spacing between beam pairs of 1085 μm. The beam

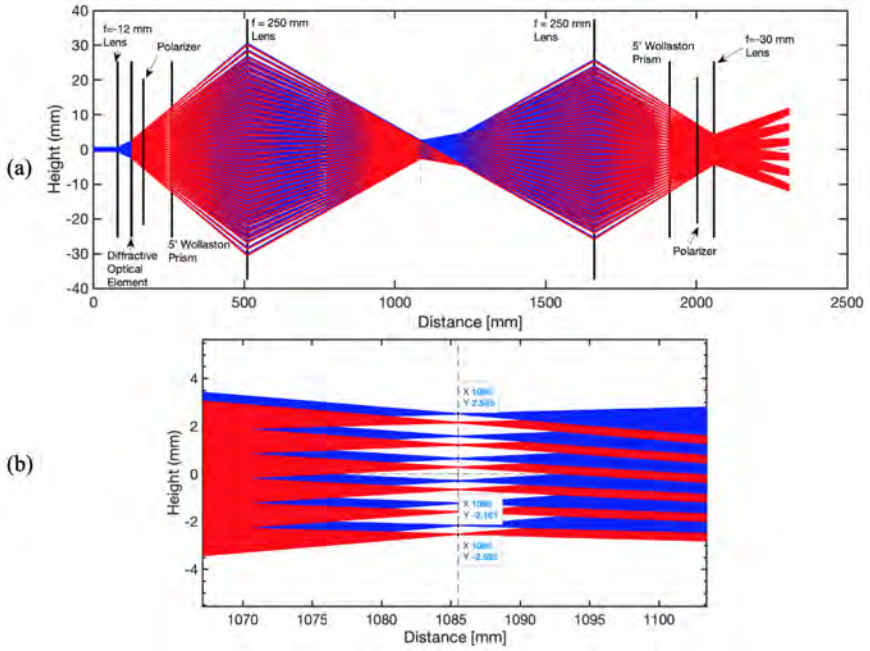

Figure 6.20: (a) A ray trace diagram of the LA-FLDI system with 5-arcminute prisms, (b) A close-up of the focus region showing the six beam pairs [316].

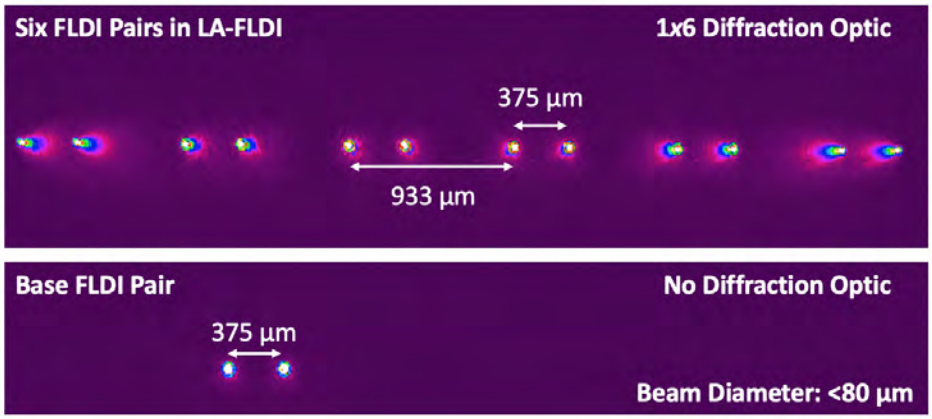

Figure 6.21: Beam pair characterization with a beam profiler for the setup with 5-arcminute prisms, shown with and without the DOE. [316].

profiler (Ophir-Spiricon SP90425) was used again to characterize the beam pairs at the focal point. Fig. 6.23 shows the beam pairs as observed with the diffractive optic. The beam-pair spacing was measured to be 130 μm and distance between beam pairs was measured to be 1070 μm. The difference in the predicted and measured values of beam spacing can be attributed to the uncertainty in placement of the DOE as this affects the beam pairs and their spacing. The beam pairs

were angled to match the slope of the cone at the measurement location which was with the most downstream beam approximately 25.4±0.5 mm from the end of the cone and 1±0.5 mm from the wall in the wall-normal direction. ([4])

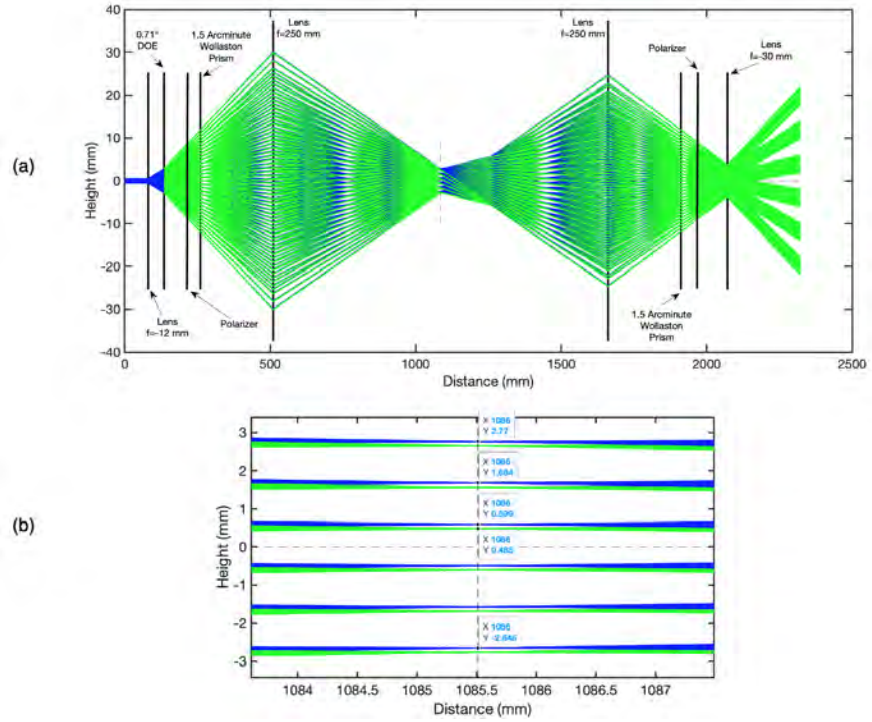

Figure 6.22: (a) A ray trace diagram of the LA-FLDI system with 1.5-arcminute prisms, (b) A close-up of the focus region showing the six beam pairs. Siddiqui et al. [5]

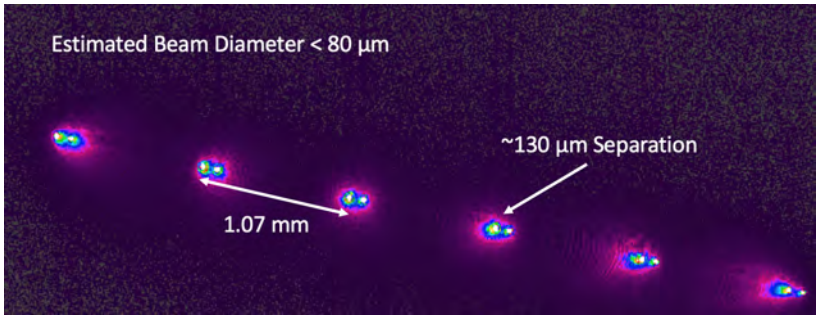

Figure 6.23: Beam pair characterization with a beam profiler for the setup with 1.5-arcminute prisms. Siddiqui et al. [5]

6.4 PHACENATE Mach Stem Experimental methods and data reduction

This section follows from McManamen [17] and McManamen et al. [3].

6.4.1 Total pressure measurements

Total pressure measurements were conducted using a constructed Pitot pressure probe. A Kulite XCEL-100-5A pressure sensor was flush mounted in precision stainless steel tubing. Three sections of increasing diameter tubing were connected downstream of the sensor head with epoxy-smoothed transitions to bring the outer diameter from the size of the transducer (0.26 cm) up to 0.6 cm (further described in [320]). The Pitot probe could then be mounted in a sting assembly to position it in the test section. The Kulite sensor was sampled at 300 kHz and the signal was low pass filtered at 50 kHz before being recorded on the computer's data acquisition (DAQ) system. Total pressure measurements were taken along the centerline of the nozzle exit plane in vertical and horizontal directions. Fifty runs were recorded at each of 9 locations across the nozzle exit plane while the probe was moved manually using a transition stage. Target locations of the probe were measured with a ruler across the nozzle exit and marked on the transition stage, accuracy of the location of the probe is of the order 0.2 cm. For each location a 2 ms section of data was taken from each run in the region of stable pressure. The same 2 ms section of data from the settling chamber pressure was normalized against itself and used to correct the Pitot signal to account for shot-to-shot influences over time. This was done for both vertical and horizontal rakes. ([17, 3])

6.4.2 Laser system description and experiment configuration

This section follows from McManamen et al. [3]. Two identical pulsed laser systems were used in this study for excitation of nitric oxide in various LIF techniques. Each system consisted of an injection seeded Spectra Physics PRO-290-10 Nd:YAG laser and a Sirah Cobra Stretch dye laser with a sum frequency mixing unit. The YAG laser operated at 10 Hz with a linewidth of 0.003 cm^{-1}, and was tuned for output in both second and third harmonics (532 nm and 355 nm respectively). A fundamental beam was generated in the dye laser by pumping a dye solution consisting of Rhodamine 610 and Rhodamine 640 in methanol with the first harmonic output of the YAG. The resulting fundamental beam was tunable in the range of 600 nm to 630 nm. The dye fundamental beam was then mixed with the third harmonic output from the YAG in a Sirah SFM-355 mixing unit, resulting in an ultraviolet (UV) 223 nm to 227 nm output beam. Typical linewidth and power of the UV beam was 0.08 cm^{-1} and 5-12 mJ/pulse, respectively. The experimental configuration used for both laser based methods is depicted in 6.24. The model wedges were installed flush with the exit plane of the nozzle and spaced 5.1 cm apart vertically. The optimal vertical spacing for the wedges was determined via schlieren imaging flow visualization, where the Mach stem's height was maximized while remaining downstream of the wedge geometry. A Pitot pressure probe was mounted outside of the laser diagnostic area, in the lower corner of the core flow, to monitor tunnel conditions. A Princeton Instruments PI-MAX4 ICCD camera was mounted for viewing from the right hand side of the tunnel. ([17, 3])

The tunnel N_2 supply was pre-seeded with 0.5-1.0 % NO and pre-heated to achieve 375 K in the tunnel settling chamber. The initial laser was timed at 30-32 ms following initial tunnel valve opening and the second laser followed at a 1.7 μs time delay. This time delay was selected to

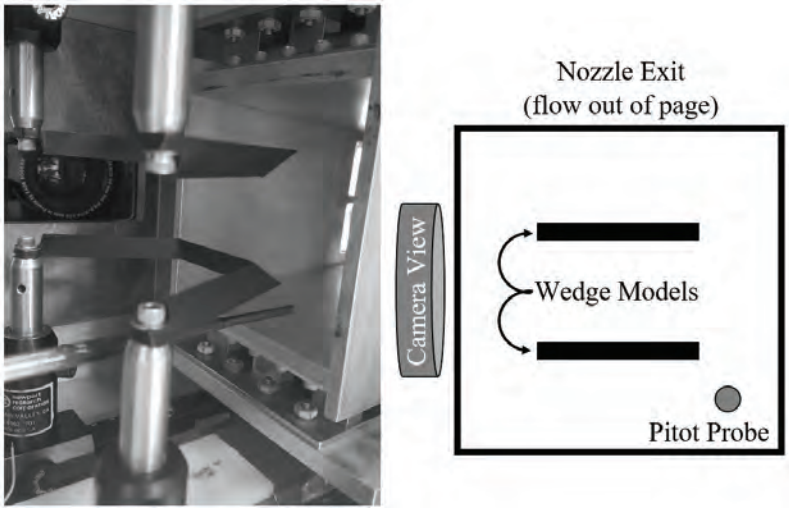

Figure 6.24: Model wedge configuration for MTV and PLIF Thermometry experiments. Left: image of actual configuration in tunnel; right: diagram showing model wedge and Pitot probe position from behind, looking straight into nozzle exit. [3]

minimize the uncertainty in the velocimetry technique, and was used in both laser based methods for consistency. The camera was liquid cooled to -35 C with the intensifier enabled. The dual image feature setting was used and camera gates were set to 3ns/100ns for the velocimetry "write"/"read" exposures and 10-15ns for both PLIF exposures. ([3])

6.4.3 Molecular Tagging Velocimetry

This section follows from McManamen et al. [3]. Velocity measurements were made across a normal shock using a single component molecular tagging velocimetry approach. Two lasers were used in the MTV technique, one "write" laser to initially excite the ground state NO, and one "read" laser that would later target the tagged v"=1 NO, as previously demonstrated in [321]. The final turning mirrors and sheeting optics for both lasers were mounted to an optical breadboard, which in turn was mounted to a linear transition stage on a rail system. A diagram of this setup is shown in 6.25. The linear transition stage was used to optimize the location of the "write" laser lines in relation to the normal shock wave during operation of the tunnel. The camera gate was set to 100 ns exposure so that signal from the scattered laser between the focused lines could be detected in order to reveal the shock location. The transition stage was then adjusted until the "write" line was just downstream of the shock wave, usually with a separation of roughly 5 pixels. Once the lines were in optimal location, the transition stage was locked to prevent accidental motion. ([3])

For each Reynolds number condition a series of images was taken. First a dotcard image was taken to align and focus the camera on the laser excitation region, as well as provide a distance conversion factor to be used in post processing. The background intensity was corrected by taking a 'dark-charge' image of the covered camera lens and subtracting this from each frame. In order to confirm the location of the shock wave in post-processing, a long term PLIF exposure of NO(0,0) was recorded and averaged over 100 frames. Finally, the MTV images were recorded at several

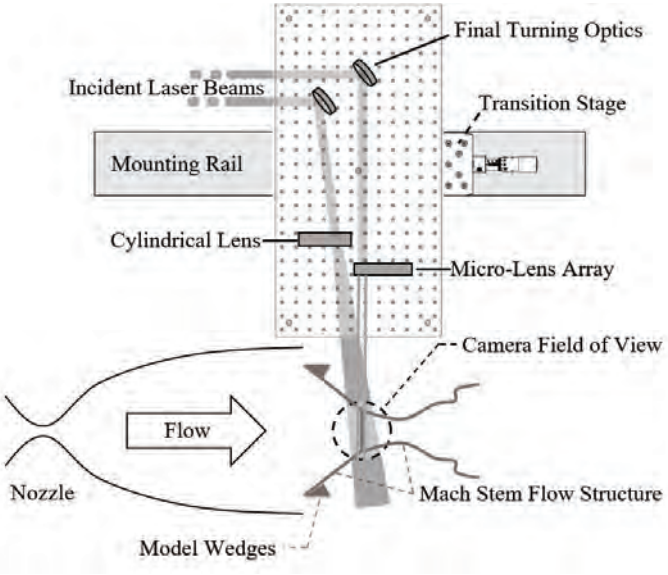

Figure 6.25: Diagram of experiment setup for MTV measurements. [3]

locations. 500 image pairs were taken in the 'optimal' position described previously. The transition stage would then be adjusted to shift the laser lines 5-10 pixels farther downstream, and 500 image pairs were taken at the new location. This was repeated until 4 total locations had been recorded. All velocimetry images in this study were processed using a custom program written in Matlab. Cross correlation was performed using the built in "x-corr" Matlab function. First, each image pair was divided into 'sub-images' representing a region of single pixel height surrounding the location of the initial 'write' laser line. A threshold value was subtracted from each sub-image to remove the background signal and avoid corruption of the cross-correlation results. The "x-corr" function was then applied and the resulting correlation matrix was cropped around the peak value and fitted with a third order polynomial with centering and scaling applied. A goodness of fit (r^2) value was recorded for the correlation function so that the user could remove poor correlation results. An example cross-correlation result is shown in 6.26. The far left figure shows the normalized and thresholded sub-images, where the delayed image has been shifted by the correlation peak. In the middle is the primary cross-correlation fit, and to the right is the secondary cross-correlation fit. Each is cropped around the peak value. A third order polynomial fit is applied with 95% confidence bounds, and the resulting peak and goodness-of-fit r^2 value are displayed at the top. It was found that the correlation fit would underestimate the correlation peak value in most cases with the polynomial fit. While the peak value itself is not meaningful, in order to make sure the location of the peak was as accurate as possible a secondary fitting procedure was applied. If the initial polynomial fit returned a goodness of fit value above a user specified threshold (typically 0.95), the application would crop even closer around the peak and perform another polynomial fit. Including more points initially allows for poor correlations, without strong peaks, to be excluded from further processing; and it was found to be within 0.5 pixels of the true peak. The secondary fitting further reduced this uncertainty to 0.1 pixels. ([3])

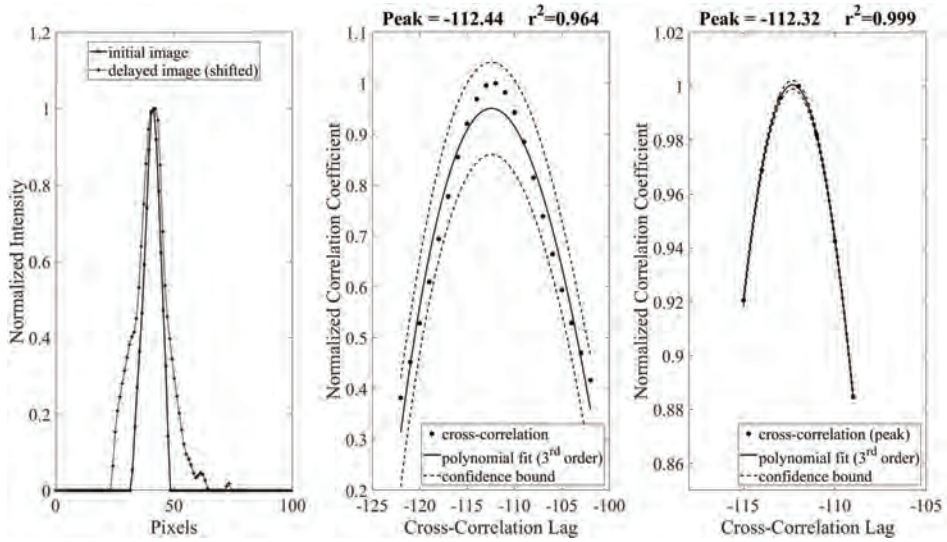

Figure 6.26: Cross correlation example of a selected sub-image pair. [3]

The recorded sub-pixel correlation peak was then converted to a velocity value via the pixel-to-meter conversion factor and time delay. This was repeated for all 'sub-image' regions across each image pair recorded in the series. The velocity and goodness of fit values were then sent to post-processing where mean and fluctuating values could be determined across the region of interest. (McManamen et al. [3])

6.4.4 Planar Laser Induced Fluorescence Thermometry

This section follows from McManamen et al. [3]. Temperature measurements were made across a normal shock wave by a two-line PLIF thermometry technique, similar to that of [321]. The "read" lasers in this study were tuned to probe transitions in the $A^2\Sigma^+(v'=0) - X^2\Pi(v''=0)$ band for ground state NO. For the nominal flow Mach number of 4.4, the expected mean temperature conditions were 77 K in the freestream and 361 K downstream of the normal shock wave. Target rotational states were chosen based on the Boltzmann population distributions of ground state NO at these temperatures. The rotational states $J''=1$ and $J''=8$ were chosen to maximize temperature sensitivity, particularly in the region downstream of the normal shock, while retaining reasonable signal potential from both regions of flow. Laser wavelengths were set for these rotational states and the power was balanced to $\sim$1.5 mJ/pulse for both lasers. A schematic of the experimental setup for PLIF thermometry is shown in 6.27. Both lasers were introduced through the top window of the tunnel. In order to optimize the overlap of the laser sheets, the angle between the beams was minimized by mounting the final turning mirrors as close to each other as possible without clipping the beams. Both lasers were sent through a cylindrical lens to alter the circular profile into a planar sheet oriented in the direction of flow. A Princeton Instruments PI-MAX4 ICCD camera was mounted on the right hand side of the tunnel for image collection. (McManamen et al. [3])

A dotcard image was taken first, to focus the camera on the plane of the laser sheets. The back-

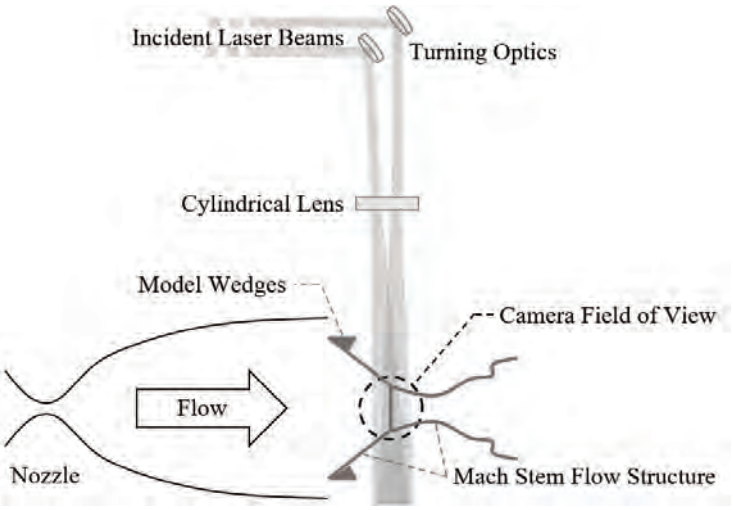

Figure 6.27: Diagram of experimental setup for PLIF thermometry. [3]

ground intensity was corrected in-situ by subtracting a "dark-charge" image of the covered camera lens from each frame. 500 image pairs were taken of the normal shock region for each Reynolds number condition and processed as described below. This was repeated in the same region of flow with the model wedges removed to further characterize the freestream conditions. Additional image pairs were taken in regions of known temperature for calibration and image correction purposes during processing. Thermometry images were processed using a custom application, written in Matlab. Free-stream images were initially processed following a conventional approach for linear LIF thermometry to establish baseline conditions. It was believed that the high laser intensity needed to obtain signal in the low density freestream led to a LIF response in the higher density post-shock region that was at the edge of the linear limit, possibly in the transitional to saturated regime for LIF thermometry. A separate processing routine was written to examine the Mach stem PLIF images, where each region of the flow was individually analyzed for an assumed mean temperature based on the previously established conditions. Because the quantities of interest in this study were fluctuations, and the mean flow conditions are well known conventionally, it was determined that this 'in-situ' processing would be sufficient for the scope of this analysis. ([3])

In this two-line PLIF technique, temperature is determined via 6.35, where R_{12} is the ratio of LIF signals from rotational states '1' and '2', C_{12} is a calibration constant based on experimental conditions, ΔE is the energy separation between the states, k is Boltzmann's constant, and T is the rotational temperature.

$$R_{12} = C_{12} e^{-\Delta E/kT} \tag{6.35}$$

The processing routine analyzed the upstream and downstream locations as separate images. Calibration images were not used in this routine. Instead, a mean temperature was assumed based on the previous freestream measurements and conventional shock-jump relations. The calibration constant (C_{12}) was then specified to match this assumed temperature for the image intensity ratio (R_{12}) values at each pixel. This temperature specification method essentially acts as a laser profile

correction step, combined with a temperature calibration, as is typically seen in the conventional approach. The raw images were cropped to view only the normal shock region with fluorescence signal, and then a region in front of and behind the normal shock was selected for further processing. Next, the images were binned in two dimensions for both pre- and post-shock regions, in this case a bin size of 4x4 was selected to optimize both signal and resolution. The mean value of the pixels within each bin, excluding negative or "not a number" values, was recorded and returned as the value for the entire bin. Each pixel was then analyzed individually to determine the appropriate C_{12} value and resulting mean and fluctuating temperatures. For each pixel coordinate, R_{12} was first determined for all image pairs. Spurious R values beyond three standard deviations from the mean R value were removed for the determination of $C_{12}{}'$. A $C_{12}{}'$ value was then selected such that the resulting mean temperature, calculated for the range of R values, would match the specified mean temperature of the region. This was done through manipulation of the standard PLIF thermometry equation into 6.36 to find "$\langle C_{12}{}' \rangle$" based on the given R_{12} range and specified mean temperature. ([3])

$$\left\langle C_{12}{}' \right\rangle = \left\langle e^{\left(ln(R_{12}) + \Delta E / k\overline{T}\right)} \right\rangle \tag{6.36}$$

Once the appropriate $C_{12}{}'$ value was determined for a given pixel coordinate, temperature values for each image pair at that coordinate were calculated and recorded. This was repeated across both regions of interest, and the resulting temperature data was sent to post processing. Mean and fluctuating temperatures were analyzed for each region, the results of which are discussed in the next section. (McManamen et al. [3])

6.5 HXT Mach Stem Experimental Setup

This section follows from Dean [11].

6.5.1 HXT Setup

All experiments in this campaign took place at Mach 8.5. As shown in Table 6.8, Mach reflections generated by four different air flows and a nitrogen flow were analyzed. Cases 1, 2, and 3 had different stagnation enthalpies and the same post-shock density, assuming equilibrium chemistry. As stagnation enthalpy increased, the thermochemical nonequilibrium in the Mach reflection flow fields also increased. Therefore, these cases enabled an analysis of how thermochemical nonequilibrium influences turbulence. The freestream conditions of cases 3 and 4 were identical except for density. Comparing results from these two cases enabled analysis of the influence of density on turbulence. Finally, cases 1 and 5 were nearly identical, except the test gases were air and nitrogen, respectively. Significantly less chemistry occurred in the post-shock relaxation region of the pure nitrogen case because nitrogen requires more energy to dissociate than oxygen. The difference in dissociation energy is due to bond strength. Diatomic nitrogen has a triple bond where each atom shares 3 electrons, and diatomic oxygen only has a double bond. Contrasting the nitrogen and air cases allowed an analysis of how chemistry influences turbulence. In summary, the main cases allowed evaluation of the influence of stagnation enthalpy, density, and chemistry on high enthalpy turbulence. Two additional cases, listed in Table 6.9, were partially studied. Multiple runs were conducted at an air case with a stagnation enthalpy of 8.9 MJ/kg. However, the freestream

density of this case was too low for the FLDI measurements. In addition, two nitrogen runs with a stagnation enthalpy of 5.2 MJ/kg were conducted. ([11])

Case	Gas	Mach	Enthalpy (MJ/kg)	Density (g/m3)	Temp (K)	V (km/s)
1	air	8.5	7.2	9.4	470	3.7
2	air	8.5	5.2	10	330	3.1
3	air	8.5	1.8	14	120	1.9
4	air	8.5	1.8	43	120	1.9
5	N2	8.5	7.2	9.2	460	3.7

Table 6.8: Freestream flow conditions of main cases that were studied.

Case	Gas	Mach	Enthalpy (MJ/kg)	Density (g/m3)	Temp (K)	V (km/s)
6	air	8.5	8.9	3.1	580	4.1
7	N2	8.5	5.2	10	330	3.1

Table 6.9: Freestream flow conditions of partially studied cases.

The operation and configuration of a wind tunnel could directly influence the measurements made inside of it. For example, changing the thickness of mylar used in an expansion tunnel changed the size and quantity of mylar debris. Therefore, it was important to note the changes in the HXT facility that were required to generate the different flow conditions overviewed in the previous section. These changes are summarized in Table 6.10 and Table 6.11 include pressures, driver gasses, driver lengths, primary diaphragms thicknesses, and mylar diaphragm thicknesses. Cases with a driver length of 1.25 ft required a single primary diaphragm, and two primary diaphragms were used in cases with a driver length of 5 ft. Small variations in driver pressure occurred at testing conditions with only a single primary diaphragm. The driver pressures reported in Table 6.9 are the average pressure of all the runs conducted at that condition. The standard deviation in the driver pressures of cases 1, 5, and 6 were 57, 38, and 53 psia, respectively. ([11])

The x-t diagrams for the 5 main cases are shown in Fig. 6.28. Although the method of characteristics code used to generate the diagrams did not account for thermochemistry, viscous effects, or the steady nozzle expansion, the diagrams show reasonable estimates for the durations of test times and other flow processes. Only one x-t diagram is shown for cases that had nearly identical flows. HXT repeatability was important because run conditions were reproduced multiple

Case	Driver Gas	Driver Length (ft)	Driver Pressure (psia)
1	He	1.25	1760
2	He	5	600
3	air	5	600
4	air	5	1900
5	He	1.25	1740
6	He	1.25	1450
7	He	5	600

Table 6.10: HXT parameters used to generate the testing conditions.

Case	Driven Press. (psia)	Exp. Press. (Torr)	Dia. Thick. (in)	Mylar Thick. (in)
1	1.04	0.230	0.25	0.001
2	1.30	0.250	0.125	0.001
3	3.45	0.325	0.125	0.002
4	10.7	1.03	0.25	0.003
5	1.04	0.229	0.25	0.001
6	0.32	0.075	0.25	0.0005
7	1.29	0.250	0.125	0.001

Table 6.11: Continued HXT parameters used to generate the testing conditions.

times to enable measurements at different locations. Measurements of the shock speed through the nozzle and static pressure at the nozzle exit substantiated the consistency of runs. The average shock speed and static pressure measured at each case are reported in Table 6.12. In addition, the number of runs conducted at each condition and the standard deviations in the measured values are reported. The standard deviations in shock speeds were within about 2% of the averages, indicating a high degree of repeatability at each condition. The primary sources of uncertainty in the shock speed measurements included the accuracy of the distance measured between the time of arrival sensors ($\pm$4 mm) and the time between samples saved by the DAQ (1e-6 s). With these considerations, the highest shock speed measurement uncertainty was less than $\pm$10 m/s. Sources of uncertainty in the static pressure measurements include a relatively low signal-to-noise ratio, measuring low pressures in the non-linear response region of the sensors, inaccuracies in the sensor calibrations, sensor damage, and thermal effects on the sensor. The static pressure sensor was recalibrated five times throughout this experimental campaign because the zero of the sensor decreased by as much as 5mV (0.013 psi) between runs. The drifting zero is a known failure mode of Kulites, likely caused by the harsh conditions inside the tunnel. Since MKS 925 and MKS 902B vacuum pressure transducers accurately measured the vacuum pressure in the expansion section

before each run, DC offsets in the zero of the nozzle static pressure Kulite could be corrected in post-processing. ([11])

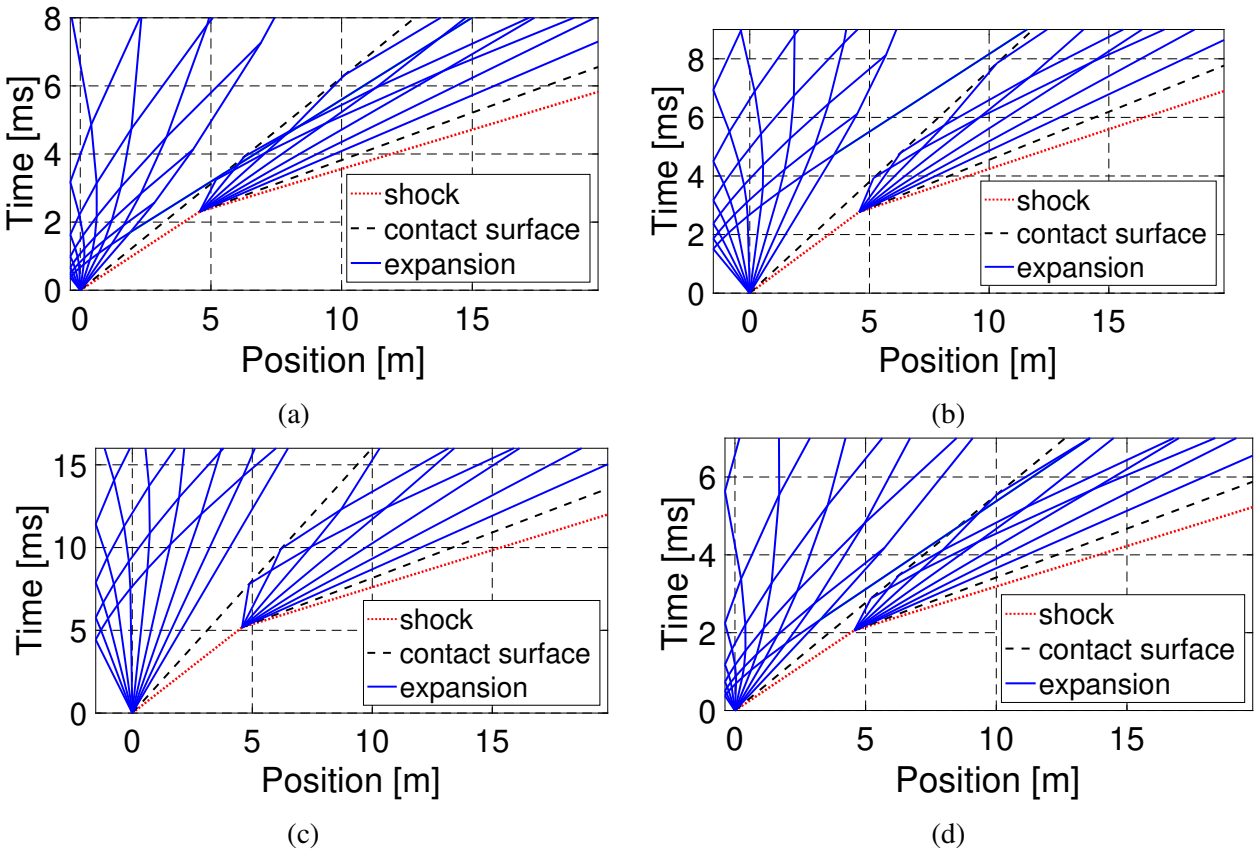

Figure 6.28: X-t wave diagrams for cases a) 1 & 5, b) 2 & 7, c) 3 & 4, and d) 6. [11]

Since measuring most flow parameters in an expansion tunnel is difficult, many must be determined theoretically. Shock speeds and static pressures computed using the same ideal theory discussed for FLDI are included in Table 6.12 to allow evaluation of the accuracy of the theoretical computations. The percent errors between the theoretical and experimental parameters are also included in Table 6.12. It is not uncommon for theoretical calculations to overpredict shock speeds in an expansion tunnel [322]. Inaccurate viscous modeling that does not capture shock attenuation and non-ideal diaphragm rupture are possible causes of the shock speed overpredictions [323, 324]. Note that shock speed error does not directly quantify the error in other theoretical values. Assuming most attenuation occurs as the shock travels down the expansion section and through the nozzle of the HXT, the test time test gas is shock heated and processed by the unsteady expansion before the shock strength has appreciably attenuated. The static pressure errors were about half the shock speed errors, validating the previous statement. The FLEET measurements also showed that the errors in the theoretical freestream velocities were less than half of the shock speed errors. The

		Shock Speed [m/s]				Static Pressure [psia]			
Case	**Runs**	**Measured**	**STD**	**Theo.**	**Error**	**Measured**	**STD**	**Theo.**	**Error**
1	8	3830	82	4350	14%	0.19	0.013	0.18	5.3%
2	3	3360	67	3690	9.8%	0.13	0.006	0.14	7.7%
3	4	1950	9.6	2220	14%	0.073	0.009	0.067	8.2%
4	3	1970	10	2230	13%	0.22	0.006	0.21	4.5%
5	11	3550	61	4360	23%	0.18	0.009	0.18	0%
6	9	3930	190	4820	23%	0.091	0.01	0.073	25%
7	2	3230	110	3710	15%	0.14	0	0.14	0%

Table 6.12: Experimental and theoretical shock speeds and nozzle exit static pressures for each flow condition.

Case	**h (cm)**
1	20.70
2	21.65
3	23.65
4	23.65
5	21.97
6	20.70
7	22.61

Table 6.13: Tip to tip distance between the wedges at each run condition.

case 6 static pressure error was an outlier because those runs were performed before the first high-quality calibration. Overall, the values in Table 6.12 indicate that the theoretical computations of the test time flow parameters were reasonably accurate. ([11])

6.5.2 Model Setup

This section follows from Dean [11]. The tip-to-tip distance between the wedges of the model (h), shown in Fig. 6.29a, was adjusted using spacers so the Mach stem would form in the same location downstream from the wedges at each run condition. A significant motivation for changing the wedge gap was to keep the influence of the favorable pressure gradients on the shear layers as consistent as possible. The pressure gradients were produced as the flow expanded around the back of the wedges. Thermochemistry caused the forward Mach line angles of each expansion fan to vary slightly with stagnation enthalpy; however, this variation was slight. The tip-to-tip distances between the wedges for each run condition are listed in Table 6.13. A combination of US3D simulations and trial and error determined the spacings. ([11])

Rather than moving all of the diagnostics, the model position was adjusted to probe different

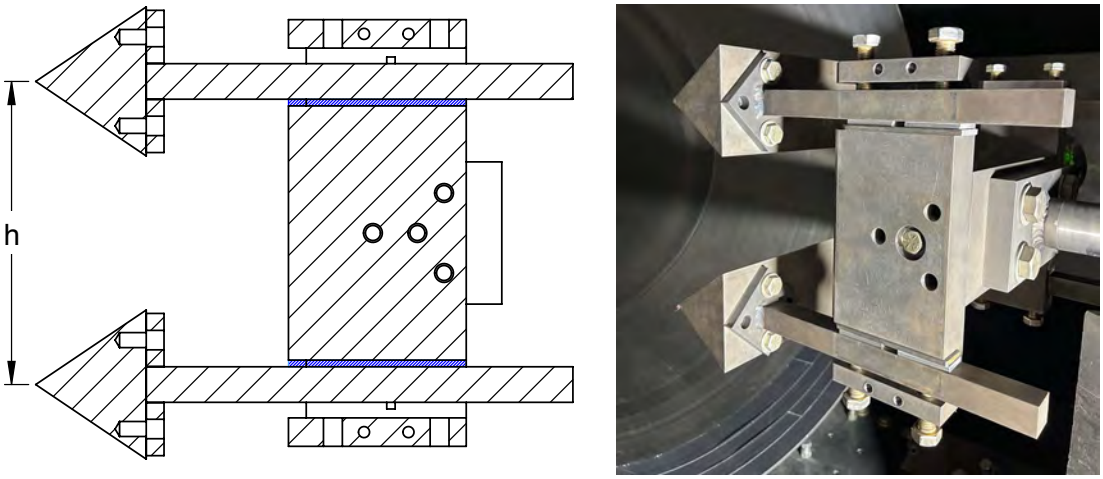

(a) (b)

Figure 6.29: Mach stem model a) section view drawing showing position where spacers go in blue and the tip to tip distance between the wedges *h* and b) image showing what the spacers look like before the cover plate is installed. [11]

locations in the Mach stem flowfields. The model height was adjusted using spacers placed between the breadboard floor of the test section and the bottom plate of the model holder, as shown in Fig. 6.30. The streamwise position of the model was also adjusted using spacers cut from a 7/8" diameter steel rod that could fit through the hole in the back of the model holder. When changing the spacers, the whole model assembly was pushed slightly upstream. Then a stick magnet was used to change out the spacers. Finally, the model was pulled back as far as it could go, pinching the spacer. Since the model is heavy, this method avoided the need to completely take out the model each time the streamwise position was adjusted. Using the spacers was also better than relying on the friction produced by tightening the bolts that pinch the model shaft to keep the model from moving downstream.([11])

6.5.3 Measurement Locations

This section follows from Dean [11]. Each of the five main run conditions were probed with FLDI at least 3 times in the regions shown in Fig. 6.31. The three main measurement location were the freestream (FS), post-shock (PS), and shear layer (SL). Each post-shock measurement was wade 1 cm downstream from the normal shock, and each shear layer measurement was made 3.5 cm downstream from the normal shock. The FLEET measurements were always made in the same freestream location about 12 cm in front of the model. OES measurements were made in both the post-shock and shear layer regions. ([11])

6.5.4 Simultaneous Diagnostics Setup

The simultaneous capture of schlieren, FLDI, OES, and FLEET required a complex optical setup. The pitch side of the schlieren and OES setups is shown in Fig. 6.32a. The green and red regions in the edited image show the optical paths of the FLDI and schlieren, respectively.

Figure 6.30: Image of spacers used to adjust the vertical position of the model.

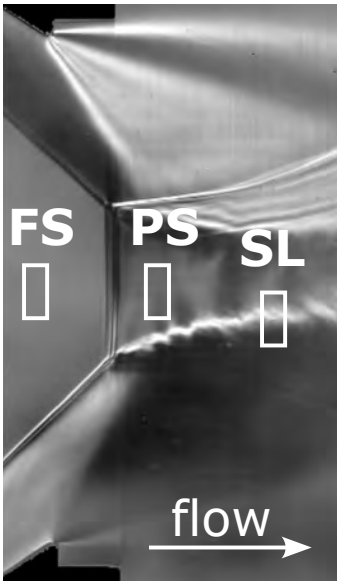

Figure 6.31: Schlieren image of Mach stem flowfield showing the three main FLDI measurement locations: freestream (FS), post-shock (PS), and shear layer(SL).

The schlieren mirror, shown in Fig. 6.32b, was just out of frame on the right side of Fig. 6.32a. An image of the true optical paths of the schlieren and FLDI is shown in Fig. 6.33. The image was captured after a run where scatter from smoke inside the test section made the FLDI beams easy to see. The schlieren and FLDI were intentionally pitched from the same side so the FLDI measurement locations could be captured with the schlieren camera, making spatial correlations trivial. ([11])

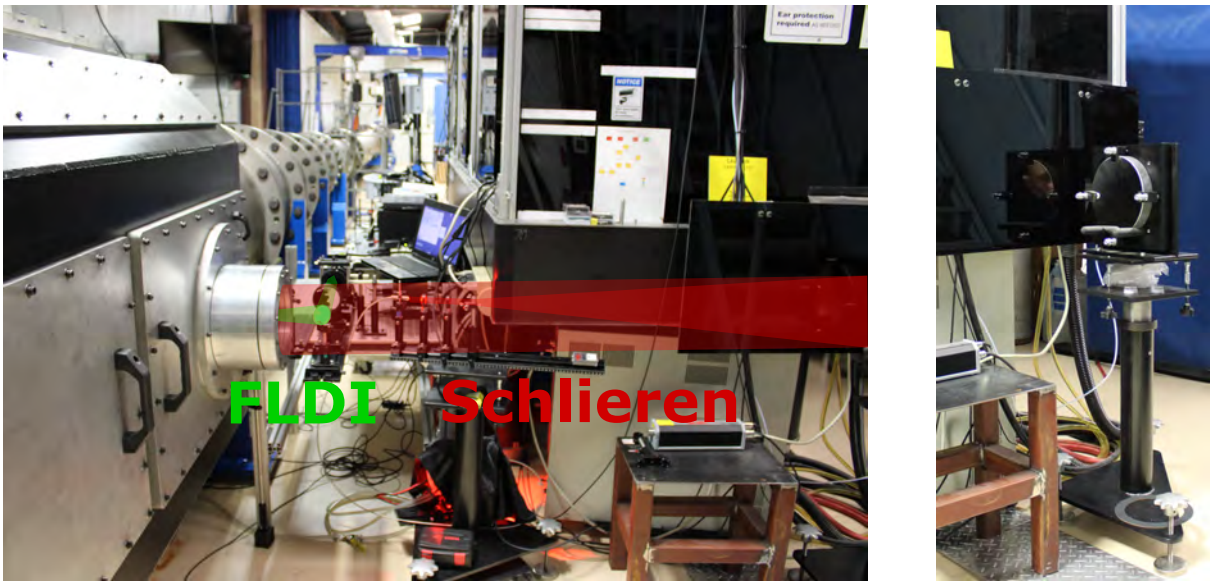

(a) (b)

Figure 6.32: Pitch side of schlieren and FLDI optical setups showing a) light paths and b) schlieren mirror. [11]

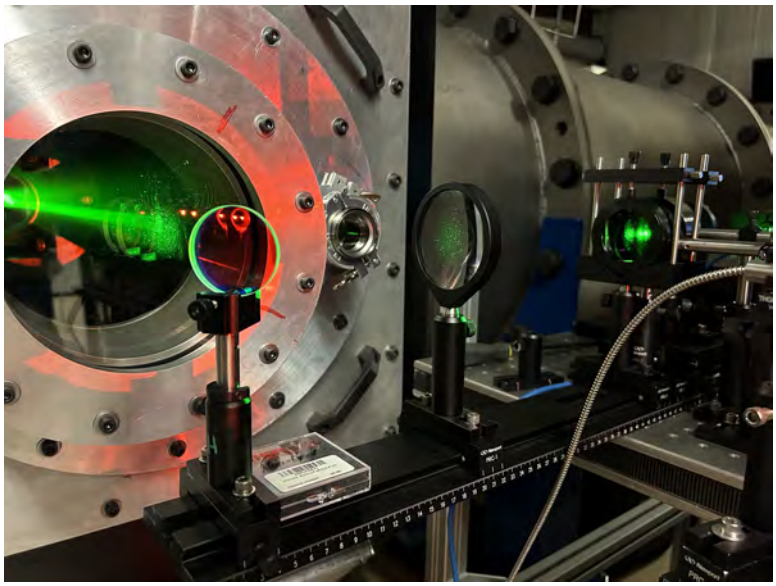

Figure 6.33: Image where smoke inside the test section made the FLDI beams visible. [11]

The catch side of the schlieren, FLDI, and OES optical paths are shown in Fig. 6.34. The femtosecond laser pulses for FLEET were also pitched from this side. In Fig. 6.34, the white optical path for the OES is shown immediately downstream from the long-pass dichroic mirror used for FLDI, which was the arrangement when freestream and post-shock FLDI measurements

were made. Since shear layer FLDI measurements were made relatively far from the shock, the OES was occasionally switched to an optical path upstream from the long-pass filter, allowing emission measurements of the region immediately downstream from the shock. ([11])

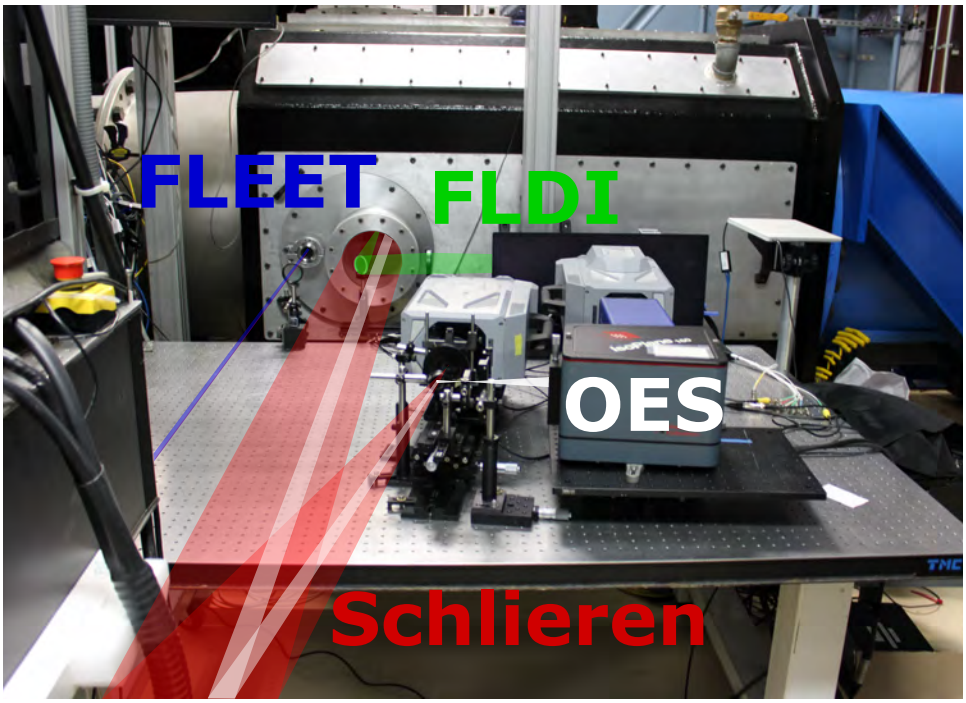

Figure 6.34: Catch side of the schlieren, FLDI, and OES setups edited to show the optical paths. Pitch side for FLEET. [11]

6.5.5 Schlieren Setup

This section follows from Dean [11]. A CAVILUX HF with an output of 810 nm was used as the light source. The 810 nm pulses from the CAVILUX were set to a width of 30 ns and synced with the Photron SAZ camera, which operated at a frame rate of 80 kHz. At this pulse rate, the CAVILUX was able to produce over 1000 consecutive pulses before starting to skip triggers. Since 810 nm is invisible to the human eye, the input of the fiber that comes with the CAVILUX was temporarily coupled with a 613 nm LED (Luminus Devices PT-120) so all of the optics could be aligned, as shown in Fig. 6.35a. ([11])

Before each run, the LED coupling was used to capture spatial calibration images for the schlieren and OES. An air gap was intentionally kept between the fiber and the LED to prevent the fiber from getting too hot. In addition, the LED was not operated continuously with more than 6 mA. The output of the CAVILUX fiber was focused onto a slit using two spherical lenses, as shown in Fig. 6.35b. The CAVILUX laser was placed on a small table between the schlieren source optics and the schlieren mirror, as shown in Fig. 6.32. The sync input for the CAVILUX was plugged

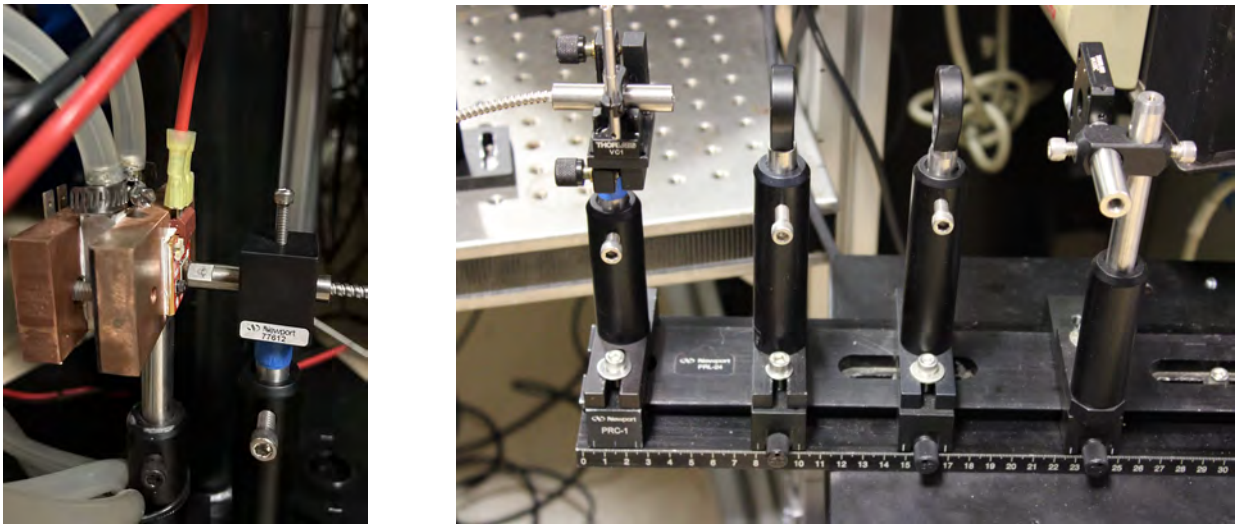

(a) (b)

Figure 6.35: Schlieren light source a) fiber coupled with an LED for alignment and b) optics used to set the light divergence angle and focus on the slit, where the optics from left to right are the fiber output, f= 50 mm plano-convex lens, f=100 mm plano-convex lens, and slit (Thorlabs VA1OOC). [11]

into the general output 1 port of the SAZ, which was set to output positive TTL signals for each camera exposure. The general output 2 port of the SAZ was set to output a positive TTL signal when recording and plugged into the CAVILUX trigger input port. The trigger setting ensured that the CAVILUX would only pulse during the test time. The schlieren mirrors were 20.3 cm in diameter with a focal length of 1.22 m (Edmund Optics 32-074-522). Since the schlieren mirror on the catch side was also used for spectroscopy, it was enhanced with a deep UV aluminum coating. A detailed image of the individual schlieren catch optics is shown in Fig. 6.36. Separate bandpass filters were needed for the calibration images (613 nm) and to capture the run (810 nm). When a bandpass filter was not placed in front of the camera, the position of each FLDI beam pair was visible. The iris was important for ensuring the quality of the schlieren in the HXT. Without it, bright background emission would make it through the bandpass filter and optical reflections would be visible. ([11])

6.5.6 FLDI Setup

This section follows from Dean [11]. This setup was comprised two columns of six beam pairs, whereas the earlier discussed configuration only had one beam pair. The setup was created with the help of Mark Gragston and Farhan Siddiqui from the University of Tennessee Space Institute [325]. The FLDI source light was a 532 nm laser (Cobolt Samba 1500). First, the beam passed through a linear polarizer (Thorlabs LPVISE100-A), followed by a f=-6.0 mm plano-concave lens. The expanding beam then propagated through a diffractive optic (Holo/Or M5-474-Q-Y-A), splitting the 55° polarized beam into six beam spots with a separation angle of 1.2°. Next, the six beam spots

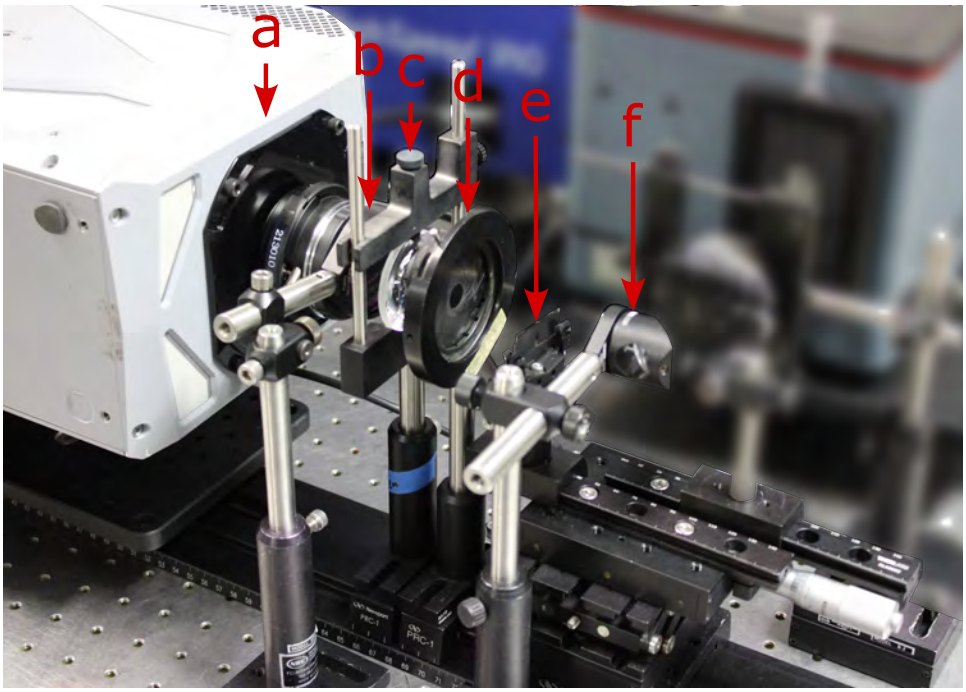

Figure 6.36: Schlieren catch optics. The labeled components are as follows: a) Photron Fastcam SAZ, b) 810 nm bandpass filter (Edmund 88021), c) f=100 mm plano-concave lens d) iris, e) knife edge, and f) 50-50 beam splitter (Thorlabs BSW10). [11]

passed through a 20 arcminute Wollaston prism (United Crystals SN 2020727), generating a 6 x 2 matrix of beam spots with one column vertically polarized and one column horizontally polarized. Then, the twelve beam spots passed through another linear polarizer (Thorlabs LPVISE200-A) and a 2 arcminute Wollaston prism, converting the 12 beam spots into 12 beam pairs of horizontal and vertical polarization. The beam pairs were focused using a f=250 mm plano-convex lens. Before entering the test section, a dichroic mirror (Thorlabs DMLP550L) turned the beam pairs 90° degrees. The dichroic was transparent to the schlieren light, allowing simultaneous schlieren imaging of the region probed with FLDI. Images showing all the FLDI pitch optics are displayed in Fig. 6.37. In addition, the approximate optical path lengths of each optic from the laser source are listed in Table 6.14.([11])

Table 6.14: Approximate distances of FLDI pitch optics from laser source with component labels following Fig. 6.37. [11]

Component	a	b	c	d	e	f	g	h	i	j
Distance [cm]	0	23	25	28	30	32	34	58	76	88

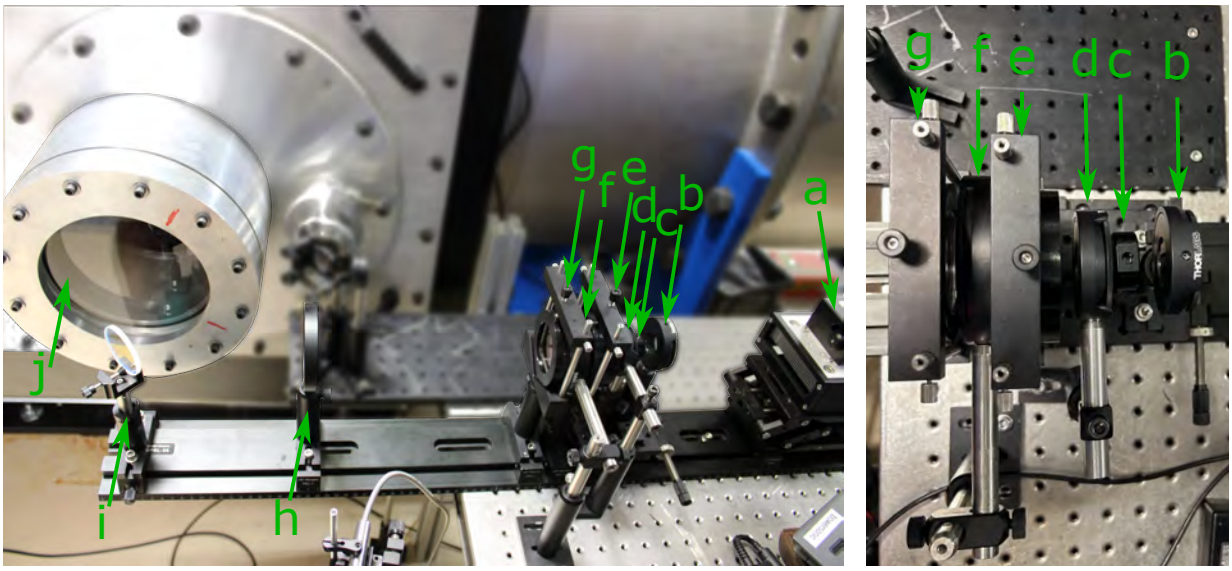

(a) (b)

Figure 6.37: FLDI pitch optics. The labeled components are as follows: a) 532 nm laser, b) polarizer, c) f=-6 mm lens, d) diffractive optic, e) 20 arcminute Wollaston prism, f) polarizer, g) 2 arcminute Wollaston prism, h)f=250 mm lens, i) longpass dichroic mirror, and j) fused silica tunnel window. [11]

After coming to a focus at the center of the test section, the twelve beam pairs exit through a fused silica window and turn 90° as they reflect off another dichroic mirror (Thorlabs DMLP550L). The beams then passed through an f= 250 mm plano-convex lens and another 2 arcminute Wollaston prism, which made each pair of beams collinear. Next, the collinear beams passed through two plano-concave lenses. The first lens had a focal length of f -30mm, and the second had a focal length of -20mm (Thorlabs LC4924). The beams passed through a 532 nm bandpass filter (Edmund 65216) to minimize interference from gas emission and femtosecond laser pulses. Finally, the beams passed through a linear polarizer (Thorlabs LPVISE200-A), which interfered each collinear beam. A custom-built, 12-channel photodetector assembly measured the interfered light intensity. Kirk Davenport at the University of Tennessee Space Institute built the photodetector assembly with Thorlabs FDS100 photodiodes and switchable gain OEM photodetector amplifiers (Thorlabs PDAPC1) [326]. Images showing all the FLDI catch optics are displayed in Fig. 6.38. In addition, the approximate optical path lengths of each optic from the tunnel window are listed in Table 6.15. Although it is not shown in Fig. 6.38, black fabric was used to surround everything behind the bandpass filter. ([11])

FLDI measurements were made with the Cobolt Samba 1500 laser set to 50 mA. It was important that the laser was shuttered before being turned on because it goes to a full power warmup mode before settling at the prescribed power setting. A Spiricon BM-USB-SP907-OSI beam profiler measured the beam pairs at the focus of the FLDI setup, resulting in the image shown in Fig. 6.39a. This model has a pixel size of 7.38 μm. According to the beam profile measurement,

(a) (b)

Figure 6.38: FLDI catch optics. The labeled components are as follows: k) fused silica tunnel window, l) longpass dichroic mirror, m) f=250 mm lens, n) 2 arcminute Wollaston prism, o) f=-50 mm lens, p) f=-20 mm lens, q) 532 nm bandpass filter, r) polarizer, and s) photodetectors. [11]

Table 6.15: Approximate distances of FLDI catch optics from laser source with component labels following Fig. 6.38. [11]

Component	k	l	m	n	o	p	q	r	s
Distance [cm]	0	9	26	50	56	62	65	68	83

the foci of each beam pair were separated by 155 μm. In addition, the two columns of pairs were about 893 μm apart. ([11])

A Spectrum DN2.292-16 data acquisition system recorded the voltage outputs from the photodiodes. The sample rate was 10 MHz, and 10 ms of data was recorded during each run. The labels in Fig. 6.39b show the DAQ channels used for each beam pair. This naming convention will be used to specify individual beam pairs throughout the remainder of this document. The data acquisition was triggered using the signal from the third shock time of arrival sensor embedded in the nozzle with a digital delay generator. Each beam in a pair traversed essentially the same path throughout the test section except for a characteristic length L near the focus. To estimate L, a needle nozzle was mounted on a rail, as shown in Fig 6.40a, to generate a small, turbulent region. RMS voltages of the second FLDI beam pair were recorded with the needle nozzle at different

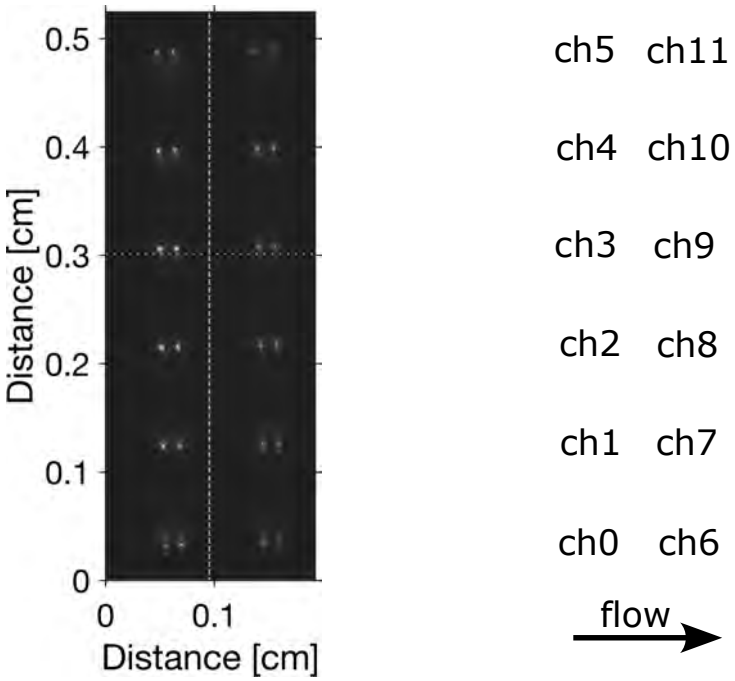

(a) (b)

Figure 6.39: FLDI beam pair a) profile image showing length scales and b) labels for DAQ channels and orientation to flowfield. [11]

points along the rail, which are plotted in Fig. 6.41. A Lorenz curve was fit to the experimental data, and the distance between the 1/e dropoffs in the Lorenz curve defined L. A similar method for finding the characteristic length was used by Benitez et al. [327]. The estimated characteristic length L for this FLDI setup was 79 mm. ([11])

A phase sweep was recorded before each run. During the phase sweep, the DAQ stored 42 seconds of data while the spanwise position of the Wollaston prism on the catch side was swept. An example of the voltages measured during a phase sweep is shown in Fig. 6.42. Due to an imperfect optical setup, the upstream and downstream columns of beam pairs were slightly out of phase. The ideal position for the Wollaston prism is where the voltage of each channel is precisely between the max and min measured during a phase sweep. Rather than setting the Wollaston prism at a biased point that evenly compromised the phases of both columns, the upstream column of FLDI measurements was favored. Since the upstream column was prioritized, the fringes were centered on the photodetectors in that column. The limited adjustability of the photodetector assembly made it challenging to get the spacing between the columns of photodetectors to match the spacing between the columns of fringes. As a result, the fringes of the downstream column were only partially covering their corresponding detector faces, causing comparatively lower voltage readings. ([11])

When making FLDI measurements in an expansion tunnel, a significant challenge arises due to the presence of mylar diaphragm debris convected with the test time flow. The debris particles

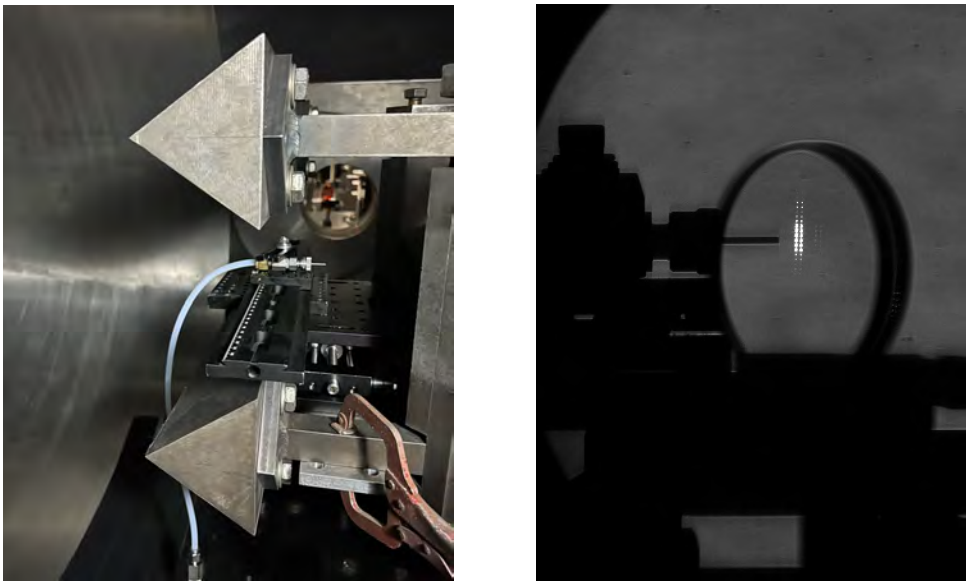

(a) (b)

Figure 6.40: Needle nozzle rig used to find the characteristic length of the FLDI setup captured with a) a regular camera and b) the schlieren setup. [11]

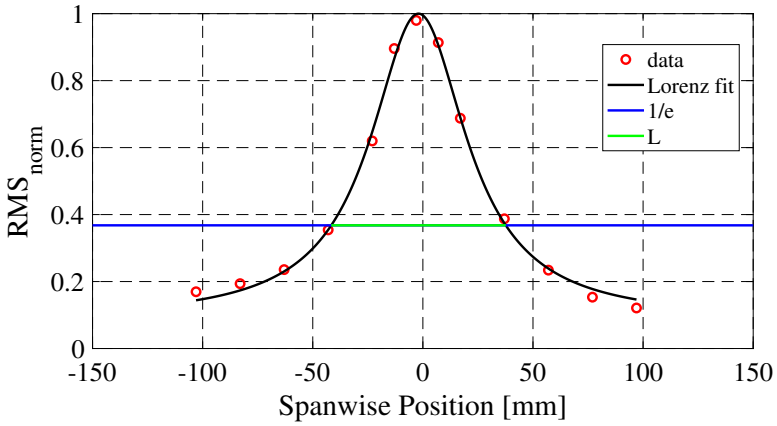

Figure 6.41: Spanwise RMS fluctuations of the needle nozzle flowfield used to determine the characteristic length of the FLDI setup. [11]

create high-frequency voltage dips in the FLDI signal because they block and scatter light when passing through the FLDI beams. The freestream measurement from a case 1 run condition, shown in Fig. 6.43, is an example of a particle-laden FLDI measurement. The blue line represents the raw voltage signal, while the black line, superimposed on the raw voltage signal, shows the reduction in particle voltage dips achieved using Matlab's filloutliers function. ([11])

The filloutlier function defined outlier voltages as points with a value of more than three median absolute deviations (*MAD*) from the median. The *MAD* of a voltage signal V is defined with the

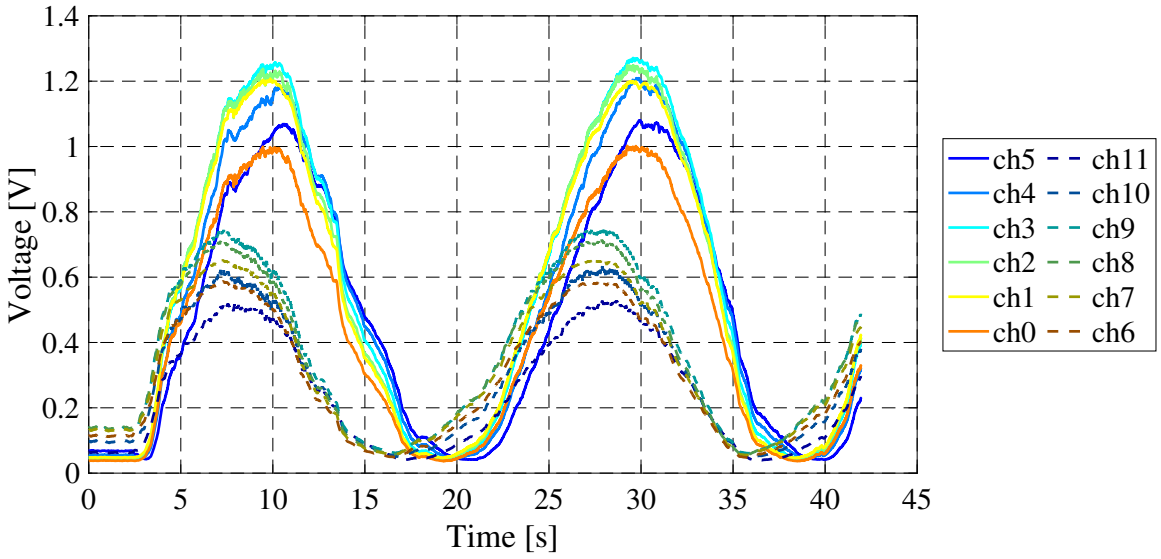

Figure 6.42: FLDI voltages measured during phase sweep calibration. [11]

equation:

$$MAD = \frac{1}{\sqrt{2} * erfcinv(3/2)} * median(|V - median(V)|) \tag{6.37}$$

where erfcinv is the inverse complementary error function. A sliding window containing 70 points was used to compute the median. Outlying voltages were replaced using a cubic spline interpolation. Unfortunately, this signal-cleaning technique only reduced large-magnitude disturbances, leaving a signal that could still be dominated by particle disturbances. Particles were most problematic in case 1 and 5 flows. For example, the results in Fig. 6.44 show freestream FLDI voltages measured during the test time of a low-enthalpy case 3 run had no signs of particles. However, evident signs of particles show up in the voltage signal plotted in Fig. 6.44a after the test time at around the 4.25 ms mark. Thinner mylar was used with higher enthalpy runs. The reduction in drag needed to accelerate thinner mylar and increased mylar incineration from higher temperatures likely contributed to the earlier arrival of diaphragm debris at higher enthalpy. Freestream FLDI measurements made at an 8.9 MJ/kg (case 6) run condition were indistinguishable from the background FLDI measurements. No discernible signal was measured at this condition because the freestream density was too low for the sensitivity of the FLDI setup. The absence of voltage dips in the 8.9 MJ/kg run condition indicates that the mylar was mostly vaporized at this condition. This evidence suggests that low and high stagnation enthalpy testing conditions are generally devoid of significant particles. However, moderate enthalpy testing conditions can have substantial quantities of particles. ([11])

Since the spectral analysis of FLDI measurements is central to this study, the influence of reducing the particle disturbance dips on power spectra is consequential. The plots in Fig. 6.45 show the power spectra of the raw and cleaned voltage signals from the case 1 run overviewed in Fig. 6.43. The sharp dips caused by debris have a width on the order 1 μs. Consequently, reducing the magnitude of the dips reduced the high-frequency power spectra. The objective of the FLDI

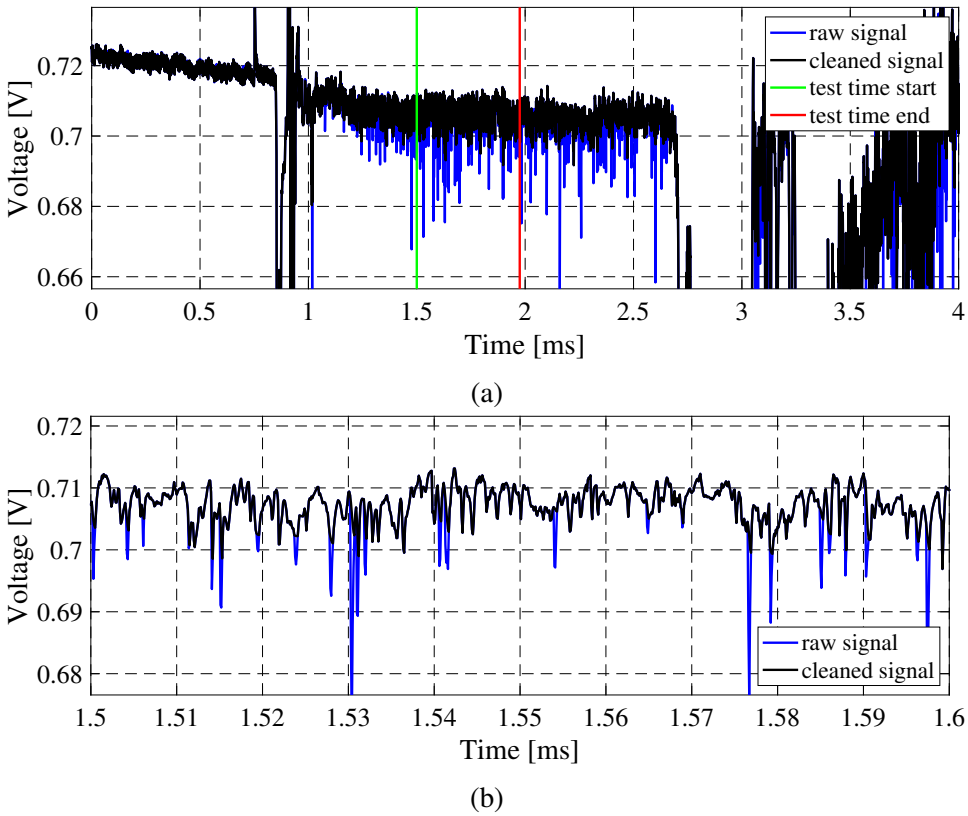

Figure 6.43: Freestream FLDI voltage plots from a 7.2 MJ/kg air run (case 1) showing a) the majority of the run and b) a zoomed-in portion of the test time, highlighting the influence of particles and the method used to clean the signals. [11]

measurements was to measure turbulent spectra. Cleaning the signals helped isolate the desired turbulent structure measurements from inaccuracies caused by particle debris. However, the high-frequency content of the freestream and post-shock FLDI measurements made in the particle-laden flows of cases 1, 2, and 5 remained dominated by particle disturbances. ([11])

After the primary experimental campaign, a test was performed with the FLDI setup to quantify the influence of particles further. The test entailed a freestream measurement at the case 1 run condition where the polarizer on the catch side of the FLDI optics was removed. Without the last polarizer, the beam pairs did not interfere, so changes in the voltage of the photodetectors could only be caused by subtle beam steering or particles blocking the laser. The results from this test are presented in Fig. 6.46 with the same format as the results from the equivalent FLDI test shown previously in Fig. 6.43. The blockage test results reveal particles had significant influence on the FLDI measurements. The similarities between the data in Figs. 6.46 and 6.43 are striking. ([11])

The power spectra of the voltages measured during the blockages test are shown in Fig. 6.47. The results show that particles can contribute significantly to the high-frequency content of an FLDI measurement. In addition, particles can have a mild influence on the low-frequency content of the FLDI measurements. It is believed that the freestream and post-shock FLDI measurements

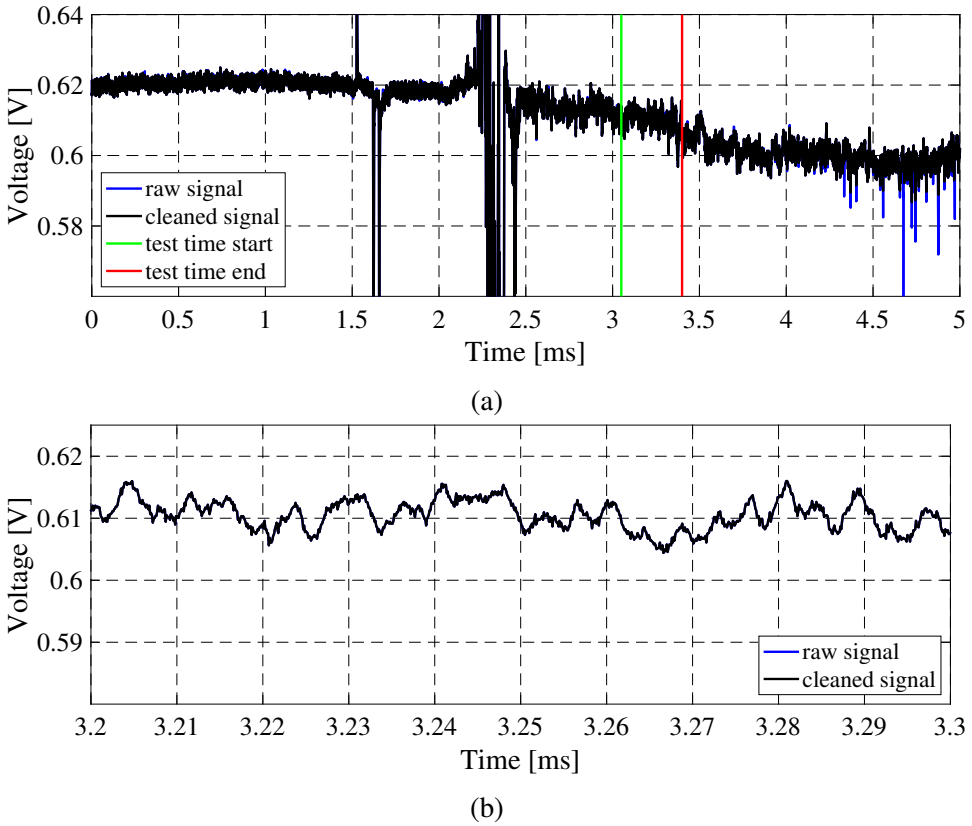

Figure 6.44: Freestream FLDI voltage plots from a 1.8 MJ/kg air run (case 3) showing a) the majority of the run and b) a zoomed-in portion of the test time, highlighting the influence of particles and the method used to clean the signals. [11]

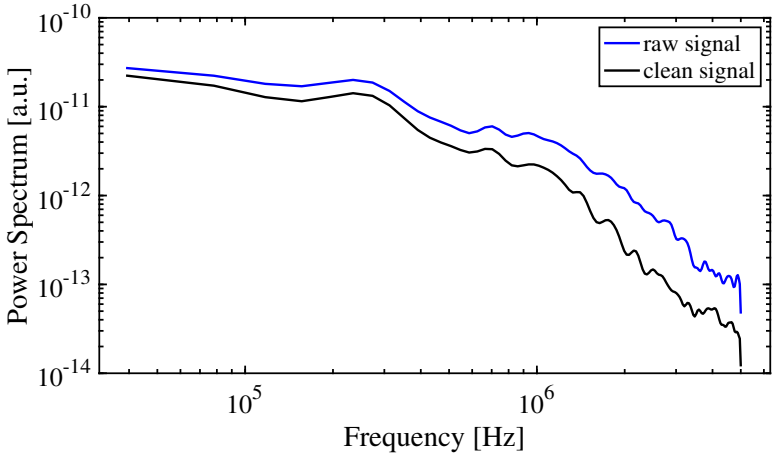

Figure 6.45: Power spectra of raw and clean voltage signals from freestream measurements performed at run condition 1. [11]

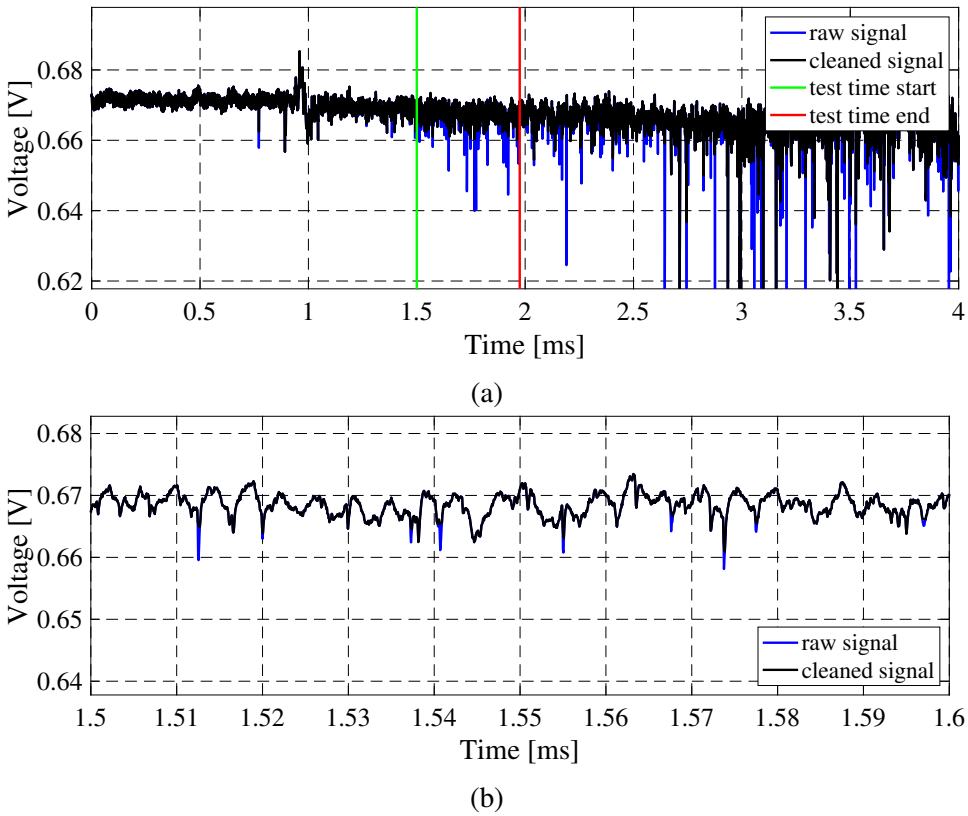

Figure 6.46: Freestream FLDI optical path blockage test at a case 1 run condition showing a) the majority of the run and b) a zoomed-in portion of the test time, highlighting the influence of particles. [11]

were impacted the most. The substantial refractive index fluctuations measured in the shear layers meant that the influence of particles was comparatively less significant in those regions. ([11])

6.5.7 OES Setup

Optical emission spectroscopy is a powerful diagnostic for high enthalpy flows. It was employed in this experimental campaign to explore how population distributions among electronically excited particles change through the turbulent shear layers of the Mach reflections. Sufficient radiation given the sensitivity of the emission spectroscopy setup was only produced during cases 1, 5, and 6. The OES measurements would have benefited from even higher enthalpy testing conditions, where emission is much brighter. However, probing higher enthalpy testing conditions in this study would have compromised the FLDI measurements due to lower freestream densities. The OES setup used in this experimental campaign, shown in Fig. 6.48, was similar to the first pathfinding OES experiments. Some of the emission generated downstream of the Mach stems would follow the path of the collimated schlieren light, reflecting off the 20.3 cm diameter, f=1.22 m, deep UV enhanced aluminum-coated mirror (Edmund Optics 32-074-522) toward the 50-50 beam splitter (Thorlabs BSW10). Although not rated for UV, the UV reflectance of the beam split-

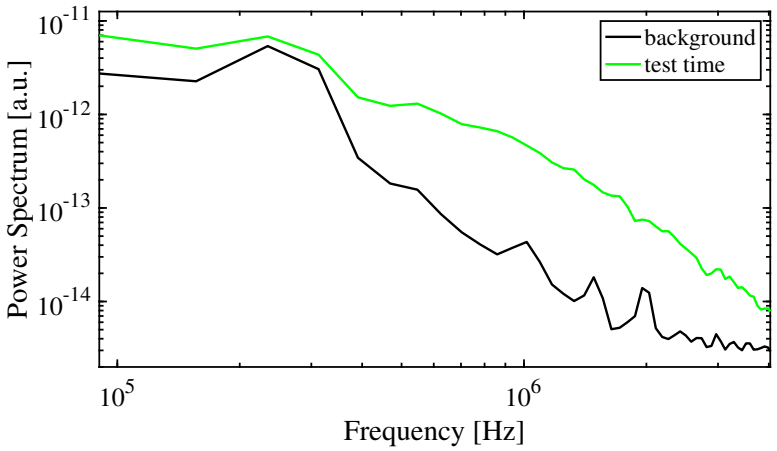

Figure 6.47: Power spectra of test time and background noise floor of voltages measured during particle blockage test. [11]

ter proved sufficient for this application. The emission light reflected from the beam splitter passed through an f=200 mm fused silica plano-convex lens (Thorlabs LA4102), through a slit (Thorlabs VA100C), and through an iris. The slit was placed where the schlieren light came to a focus, preserving the spatial accuracy of the OES measurements by ensuring the acceptance angle for light making it to the spectrometer was small. The slit of the Princeton Instruments IsoPlane160 spectrometer was set to a width of 50 μm. The light diffracted by the grating inside the spectrometer was intensified using a LaVision IRO X S20. Then, the output from the IRO was captured at 40 kHz using a Photron Fastcam SAZ. ([11])

Throughout the various runs, only three main adjustments were made to the OES setup: the spectrometer grating, the IRO gain setting, and the beam splitter orientation. Ultraviolet emission measurements targeting nitric oxide were performed using a grating with 1,800 groves/mm blazed holographic - UV optimized. All other emission measurements were performed using a grating with 1,800 groves/mm blazed to 500 nm. The gain setting on the IRO was set between 60% and 85% to maximize the signal captured during each run without overexposure. ([11])

Emission spectroscopy measurements were not performed in the same spatial location as FLID measurements during a given run because the dichroic mirror used for the FLDI would block the emission. Therefore, slight adjustments were made to the beam splitter orientation to control the OES measurement location. Adjustments were also made to the positions of the f=200 mm focusing lens, slit, and iris accordingly. Note that the reflectance of a beam splitter can change with slight changes in the angle of incidence, causing some uncertainty in the OES relative intensity calibration. The OES optics were aligned using a skinny bolt temporarily placed on the model to mark the desired measurement location. The schlieren setup was used to verify that the FLDI dichroic would not interfere with that position. In addition, the orientation of the beam splitter was adjusted so the shadow caused by the bolt in the schlieren light was aligned with the spectrometer slit. The ease of this process was a considerable advantage of spatially and temporally syncing schlieren with the OES. An example schlieren image showing the OES and FLDI measurement locations during one of the runs is shown in Fig. 6.49. ([11])

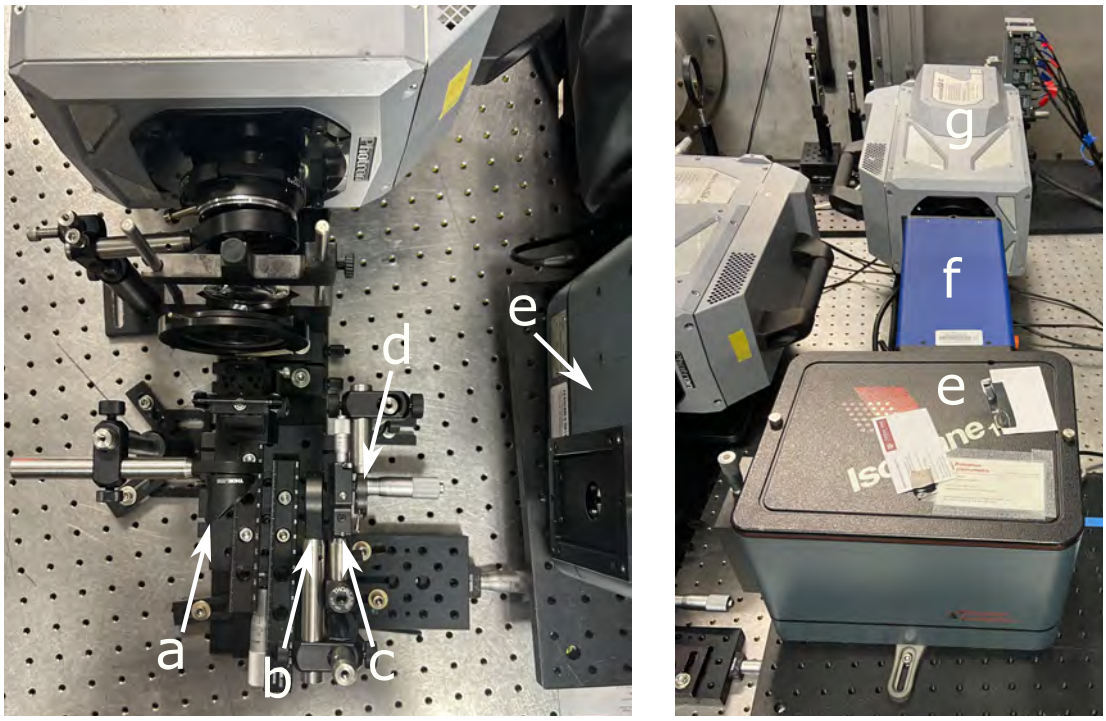

(a) (b)

Figure 6.48: OES catch optics. The labeled components are as follows: a) 50-50 beam splitter, b) f=200 mm plano-convex lens, c) slit, d) iris, e) IsoPlane 160 spectrometer, f) LaVision IRO X S20, and g) Photron Fastcam SAZ camera. [11]

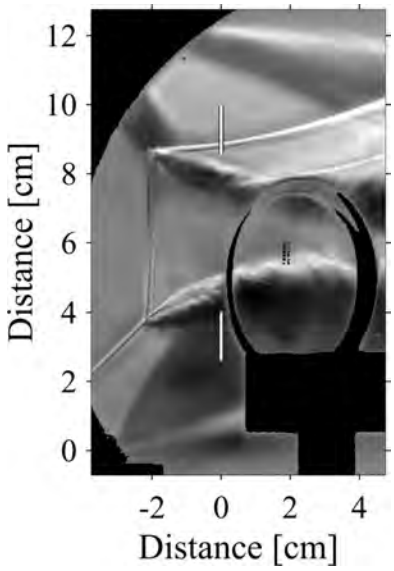

Figure 6.49: Schlieren image with the OES measurement location marked with white lines. [11]

Spatial correlations between schlieren and optical emission spectroscopy (OES) measurements were computed using calibration images captured before each run. These images of bolts positioned at the center of the model were illuminated by the schlieren LED and captured by both the schlieren and OES systems. The schlieren calibration images did not require any optic repositioning. The OES calibration images were captured by completely opening the slit of the spectrometer and configuring the grating to act as a mirror by setting it to a center wavelength of zero. An example of calibration images captured with the schlieren and OES cameras was presented in earlier. A MATLAB script was created to determine the correlation between pixels using the calibration images. The 1.27 cm thickness of the bracket on the back of the wedges was used as a length scale reference. Note paper was placed on the schlieren catch side of the model before runs to confirm that no shadow was visible, ensuring the schlieren light was aligned and collimated to accurately capture the scales of the model features. Distances could not be resolved to a scale smaller than a pixel, so the uncertainty in the spatial calibration was equivalent to the dimension of a pixel, which was about 0.28 mm for the schlieren images and 0.18 mm for the OES images. A Princeton Instruments IntelliCal configured to produce mercury emission was used for wavelength calibrations before each run. A 40 nm wavelength range was visible with the gratings and imaging hardware used in the campaign. It was impossible to capture more than one mercury line within the wavelength regions of interest. Consequently, the center wavelength of the spectrometer was systematically adjusted in 10 nm increments, and the displacement of the mercury line was used to derive a linear pixel-to-wavelength correlation. Three different center wavelength positions were used, which included the position of the center wavelength during the run. The mercury line would fill about 13 pixels, and the center pixel was evaluated using a zoomed-in visual inspection. It is assumed that the center was correctly identified to within 3 pixels each time. The wavelength scale of each pixel was approximately 0.048 nm. Therefore, the calibration process resulted in an uncertainty of about 0.14 nm. Other smaller sources of uncertainty include the consistency in the diffraction of the grating for slightly different orientations and the advertised 0.02 nm wavelength reproducibility of the AccuDrive system inside the IsoPlane160, which sets the center wavelength [328]. The measured spectra always aligned with NEQAIR spectra to within 0.3 nm. The wavelength calibrations were improved during post-processing, so measured iron emission lines aligned perfectly with NEQAIR iron spectra. The transmittance and reflectance of optics are functions of wavelength and angle of incidence. In addition, the wavelength sensitivity of lenses and mirrors is often substantial in the UV region. When making spectroscopy measurements, it is important to quantify the losses caused by each optical component using a relative intensity calibration. Unfortunately, a broadband UV light source for making relative intensity calibrations was not available until after the experimental campaign. Further, the light source that was eventually used did not have a NIST traceable calibration. As a result, the uncertainty in the calibrated spectra, although likely small, was difficult to quantify. Nevertheless, the objective of the OES measurements was to quantify changes in emission through the turbulent shear layers. Assuming the spatial variation in relative intensity was small throughout the system, the lack of a perfect intensity calibration did not render the primary objective infeasible. A single intensity calibration was simultaneously executed on the beam splitter, the f=200 mm focusing lens, the optics inside the spectrometer, and the IRO, as shown in Fig. 6.50. A BDS130 deuterium light source was used to generate the broadband UV

emission. The ratio between the spectra measured during the calibration and the typical emission curve of the BDS130 deuterium light source was used to calibrate spectral measurements for losses caused by the aforementioned optics. ([11])

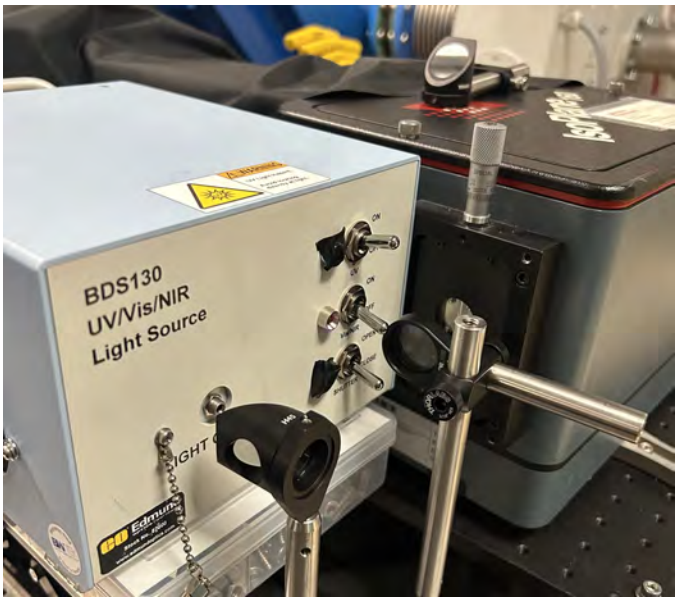

Figure 6.50: Setup used for the relative intensity calibration. [11]

An intensity correction for the schlieren mirror was computed separately using a fiber coupled to the BDS130 deuterium light source. Emission was measured using a second fiber coupled to an Ocean Optics USB2000+ spectrometer that was also fiber-coupled and used to measure the emission. The ratio between the emission measured when the deuterium was reflected off the center of the schlieren mirror and the emission measured when the fibers were placed in line with each other was used to calibrate spectral measurements for losses caused by the schlieren mirror. The schlieren light angle of incidence was approximately matched by the positioning of the fibers during the calibration. The intensity calibration curve computed for all optics in the OES setup is shown in Fig. 6.51. Better OES calibration techniques are possible with the proper equipment. Brett Cruden's 2014 NATO paper is a helpful reference for supreme spatial, wavelength, relative intensity, and instrument line shape OES calibrations Cruden [329]. ([11])

6.5.8 FLEET

This section follows from Dean [11] and Dean et al. [16]. Femtosecond laser electronic excitation tagging (FLEET) is a nonintrusive molecular tagging technique developed at Princeton University with a demonstrated ability to tag and follow lines and patterns in nitrogen and air flows without requiring seeding Michael et al. [330], Miles et al. [331]. The tagging process involves the interaction of a high-intensity, short-pulse laser with molecules. A femtosecond laser is used for multiphoton dissociation of the molecular species to create long-lived fluorescent tracers that are

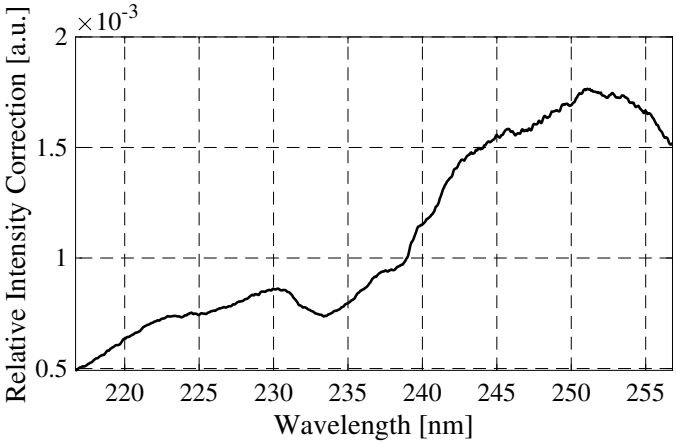

Figure 6.51: Relative intensity calibration curve used to correct UV OES spectra for losses caused by optics. [11].

imaged several microseconds later with a single time-gated intensified camera. A simplified energy–level diagram for molecular nitrogen, the target molecule dissociated to create fluorescence, is shown in Fig. 6.52. A relatively long timescale delay of tens to hundreds of microseconds between the dissociation of the nitrogen caused by the femtosecond laser and fluorescence emission occurs due to the time it takes for dissociated nitrogen atoms to find each other and recombine. The recombination produces nitrogen molecules excited in the B-state. Relaxation transitions of the excited B-state molecules to the metastable A-state result in N_2 first positive emission. The delay in emission allows time for a line of dissociated N_2 produced by a femtosecond laser pulse to convect downstream. Velocity estimates are obtained by measuring the displacement between the position of the laser beam and the location where the fluorescence emission is captured at a known time delay after the laser pulse. The possibility of capturing FLEET data at kilohertz rates and following the real-time evolution of continuous line patterns at intervals as short as microseconds has been demonstrated in laboratory and field conditions. Since FLEET emission lines in nitrogen are significantly stronger than in air [330], the application of this technique is particularly suitable for large-scale nitrogen-based ground test facilities [332, 333, 334].

Spectral and temporal filtering enables the use of FLEET in the presence of plasma emission, such as in arc jet tunnels [335], expansion tunnels, and other high enthalpy facilities. In this experimental campaign, FLEET was used to characterize freestream flow velocities inside the HXT. Before the campaign, two ISO-KF 50 flanges were added to the HXT test section doors to allow easy installation of standard vacuum viewports for laser diagnostics. The new, small optical access ports, shown on the left of Fig. 6.53, were located immediately downstream from the nozzle exit, allowing freestream flow measurements while other experiments occur downstream. The window material was KODIAL Glass (Lesker QF50-200-VP). ([11, 16])

The laser source used to dissociate nitrogen molecules was a Ti:Sapphire amplified system delivering 800nm, 90fs pulses at 1kHz. The laser beam was focused in the middle of the tunnel using a spherical lens with a focal distance of 80cm, shown in front of the small window in Fig. 6.53. The FLEET emission was captured by the detection system shown above the tunnel in Fig. 6.54.

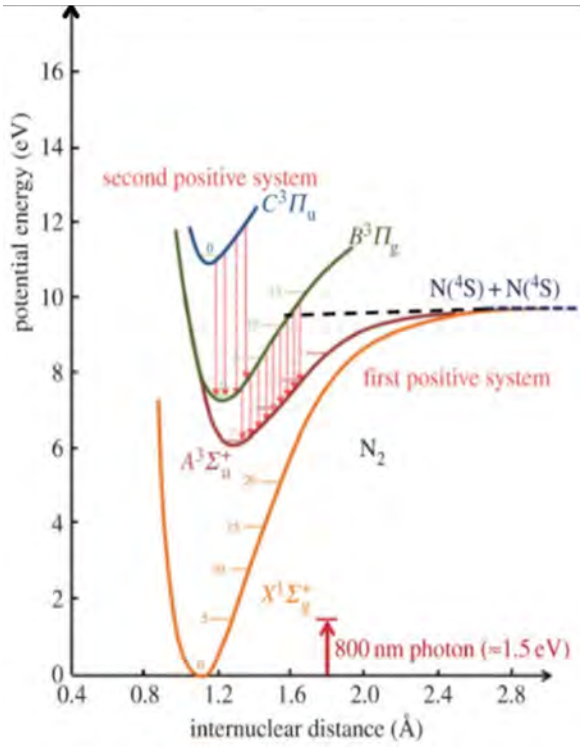

Figure 6.52: FLEET mechanism. N atom recombination following molecular dissociation results in a delayed B $\rightarrow$ A emission. [11].

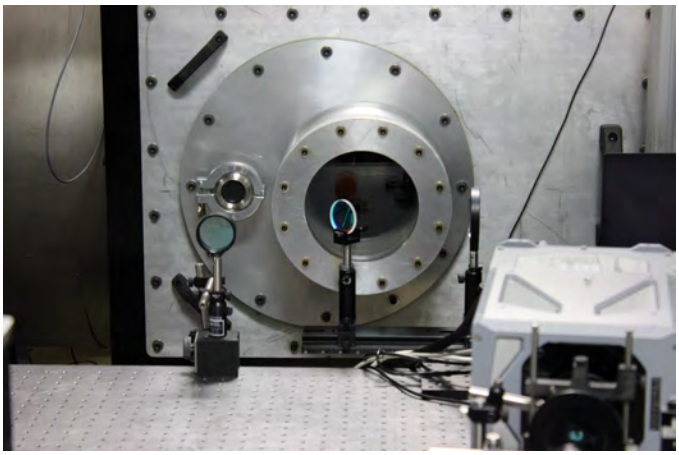

Figure 6.53: View of the test section door showing the small viewport on the left used for FLEET measurements. [11]

The PCO Dicam fast gated intensified camera was equipped with a Nikkor F/2 200mm lens, allowing imaging from a distance of approximately 1 m with a pixel resolution of 50 microns/pixel. Fig. 6.55 shows the system imaging a grid card used to determine the length scale, which was 21.2 $\pm$0.6 px/mm. ([11, 16])

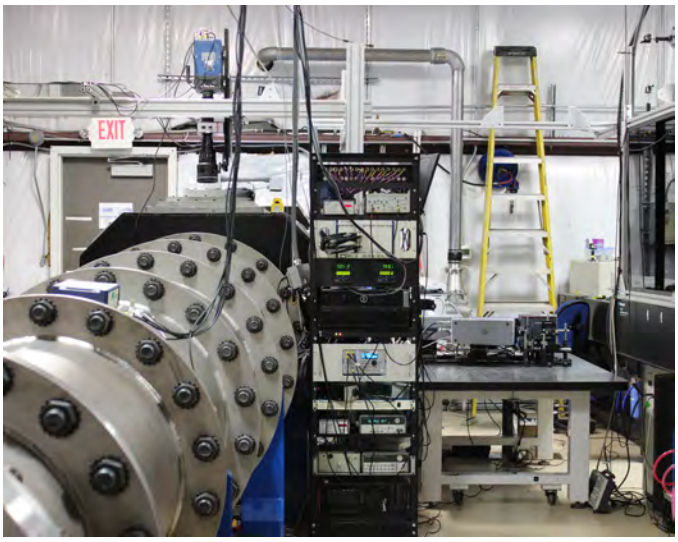

Figure 6.54: Image showing the camera mounted above the test section and the femtosecond laser in the back right corner. [11]

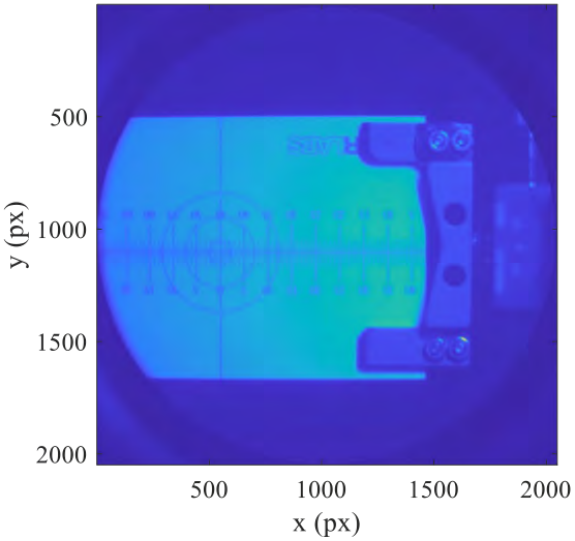

Figure 6.55: Image of grid card used to determine length scales. [11]

The camera looked through a 20.3 cm diameter fused silica window (Edmund Optics 43434). Since test times were on the order of 1 ms, only 1 FLEET image was captured during each test time. Nevertheless, 11 images were stored during each run because the velocity conditions before and after the test times are useful for validating full simulations of the HXT facility. FLEET images captured during an air run with a stagnation enthalpy of 1.8 MJ/kg (case 3) are shown in Fig. 6.56. The image in Fig. 6.56a marks the position of the laser, captured before running the facility with the test section at a favorable pressure for the nitrogen emission. The other images in Fig. 6.56

show the displacement of the nitrogen emission line at 1 ms intervals relative to the test time. Since the FLEET system operated at 1 kHz and the test times in the HXT were on the order of 1 ms, it was critical to time the laser and camera system with the HXT tunnel flow. A system of pulse delay generators triggered with a PCB 132B38 shock time of arrival sensor were used to trigger the laser and the intensified camera, ensuring a fleet measurement would occur in the center of each test time. ([11, 16])

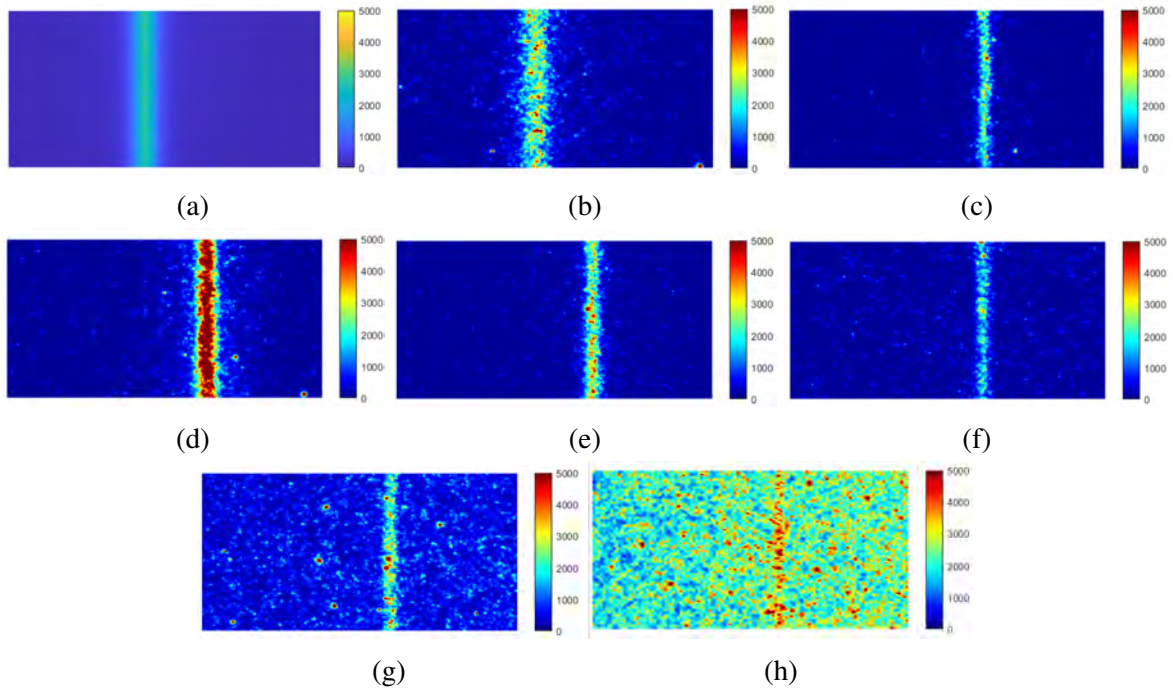

Figure 6.56: FLEET images with colorbars showing intensity captured a) before the run, b) -1 ms, c) -1 ms, d) 0 ms, e) 1 ms, f) 2 ms, g) 3 ms, and h) 4 ms relative to the test time. The flow direction was left to right. [11]

7. RESULTS

7.1 Preamble

The descriptions or results presented in this section were drawn from selected dissertations, theses, and articles associated with the execution of this project: McManamen [1], Buen et al. [2], McManamen et al. [3], Siddiqui [4], [5], Siddiqui et al. [6], Broslawski [7], Dean et al. [8],Bryan et al. [52], Bryan et al. [10], Dean [11], Broslawski et al. [12], Broslawski et al. [13], Broslawski et al. [14], Smotzer et al. [15], and Dean et al. [16]. The original citations are also included in the subsequent text.

7.2 Hypersonic Boundary Layer with Thermal Nonequilibrium

7.2.1 Boundary Layer Solver Results

The results described in this section follow from Broslawski [7]. The results of the boundary layer solver are shown below, along with a discussion of their implications.

7.2.1.1 Grid Convergence Study and Validation

Simulations were run for both laminar and turbulent boundary layers, with the Cebeci-Smith model [43] used for the latter. The solution domain covered $25-125$mm in the streamwise direction and $0-25$mm in the wall-normal direction with transition forced at the test article's trip location, 63.5mm. The turbulent grid used Malik clustering with half of the points placed below the critical value of 3mm; this was selected after preliminary testing with the laminar boundary layer. Standard air at the test conditions was used. The predictor-corrector tolerance was set to 1×10^{-6}. A total of three different grids were produced for both the implicit and explicit schemes, coarse, medium, and fine; thus there were six in total. The stability requirements of the explicit scheme required far finer streamwise steps than the implicit scheme, and limited the wall-normal resolution. These grids are defined in Table 7.1. Note that in the streamwise direction, the streamwise step within the domain was the controllable parameter, not the number of streamwise points. In the wall-normal direction, the number of wall-normal points was used as the controllable parameter because clustered spacing made the wall-normal step a variable. ([7])

Grid	**Implicit**		**Explicit**	
	$X\times Y$	ΔX (mm)	$X\times Y$	ΔX (m)
Coarse	51×50	2	10001×50	1×10^{-2}
Medium	251×250	0.4	20001×75	5×10^{-3}
Fine	1251×1250	0.08	40001×100	2.5×10^{-3}

Table 7.1: Grids for convergence study; here X denotes the streamwise coordinate, and Y denotes the wall-normal coordinate.

The results of the grid convergence study are shown in Table 7.2. The fidelity of a grid was quantified by comparing its results to those of the finest mesh, which was assumed to be the most accurate. For example, for the coarse/turbulent/implicit grid the u, v, and T data from the finest turbulent, implicit run were interpolated to match the coordinates of the test grid, then the Euclidean norm of the absolute value of the difference was calculated. The data were taken from the ends of the domains to allow errors to accumulate and were normalized by the edge values. This process mirrored the predictor-corrector convergence procedure in the boundary layer solver itself, and these three variables were chosen as they were the primary variables calculated directly from the conservation equations; again, v was normalized by u_e as v_e could be near zero. From the results in Table 7.2, it seemed that in order to keep the cumulative error below 1% the computational effort required for the medium grid was necessary. This grid performed well for all four combinations tested, and should be used for future simulations. A more thorough grid convergence study, one to test if fewer points could be used or the error had become asymptotic, was deemed unnecessary for the efficiency and fidelity required here. ([7])

Scheme	**Coarse**		**Medium**	
	Laminar	Turbulent	Laminar	Turbulent
Implicit	0.81%	1.57%	0.12%	0.08%
Explicit	0.37%	1.00%	0.12%	0.24%

Table 7.2: Grid convergence study results.

Validation was conducted analogously to the grid convergence tests. The reatment was the same as for the grid convergence study, with the self-similar data taking the place of the fine grid. Unfortunately, this approach was applicable only to laminar data; these results would need to be compared against the experimental data (schlieren, IR thermography, Pitot pressure, *etc.*), and this was periodically done throughout this chapter. The results are shown in Table 7.3. Careful inspection revealed inherent differences between the finite difference and self-similar approaches. Consider the implicit, laminar case. Table 7.2 reports a difference between the medium and fine grids of 0.12%. Now, in Table 7.3 the differences between the medium and fine grids and the self-similar solution were 1.1% and 1.23% respectively; thus the fine grid was 0.13% more inaccurate than the medium grid, nearly identical to the 0.12% difference between the two grids themselves. The same pattern was repeated throughout the data; for example, the medium/laminar/explicit" case was 0.12% off from the fine/laminar/explicit grid, and was 0.10% more accurate than the fine grid as compared to the self-similar solution. This suggested there was some baseline discrepancy between the self-similar and finite difference calculations, where v was identified as the likely source. Such a systematic error may be exacerbated by finite differencing with finer and finer grids, which somewhat diminished the efficacy of the studies at hand; interpolation between the self-similar and fine grids was another potential source of error. Looking at the overall objective

and balancing the comparisons between the fine and self-similar grids, it was sufficient to say the medium grid provided a good trade off between speed, resolution, and fidelity to both optimized finite difference and self-similar solutions. ([7])

Grid	Coarse	Medium	Fine
Implicit	0.55%	1.10%	1.23%
Explicit	0.67%	0.83%	0.93%

Table 7.3: Validation study results.

7.2.1.2 Full Boundary Layer Simulations

Simulations were run studying the effect of the boundary layer, numerical scheme, and heat flux method. The domain covered $25-405$mm in the streamwise direction and $0-25$mm in the wall normal direction. For turbulent simulations, transition was forced at 63.5mm, matching the trip location on the physical test article. For all tests, the "Medium" grid was used (see Table 7.2); though the streamwise step size stayed the same, now there were 951 and 76001 streamwise grid points due to the larger domain. For turbulent codes, the "Cebeci-Smith" eddy viscosity model was exclusively used, though the heat flux model varied between the gradient diffusion and AEF approaches. The Predictor-Corrector tolerance was set at 1×10^{-6}. The simulated flow matched the test conditions shown in Table 4.1: $M=5.7$; $P_o=496.4$kPa; and $T_o=430$K. These provided a flow Reynolds number of $Re_\infty=5.51\times10^6/$m. The discrepancy between this Reynolds number and that calculated by the NALDAQ was due to the low-temperature correction for viscosity in the boundary layer solver which was absent from the NALDAQ; it was acceptable because it only meant the code better matched the actual flow physics, not the tunnel's estimation thereof. The test article's 2.75° half-angle was included, and the calculated shock angle was 11.95°. The pre- and post-shock conditions are summarized in Table 7.4. Preliminary IR thermography data showed an isothermal wall condition at 350K was an appropriate boundary condition. ([7])

Location	M	P (Pa)	T (K)
Pre-shock	5.7	430.07	57.35
Post-shock	5.35	626.89	63.97

Table 7.4: Simulation pre- and post-shock conditions. [7]

The results are shown in Figures 7.1 through 7.4. The 2D plots show the expected behavior, that the boundary layer grew with $\sqrt{x}$. The v data required some analysis because there was a

jump at the leading edge and then decay along the plate, as well as nonphysical results exactly at the numerical trip. The discontinuity at the start of the domain was due to a discrepancy between the self-similar prediction for v at the inlet plane and the finite difference result at the next location; Figure 7.1 shows it mostly dissipated within a few iterations. The streamwise decay in the freestream and noise at the trip location were both attributed to a lack of a freestream boundary condition for the conservation of mass equation. Consider the laminar case. As the boundary layer grew, the mass flow at a single plane decreased. In order to prevent violating the conservation of mass, less mass could be ejected out of the vertical domain by v. Again, v was the only conservation variable which could perform such a task because it was not constrained by a freestream boundary condition. Thus v_e could change along the domain. This effect was exacerbated at the trip location, where the boundary layer instantly, artificially, and dramatically grew. However, while the total boundary layer thickness increased, the slowest portion suddenly shrunk, forcing v_e to "suck in" mass from the upper boundary and providing nonphysical negative velocities. Eventually, the code corrected, v_e was effectively re-initialized for a turbulent boundary layer, and the streamwise decay occurred once again, this time more rapidly due to the faster-growing turbulent boundary layer. A numerical transition process would help smooth the streamwise v component, but because $v \ll u$ and the error in v was normalized by the much larger u_e, v was not very impactful and convergence was achieved even with some error. ([7])

The plots of heat flux (7.1(e) through 7.4(e)) show several interesting trends. To begin, it was immediately clear that the laminar boundary layer provided less heating than the turbulent one. This was entirely in line with theory and owed to the increase in dissipation due to the presence of eddy viscosity. The general decay in both laminar and turbulent cases owed to the growth of the boundary layer; as the thermal boundary layer thickened, the gradients near the wall became less severe and thereby reduced the heat flux. For the velocity profiles of laminar boundary layers, $\delta(x) \propto \sqrt{x}$ [19], so the expected trend for the thermal boundary layer was fastest growth near the leading edge followed by a leveling off along the plate. Therefore heat flux should decay rapidly near the leading edge before reaching a "steady state" towards the end of the plate, which was exactly what the data show. The discontinuities and bumps in heat flux at the transition point were due to the harmonic nature of the conservation equations and needed to be corrected with numerics too advanced for the present code. The heat flux data could be used to check the state of the boundary layer. IR thermography could provide the heat flux along the plate, and if the value better matched the turbulent prediction, then one could expect the flow to be turbulent and *vice versa* for the laminar prediction; where the heat flux quickly jumped between the two lines denoted transition. As was expected from the DNS [24], "AEF" and "Gradient Diffusion" approaches for this ZPG environment predicted similar results for the wall normal component of the heat flux, as well as for the off body variables; studying the streamwise component of heat flux would have shown a larger discrepancy. The plots of boundary layer thickness (7.1(f) through 7.4(f)) were useful for sizing the boundary layer before schlieren, PLIF, and Pitot measurements. It was useful to have an estimate of the boundary layer size before setting up these techniques to ensure they captured the entire region; once the measurements were complete, they could be used to validate the code. For the laminar case, the $\delta_{99.5\%}$ boundary layer thickness was calculated from u, T, and H_o; for the turbulent cases, the latter was omitted due to its esoteric nature and the complex shape

of the total enthalpy profile. ([7])

The boundary layer profiles 405mm from the leading edge for several key variables are provided and compared in Figures 7.5 and 7.6. The former shows that in practice there was little to choose between the implicit and explicit turbulence schemes, and that the AEF model did provide some alteration to the profiles, most notably the one using the total enthalpy. The discrepancy in v_e would be unexpected if not for the preceding analysis of the sensitivity of this parameter to any change in boundary layer thickness and its loose convergence criteria. The expected trends such as thicker turbulent boundary layers and thin near-wall regions were correctly manifested. Figures 7.5(c) and (f) show how the Ideal Gas Law, with a constant pressure, causes n to exactly mirror T; this had implications for PLIF, where the signal was dependent on the number density of the gas. ([7])

By using the van Driest effective velocity, Figure 7.6 shows the distinct regions of the turbulent boundary layer 405mm from the leading edge. The viscous sublayer existed below $y^+ \lesssim 10$ ($y \lesssim$ 0.59mm), the buffer layer between $10 \lesssim y^+ \lesssim 30$ ($0.59 \lesssim y \lesssim 1.8$mm), the log layer between $30 \lesssim y^+ \lesssim 100$ ($1.8 \lesssim y \lesssim 5.9$mm), and the wake beyond that; the wake was weak for the low-Reynolds number boundary layer simulated, though in the experiment it would be strong due to the presence of the trips. These data were useful for guiding subsequent analyses, especially Pitot experiments. Despite having the proper shape and slope, the data appear to under predict velocity in the log layer. Possible reasons for this include poor simulation of the transition process, improperly accounting for the low densities in the ACE tunnel, or overprediction of τ_w. Of these challenges, the lattermost seemed to be the most likely cause for the disagreement. It will be shown in the Pitot pressure and PLIF velocimetry results (Sections 7.2.3.5 and 7.2.5.3, respectively) that by the "Back" test location referenced in Figure 7.6 $\tau_w \approx 18$Pa to get the boundary layer profile to sit on the theoretical line for the log layer. However, the simulation's results, shown in Figure 7.7(a), put $\tau_w \approx 19.6$Pa. This increased the friction velocity, which in turn decreased u^+_{eq}. Increasing the order of the differentiation in calculating $\tau_w = \mu_w \frac{du}{dy}$ and checking the numerics by differentiating without Malik mapping did not resolve the issue. Hard-coding $\tau_w = 18$Pa did yield better agreement with the theory, though it was still imperfect. Ultimately it was decided that for the fidelity expected and required of this in-house boundary layer solver, and remembering program's main goals were to provide order-of-magnitude estimates of flow properties through the boundary layer and to work as an educational tool for turbulence modeling, the agreement was deemed sufficient. The Stanton number is also shown in Figure 7.7(b) for completeness, as Stanton number was the main heat flux parameter discussed in subsequent sections. The wall and off body data are directly compared to the experimentally measured values in Section 7.2.6. ([7])

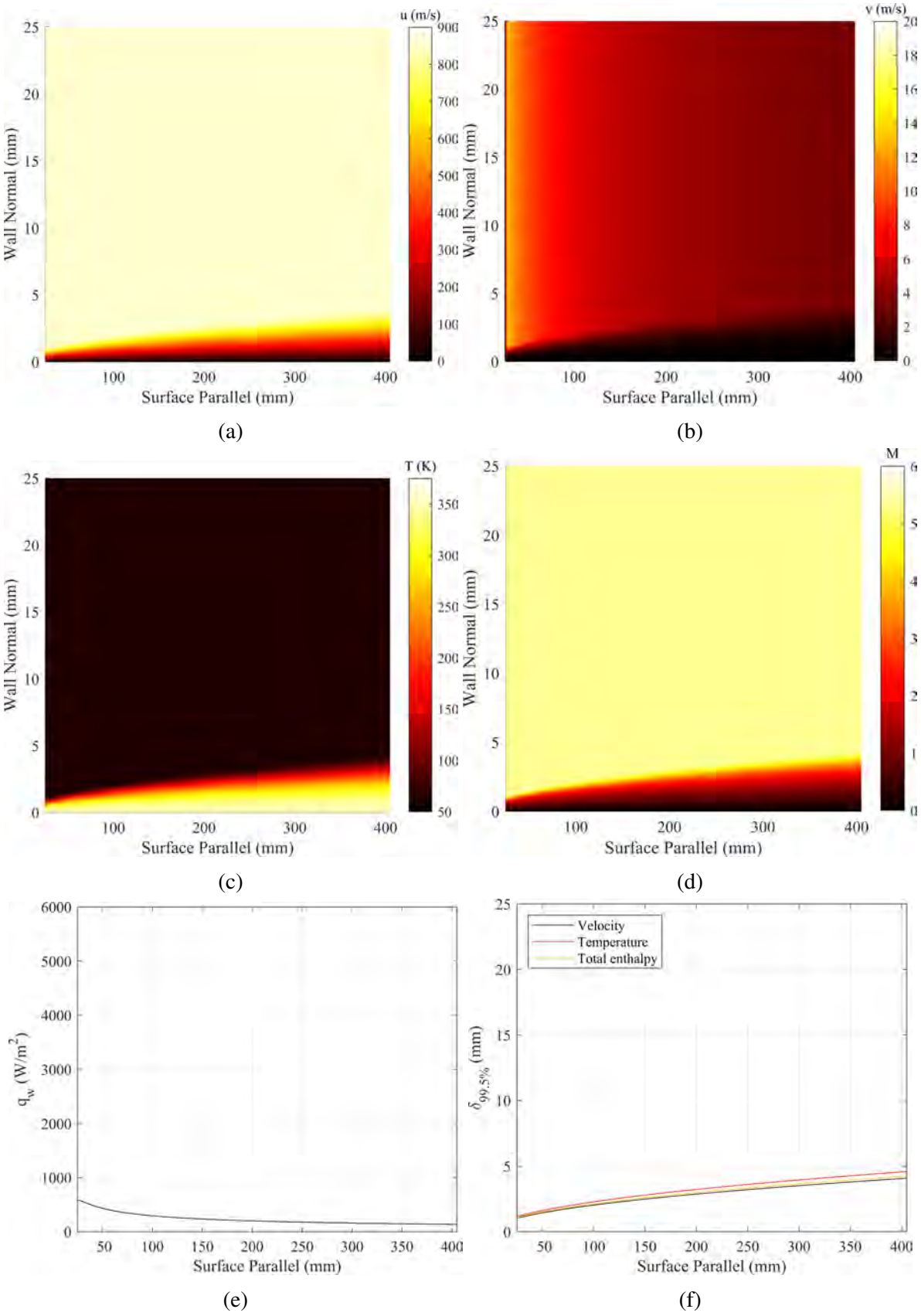

Figure 7.1: Laminar boundary layer implicit simulation results. [7]

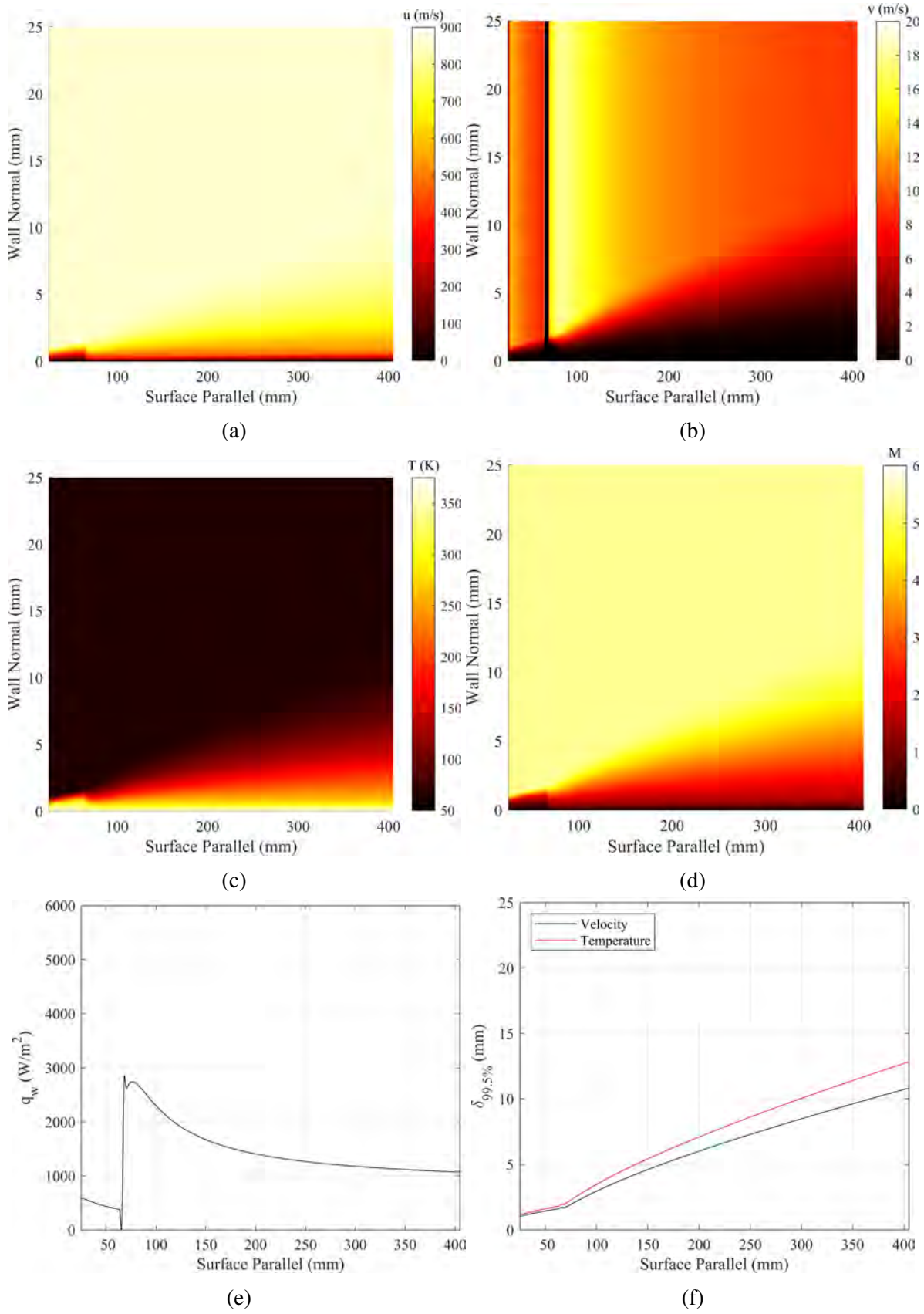

Figure 7.2: Turbulent boundary layer implicit simulation results. [7]

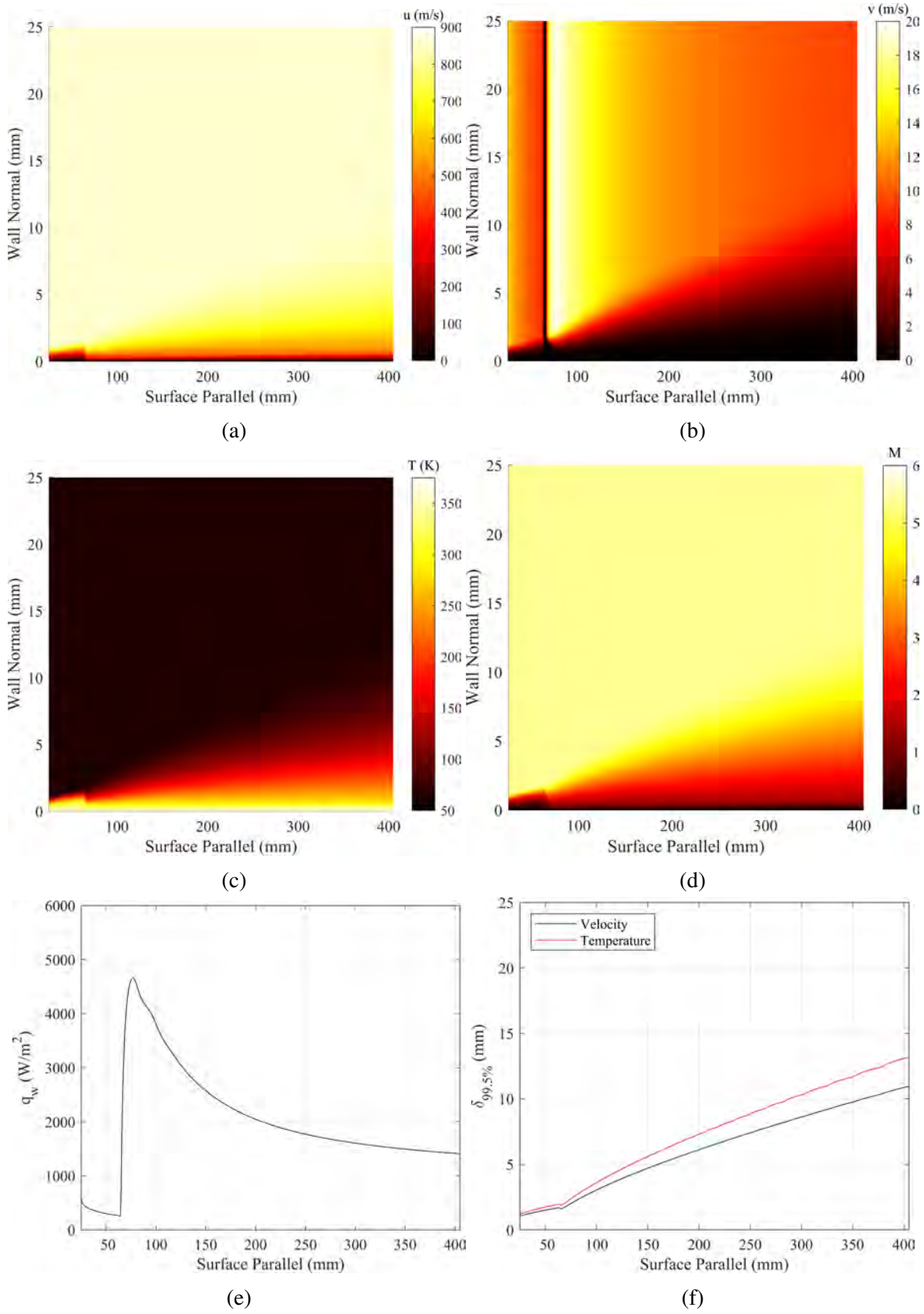

Figure 7.3: Turbulent boundary layer explicit simulation with gradient diffusion heat flux model results. [7]

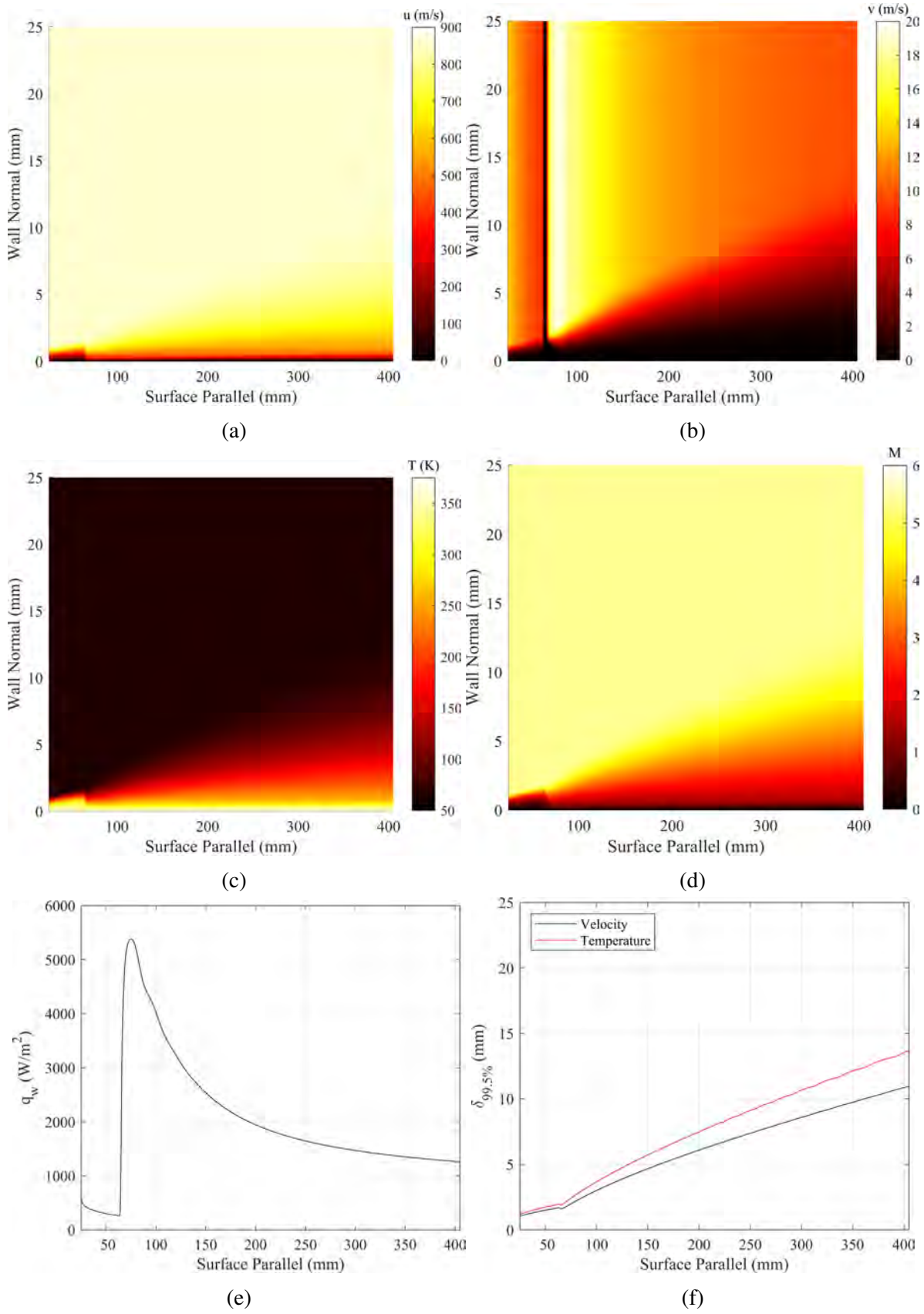

Figure 7.4: Turbulent boundary layer explicit simulation with AEF heat flux model results. [7]

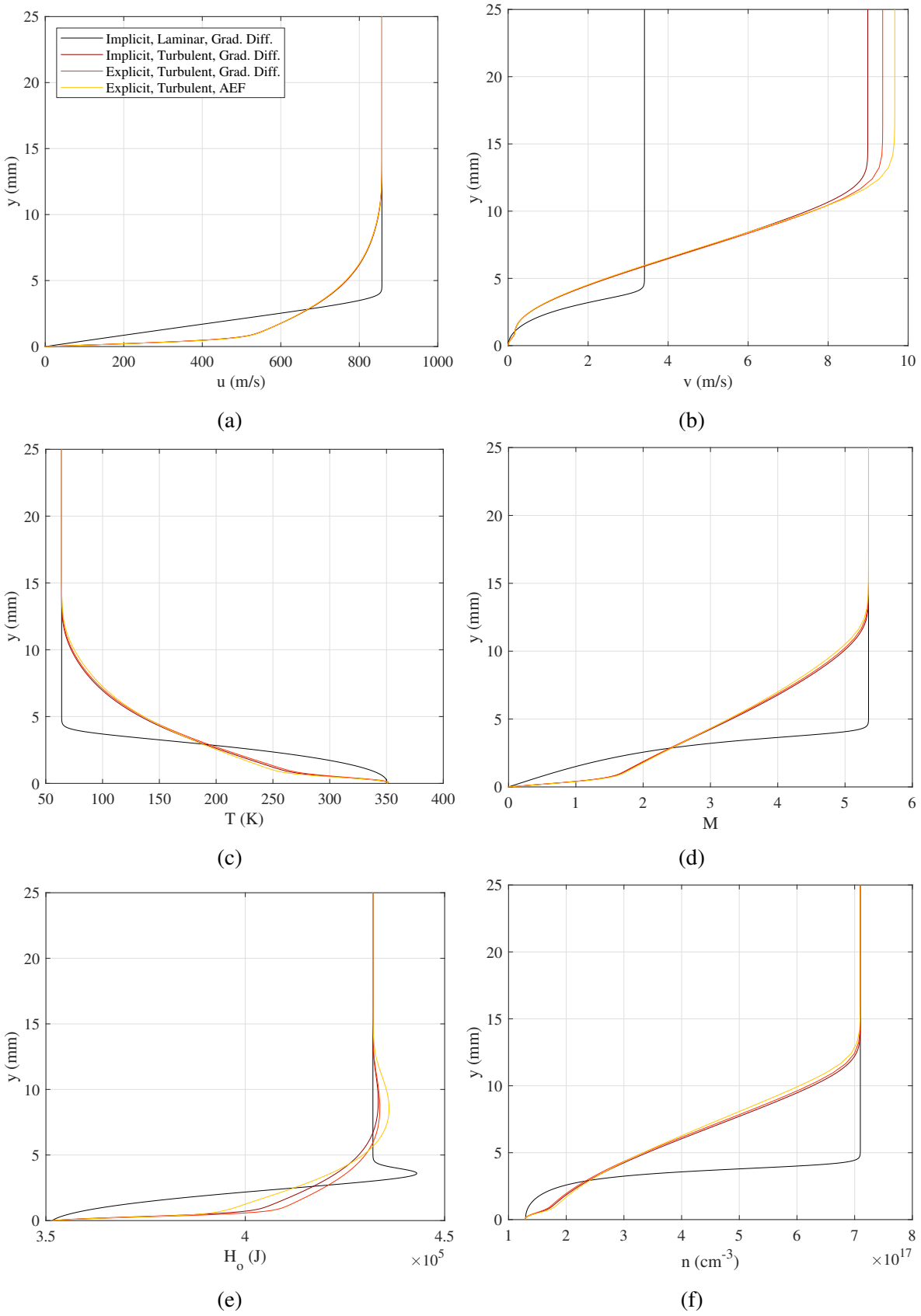

Figure 7.5: Simulation boundary layer profiles at 405mm; same legend applied to all figures. [7]

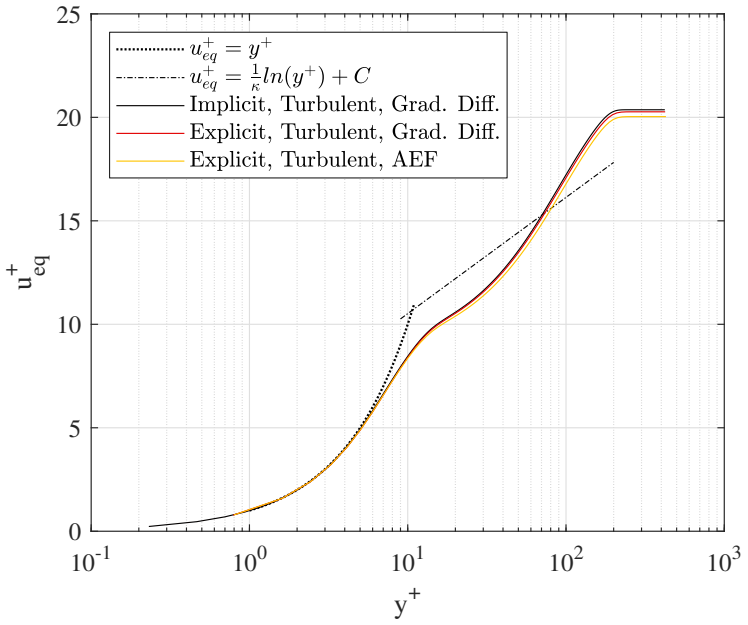

Figure 7.6: Simulated velocity boundary layer profiles at 405mm with inner variable scaling. Following Clauser [40], $\kappa = 0.41$ and $C = 4.9$. [7]

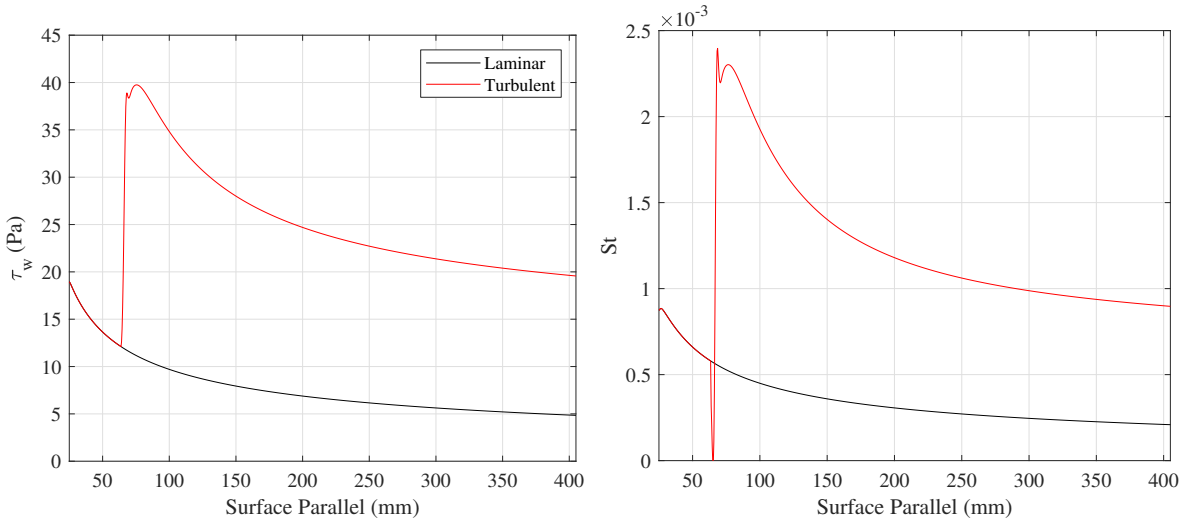

(a) (b)

Figure 7.7: Plot of wall shear stress and Stanton number from simulations; same legend applies to both figures. [7]

7.2.2 Test Article Characterization

The results described in this section follow from Broslawski [7]. Before beginning with the main experimental campaigns, several tests were conducted to aid with the development of the test article, characterize its behavior, and study its baseline performance. While these tests were preliminary, the data play a crucial role in the broader research objectives. The experiments described here include plasma characterization via its power performance, trip sizing with IR thermography, and leading edge uniformity checks using surface profilometry. ([7])

7.2.2.1 Plasma Characterization

This section covers the development of the glow discharge used for the remainder of the tunnel runs in this report. The test matrix is provided in Table 7.5 and includes four different experiments. The first five "Power characterization" runs studied the effect of varying system parameters like Reynolds number, the power supply voltage, the power supply current, and the Reynolds number. The next five runs studied the breakdown voltage ("Breakdown characterization") and the appearance of the plasma from both the top ("Visualization") and side ("Cathode layer") to identify interesting features, attempt to measure the thickness of the cathode layer, determine if the glow discharge was normal or abnormal, and to test the effect of Reynolds number on these parameters; these experiments were repeated for the turbulent boundary layer in the final three runs to study the effect of the trips. ([7])

Additionally, the polarity of the electrodes (cathode upstream of anode and *vice versa*) was also varied. Runs 4469-4475, 4483, and 4476 all had the cathode upstream of the anode; indeed all the runs were initially performed in this configuration, but those not just listed (after Run 4483) were repeated with the final "cathode downstream" orientation. This change was unplanned and a direct result of the preliminary testing reviewed here, so while it was not included in the test matrix its effects are discussed below. The only circuit data collected was the power supply's current and voltage, both of which were linked to the NALDAQ by a synchronous trigger. However, because the ballast resistance was measurable and it was the only other load besides the plasma, one could use Ohm's Law to determine the plasma's voltage and then $P = IV$ to calculate its power. It is important to be clear, this power represented the rate of all energy loss across the electrodes. It could not differentiate between Joule and cathode heating, nor energy deposited into internal *versus* external modes (η). An effort to approximately differentiate the degrees of Joule and cathode heating is included below. Here it is noted that the visual data taken in Runs 4547, 4483, and 4549 to attempt to measure the size of the cathode layer and the effect of Reynolds number on it were largely inconclusive due to the challenging orientation of the camera (looking directly at the side of the plate) and diffuse nature of the plasma. The information lost could be partially recovered via other runs and the theory provided in Section 2.3, but no attempt was made to do so as it was of secondary importance. ([7])

The analysis begins with a study of the effect of the ballast resistance R_b captured in Runs 4470, 4469, and 4474. For these tests the voltage was slowly increased until the plasma was ignited, then increased until the current approached the power supply's upper limit of 100mA; this meant the supply was "voltage limited". Here the data were truncated to only include the "plasma on" results. Following the convention in literature [97, 98, 336], it was illuminating to plot the variables

No.	Experiment	Trip	Power Supply	Reynolds ($\times 10^6/m$)	Run/Date
1	Power characterization	Laminar	I_{Max}, V_{Sweep}, $R_b = 10\text{k}\Omega$	6	4470, 9/15/2020
2	Power characterization	Laminar	I_{Max}, V_{Sweep}, $R_b = 20\text{k}\Omega$	6	4469, 9/15/2020
3	Power characterization	Laminar	I_{Max}, V_{Sweep}, $R_b = 30\text{k}\Omega$	6	4474, 9/16/2020
4	Power characterization	Laminar	I_{Sweep}, V_{Max}, $R_b = 10\text{k}\Omega$	6	4472, 9/15/2020
5	Power characterization	Laminar	I_{Max}, V_{Max}, $R_b = 10\text{k}\Omega$	$4.75 - 6.5$	4475, 9/16/2020
6	Breakdown measurement	Laminar	I_{Max}, V_t, $R_b = 10\text{k}\Omega$	6	4542, 10/7/2020
7	Cathode layer visualization	Laminar	I_{Max}, V_{Sweep}, $R_b = 10\text{k}\Omega$	6	4547, 10/8/2020
8	Cathode layer visualization	Laminar	I_{Max}, V_{Max}, $R_b = 10\text{k}\Omega$	$4.75 - 6.5$	4483, 9/17/2020
9	Visualization to determine normal or abnormal glow	Laminar	I_{Max}, V_{Sweep}, $R_b = 10\text{k}\Omega$	6	4544, 10/8/2020
10	Visualization to determine normal or abnormal glow	Laminar	I_{Max}, V_{Max}, $R_b = 10\text{k}\Omega$	$4.75 - 6.5$	4476, 9/16/2020
11	Breakdown measurement	Turbulent	I_{Max}, V_t, $R_b = 10\text{k}\Omega$	6	4541, 10/7/2020
12	Cathode layer visualization	Turbulent	I_{Max}, V_{Max}, $R_b = 10\text{k}\Omega$	6	4549, 10/9/2020
13	Visualization to determine normal or abnormal glow	Turbulent	I_{Max}, V_{Sweep}, $R_b = 10\text{k}\Omega$	6	4545, 9/17/2020

Table 7.5: Plasma characterization test matrix.

against current; this acted almost as a normalization because it removed the temporal dependence and related everything to a fundamental circuit parameter. The results are shown in Figure 7.8. These data revealed several interesting trends. Consider Figure 7.8(a). For the 30kΩ resistor, the slope was high enough that the power supply's 3000V limit was reached before the current hit the 100mA limit. Decreasing the ballast resistance to 10kΩ reduced this slope to the point that the current's limit was reached before even half of the available voltage was requested. As one would expect and Figure 7.8(b) confirmed, the case with highest voltage at a set current had the highest power supply usage; the exponential shape of the curves, however, was surprising and must be

somehow due to the plasma. Figures 7.8(c) and (d) reveal the plasma was completely unaffected by the ballast resistance. This implied the plasma was the driving factor for the circuit's behavior, and was itself a function of the flow. It seemed that for the configuration used, the original "cathode upstream" polarity, the present flow could only sustain a voltage drop of $350 - 380$V regardless of the current used; recall that the slight rise in voltage was not unexpected, even for normal glow discharges. Now, because the plasma voltage was effectively a constant and the current was increasing, it made sense Figure 7.8(d) displays a linear dependence between power and current. Synthesizing the results, if one wanted to increase the plasma power, one would need a higher current power supply. Current could then be increased until the power supply's voltage limit was reach, at which time a smaller ballast resistance could be used; this could continue until either the ballast resistor became impractically small or the plasma constricted into an arc discharge. ([7])

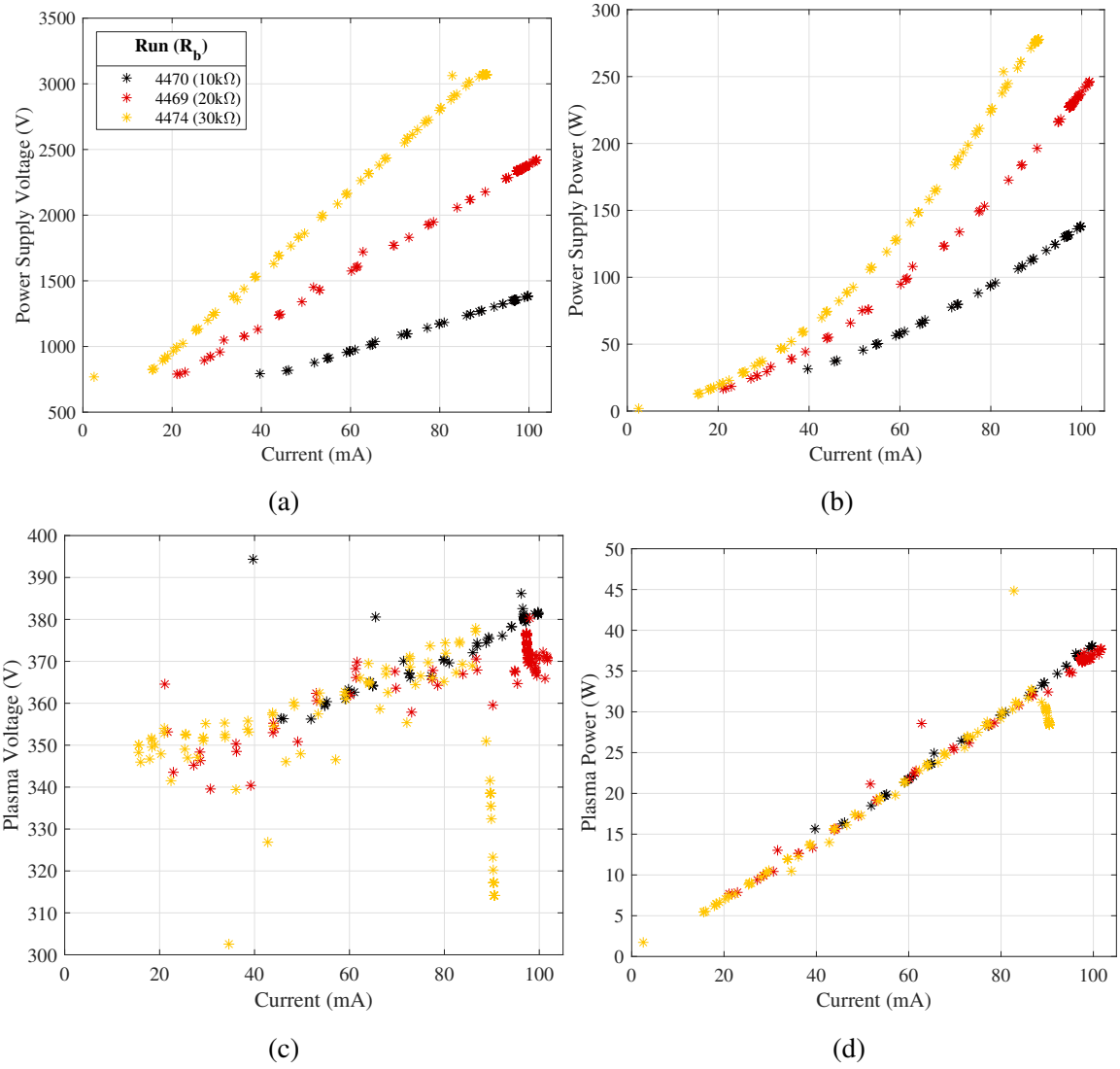

Figure 7.8: Effect of ballast resistance on plasma. [7]

The preceding analysis is for a switching power supply and the runs covered were "voltage limited"; while the behavior with a current- or voltage-fixed power supply was not studied, the effect of running in a "current limited" capacity was. Ultimately it exactly followed the same relationships seen above. This further abetted the claim that it was the flow, not the circuit, that defined the plasma behavior. If that was the case, then what effect would the Reynolds number have on the plasma? Run 4475 directly addressed this question. Both the current and voltage were held just below the safe maximum value for the 10kΩ resistor, $\sim$ 95mA and 1350V respectively, then once the plasma was on condition, the Reynolds number was ramped from $4.75 \rightarrow 6.5\times10^6/\text{m}$. The condensed results are shown in Figure 7.9 and revealed the plasma's weak dependence on Reynolds number. As the Reynolds number rose, more current was passed through the electrodes; this meant more energy was lost to the ballast resistor, so the plasma voltage dropped. The increased current and dropped voltage somewhat offset one another to maintain a mostly constant plasma power. Visually inspecting the plasma, as the Reynolds number increased, the plasma appeared to dim and even ceased to cover the cathode at the uppermost Reynolds number. This implied the plasma was constricting, which may explain the rise in current. The effect of cathode heating on the plasma performance was deemed negligible because past studies at constant conditions did not show the same behavior. The findings for Run 4475 held for Runs 4483 and 4476, which also used the preliminary "cathode upstream" configuration; because preliminary tests did not reveal dramatic trends, these runs were not repeated with the final "cathode downstream" configuration. ([7])

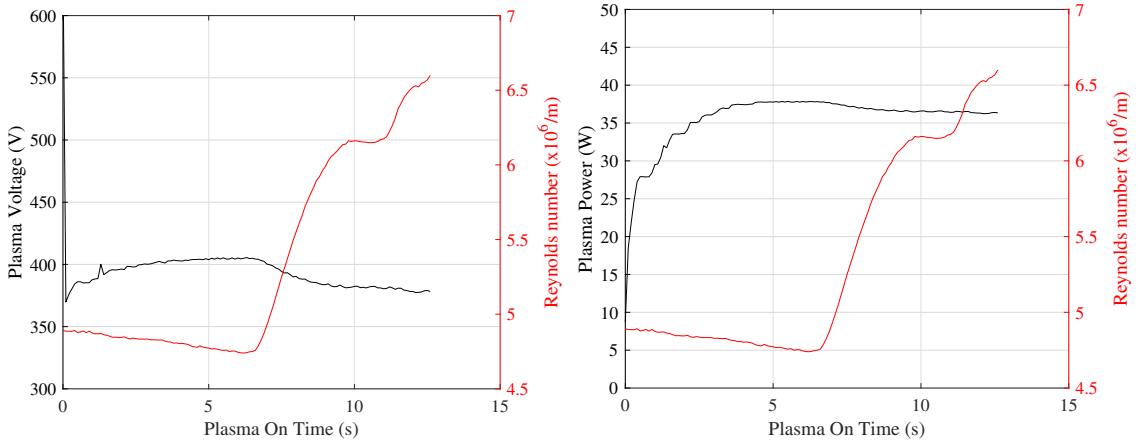

(a) (b)

Figure 7.9: Effect of Reynolds number on plasma. [7]

Another important element of plasma characterization was the determination of the threshold voltage. The parameter was measured by recording the voltage when the current spiked to 1mA, signifying electrical conduction due to the ignition of the plasma; the plasma was cycled three times in a given run to provide extra data points and to check for any effect of plate heating. It

was important that the measurement was made with the electrodes in the proper polarity, because, as will be seen shortly, polarity greatly affected electrical performance. Thus for both Runs 4542 and 4541 the cathode was placed downstream of the anode, which was the final test orientation. Qualitative results are shown in Figure 7.10 while quantitative values are provided in Table 7.6. While the turbulent flow did appear to have a slightly lower breakdown voltage, the sensitivity of the measurement apparent in Figure 7.10 made a definitive conclusion elusive. Similarly, there seemed to be little effect of plate and electrode heating, which made sense because the plasma was only briefly ignited, and due to their placement so near the leading edge the electrodes should be thermally saturated from the preheat. It is worth noting that the mean breakdown voltage from the six plasma cases from the IR/schlieren diagnostic campaign to be discussed was 843V. The theoretical pressure behind the bow shock was 4.70Torr (626.89Pa) and the edge-to-edge electrode spacing is 0.635cm, so $PD = 2.98\text{Torr} \cdot \text{cm}$. From Figure 4.15 depicting Paschen curves over a range of temperatures, it appeared the "effective breakdown temperature" was somewhere between $150 - 250\text{K}$. This number was highly qualitative for the reasons discussed in Section 4.5.8 (i.e.-temperature-dependent conditions and unreliable constants), but it was feasible for the boundary layer and underscored the challenge of a traditional Paschen prediction of V_t. Finally, if the breakdown voltage was $\sim$ 800V and the power supply's maximum current was 100mA, then the ballast resistor must dissipate 80W during breakdown. The resistors purchased were rated to 100W, so the 10kΩ resistor was the weakest that could handle breakdown with a reasonable factor of safety. ([7])

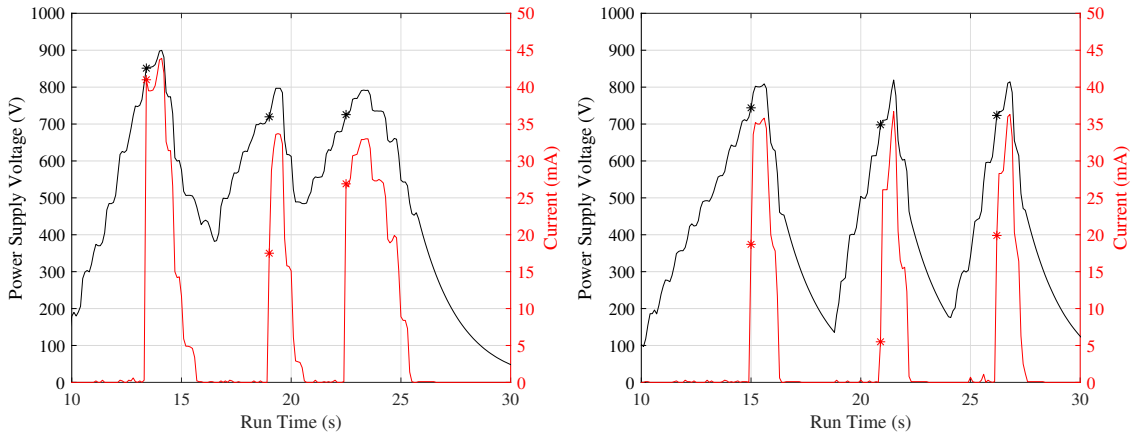

(a) Laminar (Run 6)

(b) Turbulent (Run 11)

Figure 7.10: Measured breakdown voltage (Run 6, laminar flow). [7]

Runs 4544 and 4545 were the best representation of true run conditions because the plasma and tunnel were both run as they would be for the experimental test campaign, though the plasma voltage was ramped slowly to improve the data's temporal resolution. In addition to the aforementioned circuit data, the same camera in Section 6.2.2 recorded the plasma from above to study

Point	Laminar (Run 6)	Turbulent (Run 11)
1	851	744
2	720	698
3	725	723
	Average	
	765	722

Table 7.6: Comparison of breakdown voltages over time and with different boundary layers

breakdown, stability, and the effect trips had on the plasma's structure. The data are shown in Figures 7.11 and 7.12; the plasma images were true color. In both cases, the edges of the electrodes ignited first. The cathode's wire was connected in the center of each electrode, and the anode's wire was connected on the side nearer the top of the images. That the breakdown was symmetric meant this was not due to the wiring; another explanation would be slight bowing at the edges of the electrodes, causing them to protrude slightly from their pockets in the PEEK at the edges. Continuing in time, it was clear that the cathode became fully covered well before the maximum current was applied. This would imply the plasma was just above the normal glow discharge regime. However, the current was not orders of magnitude larger than the normal limit, nor was there a large rise in voltage, so it was likely safe to say the plasma was still within the upper limit of the normal regime. This was useful, because many of the formulas and theory covered in Section 2.3 were for normal glow discharges. It was surprising to see how suddenly the plasma grew to cover the cathode between (b) and (c) in both Figures. Also, the plasma did seem to become slightly brighter between (c), when it first covered the cathode and (d), when the power was maximized. Finally, the plasma was indeed uniform across the span, which was a critical design goal for the test article. ([7])

When comparing the effect of the trips, there was no noticeable effect on plasma power; it was $\sim$ 47W for both configurations. That being said, it did take slightly more current to fully cover the cathode in the turbulent case, $\sim$ 75mA *versus* the laminar case's $\sim$ 65mA. This could imply the presence of the trips and their complex shock structure affected the flow enough to alter the plasma's performance, but then the breakdown voltage remained at $\sim$ 800V for both cases so this argument was assailable. Ultimately the important parameter was the plasma power, which was indeed identical between the two cases, so for the purpose of this report it was safe to say the two cases were functionally identical. ([7])

The flow structures present in the turbulent plasma case in Figure 7.12 were worth discussion. Corner vortices were present as pinkish streaks in the negative glow. Meanwhile, in the positive column, the troughs in between the trips had the highest signal, followed by the wakes; the corner vortices seemed to fully suppress the positive column. It was possible that the pressure differential or temperature [337] in the corner vortices was indeed changing the negative glow analogously to the positive column, but the exact mechanism was not determined. The latter explanation seemed more likely, as evinced by Figure 7.13. This image was taken near the end of the PLIF campaign.

It shows different degrees of electrode "burning" on the cathode in the corner vortex, wake, and trough regions. The PEEK was most damaged downstream of the corner vortices, which implied these regions were hotter than the rest of the flow; IR thermography was later used to confirm this was a thermal effect and not a result of copper sputtering. ([7])

The authors covered in Section 2.3.1 placed the cathode upstream of the anode, largely to maximize its impact near the viscous-inviscid interaction region at the leading edge. While they did mention similar degradation around the test article, their orientation was preserved and thus was initially adopted here; note that these authors used a ceramic insert, which should be impervious to burning at the plasma temperatures experienced and thus lending credence to the sputtering hypothesis. Still, even after about ten runs of preliminary testing with the cathode upstream of the anode, here Runs 4469-4475, 4483, and 4476 in Table 7.5, some degradation became noticeable. The concern was that over time, whatever its cause, it would provide a conductive path between the electrodes and form a short circuit. This would destroy the PEEK insert, and so the cathode was moved downstream of the anode. A surprising consequence of this decision was the improvement in plasma performance. Comparing Figure 7.8(d) and 7.11(h), the plasma power rose from $\sim$ 37W to $\sim$ 47W. Furthermore, the positive column was established only with the latter polarity. This was potentially a manifestation of the velocity analysis conducted in Section 2.3. Recall that absent of the flow the ion and electron velocities were roughly predicted to be $\mathcal{O}(10^2 \frac{m}{s})$ and $\mathcal{O}(10^6 \frac{m}{s})$ respectively. This implied the ions, which traveled towards the cathode, could be largely impeded by the hypersonic flow through most of the boundary layer. A reduction in ion current would lower the overall current, and thus drop the plasma power. The opposite effect was possible if the ions traveled with the flow towards the cathode. Finally it is worthwhile to return to the theory in Section 2.3 to try and determine the total amount of Joule heating. With $CV_c \approx 6$ for a normal glow discharge and $A = 15\text{cm}^{-1}\text{Torr}^{-1}$, $B = 365\frac{\text{V}}{\text{cmTorr}}$, and $\gamma = 2.5 \times 10^{-4}$ (constants from Section 4.5.8), then the cathode fall voltage was $V_c = 605\text{V}$. This exceeded the entire voltage drop across the electrodes; the discrepancy was most likely due to the failure of the constants at the temperatures experienced in the boundary layer. Meanwhile, taking the approach of Nishihara et al. [91] and extrapolating the data yielded $V_c = 438.5\text{V}$ ($V = 438.5 + 0.374i$, $R^2 = 0.56$), a much more reasonable result. However, the data (excluding outliers) shown in Figure 7.14 was not perfectly linear, nor would one expect it to be. Thus all that could be said was that one could assume most of the voltage drop, $\sim$ 475V from Figures 7.11 and 7.12, did indeed occur in the cathode layer. If one did take $d_c \approx 0.1\text{cm}$ from the pseudo-qualitative data in Runs 4544 and 4549, a maximum current of $i = 0.095\text{A}$, and a cathode area of $A = 8.31\text{cm}^2$ then $P_J = 54.3\frac{\text{W}}{\text{m}^3}$. Again, this was simply the plasma power as discussed above (here $\sim$ 45W) divided by the approximate volume of the cathode sheath. ([7])

7.2.2.2 Trip Sizing Study

IR thermography was used to determine the efficacy of different trip heights (h), widths (d, "diameters"), and spacings (w). The goal was to determine if the trips could produce a uniform TBL by the back of the test article at Reynolds numbers attainable in the ACE tunnel. The temperature data was used to calculate a spanwise Stanton number 405mm from the leading edge over a range of Reynolds numbers for each trip. Recall here that following [213, 214] the Stanton number was

calculated with T_o and not T_{aw} as the state of the boundary layer would change as the Reynolds number and trips were varied, so the results cannot be compared to those elsewhere in report. Nevertheless, due to the normalization, turbulence was achieved when the Stanton numbers collapsed on one another, and this approach afforded sufficient fidelity to show that effect. An example of the data is provided in Figure 7.15, which also shows the result for the control "untripped" case; all traces were taken at $x = 405$mm from the leading edge. An analysis of the plate's thermal response and its implications is provided in the dedicated IR thermography section (Section 7.2.3.3). ([7])

The test matrix for the trip sizing campaign is provided in Table 7.7. See that the runs were generally grouped into three sets, where the four h's were tested for a set (d, w) combination. The data are presented in this manner in Figures 7.16, 7.17, and 7.18. The wedge was mounted as far back on the struts as possible to maximize the visible area and check for shock impingement (discussed alongside the schlieren results, Section 7.2.3.2). ([7])

No.	**Location**	**Re** ($\times 10^6/m$)	**Trip** ($\delta_{H_o,99.5\%} * (h,\, d,\, w)$)	**Run/Date**
1	Back	$2-6$	*None*	4442, 9/2/2020
2	Back	$2-7$	(1, 1, 2)	4436, 9/1/2020
3	Back	$2-7$	(1.25, 1, 2)	4434, 9/1/2020
4	Back	$2-7$	(1.5, 1, 2)	4435, 9/1/2020
5	Back	$2-7$	(1.75, 1, 2)	4429, 8/31/2020
6	Back	$2-7$	(1, 1.5, 3)	4441, 9/2/2020
7	Back	$2-7$	(1.25, 1.5, 3)	4439, 9/2/2020
8	Back	$2-7$	(1.5, 1.5, 3)	4433, 9/1/2020
9	Back	$2-7$	(1.75, 1.5, 3)	4428, 8/31/2020
10	Back	$2-7$	(1, 2, 4)	4438, 9/2/2020
11	Back	$2-7$	(1.25, 2, 4)	4437, 9/2/2020
12	Back	$2-7$	(1.5, 2, 4)	4432, 9/1/2020
13	Back	$2-7$	(1.75, 2, 4)	4427, 8/31/2020
14	Back	3	(1.5, 2, 4)	4443, 9/3/2020
15	Back	6	(1.5, 2, 4)	4444, 9/3/2020

Table 7.7: Trip sizing study IR thermography test matrix.

Apart from the most modest trips (Figure 7.16a), all of the geometries were successful at fomenting transition. In Figure 7.16, the Stanton numbers collapsed for both the $h = 1.5$ and $h = 1.75$ orientations. Increasing the size and spacing (Figure 7.17), full turbulence was achieved by $Re = 6 \times 10^6/m$ for all of the heights tested. This suggested larger, more independent vortices were more effective at transitioning a flow than those from the smaller, clustered trips. This could be because the sets of smaller trips acted more like a blockage than a vortex generator, or because turbulent production occurs in large scales Pope [51]; additional credence was lent to the former

theory as there was little evidence of individual trip wakes in the data for the smallest trip cases, just sudden and uneven rises. Either way, the largest trips (Figure 7.18) performed the best, with all heights achieving turbulent flow by $Re = 5 \times 10^6/m$. This provided a factor of safety to ensure the flow is turbulent at the test condition. Furthermore, the heating was uniform over the region of interest, which was not always the case for the smallest trips (Figure 7.16). Finally, at higher Reynolds numbers, say above $5 \times 10^6/m$, the waviness of the profiles due to the trip wakes and vortices was diminished. These effects were tolerable ([206, 213]), but it was preferable to avoid them if possible. Finally, it was understood that the consistent rise in heating above $Re = 3 \times 10^6/m$ was due to the tunnel nozzle's sidewalls transitioning and increasing the freestream noise environment. ([7])

Of all the trips tested, the best performing, as defined by the earliest collapse and most spanwise uniformity, were the $\delta_{H_o,99.5\%} * (1.5, 2, 4)$ trips. It was surprising they outperformed the $h = 1.75$ trips in the same family, but perhaps the largest trips produced oversized wakes and not clean vortices. A few preliminary MTV runs were conducted with the trips to further confirm their efficacy, but any quantitative analysis was reserved for the more careful studies in the dedicated PLIF review. For all subsequent tests hereafter the $\delta_{H_o,99.5\%} * (1.5, 2, 4)$ trips were used. As an addendum to this study, the degree of plate heating was briefly studied. The IR thermography tunnel runs typically lasted just under 30s, during which time the plate heated up under 5K, even for turbulent flows. This implied an isothermal wall condition, but not necessarily an adiabatic one, so there was a risk the Stanton number would change as a function of time. To study this effect on both a laminar/transitional and turbulent boundary layers, the $\delta_{H_o,99.5\%} * (1.5, 2, 4)$ trips were run at a constant $Re = 3$ and $6 \times 10^6/m$. The results are shown in Figure 7.19. The data suggested that there was very little temporal dependency on the results, validating the use of long tunnel runs. ([7])

7.2.2.3 Leading Edge Uniformity and Roughness

Surface profilometry revealed the leading edge was well-machined and uniform across the model span. Characteristic results for one of the tests are shown in Figure 7.20. A dashed line at 20.65mm separated the leading edge polynomial from the flat wedge geometry. The leading edge was approximately merged with the wedge slope within $\sim$ 5mm of the leading edge, which underscored the need for the definition of the geometry's effective radius of curvature. Data upstream of this point was somewhat noisy, which was expected as this section was less finely ground. That being said, while some machine chatter exactly at the leading edge was visible, it did not appear to have been captured by the surface profilometer beyond the noise floor. The data also suggested the leading edge polynomial did indeed merge smoothly with the wedge slope, which was the entire reason for its inclusion in the design. With regard to the spanwise uniformity of the leading edge, there did seem to be a slight depression in the center of the span; it was $\mathcal{O}(100)\mu$m; this value, which was consistent among all three tests, was acceptable over the $\sim$ 200mm test article. The depression deepened as one moved downstream, but it remained tolerable; this may be due to minor misalignment of the profilometer in the Y-direction. ([7])

The roughnesses for the "even" and "odd" scans from the three tests were included in Table 7.8 to the resolution of the profilometer. The repeatability between all six data sets was encouraging.

Furthermore, the model was specified to be ground to $R_{avg} = 32\mu\text{in} = 0.81\mu\text{m}$, which strongly agrees with the experimental result. Broslawski [7])

	R_{avg}	R_{ptp}	R_{rms}
Test 1			
Even	0.73	3.12	0.95
Odd	0.74	3.14	0.97
Test 2			
Even	0.73	3.14	0.96
Odd	0.74	3.16	0.97
Test 3			
Even	0.74	3.18	0.98
Odd	0.74	3.18	0.98
Average			
	0.74	3.15	0.97

Table 7.8: Results of three redundant roughness tests; all data are in microns.

7.2.3 Flow Physics Data

The results described in this section follow from Broslawski [7]. These data used classical diagnostic techniques to gather as much information about the test environment as was feasible. Data was collected at the wall from oil flow and IR thermometry, off-body from schlieren and Pitot probe surveys, and in spectral space using high frequency pressure transducers. These results paint a detailed picture of the test environment, the hypersonic turbulent boundary layer with zero pressure gradient, and they provide further information on specific features such as the flow near the leading edge or just downstream of the trips. ([7])

7.2.3.1 Oil Flow Results

The primary purpose of oil flow visualization was to ensure the quality of the flow within the test area; through their own oil flow campaigns Semper [206] and Leidy [213] showed sting effects, edge effects, pressure gradients, separation, shocks, *etc.* could all effect hypersonic boundary layers in the ACE tunnel. Additionally, oil flow communicates the presence and longevity of flow features like trip wakes, which could inform the placement of later sensors and measurements. Both full images and spanwise traces of the test area are provided at different stations along the plate and over a range of times to study how the flow evolved both spatially and temporally. For all runs, the test Reynolds number of $6 \times 10^6/m$ was used. Because the oil behaved unpredictably during unstart and is electrically conducting, for safety the plasma was never ignited during these runs. The test matrix is shown in Table 7.9. ([7])

Figure 7.21 compares laminar and turbulent results at each of the three test locations. The clearest observation was a slight outward motion of the streaks, especially in downstream images.

No.	Location	Trip	Run/Date
1	Back	Laminar	4508, 9/28/2020
2	Back	Turbulent	4507, 9/28/2020
3	Middle	Laminar	4509, 9/28/2020
4	Middle	Turbulent	4510, 9/29/2020
5	Forward	Laminar	4513, 9/29/2020
6	Forward	Turbulent	4511, 9/29/2020

Table 7.9: Oil flow test matrix.

This was present in both the laminar and turbulent images, so it was not due to trip blockage, and the images were dewarped and rotated, so it was not a camera effect. This suggested the top surface of the wedge was at a slightly higher pressure than the underside, causing streamlines to "wrap around" the sides of the model. This was not surprising given the challenges outlined by Leidy [213]; it may be caused by a very slight angle of attack (recall the model was constrained to $\pm 0.1°$) or the fact the model was mounted 2.54cm below the test section's centerline (a necessity discussed in Section 7.2.3.2). Nevertheless, the streamlines remained relatively straight in a core region roughly $\pm$25mm from the centerline. ([7]))

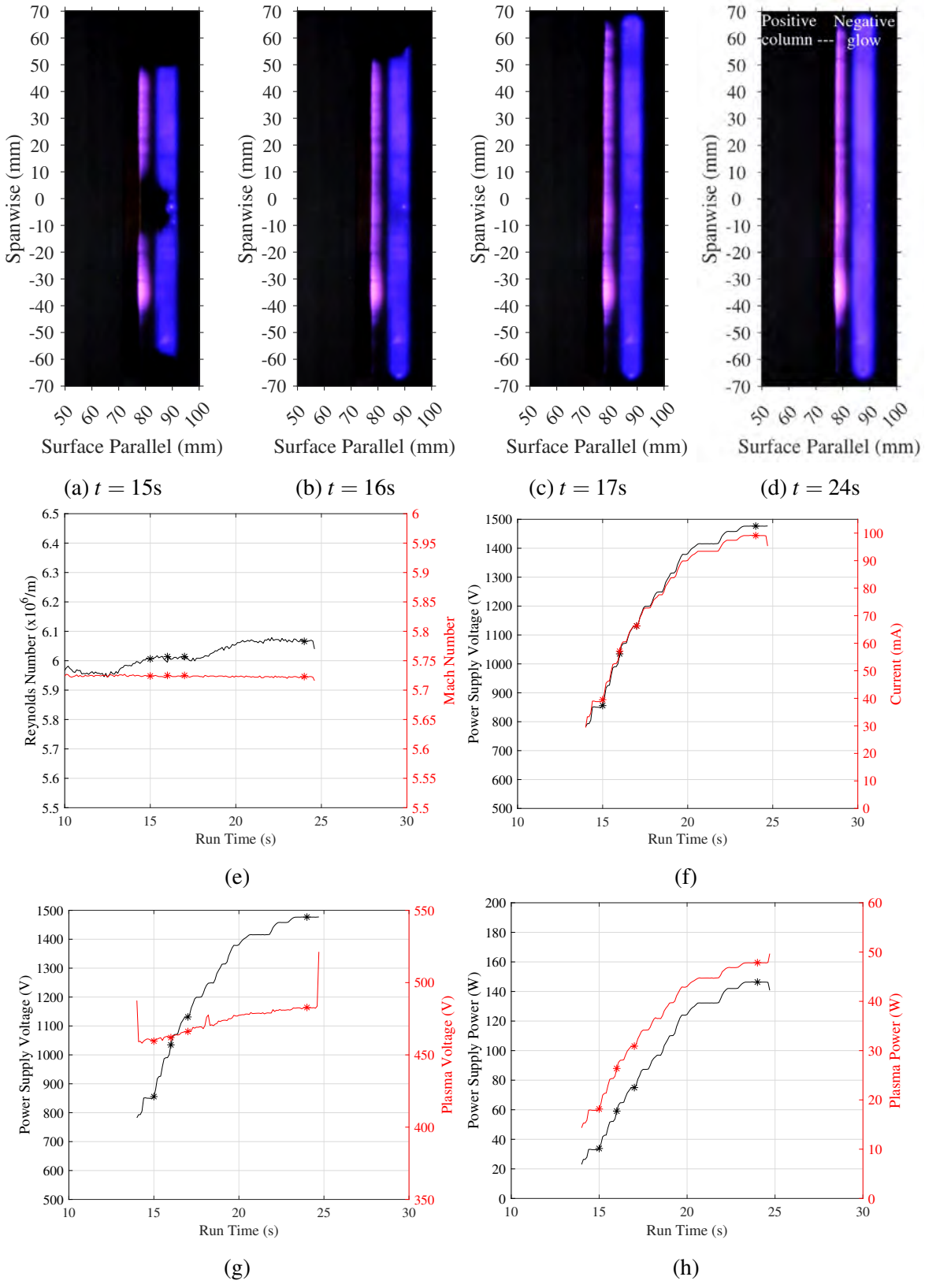

Figure 7.11: Plasma performance in a laminar boundary layer (Run 9). [7]

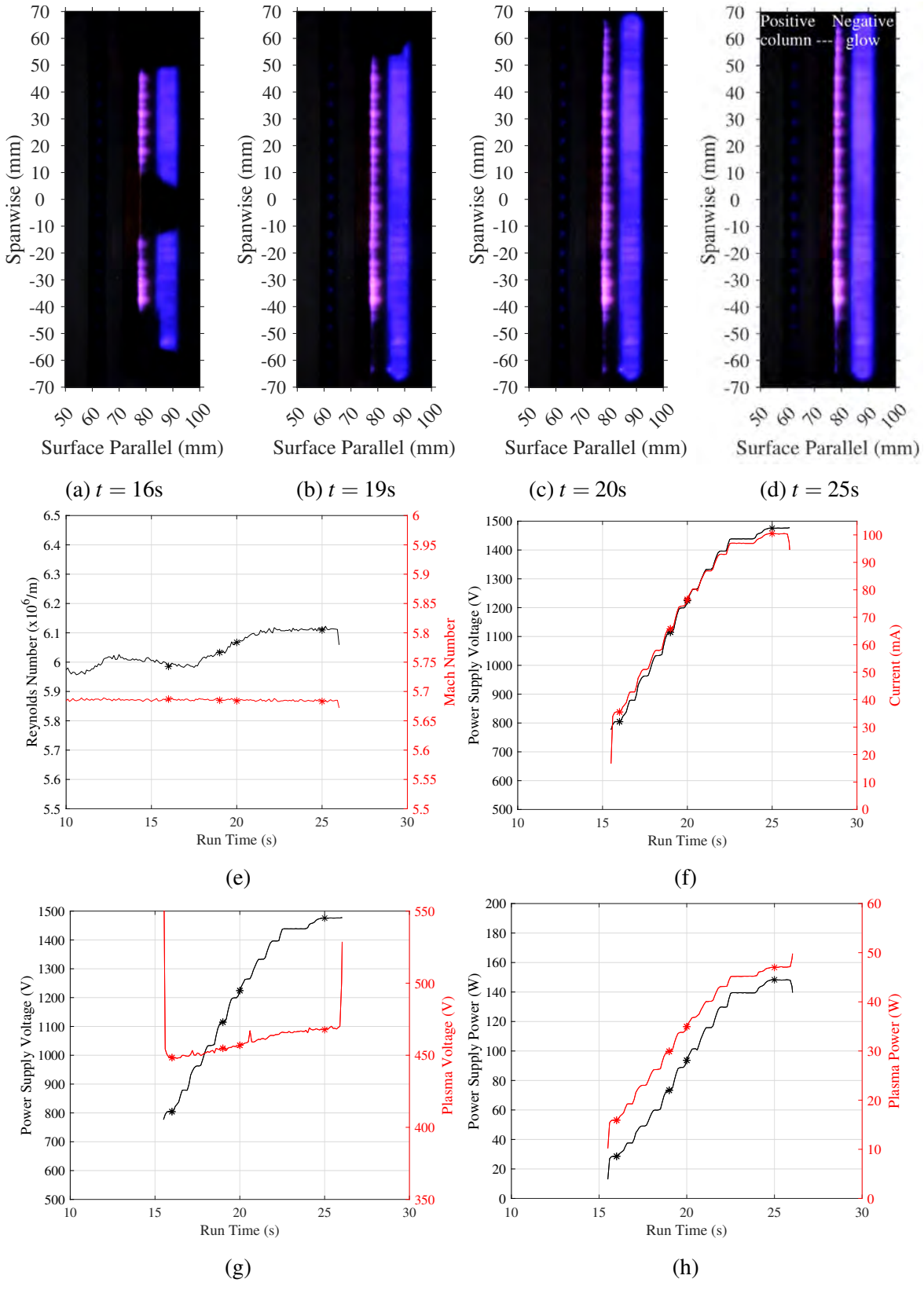

Figure 7.12: Plasma performance in a turbulent boundary layer (Run 13). [7]

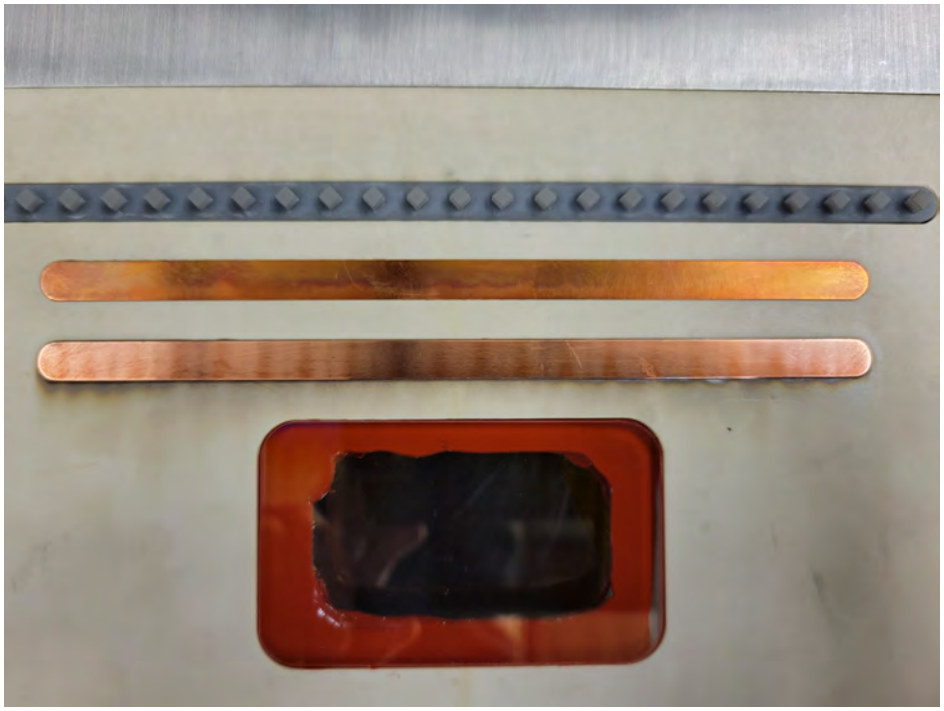

Figure 7.13: Burned electrodes; flow is top to bottom. [7].

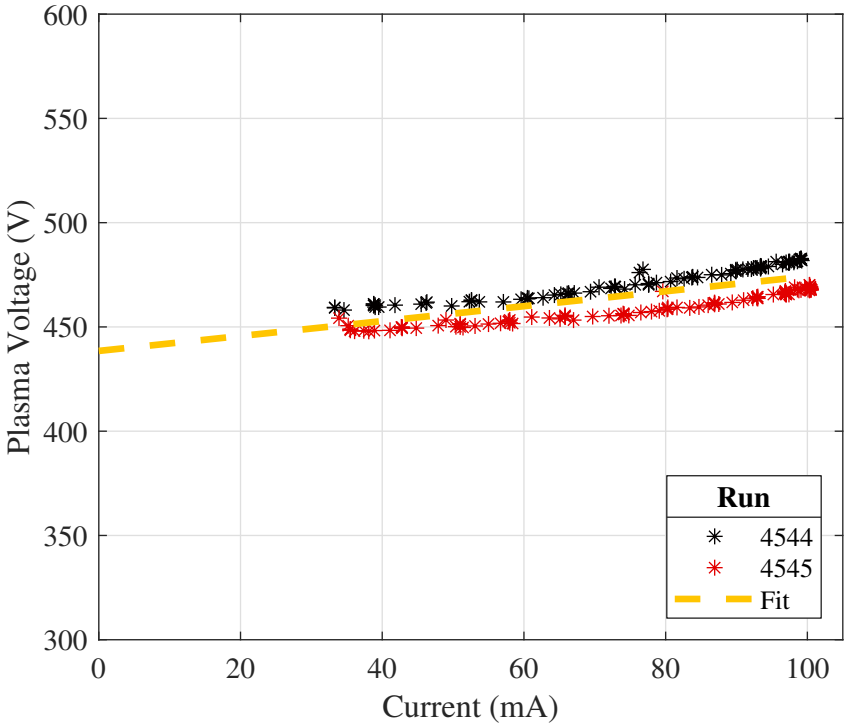

Figure 7.14: Cathode voltage drop following the method of Nishihara et al. [91]. [7].

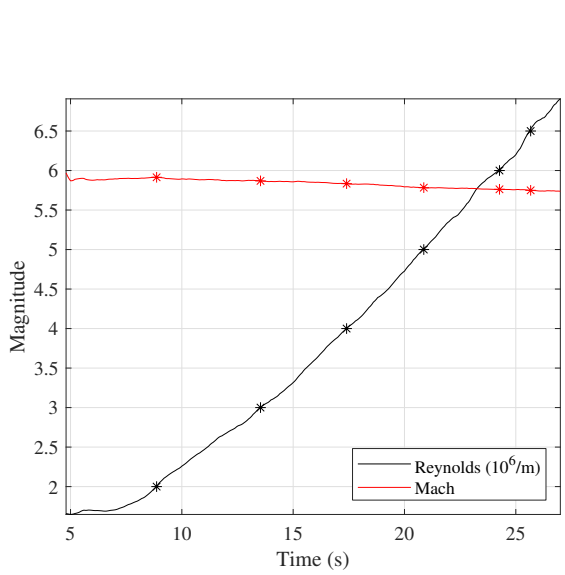

(a) Tunnel conditions with sample points

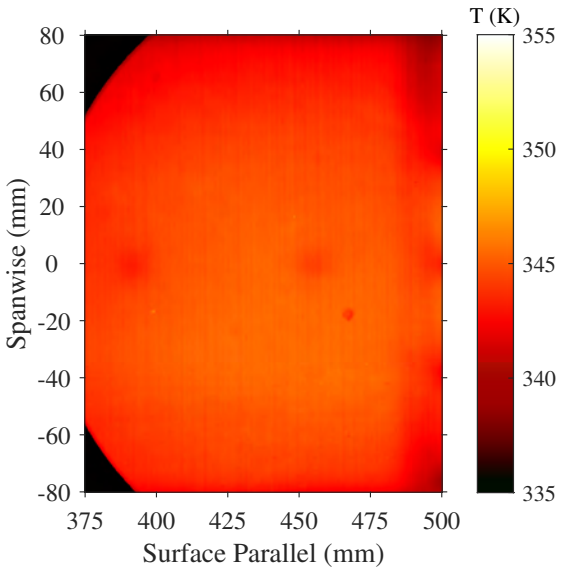

(b) Full temperature image at $Re = 6 \times 10^6/m$

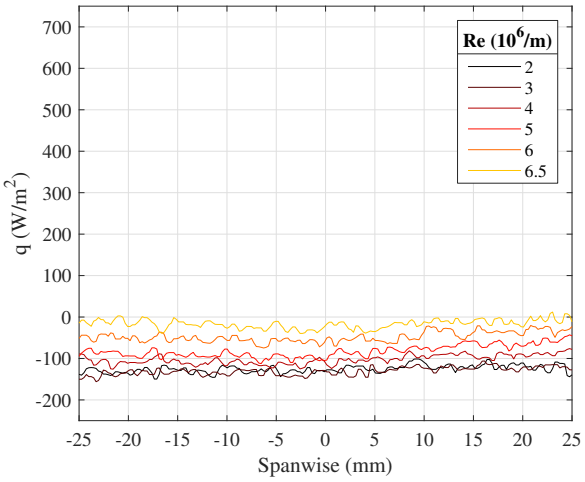

(c) Heat flux traces

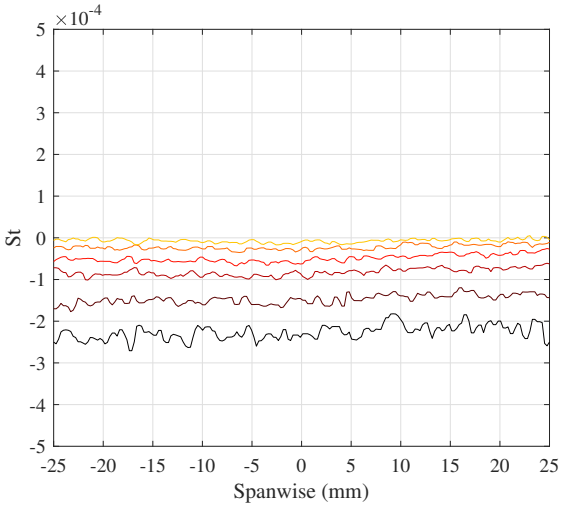

(d) Stanton number traces

Figure 7.15: Sample of IR data for trip sizing from control case. Traces taken at $x = 405$mm from the leading edge; same legend applies to (c) and (d). [7].

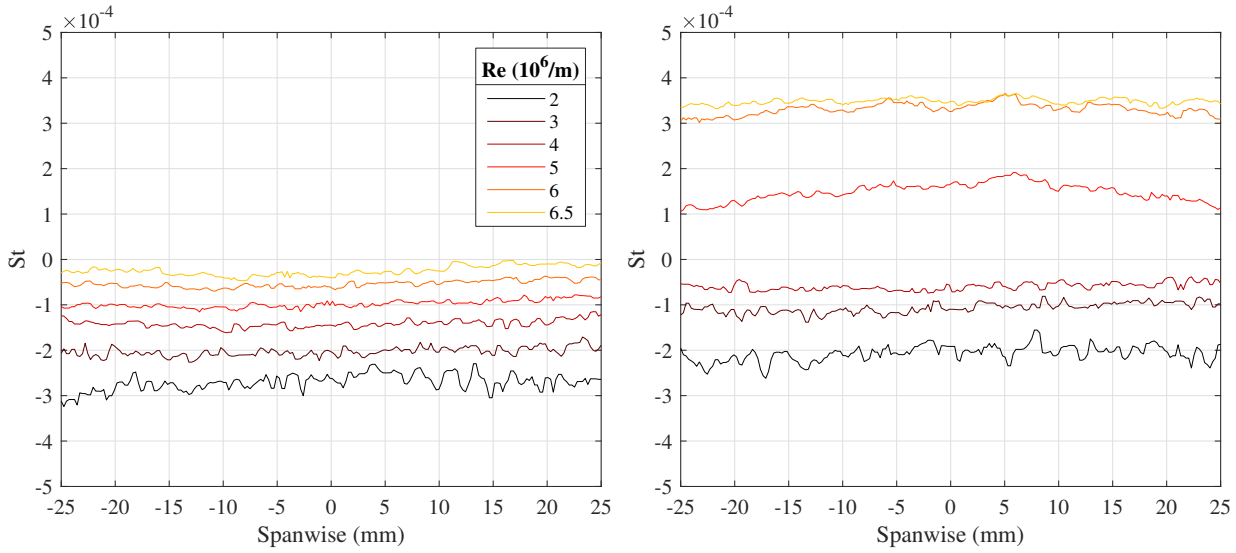

(a) $\delta_{H_o,99.5\%} * (h = 1, d = 1, w = 2)$

(b) $\delta_{H_o,99.5\%} * (h = 1.25, d = 1, w = 2)$

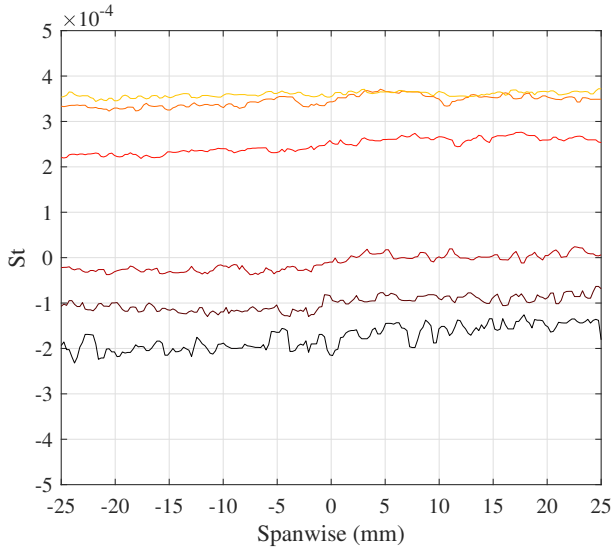

(c) $\delta_{H_o,99.5\%} * (h = 1.5, d = 1, w = 2)$

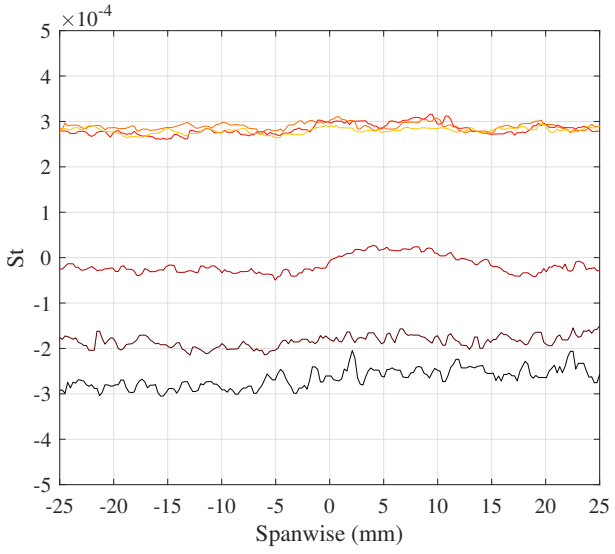

(d) $\delta_{H_o,99.5\%} * (h = 1.75, d = 1, w = 2)$

Figure 7.16: IR studying sweep of trip heights for ($d = 1$, $w = 2$) family. Same legend applies for all figures. [7]

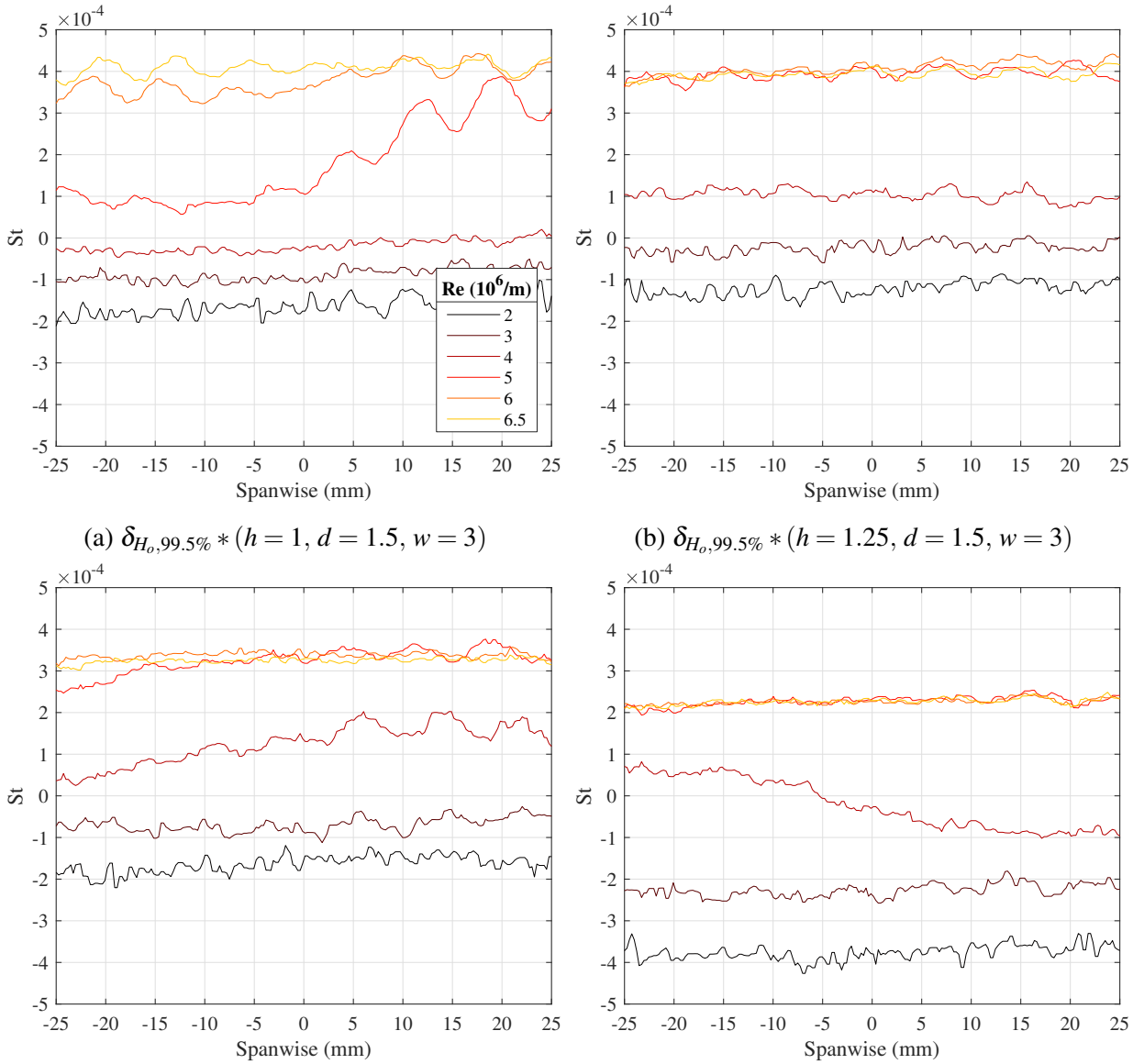

(a) $\delta_{H_o,99.5\%} * (h = 1,\ d = 1.5,\ w = 3)$

(b) $\delta_{H_o,99.5\%} * (h = 1.25,\ d = 1.5,\ w = 3)$

(c) $\delta_{H_o,99.5\%} * (h = 1.5,\ d = 1.5,\ w = 3)$

(d) $\delta_{H_o,99.5\%} * (h = 1.75,\ d = 1.5,\ w = 3)$

Figure 7.17: IR studying sweep of trip heights for ($d = 1.5$, $w = 3$) family. Same legend applies for all figures. [7]

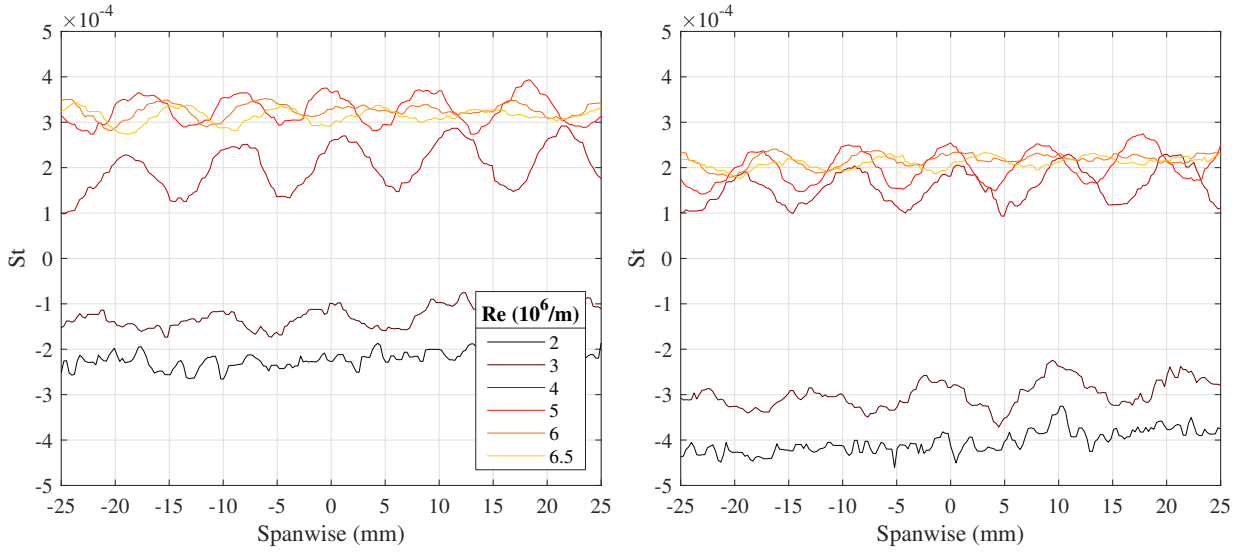

(a) $\delta_{H_o,99.5\%} * (h = 1, d = 2, w = 4)$

(b) $\delta_{H_o,99.5\%} * (h = 1.25, d = 2, w = 4)$

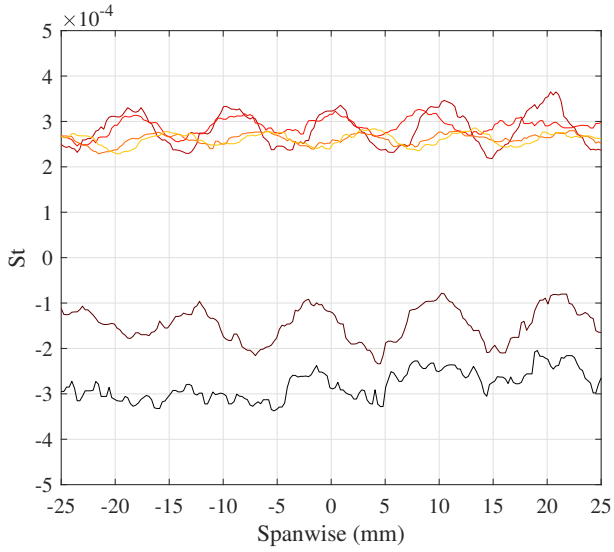

(c) $\delta_{H_o,99.5\%} * (h = 1.5, d = 2, w = 4)$

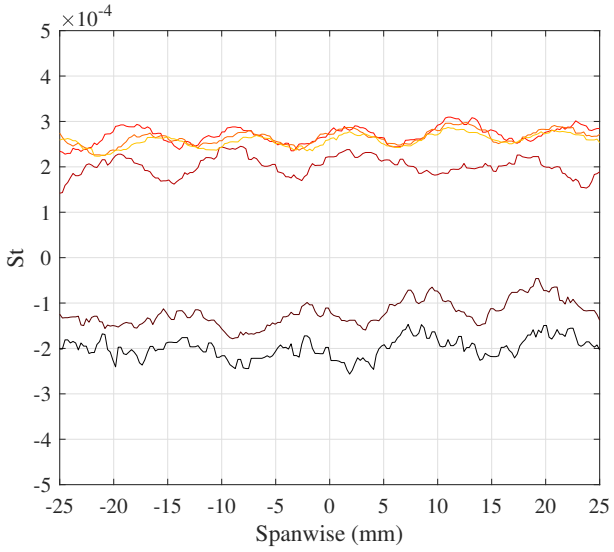

(d) $\delta_{H_o,99.5\%} * (h = 1.75, d = 2, w = 4)$

Figure 7.18: IR studying sweep of trip heights for ($d = 2$, $w = 4$) family. Same legend applies for all figures. [7]

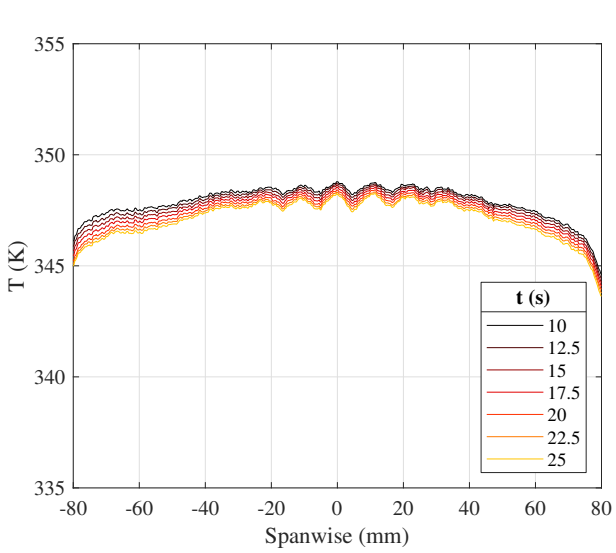

(a) Temperature at $Re = 3 \times 10^6/m$

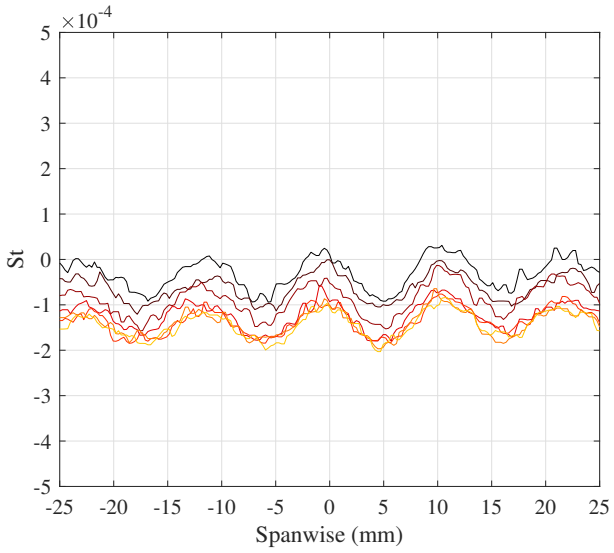

(b) Stanton number at $Re = 3 \times 10^6/m$

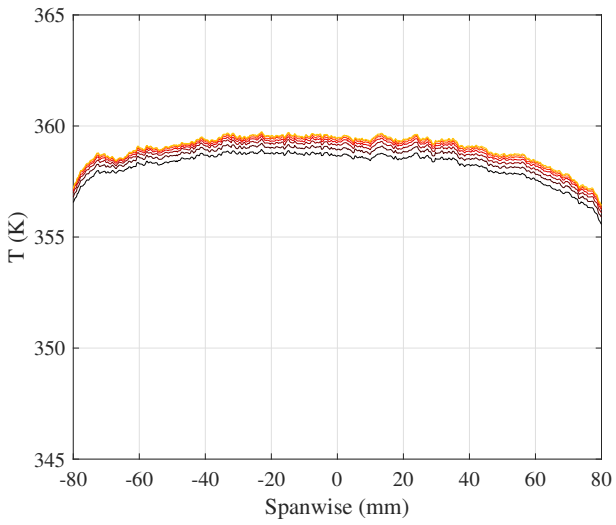

(c) Temperature at $Re = 6 \times 10^6/m$

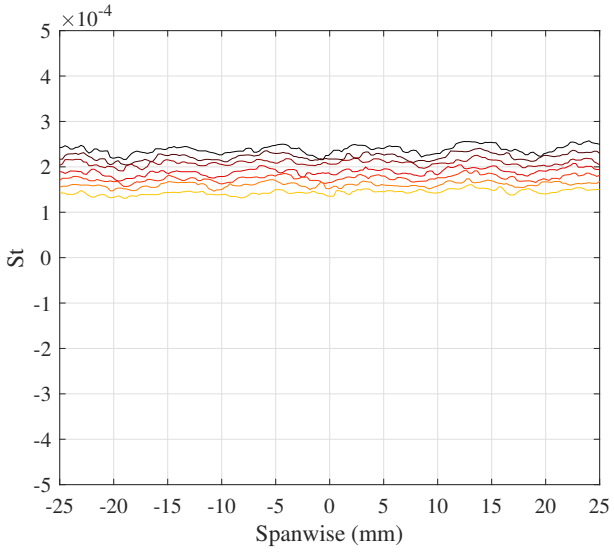

(d) Stanton number at $Re = 6 \times 10^6/m$

Figure 7.19: IR studying temporal effect on heating. Same legend applies for all figures, but note the change in axis between (a) and (c). [7]

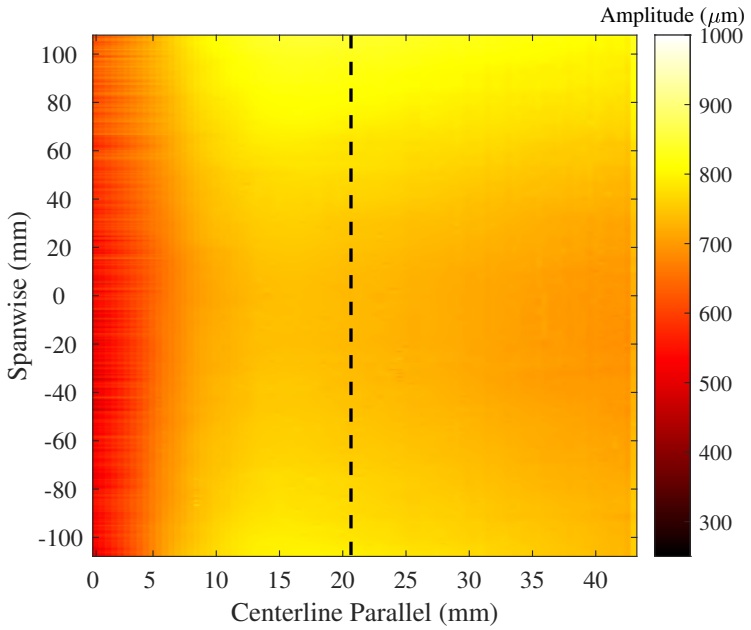

Figure 7.20: Characteristic result of a full profilometer scan. A dashed line at 20.65mm separates the leading edge polynomial from the flat wedge region.

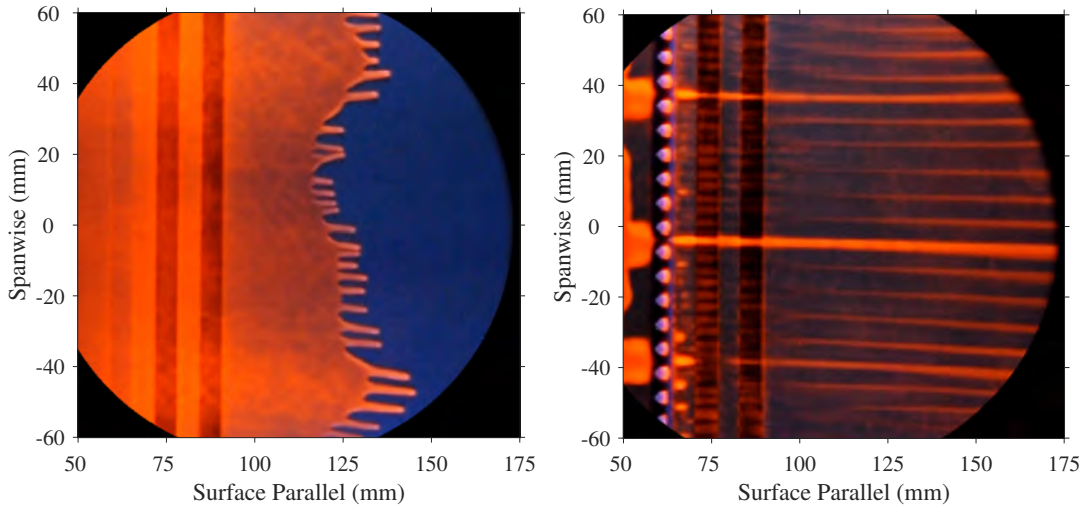

(a) Forward/Laminar

(b) Forward/Turbulent

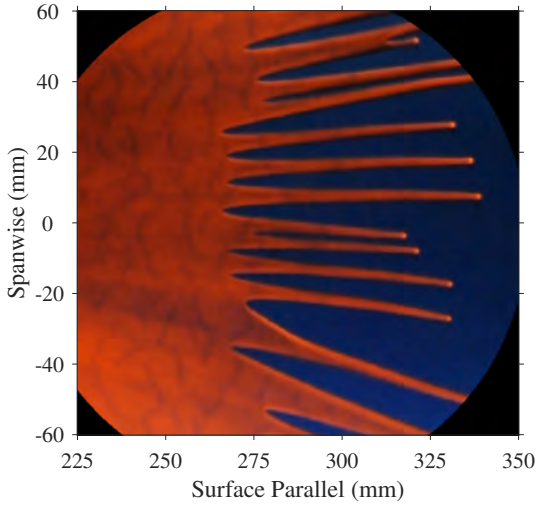

(c) Middle/Laminar

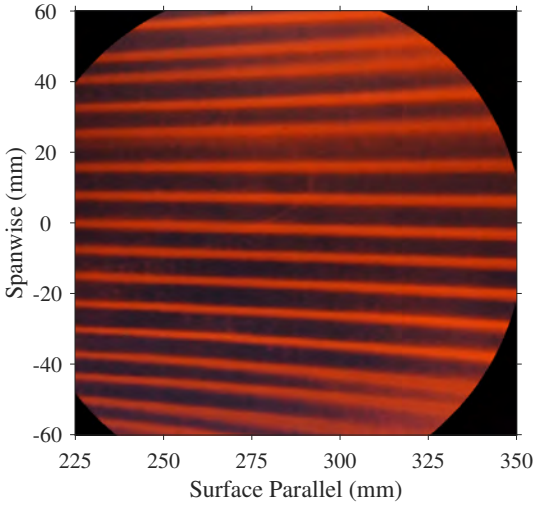

(d) Middle/Turbulent

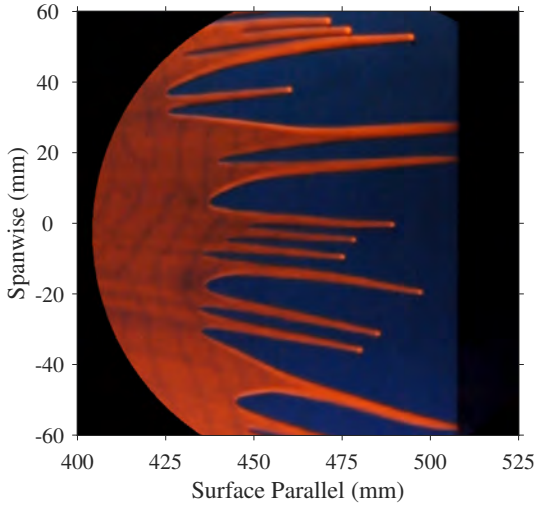

(e) Back/Laminar

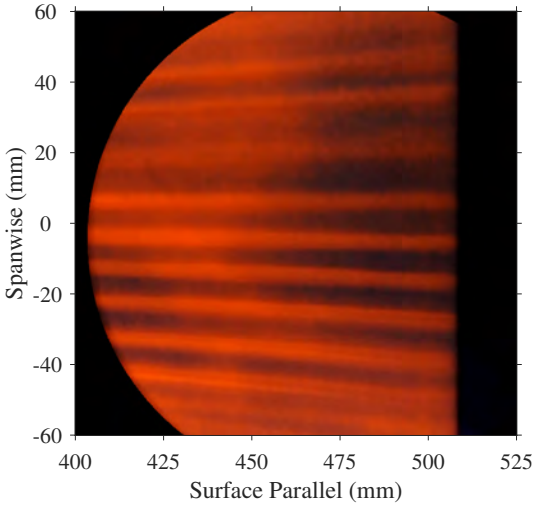

(f) Back/Turbulent

Figure 7.21: Raw color oil flow images along the plate with and without trips. [7]

Another feature present in Figure 7.21 was the thickening of the streaks as one moved downstream. This was likely due to the streamlines merging, and was described by Semper [206]. This was explored in Figure 7.22. Note that due to inherent difficulties with analyzing oil flow data the times displayed count the seconds from a manually identified tunnel start. They were therefore somewhat arbitrary and disconnected from the ACE tunnel's DAQ, but were nevertheless sufficient for the current discussion. Similarly, the "Normalized Intensity" axis was relative only to the camera; the data were normalized to account for the drop in signal as the oil was blown out of frame. The data showed that as one moved downstream, the flow became more unstructured and the periodic trip effects broke down. The regularity of the streaks decreased while their wavelength increased, with an expected drop in their frequency. The location of the streaks changed slightly as one moved downstream, which was understandable due to the aforementioned divergence. At a given location, however, the locations of the structures were fairly constant. The progressive clarity of the waves over time at the "Back" location (Figure 7.22(c)) may be explained by the time it took for weak (compared to the trip effects) flow structures to manifest in the slow-moving oil. The large spikes in signal at the "Forward" location (Figure 7.22a) were due to the pooling seen in 7.21(b), the cause of which was unclear but may have been due to waviness in the plastic trip insert or the thin portion of the PEEK used for attachment to the metal wedge frame; for example, screwing the trip insert into the model produced slight valleys at the attachment points, though their locations were at -63.5, 0, and 63.5mm. Fortunately this effect seemed to dissipate as one moved away from the leading edge. Note that upstream trip effects were studied by Semper [206]. Figure 7.22(a) was of specific interest. By $t \approx 12-15$s the majority of the oil had blown into the troughs and then off of the plate; the low velocity in the wakes and high velocity in the troughs led to this spanwise pressure differential. Once the bulk of the oil was removed, however, new peaks in the data appeared in the traces. These new peaks formed exactly in between the "trough" peaks and corresponded well to the location of the trips. ([7])

This dynamism in the data was unexpected and motivated deeper investigation. Greater detail on streamline merging and the transition process was provided in Figure 7.23. Just after the run began, at $t = 3$s, there was high signal in between the trips, no signal at the corner vortices, and then some signal in the centerline of the trip wakes. This may have been due to counter-rotating corner vortices pushing oil into the channels, a velocity deficit in the wake, low speeds in the channels due to shock-shock interaction (Semper [206] explored the near-trip shock behavior), or some combination of the three. Whatever the cause, just three seconds later, the channel structures were all that remained. However, evidence of the corner vortices appeared on the upstream electrode; this was a complete reversal of the signal at this location from just three seconds prior. It was possible that it was not until only a thin coat of oil remained weak flow effects have sufficient force to manifest in the oil. This may have been the case, because another three seconds later at $t = 9$s the bulk of the oil had traveled past the second electrode. At ~ 100mm from the leading edge in Figure 7.23(c), there appeared to be the corner vortices from two adjacent trips merging across a channel. It was possible this was the initiation of the breakdown process. Studying the subsequent images, Figure 7.23(d-f), where a trip's two corner vortices bifurcated, there was a faint rise in signal in the now free wake region. It was possible this was simply residual oil left on the plate, so one could ask if the wakes were breaking down, causing a pressure rise which splits

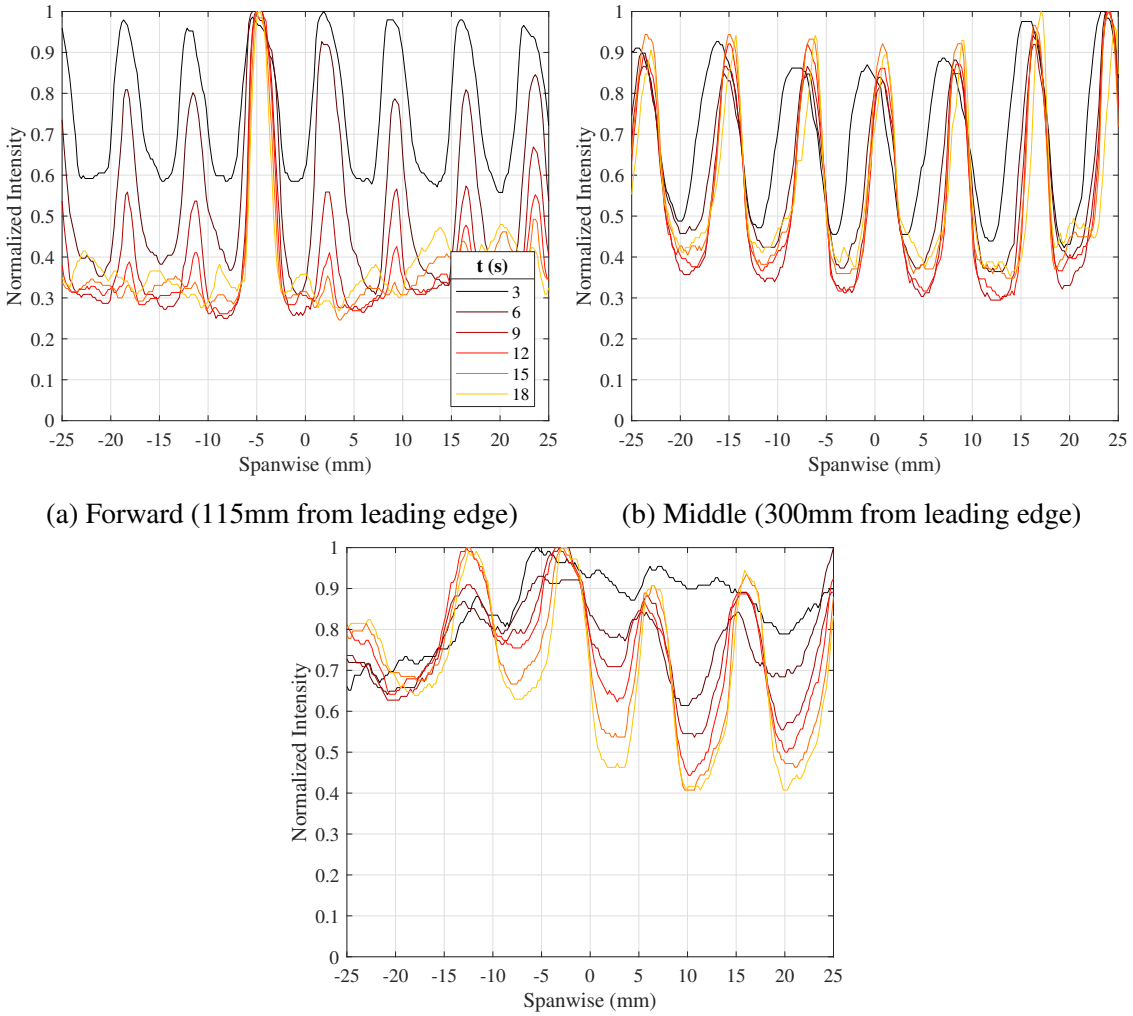

(a) Forward (115mm from leading edge)

(b) Middle (300mm from leading edge)

(c) Back (425mm from leading edge)

Figure 7.22: Spanwise traces of oil flow intensity with temporal evolution. Same legend applies for all figures. [7]

the vortices apart like a wedge, or were the vortices constructively interfering once they reached a critical size? The location of the new vortex structures matched what was seen at downstream locations in Figure 7.21, and Figure 7.21(f) even seemed to have two "sub-streaks" in some of its features. Furthermore, in reviewing the video the streaks at the downstream locations formed immediately and with no obvious difference in streamwise oil velocity, which implied oil was being blown laterally by strong vortices. All of this implied the trip vortices evolved, but remained the dominant flow mechanism along the entire length of the test article. Ultimately, to better explore the space in between other techniques were required. Such a comparison to the features identified with IR thermography is provided in Section 7.2.6. ([7])

7.2.3.2 Schlieren Results

Schlieren imaging serves many useful roles. It visualizes shock structures, boundary layers, and separation/reattachment zones. Seeing shocks is necessary to study the leading edge, as well as identify any issues with the quality of the test volume such as Mach waves or impinging shocks; it is even possible to view the shock produced by a glow discharge [125, 124, 113]. Measuring the boundary layer height is helpful for CFD validation, offers an excellent comparison point for other diagnostics like PLIF or Pitot surveys, and can help scale test article features like the trips; simply showing the boundary layer also describes its state: laminar; transitional; or turbulent. Checking that separation is prevented at the leading edge is an additional application because such a result would adversely affect the flow's temporal stability, and even fatigue the model's sting; it is interesting to study the separation and reattachment structures near the trips as well, as was done by Semper [206]. ([7])

The schlieren campaign is summarized in Table 7.10; note that IR data was collected concurrently, so the test matrices overlap. Runs were conducted at four test locations, with the test article and test section windows adjusted to maximized the amount of boundary layer seen. The plasma was run on and off and the trips were installed and omitted for four runs at each location. Two additional runs (Runs 4551 and 4550) visualized the shocks at the leading edge with the trips and a blank insert installed; no plasma was ignited as the view was entirely upstream of the electrodes, and the entire wedge itself was moved backwards on the struts to allow visualization of the leading edge. It was helpful to reiterate some elements of the data processing. For all runs data was collected at 1000fps with a 1.25μs gate to capture high-speed effects without restricting the field of view or sacrificing too much signal. The tunnel started at and was left on the test condition of $Re = 6 \times 10^6/\text{m}$. A large area was left above the boundary layer to show the development of shocks in the freestream; this was helpful for comparing to the PLIF data. Finally, the mean images were the average of 100 frames surrounding an instant, so the frame rate of mean images effectively matched the NALDAQ's 10Hz collection frequency. The plasma properties for these runs are summarized in Table 7.11. These data represented each run's average once the plasma reached it's operational condition. As was shown in Figure 7.24, the plasma was nominally switched on at $\sim$ 10s, reached its operational condition by $\sim$ 15s, and was switched off at $\sim$ 27s, so $\sim$ 10s of data were averaged. ([7])

Figure 7.25 shows the leading edge behavior. It is noted the images were rotated such that the top surface was flat to allow better comparison with subsequent images, and that the vertical scale started at the wedge centerline, not the top surface. In reviewing the high speed footage, there was no evidence of separation at the leading edge, and the test article was relatively free of vibration. There was no clear evidence of the trips in this view to distinguish the turbulent run from the laminar run, so the data from the latter was not shown. The characteristic curvature of the hypersonic shock [19], especially near the intentionally blunted leading edge, was present. The thickness of the shock and perceived deformity of the leading edge were a consequence of imperfect alignment between the 3D object (a 2D extrusion) and the schlieren system. The measured shock angle between the shock and the top surface was $\sim 15.25°$, so considering the 2.75° wedge half-angle the total shock angle is $\sim 18°$. This deviated strongly from the 11.95° predicted by the theory in the boundary layer solver (see 7.2.1, [205]) but it was potentially explained by the bluntness of the

No.	Location	Trip	Plasma	Run/Date
1	Back	Laminar	Off	4518, 10/1/2020
2	Back	Turbulent	Off	4522, 10/2/2020
3	Back	Laminar	On	4533, 10/5/2020
4	Back	Turbulent	On	4532, 10/5/2020
5	Middle	Laminar	Off	4527, 10/3/2020
6	Middle	Turbulent	Off	4524, 10/2/2020
7	Middle	Laminar	On	4529, 10/4/2020
8	Middle	Turbulent	On	4530, 10/4/2020
9	Forward	Laminar	Off	4538, 10/7/2020
10	Forward	Turbulent	Off	4539, 10/7/2020
11	Forward	Laminar	On	4537, 10/6/2020
12	Forward	Turbulent	On	4540, 10/7/2020
13	Forward (LE)	Laminar	Off	4551, 10/9/2020
14	Forward (LE)	Turbulent	Off	4550, 10/9/2020

Table 7.10: Schlieren test matrix.

No.	Current (mA)	Power Supply Voltage (V)	Power Supply Power (W)	Plasma Voltage (V)	Plasma Power (W)
3	93.9	1406	132.1	463.8	43.6
4	94.8	1399	132.7	447.9	42.5
7	88.4	1341	118.5	454.4	40.2
8	89.5	1342	120.1	444.1	39.7
11	93.6	1409	131.9	470.1	44.0
12	93.4	1402	130.9	465.5	43.5
Average					
	92.3	1383	127.7	457.6	42.2

Table 7.11: Plasma conditions for schlieren campaign.

leading edge polynomial, the thickness perceived by the technique, the curvature of the shock, and viscous effects like those described by Hayes and Probstein [115]. In the next downstream view (Figure 7.27), the shock was straighter and the measured shock angle was $\sim 12°$ for a cumulative angle of ~ 14.75, which aligned more reasonably with the theory. ([7])

There bulk of the data are presented in Figures 7.26, 7.27, 7.28, and 7.29. The former two figures are instantaneous and mean images from runs without the plasma while for the latter two the plasma was ignited. The mean images generally provided clearer trends as it seemed the 1.25μs camera gate was, unsurprisingly, too large to freeze the flow; it will become clear in Section 7.2.5 PLIF remedied this issue. Comparing the data, it seemed the plasma had no effect on the boundary layer height, and any shocks formed above the cathode were too weak to see. This was

not surprising, as the plasma was sized not to be a direct flow perturbation like the studies in Section 2.3.1 but to seed in vibrational nonequilibrium. Any boundary layer thickening due to cathode or Joule heating would convoluted any effects of vibrational relaxation, which were the focus of this report. For simplicity, the remainder of the analysis was conducted on Figure 7.27. Consider the laminar images first. The Mach waves introduced by the electrodes and PEEK insert were clearly visible. Evidence of the latter was arguably present beyond 45mm in Figure 7.25 as the seam was approximately 44mm from the leading edge. Of greater interest was the boundary layer height. It appeared that the boundary layer was nearly a constant 5mm. This defied the expected growth with the streamwise coordinate [19]. Looking more closely at Figure 7.25, it seemed this feature was faintly present within 20mm of the leading edge, which was further evidence it was not a boundary layer. A likely explanation was that this was the entropy layer. The true boundary layer appeared to be the thin streak entrained within this larger structure. If this was the case, the laminar boundary layer appeared to be $1-2$mm in 7.27(a), $2-3$mm in 7.27(c), and $3-4$mm in 7.27(e); these values were much closer in agreement to the theory of van Driest [223] and predicted by the boundary layer solver in Section 7.2.1. Interestingly, in the instantaneous Figures 7.26(e) and 7.28(e), and impinging shock appeared to be causing the boundary layer to transition at 455mm. The shocks presented in the "Back" view were known wind tunnel imperfections caused by the 22.86cm nozzle merging abruptly with the 23.18cm test section. These were so strong that in preliminary IR testing they caused a sudden rise in surface heating. To avoid them, the entire test article was lowered 2.54cm in the test section by machining shorter struts. All runs were conducted with these shorter struts and usually with the wedge in a "Forward" position, and the present schlieren showed these efforts were mostly successful in preventing or delaying the impingement of the strongest shock. For safety, all tests were be conducted upstream of the shock impingement. ([7])

The turbulent images contained a wealth of information. Figure 7.27 showed the turbulent boundary layer to be $4-6$mm in 7.27(b), $8-10$mm in 7.27(d), and $10-12$mm in 7.27(f). As expected, the turbulent boundary layer was much thicker than the laminar analog, and while it was not frozen Figure 7.26 does show the chaotic eddies characteristic of turbulence. The laminar boundary layer appeared to be impinging two-thirds of the way up the trips, which was exactly how they were designed. Furthermore, Figure 7.27(b) shows the upstream recirculation, oblique shock, and shear layer produced by the trips and described by Semper [206]. To be clear, the shear layer produced by the trips was present between $70-90$mm in Figure 7.27(b). Semper directly attributed this behavior to the corner vortices. It was interesting to note that this was roughly the range in which the corner vortices were visible in the oil flow data (Figure 7.23). An inspection of the instantaneous schlieren image Figure 7.26(b) revealed the boundary layer was transitional after this point, perhaps becoming turbulent between $130-150$mm. This supported the theory introduced in Section 7.2.3.1, that the merging of the streamlines in Figure 7.23 approximately 100mm from the leading edge was indeed transition to turbulence. Further experimentation was warranted, but an important finding has been introduced and corroborated between two independent techniques. Again, the presence of the glow discharge did not have any apparent effect on this transition process (Figure 7.28(b)), but this was not a concern for meeting the project's goals. ([7])

7.2.3.3 IR Results

IR thermography measures the wall's thermal conditions. This can be used to set the thermal boundary condition needed for both CFD and PLIF, provide validation data for CFD, inform the state of the boundary layer, and reveal some flow structures like wakes or impinging shocks. Here temperatures were converted into heat flux, and then nondimensionalized into Stanton number. The heat flux, and thereby the Stanton number, both required an internal wall boundary condition to be known for calculation, so data was only provided within the bounds of the embedded thermocouples (with a few millimeters' exception to provide traces at 260mm); enough data was shown in the spanwise direction to study any effect of a free PEEK or metal-supported PEEK wall condition may have. Recall from Section 4.5 that the test article was hollow to allow for laser diagnostics, but outside of the $\pm$25.4mm span along the centerline the PEEK was in contact with the metal wedge frame. To prevent any contamination from these differing wall conditions, heat flux and Stanton number data is not provided beyond $\pm$25.4mm. The temperature measurements had no such limitations, and thus were provided over a larger domain. Again, the schlieren and IR runs were conducted concurrently, so the test matrix and plasma conditions are included in Tables 7.10 and 7.11 respectively. All still images were provided after the plasma had reached its operating condition and at the same time as the above schlieren images. Finally, it is noted that the glass used for laser diagnostics likely behaved differently from the PEEK measurements here; no correction is offered here, though Buen [212] used a thermocouple to measure the glass wall temperature for their PLIF work. Similarly, heating of the thermocouple by conduction through its mounting must be ignored. Note that thermocouples were mounted $[104.6, 122.1, 139.5, 157.0, 263.5, 327.0, 390.5, 454.0]$mm from the leading edge in the surface parallel coordinate. ([7])

The results are shown below. It is noted that they are compared to the numerical boundary layer solver's predictions and the oil flow's features in Section 7.2.6. Figure 7.30 provides the PEEK temperature under the maximum domain attainable. The forward views, 7.30(a) and (b) show slight heating near the electrodes; this was explored directly in a later figure. Figure 7.30(b) was especially important because it studied the streak behavior seen in the oil flow data. In Figure 7.23, the trip vortices merged just downstream of the electrodes. In IR, the corner vortices were apparent just downstream of the trip, and they seemed to blur together into a wake structure downstream of the electrodes. This may have implied that the same mechanism which drove the corner vortices apart in the oil flow data was the main turbulent structure, that the combined "wake" was the true breakdown mechanism and it pushed the oil into the troughs. It was noted that the strong thermal perturbations produced by the trips and enhanced by the plasma were likely to be the source of the degredation of the cathode and evident structures in the glow discharge discussed in Section 7.2.2.1. The middle and downstream views in Figure 7.30(c-f) show how the cutout beneath the PEEK did produce some spanwise nonuniformity, as did the thermocouples. The effects were small and were mostly corrected via heat flux calculation; this "heat flux normalization" allowed Leidy [213], who used a 6.35mm PEEK insert instead of the present 15.62mm, to produce workable data. Nevertheless, to be conservative it was best to focus on data from the core area where the thermocouples directly measured the internal conditions, and to take spanwise traces away from the location of the thermocouples. ([7])

Figures 7.31 through 7.36 show the effect turbulence and plasma had on temperature, heat

flux, and Stanton number. First considering the temperature data, Figures 7.31 and 7.32, there seemed to be little change over time, which suggested an isothermal wall condition of $\sim$ 350K was roughly appropriate throughout the majority of the domain in the core flow. It was surprising that the temperature was not significantly higher for the turbulent case than the laminar case, but this was likely a consequence of leaving the test article in the test section during preheat, which "set" the wall temperature near the adiabatic wall temperature. For the laminar and turbulent cases, the boundary layer solver calculated the adiabatic wall temperature to be 372.4K and 390.5K respectively. It was in this detail that the laminar and turbulent flows differentiated themselves as the turbulent case, being much farther from the adiabatic condition, had much higher heat flux (Figures 7.33 and 7.34). Naturally, the effects of the trips were strongest in the "Forward" location and smoothed out as one moved downstream; this suggested that the boundary layer became more uniform as the turbulence became fully developed, which was important in describing the quality of the test environment. To that end, by the "Back" location, the heat flux agreed reasonably well with the boundary layer solver's turbulent prediction (Figure 7.2(e)), both validating the code and the state of the turbulent boundary layer; the agreement in the laminar case (Figure 7.1(e)) was not as strong, the consequence of which will be discussed in Section 7.2.3.5. The collapse of heat flux traces over time was due to the internal PEEK becoming hotter. Any evidence of the free space or metal contact on the back of the model was not present in the heat flux data, which meant not only that the temperature difference was locally normalized, but that the thermocouples provided reasonable boundary conditions throughout the domain. Any trends noticed in heat flux extend to Stanton number, but because the latter was normalized by tunnel and wall conditions it allowed for run-to-run comparisons. Recall that when the trips were installed, the flow was considered "Turbulent" and the T_{aw} in the Stanton number was calculated with $Pr^{\frac{1}{3}}$, so the results in the "Forward" location (Figures 7.33 and 7.34) were suspect as the flow was likely transitional. Also at this location, the "Laminar" results were considerably higher than one might expect, and they varied largely from run-to-run with q_w. This was because $T_w \rightarrow T_{aw}$, but q_w did not approach 0; again, T_{aw} is considerably lower for laminar flows than for turbulent flows. This was likely a result of the thin PEEK at the leading edge, exposed on both the top and bottom surfaces. Here perhaps the temperature could change more rapidly, faster than the internal condition, as measured by the thermocouples, could. This would explain why the St fell so sharply as the flow started. Background subtracting the data may have helped account for the effect of being so near the leading edge during preheat, but it could not help if these elevated temperatures changed the test article's response to the flow. ([7])

Otherwise, the run-to-run normalization afforded by the Stanton number was useful when comparing the plasma on and off cases. The plasma had no obvious effect on the data, and despite normalization most of the variation between runs at the same location seemed to be from tolerable wall or tunnel differences. This meant that the plasma did not have a noticeable impact on the state of the boundary layer and thermal boundary condition, at least to within the fidelity of the IR thermography employed here. This was not problematic because the goal was always to seed in nonequilibrium, not modify the boundary layer. Furthermore, this was not to say the plasma had no thermal impact whatsoever. Figure 7.37 shows how the cathode heated up over time. In under 20s of total operation, it heated the PEEK immediately downstream $\sim$ 15K, a considerable

amount given the short duration. This underscored the real impact cathode heating could have. The downstream side of the cathode was more greatly affected which implied the heat was convected off the surface as well as conducted through the PEEK. ([7])

7.2.3.4 High Frequency Pressure Transducer Results

High frequency pressure measurements provide the spectral content in the boundary layer, from which one can infer its state: laminar; transitional; or turbulent. By varying their placement along the plate, these sensors can track the breakdown process; analogously, moving them to different positions along the span can provide detail on specific physics such as the effect of wakes, corner vortices, and troughs. As was discussed in Section 6.2.5, uncalibrated Kulite XCE-062A pressure transducers with a Kulite KSC2-C3 signal conditioning box were used for all of these measurements which should provide voltage fluctuations from $f = 0 \sim f_r \approx 250$kHz. Because all analyses were done in the frequency space and these Kulites scaled linearly between voltage and pressure, it was sufficient to measure voltage fluctuations alone. The Kulites were placed 130, 260, and 405mm from the leading edge to match, as best as possible, the measurements from other techniques; extra space was added near the electrodes to attempt to prevent electrical interference. The sensors were placed 0 (wake), -3.42 (trough), -6.84 (wake), and -10.26mm (trough) along the span to again match previous off-centerline measurements, and to attempt to make measurements in wakes, troughs, and corner vortices. IR measurements were taken alongside the Kulite data for the express purpose of recording the placement of flow features with respect to the sensors. The test matrix and plasma conditions from what ended up being the few successful plasma runs are shown in Tables 7.12 and 7.13 respectively; Figure 7.38 shows the plasma power traces for the corresponding runs. ([7])

Before and test data could be taken, the efficacy of the new REZCOMP™ technology needed to be verified. To do so, the tunnel was run three times with the trips installed and the Kulites in the downstream location as it was desirable to pass as noisy of a signal as possible into the signal conditioning boxes. For the first run the signals were passed through a 200kHz Krohn-Hite low-pass filter (this is the "lab standard" approach), then for the next run through the Kulite KSC-2 with the REZCOMP™ feature turned off, and finally for the last run passed through the Kulite KSC-2 box with REZCOMP™ turned on and optimized. The results from the centerline Kulite, shown in Figure 7.39, show the clear superiority of the REZCOMP™ technology. As expected, the 200kHz low-pass filter did at least partially remove the resonant frequency spike at ~ 250kHz, but it still mostly remained and bled back into the otherwise flat-frequency response regime. The REZCOMP™ filter, however, reduced the resonant frequency to the amplitude of electrical noise like the spikes above 250kHz and extended the desired flat-frequency regime. It is noted that the data were cut off at 500kHz as this is where the Kulite KSC-2 boxes natural roll-off was reported. ([7])

It is also worthwhile here to quickly address the effect of the plasma on the boundary layer's spectra. In short, there was no meaningful effect, as evinced by Figure 7.40. These data were taken from the centerline Kulite both with and without the trips installed; the "No plasma" case was the instantaneous trace when the tunnel reached $Re = 6 \times 10^6/\text{m}$ and the "Plasma" case represented the average of 15s of data when the tunnel was parked at $Re = 6 \times 10^6/\text{m}$ and the plasma was

No.	Location	Trip	Plasma	Filter	Run/Date
1	Back	Turbulent	Off	Low-pass filter	5053, 11/9/2021
2	Back	Turbulent	Off	None	5052, 11/9/2021
3	Back	Turbulent	Off	REZCOMP™	5054, 11/9/2021
4	Back	Turbulent	On	REZCOMP™	5055, 11/9/2021
5	Back	Laminar	Off	REZCOMP™	5057, 11/9/2021
6	Back	Laminar	On	REZCOMP™	5056, 11/9/2021
7	Middle	Turbulent	Off	None	5058, 11/11/2021
8	Middle	Turbulent	Off	REZCOMP™	5064, 11/11/2021
9	Middle	Laminar	Off	REZCOMP™	5065, 11/15/2021
10	Front (K3, K2, K1)	Turbulent	Off	None	5068, 11/16/2021
11	Front (K3, K2, K1)	Turbulent	Off	REZCOMP™	5069, 11/16/2021
12	Front (K3, K2)	Laminar	Off	REZCOMP™	5070, 11/16/2021
13	Front (K4)	Turbulent	Off	None	5075, 11/18/21
14	Front (K4)	Turbulent	Off	REZCOMP™	5076, 11/18/2021
15	Front (K4)	Laminar	Off	REZCOMP™	5077, 11/18/2021

Table 7.12: High frequency pressure transducer test matrix.

No.	Current (mA)	Power Supply Voltage (V)	Power Supply Power (W)	Plasma Voltage (V)	Plasma Power (W)
4	95.2	1409	134.1	455.7	43.4
6	95.0	1425	135.3	473.5	45.0
			Average		
	95.1	1417	134.7	464.6	44.2

Table 7.13: Plasma conditions for high frequency pressure campaign.

on-condition. In both cases, the traces were almost identical, with some discrepancy likely owing to run-to-run variation and smoothing due to averaging the plasma traces. Specifically, the offset between the traces in Figure 7.40(a) was not consistent, or even present, for the other three Kulites when comparing these runs. These plasma traces were only available for the "Back" test location 405mm from the leading edge; efforts to take data at the stations nearer to the electrodes were foiled by electromagnetic interference, even with the Kulites 168.7mm from the cathode. Thus there remained some tangible consequence of the plasma, but it was too weak to manifest in the boundary

layer's spectra; this heavily implied the plasma was not affecting the turbulence as described in Section 2.2.4. ([7])

One of the objectives of this campaign was to identify any spanwise variation in the flow, especially as it pertained to wakes and troughs from the boundary layer trips. In order to understand exactly where the Kulites were with respect to flow features, IR thermography was conducted in conjunction with the pressure data collection. The results for characteristic runs at each location and for the laminar and turbulent flows are included in Figures 7.41 and 7.42 respectively. Each figure contains an IR temperature reading from the region of interest at the test condition $Re = 6 \times 10^6/\text{m}$ and a corresponding temperature trace, with the Kulite locations included on the bottom axis. Because the PEEK needed to be pocketed to allow the short Kulites to be installed, the results near the actual sensors were unclear, and so the temperature traces were taken 30mm downstream of the Kulites. As the flow developed downstream there was some movement of the wakes and troughs, but it was observed to be minor and thus this separation was tolerable. In regards to Figure 7.42, in the "Front" location Kulites 4 and 2 (recall these were 0 and -6.84mm from the centerline respectively) were solidly in the wakes while Kulites 3 and 1 were solidly in the troughs, which followed from their placement with respect to the trips. By the downstream locations, however, the placement became more ambiguous. For example, in the "Rear" location Kulites 4 and 3 were solidly in a wake and trough respectively, but Kulites 2 and 1 were on the boundary between the two; should they still exist so far into the fully turbulent environment, these sensors may have been in corner vortices. This again shows the development of the boundary layer, movement of the flow features, and physical size of the Kulites complicated their precise placement, and it also underscored the importance of taking real-time IR measurements. Additional results from IR thermography are provided in Section 7.2.3.3. ([7])

The bulk of the results are included in Figures 7.43 through 7.48, grouped by location and the boundary layer's state. Every plot contains mean "Pre-run" data from each Kulite, collected over a few seconds before the tunnel started; this allowed the identification of the noise floor as well as any inherent frequencies in the circuit, though in general the signal was clean. Each figure shows the spectra from each of the four Kulites at that streamwise location, with the exception of Figure 7.43 owing to the failure of Kulite 1 during this run; due to the uniformity of the laminar data from the other spanwise and streamwise locations, this run was not repeated to fill this gap in the data. To that end, in general the laminar data showed little variation between spanwise locations and even streamwise locations. The former was important as it confirmed the spanwise uniformity of the test article, at least between the "Wake" (0mm) and "Trough" (10.26mm) test locations used throughout this project. It was interesting to see that the signal intensified significantly between $Re = 3$ and $3.5 \times 10^6/\text{m}$ owing to the transitioning nozzle sidewalls increasing the freestream noise at this Reynolds number [214, 206]. Beyond this transitory point, the laminar data tended to collapse for the remainder of the Reynolds numbers in the run, with any variation more likely due to the different sensors than true flow physics. In their laminar wedge experiments in the ACE tunnel, Leidy [213] was able to borrow from low speed theory and observe the frequency of the Type-I secondary instability at $f_I = U_e/(2\delta)$ Craig and Saric [338], but here no such frequency was clear. There may be some content at ~ 40kHz at the "Middle" and "Back" locations owing to the slope change in the frequency decay, but the evidence was weak. ([7])

The turbulent boundary layer results contained more interesting physics. Begin with the data from the "Front" of the plate, Figure 7.44. For those sensors in the trip wake, K4 and K2, there appeared to be two distinct frequencies at ~ 20 and ~ 50kHz. The latter was established as soon as the freestream became noisy at $Re = 3.5 \times 10^6/\text{m}$, but the former only became defined at $Re = 5 \times 10^6/\text{m}$. In the troughs, only the ~ 50kHz frequency was apparent. This suggested the corner vortices in the wake fomented turbulence through, in part, this higher frequency. Also, in general, that the frequency of a disturbance tended to grow with the Reynolds number likely stemmed from the thinning of the boundary layer; see [5]. Plotted on all tripped figures is a line with a slope of $-5/3$. This is taken from Kolmogorov's theory Kolmogorov [339, 340] that the turbulent kinetic energy $E = f(k, \varepsilon, \nu)$, where k is the wavenumber, ε is the dissipation, and ν is the viscosity. In the so-called inertial subrange, viscosity can be neglected and one can write $E(k) = \alpha \varepsilon^{2/3} k^{-5/3}$. Thus when plotted on a logarithmic wavenumber axis or, here, the frequency (Semper [206] compared the two using $f = \frac{k u_\infty}{2\pi}$), one would expect the kinetic energy of isotropic turbulence to cascade with a slope of $-5/3$. This is Kolmogorov's $-5/3$ Law, which is well described in Pope [51], Tennekes [341], Ortiz-Suslow and Wang [342]. Although boundary layers cannot be considered isotropic, here the theory was used to check if flow was turbulent by qualitatively comparing the slope of the cascade portion of the spectrum with the $-5/3$ line. At this upstream location, the agreement was poor, especially in the wakes. This implied the boundary layer was still at least partially transitioning, which followed from the measurements in Sections 7.2.3.1 and 7.2.3.2. As one moved downstream to 260mm from the leading edge, the data better agree with the theory. In Figure 7.46, it seemed the two frequencies had merged to create one production [51, 341] frequency at ~ 30kHz; again, these results only turned on with the presence of freestream noise above $Re = 3.5 \times 10^6/\text{m}$. This energy was passed into progressively higher frequencies until it decayed into the noise floor near the sensors' f_r; again, due to the inability to perfectly predict Q, the depression around f_r made it challenging to definitively say if the turbulent structures had fully dissipated by this point, though the relatively high energy levels at higher Reynolds numbers made this seem unlikely. Moving downstream to 405mm from the leading edge, the boundary layer continued to develop and grow, meaning there was still better agreement with the $-5/3$ Law and the production frequency fell to ~ 20kHz respectively. At both of these turbulent locations, there was no clear difference in the response from any of the sensors, so while Figure 7.42 showed their placement in wakes and troughs may be imperfect, there was a strong case the more turbulent boundary layer become homogenized in the spanwise direction. ([7])

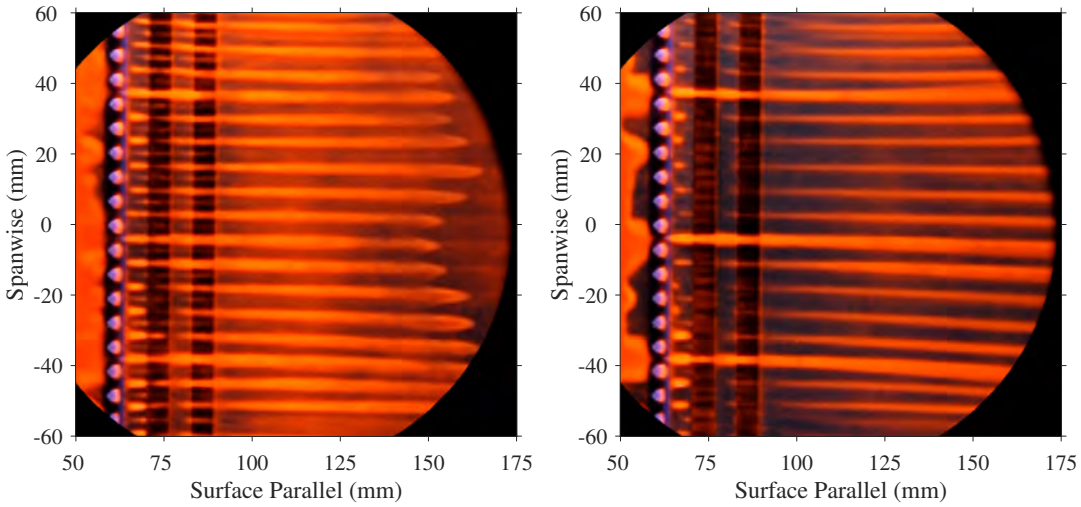

(a) $t = 3$s

(b) $t = 6$s

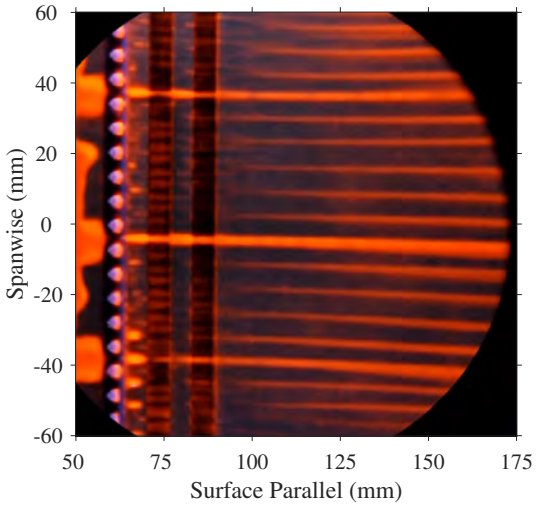

(c) $t = 9$s

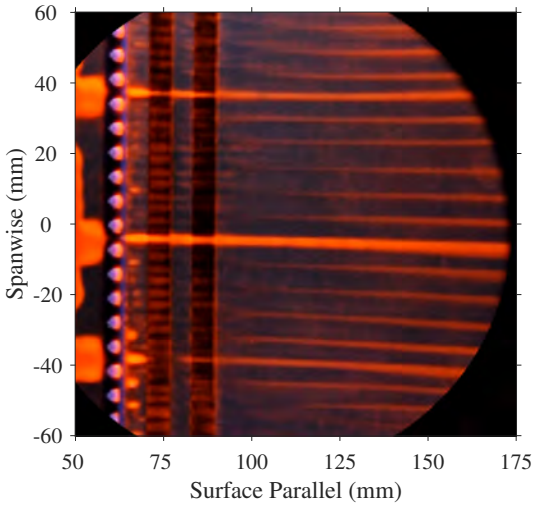

(d) $t = 12$s

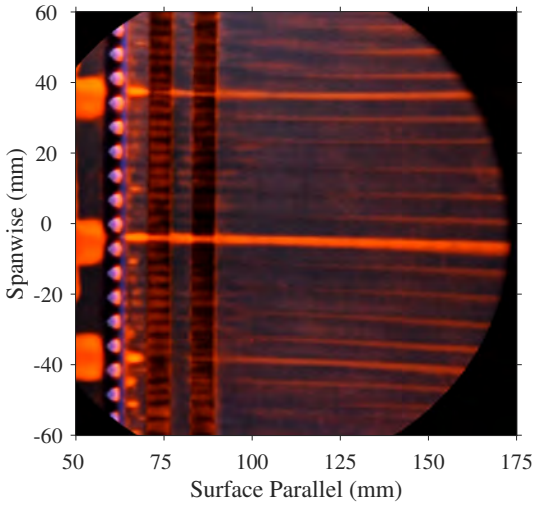

(e) $t = 15$s

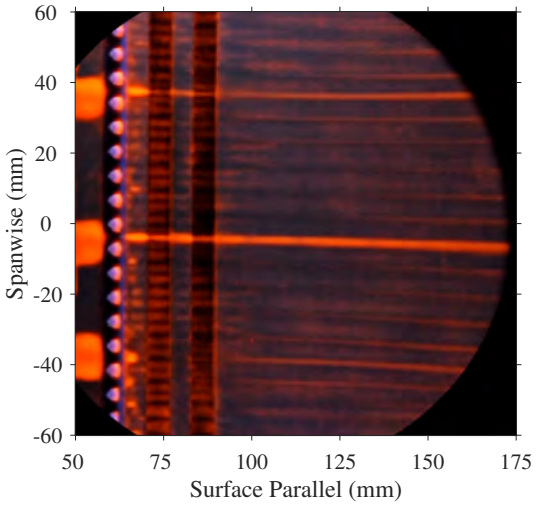

(f) $t = 18$s

Figure 7.23: Temporal evolution at the Forward location. [7]

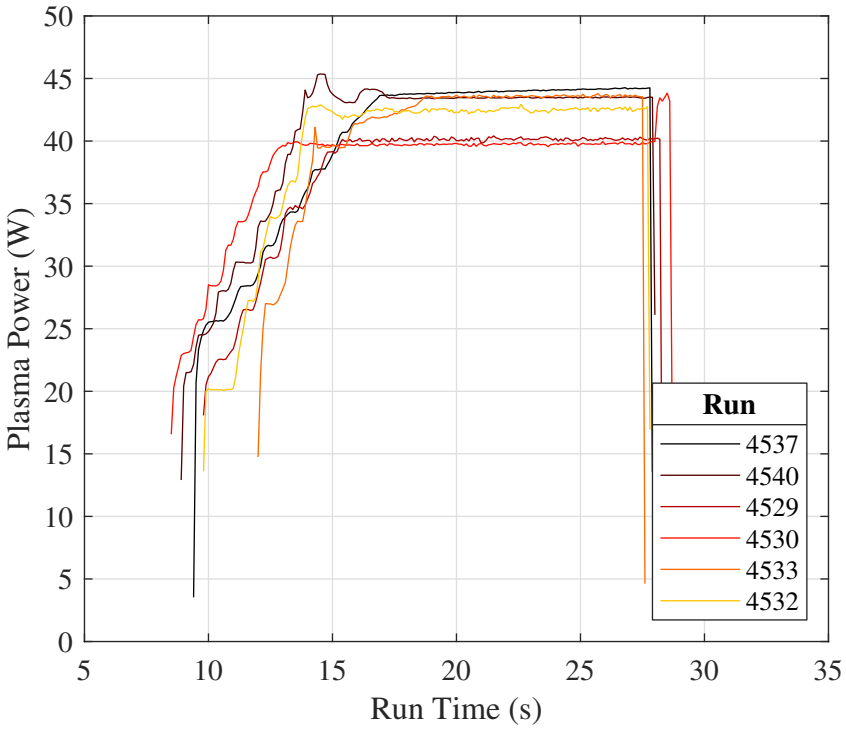

Figure 7.24: Plasma power traces for schlieren and IR thermography runs. [7].

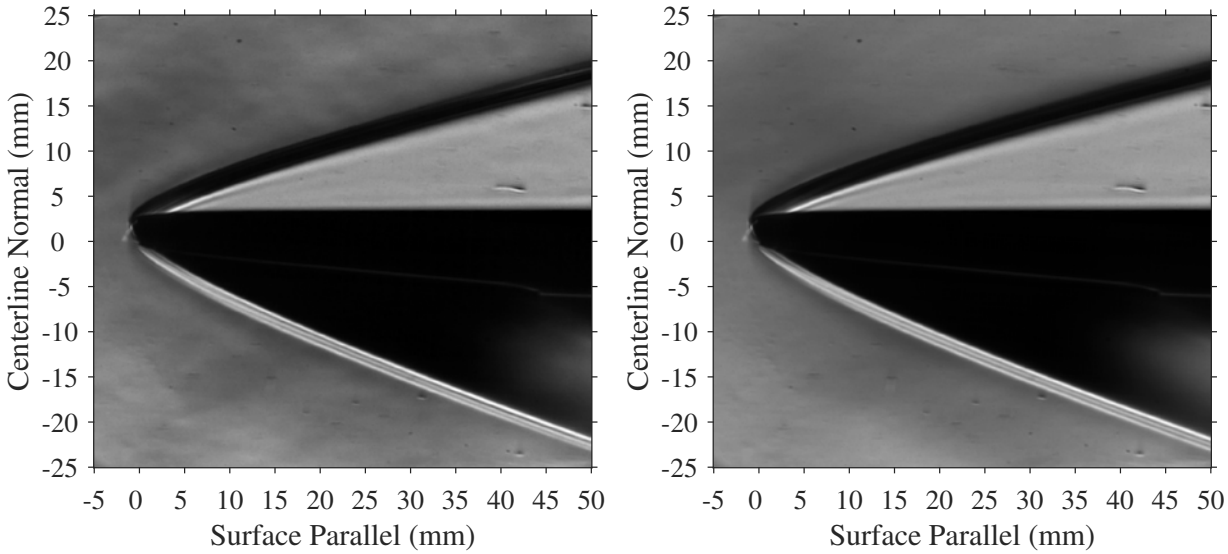

(a) Instantaneous

(b) Mean

Figure 7.25: Instantaneous and mean schlieren images of the leading edge. Trips are installed, but out of view. [7].

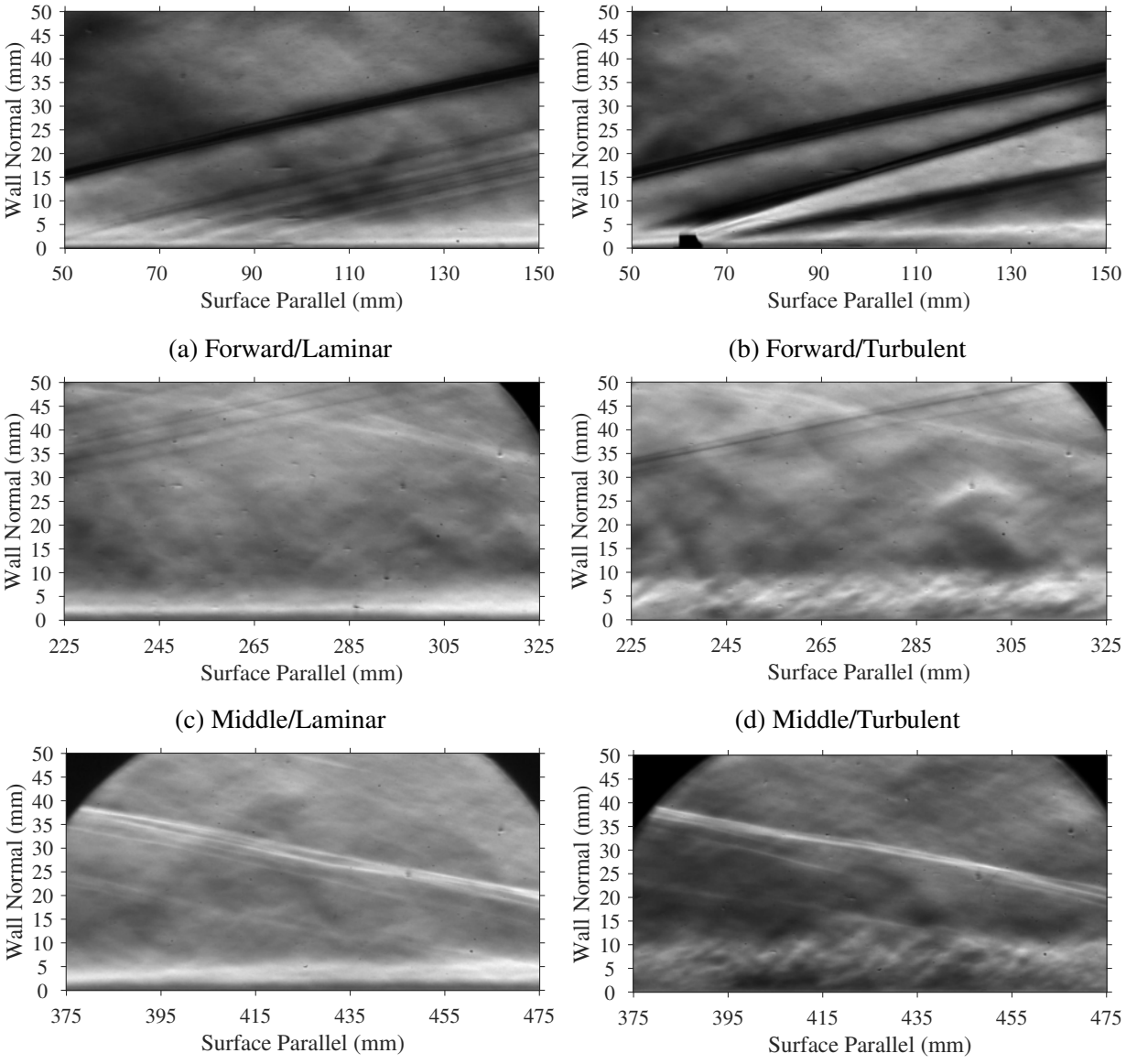

(a) Forward/Laminar

(b) Forward/Turbulent

(c) Middle/Laminar

(d) Middle/Turbulent

(e) Back/Laminar

(f) Back/Turbulent

Figure 7.26: Instantaneous schlieren images with the plasma off. [7]

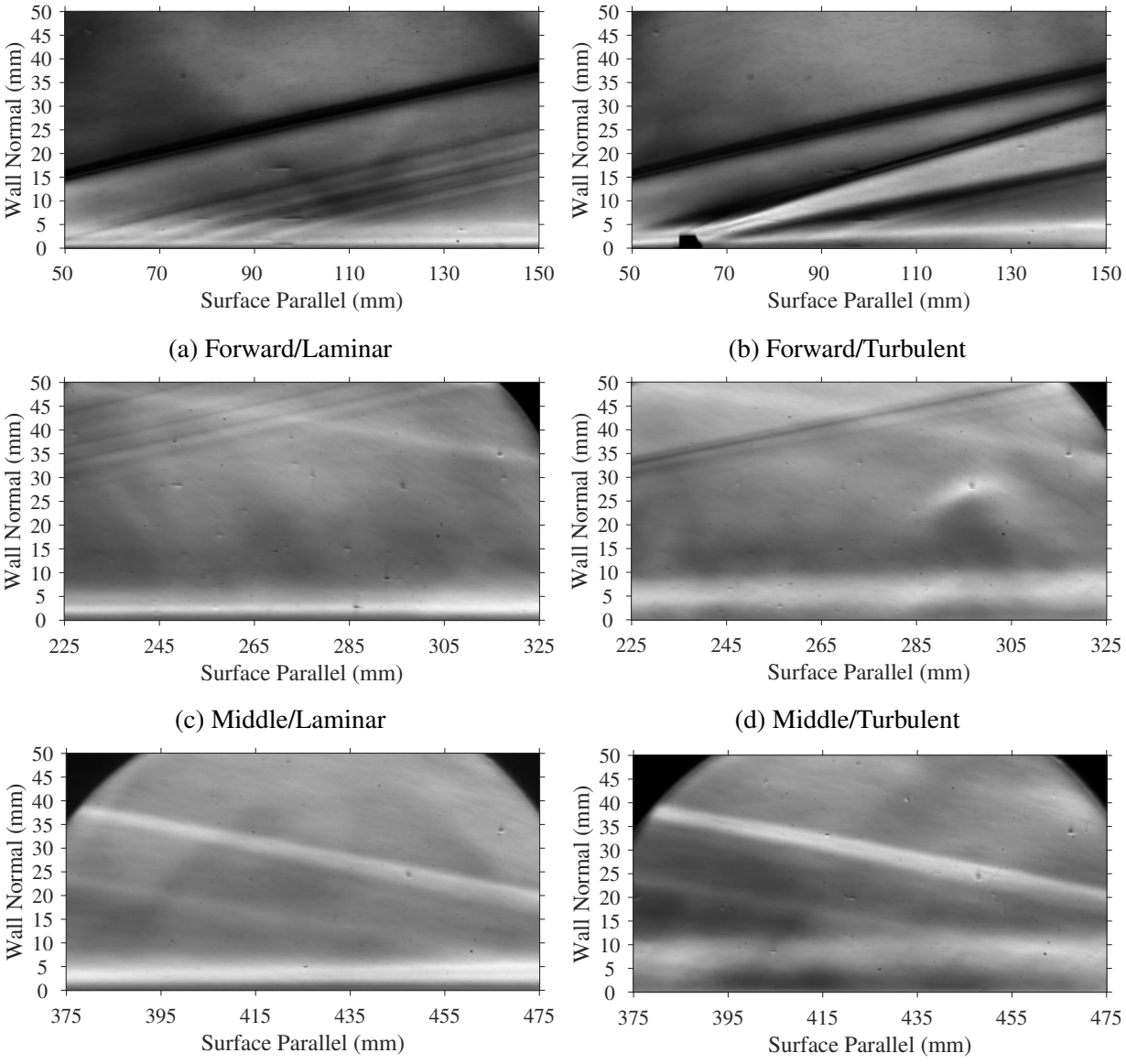

(a) Forward/Laminar

(b) Forward/Turbulent

(c) Middle/Laminar

(d) Middle/Turbulent

(e) Back/Laminar

(f) Back/Turbulent

Figure 7.27: Mean schlieren images with the plasma off. [7]

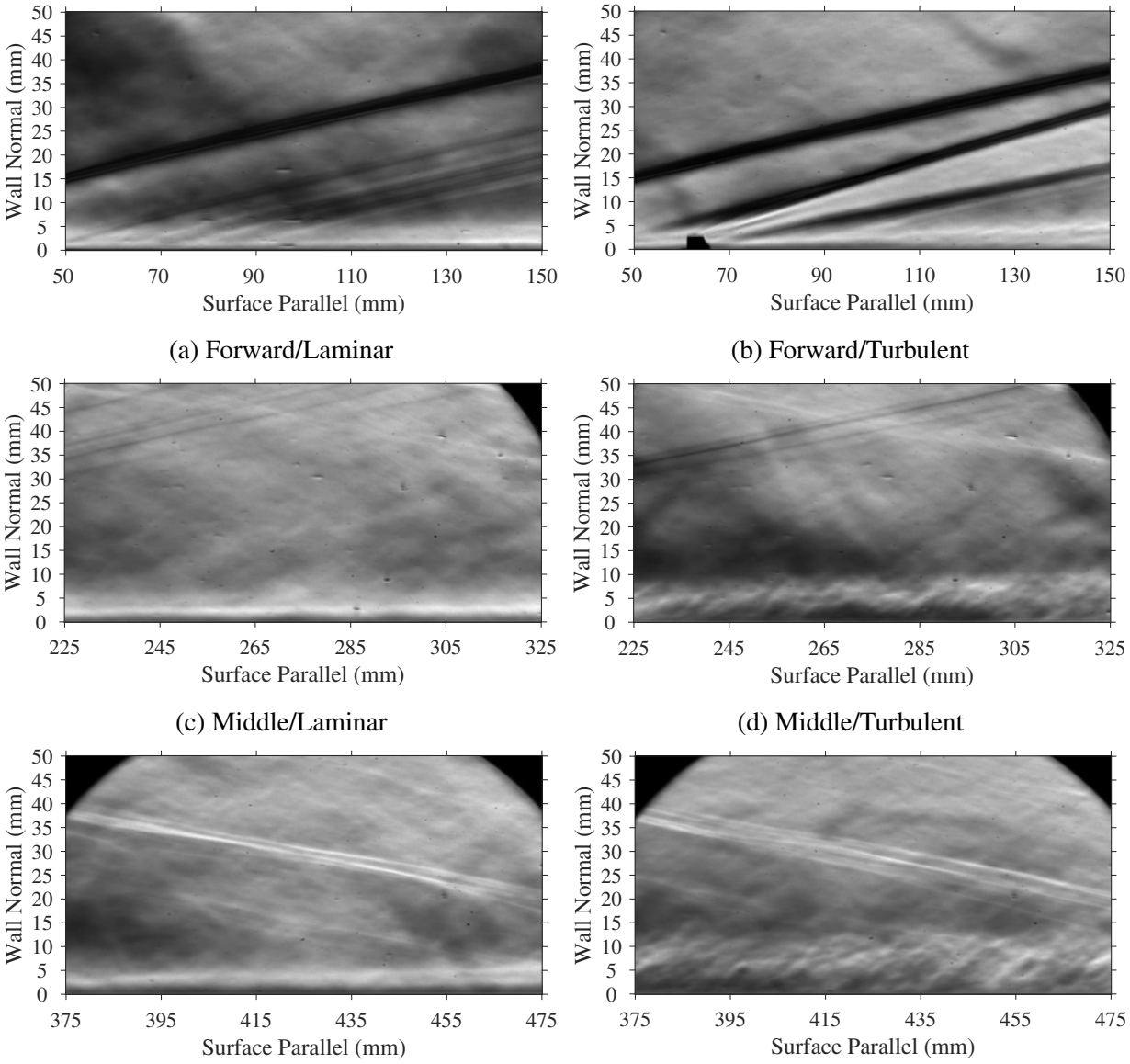

(a) Forward/Laminar

(b) Forward/Turbulent

(c) Middle/Laminar

(d) Middle/Turbulent

(e) Back/Laminar

(f) Back/Turbulent

Figure 7.28: Instantaneous schlieren images with the plasma on. [7]

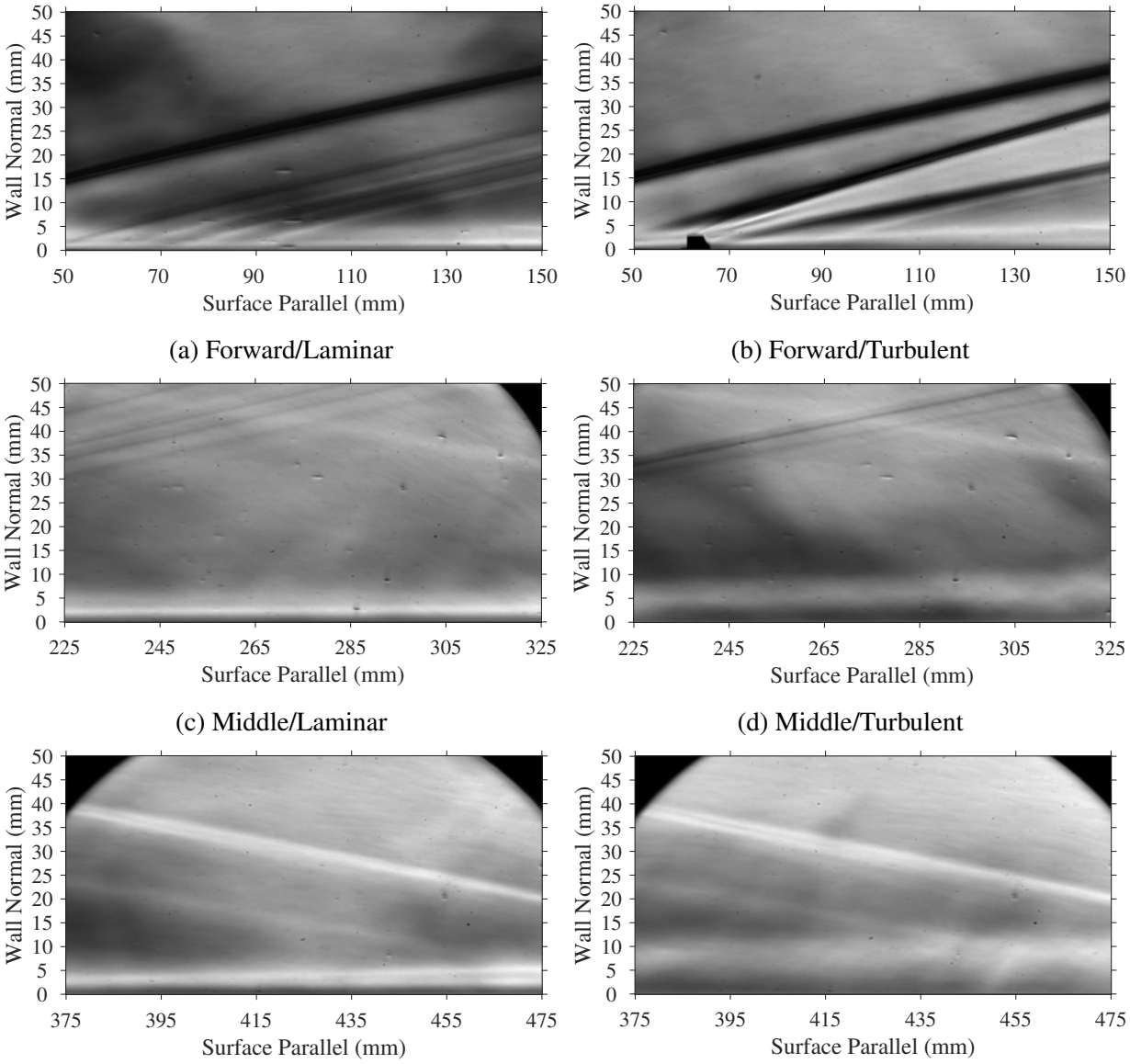

(a) Forward/Laminar

(b) Forward/Turbulent

(c) Middle/Laminar

(d) Middle/Turbulent

(e) Back/Laminar

(f) Back/Turbulent

Figure 7.29: Mean schlieren images with the plasma on. [7]

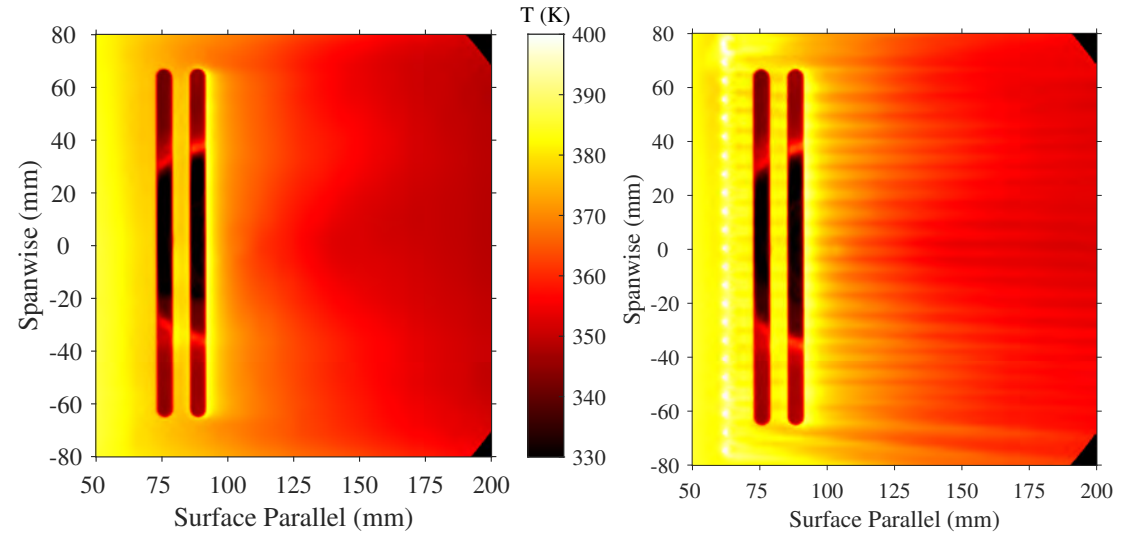

(a) Forward/Laminar

(b) Forward/Turbulent

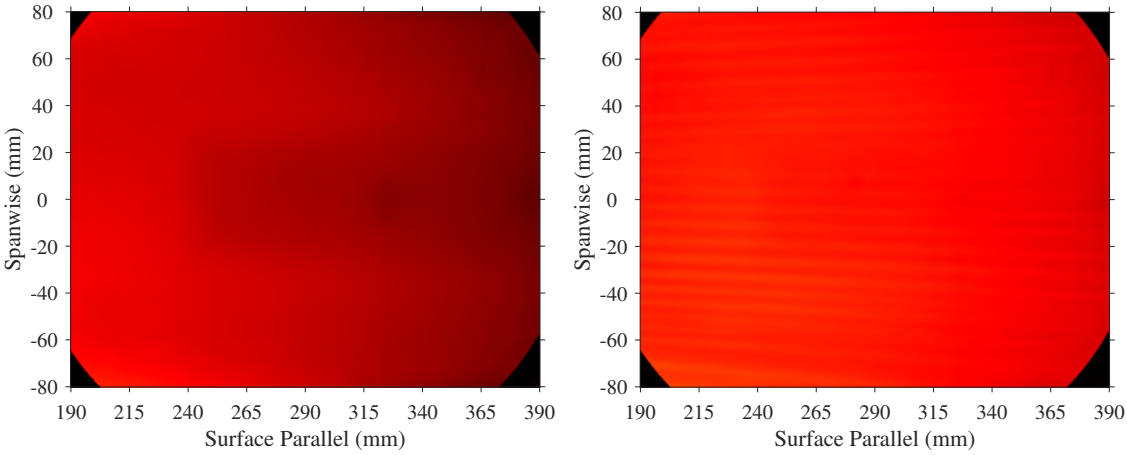

(c) Middle/Laminar

(d) Middle/Turbulent

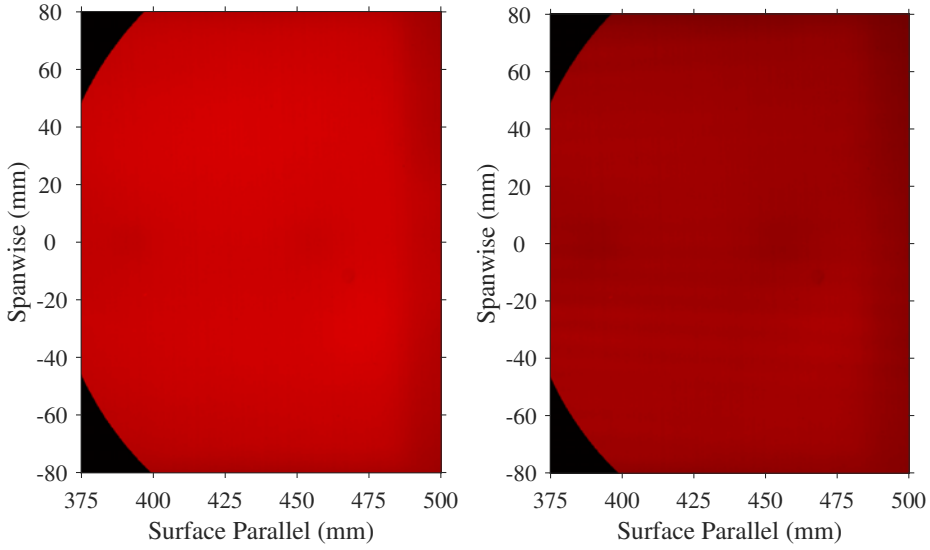

(e) Back/Laminar

(f) Back/Turbulent

Figure 7.30: IR temperature maps with the plasma on. Same legend applies for all figures. [7]

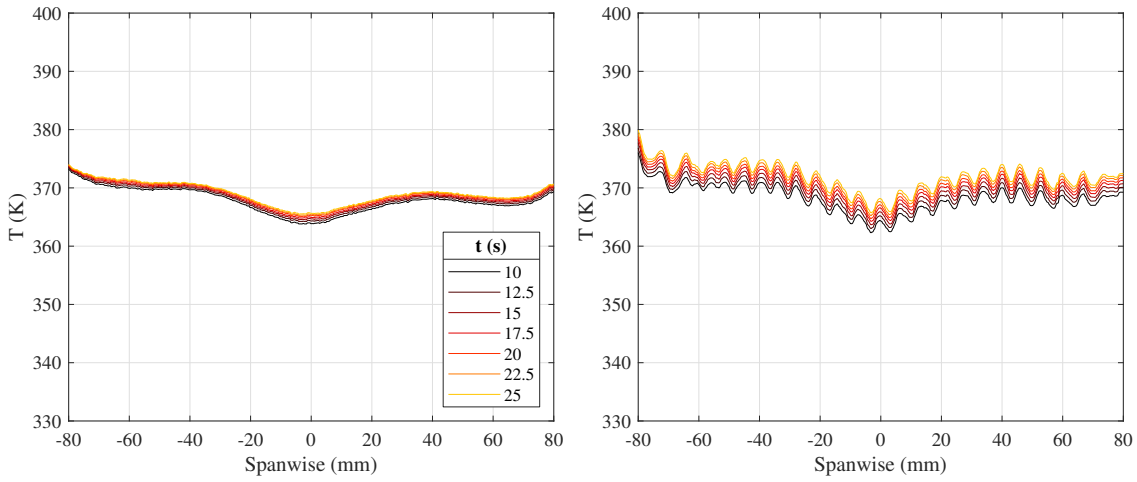

(a) Forward/Laminar

(b) Forward/Turbulent

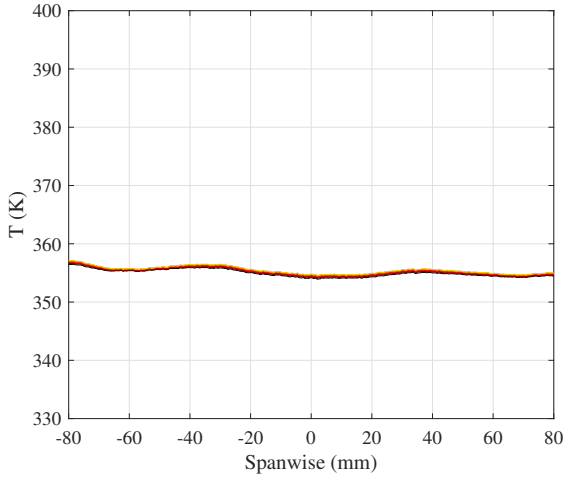

(c) Middle/Laminar

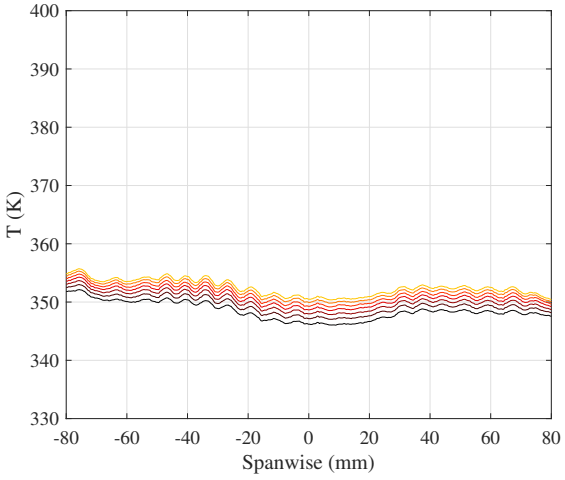

(d) Middle/Turbulent

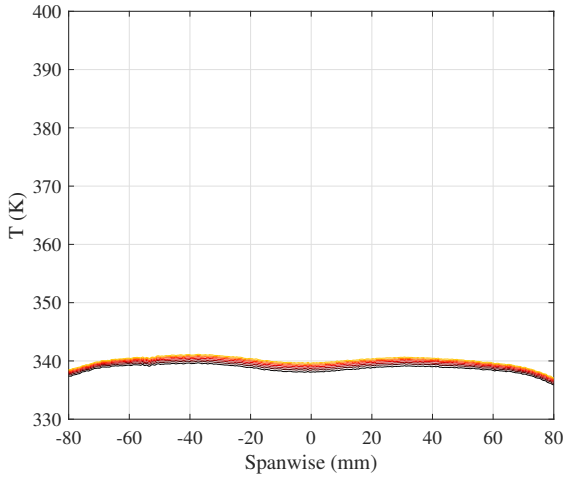

(e) Back/Laminar

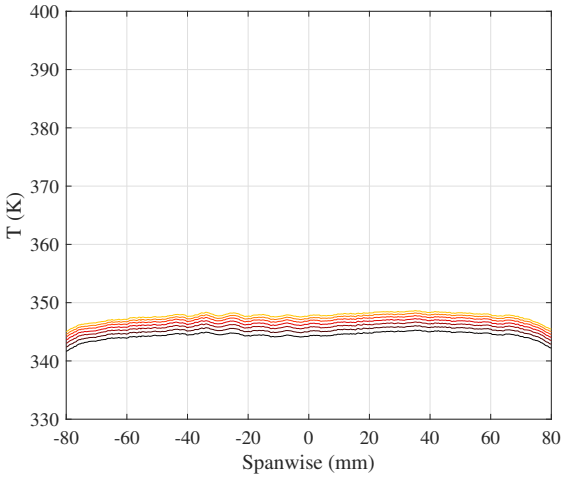

(f) Back/Turbulent

Figure 7.31: IR temperature spanwise traces with the plasma off. Traces are 115 ("Forward"), 260 ("Middle"), and 405mm ("Back") from the leading edge. Same legend applies for all figures. [7]

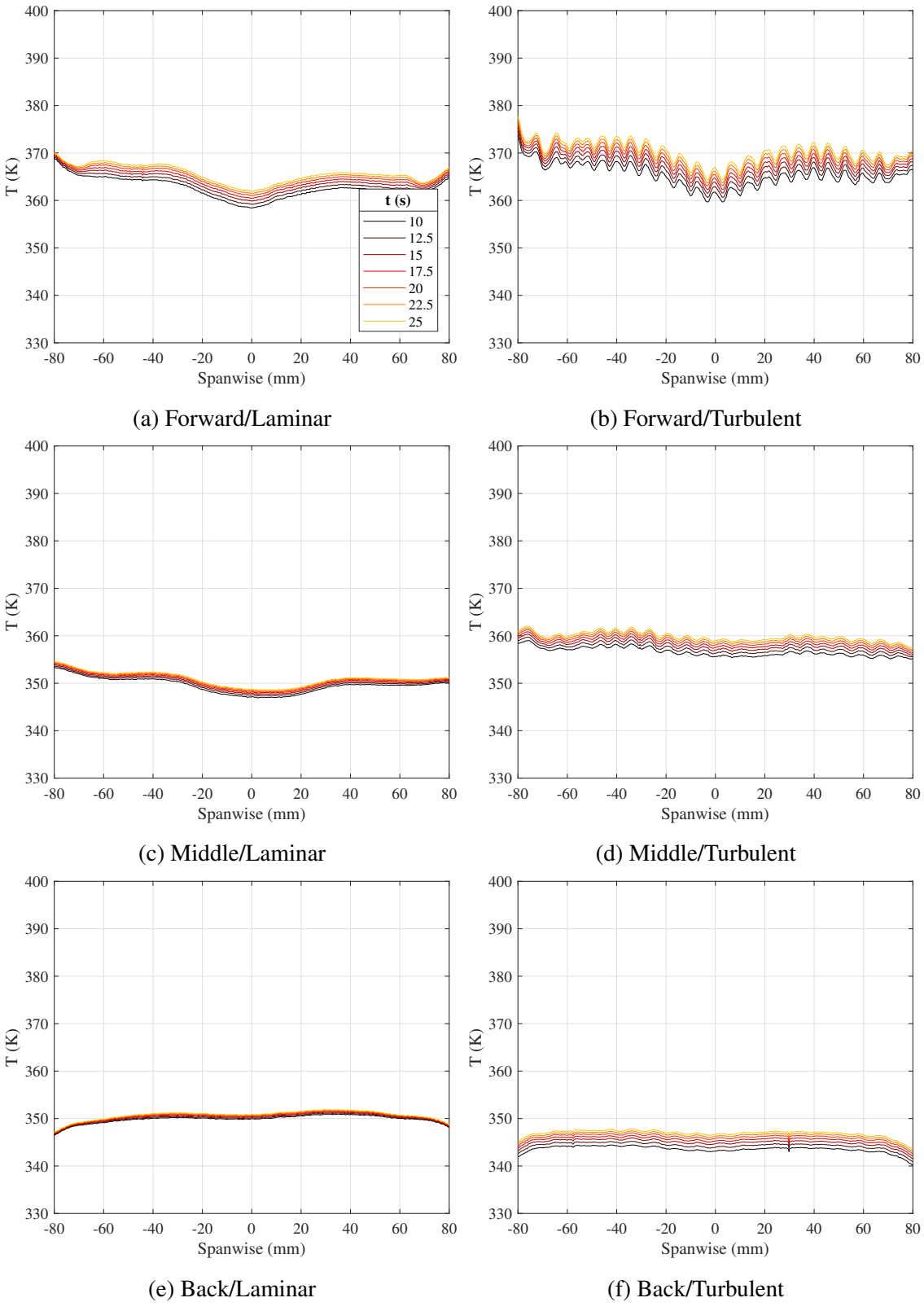

(a) Forward/Laminar

(b) Forward/Turbulent

(c) Middle/Laminar

(d) Middle/Turbulent

(e) Back/Laminar

(f) Back/Turbulent

Figure 7.32: IR temperature spanwise traces with the plasma on. Traces are 115 ("Forward"), 260 ("Middle"), and 405mm ("Back") from the leading edge. Same legend applies for all figures. [7]

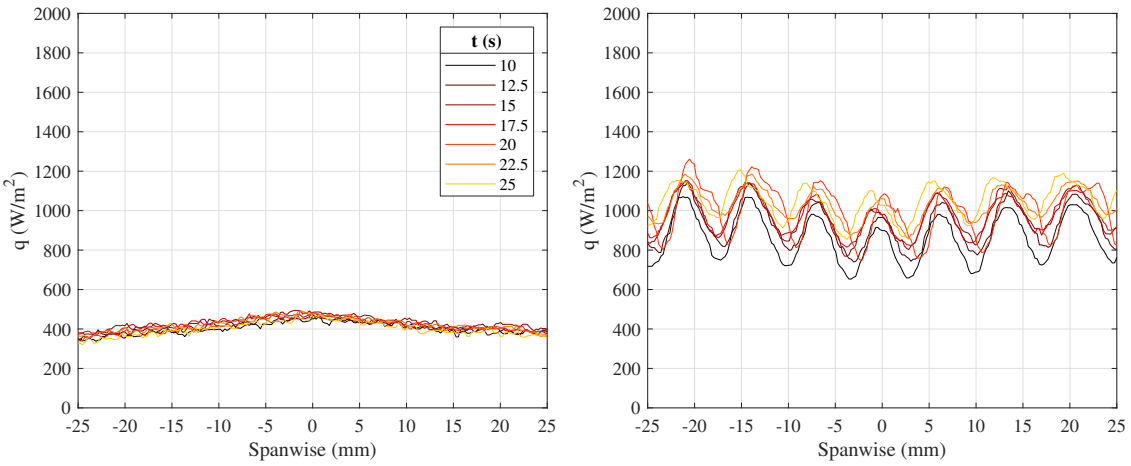

(a) Forward/Laminar

(b) Forward/Turbulent

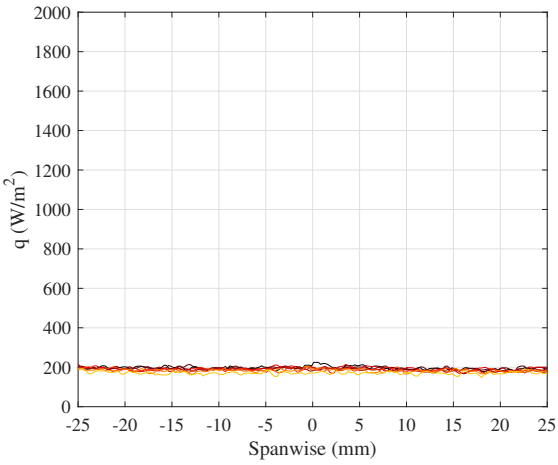

(c) Middle/Laminar

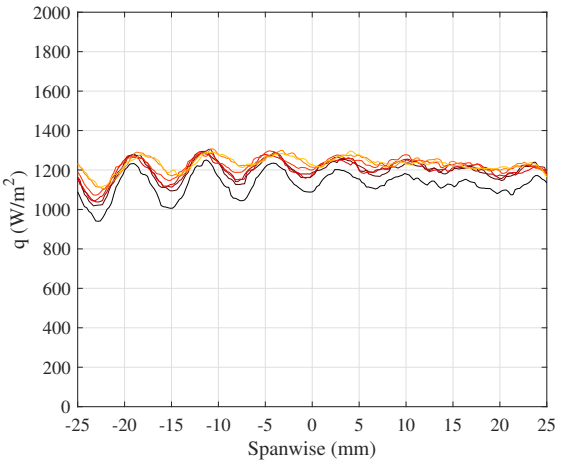

(d) Middle/Turbulent

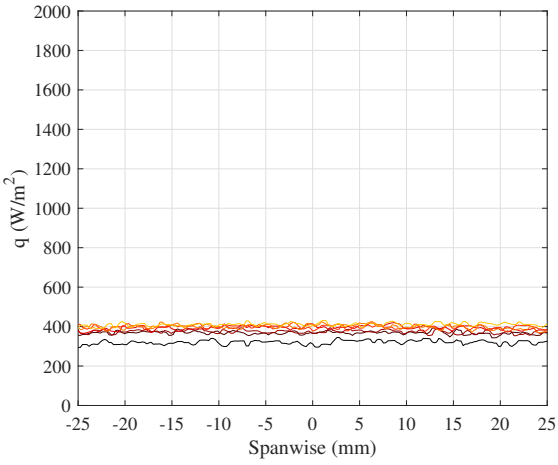

(e) Back/Laminar

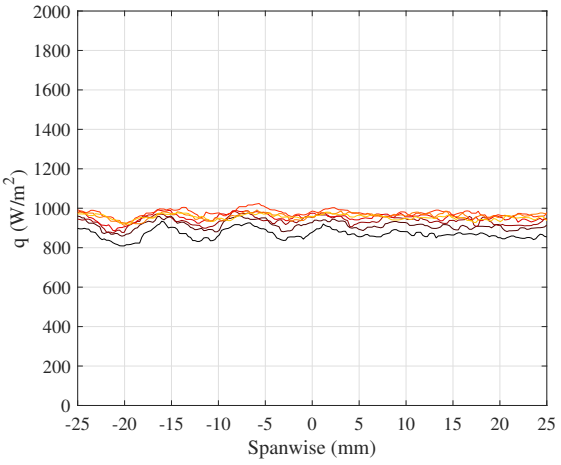

(f) Back/Turbulent

Figure 7.33: IR heat flux spanwise traces with the plasma off. Traces are 115 ("Forward"), 260 ("Middle"), and 405mm ("Back") from the leading edge. Same legend applies for all figures. [7]

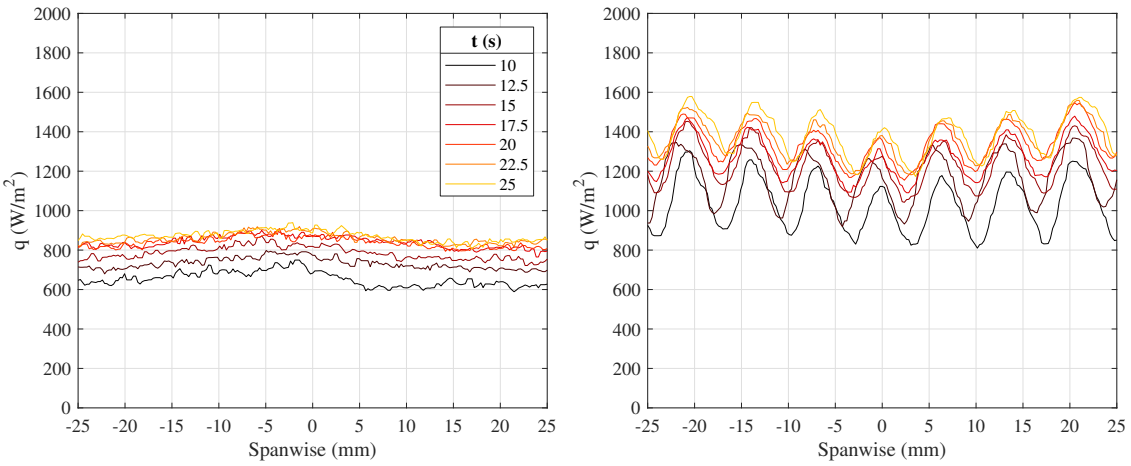

(a) Forward/Laminar

(b) Forward/Turbulent

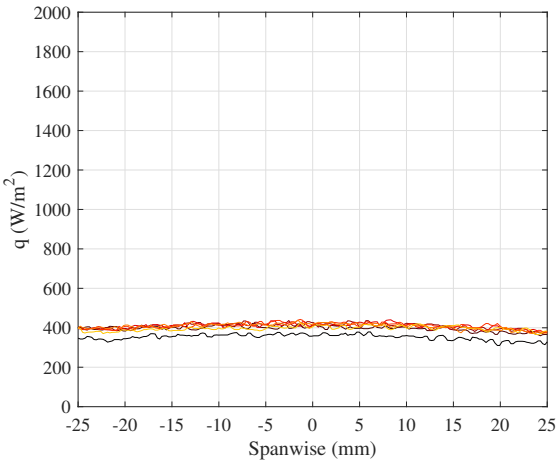

(c) Middle/Laminar

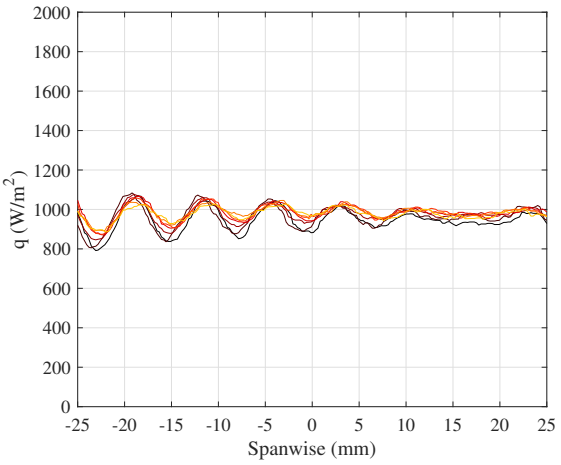

(d) Middle/Turbulent

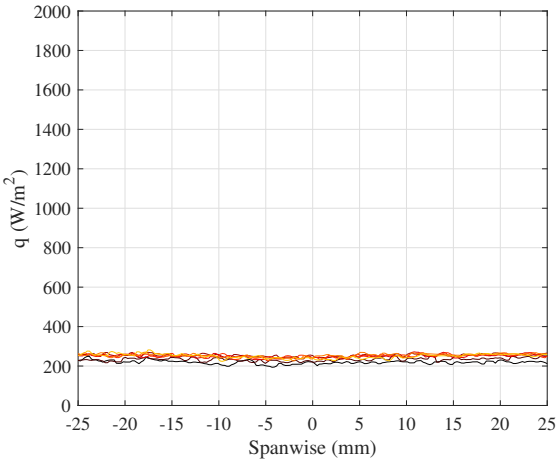

(e) Back/Laminar

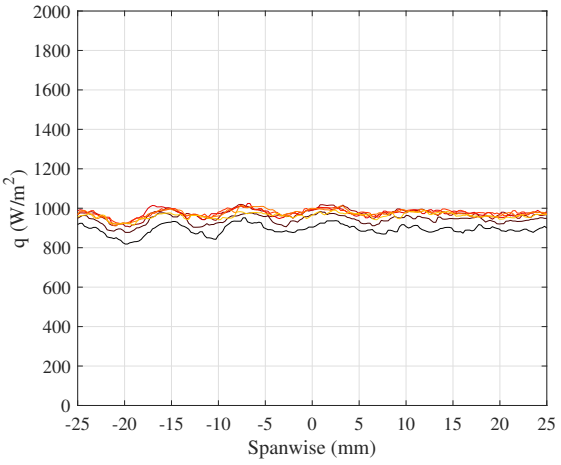

(f) Back/Turbulent

Figure 7.34: IR heat flux spanwise traces with the plasma on. Traces are 115 ("Forward"), 260 ("Middle"), and 405mm ("Back") from the leading edge. Same legend applies for all figures. [7]

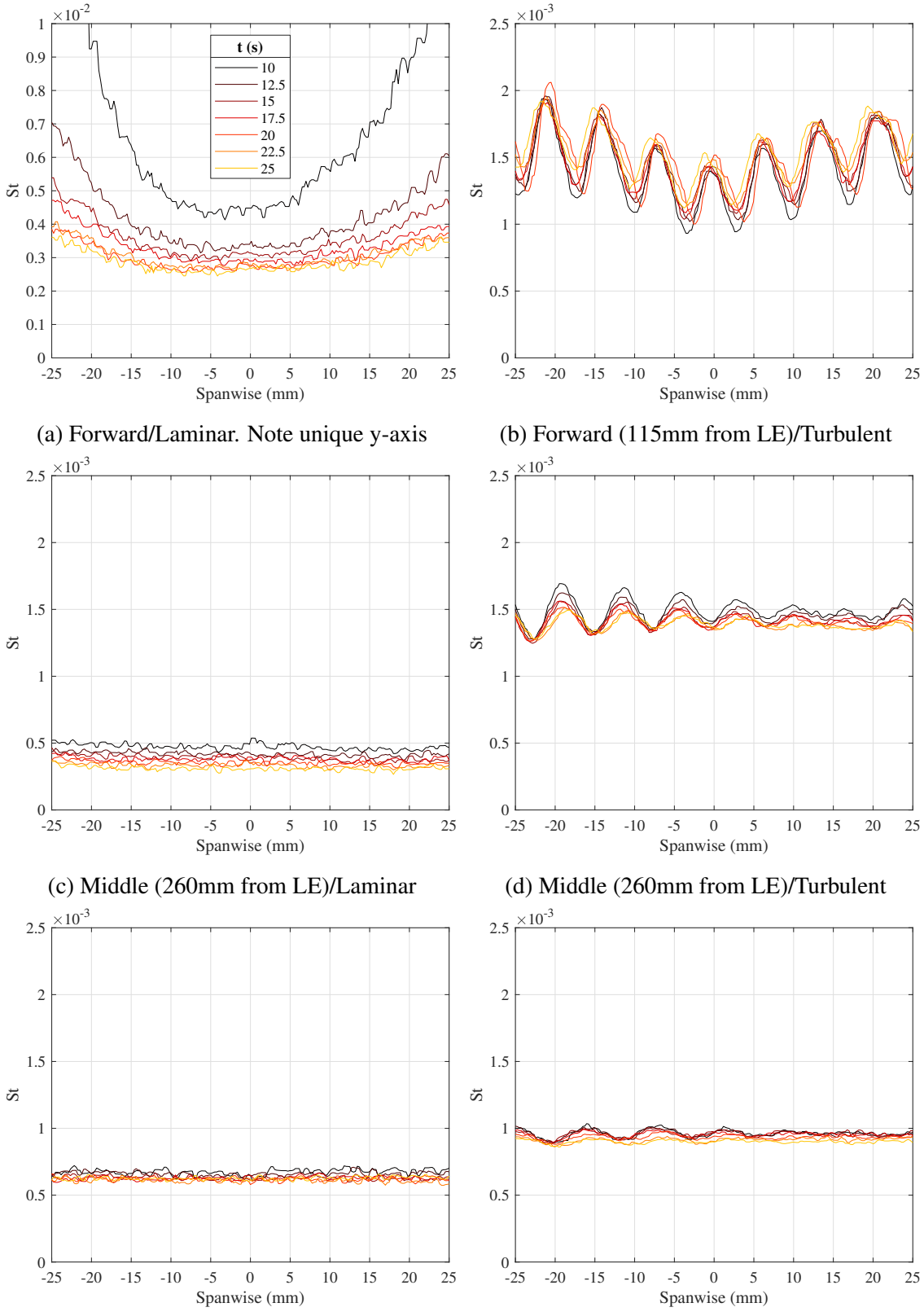

(a) Forward/Laminar. Note unique y-axis

(b) Forward (115mm from LE)/Turbulent

(c) Middle (260mm from LE)/Laminar

(d) Middle (260mm from LE)/Turbulent

(e) Back (405mm from LE)/Laminar

(f) Back (405mm from LE)/Turbulent

Figure 7.35: IR Stanton number spanwise traces with the plasma off. Traces are 115 ("Forward"), 260 ("Middle"), and 405mm ("Back") from the leading edge. Same legend applies for all figures. [7]

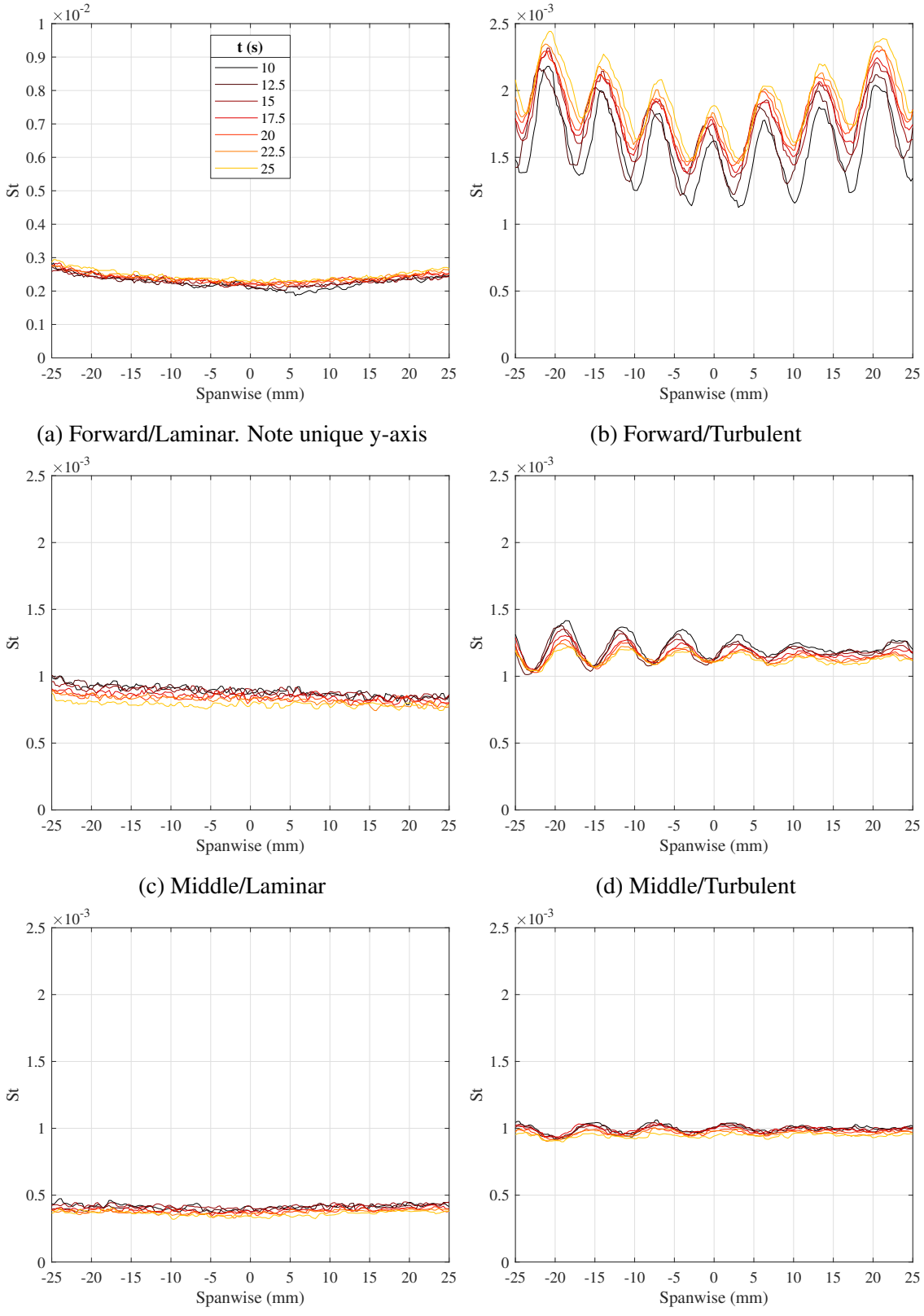

(a) Forward/Laminar. Note unique y-axis

(b) Forward/Turbulent

(c) Middle/Laminar

(d) Middle/Turbulent

(e) Back/Laminar

(f) Back/Turbulent

Figure 7.36: IR Stanton number spanwise traces with the plasma on. Traces are 115 ("Forward"), 260 ("Middle"), and 405mm ("Back") from the leading edge. Same legend applies for all figures. [7]

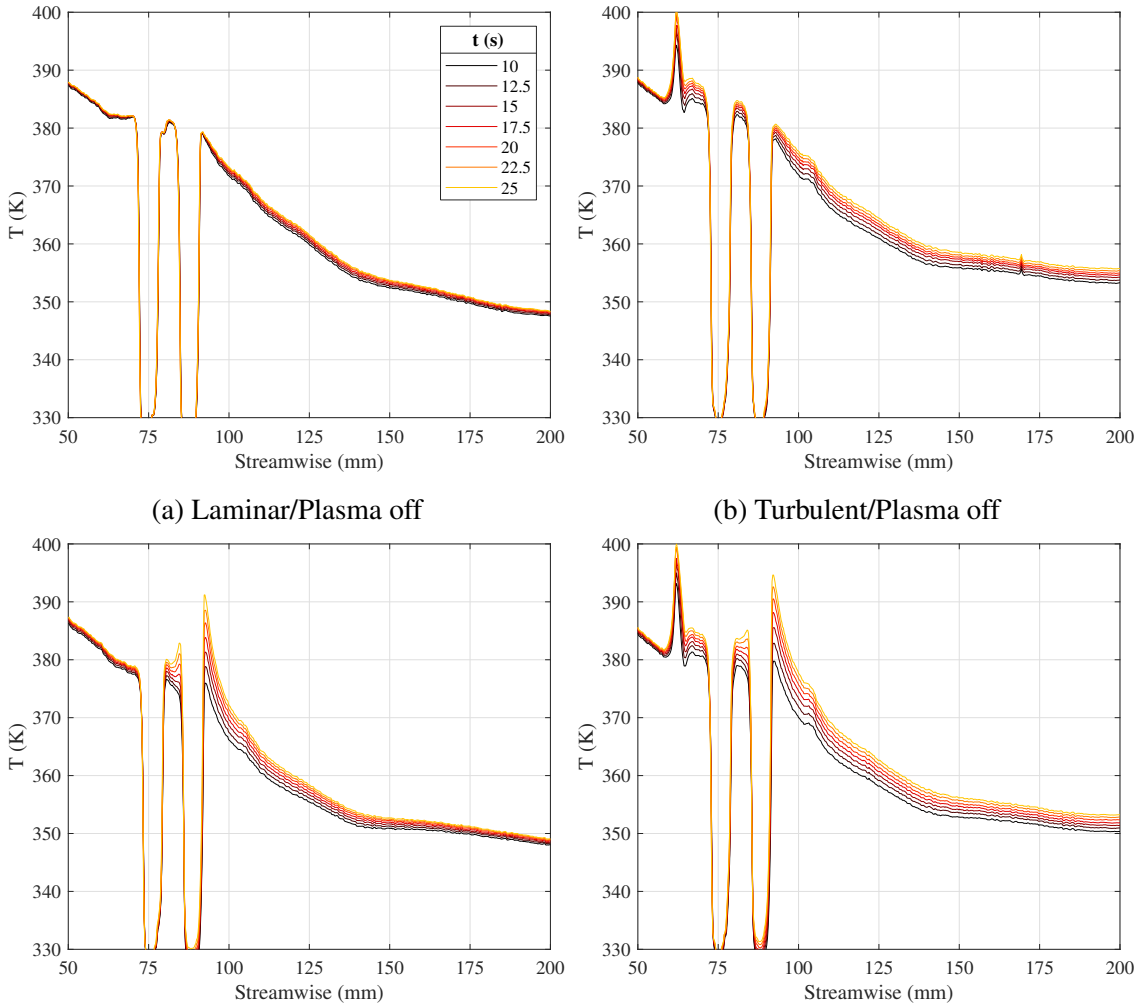

(a) Laminar/Plasma off

(b) Turbulent/Plasma off

(c) Laminar/Plasma on

(d) Turbulent/Plasma on

Figure 7.37: IR Stanton number streamwise traces at the model centerline. Same legend applies for all figures.[7]

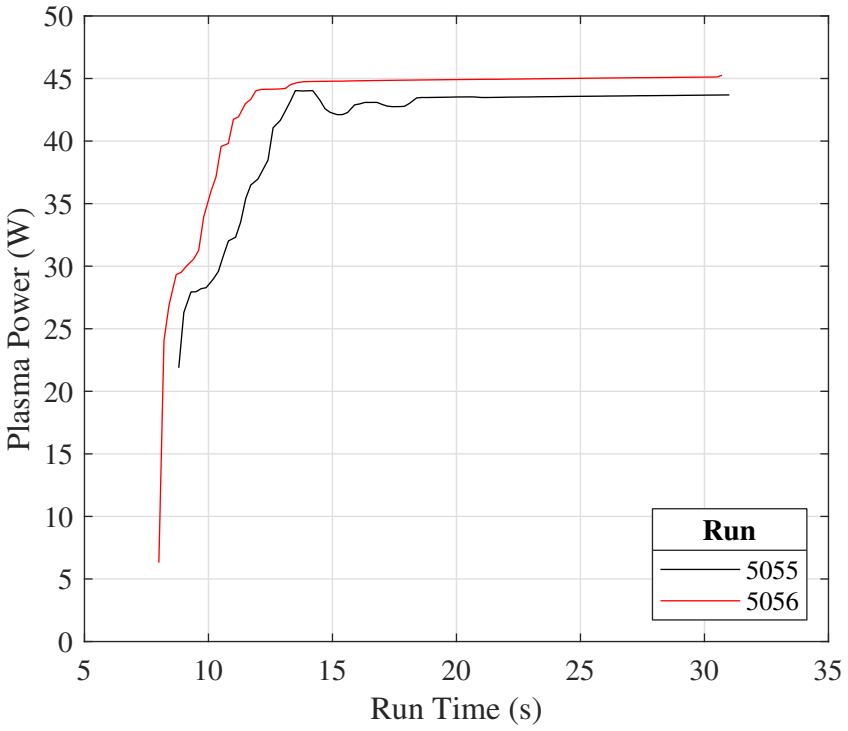

Figure 7.38: Plasma power traces for high frequency pressure runs. [7].

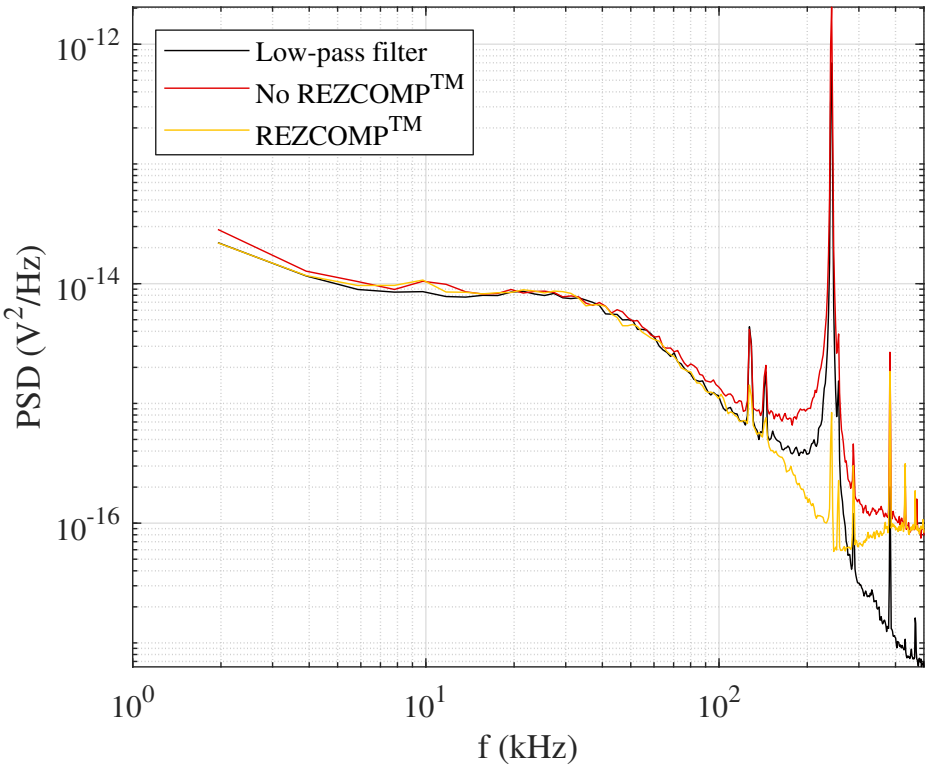

Figure 7.39: Effect of REZCOMP™ on Kulite data. [7].

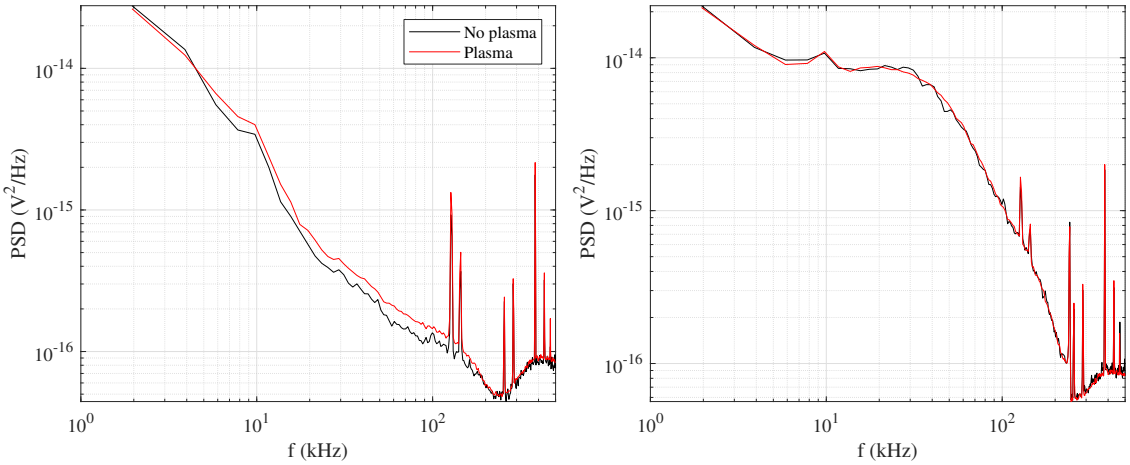

(a) Laminar (b) Turbulent

Figure 7.40: Effect of plasma on fluctuation frequency. [7]

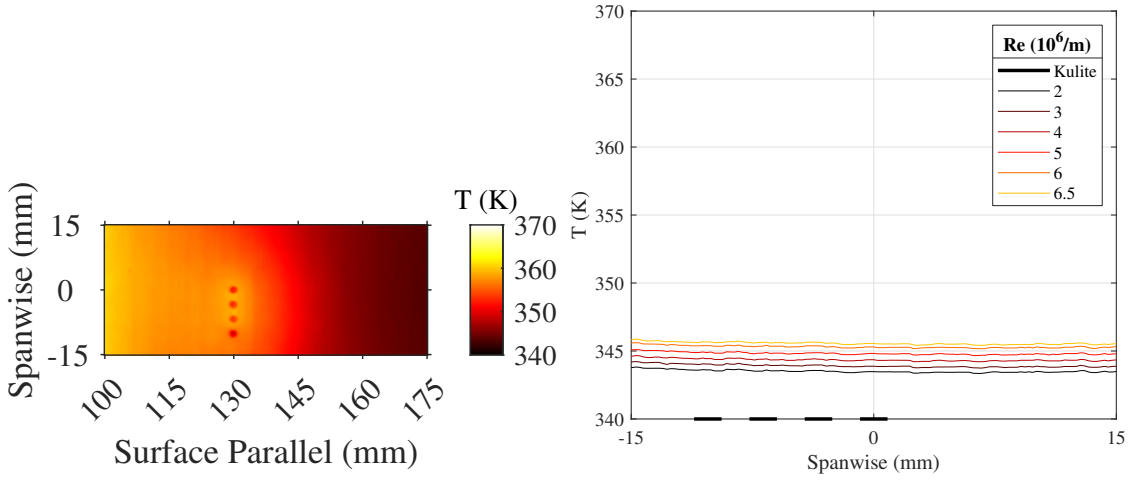

(a) Run 5070 (Forward)

(b) Run 5070: Spanwise trace 160mm from LE

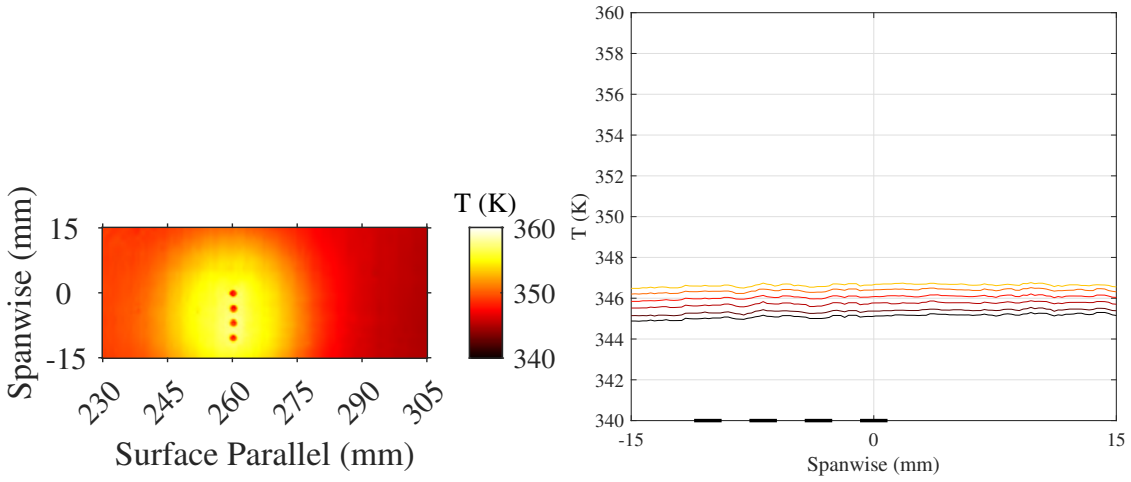

(c) Run 5065 (Middle)

(d) Run 5065: Spanwise trace 290mm from LE

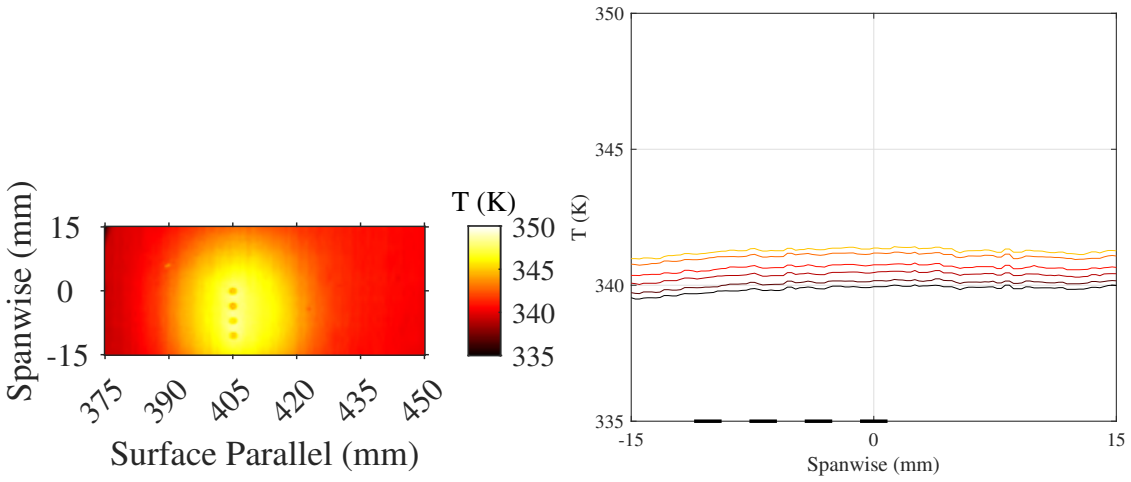

(e) Run 5057 (Back)

(f) Run 5057: Spanwise trace 435mm from LE

Figure 7.41: IR temperature data for laminar Kulite runs. Same legend applies to all trace figures. [7]

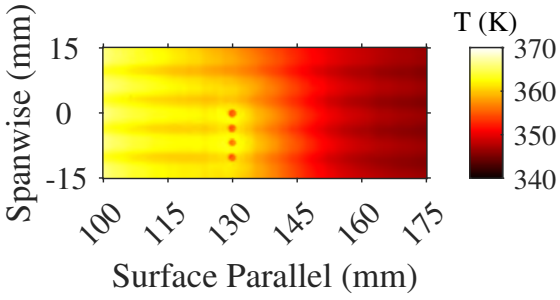

(a) Run 5069 (Forward)

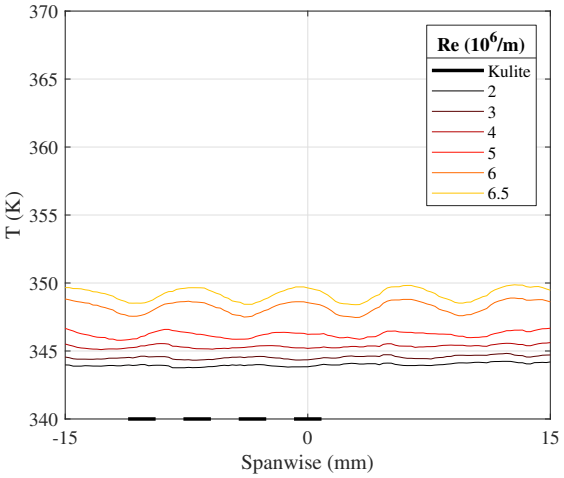

(b) Run 5069: Spanwise trace 160mm from LE

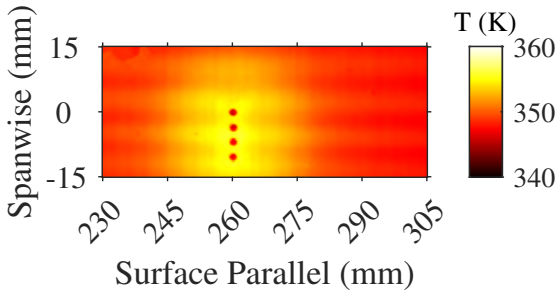

(c) Run 5064 (Middle)

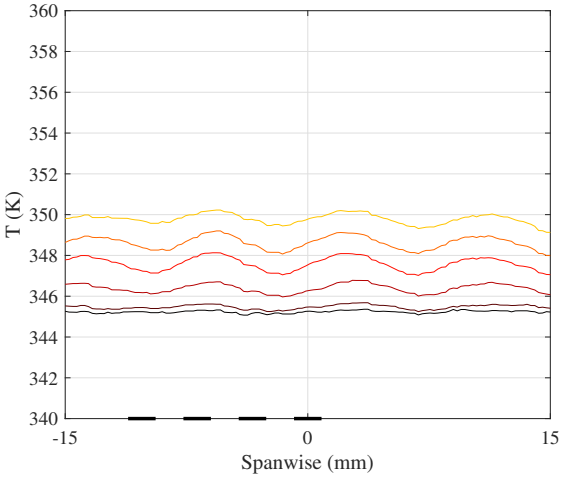

(d) Run 5064: Spanwise trace 290mm from LE

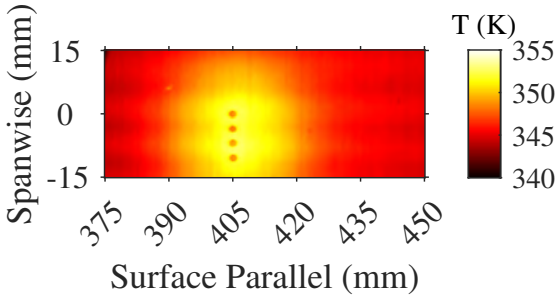

(e) Run 5054 (Back)

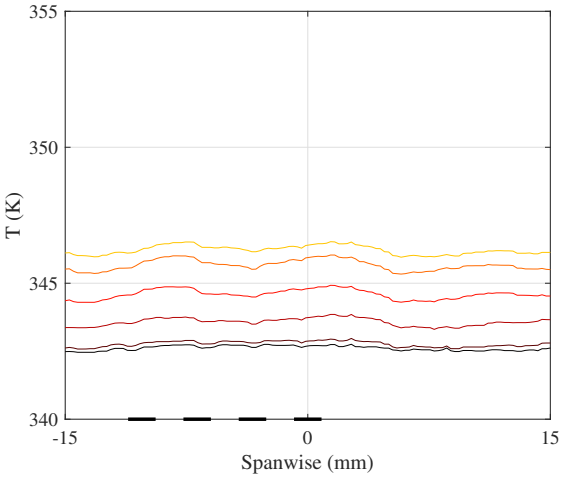

(f) Run 5054: Spanwise trace 435mm from LE

Figure 7.42: IR temperature data for turbulent Kulite runs. Same legend applies to all trace figures. [7]

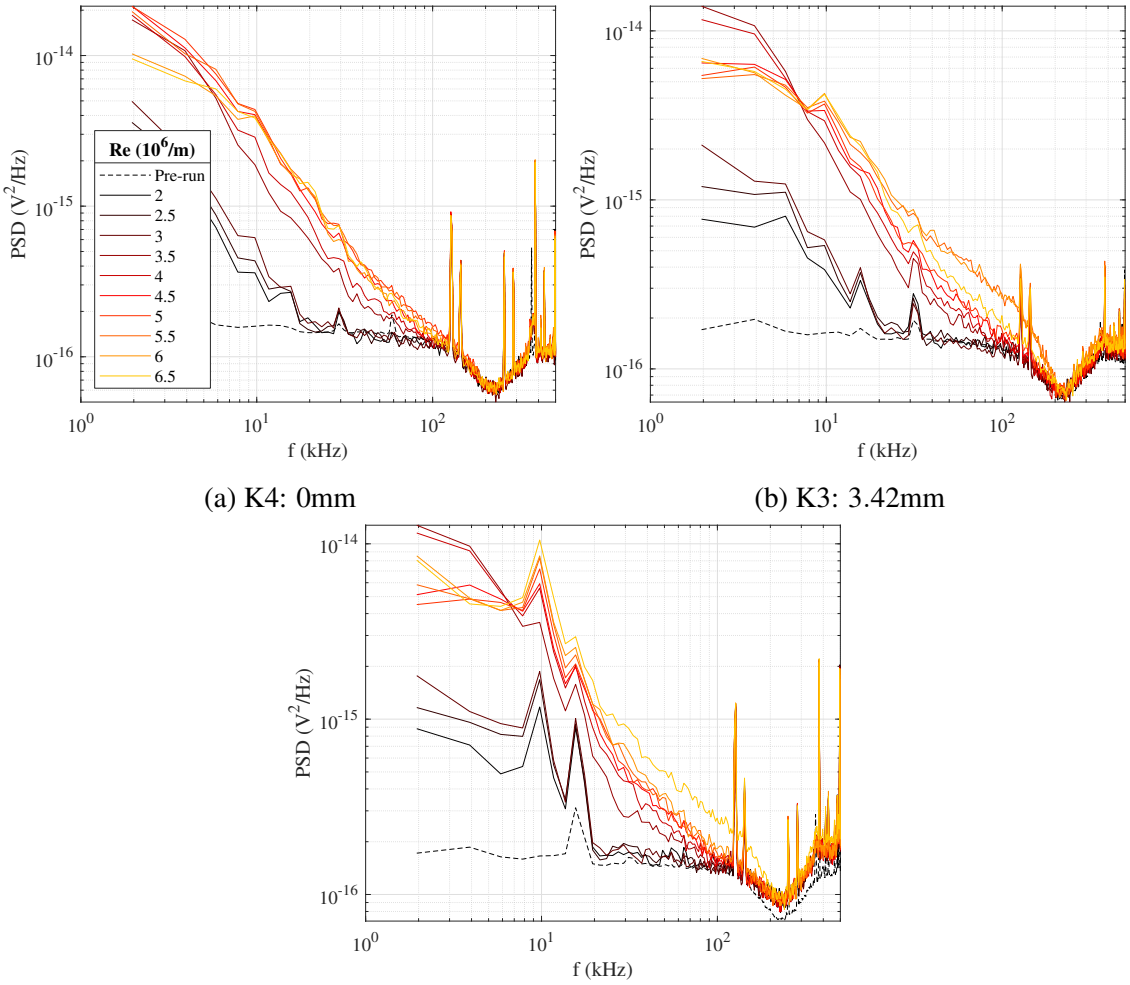

(a) K4: 0mm

(b) K3: 3.42mm

(c) K2: 6.84mm

Figure 7.43: Laminar Kulite pressure fluctuation data, 130mm from the LE. [7].

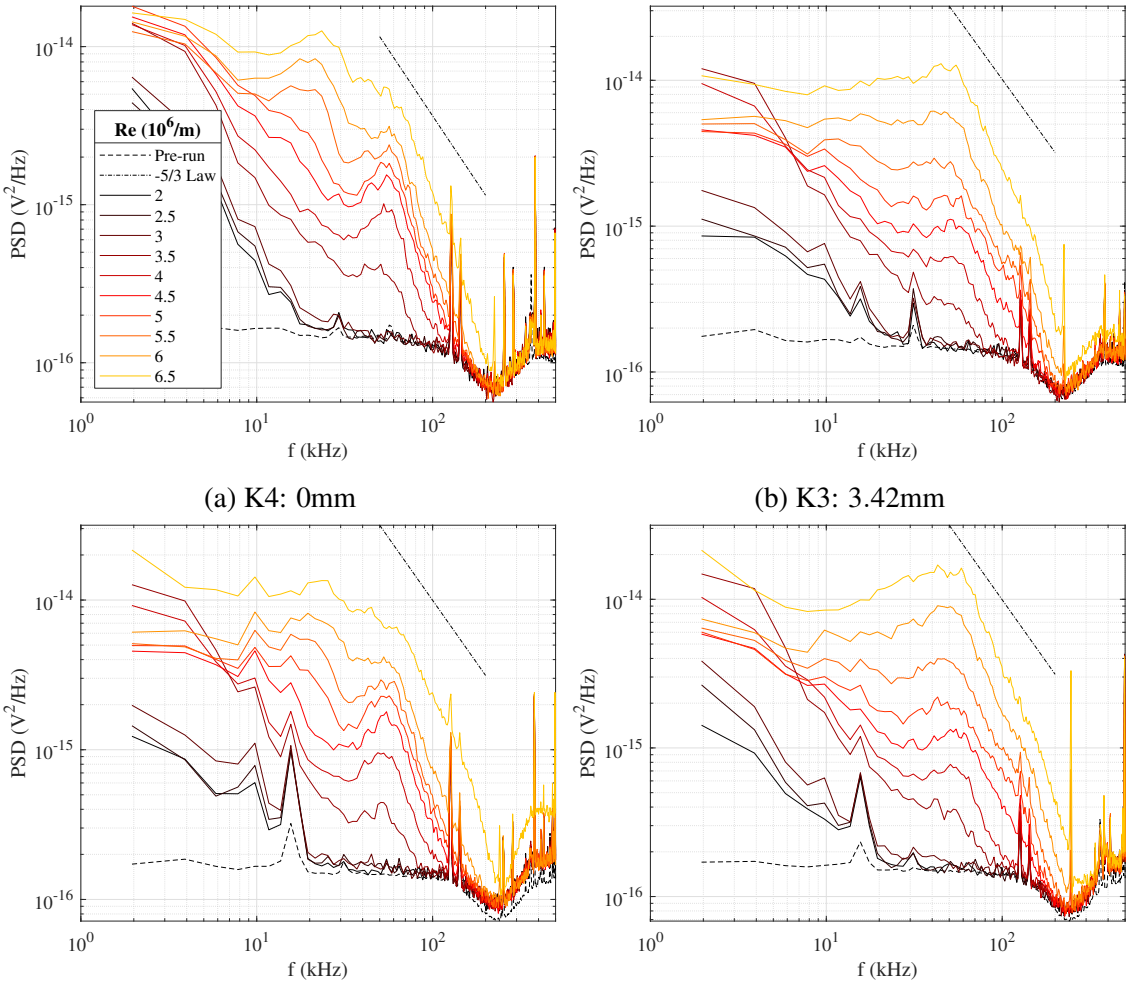

(a) K4: 0mm

(b) K3: 3.42mm

(c) K2: 6.84mm

(d) K1: 10.26mm

Figure 7.44: Turbulent Kulite pressure fluctuation data, 130mm from the LE. [7]

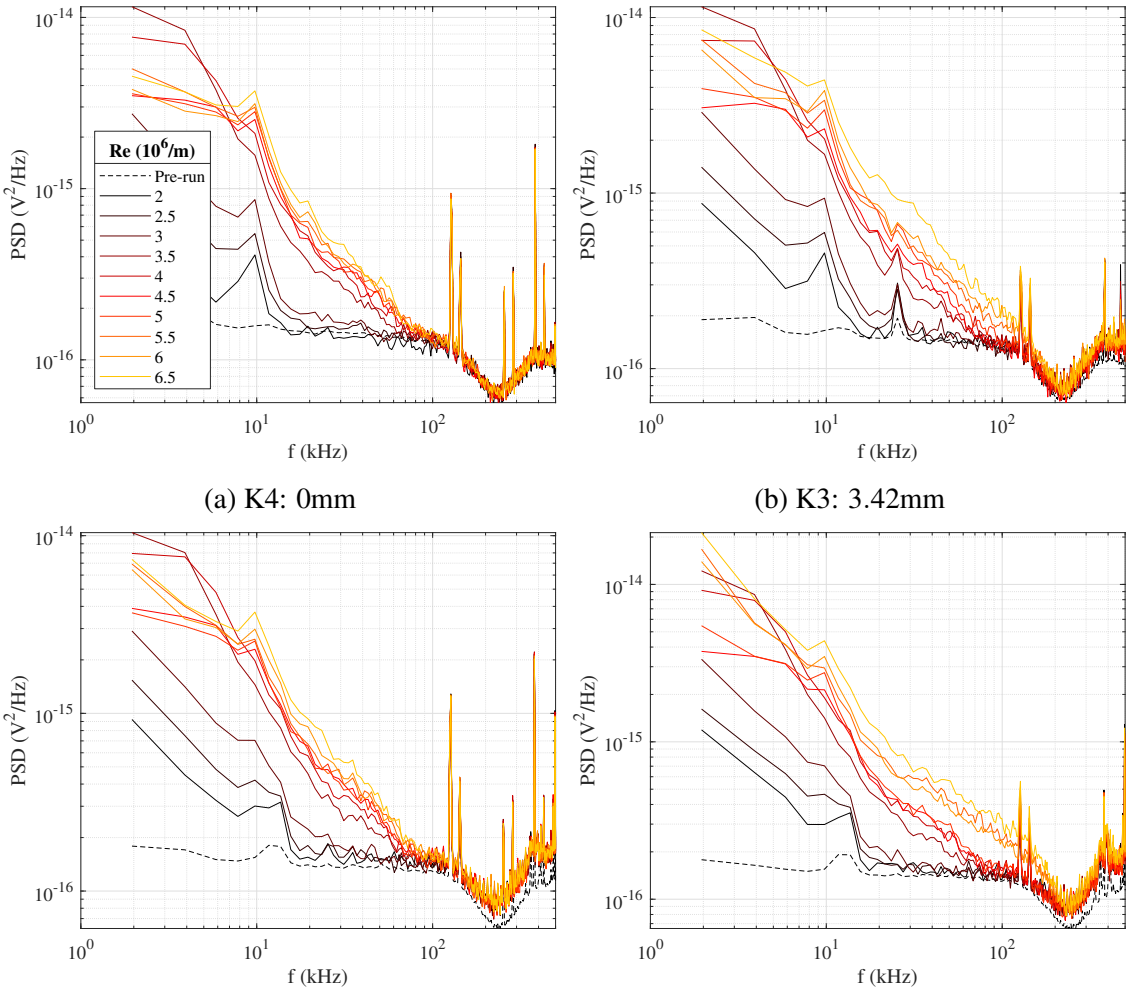

(a) K4: 0mm

(b) K3: 3.42mm

(c) K2: 6.84mm

(d) K1: 10.26mm

Figure 7.45: Laminar Kulite pressure fluctuation data, 260mm from the LE. [7]

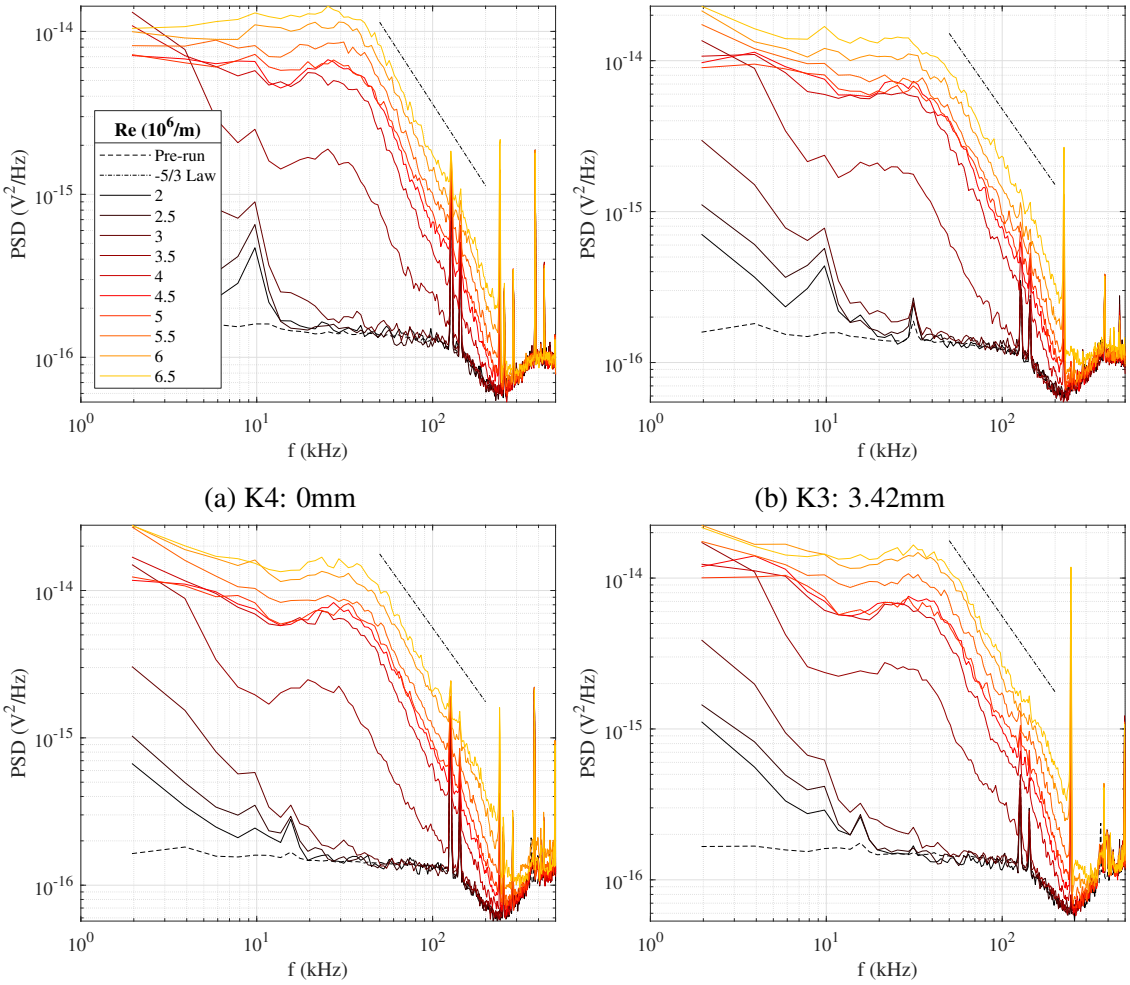

(a) K4: 0mm

(b) K3: 3.42mm

(c) K2: 6.84mm

(d) K1: 10.26mm

Figure 7.46: Turbulent Kulite pressure fluctuation data, 260mm from the LE. [7]

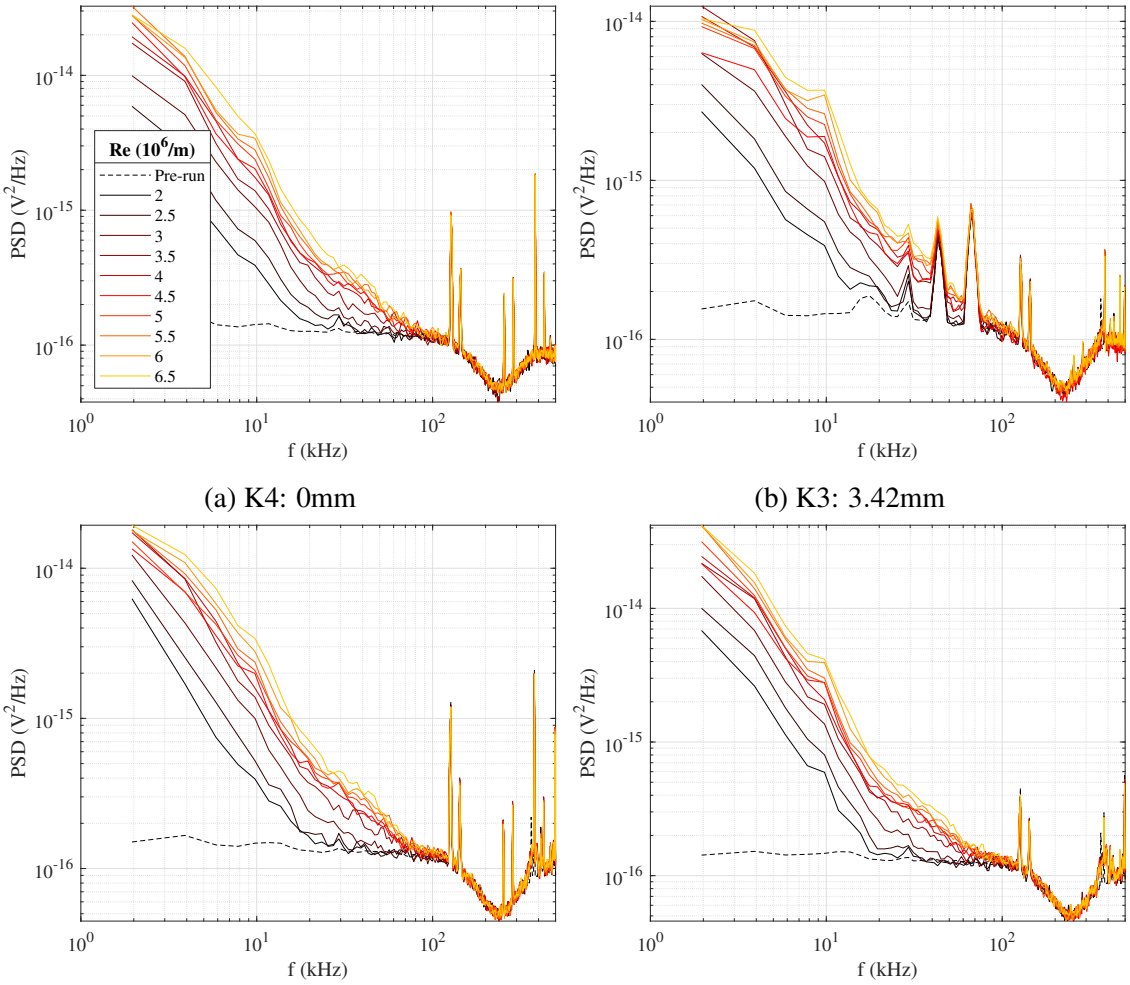

(a) K4: 0mm

(b) K3: 3.42mm

(c) K2: 6.84mm

(d) K1: 10.26mm

Figure 7.47: Laminar Kulite pressure fluctuation data, 405mm from the LE. [7]

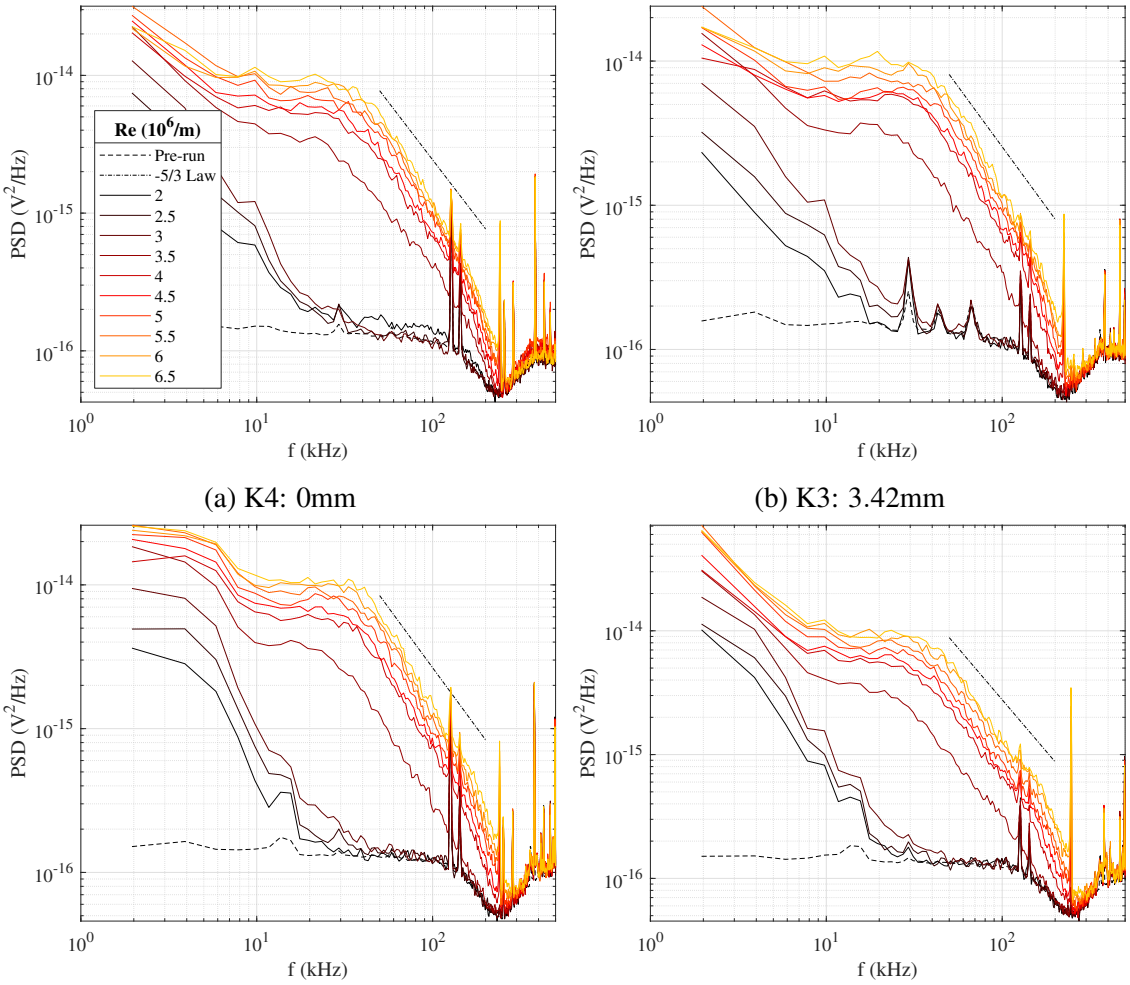

(a) K4: 0mm

(b) K3: 3.42mm

(c) K2: 6.84mm

(d) K1: 10.26mm

Figure 7.48: Turbulent Kulite pressure fluctuation data, 405mm from the LE. [7]

7.2.3.5 Pitot Probe Results

Pitot probes are classic fluid dynamics tools because they provide a wealth of data with only two simple measurements. Here the Mach number was directly measured, and through well-established theory [48, 50, 43] velocity profiles were calculated. These profiles allowed for classical boundary layer theory like inner variable plots to be produced, the inference of key physics such as transition and wall shear stress, and the validation of other data like that from the numerical boundary layer solver or PLIF. A detailed Pitot campaign was conducted in the ACE tunnel, with the test matrix included in Table 7.14. The plasma conditions and powers for each run are provided in Table 7.15 and Figure 7.49 respectively. Due to an experimental inconsistency, the results for the plasma runs in the "Middle" location were not included in this report; because the plasma was shown to have little to no effect in the "Front" test location and due to the tertiary importance of the "Middle" test location, this was deemed an unfortunate but acceptable loss.

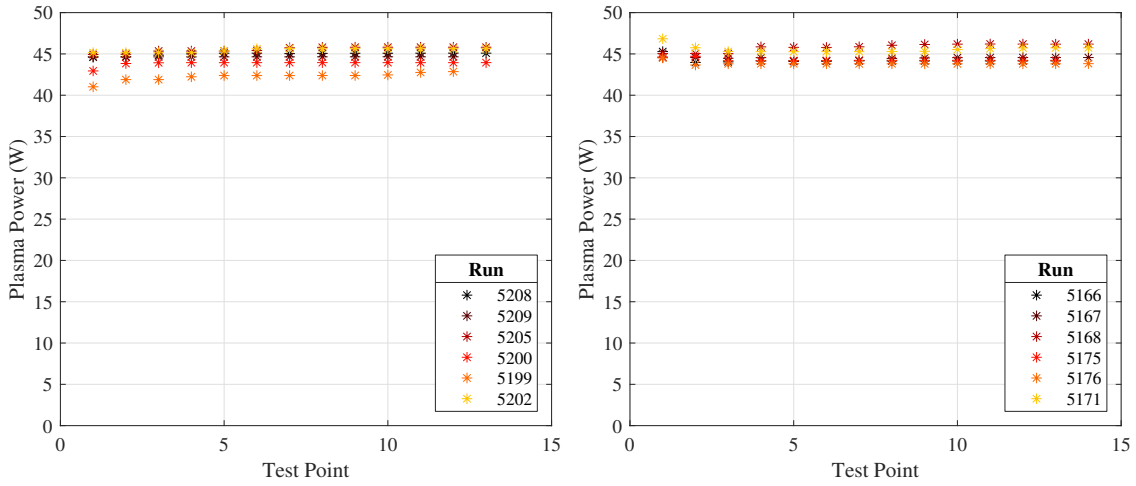

(a) Front run (b) Back runs

Figure 7.49: Plasma power traces for Pitot runs. [7].

Figure 7.50 shows two representative schlieren images taken with the probe in the "Front" test location. Of the hundreds of available images from the entire campaign, these were selected for the unique physics they capture. Note that schlieren images with better contrast are available in Section 7.2.3.2; those included here were intentionally brightened to increase the contrast between the probe and the flow for better edge detection, not to necessarily describe flow physics. ([7])

To begin, the entropy layer is visible in Figure 7.50(a), which served as a reminder that its effect may be visible in the Pitot data. Next, 0mm fell a couple pixels below the observed wall. This underscored the importance of measuring the wall offset, and trying to align the schlieren system with the roll of the plate. Similarly, in both images, there is a faint shock passing just below the probe; it was believed that this was the oblique shock generated by the static pressure

No.	Location	Trip	Plasma	Sweep	Run/Date
1	Back, wake	Turbulent	Off	Inner	5163, 1/20/2022
2	Back, wake	Turbulent	Off	Outer	5165, 1/21/2022
3	Back, wake	Turbulent	On	Inner	5166, 1/21/2022
4	Back, wake	Turbulent	On	Outer	5167, 1/21/2022
5	Back, wake	Laminar	Off	Full	5169, 1/22/2022
6	Back, wake	Laminar	On	Full	5168, 1/21/2022
7	Back, trough	Turbulent	Off	Inner	5173, 1/23/2022
8	Back, trough	Turbulent	Off	Outer	5174, 1/23/2022
9	Back, trough	Turbulent	On	Inner	5175, 1/23/2022
10	Back, trough	Turbulent	On	Outer	5176, 1/23/2022
11	Back, trough	Laminar	Off	Full	5172, 1/22/2022
12	Back, trough	Laminar	On	Full	5171, 1/22/2022
13	Middle, wake	Turbulent	Off	Inner	5179, 1/26/2022
14	Middle, wake	Turbulent	Off	Outer	5182, 1/27/2022
15	Middle, wake	Laminar	Off	Full	5184, 1/27/2022
16	Middle, trough	Turbulent	Off	Inner	5187, 1/29/2022
17	Middle, trough	Turbulent	Off	Outer	5188, 1/29/2022
18	Middle, trough	Laminar	Off	Full	5185, 1/28/2022
19	Forward, wake	Turbulent	Off	Inner	5206, 2/4/2022
20	Forward, wake	Turbulent	Off	Outer	5207, 2/4/2022
21	Forward, wake	Turbulent	On	Inner	5208, 2/4/2022
22	Forward, wake	Turbulent	On	Outer	5209, 2/4/2022
23	Forward, wake	Laminar	Off	Full	5204, 2/3/2022
24	Forward, wake	Laminar	On	Full	5205, 2/3/2022
25	Forward, trough	Turbulent	Off	Inner	5195, 2/1/2022
26	Forward, trough	Turbulent	Off	Outer	5198, 2/1/2022
27	Forward, trough	Turbulent	On	Inner	5200, 2/2/2022
28	Forward, trough	Turbulent	On	Outer	5199, 2/2/2022
29	Forward, trough	Laminar	Off	Full	5201, 2/2/2022
30	Forward, trough	Laminar	On	Full	5202, 2/2/2022
31	Probe in center of test section	$Re = 2-6\times10^6/\mathrm{m}$	N/A	N/A	5212, 2/5/2022

Table 7.14: Pitot probe test matrix.

taps at 130mm; this theory seemed more likely than blowing from the port as preliminary schlieren imaging showed the static ports mostly vented even before the flow was started. This was remarkable because despite their small diameter (0.508mm) and 3.42mm spanwise displacement from the probe, it will be seen shortly that they still interfered with the results. While there was no choice but to offset the probe from the holes in this "Front" location, this result stood as a lesson for future work, and as a warning that the stronger shocks from the electrodes and trips may have had a more

No.	Current (mA)	Power Supply Voltage (V)	Power Supply Power (W)	Plasma Voltage (V)	Plasma Power (W)
3	95.4	1418	135.2	463.7	44.2
4	94.8	1418	134.4	469.0	44.5
6	95.1	1434	136.3	482.0	45.8
9	95.2	1418	135.0	465.2	44.3
10	95.1	1413	134.4	461.0	43.8
12	94.9	1430	135.8	480.0	45.6
21	95.2	1426	135.7	472.5	45.0
22	95.0	1421	135.0	470.0	44.6
24	94.5	1428	134.9	482.1	45.5
27	95.0	1412	134.1	461.8	43.9
28	94.0	1391	130.8	449.4	42.3
30	95.4	1431	136.5	476.8	45.5
Average					
	95.0	1420	134.8	469.4	44.6

Table 7.15: Plasma conditions for Pitot probe campaign.

pronounced impact. To address that concern, it would have been beneficial to measure the pressure jump across, say, the trip shocks, but due to their complex nature it was not expected they would follow any simple theory. Furthermore, this measurement was already done with the PLIF results, and could be replicated here by comparing any freestream reading at any point along the plate with the trips installed to one without them; this approach was discussed below. Finally, in the "Front" test location it was more important to add points in the boundary layer to improve its resolution due to its thin size. ([7])

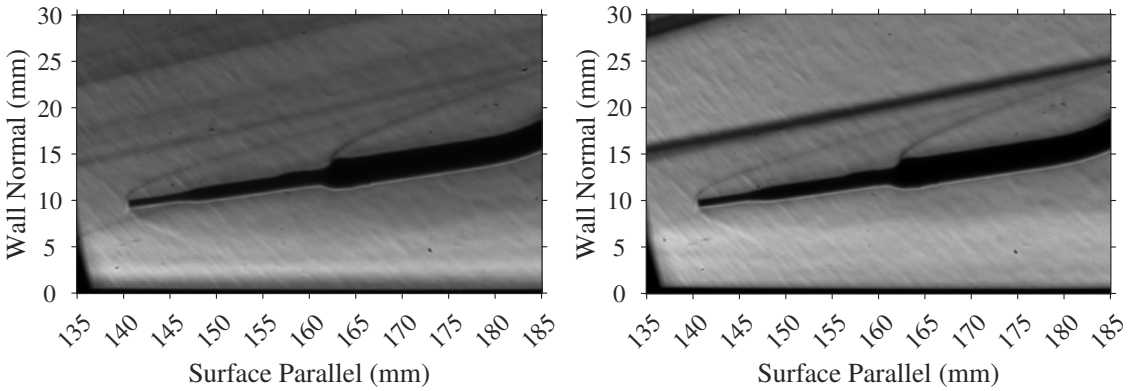

(a) Laminar

(b) Turbulent

Figure 7.50: Schlieren images for Pitot probe placement, "Front" location. [7]

7.2.3.6 *Wall Shear Stress Results*

The wall shear stress for each of the six main test cases (three locations, laminar and turbulent flow) is provided in Tables 7.16-7.21. The results from the numerical boundary layer solver for generalized laminar and turbulent flow ("Implicit" scheme, "Gradient Diffusion" heat flux, same inputs as Section 7.2.1) are also shown in Figure 7.7(a), and the results for each specific location are provided in the caption of the corresponding table. The van Driest II skin friction model ($\tau_{w,VD}$) was solved for the turbulent cases using Matlab's inbuilt "fsolve" function, but because it is restricted to only adiabatic flows its results were meant to used for reference only; that being said, based on the actual flow conditions, $T_{aw} \approx [375, 395\text{K}]$ for the laminar and turbulent flows respectively, so for example if for the intermediary "Middle" case $T_w = 355\text{K}$ then $\frac{T_w}{T_{aw}} = [0.947, 0.899]$ and the plate was reasonably close to adiabatic conditions, especially near the leading edge and at least to within the other approximations used throughout these calculations. ([7])

The Preston tube results were, in general, a factor of two below the expected value for all turbulent cases and near the correct answer for the laminar cases, though the latter was likely coincidental. There were several possible explanations for this error. Preston [281] recommended $\log \frac{(P-P_o)d^2}{4\rho\nu^2} > 5$, which, if one follows Semper [206] and considers d to be the height of the tube in the wall-normal direction, the data did not satisfy. Similarly, the $R_d^2 C_p$ and $R_d^2 C_f$ results did not fall onto the linear portion of the scaled plots in [286]. The reasons for these discrepancies were unknown, but likely stemmed from the probe itself. The Preston approach was attempted for convenience as the data was already being taken; a more intentional effort would have included a range of truly circular probes of varying diameter precisely fixed to the wall. Even if this was done, the approach was fundamentally imperfect; in their review of several calibrations, Allen [343] said the approach of Keener and Hopkins [286] could have errors up to 50%. The finding here was not to disregard Preston tube for measurement of wall shear stress, but that a dedicated study should be conducted before it is insouciantly attempted.([7])

In general, in all cases except the Preston tube, the agreement between the experimental and numerical for the "Turbulent" flows was much better than in the "Laminar" cases. The numerical, Reynolds Analogy, van Driest II approaches never differed by more than 25%, even at the "Front" test location. At least for the Reynolds Analogy approach, the higher adiabatic wall temperature and better agreement in the heat flux values ($q_w = [1752.7, 1243.9, 1069.0] \frac{\text{W}}{\text{m}^2}$ for the "Implicit/Gradient Diffusion" scheme), especially in the "Back" test location, explained this result. Indeed, by this point all of the techniques except the Preston tube yielded results within $20 \pm 3\text{Pa}$. ([7])

The Clauser approach warranted special attention. As described in Section 7.2.1, the τ_w predicted by the boundary layer solver will cause the inner variable scaled plot of u_{eq}^+ *versus* y^+ to fall below the theoretical lines. Clauser's method allowed one to manually alter τ_w until the experimental and theoretical results agreed. Ignoring the transitional flow at the "Front" test location, this did allow for the production of classical inner variable plots at the "Middle" and "Back" test location, indicating fully turbulent flow. However, one must ask, especially given that the Reynolds Analogy and van Driest II wall shear stresses also overpredicted $\tau_{w,Clauser}$, if this approach was not fitting the data? Put another way, theory should explain data, not the other way around. While the

Clauser method was helpful because it allowed direct manipulation of the data when there were five competing techniques, one must appreciate its implication. Looking at the data holistically, it seemed that the numerical, Reynolds Analogy, and Clauser approaches were converging on the same result as the flow moved from the "Middle" to the "Back" test locations, with the van Driest II approach lagging only slightly behind, perhaps due to its adiabatic assumption. What would happen if the test article was 1m long? Inserted into the tunnel after preheat? Its leading edge sharpened? Its material entirely PEEK? Its trips altered; and in the CFD, what if the trips were themselves modeled? At least numerically, increasing the streamwise domain did seem to yield results tending towards better agreement with the theory. The point here was that in experimentation theory should be used to interpret data, and data should be taken only as far as their real-world limitations will allow. These wall shear stress data suggested that the boundary layer was becoming fully developed, and the agreement with classical theory was milquetoast; to that end, perhaps increasing the length of the plate would allow for better interpretation of the observed trends, as the turbulence may become more fully developed. ([7])

In summation, the Reynolds Analogy, van Driest II, Clauser, and numerical approaches to the estimation of the skin friction were all reliable for the turbulent flow, provided it had enough time to fully develop. There were significant issues in "Laminar" cases, likely stemming from the thermal response of the test article. Finally, the Preston tube method warrants further investigation, especially because it could offer a useful validation of the Reynolds Analogy approach for laminar boundary layers. A comparison of the wall shear stress results measured with the Pitot probe with other techniques is included in Section 7.2.6. ([7])

7.2.3.7 Boundary Layer Profiles

The wall shear stress for each of the six main test cases (three locations, laminar and turbulent flow) is provided in Tables 7.51-7.56. For each case, the Mach number, temperature, and velocity profiles are shown, as well as the inner variable velocity profile for the turbulent runs. The data are grouped such that all tests that a given location (plasma "On/Off" and "Wake/Trough") were plotted on the same figure to elucidate any effect. ([7])

In general, the uncertainties for the Mach number and displacement were so small that including error bars only served to clutter the figures. The error in the Mach number was $\sim 1\%$ at the wall and $\sim 0.5\%$ in the freestream, values so small the error was not carried into the calculations for temperature or velocity. The displacement error went from $y \approx [0.3, 0.8]$mm at the wall and freestream, respectively. While more significant, the error bars still tended to obfuscate the results. Instead, when the measured height of a point was below half the probe diameter plus the base two pixels of uncertainty, it was called a "wall point" and plotted with an open circle. This denoted a proportionally high degree of uncertainty in the position of the probe, but also in the data itself; recall that no correction was available for the probe's effective center near the wall, and the Preston tube results were relatively inaccurate. Indeed, when plotted using inner variables, these wall points followed unrealistic trends. The "Front" plots were perhaps the most dynamic. All cases showed a distinct bump at $\sim$ 7mm owing to the weak shock produced by the static pressure holes. And it was indeed weak, as the final points in the "Laminar" and "Turbulent" plots were nearly identical; this implied that the complex shock/separation/reattachment feature produced by

the trips was weak enough to not significantly manifest in the Pitot results, so the far weaker static port shock should have had no effect. The lent credence to the decision to not measure the Mach number on both sides of the trips' shocks and to instead add resolution to the thin boundary layer. That being said, the Mach number did not fully reach the expected freestream value by 10mm above the surface, a factor several times δ. Again, that this occurred in both the "Laminar" and "Turbulent" cases meant that it could not be attributed to the trips' shocks. The more likely explanation would be a prolonged leading edge effect, though this did extend even above the entropy layer. To that end, the decision to add resolution to the boundary layer instead of the freestream proved fortuitous in that one can see a slight change in the slope of the profiles in Figure 7.51 at $\sim$ 3mm. Taken with the results in Section 7.2.3.2 it was probable this was the entropy layer. It was interesting to see it represented in the Pitot data. ([7])

The added resolution was helpful for the "Turbulent" case as well, though evidently that was a misnomer. As far back as 140mm from the leading edge, downstream of the PLIF measurements, there remained clear evidence of the trips in the "Wake" plots. Indeed, between $3-6$mm, well below the trips' shear layer identified both in the shlieren data in Section 7.2.3.2 and in the images taken concurrently with the Pitot data, the velocity in the "Wake" lagged behind that in the "Trough". This implied there was some lingering velocity deficit in the boundary layer owing to the wake. The run-to-run repeatability of the feature confirmed it was not likely due to any probe misalignment, and there were no known issues with the probe used as such physics were not measured at the the "Middle", where it was also used. That the "Troughs" remained relatively unaffected and even collapsed onto the inner variable log layer added further evidence of the longevity of the trips' wakes, even in the transitional environment. Cumulatively, therefore, this location must be considered transitional, not fully turbulent. This implied that the use of r_{turb} in T_{aw} in the Crocco-Busemann's equation inaccurate, though it was the best approximation available. ([7])

It is noted that the discrepancy between the plasma "Off" (Runs 5206, 5207) and "On" (Runs 5208, 5209) in Figure 7.52 was not attributed to the plasma as there was no similar behavior in the "Trough" case or any of the laminar data. The cause remained unclear at the time of publication but run-to-run variability, the affect of the bend in the "Trough" probe, the slightly larger (almost 0.1mm) height of the "Trough" probe), elastic rotational deflection of the probe in the presence of the flow, and slight probe misalignment remained possible culprits. In the "Middle" test location, the boundary layer seemed to follow a more classical path. Near the wall, the "Laminar" data curled downwards at an expedited rate. This was most likely a physical probe effect and could be improved by the inclusion of an effective probe center or a smaller probe. The "Turbulent" data also follow the theoretical trend, and indeed the flow appeared fully turbulent. There was again disagreement between "Wake" and "Trough" data in this "Middle" location. Here, however, the most likely culprit was the physical probe itself as the data maintained a near-constant offset in the Mach number between all of the runs considered in Figures 7.53 and 7.54. It was interesting to see that as the Mach number was high, the temperature calculated by the Crocco-Busemann relation was low, so when combined the competing effects partially canceled in the calculation of the velocity. Fortunately, in the "Back" location only one probe was used, and the data collapse closely together. Again, both laminar and turbulent theoretical shapes were recovered; for example, it was encouraging to see the "bent knee" shape in Figure 7.56(c). There was the same downward curl

in the points near the wall, but this was again attributed to probe-wall effects. Taken together, the Pitot campaign was successful in that it provided insight on the laminar, transitional, and turbulent nature of the boundary layer, recovered classical theory, and provided off-body measurements of the flow; this is best shown in Figure 7.57, which compares the evolution of the Mach number, temperature, and velocity profiles along the test article for the "Wake/Plasma off" case. Additionally, it confirmed that, again, there was no tangible impact of the plasma on the flow, and provided a means to study various techniques for the calculation and measurement of wall shear stress. Its data are compared to that of other techniques in Section 7.2.6. In the future, the results could be improved with more time spent testing the effect of different probes and trying to use the same one for all tests. (Broslawski [7].)

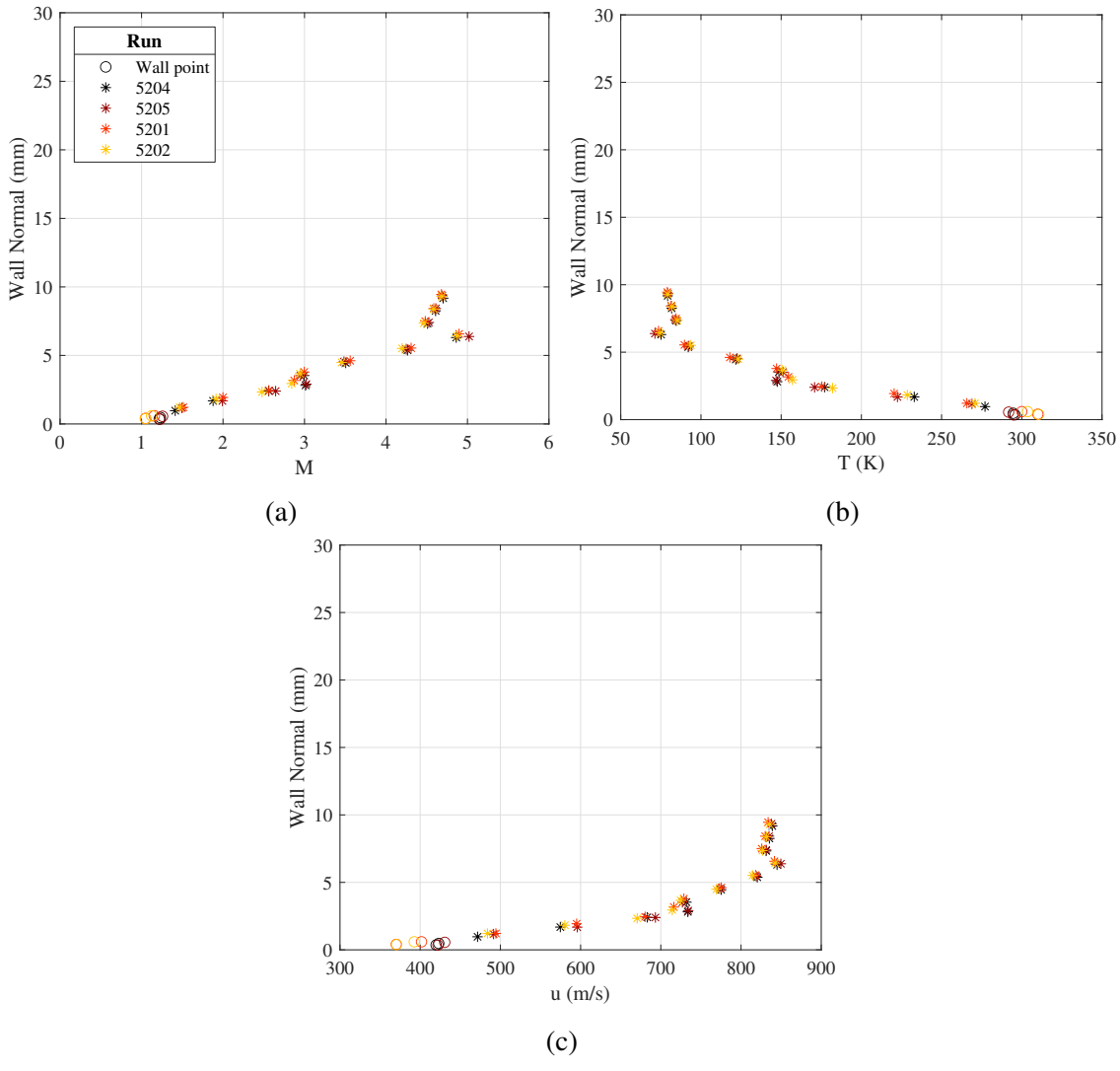

Figure 7.51: Laminar Pitot data, 140mm from the LE. Same legend applies for all figures. [7]

Run	$\tau_{w,RA}$	$\tau_{w,Preston}$
5204	49.6	10.1
5205	49.7	10.3
5201	49.7	7.7
5202	49.9	7.8

Table 7.16: Pitot campaign wall shear stress, laminar flow, 140mm from the LE. $\tau_{w,CFD} = 8.2$. All values are in Pa.

Run	$\tau_{w,VD}$	$\tau_{w,RA}$	$\tau_{w,Preston}$	$\tau_{w,Clauser}$
5206, 5207	27.7	34.7	12.2	17.5
5208, 5209	28.1	35.2	12.3	17.5
5195, 5198	27.9	34.8	8.8	19.5
5200, 5199	27.8	34.6	8.5	19.5

Table 7.17: Pitot campaign wall shear stress, turbulent flow, 140mm from the LE. $\tau_{w,CFD} = 29.0$. All values are in Pa.

Run	$\tau_{w,RA}$	$\tau_{w,Preston}$
5184	12.1	10.1
5185	12.2	7.1

Table 7.18: Pitot campaign wall shear stress, laminar flow, 260mm from the LE. $\tau_{w,CFD} = 6.0$. All values are in Pa. [7]

7.2.3.8 Freestream Mach Number Results

The freestream Mach number test produced complex results, shown in Figure 7.60. There were two trends to consider, the amount of variation in each result, and its response as the Reynolds number changed. The $P_{o,TS}/P_{TS}$ (TS- test section, SC- settling chamber) result showed the most sensitivity to the Reynolds number, followed by the $P_{o,SC}/P_{TS}$ result, and lastly the $P_{o,TS}/P_{o,SC}$ result. Figure 7.60(b) was produced to elucidate these findings by plotting each pressure reading normalized by its value when the tunnel started. It shows that the stagnation pressures track one another closely, maintaining a near-constant pressure ratio. The static pressure readout defied this

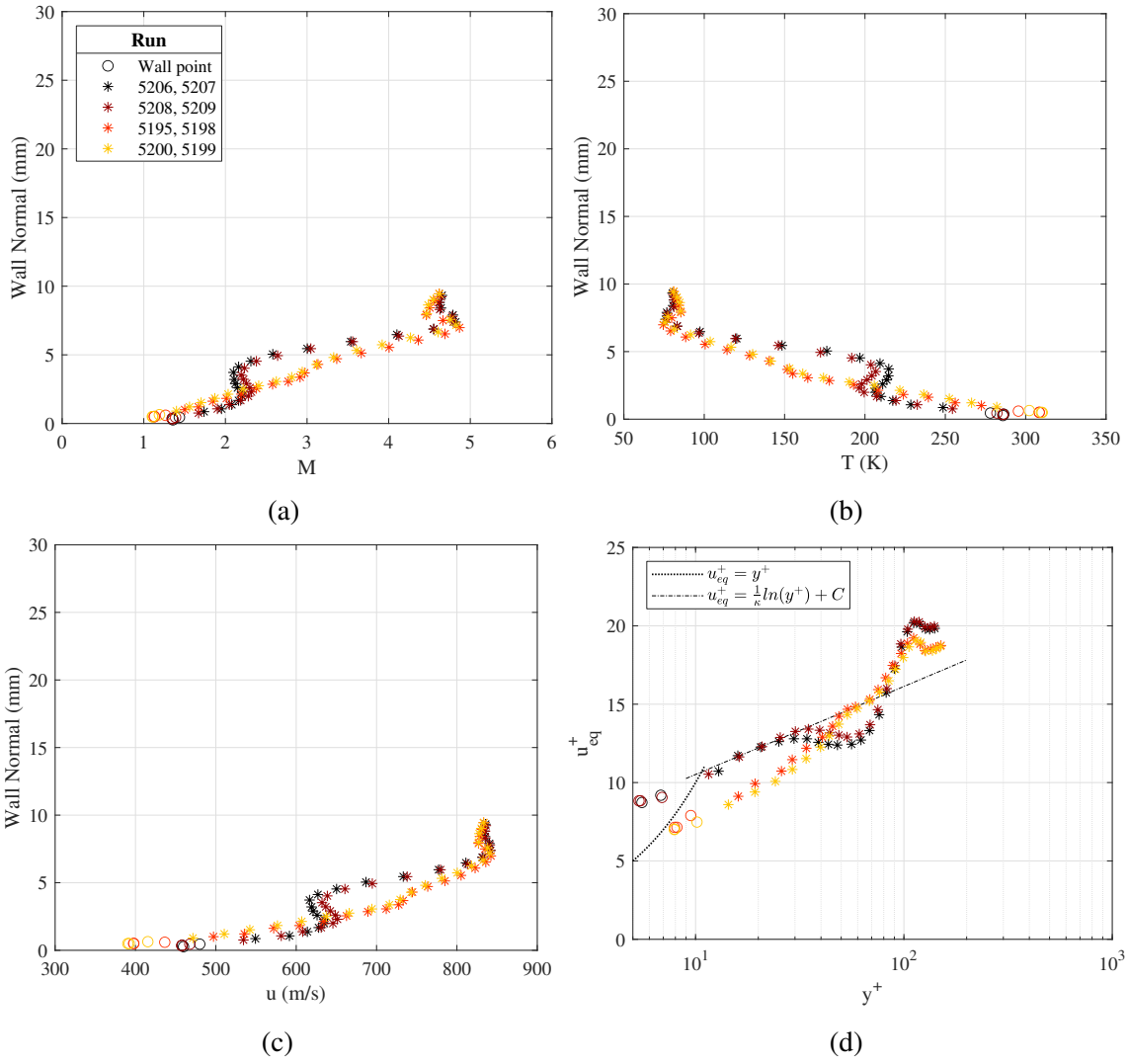

Figure 7.52: Turbulent Pitot data, 140mm from the LE. Same legend applies for all figures. [7]

Run	$\tau_{w,VD}$	$\tau_{w,RA}$	$\tau_{w,Preston}$	$\tau_{w,Clauser}$
5179, 5182	24.9	25.2	10.1	16.5
5187, 5188	24.8	25.1	7.5	16

Table 7.19: Pitot campaign wall shear stress, turbulent flow, 260mm from the LE. $\tau_{w,CFD} = 22.4$. All values are in Pa. [7].

trend, growing $\sim 50\%$ more than the stagnation pressures. The reason for this sensitivity remained under investigation at the time of publication. Still, the variation in the static pressure explained why the Mach numbers calculated using P_{TS} were the most for susceptible to change. This effect

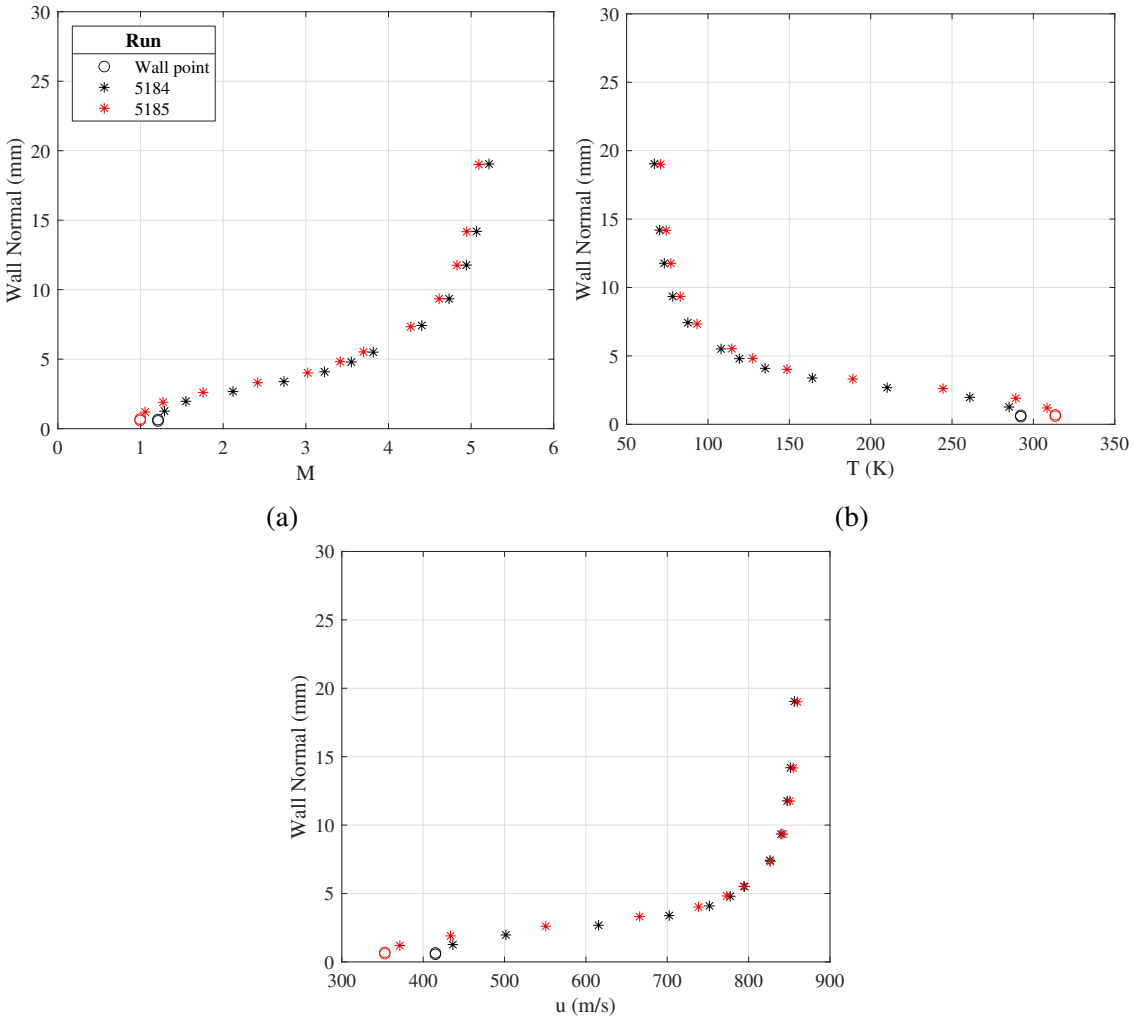

Figure 7.53: Laminar Pitot data, 260mm from the LE. Same legend applies for all figures. [7]

Run	$\tau_{w,RA}$	$\tau_{w,Preston}$
5169	10.2	8.2
5168	10.0	8.4
5172	10.0	8.9
5171	10.1	8.8

Table 7.20: Pitot campaign wall shear stress, laminar flow, 405mm from the LE. $\tau_{w,CFD} = 4.8$. All values are in Pa.

was enhanced in the Mach number calculated entirely from TS instruments. This was attributed

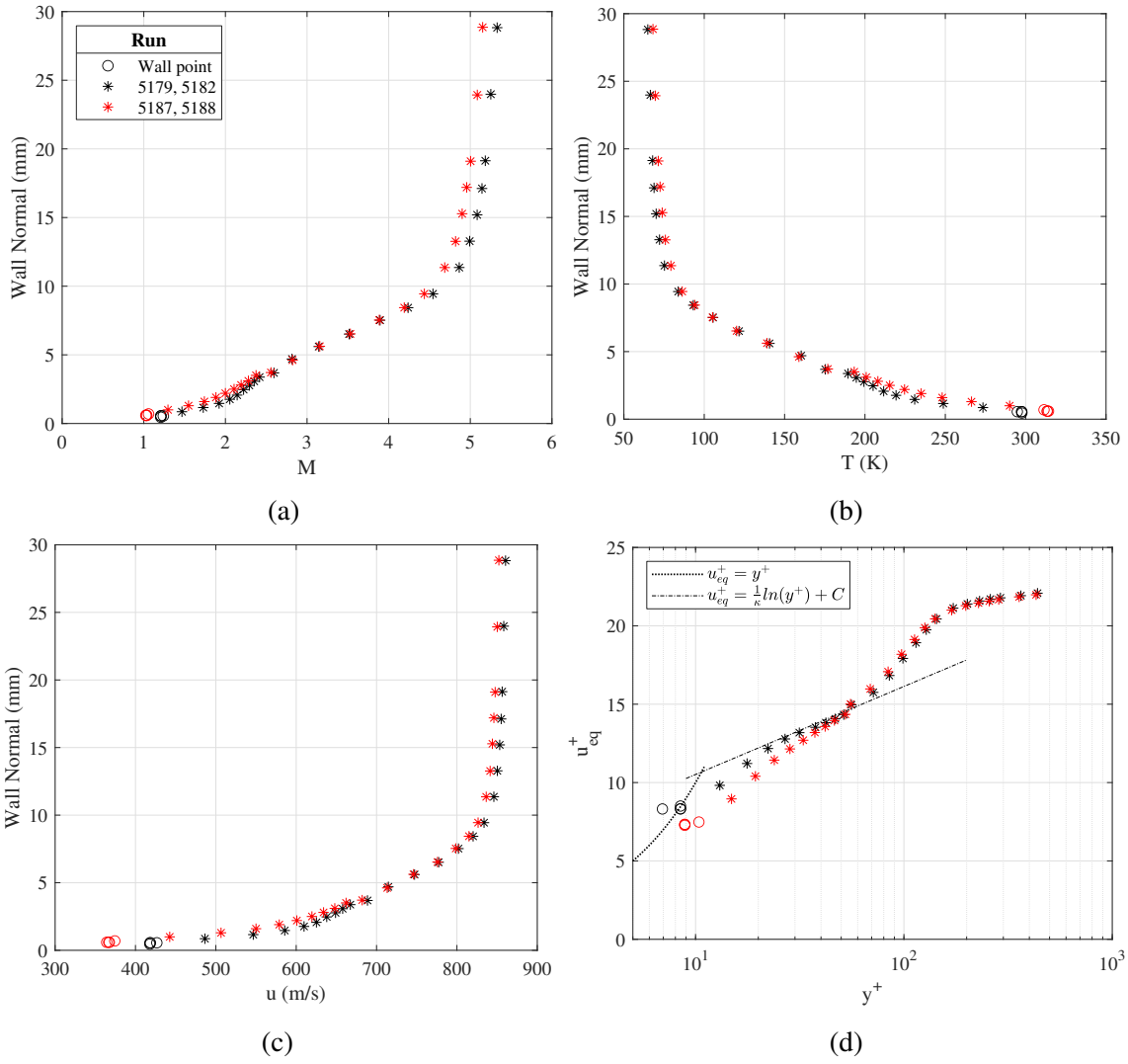

Figure 7.54: Turbulent Pitot data, 260mm from the LE. Same legend applies for all figures. [7]

Run	$\tau_{w,VD}$	$\tau_{w,RA}$	$\tau_{w,Preston}$	$\tau_{w,Clauser}$
5163, 5165	23.4	20.6	8.7	18.0
5166, 5167	22.9	20.2	8.7	18.0
5173, 5174	23.0	20.2	9.8	18.0
5175, 5176	22.9	20.2	10.7	18.5

Table 7.21: Pitot campaign wall shear stress, turbulent flow, 405mm from the LE. $\tau_{w,CFD} = 19.6$. All values are in Pa.

to the role Reynolds number had on the boundary layer. As it was increased, the flow's inertial

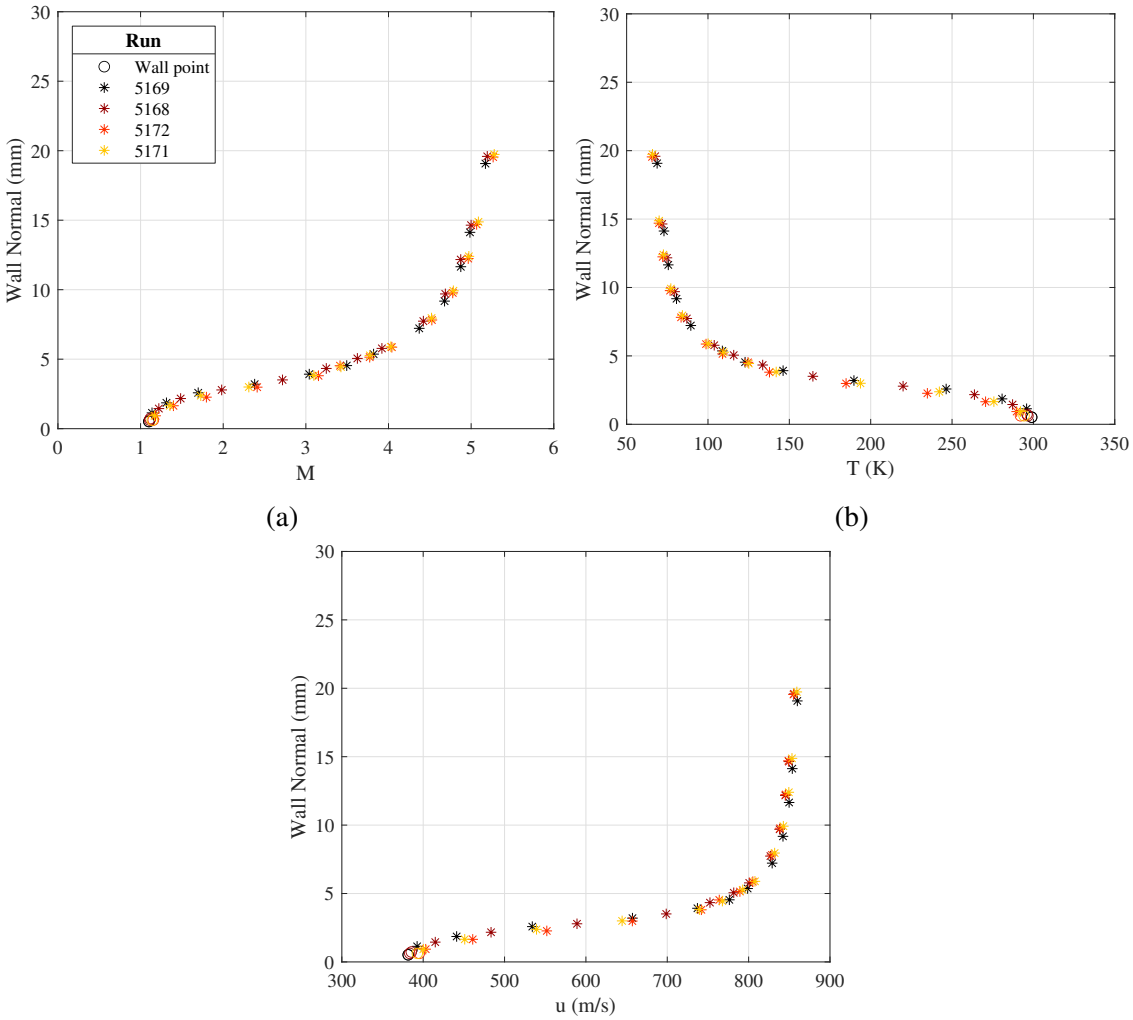

Figure 7.55: Laminar Pitot data, 405mm from the LE. Same legend applies for all figures. [7]

forces dominated its viscous forces, so the boundary layer thinned; this was captured in the laminar equation $\delta \propto \frac{M_e^2\sqrt{x}}{\sqrt{Re}}$ [19] (*Re* refers to the unit Reynolds number). Here the thinning boundary layer would affect the nozzle's effective area ratio. Both TS instruments would be affected by this behavior at the nozzle exit, while the SC probe would be largely insulated from it, producing a more invariant Mach number. The linearly-scaling 0.5% error of the MKS Baratron 631C-10 may have had some effect, but was likely too small to be the sole source of the trend. While the variation in the Mach number could be explained, the general trend, that the Mach number decreased with as the Reynolds number grew, could not. As the boundary layer thinned, the Mach number should have increased, with the exception of the boundary layer rapidly thickening as the flow became turbulent at $Re = 3-4\times10^6/\text{m}$ [207]. In the case of the turbulent flow, it may have been that the transition point in the nozzle moved upstream, which gave the boundary layer more time to

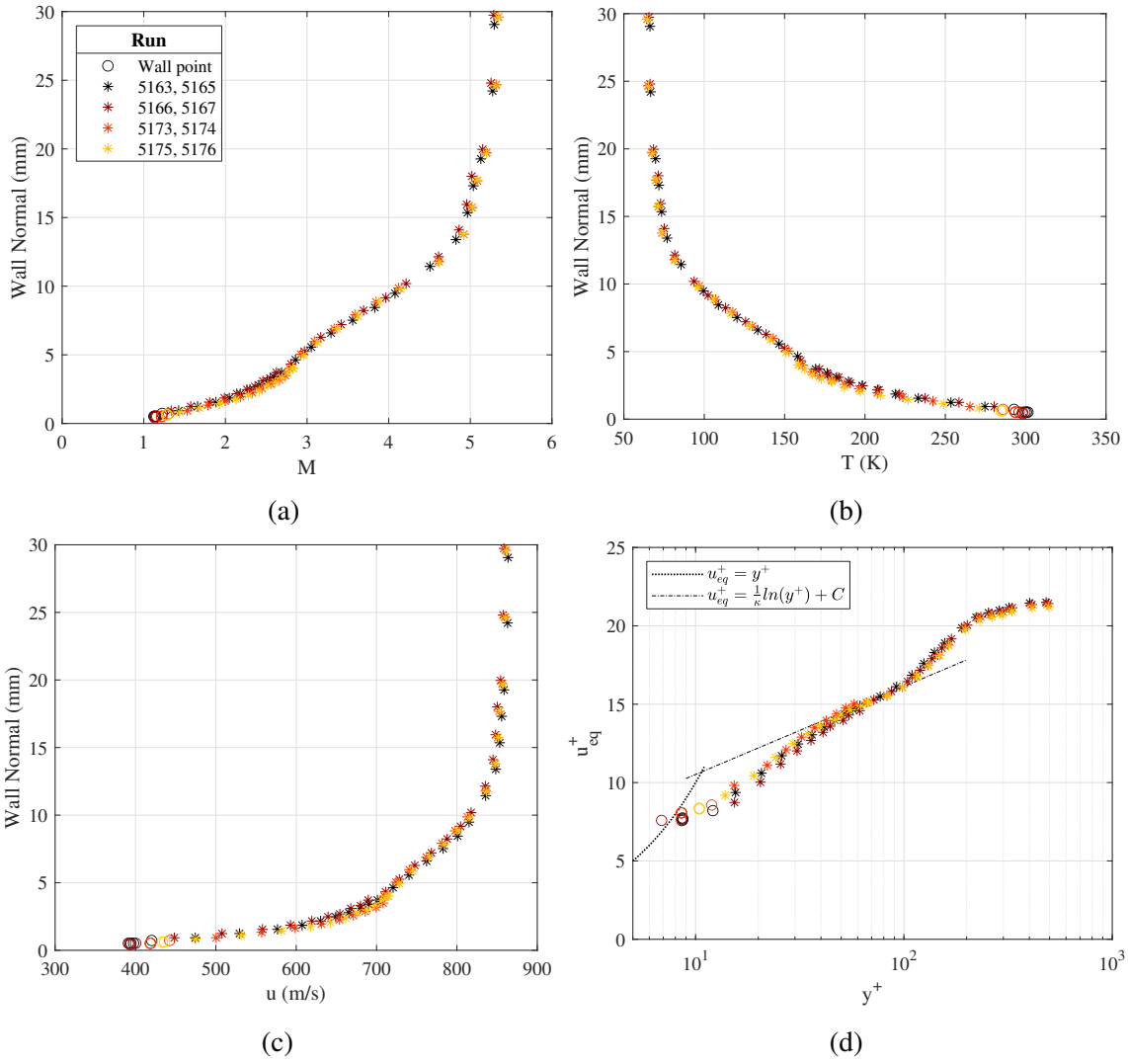

Figure 7.56: Turbulent Pitot data, 405mm from the LE. Same legend applies for all figures. [7]

develop and grow despite the higher Reynolds number. Another possible explanation would be that the laminar flow in the nozzle's throat was proportionally affected more than the exit area ratio, effectively driving down the cumulative area ratio. A final theory would be that as the tunnel was run, it heated slightly, increasing the speed of sound and thereby lowering the Mach number, but in constant Reynolds number tests the Mach number remained constant. ([7])

As part of the development of the PLIF technique, Buen [212] made freestream temperature and velocity measurements of the ACE tunnel at comparable Reynolds numbers. The former were mostly to measure freestream fluctuations and the uncertainty of the technique, however, because to make a thermometry measurement a known temperature must be input, and the only reasonable input for the entire homogeneous data set was the NALDAQ's calculated temperature; as such the freestream temperature 57.35K from Table 4.1 was used hereafter. The velocimetry results from a

spanwise (across the test section) and top-down (from the ceiling to the floor) test were 869.8 ± 7.7 and $822.5 \pm 9.0\text{m/s}$ respectively. Combined with the NALDAQ's temperature, the Mach number ranged from $M = 5.42 - 5.73$, only the latter of which was feasible and matched both the Pitot probe's and NALDAQ's results; no explanation was offered in [212] for the discrepancy in the top-down measurement. Additionally, the temperature fluctuations in the core of the NO cloud were $2 - 8\%$ and the velocity fluctuations were $0.5 - 1\%$ for both the spanwise and top-down techniques [212]; the large temperautre fluctuations were attributed to the uncertainty of the technique. What was worth noting was that, for the spanwise measurement, the velocity tended to grow as the run progressed, both in the NALDAQ and MTV data. Buen [212] attributed this behavior to the tunnel heating, but it could also have occurred due to the tunnel operator increasing the stagnation pressure, and thereby changing the velocity, to maintain the Mach number as the temperature elevated. Were it solely due to tunnel heating, then at the very least the heating's effect on the freestream temperature dominated any effect on the velocity, as the Mach number was known to fall during a run. ([7])

In summation, the Pitot-Pitot data confirmed the tunnel's standard calculation of the Mach number to be 5.7 at the test condition of $6 \times 10^6/\text{m}$ to within $\sim 2\%$, though further understanding of the behavior of the Mach number was warranted. These findings were abetted by PLIF diagnostics. As a final note, it was interesting to see the delay in the response of the static pressure data as the MKS Baratron 631C-10 vacuumed out manifest in the Mach numbers as a brief spike as the settling chamber pressure was increased; neither Pitot tube showed evidence of a delayed response. ([7])

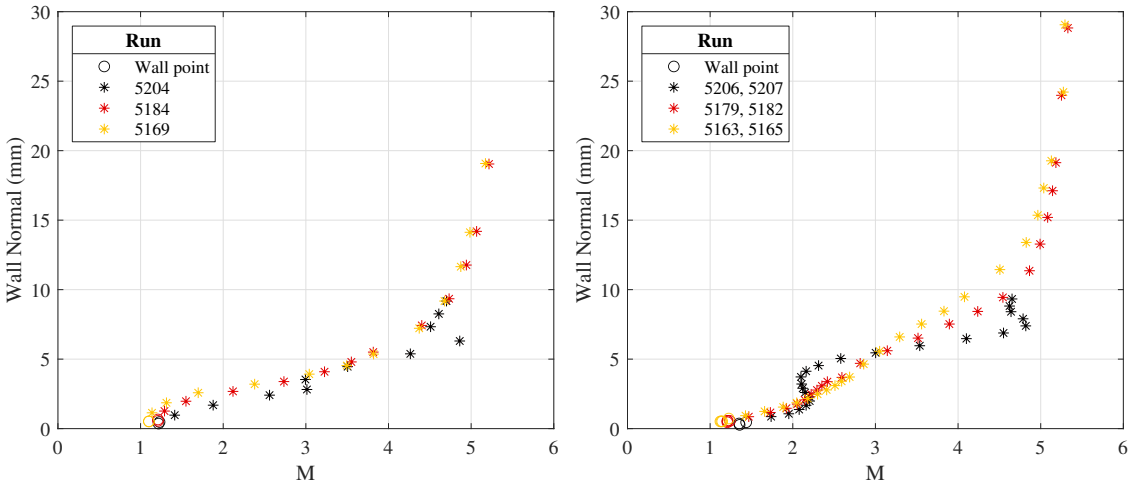

(a) Laminar, Mach number

(b) Turbulent, Mach number

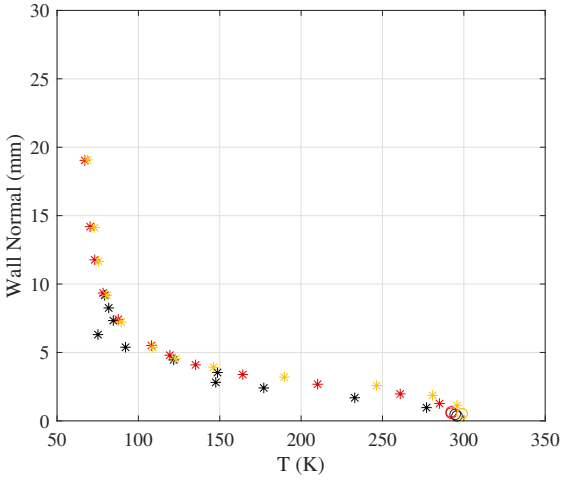

(c) Laminar, temperature

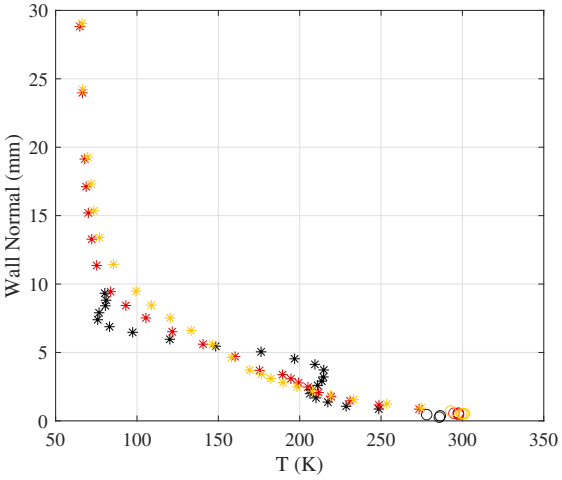

(d) Turbulent, temperature

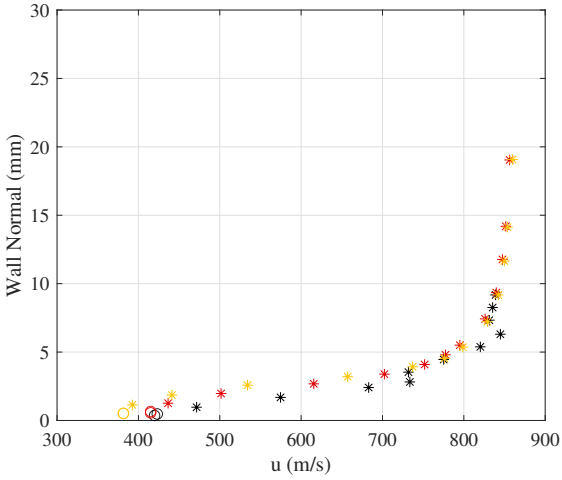

(e) Laminar, velocity

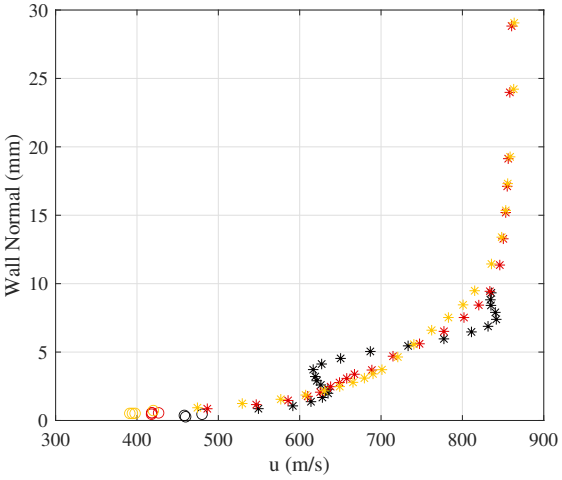

(f) Turbulent, velocity

Figure 7.57: Streamwise plots of Pitot data. All figures in the "Wake" with the plasma "Off". Same legend applies for all figures in column. [7]

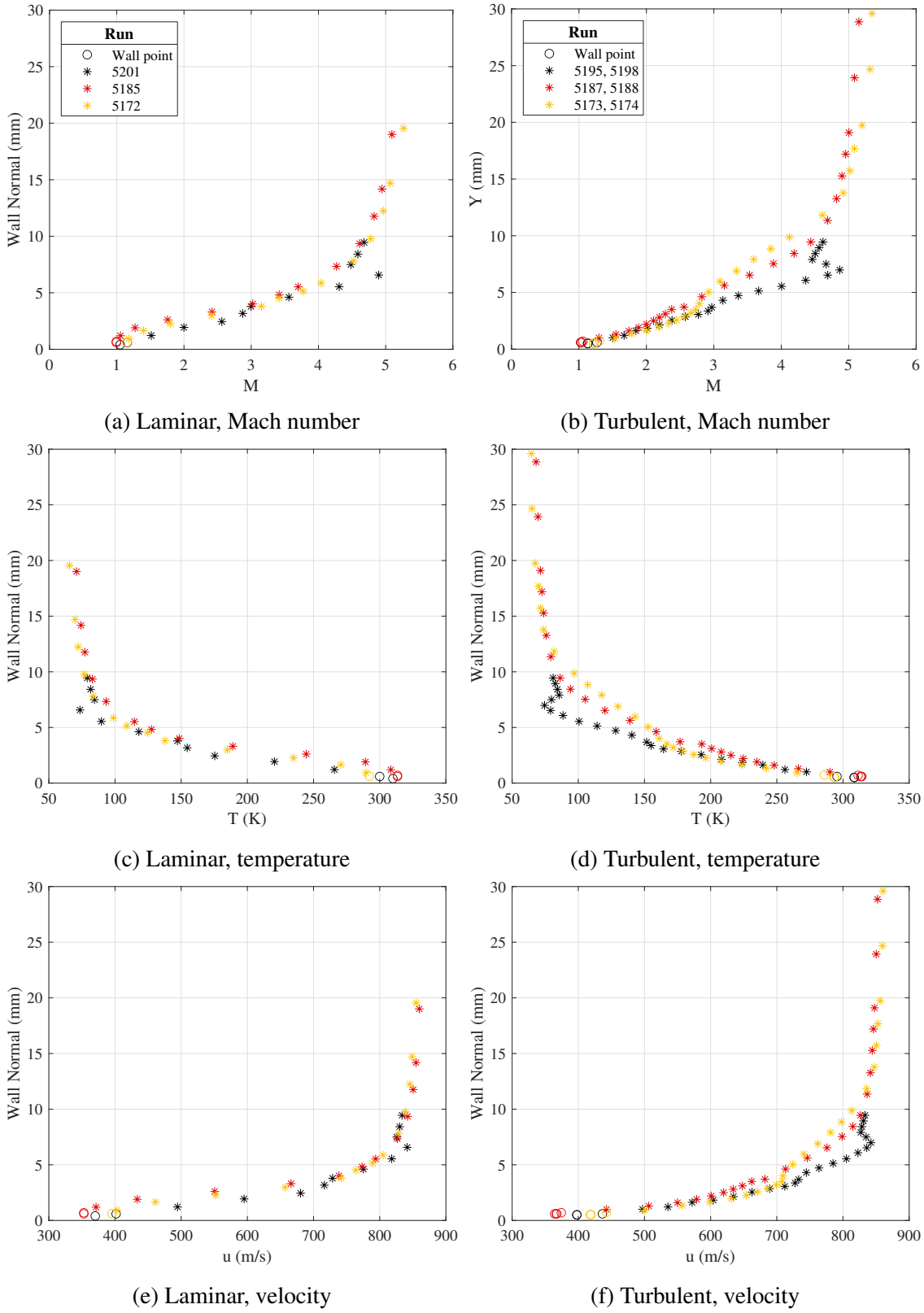

(a) Laminar, Mach number

(b) Turbulent, Mach number

(c) Laminar, temperature

(d) Turbulent, temperature

(e) Laminar, velocity

(f) Turbulent, velocity

Figure 7.58: Streamwise plots of Pitot data. All figures in the "Trough" with the plasma "Off". Same legend applies for all figures in column. [7]

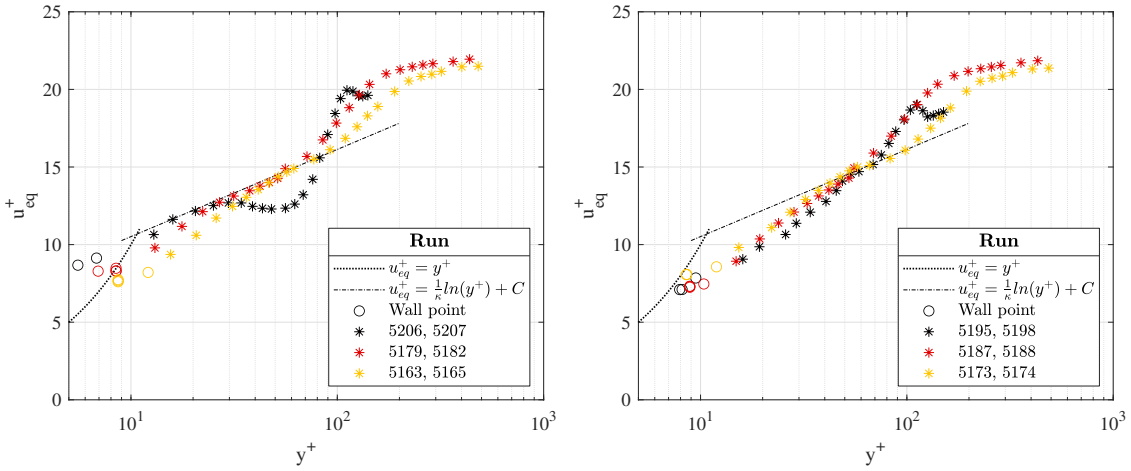

(a) Wake

(b) Trough

Figure 7.59: Streamwise plots of Pitot inner variable data. All figures had the plasma "Off". [7]

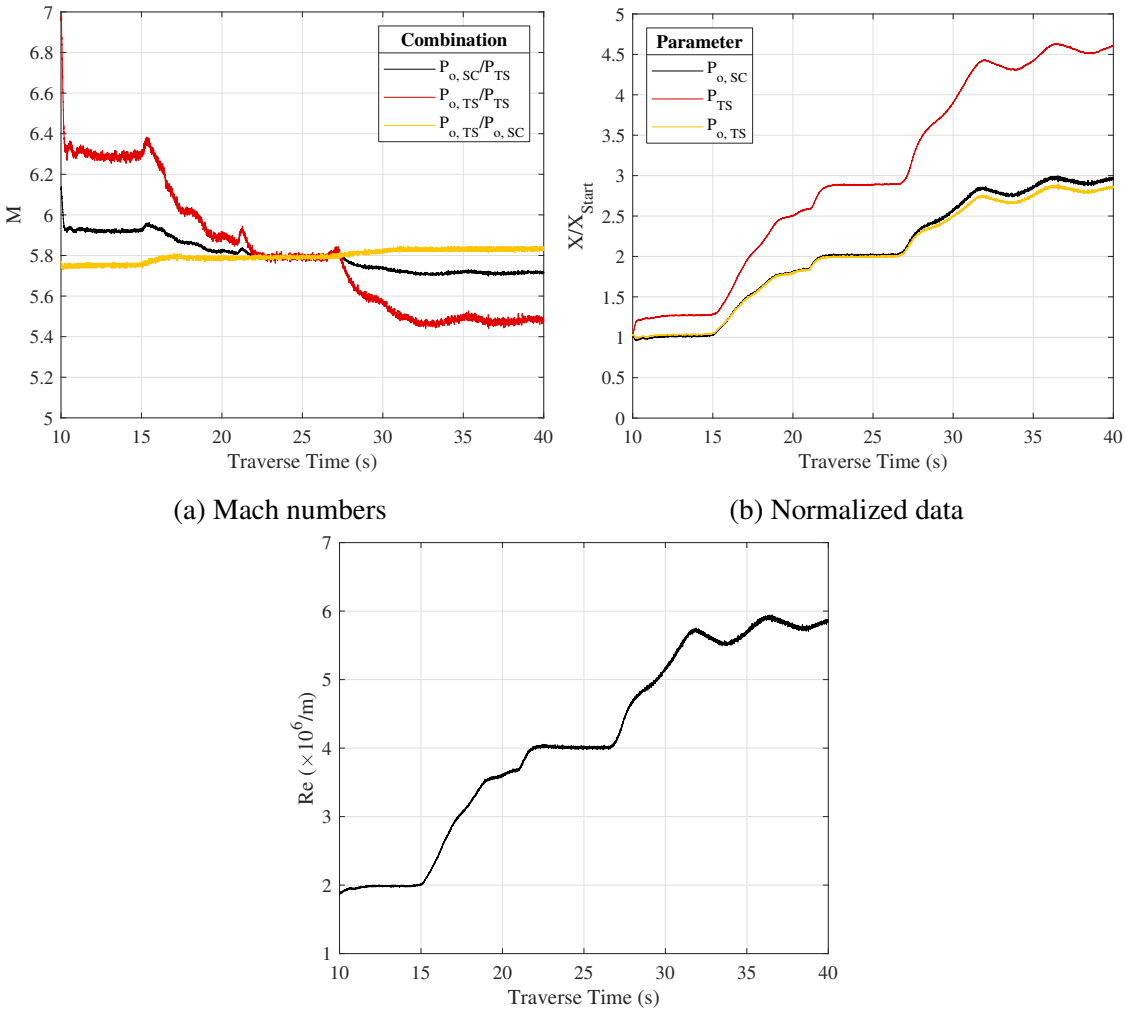

(a) Mach numbers

(b) Normalized data

(c) Reynolds number

Figure 7.60: Tunnel Mach number calculated from various pressure sources. [7]

7.2.4 Advanced Optical Techniques

The results described in this section follow from Broslawski [7]. The techniques in this section were well-established in hypersonic wind tunnel testing, but the results presented were the first from the ACE tunnel. As such they are distinguished from other, more standard optical techniques like schlieren imaging or surface profilometry. The data were relevant to the behavior of the plasma, the flow physics in the boundary layer, and the system's nonequilibrium. ([7])

7.2.4.1 OES Results

The OES data can be split into three parts, the HCLs' spectra, the broadband data taken with the OceanOptics spectrometer, and the rotationally-resolved data taken with the Spex spectrograph. The broadband measurements were useful for identifying species and their degree of excitation as well as studying the effect of general parameters including flow condition and measurement location. Rotationally-resolved data were collected to allow estimation of the bulk plasma temperature to determine if it would produce a significant and undesirable thermal perturbation. The spectra from the HCLs were also recorded using both techniques; the broadband data provided the location of relevant lines, and then certain lines of interest were probed to provide a measurement of the instruments' resolutions. The test matrix for ACE tunnel spectroscopy measurements is shown in Table 7.22, and the corresponding plasma conditions in Table 7.23 and Figure 7.61. ([7])

No.	Resolution	Location	Trip	Nitric Oxide	Run/Date
1	Broadband	Positive column	Laminar	Yes	4921, 8/31/2021
2	Broadband	Negative glow	Laminar	Yes	4919, 8/30/2021
3	Broadband	Positive column	Laminar	No	4922, 8/31/2021
4	Broadband	Negative glow	Laminar	No	4918, 8/30/2021
5	Broadband	Positive column	Turbulent	No	4923, 8/31/2021
6	Broadband	Negative glow	Turbulent	No	4917, 8/30/2021
7	Resolved	Positive column	Laminar	No	4929, 9/2/2021
8	Resolved	Negative glow	Laminar	No	4930, 9/2/2021
9	Resolved	Positive column	Turbulent	No	4928, 9/2/2021
10	Resolved	Negative glow	Turbulent	No	4935, 9/3/2021

Table 7.22: OES test matrix.

7.2.4.2 HCL Spectra

It was first necessary to measure the performance of the HCLs. The $Hg-Ar$ lamp was used to calibrate the OceanOptics USB2000+, then broadband measurements were taken of the remainder of the lamps. This provided the capability to check for metal lines in the plasma such as Cu sputtered from the electrodes, isolated peaks to determine both instruments' resolutions, and aided with the calibration of the Spex spectrograph. The full broadband results for each of the four

No.	Current (mA)	Power Supply Voltage (V)	Power Supply Power (W)	Plasma Voltage (V)	Plasma Power (W)
1	93.5	1427	133.5	489.6	45.8
2	94.2	1433	135.0	487.6	45.9
3	93.9	1427	133.9	485.3	45.6
4	93.9	1427	134.0	484.6	45.5
5	95.9	1430	137.2	468.5	44.9
6	95.0	1426	135.5	472.5	44.9
7	93.8	1426	133.7	485.5	45.5
8	93.9	1427	134.0	485.4	45.6
9	95.5	1429	136.5	471.4	45.0
10	95.8	1428	136.9	467.1	44.8
Average					
	94.5	1428	135.0	479.7	45.4

Table 7.23: Plasma conditions for OES campaign.

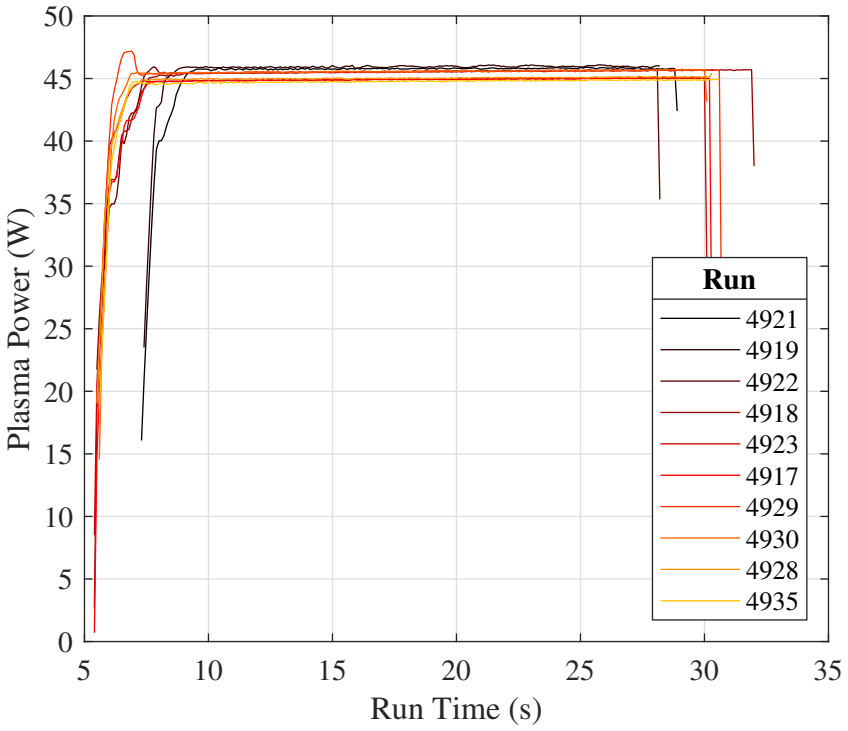

Figure 7.61: Plasma power traces for OES runs. [7].

HCLs are shown in Figure 7.62; these plots were normalized by the absolute maximum intensity in the entire spectra. In general, the lines below 600nm were attributed to the metal cathode while

those above 600nm were attributed to the inert gas. This was why the *Rh*, *Ti*, and *Cu* plots all had the same IR spectra, they all used *Ne* as their fill gas. Figure 7.63 focuses on the UV region of interest; here the data were normalized by the maximum intensity in the bandwidth shown. This was appropriate because these data were taken by maximizing the output in the region shown and letting the brighter IR spectra saturate in order to provide additional clarity in the UV region, that of the greatest relevance to the plasma. While these data mostly served as a reference and as a calibration source, there were several additional findings. Figure 7.63(a) shows a strong, isolated spike in the *Hg* spectra at 365.02nm (according to the NIST tables[1] discussed in Section 6.2.7). This was in a good position for both the calibration and resolution measurement of the Spex spectrograph. Indeed, the same line was used to measure the resolution of the OceanOptics spectrometer as well. For the OceanOptics spectrometer, the isolated *Ne* line at 692.95nm (again, from NIST) shared between the *Rh*, *Ti*, and *Cu* lamps provided another point. Using the dataset that maximized the signal of each line and taking the average of the results from all four lamps yielded a resolution of $[Hg, Rh, Ti, Cu] = [2.5039, 2.1443, 2.2021, 2.1866]\text{nm} \rightarrow 2.2592\text{nm}$. The four runs with the Spex spectrometer and *Hg* lamp yielded a resolution of $[4929, 4930, 4928, 4935] = [0.0804, 0.0727, 0.0804, 0.0770]\text{nm} \rightarrow 0.0776\text{nm}$; it was unknown why this value differed from the 0.025nm reported by Hsu [53]. Nevertheless the Spex spectrograph had $\sim 30\times$ the resolution of the broadband spectrometer, underscoring its value and enhanced capability. ([7])

7.2.4.3 Broadband Spectra

The broadband plasma spectra addressed several fundamental questions. Note that for the following figures the data were normalized by each run's maximum intensity in the full spectra. Figure 7.64 shows that the presence of the trips had no measurable effect on the negative glow or positive column. This was somewhat surprising, because the trips did have a visible impact on the plasma's shape and color; further investigation on the bulk temperature was used to confirm this result, and this will be discussed shortly. For now, however, it was no longer necessary to distinguish between the two cases. The performance of negative glow and positive column is compared in Figure 7.65. There was a series of three lines present only, or at least predominantly, in the negative glow. This was the first negative system $N_2^+ \left(B^2\Sigma \rightarrow X^2\Sigma\right)$. Recall from Section 2.3 that the positively charged ions were expected to aggregate above the cathode, so it followed purely from the perspective of number density that their spectra should be strongest in this region. Rajzer [97] offered such effects as this and the high bulk and electron temperatures above the cathode as explanations for the color difference between the negative glow and the positive column and suggested these same effects could lead to differences in the spectra as well. All told this figure was predicted from plasma theory. The difference in the signal also ensured that the collimator was not so large as to fully conflate the two regions. The data in Figure 7.66 demonstrates the effects of a 10% *NO* injection to see if the *NO* was directly excited by the plasma as Hsu [53] observed. Its results are both clear and provocative: in both the negative glow and positive column regions the *NO* was electronically excited by the plasma. The higher energy region produced more intense lines. ([7])

[1] https://www.nist.gov/pml/handbook-basic-atomic-spectroscopic-data

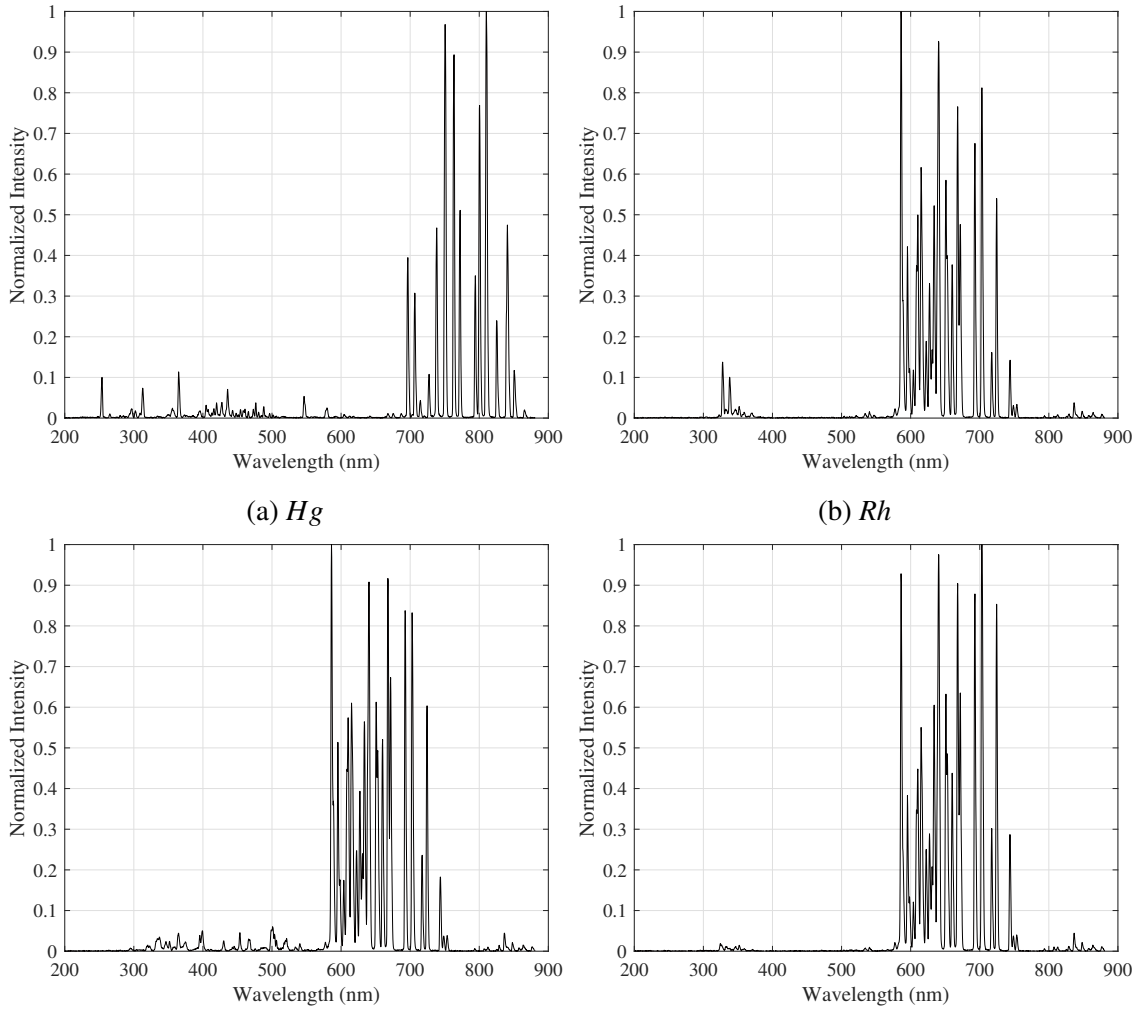

(a) Hg (b) Rh

(c) Ti (d) Cu

Figure 7.62: Broadband spectra of HCLs. Data normalized by maximum intensity in range. [7]

Buen [212] attributed the vibrational excitation of NO through the plasma, as observed through PLIF thermometry, to one of two processes, inelastic scattering (Equation 7.1) and/or electron-impact ionization (Equation 7.2)

$$NO^{v=0} + e^- \rightarrow NO^- \rightarrow NO^{v=1} + e^- \tag{7.1}$$

$$NO\,X^2\Pi + e^- \rightarrow NO\,A^2\Sigma^+ + e^- \tag{7.2}$$

The latter pathway would produce $NO^{v=1}\,X^2$ through fluoresence and collisional quenching. Song et al. [344] stated the resonant absorption energy range for the inelastic scattering process was $0.5-2\text{eV}$ with an absorption cross-section of $\sim 2-5\times10^{-16}\text{cm}^2$. The absorption energy range for the electron-impact ionization had a maximum of 1.9eV with an absorption cross-section of $1.1\times10^{-17}\text{cm}^2$. From the characteristic parameters listed by Roth [98], the glow discharge's

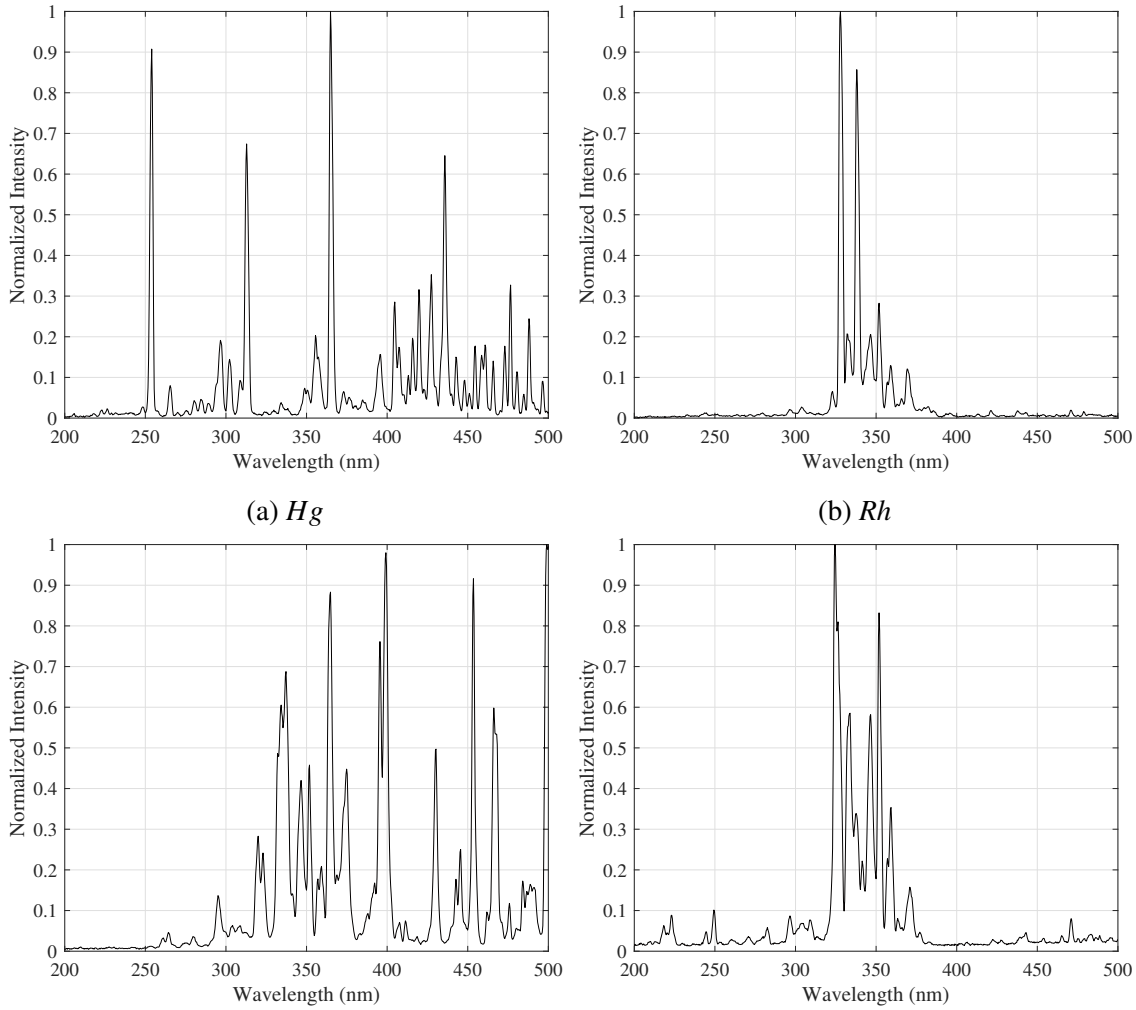

(a) Hg (b) Rh

(c) Ti (d) Cu

Figure 7.63: Focused spectra of HCLs. Data normalized by maximum intensity in range. [7]

temperature of $1-2$eV was well-suited to excite these transitions. The spectrometers here could only study the fluorescence, providing little guidance as to the source of the initial excitation, but owing to the lower absorption cross-section and upper energy limit of the electron-impact ionization process, Buen [212] concluded the inelastic scattering process was likely the dominant source of NO excitation within the plasma. ([7]))

An unexpected finding was the presence of NO lines even in the absence of injected gas. This was not due to leftover gas in the chamber because the first run in the series, Run 4918, did not have NO and occurred months and many runs after the last NO run. Furthermore, NO venting procedures were built into the post-run procedure whenever the gas was injected, so none should ever be left in the line. A pickup run where the NO injection was started halfway through the run confirmed the lines were indeed excited NO because the small lines grew in intensity after the NO was introduced. The HCL spectra in Figure 7.63(d) shows these are not lines from sput-

tered Cu. The question became, then, where did the NO come from? Its formation required the presence of atomic N and O, but the ACE tunnel is a cold blowdown facility and should not have produced temperatures at any point in the entire air supply system or across the shock high enough to dissociate N_2 or even O_2. Recall from Anderson [19], these species dissociate at ~ 4000K and ~ 2500K respectively, though fsome N_2 dissociation is possible at $\lesssim 2000$K [19], especially at the low pressures observed in the ACE tunnel. Taken together, this could imply a lower limit for the plasma's internal temperature, that in the nonequilibrium of the plasma, vibrational temperatures could reach these temperatures and been sufficiently excited enough to cause dissociation; because electron temperatures on the order of $1-2$eV corresponding to $11604.5-23209.1$K were expected [98], vibrational modes $\mathscr{O}(1000\text{K})$ were reasonable. An alternative hypothesis comes from the work of Kossyi et al. [345], who identifies hundreds of reactions and their rate constants in air plasmas, including those involving N, O, and NO. These reactions illustrate the complexity of plasma chemistry, and show ionization, recombination, electronic excitation, *etc.* were all equally valid and significant contributors to the formation of NO. These reactions may not have required excessively high neutral molecule internal temperatures. Either way, the spectroscopy available did conclude NO was being formed, and that the plasma was the most likely source of the constituent atoms, specifically the negative glow where the electrons are more energetic. Further work to resolve the vibrational temperature through OES could further clarify the mechanism by which NO formation occurred. Comparing the spectra in Figure 7.66(c) to the NIST tables, O lines were present at 777.19 and 844.63/844.64/844.68nm and N lines were present at 821.63 and 868.03/868.34nm. As expected, these lines faded away in the positive column, Figure 7.66(d); the unidentified bands at 600, 675, and 750nm, perhaps carbon bands from burning PEEK between the electrodes or N_2 first positive bands generated by the anode, did seem to become stronger in the positive column, defying the general trend. That the data overlapped so well between the cases with and without NO injection also showed the NO was not being dissociated. This was an unexpected finding, not least because the OceanOptics spectrometer has $< 30\%$ efficiency above 575nm. It showed that the plasma, though it may have been, weak and ro-translationally cold, had sufficient energy to break apart very stable molecules and thereby foment species recombination. This would imply that a sufficiently strong plasma could remove the need for any NO injection for PLIF measurements. It also suggests that the NO that was probed with PLIF was being electronically excited by the plasma, not just vibrationally excited by relaxing NO or the laser, complicating the system's thermodynamics. ([7])

7.2.4.4 Spectra for Thermometry

N2SPECFIT was run for the rotational lines of the $N_2\left(C^3\Pi_u \rightarrow B^3\Pi_g\right)$ $(v',v'')=(0,2)$ band (notation from Gilmore et al. [295]). The average of the twenty acquisitions were background subtracted by the mean of the twenty background frames. The maximum of resulting single spectra was used to normalize the data from zero to one. The standard deviation for each pixel was calculated from the result of subtracting the mean background signal from each spectra, then again normalizing by the maximum of the average background subtracted spectra. Despite the careful calibration and background subtraction, the best results were obtained when the program was allowed to calculate and apply a small wavescale shift and dark current offset. Similarly, omitting

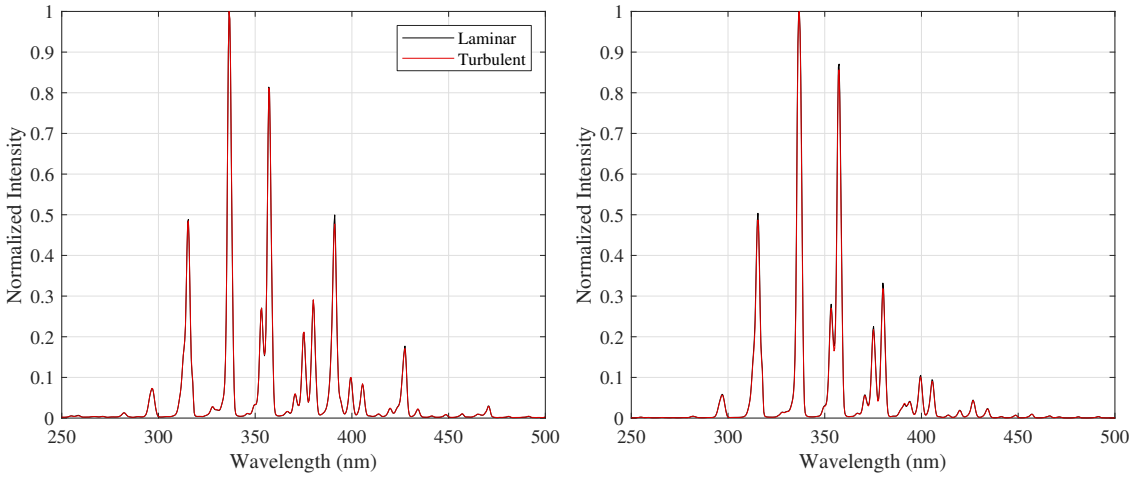

(a) Negative glow (b) Positive column

Figure 7.64: Comparison between spectra of laminar and turbulent flow. [7]

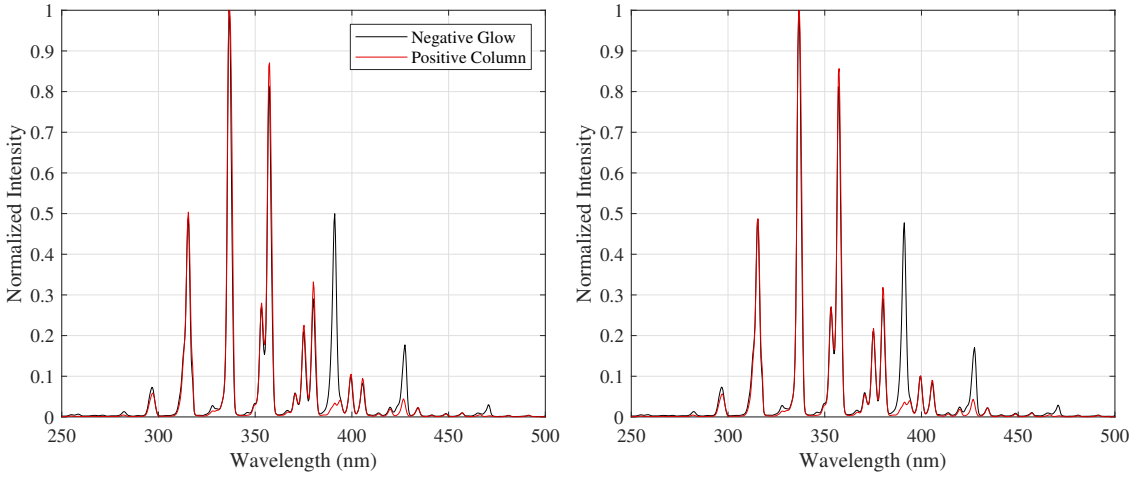

(a) Laminar (b) Turbulent

Figure 7.65: Comparison between spectra of negative glow and positive column. [7]

the vibrational peaks and fitting only the rotational lines of the aforementioned band were analyzed produced the strongest fits. The reason for this limitation was unknown, but including the vibrational peaks caused the program to converge on an incorrect wavescale shift, perhaps because the code tried to use the few and broad vibrational peaks to determine the shift instead of the more numerous rotational lines. Nevertheless, because the goal was only ever to determine a rotational temperature, cutting the vibrational peaks to improve the accuracy of the ro-translational temperature was a worthwhile sacrifice. The $(v', v'') = (0, 2)$ band's rotational lines were used because it was the dominant peak in the observed spectra. ([7])

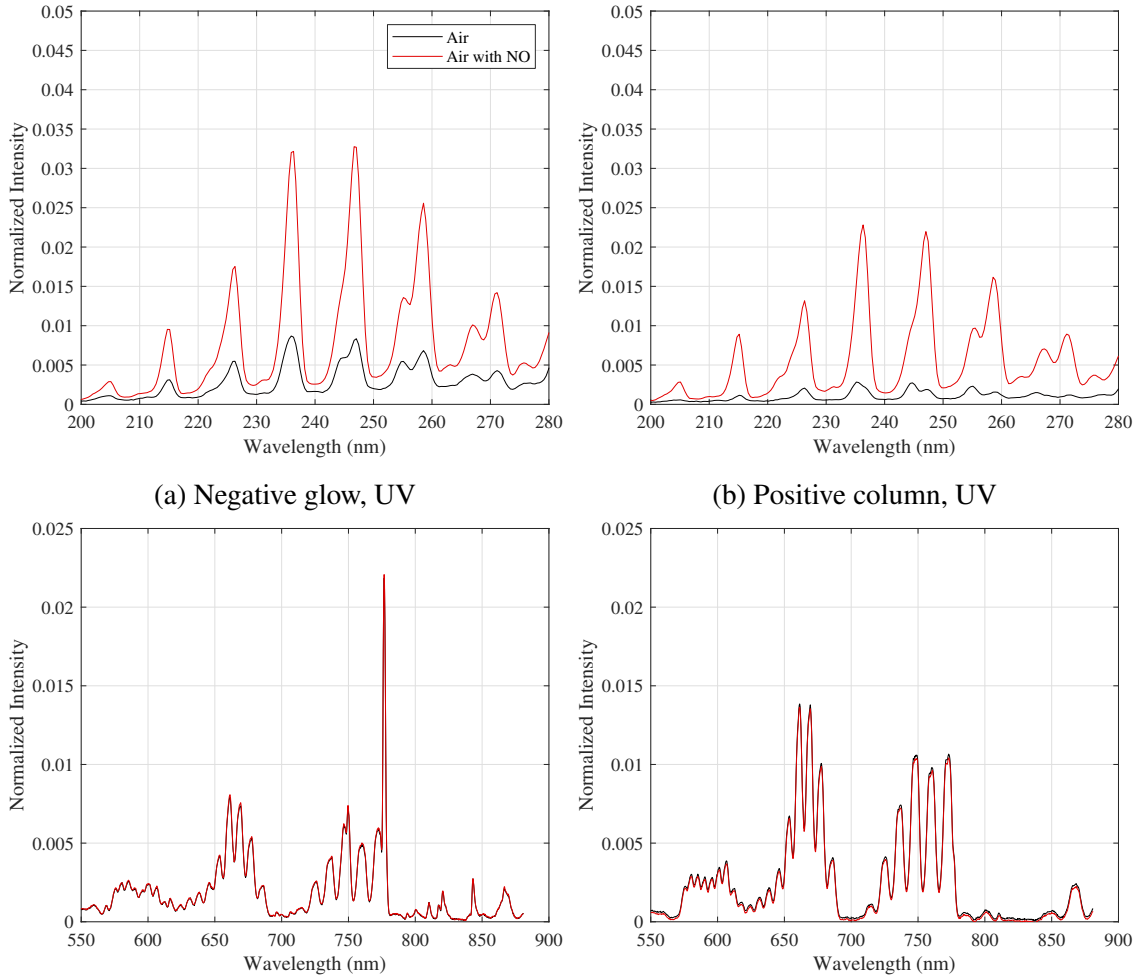

(a) Negative glow, UV

(b) Positive column, UV

(c) Negative glow, Vis-IR

(d) Positive column, Vis-IR

Figure 7.66: Comparison between spectra of air and air mixed with *NO*. [7]

There are three relevant mechanisms by which a spectra can broaden itself, natural (lifetime), Doppler, and pressure (collisional) broadening [346]. The first is mostly attributed to the uncertainty arising from the short lifetime of the upper state of the transition, but can often be neglected [346]; it was not even included as a correction in N2SPECFIT. Doppler broadening arises as gas molecules move towards and away from the detector, shifting their frequencies relative to the observer; Ellis et al. [346] write that this is perhaps the most common broadening mechanism, and it is especially pervasive in UV spectroscopy. For gases in thermal equilibrium this will manifest as a one-dimensional Maxwellian-Bolztmann distribution and could be included in the simulation with an assumed Gaussian profile shape [347]. Like lifetime broadening, collisions between the gas or the wall which depopulate states add to the overall uncertainty of the measurement and produce so-called pressure broadening; this is often accounted for by assuming a Lorenztian profile [348]. N2SPECFIT allowed the use of either a triangular, Gaussian, or "pseudoVoigt" profile, the lattermost being a convolution of the Gaussian and Lorenztian profiles which the user could adjust

to capture their system's unique physics. Ultimately the best results were found with the a purely Gaussian instrument lineshape function with the Spex spectrograph's 0.0776nm FWHM resolution. Figure 7.67 shows the detailed view of the $(v',v'') = (0,2)$, $(1,3)$, $(2,4)$, $(3,5)$ vibrational bands of the second positive system (in order of decreasing wavelength). Because this data was taken in the negative glow, some rotational lines from the $(v',v'') = (0,0)$ band of the first negative system were visible; as expected, these were absent in positive column data. The cause of the bumps slightly to the right of each of the vibrational bands was unknown, but these regions were cut from the temperature fitting and are therefore of minor importance to the main objectives. ([7])

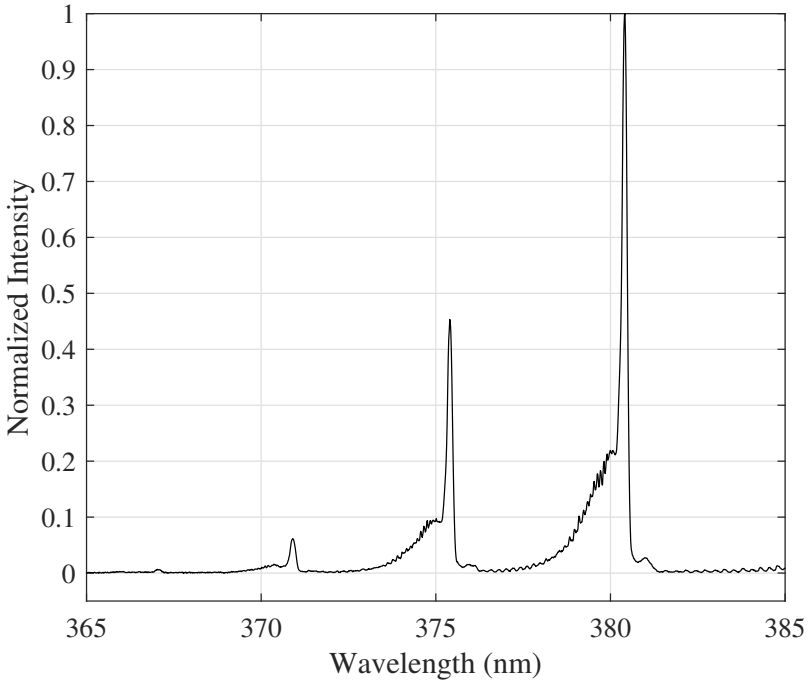

Figure 7.67: Full view of rotationally resolved spectra. Data taken from the "Negative Glow", "Turbulent" run. Data normalized by each run's maximum intensity in full spectra. [7]

The temperature fitting results are shown in Figure 7.68 and quantified in Table 7.24. While there were some offshoots at high wavelengths and the undershoots at lower wavelengths, overall in each case the fit was strong. That being said, the fits produced a spread with no discernible pattern between $315-340$K. While N2SPECFIT did provide some uncertainty, the differences between the temperatures exceeded this margin. That the "Laminar" and "Turbulent" runs yielded different results for the same region despite any notable difference in the broadband spectra reviewed above suggested the variation was indeed due to different convergence conditions in the software. Other possible sources of error could include vibration in the plate (though the diameter of the collimating lens should have been large enough to capture the entire plasma regardless of any such movement), poor estimation of the spectrometer's resolution, or slight differences in the tunnel's conditions

between runs. The lattermost idea could be probed with repeated testing at the same condition. For the fidelity of this report, however, estimating the bulk temperature of a glow discharge through a sheath, boundary layer, entropy layer, and wake, it is enough to say the plasma was approximately 330 ± 15K. Put more practically and qualitatively, the bulk of the plasma is likely to be on the order of the temperature of the hot wall and therefore is unlikely to produce a strong thermal perturbation. ([7])

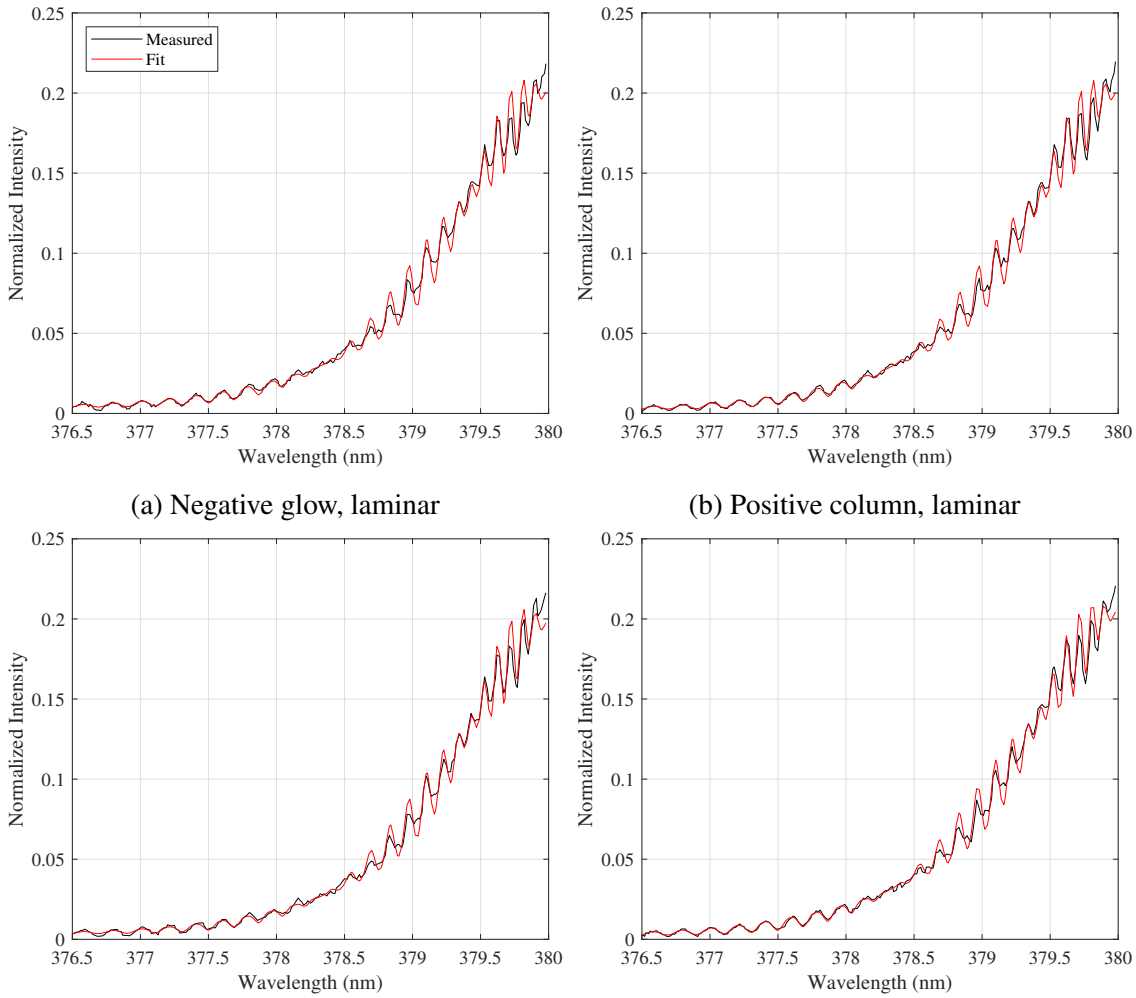

(a) Negative glow, laminar

(b) Positive column, laminar

(c) Negative glow, turbulent

(d) Positive column, turbulent

Figure 7.68: Ro-translational temperature fits of rotationally resolved $(v', v'') = (0, 2)$ band. Data normalized by each run's maximum intensity in full spectra. [7]

Run	Temperature (K)	χ^2_{Red}	Dark current offset (normalized intensity)	Wavescale shift (nm)
4930	328.3 ± 2.17	2.106	$0.371 \times 10^{-2} \pm 0.185 \times 10^{-3}$	$0.499 \times 10^{-1} \pm 0.581 \times 10^{-3}$
4929	330.9 ± 1.92	2.791	$0.244 \times 10^{-2} \pm 0.153 \times 10^{-3}$	$0.491 \times 10^{-1} \pm 0.517 \times 10^{-3}$
4935	313.8 ± 1.97	2.180	$0.333 \times 10^{-2} \pm 0.164 \times 10^{-3}$	$0.500 \times 10^{-1} \pm 0.579 \times 10^{-3}$
4928	341.6 ± 2.18	2.331	$0.234 \times 10^{-2} \pm 0.176 \times 10^{-3}$	$0.549 \times 10^{-1} \pm 0.531 \times 10^{-3}$

Table 7.24: OES temperature fitting results.

7.2.5 PLIF Results

The results described in this section follow from Broslawski [7]. The results of the three PLIF campaigns are split into individual sections below corresponding to the rotational thermometry, vibrational thermometry, velocimenty, and spanwise velocimetry; flow visualization is discussed throughout, but especially in the rotational thermometry and spanwise velocimetry sections. The implementation, development, and analysis of these techniques and their corresponding data was the sole focus of Buen's [212] doctoral research, and as such a more detailed discussion is found therein. The goal here was an interpretation of the results in the context of turbulent boundary layers, especially as the data informed the above theories and techniques. Of special interest was the off-body measurement of fundamental variables (*i.e.*- u and T) and their fluctuations, as well as the NEQ measurements of T^{vib}_{NO} along the test article. ([7])

7.2.5.1 Rotational Thermometry

The rotational thermometry campaign measured the thermal boundary layer as it developed along the plate. Measurement of this profile was useful in its own right, but its impact was multiplied owing to the necessity of temperature when calculating other variables such as density and viscosity. Of special interest was the measurement of the temperature just downstream of the glow discharge; the sensitivity of PLIF thermometry and its immunity to electromagnetic interference made it uniquely suited to this task. Additionally, because planar (sheet width $\sim 800\mu$m [212]) measurements were made, the raw data acted as spatially resolved flow visualization. The test matrix for this campaign is shown in Table 7.25, and the corresponding plasma conditions in Table 7.26 and Figure 7.69. ([7])

For each case instantaneous and mean "Hot" images are shown for flow visualization, rotated and cropped but otherwise just as they appeared out of the ICCDs. The corresponding instantaneous and mean temperature maps were also provided next, as well as the mean (RMS) fluctuations and uncertainty maps. Gaps in the instantaneous temperature due to low signal or nonphysical results were filled with black space. The RMS of the fluctuations $T' = T - \overline{T}$ was provided because the mean of the Reynolds averaged data should be, and in fact was, zero. The calculation of uncertainty is described in [212]. All of these data are contained in Figures 7.71-7.82, but they are succinctly summarized in Figure 7.70, which collapses the 2D maps into boundary layer profiles and compares the effect of plasma and location; here the fluctuation profile is the average of the RMS along the streamwise direction. It is noted that the error bars on the mean temperature and

No.	Location	Trips	Plasma	Run/Date
1	Forward, wake	Laminar	Off	4608, 1/14/2021
2	Forward, wake	Turbulent	Off	4610, 1/16/2021
3	Forward, trough	Turbulent	Off	4615, 1/19/2021
4	Forward	Laminar	On	4609, 1/15/2021
5	Forward, wake	Turbulent	On	4613, 1/18/2021
6	Forward, trough	Turbulent	On	4614, 1/18/2021
7	Back, wake	Laminar	Off	4621, 1/22/2021
8	Back, wake	Turbulent	Off	4616, 1/19/2021
9	Back, trough	Turbulent	Off	4619, 1/21/2021
10	Back, wake	Laminar	On	4620, 1/21/2021
11	Back, wake	Turbulent	On	4617, 1/20/2021
12	Back, trough	Turbulent	On	4618, 1/20/2021

Table 7.25: PLIF rotational thermometry test matrix.

No.	Current (mA)	Power Supply Voltage (V)	Power Supply Power (W)	Plasma Voltage (V)	Plasma Power (W)
4	94.1	1430	134.6	486.5	45.8
5	95.0	1434	136.3	481.0	45.7
6	95.0	1432	136.1	478.7	45.5
10	95.2	1446	137.7	490.9	46.7
11	94.9	1430	135.8	478.3	45.4
12	94.9	1432	135.8	479.9	45.5
Average					
	94.9	1434.1	136.0	482.6	45.8

Table 7.26: Plasma conditions for PLIF rotational thermometry campaign.

fluctuation profiles in Figure 7.70 were not calculated from the 2D uncertainty image for the corresponding run (Figures 7.71-7.82(f)). Instead, new uncertainties were calculated when the mean temperature (d) and fluctuation (e) 2D maps were horizontally averaged to produce the boundary layer profiles. While this greatly simplified the calculation of the error bars, it meant effectively taking and "average of an average", which Buen [212] stated led to a conservative estimation of the total error. More formally, the results from each row of pixels in each frame of a run should have been used as this would yield a more complete representation of the statistics, but such rigor was taken in neither [212] nor here. The condensed data in Figure 7.70 answers several general questions. Perhaps the clearest is the plasma's inefficacy in perturbing the boundary layer, either its temperature or its fluctuations. Recall from Section 2.2.4 that in the work of Fuller et al. [27], a strong RF plasma increased the vibrational temperature of N_2, which then relaxed via H_2O to

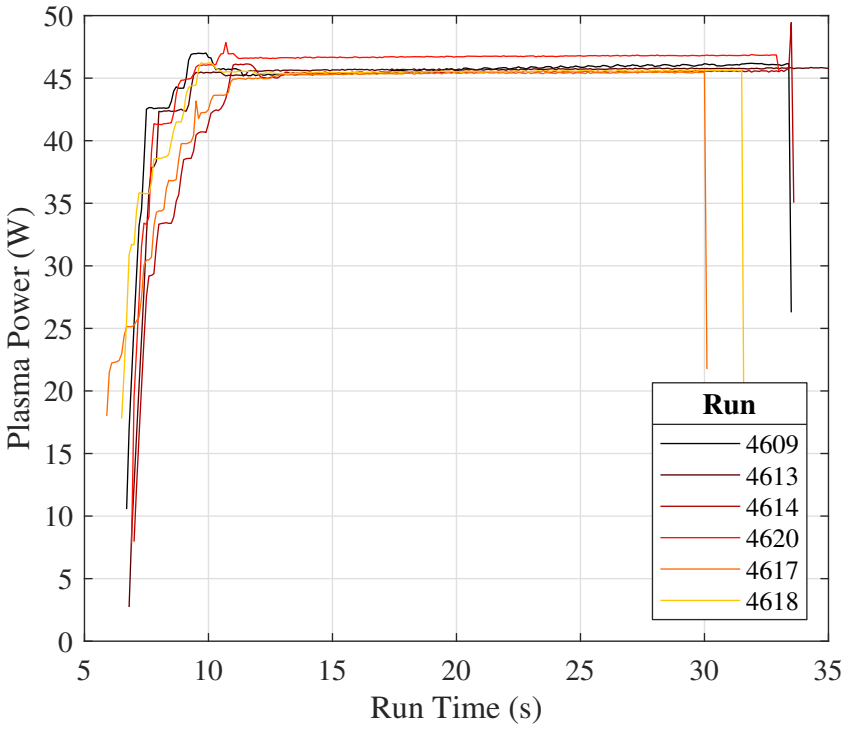

Figure 7.69: Plasma power traces for PLIF rotational thermometry runs. [7]

increase the bulk ro-translational temperature of the air, increasing its viscosity, and thereby reducing the turbulent fluctuations. Be it due to the weaker plasma used, the absence of water in the dry air air supply, or large mean free path in the ACE test section, this process was not appreciably replicated here. In nearly all cases, the the plasma "Off" and "On" cases fell within one another's uncertainties. Even at the wall, where there should have been some collisional quenching of the vibrationally excited N_2, any change was well within the uncertainty limits. There was a delicate balance between sizing the plasma to instill NEQ and thermally perturbing the flow, and a more conservative power supply was used to aim for the former, rather than the later as the goal of this work was to study NEQ, not flow control. The spectroscopic measurements in Section 7.2.4.1 confirmed N_2 was indeed being excited, so either an insufficient amount of it existed to meaningfully heat the boundary layer, or it remained frozen; given the calculations in [53], Buen [212], the latter case was more probable. ([7])

The boundary layer growth was clearest in the turbulent flows, and indeed there was little difference between the wake and trough cases, at least as viewed from these averaged profiles. While this was expected in the more isotropic downstream location, it did confirm that the trip's vortices were indeed breaking down even by this upstream location (see Section 7.2.3.1). In these cases, the fluctuation profiles provided the clearest demarcation of the boundary layer's edge as the temperature profiles tended to rise slowly but consistently well above the expected edge. This result, $\sim$ 12.5mm, agrees well with the other off body diagnostics available, schlieren imaging, CFD, and Pitot pressure. While the uncertainty in the fluctuation profiles increased considerably

near the wall, approaching 50% in places, it was encouraging to see the general shape of the turbulent fluctuation profiles peak near the middle of the boundary layer then fall back towards the wall as they passed from the overlap region into the laminar sublayer; Buen [212] attributed the high uncertainty in this region to low signal and surface reflections. The lack of growth of the laminar thermal boundary layer was initially surprising, until one recalls the presence of the entropy layer seen in the schlieren data in Section 7.2.3.2. It sat $\sim$ 5mm above the surface all along the length test article. Here it acted to mask the laminar flow's thermal boundary layer. That the laminar cases' fluctuations matched the tripped cases' at the "Front" test location abetted the claim the flow was still transitioning and was not fully turbulent; the clearest difference between the laminar and tripped cases at this location would be that the temperature and fluctuation profiles for the tripped boundary layers were slightly thinner. ([7])

The raw fluorescence images and temperature maps provide greater context for the behavior studied in the above profiles. The simplest case with which to start would be the laminar flow in the upstream test location. Here the mean fluorescence image shows the strong rise in signal across the bow shock, as well as the presence of weaker Mach waves stemming from slight steps at the interface of the PEEK insert, electrodes, trip insert, and window. The large rise in signal from the bow shock stemmed from the increase in both pressure, temperature, and density it produced. For an idealized flow at $M = 5.7$ and $\delta = 2.75°$, $P_2/P_1 = 1.458$ and $T_2/T_1 = 1.115$ and $\rho_2/\rho_1 = 1.307$ [205]. This improved signal led Buen [212] to use the post-shock region as the known calibration temperature in the thermometry calculations. They adjusted this temperature until the pre-shock temperature was 58K; as a check, under these conditions the wall temperature approached the 360K measured on the glass with a thermocouple, at least with the measurement uncertainty. What remained unclear, however, was why the temperature jump across the shock went from $\sim$ 64 (accounting for the slight rise in the freestream) to $\sim$ 82K, or $T_2/T_1 = 1.281$. Moreover, that the temperature rose at all above the shock was unexpected. The best theories at present include nonuniform gas seeding leading to the formation of nascent N_xO_y species, NO dimer breakup across the shock, and shock curvature causing deviation from the ideal 11.95°. Buen [212] extensively explored the first two cases and found they could be meaningful, and a rough measurement from Figure 7.71(b) yielded a shock angle of $\sim 12.5°$ ($T_2/T_1 = 1.149$), so a convolution of all effects was likely. Buen [212] also attributed the steady rise in temperature moving towards but above the boundary layer to the series of weak Mach waves and the local minimum in the laminar fluctuation profiles in the upstream location to the location of the calibration region. Finally, O'Byrne et al. [349] reminds readers that horizontally averaging an angled shock causes its temperature jump to spread and appear continuous. ([7])

The insertion of the trips added a separation/reattachment shock below the bow shock, followed by a shear layer formed by the counter-rotating vortices exchanging slow, hot surface air with fast, cool edge air [206]; this complex shock structure is shown with better optical access with the schlieren data in Section 7.2.3.2. These physics tended to obscure the Mach waves, but they were indeed present, most visibly in the average turbulent trough fluorescence images, Figures 7.73 and 7.76. Of particular interest was the decrease in temperature downstream of the separation/reattachment shock. Buen [212] follows O'Byrne et al. [349], who used PLIF thermometry to study laminar flow on a flat plate and attributed the fall in temperature between the bow shock

and wall to expansion as the flow turned from the shock to follow the wall. Still, one would have expected the vortices to have spread the perceived thermal boundary layer as they exchanged hot and cold gas from the wall and edge, but evidently this did not occur; that being said, this process may be at least partially responsible for the lack of Mach waves in the wake case. Much of the same behavior was observed in the upstream "Trough" data, though as Buen [212] notes the temperature jumps across the shocks were less severe. That there were even shocks at all is important, because it showed that the trips did not act individually and instead merged together to create a single, albeit complex, shock structure along their entire surface. Only a spatially-resolved flow visualization technique could have produced this finding. It was also interesting to observe the presence of regular, wave-like structures in the instantaneous wake images, Figures 7.73 and 7.73. These were a clear indication of the singular behavior of the trips as they were absent in the trough images, and that they appeared regular showed again that the flow was transitioning and not yet fully turbulent. Nevertheless, they appeared to have little tangible impact on the temperature because, as was mentioned above, there was little difference between the mean temperature and fluctuation images. Finally, that the signal dropped so low near the wall, even for these "Hot" images, reinforced the challenge of near-wall PLIF measurements. ([7])

The largest change in the downstream test location came from the raw fluorescence images. By this point, the bow and trip shocks were well above the cameras' field of view, making measurement of the freestream temperature impossible. To circumvent this, Buen [212] used the result for the post-bow shock temperature from the upstream cases, 82K, for all downstream analyses; this did not account for the temperature rise across the trip shocks. The known shock from the junction between the ACE tunnel's nozzle and test section was also present; recall that when positioning the test article, great care was taken to avoid this known aberration. Here the temperature did rise slightly, $\sim$ 2K the flow moved across this shock. In the laminar cases, there was no evidence of the entropy layer. Meanwhile, in all turbulent cases, the instantaneous images provided excellent, frozen images of the turbulent boundary layer. The classical elements such as the chaotic appearance, entrained eddies, varying length scales, superlayer, *etc.* were all present [48, 43, 51], and the common appearance between the wake and trough images conveyed the flow's spanwise homogeneity, suggesting it was truly fully developed. ([7])

7.2.5.2 Vibrational Thermometry Results

These data represented the first ever known, direct measurement of the development of a vibrational temperature boundary layer in a hypersonic blow down wind tunnel, at least with the PLIF technique. This campaign began when "noise" was observed in the "Read" images of preliminary MTV tests. Why did the sheet probing vibrationally excited species extend beyond the tagged "Write" line in Section 7.2.5.3? And why was the signal near the wall so much brighter when the plasma was on? The realization that not only did $NO^{v=1}$ exist in the freestream, but was being produced by the plasma was perhaps the greatest moment of discovery in this entire body of work. It is with this enthusiasm the data were analyzed. The results here introduce the data and make generalized observations. ([7])

These tests were conducted after the rotational thermometry and velocimetry campaigns showed there was no effect of being in the on- or off-centerline location, so the "Trough" runs were cut

from the standard test matrix for time. In their place, measurements were taken at the "Middle" test location $\sim$ 260mm from the leading edge so as to better capture the evolution of the vibrational temperature boundary layer along the plate. Of course, studies of the roles of the trips and the plasma were included. The final test matrix is shown in Table 7.25, and the corresponding plasma conditions are shown in Table 7.28 and Figure 7.83. Before starting, note that the results shown below used $T^v_{e,NO} = 230$K to be consistent with Buen's [212] the assumptions and analyses. However, the same figures are re-plotted for $T^v_{e,NO} = T^v_{e,N_2,O_2} = 358$K in Appendix A. Although scaling PLIF data is a nonlinear process and the temperature ranges changed depending on $T^v_{e,NO}$, the same line shapes and trends held for both data sets, so most of the relative analysis below can readily be extended from one case to the other. It must also be understood that the actual T^v_{NO} most likely fell between the bounds generated by these two edge conditions. ([7])

No.	Location	Trips	Plasma	Run/Date
1	Forward	Laminar	Off	4678, 3/26/2021
2	Forward	Turbulent	Off	4681, 3/27/2021
3	Forward	Laminar	On	4679, 3/27/2021
4	Forward	Turbulent	On	4682, 3/28/2021
5	Middle	Laminar	Off	4688, 3/30/2021
6	Middle	Turbulent	Off	4691, 3/31/2021
7	Middle	Laminar	On	4687, 3/30/2021
8	Middle	Turbulent	On	4690, 3/31/2021
9	Back	Laminar	Off	4685, 3/29/2021
10	Back	Turbulent	Off	4684, 3/29/2021
11	Back	Laminar	On	4686, 3/30/2021
12	Back	Turbulent	On	4683, 3/29/2021

Table 7.27: PLIF NO vibrational thermometry test matrix.

As with the rotational thermometry, it was helpful to first consider the mean boundary layer profiles before analyzing the 2D images for each run individually. As in Section 7.2.5.1, it is noted that the error bars on the profiles came from the corresponding run's mean temperature and fluctuation images, not the uncertainty image; these 2D maps will be introduced shortly. The laminar profiles are shown in Figure 7.84. With the plasma off, the profiles at all three locations and their corresponding fluctuations matched to within the uncertainty of the measurement. There was a decay in the temperature as the flow approached the wall, which Buen [212] attributed to either a temperature gradient in the freestream (recall that the test article was mounted 25.4mm below the tunnel centerline) or the progressive activation of the VT and VV relaxation pathways as the rotranslational temperature increased towards the boundary layer. The N_xO_y species formed due to injecting NO at 15% may have exacerbated any effect of being off-centerline. Without freestream T^v_{NO} measurements, the exact source of the decay was difficult to explain, but the increased rate of

No.	Current (mA)	Power Supply Voltage (V)	Power Supply Power (W)	Plasma Voltage (V)	Plasma Power (W)
3	94.5	1439	136.0	491.0	46.4
4	95.3	1433	136.6	477.3	45.5
7	95.5	1451	138.5	492.7	47.1
8	95.4	1440	137.4	482.8	46.1
11	95.5	1451	138.5	493.9	47.1
12	95.5	1443	137.8	484.8	46.3
Average					
	95.3	1442.8	137.5	487.1	46.4

Table 7.28: Plasma conditions for PLIF vibrational thermometry campaign.

said decay between $2.5-5$mm was likely due to VT and VV relaxation; using the ro-translational thermometry results to calculate the energy exchange rates through the boundary layer, Buen [212] found the efficacy of many of the relaxation pathways to increase by several orders of magnitude in this range, but the dominant NO VT and $NO-O_2$ VV reactions were relatively unaffected, rising $\mathcal{O}(10-100\times)$. An alternative explanation for the vibrational temperature deficit near the wall could be some effect due to the shock curvature at the leading edge and the corresponding entropy layer observed in Section 7.2.3.2, but such a process was less understood. The slight recovery below $\sim$ 1mm was likely due to the partial satisfaction of the no-slip condition. ([7])

The introduction of the plasma fomented a general trend in the laminar boundary layer. Indeed, the vibrational temperature boundary layer seemed to be growing alongside the laminar velocity boundary layer, thickening as it traveled along the test article. In doing so, the temperature dropped from a peak of $\sim$ 275K $\sim$ 1mm above the surface at the first test location, to $\sim$ 260K $\sim$ 2mm above the surface at the second test location, and finally $\sim$ 250K $\sim$ 2mm above the surface at the final test location. While the temperature peak did not move appreciably between the "Middle" and "Back" test locations, in the "Front" test location the peak temperature corresponded well with the observed height of the plasma's cathode layer, and the short distance between the plasma and test location left little room for relaxation or boundary layer growth. Above $\sim$ 10mm the plasma "Off" and "On" cases appeared identical. Between $\sim 5-10$mm the general shape of each location's curve was maintained, but they appeared consistently $\sim$ 5K colder when the plasma was on, a small but meaningful amount. That the vibrational temperature boundary layer thickness matched the ro-translational boundary layer's thickness was expected. In order to explain the motion of the peak temperature, Buen [212] performed some calculations using Fick's Law of Diffusion and found it was a decent explanation for the observed results. When added to the boundary layer growth, this helped explain how any why the peak vibrational temperature moved up from the wall. That the vibrational temperature dropped could either have been due to this same diffusive pathway or vibrational relaxation, but the lack of meaningful difference in the ro-translational temperature profiles between the plasma "Off" and "On" cases, and the general thickening of the downstream vibrational temperature profiles, meant that should the latter case be significant, an insufficient amount

of vibrational energy was relaxing to affect the gases' properties. In both cases, the fluctuations increased as the flow approached the boundary layer, perhaps due to whatever trend drove down the vibrational temperature. Interestingly, the relative fluctuation percentage was roughly matched in this region between the ro-translation and vibrational measurements. This was surprising, because one would expect the larger temperatures would have reduced the fluctuation percentage accordingly. Also, it was hypothesized the vibrational temperature would have been more insulated from the pressure perturbations which lead to ro-translational temperature fluctuations, but evidently this was not the case; this complex relationship was discussed in Section 2.2.5 based on the work of Khurshid and Donzis [29]. Near the wall the fluctuations did not spike to the same degree as the ro-translational case. This may be due to the increased signal in this regime; the $v = 0$ beam could be optimized for the "Hot" boundary layer (high J state), and when it was turned on the plasma directly increased the number density of vibrationally-excited target molecules for the $v = 1$ beam. Buen [212] asserted that the interface between the boundary and entropy layers was the source of fluctuation peak at $\sim$ 5mm. There was little change in the shape or magnitude of the fluctuation profiles between and of the three test locations, and the plasma seemed to have no effect as well. ([7])

The turbulent profiles are shown in Figure 7.85. Once again, the calculation of the error bars by Buen [212] is described in Section 7.2.5.1. The "Front/Plasma off" case agreed strongly with its laminar counterpart. The "Middle" and "Back" cases, however, did not show the same deficit below $\sim$ 5mm; they also did not show the same general decay towards the boundary layer, but this was likely due to the thickness of the boundary layer itself. All three profiles reached a wall temperature of $\sim$ 225K, which matched that of the laminar flow. With the plasma activated, there again became a clear trend as the flow moved along the test article. The profile for the first location agreed well with the laminar case, with a peak temperature of $\sim$ 270K $\sim$ 1mm above the surface. In general, this implied that the transitional boundary layer was not yet capable of having an impact on the vibrational energy profile, but the addition of the slight "hump" in the profile at $\sim$ 3mm showed there was some effect; Buen [212] postulated this bump was due to turbulent mixing, perhaps the ejection of vibrationally hot gas from the wall and into the trips' shear layer due to the corner vortices. By the "Middle" location, the boundary layer had thickened to $\sim$ 9mm, and the temperature peaked at $\sim$ 255K at the wall; this was the only profile to peak at the wall, casting some doubt onto its veracity below $\sim$ 2mm, especially when considering the sudden and unexplained spike in its fluctuation profile in this region. By the final test location, the peak temperature was $\sim$ 240K $\sim$ 11mm from the wall, agreeing well with the ro-translational boundary layer thickness. Comparing the "Laminar" and "Turbulent" cases, it would seem the wall temperature was independent of the flow and was $\sim$ 270mm at the first test location, and then $\sim$ 240K at the second two test locations. Also, recall from Khurshid and Donzis [29] that turbulent flows should be able to store a greater degree of their energy in vibrational modes than laminar flows, potentially explaining some degree of the hotter temperatures seen in Figure 7.85 as compared to Figure 7.84; still, mixing likely played a more dominant role in the resulting temperature profiles. The decrease in the peak temperature and thickening of the boundary layer was attributed to turbulent mixing, or the combination of convection and diffusion [212]. Again, this would imply that the vibrational relaxation may have played a secondary role in the vibrational temperature decay, a position Buen supported with the

absence of any ro-translational temperature rise along the plate. They plotted the relaxation reaction rates, now calculated using the turbulent ro-translational temperature profiles, and as with the laminar case the less important reactions had remarkable increase in efficiency. The dominant NO VT and $NO-O_2$ VV reactions had the same $\mathcal{O}(10-100\times)$ increase within the boundary layer. While the exact effect of these increases was difficult to quantify given the intensity of the turbulence and lack of any perceptible impact of the plasma in the other PLIF techniques, despite the growth of the reaction rates in the boundary layer Buen stated NO vibrational relaxation was likely to play a secondary role to turbulent mixing; the low number density of vibrationally excited NO molecules could only have lessened the impact of the relaxation. Recall that other experiments [27, 94] used a stronger plasma and more efficient relaxers like H_2O and CO_2 to generate a measurable impact from the more plentiful N_2. There was surprisingly little difference in magnitude of the fluctuating profiles between the laminar and turbulent flows save for the larger boundary layer in the latter case. In all cases, the fluctuations seldom exceeded 4%. A possible explanation could be the relative invariance of the vibrational temperature to turbulent pressure fluctuations; it takes considerably more collisions to cause vibrational equilibration ($\mathcal{O}(10^4)$) than ro-translational equilibration ($\mathcal{O}(10^{0-1})$), so the timescales for the pressure perturbations and low densities in the ACE tunnel may have been such that there could be little vibrational energy exchange; possible mechanisms are provided by Khurshid and Donzis [29]. Upon entering the boundary layer, the profiles for the turbulent case appeared more constant, as one might expect for the fully developed turbulent flow; Buen [212] expected a decrease in fluctuations near the wall owing to the presence of the laminar sublayer, but the low signal in this region and presence of vibrational slip may have confounded this behavior. There was a distinct hump in both the "Laminar" and "Turbulent", plasma "On", "Front" fluctuation plots at $\sim$ 2mm; Buen [212] attributed other such bumps in these profiles to the interface of the freestream and entropy layers or the trips' wake structure, but this one remained unexplained. That it occurred so close to the cathode layer meant it may have been due to some effect of the vibrational energy seeding. ([7])

The individual run data is presented analogously to the ro-translational results in Figures 7.86-7.97. For each run, an instantaneous and mean fluorescence image is shown; here the $v=1$ frame was selected because $v=0$ images can be seen in the ro-translational results. The corresponding instantaneous 2D temperature map from this frame is provided next, as well as the mean temperature map from all of the images. The bottom row contains the RMS fluctuation ($T'=T^v-\overline{T}^v$) and mean uncertainty maps. Again, any gaps in the data were filled with solid black regions. The laminar data showed several key trends. To begin, compare any set of raw images without and with the plasma, for example Figures 7.86(b) and 7.88(b) respectively. In the freestream, there was a gradual decrease in signal as the flow approached the wall, perhaps due to absorption, the rising temperature reducing the number density of the NO, or chemistry effects. No Mach waves were visible, likely due to their weak effect even ro-translational temperature. The main feature, however, was the bright region near the wall, contained entirely within the boundary layer, that was only present when the plasma was activated. This represented direct evidence the plasma was vibrationally exciting the NO. In those laminar runs with the plasma on it was especially clear where the boundary layer began. The turbulent run data showed the same impact of the plasma. The instantaneous images of the fully developed turbulent boundary layer, such as 7.95(a) were partic-

ularly striking, provide excellent resolution of the turbulent structures. In the upstream location, Figure 7.89, it was interesting to view the trip shock. This shock was strong enough to be visualized, likely due to its effect on the NO's number density. However, it seemed to have little tangible effect on any of the thermometric results. This may have been due to the relative invariance of the vibrational temperature to shocks in low density blowdown facilities like the ACE tunnel[90]. An additional detail in Figure 7.89(b) was a weak glowing region between $\sim 2-4$mm; this was attributed to the trips' corner vortices convecting vibrationally excited NO out of the cathode layer [212]. ([7])

7.2.5.3 Velocimetry Results

Velocity was the final fundamental, and perhaps the most classical, boundary layer variable measured. Many of the theories developed for subsonic, and then extended to supersonic, boundary layers were developed to predict the velocity profile, and as such the ability to directly and unobtrusively measure it to excellent resolution was invaluable in testing these models. As such the main goal of this campaign was to collect canonical, high-quality data that could be used to compare to past and future hypersonic turbulent boundary layer experiments and models. This included those for the shape and magnitude of the velocity fluctuation profile. The test matrix for this campaign is shown in Table 7.29, and the corresponding plasma conditions in Table 7.29 and Figure 7.98. ([7])

No.	Location	Trips	Plasma	Run/Date
1	Forward, wake	Laminar	Off	4672, 3/23/2021
2	Forward, wake	Turbulent	Off	4662, 3/18/2021
3	Forward, trough	Turbulent	Off	4664, 3/19/2021
4	Forward	Laminar	On	4671, 3/23/2021
5	Forward, wake	Turbulent	On	4661, 3/18/2021
6	Forward, trough	Turbulent	On	4663, 3/19/2021
7	Back,wake	Laminar	Off	4652, 3/15/2021
8	Back, wake	Turbulent	Off	4654, 3/16/2021
9	Back, trough	Turbulent	Off	4657, 3/17/2021
10	Back, wake	Laminar	On	4653, 3/15/2021
11	Back, wake	Turbulent	On	4655, 3/16/2021
12	Back, trough	Turbulent	On	4656, 3/16/2021

Table 7.29: PLIF velocimetry test matrix.

While these detailed datasets were valuable on an individual basis, it was perhaps best to first establish general trends by looking at a cumulative comparison of the laminar, turbulent wake, and turbulent trough velocity and fluctuation profiles. These plots are contained in Figure 7.99; here the results from both lines from any given run were drawn with the same style for clarity. In general,

No.	Current (mA)	Power Supply Voltage (V)	Power Supply Power (W)	Plasma Voltage (V)	Plasma Power (W)
4	95.0	1444	137.2	490.9	46.6
5	95.2	1437	136.9	482.2	45.9
6	94.6	1433	135.6	484.0	45.8
10	95.1	1447	137.6	493.0	46.9
11	95.0	1436	136.5	483.1	45.9
12	95.1	1438	136.8	483.7	46.0
Average					
	95.0	1439.3	136.8	486.2	46.2

Table 7.30: Plasma conditions for PLIF velocimetry campaign.

there was no perceptible effect of the plasma, either on the velocity profile or its fluctuations. This further supported the finding in Section 7.2.5.1 that there was little chance of relaminarization owing to $N_2^{v=1}$ relaxation, or any other species for that matter. There also appeared to be a tendency for the velocity profiles to curl towards the wall in an non-physical manner below $\sim$ 1mm from the wall. This, alongside the ostensible slip at the wall, likely stemmed from the challenge in making measurements in the near wall region owing to low signal and high noise; this manifested in the high uncertainty in this region. When reviewing these plots, it was also helpful to remember the theoretical edge velocity calculated by the boundary layer solver was 857.6m/s. ([7])

The laminar data in Figure 7.99(a) and (b) shows considerable overlap for all cases, especially after taking into account the uncertainty. In general, however, one can see that the red, downstream traces took slightly longer to reach the edge condition, $\sim$ 4mm as opposed to $\sim$ 2mm for the downstream and upstream cases respectively; these values matched the predicted boundary layer heights from other techniques (ex.- the boundary layer solver), but the lack of clarity underscored the challenge in experimentally determining the boundary layer edge. This problem was somewhat alleviated by the laminar fluctuation profile plot, wherein the departure from the perceived freestream value showed more clearly where the boundary layer started. The greater uncertainty for the upstream case may have been due to the Mach wave coming off the window/PEEK interface 97.9mm from the leading edge. Buen [212] attributed the gradual decrease in velocity as the flow approaches the boundary layer to the same series of weak Mach waves described in the rotational thermometry results, Section 7.2.5.1. These trends were more apparent in the turbulent cases. Consider first the wake data, Figures 7.99(c) and (d). The black, upstream profiles initially sat above the red, downstream profiles, but the trend reversed at $\sim$ 3mm. Remember, a turbulent boundary layer velocity profile lays almost flat against the wall, rapidly recovering towards the edge velocity, then shifts to very gradually approach the edge velocity. In laminar boundary layer profiles, this process is more uniform through the boundary layer. These physics were displayed here. Indeed, the two cases did not overlap until $\sim$ 13mm. This was reflected in the fluctuation profile, where in the downstream location the fluctuation profiles departed the edge condition at $\sim$ 13mm and in the upstream case the results more closely matched those from the laminar plot. That being said,

as one would expect the magnitude of the fluctuations were larger in the tripped case as opposed to the fully laminar case. As the boundary layer became fully turbulent, the fluctuations should become zero at the wall, but this did not occur, likely due to the high uncertainty in this region. Surprisingly, in the upstream profiles there was little evidence beyond the uncertainty limits of the trip separation/reattachment shock structure, the trips' shear layer, or the wake behavior seen in Section 7.2.3.5. For these profiles Buen et al. [2] did attribute the slight rise in the velocity from 20 to 15mm above the surface to the expansion after the trip separation/reattachment shock and the decay above the boundary layer to the trips' shear layer. Similarly, the spread of the line-to-line data for a single run may have owed partially to the lines' $5-10$mm streamwise separation in the highly transitional region. The trough data in Figures 7.99(e) and (f) followed the same general trends. These data appeared far more orderly, but whether this was due to the fact the trips' effects should have been weaker or there were fewer analyzable lines was unclear. ([7])

The full dataset available from each run are contained in Figures 7.100-7.111. "Write" and "Read" images are shown as they appeared out of the ICCD, the only processing being image rotation and cropping. These images underscored several experimental challenges, including: low signal near the wall; strong reflections despite the anti-reflective coating; "hot spots" on the wall from dust, burn marks, damage, *etc.* causing excessive scatter; excitation of naturally occurring vibrationally excited NO in the read images; beam spreading (the beams' waists were usually set just above the cameras' field of view). For example, the strong signal of one line could be independent of that of the other, which for Runs 4657 and 4656 manifested as only one line having sufficient accuracy for worthwhile analysis. This also meant that some of the raw images shown below appeared either too dark or too saturated, as a balance was attempted to be struck for clearly showing both lines with just one color bar; when analyzing the data, each line was separately identified using its own region of interest (see [212]). In such instances when the line locations were unclear, it is recommended to defer to the mean line location plot. For each run, the two lines' velocity and fluctuation profiles were shown. Again, for the mean fluctuation profiles the RMS average of the temporally-fluctuating velocities $u' = u - \overline{u}$ was shown as, by definition, $\overline{u'} = 0$. Recall from Section 6.2.6 that during the Pitot pressure campaign, the measured Mach number was used in the second Crocco-Busemann relation to calculate the temperature profile, and from these two parameters provided the velocity profile. An analogous process was implemented here; the velocity profile for each line was inputted into the Crocco-Busemann relations, and then the Mach number was computed from $M = u/\sqrt{\gamma R_{air} T}$. Hereafter, these parameters will be referred to as T_{C-B} and M_{C-B} respectively. Of course, here one could skip the estimation of the temperature profile and interpolate the ro-translational thermometry data from Section 6.2.6; in this way, one could validate the Crocco-Busemann theory. These results are subsequently denoted T_{PLIF} and M_{PLIF}. In these calculations, uncertainties were calculated by finding the extrema for the ratios in each calculation. For example,

$$T_{C-B,low} = T_w + (T_{aw} - T_w)\frac{u - u_{unc}}{u_e - u_{e,unc}} + (T_e - T_{aw})\left(\frac{u - u_{unc}}{u_e - u_{unc,e}}\right)^2 \tag{7.3}$$

$$M_{C-B,low} = \frac{u - u_{unc}}{\sqrt{\gamma R_{air}(T_{C-B,low})}} \tag{7.4}$$

The process was reversed for the upper limit. Due to the relatively large uncertainties, and the sensitivity of Mach number to both temperature and velocity, the more conservative approach in Section 7.2.3.5 yielded nonphysical results. ([7])

This form of the Crocco-Busemann equation was used because it guaranteed that at the edge of the boundary layer $u = u_e$ and $T = T_e$, regardless of data coming from different sources (PLIF thermometry, PLIF MTV, NALDAQ/theory, *etc.*); for example, T_e was set using oblique shock relations [205] and NALDAQ data for consistency with the Pitot data reduction (Section 6.2.6), and T_w was set from the PLIF thermometry as no single wall temperature value was hard-coded into Buen's [212] analysis. Again, for simplicity when comparing the reduced data, this was the same form used in Section 7.2.3.5. The adiabatic wall temperature was calculated using the PLIF results for the "PLIF" dataset, and from the NALDAQ/shock jump equations for the "C-B" dataset. This step was important, as it meant that the PLIF and Crocco-Busemann results could have different T_e, and thus different profiles. This discrepancy manifested in the data, and will be discussed shortly. Note that in the "Turbulent/Front" case, the flow was transitional, not turbulent, so using r_{turb} in T_{aw} became an unwanted but necessary approximation. The results contained in Figures 7.100-7.111 matched the general trends discussed for Figure 7.99, but with greater clarity. Because MTV is conceptually straightforward, it was instructive to look at the raw images, then observe how the computer interpreted them in order to understand certain features; for example, the curling behavior of the velocity profiles near the wall most likely arose from ambiguity in the read images. ([7])

The Crocco-Busemann-derived temperature plots differed significantly from the PLIF results. For the laminar cases, the results were decent, albeit inconsistent, below $\sim$ 6mm; even the transitional ("Turbulent/Front") boundary layers had some agreement between the two techniques despite the use of r_{turb} in T_{aw}. This was no doubt helped by the decision to use $T_{w,PLIF}$ to anchor the Crocco-Busemann results. In the fully turbulent cases, the PLIF results more gradually approached T_w, almost with a laminar profile shape. The Crocco-Busemann results, however, under predicted these temperatures and recovered the bulk of the temperature below $\sim$ 2mm, where unfortunately the velocity data had the highest uncertainty. In general, the Crocco-Busemann profile matched the velocity data due to its explicit dependence on $\frac{u}{u_e}$. In the freestream, $T_{e,C-B} < T_{e,PLIF}$ owing to the different scaling used for the two techniques. This discrepancy led, at least in part, to the poor agreement elsewhere in the curve. The higher-than-expected value for $T_{e,PLIF}$ were discussed in Section 7.2.5.1. Because it is a function of $\sqrt{T}$ and scales between $0-6$ instead of $360-60$K, the Mach number appeared somewhat insulated from the discrepancies in the temperature profiles. In the "Front" test locations, the profiles from at least one of the laser lines fell within the uncertainties of the PLIF and Crocco-Busemann techniques typically up to $\sim$ 5mm, and for the "Back" locations this agreement could extend up to $\sim$ 10mm. In the freestream, however, the significantly higher $T_{e,PLIF}$ drove the Mach number down to $M \approx 4.5$. The error did not stem from a lower-than-expected u_e, as in most cases u_e fell only $1-3\%$ lower than the ideal 857.6m/s, and they did reach this value including their uncertainty. Before calling M_{C-B} a resounding success, one must remember T_e was set using the theoretical result, so any agreement it had in the freestream was

more a testament to the velocity data than the temperature results. Further discussion and validation of these data and theories using the Pitot probe's results is included in Section 7.2.6. As a final note, in some figures (ex.- Figure 7.106(f), Run 4652), the Mach number grew erroneously high before curling back to the expected edge value. This stems back to the specific shape of the velocity profile. For whatever reason (freestream shocks, wide beams, *etc.*) the velocity profile decayed in the freestream, meaning $u_{max} \neq u_e$. However, Crocco-Busemann forces the temperature to T_e at the edge of the boundary layer, and derives temperature profile's shape entirely from the velocity profile. So, $\frac{u}{u_e} > 1$ yielded $T < T_e$, a nonphysical result within the current context. For the present example, this produced $T_{min} \approx \frac{1}{2}T_e$, which, despite the $\sqrt{T}$ dependency, had a large effect on the Mach number. Thus the Mach number axes were not extended above $M = 6$ because anything above this threshold far exceeded even the nozzle's maximum Mach number and was therefore considered erroneous. ([7])

Inner variable plots were generated using T_{PLIF} for the tripped cases. The viscosity was calculated from the temperature by blending Keyes' and Sutherland's Laws in the cold and hot regions, respectively. Following the procedure outlined in 7.2.3.5, the τ_w was estimated using Clauser's chart method [40]. The results are shown in Figures 7.112 and 7.113 alongside the theoretical Law of the Wall ($u^+_{eq} = y^+$) and log layer ($u^+_{eq} = \frac{1}{\kappa}\ln y^+ + C$ with $\kappa = 0.41$ and $C = 4.9$, following [40, 50]) plots. The uncertainty in y^+ was too small to be shown clearly on the logarithmic axis. These plots follow the trends observed in Section 7.2.3.5. In the upstream location the data did not follow the expected trends because the flow was likely to be transitional, not fully turbulent; τ_w should not be trusted in this region. However, by the downstream location, it was known the boundary layer was more fully developed and turbulent. The difference between the results calculated from the PLIF and Crocco-Busemann data were generally only present in the outer layer, which was of little consequence to the region of interest. For the wake case, the results tended to show the sensitivity of u^+_{eq} to the realities of near wall measurements. The near wall results matched those observed with the Pitot probe, and indeed were superior in the case of Figure 7.112(d), giving the impression the error in Figure 7.112(c) was largely due to a poor run; note the spread in the data in Figure 7.99(c). The downstream plots in Figure 7.113, however, were excellent and strongly correlated with the theory within the bounds shown. The deviation in the linear sublayer was likely due to the large uncertainty in the velocity data ($y^+ \approx 10 \implies y < 1$mm). Due to the spanwise homogeneity by this point on the test article, it was safe to assume these plots were representative of the true condition of the boundary layer. Note that in both cases, τ_w the results predicted by both the boundary layer solver and Pitot probe, and the same concerns about the veracity of Clauser's method remained (see Section 7.2.3.5). ([7]

7.2.5.4 Spanwise Velocimetry

The spanwise velocimetry test matrix is provided in Table 7.31. Because the focus of this campaign was to confirm there were no spanwise gradients across the plate and to study the isotropy of the turbulence, only a small number of runs were conducted. None of these runs used the plasma. ([7])

The data are shown in Figure 7.114. Of the four runs, only the turbulent ones yielded reliable results. The laminar runs tended to have regular changes in the velocity across the plate. The test

No.	Location	Trips	Run/Date
1	Forward	Laminar	4697, 4/8/2021
2	Forward	Turbulent	4695, 4/7/2021
3	Back	Laminar	4698, 4/9/2021
4	Back	Turbulent	4699, 4/9/2021

Table 7.31: PLIF spanwise velocimetry test matrix.

article and tunnel shifting upon startup offered an explanation for this result. During setup, care was taken to unsure the "Write" beam and "Read" sheet were at a constant height above the plate. It was known, however, that the tunnel shifted when the flow was turned on, ruining this precise alignment. It is for this reason that during other off-body campaigns (Pitot pressure, schlieren imaging, boundary layer MTV) the wall needed to be identified for each image, but here this was impossible. Due to the thin nature of the laminar boundary layers, the velocimetry would be highly susceptible to any plate roll. Because they were thicker, measured higher off the surface, and had less of a velocity gradient in the outer layer, the turbulent profiles would be more insulated for such discrepancies; this challenge did remain, however, as a source of systematic error. What can at least be said about the laminar data is that the velocity did drop considerably between the upstream and downstream test locations, and that the fluctuations were consistently below those of the turbulent runs. The turbulent runs yielded exciting results, especially Figure 7.114(e). One could see the dramatic reduction in velocity as one moved into a wake. The regular spacing of these wakes matched the 6.84mm spacing of the trips. Furthermore, at the edges of each wake, where the corner vortices were present, there was a distinct spike in the velocity fluctuation on top of the already enhanced fluctuations in the wake itself. This represented direct evidence of not only the presence of the vortices, but their role in fomenting turbulence. By the downstream location described in Figure 7.114(f), the velocity dropped as the boundary layer thickened and both the velocity and fluctuation profiles homogenized. One could argue modest, regular fluctuations did indeed persist in the data, and this was observed in other data such as IR thermography (see Section 7.2.3.3), but it was reasonable to assume many techniques would be unable to resolve such weak and broad features. Oversaturated instantaneous "Read" images are included in Figures 7.114(a) and (b) to show the breakdown of these vortical structures just upstream of each of the true lines. Enough naturally occurring $NO^{v=1}$ was detectable via the "Read" beam to show that in the upstream location there were orderly vortical structures, but they decayed by the downstream location; the contrast was adjusted such that these features were visible even though doing so saturated the "Write" line data. That the signal was brightest in the wakes follows from their velocity defecit as compared to the troughs. Lower velocity means higher pressure, and therefore greater NO density and signal. This effect seemed most pronounced in the trips' vortices. ([7])

In order to better illustrate the behavior of the trips, spanwise visualization images were taken as part of the NO characterization study discussed Section 4.2.3. The beams were 3 and 5mm above the plate in the upstream and downstream locations, respectively. Both beams were angled 2.75mm to match the plate's tilt, but the cameras were not for simplicity. One can see the ordered, vortical

structures in the upstream image, and the chaotic, fully developed turbulence in the downstream image. The streaks in the images may have been due to NO clustering through the aerogrids, but more likely arose from the trips. Interestingly, the vortices seemed to be spreading at 130mm, which was observed in the oil flow results. The bias of the gas towards one side of the image may have been due to injector misalignment, and the streamwise variation of the image may have been due to plate pitch with respect to the beam. In general, the plate and tunnel tended to shift down during a test. If they pitched down as well, then in the upstream image the data is likely to be above the boundary layer until it grew large enough to reach the beam at $\sim$ 130mm; at 3mm, even under ideal conditions the beam would have been in the outer edge of the boundary layer and was taller than the trips. In the downstream image, meanwhile, a negative pitch would mean the laminar sublayer was observed past $\sim$ 445mm; this was a more likely explanation than the beam exiting the boundary layer, as the tunnel did not shift down $\mathscr{O}(1\text{cm})$, only $\mathscr{O}(1\text{mm})$. ([7])

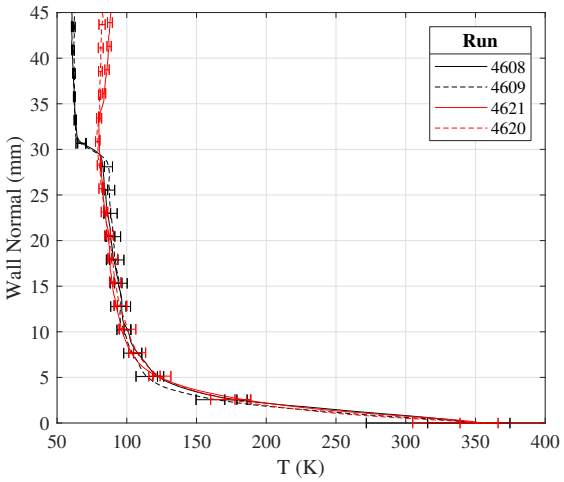

(a) Laminar, temperature

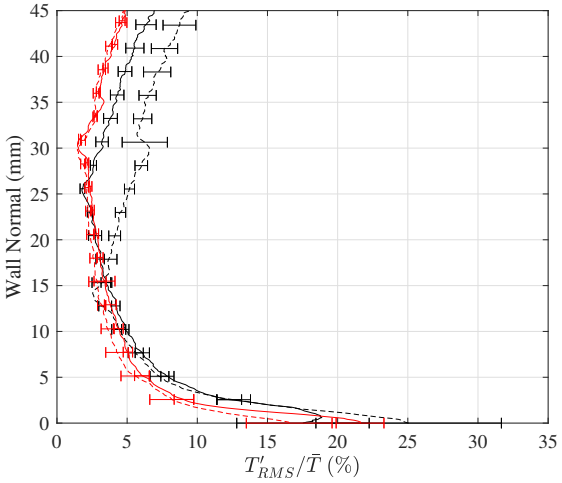

(b) Laminar, fluctuation

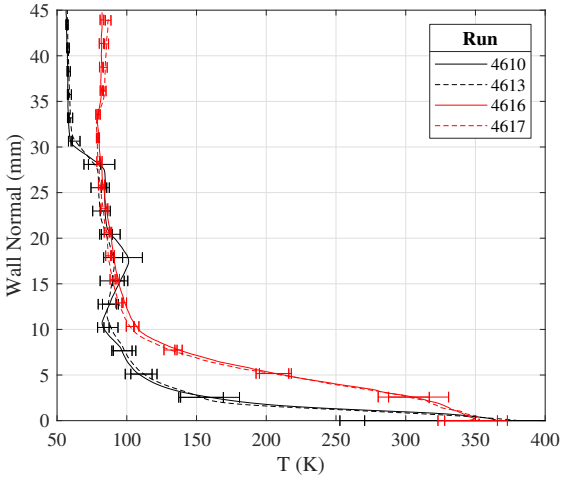

(c) Turbulent wake, temperature

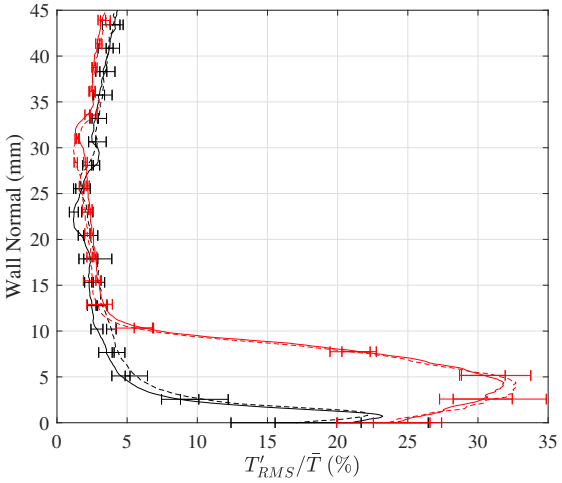

(d) Turbulent wake, fluctuation

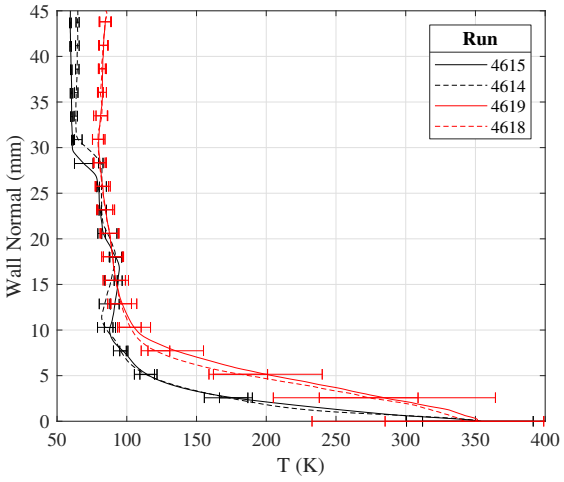

(e) Turbulent trough, temperature

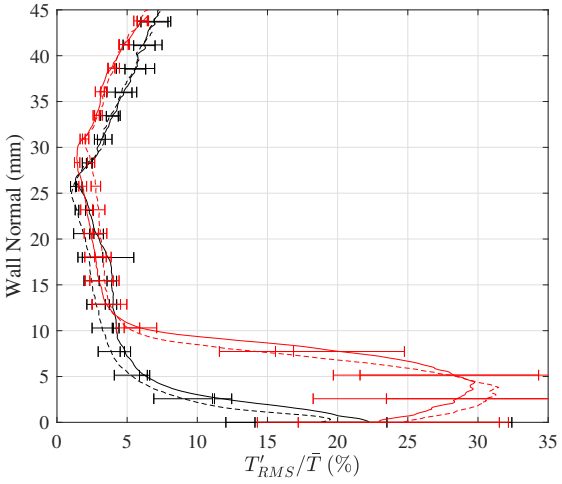

(f) Turbulent trough, fluctuation

Figure 7.70: PLIF rotational thermometry: temperature and fluctuation profile comparison; error bars were set from the corresponding mean temperature and fluctuation images. Same legend applies to all figures in a row. [7]

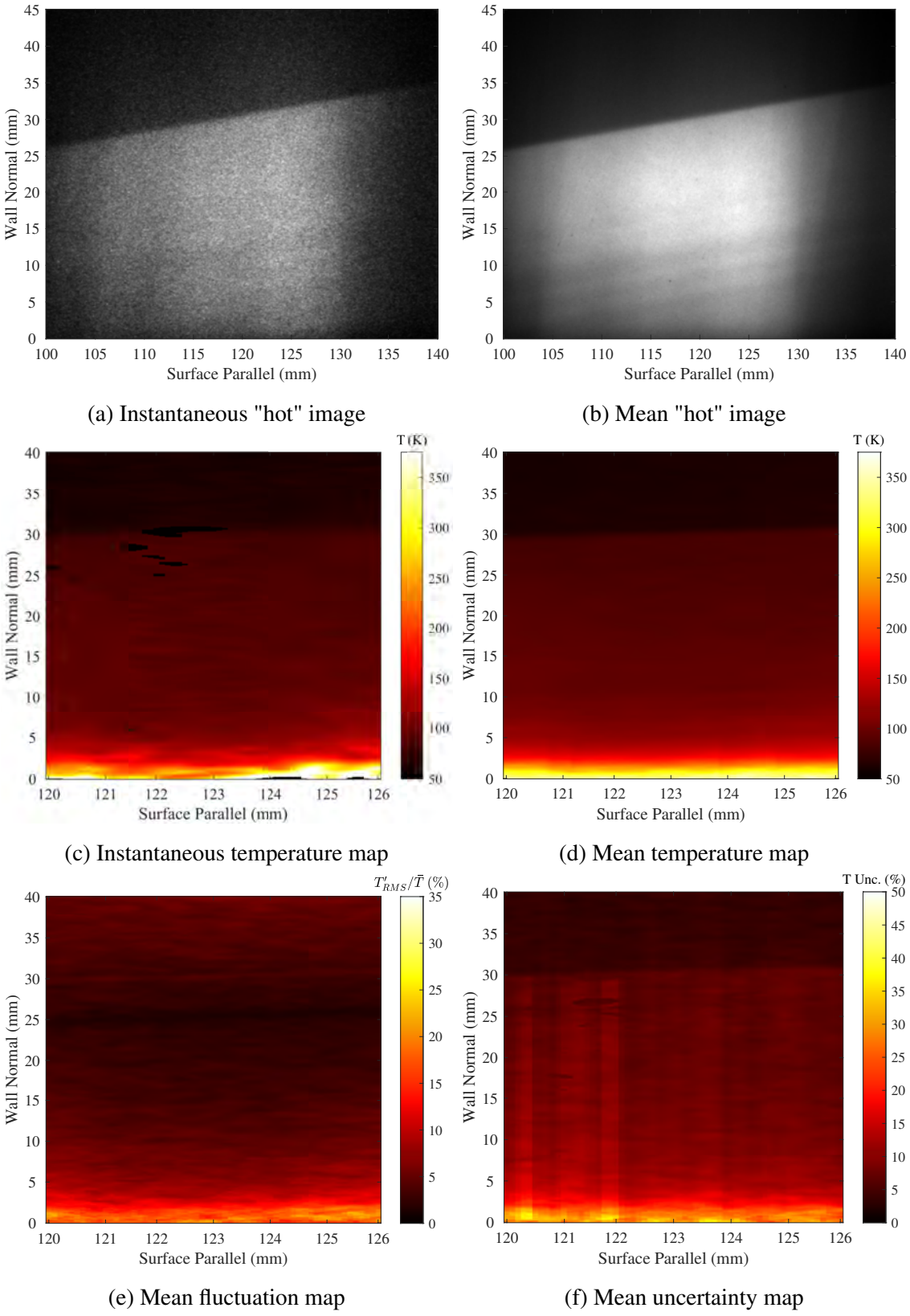

(a) Instantaneous "hot" image

(b) Mean "hot" image

(c) Instantaneous temperature map

(d) Mean temperature map

(e) Mean fluctuation map

(f) Mean uncertainty map

Figure 7.71: PLIF rotational thermometry, Run 4608: upstream; laminar; plasma off. [7]

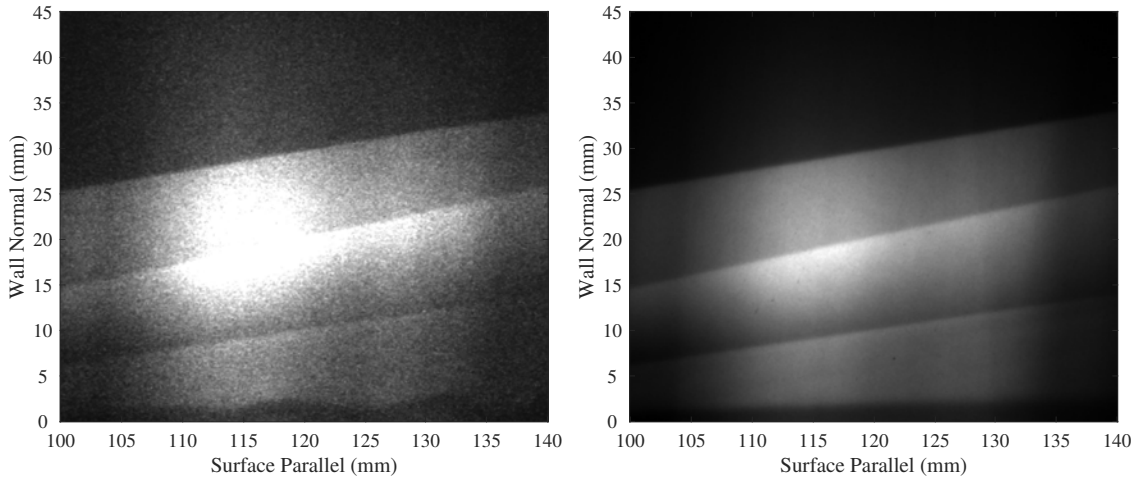

(a) Instantaneous "hot" image

(b) Mean "hot" image

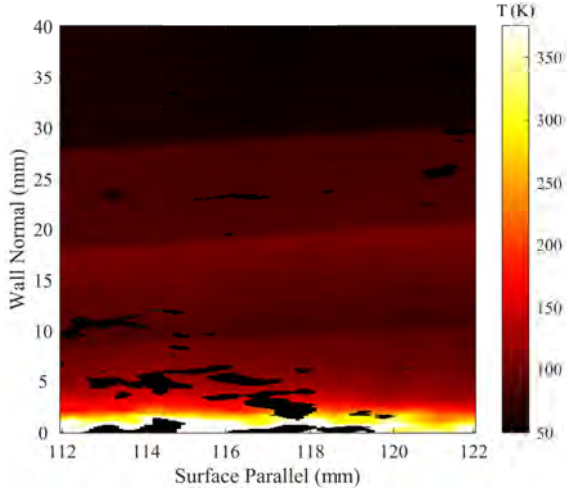

(c) Instantaneous temperature map

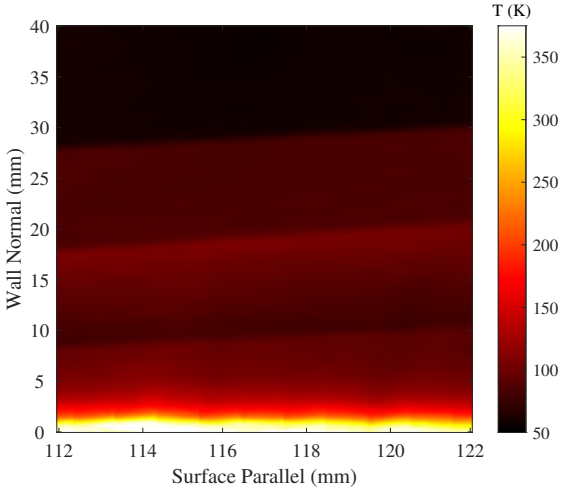

(d) Mean temperature map

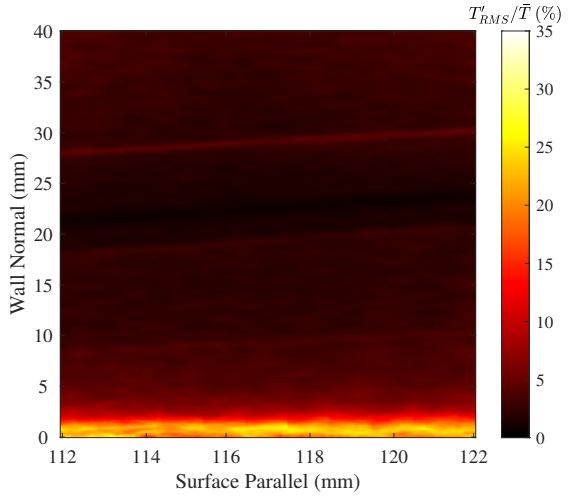

(e) Mean fluctuation map

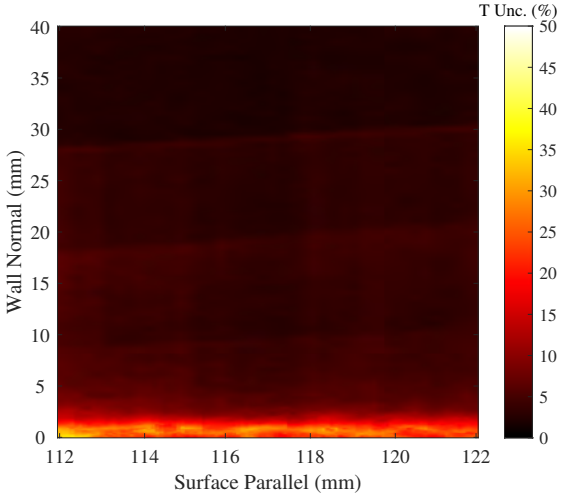

(f) Mean uncertainty map

Figure 7.72: PLIF rotational thermometry, Run 4610: upstream; turbulent wake; plasma off. [7]

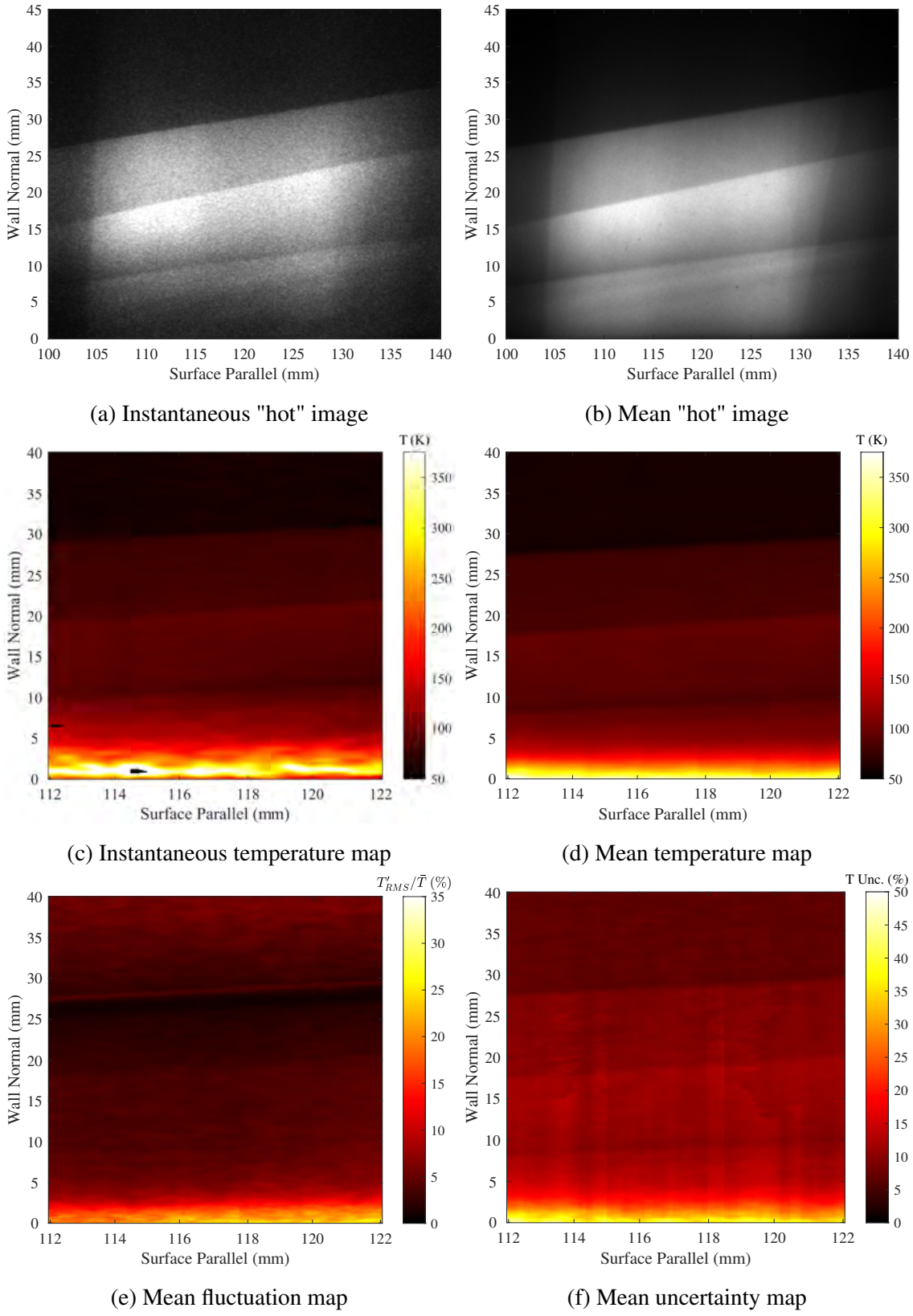

(a) Instantaneous "hot" image

(b) Mean "hot" image

(c) Instantaneous temperature map

(d) Mean temperature map

(e) Mean fluctuation map

(f) Mean uncertainty map

Figure 7.73: PLIF rotational thermometry, Run 4615: upstream; turbulent trough; plasma off. [7]

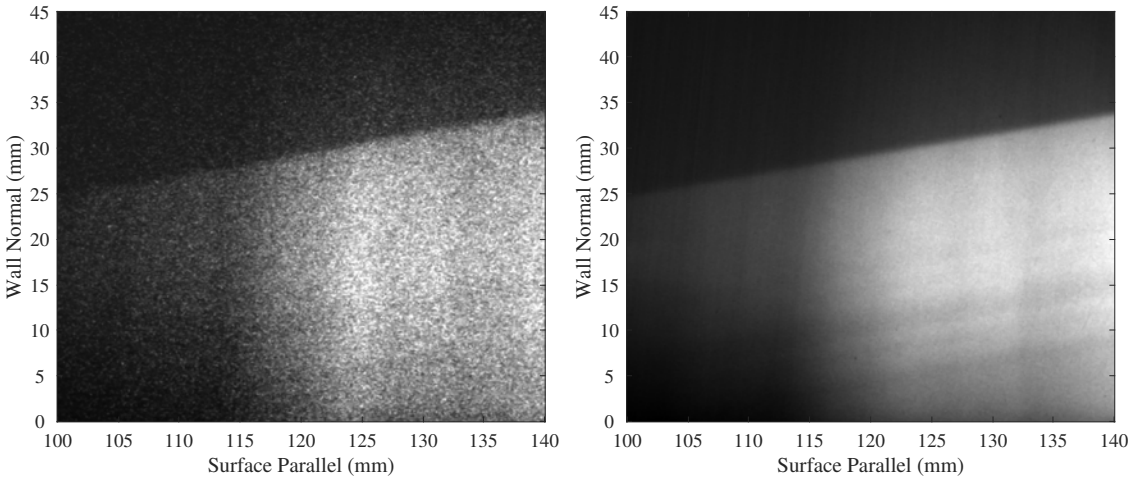

(a) Instantaneous "hot" image

(b) Mean "hot" image

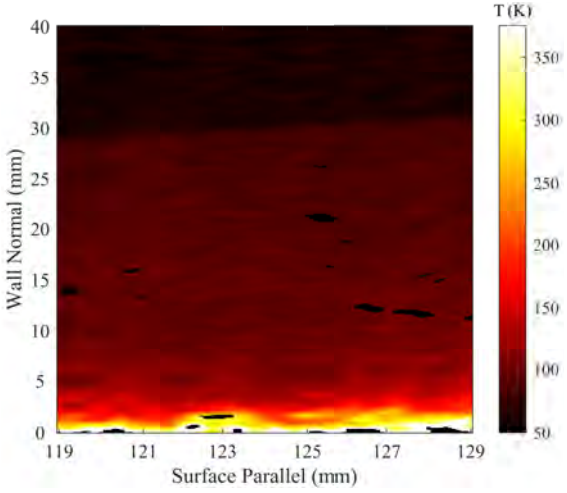

(c) Instantaneous temperature map

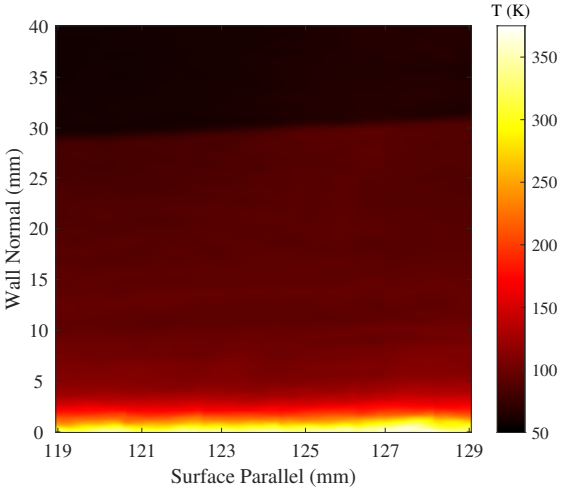

(d) Mean temperature map

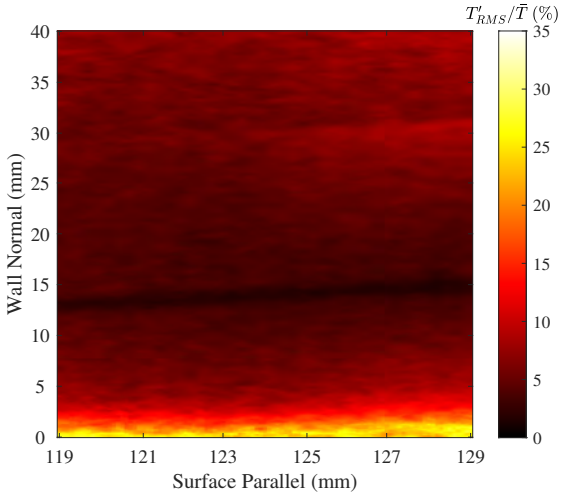

(e) Mean fluctuation map

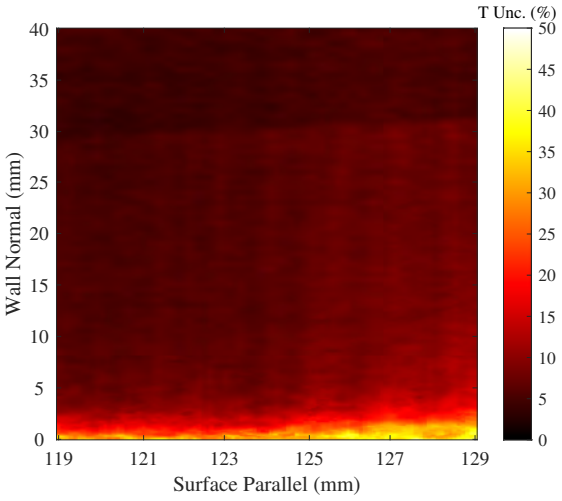

(f) Mean uncertainty map

Figure 7.74: PLIF rotational thermometry, Run 4609: upstream; laminar; plasma on. [7]

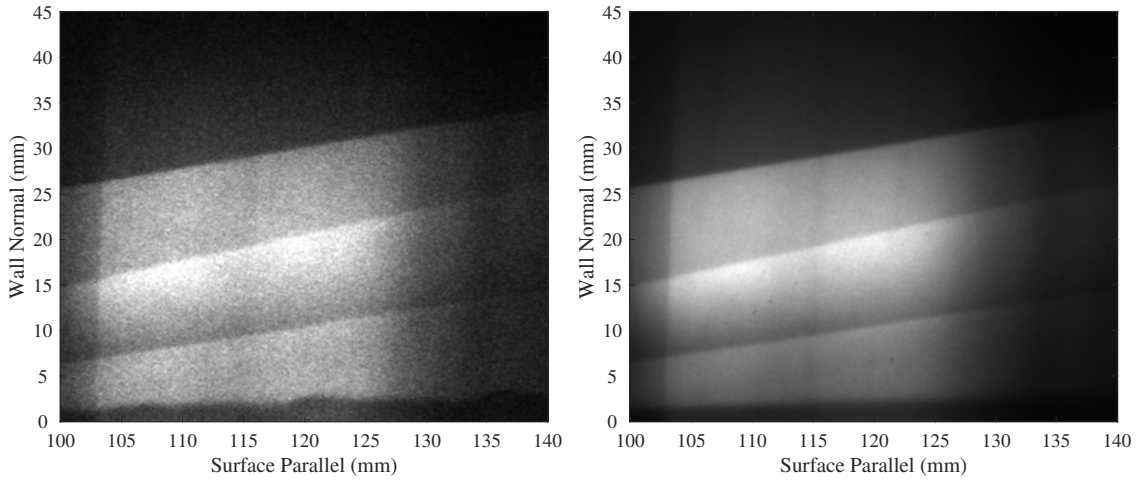

(a) Instantaneous "hot" image

(b) Mean "hot" image

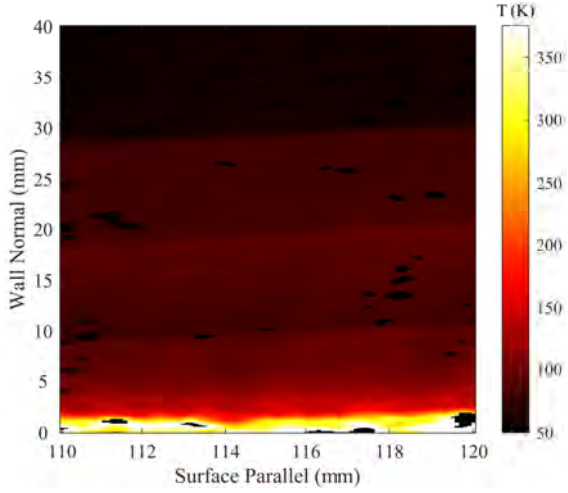

(c) Instantaneous temperature map

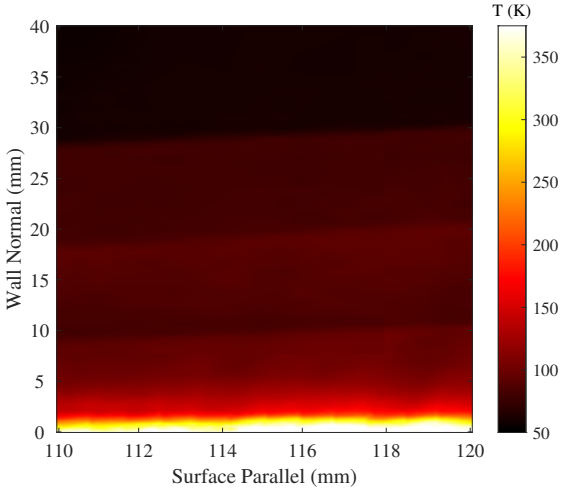

(d) Mean temperature map

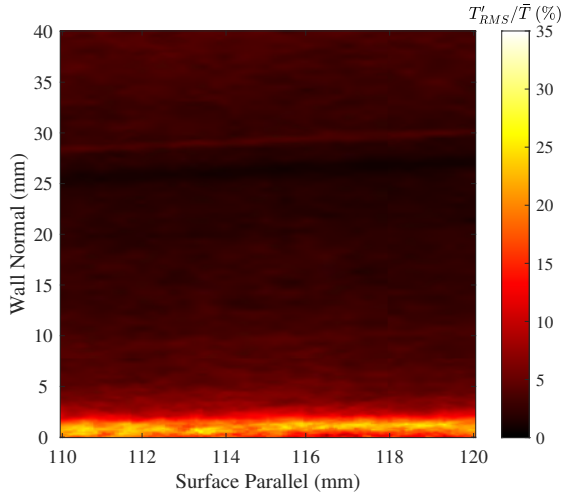

(e) Mean fluctuation map

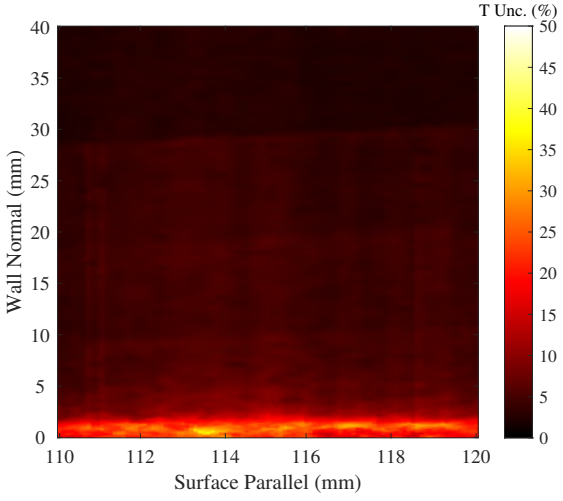

(f) Mean uncertainty map

Figure 7.75: PLIF rotational thermometry, Run 4613: upstream; turbulent wake; plasma on. [7]

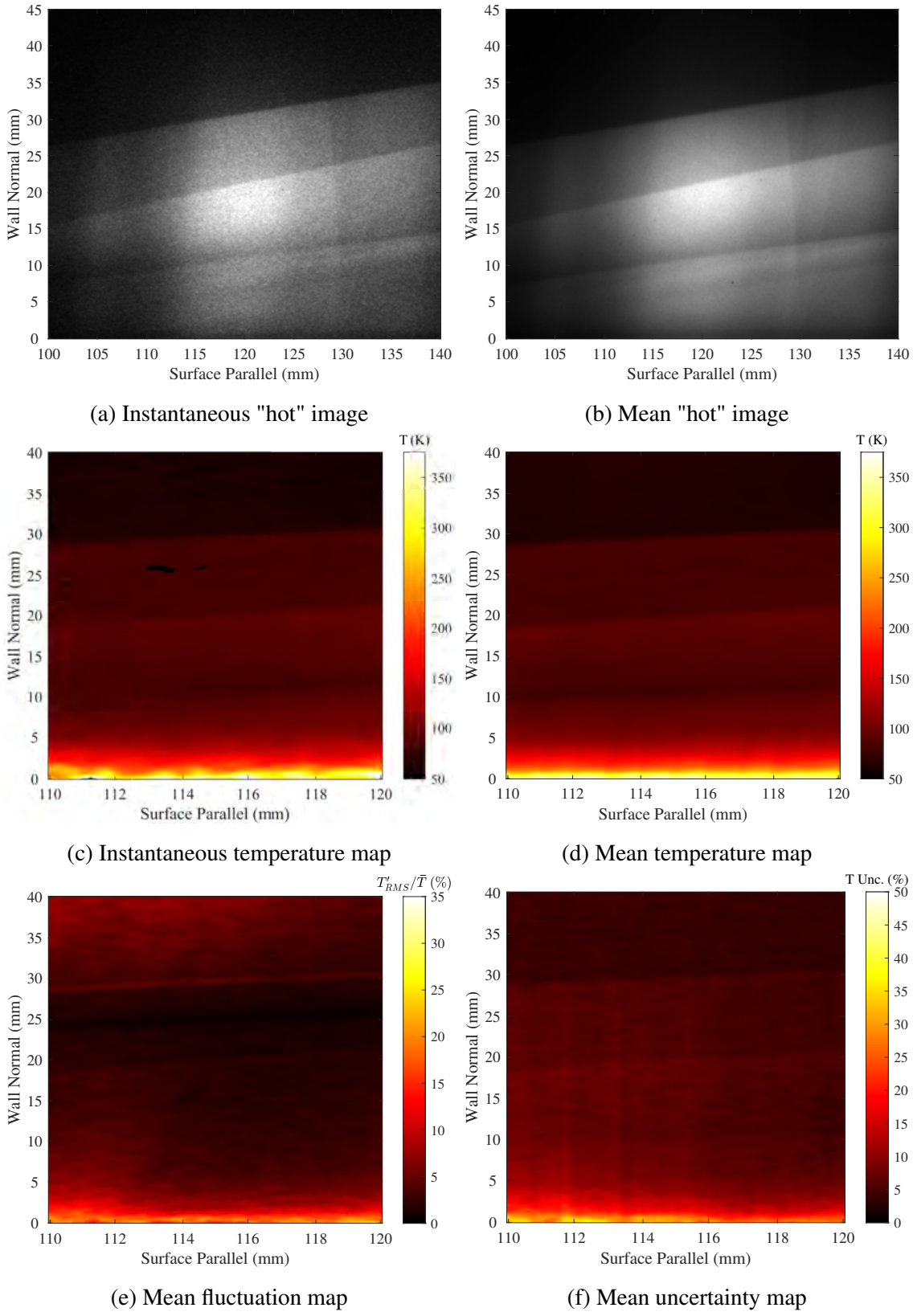

(a) Instantaneous "hot" image

(b) Mean "hot" image

(c) Instantaneous temperature map

(d) Mean temperature map

(e) Mean fluctuation map

(f) Mean uncertainty map

Figure 7.76: PLIF rotational thermometry, Run 4614: upstream; turbulent trough; plasma on. [7]

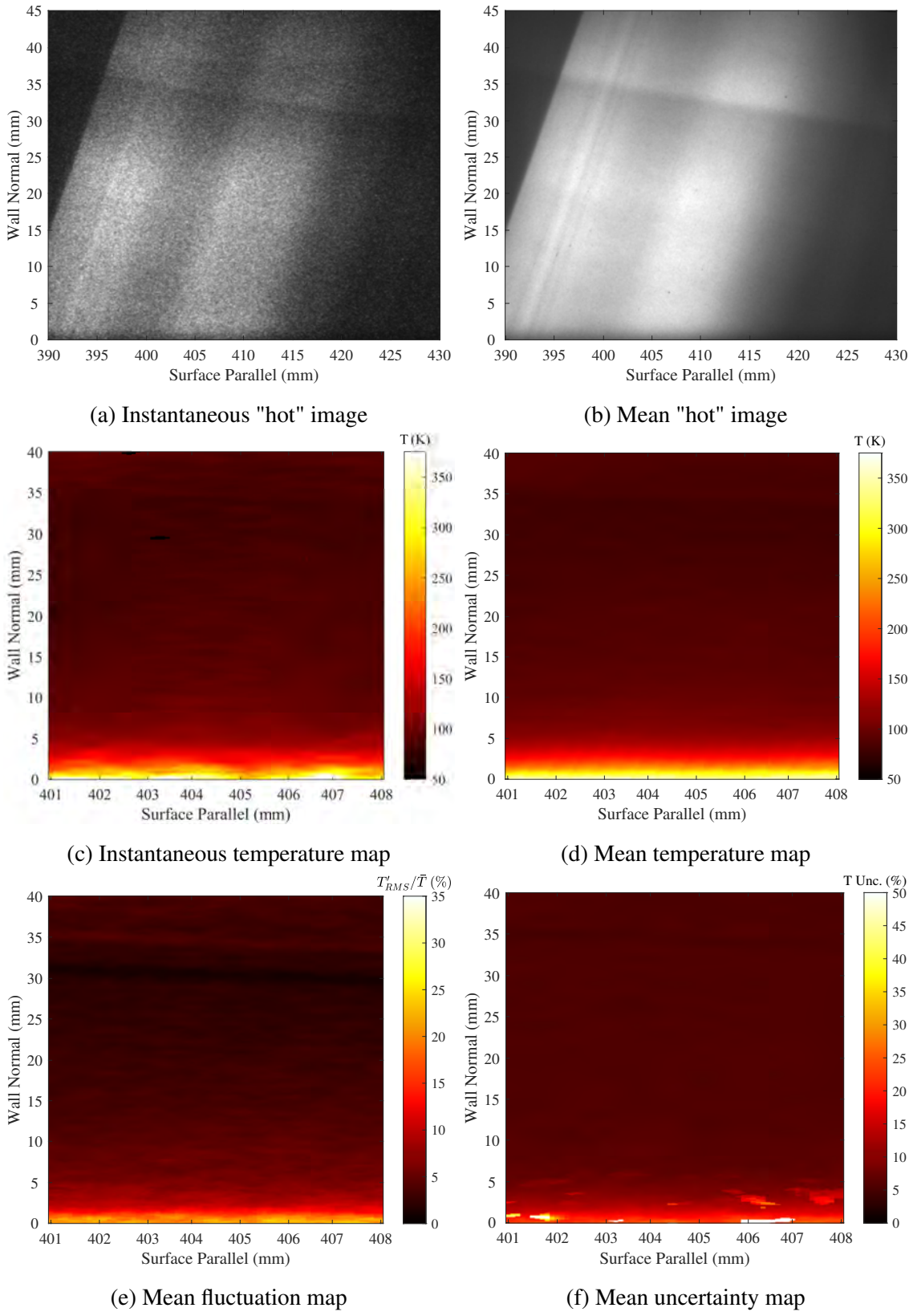

(a) Instantaneous "hot" image

(b) Mean "hot" image

(c) Instantaneous temperature map

(d) Mean temperature map

(e) Mean fluctuation map

(f) Mean uncertainty map

Figure 7.77: PLIF rotational thermometry, Run 4621: downstream; laminar; plasma off. [7]

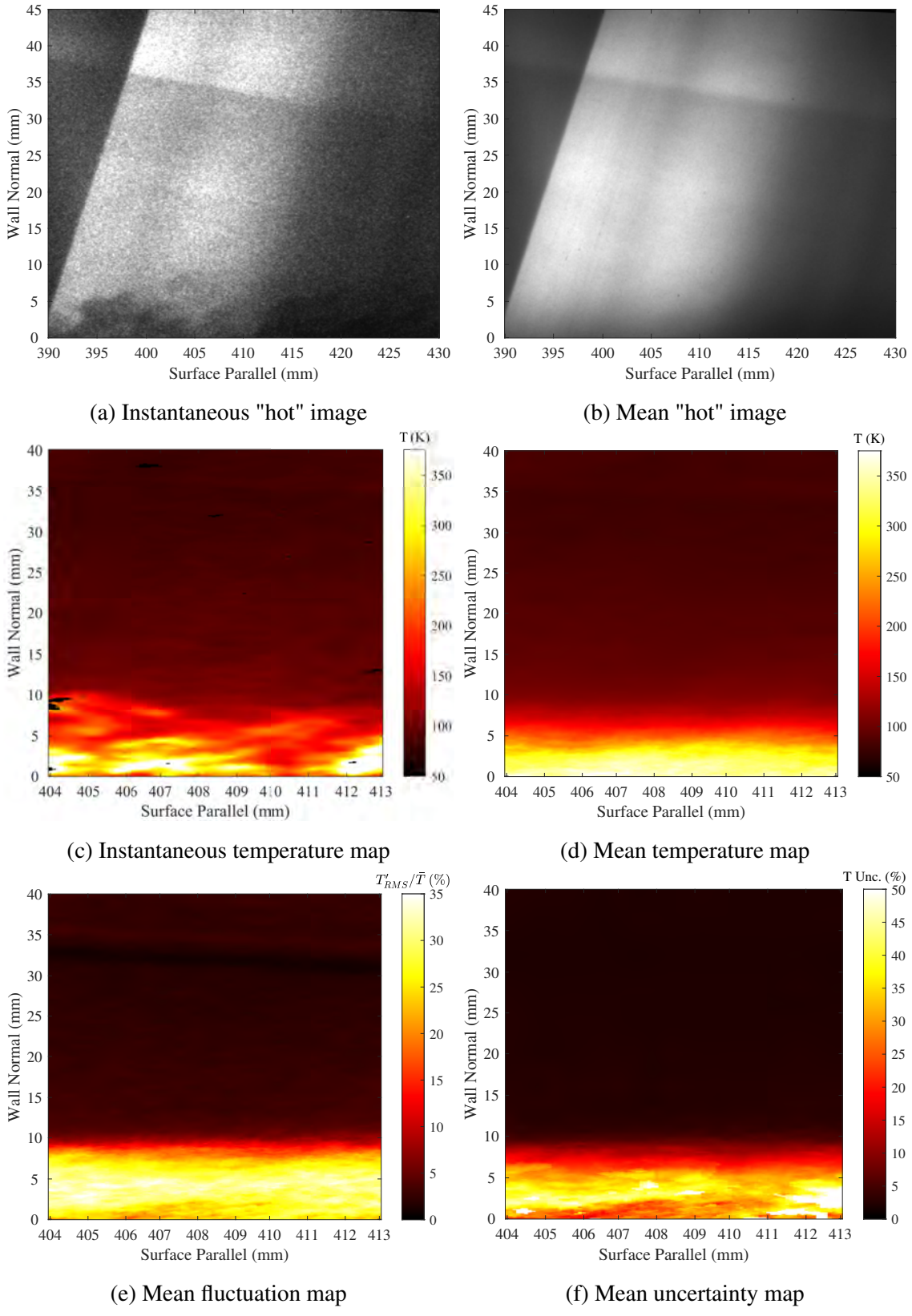

(a) Instantaneous "hot" image

(b) Mean "hot" image

(c) Instantaneous temperature map

(d) Mean temperature map

(e) Mean fluctuation map

(f) Mean uncertainty map

Figure 7.78: PLIF rotational thermometry, Run 4616: downstream; turbulent wake; plasma off. [7]

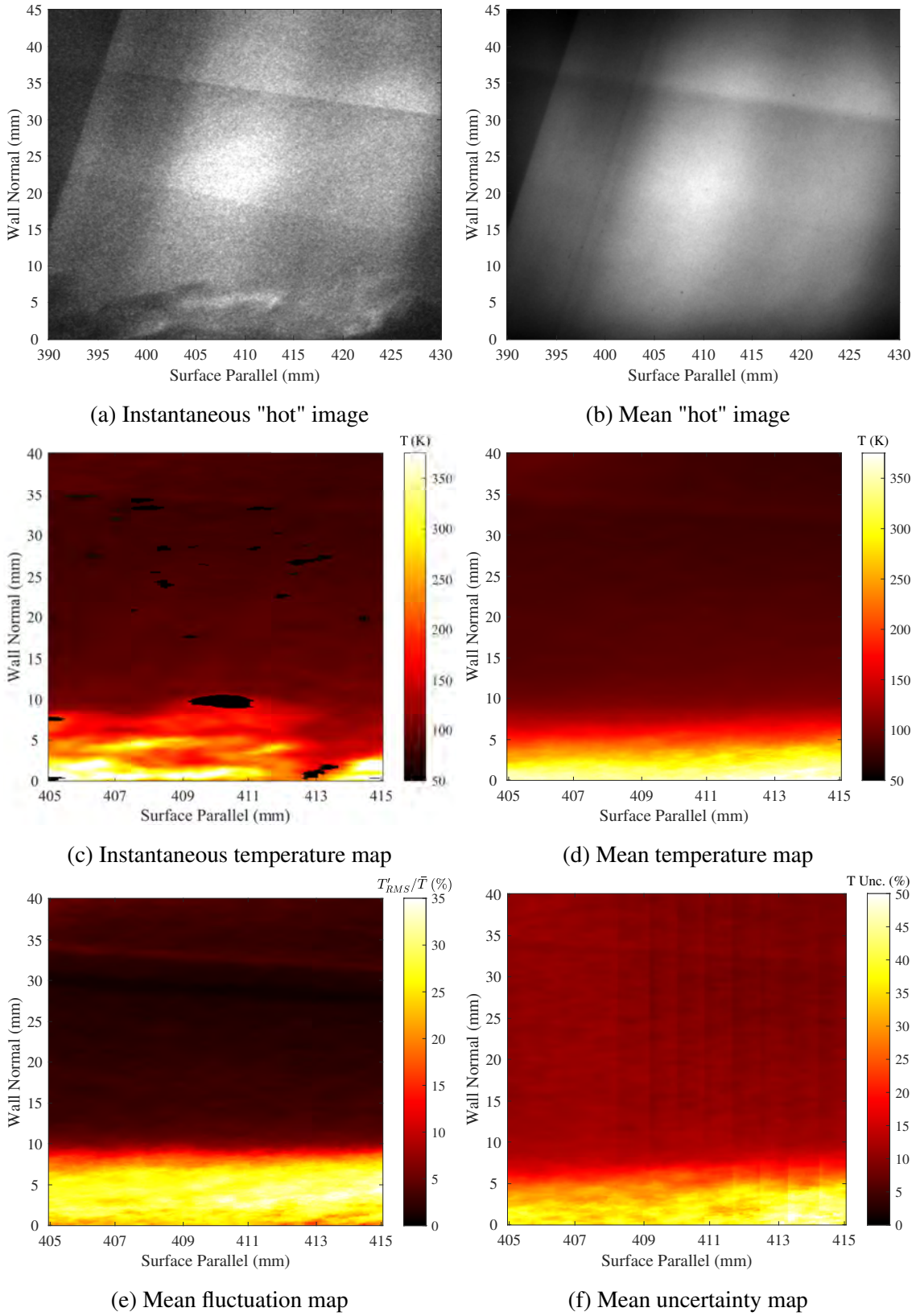

(a) Instantaneous "hot" image

(b) Mean "hot" image

(c) Instantaneous temperature map

(d) Mean temperature map

(e) Mean fluctuation map

(f) Mean uncertainty map

Figure 7.79: PLIF rotational thermometry, Run 4619: downstream; turbulent trough; plasma off. [7]

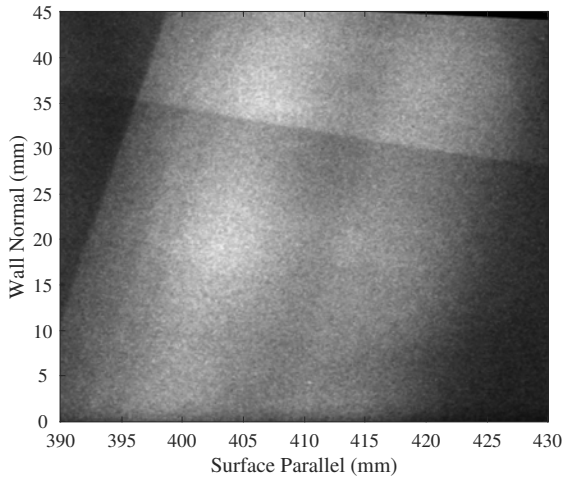

(a) Instantaneous "hot" image

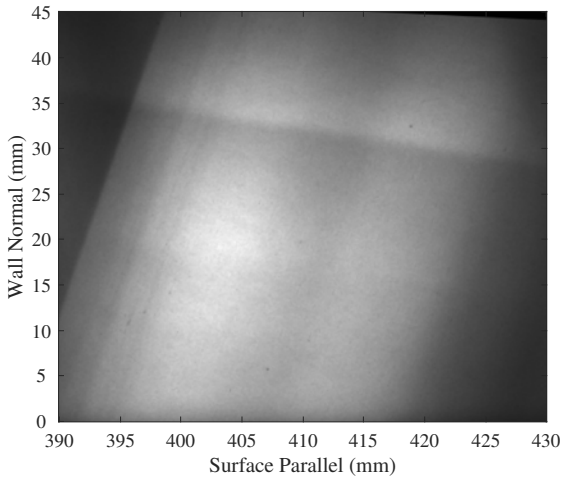

(b) Mean "hot" image

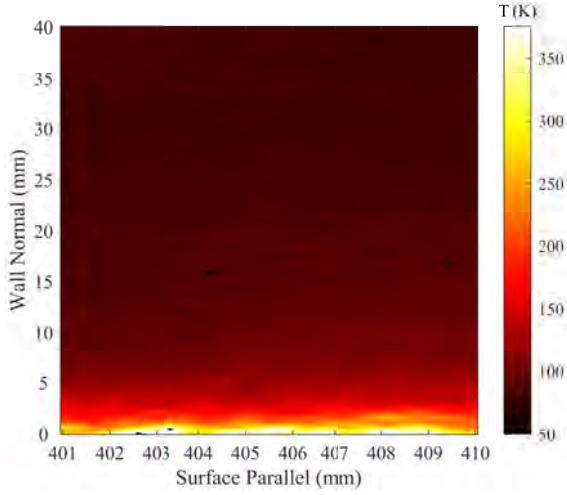

(c) Instantaneous temperature map

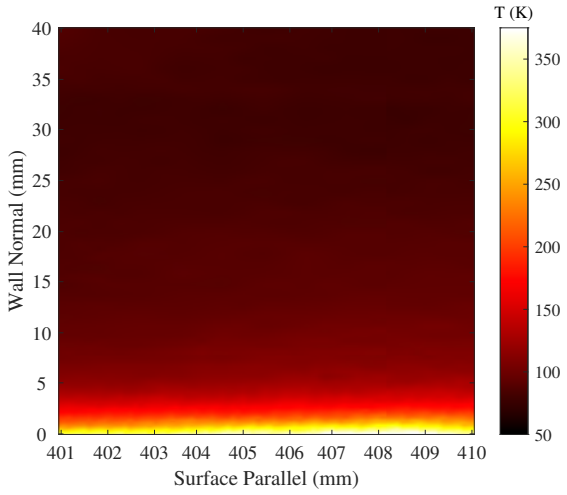

(d) Mean temperature map

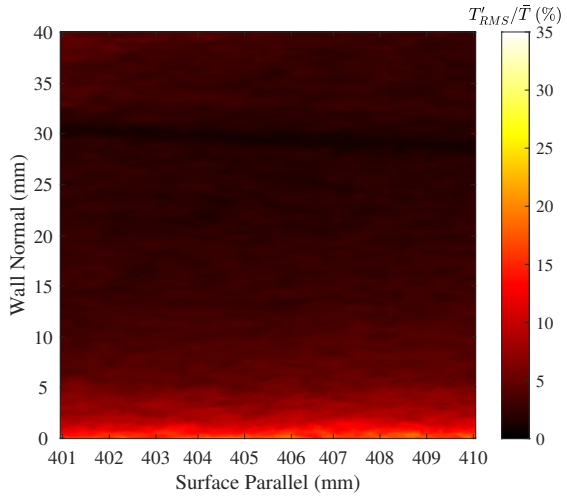

(e) Mean fluctuation map

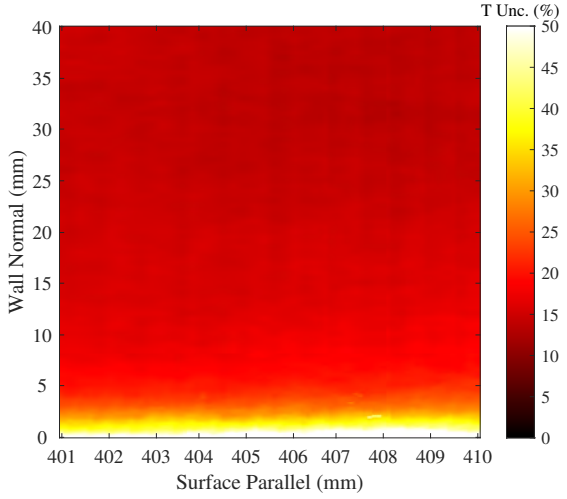

(f) Mean uncertainty map

Figure 7.80: PLIF rotational thermometry, Run 4620: downstream; laminar; plasma on. [7]

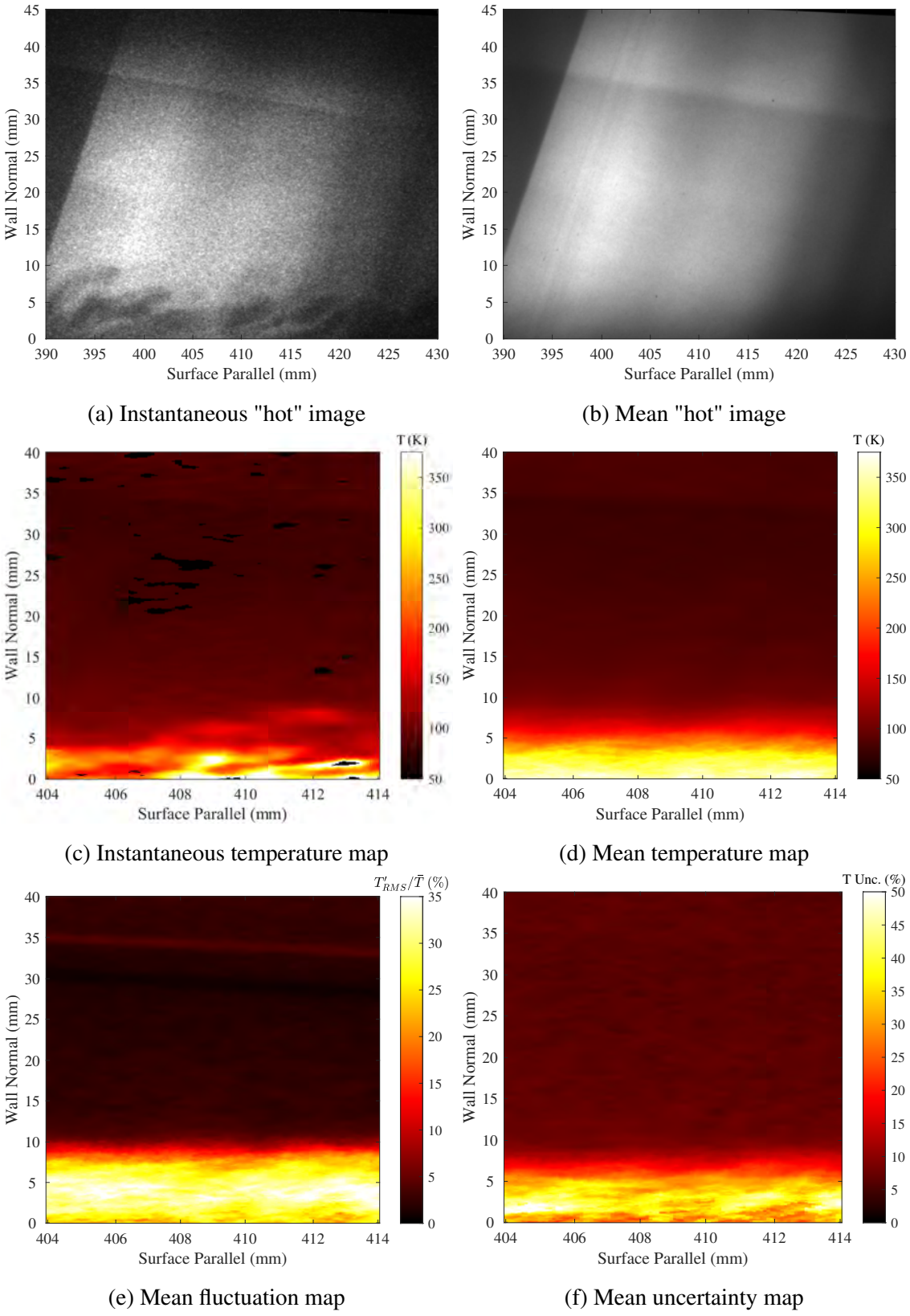

(a) Instantaneous "hot" image

(b) Mean "hot" image

(c) Instantaneous temperature map

(d) Mean temperature map

(e) Mean fluctuation map

(f) Mean uncertainty map

Figure 7.81: PLIF rotational thermometry, Run 4617: downstream; turbulent wake; plasma on. [7]

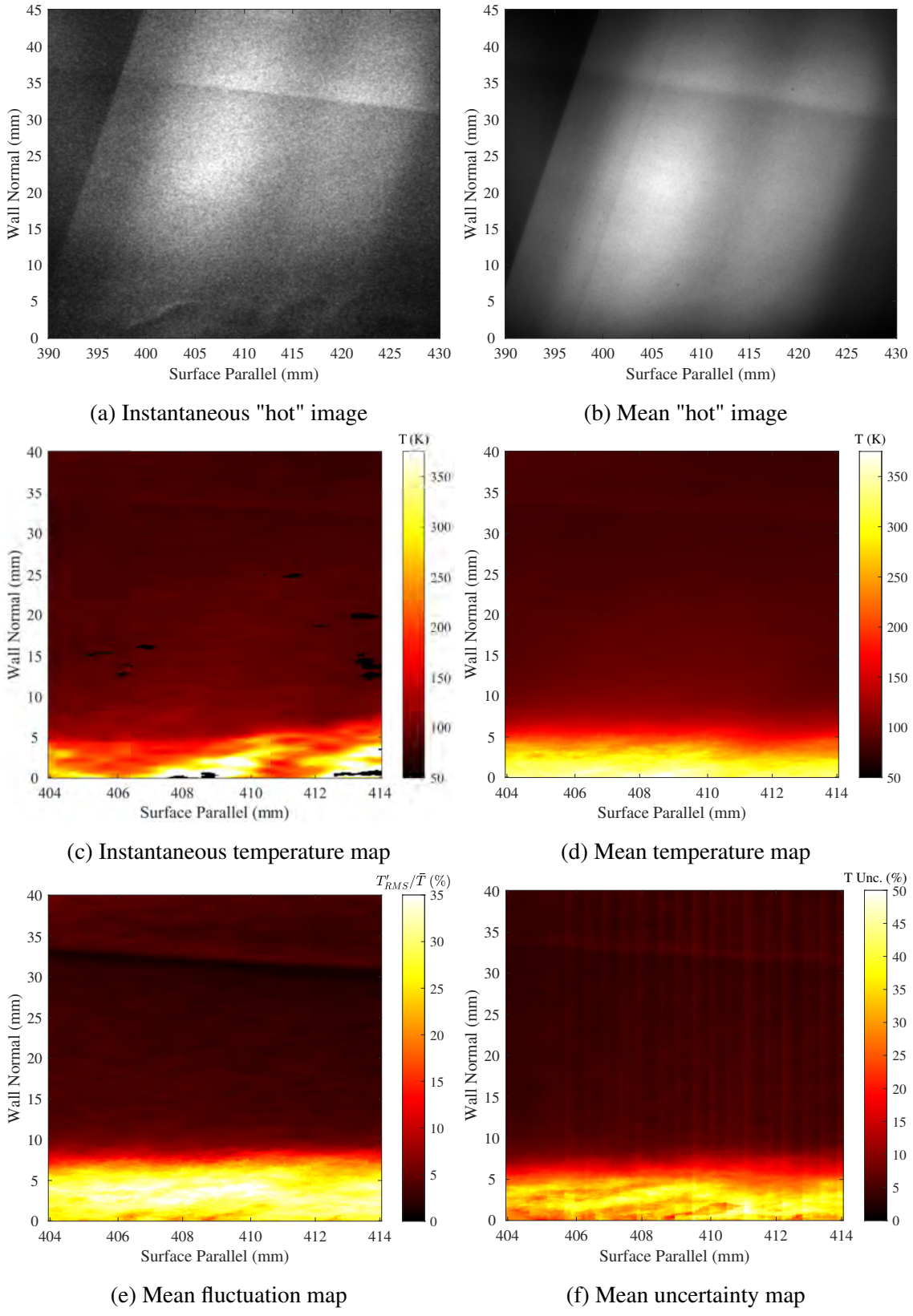

(a) Instantaneous "hot" image

(b) Mean "hot" image

(c) Instantaneous temperature map

(d) Mean temperature map

(e) Mean fluctuation map

(f) Mean uncertainty map

Figure 7.82: PLIF rotational thermometry, Run 4618: downstream; turbulent trough; plasma on. [7]

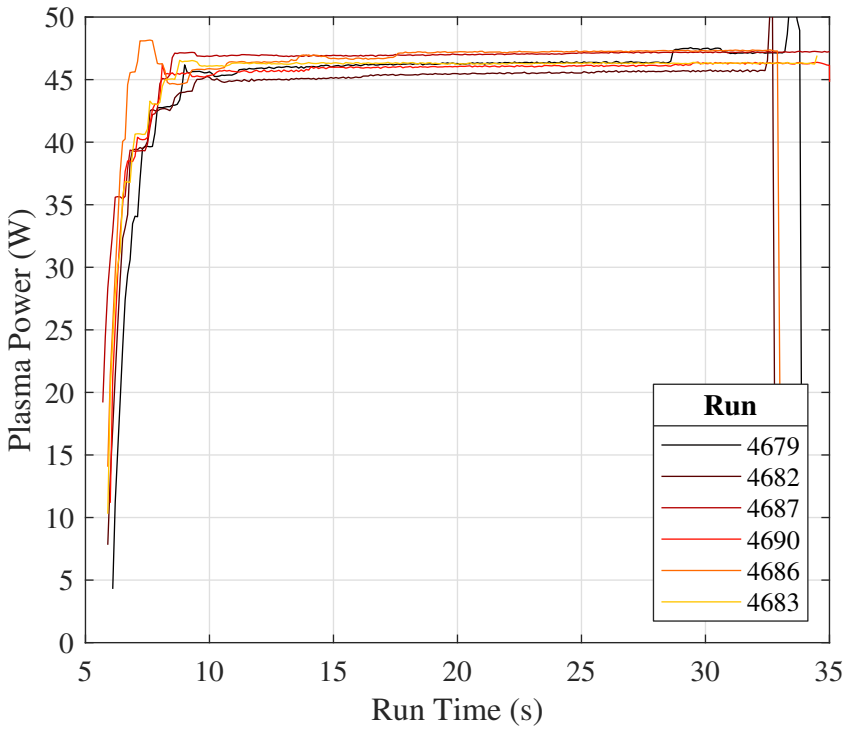

Figure 7.83: Plasma power traces for PLIF vibrational thermometry runs.

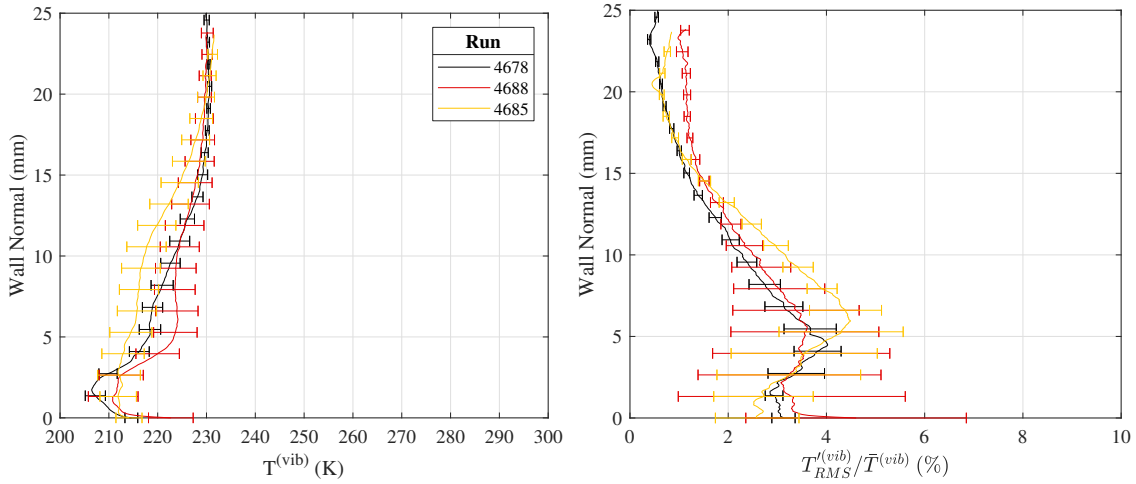

(a) Plasma off, temperature

(b) Plasma off, fluctuation

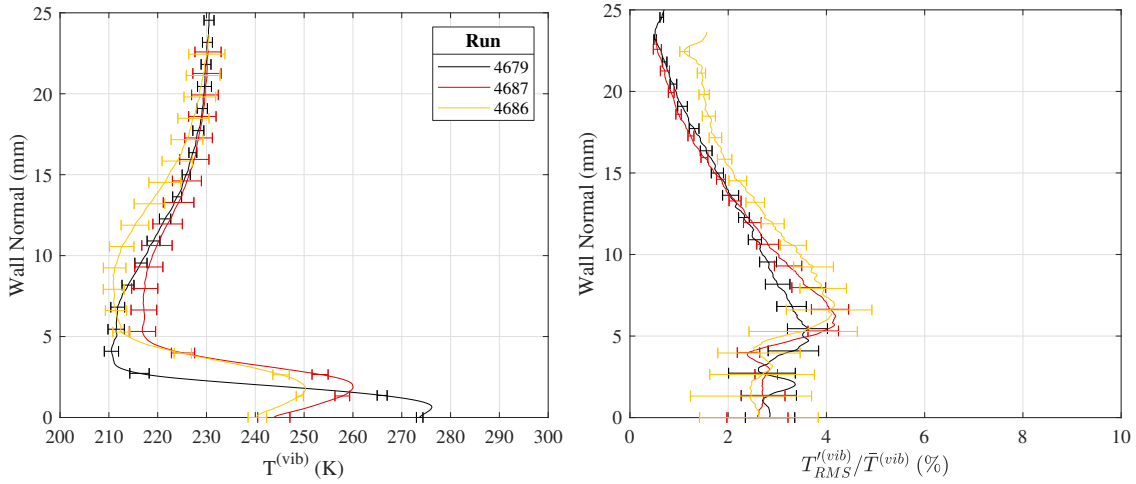

(c) Plasma on, temperature

(d) Plasma on, fluctuation

Figure 7.84: PLIF vibrational thermometry, laminar temperature profile comparison assuming $T^{v}_{e,NO} = 230K$; error bars were set from the corresponding mean temperature and fluctuation images. Same legend applies to all figures in a row. [7]

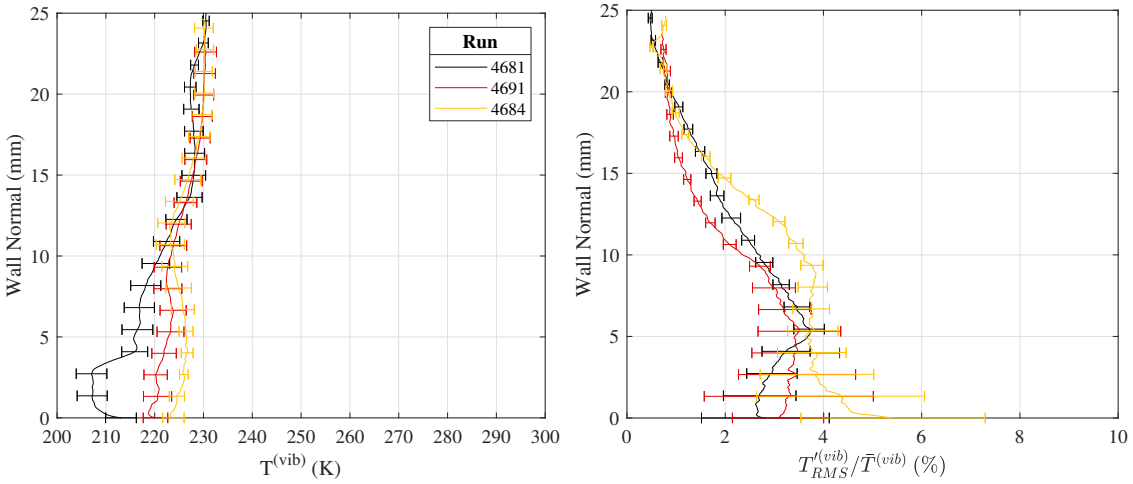

(a) Plasma off, temperature

(b) Plasma off, fluctuation

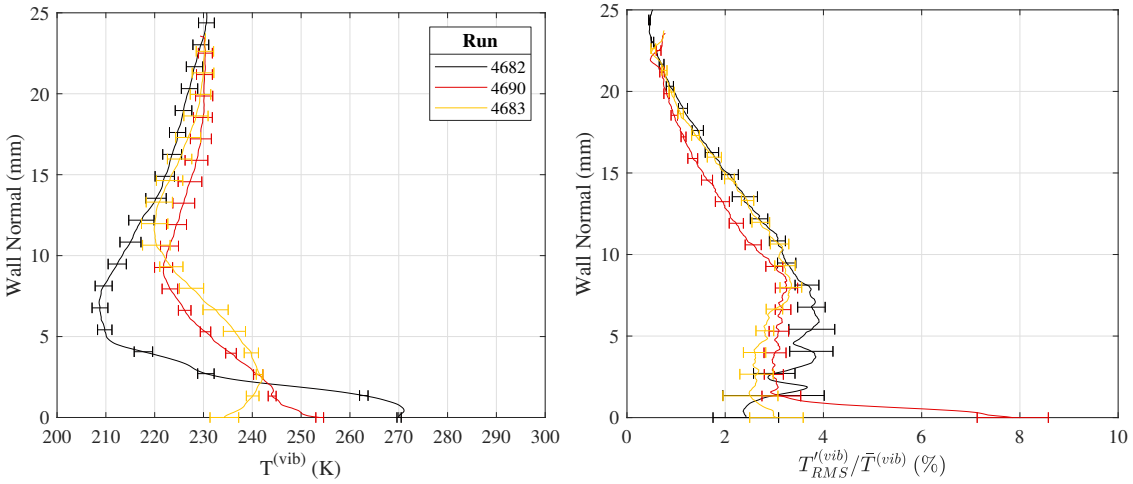

(c) Plasma on, temperature

(d) Plasma on, fluctuation

Figure 7.85: PLIF vibrational thermometry, turbulent temperature profile comparison assuming $T^{v}_{e,NO} = 230K$; error bars were set from the corresponding mean temperature and fluctuation images. Same legend applies to all figures in a row. [7]

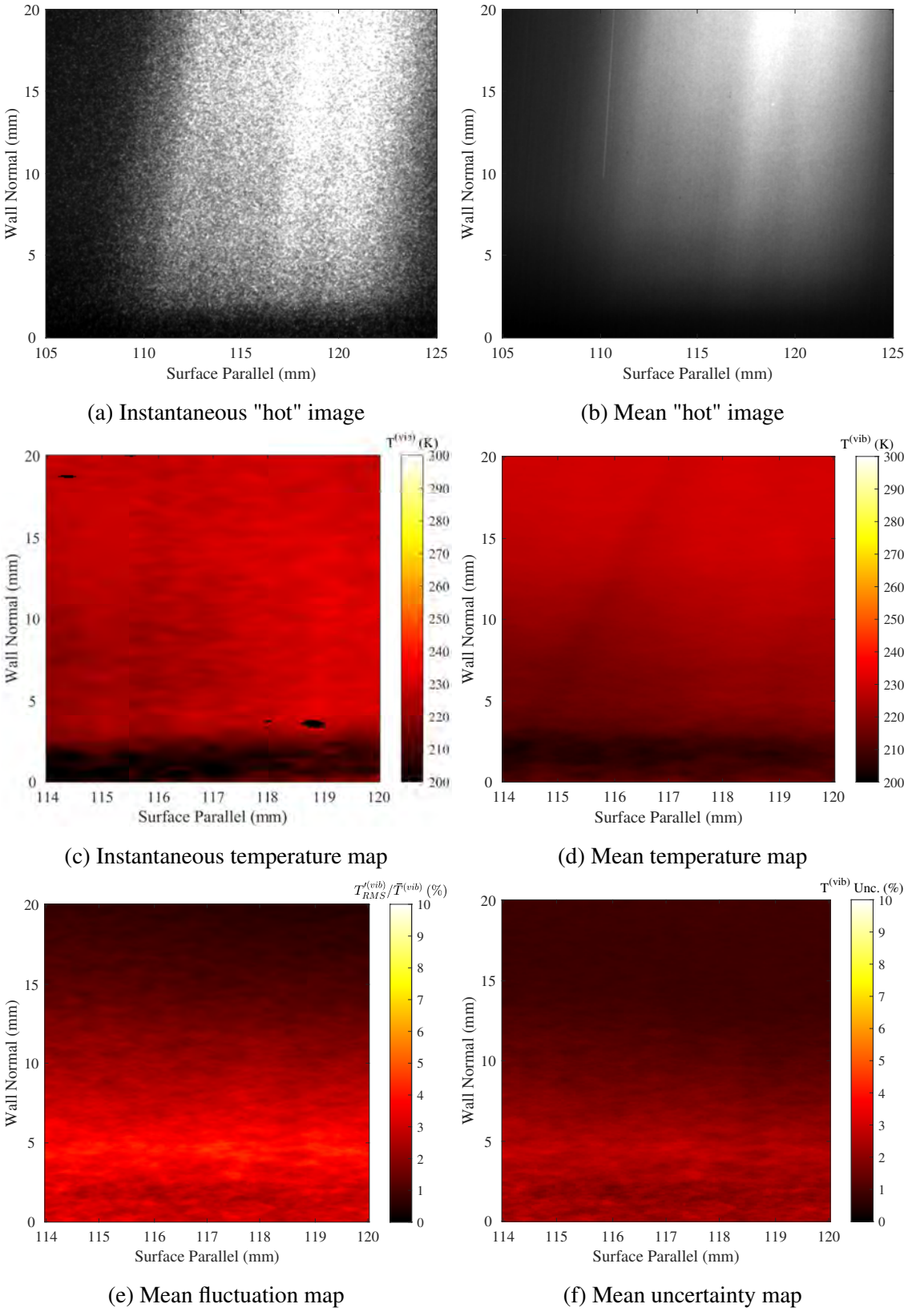

(a) Instantaneous "hot" image

(b) Mean "hot" image

(c) Instantaneous temperature map

(d) Mean temperature map

(e) Mean fluctuation map

(f) Mean uncertainty map

Figure 7.86: PLIF vibrational thermometry assuming $T^{v}_{e,NO} = 230K$, Run 4678: upstream; laminar; plasma off. [7]

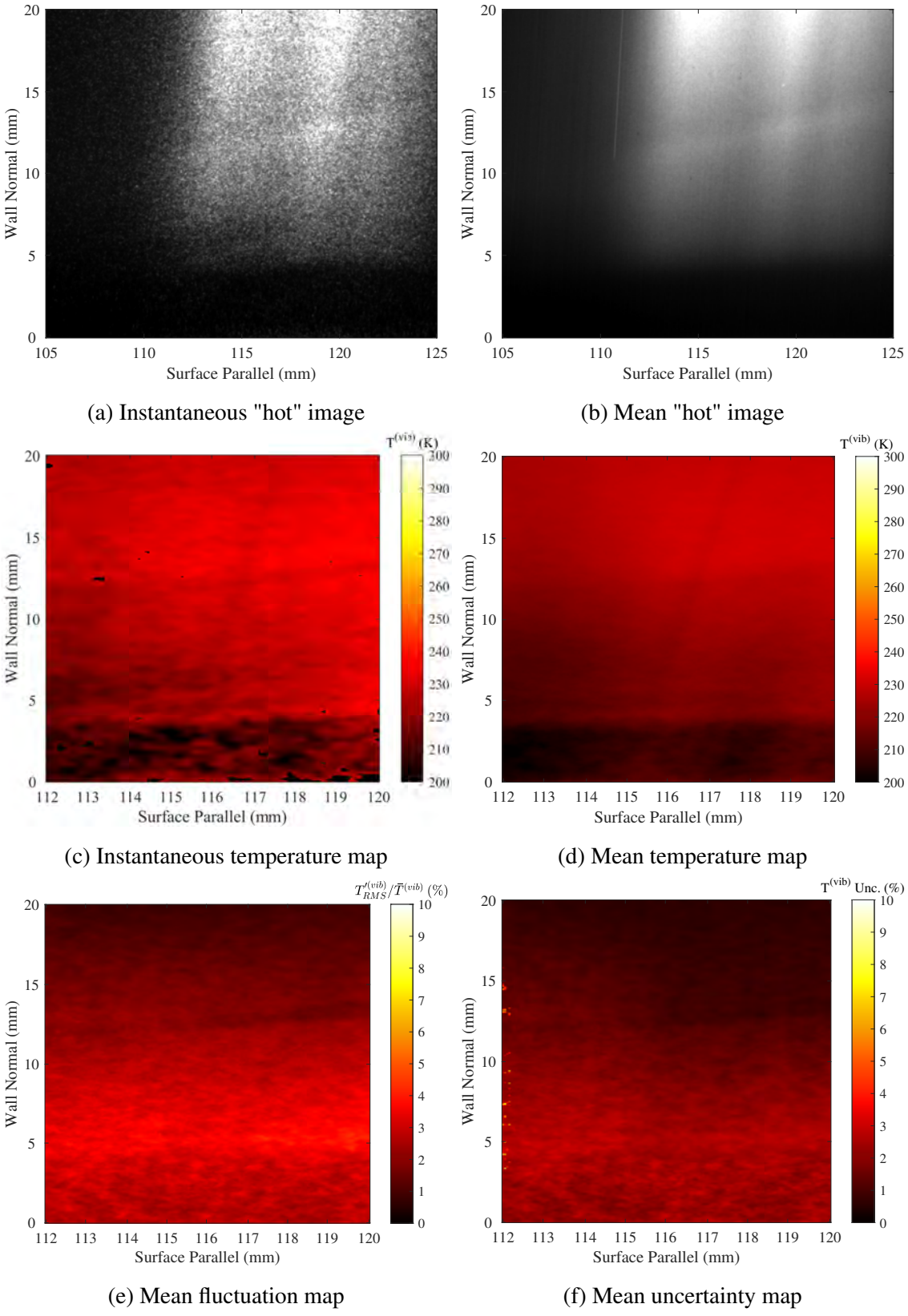

(a) Instantaneous "hot" image

(b) Mean "hot" image

(c) Instantaneous temperature map

(d) Mean temperature map

(e) Mean fluctuation map

(f) Mean uncertainty map

Figure 7.87: PLIF vibrational thermometry assuming $T^v_{e,NO} = 230K$, Run 4681: upstream; turbulent; plasma off. [7]

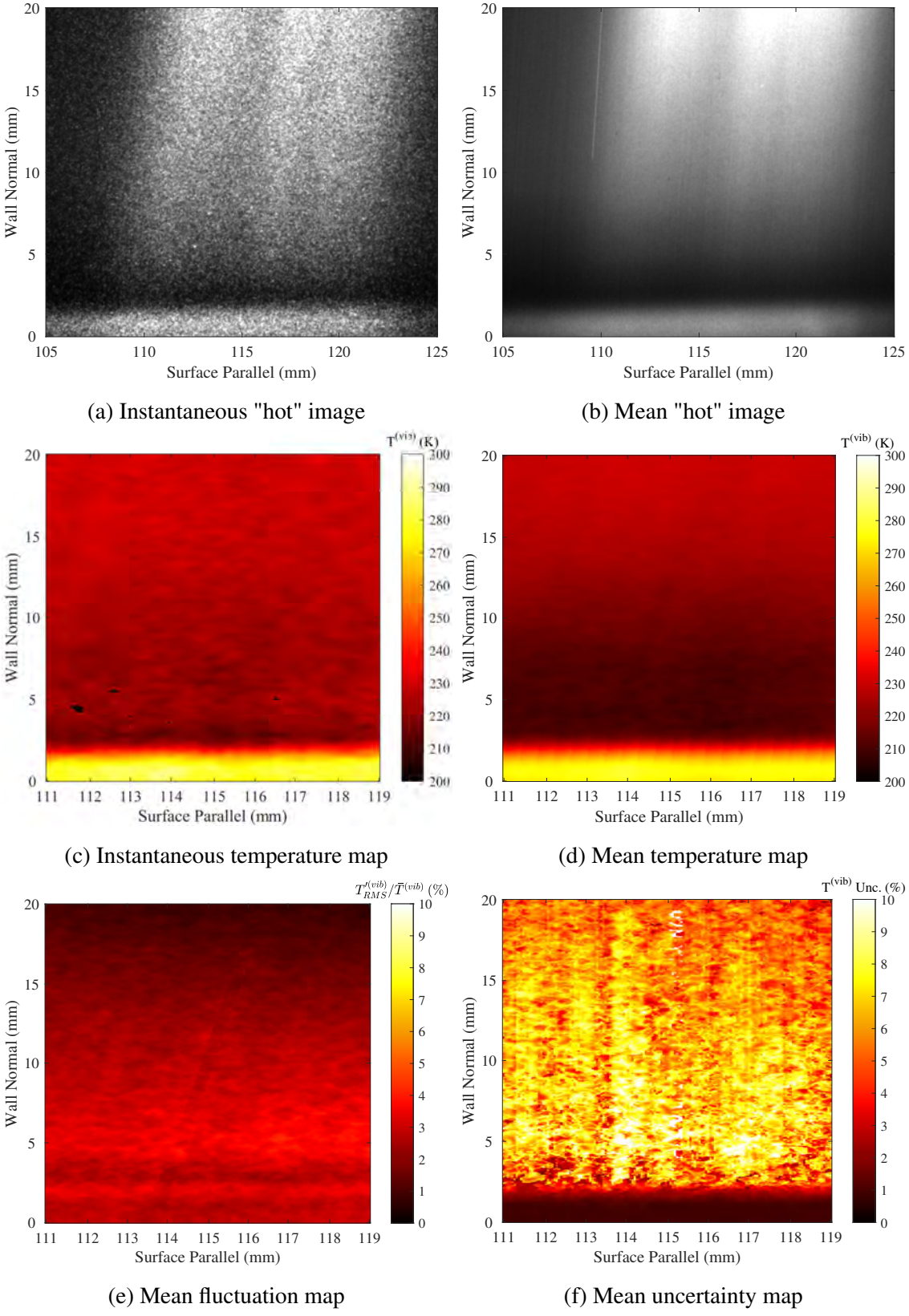

(a) Instantaneous "hot" image

(b) Mean "hot" image

(c) Instantaneous temperature map

(d) Mean temperature map

(e) Mean fluctuation map

(f) Mean uncertainty map

Figure 7.88: PLIF vibrational thermometry assuming $T^{v}_{e,NO} = 230K$, Run 4679: upstream; laminar; plasma on. [7]

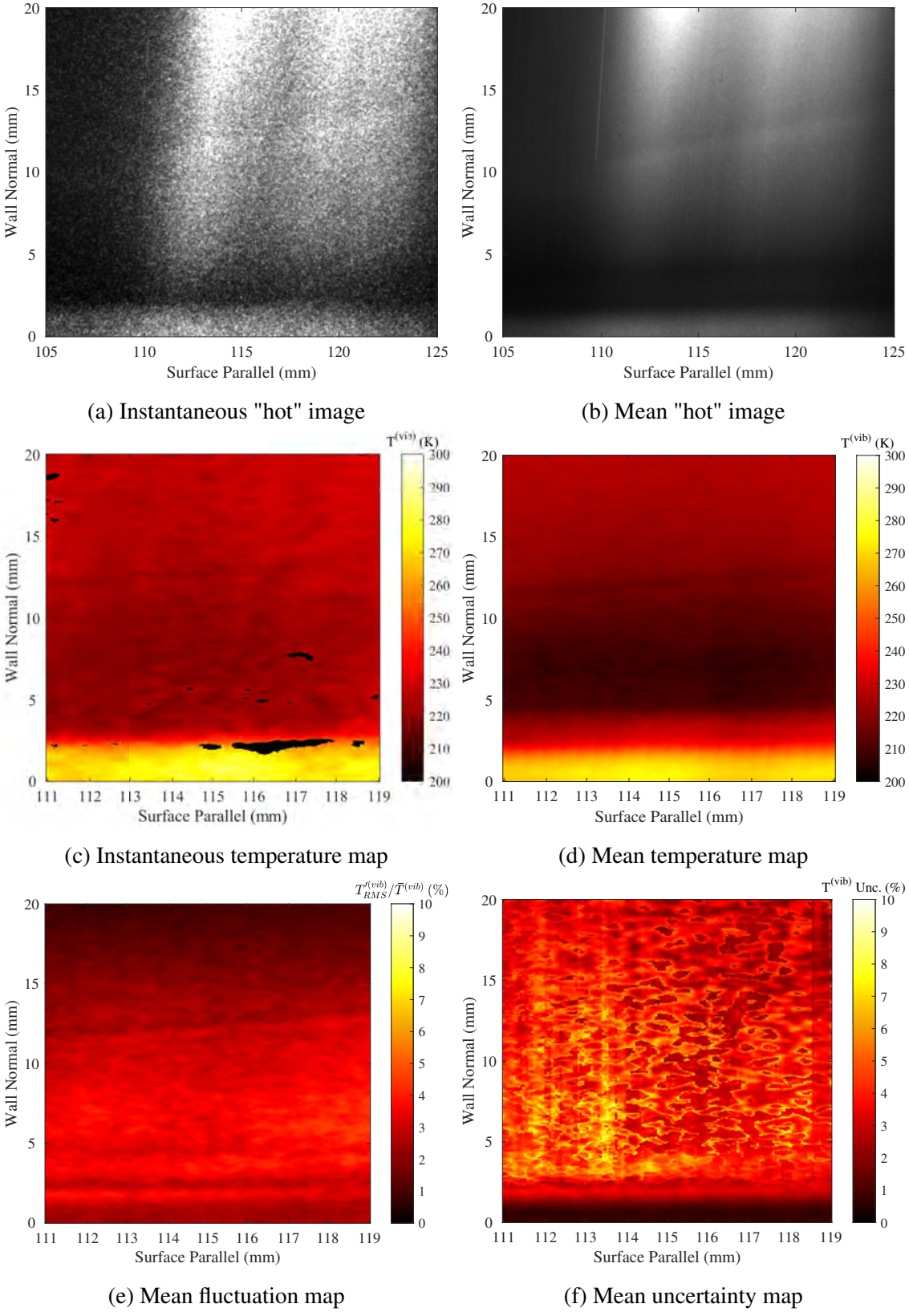

(a) Instantaneous "hot" image

(b) Mean "hot" image

(c) Instantaneous temperature map

(d) Mean temperature map

(e) Mean fluctuation map

(f) Mean uncertainty map

Figure 7.89: PLIF vibrational thermometry assuming $T^v_{e,NO} = 230K$, Run 4682: upstream; turbulent; plasma on. [7]

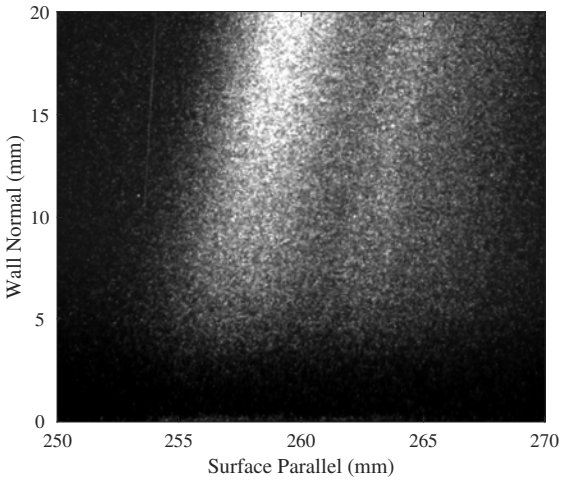

(a) Instantaneous "hot" image

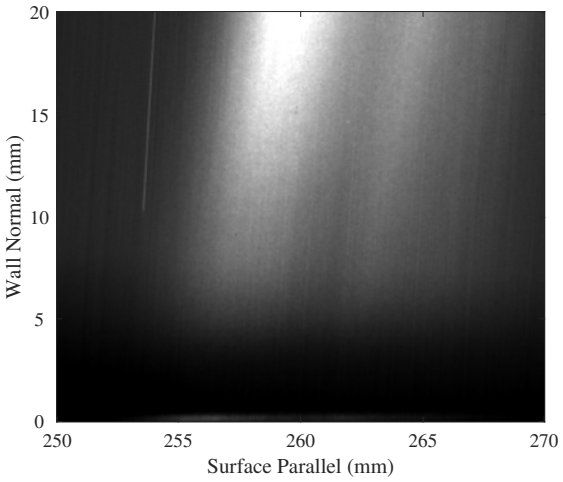

(b) Mean "hot" image

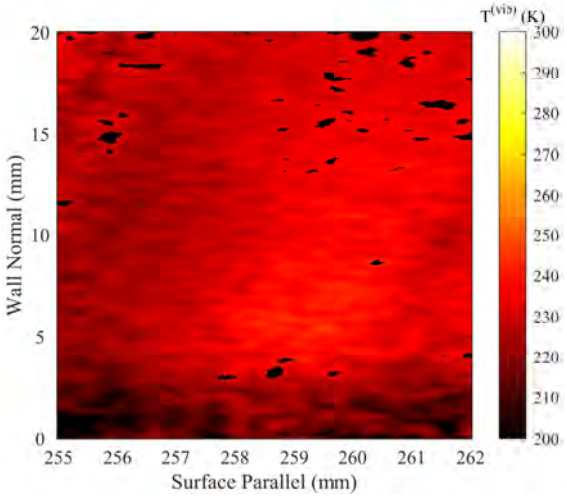

(c) Instantaneous temperature map

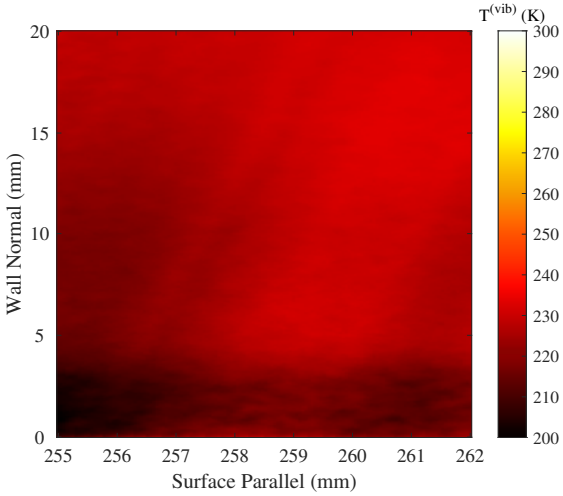

(d) Mean temperature map

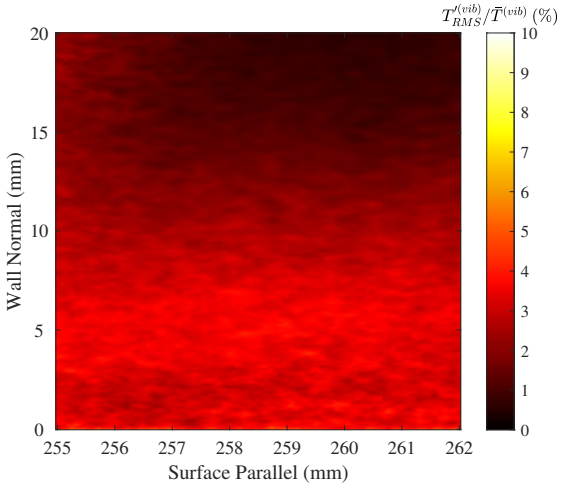

(e) Mean fluctuation map

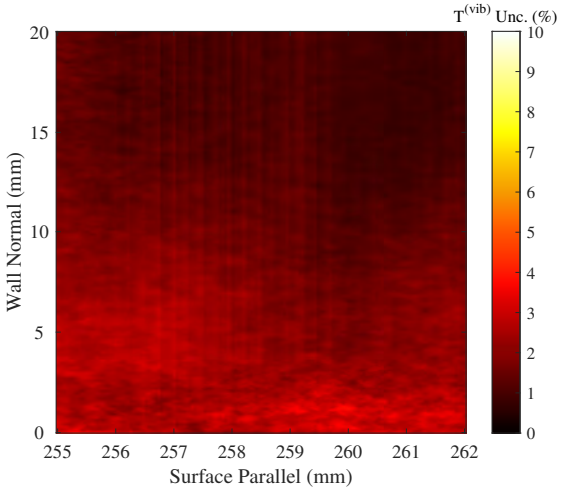

(f) Mean uncertainty map

Figure 7.90: PLIF vibrational thermometry assuming $T^{v}_{e,NO} = 230K$, Run 4688: middle; laminar; plasma off. [7]

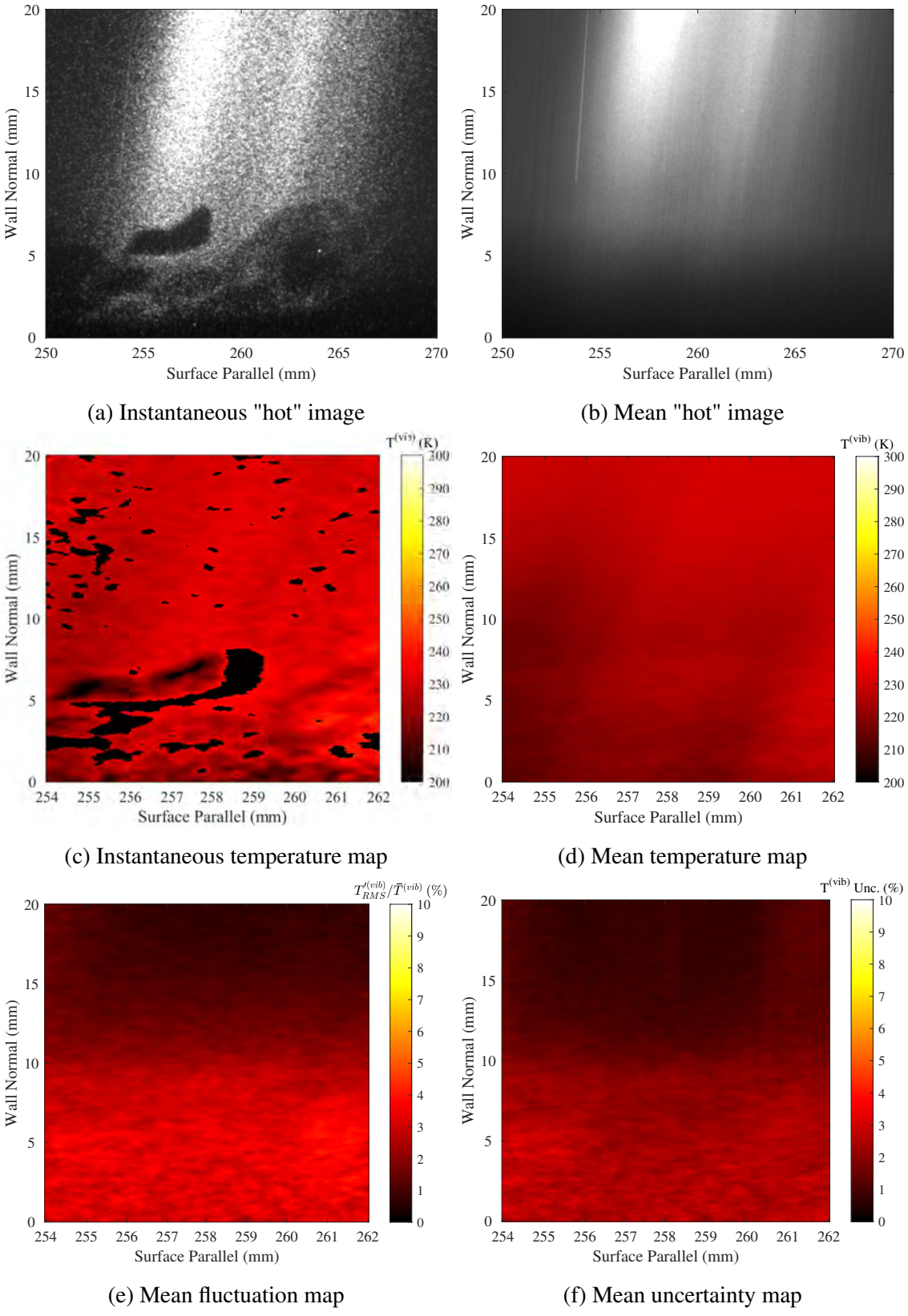

(a) Instantaneous "hot" image

(b) Mean "hot" image

(c) Instantaneous temperature map

(d) Mean temperature map

(e) Mean fluctuation map

(f) Mean uncertainty map

Figure 7.91: PLIF vibrational thermometry assuming $T^{v}_{e,NO} = 230K$, Run 4691: middle; turbulent; plasma off. [7]

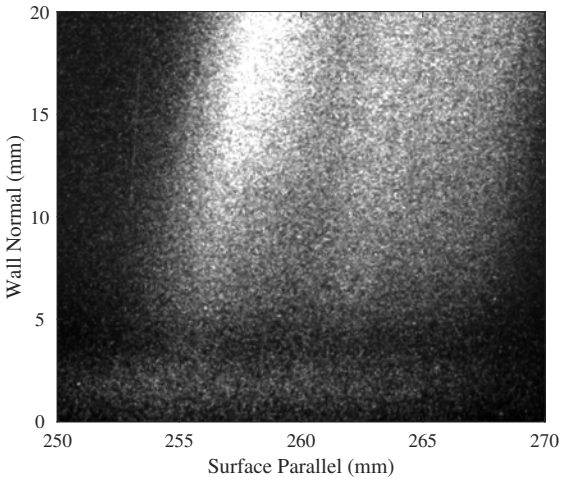

(a) Instantaneous "hot" image

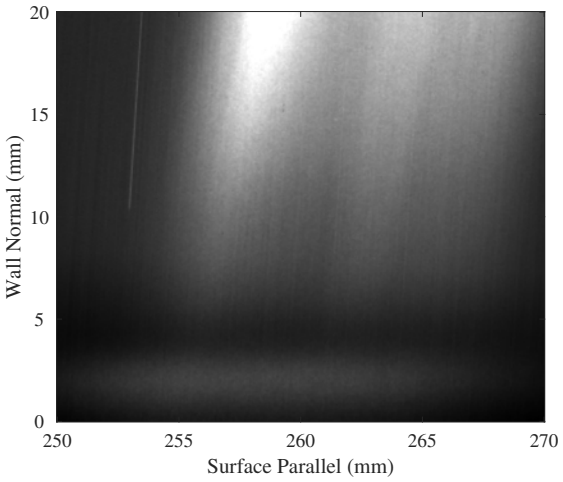

(b) Mean "hot" image

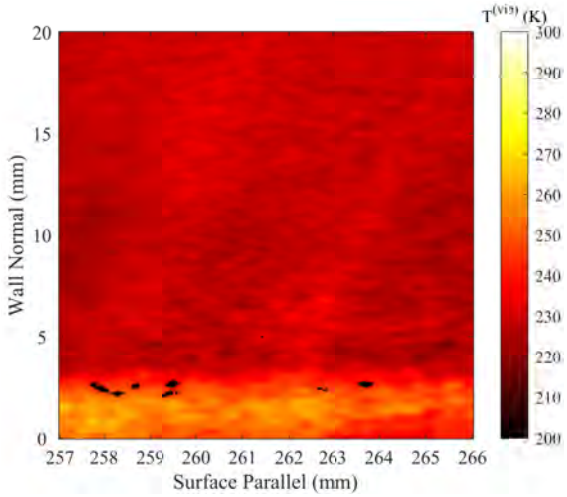

(c) Instantaneous temperature map

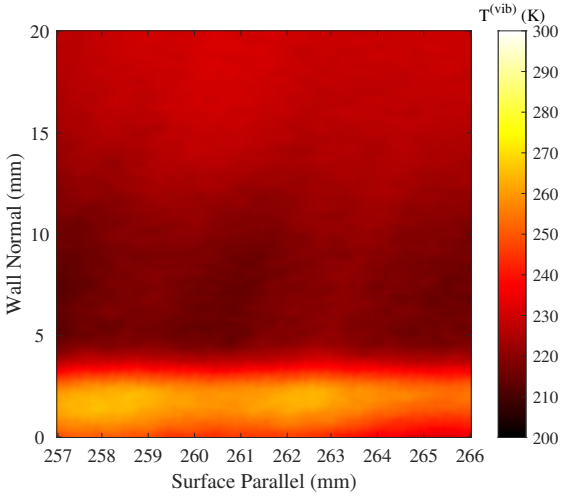

(d) Mean temperature map

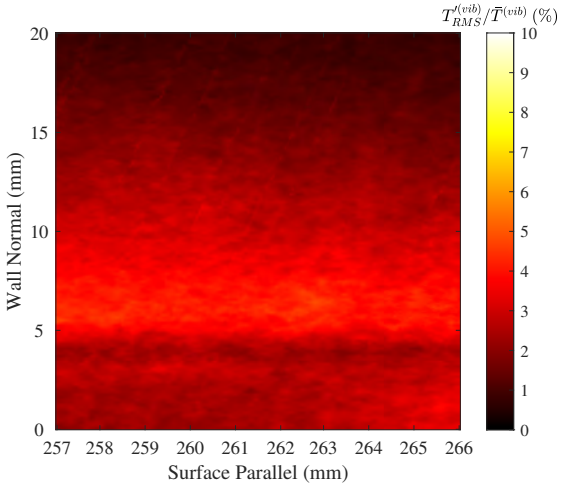

(e) Mean fluctuation map

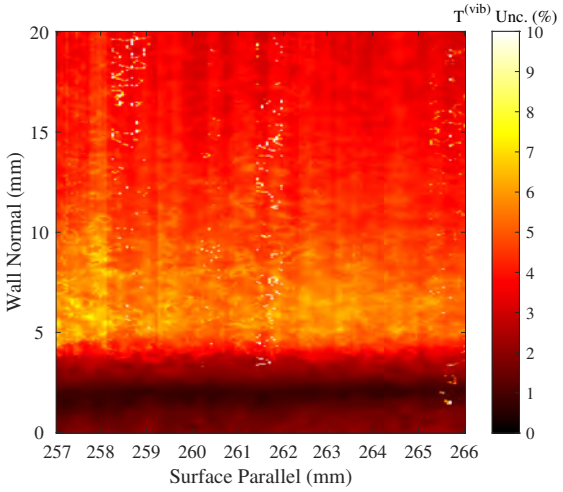

(f) Mean uncertainty map

Figure 7.92: PLIF vibrational thermometry assuming $T^{v}_{e,NO} = 230K$, Run 4687: middle; laminar; plasma on. [7]

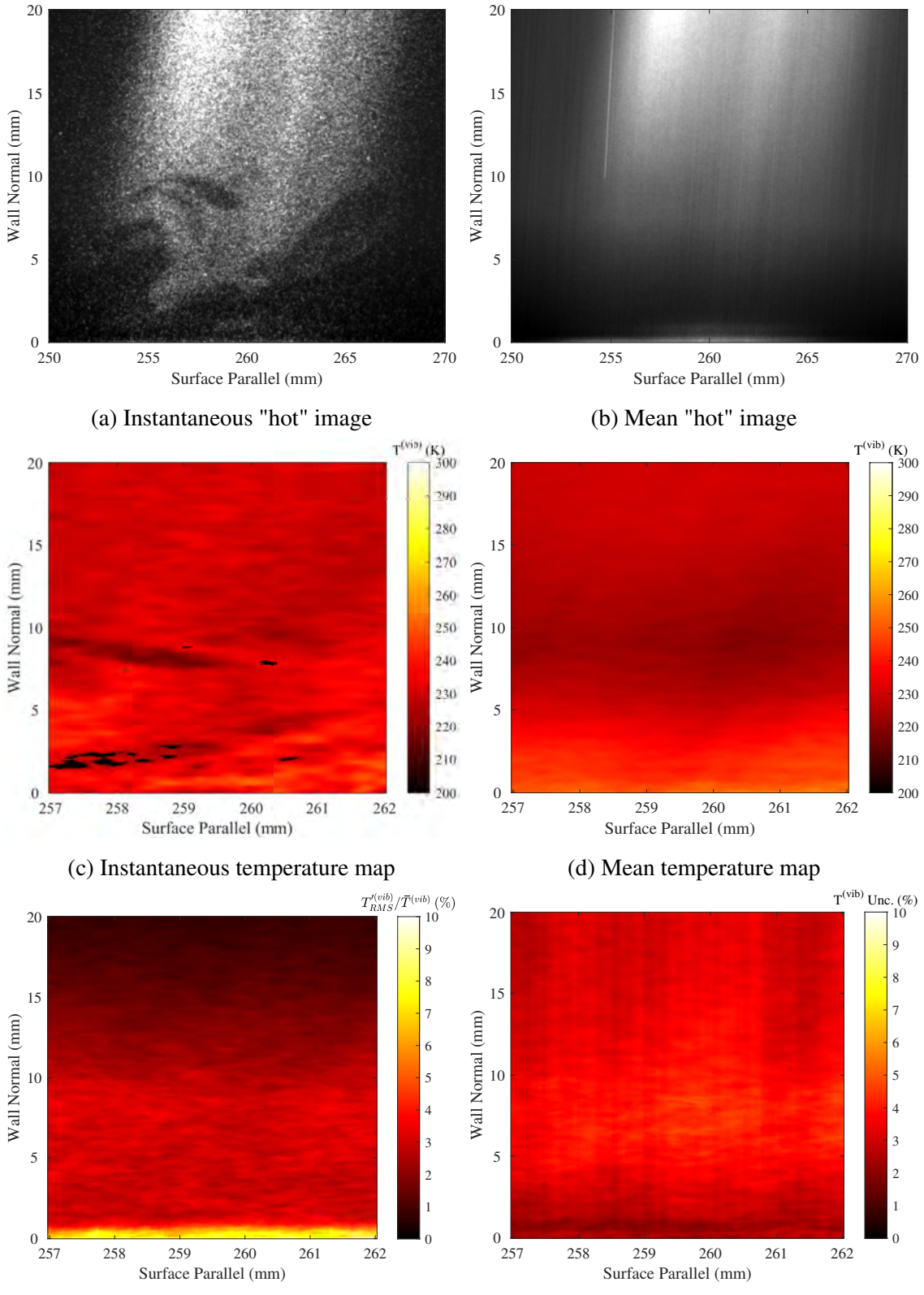

(a) Instantaneous "hot" image

(b) Mean "hot" image

(c) Instantaneous temperature map

(d) Mean temperature map

(e) Mean fluctuation map

(f) Mean uncertainty map

Figure 7.93: PLIF vibrational thermometry assuming $T^{v}_{e,NO} = 230K$, Run 4690: middle; turbulent; plasma on. [7]

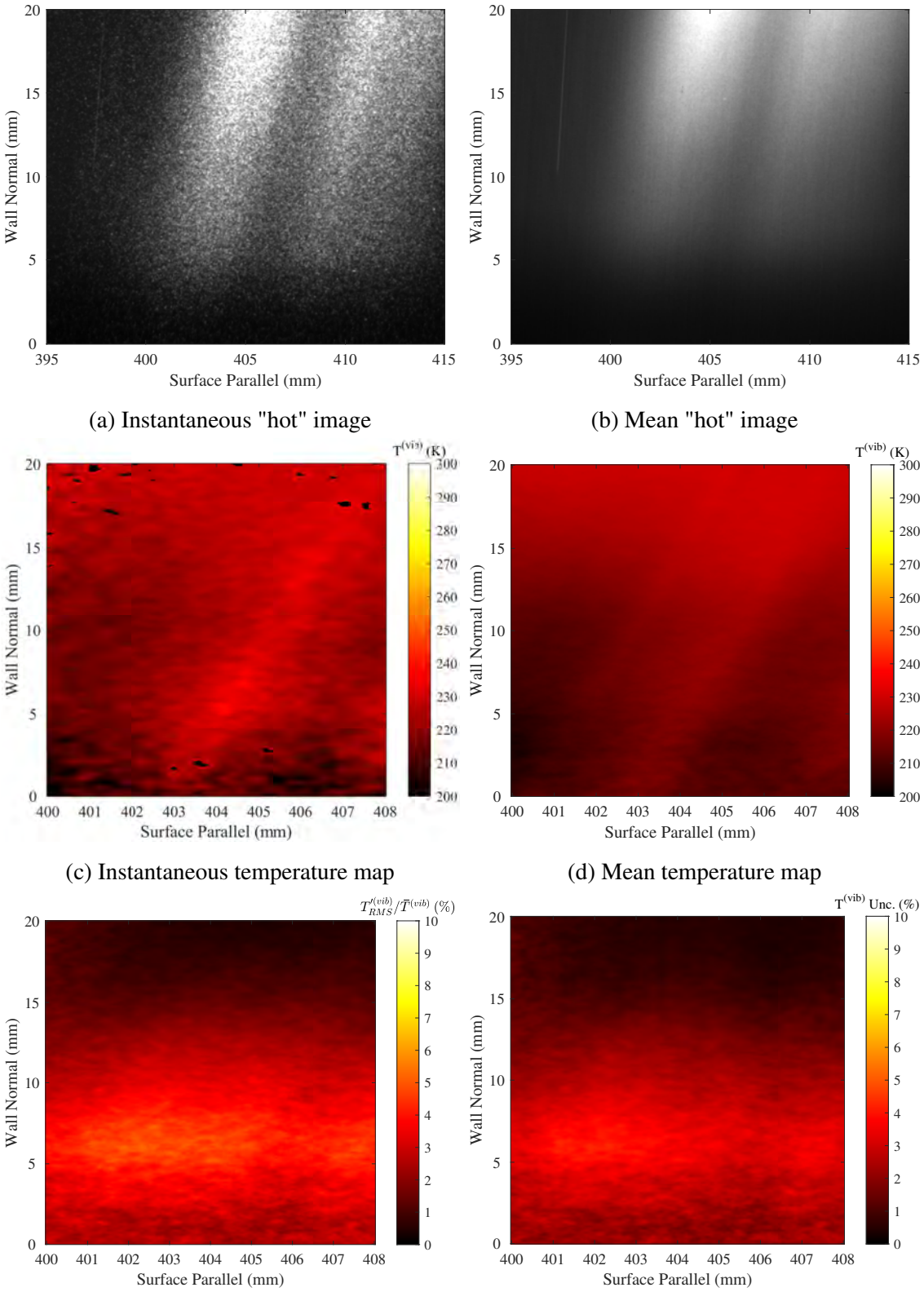

(a) Instantaneous "hot" image

(b) Mean "hot" image

(c) Instantaneous temperature map

(d) Mean temperature map

(e) Mean fluctuation map

(f) Mean uncertainty map

Figure 7.94: PLIF vibrational thermometry assuming $T^v_{e,NO} = 230K$, Run 4685: back; laminar; plasma off. [7]

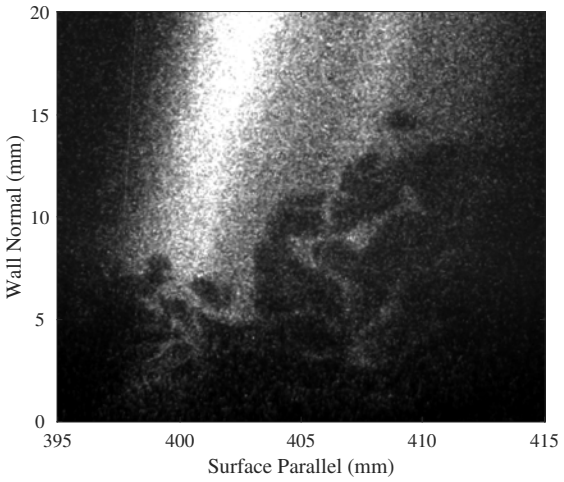

(a) Instantaneous "hot" image

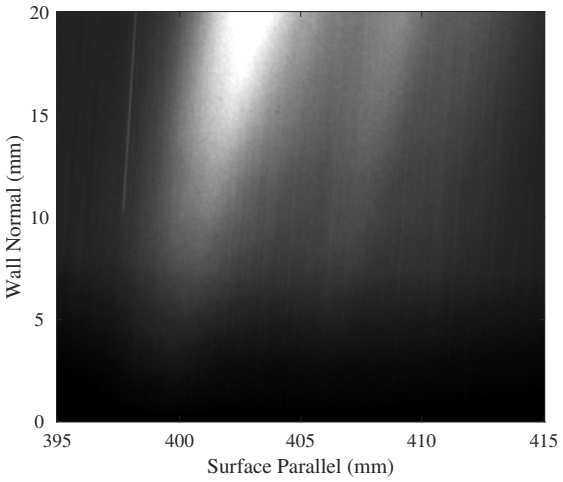

(b) Mean "hot" image

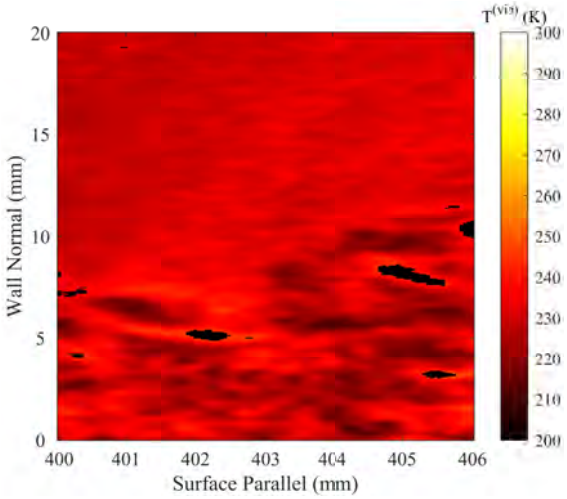

(c) Instantaneous temperature map

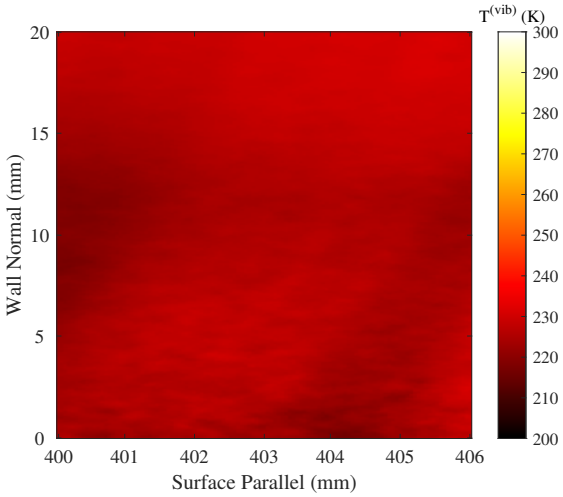

(d) Mean temperature map

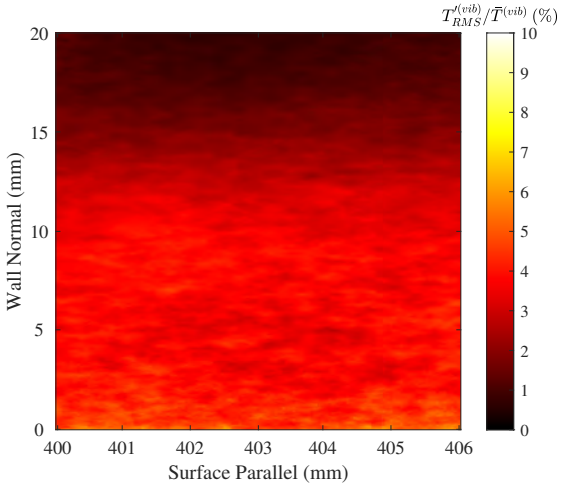

(e) Mean fluctuation map

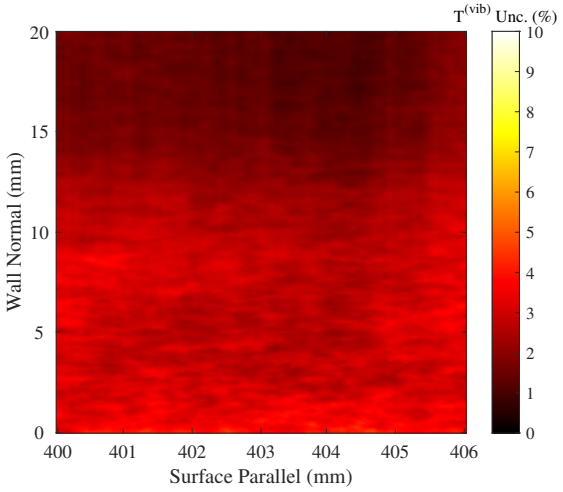

(f) Mean uncertainty map

Figure 7.95: PLIF vibrational thermometry assuming $T^{v}_{e,NO} = 230K$, Run 4684: back; turbulent; plasma off. [7]

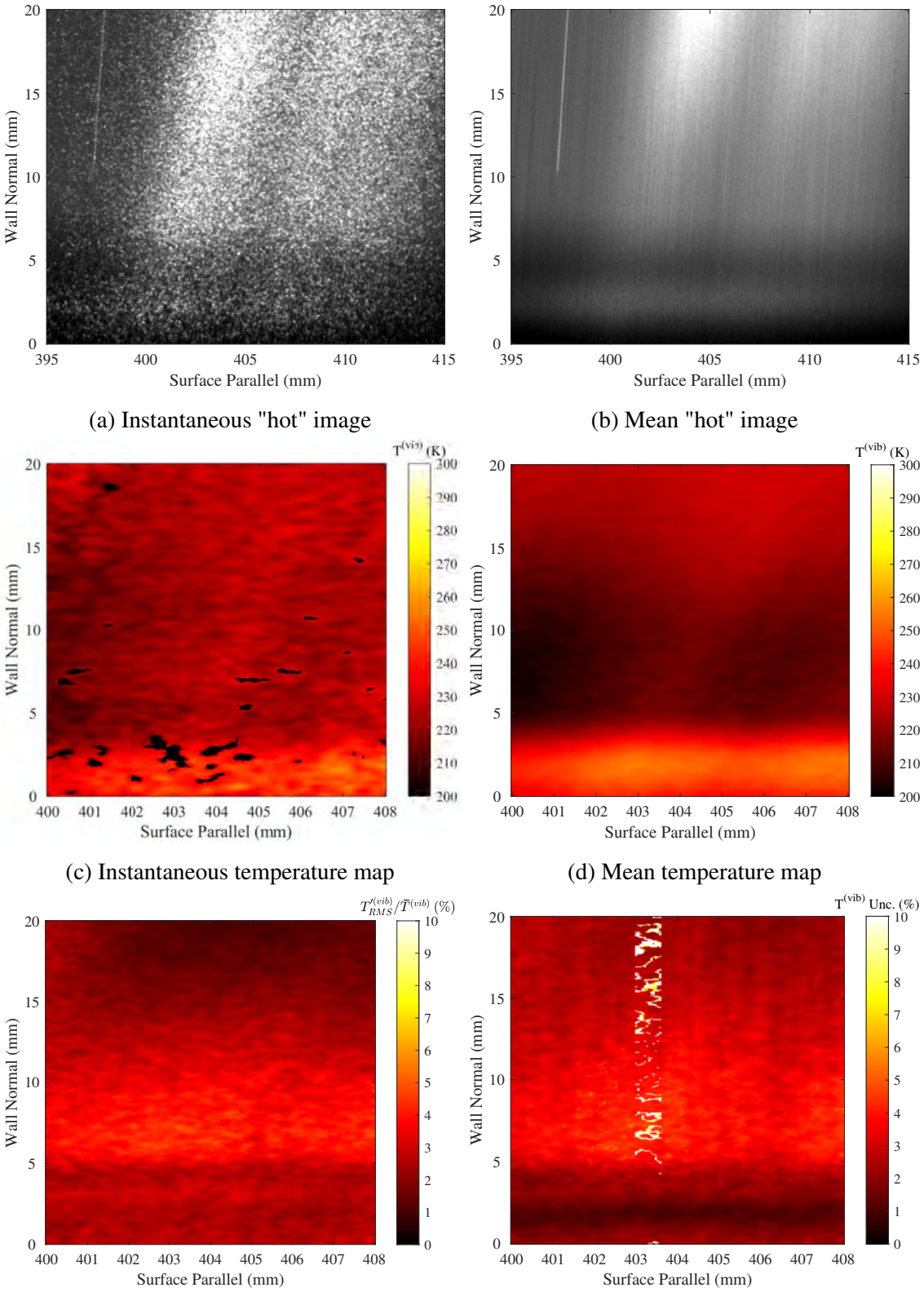

(a) Instantaneous "hot" image

(b) Mean "hot" image

(c) Instantaneous temperature map

(d) Mean temperature map

(e) Mean fluctuation map

(f) Mean uncertainty map

Figure 7.96: PLIF vibrational thermometry assuming $T^{v}_{e,NO} = 230K$, Run 4686: back; laminar; plasma on. [7]

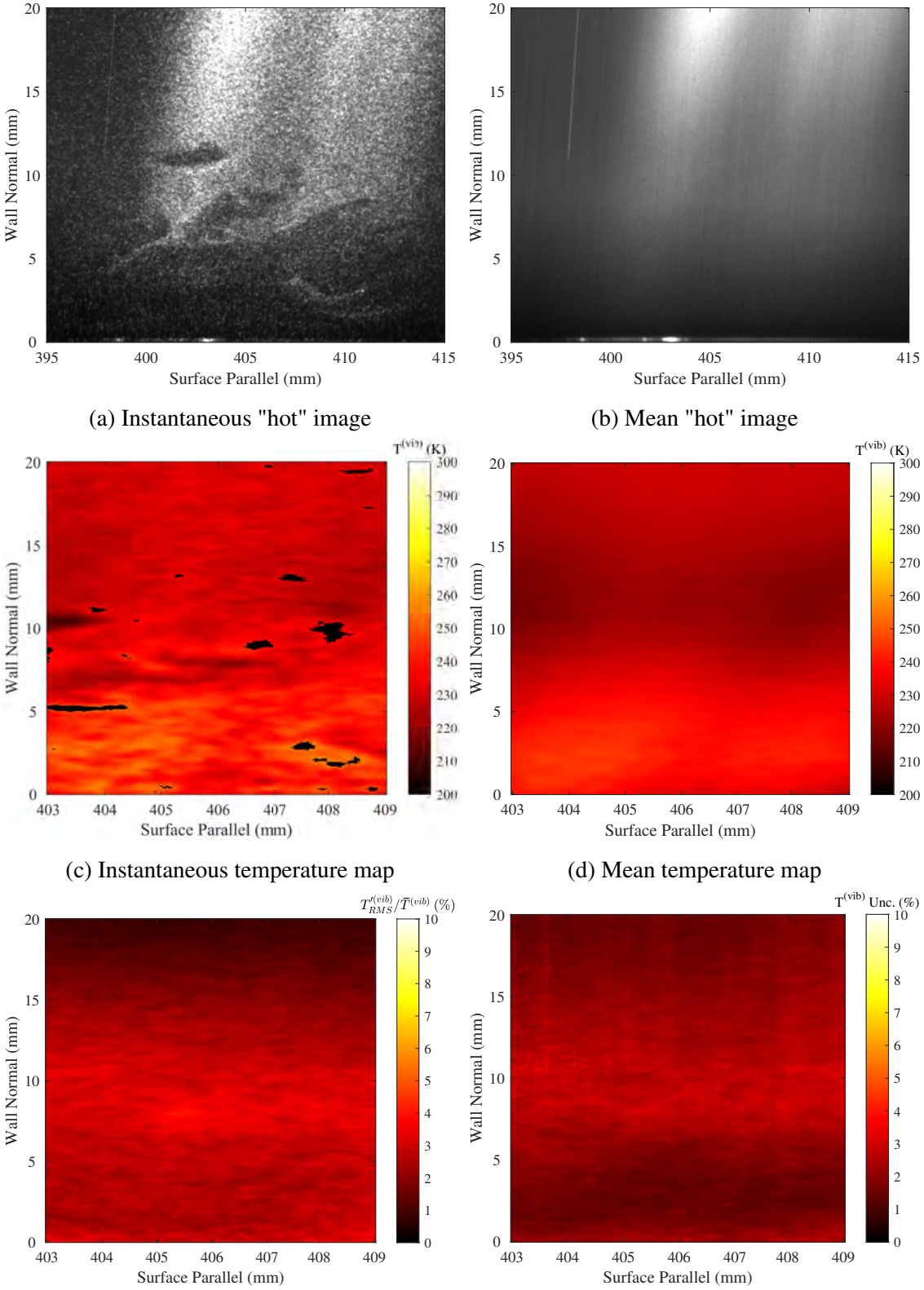

(a) Instantaneous "hot" image

(b) Mean "hot" image

(c) Instantaneous temperature map

(d) Mean temperature map

(e) Mean fluctuation map

(f) Mean uncertainty map

Figure 7.97: PLIF vibrational thermometry assuming $T^{v}_{e,NO} = 230K$, Run 4683: back; turbulent; plasma on. [7]

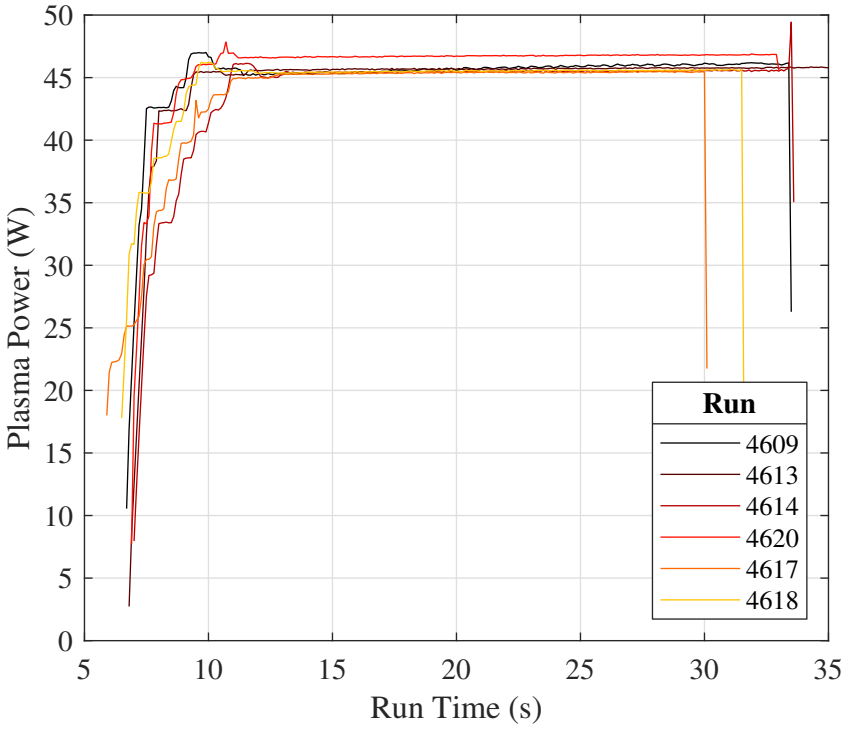

Figure 7.98: Plasma power traces for PLIF velocimetry runs.

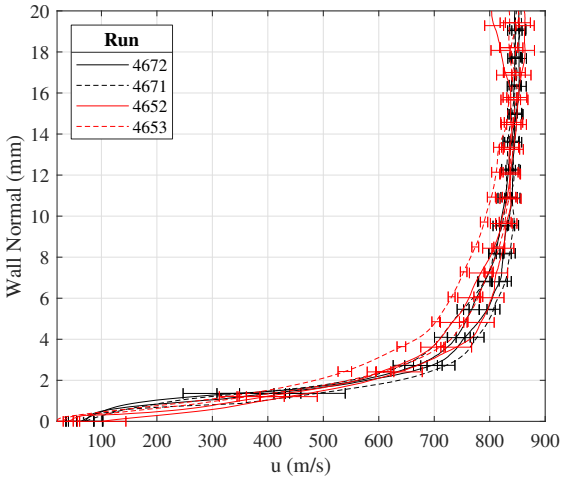

(a) Laminar, velocity

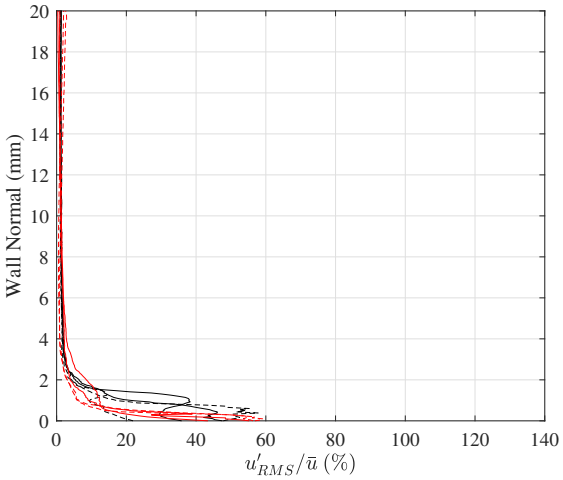

(b) Laminar, fluctuation

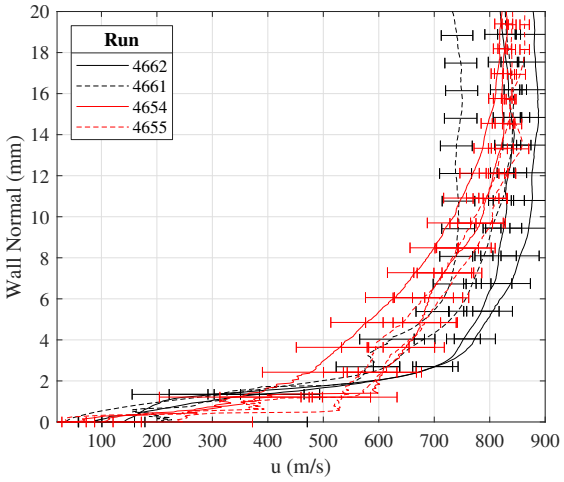

(c) Turbulent wake, velocity

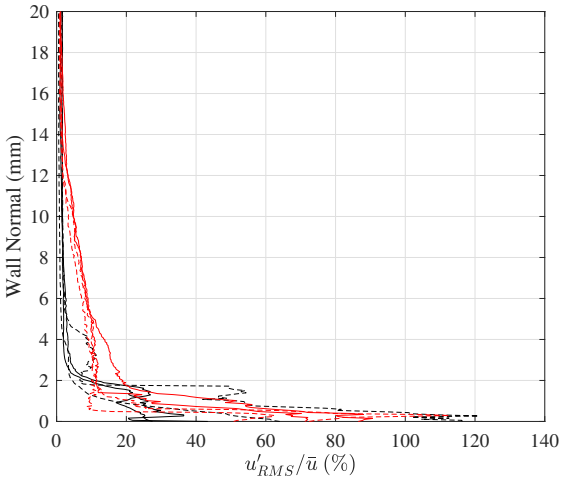

(d) Turbulent wake, fluctuation

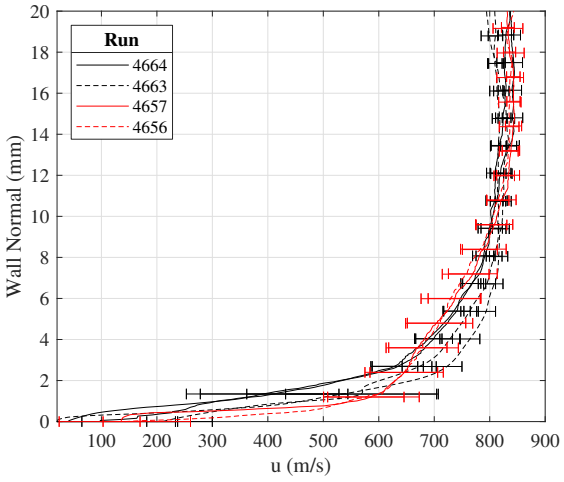

(e) Turbulent trough, velocity

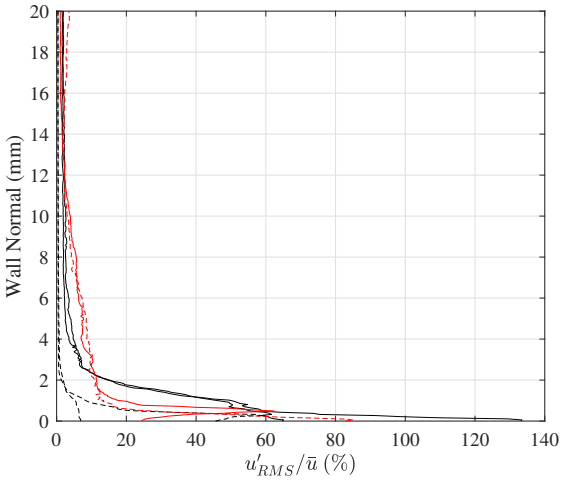

(f) Turbulent trough, fluctuation

Figure 7.99: PLIF MTV velocity and fluctuation profile comparison. [7]

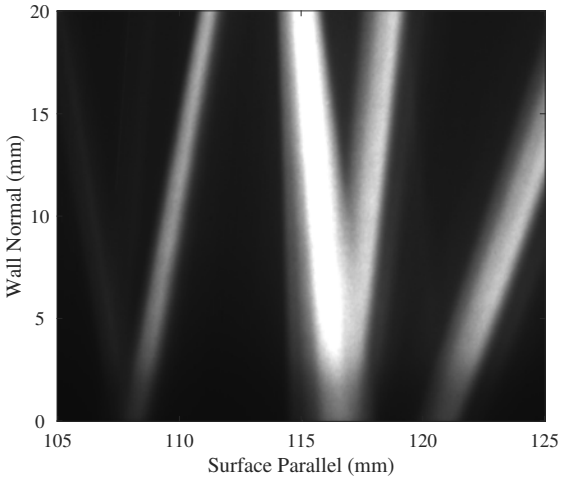

(a) Mean write image

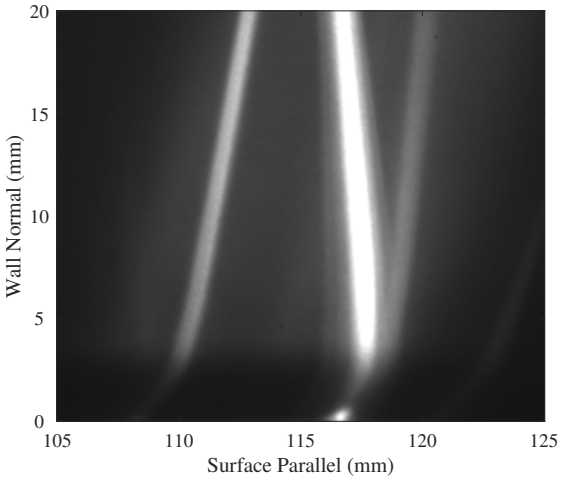

(b) Mean read image

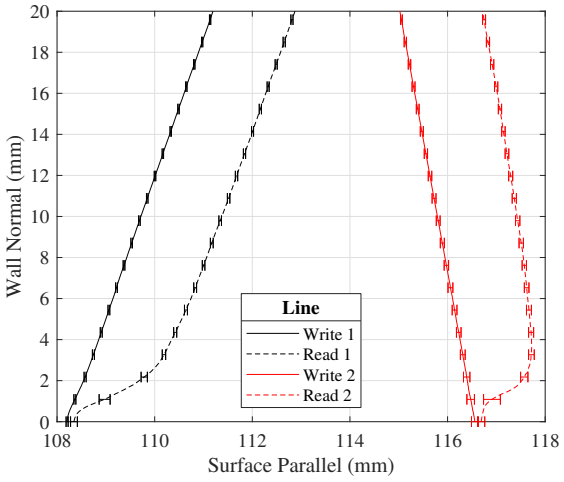

(c) Mean line locations

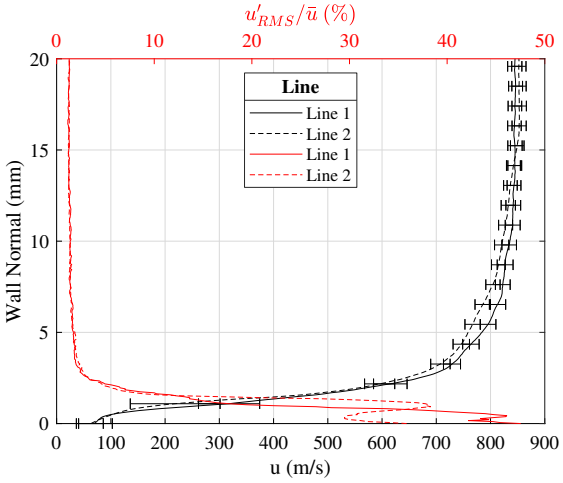

(d) Mean velocity and fluctuation profiles

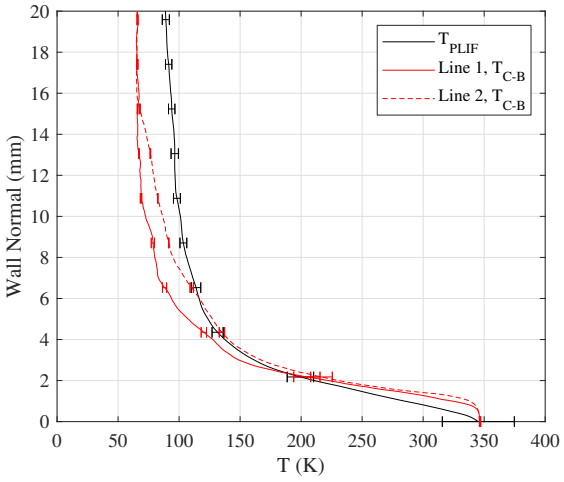

(e) Mean temperature profiles

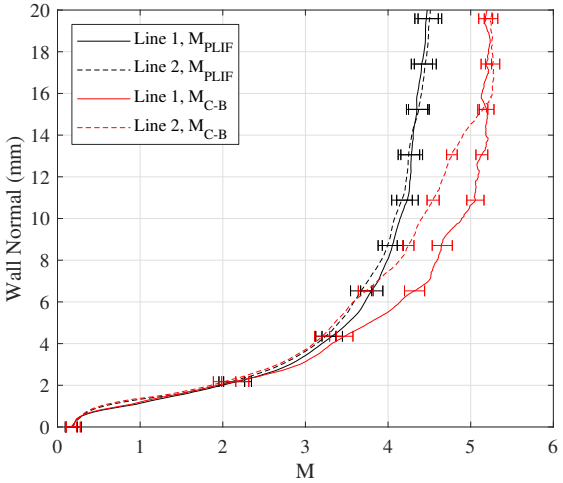

(f) Mean Mach number profiles

Figure 7.100: PLIF MTV, Run 4672: upstream; laminar; plasma off. [7]

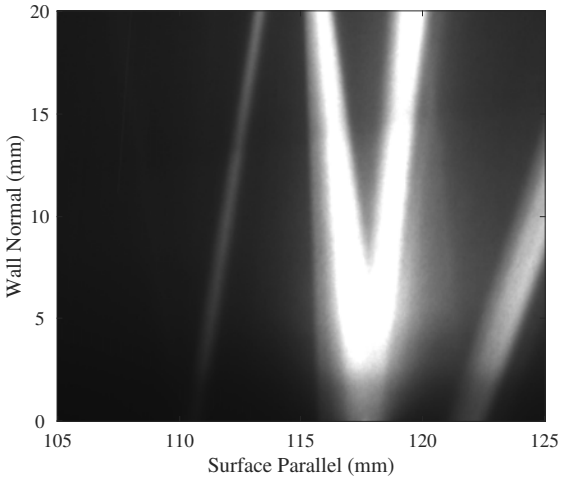

(a) Mean write image

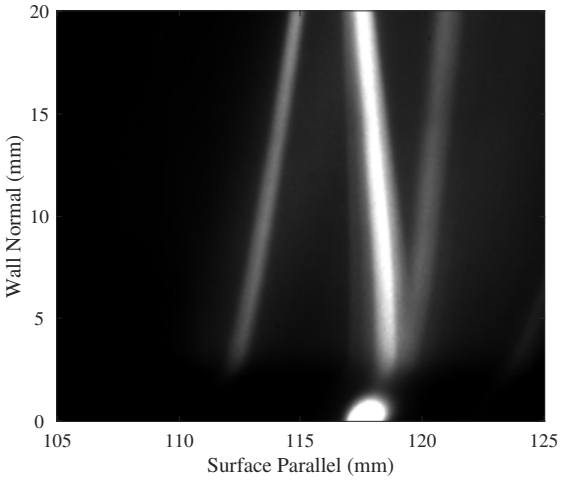

(b) Mean read image

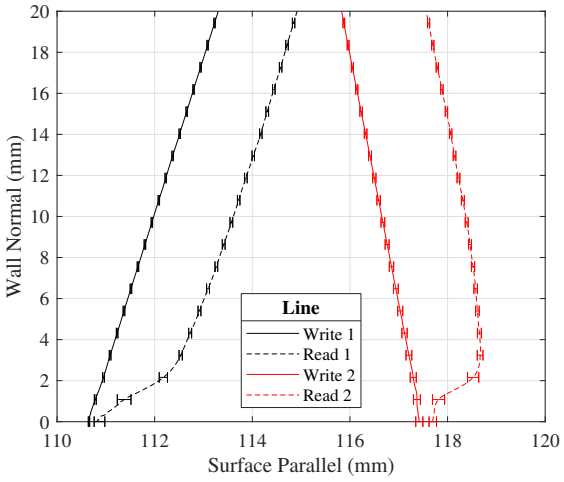

(c) Mean line locations

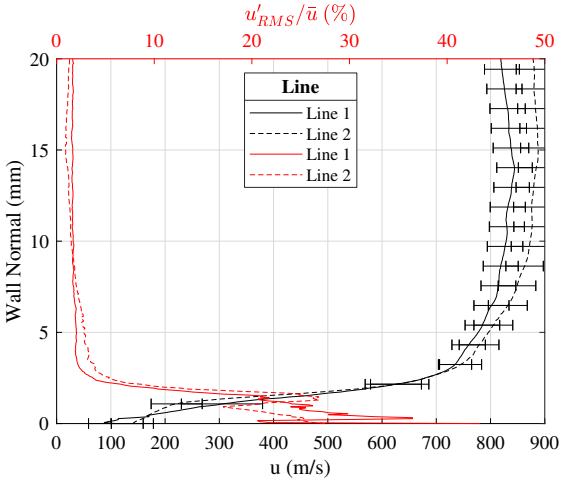

(d) Mean velocity and fluctuation profiles

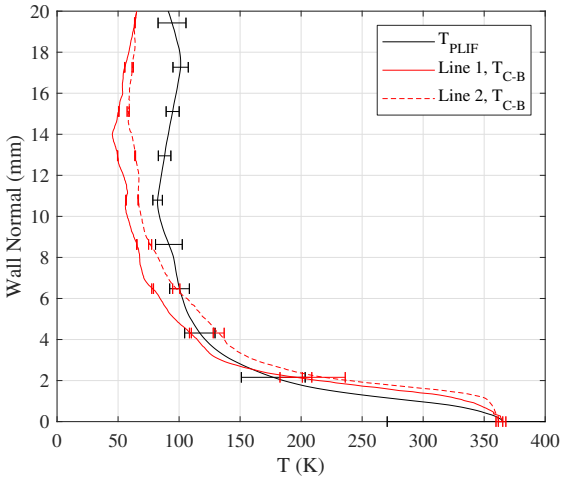

(e) Mean temperature profiles

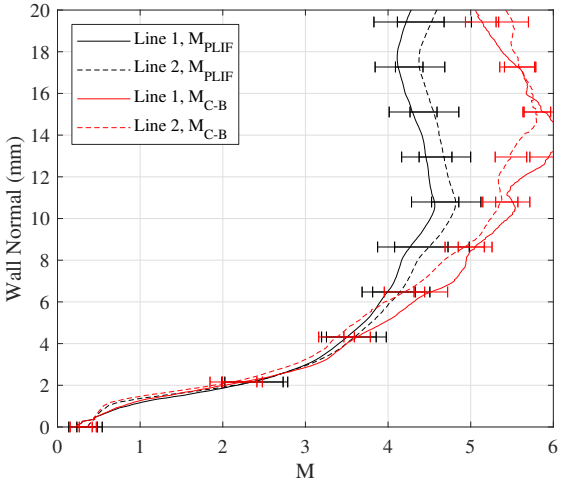

(f) Mean Mach number profiles

Figure 7.101: PLIF MTV, Run 4662: upstream; turbulent wake; plasma off. [7]

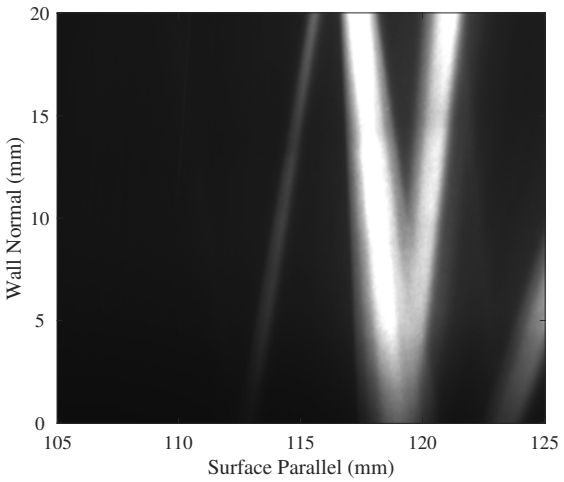

(a) Mean write image

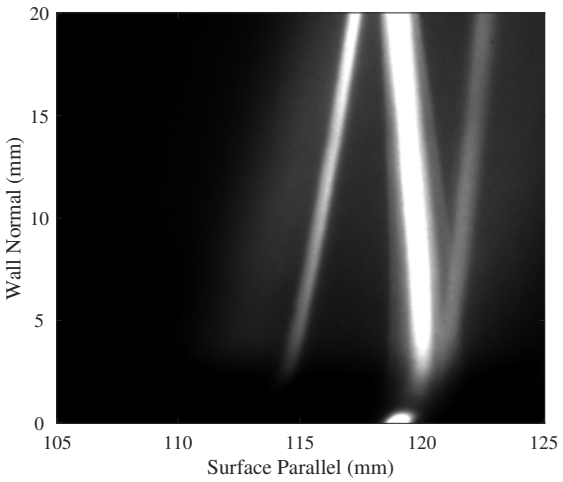

(b) Mean read image

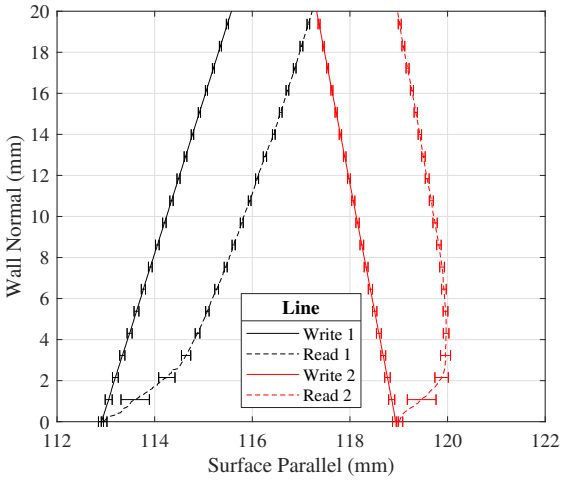

(c) Mean line locations

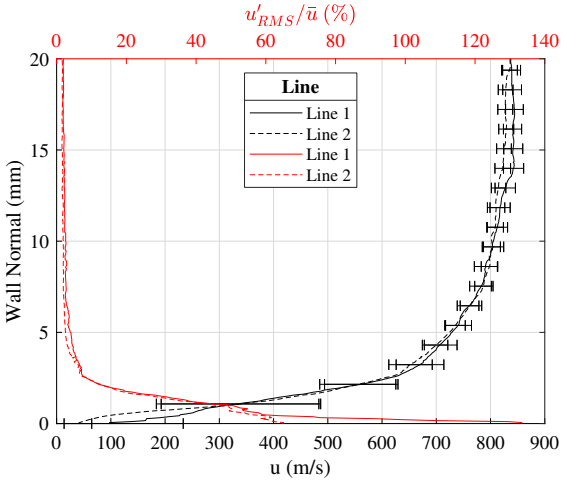

(d) Mean velocity and fluctuation profiles

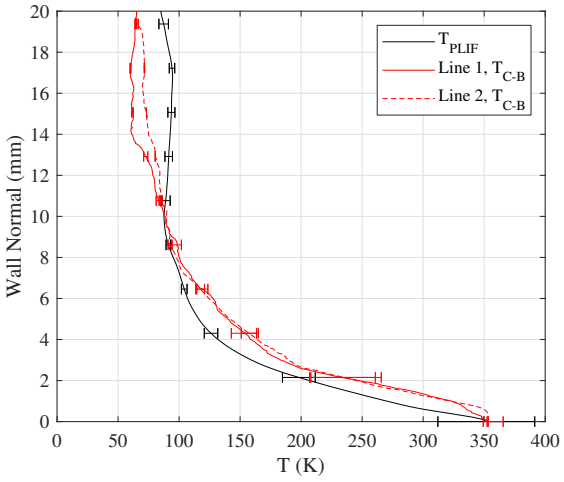

(e) Mean temperature profiles

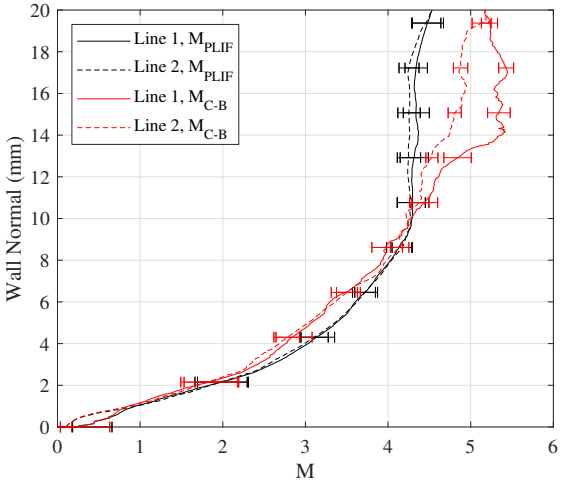

(f) Mean Mach number profiles

Figure 7.102: PLIF MTV, Run 4664: upstream; turbulent trough; plasma off. [7]

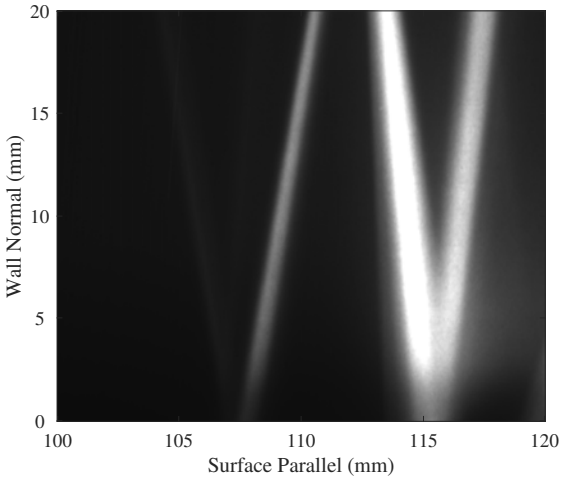

(a) Mean write image

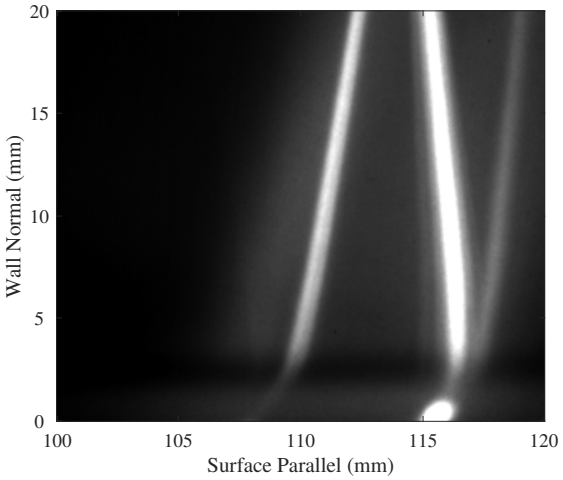

(b) Mean read image

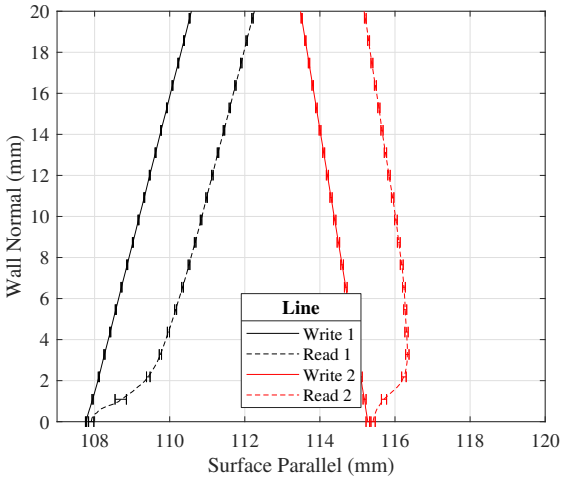

(c) Mean line locations

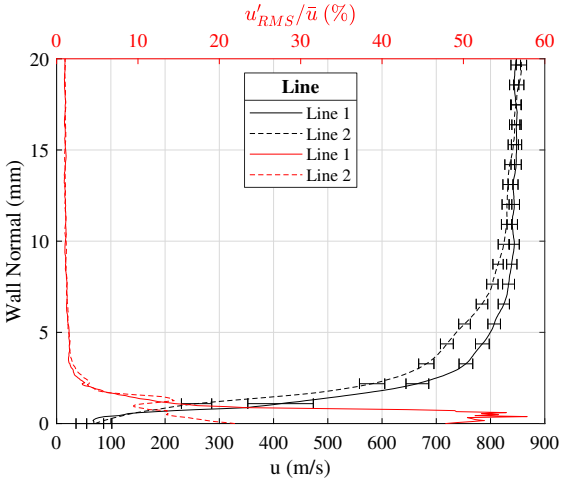

(d) Mean velocity and fluctuation profiles

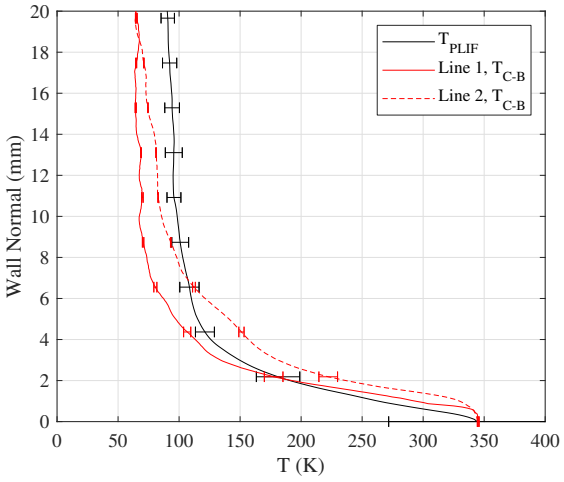

(e) Mean temperature profiles

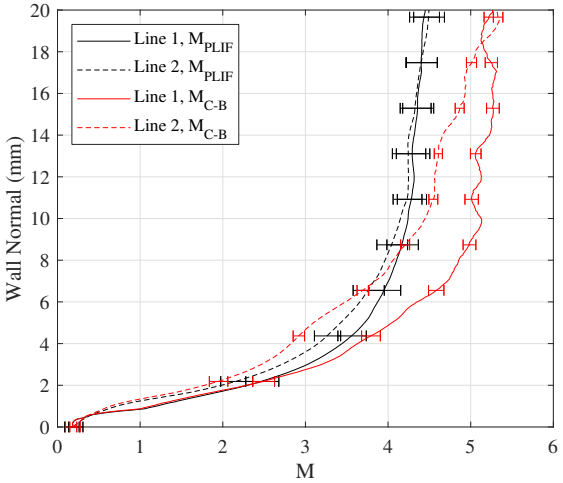

(f) Mean Mach number profiles

Figure 7.103: PLIF MTV, Run 4671: upstream; laminar; plasma on. [7]

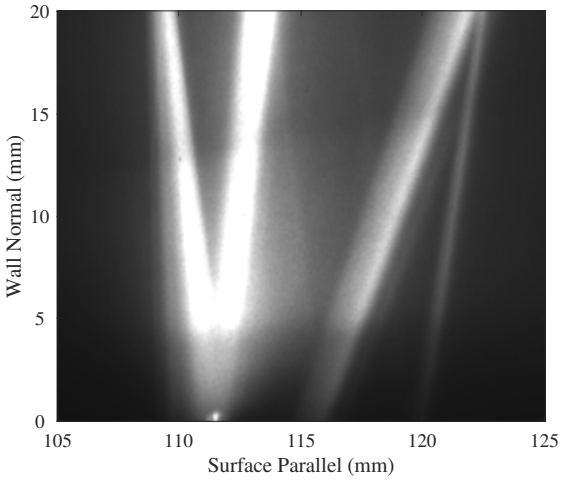

(a) Mean write image

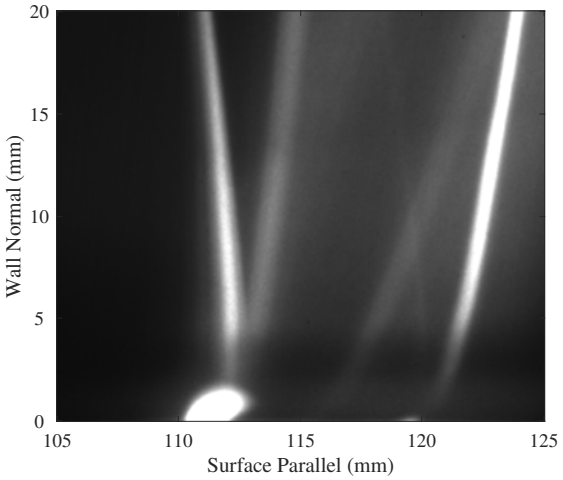

(b) Mean read image

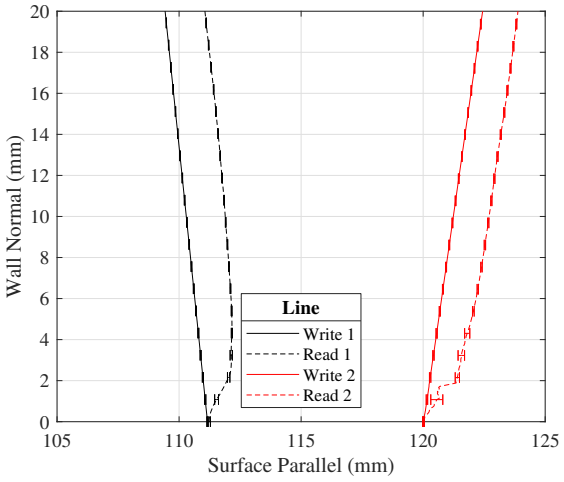

(c) Mean line locations

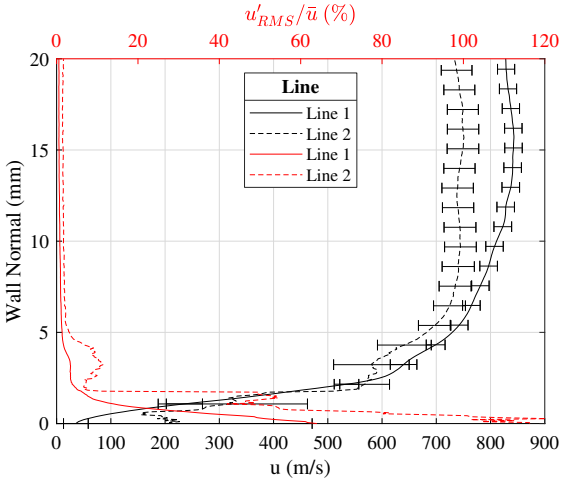

(d) Mean velocity and fluctuation profiles

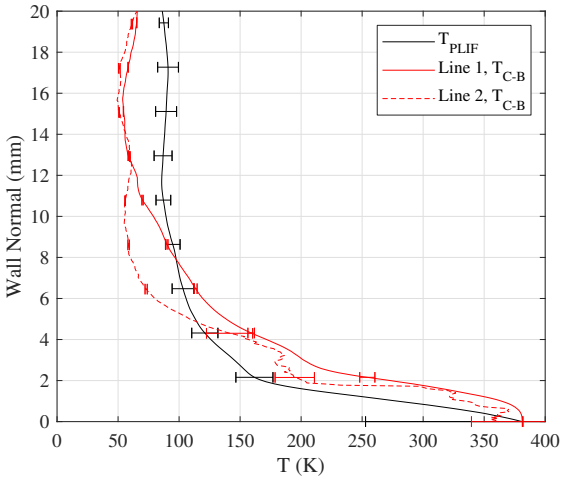

(e) Mean temperature profiles

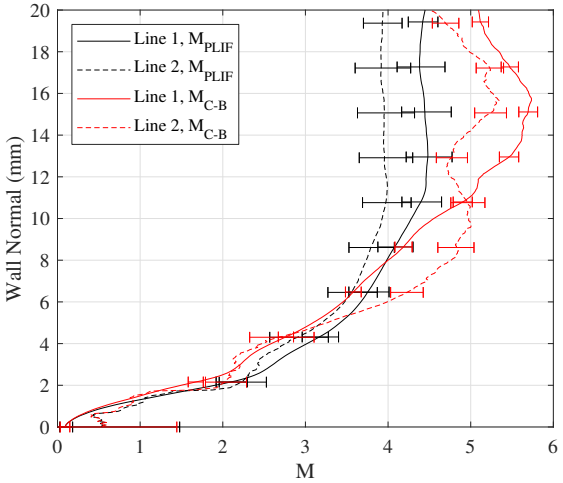

(f) Mean Mach number profiles

Figure 7.104: PLIF MTV, Run 4661: upstream; turbulent wake; plasma on. [7]

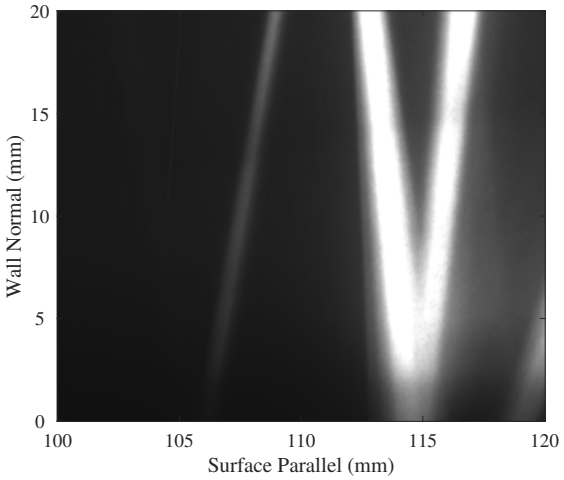

(a) Mean write image

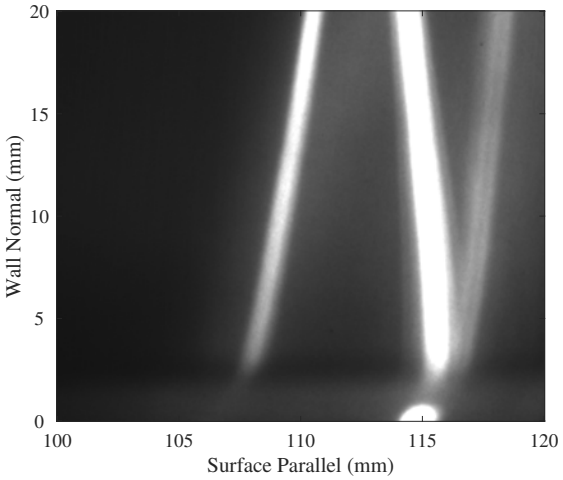

(b) Mean read image

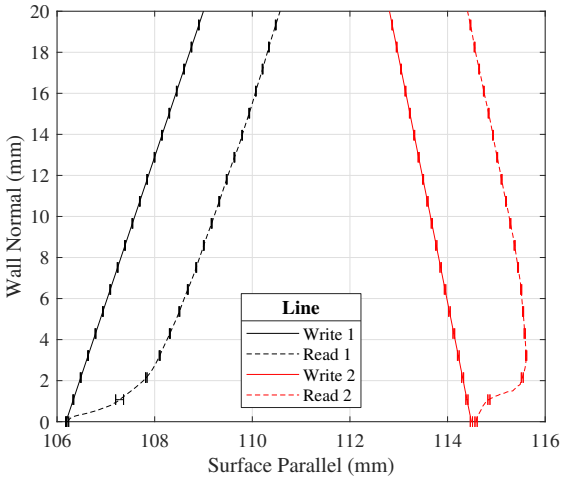

(c) Mean line locations

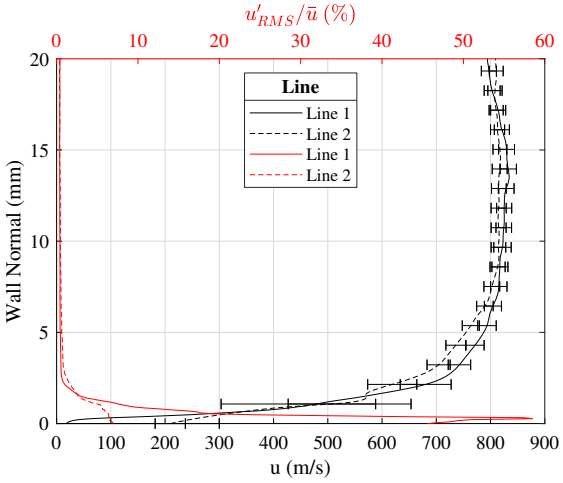

(d) Mean velocity and fluctuation profiles

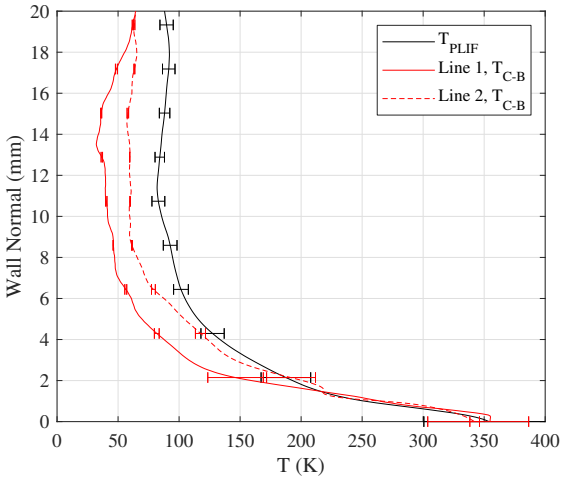

(e) Mean temperature profiles

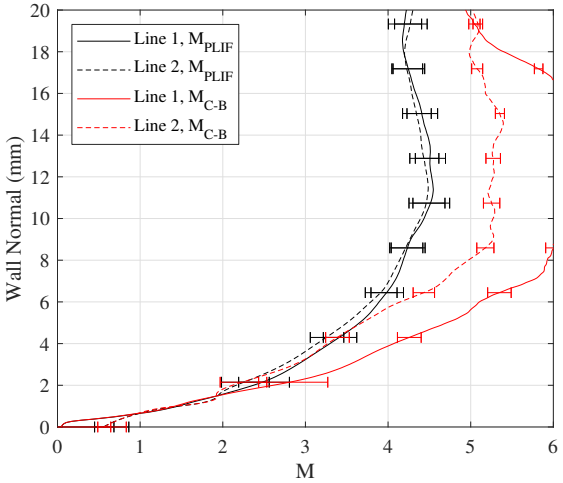

(f) Mean Mach number profiles

Figure 7.105: PLIF MTV, Run 4663: upstream; turbulent trough; plasma on. [7]

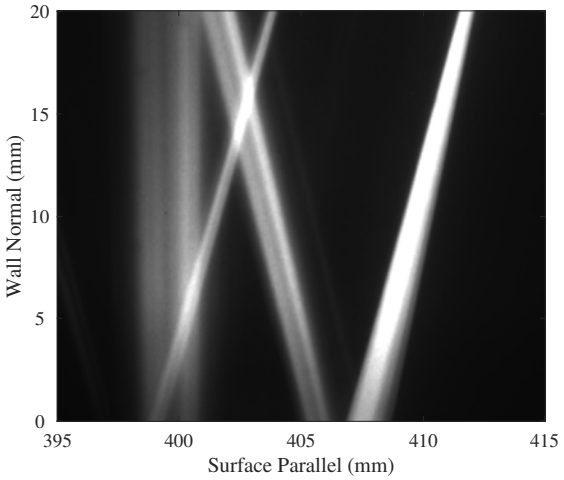

(a) Mean write image

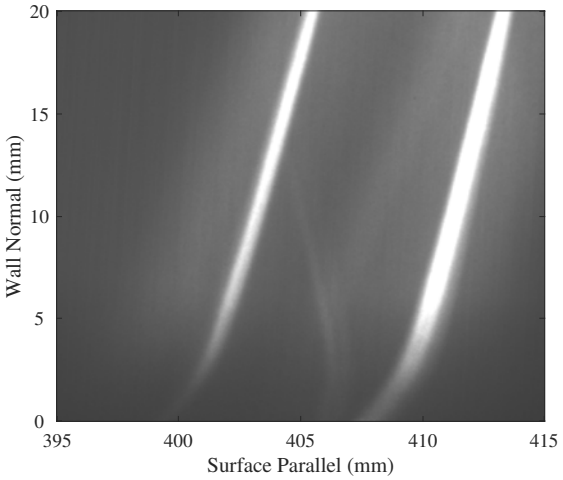

(b) Mean read image

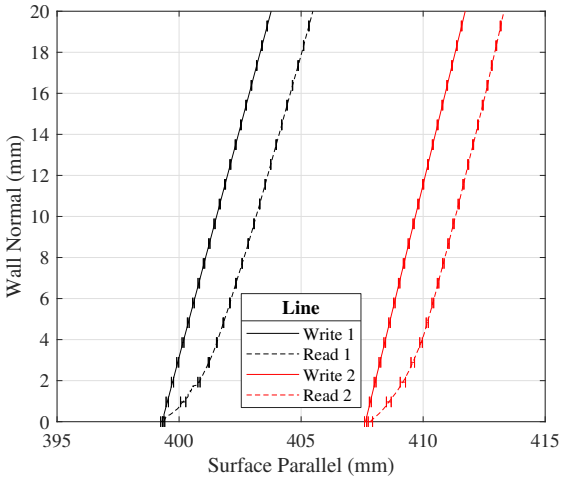

(c) Mean line locations

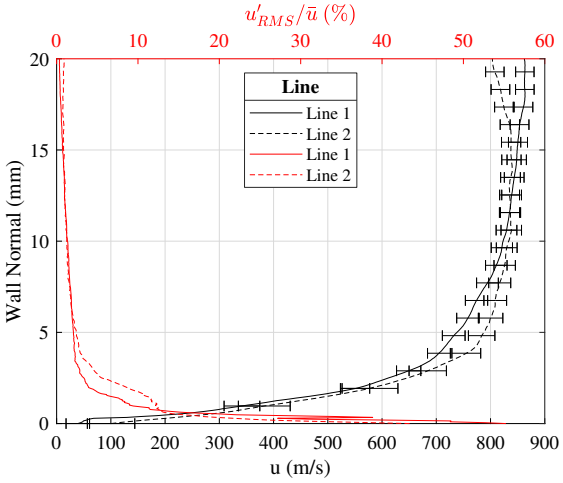

(d) Mean velocity and fluctuation profiles

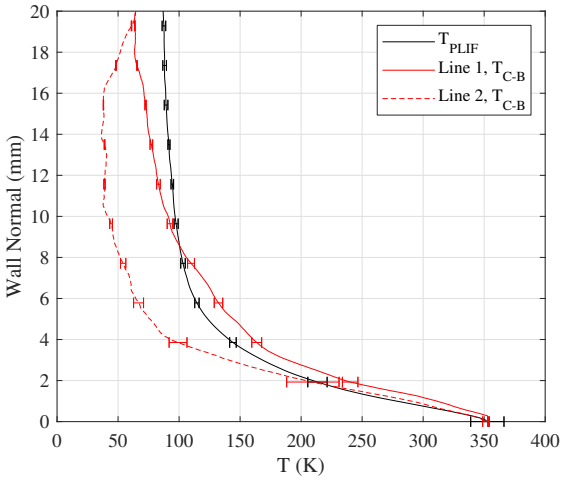

(e) Mean temperature profiles

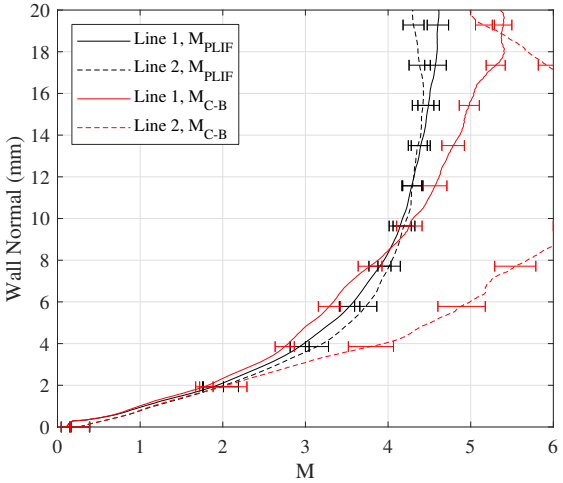

(f) Mean Mach number profiles

Figure 7.106: PLIF MTV, Run 4652: downstream; laminar; plasma off. [7]

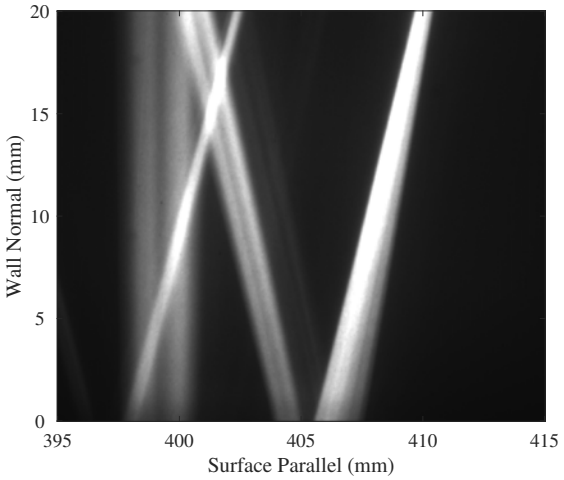

(a) Mean write image

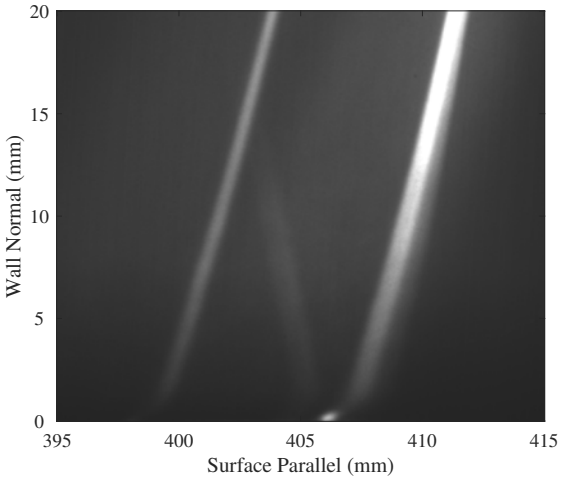

(b) Mean read image

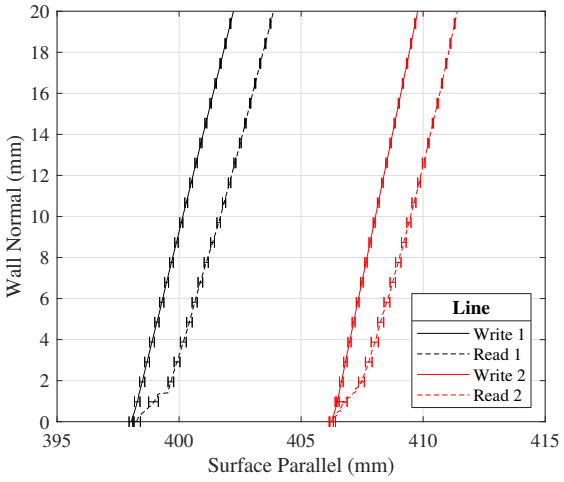

(c) Mean line locations

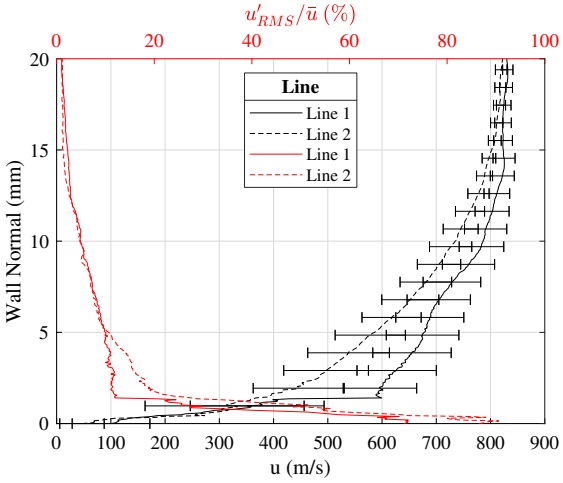

(d) Mean velocity and fluctuation profiles

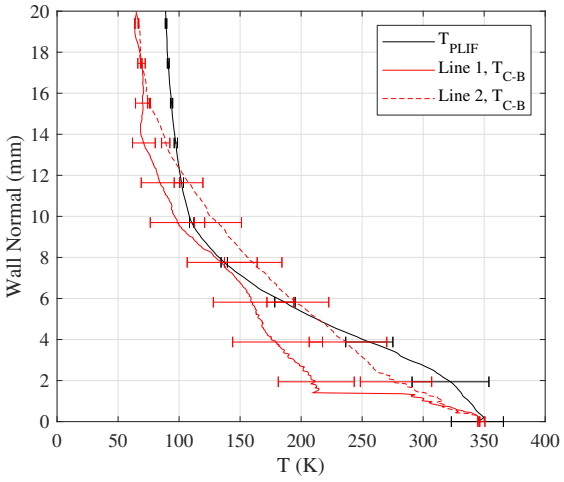

(e) Mean temperature profiles

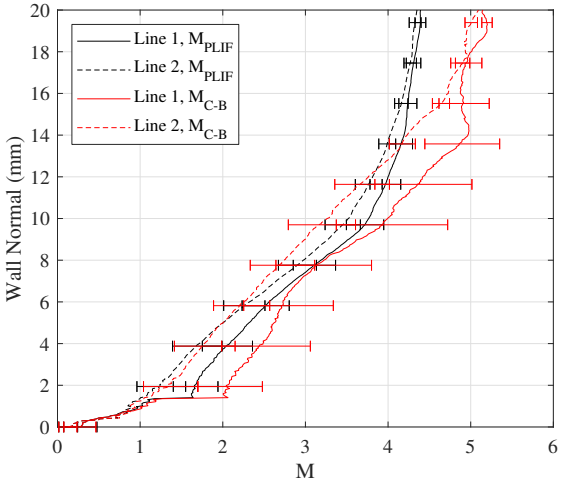

(f) Mean Mach number profiles

Figure 7.107: PLIF MTV, Run 4654: downstream; turbulent wake; plasma off. [7]

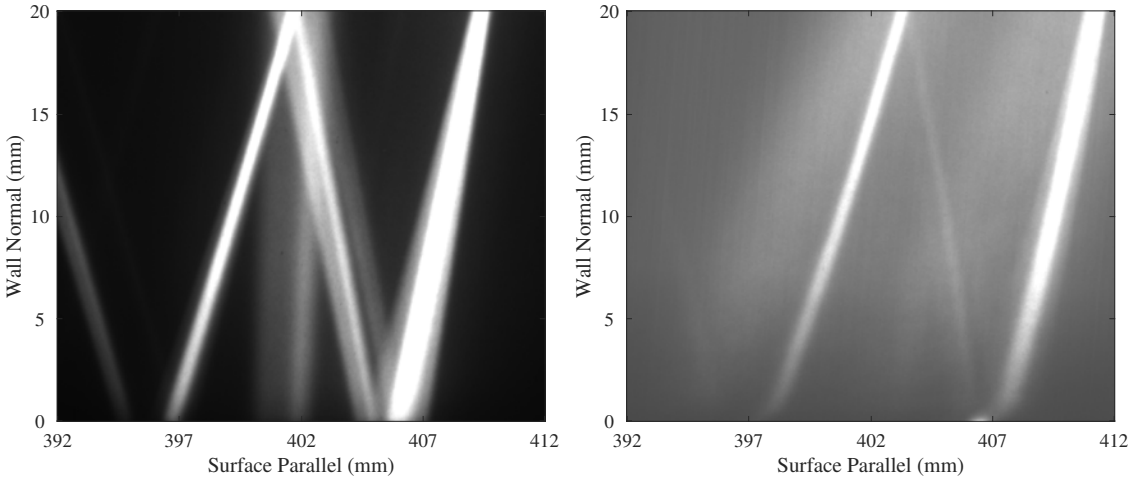

(a) Mean write image

(b) Mean read image

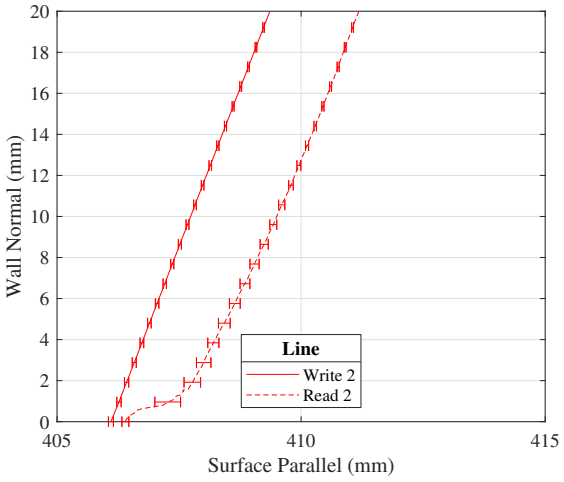

(c) Mean line locations

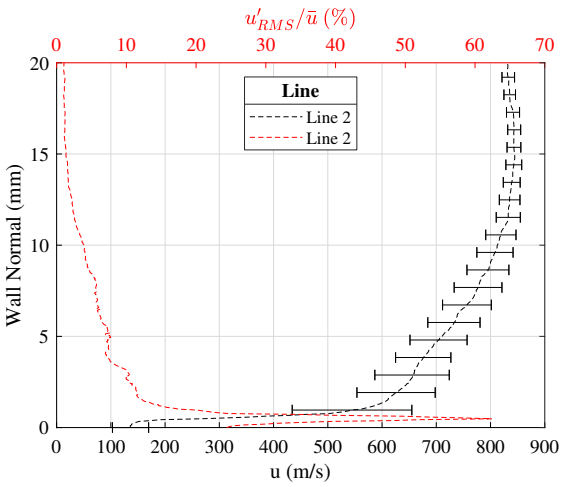

(d) Mean velocity and fluctuation profiles

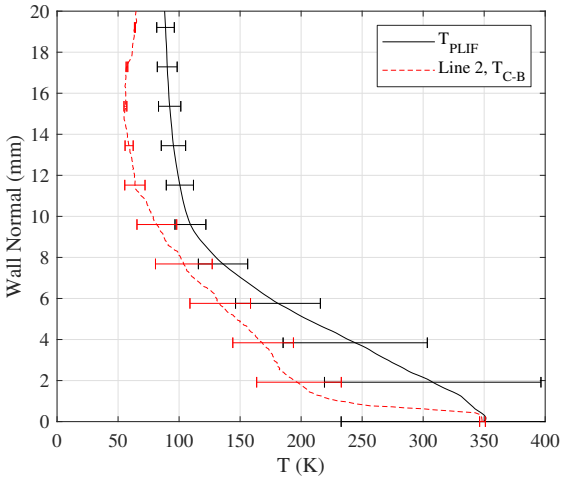

(e) Mean temperature profiles

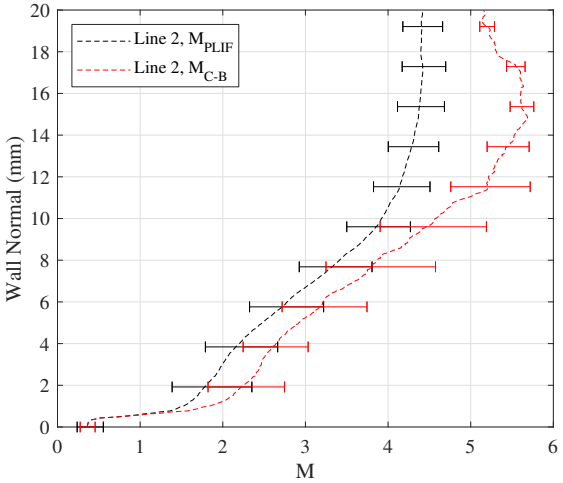

(f) Mean Mach number profiles

Figure 7.108: PLIF MTV, Run 4657: downstream; turbulent trough; plasma off. [7]

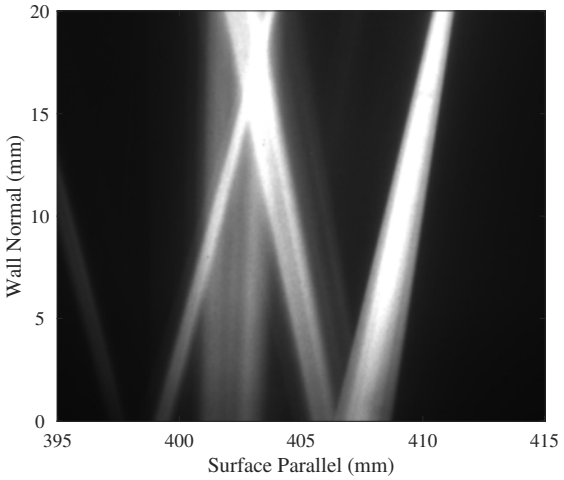

(a) Mean write image

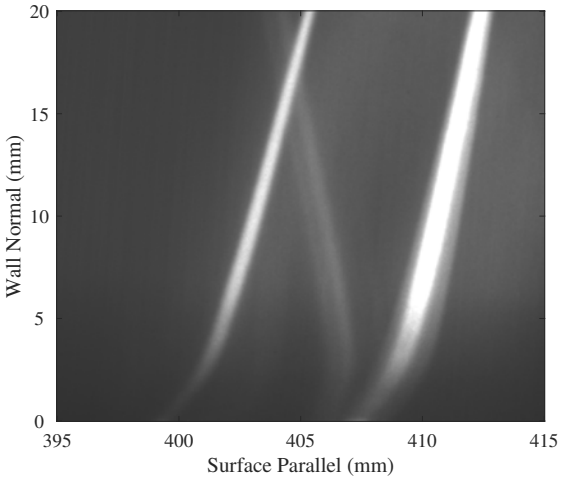

(b) Mean read image

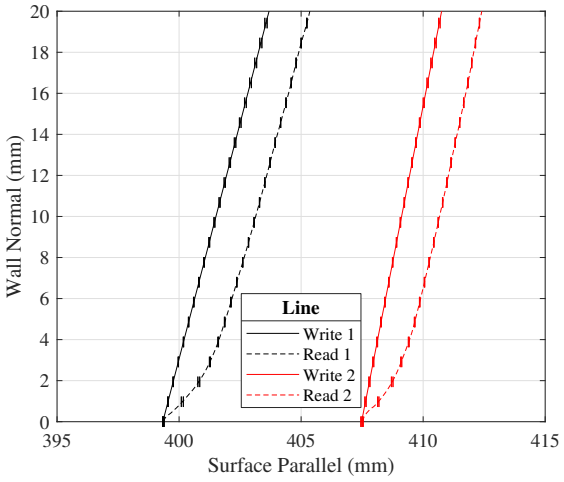

(c) Mean line locations

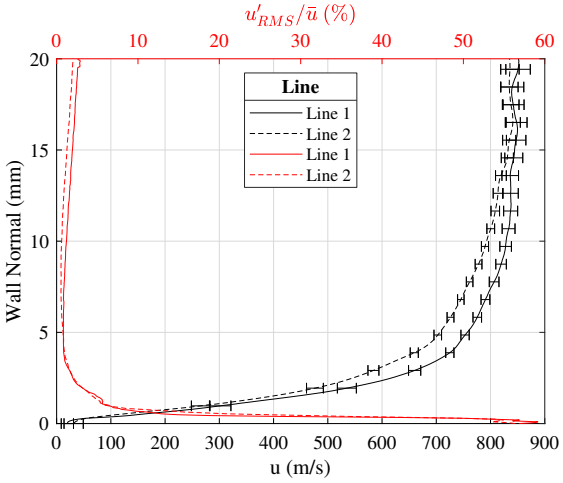

(d) Mean velocity and fluctuation profiles

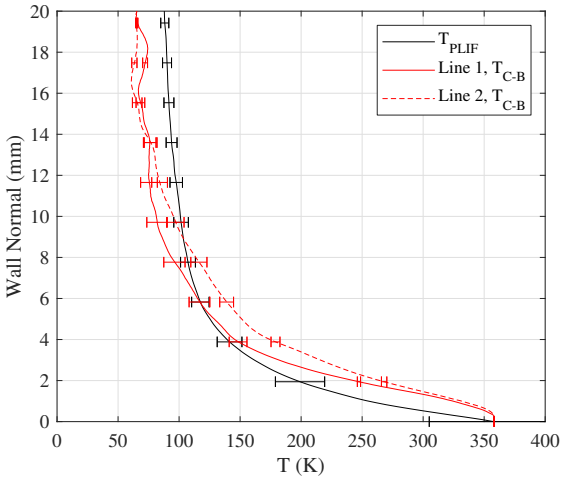

(e) Mean temperature profiles

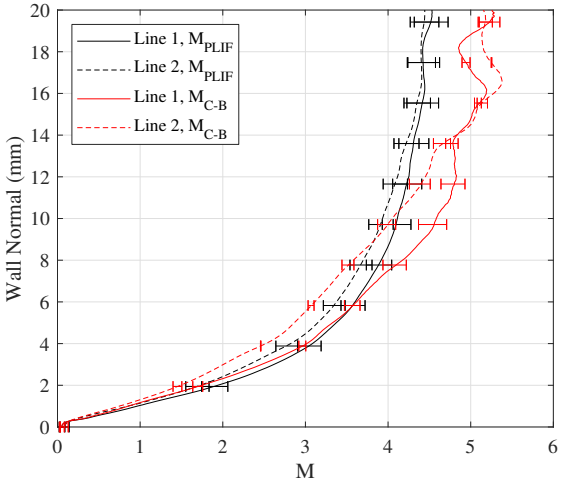

(f) Mean Mach number profiles

Figure 7.109: PLIF MTV, Run 4653: downstream; laminar; plasma on. [7]

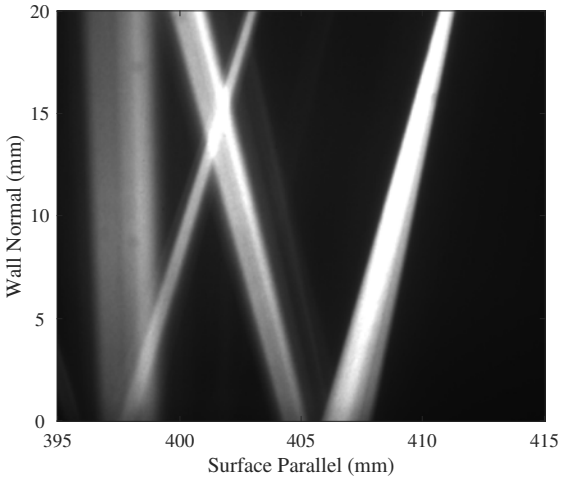

(a) Mean write image

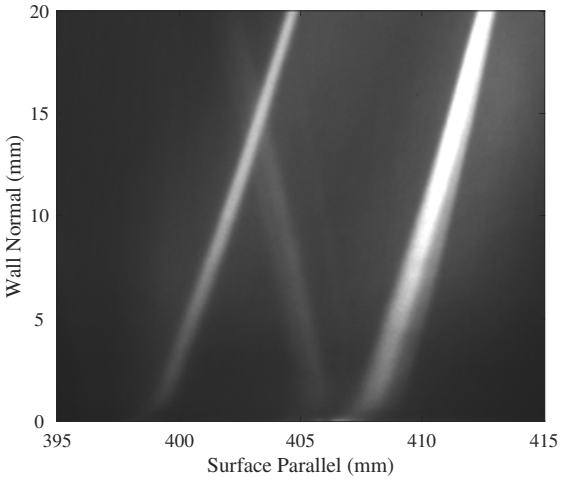

(b) Mean read image

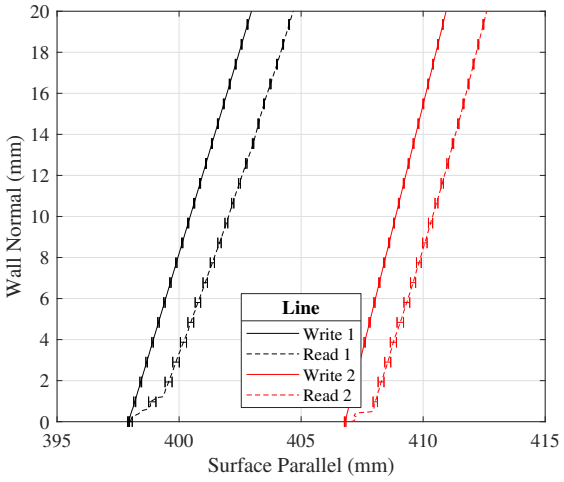

(c) Mean line locations

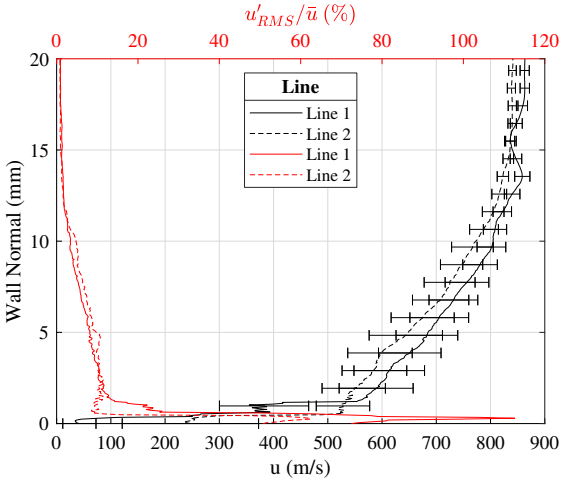

(d) Mean velocity and fluctuation profiles

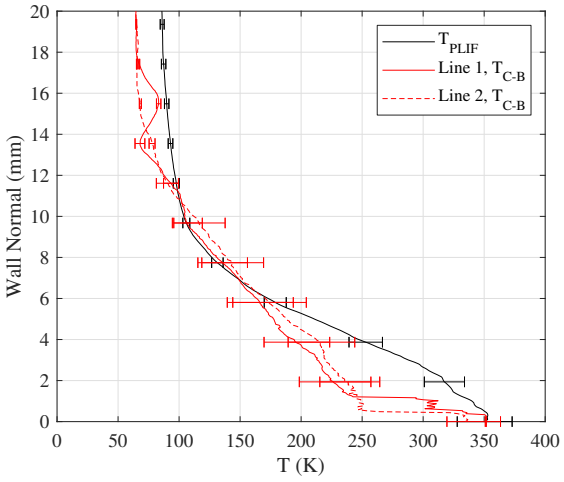

(e) Mean temperature profiles

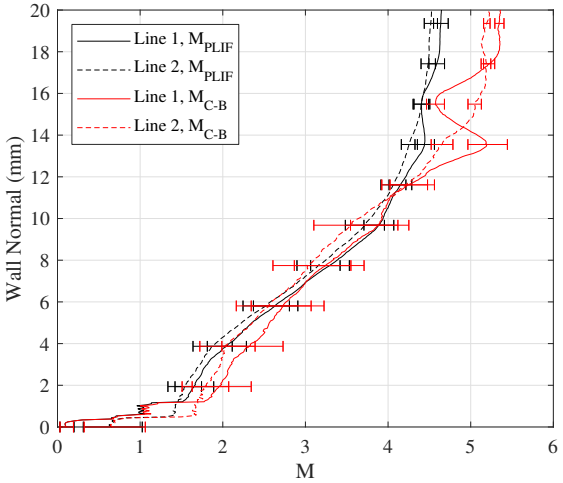

(f) Mean Mach number profiles

Figure 7.110: PLIF MTV, Run 4655: downstream; turbulent wake; plasma on. [7]

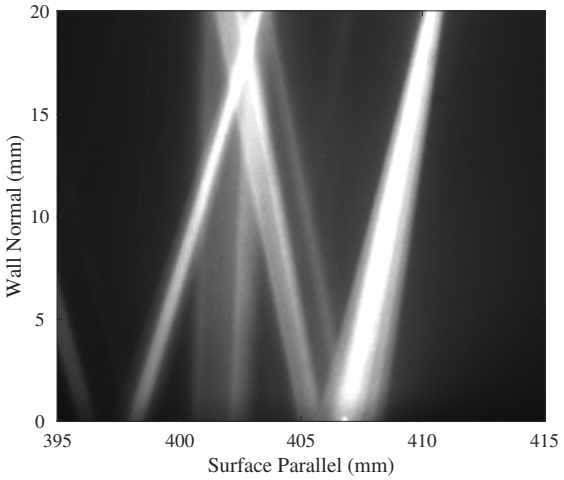

(a) Mean write image

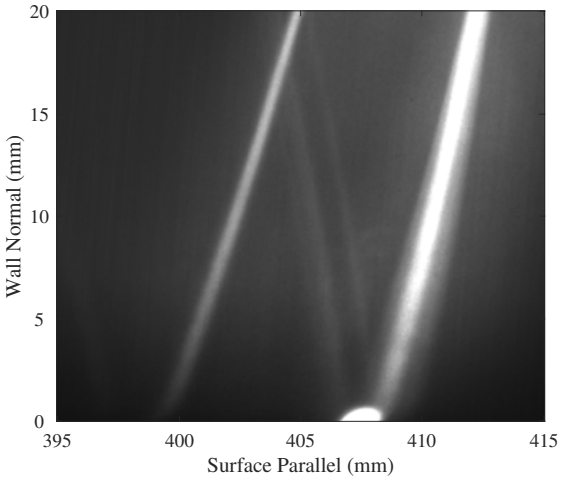

(b) Mean read image

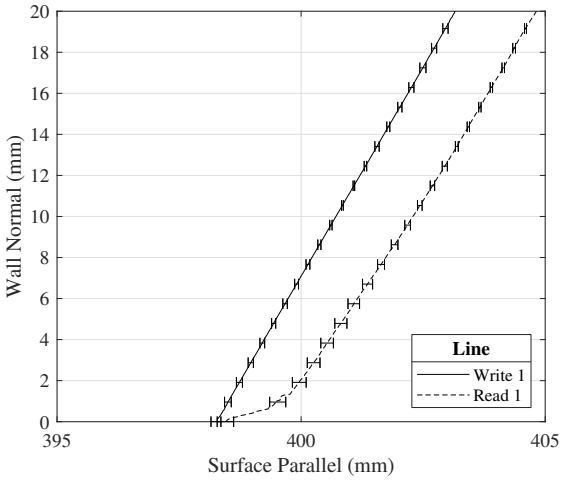

(c) Mean line locations

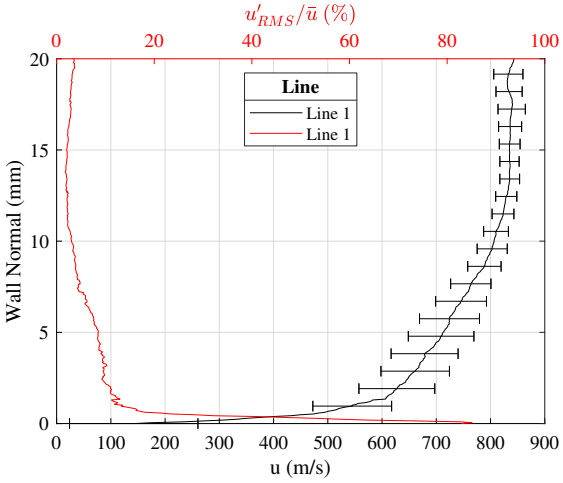

(d) Mean velocity and fluctuation profiles

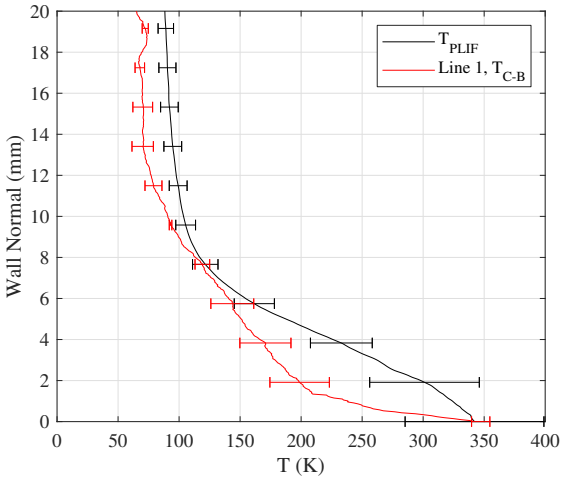

(e) Mean temperature profiles

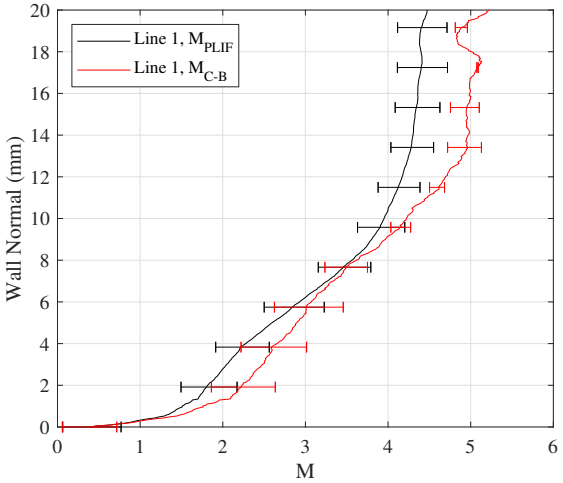

(f) Mean Mach number profiles

Figure 7.111: PLIF MTV, Run 4656: downstream; turbulent trough; plasma on. [7]

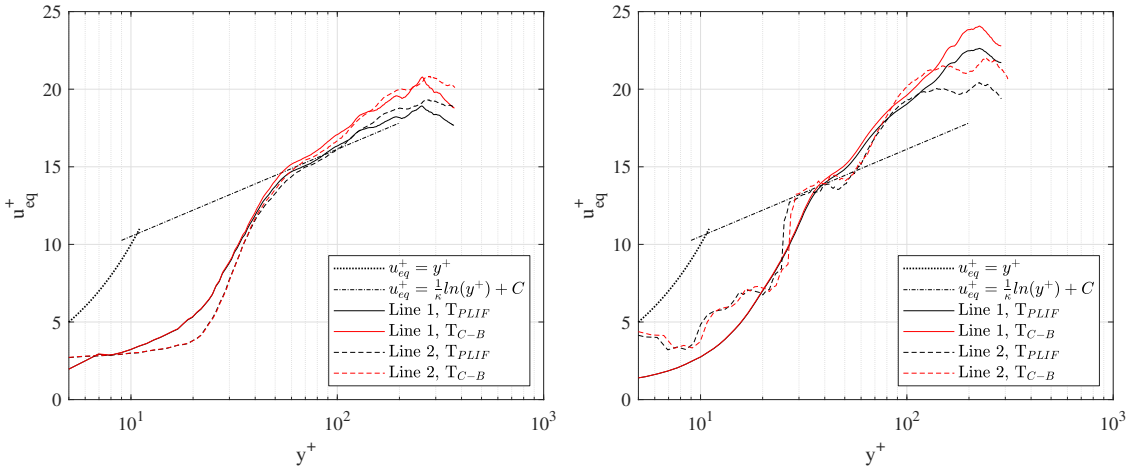

(a) Upstream, plasma off, $\tau_w \approx 23$Pa

(b) Upstream, plasma on, $\tau_w \approx 15.5$Pa

(c) Downstream, plasma off, $\tau_w \approx 13$Pa

(d) Downstream, plasma on, $\tau_w \approx 13$Pa

Figure 7.112: PLIF MTV inner variable plots, wake. [7]

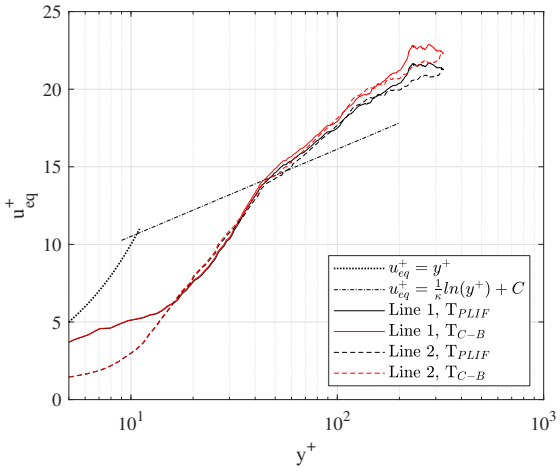

(a) Upstream, plasma off, $\tau_w \approx 17$Pa

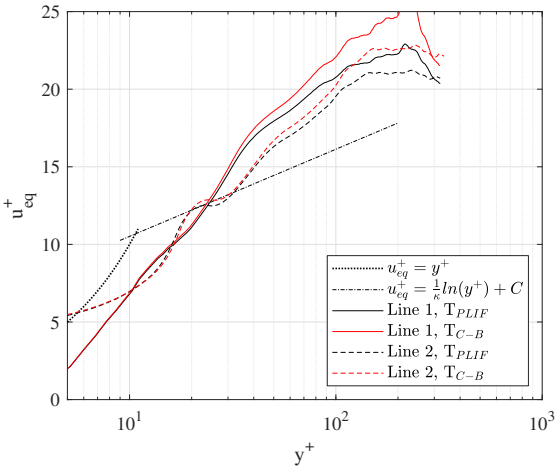

(b) Upstream, plasma on, $\tau_w \approx 16.5$Pa

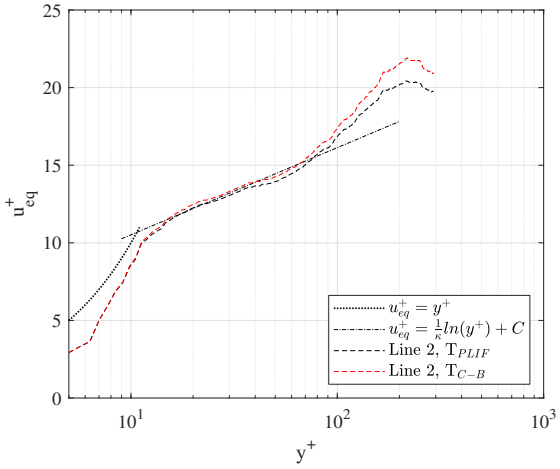

(c) Downstream, plasma off, $\tau_w \approx 15.5$Pa

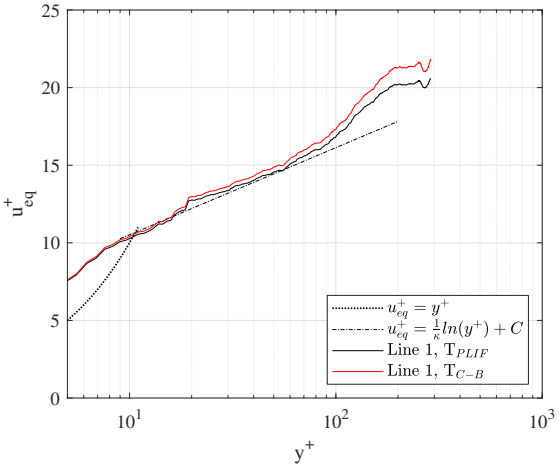

(d) Downstream, plasma on, $\tau_w \approx 15$Pa

Figure 7.113: PLIF MTV inner variable plots, trough. [7]

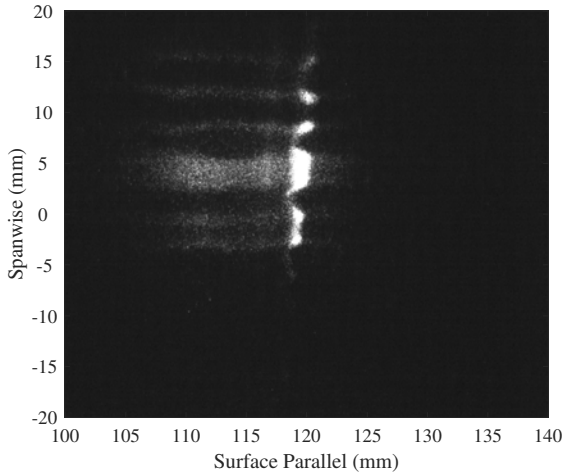

(a) Upstream instantaneous read image

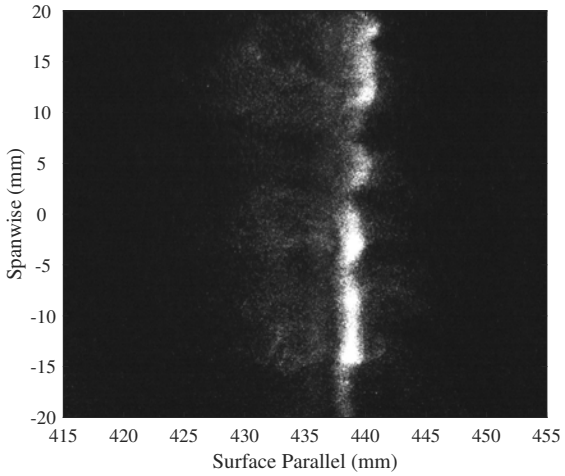

(b) Downstream instantaneous read image

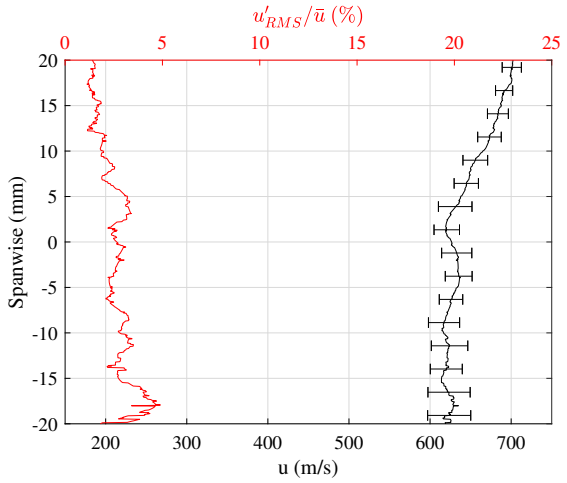

(c) Upstream laminar profiles

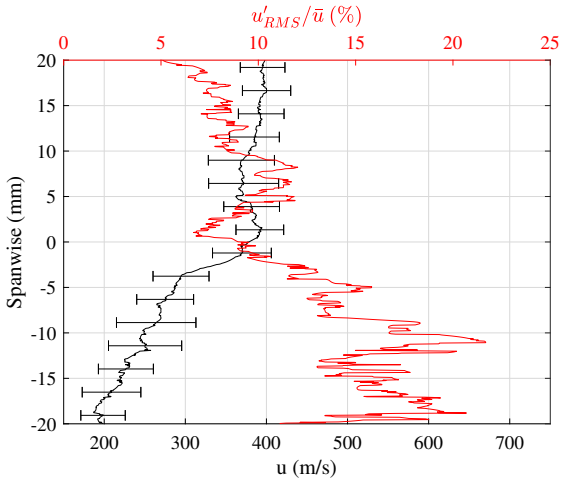

(d) Downstream laminar profiles

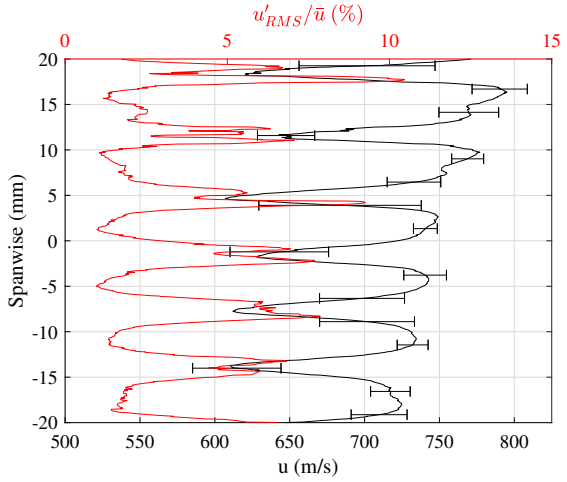

(e) Upstream turbulent profiles

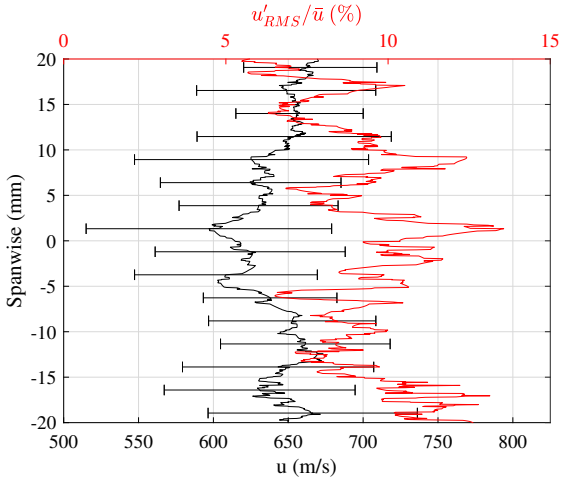

(f) Downstream turbulent profiles

Figure 7.114: Spanwise PLIF MTV. [7]

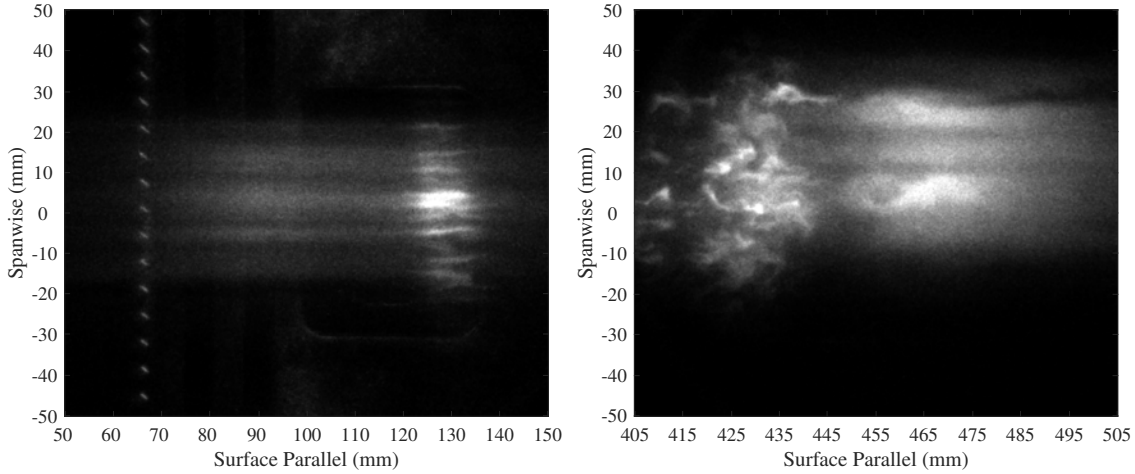

(a) Upstream (b) Downstream

Figure 7.115: Spanwise PLIF visualization. [7]

7.2.6 Comparisons

This section follows from Broslawski [7]. The purpose of this section is to compare data collected for the same parameter by different techniques. This process can validate measurements, provide a more detailed picture of the flow physics, or motivate further work. Some comparisons were made in the above sections as each result was introduced, but here the results are directly plotted alongside one another; that being said, greater context and analysis of each individual experiment are provided in its corresponding section above. The goal here is to provide better understanding not just of the data, but the inherent strengths and weaknesses of each diagnostic.([7])

7.2.6.1 Off Body Variables

Perhaps the variables of greatest interest to a turbulence model are the velocity and temperature, and by extension the Mach number. Four independent methodologies were used in this report to predict or measure these fundamental parameters: the numerical boundary layer solver; PLIF thermometry; PLIF velocimentry; and Pitot probe. Data for each of these techniques are plotted for the laminar, turbulent (wake), and turbulent (trough) cases in Figures 7.116-7.118 respectively; the inner variable plots for the turbulent cases with and without the plasma are shown in Figures 7.122 and 7.123 respectively. As was done in their corresponding sections, the Crocco-Busemann relation was used to relate the Mach number to temperature (Pitot) or velocity to temperature (PLIF velocimetry), which allowed these techniques to produce velocity, temperature, and Mach number plots. For the PLIF measurements, when the temperature was derived from velocity via Crocco-Busemann, the label "MTV" was used, and when it came from the direct PLIF thermometry campaign the label "$\text{PLIF}_{\text{Them}}$" was used. Recall from Section 7.2.3.5 that the Pitot probe made measurements 140mm from the leading edge in the "Front" test location and observed a weak shock due to the static pressure tap $\sim$ 6mm from the surface, and that for "Turbulent" runs M_e was taken $\sim$ 30mm above the surface, though for consistency with other techniques only 20mm of data are shown here. This meant, in general, the Pitot data might not be fully converged on its edge condition in the plots shown, even though theoretically no boundary layer should have been $>$ 15mm. Also, the "Trough" PLIF measurements were conducted between the first and second trip, while the Pitot's "Trough" measurements were conducted between the second and third trip. Finally, the for the "Turbulent/Front" cases r_{turb} was used in T_{aw} in the Crocco-Busemann equation when this location was only transitional, an approximation born of necessity. It is important to remember the variable directly measured by the experimental techniques: Pitot probes measure Mach number; PLIF thermometry temperature; PLIF MTV velocity; PLIF thermometry and MTV combine to provide Mach number. Any variables produced outside of these fundamental results are subject to assumptions. Perhaps the most relevant is the definition of boundary conditions for the wall and freestream temperature used in the Crocco-Busemann equation. Recall that in both cases T_w was taken from experimental measurements, and T_e (and u_e, for the Pitot probe implementation) came from the NALDAQ and oblique shock relations. Analogously, T_e was set in the PLIF thermometry results to provide realistic values for T_w, which, for any of the reasons discussed in Section 7.2.5.1 and in [212], led to a higher-than-expected value for T_e. All of this to say that when comparing the data, the best gauge of the performance of a technique is to study its original and unprocessed form. Otherwise, one must be cognizant of the limitations of the assumptions applied. Finally, note that

deviations from the expected theory, especially in the MTV temperature results in Figures 7.116(f) and 7.121(e) and in the inner variable plots in Figures 7.122 and 7.123 were discussed in their corresponding sections. Briefly, issues with the former stemmed from unexpected shaped of the MTV profile and issue with the later may be due to wake, transition, or low density effects in the boundary layer, continued turbulence development, or issues with Clauser's method for estimating τ_w. ([7])

The analysis begins with the identification of a global trend, that the numerical boundary layer solver tended to under predict the size of the boundary layer, and miss the gradual slope from the boundary layer to the freestream. This was unfortunate but not surprising, as it was a purely theoretical code which neglected: leading edge bluntness; entropy layer effects; shock curvature; viscous/inviscid interaction pressure features at the leading edge; transition; Mach waves due to seams at junctions in the test article; and for turbulent flows trip effects (wakes, shock structure, shear layer, 3D effects). In practice, no doubt some of these features were more important than others, but any one of them would complicate the final result. It is tempting to view the numerical results as the "correct answer", but one must recognize their own unique limitations. The experimental analysis should begin with the laminar plots in Figure 7.116. The velocity data show excellent agreement between all three velocimetry techniques. The Pitot data, derived from the Mach number, captured the same shape observed in the MTV data, with the exception of the bump at $\sim$ 6mm in the "Front" test location due to the static pressure port. Between $\sim 2-5$mm, the experimental techniques had decent agreement with the PLIF thermometry data. Caution should be exercised before declaring the MTV and Pitot results in complete agreement as both rely on Crocco-Busemann assumptions to produce temperature data and were forced to effectively the same T_e; this forcing was validated by the Pitot measurements for M_e matching the theoretical result far from the wall, even with the trips installed. The agreement, especially in the "Front" location, was striking. Thus it makes sense that parameters that agreed well in both u and T should match in M. The nonphysical result in the MTV data at the "Back" test location stemmed from the unique shape of the velocity profile via a process described in Section 7.2.5.3. As expected, the PLIF and Pitot Mach numbers agree well in the boundary layer, but the PLIF result under predicts the Pitot-validated M_e, again pointing to a problem in T_e from the PLIF thermometry data. The turbulent/wake data from Figure 7.117 are analyzed next. Immediately one sees that the PLIF data completely misses the trips' wake structure in the front test location. This was unexpected, but it was hypothesized that the Pitot data was especially sensitive to this pressure effect in a way the laser diagnostics were not. Alternatively, the Pitot probe may have been large enough to "smear" physics in this complex region, while the PLIF results would have better resolution. In general, the agreement in the velocity data was not as strong as in the "Laminar" case, especially in the "Back" test location. For the "Front" test location, the MTV and $\text{PLIF}_{\text{Therm}}$ temperature results had decent agreement between $\sim 2-6$mm, and the Pitot data eventually fell between them from $\sim 6-10$mm. Any discrepancies between these MTV and $\text{PLIF}_{\text{Therm}}$ data were masked in the Mach number, which agreed analogously up to $\sim$ 10mm. PLIF thermometry of the fully turbulent boundary layer in the back location produced a thermal boundary layer far larger than that predicted by either Crocco-Busemann technique. That being said, at least one PLIF line did agree with the Pitot data to within the uncertainty. As expected then, this line produced decent agreement in the Mach

number profiles. The turbulent/trough data in Figure 7.118 performed the best out of the three sets described. The Pitot probe over predicted the PLIF MTV data in the "Front" location, but it was by a consistent margin; note that the trip effect was diminished in the trough as compared to the wake. However, the PLIF MTV, Pitot, and even numerical velocity data in the back location matched almost perfectly. With such excellent agreement in both cases, one would expect the temperature profiles to match, and indeed they did. While the Pitot data actually more closely matched the PLIF thermometry result through the boundary layer in the "Front" location, all three techniques agreed well up to $\sim$ 10mm. In the "Back" location, MTV data agreed nearly perfectly with the simulation, and the Pitot data split the MTV and $PLIF_{Therm}$ results. This made sense, because the simulation and MTV data matched so closely, so the Crocco-Busemann derived temperature should fit the computational result; this validated the Crocco-Busemann approach. The temperature profile's shape from all four curves matched. The Mach number fit similarly excellently; all three experimental techniques agreed at both the front and back locations up to $\sim$ 10mm. ([7])

It is unclear why the trough data outperformed the wake data. To check if it was simply a coincidence, the plasma on data is included in Figures 7.119 through 7.121, taking advantage of the fact that the plasma had no tangible effect on these parameters. The results not only support the aforementioned trends, but in fact the agreement was even better in some cases. It was interesting to note the slight presence of the shear layer in the front test location in the laser diagnostics results; this validated the physics captured by the Pitot probe, but it was unclear why the result was only visible in the plasma on data. Finally, for completeness, the inner variable plots from the plasma "Off" and "On" cases are included in Figures 7.122 and 7.123 respectively. Due to the variability inherent to Clauser's method and the heavy scaling applied, these data are not too instructive. For clarity, data from the transitional flows in the "Front" test location were not shown, as the scaling only was appropriate for turbulent flows. (Broslawski [7].) Overall these results were highly encouraging. They suggested that with proper scaling in the freestream, all three experimental techniques were working well; the simulation results were somewhat lacking owing to their known simplicity. The agreement in the boundary layer especially was strong. The results underscored the importance of confirming results as every tool has its own strengths and weaknesses: the simulations could not capture all of the flow's physics; the PLIF thermometry and Crocco-Busemann approach were both beholden to their scaling; the Pitot probe was very sensitive to pressure features. Even for a flat plate boundary layer, these data show accurately quantifying the flow requires the application and deep understanding of many techniques. ([7])

7.2.6.2 Surface Streaks

Oil flow visualization and IR thermography shared the ability to visualize fluid-wall interactions across the 2D region of interest. Summarizing the mechanisms by which this occurs, oil flows from regions of high pressure to regions of low pressure, such as along the test article or from wake to trough, while IR thermography, analogously, shows heating where wall shear stress is elevated, such as from vortical structures or turbulence. Both techniques are dynamic, able to manifest changes in the interaction over time, so for this reason traces were taken once the flow had time to establish a trend (of particular concern for the oil flow in the low density ACE tunnel) and then at the end of the data collection cycle; thus traces were taken from the third ("Early")

and final ("End") test time from the figures in the corresponding sections for a total difference of $\sim$ 10s. The IR data was normalized just like the oil flow results, and the Stanton number data was used as it clearly showed the wakes and troughs. (([7])

The results for the three test locations are shown in Figure 7.124. At all three locations, the oil flow and IR streaks were offset by half a wavelength such that a peak in the oil flow signal was in a trough in the Stanton number. The IR results in Figure 7.124(a) show the heating falls regularly behind the trips at both the start and end of the test, implying that high signal in IR corresponds to the trips' wakes. Visual inspection of the oil flow data in Section 7.2.3.1 shows that everywhere but a portion of the "Front" test location, the oil collected in the troughs. Taken together, this implied that the wakes formed by the trips caused higher pressures due to their velocity deficit (see also Section 7.2.5.4) which pushed oil into the troughs and led to increased skin friction due to turbulent heating. These trends persisted along the length of the test article, but by the "Back" test location their effect was diminished as the flow become more isotropic. One trace defied the analysis just introduced, the "End" oil flow trace at the "Front" test location. Recall from Section 7.2.3.1 how the transition process became visible once the bulk of the oil had been removed from the plate. It remained unclear if the unexpected, in some places inverse, trends were due to a thin oil residue being left behind by the flow or just the ability for weaker trends to be given time to manifest, but nevertheless here one can see that the peaks were produced not only offset half a wavelength from those from the "Early" trace, but they lined up well with the peaks in the IR data. This suggested that the trips' wakes were indeed being visualized with the oil flow technique at this upstream location at the end of the run.([7])

7.2.6.3 Wall Variables

Here predictions, measurements, and calculations of the wall heat flux, Stanton number, and wall shear stress are compared. Data was provided from the numerical boundary layer solver, IR thermography, Pitot probe, and PLIF velocimetry. These results, especially those for the wall shear stress, were discussed in great detail in the aforementioned sections. The goal here was to visualize the trends in the data to further support these arguments.

Data were provided for both plasma "Off and On" cases under the understanding that its presence had little impact on these parameters. For the IR data, the final 2D frame for which trace data was shown in Section 7.2.3.3 was averaged along its span to provide a streamwise plot of the variable of interest; this trace was then averaged with its corresponding plasma "Off/On" partner to attempt to account for the large run-to-run variability in these parameters, especially the heat flux. Recall that the IR results were limited by the placement of the thermocouples, and that the Stanton number for the turbulent case near the leading edge was suspect as the flow was likely transitional, but the turbulent recovery factor was used. Finally, the simulations were extended to cover the range observed with the IR camera using the same settings as in Section 7.2.1 and a "Gradient Diffusion" heat flux calculation with the Cebeci-Smith turbulence model [43]. ([7])

The IR data, Figure 7.125(a-b), are discussed first. The data showed that near the leading edge the experiment did not match the simulations. For the turbulent case, this could either be attributed to any number of factors, including: the code's inability to actually simulate transition; the physical 3D trip effects; the high heating due to the thin PEEK and closeness to the stainless

steel frame; the exposure of both sides of the PEEK to the flow; the codes constant 350K boundary condition; leaving the test article in the tunnel during preheat; using r_{turb} in the data reduction code for this transitional region; *etc.*. Many of these same arguments could be extended to the laminar case in the same region. However, farther from this dynamic region the results found much greater agreement, especially for the turbulent case. For the laminar case, the code under predicted the heat flux, and thereby the Stanton number, by a factor of two. Some testing showed reducing the wall temperature in the simulation could partially account for this discrepancy; because the heating was already so low in the "Laminar" case and both q_w and St are so sensitive to T_w, a change of only a few Kelvin in T_W could change q_w by $\sim 100\mathrm{W/m^2}$, thereby affecting the perceived difference between the results. Run-to-run repeatability could also partially explain the error; where the laminar data overlap at $\sim 375\mathrm{K}$ there was a large enough discrepancy to include the simulation's results in the margin of error. The turbulent case performed much better, perhaps because the large magnitude of heating better masked discrepancies; a difference of $\sim 100\mathrm{W/m^2}$ is a 50% error if $q_w = 200W/m^2$ but only 10% if $q_w = 1000W/m^2$. In either case, these results were encouraging and showed that given sufficient time for both the simulation and flow to develop past regions of high complexity, the boundary layer solver did provided reasonable predictions of the wall heat flux and Stanton number. ([7])

The shear stress results in Figure 7.125(c) were discussed in Section 7.2.3.6. Summarizing, the laminar results were likely hindered by the assumed plate temperatures, both when analyzing the experimental data and also when setting T_w in the boundary layer solver. The turbulent data were all converging as the flow traveled downstream, which may have been evidence it was not yet entirely fully developed. The results using Clauser's method from the Pitot and PLIF data had close agreement, which was encouraging. Just as for the laminar case, that the Reynolds Average (RA) and van Driest II (VD) techniques data better matched the simulation towards the end of the test domain likely stemmed from the strong agreement in the heat flux at this point; to that end, the discrepancy at the leading edge could well have been due to the assumption of fully developed turbulence at the "Front" test location. It is noted that the boundary layer solver may have been slightly overpredicting τ_w as the boundary layer profile at the "Back" test location did not reach the log layer theory (see Figure 7.6); an alternative explanation may have been the low densities in the ACE tunnel being outside the range for which the Cebeci-Smith model was developed. Details aside, the wall shear stress was likely $5\mathrm{Pa} < \tau_w < 10\mathrm{Pa}$ and $17\mathrm{Pa} < \tau_w < 22\mathrm{Pa}$ for the laminar and turbulent flows respectively. ([7])

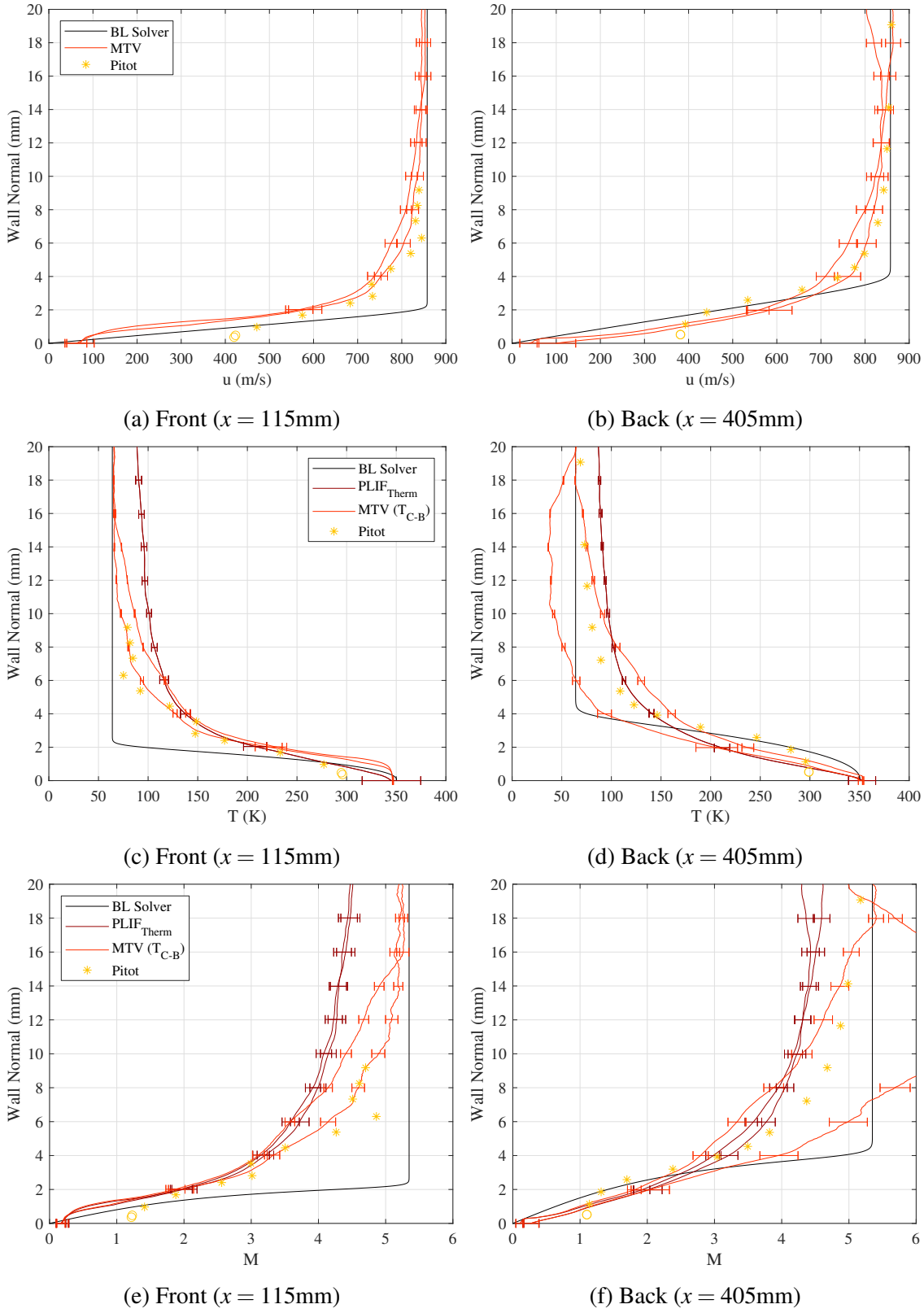

(a) Front ($x = 115$mm)

(b) Back ($x = 405$mm)

(c) Front ($x = 115$mm)

(d) Back ($x = 405$mm)

(e) Front ($x = 115$mm)

(f) Back ($x = 405$mm)

Figure 7.116: Comparison of laminar off body techniques (no plasma); same legend applies to each row. [7]

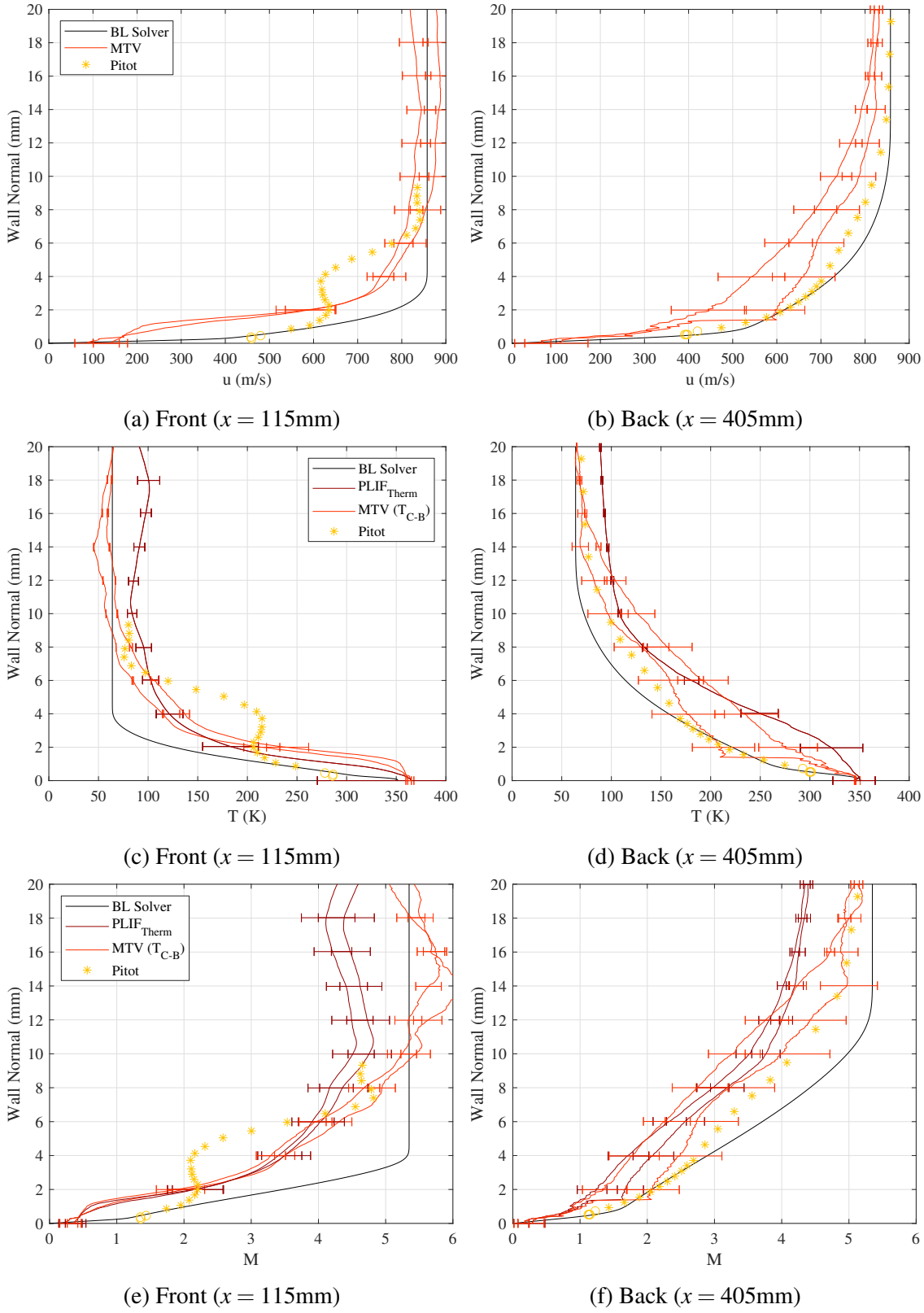

(a) Front ($x = 115$mm)

(b) Back ($x = 405$mm)

(c) Front ($x = 115$mm)

(d) Back ($x = 405$mm)

(e) Front ($x = 115$mm)

(f) Back ($x = 405$mm)

Figure 7.117: Comparison of turbulent off body techniques (wake, no plasma); same legend applies to each row. [7]

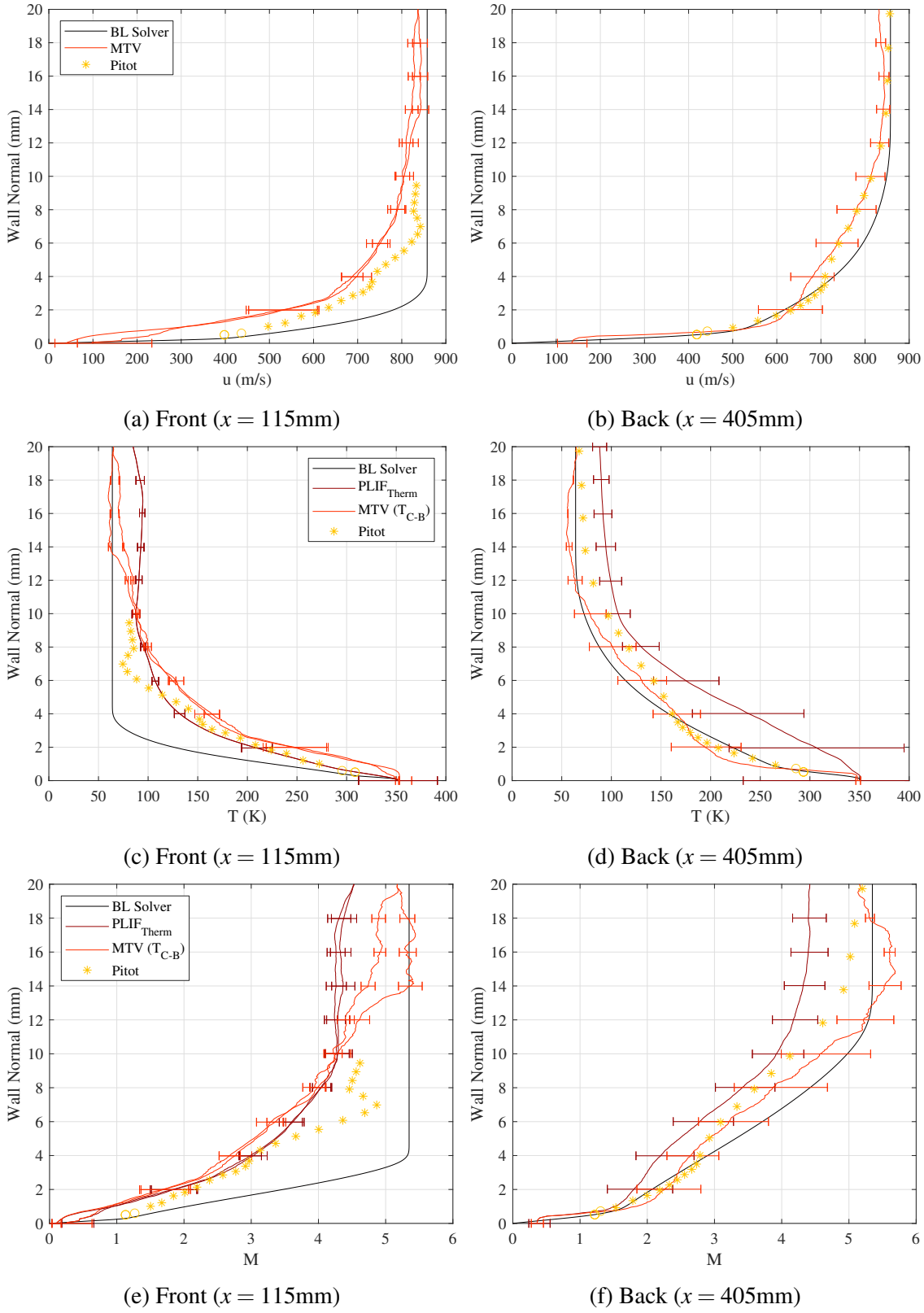

(a) Front ($x = 115$mm)

(b) Back ($x = 405$mm)

(c) Front ($x = 115$mm)

(d) Back ($x = 405$mm)

(e) Front ($x = 115$mm)

(f) Back ($x = 405$mm)

Figure 7.118: Comparison of turbulent off body techniques (trough, no plasma); same legend applies to each row. [7]

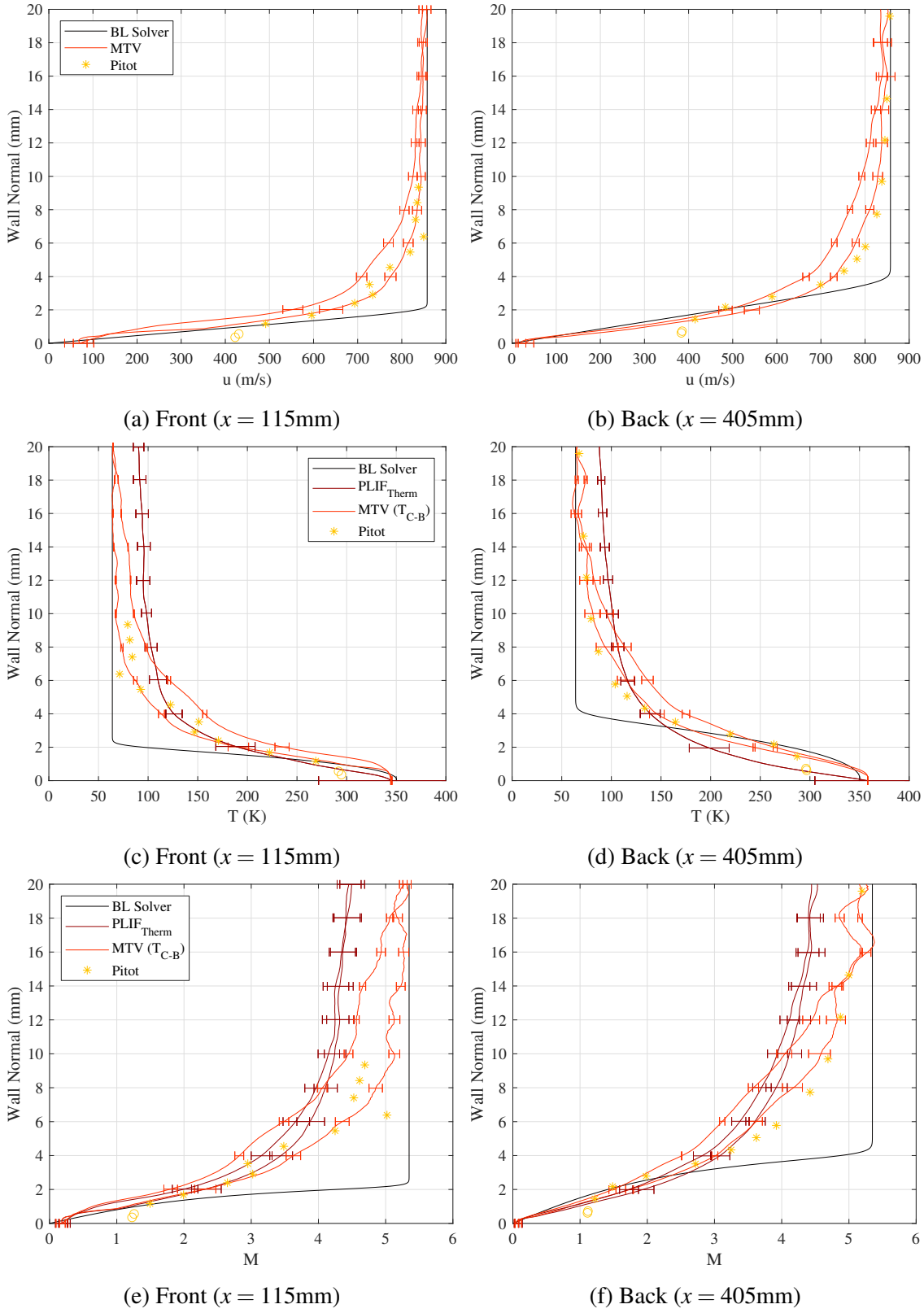

(a) Front ($x = 115$mm)

(b) Back ($x = 405$mm)

(c) Front ($x = 115$mm)

(d) Back ($x = 405$mm)

(e) Front ($x = 115$mm)

(f) Back ($x = 405$mm)

Figure 7.119: Comparison of laminar off body techniques (plasma); same legend applies to each row. [7]

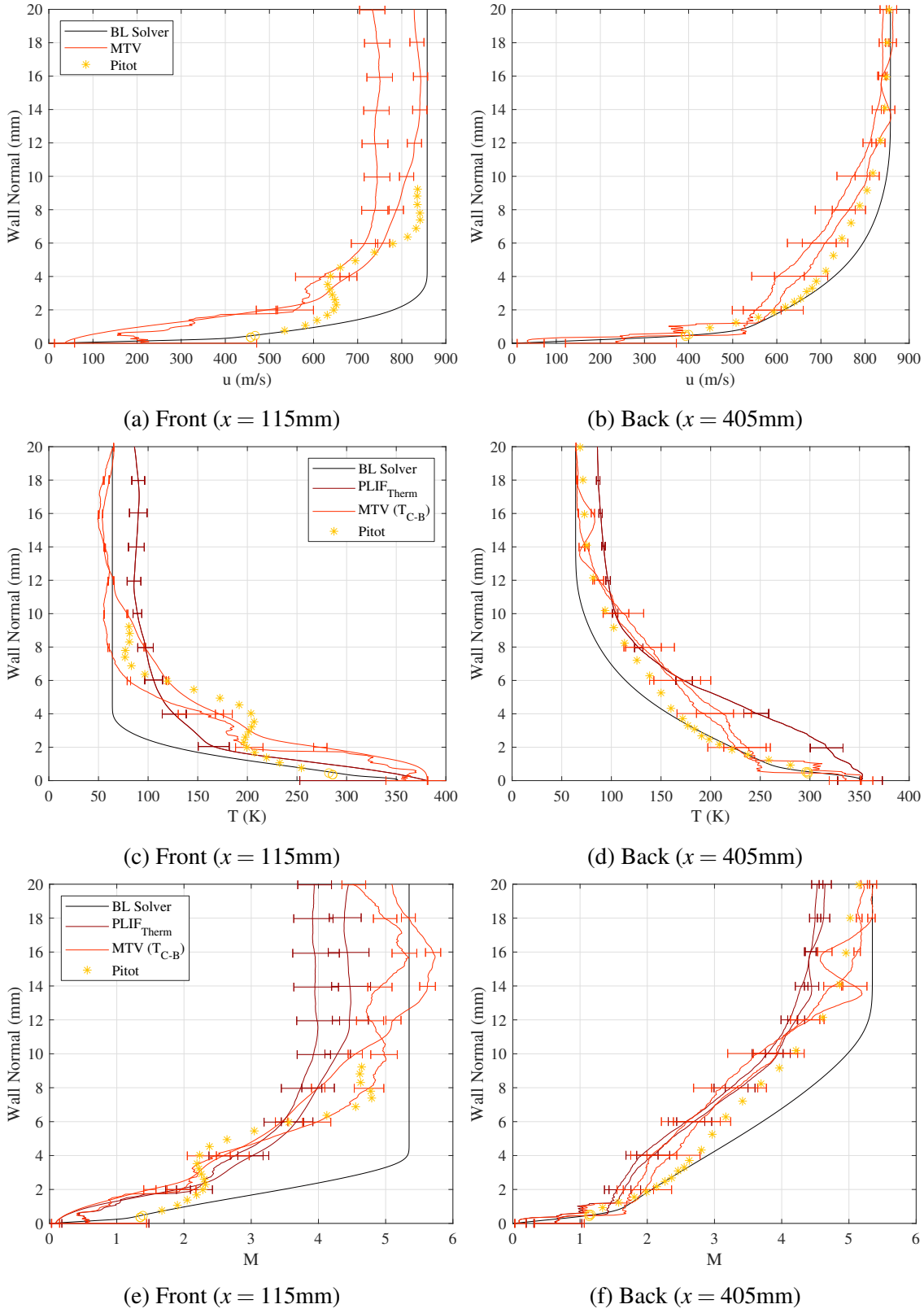

(a) Front ($x = 115$mm)

(b) Back ($x = 405$mm)

(c) Front ($x = 115$mm)

(d) Back ($x = 405$mm)

(e) Front ($x = 115$mm)

(f) Back ($x = 405$mm)

Figure 7.120: Comparison of turbulent off body techniques (wake, plasma); same legend applies to each row. [7]

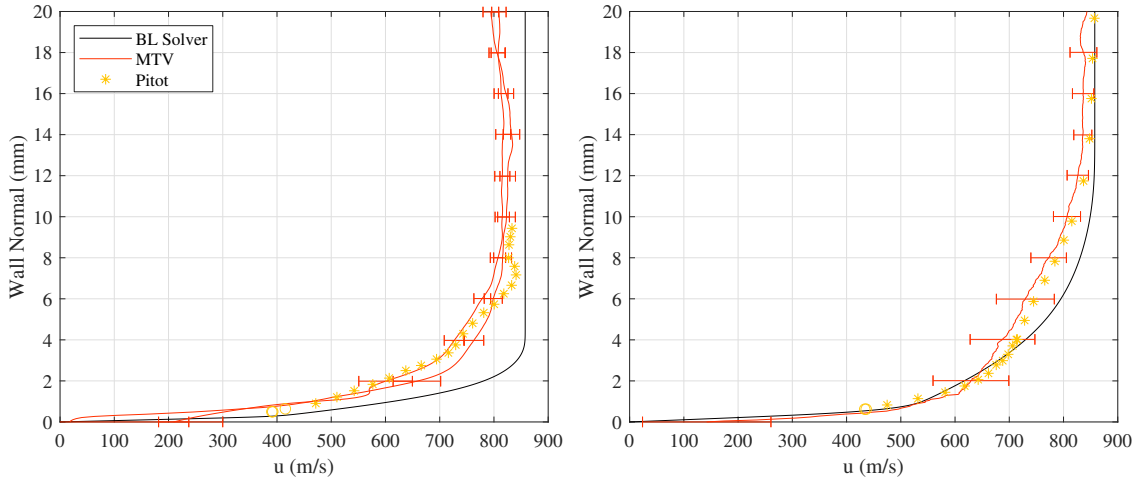

(a) Front ($x = 115$mm)

(b) Back ($x = 405$mm)

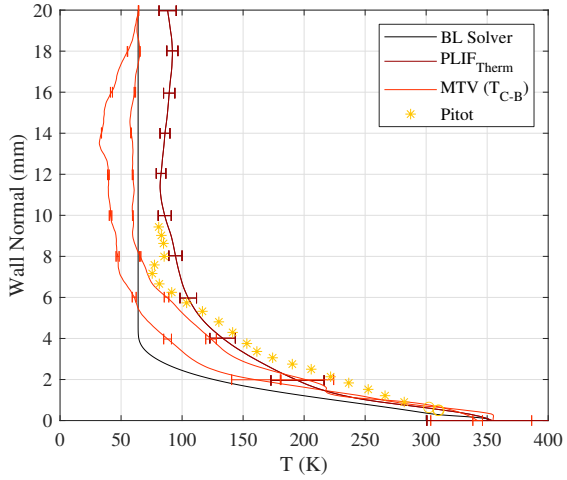

(c) Front ($x = 115$mm)

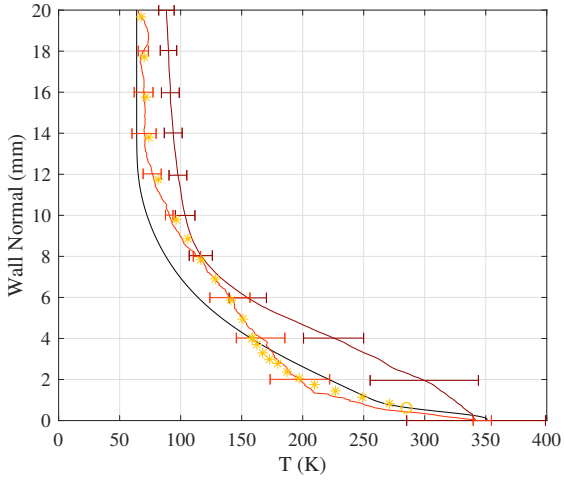

(d) Back ($x = 405$mm)

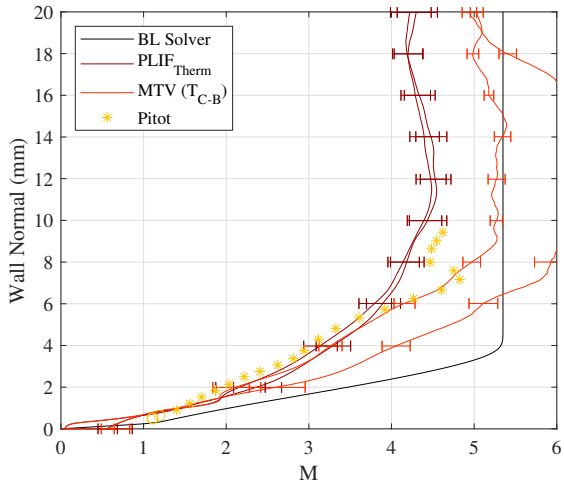

(e) Front ($x = 115$mm)

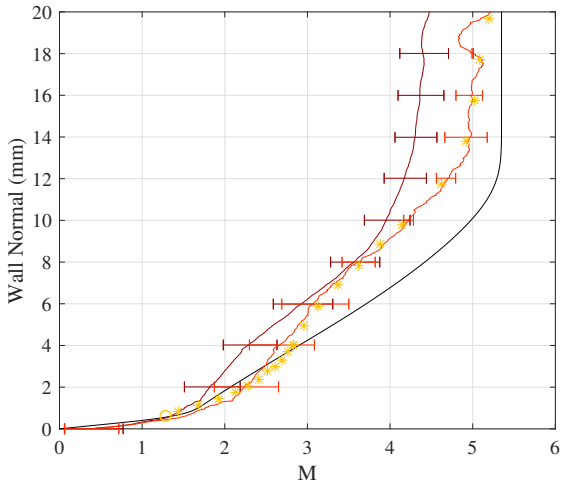

(f) Back ($x = 405$mm)

Figure 7.121: Comparison of turbulent off body techniques (trough, plasma); same legend applies to each row. [7]

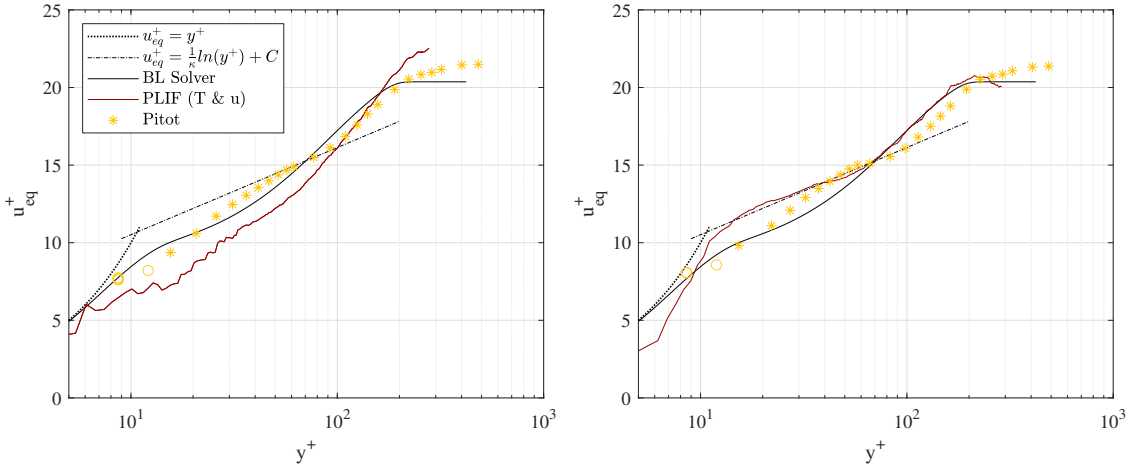

(a) Back, wake ($x = 405$mm)

(b) Back, through ($x = 405$mm)

Figure 7.122: Comparison of turbulent off body techniques, inner variable plot (no plasma); same legend applies to all figures. [7]

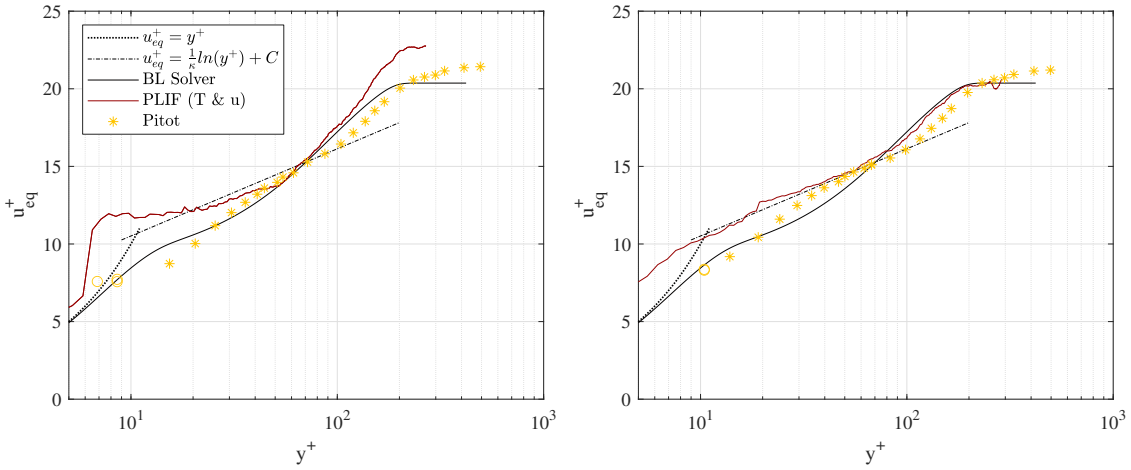

(a) Back, wake ($x = 405$mm)

(b) Back, through ($x = 405$mm)

Figure 7.123: Comparison of turbulent off body techniques, inner variable plot (plasma); same legend applies to all figures. [7]

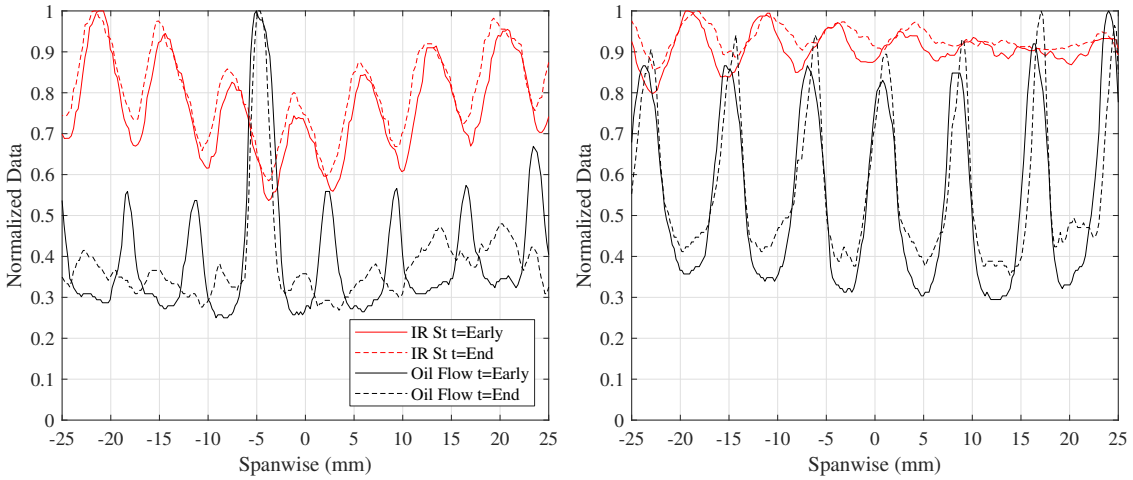

(a) Front ($x = 115$mm)

(b) Middle ($x = 260$mm)

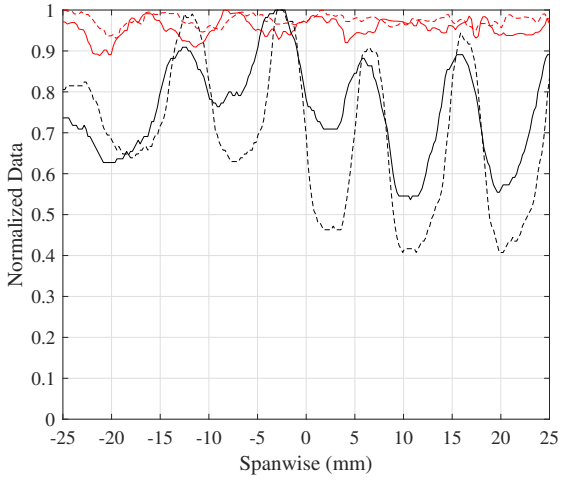

(c) Back ($x = 405$mm)

Figure 7.124: Comparison of surface streak visualization techniques; same legend applies to all figures. [7]

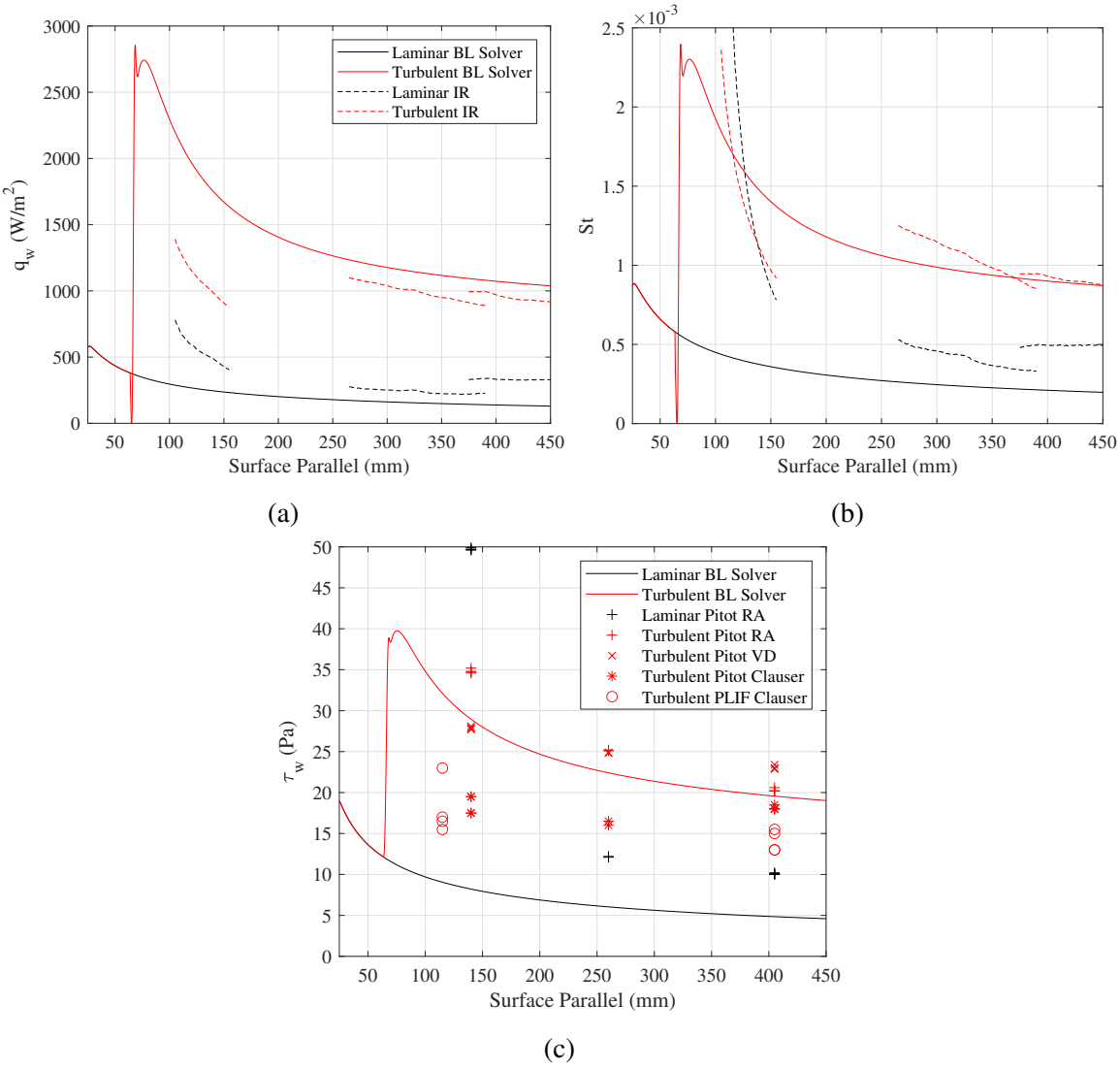

Figure 7.125: Comparison of wall variable measurement techniques; same legend applies to (a) and (b). [7]

7.3 Mach 6 Quiet Tunnel Boundary Layer Transition Experiments

7.3.1 Smooth Cone

The results described here follow from Siddiqui [4] and Siddiqui et al. [5].

7.3.1.1 Temperature profiles

There were 51 type-T thermocouples aligned streamwise along the port side of the model starting at 50.8 mm from the tip and ending at 444.5 mm from the tip. The first five thermocouples were spaced 25.4 mm apart. The remaining forty-six thermocouples were spaced 6.35 mm apart. The temperature profiles were examined over several runs to ascertain the state of the boundary layer. The recirculating chiller was set to coolant set points 20 °C, -20 °C, and -60 °C. Fig. 7.126 shows the typical temperature profiles that are seen for the different coolant set points. There is a distinctive shape to the temperature profile caused by how the coolant flows through the model. The coolant enters the model in a tube in the centre and recirculates to the back before exiting the model, this causes the shape of the temperature profile in addition to higher heating near the nose tip as the detachable tip does not get cooled. There was some concern that the pattern was caused by the nozzle shear layers interacting with the boundary layer on the model. To alleviate these concerns the model was moved as far into and out of the nozzle as possible while the temperature profiles were observed. The profiles did not change with the position of the model. ([4])

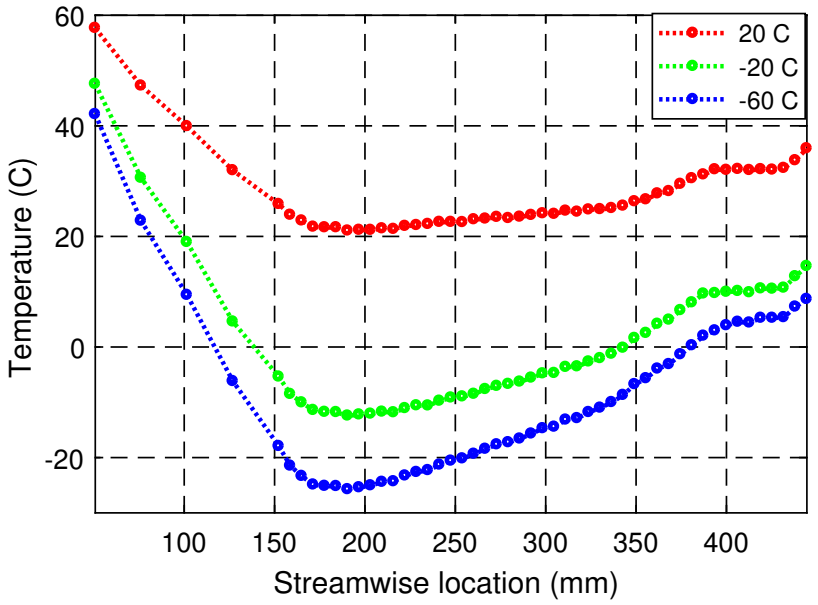

Figure 7.126: Temperature profiles at three coolant set points of 20 °C, -20 °C, and -60 °C on the smooth cone at unit Reynolds number of 9×10^6 /m. [4].

For all temperature cases, an increase in heating was observed followed by a plateau, this was attributed to the boundary layer starting to transition (increased heating). Qualitatively, the increase

in heating happened earlier for the colder wall cases. This was quantified by drawing straight lines on the temperature profiles and using the intersection points as locations of start of transition as shown in Fig. 7.127. The transition onset location moves from 342.9 mm from the tip for the 20 °C case to 330.2 mm for the -20 °C case and then to 317.5 mm for the -60 °C case. The earlier onset of transition was caused by the boundary layer thickness decreasing and moving the sonic line closer to the surface, thus increasing the Mack-mode frequency and accelerating the associated destabilization. ([4])

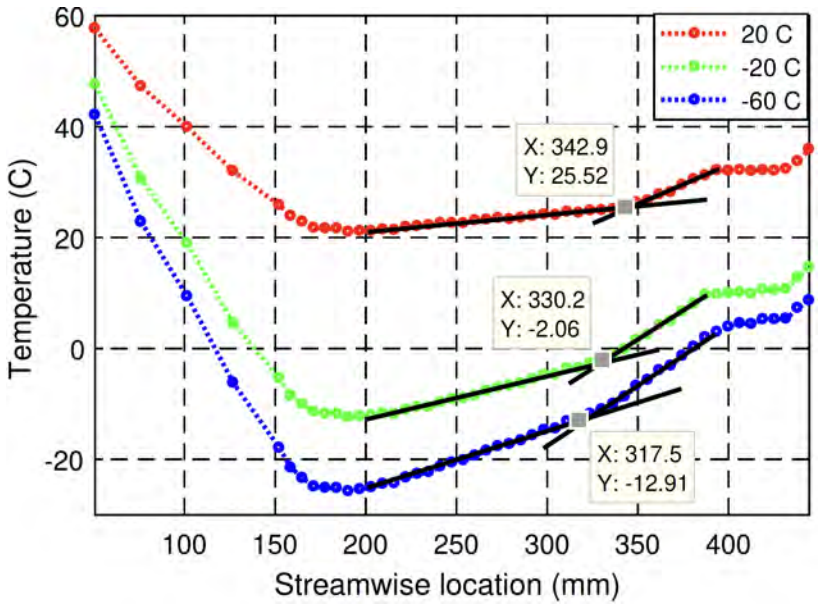

Figure 7.127: Temperature profiles on the smooth cone at unit Reynolds number of 9x10^6 /m with quantification of transition onset location. [4]

The unit Reynolds number was swept from 8x10^6 /m to 11x10^6 /m by steadily increasing the pressure in the settling chamber over the course of a wind tunnel run. The same three coolant set points of 20 °C, -20 °C, and -60 °C were used. The objective was to observe the temperature profiles as the boundary layer destabilizes from laminar to transitional and eventually become fully turbulent. The temperature profiles at unit Reynolds numbers of 8, 9, 10, and 11 x10^6 /m have been plotted for each coolant set point. Fig. 7.128 shows the temperature profiles from the smooth cone at coolant set point 20 °C. The onset of transition moved upstream as the Reynolds number increased. The heating also increased as the Reynolds number was increased. The temperature profiles at the aft end of the cone were very similar for the 8x10^6 /m and 9x10^6 /m profiles but an increase was observed for the 10x10^6 /m profile. The 11x10^6 /m profile showed a significant increase in temperature compared to the lower Reynolds numbers, indicating a turbulent boundary layer. ([4])

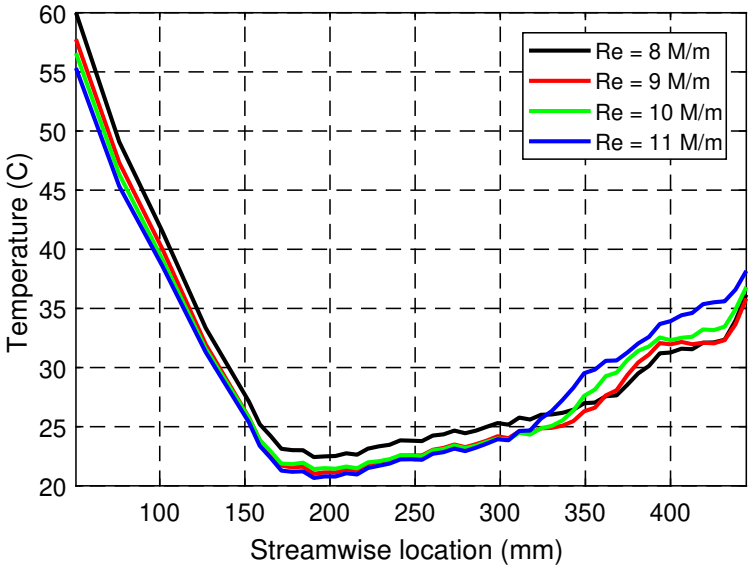

Figure 7.128: Temperature profiles over Reynolds number sweeps for the smooth cone at 20 °C coolant set point. [4]

Fig. 7.129 shows similar behavior for the -20 °C case. The transition onset location moves upstream with higher Reynolds number. The temperature profiles are seen to again be similar for the 8x10^6 /m and 9x10^6 /m unit Reynolds number profiles. The profile at unit Reynolds number 10x10^6 /m is significantly higher at the aft end of the cone than that seen for the 20 °C case, this signifies greater destabilization with wall cooling. The 11x10^6 /m profile shows higher heating again and signifies a fully turbulent boundary layer. ([4])

Fig. 7.130 shows the temperature profiles over the course of a Reynolds number sweep for the -60 °C coolant set point case. Similar trends to the two previous cases are observed with the transition onset locations moving further upstream as the Reynolds number is increased. The 8x10^6 /m and 9x10^6 /m unit Reynolds number profiles are observed to be very similar and the 10x10^6 /m profile shows increased heating at the aft end. The 11x10^6 /m unit Reynolds number profile shows even higher heating as expected. (Siddiqui [4])

7.3.1.2 Mack-mode instabilities

The Mack-mode instability has been identified as the dominant cause of boundary-layer transition and is the focus of this study. The Mack mode was studied using the focusing schlieren technique to visualize the Mack-mode "rope-like" structures using a camera. Then point measurements were taken with a fiber-optic coupled photodetector to analyze spectral content in the boundary layer. ([4])

The focusing schlieren camera settings were set to a frame rate of 1500 fps and a shutter time of 0.16 μs This provided the field of view needed to capture the entirety of the cone that was outside the tunnel nozzle with enough data storage to record the full wind tunnel run. Figure 7.131 shows the Mack-mode instability on the aft end of the model as visualized using the focusing schlieren

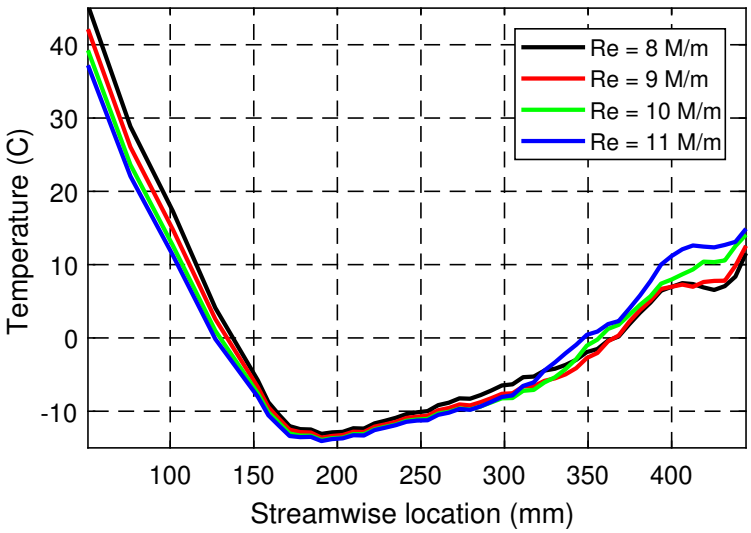

Figure 7.129: Temperature profiles over Reynolds number sweeps for the smooth cone at -20 °C coolant set point. [4]

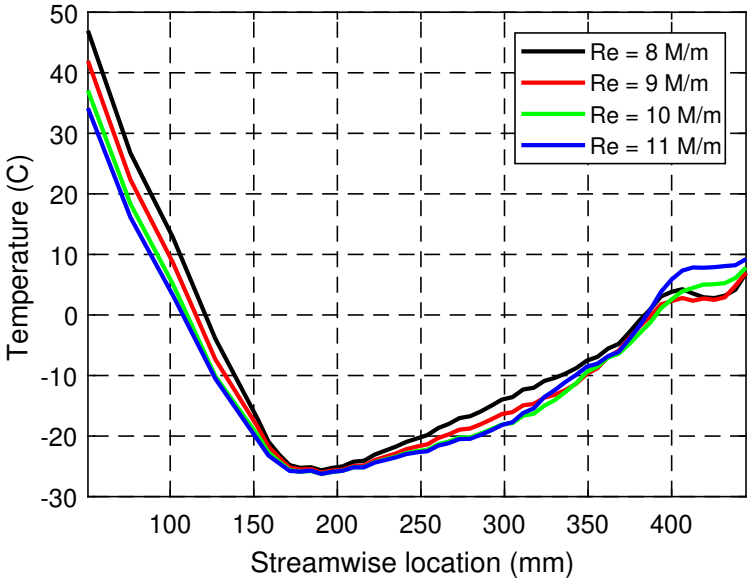

Figure 7.130: Temperature profiles over Reynolds number sweeps for the smooth cone at -60 °C coolant set point. [4].

diagnostic. The wavelength of the waves seen equate to a frequency of ∼300 kHz as expected for the Mack mode. The boundary layer was seen to decrease in thickness as the Reynolds number was increased and intermittently lost structure. The intermittency of the breakdown increased as Reynolds number was increased untill eventually there was no observable structures and the boundary layer was turbulent. Quantifying transition onset was difficult from these data as some

arbitrary definition of transition dependent on intermittency level would have to be made. Instead the data collected using the camera were used as a qualitative measurement showing presence of Mack-mode waves and confirming the trends seen in the data from the other diagnostics. ([4])

Figure 7.131: Focusing schlieren image showing Mack-mode structures on the smooth cone at coolant setpoint -60 °C. [4]

The time-domain voltage data from the photodetector were acquired by the DAQ at a sampling rate of 2 MHz as this was the maximum for the DAQ. It should be noted that the photodetector was capable of far higher frequencies and the DAQ was the limiting factor. The time-domain data were converted to frequency domain using Welch's method where segment size was 2^8 and overlap was 50%. This gives us data in the frequency domain to 1 MHz with a resolution of 7.8 kHz. Thus there is an uncertainty of $\pm$3.9 kHz in these data. The fiber optic was positioned to take data at a point in the boundary layer 25.4 mm from the aft end of the cone. The focusing schlieren diagnostic with the photodetector was also used as an alignment tool to zero the angle of attack of the model. Hofferth [299] observed a variation in the frequency of the Mack mode with angle of attack on the 93-10 cone. A study was conducted with the angle of attack changed and runs repeated and showed that the Mack-mode frequency changed by 84 kHz for 1° change in angle of attack. Kocian [350] carried out LPSE computations for the 93-10 cone and found the Mack-mode frequency to vary by 73 kHz per 1° angle of attack. Fig. 7.132 shows the experimental and computational results. Thus the Mack-mode frequency is very sensitive to angle of attack. Since the 91-6 cone is a very similar geometry to the 93-10 cone, we assumed high sensitivity. This sensitivity was used to align the model by varying the angle of attack and quantifying the difference in frequency at the same wind tunnel conditions. This was repeated untill the frequencies matched. This procedure was repeated every time the 91-6 cone model was installed. ([4])

The unit Reynolds number was steadily increased from 8x10^6 /m to 11x10^6 /m for the three coolant set points. Fig. 7.133 shows the data for the coolant set point 20 °C case. The Mack-mode peak frequency was measured at 289.1$\pm$3.9 kHz at a unit Reynolds number of 8x10^6 /m and

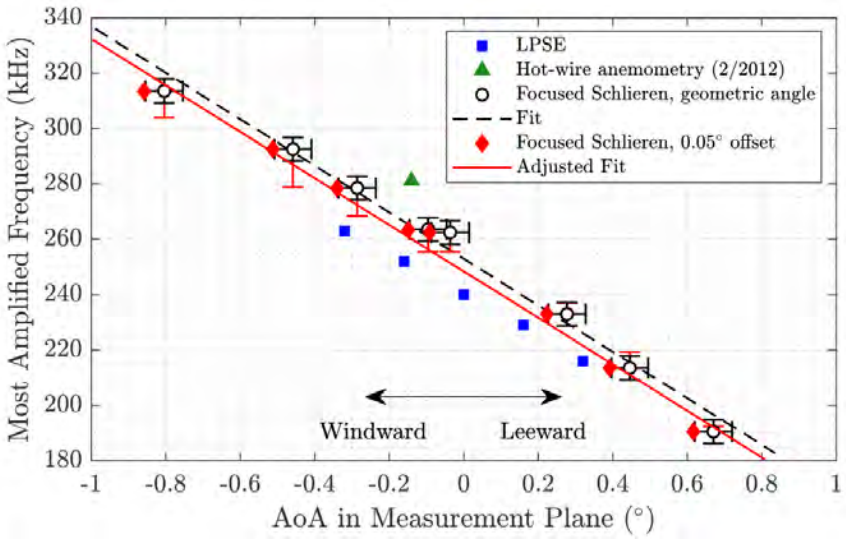

Figure 7.132: Variation of Mack-mode frequencies as seen from experiments and computations on the 93-10 cone. [4]

as the Reynolds number increased, the frequency increased. The spectral energy away from the peak stayed the same up to a unit Reynolds number of 9.2x10^6 /m and after, the spectral energy increased and the peak diminished. The increase in spectral energy was thought to be the onset of transition and further breakdown as it keeps increasing. Eventually the spectral energy and peak come together to form a line at a unit Reynolds number of 10.5x10^6 /m, at this point the boundary layer appeared turbulent. ([4])

Figure 7.134 shows the spectral data for the -20 °C coolant set point case. The frequency of the Mack mode at a unit Reynolds number of 8x10^6 /m is seen to be 296.9±3.9 kHz. This is higher than that seen for the 20 °C case, this increase can be attributed to the decrease in boundary-layer height from wall cooling. The increase in frequency has a destabilizing effect, the spectral energy increases at a unit Reynolds number of 9x10^6 /m and the boundary layer is turbulent at 9.8x10^6 /m. ([4])

Figure 7.135 shows the spectral data for the -60 °C coolant set point case. The frequency of the Mack-mode peak is seen to be 296.9 kHz at a unit Reynolds number of 8x10^6 /m. This is perplexing at first as it is the same as that seen for the -20 °C case but there is an uncertainty of ±3.9 kHz on these values so it is possible that the frequency is higher for the colder wall case. The destabilizing effects of wall cooling are observed again with the spectral energy increasing at a unit Reynolds number of 8.8x10^6 /m and the boundary layer fully turbulent at a unit Reynolds number of 9.5x10^6 /m. ([4])

7.3.1.3 Görtler instabilities

The results described in this Section follows from Siddiqui [4] and (Siddiqui et al. [5]. The Görtler instability results from curvature and leads to 3-D vortex structures in the boundary layer [132]. Constant Temperature Anemometry (CTA) was used with a hot-film probe to probe the

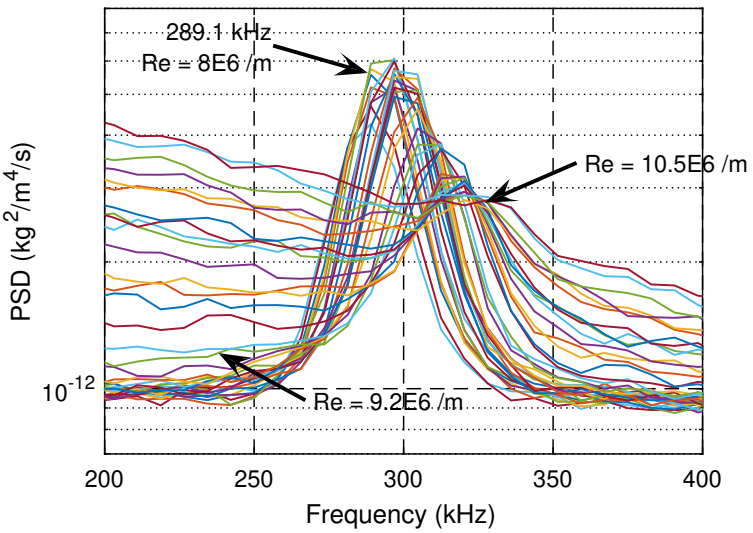

Figure 7.133: Spectral data from focusing schlieren on the smooth cone at coolant setpoint 20 °C. [4]

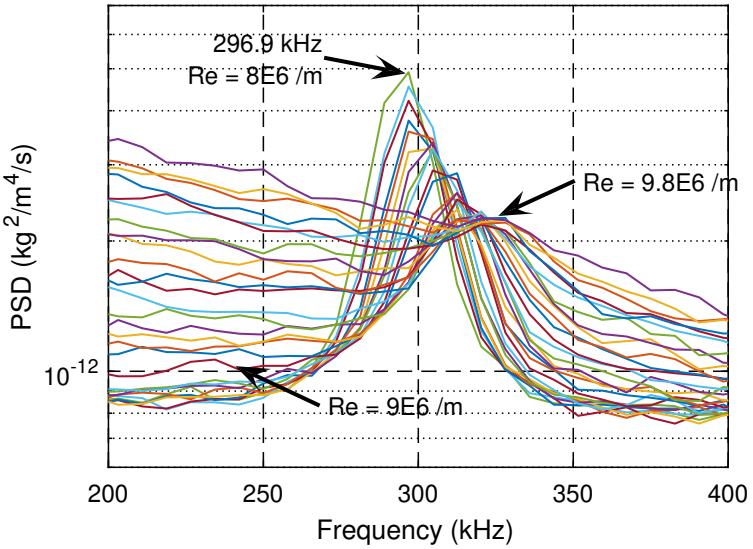

Figure 7.134: Spectral data from focusing schlieren on the smooth cone at coolant setpoint -20 °C. [4]

boundary layer and the voltage output was mapped to study the mass-flux variation. The hot-film survey location was 35±0.5 mm from the aft end (422.2±0.5 mm from the tip) of the cone. The raw voltage and filtered/amplified voltages were sampled at 500 kHz for 100 ms at each measurement point. Azimuthal sweeps were performed from 80° to 100° with a standard coordinate system where 0° was defined as the centerline streamline along the port side. Only two sweeps could be

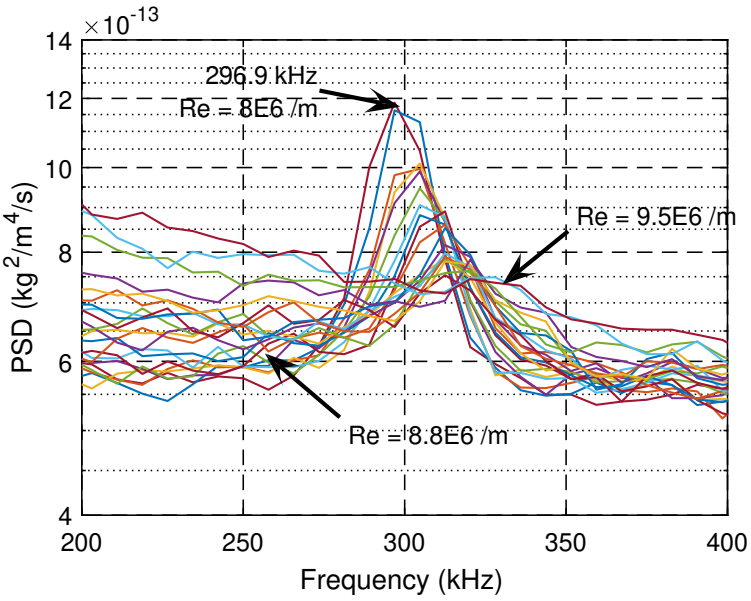

Figure 7.135: Spectral data from focusing schlieren on the smooth cone at coolant setpoint -60 °C. [4]

completed during one wind tunnel run so multiple wind tunnel runs had to be carried out to map the boundary layer. The distance from the surface was estimated by placing the hot-film sensor in its probe holder very close to the surface as it would be during a wind tunnel run and taking pictures. The pictures were then used to measure wall-normal distance from model surface to the sensor using ImageJ software and also measuring known quantities like the length and width of the sensor holder. These measurements were then used to recover the distance from the sensor to the model. Figure 7.136 shows the voltage variation (representative of mass-flux variation) maps created from wind tunnel runs where hot films were traversed through the boundary layer to collect data. Fig. 7.136a is for the 20 °C coolant set point case and does not show strong structure but some periodic variation is seen. In Fig. 7.136b the structures get more defined and definite peaks are seen, five peaks can be discerned which on average over a 20° span equates to a wavenumber of 90. Fig. 7.136c shows the data collected for the -60 °C coolant set point case and shows a reduction in the boundary-layer height as expected when the model wall is cooled and the same peaks observed earlier with more structure. Overall it can be concluded that the wall cooling caused the boundary-layer height to decrease and made the Görtler vortices more prominent. ([4])

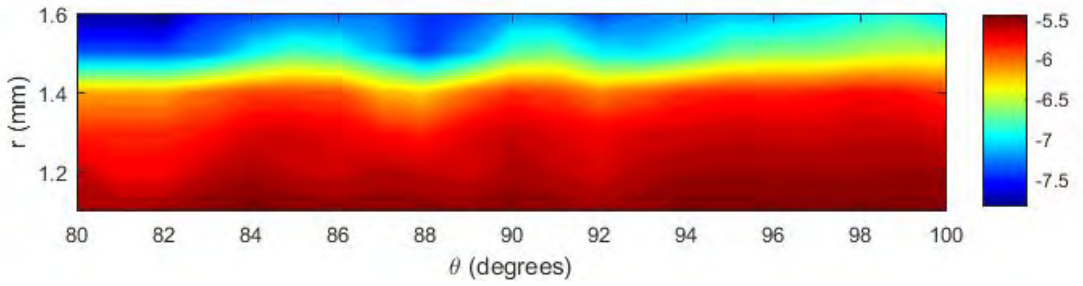

(a) Coolant set point 20 °C

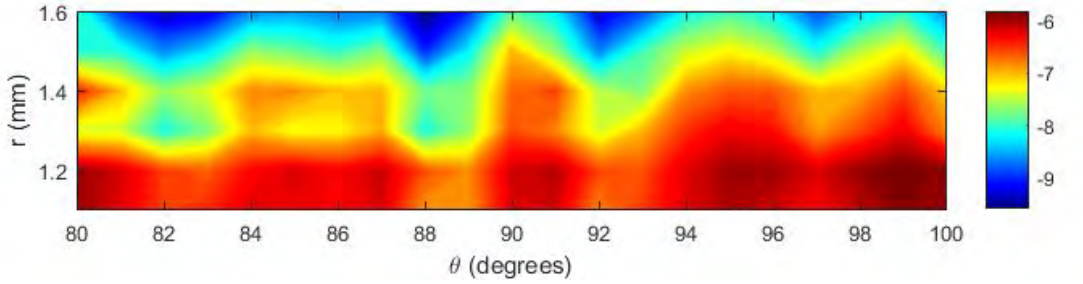

(b) Coolant set point -20 °C

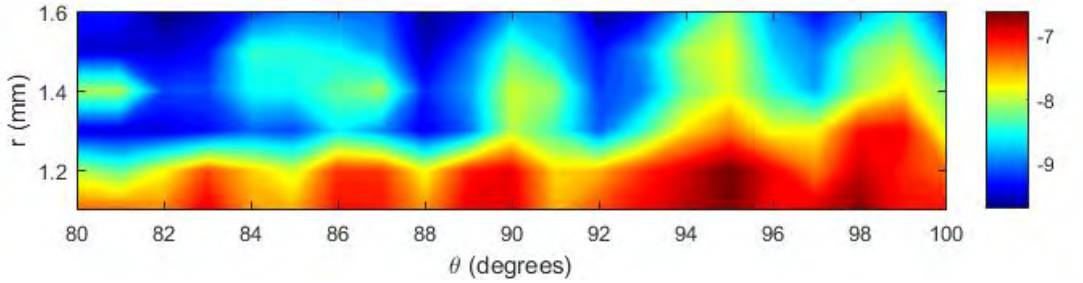

(c) Coolant set point -60 °C

Figure 7.136: Hot-film voltage variation over a 20° azimuthal sweep on the smooth cone at a unit Reynolds number of 9x10^6 /m. [4]

7.3.2 Cone with DREs

The results described in this Section follows from Siddiqui [4] and (Siddiqui et al. [5]. After all the available diagnostics were used on the smooth cone, periodic spanwise (azimuthal) distributed roughness elements (DREs) were added. The goal of DREs was to further destabilize the flow so that the transition process could more readily be observed. The spacing was chosen to match the Görtler vortex pattern wavenumber. The DREs were circular, and the diameter matched the spacing. The height was measured by a profilometer as 81$\pm$3.6 μm and the diameter (and spacing) measured to be 465$\pm$7.6 μm. The streamwise location was based on companion stability computations [351] as being where the flare starts, 152.4 mm from the tip, as this is where the Görtler instability starts. All the diagnostics used on the smooth cone were used again on the cone with DREs with the addition of Focused Laser Differential Interferometry (FLDI). ([4])

7.3.2.1 Temperature profiles

The results described in this Section follow from Siddiqui [4] and (Siddiqui et al. [5]. As for the smooth cone, the surface thermocouples provided a diagnostic via temperature profiles. The increase in heating observed in the temperature profiles were quantified by drawing lines and marking the points where the slope changed; a similar approach was used by Blanchard and Selby at NASA Langley [226]. Fig. 7.140 shows the lines drawn on the temperature profiles and points marked. The transition onset location moves from 336.5 mm from the tip for the 20 °C case to 317.5 mm for the -20 °C case and then to 311.1 mm for the -60 °C case. As the temperature of the model wall decreases the boundary-layer height decreases and the sonic line moves closer to the surface, thus increasing the Mack-mode frequency and increasing its destabilizing effect [319]. Figure 7.140 shows the temperature profiles for the three coolant set points. The distinctive shape of the temperature profile is due to the way coolant flows in the shell. The temperature is highest near the tip as the tip is detachable and the cavity for the coolant does not extend into it. Moving backwards from the tip the temperature decreases as the coolant is able to cool the cone, and after a certain point the temperature rises as the coolant warms up on its way to the exit channel. The temperature is linear to a certain point where the slope changes, this point is thought to be where the boundary layer starts to transition. This point is termed the transition onset location and after this the temperature plateaus and then has a final uptick. The plateau and uptick are thought to be from the way the coolant flows through the cone as well, the final uptick is likely from heat conducting forward from the hot sting assembly. Blanchard and Selby [226] marked the point where the temperature profile plateaued to be the transition location but other diagnostics used for this work show that the boundary layer is not fully turbulent at low Reynolds numbers (where the plateau is also seen) and so their conclusion is not accurate. ([4])

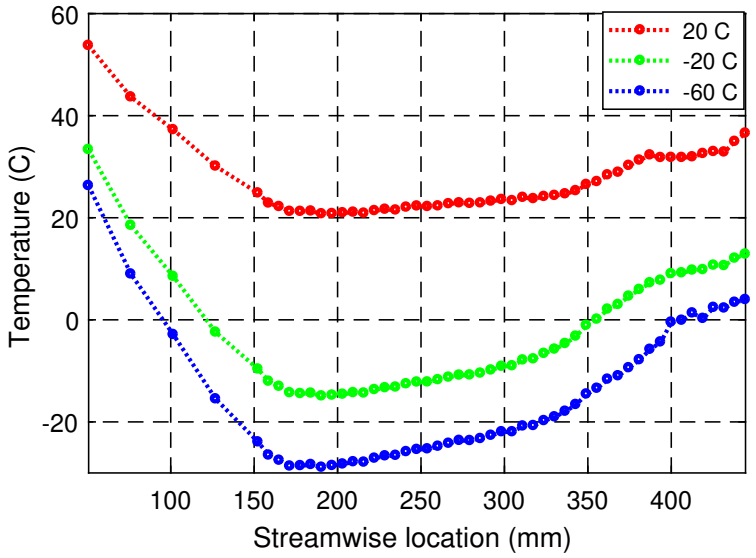

Figure 7.137: Temperature profiles over Reynolds number sweeps for three coolant set points. [4]

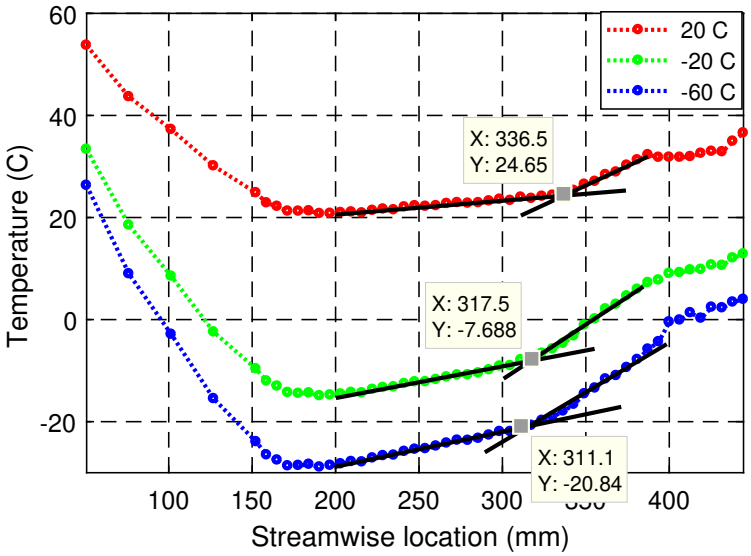

Figure 7.138: Temperature profiles over Reynolds number sweeps for the DRE cone at -20 °C coolant set point. [4]

The temperature profiles at unit Reynolds numbers of 8, 9, 10, and 11 x10^6 /m have been plotted for each coolant set point. Fig. 7.139 shows the temperature profiles from the cone with DREs at coolant set point 20 °C. The onset of transition was observed to move upstream as the Reynolds number increased. The heating also increased as the Reynolds number was increased. The temperature profiles at the aft end of the cone show the 8x10^6 /m and 9x10^6 /m profiles to be near identical. The temperature profile for the 10x10^6 /m unit Reynolds number profile shows an increase in heating. The 11x10^6 /m profile shows a significant increase in temperature compared to the lower Reynolds numbers, indicating a fully turbulent boundary layer. ([4])

The coolant temperature set point was set to -20 °C and the Reynolds number sweep repeated. The temperature profiles are shown in Fig. 7.140. The temperature profiles at unit Reynolds numbers of 8x10^6 /m and 9x10^6 /m were almost identical with the 9x10^6 /m profile slightly hotter. Above this, the temperature increased with increasing Reynolds number. The 10x10^6 /m unit Reynolds number profile showed an onset to transition, with higher heating near the aft region of the cone. Figure 7.141 shows the temperature profiles at increasing unit Reynolds numbers as the Reynolds number is swept and the coolant set point is set to -60 °C. The 8x10^6 /m and 9x10^6 /m profiles are seen to be different for this case as the higher Reynolds number shows higher heating. This indicates the boundary layer is further destabilized than in the previous cases. The 10x10^6 /m and 11x10^6 /m unit Reynolds number profiles show earlier onset of transition and higher heating as Reynolds number is increased. ([4])

7.3.2.2 Mack-mode instabilities

The results in this section follow from Siddiqui [4] and Siddiqui et al. [5]. The Mack-mode instabilities on the cone with DREs have been studied using focusing schlieren as was done for the smooth cone. Focused Laser Differential Interferometry (FLDI) has recently been implemented at

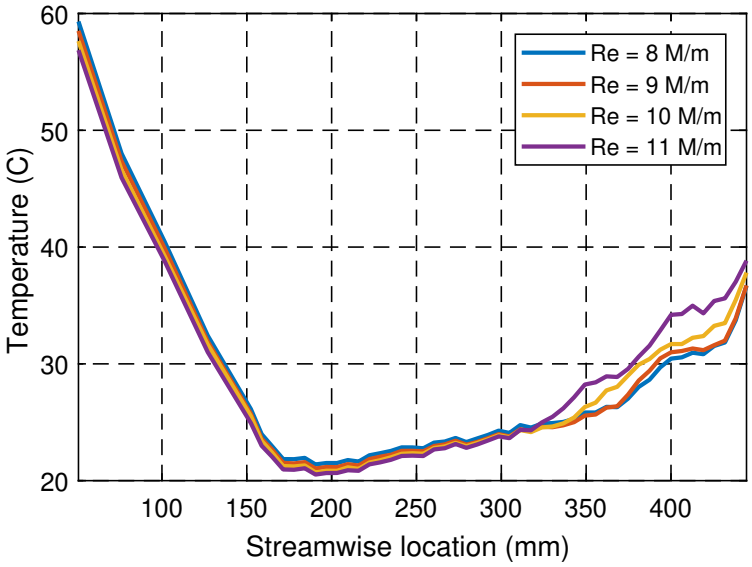

Figure 7.139: Temperature profiles over Reynolds number sweeps for the cone with DREs at 20 °C coolant set point. [4]

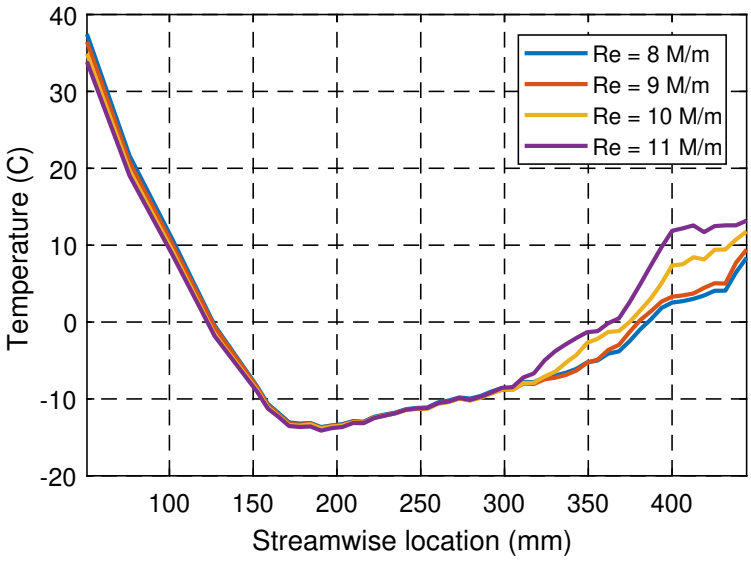

Figure 7.140: Temperature profiles over Reynolds number sweeps for the cone with DREs at -20 °C coolant set point. [4]

the NAL and has also been used to study the Mack-mode instability.

The focusing schlieren system was setup with the high-speed camera (Photron FASTCAM SA-Z). The camera settings were identical to those used for the smooth cone, 1500 fps and 0.16 μs. These settings allow for the entirety of the cone outside the nozzle to be captured in the frame and

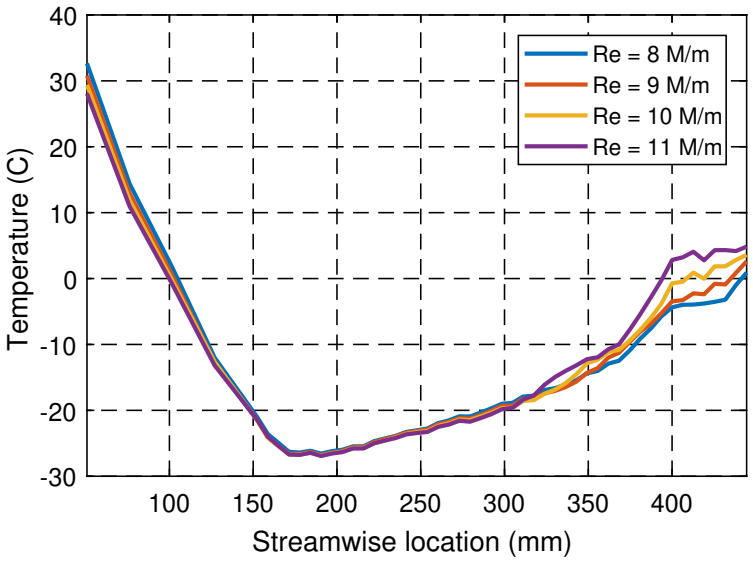

Figure 7.141: Temperature profiles over Reynolds number sweeps for the cone with DREs at -60 °C coolant set point. [4].

an entire wind tunnel run to be recorded. Wind tunnel runs were done with the coolant set point at 20 °C, -20 °C, and -60 °C. The Reynolds number was increased from 7.5x10^6 /m to 11x10^6 /m for the wind tunnel runs where the camera was part of the diagnostic to observe the boundary layer on the aft end of the cone and its transition from laminar to turbulent. Fig. 7.142 shows the Mack-mode "rope-like" structures present in the boundary layer on the cone with DREs at a coolant set point of -60 °C. Again, this diagnostic was used as a qualitative tool to confirm presence of Mack-mode waves and confirm the boundary-layer transition trends seen from the other diagnostics. The uncertainties when defining transition using this diagnostic are too high for quantification to be useful. Qualitatively the Mack-mode instability was observed to have a wavelength indicating a frequency of $\sim$300 kHz as expected. The intermittency of breakdown of the boundary layer was seen to increase as the unit Reynolds number was increased and resulted in full breakdown to transition at the higher Reynolds numbers. ([4])

Figure 7.143 shows the photodetector spectral data for the cone with DREs with the recirculating chiller set to 20 °C. The resolution of the spectral data was 7.8 kHz which translates to an uncertainty of $\pm$3.9 kHz. The fiber optic was positioned to take data at a point in the boundary layer 25.4 mm from the aft end of the cone. The unit Reynolds number was swept from 8x10^6 /m to 11x10^6 /m. The frequency of the Mack-mode instability was observed at 281.3$\pm$3.9 kHz at a unit Reynolds number of 8x10^6 /m. As the Reynolds number was increased, the Mack-mode frequency increased. At a unit Reynolds number of 8.6x10^6 /m, the overall spectral energy was seen to increase and the with diminishing peaks, which was presumed to be the onset of boundary-layer transition. As the Reynolds number was increased further, the spectral energy rose and the Mack-mode peak was no longer observable at a unit Reynolds number of 9.7x10^6 /m. The boundary layer was thought to be fully turbulent. Note the differences from the smooth cone at the same tempera-

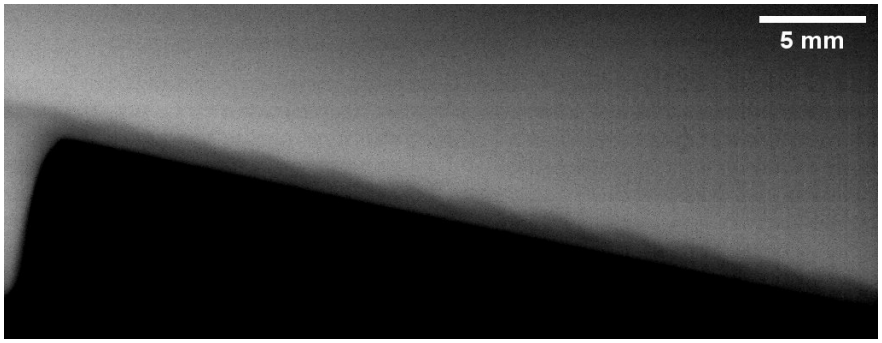

Figure 7.142: Focusing schlieren image on the aft end of the cone with DREs at coolant setpoint -60 °C. [4]

ture, the Mack-mode frequency is lower (289.1±3.9 kHz for the smooth cone), because the DREs resulted in an increased boundary-layer thickness. The rise in spectral energy(9.2x10^6 /m for the smooth cone) and turbulence (10.5x10^6 /m for the smooth cone) are observed earlier as the DREs destabilized the boundary layer. Figure 7.144 shows the spectral data on the cone with DREs at coolant setpoint -20 °C as the unit Reynolds number is swept from 7.5x10^6 /m to 11x10^6 /m. The sweep was started at an earlier Reynolds number for this case because the spectral energy starts increasing earlier. For consistency the Mack-mode frequency at unit Reynolds number of 8x10^6 /m is shown, it is 289.1±3.9 kHz. This is lower than that for the smooth cone (296.9±3.9 kHz), again due to the boundary-layer height increasing from the DREs. The spectral energy is observed to increase at a unit Reynolds number of 8.2x10^6 /m as opposed to 9x10^6 /m for the smooth cone. The spectral energy increases and the Mack-mode peak is no longer observed at a unit Reynolds number of 9.2x10^6 /m as opposed to 9.8x10^6 /m for the smooth cone. The DREs again result in earlier transition. Figure 7.145 contains the spectral data obtained from the cone with DREs at coolant set point to -60 °C. For these data, the unit Reynolds number was swept from 7.5x10^6 /m to 11x10^6 /m. The Mack-mode frequency at a unit Reynolds number of 8x10^6 /m was observed at 289.1±3.9 kHz, as compared to 296.9±3.9 kHz for the smooth cone at the same coolant set point. The spectral energy was observed to increase at a unit Reynolds number of 8x10^6 /m as opposed to 8.8x10^6 /m for the smooth cone. The Mack-mode peak was no longer observable at a unit Reynolds number of 9x10^6 /m, as opposed to 9.5x10^6 /m on the smooth cone. (Siddiqui [4])

Focused Laser Differential Interferometry (FLDI) was used to study the Mack-mode instability on the 91-6 flared cone. The technique used here has been named Linear Array-Focused Laser Differential Interfereometry (LA-FLDI) owing to the multiple beam pairs that can be created and used to probe the flow. The diffractive optic being used for this work splits the laser beam into a 1x6 array but it is possible to split the beam into 2-D arrays using the right optic or by stacking optics that create 1-D arrays. The ability to simultaneously probe multiple points in a boundary layer using a non-intrusive diagnostic is very useful for studying hypersonic flows. In this case the linear array of beam pairs is being placed in the boundary layer either parallel or perpendicular to the model wall. Initially the array of beam pairs was placed parallel to the model wall at a wall-normal height of 1±0.5 mm and with the furthest-downstream beam 25.4±0.5 mm from the

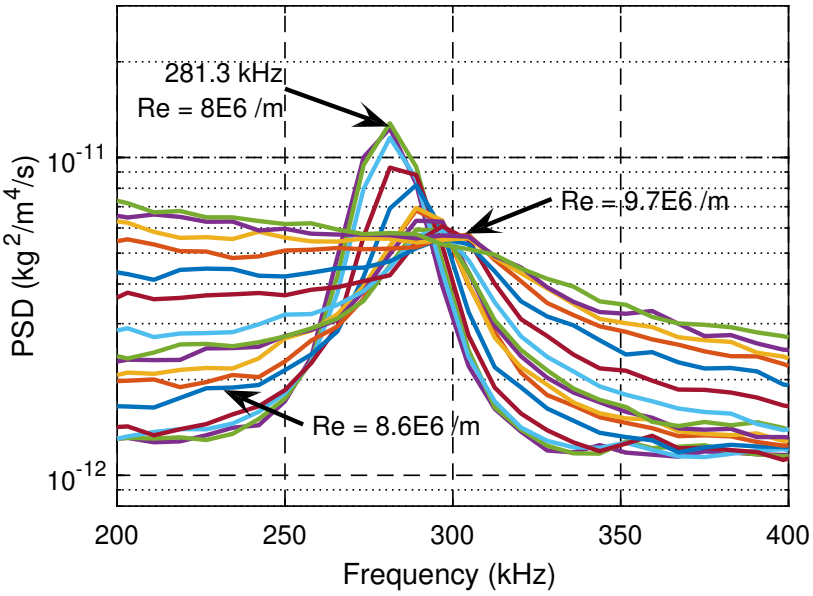

Figure 7.143: Spectral data from focusing schlieren on cone with DREs at coolant setpoint 20 °C. [4]

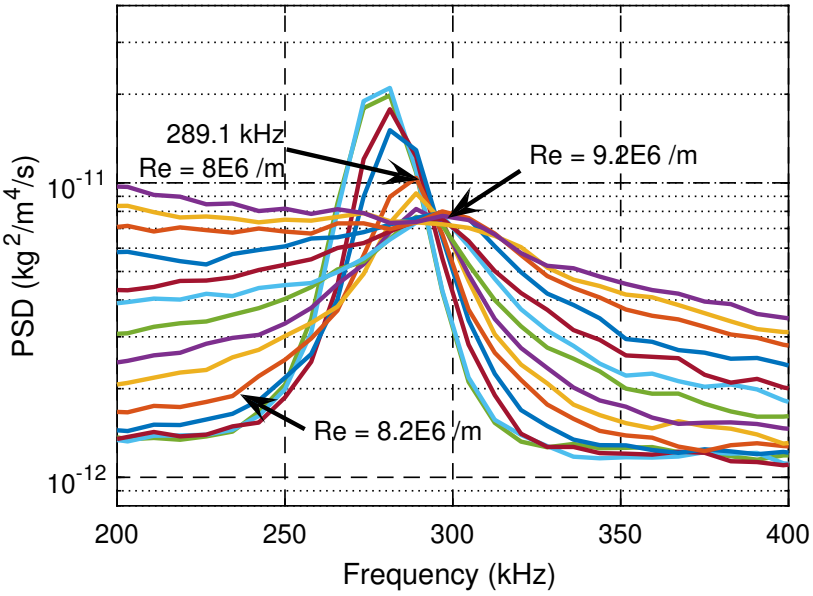

Figure 7.144: Spectral data from focusing schlieren on cone with DREs at coolant setpoint -20 °C. [4]

aft end of the cone. Wind tunnel runs were done with the beam pairs in this orientation and the Reynolds number was increased from 8x10^6 /m to 11x10^6 /m. The LA-FLDI technique provides spectral data similar to the focusing schlieren technique. The data were sampled at 2 MHz as this

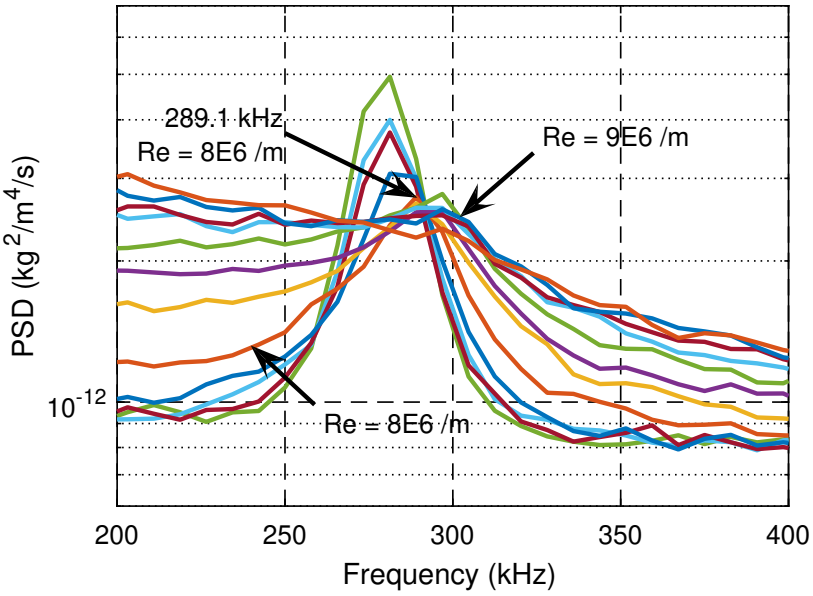

Figure 7.145: Spectral data from focusing schlieren on cone with DREs at coolant setpoint -60 °C. [4]

was the highest the DAQ system was capable of. It should be noted that the photodetectors are capable of higher frequencies and the DAQ system is the limiting factor here. Future experiments may be able to use higher bandwidth data acquisition systems to analyze higher frequency content in the spectral data. Fig. 7.146 shows the spectral data from all 6 channels as the unit Reynolds number is swept up. At a unit Reynolds number of 8.2x10^6 /m the Mack-mode peak is seen to have a frequency of ∼290 kHz and the harmonics of the Mack mode are seen as well. At a unit Reynolds number of 9.2x10^6 /m the Mack-mode frequency has increased to ∼305 kHz and the frequency of the harmonics has increased too. At a unit Reynolds number of 10.2x10^6 /m the boundary layer is transitional and the harmonics are no longer seen. The Mack mode is a diffuse peak and more importantly there is some separation between the spectral energy from the six channels. This indicates that the most upstream channel (channel 6) was transitioning later than the most downstream channel (channel 1). At a unit Reynolds number of 10.9x10^6 /m a classic turbulence hump is observed in the spectra. (Siddiqui [4])

The spectral data were plotted as colormaps to better understand trends as the Reynolds number was increased. Fig. 7.147 shows the colormaps showing the evolution of the Mack-mode instability and eventual disappearance as the boundary layer transitions to turbulence. The frequency of the Mack-mode and its harmonics increase as the Reynolds number is increased. For the coolant set point of 20 °C the Mack-mode instability diffuses and cannot be ascertained after a unit Reynolds number of 10.2x10^6 /m. For the -20 °C case the Mack-mode instability cannot be ascertained past a unit Reynolds number of 9.2x10^6 /m, indicating earlier transition.

For better quantification, the peaks of the Mack-mode instability and its harmonics were plotted separately as Reynolds number was increased for the two coolant set points. The results are plotted

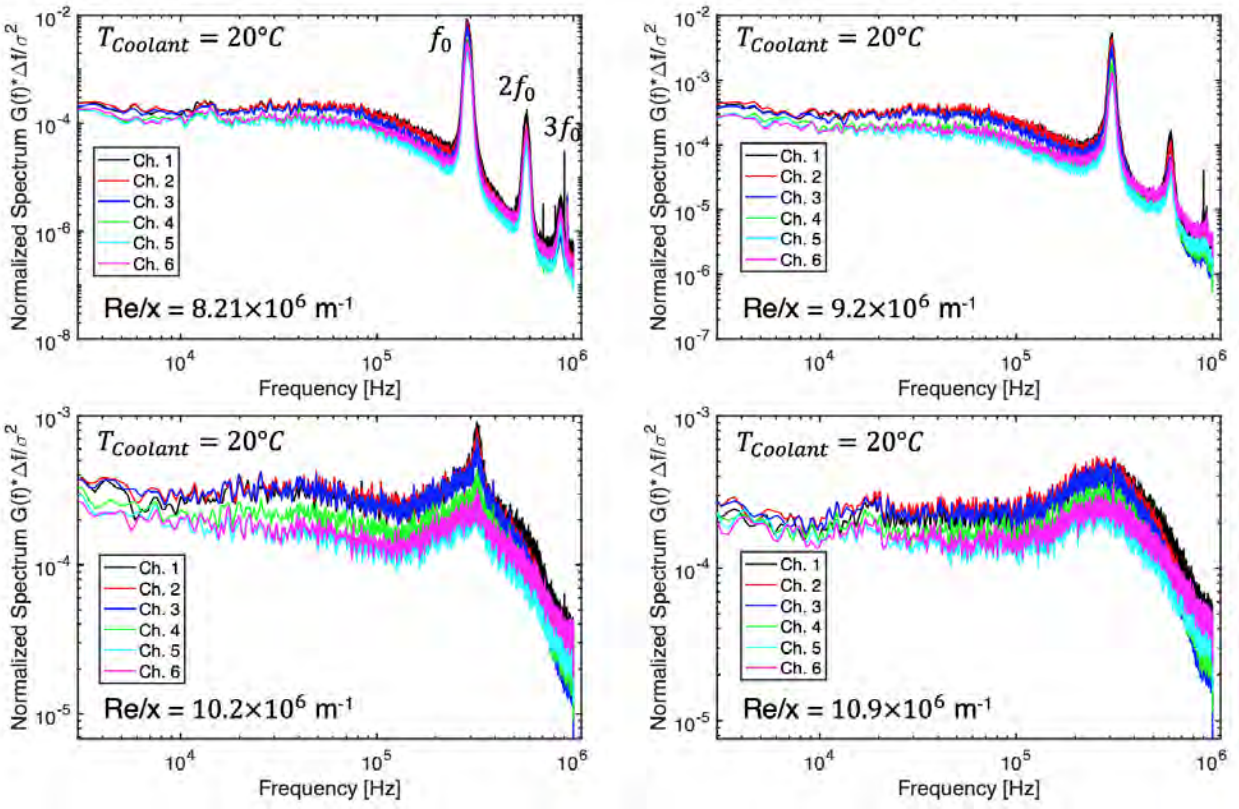

Figure 7.146: Spectral data obtained using the LA-FLDI diagnostic at six points in the boundary layer on the cone with DREs over the course of a Reynolds number sweep. [5]

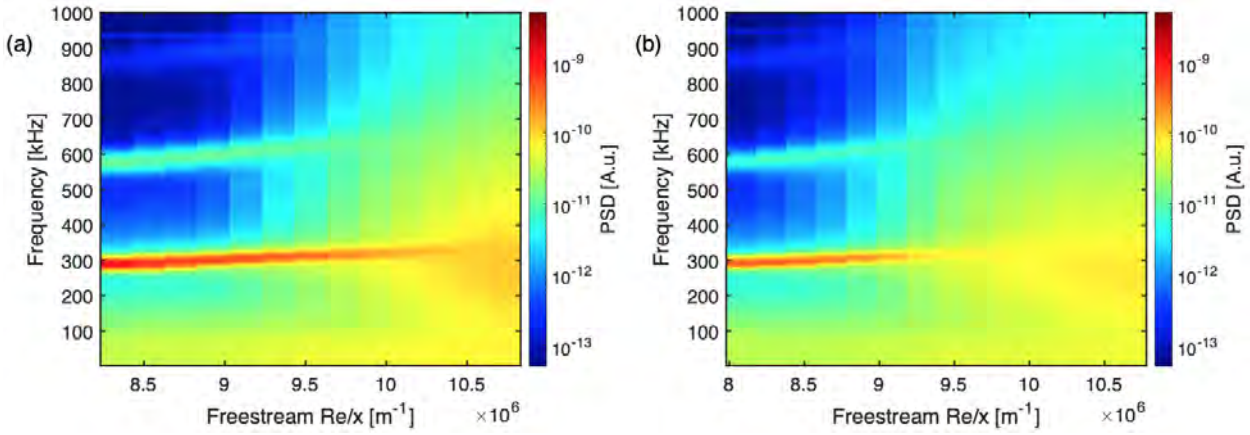

Figure 7.147: Spectral data in the form of colormaps over the course of a unit Reynolds number sweep on the cone with DREs. (a) Coolant temperature set point 20 °C, (b) Coolant temperature set point -20 °C. [4]

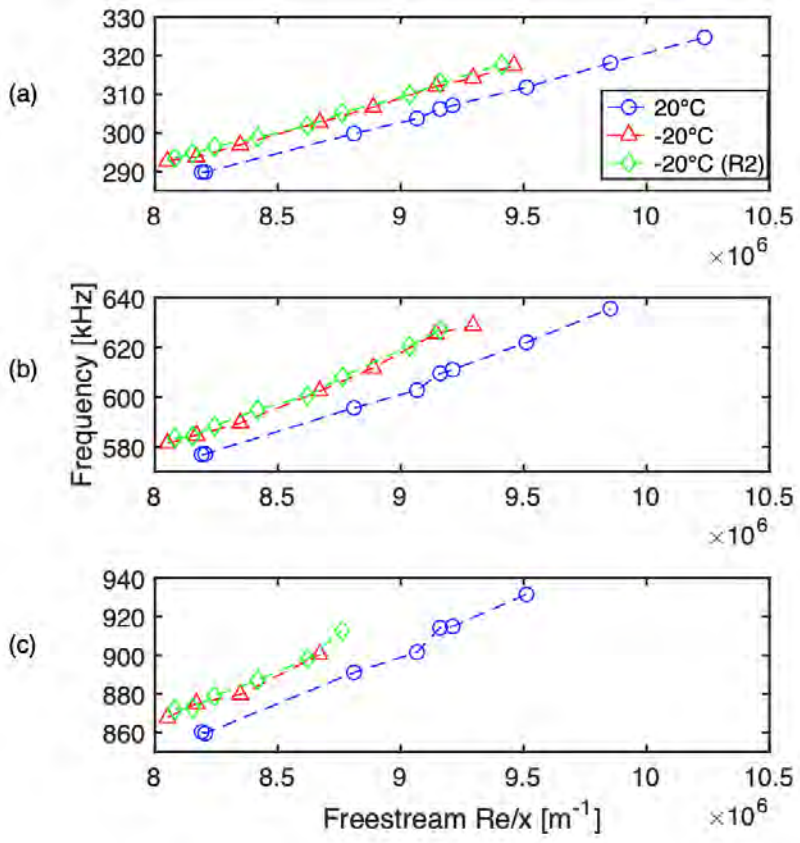

Figure 7.148: Peaks of the Mack-mode instability and its harmonics plotted separately over the course of a unit Reynolds number sweep for different coolant set points at Channel 1. (a) Mack-mode frequency, (b) its first harmonic, and (c) its second harmonic. [4]

in Fig. 7.148. The Mack-mode frequency and the harmonics were observed to be higher when the coolant set point was decreased due to the sonic line moving closer to the model wall. The harmonics also dissipated earlier than the Mack-mode peaks. The wall-normal orientation of the beam pairs is shown in Fig. 7.149. The lowest beam pair was placed so as to mark the wall location, and then the location of the other beam pairs was determined using beam-profiler imaging. A Reynolds number sweep was carried out with the coolant set point at 20 °C on the cone with DREs. The data collected were converted to the frequency domain and plotted. The point closest to the wall was eclipsed by the model and the point furthest away showed no content due to being outside the boundary layer. Thus the four points in the middle have been analyzed and the spectral data plotted in a colormap, as seen in Fig. 7.150. The Mack-mode instability and its harmonics are observed at wall-normal distances of 0.38 mm, 0.76 mm, and just barely for the 1.14 mm. At 1.52 mm from the wall there was no content and this confirmed that the spectral content in the lower points was due to boundary layer instabilities. (Siddiqui [4])

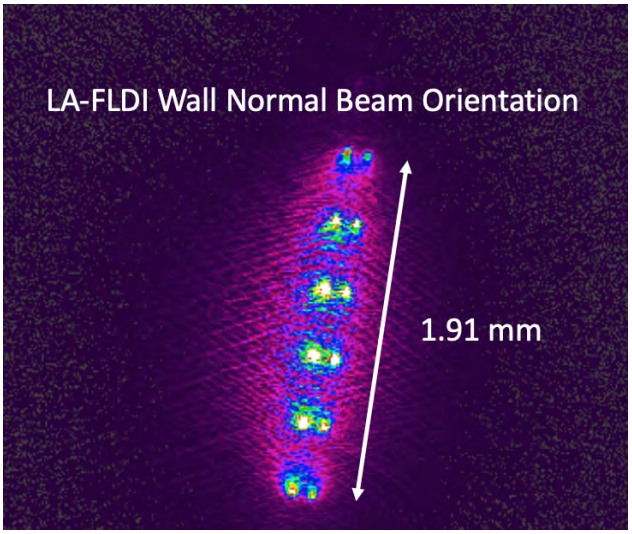

Figure 7.149: Beam profile of the beam pairs in wall-normal orientation for boundary-layer profile analysis. [5]

7.3.2.3 Görtler Instabilities

Constant Temperature Anemometry (CTA) was used to map the boundary layer over the aft end of the cone. The map was created in a plane parallel to the nozzle exit and 35±0.5 mm from the aft end (422.2±0.5 mm from the tip) of the cone. The data were sampled at 500 kHz for 100 ms at each point. The hot-film probe was traversed in 0.5° steps to do azimuthal sweeps from 80° to 101° using a conventional cylindrical coordinate system. Only one sweep could be accomplished in one wind tunnel run and thus several wind tunnel runs were carried out at the same flow condition to create the map. The step size for the sweep on the cone with DREs was half what it was on the smooth cone to better capture the structure of the Görtler instability. The range was also increased slightly from 20° to 21° to fully capture the last peak. The distance of the sensor from the surface was estimated by placing the sensor very close to the model and taking images. The images were processed using known distances like dimensions of the probe holder to estimate the wall-normal distance of the probe from the model surface. Fig. 7.151 shows the map of voltage variations created from data collected over several wind tunnel runs. The coolant set point 20 °C case is shown in Fig. 7.151a and shows some structure and periodicity. Fig. 7.151b shows more definition and a periodicity of peaks every 4° can be seen. The boundary layer is also seen to decrease in thickness with the lower wall temperature. Fig. 7.151c shows the variations captured using the hot-film sensor over the cone with DREs at a coolant set point of -60 °C. The boundary-layer height was observed to decrease further as the structure of the Görtler vortices became stronger. The periodicity was again 4° which equates to a wavenumber of 90. (Siddiqui [4])

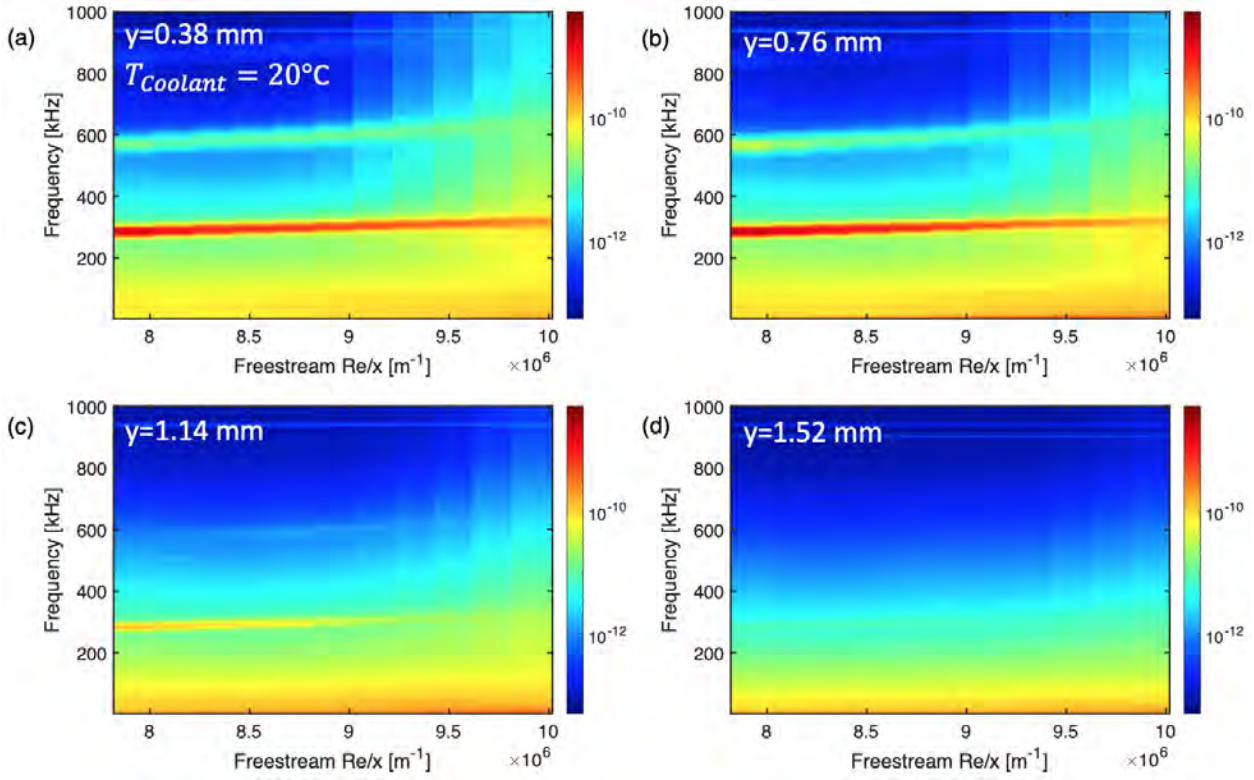

Figure 7.150: Spectral data from channels 2-5 of the LA-FLDI setup with wall-normal orientation over the course of a unit Reynolds number sweep on the cone with DREs. Coolant set point at 20 °C. [5]

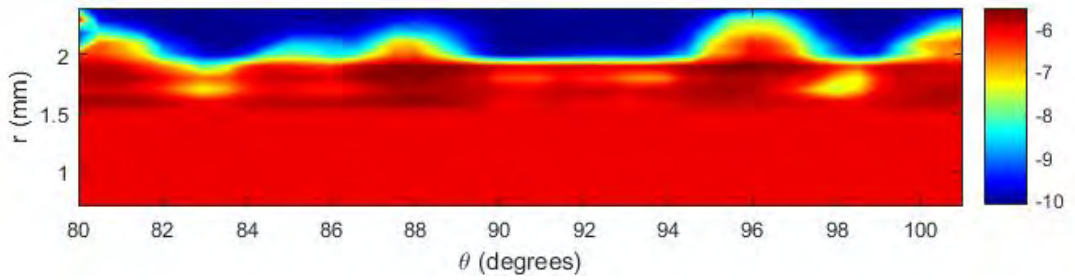

(a) Coolant set point 20 °C

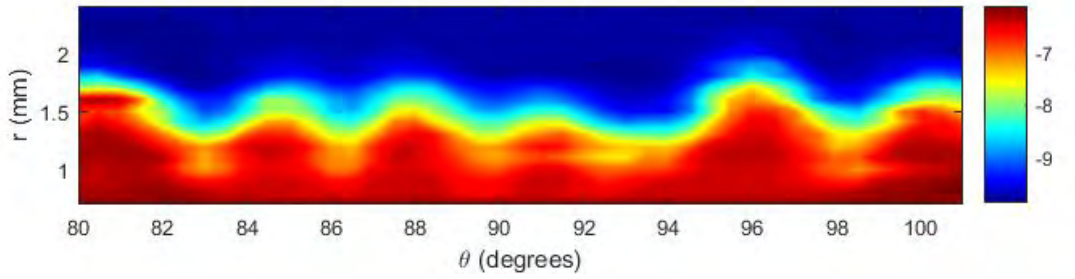

(b) Coolant set point -20 °C

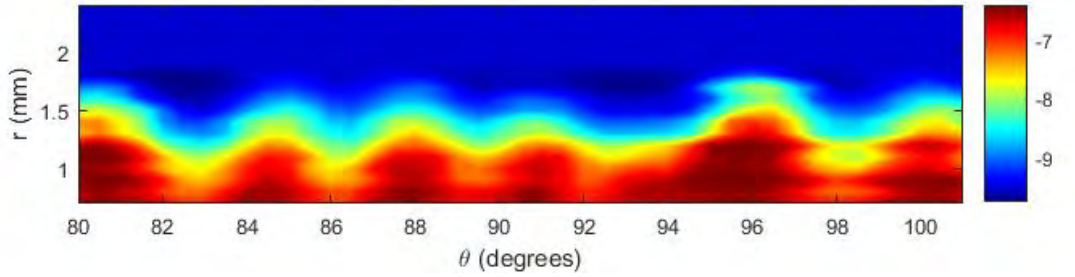

(c) Coolant set point -60 °C

Figure 7.151: Hot-film voltage variation over a 21° azimuthal sweep on the cone with DREs at a unit Reynolds number of $9x10^6$ /m. [4]

7.4 PHACENATE High-Speed Mach Stem Results

This section follows from [17] and McManamen et al. [3]. A list of the experiments performed in this work and the coinciding tunnel conditions is given in 7.32. The freestream Mach number was set to 4.4 for all tests. Total pressure measurements were taken during 'freestream' studies only, while 'Mach stem' investigations were purely optical investigations with wind tunnel models installed. The tunnel conditions remain comparable across the individual measurement campaigns, and the results between freestream and pre-shock Mach stem measurements show good agreement. During two of the Mach stem investigations, it was noted that a heater malfunction warning occurred. During these tests, the PID loop was reset during tunnel operation, and it was observed that the reservoir temperature increased above the desired temperature range by not more than 2 K for a period of several minutes (3-9 tunnel shots). Interrogation of the PLIF images for the course of these measurement campaigns showed no distinguishable indication of the isolated heater events, and the mean behavior of the results again show good agreement with the measurements where no heater warnings occurred; thus it is believed that the effects were negligible.

7.4.1 Total pressure characterization

Characterization of the freestream total pressure was performed by traversing a Pitot pressure probe across the center-line of the nozzle exit taking snapshots of data. The total pressure was measured at nine locations across the vertical and horizontal nozzle exit center-line. Following the procedure previously described, a section of data was analyzed for each location to determine the mean and fluctuating total pressure components across the nozzle exit plane. Plots of these are shown in 7.152 and 7.153 below. The uncertainty in the location of the probe at each point is of the order 0.2 cm. The model wedges, when installed, inhabit the area within $\pm$0.5 x/l and $\pm$0.5 y/h. Within this region, no significant anomalies in the mean or fluctuating total pressures are seen. Total pressure fluctuations were found to be $\sim$2 % for all three cases. The Re/m=2.1e6 case was marginally lower. It is noted that it is expected that a significant portion (up to 50%) of the fluctuating content was not resolved due to filtering and the physical size of the total pressure sensor. This would indicate an increase in the reported total pressure fluctuations by up to a factor of 2. However, the level of freestream disturbances observed here are comparable to the results of Mai and Bowersox [232] when their facility experienced turbulent boundary layers. Whereas the laminar boundary layer cases in their facility had significantly reduced freestream disturbances. This comparison indicates that the present nozzle experienced turbulent boundary layers at all conditions. The pressure and temperature data taken during each tunnel run was used in conjunction with isentropic and shock-jump relations to determine the expected bulk conditions for velocity and temperature in the Mach stem flow. These values and their uncertainties are listed in 7.33. ([17, 3])

7.4.2 MTV across normal shock

This section follows from McManamen et al. [3]. MTV experiments were performed on the Mach stem flow at four locations downstream of the normal shock wave for each Reynolds condition. The measurement locations were determined in post processing and were found to inhabit the region within 0.1 to 0.4 mm downstream of the normal shock wave. Early measurements taken

Re/m (10^6)	Total Press. (kPa)	Pitot Press. (kPA)	Repeat. (RMS) (RMS)	Heater Temp. (K)	Measurement Type
2.1	87.6 ± 1.0	8.2 ± 0.1	2.3	375	Freestream
3.5	145.1 ± 1.4	13.4 ± 0.2	1.4	374	Velocimetry (1D)
5.1	213.0 ± 1.8	20.1 ± 0.3	0.8	375	
2.1	86.0 ± 0.9	8.6 ± 0.1	not avail.	374	Mach Stem
3.5	145.3 ± 1.4	15.0 ± 0.2	0.6	374	Velocimetry (1D)
5.2	214.0 ± 1.7	22.1 ± 0.3	0.7	374	
2.1	87.0 ± 1.0	8.2 ± 0.1	0.8	374	Freestream
3.5	145.1 ± 1.4	13.4 ± 0.2	1.4	374	Thermometry
5.2	212.5 ± 1.8	20.5 ± 0.3	0.8	375	
2.1	86.8 ± 1.0	8.8 ± 0.2	0.7	375*	Mach Stem
3.5	146.5 ± 1.1	15.1 ± 0.2	0.6	375	Thermometry
5.2	212.5 ± 1.8	21.4 ± 0.3	1.0	375*	

Table 7.32: List of experiments and relevant tunnel conditions.(*Denotes a heater malfunction warning, the pebble bed heater PID loop was reset during tunnel operation and the supply temperature may have temporarily increased above the desired range.

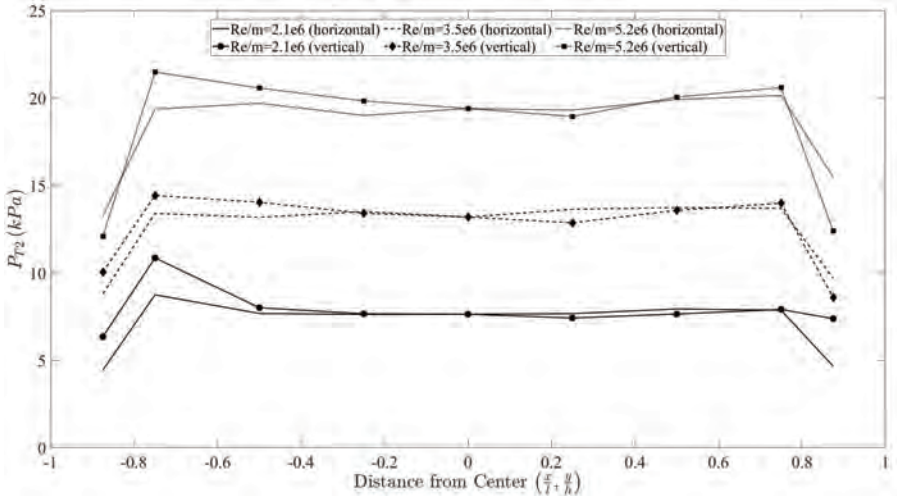

Figure 7.152: Total pressure traverse measurements for three Reynolds conditions in horizontal and vertical directions. [3]

M_1	T_1 (K)	T_2 (K)	U_1 (m/s)	U_2 (m/s)
4.4 ± 0.1	77 ± 3	361 ± 13	773 ± 23	162 ± 5

Table 7.33: Expected Mach stem conditions.

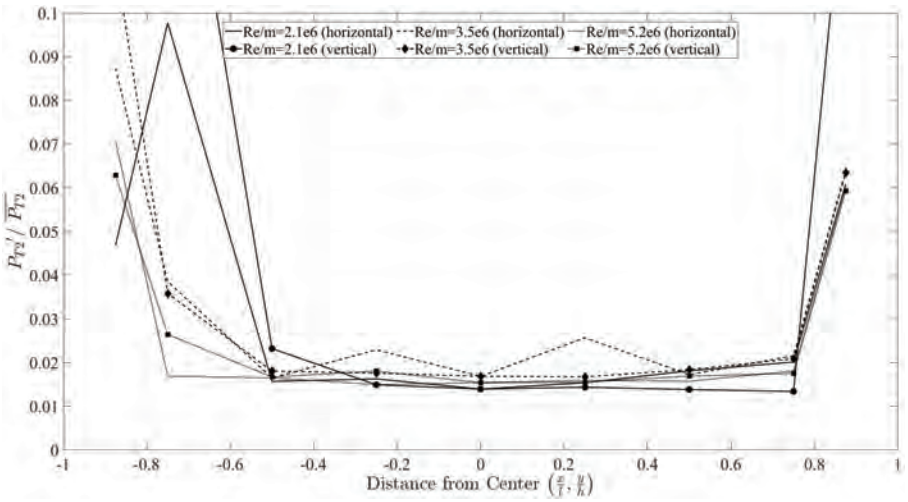

Figure 7.153: Total pressure fluctuation measurements for three Reynolds conditions in horizontal and vertical traverse directions. [3]

further downstream showed signs of significant acceleration due to the convergence of the shear layer, thus the domain was restricted to the close region where this influence was minimized. The freestream measurements were taken at a distance 1.6 to 2.0 mm upstream of the shock wave. Further, the center 300 pixels were extracted for analysis to avoid potential interactions with the shear layer or influences of shock curvature. It was determined that the curvature led to a maximum change in shock angle of 2.5 degrees across the domain, which accounts for a maximum difference of 0.004 in the normal Mach number component. Given this analysis, it is believed the slight curvature had no measurable effect within the region. This final interrogation window is shown in 7.154, overlaid on a PLIF image of the Mach stem at Re/m = 5.2e6 for visual reference. The mean and fluctuating velocities across the shock wave for each of the Reynolds conditions is presented in 7.34 below. The mean velocities are found to be within the uncertainty of the expected conditions. The uncertainty in cross-correlation peak estimation is believed to be on the order of 0.1 pixels following secondary fitting procedures, which does not account for the 3% difference in mean velocities observed. It is believed the main source of variability in velocity determination arises from the uncertainty of actual tunnel conditions during typical operation. Higher freestream and post-shock velocity fluctuations are noted in the lowest Reynolds condition, opposed to expectation. This trend is consistent with the freestream measurements performed without model wedges installed, thus it is believed that the operation of the facility at such a low pressure leads to an increase in freestream disturbances, possibly due to mass flow inconsistencies through the control valves at this condition. ([17, 3])

The mean velocities discussed above for the three Reynolds conditions were time-averaged over 500 samples. 7.155 shows 10 randomly selected velocity profiles in comparison with the mean velocity for a single line location in the middle Reynolds condition. This shows the overall spread of the data, and the result of the 500 sample averaging.

The number of data points (or image pairs) that were above the uncertainty cutoff of $r^2 = 0.95$

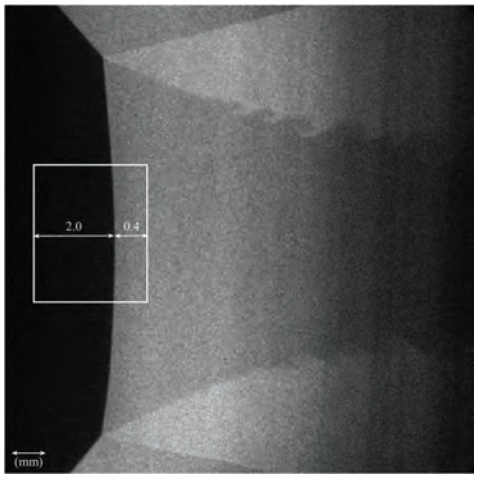

Figure 7.154: MTV measurement domain overlaid on PLIF image of Mach stem at Re/m = 5.2e6. [3]

$Re/m(10^6)$	$\overline{U}_{FS}$ (m/s)	$\overline{U}_{DS}$ (m/s)	$U'/\overline{U}_{FS}$ (%)	$U'/\overline{U}_{DS}$ (%)
2.1	$775-780$	$155-165$	$1-1.5$	$5-6$
3.5	$785-790$	$155-165$	$0.7-0.8$	$3.5-4.5$
5.2	$763-767$	$163-173$	$0.65-0.8$	$3-4$

Table 7.34: Mean and fluctuating velocities across a normal shock. Ranges shown for the four measurement locations of each Reynolds condition.

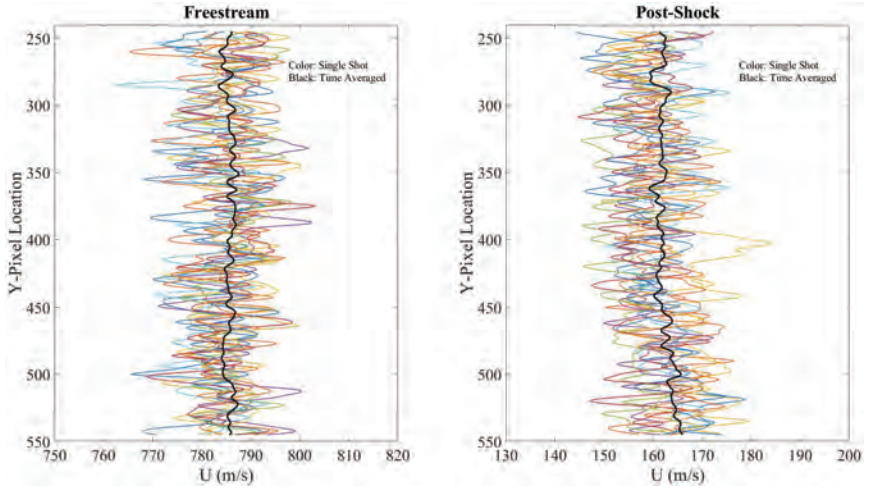

Figure 7.155: Several single-shot velocity profiles (color) in comparison to the time-averaged mean velocity (black). [3]

across the measurement domain for each measurement location and Reynolds condition is listed in 7.35. For the Re/m = 2.1e6 condition, the freestream shows 98-100% of data points are retained using this cutoff. Downstream of the shock wave, however, there is an increase in the number of data points that are cutoff. The closest and farthest locations from the shock wave in the downstream case show the highest loss of data, at only 85-95% retention. The discrepancy of the first location is possibly due to the proximity of the shock wave. In post processing, the shock wave was found to alter the line shape at this first location in some of the image pairs (due to shot-to-shot inconsistency in shock formation). These images were excluded from further processing, however it is possible that some inconsistency at this proximity was carried through in the remaining images as well. The low retention of the final location is presumably due to a discrepancy of laser intensity compared to the other cases. The Re/m = 3.5e6 condition experiences virtually no loss of data points to the uncertainty cutoff across the domain at all four measurement locations in both freestream and downstream of shock wave measurements. Similarly, the highest Reynolds condition (Re/m = 5.2e6) experiences only minor data loss to the uncertainty cutoff, mostly occurring at the third measurement location downstream of the normal shock, though not at a level that produces concern. The velocity amplification factor is defined as the square of downstream fluctuations divided by upstream fluctuations, $G = (U_{DS}')^2 / (U_{FS}')^2$, in this work. Amplification factor is plotted against distance downstream of the shock at each point in 7.156, 7.157, and 7.158 for the Re/m = 2.1e6, 3.5e6, and 5.2e6 conditions respectively. All four measurement locations are included, and the mean value for each location is shown in black over the raw data. In the lowest Reynolds condition, the larger scatter observed closer to the shock is likely due, again, to the shock proximity and decrease in data retention. Moving farther downstream the amplification factor is found to trend towards unity with a spread of ± 0.2. Similar data point spread is observed in the Re/m=3.5e6 and Re/m=5.2e6 conditions, having mean values across the domain of 1.2 and 1.1 respectively. Average amplification factors of the three Reynolds conditions are plotted together in 7.159. There does not appear to be a significant Reynolds number trend in velocity amplification for these conditions. The low Reynolds condition is perhaps an anomaly, due to discrepancies described previously. The final two conditions lie in close proximity to each other, with perhaps a slight reduction in amplification with increasing Reynolds number. Finally, the velocity amplification factors from this work are shown in relation to the LIA predictions from Donzis [32] in 7.160. The mean values fall just below the LIA curve, with no distinct Reynolds number trend. Error bars representing the spread of the data in this study are found to almost reach the LIA prediction. In contrast, the other works included in Donzis' study around this Mach number all lie well above the LIA prediction line. Although transverse velocity components were not measured in this work, an attempt can be made to estimate the turbulent kinetic energy by assuming the post shock anisotropy is somewhere between 1 and 1.1 [33, 183]. This would result in estimated amplification factors for TKE, 'G_{TKE}', in the ranges 1.05-1.16, 1.18-1.30, and 1.10-1.21 for the Reynolds conditions 2.1e6 1/m, 3.5e6 1/m, and 5.2e6 1/m respectively. In many cases, G_{TKE} may be preferred for comparison (and may be considered a more fair comparison to LIA), thus this estimate is provided as a basis. However, due to the inability to measure the transverse velocity components, and for consistency with Donzis [32] where G is defined as in this study, this work focuses on amplification of only the axial velocity in discussion.([17, 3])

$Re/m(10^6)$	Loc 1	Loc 2	Loc 3	Loc 4
2.1	>98, 85–99	>98, >95	>98, >95	>98, 85–95
3.5	100, >99	100, >99	100, 100	100, 100
5.2	>99, >97	>99, >97	>99, >95	>99, >98

Table 7.35: Percent of data points above the uncertainty cutoff of $r^2 = 0.95$ across the domain for each measurement location and Reynolds condition. The data are summarized as FS, DS.

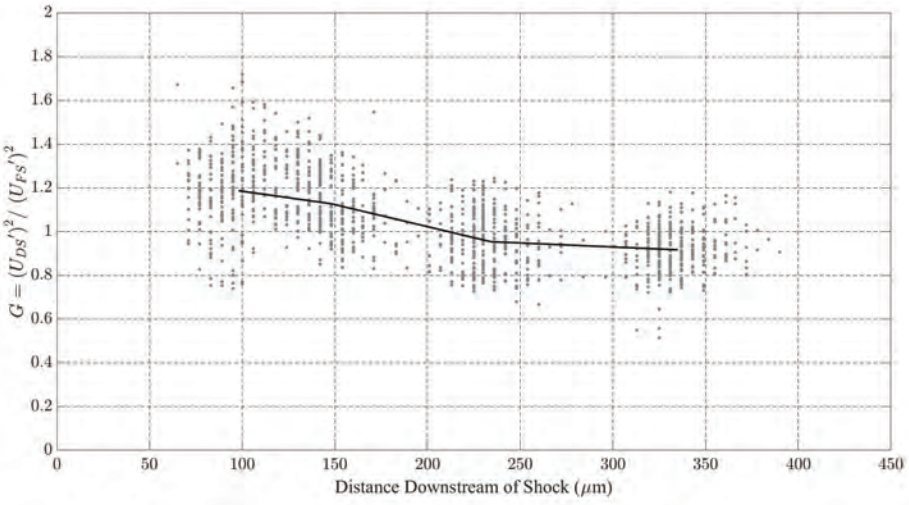

Figure 7.156: Velocity amplification factor as a function of distance downstream of shock for Re/m=2.1e6. [3]

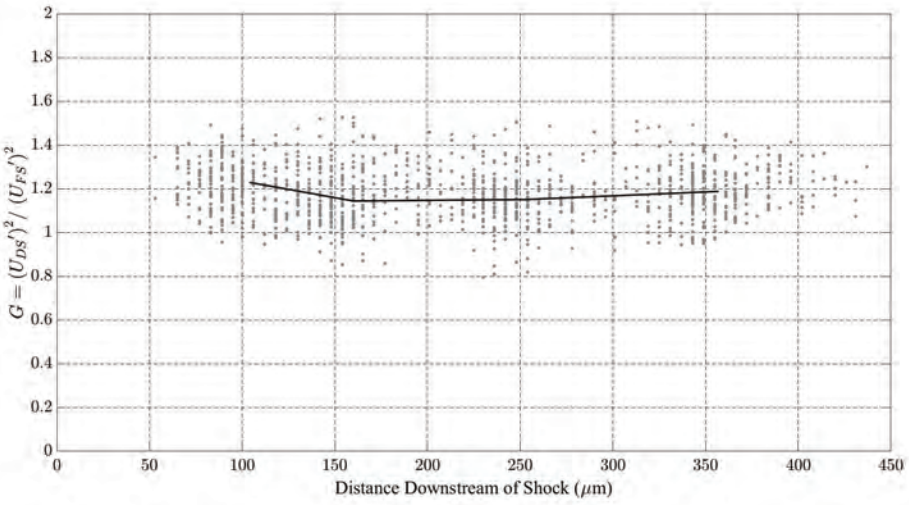

Figure 7.157: Velocity amplification factor as a function of distance downstream of shock for Re/m=3.5e6. [3]

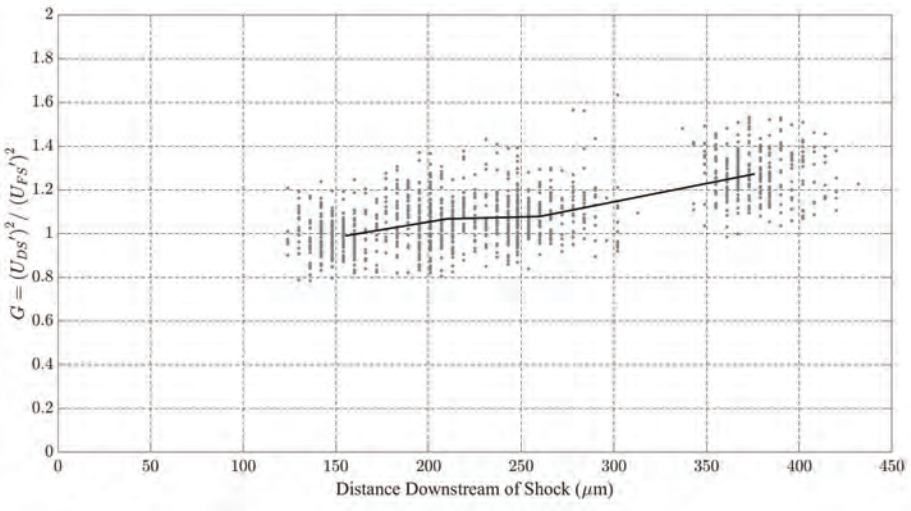

Figure 7.158: Velocity amplification factor as a function of distance downstream of shock for Re/m=5.2e6. [3]

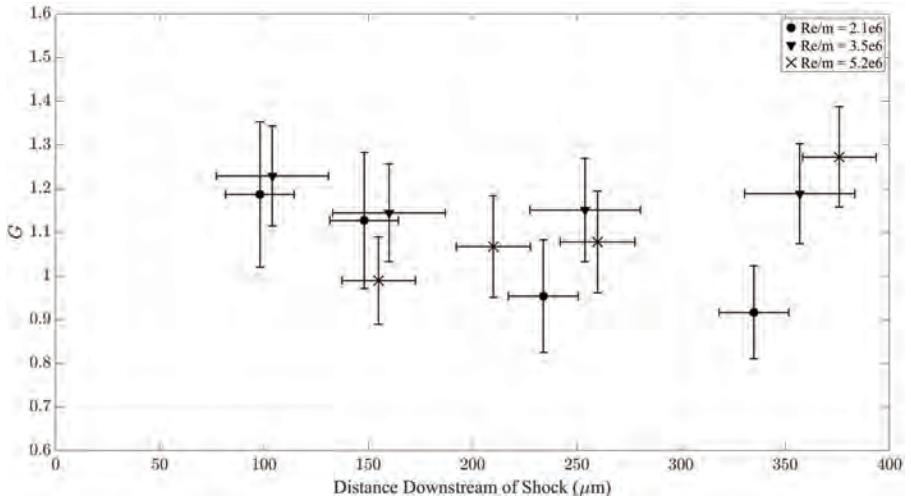

Figure 7.159: Velocity amplification factors across shock for all Reynolds conditions. [3]

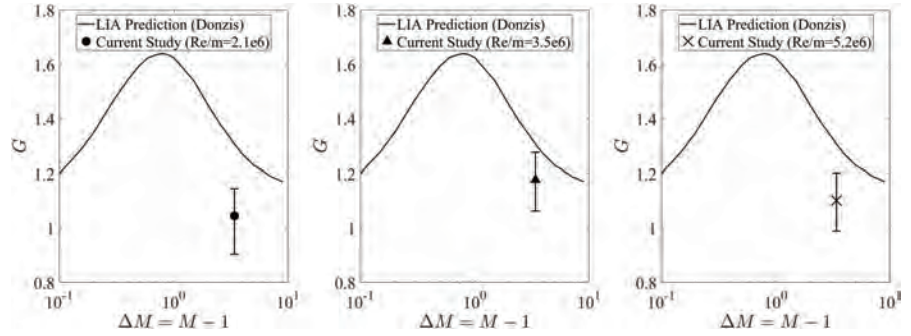

Figure 7.160: Velocity amplification factors in relation to LIA predictions (adapted from [32]). [3]

7.4.3 Thermometry across normal shock

This section follows from McManamen et al. [3]. As previously discussed, the PLIF thermometry experiments were found to be outside of the linear regime. The mean temperature was specified for two defined regions in front of and behind the shock wave, based on the expected conditions determined previously. Each region was processed using averaged 4x4 pixel bins, and temperature outliers beyond three standard deviations from the mean were excluded. Using these techniques, there was at least 98% retention of data points (image pairs) across the domain for all three Reynolds conditions. Contour plots of the fluctuating temperatures for each Reynolds condition are shown in 7.161. The two analysis regions are overlaid on the average PLIF image for each case for visual representation. In thermometry processing, laser intensity fluctuations play into the systematic error of the results. It could be suggested that the observed fluctuations are truly a result of laser intensity and not turbulent properties. 7.162 below shows the evolution of temperature fluctuations at 10 randomly selected pixels in each of the pre- and post shock domains for the highest Reynolds condition. The scale is set to view only the first 200 image pairs to better visualize the correlation. It is expected that dominating laser intensity fluctuations would lead to correlated behavior between all of the pixels, where true temperature fluctuations would be represented by 10 randomly fluctuating lines. While there are some common peaks, it can be seen that the 10 pixels act independently, therefore, it is believed that the systematic error did not dominate these measurements. Line plots representing the average temperature fluctuation across the vertical direction are shown in 7.163. Again, similar to the velocity results, the lowest Reynolds condition is found to have increased fluctuations in both the freestream and post-shock regions, while the remaining Reynolds conditions lie in close proximity to each other. Freestream fluctuations range 4.5-6%, increasing to 15-25% in the region downstream of the shock wave. Due to the significant temperature fluctuations observed downstream of the shock wave, the temperature amplification factor is defined in reference to the normalized fluctuations in this work. Specifically, $G_T = \sqrt{\left(T_{DS}'/\overline{T_{DS}}\right)^2 / \left(T_{FS}'/\overline{T_{FS}}\right)^2}$, where the upstream and downstream fluctuations are normalized by their respective mean temperatures. Under this definition, the lowest Reynolds condition settles to an amplification factor of 4.5, while the middle and high Reynolds conditions converge around 3. Moving towards the shock wave, the temperature amplification increases dramatically in all three cases. It is not truly possible to measure temperature fluctuations within the shock in this study, due to the time delay between images and uncertainty in specific shock location. Thus, the peak amplification is rather uncertain. In fact, due to pixel binning effects, only the region beyond 100 μm is considered further, and the region closer to the shock can only be a rough approximation of behavior. ([17, 3])

7.4.3.1 Uncertainty analysis

A large concern in this work was signal-to-noise (SNR) limitations, particularly in the low temperature and low density freestream. To mitigate this, the camera was liquid cooled to -35 C, which reduces the charge buildup on the sensor. Additionally, the dark-charge was subtracted within the camera software, which brought the base noise level down to approximately 60 counts. The lowest signal applications in this study experienced approximately 600 counts, thus, the SNR was found to be 10 or higher. Another source of error in the MTV application arises from the timing jitter of

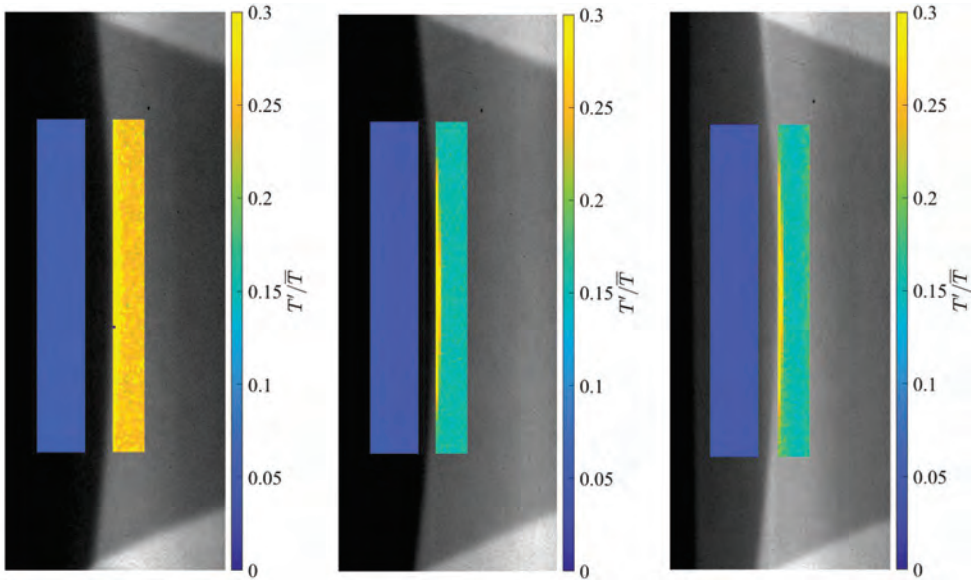

Figure 7.161: Temperature RMS fluctuations across shock for three Reynolds conditions. Left: Re/m =2.1e6, Center: Re/m = 3.5e6, Right: Re/m = 5.2e6. [3]

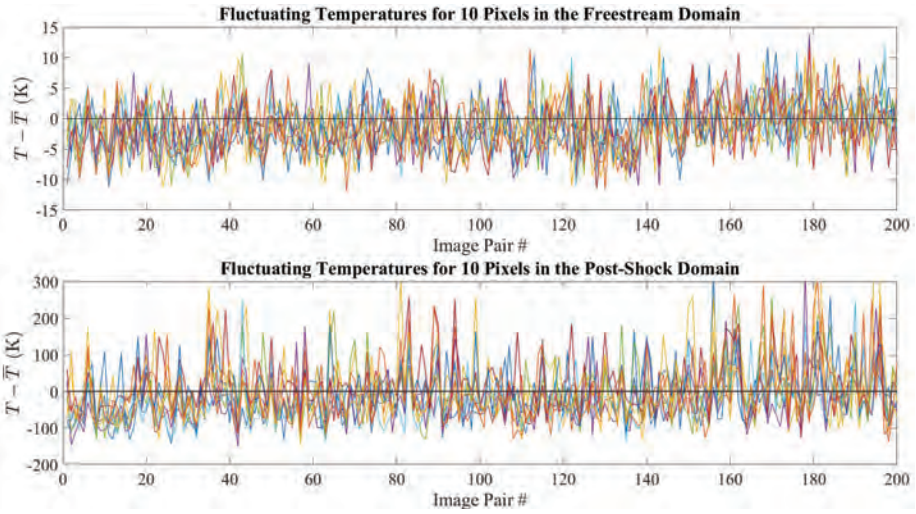

Figure 7.162: Temperature fluctuation evolution for the first 200 image pairs of 10 randomly selected pixels in the pre- and post-shock domains. [3]

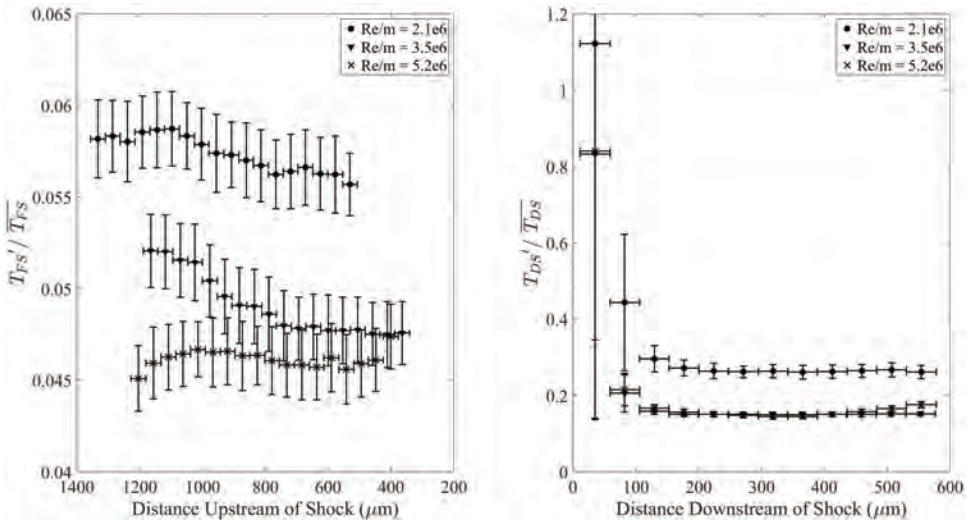

Figure 7.163: Average temperature RMS fluctuations as a function of distance downstream of shock for three Reynolds conditions. [3]

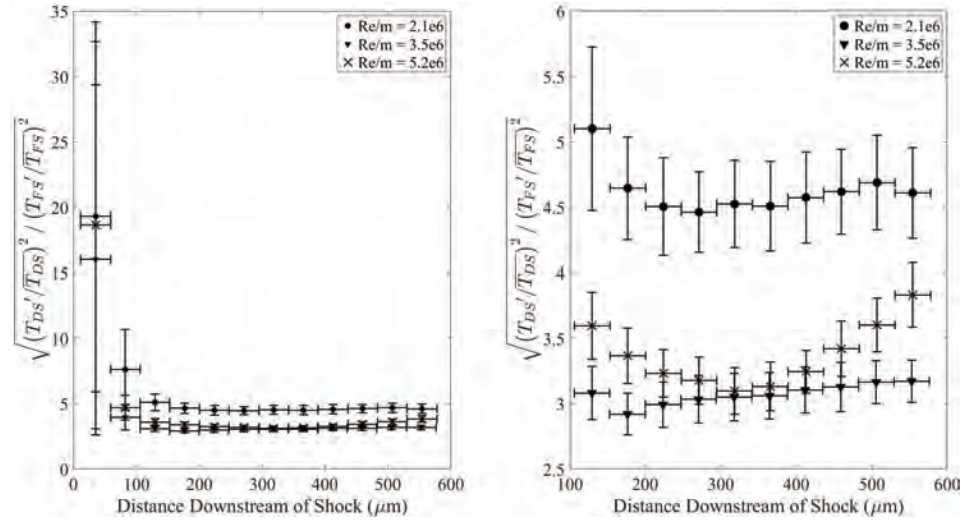

Figure 7.164: Average temperature amplification factor as a function of distance downstream of shock for three Reynolds conditions. To the left, the entire domain is included, to the right, only the region downstream of 100 μm is shown. [3]

the system (pulse/delay generator, camera, and lasers). The maximum reported timing jitter from each of these components arises from the YAG laser, at <0.5 ns, and the expected uncertainty from the system is <0.06%. The uncertainty of the MTV data processing algorithm was 0.1 pixels (as discussed in 6.4.3), which in the low velocity region downstream of the shock results in an uncertainty of 0.4%. The random error was reduced by taking large sample data sets. The total number of data points was of the order 600 thousand samples, and the expected error is <0.2%. Thus, the total error in the MTV application is expected to be of the order 0.5%. The thermometry application experienced similar sources of error, including SNR, data processing, and laser intensity fluctuations. Due to the pixel binning routine, the random error for thermometry is expected to increase to 0.25%. There was a reported 4% uncertainty in the mean temperature estimate, however, once established it is believed that this does not translate directly to the uncertainty in determination of the fluctuating temperatures. Overall, the total uncertainty from systematic and random sources is expected to be less than 0.5%. ([17, 3])

7.5 HXT Hypervelocity Mach Stem Results

This section follows from Dean [11] and Dean et al. [16].

7.5.1 FLEET Results

The runs probed with FLEET are listed in Table 7.36. Significant broadband emission was generated around the Mach stem model at the higher stagnation enthalpy cases. The broadband emission substantially increased the background noise in each FLEET image. A bandpass filter was added to the FLEET collection system, and light-absorbing tape was added inside the test section to mitigate interference from background emission. Some of the tape placed on the nozzle floor is visible in Fig. 6.29b. In addition to spectral filtering, a temporal filter was imposed by minimizing the gating time for the FLEET measurements. The FLEET images were processed using a Gaussian fit to determine the position of each FLEET line. Examples of the Gaussian fits for images captured during a case 3 run are shown in Fig. 7.165a and Fig. 7.165b at t=0 and t=5 ms, respectively. The Gaussian centered at x=0 mm in each figure marks the laser position captured before the run. The other curves show the displacement of the FLEET lines. Note the black lines show the raw data, and the red lines show the Gaussian curve fits. The elevated noise floor in Fig. 7.165b was caused by broadband emission likely produced by mylar combusting inside the test section after the test time. The FLEET velocities listed in Table 7.36 were computed using the single fleet image captured during each test time. FLEET velocity results are also listed in Table 7.36 next to test time flow velocities that were theoretically computed. The theoretical velocities agreed reasonably well with FLEET velocities measured in this study, validating the HXT computations. The static pressure measured at the nozzle exit and the FLEET velocities measured during a case 3 run are plotted in Fig. 7.166. The x-axis shows time relative to the test time fleet image, which is consistent with the times of Fig. 6.56. Error bars indicate the uncertainty of each velocity measurement. The flow after the test time is not fully processed by the unsteady expansion generated when the secondary diaphragm ruptures in HXT. As a result, the velocity decreased, and the static pressure increased after the test time. Comparing the velocity roll-off measured using FLEET with future CFD simulations of the HXT facility will help verify the accurate simulation of the unsteady expansion within the facility. ([11], Dean et al. [16])

Case	Mach	Enthalpy (MJ/kg)	Gas	Theo. Vel. (m/s)	FLEET Vel. (m/s)	Unc. (m/s)
2	8.5	5.2	air	3110	3350	46
2	8.5	5.2	air	3110	3340	50
3	8.5	1.8	air	1840	1920	45
3	8.5	1.8	air	1830	1860	29
3	8.5	1.8	air	1850	1950	23
5	8.4	7.2	N2	3670	3160	60
5	8.4	7.2	N2	3670	3270	43
7	8.4	5.9	N2	3310	3440	41

Table 7.36: Comparison between theoretically computed and FLEET measured freestream velocities in HXT.

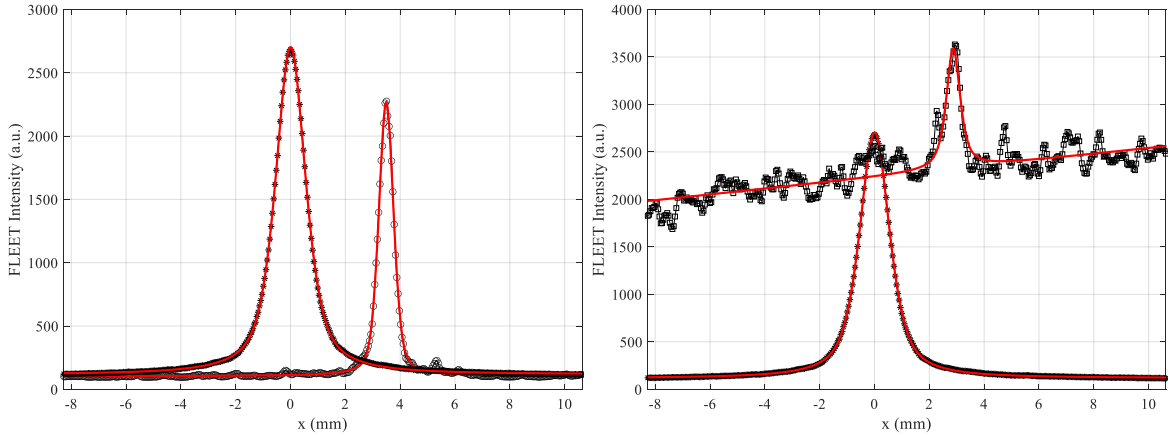

(a) (b)

Figure 7.165: FLEET image data and Gaussian curve fits showing the displacement of the FLEET lines during a case 3 run at a) the test time and b) 4 ms after the test time. [11]

7.5.2 Schlieren Results

This section follows from Dean [11]. The main reason schlieren was captured during these experiments was to spatially correlate the other diagnostic measurements to the positions of Mach stem flow features like the normal shock and shear layers. Before each run, schlieren images were used to ensure the model and the diagnostics were in the correct locations. In addition, schlieren was used to iterate on the thickness of spacers needed in the model for each flow case so the normal shocks would form 1 cm downstream from the back of the wedges. Schlieren was also used to evaluate the start, stop, and steadiness of test times. Raw high-speed schlieren videos were captured at 80 kHz during each run. The raw videos were processed with background subtractions and linear contrast enhancements. In addition, the FLDI and OES measurement locations were marked. A small amount of FLDI laser light would make it through the longpass dichroic mirrors

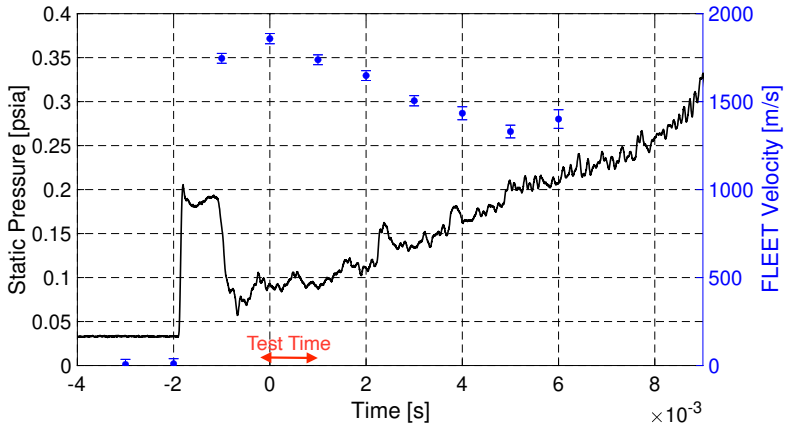

Figure 7.166: FLEET velocity plotted with static pressure measured at the nozzle exit during a case 3 run. [11]

used to turn the FLDI beams. The schlieren camera captured this light, revealing the positions of the FLDI beam pairs in the spanwise center of the model where the camera was focused. The FLDI laser was blocked by the bandpass filter placed in front of the schlieren camera during the runs, so the FLDI beam locations were captured in a schlieren snapshot before each run with the bandpass filter removed. An example of a raw and processed schlieren image is shown in Fig. 7.167. The ring-shaped shadows were caused by the edges of the dichroic mirrors used for the FLDI measurements. In the processed image of Fig. 7.167b, the vertical white lines along x=0 cm mark the location of an OES measurement. In addition, the cluster of dots around x=-4.25 cm shows the location of FLID measurements. A code was written to determine the position of the normal shock in each schlieren image. The positions of the normal shocks relative to the back of the wedges during different runs at each flow condition are plotted with static pressure in Fig. 7.168. The results in Fig. 7.168 show a consistent low-frequency variation of about 5 mm in the shock positions during the test times. There was an anti-correlation between shock position changes and static pressure changes. The results in Fig. 7.168 also show that the variation in shock position between different runs of the same case was a couple of millimeters. Cases 3 and 4 were the only air-driven conditions, and they both appeared to have the most test time unsteadiness. When operating an expansion tunnel, it is important to ensure the speed of sound in state 2 is greater than in state 3 to suppress acoustic disturbances generated by the primary diaphragms Paull and Stalker [241]. The speed of sound ratios a_3/a_2 for each flow case shown in Table 7.37 reveal that the two air-driven runs had the best sound speed ratios, so the unsteadiness was not related to disturbances generated by the primary diaphragms. The unsteadiness could be attributed to the secondary diaphragm material because cases 3 and 4 required thicker Mylar diaphragms than the other run conditions. In addition, Sharma found a qualitative correlation between the characteristic acoustic impedance across the initial secondary diaphragm and test gas noise levels [352]. ([11])

Schlieren snapshots captured during freestream FLDI measurements at each run condition are shown in Fig. 7.169. The scale of each image in Fig. 7.169 is the same, highlighting the different Mach stem sizes caused by the thermochemistry of each case. In some of the images, the edges

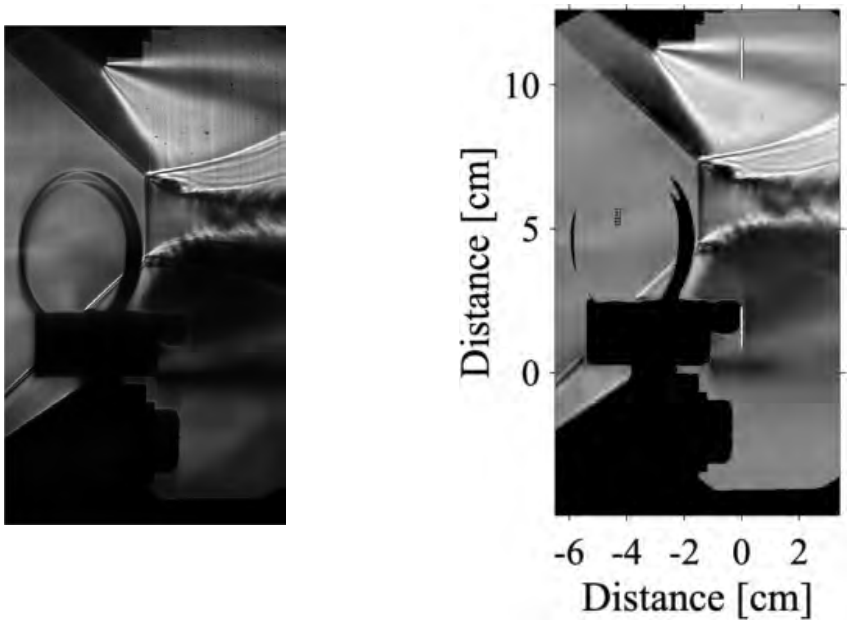

(a) (b)

Figure 7.167: Schlieren snapshots from a case 1 run showing a) raw and b) processed images. [11]

Case	1	2	3	4	5
a_2/a_3	2.0	1.4	2.3	2.3	2.0

Table 7.37: Sound speed ratios across the first contact surface of each flow case, which are relevant for the suppression of acoustic disturbances generated by the primary diaphragms. [11]

of the FLDI dichroic mirrors were visible. Although the positions of the FLDI optics were kept constant, the model location was adjusted. Therefore, the relative position between the model and the optics varied, and the mirror edges do not provide insight into the absolute positions of the Mach stems. Fewer turbulent structures are visible in Fig. 7.169c compared to the others because an LED light source was used instead of the CAVILUX during that run. Weak shocks generated by structures in the shear layers are visible in the schlieren results shown in Figs. 7.169a and 7.169b. Interestingly, the schlieren images also show a bifurcation in the shear layers generated at the shock triple points. The splitting of the shear layers is especially visible in the lower half of Fig. 7.169d. To our knowledge, this phenomenon had not been reported in literature, and it did not show up in US3D simulations Bryan et al. [10]. The bifurcation could have been an artifact of edge effects. ([11])

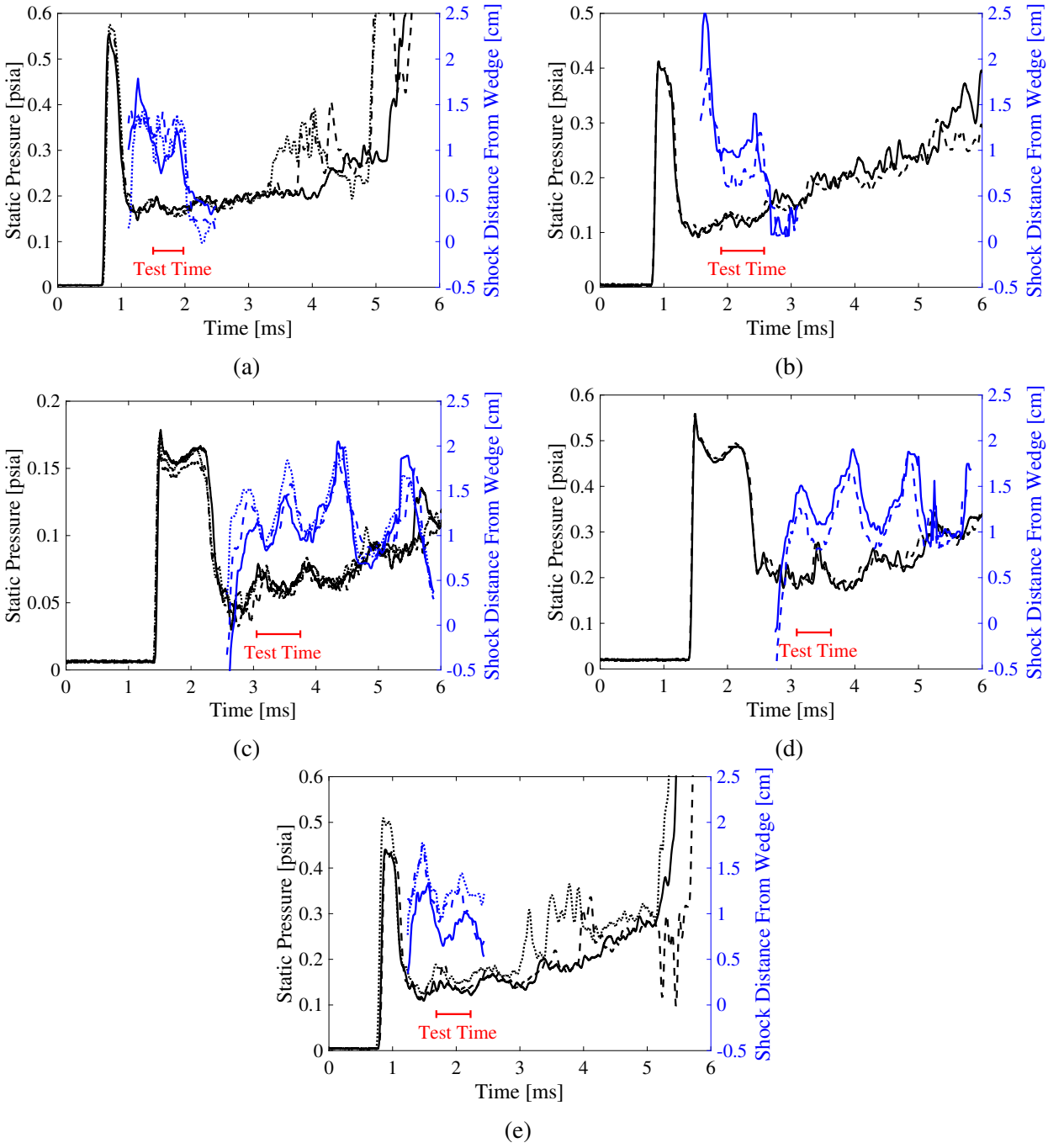

Figure 7.168: Plots showing normal shock positions relative to the back of wedges and static pressures measured during runs of a) case 1, b) case 2, c) case 3, d) case 4, and e) case 5. [11]

7.5.3 FLDI Results

The FLDI measurements were used to evaluate convective velocities, shock turbulence interactions, and shear layer turbulence.

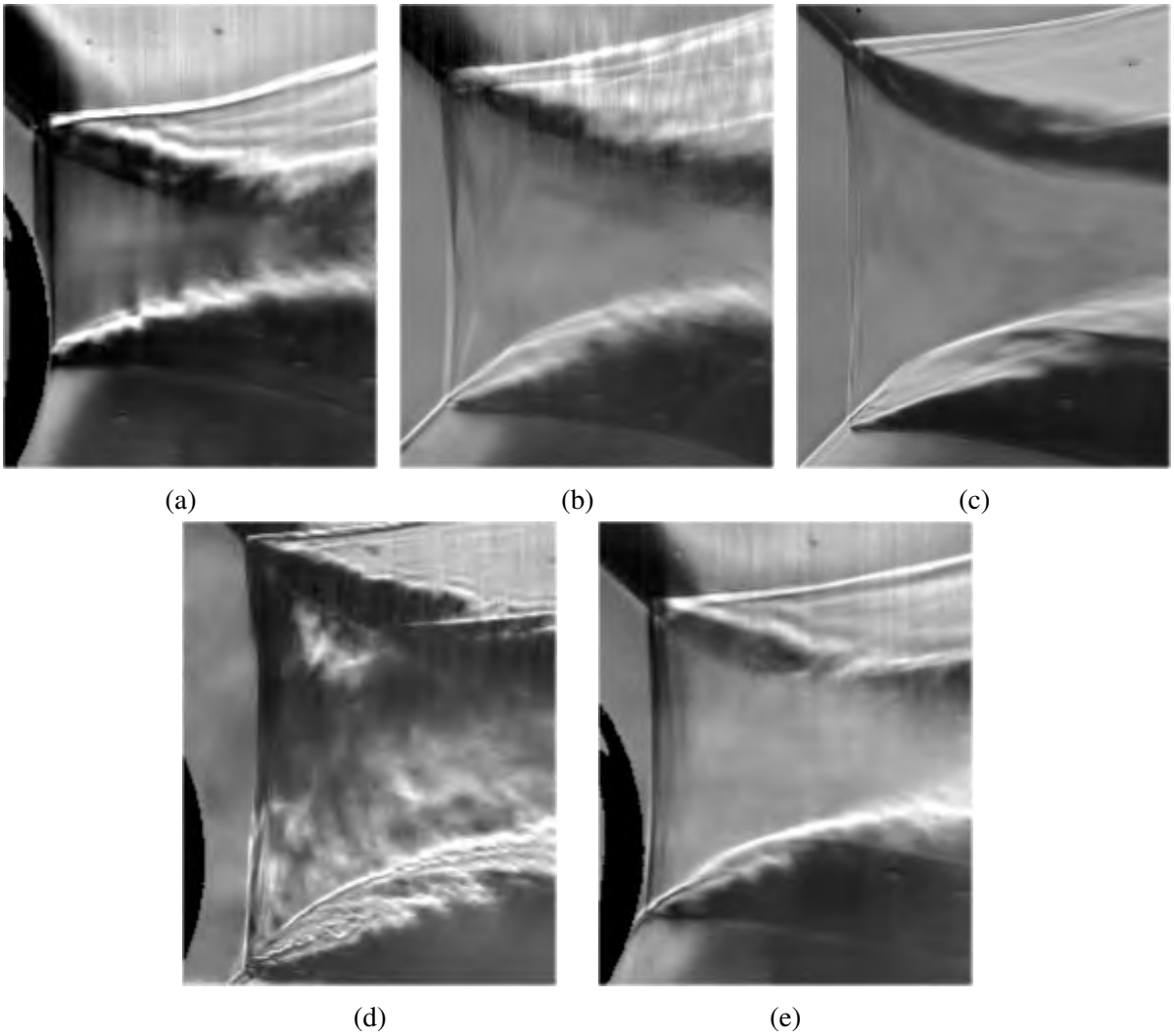

Figure 7.169: Schlieren snapshots captured a) case 1, b) case 2, c) case 3, d) case 4, and e) case 5. [11]

Many studies have employed FLDI setups capable of measuring the convective velocities of turbulent structures [353, 354, 355, 356, 325]. A 6 by 2 FLDI array was used in this study because it enabled simultaneous convective velocity measurements at 6 locations in the flowfield. Convective velocities (u_c) were computed using the distance between the foci of the two FLDI columns (ℓ), the DAQ sample rate (f_s), and the lag value (N_{lag}) corresponding to the peak normalized cross-correlation of adjacent sensor signals:

$$\langle u_c \rangle = \frac{\ell}{t_{corr}} = \frac{\ell}{N_{lag}/f_s} \tag{7.5}$$

The convective velocity is shown in angled brackets $\langle\rangle$ because it is a time-averaged velocity over the sample period corresponding to the total number of samples (N) used in the correlation. Ac-

cording to the beam profiler measurements discussed in Sec. 6.5.6, the length of ℓ was 897 μm for these experiments. Low-frequency trends in the data were removed by subtracting a third-order curve fit from each signal. Then, normalized cross correlations (R_{12}) were computed for all possible data shifts (ΔN) between each adjacent signal $s_1(n)$ and $s_2(n)$. MATLAB's xcorr function was used to compute the cross correlations. The general equation for a normalized cross-correlation is:

$$R_{12}(\Delta N) = \frac{\sum_{n=1}^{N} s_1(n) s_2(n+\Delta N)}{\sqrt{\sum_{n=1}^{N} s_1(n) \sum_{n=1}^{N} s_2(n)}} \tag{7.6}$$

The ΔN value that maximized the magnitude of R_{12}, designated N_{lag}, corresponded to the shift in time steps that caused the best overlap between signals. An example of two raw and aligned voltage signals is shown in Fig. 7.170. ([11])

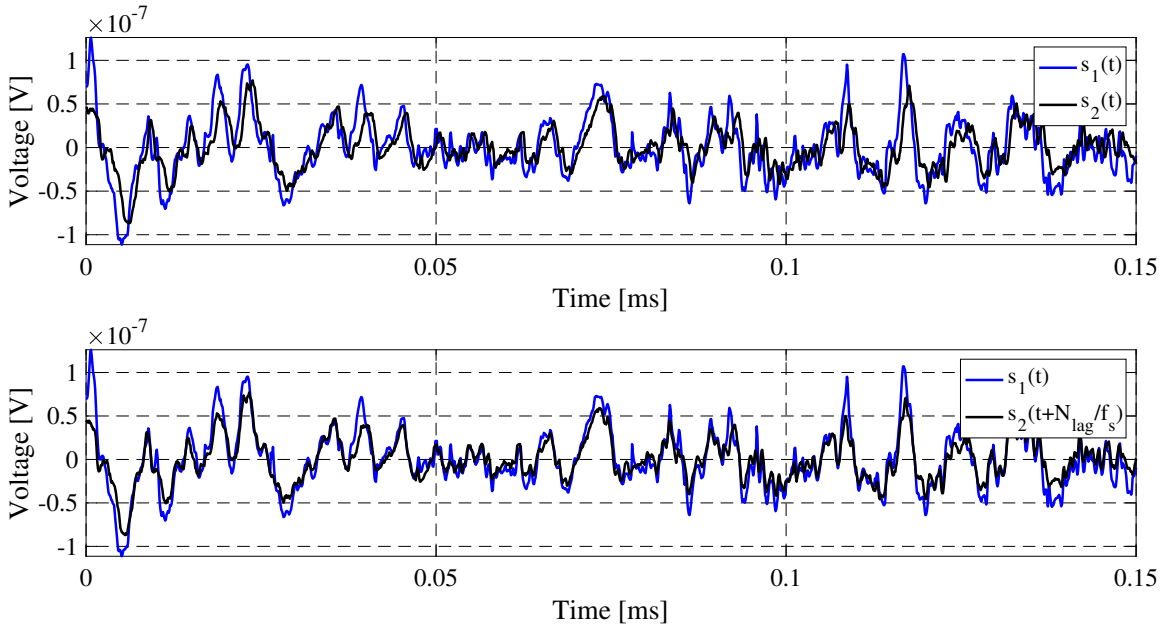

Figure 7.170: Example of signal correlation for convective velocity measurements with two raw signals in the top plot and two aligned signals in the bottom plot. [11]

FLDI measurements were made in the freestream, post-shock, and shear layer regions around the Mach reflections, as shown in Fig. 6.31. The average freestream convective velocity measured with the FLDI setup at each flow condition is listed in Table 7.38. The FLDI measured velocities agree reasonably well with the theoretically expected test time velocities, which are also listed in Table 7.38, despite large FLDI velocity uncertainties. The DAQ sample rate of f_s=10 MHz was a limiting factor for the accuracy of the freestream convective velocities, leading to the sizeable uncertainties. Future experiments would benefit from splitting pairs of adjacent FLDI voltage signals and simultaneously recording them with an oscilloscope at much higher sample rates. ([11])

Case	Theo. Vel. [m/s]	FLDI Vel. [m/s]	Unc. [m/s]
1	3700	3000	720
2	3100	3000	720
3	1900	1800	360
4	1900	1800	360
5	3700	3000	720

Table 7.38: Freestream convective velocities measured with FLDI and the corresponding uncertainties. The theoretical freestream velocities are included for comparison.

Similar to Davenport [326], the uncertainty of each velocity measurement was computed using the law of propagation of uncertainty as outlined by the National Institute of Standards and Technology [357]. As shown by Eqn. 7.5, the two inputs for the calculation of velocity were the measurement pair spacing ℓ and the correlation delay time t_{corr}. The uncertainty associated with the measurement pair spacing is the distance between beam pairs ℓ_{bp} because it is impossible to resolve the position of a disturbance between beam pairs. The uncertainty associated with the t_{corr} was defined as $u(t_{corr}) = 1/(2f_s)$ because it is impossible to resolve the time a disturbance passes between sample points. The total uncertainty of each convective velocity measurement (u_c) was computed with the equation:

$$u_c = \sqrt{\ell_{bp}^2 * \frac{1}{t_{corr}^2} + \frac{1}{4f_s^2} * \frac{\ell^2}{t_{corr}^4}} \tag{7.7}$$

Attempts to correlate adjacent FLDI signals in the post-shock regions were unsuccessful. The chemistry in the shock relaxation regions likely caused gradients and non-uniformities in the refractive index field, obscuring the convection of turbulent disturbances. The best convective velocity measurements were made in the shear layers. The shear layers were lower velocity and higher density than the freestream, lessening uncertainty caused by the sample rate and increasing the FLDI signal strength. ([11])

A limitation of the basic cross-correlation is that the signal sample rate dictates the resolution when computing the lag between signals. Similar to McManamen [17], correlation resolutions were enhanced using a fifth-order polynomial fit. Computing the lags between signals using the positions of the fitted curve maximums resulted in sub-sample time step estimations. An example of a shear layer velocity distribution evaluated using the standard cross-correlation and the enhanced curve fitting method is shown in Table 7.39. A substantial increase in velocity resolution was achieved because there was variation between the convective velocities of structures in shear layers, and the correlation found the average convective velocity over a time interval. Similar results were not achieved when applying this method to the freestream cases because the convective velocities of freestream flow features were practically constant. ([11])

Convective velocity distributions measured in the shear layers of each run condition are plotted in Figs. 7.171-7.175. Schlieren snapshots accompany each plot to provide context for the position

Basic Correlation	Curve Fit Correlation
1790 m/s	1780 m/s
1790 m/s	1770 m/s
1790 m/s	1750 m/s
1790 m/s	1660 m/s
1790 m/s	1590 m/s
1790 m/s	1530 m/s

Table 7.39: Shear layer velocity distributions of case 1 flowfield evaluated with normal cross-correlations and a cross-correlation enhanced using a curve fit.

of each FLDI measurement. The results show how the average convective velocity of flow structures in the shear layers changed with position. Points that appear as outliers in Figs. 7.172a and 7.173a could be caused by particles in the flow. It is also possible that something related to the upper portion of the bifurcated shear layer affected the correlations, as outliers consistently appeared near that region. The vertical positions in Figs. 7.171-7.175 are measured relative to the upper tip of the lower wedge. The streamwise distances between the upper tip of the lower wedge and the lowest, upstream most FLDI beam pair (channel 0) are listed in Table 7.40. ([11])

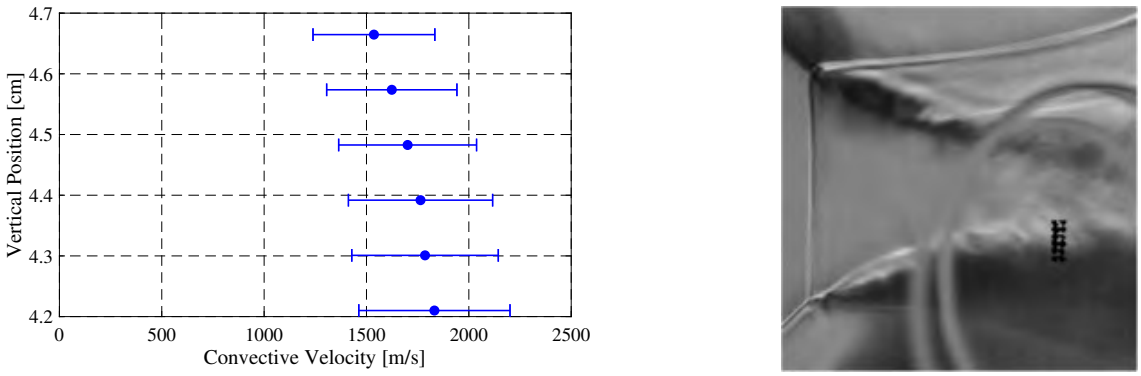

(a) (b)

Figure 7.171: Plot of FLDI convective velocities measured in a case 1 shear layer with a schlieren image for spatial reference. [11]

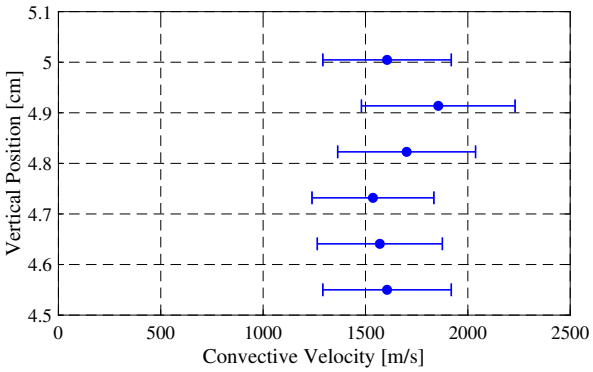

(a)

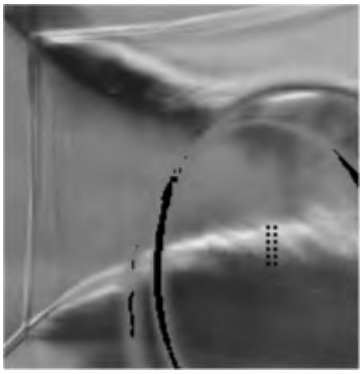

(b)

Figure 7.172: Plot of FLDI convective velocities measured in a case 2 shear layer with a schlieren image for spatial reference. [11].

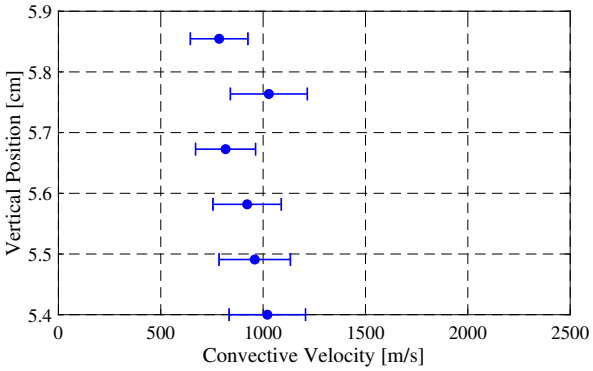

(a)

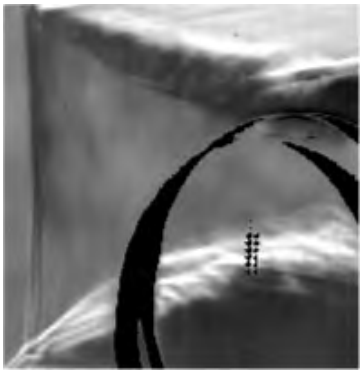

(b)

Figure 7.173: Plot of FLDI convective velocities measured in a case 3 shear layer with a schlieren image for spatial reference. [11].

Case	1	2	3	4	5
Streamwise Distance (cm)	4.6	4.3	4.6	4.6	4.7

Table 7.40: Streamwise distances between the upper tip of the lower wedge and the lowest, upstream most FLDI beam pair (channel 0) for the measurements shown in Figs. 7.171-7.175.

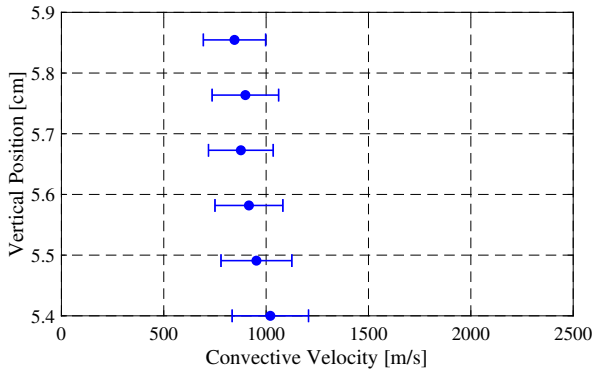

(a)

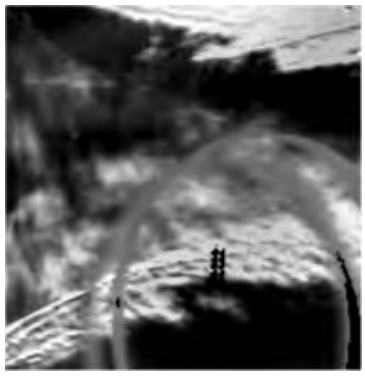

(b)

Figure 7.174: Plot of FLDI convective velocities measured in a case 4 shear layer with a schlieren image for spatial reference. The shock was just upstream of the left edge of the schlieren frame. [11].

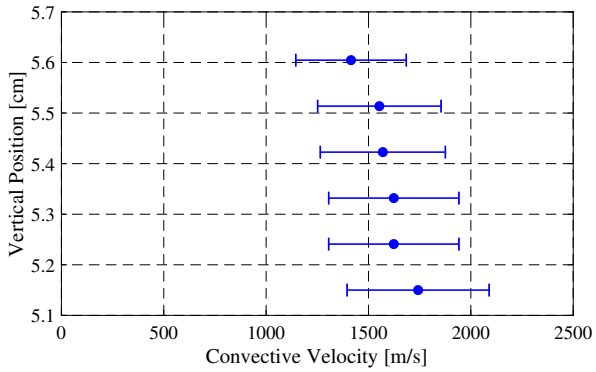

(a)

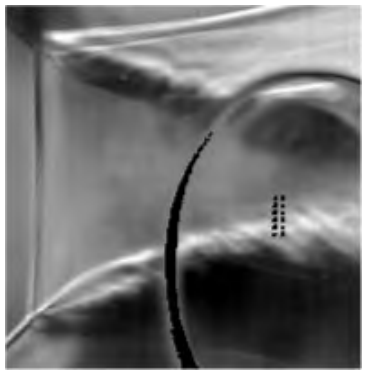

(b)

Figure 7.175: Plot of FLDI convective velocities measured in a case 5 shear layer with a schlieren image for spatial reference. [11].

7.5.4 Shock Turbulence Interaction

One aim of this experimental campaign was to use FLDI measurements to quantify the change in the index of refraction fluctuations across the normal shocks of the Mach reflections at each run condition. In order to calculate refractive index fluctuations, raw FLDI voltages were processed using the method outlined in Sec. 6.5.6 to reduce inaccuracies caused by particles. Note that this process did not entirely remove inaccuracies caused by particles, and the influence of particles passing through the FLDI beams could still be significant. Then, the voltages were converted to differential index of refraction. A trend removal using a third-order curve fit was performed on the data to isolate *dn* fluctuations from low-frequency changes. Then, the power spectra were computed using fast Fourier transforms with hanning windows of duration 1e-5 s and 50% overlap. The test times for each flow condition varied, but this window duration ensured that at least 100 windows were used for computing power spectra. The freestream power spectra measured with the upstream column of FLDI measurements during a case 5 run condition are shown in Fig. 7.176. The channel labels follow the convention outlined in Fig. 6.39b. The colored lines correspond to test time measurements, and the black lines correspond to the background noise floor of each beam pair. Backgrounds were measured immediately before each run while the test section was still under vacuum. The results in Fig. 7.176 highlight the consistency in the measurements made by each beam pair. The power spectra computed using channels 1-4 were averaged together, creating a single line for comparisons with other cases. The results in Fig. 7.177a show the average refractive index power spectra measurements made in the freestream of each flow case, where dotted lines show the average background spectra and solid lines show the average test time spectra. Cases 1 and 3 were both performed twice, and those results show great repeatability. Variations in the backgrounds were caused by changes to the FLDI setup throughout the campaign. Power spectra are not relative measurements, so the background variation only influenced the detection threshold of frequencies with very low energy. ([11])

The flow conditions of cases 1, 2, 3, and 5 were selected such that the post-shock densities would be equivalent, assuming equilibrium chemistry. Since thermochemistry causes an increase in post-shock density relative to an ideal gas, the freestream densities of higher enthalpy cases were slightly lower. In addition, the freestream density of case 4 was much higher than all of the other cases. The Power spectra shown in Fig. 7.177b were computed from *dn* normalized by ρ_{atm}/ρ_{∞} to better compare the freestream refractive index fluctuations between cases given the different densities. In order to avoid confusion, the power spectra plot was cropped to prevent ambiguity caused by the different background levels. The results in Fig. 7.177b show mild variation in power spectra between all cases on the low-frequency side of the plot. In addition, cases 1 and 5 show the same high-frequency content. No high-frequency content was measured in either case 3 run. Some small-scale flow structures could have contributed to the elevated high-frequency content of cases 1, 3, and 5. However, most of the high-frequency content shown in these cases were likely artifacts of particles passing through the FLDI beams. Similar to the freestream results presented in Fig. 7.177a, the average power spectra of post-shock *dn* measurements are plotted in Fig. 7.178a. The background noise floors are shown with dotted lines. Case 4 appears as an anomaly because it had a post-shock density more than three times greater than the other cases. In addition, the only case without high-frequency content was case 3. Given the dissimilarity in post-shock densities,

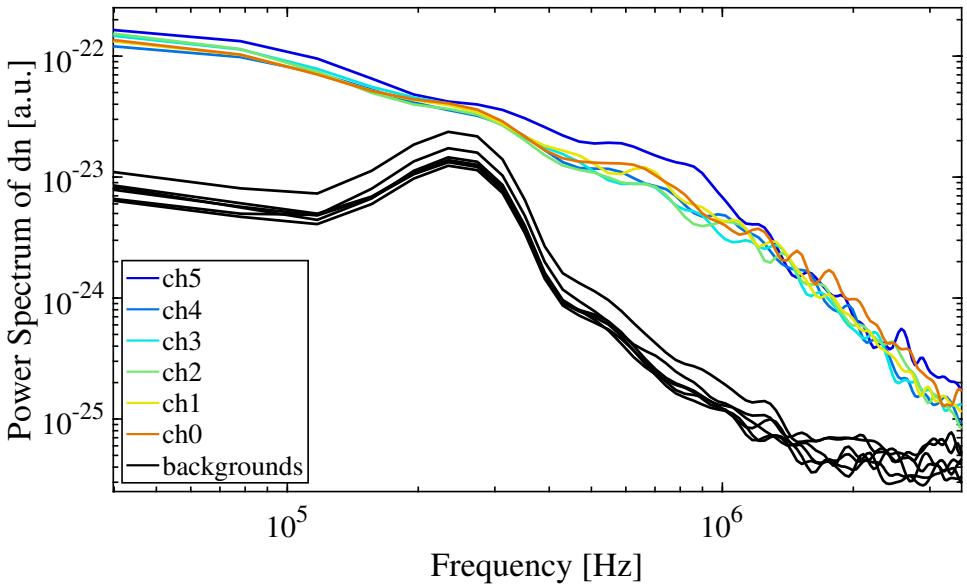

Figure 7.176: Power spectra of *dn* measured with the upstream column of the FLDI setup in the freestream of a case 5 run condition. [11]

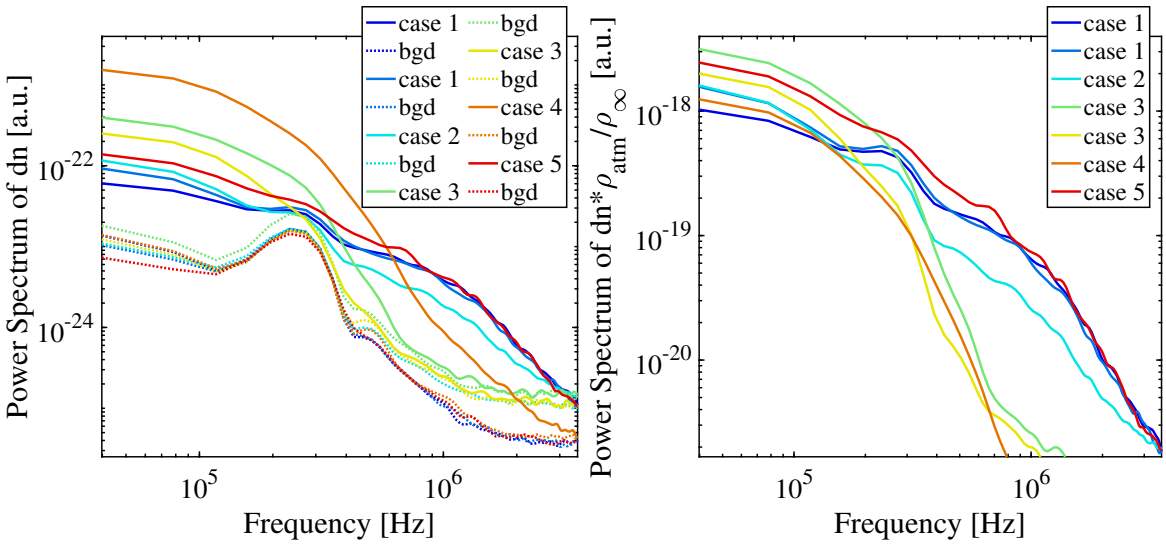

Figure 7.177: Freestream refractive index power spectra, where a) shows the power spectra with the corresponding noise floor backgrounds (bgd) and b) shows density-normalized power spectra. [11]

the power spectra shown in Fig. 7.178b were derived from *dn* normalized by ρ_{atm}/ρ_2, where ρ_2 is the post-shock density assuming equilibrium chemistry. Analogous to the normalized freestream findings, the normalized post-shock spectral results exhibit mild variations between cases in the

lower frequency range. In addition, high-enthalpy cases 1, 2, and 5 demonstrated similar high-frequency characteristics. The case 4 result will be discussed later in this section. A comparison between unnormalized freestream and post-shock power spectra is presented in Fig. 7.179a. The results on the low-frequency end show elevated refractive index fluctuations were present in the post-shock regions, which is logical considering density rises significantly across shocks. The only notable difference in high-frequency power spectra measured across the shock was in case 4. The high-frequency content of case 3 did not change because no high-frequency content was measured in the freestream or post-shock regions of case 3. A plausible explanation for the lack of high-frequency amplification in cases 1, 2, and 5 is that particles, which remained relatively unchanged when passing through the post-shock regions, caused most of the high-frequency content. Only case 4 exhibited an increase in high-frequency refractive index fluctuations across the shock. A more straightforward way to visualize the amplification across the shocks is presented in Fig. 7.179b, where the ratios between the unnormalized post-shock and freestream power spectra curves are plotted. The ratio results show that the amplification in case 4 was almost two orders of magnitude. The lower frequency ratio results also show that, aside from cases 1 and 4, higher enthalpy cases had increased amplifications in low-frequency refractive index fluctuations. The underlying mechanism for this trend was likely real gas effects, where the density ratios across the shocks increased as enthalpy increased. A comparison between the density normalized freestream spectra of Fig. 7.177b and post-shock spectra of Fig. 7.178b is presented in Fig. 7.180a. The results show that higher enthalpy air runs had progressively reduced low-frequency post-shock refractive index fluctuations relative to the local flow density. However, these findings do not unequivocally imply a damping of low-frequency density fluctuations because changes in the Gladstone-Dale constant accompanied chemistry changes within the post-shock regions. The fact that the low-frequency, post-shock results of case 5, which had minimal chemistry changes since it was pure nitrogen, is bounded by the low enthalpy air runs is further evidence that post-shock chemistry played a role in the low-frequency post-shock trends of Fig. 7.180a. ([11])

In most cases, high-frequency content was caused by particles, which were independent of the initial change in density across the shock. As a result, there is little meaning in the normalized high-frequency content of all cases except case 4. The ratios between the density normalized post-shock and freestream power spectra curves presented in Fig. 7.180b show that the change in the density normalized fluctuations of case 4 was around unity until 1 MHz. Interestingly, the ratio of Case 4 shows that the normalized refractive index fluctuations increased slightly at the lowest measurable frequencies. Although the Gladstone-Dale constant changes across the shocks Merzkirch [358], the change is independent of disturbance frequency. Therefore, the ratio results in Fig. 7.180b indicate that at the case 4 condition, either the amplification in density fluctuations around 300 kHz was less than lower frequency density fluctuations or the attenuation in density fluctuations around 300 kHz was greater than lower frequency density fluctuations. Ambiguity regarding whether or not the results indicate density fluctuations were amplified or attenuated is due to uncertainty surrounding the Gladstone-Dale constant in the post-shock region, which is an analysis left to future work. Another noteworthy trend in Fig. 7.180b is the order of magnitude difference between the low-frequency ratios of cases 3 and 4, which were identical run conditions except density. The ratio difference could be attributed to particles. A comparison between the freestream and post-

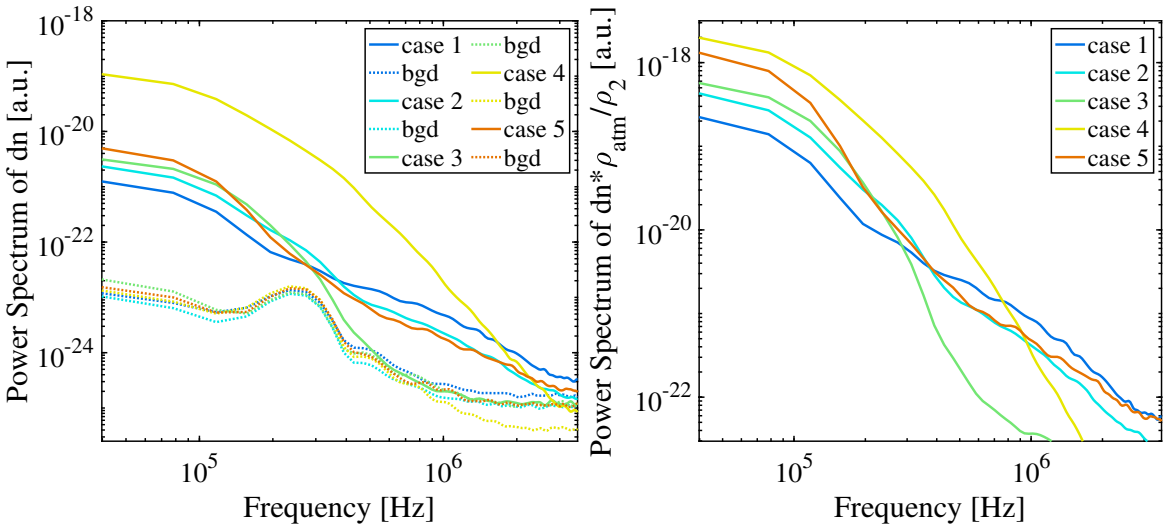

(a) (b)

Figure 7.178: Post-shock refractive index power spectra, where a) shows the power spectra with the corresponding noise floor backgrounds (bgd) and b) shows density-normalized power spectra. [11]

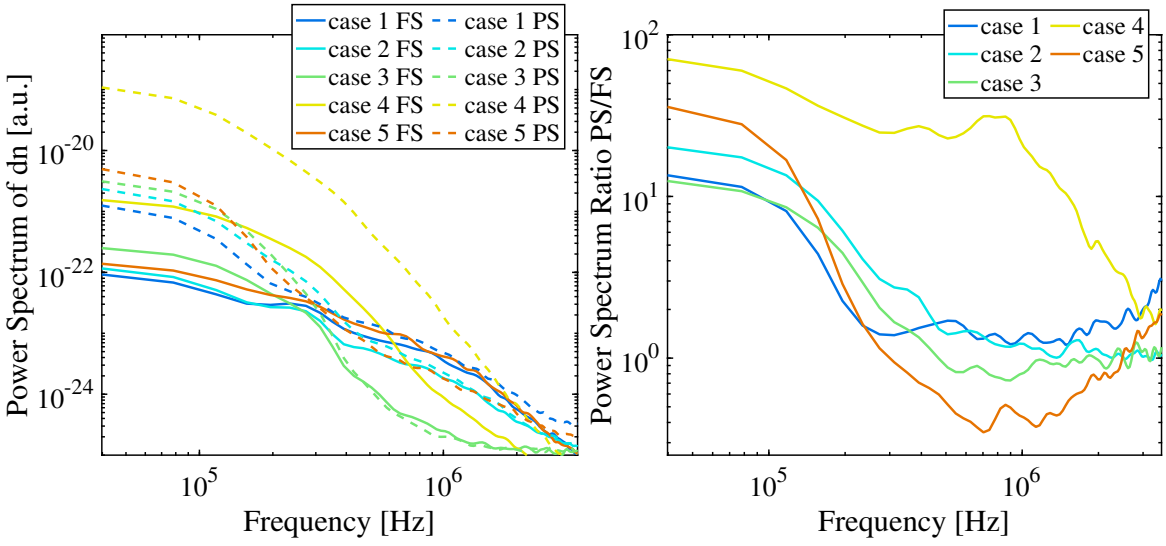

(a) (b)

Figure 7.179: Comparisons between unnormalized *dn* freestream (FS) and post-shock (PS) power spectra, where a) shows the power spectra and b) shows the ratios between the power spectra curves. [11]

shock root mean square (RMS) refractive index fluctuations (*dn*) is shown in Fig. 7.181a with the

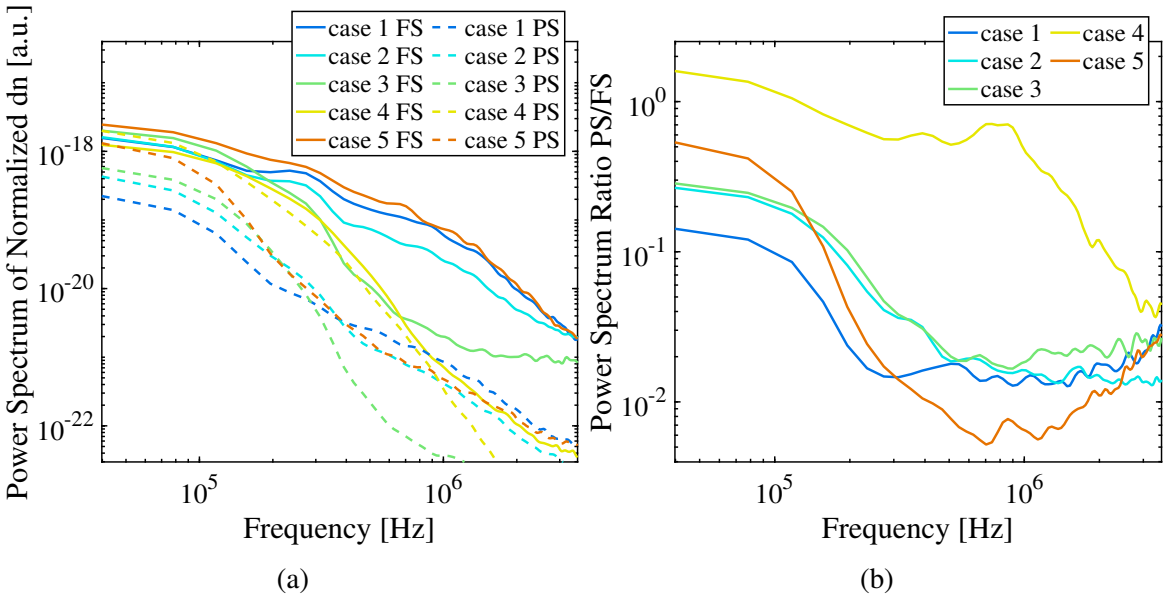

Figure 7.180: Comparisons between density normalized *dn* freestream (FS) and post-shock (PS) power spectra, where a) shows the power spectra and b) shows the ratios between the power spectra curves. [11].

corresponding RMS backgrounds. Similar to the power spectra results of Fig. 7.179a, the RMS was substantially greater in the post-shock regions, which had locally higher densities. A comparison of the RMS of density normalized refractive index fluctuations is shown in Fig. 7.181b. Contrary to the RMS of unnormalized *dn*, the RMS of the density normalized refractive index fluctuations were lower in the post-shock region for all cases except case 4. It is worth noting that the influence of particles was most significant in the high-frequency regions, which contained relatively low power. Therefore, the RMS results were less susceptible to measurement error caused by particles than the power spectra results may imply. ([11])

7.5.5 Shear Layer Turbulence

FLDI measurements were performed in the shear layers for each flow condition. Complexities of these turbulent shear layers included supersonic flow in thermal nonequilibrium on one side and dissociated, subsonic flow on the other. In addition to velocity, thermal, and chemical discontinuities, the shear layers are exposed to a favorable pressure gradient caused by the expansion generated at the back corners of the wedges.

Power spectra and RMS fluctuations from the same shear layer FLDI measurements discussed in the convective velocity results of Sec. 7.5.3 are presented in Figs. 7.182-7.186. All of the measurements were made approximately 3.5 cm downstream from the normal shocks. The vertical location of the measurements made during the case 1 flow condition, shown in Fig. 7.182c, slightly favored the oblique shock side of the shear layer. Interestingly, the power spectrum results show the power of frequencies near the middle of Fig. 7.182a decreased with position into the post oblique shock region. According to the work of Fujji and Hornung, the peak absorption rate for

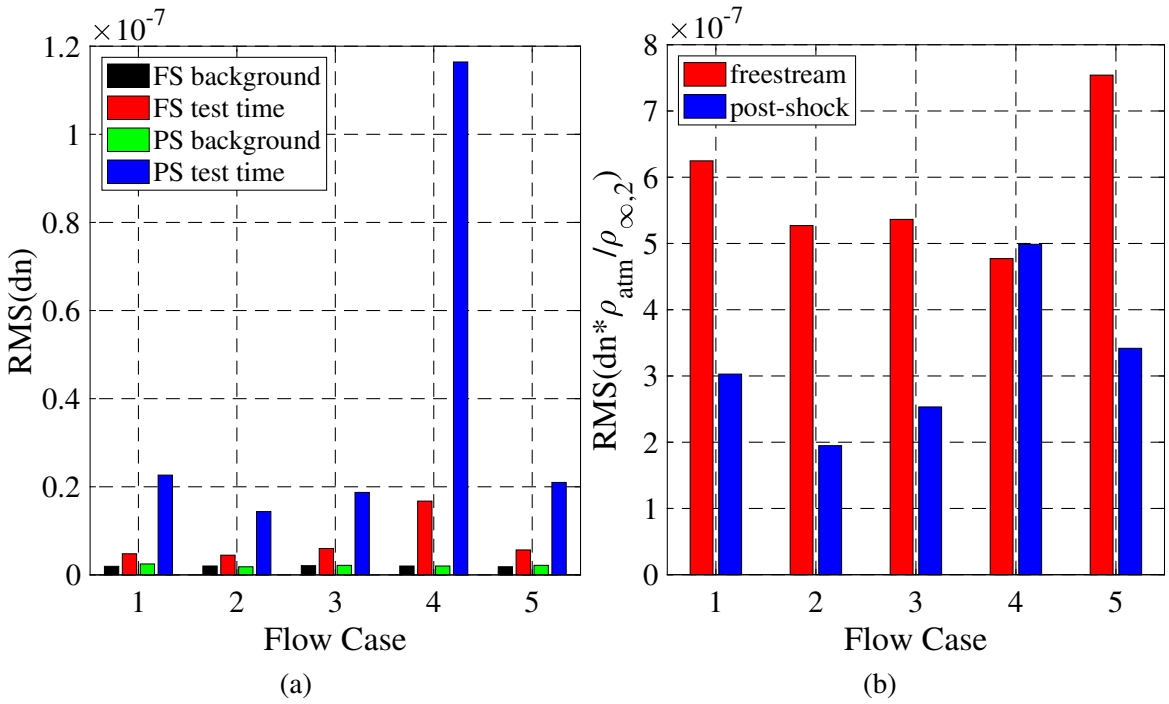

Figure 7.181: RMS for freestream (FS) and post-shock (PS) dn measurements with a) showing background RMS next to the test time RMS of each flow case and b) showing RMS of $dn * \rho_{atm}/\rho_{\infty}$ for the freestream and $dn * \rho_{atm}/\rho_2$ for the post-shock region. [11]

air at a temperature of 5,000 K and a density of 0.1 kg/m^3 is between 10^5 and 10^6 Hz. Therefore, it is possible that variation in power spectra shown in Fig. 7.182a was caused by acoustic damping [86]. Nothing particularly interesting was measured in the shear layer of the case 2 run shown in Fig. 7.183. The RMS results indicate that the measurements were made near the center of the shear layer. In addition, the refractive index power spectra was invariant with position. The vertical location of the measurements made during case 3, shown in Fig. 7.184c, slightly favored the normal shock side of the shear layer. Whereas the case 1 measurements on the other side of the shear layer only demonstrated variation in the medium frequency range, the results in Fig. 7.184a show uniform variation in the highest frequency range. Identical trends are present in the case 4 results of Fig. 7.185. It should be noted that since the flowfields were not perfectly steady throughout the test times, some spatial blurring in the results is expected. In addition, the freestream and post-shock FLDI results exhibited remarkable uniformity across all channels, indicating that particle distribution was uniform throughout the flow. Therefore, spatial variation in spectra throughout the shear layers can be predominantly attributed to variations in local turbulence. The case 5 measurement location strongly favored the normal shock side of the shear layer. The FLDI measurements at this location, presented in Fig. 7.186, reveal moderate variation in all frequencies with vertical position. Notably, the power spectra exhibited a consistent trend of decreasing magnitude as the distance from the center of the shear layer increased. The most pronounced variation in power spectra occurred around 1 MHz, and the frequency with the highest power occurred around 160

kHz. Despite the substantial overall variation in power spectra, it is interesting to note that the refractive index fluctuations measured at channels 2, 4, and 5 all exhibited the same high-frequency characteristics. ([11])

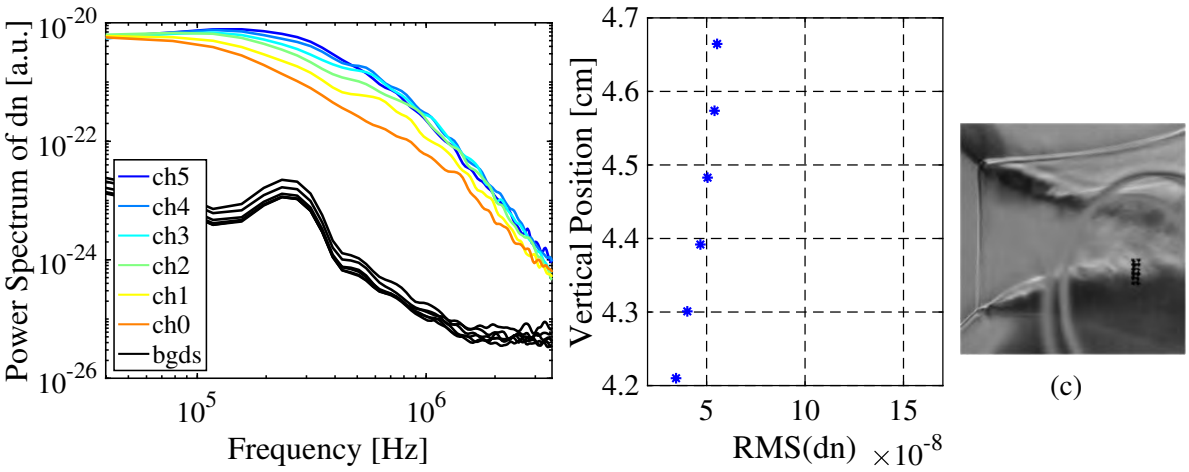

Figure 7.182: Plots of the a) refractive index power spectra and b) RMS measured with FLDI in a case 1 shear layer with c) a schlieren image for spatial reference. [11]

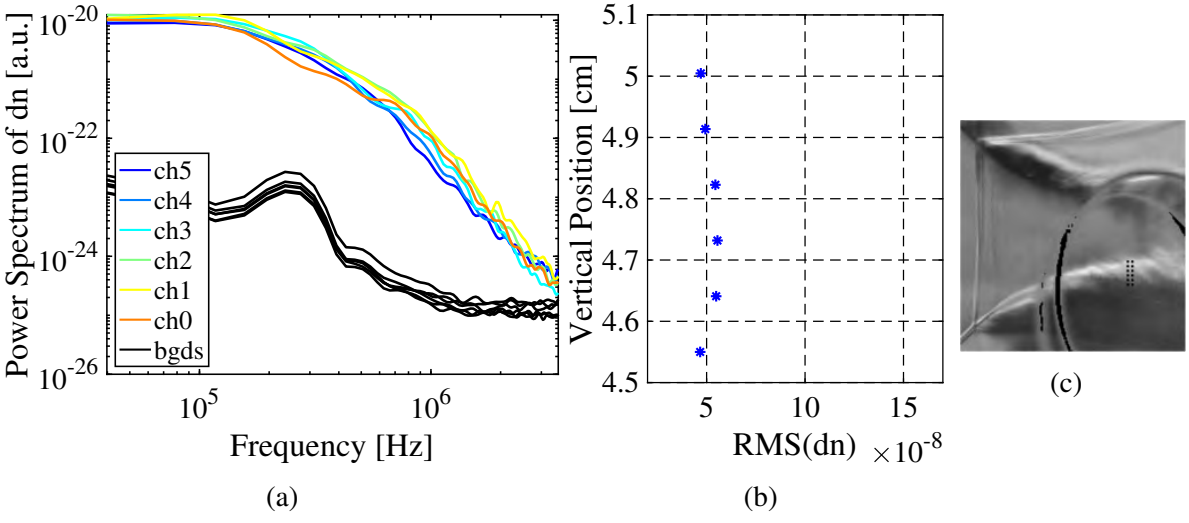

Figure 7.183: Plots of the a) refractive index power spectra and b) RMS measured with FLDI in a case 2 shear layer with c) a schlieren image for spatial reference. [11]

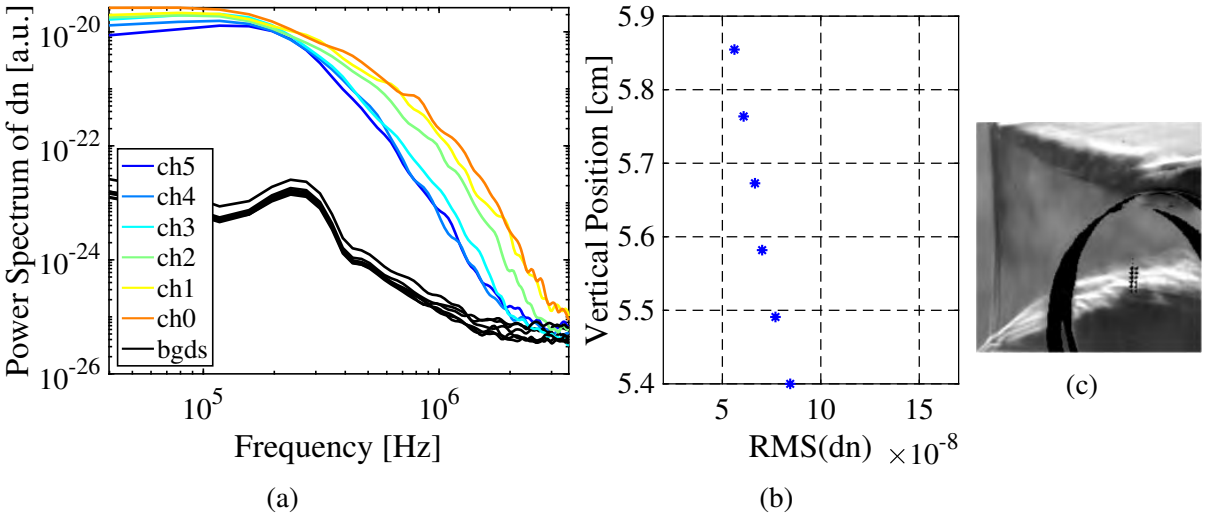

Figure 7.184: Plots of the a) refractive index power spectra and b) RMS measured with FLDI in a case 3 shear layer with c) a schlieren image for spatial reference. [11]

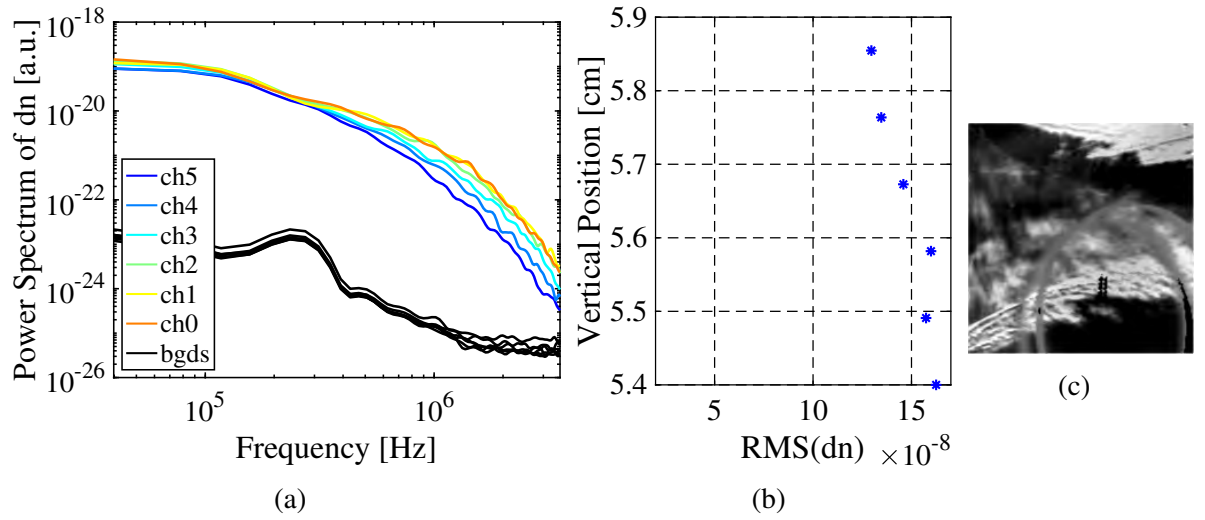

Figure 7.185: Plots of the a) refractive index power spectra and b) RMS measured with FLDI in a case 4 shear layer with c) a schlieren image for spatial reference. [11]

7.5.6 OES Results

Optical emission spectroscopy measurements were conducted at the highest stagnation enthalpy flow cases to evaluate the turbulence in the Mach stem shear layers. Spatially and temporally synced with high-speed schlieren, the OES measurements produced data useful for modeling

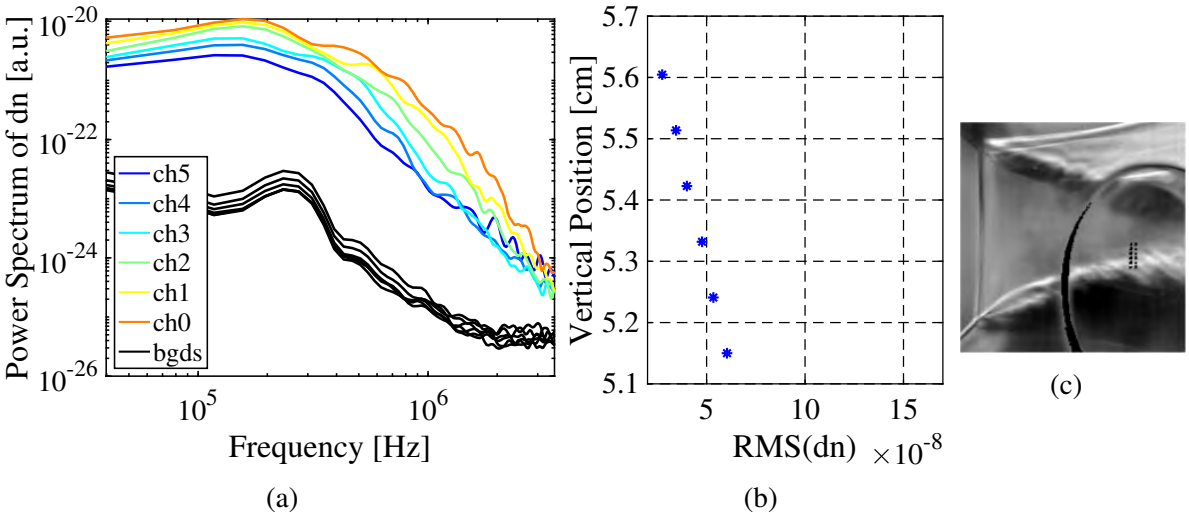

Figure 7.186: Plots of the a) refractive index power spectra and b) RMS measured with FLDI in a case 5 shear layer with c) a schlieren image for spatial reference. [11]

high-enthalpy turbulence. A time-averaged OES image was generated for each run using four consecutive test time images to improve the signal-to-noise ratio of the measurements. Given that the Mach reflection structures exhibited minor temporal variations, only images captured during the most stable segment of each test time were utilized, thereby minimizing potential spatial inaccuracies. Moreover, the OES was captured at a frequency of 40 kHz, resulting in the average only spanning 0.1 ms. An example of the raw images used to produce an average OES image for an air run (case 1) is shown in Fig. 7.187. Since the Mach reflections were symmetric, an additional average was taken using the top and bottom portions of the image. The location of the symmetry plane was determined using a curve of the total intensity in each row of pixels normalized by the maximum, as shown in Fig. 7.188. Quadratic fits were computed for the emission through the shear layers of the intensity curve, which are shown as solid green lines. The position of the symmetry plane was defined using the midpoint between reference points located on the curve fits where the normalized intensity was 0.5. Note that the dip in normalized intensity around 4.7 cm was likely caused by a small chip in the wind tunnel window. The result of averaging the two halves and mirroring them to resemble the original image is shown in Fig. 7.189. Spatial, wavelength, and intensity calibrations were also applied to the spectra shown in Fig. 7.189. The red, green, and blue square brackets on the right side of the figure mark the bounds of pixels that were binned together to generate line plots. The binning was a compromise between obtaining enough pixels to extract a clean spectrum and limiting averaging over a large portion of the flow. The curve fit for the lower shear layer shown in Fig. 7.188 was used to define the bounds of the binned regions. The blue region goes from the lowest position shown by the curve fit, where the normalized intensity is 0.2, to the reference point position, where the normalized intensity is 0.5. The green region goes from the reference point to the top of the curve fit, where the normalized intensity is 0.85. The red region covers the uniform post-shock region between the position indicated by the end of the curve

fit and the symmetry position. In subsequent discussions, the red region will be referred to as the centerline region, and the blue region will be referred to as the shear layer region. ([11])

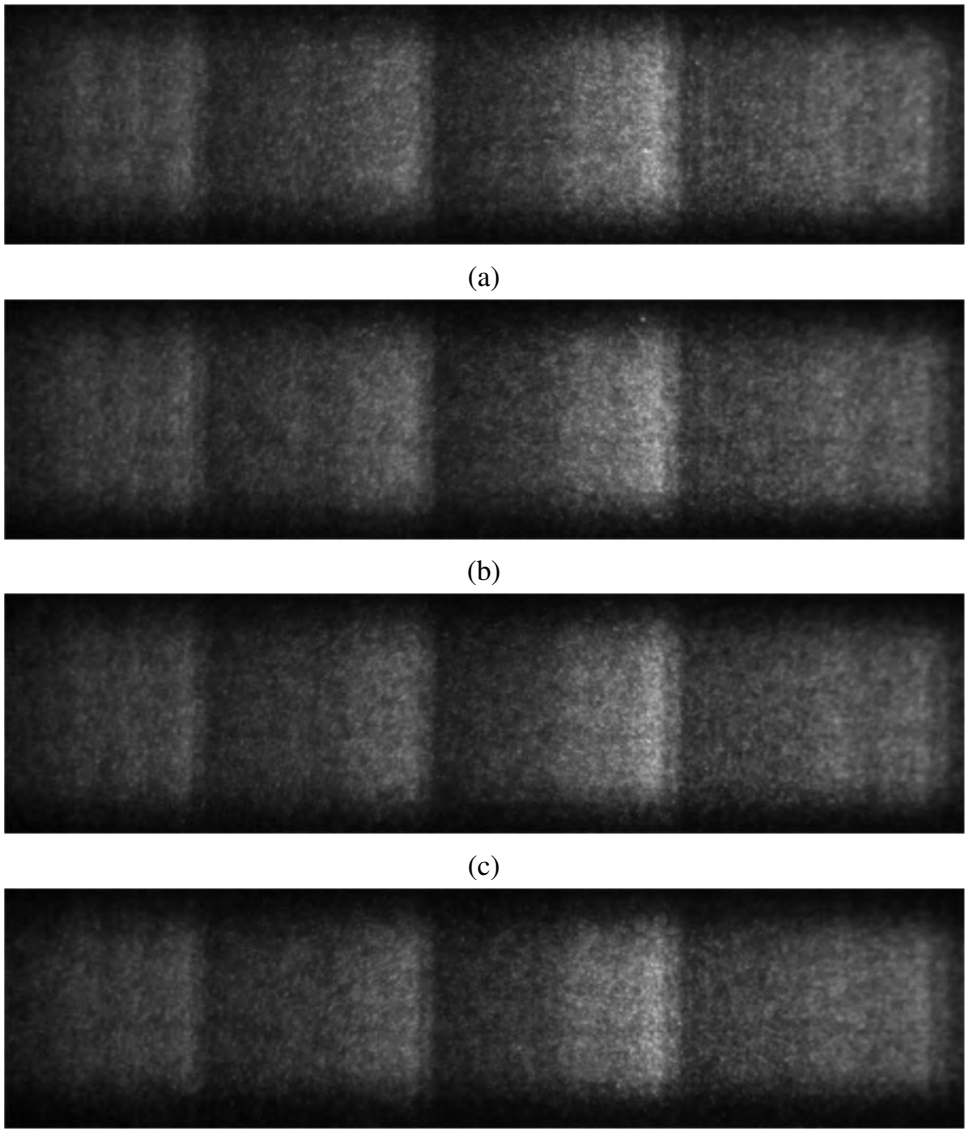

(a)

(b)

(c)

(d)

Figure 7.187: Raw OES images captured during a case 1 run used to produce an average image. [11]

7.5.6.1 Air NO Results

Nitric oxide emission was the primary target of OES measurements during case 1 air runs because few other species emit within the UV emission range of NO. In addition, NO is naturally

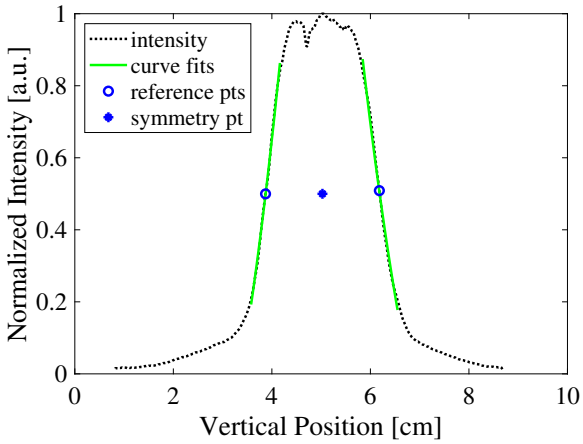

Figure 7.188: Normalized total intensity plotted as a function of position for determining the symmetry location of a case 1 run. [11]

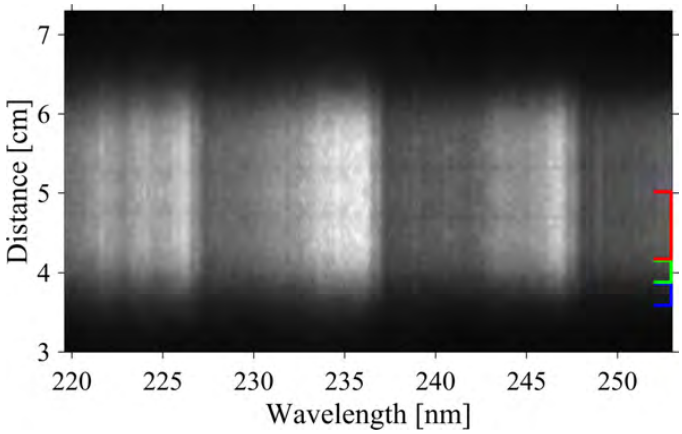

Figure 7.189: Example of an average emission image for a case 1 run condition. [11]

produced in high-temperature air, is considered in the finite rate chemistry computations of all high fidelity hypersonic CFD codes, and has been studied using a similar technique [352, 359]. Nitric oxide emission measured approximately 1.5 cm downstream from the Mach stem during a case 1 run is shown in Fig. 7.190. The y-axis of the schlieren image in Fig. 7.190a is spatially correlated with the y-axis of the OES image in Fig. 7.190b. In addition, the white vertical lines in the schlieren image mark the location of the OES measurements. The darker regions that run horizontally through the middle of the emission around y= 4.7 and y= 5.3 cm were likely caused by a chip in the tunnel windows. They were not artifacts of the flow. Since these measurements were relatively close to the shock, the emission intensity was moderate, and the IRO gain was set to 75%. Line plots of the emission binned within the regions marked by the red, green, and blue square brackets on the right side of Fig. 7.190b are presented in Fig. 7.190c. Red corresponds to centerline measurements, and blue corresponds to shear layer measurements. The intensity in the line plots was area normalized for easy comparisons between the spectra in the different

regions. Note the trend where the blue shear layer line is above the centerline emission at some wavelengths and below it in others. The synthetic NO spectra for equilibrium temperatures ranging from 2,800 to 9,200 K produced using NEQAIR and shown in Fig. 7.191 exhibit the same trend for increasing temperatures. This evidence indicates that the NO molecules emitting light within the shear layers were at a higher equilibrium temperature than the NO molecules emitting in the centerline region. Estimations of rotational and vibrational temperatures based on emission spectra from these experiments are being left to future work. ([11])

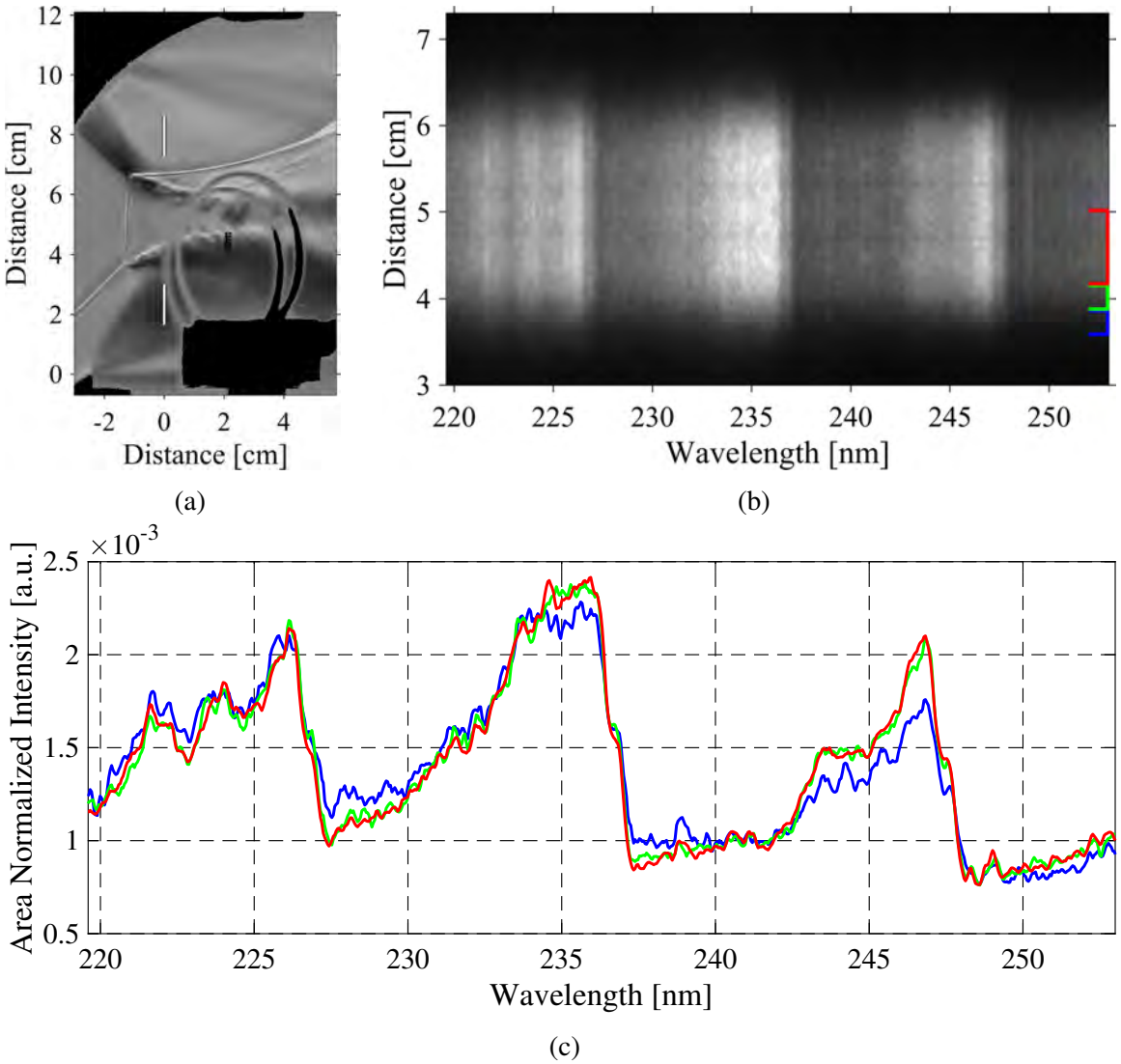

Figure 7.190: OES measurements of primarily NO made 1.5 cm downstream from the Mach stem during a case 1 run where a) shows a spatially and temporally correlated schlieren image marking the OES measurement location with white lines, b) shows the average OES image from the test time with colored brackets on the right side marking the regions binned for line emission plots, and c) shows area normalized line plots of the binned emission. [11]

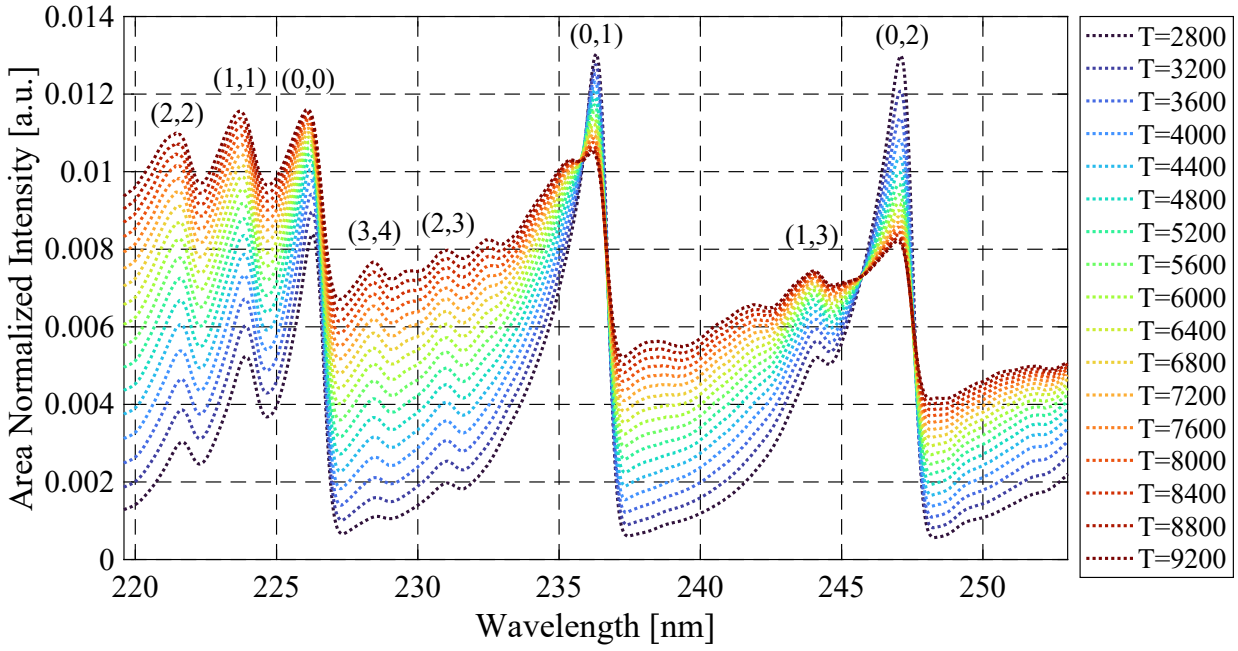

Figure 7.191: Synthetic NO A-X (γ band system) spectra for equilibrium temperatures ranging from 2,800 to 9,200 K generated using NEQAIR with a non-Boltzmann assumption. Vibrational bands are labeled using (v',v"). [11]

Previous studies have assumed Boltzmann and non-Boltzmann distributions for NO produced by the first and second Zeldovich reactions, respectively [360, 361]. NEQAIR spectra assuming both Boltzmann and non-Boltzmann distributions for NO were considered, and the non-Boltzmann results, shown in Fig. 7.191, appeared to match the measured spectra better. It is interesting to note that variation in emission between the shear layer and the centerline was disproportionately larger at the (1,3) and (0,3) vibrational transitions (243 to 247 nm) compared to all the other transitions. It is also interesting to note that the spin splitting of electronic states caused by the unpaired electron in NO molecules is visible on the right sides of the (0,0), (0,1), and (0,2) transition peaks in the OES spectra. These small step features are absent in the NEQAIR spectra because NEQAIR v15.1 did not account for spin splitting. Nitric oxide emission measured approximately 3.5 cm downstream from the Mach stem during a case 1 run is shown in Fig. 7.192. This is the same streamwise position where FLDI measurements were made in the shear layer. The emission generated at this position was not as bright as it was 1.5 cm downstream from the shock, so the IRO gain was set to 83%. The lower radiative emission and larger IRO gain resulted in a comparatively lower signal-to-noise ratio than the measurements made 1.5 cm downstream from the Mach stem. The gray area in Fig. 7.192c shows NEQAIR computed iron emission spectra for an arbitrary concentration with an equilibrium temperature of 4,000 K. The synthetic iron emission aligns with the four small emission peaks not characteristic of NO, indicating a small amount of iron emission was likely captured. While variations in emission measured 1.5 cm downstream from the Mach stem indicated an elevated temperature in the shear layer region, there were hardly any discernible differences

among the emission plotted in Fig. 7.192c. The two iron emission lines at 248.3 and 248.9 nm were the only clear demonstrations of spatial variation in emission. Both lines appeared brighter in the shear layers. Interestingly, these two iron emission lines were barely distinguishable in the results measured 1.5 cm downstream from the shock. Another noteworthy distinction between the 1.5 cm and 3.5 cm results pertains to the (0,1) band of nitric oxide. The (0,1) band measured 3.5 cm downstream of the shock exhibited a clear peak. However, the (0,1) peak measured 1.5 cm downstream from the Mach stem was relatively broad and lacked a pronounced peak. Since the OES measurements made 3.5 cm downstream from the Mach stem at the case 1 run condition were limited by relatively low emission intensity, the measurements were repeated at the case 6 run condition. Although the higher 8.9 MJ/kg stagnation enthalpy of the case 6 condition resulted in a completely different flowfield, the OES measurements made at this condition, shown in Fig. 7.193, had a much better signal-to-noise ratio. The IRO gain for this run was 83%. The OES trends shown in Fig. 7.193c resemble the trends observed in the measurements made 1.5 cm downstream from the Mach stem during the case 1 run shown in Fig. 7.190c. Recall, however, that there was no evidence in the emission measured 3.5 cm downstream from the Mach stem at the case 1 condition that the shear layer region was hotter than the center of the shock relaxation region. It is possible that the emission in the hotter appearing region of the shear layer was too dim 3.5 cm downstream from the Mach stem at the case 1 flow condition to measure accurately. It is also possible that the lower Reynold's number and longer relaxation distances caused by the lower density of the case 6 flow resulted in similar flowfield characteristics appearing farther downstream. Due to the complexity of the flowfields, it is difficult to state a definitive underlying cause for the discrepancy. It is recommended that this be investigated further in future work. ([11])

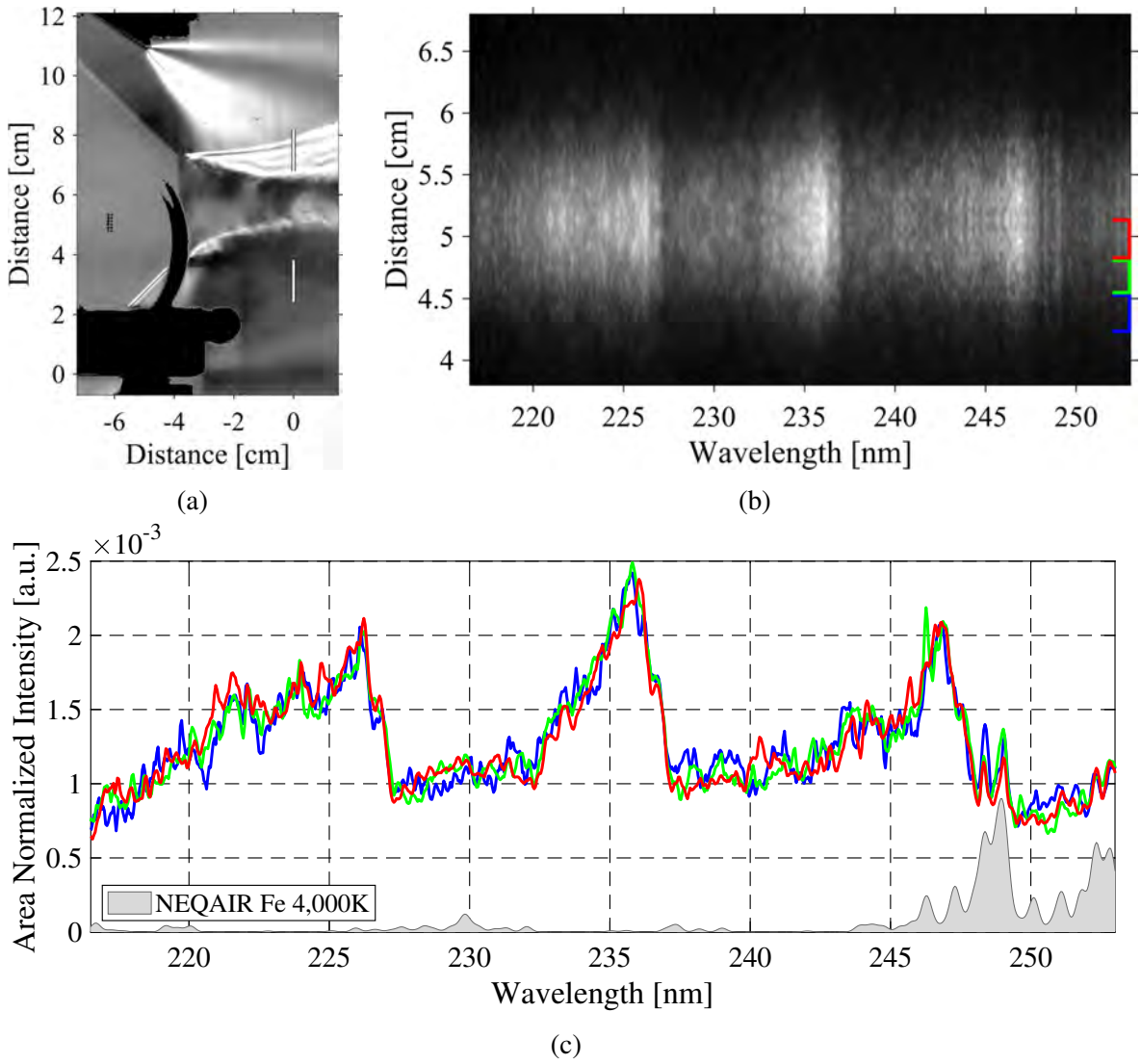

Figure 7.192: OES measurements of primarily NO made 3.5 cm downstream from the Mach stem during a case 1 run where a) shows a spatially and temporally correlated schlieren image marking the OES measurement location with white lines, b) shows the average OES image from the test time with colored brackets on the right marking the regions binned for line emission plots, and c) shows area normalized line plots of the binned emission and NEQAIR generated spectra for iron. [11]

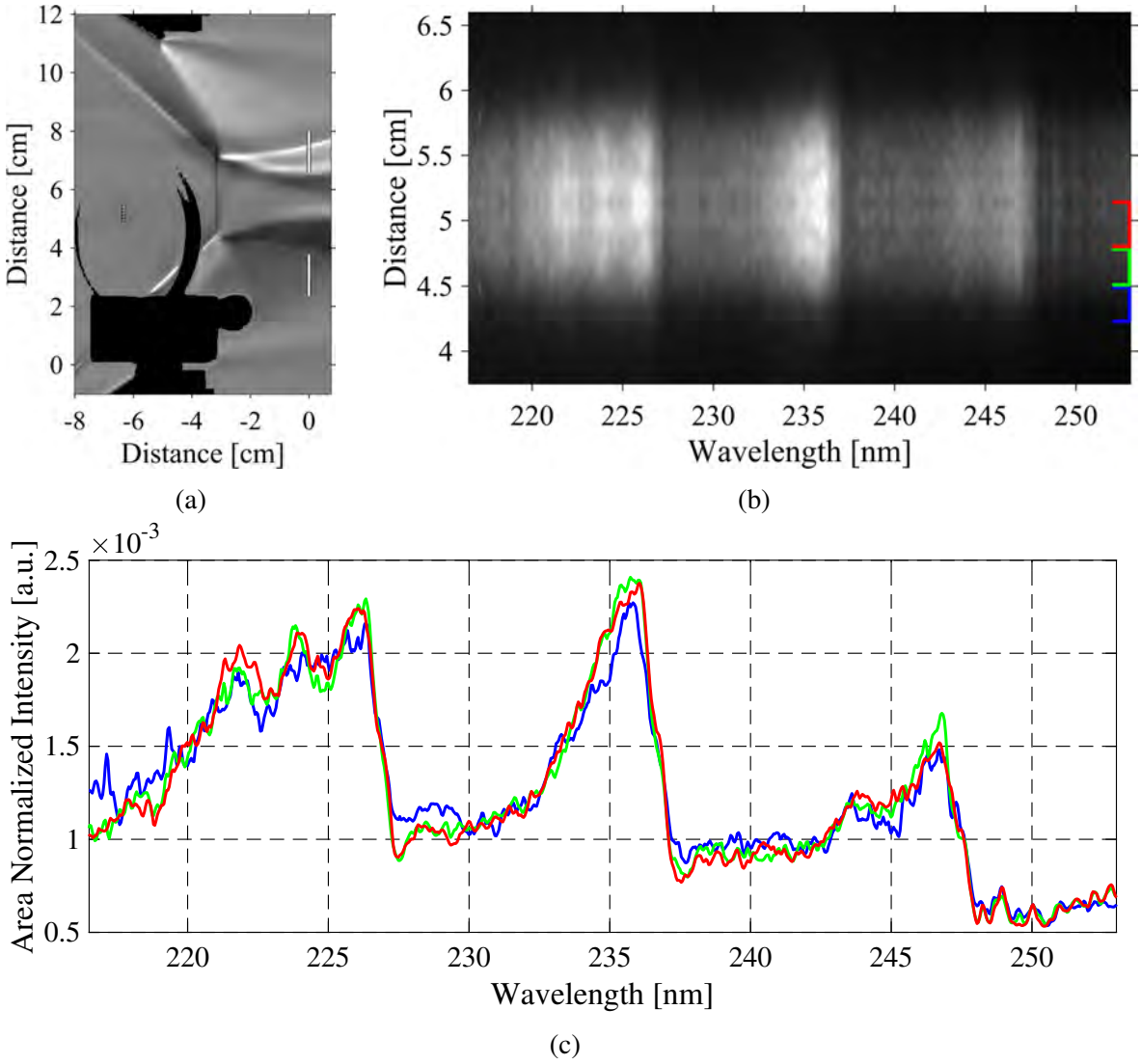

Figure 7.193: OES measurements of primarily NO made 3.5 cm downstream from the Mach stem during a case 6 run where a) shows a spatially and temporally correlated schlieren image marking the OES measurement location with white lines, b) shows the average OES image from the test time with colored brackets on the right marking the regions binned for line emission plots, and c) shows area normalized line plots of the binned emission. [11]

7.5.6.2 Air Fe Results

Two runs were performed at the case 1 condition to investigate the presence of N2 emission. Emission measurements were made 3.5 cm downstream from the Mach stem during both runs, and the results were identical. For the sake of brevity, only the results from the first run are shown in Fig. 7.194. In this case, an IRO gain of 70% was used. The gray area included in Fig. 7.192c shows NEQAIR computed iron emission at an equilibrium temperature of 4,000 K. The synthetic iron emission aligns with nearly every OES measured feature, indicating the majority of the emission between 360 and 400 nm was iron. The presence of iron is not uncommon in high enthalpy facilities [362]. Although the enthalpy of this run condition was too low for appreciable nitrogen emission, these measurements were important for characterizing the presence of minor flow contaminants. It should be noted that the OES measurements in this wavelength range were not calibrated for relative intensity, making exact comparisons with NEQAIR difficult. Nevertheless, the binned intensities plotted in Fig. 7.194c demonstrate some mild variation in emission between the blue shear layer region and the red centerline region. Synthetic spectra produced from NEQAIR simulations of iron at equilibrium temperatures ranging from 2,800 to 9,200 K are shown in Fig. 7.195. Most differences between the centerline and shear layer emission are consistent with temperature trends in the NEQAIR spectra, indicating elevated temperatures were present in the shear layers. Higher fidelity efforts of future work may allow the evaluation of translational and electronic temperatures based on the measured iron emission. ([11])

7.5.6.3 Nitrogen Results

Several OES measurements were conducted within the pure nitrogen flows of the case 5 experimental condition. Results obtained from an OES measurement made 2 cm downstream from the Mach stem during one of these case 5 runs are shown in Fig. 7.196. In this specific run, the IRO gain was set to 60%. A NEQAIR computed spectrum of cyanide (CN) emission at an equilibrium temperature of 5,000 K is included with the binned intensity plots shown in Fig. 7.196c. The similarity between the synthetic and measured CN spectra suggests that cyanide was the only distinguishable emission measured during this run. The emission originated from the CN violet band system, where $\Delta v = 0$. CN violet emission was also observed in LES-XX OES measurements, which utilized low carbon, spectroscopic purity bottled test gas [363]. Minute concentrations of certain species can be sufficient to cause bright chemiluminescence behind a shock. The trace amounts of carbon in this flowfield may have originated from the stainless steel of the tunnel walls, mylar, or oil residue from hand prints. None of the OES measurements made in nitrogen flows were relative intensity corrected. It is recommended that the NAL acquire a NIST traceable integrating sphere and recreate the setup to perform a proper relative intensity calibration. Although it will be impossible to recreate the setup perfectly, this future work would reduce uncertainties in the emission spectra, potentially leading to temperature computations. High-level discrepancies between the measured emission and the synthetic CN spectra shown in Fig. 7.196c were likely a result of relative intensity losses through the various OES optics. Although the emission results were not relative intensity calibrated, the calibration error should be approximately uniform throughout the collection optics. As a result, comparisons between the emission measured at the centerline and the shear layer were still meaningful. Synthetic emission trends for CN at equi-

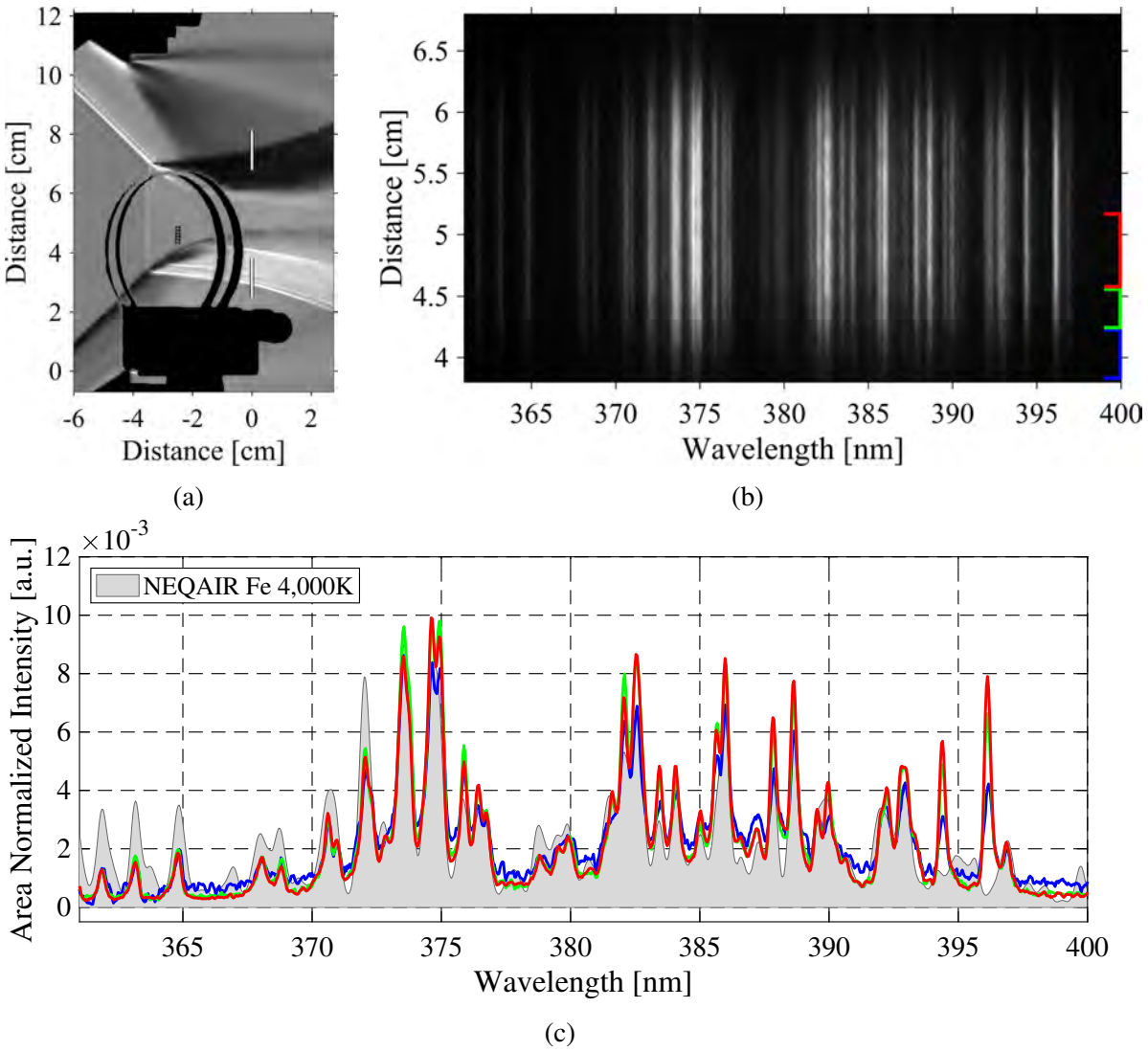

Figure 7.194: OES measurements made 3.5 cm downstream from the Mach stem during a case 1 run where a) shows a spatially and temporally correlated schlieren image marking the OES measurement location with white lines, b) shows the average OES image from the test time with colored brackets on the right marking the regions binned for line emission plots, and c) shows area normalized line plots of the binned emission and NEQAIR generated spectra for iron. [11]

librium temperatures from 2,800 to 9,200 are shown in Fig. 7.197. Consistent with observations made in the air runs, the measured CN emission trends indicated that the shear layer region was a higher temperature than the centerline region. Interestingly, CN emission was absent from the air measurements of the case 1 flow made within the same wavelength region presented in Fig. 7.194. In addition, the nitrogen emission results in Fig. 7.196c were devoid of iron emission. The CN emission in the nitrogen run was relatively bright compared to the iron emission of the air run. As a result, the IRO gain was much lower during the nitrogen run. Iron emission was likely present

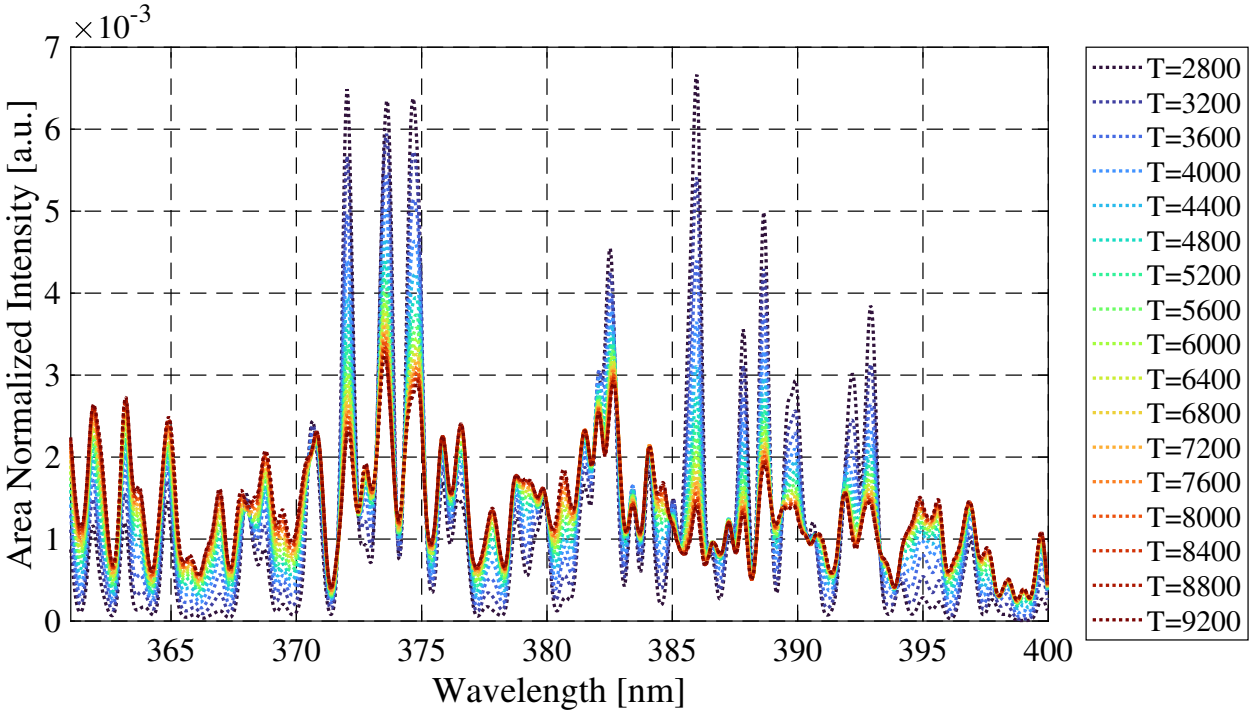

Figure 7.195: Synthetic iron spectra for equilibrium temperatures ranging from 2,800 to 9,200 K generated using NEQAIR. [11]

during the nitrogen run at an intensity below what could be detected. The lack of detectible CN emission in the air run could be attributed to lower temperatures in the post-shock region caused by the thermochemical relaxation of the air chemistry. Other possible explanations include lower CN production in the air case caused by other chemical reactions using carbon or quenching caused by species like oxygen. A second nitrogen run was performed where OES measurements were made 2 cm downstream from the Mach stem. During this run, the center wavelength of the spectrometer was adjusted to allow measurements from 330 to 370 nm, avoiding the relatively bright CN violet emission. Without overexposure danger from the CN emission, the IRO gain was increased from 60% to 70%. The spectra from this location, shown in Fig. 7.198, align well with the NEQAIR computed spectra for imidogen (NH), CN, and Fe. The synthetic spectra, plotted with various shades of gray in Fig. 7.198c, were computed assuming Boltzmann distributions and equilibrium temperatures of 5,000 K. The CN emission was from the violet band system where $\Delta v = +1$. Similar to the results in the previous case, the measured CN emission trends indicate that a higher equilibrium temperature was present in the shear layer. ([11])

NEQAIR generated NH $A^3\Pi - X^3\Sigma^-$ emission spectra for equilibrium temperatures ranging from 2,800 to 9,200 K are shown in Fig. 7.199. The temperature trends in the synthetic spectra indicate that the NH molecules emitting in the shear layers were at a higher equilibrium temperature than in the center of the post-shock relaxation region. Several other emission spectroscopy studies have identified the presence of NH in expansion tunnels [363, 364, 365]. The hydrogen in

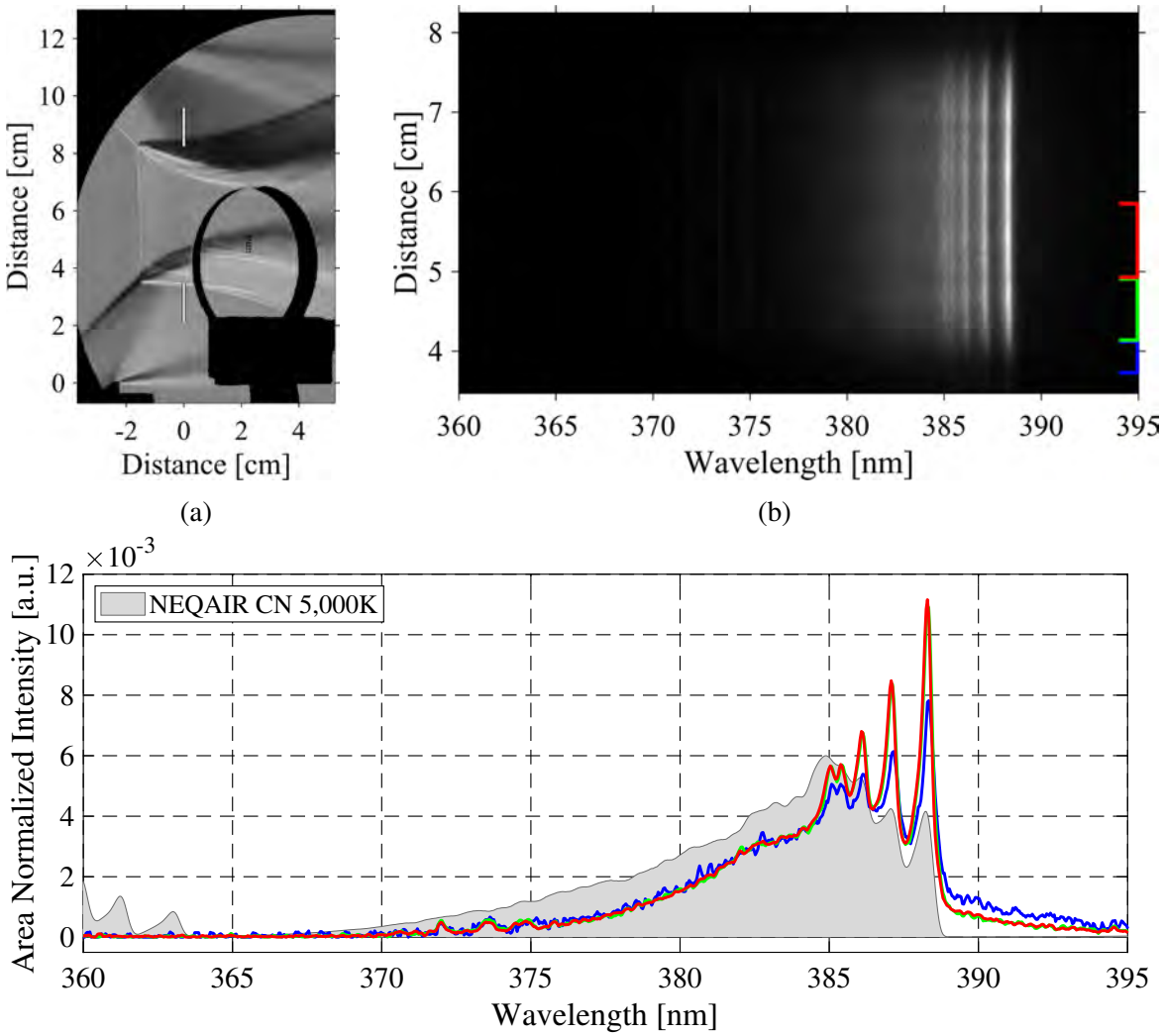

Figure 7.196: OES measurements made 2 cm downstream from the Mach stem during a case 5 run where a) shows a spatially and temporally correlated schlieren image marking the OES measurement location with white lines, b) shows the average OES image from the test time with colored brackets on the right marking the regions binned for line emission plots, and c) shows area normalized line plots of the binned emission and NEQAIR generated spectra for CN. [11]

the NH molecule likely originated from water vapor outgassed from the metal surfaces of the test gas section. Results from a third case 5 run are shown in Fig. 7.200, where OES was performed 3.5 cm downstream from the Mach stem. This was the same streamwise position as the FLDI measurements in Fig. 7.186. Note that the same wavelength region was measured as the previous case 2 cm downstream from the Mach stem. Since emission typically decreases with distance from the Mach stem, the IRO gain was increased to 75%. Using the CN violet emission as a reference, the binned intensities in Fig. 7.200c show that emission from NH was substantially lower at 3.5 cm

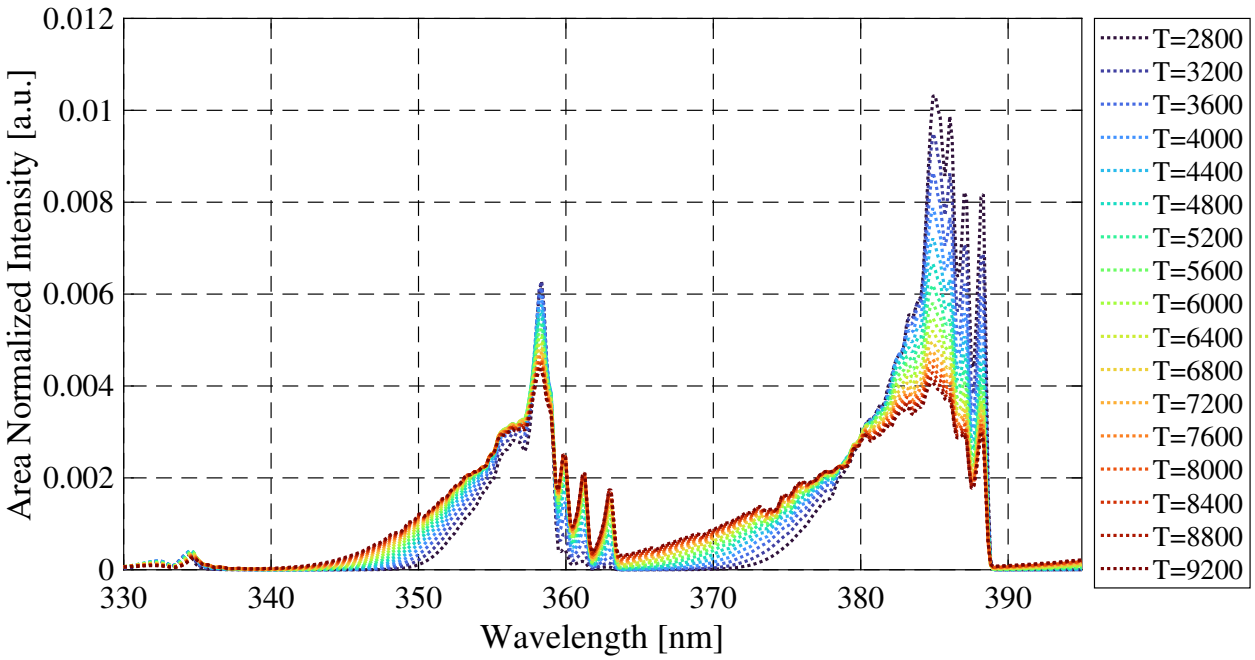

Figure 7.197: Synthetic CN $B^2\Sigma^+$ - $X^2\Sigma^+$ (violet band) spectra for equilibrium temperatures ranging from 2,800 to 9,200 K generated using NEQAIR. [11]

downstream from the Mach stem than 2 cm. It is also interesting to note that almost no variation in NH emission was demonstrated between the shear layer and the centerline region during this run. Contradictorily, there was more variation in the CN emission between the shear layer and the centerline regions at 3.5 cm than 2 cm downstream from the Mach stem, particularly around 355nm. ([11])

7.6 Computation of the Hypervelocity Mach Stem

7.6.1 Validation

This discussion in this section follows from Bryan et al. [52]. For the CFD verification, a coarse grid of $\sim$ 416k cells, a medium grid of $\sim$ 624k cells, and a fine grid of $\sim$ 834k cells were used. *Tab.* 7.41 and *Tab.* 7.42 provide the estimated HXT test conditions and simulation initial conditions that were used to do solution verification on the grid. It is important to state that the grids used were two-dimensional planes that were extruded one cell thick in the $z-$direction. *Fig.* 7.201 and 7.202 provide two of the many parameters that were used to computationally validate the grids. The first figure presented compares the Mach value along an $x-$slice at the axial $x-$location of the Mach stem. To prevent bias and uncertainty in determining where the $x-slice$ was in relation to the axial $x-$location of the Mach stem, a systematic approach was developed. First, a horizontal $y-$slice was taken along the symmetry plane, and the data from that slice was then used to plot a simple Mach versus x. A probe was then used to grab the $x-$location of exactly where the Mach number drops in value, meaning the flow passed through the Mach stem. With this x value now

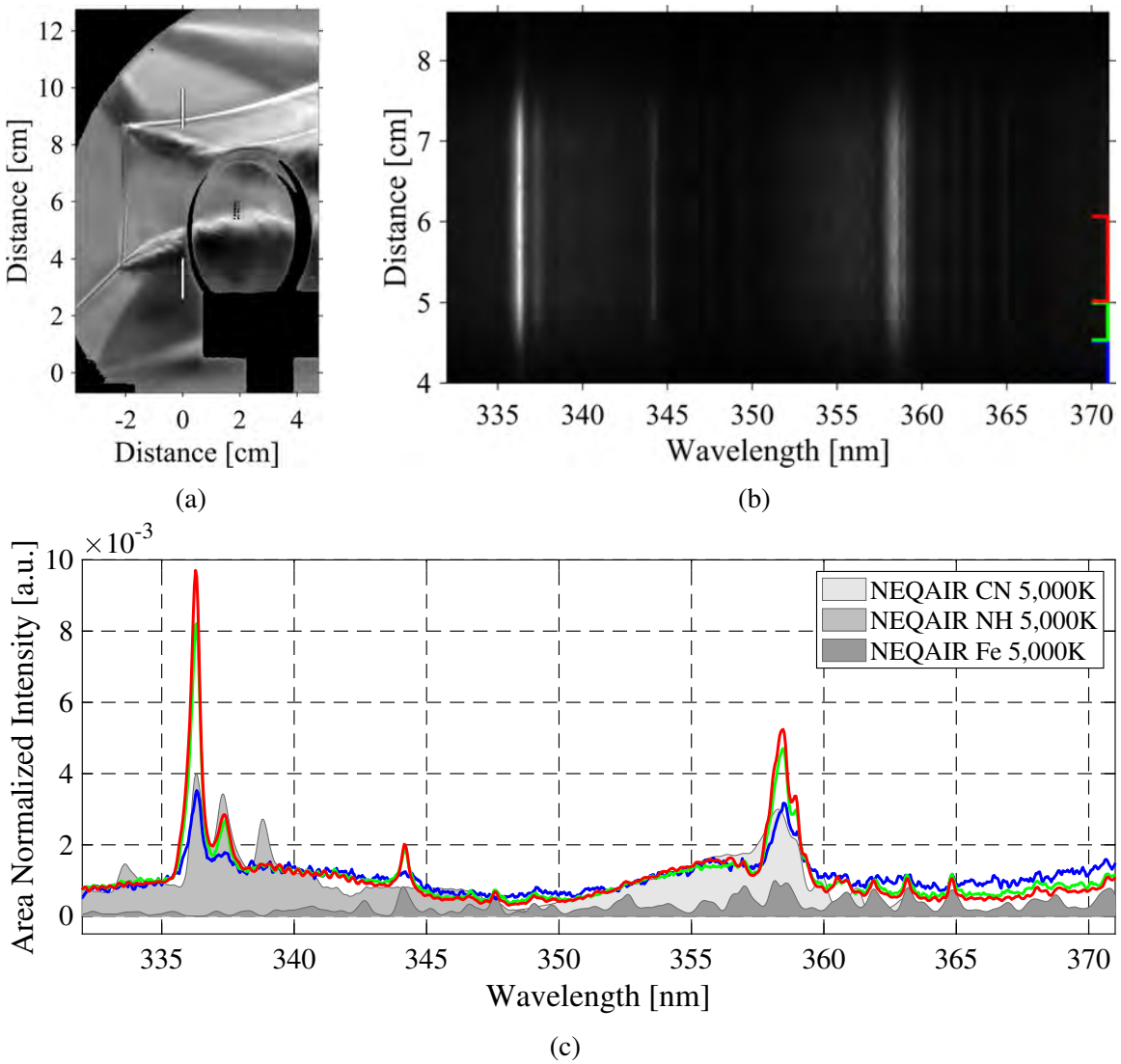

Figure 7.198: OES measurements made 2 cm downstream from the Mach stem during a case 5 run where a) shows a spatially and temporally correlated schlieren image marking the OES measurement location with white lines, b) shows the average OES image from the test time with colored brackets on the right marking the regions binned for line emission plots, and c) shows area normalized line plots of the binned emission and NEQAIR generated spectra for CN. [11]

marked, a vertical $x-$slice was taken at that axial $x-$location. This process was repeated for the three different grids used and it can clearly be seen that all three grids do not change the results appreciably. The second figure presented compares the atomic oxygen number density along the symmetry plane. The atomic oxygen number density was calculated using $O_{nd} = \frac{\rho_o Na}{MM}$. Here ρ_o $[kg/m^3]$ is the atomic oxygen density, MM $[kg/mol]$ is the molar mass of atomic oxygen, and Na $[particles/mol]$ is Avogadro's number. This approach simply extracted the horizontal $y-$slice along the symmetry plane, and then plots the variable of interest with respect to x. In this case, it

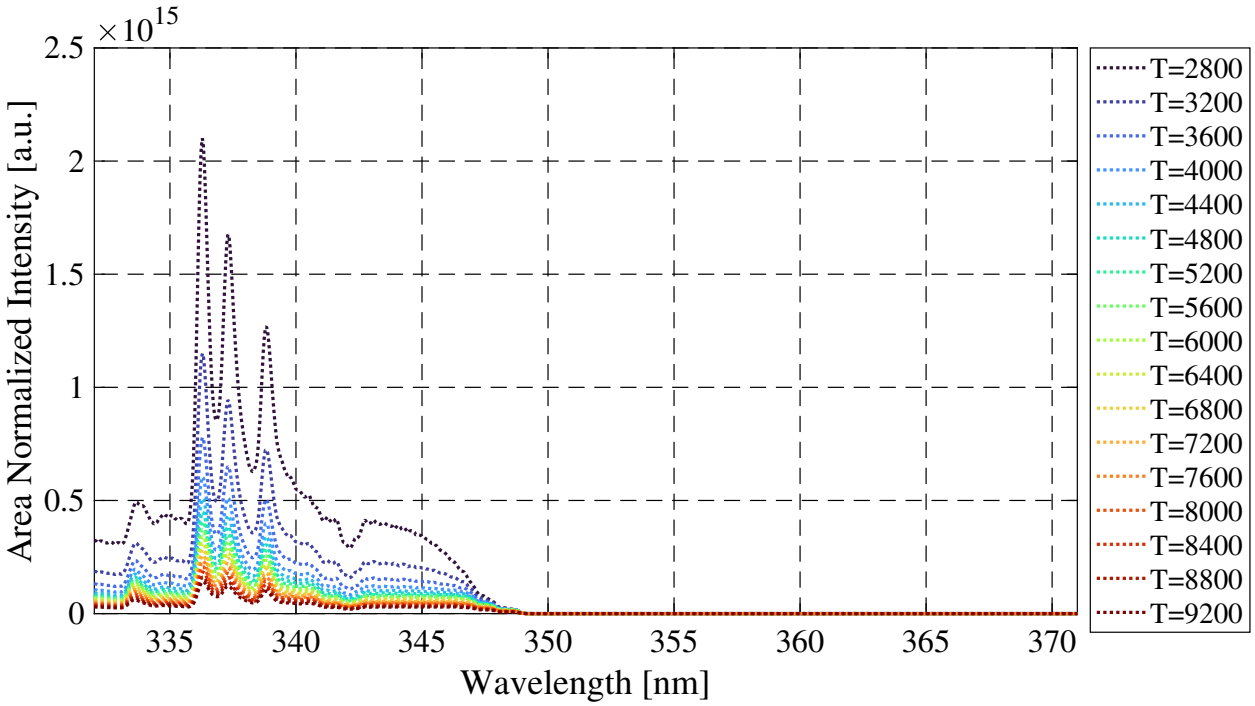

Figure 7.199: Synthetic NH (A-X) spectra for equilibrium temperatures ranging from 2,800 to 9,200 K generated using NEQAIR. [11]

can clearly be seen that there is no discrepancy or variation of the atomic oxygen number density for the three different grids used. Both the Mach versus y plot and atomic oxygen number density plot have successfully validated the grids and the validity of the results. Many other quantities of interest also justified the accuracy of the results, and were not presented. ([52]).

Table 7.41: Estimated HXT test conditions for simulation validation.

Case	M	h_0	Re/m	T	U	P	P_0	ρ
	$[\sim]$	$[MJ/kg]$	$[1/m]$	$[K]$	$[m/s]$	$[Pa]$	$[Pa]$	$[kg/m^3]$
127/158	8.5	11	$1.3e5$	710	4600	210	$19e3$	0.00098

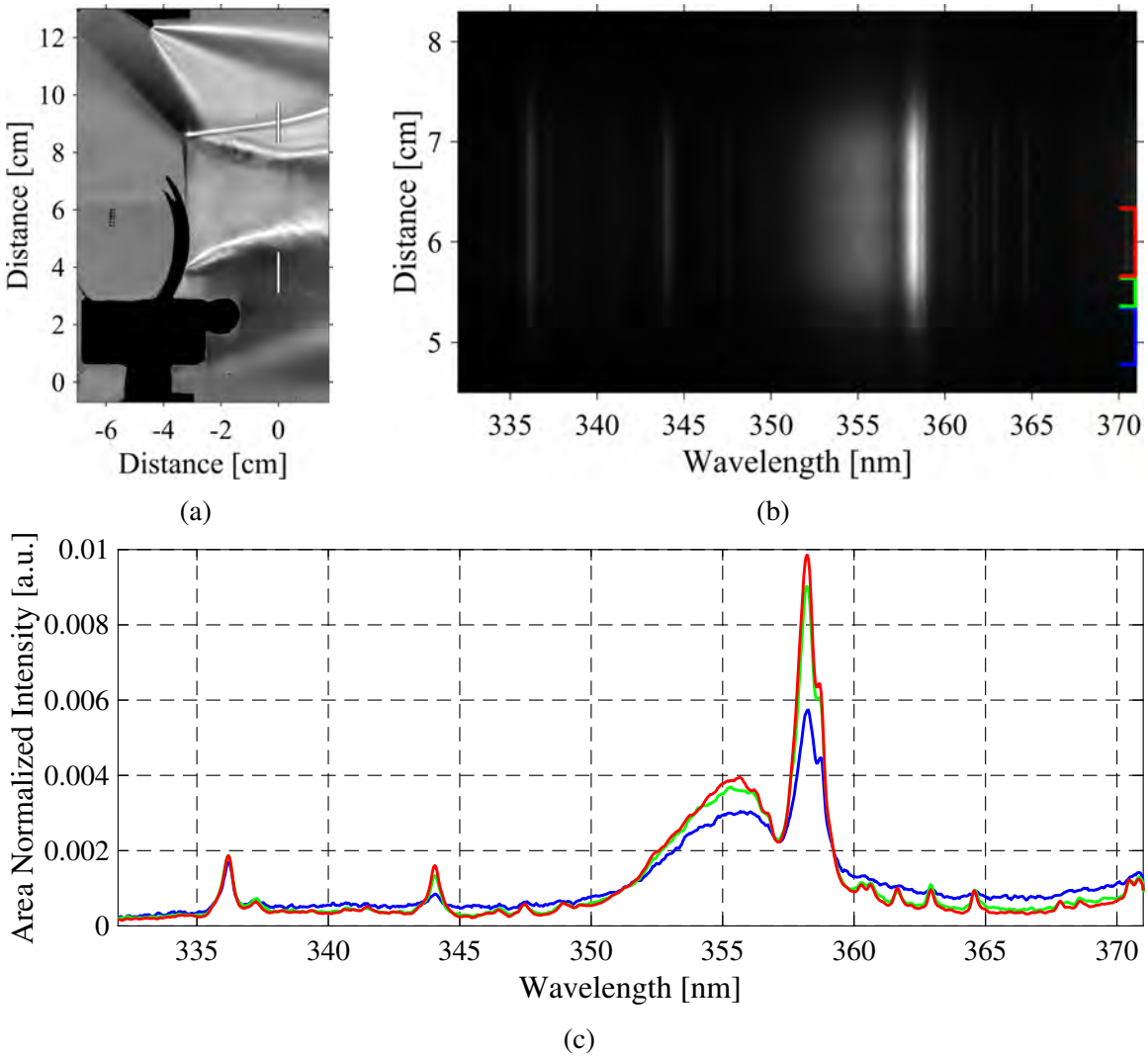

Figure 7.200: OES measurements made 3.5 cm downstream from the Mach stem during a case 5 run where a) shows a spatially and temporally correlated schlieren image marking the OES measurement location with white lines, b) shows the average OES image from the test time with colored brackets on the right marking the regions binned for line emission plots, and c) shows area normalized line plots of the binned emission and NEQAIR generated spectra for CN. [11]

Table 7.42: Simulation initial conditions obtained from estimated HXT test conditions for simulation validation.

Case	ρ $[kg/m^3]$	T, T_v $[K]$	U $[m/s]$	ρ_{vol} $[kg/m^3]$	T_{vol}, T_{vol_v} $[K]$	U_{vol} $[m/s]$	DCM	X_{N_2}	X_{O_2}	Air Model
127/158	0.00098	710	4600	0.00098	220	0	[1,0,0]	0.77	0.23	11 species

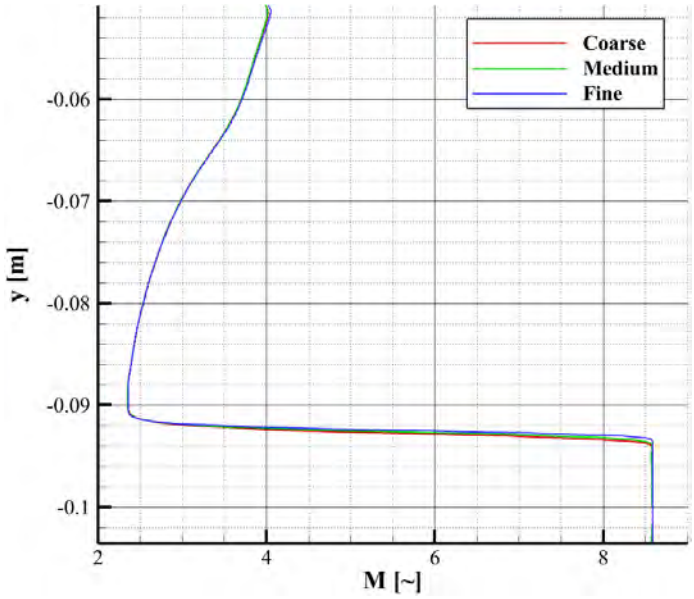

Figure 7.201: Mach versus y along x-slice at Mach stem location.

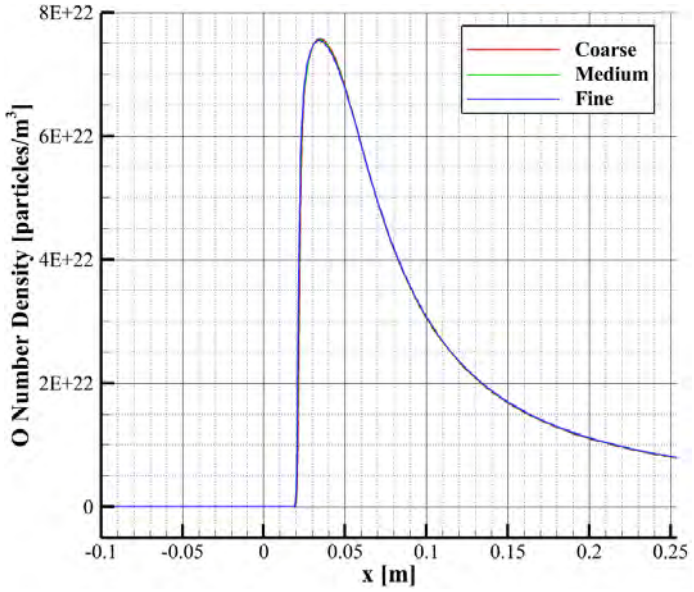

Figure 7.202: Oxygen number density along symmetry plane for Mach 8.5 flow with 11 MJ/kg stagnation enthalpy. [52]

For the validation with experimental results, both the $y-$gradient of density and Mach number contours were compared and overlayed directly with experimental schlieren. The computational

grid used for the experimental validation was the coarse grid as it was proven previously to provide accurate results. *Tab.* 7.41 and *Tab.* 7.42 provide the HXT run conditions and simulation initial conditions for the results presented in this section. It can be seen in *Fig.* 7.203 that the overall shock structure matches well with the experimental schlieren. The only noticeable differences between the experimental and computational schlieren are the intensity of the shock and shear layer. This discrepancy could be a result of how the experimental schlieren was processed, which consisted of performing a background subtraction and adjusting the image contrast. It is also possible that the difference is due to numerically capturing discontinuities, like shocks, in a thin slice free of 3D edge effect, versus the schlieren experiment which was dependant on the full spanwise path through the test section. Furthermore, in *Fig.* 7.204 the Mach number contour lines are placed directly on top of the experimental schlieren. This figure illustrates how the incident oblique shock, reflected oblique shock, shear layer, expansion fan, and normal shock match with the experiment. These two experimental validation techniques further justify that the grid and solver configurations used were sufficient to obtain accurate flow simulations. (Bryan et al. [52].)

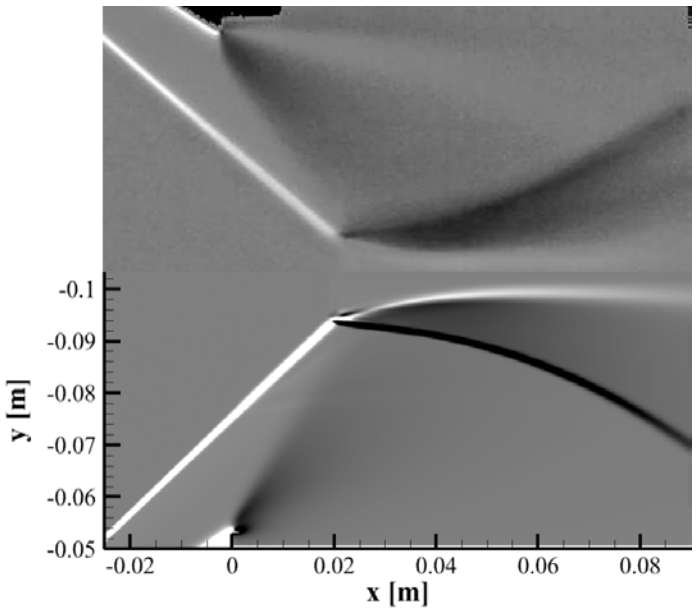

Figure 7.203: Experimental (top) and computational (bottom) schlieren comparison for Mach 8.5 flow with stagnation enthalpy 11 MJ/kg. [52]

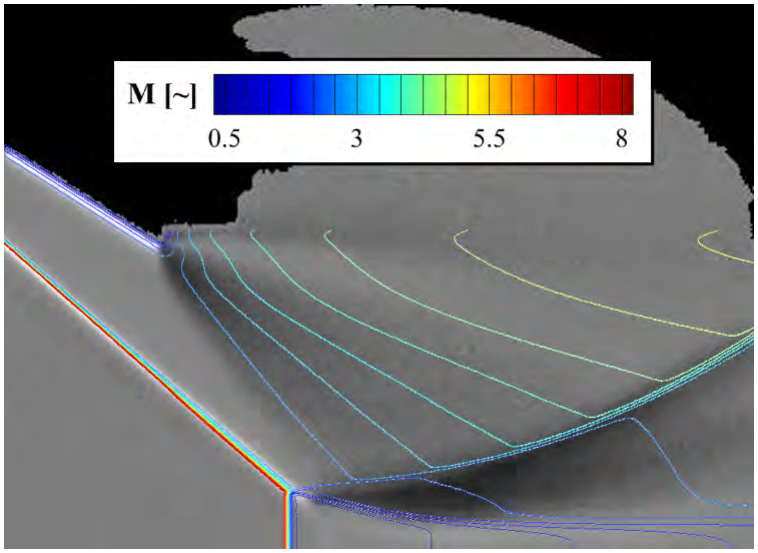

Figure 7.204: Experiment schlieren and simulation Mach number contour overlay for Mach 8.5 flow with stagnation enthalpy 11 MJ/kg. [52]

7.6.2 Stagnation Enthalpy Sweep at Mach 8.5

This discussion in this section follows from Bryan et al. [52]. The results in this section were produced using the coarse grid with inlet conditions that were Mach 8.5 with stagnation enthalpies 3.8 5.4, 6.9, and 11 MJ/kg. Each of these test conditions have a corresponding "Case" number which represent a particular HXT experiment. Multiple HXT experiments were performed at each condition. Because all of the results presented in this paper occur at Mach 8.5, only the stagnation enthalpies will be used to differentiate between the results from now on. *Tab.* 7.43, *Tab.* 7.44 and *Tab.* 7.45 provide the estimated HXT test conditions and simulation initial conditions. It can be seen in *Tab.* 7.44 that two of the test conditions use an 11 species air model and the other two use a 5 species air model. A 5 species air model was used for the two lower enthalpy cases because there wasn't significant ionization or excitation occurring. Therefore, running an 11 species air model was excessive and computationally inefficient for those cases. Although not shown, 5 and 11 species simulations were performed for the 5.4 MJ/kg condition. There were not any appreciable differences between these simulations, validating the use of a 5 species air model. ([52].)

Case	M	h_0	Re/m	T	U	P	P_0	ρ
	$[\sim]$	$[MJ/kg]$	$[1/m]$	$[K]$	$[m/s]$	$[Pa]$	$[Pa]$	$[kg/m^3]$
127/158	8.5	11	$1.3e5$	710	4600	210	$19e3$	0.00098
160/161/162	8.5	6.9	$1.3e6$	440	3600	1200	$110e3$	0.0092
166/167	8.5	5.4	$3.3e6$	350	3200	2100	$200e3$	0.021
163/164/165	8.5	3.8	$9.8e6$	250	2700	4100	$380e3$	0.058

Table 7.43: Estimated HXT test conditions.

Case	ρ	T, T_v	U	ρ_{vol}	T_{vol}, T_{vol_v}	U_{vol}
	$[kg/m^3]$	$[K]$	$[m/s]$	$[kg/m^3]$	$[K]$	$[m/s]$
127/158	0.00098	710	4600	0.00098	220	0
160/161/162	0.0092	440	3600	0.0092	220	0
166/167	0.021	350	3200	0.021	220	0
163/164/165	0.058	250	2700	0.058	220	0

Table 7.44: Simulation initial conditions.

Case	DCM	X_{N_2}	X_{O_2}	Air Model
127/158	$[1,0,0]$	0.77	0.23	11 species
160/161/162	$[1,0,0]$	0.77	0.23	11 species
166/167	$[1,0,0]$	0.77	0.23	5 species
163/164/165	$[1,0,0]$	0.77	0.23	5 species

Table 7.45: Continuation of simulation initial conditions.

Fig. 7.205 provides the $x-$velocity for the various stagnation enthalpies presented. Each of the subplots in this figure all utilize the same colorbar bounds to provide an equal comparison in velocities and shock patterns. The stagnation enthalpy of the 11 MJ/kg case had the smallest Mach stem height, and the stagnation enthalpy of 3.8 MJ/kg case had the largest Mach stem height. From this it can be seen that the higher the stagnation enthalpy, the smaller and more downstream the Mach stem. This trend is due to chemical dissociation and the excitation of internal energy modes, and it was noted in the results by Grasso *et al.* [158]. Another interesting shock pattern to observe involves the reflected oblique shock. For the stagnation enthalpy of 11 MJ/kg case, the

reflected oblique shock was noticeably steeper than the lower enthalpy cases. The final shock pattern of interest was the relative size of the wake region, bounded by the shear layer and symmetry plane. Comparing the wake region encompassed by the shear layer for the four different enthalpy cases, it is clear that for the lower stagnation enthalpy cases the wake region was much larger and more prominent than the higher stagnation enthalpy cases. Furthermore, *Fig.* 7.206 presents the translational-rotational temperature for each of the different stagnation enthalpy cases. Utilizing a single colorbar allows the intensities of the temperatures to be equally compared. The temperature pattern amongst the different enthalpies was trivial, as the higher the stagnation enthalpy, the higher the temperature. The shock patterns shown in *Fig.* 7.205 were also explicitly illustrated here. It is important to note that the region of the highest temperature amongst all of the cases was directly after the normal shock, which was where the non-equilibrium was highest. A method for determining non-equilibrium will be discussed later in this paper. The species mole fractions of nitric oxide, NO, and atomic oxygen, O, will be discussed next. ([52].)

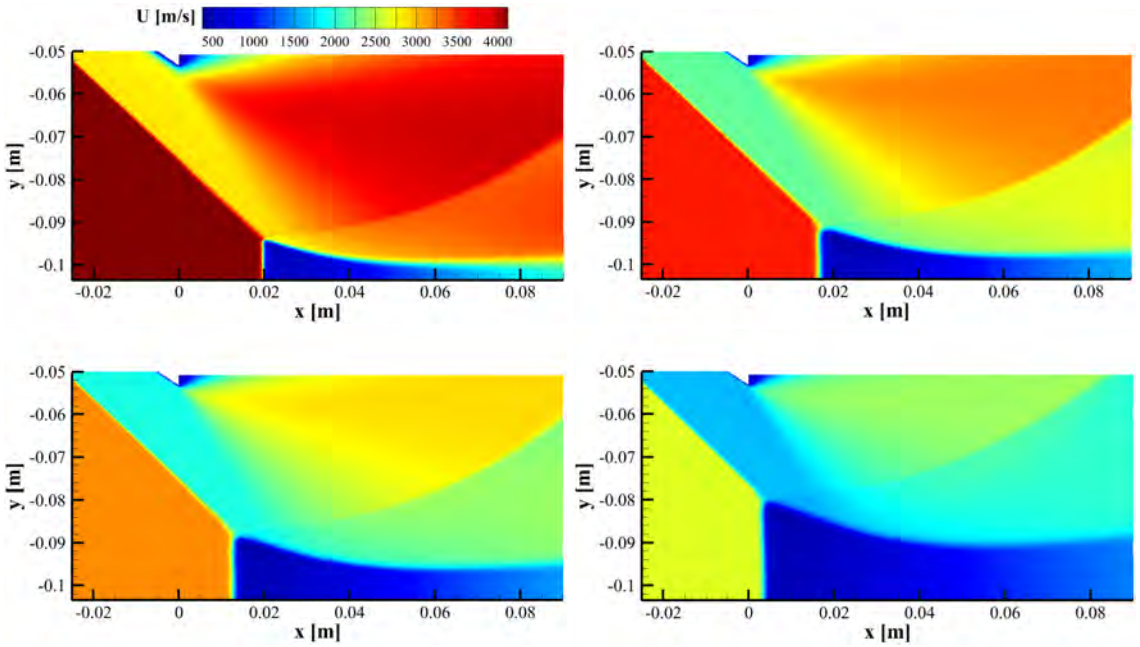

Figure 7.205: X-velocity results for Mach 8.5 flow with stagnation enthalpies of a) 11, b) 6.9, c) 5.4 and d) 3.8 MJ/kg. Bryan et al. [52]

The mole fractions of nitric oxide for the various stagnation enthalpies studied is provided in *Fig.* 7.207. The results show that nitric oxide existed solely in the wake regions. Following the wake region trend discussed previously, the size of the nitric oxide region in the domain increased as the stagnation enthalpy decreased. Also, as stagnation enthalpy decreased, the region with the highest mole fraction of nitric oxide in each flow field moved downstream. Going from a stagnation enthalpy of 3.8 MJ/kg to 5.4 MJ/kg, the mole fraction of nitric oxide increased significantly.

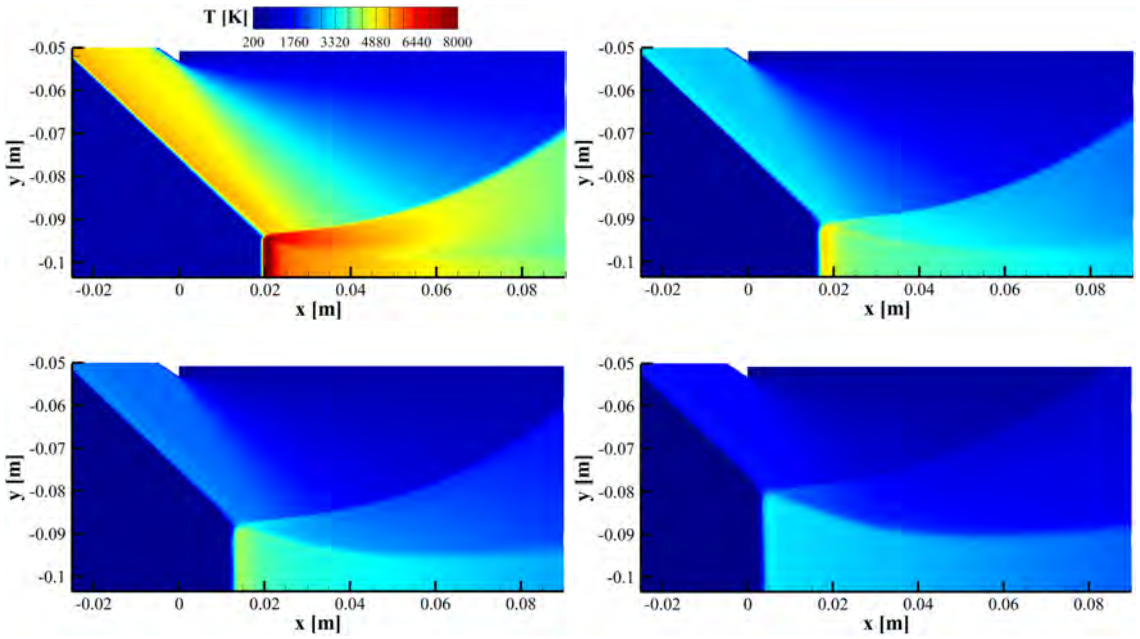

Figure 7.206: Translational-Rotational Temperature for Mach 8.5 and stagnation enthalpies of a) 11, b) 6.9, c) 5.4 and d) 3.8 MJ/kg. Bryan et al. [52]

Further increases in enthalpy resulted in progressively lower mole fractions of nitric oxide. Another interesting observation to note is that the highest stagnation enthalpy case of 11 MJ/kg had the lowest nitric oxide mole fraction among the enthalpies simulated. Furthermore, unlike the other stagnation enthalpies simulated, the 11 MJ/kg case showed nitric oxide concentrated close to the normal shock and predominantly existing along the shear layer. It would be an interesting and worthwhile case study in the future to simulate additional stagnation enthalpies between 6.9 MJ/kg and 11 MJ/kg to explore the transition in nitric oxide concentrations from the entire wake region to just the shear layer. The mole fractions of atomic oxygen for the various stagnation enthalpies are given in *Fig.* 7.208. Similar to nitric oxide, the mole fraction of O lies in the wake region of the Mach stem, bounded by the shear layer and symmetry plane. Unlike nitric oxide, the local region with the highest O mole fraction didn't appear to move around from case to case. Nevertheless, the gradient region between the normal shock and the region with maximum O mole fraction decreased in length as stagnation enthalpy increased. Also, as the stagnation enthalpy increased the maximum mole fraction of O also increased. It should be noted that in the case of 11 MJ/kg, there was nearly complete dissociation of diatomic oxygen. ([52])

7.6.3 Analyzing Thermochemical Non-equilibrium of Mach 8.5 Flow at Stagnation Enthalpy 11 MJ/kg

This discussion in this section follows from Bryan et al. [52]. An important area of interest in high enthalpy, hypersonic flow is thermochemical non-equilibrium. A gas in both thermal non-equilibrium and chemical non-equilibrium is considered to be in thermochemical non-equilibrium. To analyze both of these properties, flow at Mach 8.5 with stagnation enthalpy of 11 MJ/kg was

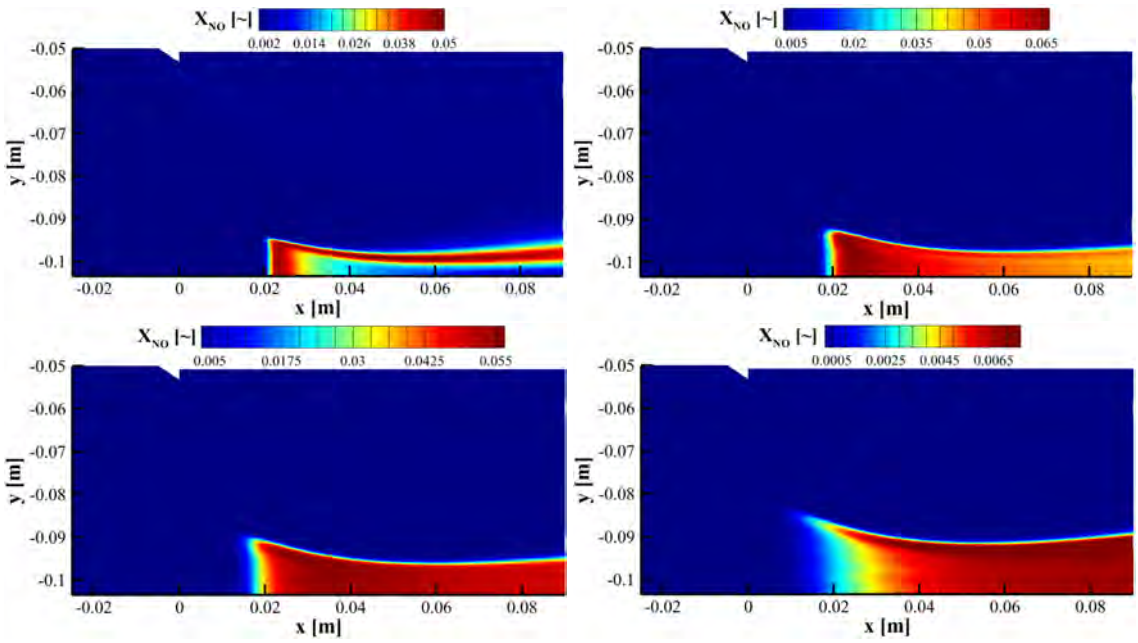

Figure 7.207: Mole Fraction of nitric oxide for Mach 8.5 flow with stagnation enthalpies of a) 11, b) 6.9, c) 5.4 and d) 3.8 MJ/kg. Bryan et al. [52]

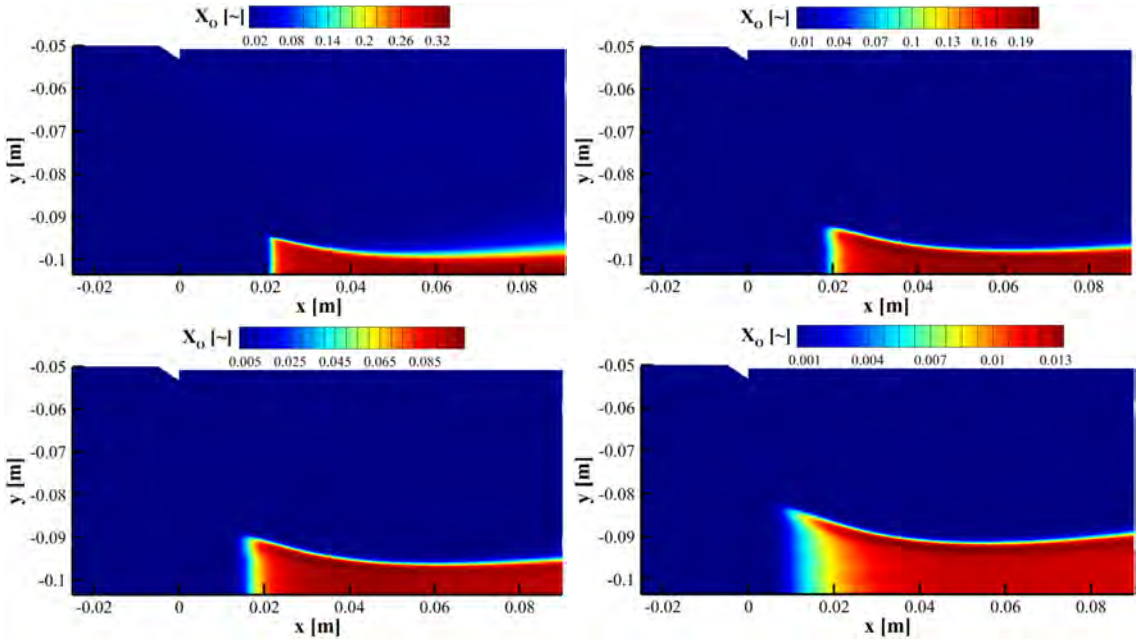

Figure 7.208: Mole Fraction for molecular oxygen for Mach 8.5 flow with stagnation enthalpies of a) 11, b) 6.9, c) 5.4 and d) 3.8 MJ/kg. Bryan et al. [52]

simulated with the coarse grid discussed previously. A gas is said to be in thermal non-equilibrium if its internal energy cannot be characterized by a single temperature. The thermal non-equilibrium in the 11 MJ/kg case was evaluated using the difference between the translational-rotational temperature, T, and the vibrational-electronic temperature, T_v at each location in the flow field. The results, shown in *Fig.* 7.210, indicate that there was thermal non-equilibrium along the incident oblique shock, the Mach stem, and between the reflected oblique shock and shear layer. Although the greatest thermal non-equibrium occurred downstream of the normal shock, it is interesting to note that the streamwise length of the thermal non-equibrium region is longest downstream of the oblique shocks. ([52])

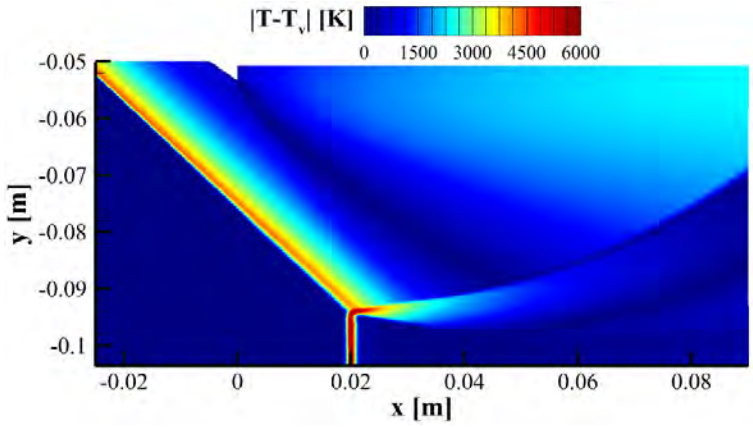

Figure 7.209: Difference between T and T_v for Mach 8.5 flow with stagnation enthalpy 11 MJ/kg. [52]

To determine if a gas species was in chemical non-equilibrium, the Damköhler number, *Da*, was calculated. The Damköhler number is the ratio of the fluid motion timescale to the chemical reaction timescale. The Damköhler number was calculated using the formula Candler [366]

$$Da = \frac{\tau_f}{\tau_c} = \frac{l w_s}{\rho V}$$

Here l is a characteristic length scale chosen to be the length of the wedge, ρ is the total density, V is the magnitude of velocity, and w_s is the rate of production/destruction of a species from chemical reactions. Two different methods for calculating w_s were considered. The first method used the equation provided by Candler *et al.*, $\frac{\partial}{\partial x_j}(\rho_s u_j) = w_s$ [366]. The second used a more general approach, which was discussed in Anderson *et al.* [19] and Kee *et al.* [367]. In the general approach, all of the possible chemical reactions needed to be specified. Then, the partition functions for each species, the zero-point energies for each reaction, the equilibrium constants for each reaction, the forward and reverse reaction constants for each reaction, the rate of progress for each reaction, and the rate of production/destruction for each species needed to be computed.

Ultimately, the first approach was selected to calculate the Damköhler number for most of the results. For completeness, a direct comparison of the nitric oxide Damköhler number was made, which is presented in *Fig.* 7.210, using the two different methods for calculating w_s and *Da*. The grey region in *Fig.* 7.210 simply signifies either that NO was in equilibrium or only trace amounts of NO were present. If the Damköhler number approached zero then the chemical reaction time scale were much larger than the flow timescale, implying the reactions are slow and the gas is frozen [366]. On the other hand, if the Damköhler number approached infinity then the chemical reaction time scale was much smaller than the flow timescale, implying the reactions occur instantly and the gas is in equilibrium [366]. The Damköhler number was calculated for NO, O, N, and NO^+, which is shown in *Fig.* 7.211. The results show that NO, O, and N all exhibit strong chemical non-equilibrium as the Damköhler number is of order 1. Qualitatively, atomic oxygen had a larger region of non-equilibrium than both NO and N. Furthermore, NO had a larger region of non-equilibrium than N. The subplots for NO, O contain the same colorbar, whereas N and NO^+ have a different colorbar. These results show that NO and N had similar regions of chemical non-equilibrium. Also, the degree of non-equilibrium was less for N and much less for NO^+. ([52].)

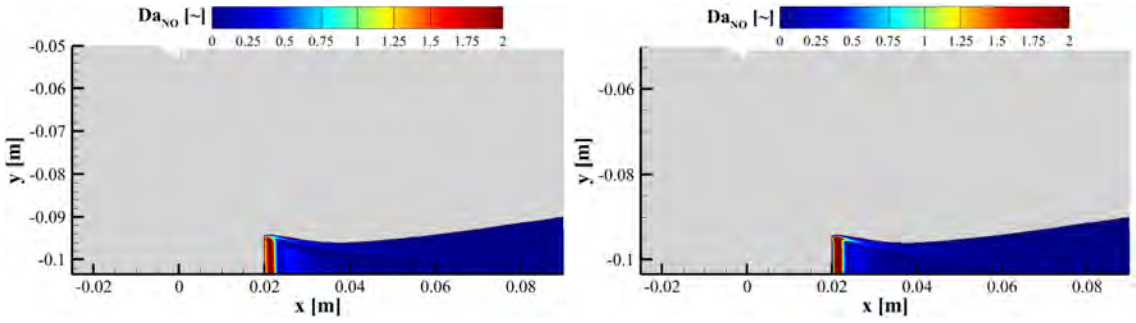

Figure 7.210: Damköhler number of NO for a) Candler *et al.* [366] and b) Anderson *et al.* [19] for Mach 8.5 and stagnation enthalpy 11 MJ/kg. Bryan et al. [52]

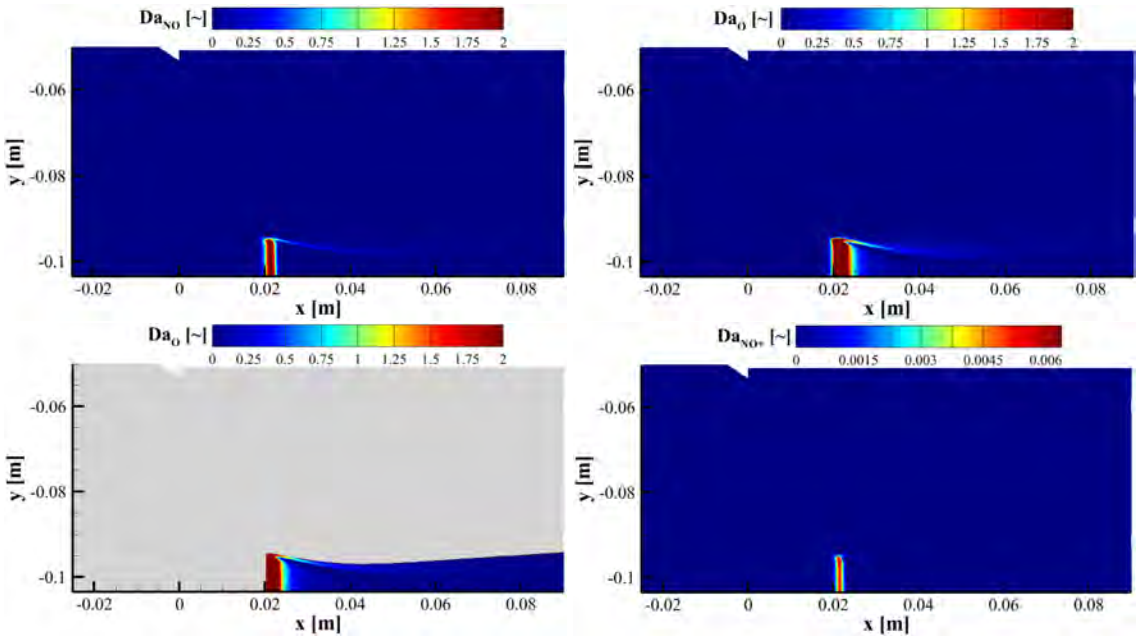

Figure 7.211: Damköhler number of a) NO, b) O, c) N, and d) NO^+ for Mach 8.5 with a stagnation enthalpy 11 MJ/kg. Bryan et al. [52]

8. CONCLUSIONS

8.1 Preamble

The conclusions presented in this section were drawn from selected dissertations, theses, and articles associated with the execution of this project: McManamen [1], Buen et al. [2], McManamen et al. [3], Siddiqui [4], [5], Siddiqui et al. [6], Broslawski [7], Dean et al. [8],Bryan et al. [52], Bryan et al. [10], Dean [11], Broslawski et al. [12], Broslawski et al. [13], Broslawski et al. [14], Smotzer et al. [15], and Dean et al. [16]. The original citations are also included in the subsequent text.

8.2 Hypersonic Boundary Layer with Thermal Nonequilibrium

The objectives for the non-equilibrium hypersonic turbulent boundary layer study were 1) Produce a test article capable of canonical boundary layers, excitation of thermal nonequilibrium, and both modern physical and optical diagnostics; 2) Re-derive the algebraic energy flux model in great detail; 3) Create a database of experimental turbulence data to validate turbulence models; 4) Extend this database to flows in thermal nonequilibrium. Taken together, the goal was to provide a database of parameters collected in a hypersonic turbulent boundary layer with and without thermal nonequilibrium to improve understanding and modeling of these environments. Despite its recognized critical importance, there was little to no canonical experimental data of these flows in thermal nonequilibrium for validation of proposed theories and models, hindering progress. Therefore this work served the broader community by encouraging the development of low cost predictions of aerodynamic heating, and thereby more judicious use of high fidelity computations when designing thermal protection systems. The test article was designed and fabricated, with attention on the leading edge, trips, and electrodes, as they directly control the quality of the boundary layer produced and thereby. The success of the test article was quantified, where the plasma was characterized using circuit measurements, the trip efficacy was tested with IR thermography, and the leading edge uniformity was confirmed using surface profilometry. This geometry operating in ACE provided a low Reynolds number turbulent boundary layer test bed for the theoretical and experimental study described herein, but is also DNS accessible with current computational resources. The derivation and implementation of an algebraic energy flux model for flows in thermal equilibrium was described. The results matched those of the source material [22] on which they were meant to elaborate. The theory was extended for the first time to a flow in a favorable pressure gradient as well, and its results were encouraging [25]. What remains is the implementation and tuning of the model in a CFD code and validation with DNS and experimental data. Without considering thermal nonequilibrium, the theoretical developments pointed to the need for improved hypersonic Reynolds stress models and showed areas where the present model could be enhanced such as its performance near the wall or the use of the weak (mechanical) equilibrium assumption in the presence of pressure gradients. The experimental campaigns provided surveys of the wall temperature, heat flux, shear stress, freestream velocity, temperature, Mach number, plasma power, constituents, internal temperatures, freestream Pitot, surface pressure measurements, high-frequency pressure measurements, boundary layer and shock visual-

ization, leading edge uniformity and roughness along the test article. The temperature, velocity, Mach number, and pressure data were all taken to resolve the turbulent fluctuations, and data were taken at up to six test locations along the streamwise and spanwise direction for the laminar/turbulent and plasma off/on cases. Thus, through a variety of techniques, including some redundant measurements, the flow was exceptionally well characterized. The plasma was used to allow the study the effect of controlled vibrational nonequilibrium in a hypersonic boundary layer. Specifically, PLIF thermometry of T^v_{NO} was especially successful in studying the effect of the nonequilibrium by measuring the change in the vibrational temperature along the test article and through the boundary layer. These measurements represent the first known such measurement. The unique time scales of $NO^{v=1}$ relaxation were estimated to be at least comparable to the flow over the test article, leaving the potential open for turbulence and nonequilibrium coupling. All evidence suggested that this would not have been observed with N_2 or O_2, which were likely thermally frozen; this freezing of the dominant species and the low concentration of the relaxing NO meant that the re-laminarization process identified in [27] could not occur, a finding supported the data. That these data leveraged the data from the numerical boundary layer solver, experimental PLIF measurements, and thermodynamic and turbulence theories in their analyses united the three fields at the core of this work. These data may also inform additional exploration of the reaction time scales and validate novel vibrational energy turbulence models. The summary in Figure 8.1 demonstrates the manner in which the present data, coupled with finite rate chemistry models, are being used to advance turbulence models that include thermal non-equilibrium. (Broslawski [7]).

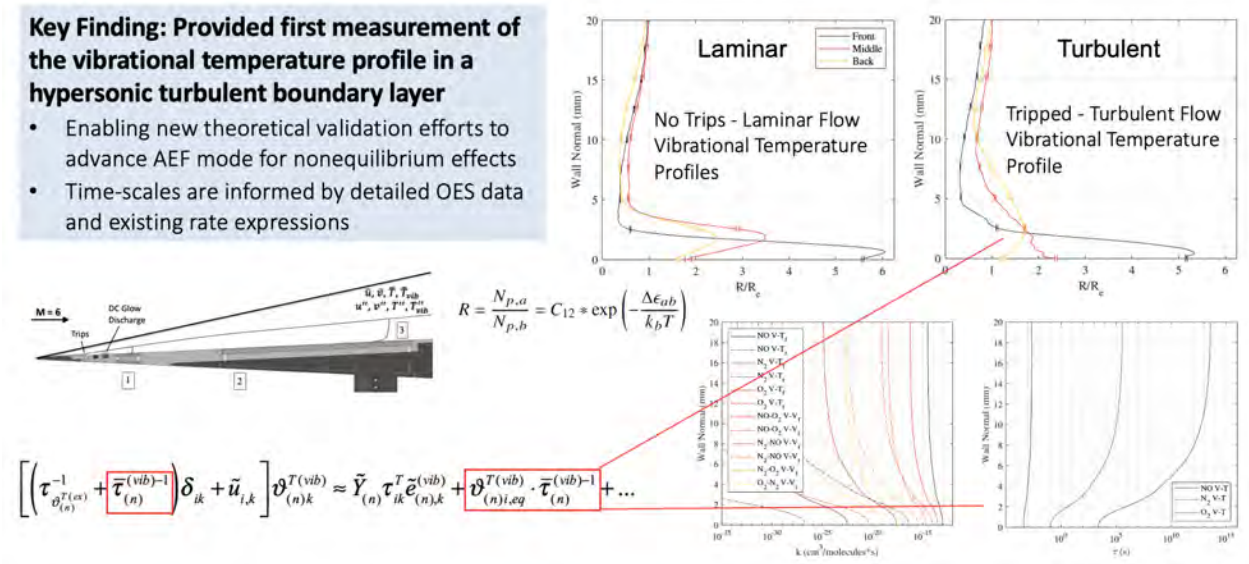

Figure 8.1: Key finding 1: Experimental quantification of a 2-D Mach 6 boundary layer with thermal non-equilibrium, including providing first known excited vibrational temperature profile across turbulent and laminar hypersonic boundary layers. These data enable validation of energy (heat) flux turbulence closure models and are DNS accessible with current computational resources. ([7]

The second boundary layer study was performed to examine the instabilities associated with boundary layer transition that included both the Mack second mode and DRE excited stationary Görtler instabilities. The aim for this study was to provide additional fundamental boundary layer stability and breakdown to turbulence that may help inform interpretation of the tripping mechanism for the above non-equilibrium hypersonic boundary layer study. The experiments were conducted in the TAMU M6QT on the a canonical 91-6 flared cone. The 91-6 is a flared cone with embedded thermocouples and active cooling. The experiments were carried out first on the smooth cone and then DREs added and experiments repeated. The diagnostics included surface temperatures, hot-film anemometry, focusing schlieren, and focused laser differential interferometry (FLDI). Wind tunnel runs were performed at coolant set points set of 20 °C, -20 °C, and -60 °C. The unit Reynolds number was held constant at $9x10^6$ /m. Analysis of the temperature profiles obtained from the embedded thermocouples showed an earlier increase in heating for the cases with lower wall temperature. This is in agreement with previous experiments that show increased destabilization with lower wall temperature due to a decrease in boundary-layer height causing higher frequencies of the Mack-mode instability. This trend was observed for both the smooth cone and the cone with DREs and has been quantified for both cases. When comparing the smooth cone and cone with DREs at the same coolant set points, earlier heating was observed for the cone with DREs due to the destabilizing effect of the DREs. The temperature profiles were also analyzed over the course of a Reynolds number sweep for the same three coolant set points on the smooth cone and the cone with DREs. Earlier heating was observed for all profiles for the higher Reynolds numbers. For the smooth cone case the temperature profiles were near identical at the aft end of the cone for unit Reynolds numbers of $8x10^6$ /m and $9x10^6$ /m. An increase in heating was observed for the $10x10^6$ /m case and continued increase for the $11x10^6$ /m as the boundary layer transitioned to turbulence. For the cone with DREs similar trends were observed except for coldest wall Re/m = $9x10^6$ /m, where higher heating was seen compared to the smooth cone profile signifying earlier transition of the boundary layer. Spectral data were also collected and showed peaks ranging from $\sim$280 to $\sim$320 kHz. The frequencies were seen to increase as the Reynolds number was increased due to a decrease in boundary-layer height. An increase was seen in the spectral energy at certain Reynolds numbers and grew until the Mack-mode peak was no longer visible, which was then considered a turbulent boundary layer. For the smooth cone and cone with DREs the spectral energy was observed to increase at lower Reynolds numbers for lower wall temperatures. The Mack-mode peak was not observed at lower Reynolds numbers as the wall temperature was decreased. The Mack-mode frequencies were observed to be lower in general for the cone with DREs due to a higher boundary-layer height caused by the DREs. The cone with DREs was also observed to be more unstable as the increase in spectral energy and disappearance of Mack-mode peak were observed at earlier Reynolds numbers for the same wall temperatures. Hot-film maps showed peaks every 4° for the smooth cone and the cone with DREs. The structure became more prominent and the height of the boundary layer was observed to decrease for the lower wall temperatures. The boundary-layer height was observed to be higher for the cone with DREs than for the smooth cone, in agreement with the focusing schlieren data. These peaks were assumed to be from Görtler vortices caused by the flare and this was confirmed by computational work. Spectral data were obtained and the Mack-mode instability and two harmonics documented. Unit

Reynolds number sweeps were performed and the spectral data showed boundary-layer transition as the Reynolds number was increased. The present data are summarized in Figure 8.2. (Siddiqui [4]).

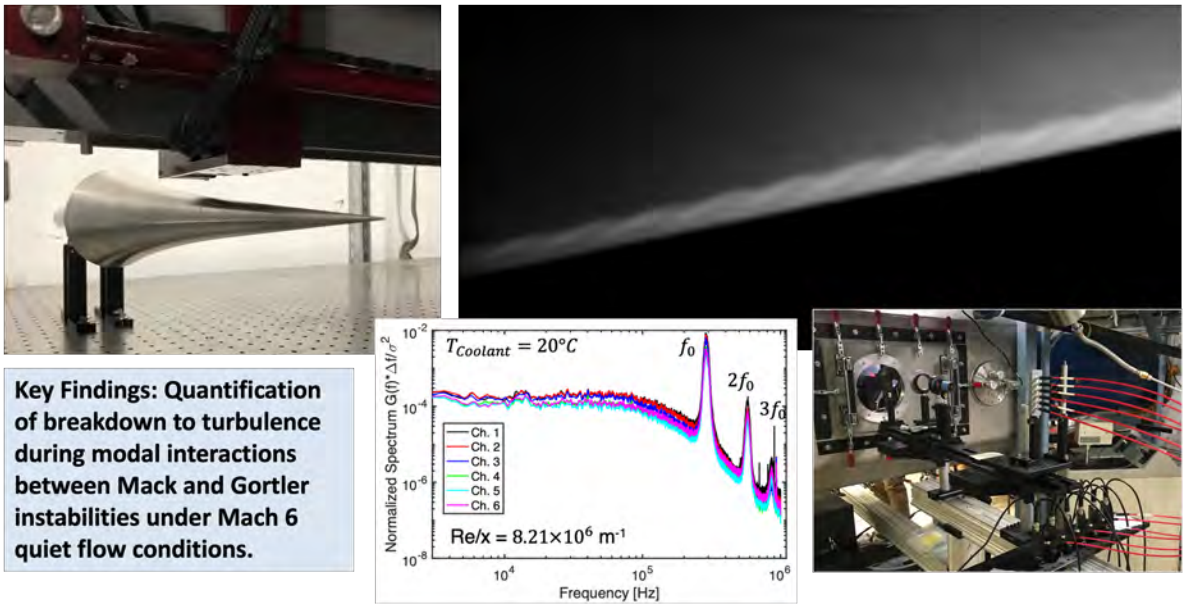

Figure 8.2: Key Finding 2: Experimentally quantified the breakdown to turbulence for the case of interacting Mack and Görtler instabilities, which is of direct relevance to the tripped Mach 6 thermal nonequilibrium boundary layer study. ([4]

8.3 Hypervelocity Mach Stem Experiments

The primary purpose of the hypervelocity Mach stem study was the experimental quantification of high-enthalpy, hypersonic turbulence. The first deliverable from this work was the final commissioning and characterization of a national resource scale, high enthalpy ground testing facility called the Hypervelocity Expansion Tunnel (HXT) within the National Aerothermochemistry and Hypersonic Flight Laboratory at Texas A&M University. Noteworthy design aspects of the facility included energy-damping structural supports, a double diaphragm system for repeatability, and a nozzle with a 0.91 m diameter exit, which ranks it among the largest expansion tunnels in existence. The HXT was characterized at conditions throughout its operational envelope using high-frequency pressure measurements, schlieren, Mie scattering, optical emission spectroscopy (OES), focused laser differential interferometry (FLDI), femtosecond laser electronic excitation tagging (FLEET), and planar laser-induced fluorescence (PLIF). The characterization measurements validated a theoretical prediction code for the facility and demonstrated high flow condition repeatability. The commissioning of the HXT led to multiple pathfinding experimental campaigns. One of these campaigns employed PLIF to visualize nitric oxide mixing in the shear layers of

Mach reflections. Mach reflections, generated using a pair of large wedges, served as canonical flows for studying turbulence. The freestream flow conditions of the campaign were Mach 6.5 with stagnation enthalpies of 6, 7, and 8 MJ/kg. The PLIF experiments served dual roles, spatially quantifying the turbulent mixing of nitric oxide at 250 kHz and progressing the development of an ultra-fast laser diagnostic technique. The resulting visualizations provided useful insight into the behavior of turbulent structures within Mach reflection shear layers. In addition, the size and relative concentrations of the nitric oxide flow features were relevant for computer simulation validation. Other pathfinding campaigns focused on maturing diagnostic techniques, including FLDI and OES, for studying Mach reflection flows inside the HXT. The culmination of this work materialized in an experimental campaign that leveraged simultaneous FLEET, FLDI, OES, and high-speed schlieren to study the extreme turbulence around Mach reflections. Five distinct Mach 8.5 flowfields with stagnation enthalpies ranging from 1.8 to 8.9 MJ/kg were studied. Including air and nitrogen test gasses at two different densities and three different stagnation enthalpies, the different cases allowed evaluation of the influence of stagnation enthalpy, density, and chemistry on high enthalpy turbulence. The turbulence measurements within the Mach reflection free shear layers were the first of their kind. The presence of high-temperature effects like thermal and chemical non-equilibrium made the measurements particularly valuable to the hypersonics community. In addition, to the best of the authors' knowledge, the experimental setup devised for simultaneous FLDI and high-speed schlieren was original and uniquely valuable for measurements in flowfields that exhibit mild temporal variations. Noteworthy variations in turbulent energy distributions based on refractive index power spectra at the different flow conditions were identified using the FLDI results. In addition, the turbulence statistics of the index of refraction fluctuations were valuable for validating upcoming direct numerical simulations (DNS) of the flowfields. The FLDI measurements also yielded convective velocity distributions through the shear layers, which provided additional insight into the turbulence. Shock turbulence interactions were studied by performing FLDI measurements on both sides of the normal shocks of the Mach reflections. These measurements were complicated by the presence of particles at some run conditions. The change in chemistry across the shocks at the higher enthalpy conditions introduced additional complexity in correlating the refractive index measurements to the underlying turbulence. Nevertheless, the results were valuable for wind tunnel characterization, and interesting trends were identified, particularly at the highest density run condition. The final component of the extreme turbulence measurements was the use of OES to quantify the thermochemistry present in both the shear layers and the post-shock regions. Emission from the gamma band system of nitric oxide was primarily measured during air runs, and emission from the cyanide (CN) violet band system was the primary emission measured during nitrogen runs. Other emission sources identified within the probed wavelength ranges included iron and imidogen (NH). The spatial distributions of emission measured vertically through the shear layers and post-shock region during each run consistently indicated that the equilibrium temperatures of electronically excited species emitting with the shear layers were higher than in the post-shock regions. The computation of specific rotational and vibrational temperatures based on the emissions was left to future work. Another observation was the absence of CN emission during the high enthalpy air runs, which contrasted with the prominence of CN emission during nitrogen runs. The summary in Figure 8.3 demonstrates the profound effect of thermochemistry

on the structure of the Mach stem flow, with associated spectra. The translational temperature just downstream of the normal shock was about 7,000K, and the equilibrium temperature from the spectra was about 5,000K. Example results are summarized in Figure 8.3. (Dean [11])

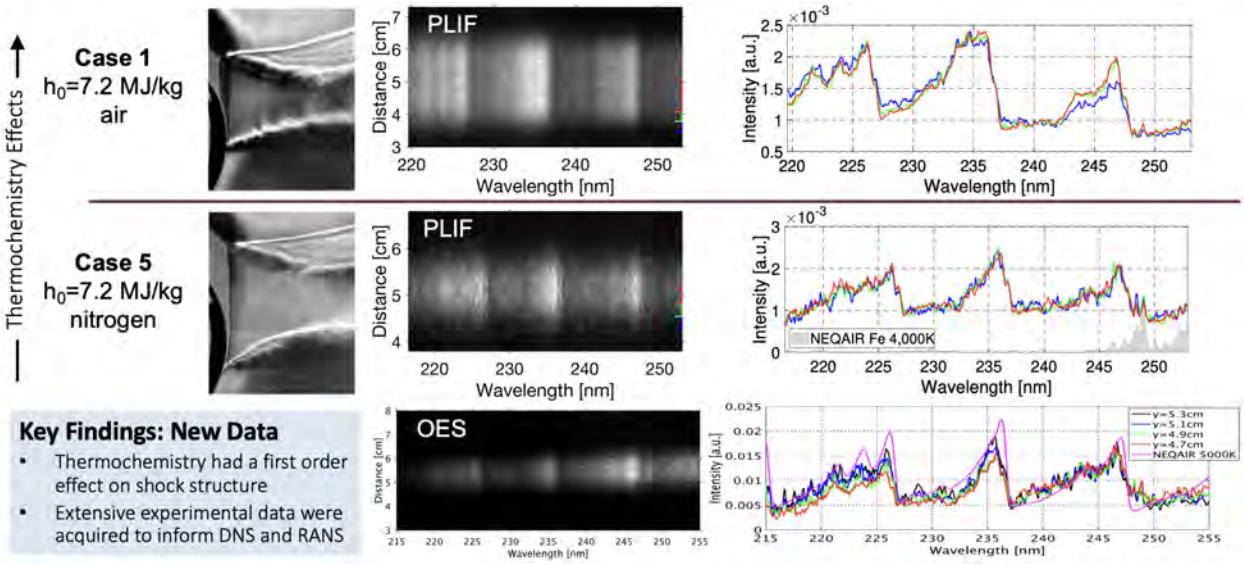

Figure 8.3: Key Finding 3: Experimentally quantified the role of thermochemistry on Mach stem flows, including shock turbulence interaction and the free shear layer region. Temperature estimates are available from molecular fits to emission and PLIF spectra. The flow is DNS accessible with current computational methods. [11]

The low-enthalpy study provided observations of velocity and temperature fluctuation behavior through a stationary normal shock wave at Mach 4.4. This Mach number was selected for observation due to the high discrepancy between current theoretical and computational works, as well as the lack of experimental data in this regime. Experiments were performed in a small scale pulsed operation wind tunnel facility with Mach stem generator models installed to produce a normal shock wave in the freestream. No turbulence generating apparatus was used, rather the freestream fluctuations were a product of typical tunnel operation. This would include the incident noise due to flow through the tunnel supply lines and through the inlet valve orifices, as well as acoustic waves originating from the nozzle wall boundary layers. It is noteworthy that the PHACENATE facility transitioned to the Air Force with the graduate student that supported this project. Several optical techniques were employed in this work to observe amplification of vortical and entropic turbulence modes. Single component velocity measurements were taken at four locations downstream of the Mach stem for each Reynolds condition. This was followed by a PLIF thermometry investigation across the same region of interest for each case. Of the three conditions studied, the lowest Reynolds case seems to be an anomaly, having increased levels of freestream disturbances in both velocity and temperature. This is thought to be due to tunnel operation at low pressure.

The behavior is observed during all experiments, with and without model wedges installed, so it is unlikely to be an experimental error. (McManamen et al. [3]). Freestream velocity fluctuations for the axial mode were measured to be 0.7-1.2%, normalized by the mean velocity. In the post shock region, the RMS fluctuations were found to increase to 3-6%, normalized by the respective post-shock mean velocity. Transverse velocity fluctuations were not obtained in this study, therefore the role of the transverse modes are not indicated. Amplification of the axial mode was found to be 1.1-1.2, with no strong Reynolds number effect. The freestream velocity fluctuations are relatively weak compared to the other modes in this study, therefore it is difficult to separate its role in the observed amplification. The measured velocity amplification factor is found to be lower than both LIA prediction and results of computational studies in a similar Mach and K regime [see 168]. Temperature fluctuations were measured to be 4.5-6% in the freestream and 15-25% in the post-shock region. The Re/m = 2.1e6 condition had significantly higher fluctuations than the Re/m = 3.5e6 and 5.2e6 cases. Example results are summarized in Figure 8.4. Although not a focus of this study, the Kelvin-Helmholtz instability was visible in the schlieren photograph in Figure 8.4. (McManamen et al. [3])

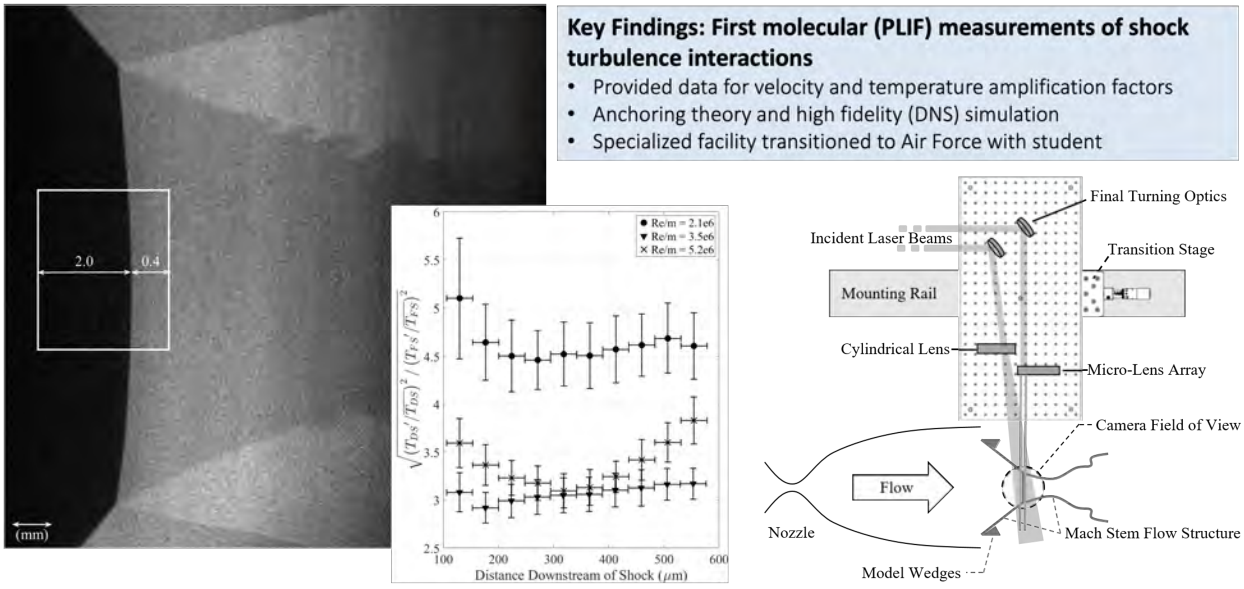

Figure 8.4: Key Finding 4: Experimentally quantified the velocity and temperature fluctuation amplifications across a normal shock (Mach stem) at Mach 4.4. These are the first known molecular based measurements using laser diagnostics (PLIF and MTV). The flow is DNS accessible with current computational methods. [3]

Finally, the high enthalpy Mach stem flows were simulated using the US3D CFD. Simulations of Mach stems in four different Mach 8.5 flow fields which had stagnation enthalpies of 3.8, 5.4, 6.9, and 11 MJ/kg were performed. The x-velocity and temperature distributions of the flow fields

were discussed in detail. The non-equilibrium regions of the flow fields were computed, which enable future experiments targeting non-equilibrium flows. Mole fraction distributions of nitric oxide and atomic oxygen were also produced for each flow condition. In addition to providing insight into the chemistry of high enthalpy Mach stems, these results were utilized to inform spectroscopy experiments. The calculations demonstrated the effectiveness of current high temperature gas models, as well as the ability capture the Kelvin-Helmholtz instability observed in the PHACENATE experiments. All of the simulations performed in this study incorporated laminar viscous effects. Example results are summarized in Figure 8.5. (Bryan et al. [52])

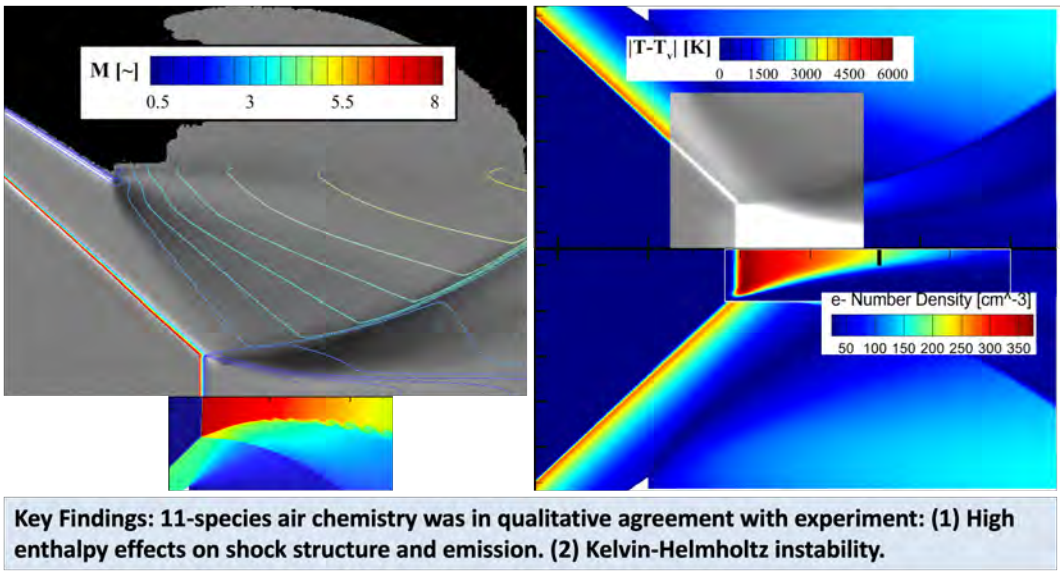

Figure 8.5: Key Finding 5: Numerical characterization of Mach stem flows using current CFD methods ([37]. The collages shown demonstrate the effectiveness of the 11-species air model and ability to resolve laminar kelvin-Helmholtz instability. [52]

REFERENCES

[1] B. McManamen. *Velocity and Temperature Measurements in a High Mach Number Shock-Turbulence Interaction*. PhD thesis, Texas A&M University, College Station, TX, 2019.

[2] Z. D. Buen, C. Broslawski, M. Smotzer, J. E. Kuszynski, S. North, and R. D. Bowersox. Towards vibrationally excited nitric oxide monitoring (venom) in a laminar, hypersonic boundary layer. *AIAA Paper 2020-1275*, 2020.

[3] B. McManamen, D. A. Donzis, S. W. North, and R. D. Bowersox. Velocity and temperature fluctuations in a high-speed shock-turbulence interaction. *Journal of Fluid Mechanics*, 913, 2021.

[4] F. Siddiqui. *Boundary-Layer Instabilities on a Cooled Flared Cone at Mach 6*. PhD thesis, Texas A&M University, College Station, TX, 2021.

[5] F. Siddiqui, M. Gragston, W. Saric, and R. Bowersox. Second-mode instabilities on a cooled flared cone with discrete roughness elements at mach 6. *Experiments in Fluids*, 62(10): 213.1–13, 2021.

[6] F. Siddiqui, M. Gragston, and R. Bowersox. Second-mode instabilities on a cooled flared cone with discrete roughness elements at mach 6. *AIAA Journal*, 60(11):6214–6224, 2022.

[7] C. Broslawski. *The Modeling and Experimentation of Hypersonic Turbulent Boundary Layers with and without Thermal Nonequilibrium*. PhD thesis, Texas A&M University, College Station, TX, 2022.

[8] T. S. Dean, T. R. Blair, M. L. Roberts, C. M. Limbach, and R. D. Bowersox. On the Initial Characterization of a Large-Scale Hypervelocity Expansion Tunnel. *AIAA Paper 2022-1602*, 2022.

[9] C. Bryan. *Computational Analysis of Hypersonic Mach Stems at High Enthalpy*. MS Thesis, Texas A&M University, College Station, TX, 2023.

[10] C. A. Bryan, T. S. Dean, B. J. Morreale, and R. D. Bowersox. Computational Simulations of Hypersonic Mach Stems at High Enthalpy. In *AIAA Science and Technology Forum and Exposition*, National Harbor, MD, 2023.

[11] T. Dean. *Experimental Investigation of Hypersonic Turbulence Around High Enthalpy Mach Reflections*. PhD thesis, Texas A&M University, College Station, TX, 2023.

[12] C. Broslawski, A. Moran, S. North, and R. D. Bowersox. The characterization of a glow discharge in a tripped hypersonic boundary layer. *Journal of Thermophysics and Heat Transfer*, 2024.

[13] C. Broslawski, A. Britt, S. North, and R. Bowersox. The characterization of a dc glow discharge in a tripped hypersonic boundary layer. *AIAA Paper 2024-1650*, 2024.

[14] C. Broslawski, Z. Buen, A. Britt, M. Smotzer, S. North, and R. Bowersox. Thermochemical relaxation of vibrationally excited no in a hypersonic turbulent boundary layer. *AIAA Paper 2024-2123*, 2024.

[15] M. Smotzer, Z. Buen, C. Broslawski, A. Britt, B. Morreale, S. North, and R. Bowersox. Nitric oxide planar laser induced fluorescence rotational thermometry characteriza-tion of a hypersonic boundary layer. *AIAA Paper 2024-1518*, 2024.

[16] T. S. Dean, J. C. Pehrson, R. D. Bowersox, and A. Dogariu. Expansion Tunnel Freestream Characterization Using Ultrafast Diagnostics. In *AIAA Scitech 2024 Forum*, 2024.

[17] B. T. McManamen. *Velocity and Temperature Measurements in a High Mach Number Shock-Turbulence Interaction*. PhD thesis, Texas A&M University, 2019.

[18] OUSD(R&E). National defense science & technology strategy 2023. 2023. URL `https://www.cto.mil/wp-content/uploads/2024/05/2023-NDSTS.pdf`.

[19] J. Anderson. *Hypersonic and High Temperature Gas Dynamics*. AIAA, Inc., 2019.

[20] J. Urzay. Supersonic Combustion in Air-Breathing Propulsion Systems for Hypersonic Flight. *Annual Review of Fluid Mechanics*, 50:593–627, 2018.

[21] A. Whitehead Jr. Nasp aerodynamics. *AIAA Paper 1989-5013*, 1989.

[22] R. D. W. Bowersox. Extension of equilibrium turbulent heat flux models to high-speed shear flows. *Journal of Fluid Mechanics*, 633:61–70, 2009.

[23] J. Poggie. Compressible turbulent boundary layer simulations: resolution effects and turbulence modeling. *AIAA Paper 2015-1983*, 2015.

[24] J. Huang, G. L. Nicholson, L. Duan, M. M. Choudhari, and R. D. Bowersox. Simulation and modeling of cold-wall hypersonic turbulent boundary layers on flat plate. *AIAA Paper 2020-0571*, 2020.

[25] C. Broslawski, B. Morreale, R. D. Bowersox, G. Nicholson, and L. Duan. Further validation and implementation of an algebraic energy flux model for high speed gaseous shear flows. *AIAA Paper 2022-0340*, 2022.

[26] R. Bowersox, S. North, and R. Srinivasan. High-speed free shear layers with molecular non-equilibrium: An example of the fluids information triad (invited). *AIAA Paper 2008-0685*, 2008.

[27] T. J. Fuller, A. G. Hsu, R. Sanchez-Gonzalez, J. C. Dean, S. W. North, and R. D. Bowersox. Radiofrequency plasma stabilization of a low-reynolds-number channel flow. *Journal of fluid mechanics*, 748:663, 2014.

[28] T. J. Fuller. *Experimental Analysis of the Effect of Vibrational Non-Equilibrium on the Decay of Grid-Generated Turbulence*. PhD thesis, Texas A&M University, College Station, TX, 2009.

[29] S. Khurshid and D. A. Donzis. Decaying compressible turbulence with thermal non-equilibrium. *Physics of Fluids*, 31(1):015103, 2019.

[30] M. T. Semper and R. D. W. Bowersox. Tripping of a hypersonic low-reynolds-number boundary layer. *AIAA Journal*, 55(3):808–817, 2017.

[31] H. Hornung and M. Robinson. Transition from regular to mach reglection of shock waves part 2. the steady-flow criterion. *Journal of Fluid Mechanics*, 123:155–164, 1982.

[32] D. A. Donzis. Amplification factors in shock-turbulence interactions: Effect of shock thickness. *Physics of Fluids*, 24(1):011705, 2012.

[33] J. Larsson, I. Bermejo-Moreno, and S. K. Lele. Reynolds-and Mach-number effects in canonical shock–turbulence interaction. *Journal of Fluid Mechanics*, 717:293–321, 2013.

[34] H. S. Ribner. Convection of a pattern of vorticity through a shock wave. Technical Report NACA-TR-1164, NACA, 1954.

[35] H. S. Ribner. Shock-turbulence interaction and the generation of noise. Technical Report NACA-TN-3255, NASA Lewis Research Center, 1954.

[36] A. Leidy, I. Neel, N. Tichenor, R. Bowersox, and J. Schmisseur. Influence of perturbations on 3-d hypersonic shock laminar boundary interactions. *AIAA Journal*, 59(7):2357–2367, 2021.

[37] G. V. Candler, H. B. Johnson, I. Nompelis, V. M. Gidzak, P. K. Subbareddy, and M. Barnhardt. Development of the us3d code for advanced compressible and reacting flow simulations. *AIAA Paper 2015 - 1893*, 2015.

[38] L. Prandtl. Über flüssigkeitsbewegung bei sehr kleiner reibung. *Proc. Third Int. Math. Congr. Heidelberg*, 1904.

[39] E. R. van Driest. Turbulent boundary layer in compressible fluids. *Journal of the Aeronautical Sciences*, 18(3):145–160, 1951.

[40] F. H. Clauser. The turbulent boundary layer. *Advances in Applied Mechanics Advances in Applied Mechanics Volume 4*, page 1–51, 1956.

[41] D. B. Spalding. A single formula for the "law of the wall". *Journal of Applied Mechanics*, 28(3):455–458, Jan 1961.

[42] W. Jones and B. E. Launder. The prediction of laminarization with a two-equation model of turbulence. *International journal of heat and mass transfer*, 15(2):301–314, 1972.

[43] T. Cebeci and A. M. O. Smith. *Analysis of Turbulent Boundary Layers*. Acad. Pr., 1974.

[44] B. E. Launder and B. I. Sharma. Application of the energy-dissipation model of turbulence to the calculation of flow near a spinning disc. *Letters in heat and mass transfer*, 1(2): 131–137, 1974.

[45] B. Baldwin and H. Lomax. Thin-layer approximation and algebraic model for separated turbulentflows. *16th Aerospace Sciences Meeting*, 1978.

[46] P. Spalart and S. Allmaras. A one-equation turbulence model for aerodynamic flows. *AIAA Paper 1992-0439*, 1992.

[47] A. J. Smits and J.-P. Dussauge. *Turbulent shear layers in supersonic flow*. Springer, 2nd edition, 2006.

[48] F. M. White. *Viscous Fluid Flow*. McGraw-Hill, 3rd edition, 2006.

[49] D. C. Wilcox. *Turbulence Modeling for CFD*. DCW Industries, 2nd edition, 2006.

[50] J. A. Schetz and R. D. W. Bowersox. *Boundary layer analysis*. American Institute of Aeronautics and Astronautics, 2nd edition, 2011.

[51] S. B. Pope. *Turbulent Flows*. Cambridge University Press, 2015.

[52] C. A. Bryan, T. Dean, B. J. Morreale, and R. D. Bowersox. Computational simulations of hypersonic mach stems at high enthalpy. *AIAA Paper 2023-0858*, pages 1–16, 2023.

[53] A. Hsu. *Application of Advanced Laser and Optical Diagnostics Towards Non-Thermal Equilibrium Systems*. PhD thesis, Texas A&M University, College Station, TX, 5 2009.

[54] H. E. Bass. Absorption of sound by air: high temperature predictions. *The Journal of the Acoustical Society of America*, 69(1):124–138, 1981.

[55] G. V. Candler, J. D. Kelley, S. O. Macheret, M. N. Shneider, and I. V. Adamovich. Vibrational excitation, thermal nonuniformities, and unsteady effects on supersonic blunt bodies. *AIAA journal*, 40(9):1803–1810, 2002.

[56] R. Jongbaik. Theoretical investigation of the vibrational relaxation of $no(v = 1-7)$ in collisions with o_2 and n_2. *Bulletin of the Korean Chemical Society*, 14(1):47–52, 1993.

[57] J. Kosanetzky, U. List, W. Urban, H. Vormann, and E. Fink. Vibrational relaxation of no (x2π, υ= 1) studied by an ir-uv-double-resonance technique. *Chemical Physics*, 50(3): 361–371, 1980.

[58] S. A. Schaaf and P. L. Chambre. *Rarefied Gas Dynamics*. Princeton University Press, 1966.

[59] I. Nompelis, G. V. Candler, and M. S. Holden. Effect of vibrational nonequilibrium on hypersonic double-cone experiments. *AIAA journal*, 41(11):2162–2169, 2003.

[60] Y.-L. Yu, X.-D. Li, Z.-H. Wang, and L. Bao. Theoretical modeling of heat transfer to flat plate under vibrational excitation freestream conditions. *International Journal of Heat and Mass Transfer*, 151:119434, 2020.

[61] R. Sauerwein and B. Hruschkaand. Influence of molecular vibrational energy accommodation modeling on cone surface heat flux at mach 10. *Journal of Energy and Power Engineering*, 10:660–666, 2016.

[62] G. Black, H. Wise, S. Schechter, and R. L. Sharpless. Measurements of vibrationally excited molecules by raman scattering. ii. surface deactivation of vibrationally excited n_2. *The Journal of Chemical Physics*, 60(9):3526–3536, 1974.

[63] J. N. Moss and G. A. Bird. Direct simulation monte carlo simulations of hypersonic flows with shock interactions. *AIAA journal*, 43(12):2565–2573, 2005.

[64] J. Méolans. Thermal slip boundary conditions in vibrational nonequilibrium flows. *Mechanics Research Communications*, 30(6):629–637, 2003.

[65] I. Boyd, W. Phillips, D. Levin, I. Boyd, W. Phillips, and D. Levin. Sensitivity studies for prediction of ultra-violet radiation in nonequilibrium hypersonic bow-shock waves. *AIAA Paper 1997-0131*, 1997.

[66] J. Clarke and M. McChesney. *The Dynamics of Real Gases*. Butterworths Scientific Publications, 1964.

[67] W. G. Vincenti and C. H. Kruger. *Introduction to physical gas dynamics*. Wiley, 1965.

[68] P. Gnoffo, R. Gupta, and J. Shin. Conservation equations and physical models for hypersonic air flows and thermal and chemical non-equilibrium. Technical Report TP No. 2867, NASA Langley, 1989.

[69] S. Deiwert and G. Candler. Reacting flows: Special course on three-dimensional supersonic/hypersonic flows including separation. Technical Report AGARD Report No. 764, NASA Ames Research Center, 1989.

[70] C. Park. *Non-Equilibrium Hypersonic Aerothermodynamics*. Wiley & Sons, 1990.

[71] R. Macdonald, R. Jaffe, D. Schwenke, and M. Panesi. Construction of a coarse-grain quasi-classical trajectory method. i. theory and application to n2-n2 system. *The Journal of chemical physics*, 148(5):054309, 2018.

[72] M. Panesi, A. Munafò, T. Magin, and R. Jaffe. Nonequilibrium shock-heated nitrogen flows using a rovibrational state-to-state method. *Physical Review E*, 90(1):013009, 2014.

[73] A. Munafo, M. Panesi, and T. Magin. Boltzmann rovibrational collisional coarse-grained model for internal energy excitation and dissociation in hypersonic flows. *Physical Review E*, 89(2):023001, 2014.

[74] M. Panesi, R. L. Jaffe, D. W. Schwenke, and T. E. Magin. Rovibrational internal energy transfer and dissociation of $n_2(^1\sigma_g^+) - n(^4s_u)$ system in hypersonic flows. *The Journal of chemical physics*, 138(4):044312, 2013.

[75] T. E. Magin, M. Panesi, A. Bourdon, R. L. Jaffe, and D. W. Schwenke. Coarse-grain model for internal energy excitation and dissociation of molecular nitrogen. *Chemical Physics*, 398:90–95, 2012.

[76] G. Chaban, R. Jaffe, D. Schwenke, and W. Huo. Dissociation cross sections and rate coefficients for nitrogen from accurate theoretical calculations. *AIAA Paper 2008-1209*, 2008. Paper no. 1209.

[77] D. W. Schwenke. Dissociation cross sections and rates for nitrogen. Technical Report RTO-EN-AVT-162, NASA Ames Research Center, 2009.

[78] R. Jaffe, D. Schwenke, G. Chaban, and W. Huo. Vibrational and rotational excitation and relaxation of nitrogen from accurate theoretical calculations. *AIAA Paper 2008-1208*, 2008.

[79] R. Jaffe, D. Schwenke, and G. Chaban. Theoretical analysis of n_2 collisional dissociation and rotation-vibration energy transfer. *AIAA paper 2009-1569*, 2009.

[80] R. Jaffe, D. Schwenke, and G. Chaban. Vibration-rotation excitation and dissociation in $n_2 - n_2$ collisions from accurate theoretical calculations. *AIAA Paper 2010-4517*, 2010.

[81] L. Landau and E. Teller. Zur theorie der schalldispersion. *Phys. Z. Sowjetunion*, 10(1): 34–43, 1936.

[82] E. Nikitin and J. Troe. 70 years of landau–teller theory for collisional energy transfer. semiclassical three-dimensional generalizations of the classical collinear model. *Physical Chemistry Chemical Physics*, 10(11):1483–1501, 2008.

[83] V. Blackman. Vibrational relaxation in oxygen and nitrogen. *Journal of Fluid Mechanics*, 1(1):61–85, 1956.

[84] G. Candler and J. Perkins. Effects of vibrational nonequilibrium on axisymmetric hypersonic nozzle design. *AIAA Paper 1991-0297*, 1991.

[85] A. G. Neville, I. Nompelis, P. K. Subbareddy, and G. V. Candler. Effect of thermal nonequilibrium on decaying isotropic turbulence. *AIAA paper 2014-3204*, 2014.

[86] K. Fujii and H. G. Hornung. A procedure to estimate the absorption rate of sound propagating through high temperature gas. Technical Report GALCIT TR FM 2001-004, California Institute of Technology Langley, 2001.

[87] R. M. Wagnild. *High Enthalpy Effects on Two Boundary Layer Disturbances in Supersonic and Hypersonic Flow*. PhD thesis, University of Minnesota, Minneapolis, MN, 5 2012.

[88] A. G. Neville, I. Nompelis, P. K. Subbareddy, and G. V. Candler. Thermal non-equilibrium effects in turbulent compressible shear flows. *AIAA Paper 2015-3218*, 2015.

[89] D. A. Donzis and A. F. Maqui. Statistically steady states of forced isotropic turbulence in thermal equilibrium and non-equilibrium. *Journal of Fluid Mechanics*, 797:181–200, 2016.

[90] M. Nishihara, K. Takashima, N. Jiang, W. Lempert, I. Adamovich, J. Rich, S. Doraiswamy, and G. Candler. Development of a mach 5 nonequilibrium-flow wind tunnel. *AIAA journal*, 50(10):2255–2267, 2012.

[91] M. Nishihara, K. Takashima, N. Jiang, W. Lempert, I. Adamovich, and J. Rich. Development of a mach 5 nonequilibrium wind tunnel. *AIAA Paper 2010-1567*, 2010.

[92] M. Nishihara, K. Takashima, N. Jiang, W. Lempert, I. Adamovich, and J. Rich. Nonequlibrium flow characterizarion in a mach 5 wind tunnel. *AIAA Paper 2010-4515*, 2010.

[93] A. Montello, M. Nishihara, J. Rich, I. Adamovich, and W. Lempert. Nitrogen vibrational population measurements in the plenum of a hypersonic wind tunnel. *AIAA journal*, 50(6): 1367–1376, 2012.

[94] M. Nishihara, I. V. Adamovich, W. R. Lempert, and J. Rich. Effect of accelerated vibrational relaxation on a supersonic shear layer. *AIAA Paper*, 577, 2015.

[95] A. Montello, M. Nishihara, J. W. Rich, I. Adamovich, and W. Lempert. Picosecond used-cars for simultaneous rotational/translational and vibrational temperature measurement of nitrogen in a nonequilibrium mach 5 flow. *AIAA Paper 2012-0239*, 2012.

[96] E. D. Lozanskii and O. B. Firsov. *Theory of Sparks*. Atomizdat, 1975.

[97] J. P. Rajzer. *Gas discharge physics*. Springer, 1991.

[98] J. R. Roth. *Industrial plasma engineering*, volume 1: Principles. Inst. of Physics Publ., 1995.

[99] A. von Engel. *Ionized Gases*. Clarendon Press, 2nd edition, 1965.

[100] P. W. Atkins and J. D. Paula. *Physical chemistry for the life sciences*. Oxford University Press, 2011.

[101] S. T. Surzhikov. Numerical simulation of two-dimensional structure of glow discharge in view of the heating of neutral gas. *High temperature*, 43(6):825–842, 2005.

[102] A. Starikovskiy and N. Aleksandrov. Plasma-assisted ignition and combustion. *Progress in Energy and Combustion Science*, 39(1):61–110, 2013.

[103] A. S. Petrusev, S. T. Surzhikov, and J. S. Shang. A two-dimensional model of glow discharge in view of vibrational excitation of molecular nitrogen. *High temperature*, 44(6):804–813, 2006.

[104] G. Herzberg. *Molecular spectra and molecular structure: I: Spectra of diatomic molecules*, volume 1. Van Nostrand, 1950.

[105] D. Storozhev and S. Surzhikov. Numerical simulation of the two-dimensional structure of glow discharge in molecular nitrogen in light of vibrational kinetics. *High Temperature*, 53 (3):307–318, 2015.

[106] S. T. Surzhikov and J. Shang. Viscous interaction on a flat plate with a surface discharge in magnetic field. *High Temperature*, 43(1):19–30, 2005.

[107] J. Shang and S. T. Surzhikov. Magnetoaerodynamic actuator for hypersonic flow control. *AIAA journal*, 43(8):1633–1652, 2005.

[108] I. Adamovich, S. Baalrud, A. Bogaerts, P. Bruggeman, M. Cappelli, V. Colombo, U. Czarnetzki, U. Ebert, J. Eden, P. Favia, et al. The 2017 plasma roadmap: Low temperature plasma science and technology. *Journal of Physics D: Applied Physics*, 50(32):323001, 2017.

[109] V. Semenov, V. Bondarenko, V. Gildenburg, V. Gubchenko, and A. Smirnov. Weakly ionized plasmas in aerospace applications. *Plasma physics and controlled fusion*, 44(12B):B293, 2002.

[110] J. Shang, R. Kimmel, J. Hayes, C. Tyler, and J. Menart. Hypersonic experimental facility for magnetoaerodynamic interactions. *Journal of Spacecraft and Rockets*, 42(5):780–789, 2005.

[111] J. Menart, J. Shang, S. Henderson, A. Kurpik, R. Kimmel, and J. Hayes. Survey of plasmas generated in a mach 5 wind tunnel. *AIAA Paper 2003-1194*, 2003.

[112] J. Menart, J. Shang, R. Kimmel, and J. Hayes. Effects of magnetic fields on plasmas generated in a mach 5 wind tunnel. *AIAA Paper 2003-4165*, 2003.

[113] J. Estevadeordal, S. Gogineni, R. Kimmel, and J. Hayes. Schlieren imaging in hypersonic plasmas. In *42nd AIAA Aerospace Sciences Meeting and Exhibit*, 2004. Paper no. 1139.

[114] J. Shang and S. Surzhikov. Magneto-fluid-dynamics interaction for hypersonic flow control. *AIAA Paper 2004-0508*, 2004.

[115] W. Hayes and R. Probstein. *Hypersonic flow theory*. Academic Press, 1959.

[116] J. Menart, S. Henderson, J. Shang, R. Kimmel, J. Hayes, and C. Atzbach. Study of surface and volumetric heating effects in a mach 5 flow. *AIAA Paper 2004-2262*, 2004.

[117] R. Kimmel, J. Hayes, J. Menart, and J. Shang. Effect of surface plasma discharges on boundary layers at mach 5. In *42nd AIAA Aerospace Sciences Meeting and Exhibit*, 2004. Paper no. 509.

[118] J. Menart, J. Shang, C. Atzbach, S. Magoteaux, M. Slagel, and B. Bilheimer. Total drag and lift measurements in a mach 5 flow affected by a plasma discharge and a magnetic field. *AIAA Paper 2005-0947*, 2005.

[119] J. Shang, R. Kimmel, J. Menart, and J. Hayes. Plasma actuator for hypersonic flow control. *AIAA Paper 2005-0652*, 2005.

[120] R. L. Kimmel, J. R. Hayes, J. A. Menart, and J. Shang. Effect of magnetic fields on surface plasma discharges at mach 5. *Journal of spacecraft and rockets*, 43(6):1340–1346, 2006.

[121] J. Menart, S. Stanfield, J. Shang, R. Kimmel, and J. Hayes. Study of plasma electrode arrangements for optimum lift in a mach 5 flow. *AIAA Paper 2006-1172*, 2006.

[122] S. Stanfield, J. Menart, J. Shang, R. Kimmel, and J. Hayes. Application of a spectroscopic measuring technique to plasma discharge in hypersonic flow. In *44th AIAA Aerospace Sciences Meeting and Exhibit*, 2006. Paper no. 559.

[123] W. Bennett, J. Menart, M. McFarland, and K. Campbell. Heating and force study of the ability of plasma discharges to modify air flows. *AIAA paper 2008-1097*, 2008.

[124] J. Shang, G. Huang, H. Yan, S. Surzhikov, and D. Gaitonde. Hypersonic flow control utilizing electromagnetic-aerodynamic interaction. *AIAA Paper 2008-2606*, 2008.

[125] J. S. Shang, R. L. Kimmel, J. Menart, and S. T. Surzhikov. Hypersonic flow control using surface plasma actuator. *Journal of Propulsion and Power*, 24(5):923–934, 2008.

[126] J. Shang, S. Surzhikov, R. Kimmel, D. Gaitonde, J. Menart, and J. Hayes. Mechanisms of plasma actuators for hypersonic flow control. *Progress in Aerospace Sciences*, 41(8): 642–668, 2005.

[127] S. T. Surzhikov and J. S. Shang. Two-component plasma model for two-dimensional glow discharge in magnetic field. *Journal of Computational Physics*, 199(2):437–464, 2004.

[128] S. Surzhikov and J. Shang. The hypersonic quasineutral gas discharge plasma in a magnetic field. In *Proceedings third MIT Conference on Computational Fluid and Solid Mechanics*, pages 1004–1005, 2005.

[129] J. Shang, R. Kimmel, J. Menart, and J. Hayes. Plasma actuator for hypersonic flow control. *AIAA Paper 2005-0562*, 2005.

[130] M. Morkovin and E. Reshotko. Dialogue on progress and issues in stability and transition research. In *Laminar-Turbulent Transition*, pages 3–29. Springer, 1990.

[131] W. S. Saric, H. L. Reed, and E. J. Kerschen. Boundary-layer receptivity to freestream distrubances. *Annual Review of Fluid Mechanics*, 34(1):291–319, 2002.

[132] W. S. Saric. Görtler vortices. *Annual Review of Fluid Mechanics*, 26(1):379–409, 1994.

[133] L. M. Mack. Boundary-layer linear stability theory. *AGARD*, Rep. No. 709, 1984.

[134] G. B. Schubauer and H. K. Skramstad. Laminar boundary-layer oscillations and stability of laminar flow. *Journal of the Aeronautical Sciences*, 14(2):69–78, 1947.

[135] A. Smith and N. Gamberoni. Transition, pressure gradient and stability theory. *Report ES-26388, Douglas Aircraft Company, Long Beach, CA*, 1956.

[136] J. Van Ingen. A suggested semi-empirical method for the calculation of the boundary layer transition region. *Technische Hogeschool Delft, Vliegtuigbouwkunde, Rapport VTH-74*, 1956.

[137] J. Kendall. Supersonic boundary layer stability experiments. In *Boundary Layer Transition Study Group Meeting*, volume 2, pages 10–1. WD McCauley. Aerospace Corporation, Air Force Report No. BSD-TR-67–213, 1967.

[138] J. M. Kendall. Wind tunnel experiments relating to supersonic and hypersonic boundary-layer transition. *Aiaa Journal*, 13(3):290–299, 1975.

[139] J. Laufer. Aerodynamic noise in supersonic wind tunnels. *Journal of the Aerospace Sciences*, 28(9):685–692, 1961.

[140] M. V. Morkovin. On supersonic wind tunnels with low free-stream disturbances. *Journal of Applied Mechanics*, 26(3):319–324, 1959.

[141] L. M. Mack. Linear stability theory and the problem of supersonic boundary- layer transition. *AIAA Journal*, 13(3):278–289, 1975.

[142] L. M. Mack. Stability of axisymmetric boundary layers on sharp cones at hypersonic mach numbers. *AIAA Paper 1987-1413*, 1987.

[143] S. P. Schneider. Effects of high-speed tunnel noise on laminar-turbulent transition. *Journal Spacecraft and Rockets*, 38(3):323–333, 2001.

[144] S. P. Schneider. Development of hypersonic quiet tunnels. *Journal of Spacecraft and Rockets*, 45(4):641–664, 2008.

[145] J. T. Lachowicz. *Hypersonic boundary layer stability experiments in a quiet wind tunnel with bluntness effects*. North Carolina State University, 1995.

[146] J. T. Lachowicz, N. Chokani, and S. P. Wilkinson. Boundary-layer stability measurements in a hypersonic quiet tunnel. *AIAA journal*, 34(12):2496–2500, 1996.

[147] G. P. Doggett. *Hypersonic boundary layer stability on a flared-cone model at angle of attack*. North Carolina State University, 1996.

[148] J. Hofferth, R. Bowersox, and W. Saric. The Mach 6 quiet tunnel at Texas A&M: quiet flow performance. *AIAA Paper 2010-4794*, 2010.

[149] J. Hofferth and W. Saric. Boundary-layer transition on a flared cone in the Texas A&M Mach 6 quiet tunnel. *AIAA paper 2012-0421*, 2012.

[150] S. A. Craig, R. A. Humble, J. W. Hofferth, and W. S. Saric. Nonlinear behaviour of the Mack mode in a hypersonic boundary layer. *Journal of Fluid Mechanics*, 872:74–99, 2019.

[151] S. A. Craig and W. S. Saric. Crossflow instability in a hypersonic boundary layer. *Journal of Fluid Mechanics*, 808:224–244, 2016.

[152] M. Ivanov, G. Markelov, A. Kudryavtsev, and S. Gimelshein. Transition between regular and mach reflections of shock waves in steady flows. *AIAA Paper 1997-2511*, 1997.

[153] D. Azevedo and C. S. Liu. Engineering approach to the prediction of shock patterns in bounded high-speed flows. *AIAA Journal*, 31(1), 1993.

[154] G. Ben-Dor, T. Elperin, H. Li, E. Vasiliev, A. Chpoun, and D. Zeitoun. Dependence of steady mach reflections on the reflecting-wedge trailing-edge angle. *AIAA Journal*, 35(11), 1997.

[155] M. Sharma, J. Austin, and N. Glumac. Influence of thermochemistry on mach reflection in hypresonic flow. *AIAA Paper 2008-5066*, 2008.

[156] Y. Burtschell, D. Zeitoun, and G. Ben-Dor. Steady shock wave reflections in thermochemical nonequilibrium flows. *Shock Waves*, August 2000.

[157] J. Li and S. Yang. Thermochemical non-equilibrium effects of shock reflection hysteresis in steady supersonic flows. *AIAA Paper 2017-2195*, 2017.

[158] F. Grasso and R. Paoli. Simulations of shock-wave reflections in nonequilibrium flows. *Journal of Spacecraft and Rockets*, 37(2):224–234, 2000.

[159] A. Trotsyuk, A. Kudryavtsev, and M. Ivanov. Computational study of mach reflection in chemically reacting steady flows. *AIAA Paper 2004-0271*, 2004.

[160] M. McGilvray, J. Austin, M. Sharma, P. Jacobs, and R. Morgan. Diagnostic modelling of an expansion tube operating condition for a hypersonic free shear layer experiment. In *Proceedings of 16th Australasian Fluid Mechanics Conference*, 2007.

[161] H. S. Ribner. Spectra of noise and amplified turbulence emanating from shock-turbulence interaction. *AIAA Journal*, 25(3):436–442, 1987.

[162] F. K. Moore. Unsteady oblique interaction of a shock wave with a plane disturbance. Technical Report 1165, NACA, 1953.

[163] S. K. Lele. Shock-jump relations in a turbulent flow. *Physics of Fluids A: Fluid Dynamics*, 4(12):2900–2905, 1992.

[164] L. Jacquin, C. Cambon, and E. Blin. Turbulence amplification by a shock wave and rapid distortion theory. *Physics of Fluids A: Fluid Dynamics*, 5(10):2539–2550, 1993.

[165] J. Ryu and D. Livescu. Turbulence structure behind the shock in canonical shock–vortical turbulence interaction. *Journal of Fluid Mechanics*, 756, 2014.

[166] D. Rotman. Shock wave effects on a turbulent flow. *Physics of Fluids A: Fluid Dynamics*, 3(7):1792–1806, 1991.

[167] M. P. Lee, B. K. McMillin, and R. K. Hanson. Temperature measurements in gases by use of planar laser-induced fluorescence imaging of NO. *Applied Optics*, 32(27):5379, 1993. ISSN 0003-6935. doi: 10.1364/ao.32.005379.

[168] C. H. Chen and D. A. Donzis. Shock-turbulence interactions at high turbulence intensities. *Journal of Fluid Mechanics*, 870:813–847, 2019. ISSN 14697645. doi: 10.1017/jfm.2019.248.

[169] R. Hannappel, T. Hauser, and R. Friedrich. A comparison of ENO and TVD schemes for the computation of shock-turbulence interaction. *Journal of Computational Physics*, 121 (1):176–184, 1995.

[170] K. Mahesh, S. K. Lele, and P. Moin. The influence of entropy fluctuations on the interaction of turbulence with a shock wave. *Journal of Fluid Mechanics*, 334:353–379, 1997.

[171] S. Jamme, J.-B. Cazalbou, F. Torres, and P. Chassaing. Direct numerical simulation of the interaction between a shock wave and various types of isotropic turbulence. *Flow, Turbulence and Combustion*, 68(3):227–268, 2002.

[172] A. Honkan and J. Andreopoulos. Experiments in a shock wave/homogeneous turbulence interaction. *AIAA Paper 1990-1647*, 1990.

[173] A. Honkan and J. Andreopoulos. Rapid compression of grid-generated turbulence by a moving shock wave. *Physics of Fluids A: Fluid Dynamics*, 4(11):2562–2572, 1992.

[174] A. Honkan, C. B. Watkins, and J. Andreopoulos. Experimental study of interactions of shock wave with free-stream turbulence. *Journal of Fluids Engineering*, 116(4):763–769, 1994.

[175] G. Briassulis and J. Andreopoulos. High resolution measurements of isotropic turbulence interacting with shock waves. *AIAA Paper 1996-0042*, 1996.

[176] S. Xanthos, G. Briassulis, and Y. Andreopoulos. Interaction of decaying freestream turbulence with a moving shock wave: pressure field. *Journal of Propulsion and Power*, 18(6): 1289–1297, 2002.

[177] J. H. Agui, G. Briassulis, and Y. Andreopoulos. Studies of interactions of a propagating shock wave with decaying grid turbulence: velocity and vorticity fields. *Journal of Fluid Mechanics*, 524:143–195, 2005.

[178] J. W. Trolier and R. E. Duffy. Turbulence measurements in shock-induced flows. *AIAA Journal*, 23(8):1172–1178, 1985.

[179] J.-F. Haas and B. Sturtevant. Interaction of weak shock waves with cylindrical and spherical gas inhomogeneities. *Journal of Fluid Mechanics*, 181:41–76, 1987.

[180] L. Hesselink and B. Sturtevant. Propagation of weak shocks through a random medium. *Journal of Fluid Mechanics*, 196:513–553, 1988.

[181] J. Keller and W. Merzkirch. Interaction of a normal shock wave with a compressible turbulent flow. *Mineralium Deposita*, 29(1):241–248, 1994.

[182] L. Jacquin, E. Blin, and P. Geffroy. An experiment on free turbulence/shock wave interaction. In *Turbulent Shear Flows 8*, pages 229–248. Springer, 1993.

[183] S. Barre, D. Alem, and J. P. Bonnet. Experimental study of a normal shock/homogeneous turbulence interaction. *AIAA Journal*, 34(5):968–974, 1996. ISSN 00011452. doi: 10.2514/3.13175.

[184] B. F. Blackwell. *The turbulent boundary layer on a porous plate: an experimental study of the heat transfer behavior with adverse pressure gradients*. PhD thesis, Stanford University, Stanford, CA, 1973.

[185] B. E. Launder. On the computation of convective heat transfer in complex turbulent flows. *Journal of Heat Transfer*, 110(4b):1112–1128, 11 1988.

[186] B. J. Daly and F. H. Harlow. Transport equations in turbulence. *The physics of fluids*, 13 (11):2634–2649, 1970.

[187] W. W. Liou and T. H. Shih. On the basic equations for the second-order modeling of compressible turbulence. Technical Report TM 105277, NASA Lewis Research Center, Cleveland, OH, 1950.

[188] A. Favre. Statistical equations of turbulent gases. *SIAM Problems of Hydrodynamics and Continuum Mechanics*, 1969.

[189] S. Pirozzoli, F. Grasso, and T. Gatski. Direct numerical simulation and analysis of a spatially evolving supersonic turbulent boundary layer at m= 2.25. *Physics of fluids*, 16(3):530–545, 2004.

[190] G. L. Nicholson, J. Huang, L. Duan, M. M. Choudhari, B. Morreale, and R. D. Bowersox. Budgets of reynolds stresses and turbulent heat flux for hypersonic turbulent boundary layers subject to pressure gradients. *AIAA Paper 2022-1059*, 2022.

[191] S. S. Girimaji and S. Balachandar. Analysis and modeling of buoyancy-generated turbulence using numerical data. *International journal of heat and mass transfer*, 41(6-7):915–929, 1998.

[192] B. E. Launder, G. J. Reece, and W. Rodi. Progress in the development of a reynolds-stress turbulence closure. *Journal of fluid mechanics*, 68(3):537–566, 1975.

[193] B. E. Launder. An introduction to single-point closure methodology. In *An Introduction to the Modelling of Turbulence, Lecture Series 1987-06*, Rhode-Saint-Genese, Belgium, 1987. Von Karman Inst. for Fluid Dynamics. Also available as UMIST Mech. Eng. Dept. Report TFD/87/7.

[194] N. R. Tichenor, R. A. Humble, and R. D. W. Bowersox. Response of a hypersonic turbulent boundary layer to favourable pressure gradients. *Journal of Fluid Mechanics*, 722:187–213, 2013. doi: 10.1017/jfm.2013.89.

[195] I. T. Neel, A. Leidy, R. D. Bowersox, and N. R. Tichenor. Hypersonic boundary layer with streamline curvature-driven adverse pressure gradient. *AIAA Paper 2016-4248*, 2016.

[196] G. Nicholson, J. Huang, L. Duan, M. M. Choudhari, and R. D. Bowersox. Simulation and modeling of hypersonic turbulent boundary layers subject to favorable pressure gradients due to streamline curvature. *AIAA 2021-1672*, 2021.

[197] G. Nicholson, J. Huang, L. Duan, and M. M. Choudhari. Simulation and modeling of hypersonic turbulent boundary layers subject to adverse pressure gradients due to streamline curvature. *AIAA Paper 2021-2891*, 2021.

[198] J. Brooks, A. Gupta, M. Smith, and E. Marineau. Particle image velocimetry measurements of mach 3 turbulent boundary layers at low reynolds numbers. *Experiments in Fluids*, 59 (5):1–15, 2018.

[199] R. A. Burns, H. Koo, V. Raman, and N. T. Clemens. Improved large-eddy simulation validation methodology: application to supersonic inlet/isolator flow. *AIAA Journal*, 53(4): 817–831, 2015.

[200] O. J. H. Williams, D. Sahoo, M. L. Baumgartner, and A. J. Smits. Experiments on the structure and scaling of hypersonic turbulent boundary layers. *Journal of Fluid Mechanics*, 834:237–270, 2018.

[201] M. Semper, N. Tichenor, R. Bowersox, R. Srinvasan, and S. North. On the design and calibration of an actively controlled expansion hypersonic wind tunnel. *AIAA Paper 2009-0799*, 2009.

[202] C. Mai. *Near-Region Modification of Total Pressure Fluctuations by a Normal Shock Wave in a Low-Density Hypersonic Wind Tunnel*. PhD thesis, Texas A&M University, College Station, TX, 5 2014.

[203] N. Tichenor. *Characterization of the Influence of a Favorable Pressure Gradient on the Basic Structure of a Mach 5.0 High Reynolds Number Supersonic Turbulent Boundary Layer*. PhD thesis, Texas A&M University, College Station, TX, 8 2010.

[204] A. H. Shapiro. *The dynamics and thermodynamics of compressible fluid flow*, volume 1 and 2. John Wiley and Sons, 1953.

[205] J. E. John and T. G. Keith. *Gas Dynamics*. Pearson Prentice Hall, 3 edition, 2006.

[206] M. Semper. *Examining a Hypersonic Turbulent Boundary Layer at Low Reynolds Number*. PhD thesis, Texas A&M University, College Station, TX, 8 2013.

[207] M. Semper, B. Pruski, and R. Bowersox. Freestream turbulence measurements in a continuously variable hypersonic wind tunnel. *AIAA Paper 2012-0732*, 2012.

[208] M. H. Bertram. Investigation of the pressure-ratio requirements of the langley 11-inch hypersonic tunnel with a variable-geometry diffuser. Technical report, National Advisory Committe for Aeronautics RM L50I13, Langley Air Force Base, VA, 1950.

[209] P. P. Wegener and R. K. Lobb. An experimental study of a hypersonic wind-tunnel diffuser. *Journal of the Aeronautical Sciences*, 20(2):105–110, 1953.

[210] P. M. Danehy, S. Obyrne, A. Frank, P. Houwing, J. S. Fox, and D. R. Smith. Flow-tagging velocimetry for hypersonic flows using fluorescence of nitric oxide. *AIAA Journal*, 41(2): 263–271, 2003.

[211] R. Sanchez-Gonzalez. *Advanced Laser Diagnostics Development for the Characterization of Gaseous High Speed Flows*. PhD thesis, Texas A&M University, College Station, TX, 5 2012.

[212] Z. D. Buen. *Implementation of NO LIF Diagnostics to Characterize the Role of Thermal Non-Equilibrium within a Hypersonic Turbulent Boundary Layer*. PhD thesis, Texas A&M University, College Station, TX, 12 2021.

[213] A. Leidy. *An Experimental Characterization of 3-D Transitional Shock Wave Boundary Layer Interactions at Mach 6*. PhD thesis, Texas A&M University, College Station, TX, 5 2019.

[214] I. Neel. *Influence of Environmental Distrubances on Hypersonic Crossflow Instability on the HiFIRE-5 Elliptic Cone*. PhD thesis, Texas A&M University, College Station, TX, 5 2019.

[215] W. Sutherland. The viscosity of gases and molecular force. *Philosophy Magazine*, 5:507–531, 1893.

[216] J. Hilsenrath, C. W. Beckett, W. S. Benedict, L. Fane, H. J. Hoge, J. S. Masi, R. L. Nuttell, Y. S. Touloukian, and H. W. Woolley. *Tables of Thermodynamic and Transport Troperties: of Air, Argon, Carbon Dioxide, Carbon Monoxide, Hydrogen, Nitrogen, Oxygen, and Steam*. Pergamon Press, 1960.

[217] A. Houpt, B. Hedlund, S. Leonov, T. Ombrello, and C. Carter. Quasi-dc electrical discharge characterization in a supersonic flow. *Experiments in Fluids*, 58(4), 2017.

[218] C. B. Cohen and E. Reshotko. Similar solutions for the compressible laminar boundary layer with heat transfer and pressure gradient. Technical Report NACA-TR-1293, NACA, 1955.

[219] R. E. Hanson, H. P. Buckley, and P. Lavoie. Aerodynamic optimization of the flat-plate leading edge for experimental studies of laminar and transitional boundary layers. *Experiments in Fluids*, 53(4):863–871, 2012. doi: 10.1007/s00348-012-1324-2.

[220] A. Dwivedi, C. J. Broslawski, G. V. Candler, and R. D. Bowersox. Three-dimensionality in shock/boundary layer interactions: a numerical and experimental investigation. *AIAA Paper 2020-3011*, 2020.

[221] S. A. Berry, A. H. Auslender, A. D. Dilley, and J. F. Calleja. Hypersonic boundary-layer trip development for hyper-x. *Journal of Spacecraft and Rockets*, 38(6):853–864, 2001.

[222] E. Reshotko and A. Tumin. Role of transient growth in roughness-induced transition. *AIAA Journal*, 42(4):766–770, 2004.

[223] E. R. van Driest. *Investigation of Laminar Boundary Layer in Compressible Fluids Using the Crocco Method*. National Advisory Committee for Aeronautics, 1952.

[224] G. Francis. *Ionization Phenomena in Gases*. Butterworth, 1960.

[225] J. W. Hofferth. *Boundary-Layer Stability and Transition on a Flared Cone in a Mach 6 Quiet Wind Tunnel*. PhD thesis, Texas A&M University, College Station, TX, 8 2013.

[226] A. E. Blanchard and G. V. Selby. An experimental investigation of wall cooling effects on hypersonic boundary-layer stability in a quiet wind tunnel. Technical report, NASA CR 198287, 1996.

[227] S. P. Wilkinson. A review of hypersonic boundary layer stability experiments in a quiet Mach 6 wind tunnel. *AIAA 1997-1819*, 1997.

[228] M. Semper, B. Pruski, and R. Bowersox. Freestream turbulence measurements in a continuously variable hypersonic wind tunnel. In *50th AIAA Aerospace Sciences Meeting including the New Horizons Forum and Aerospace Exposition*, page 732, 2012.

[229] H. G. Hornung and J. R. Taylor. Transition from regular to Mach reflection of shock waves Part 1. The effect of viscosity in the pseudosteady case. *Journal of Fluid Mechanics*, 123: 143–153, 1982.

[230] C. A. Mouton and H. G. Hornung. Mach stem height and growth rate predictions. *AIAA Journal*, 45(8):1977–1987, 2007.

[231] A. Chpoun and E. Leclerc. Experimental investigation of the influence of downstream flow conditions on Mach stem height. *Shock Waves*, 9(4):269–271, 1999.

[232] C. L. Mai and R. D. Bowersox. Effect of a normal shock wave on freestream total pressure fluctuations in a low-density mach 6 flow. *AIAA Paper 2014-2641*, 2014.

[233] E. L. Ressler and D. Bloxsom. *Very high Mach number flows by unsteady flow principles*. Cornell University Graduate School of Aeronautical Engineering limited distribution monograph, 1952.

[234] M. Nishida. Shock Tubes. In *Handbook of Shock Waves*, chapter 4, pages 553–585. Academic Press, Waltham, MA, 2001.

[235] P. H. Oosthuizen and W. E. Carscallen. *Introduction to Compressible Fluid Flow*. CRC Press, Boca Raton, 2014.

[236] R. L. Trimpi. A Preliminary Theoretical Study of the Expansion Tube , a New Device for Producing High-Enthalpy Short-Duration Hypersonic Gas Flows. Technical Report NASA TR R-133, NASA Langley Research Center, 1962.

[237] L. Trimpi and L. B. Callis. A Perfect-Gas Analysis of the Expansion Tunnel, a Modification To the Expansion Tube. Technical Report NASA TR R-223, NASA Langley Research Center, 1965.

[238] J. M. Lawson and J. M. Austin. Design of conventional and detonation-driven hypervelocity expansion tubes. *AIAA Paper 2018-3566*, 2018.

[239] S. Gu and H. Olivier. Capabilities and limitations of existing hypersonic facilities. *Progress in Aerospace Sciences*, 113(February):100607, 2020.

[240] C. G. Miller. Operational experience in the langley expansion tube with various test gases. *AIAA Journal*, 16(3):195–196, 1978.

[241] A. Paull and R. J. Stalker. Test flow disturbances in an expansion tube. *Journal of Fluid Mechanics*, 245:493–521, 1992.

[242] E. K. Marcotte. *The Design and Development of a High Enthalpy, Hypervelocity Expansion Facility.* MS Thesis, Texas A&M University, College Station, TX, 2016.

[243] A. Ben-Yakar and R. K. Hanson. Characterization of Expansion Tube Flows for Hypervelocity Combustion Studies. *Journal of Propulsion and Power*, 18(4):943–952, jul 2002. ISSN 0748-4658. doi: 10.2514/2.6021.

[244] M. Roberts. *Comparison Of An Axisymmetric and a Planar Shock Tunnel Nozzle*. MS Thesis, Texas A&M University, College Station, TX, 2021.

[245] A. Dufrene, M. MacLean, R. Parker, T. Wadhams, and M. Holden. Characterization of the New LENS Expansion Tunnel Facility. *AIAA Paper 2010-1564*, 2010.

[246] T. Furukawa, T. Aochi, and A. Sasoh. Expansion Tube Operation with Thin Secondary Diaphragm. *AIAA Journal*, 45(1):214–217, 2007.

[247] A. Dufrene, M. Sharma, and J. M. Austin. Design and Characterization of a Hypervelocity Expansion Tube Facility. *Journal of Propulsion and Power*, 23(6):1185–1193, 2007.

[248] G. S. Settles. *Schlieren and Shadowgraph Techniques*. Springer Berlin Heidelberg, Berlin, Heidelberg, 2001.

[249] R. Sánchez-González, R. Srinivasan, R. D. W. Bowersox, and S. W. North. Simultaneous velocity and temperature measurements in gaseous flow fields using the VENOM technique. *Optics Letters*, 36(2):196, jan 2011.

[250] E. C. Anderson and C. H. Lewis. Laminar or turbulent boundary-layer flows of perfect gases or reacting gas mixtures in chemical equilibrium. Technical Report NASA CR-1893., NASA, 1971.

[251] F. Blottner. Nonequilibrium laminar boundary-layer flow of ionized air. *AIAA Journal*, 2 (11), Nov 1964.

[252] J. C. Tannehill, D. A. Anderson, and R. H. Pletcher. *Computational Fluid Mechanics and Heat Transfer*. Taylor and Francis, 2 edition, 1997.

[253] M. R. Malik. Numerical methods for hypersonic boundary layer stability. *Journal of Computational Physics*, 86(2):376–413, 1990.

[254] C. R. Illingworth. Some solutions of the equations of flow of a viscous compressible fluid. *Mathematical Proceedings of the Cambridge Philosophical Society*, 46(3):469–478, 1950.

[255] G. Palmer. *Technical Java: developing scientific and engineering applications*. Prentice Hall, 2003.

[256] C. Roy and F. Blottner. Review and assessment of turbulence models for hypersonic flows: 2d/asymmetric cases. *AIAA Paper 2006-0713*, 2006.

[257] W. H. Dorrance. *Viscous Hypersonic Flow*. McGraw-Hill, 1962.

[258] A. Gilat and V. Subramaniam. *Numerical Methods for Engineers and Scientists: an Introduction with Applications using Matlab*. John Wiley & Sons, 2014.

[259] W. Chan and J. Steger. A generalized scheme for three-dimensional hyperbolic grid generation. *AIAA Paper 1991-1588*, 1991.

[260] T. S. Dean, R. D. Bowersox, S. Farahan, and M. Gragston. Index of Refraction Fluctuation Spectra in Aerothermochemical Non-equilibrium Shock Layers. *AIAA Paper 2023-0270*, 2023.

[261] R. MacCormack. The carbuncle cfd problem. *AIAA Paper*, January 2011. doi: /10.2514/6.2011-381.

[262] B. K. Crawford, G. T. Duncan, D. E. West, and W. S. Saric. Large-span, non-contact surface profilometry for laminar-flow diagnostics. *AIAA Paper 2014-2940*, 2014.

[263] B. Muralikrishnan and J. Raja. *Computational Surface and Roundness Metrology*. Springer, 2009.

[264] G. S. Settles. *Schlieren and shadowgraph techniques: visualizing phenomena in transparent media*. Springer, 2013.

[265] B. K. Crawford, G. T. Duncan, D. E. West, and W. S. Saric. Laminar-turbulent boundary layer transition imaging using ir thermography. *Optics and Photonics Journal*, 03(03): 233–239, 2013.

[266] M. Zaccara, S. Cerasuolo, G. Cardone, J. B. Edelman, and S. P. Schneider. Infrared thermography data reduction technique for heat transfer measurements in the boeing/afosr mach-6 quiet tunnel. *AIAA Paper 2019-0894*, 2019.

[267] C. L. Running, M. J. Thompson, T. J. Juliano, and H. Sakaue. Boundary-layer separation detection for a cone at high angle of attack in mach 4.5 flow with pressure-sensitive paint. *AIAA Paper 2017-3120*, 2017.

[268] A. Gülhan and S. Braun. An experimental study on the efficiency of transpiration cooling in laminar and turbulent hypersonic flows. *Experiments in Fluids*, 50(3):509–525, 2010.

[269] C. Hirschen and A. Gülhan. Infrared thermography and pitot pressure measurements of a scramjet nozzle flowfield. *Journal of Propulsion and Power*, 25(5):1108–1120, 2009. doi: 10.2514/1.41787.

[270] S. Cerasuolo. *Heat Flux Measurements by Infrared Thermography in the Boeing/AFOSR Mach 6 Quiet Tunnel*. PhD thesis, University of Naples Federico II, Naples, NA, 6 2016.

[271] C. F. Boyd and A. Howell. Numerical investigation of one-dimensional heat flux calculations. Technical Report NSWCDDI/TR-94/114, Naval Surface Warfare Center Dahlgren Division, Silver Springs, MD, 1994.

[272] T. J. Juliano, L. Paquin, and M. P. Borg. Measurement of hifire-5 boundary-layer transition in a mach-6 quiet tunnel with infrared thermography. *AIAA Paper 2016-0595*, 2016.

[273] M. P. Borg and R. L. Kimmel. Simultaneous infrared and pressure measurements of cross-flow instability modes for hifire-5. *AIAA Paper 2016-0354*, 2016.

[274] I. T. Neel, A. Leidy, and R. D. Bowersox. Preliminary study of the effect of environmental disturbances on hypersonic crossflow instability on the hifire-5 elliptic cone. *AIAA Paper 2017-0767*, 2017.

[275] S. J. Beresh, J. F. Henfling, R. W. Spillers, and B. O. Pruett. Fluctuating wall pressures measured beneath a supersonic turbulent boundary layer. *Physics of Fluids*, 23(7):075110, 2011.

[276] A. Chou, A. Leidy, R. A. King, B. F. Bathel, and G. Herring. Measurements of freestream fluctuations in the nasa langley 20-inch mach 6 tunnel. *AIAA Paper 2018-3073*, 2018.

[277] A. M. Hurst, S. Carter, D. Firth, A. Szary, and J. VanDeWeert. Real-time, advanced electrical filtering for pressure transducer frequency response correction. In *ASME Turbo Expo 2015: Turbine Technical Conference and Exposition*. American Society of Mechanical Engineers Digital Collection, 2015.

[278] J. M. Wirth. *Measurement of Heat Flux due to Fin-Induced Shock-Boundary Layer Interaction*. MS Thesis, Texas A&M University, College Station, TX, 2021.

[279] R. Volluz. Handbook of supersonic aerodynamics. section 20: Wind tunnel instrumentation and operation. Technical Report 1488, Bureau of Naval Weapons, January 1961.

[280] W. I. Grosser. Factor influencing pitot probe centerline displacement in a turbulent supersonic boundary layer. Technical Report Technical Memorandum 107341, NASA Lewis, January 1997.

[281] J. Preston. The determination of turbulent skin friction by means of pitot tubes. *The Aeronautical Journal*, 58(518):109–121, 1954.

[282] T. Wei, R. Schmidt, and P. McMurtry. Comment on the clauser chart method for determining the friction velocity. *Experiments in fluids*, 38(5):695–699, 2005.

[283] D. Neeb, D. Saile, and A. Gülhan. Experiments on a smooth wall hypersonic boundary layer at mach 6. *Experiments in Fluids*, 59(4):1–21, 2018.

[284] D. Coles. The law of the wake in the turbulent boundary layer. *Journal of Fluid Mechanics*, 1(2):191–226, 1956.

[285] E. J. Hopkins and E. R. Keener. Study of surface pitots for measuring turbulent skin friction at supersonic mach numbers. Technical Report TN D-3478, NASA, 1966.

[286] E. R. Keener and E. J. Hopkins. Use of preston tubes for measuring hypersonic turbulent skin friction. *AIAA-1669-0345*, 1969.

[287] D. H. Ferris. Preston tube measurements in turbulent boundary layers and fully developed pipe flow. Technical Report C.P. No. 831, Ministry of Aviation Aeronatucal Research Council Current Papers, 1965.

[288] N. Staff of Aerodynamics Division. On the measurement of local surface friction on a flat plate by means of preston tubes. Technical Report R&M 3185, A.R.C, 5 1958.

[289] S. Bayram and M. Freamat. Vibrational spectra of n2: An advanced undergraduate laboratory in atomic and molecular spectroscopy. *American Journal of Physics*, 80(8):664–669, 2012.

[290] H. Nassar, S. Pellerin, K. Musiol, O. Martinie, N. Pellerin, and J. Cormier. N2+/n2 ratio and temperature measurements based on the first negative n2+ and second positive n2 overlapped molecular emission spectra. *Journal of Physics D: Applied Physics*, 37(14):1904, 2004.

[291] J. M. Williamson and C. A. DeJoseph Jr. Determination of gas temperature in an open-air atmospheric pressure plasma torch from resolved plasma emission. *Journal of applied physics*, 93(4):1893–1898, 2003.

[292] S. A. Stanfield II. *A Spectroscopic Investigation of a Surface-Discharge-Mode, Dielectric Barrier Discharge*. PhD thesis, Wright State University, Dayton, OH, 9 2009.

[293] C. O. Laux. Radiation and nonequilibrium collisional-radiative models. *von Karman Institute Lecture Series*, 7, 2002.

[294] C. Laux. Optical diagnostics and collisional-radiative models. *VKI LS Course on hypersonic entry and cruise vehicles, Palo Alto, California, USA*, 2008.

[295] F. R. Gilmore, R. R. Laher, and P. J. Espy. Franck–condon factors, r-centroids, electronic transition moments, and einstein coefficients for many nitrogen and oxygen band systems. *Journal of Physical and Chemical Reference Data*, 21(5):1005–1107, 1992.

[296] L. S. G. Kovasznay. The hot-wire anemometer in supersonic flow. *Journal of the Aeronautical Sciences*, 17(9):565–572, 1950.

[297] A. J. Smits, A. K. Hawakawa, and M. C. K. Constant-temperature hotwire anemometer practice in supersonic flows – part 1: The normal wire. *Experiments in Fluids*, 1:83–92, 1983.

[298] L. M. Weinstein. Large-field high-brightness focusing schlieren system. *AIAA Journal*, 31 (7):1250–1255, 1993.

[299] J. W. Hofferth, R. A. Humble, D. C. Floryan, and W. S. Saric. High-bandwidth optical measurements of the second-mode instability in a Mach 6 quiet tunnel. *AIAA 2013-0378*, 2013.

[300] L. R. Boedeker. *Analysis and construction of a sharp focussing schlieren system*. PhD thesis, Massachusetts Institute of Technology, 1959.

[301] A. N. Leidy. *An Experimental Characterization of 3-D Transitional Shock Wave Boundary Layer Interactions at Mach 6*. PhD thesis, Texas A&M University, 2019.

[302] G. Smeets and A. George. Application of laser differential interferometers to gas dynamics. *NASA STI/Recon Technical Report N*, 75:14123, 1973.

[303] G. Smeets and A. George. Visualization methods using the differential interferometer. *NASA STI/Recon Technical Report N*, 75:25148, 1974.

[304] G. Smeets and A. George. Instantaneous laser-doppler velocimeter using a fast wavelength tracking Michelson. *Journal Review Scientific Instrum*, 49:1589, 1977.

[305] G. Smeets and A. George. Laser-Differential Interferometer Applications in Gas Dynamics. *DTIC*, 1996.

[306] A. Laderman and A. Demetriades. Detection of boundary-layer transition with a laser beam. *AIAA Journal*, 14(1):102–104, 1976.

[307] M. Azzazy, D. Modarress, and T. Hoeft. High sensitivity boundary layer transition detector. In *High speed photography, videography, and photonics III*, volume 569, pages 64–73. International Society for Optics and Photonics, 1986.

[308] M. Azzazy, D. Modarress, and T. Hoeft. High-sensitivity density fluctuation detector. *Journal of Physics E: Scientific Instruments*, 20(4):428, 1987.

[309] J. O'Hare. A nonperturbing boundary-layer transition detector. In *High speed photography, videography, and photonics III*, volume 569, pages 58–63. International Society for Optics and Photonics, 1986.

[310] G. Smeets. Laser-interferometer mit grossen, fokussierten lichtbündeln für lokale messungen. *Institut Saint-Louis Report ISL*, 11, 1973.

[311] N. J. Parziale. *Slender-body hypervelocity boundary-layer instability*. PhD thesis, California Institute of Technology, 2013.

[312] N. J. Parziale, J. E. Shepherd, and H. G. Hornung. Free-stream density perturbations in a reflected-shock tunnel. *Experiments in fluids*, 55(2):1–, 2014.

[313] N. J. Parziale, J. E. Shepherd, and H. G. Hornung. Observations of hypervelocity boundary-layer instability. *Journal of Fluid Mechanics*, 781:87–112, 2015.

[314] A. Hameed, N. J. Parziale, L. A. Paquin, C. Butler, and S. J. Laurence. Hypersonic slender-cone boundary-layer instability in the UMD HyperTERP Shock Tunnel. *AIAA Paper 2020-0362*, 2020.

[315] M. Gragston, T. J. Price, K. Davenport, J. D. Schmisseur, and Z. Zhang. An m by n FLDI array for single-shot multipoint disturbance measurements in high-speed flows. *AIAA Paper 2021-0599*, 2021.

[316] M. Gragston, F. Siddiqui, and J. D. Schmisseur. Detection of second-mode instabilities on a flared cone in Mach 6 quiet flow with linear array focused laser differential interferometry. *Experiments in Fluids*, 62(4):1–12, 2021.

[317] A. Roshko and H. Liepmann. *Elements of Gas-dynamics*. Wiley, 1957.

[318] M. Gragston, T. Price, K. Davenport, Z. Zhang, and J. D. Schmisseur. Linear array focused-laser differential interferometry for single-shot multi-point flow disturbance measurements. *Optics Letters*, 46(1):154–157, Jan 2021.

[319] F. Siddiqui, W. S. Saric, and R. D. Bowersox. Interaction of second-mode disturbances and 3-d roughness on a cooled flared cone at Mach 6. *AIAA Paper 2021-1092*, 2021.

[320] C. L. N. Mai. *Near-Region Modification of Total Pressure Fluctuations by a Normal Shock Wave in a Low-Density Hypersonic Wind Tunnel*. PhD thesis, Texas A&M University, 2014.

[321] R. Sánchez-González, R. D. W. Bowersox, and S. W. North. Vibrationally excited NO tagging by NO (A 2 Σ+) fluorescence and quenching for simultaneous velocimetry and thermometry in gaseous flows. *Optics Letters*, 39(9):2771–2774, 2014.

[322] V. Parekh, D. Gildfind, S. Lewis, and C. James. X3 expansion tube driver gas spectroscopy and temperature measurements. *Shock Waves*, 28(4):851–862, 2018.

[323] R. J. Emrich and C. W. Curtis. Attenuation in the Shock Tube. *Journal of Applied Physics*, 24(3):360–363, mar 1953.

[324] H. Mizuno, K. Sawada, and A. Sasoh. Numerical study of non-ideal diaphragm rupture in expansion tube. *AIAA Paper 2002-0650*, 2002.

[325] M. Gragston, T. J. Price, K. Davenport, J. D. Schmisseur, and Z. Zhang. An m x n fldi array for single-shot, multipoint disturbance measurements in high-speed flows. *AIAA Paper 2021-0599*, 2021.

[326] K. Davenport, S. Ledbetter, F. Siddiqui, and M. T. Gragston. Development of a Simple Compact Photodiode Array for Use with Linear Array-FLDI. *AIAA Paper 2023-1563*, 2023.

[327] E. K. Benitez, M. P. Borg, J. Luke Hill, M. T. Aultman, L. Duan, C. L. Running, and J. S. Jewell. Quantitative focused laser differential interferometry with hypersonic turbulent boundary layers. *Applied Optics*, 61(31):9203, 2022.

[328] P. Instruments. IsoPlane 160 IsoPlane 320 The Best Spectroscopy Solutions by Any Measure. *Online Brochure*, 2019.

[329] B. A. Cruden. Absolute Radiation Measurements in Earth and Mars Entry Conditions. *Radiation and Gas-Surface Interaction Phenomena in High Speed Re-Entry - STO AVT-218*, pages 1–40, 2014.

[330] J. B. Michael, M. R. Edwards, A. Dogariu, and R. B. Miles. Femtosecond laser electronic excitation tagging for quantitative velocity imaging in air. *Applied Optics*, 50(26):5158, sep 2011.

[331] R. B. Miles, A. Dogariu, J. B. Michael, and M. R. Edwards. Femtosecond Laser Excitation Tagging Anemometry. *Patent US9863975B2*, 2018.

[332] L. E. Dogariu, A. Dogariu, R. B. Miles, M. S. Smith, and E. C. Marineau. Non-Intrusive Hypersonic Freestream and Turbulent Boundary-Layer Velocity Measurements in AEDC Tunnel 9 Using FLEET. *AIAA Journal 2018-1769*, 2018.

[333] A. Dogariu, L. E. Dogariu, M. S. Smith, B. McManamen, J. F. Lafferty, and R. B. Miles. Velocity and Temperature Measurements in Mach 18 Nitrogen Flow at Tunnel 9. In *AIAA Scitech 2021 Forum*, pages 1–11, Reston, Virginia, jan 2021. American Institute of Aeronautics and Astronautics. ISBN 978-1-62410-609-5. doi: 10.2514/6.2021-0020.

[334] L. E. Dogariu, A. Dogariu, R. B. Miles, M. S. Smith, and E. C. Marineau. Femtosecond Laser Electronic Excitation Tagging Velocimetry in a Large-Scale Hypersonic Facility. *AIAA Journal*, 57(11):4725–4737, nov 2019.

[335] V. Gopal, D. Palmquist, L. Maddalena, L. E. Dogariu, and A. Dogariu. FLEET velocimetry measurements in the ONR-UTA arc-jet wind tunnel. *Experiments in Fluids*, 62(10):212, 2021.

[336] M. A. Lieberman and A. J. Lichtenberg. *Principles of plasma discharges and materials processing*. Wiley-Interscience, 2 edition, 2005.

[337] H. Itoh and M. Mizoguchi. Potential of glow-discharge flow measurement in hypersonic low-density flows. *AIAA Journal*, 58(1):291–303, 2020.

[338] S. A. Craig and W. S. Saric. Experimental study of crossflow instability on a mach 6 yawed cone. *AIAA Paper 2015-2774*, 2015.

[339] A. N. Kolmogorov. The local structure of turbulence in incompressible viscous fluid for very large reynolds numbers. *Cr Acad. Sci. URSS*, 30:301–305, 1941.

[340] A. N. Kolmogorov. Dissipation of energy in locally isotropic turbulence. *Comptes Renduc de l'Acadamie Des Sciences de l'U.R.S.S.*, 32(16):301–305, 1941.

[341] H. Tennekes. *First Course in Turbulence*. MIT Press, 2018.

[342] D. G. Ortiz-Suslow and Q. Wang. An evaluation of kolmogorov's- 5/3 power law observed within the turbulent airflow above the ocean. *Geophysical Research Letters*, 46(24):14901–14911, 2019.

[343] J. M. Allen. Evaluation of preston tube calibration equations in supersonic flow. *AIAA Journal*, 11(11):1461–1462, 1973.

[344] M.-Y. Song, J.-S. Yoon, H. Cho, G. P. Karwasz, V. Kokoouline, Y. Nakamura, and J. Tennyson. Cross sections for electron collisions with no, n2o, and no2. *Journal of Physical and Chemical Reference Data*, 48(4):043104, 2019.

[345] I. Kossyi, A. Y. Kostinsky, A. Matveyev, and V. Silakov. Kinetic scheme of the non-equilibrium discharge in nitrogen-oxygen mixtures. *Plasma Sources Science and Technology*, 1(3):207, 1992.

[346] A. M. Ellis, M. Fehér, and T. G. Wright. *Electronic and Photoelectron Spectroscopy: Fundamentals and Case Studies*. Cambridge University Press, 2005.

[347] J. M. Hollas. *Modern Spectroscopy*. John Wiley & Sons, 2004.

[348] G. Peach. Theory of the pressure broadening and shift of spectral lines. *Advances in Physics*, 30(3):367–474, 1981.

[349] S. O'Byrne, P. Danehy, and A. Houwing. Plif temperature and velocity distributions in laminar hypersonic flat-plate flow. In *20th International Congress on Instrumentation in Aerospace Simulation Facilities, 2003. ICIASF'03.*, pages 136–147. IEEE, 2003.

[350] T. S. Kocian. *Computational hypersonic boundary-layer stability and the validation and verification of EPIC*. PhD thesis, Texas A&M University, 2018.

[351] T. Kocian, D. Mullen, K. Groot, E. Beyak, and H. L. Reed. Cfd work done for 91-6 cone at tamu. Private communication, 2020.

[352] M. Sharma. *Post-Shock Thermochemistry In Hypervelocity C02 and Air Flow*. PhD thesis, University of Illinois at Urbana-Champaign, 2010.

[353] A. Ceruzzi, M. Kanapathipillai, K. H. Yu, and C. P. Cadou. Non-Intrusive Velocimetry in a Supersonic Reacting Flow using Two-Point Focused Laser Differential Interferometry. *AIAA Paper 2023-0223*, 2023.

[354] K. Davenport and M. Gragston. Simultaneous Velocity Profile and Scalar Spectra with Linear Array-Focused Laser Differential Interferometry. *AIAA Journal*, 61(2):934–939, feb 2023. ISSN 0001-1452. doi: 10.2514/1.j061945.

[355] A. P. Ceruzzi and C. P. Cadou. Interpreting single-point and two-point focused laser differential interferometry in a turbulent jet. *Experiments in Fluids*, 63(7), 2022.

[356] J. S. Jewell, A. Hameed, N. J. Parziale, and S. Gogineni. Disturbance speed measurements in a circular jet via double focused laser differential interferometry. *AIAA Paper 2019-2293*, 2019.

[357] B. N. Taylor and C. E. Kuyatt. Guidelines for Evaluating and Expressing the Uncertainty of NIST Measurement Results. *NIST Technical Note 1297*, 1994.

[358] W. Merzkirch. *Flow Visualization*, volume 22. Academic Press, 1987.

[359] N. J. Yanes. *Ultraviolet Radiation of Hypervelocity Stagnation Flows and Shock / Boundary-Layer Interactions*. Ph.d., California Institute of Technology, 2020.

[360] M. Sharma, J. M. Austin, N. G. Glumac, and L. Massa. NO and OH spectroscopic vibrational temperature measurements in a postshock relaxation region. *AIAA Journal*, 48(7): 1434–1443, 2010.

[361] D. Bose and G. V. Candler. Thermal rate constants of the O2 N NO O reaction based on the A2 and A4 potential-energy surfaces. *The Journal of Chemical Physics*, 107(16):6136–6145, oct 1997.

[362] A. Tibère-Inglesse, K. Bensassi, A. M. Brandis, and B. A. Cruden. Shock tube radiation measurement in expanding air flows. *AIAA Paper 2022-0117*, 2022.

[363] R. Parker, A. Dufrene, M. MacLean, M. Holden, P. DesJardin, J. Weisberger, and D. Levin. Emission measurements from high enthalpy flow on a cylinder in the LENS-XX hypervelocity expansion tunnel. *AIAA Paper 2013-1058*, 2013.

[364] P. A. Jacobs, R. G. Morgan, A. M. Brandis, D. R. Buttsworth, A. Dann, M. G. D'Souza, T. N. Eichmann, D. E. Gildfind, R. J. Gollan, C. M. Jacobs, M. McGilvray, T. J. McIntyre, N. R. Mudford, H. Porat, D. F. Potter, and F. Zander. Design, Operation and Testing in Expansion Tube Facilities for Super-Orbital Re-Entry. *STO-AVT-VKI Lecture Series on Radiation and Gas-Surface Interaction Phenomena in High Speed Re-Entry (2013-AVT-218)*, pages 1–65, 2013.

[365] D. Buttsworth, M. D'Souza, D. Potter, T. Eichmann, N. Mudford, M. McGilvray, T. J. McIntyre, P. Jacobs, and R. Morgan. Expansion tunnel radiation experiments to support hayabusa re-entry observations. *AIAA Paper 2010-0634*, pages 1–14, 2010.

[366] G. V. Candler. *Nonequilibrium Hypersonic Flows & Hypersonic Nozzle Flow Modeling*. Von Karman Institute For Fluid Dynamics Lecture Series, 2018.

[367] R. Kee, M. Coltrin, P. Glarborg, and H. Zhu. *Chemically Reacting Flow: Theory, Modeling, and Simulation*. Wiley, 2 edition, 2017.

APPENDIX A

VIBRATIONAL THERMOMETRY RESULTS ASSUMING VIBRATIONAL EQUILIBRIUM IN THE FREESTREAM

The figures in this section represent supplemental data to that presented in Section 7.2.5.2. The same raw data was used, but here the results were processed using assuming $T^v_{e,NO} = T^v_{e,N_2,O_2} = 358K$. The same trends described in Section 7.2.5.2 hold, but the relative amplitude of certain features may have changed do to the nonlinear scaling in PLIF thermometry data reduction; futhermore, the no-slip boundary condition is revisited. Both streamwise mean temperature comparison and detailed 2D images of all of the individual runs in Table 7.27 are included here. Finally, the calculation for the error bars in Figures A.1 and A.2 by Buen [212] is described in Section 7.2.5.1.

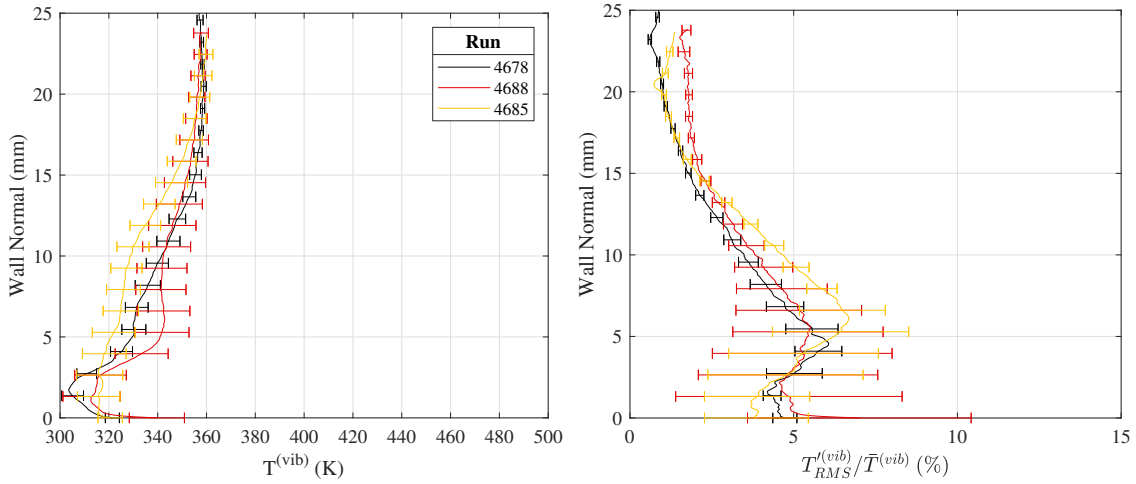

(a) Plasma off, temperature

(b) Plasma off, fluctuation

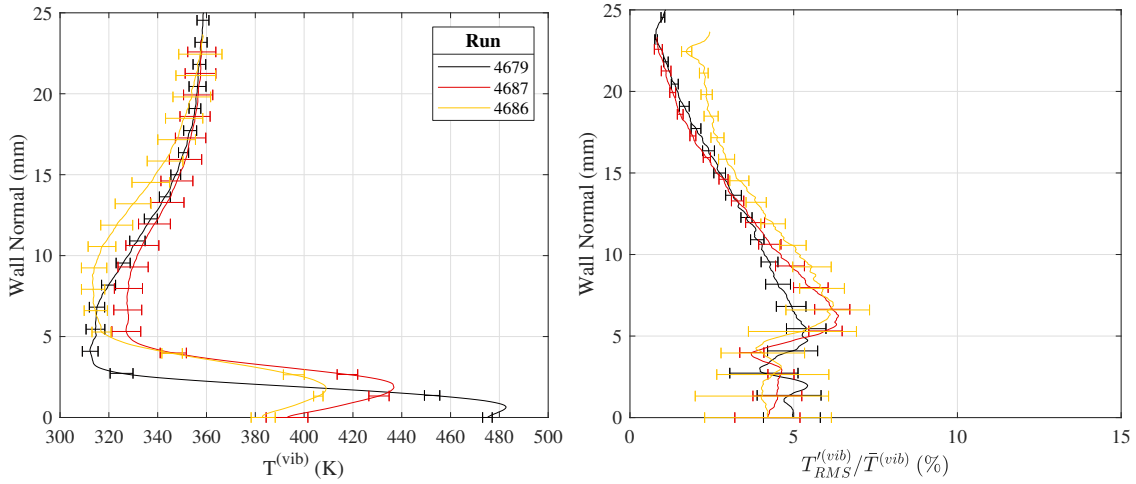

(c) Plasma on, temperature

(d) Plasma on, fluctuation

Figure A.1: PLIF vibrational thermometry, laminar temperature profile comparison assuming $T^{v}_{e,NO} = 358K$; error bars were set from the corresponding mean temperature and fluctuation images. Same legend applies to all figures in a row.

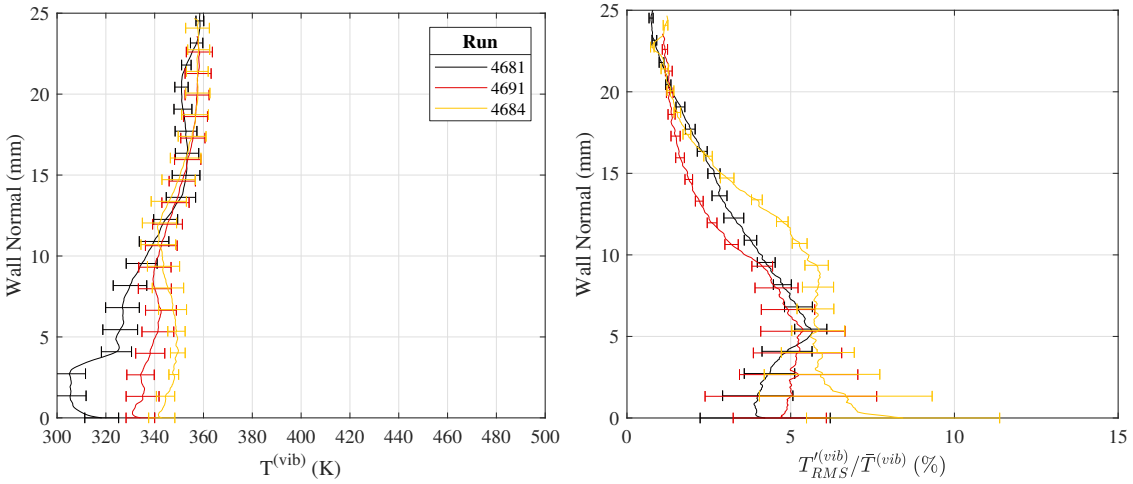

(a) Plasma off, temperature

(b) Plasma off, fluctuation

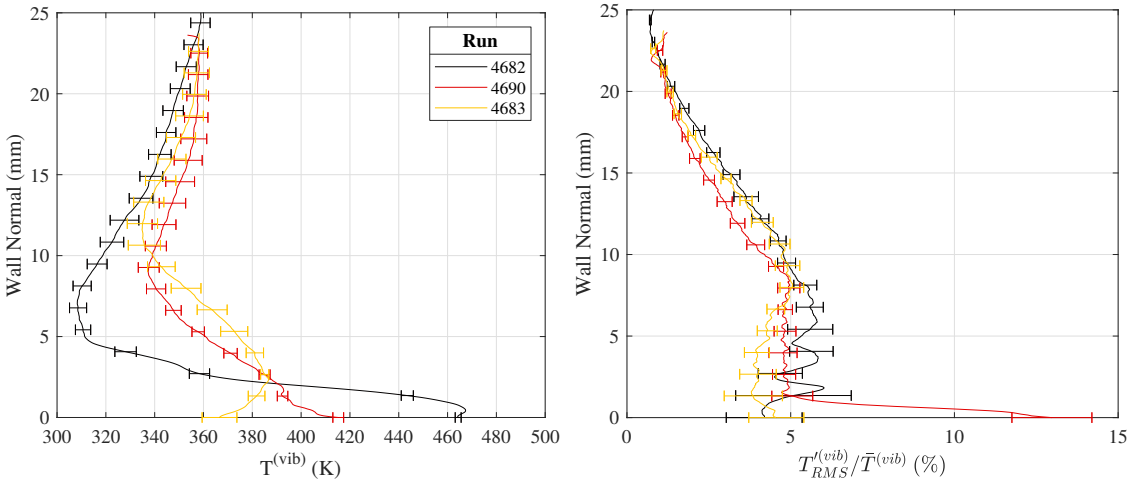

(c) Plasma on, temperature

(d) Plasma on, fluctuation

Figure A.2: PLIF vibrational thermometry, turbulent temperature profile comparison assuming $T^{v}_{e,NO} = 358K$; error bars were set from the corresponding mean temperature and fluctuation images. Same legend applies to all figures in a row.

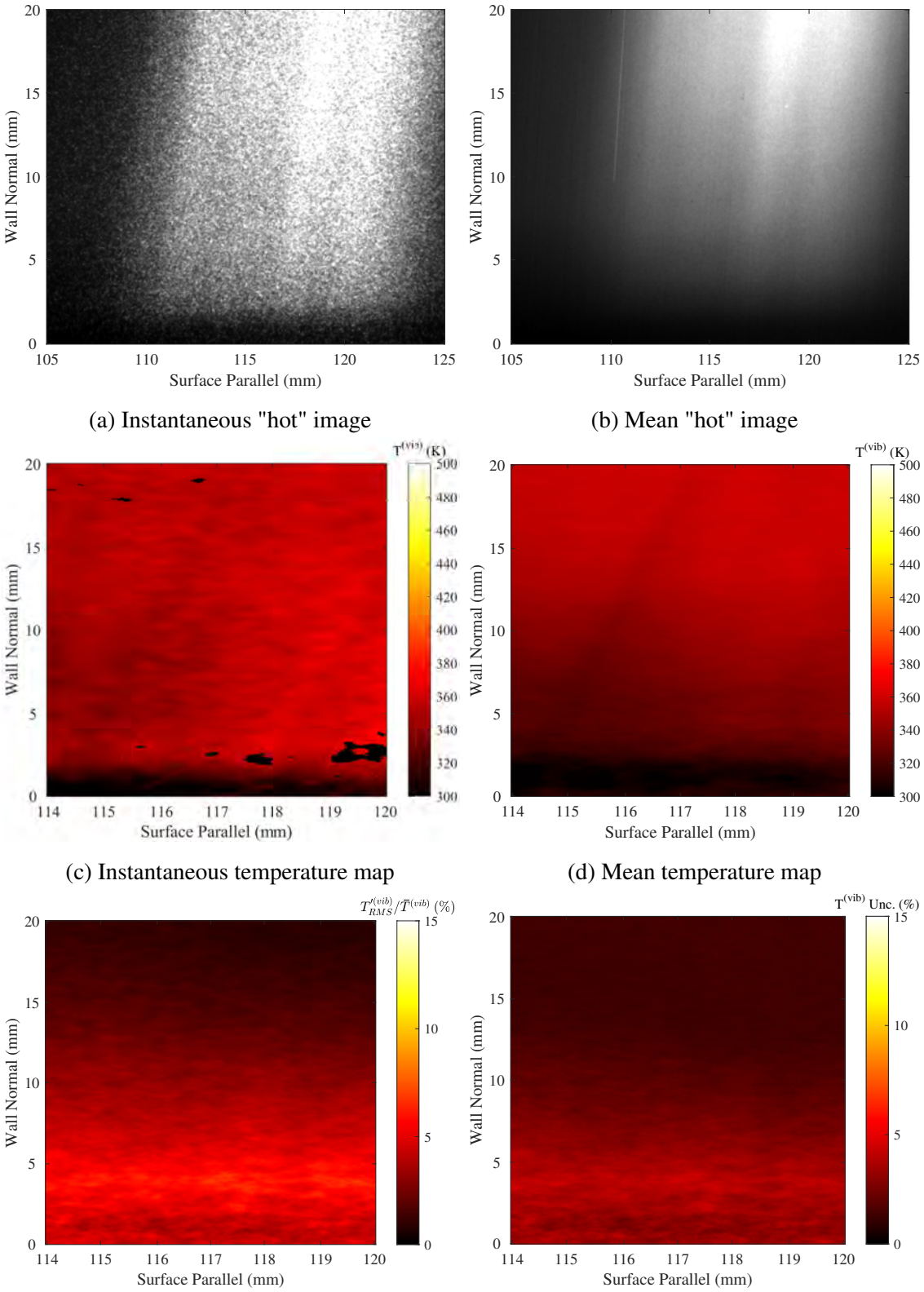

(a) Instantaneous "hot" image

(b) Mean "hot" image

(c) Instantaneous temperature map

(d) Mean temperature map

(e) Mean fluctuation map

(f) Mean uncertainty map

Figure A.3: PLIF vibrational thermometry assuming $T^{v}_{e,NO} = 358K$, Run 4678: upstream; laminar; plasma off.

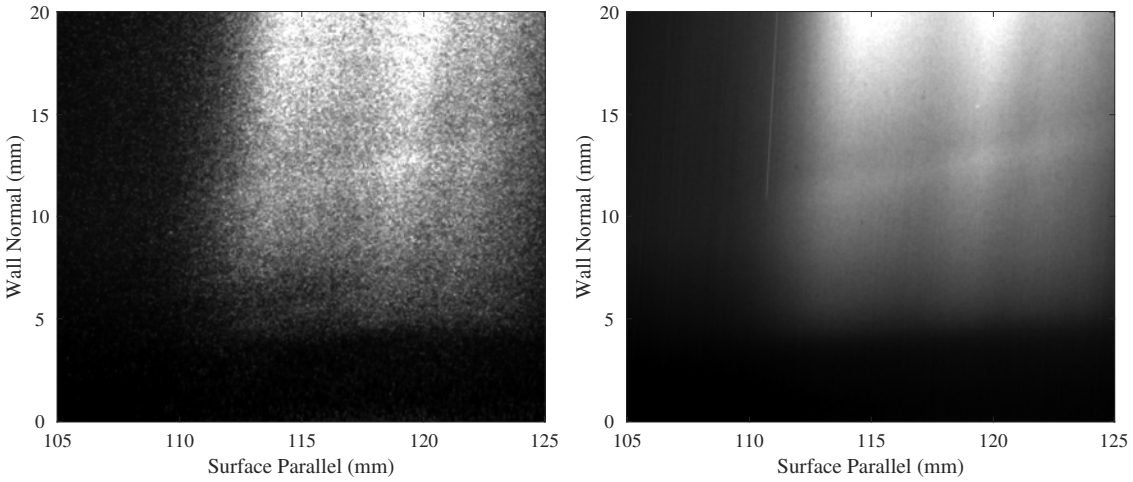

(a) Instantaneous "hot" image

(b) Mean "hot" image

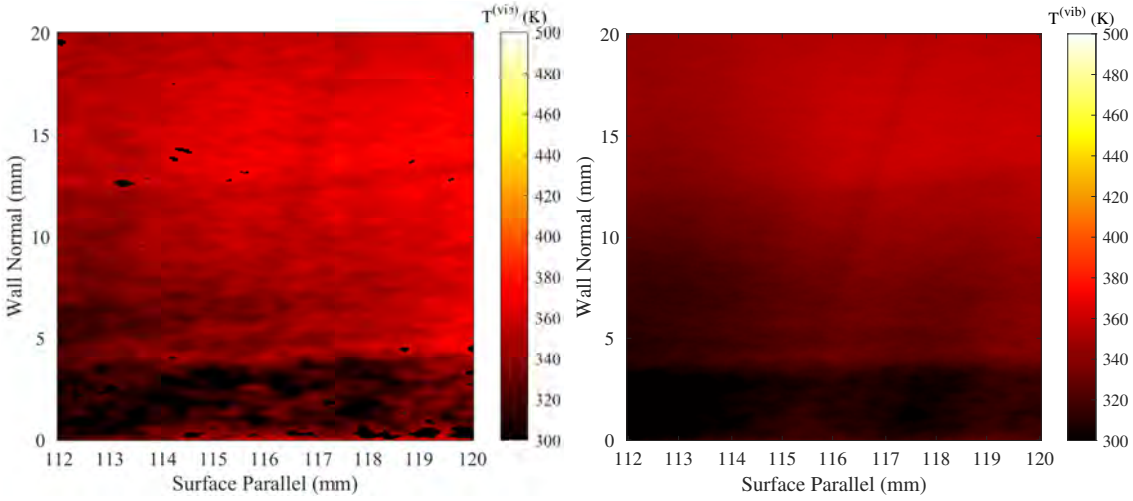

(c) Instantaneous temperature map

(d) Mean temperature map

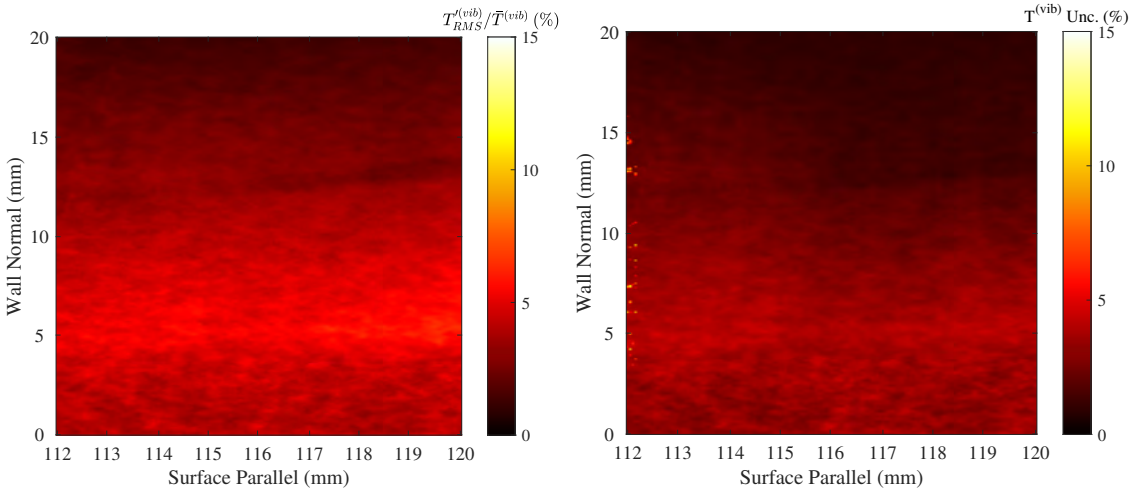

(e) Mean fluctuation map

(f) Mean uncertainty map

Figure A.4: PLIF vibrational thermometry assuming $T^{v}_{e,NO} = 358K$, Run 4681: upstream; turbulent; plasma off.

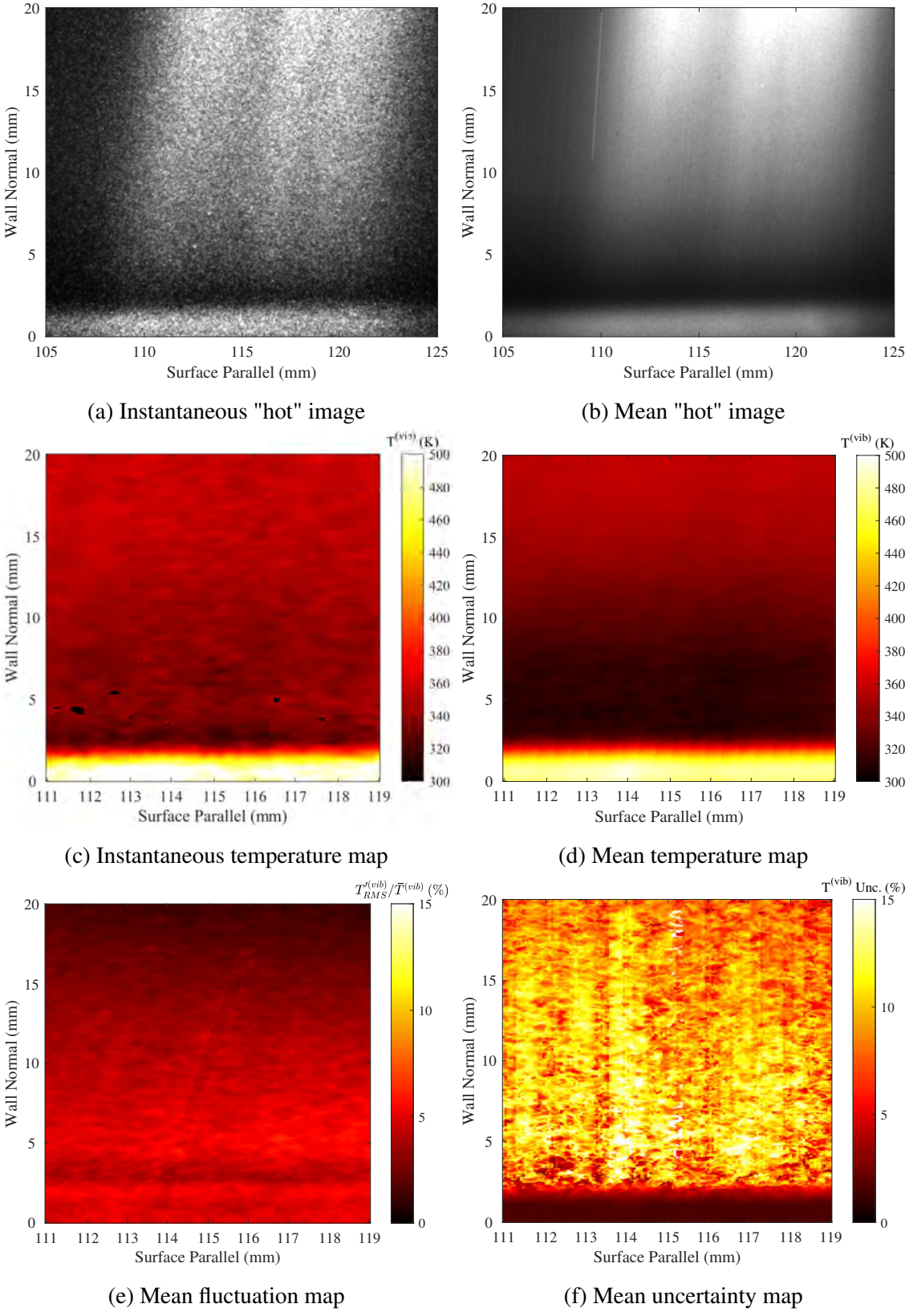

(a) Instantaneous "hot" image

(b) Mean "hot" image

(c) Instantaneous temperature map

(d) Mean temperature map

(e) Mean fluctuation map

(f) Mean uncertainty map

Figure A.5: PLIF vibrational thermometry assuming $T^{v}_{e,NO} = 358K$, Run 4679: upstream; laminar; plasma on.

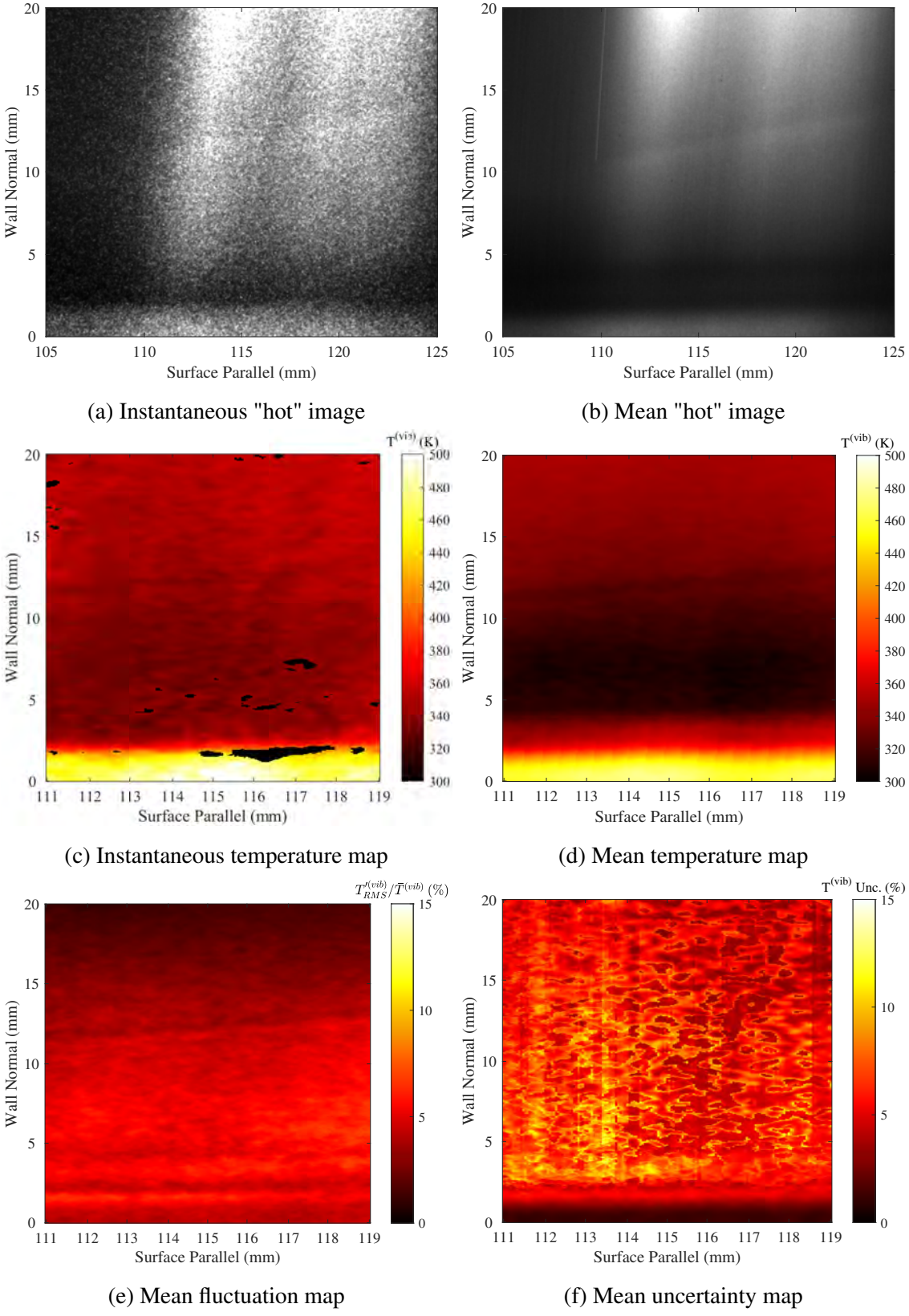

(a) Instantaneous "hot" image

(b) Mean "hot" image

(c) Instantaneous temperature map

(d) Mean temperature map

(e) Mean fluctuation map

(f) Mean uncertainty map

Figure A.6: PLIF vibrational thermometry assuming $T^{v}_{e,NO} = 358K$, Run 4682: upstream; turbulent; plasma on.

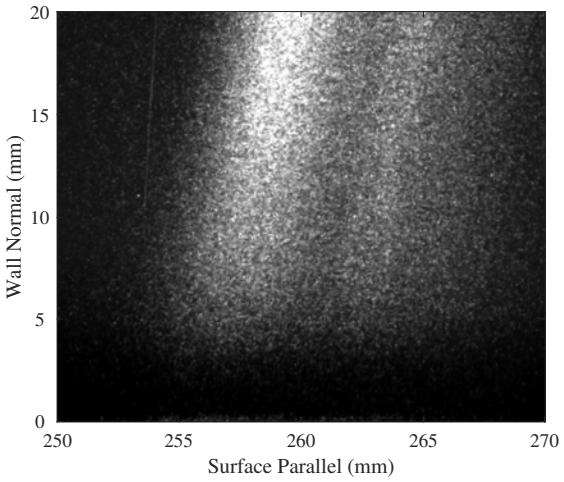

(a) Instantaneous "hot" image

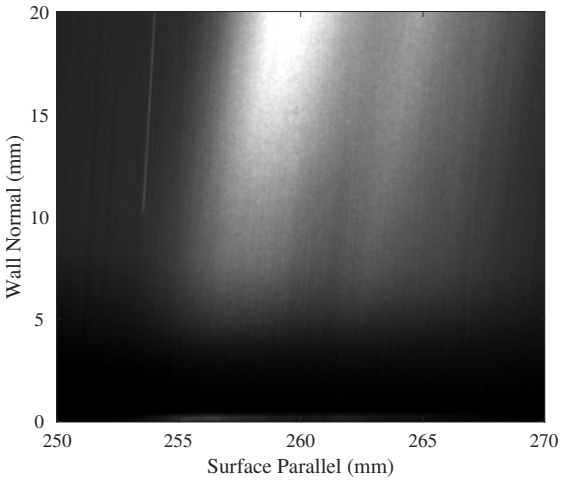

(b) Mean "hot" image

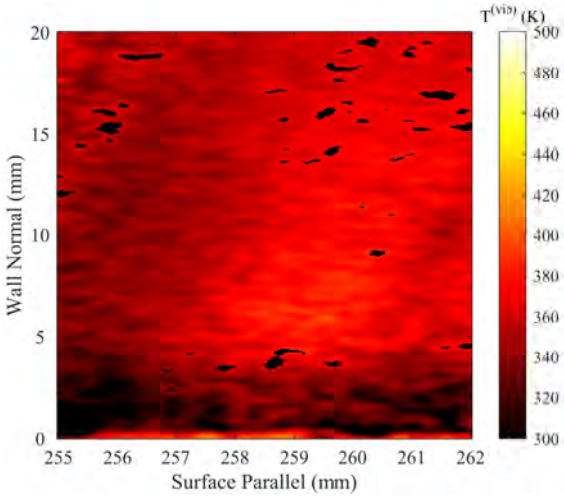

(c) Instantaneous temperature map

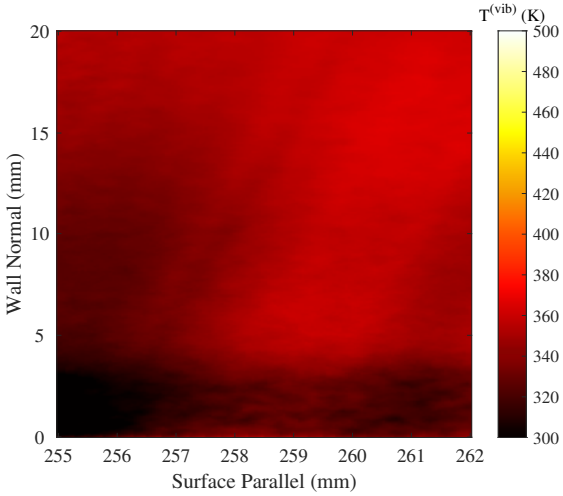

(d) Mean temperature map

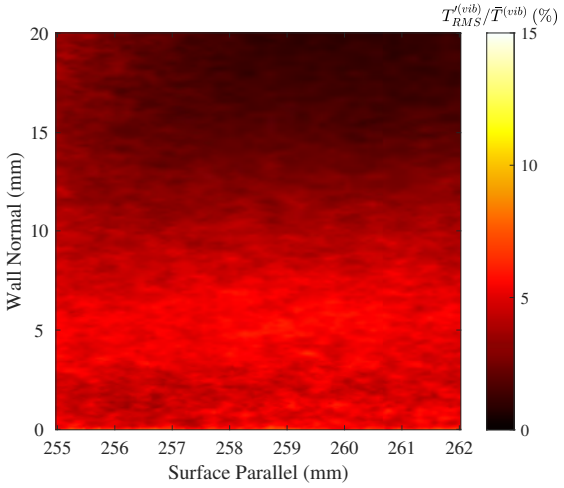

(e) Mean fluctuation map

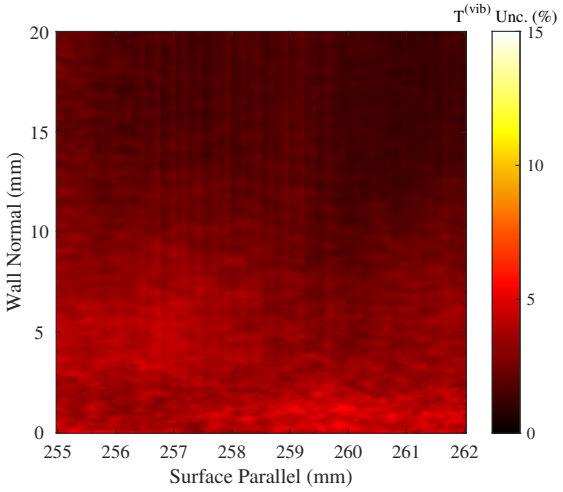

(f) Mean uncertainty map

Figure A.7: PLIF vibrational thermometry assuming $T^{v}_{e,NO} = 358K$, Run 4688: middle; laminar; plasma off.

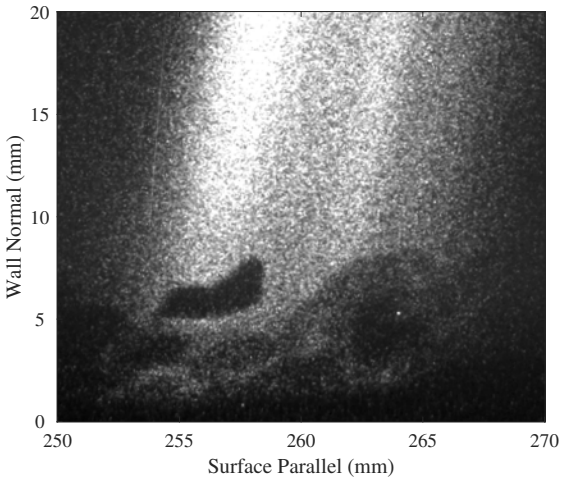

(a) Instantaneous "hot" image

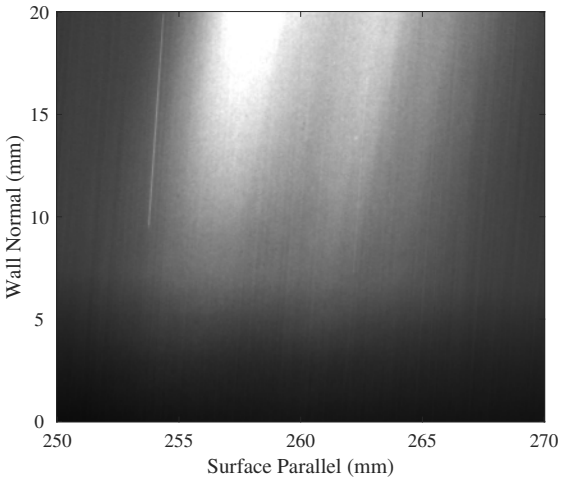

(b) Mean "hot" image

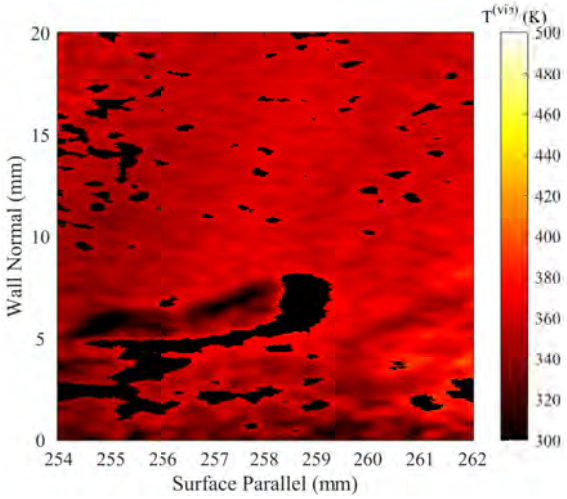

(c) Instantaneous temperature map

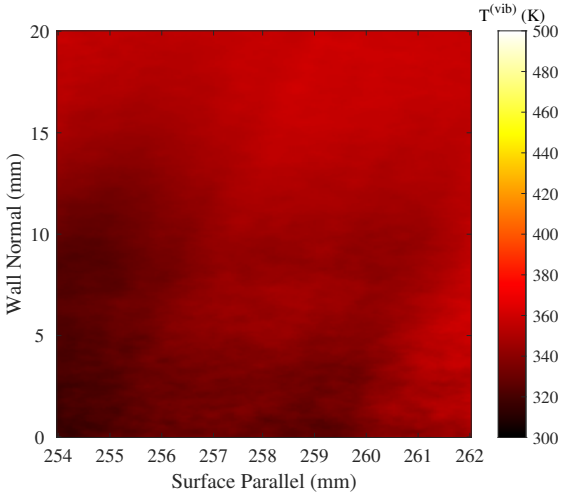

(d) Mean temperature map

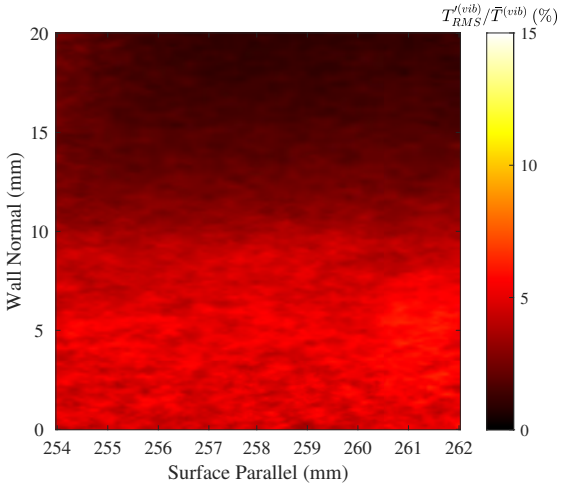

(e) Mean fluctuation map

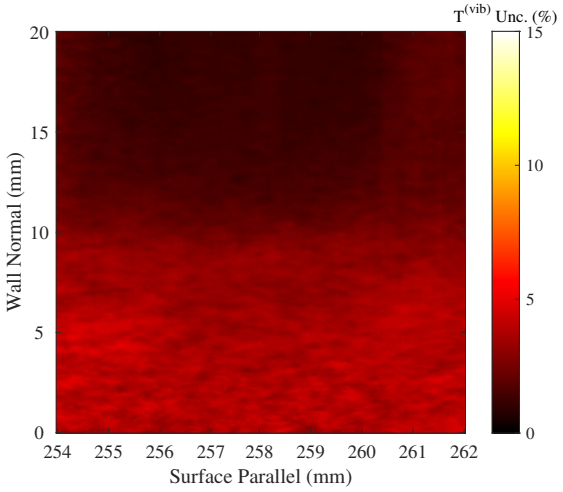

(f) Mean uncertainty map

Figure A.8: PLIF vibrational thermometry assuming $T^{v}_{e,NO} = 358K$, Run 4691: middle; turbulent; plasma off.

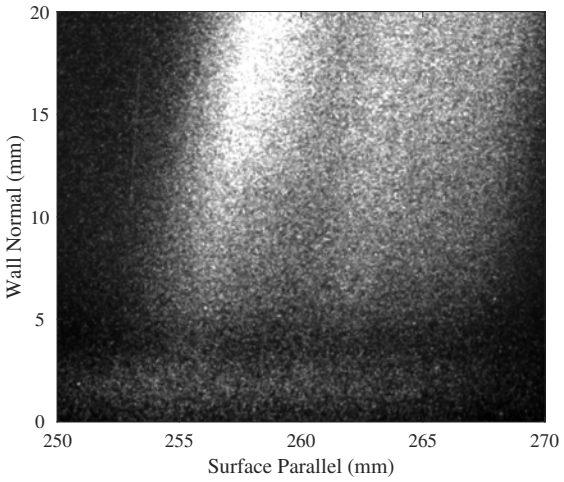

(a) Instantaneous "hot" image

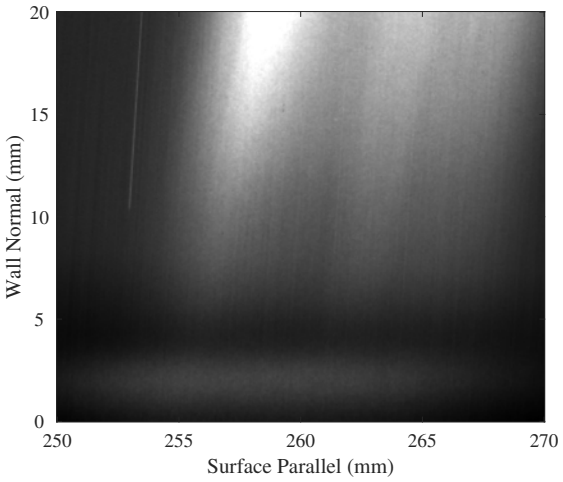

(b) Mean "hot" image

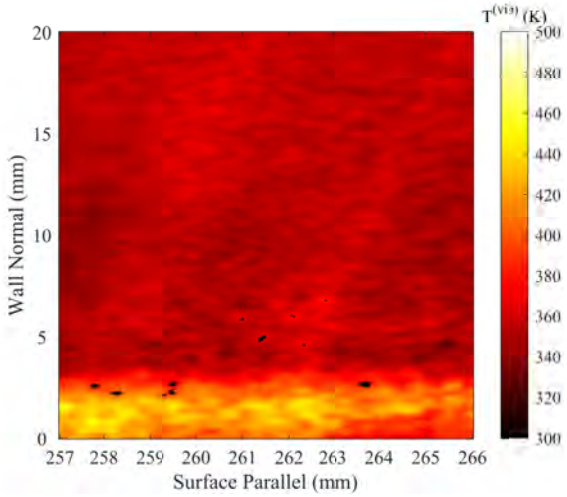

(c) Instantaneous temperature map

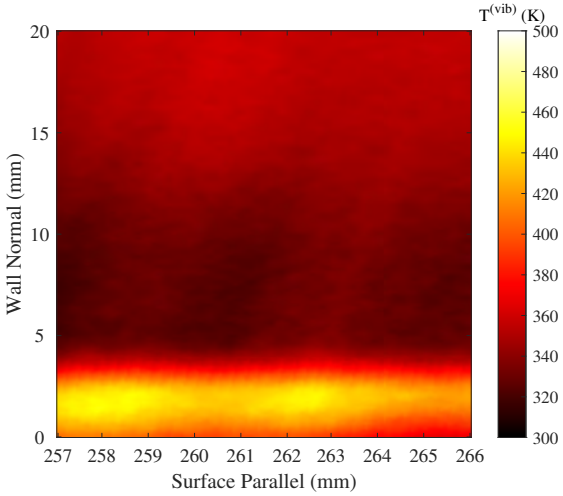

(d) Mean temperature map

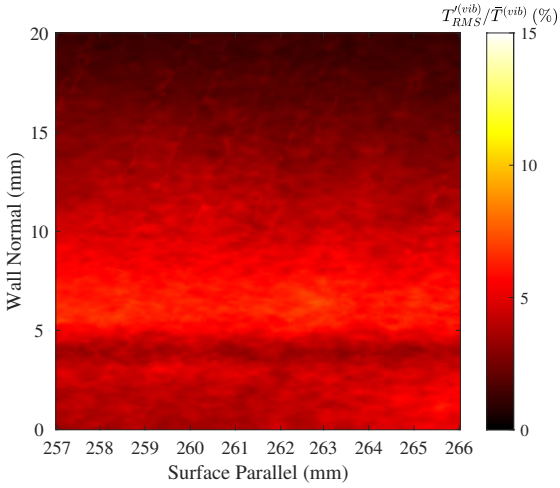

(e) Mean fluctuation map

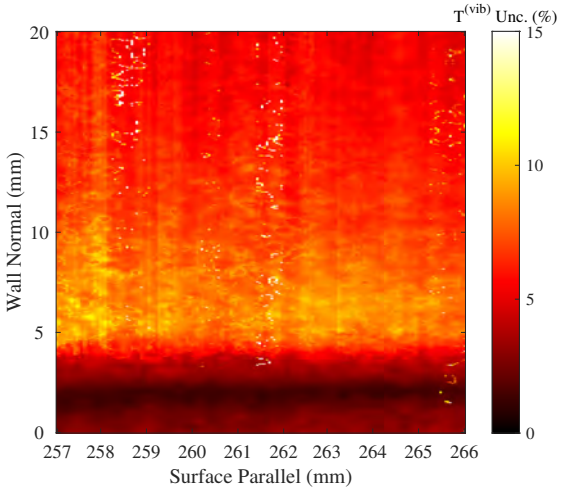

(f) Mean uncertainty map

Figure A.9: PLIF vibrational thermometry assuming $T^{v}_{e,NO} = 358K$, Run 4687: middle; laminar; plasma on.

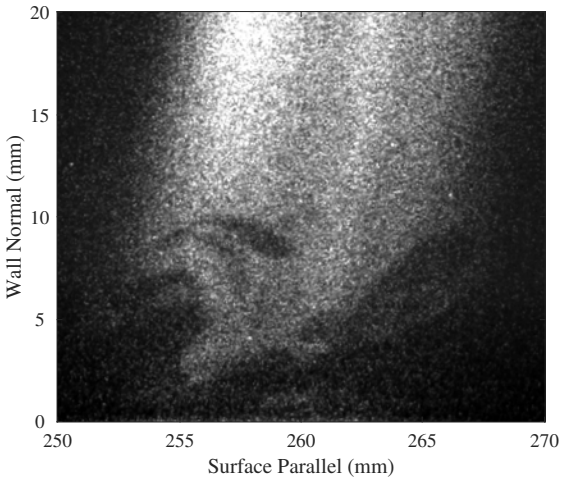

(a) Instantaneous "hot" image

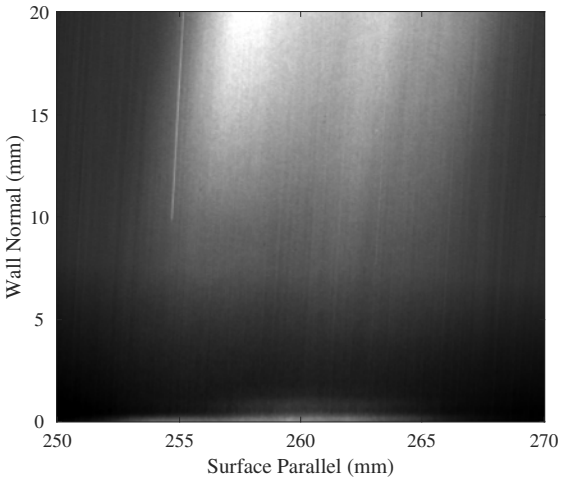

(b) Mean "hot" image

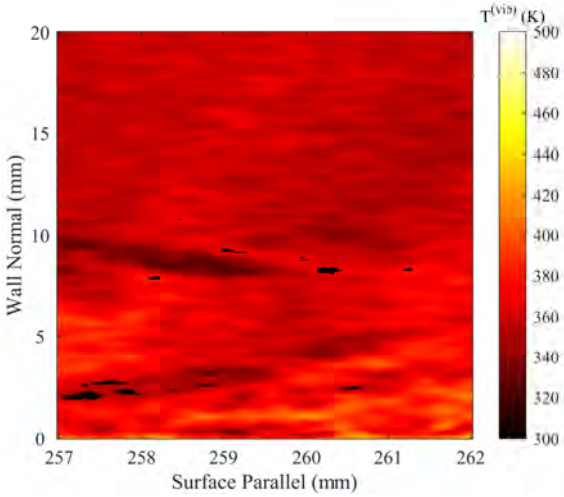

(c) Instantaneous temperature map

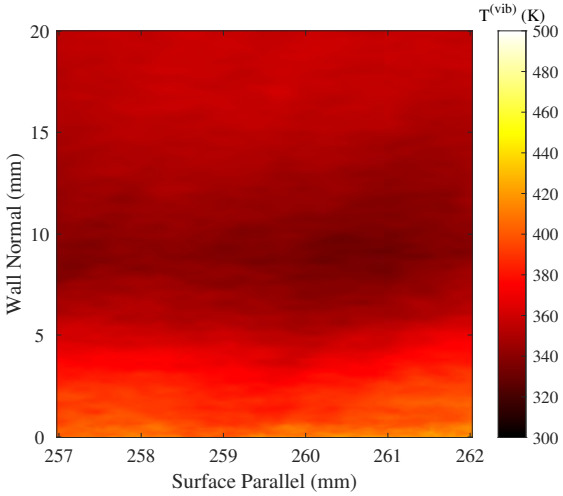

(d) Mean temperature map

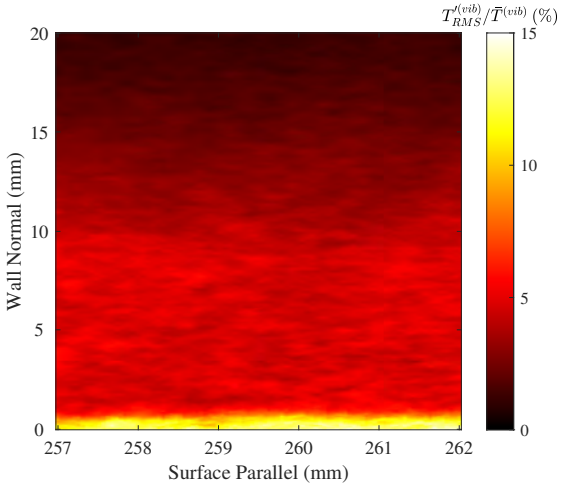

(e) Mean fluctuation map

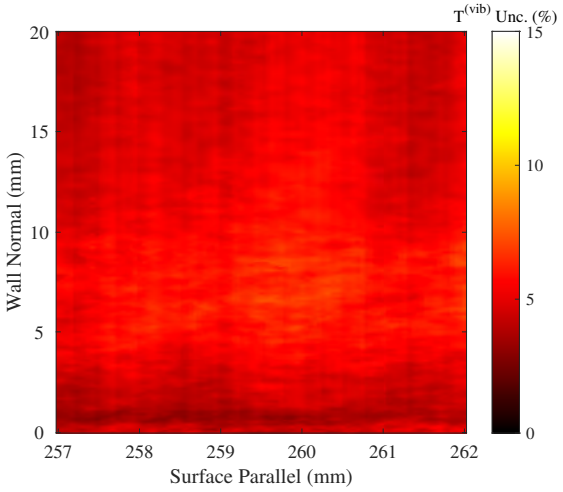

(f) Mean uncertainty map

Figure A.10: PLIF vibrational thermometry assuming $T^{v}_{e,NO} = 358K$, Run 4690: middle; turbulent; plasma on.

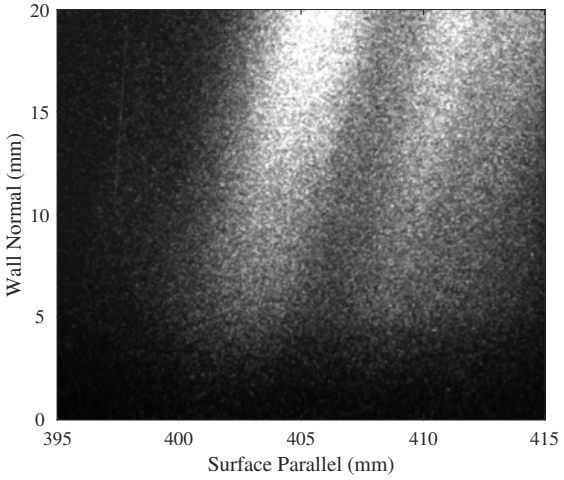

(a) Instantaneous "hot" image

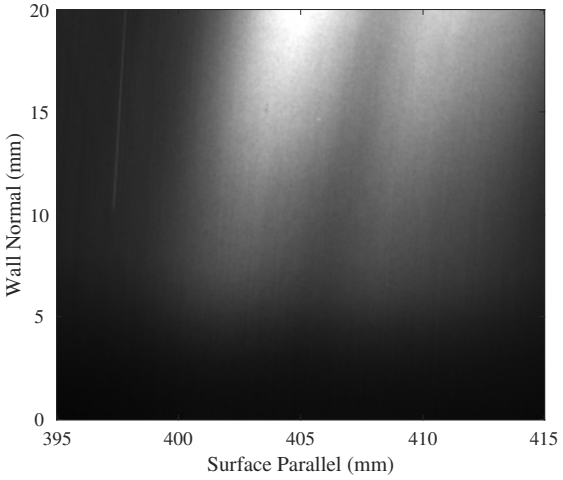

(b) Mean "hot" image

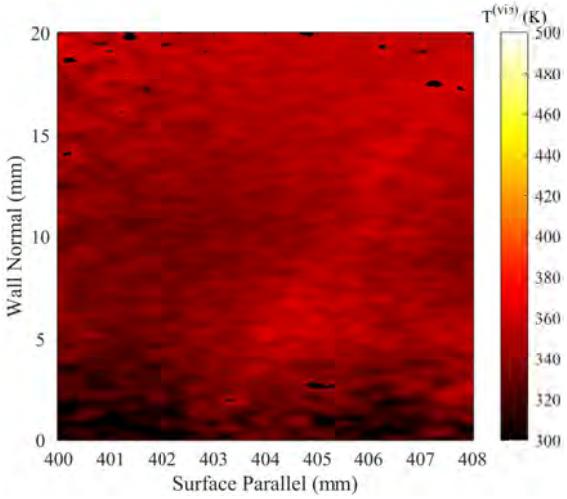

(c) Instantaneous temperature map

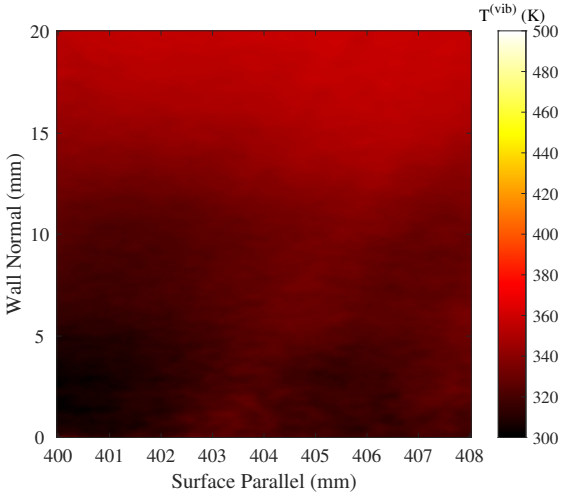

(d) Mean temperature map

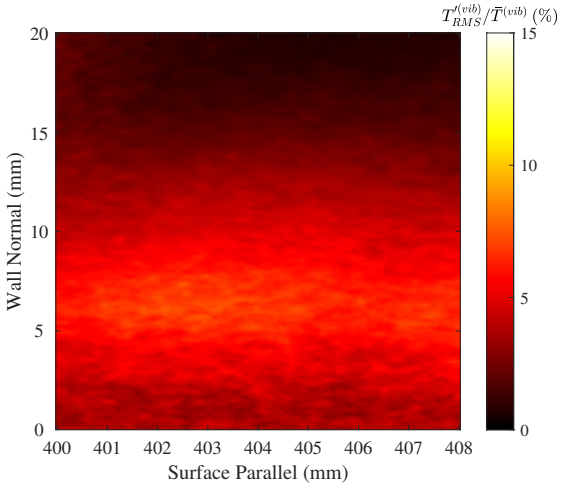

(e) Mean fluctuation map

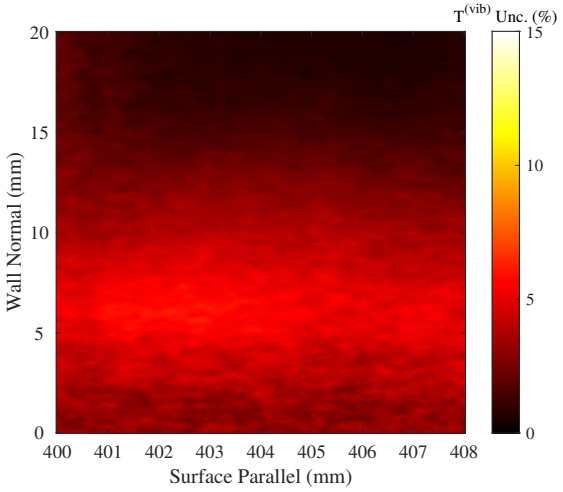

(f) Mean uncertainty map

Figure A.11: PLIF vibrational thermometry assuming $T^{v}_{e,NO} = 358K$, Run 4685: back; laminar; plasma off.

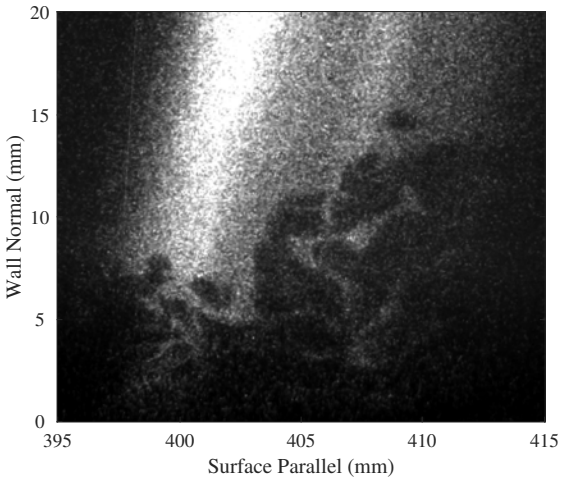

(a) Instantaneous "hot" image

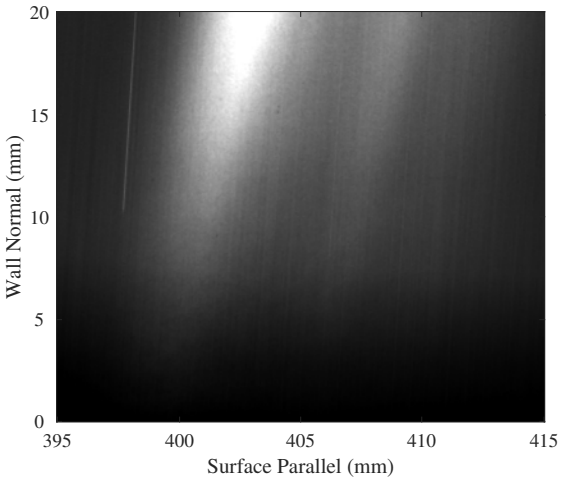

(b) Mean "hot" image

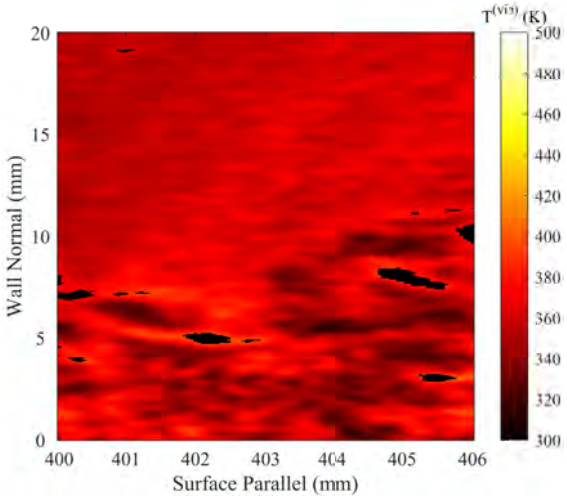

(c) Instantaneous temperature map

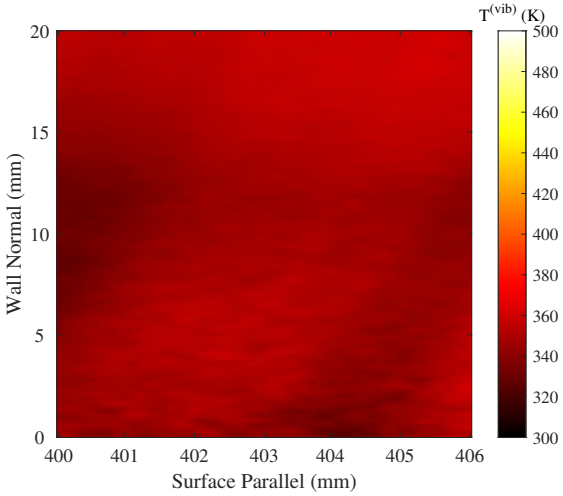

(d) Mean temperature map

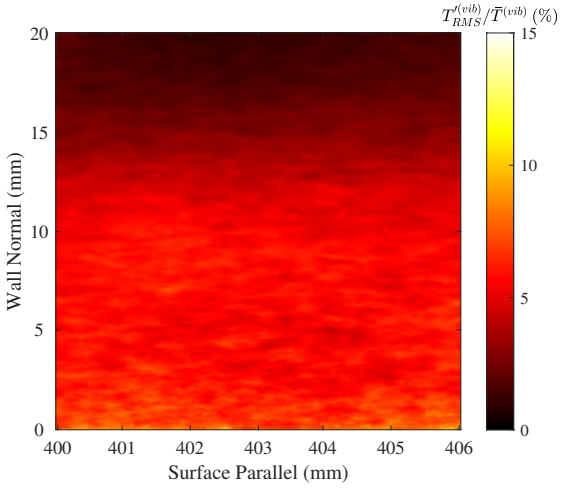

(e) Mean fluctuation map

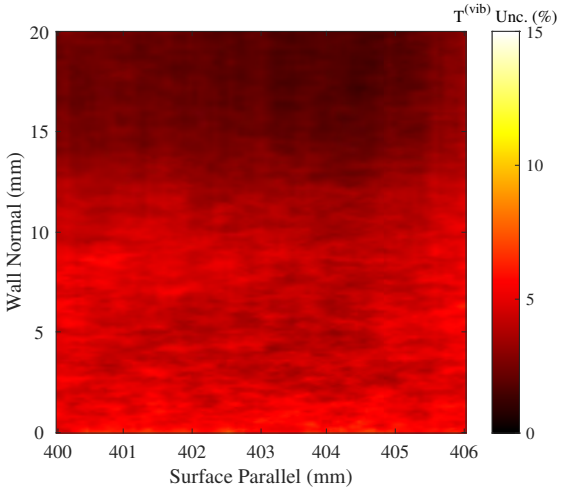

(f) Mean uncertainty map

Figure A.12: PLIF vibrational thermometry assuming $T^{v}_{e,NO} = 358K$, Run 4684: back; turbulent; plasma off.

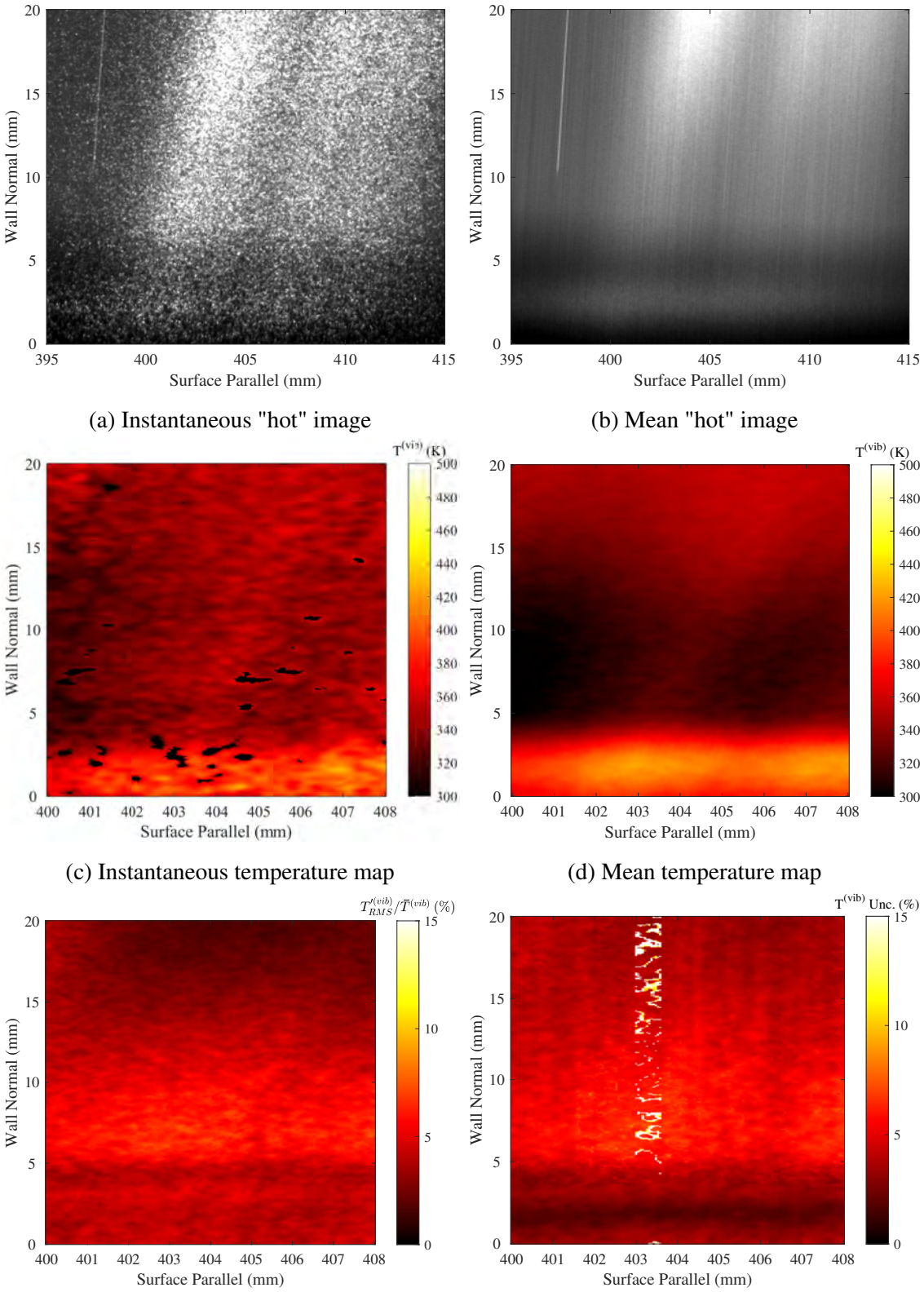

(a) Instantaneous "hot" image

(b) Mean "hot" image

(c) Instantaneous temperature map

(d) Mean temperature map

(e) Mean fluctuation map

(f) Mean uncertainty map

Figure A.13: PLIF vibrational thermometry assuming $T^{v}_{e,NO} = 358K$, Run 4686: back; laminar; plasma on.

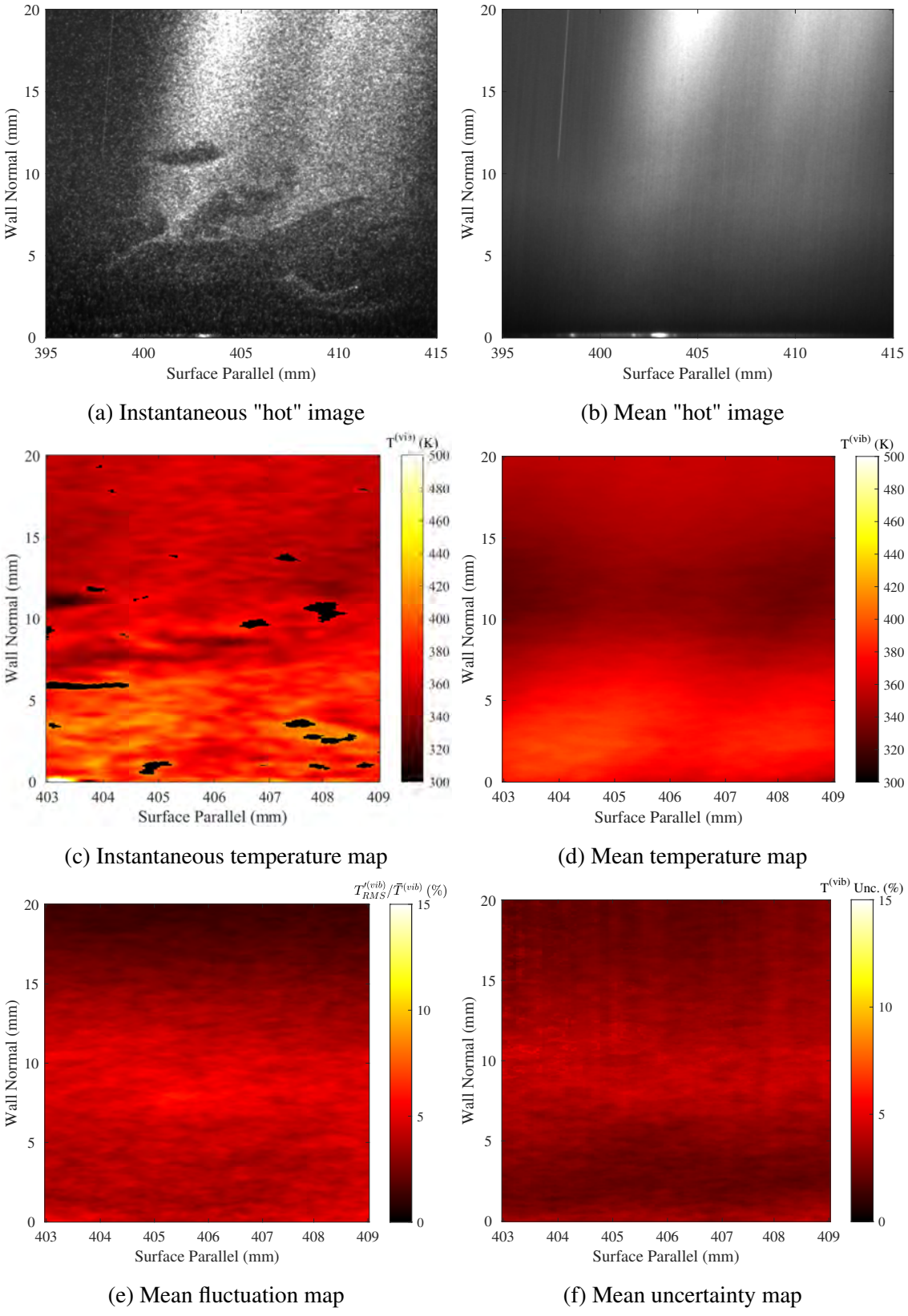

(a) Instantaneous "hot" image

(b) Mean "hot" image

(c) Instantaneous temperature map

(d) Mean temperature map

(e) Mean fluctuation map

(f) Mean uncertainty map

Figure A.14: PLIF vibrational thermometry assuming $T^{v}_{e,NO} = 358K$, Run 4683: back; turbulent; plasma on.